

## 1.1 The Current–Potential Relationship

*Ernesto J. Calvo*  
*Universidad de Buenos Aires, Buenos Aires,*  
*Argentina*

### 1.1.1 Scope

This first chapter to Volume 2 “Interfacial Kinetics and Mass Transport” introduces the following sections, with particular focus on the distinctive feature of electrode reactions, namely, the exponential current–potential relationship, which reflects the strong effect of the interfacial electric field on the kinetics of chemical reactions at electrode surfaces. We then analyze the consequence of this accelerating effect on the reaction kinetics upon the surface concentration of reactants and products and the role played by mass transport on the current–potential curves. The theory of electron-transfer reactions, migration, and diffusion processes and digital simulation of convective-diffusion are analyzed in the first four chapters. New experimental evidence of mechanistic aspects in electrode kinetics from different “in-situ” spectroscopies and structural studies are discussed in the second section. The last

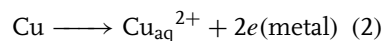
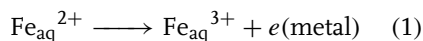
section of this volume covers kinetics and mechanisms of selected electrochemical processes.

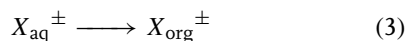
### 1.1.2 Introduction

The current–potential relationship at electrodes is set by a number of complex physical and chemical phenomena, depending on the experimental conditions.

Electrode reactions are heterogeneous chemical processes that may involve one or more electron-transfer steps across the electrochemical double layer [1, 2]. Electrode reactions provide a switch for charge to flow between phases of different type of electrical conductivity: electrodes and electrolyte [3]. Therefore, their response can be analyzed either on the basis of electrical or chemical models. The distinctive feature of reactions at electrodes is the strong dependence of both the surface concentrations and the kinetics on the electrode potential [4–10].

The following reactions at electrified interfaces are examples of electrode reactions:





The first reaction is an electron transfer across the double layer at the electrode–electrolyte interface between redox species in the electrolyte that exchange electrons with a metal electrode, the second one is an ion-transfer reaction across the double layer since the electron lost by the Cu atom remains at the metal. The third one is an ion-transfer process across the water–organic solvent interface or ion transfer at immiscible electrolyte solutions (ITIES) without the transfer of electrons. In all cases the electrochemical reaction takes place at an electrified interface and therefore the rate of these reactions follow similar exponential dependence on the interfacial electrical potential.

While electrodes can be metals, carbon or semiconductors, and so on and the charge carriers are electrons or holes, the charge carriers in liquid and solid electrolytes are solvated or nonsolvated ions in molten salts and solid electrolytes. Therefore the flow of electricity is accomplished by the electrode reactions at the interface between these electrode and electrolyte phases.

The relation between the total quantity of electricity,  $q$ , and the number of moles of each chemical being transformed during the electrolysis has been established by Michael Faraday in the eighteen century

$$q = nFN \quad (4)$$

where  $n$  is the number of charges transferred per molecule or ion,  $N$  the number of moles and  $q$  the total quantity of electricity passed through the interface and thus through the external circuit.

Differentiating the amount of charge with respect to time yields the current,

which is proportional to the rate of the electrochemical reaction (in moles per second):

$$I = nF \frac{dN}{dt} \quad (5)$$

Since we are dealing with heterogeneous reactions, we need to normalize the total current dividing by the electrode area,  $A$  and thus the current density is  $i = I/A$ . It should be noticed that the current measures an average value of the reaction rate over the electrode area, which is important to keep in mind given our present knowledge of heterogeneities at electrode surfaces in micro- and nanoscale. (At present it is possible to study electrode surfaces “in situ” in contact with electrolytes and under potential control using scanning probe microscopes with spatial resolution in the micro and nanometer.)

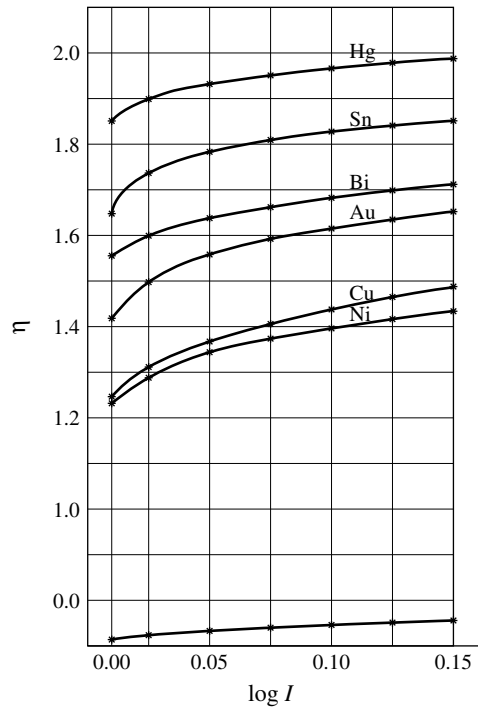
In 1905, Tafel [11] described the experimental relationship between current,  $I$ , and the overpotential  $\eta$  – the difference between the working electrode potential,  $E$ , and the equilibrium potential  $E_e$  – during the electrochemical reduction of protons to molecular hydrogen on different electrode materials such as Hg, Sn, Bi, Au, Cu, Ni, and so on:

$$\eta = a + b \log I \quad (6)$$

Figure 1 depicts a reproduction of the original current–potential curves reported by Julius Tafel for different metals, which demonstrates the electrocatalytic nature of this reaction [11].

Electrode reactions are heterogeneous chemical reactions in solution and may include elementary electron-transfer steps, ion transfer, potential-independent, or chemical steps, and so on.

**Fig. 1** Steady state overpotential versus  $\log I$  curves for the hydrogen evolution on different metals. (Taken from Ref. [11].)



### 1.1.3

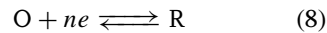
#### Thermodynamics of Electrochemical Cells

The electrode potential can be expressed by

$$E = (\phi_M - \phi_S) + \text{Const} \quad (7)$$

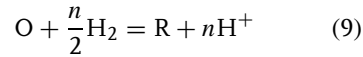
where  $\phi_M$  is the inner or Galvani potential of the metal phase and  $\phi_S$  the inner or Galvani potential of the electrolyte solution phase. In electrokinetic experiments, the electrode potential is measured with respect to a reference electrode and therefore an undetermined constant adds to the electrode potential [10].

If we consider the generic electroreduction half-reaction:



where O is the soluble oxidized and R the reduced species present in the electrolyte and  $n$  is the number of

electrons transferred from the electrode, the standard free-energy change for the overall reaction with hydrogen:



is given by

$$-\Delta G^\circ = nFE^\circ = RT \ln K_{eq} \quad (10)$$

where  $E^\circ$  is the standard potential of the O/R redox couple with respect to the standard hydrogen reference electrode (SHE) and  $K_{eq}$  is the equilibrium constant for Reaction (9).

The dependence of the electrode potential on the activities of O and R at equilibrium can be described by the Nernst equation:

$$E_e = E^\circ + \frac{RT}{nF} \ln \left( \frac{a_O}{a_R} \right) \quad (11)$$

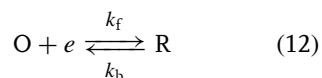
where  $a_O$  and  $a_R$  denote the activities of O and R, respectively. The use of formal or conditional equilibrium potentials,  $E'^\circ$ , is more convenient in electrode kinetics [2] since concentrations instead of activities can be used, but it must be kept in mind that activity coefficients are included in the rate coefficients.

The steady state current–potential relationship under electrode kinetics conditions has been described by Butler [12, 13] and Volmer [14].

#### 1.1.4

##### The Butler–Volmer Equation

In this section, we shall derive an expression for the current–potential relationship in electrode reactions. Since multielectron-transfer reactions at interfaces are most likely to occur in a series of one-electron steps, we shall consider first the general one-electron electrode reaction:



the rate of which is considered to be totally determined by the charge-transfer process, and mass-transport limitations or chemical step limitations will not be considered here so that the concentrations of reactant and product at the interface will be the same as the analytical concentration in the bulk of the electrolyte.

The net rate of Reaction (12) will be given by the difference between the forward and backward rates:

$$v = v_f - v_b \quad (13)$$

which, for reaction order one for reactant and product, can be expressed as

$$v_f = k_f C_O^* = \frac{i_c}{F} \quad (14)$$

and,

$$v_b = k_b C_R^* = \frac{i_a}{F} \quad (15)$$

where  $k_f$  and  $k_b$  are the corresponding rate coefficients and  $i_c$  and  $i_a$  the corresponding formal cathodic and anodic partial current densities that flow at the electrode–electrolyte interface. These partial currents cannot be measured since we cannot distinguish in the external circuit those electrons flowing towards the electrolyte from those flowing towards the electrode, and therefore we can only detect the net current,  $I = i_c - i_a$ . This difference implies that we must adopt a convention of signs for the reduction and oxidation currents [2].

The net reaction rate is

$$v = v_f - v_b = \frac{i}{F} \quad (16)$$

According to the absolute reaction rate theory of Eyring, first applied to electrode reactions, the rate coefficient of a chemical reaction,  $k$ , can be expressed as

$$k_i = \frac{k_B T}{h} \kappa \exp \left[ -\frac{\Delta G_i^\ddagger}{RT} \right] \quad (17)$$

where  $\Delta G_i^\ddagger$  is the free energy of activation for the reaction,  $k_B$  the Boltzmann constant,  $h$  the Plank constant and  $\kappa$  the transmission coefficient which for simplicity we shall consider here equal to one.

In the case of electrode reactions that occur at an electrified interface and therefore under the influence of a strong electrical field (c.a.  $10^7$  V cm<sup>-1</sup>), the driving force for the reaction of charged species  $\Delta G_i^\ddagger$  has a term of electrostatic work  $w_{el} = -FE$  as shown in the scheme of Fig. 2. The negative sign corresponds to the negatively charged electron crossing the electrical double layer.

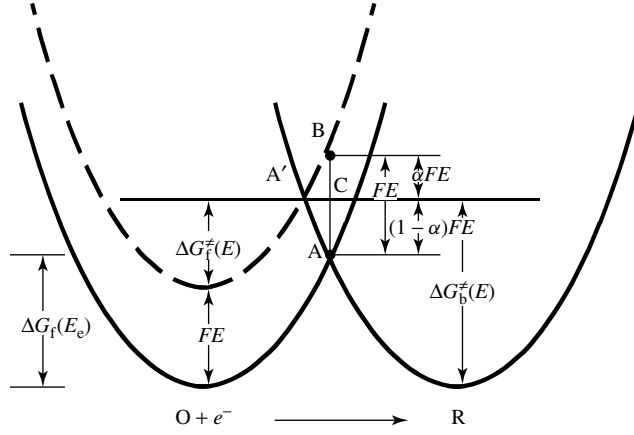


**Fig. 2** Schematic representation of the effect of electrode potential on the free energy versus reaction coordinate curves for an electron reactant at two electrode potentials:  $E = E_e$  (solid line) and  $E < E_e$  (broken line).

For convenience, we divide the free energy of activation into a potential-independent and a potential-dependent contribution:

$$\Delta G_f^\ddagger(E) = \Delta G_f^\ddagger(E_e) + \alpha FE \quad (18) \quad \text{and}$$

and,

$$\Delta G_b^\ddagger(E) = \Delta G_b^\ddagger(E_e) - (1 - \alpha)FE \quad (19)$$

where  $0 \leq \alpha \leq 1$  is the fraction of the applied potential that drives the reaction and a measure of the symmetry of the energy barrier.

Replacing in Eq. (17):

$$k_f = \frac{k_B T}{h} \exp \left[ -\frac{\Delta G_f^\ddagger(E_e)}{RT} \right] \times \exp \left( \frac{-\alpha FE}{RT} \right) \quad (20)$$

$$k_b = \frac{k_B T}{h} \exp \left[ -\frac{\Delta G_b^\ddagger(E_e)}{RT} \right] \times \exp \left( \frac{(1 - \alpha)FE}{RT} \right) \quad (21)$$

It is convenient to define

$$k_{f,o} = \frac{k_B T}{h} \exp \left[ -\frac{\Delta G_f^\ddagger(E_e)}{RT} \right] \quad (22)$$

$$k_{b,o} = \frac{k_B T}{h} \exp \left[ -\frac{\Delta G_b^\ddagger(E_e)}{RT} \right] \quad (23)$$

And therefore,

$$k_f(E) = k_{f,o} \exp \left( \frac{-\alpha FE}{RT} \right) \quad \text{and}$$

$$k_b(E) = k_{b,o} \exp \left( \frac{(1 - \alpha)FE}{RT} \right) \quad (24)$$

Thus from Eq. (16), the net current density at the electrode interface is

$$i = F \left[ k_{f,o} C_O^* \exp \left( \frac{-\alpha FE}{RT} \right) - k_{b,o} C_R^* \exp \left( \frac{(1 - \alpha)FE}{RT} \right) \right] \quad (25)$$

which has an exponential dependence on the electrode potential,  $E$ , as observed in experiments.

We note that at equilibrium  $i = 0$  and  $E = E_e$  and therefore from Eq. (25) we obtain

$$E_e = \frac{RT}{F} \left[ \ln \left( \frac{k_{f,o}}{k_{b,o}} \right) + \ln \left( \frac{C_O}{C_R} \right) \right] \quad (26)$$

which is identical to the Nernst equation for the reaction between O and R at the electrode surface. Note that the first term in Eq. (26) is the conditional or formal standard electrode potential for the reaction,  $E^{\circ'}$ , which contains the nonelectrical terms of the free energy of activation including the activity coefficients for the species O and R.

We can group all rate coefficients by substituting  $E = E_e$  in Eqs. (24 and 26) and multiplying by  $F$  and obtain the exchange current density,  $i_o$ :

$$\begin{aligned} i_o &= F k_{f,o} C_O^{1-\alpha} C_R^\alpha \exp \left[ -\alpha F \frac{E^{\circ'}}{RT} \right] \\ &= F k_{b,o} C_O^{1-\alpha} C_R^\alpha \exp \left[ (1-\alpha) F \frac{E^{\circ'}}{RT} \right] \end{aligned} \quad (27)$$

we can further define a standard state both for the electrode potential  $E = E_e$  and the reactant and product concentrations  $C_O = C_R = 1$  M:

$$\begin{aligned} k_o^\circ &= k_{f,o} \exp \left[ -\alpha F \frac{E^{\circ'}}{RT} \right] \\ &= k_{b,o} \exp \left[ (1-\alpha) F \frac{E^{\circ'}}{RT} \right] \end{aligned} \quad (28)$$

and thus,  $i_o = F k_o^\circ C_O^{1-\alpha} C_R^\alpha$ .  $k_o^\circ$  is the standard rate constant for unit surface concentration of reactants at the standard equilibrium potential.

Substituting in Eq. (25) and introducing the overpotential for the reaction as  $\eta = (E - E_e)$  and substituting  $i_o$  into

Eq. (27), we obtain the Butler–Volmer equation (29):

$$i = i_o \left[ \exp \left[ \frac{-\alpha F \eta}{RT} \right] - \exp \left[ \frac{(1-\alpha) F \eta}{RT} \right] \right] \quad (29)$$

named after Butler and Volmer, the pioneers in this field. The validity of the Butler–Volmer equation has been verified by isotopic labeling [8]. It relates the current density that flows through the electrode–electrolyte interface due to the electrode reaction to the overpotential in terms of two kinetic parameters: the exchange current density,  $i_o$ , and the transfer coefficient,  $\alpha$ .

The exchange current density introduced by Butler [12, 13] is a measure of the exchange rate between O and R at the electrode–electrolyte interface at equilibrium and measures the height of the activation barrier when both the reactant and the product of an electrode reaction are at the same free-energy level (as shown in Fig. 2).

The transfer coefficient,  $\alpha$ , introduced in electrode kinetics by Erdey–Gruz and Volmer [14] for the hydrogen evolution reaction (HER), measures the symmetry of the free-energy curves at their intersection in the transition state. Figure 3 depicts a plot of  $\ln i$  versus  $\eta$  according to Eq. (29).

Rewriting the Butler–Volmer equation, one obtains an expression for the overpotential that explains the experimental findings of Tafel:

$$\begin{aligned} \eta &= \frac{2.303 a RT}{\alpha F} \\ &\times \left\{ -\log \left[ \frac{i}{1 - \exp \left( \frac{F \eta}{RT} \right)} \right] + \log i_o \right\} \end{aligned} \quad (30)$$

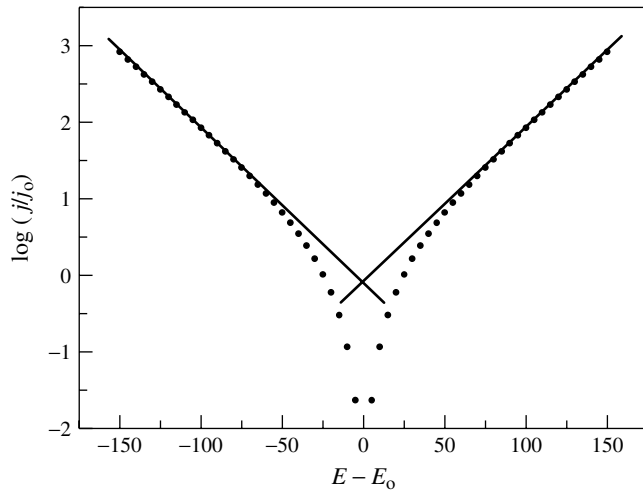


Fig. 3 Plots of  $\log |i/i_o|$  versus  $\eta$  calculated with Eq. (29).

The Tafel relationship is a linear free-energy relation of the rate coefficient for a net electrode reaction (neglecting the back reaction) and the transfer coefficient:

$$\alpha = -\frac{1}{F} \left( \frac{\partial \Delta G_f^\ddagger}{\partial E} \right)_{E_e} \quad (31)$$

and since  $E = -\Delta G^\circ/F$ , the Tafel dependence is a linear free-energy relationship between the kinetics and the thermodynamic driving force like the Brönsted relationship between the rate of proton transfer and the acid pKa in acid–base catalysis [10].

At low overpotentials ( $\eta \ll RT/\alpha nF$ ), which fulfills for 5–10 mV excursion around the equilibrium potential, the exponential expressions in Eq. (29) can be expanded in series, and the first series term in the expansion gives

$$i \cong i_o \frac{nF\eta}{RT} \quad (32)$$

a linear  $i$ – $\eta$  relationship for the flow of charge at the interface near equilibrium,

which resembles the ohmic current–potential behavior observed in conductor phases (metals and electrolytes). Notice that the slope of the current potential plot near equilibrium is independent of  $\alpha$ .

By analogy with Ohm’s law, the charge-transfer resistance,  $R_t$ , can be defined as a particular case of the polarization resistance:  $R_p = (d\eta/di)_{i \rightarrow 0}$ :

$$R_t = \frac{RT}{nF} \cdot \frac{1}{i_o} \quad (33)$$

which is a measure of  $i_o$  and is also independent of  $\alpha$ .

It should be noted that in deriving Eqs. (18 and 19), only the first term of the series expansion of the free-energy curves has been taken into account (i.e. the reactants and products parabolas have been considered linear at the crossing point) and therefore  $\alpha$  results independent of the electrode potential; this is not the case when microscopic theories like the Marcus theory based on a parabolic description are introduced. Thus, a limitation of the Butler–Volmer current–potential relation is

that it cannot account for the curvature of  $\alpha$  with the electrode potential far from the equilibrium potential and does not incorporate the temperature dependence of  $k^\circ$  explicitly.

### 1.1.5

#### Theory of Electron Transfer

Rudolf Marcus was Chemistry Nobel laureate in 1992 for his work on the theory of homogeneous and heterogeneous electron transfer (ET) in such diverse processes as the bioenergetic of photosynthesis and respiration, homogeneous redox and heterogeneous electrode reactions, corrosion, color photography, and so on. Marcus theory provides an insight on the physical and chemical phenomena of the heavy particle subsystem during electron transfer in redox reactions. Furthermore, it can accommodate disparate rates over many orders of magnitude for soluble redox species, intramolecular electron transfer in biological reactions of utmost importance, and a common framework for a comparison of redox processes in solution and at electrode surfaces.

In its simplest form the Marcus expression for the electron-transfer rate coefficient is given by [15–20]:

$$k_{\text{ET}} = Z \exp \left[ -\frac{\lambda \left( 1 + \frac{\Delta G^\circ}{\lambda} \right)^2}{4RT} \right] \quad (34)$$

with  $\lambda$  the reorganization free energy of the reactants to yield products and  $\Delta G^\circ$  the standard free energy of the reaction (thermodynamic driving force) and  $Z$  a frequency factor taken by Marcus as  $10^4 \text{ cm}^{-1}$  for heterogeneous electrode reactions [19]. The reorganization free energy,  $\lambda$  comprises the solvation,  $\lambda_o$ , and

the vibrational,  $\lambda_i$  contributions:

$$\lambda = \lambda_o + \lambda_i \quad (35)$$

Assuming the solvent as a dielectric continuum, the outer sphere component,  $\lambda_o$ , can be expressed in terms of the ionic radii  $a_1$  and  $a_2$  of the inner coordination shell ( $a_2 \rightarrow \infty$  for reactions at electrodes), the center-to-center separation distance of the reactants  $R$ , the optical ( $\epsilon_{\text{op}}$ ) and static ( $\epsilon_s$ ) dielectric constants of the solvent and the charge transferred ( $\Delta e$ ) between the reactants:

$$\lambda_o = (\Delta e)^2 \left( \frac{1}{2a_1} + \frac{1}{2a_2} + \frac{1}{R} \right) \times \left( \frac{1}{\epsilon_{\text{op}}} - \frac{1}{\epsilon_s} \right) \quad (36)$$

The inner sphere component,  $\lambda_i$  is given by

$$\lambda_i = \frac{1}{2} \sum_j k_j (q_j^r - q_j^p)^2 \quad (37)$$

where  $q_j^r$  and  $q_j^p$  are the equilibrium values for the  $j$ th normal mode coordinate  $q$  and  $k_j$  is a reduced force constant,  $k_j = 2k_j^r k_j^p / (k_j^r + k_j^p)$ .

For interfacial electrode reactions, the free energy of activation is thus given by

$$\Delta G_i^\ddagger = \frac{\lambda}{4} \left( 1 + \frac{F(E - E^\circ)}{\lambda} \right)^2 \quad (38)$$

since  $\Delta G^\circ = -F\Delta E^\circ$ .

The Marcus free-energy relation predicts a nonlinear dependence of the transfer coefficient,  $\alpha$  on electrode potential:

$$\alpha = \frac{1}{F} \frac{\partial \Delta G_i^\ddagger}{\partial E} = \frac{1}{2} + \frac{F(E - E^\circ)}{2\lambda} - \left( \frac{w_o - w_R}{2\lambda} \right) \quad (39)$$



where  $w_o$  and  $w_R$  are the electrostatic work terms due to the electrical work involved in bringing charged reactants at the reaction site or a charged reactant close to the charged electrode surface (double layer or Frumkin effects, see below). Notice that while the Butler–Volmer equation predicts  $\alpha = 0.5$  independent of the electrode potential, Marcus theory predicts curvature dependent on electrode potential and reorganization energy. Only when  $|\Delta G^\circ/2\lambda| \ll 1$ , the Marcus theory predicts  $\alpha = 0.5$ , which corresponds to low polarization and slow reactions.

The Marcus theory also allows to compare homogeneous electron-transfer reactions with the same reactions at electrode surfaces and cross-reaction rates in terms of the individual self-exchange reactions, that is,  $\lambda_{1,2} \cong 1/2(\lambda_{1,1} + \lambda_{2,2})$ . Experimental verification over 20 orders of magnitude has been the greatest success of this theory.

Another, very impressive prediction of the Marcus theory is the inverted region, coined by Marcus in 1960 [17]: For a series of related reactions of similar  $\lambda$  but different driving force,  $\Delta G^\circ$ , as  $\Delta G^\circ$  becomes negative the activation free energy,  $\Delta G^\ddagger$ , first decreases as one would expect in a Brønsted free-energy plot for acid-base catalyzed reactions, and reaches  $\Delta G^\ddagger = 0$  when  $\Delta G^\circ = -\lambda$ . Then the activation energy increases again when  $\Delta G^\circ$  becomes even more negative, leading to an inversion in the plot of logarithm of  $k_{ET}$  versus  $\Delta G^\circ$ . An experimental test of this inverted region was provided in 1984 by Miller, Calcaterra, and Closs for electron transfer between a biphenyl group to an acceptor center [21]. The difficulty with detecting the inverted region has been for many years the mass transport limit in very fast redox reactions unless the electron donor and acceptor are positioned at fixed

distance like in intramolecular electron transfer. The first evidence of the inverted Marcus region at a polarized interface was provided by the study of ET at liquid–liquid interfaces with an adsorbed C-10 lipid layer by scanning electrochemical microscopy (SECM) [22–25] and is described in Chapter 4.2.

Since the appearance of the Marcus theory, for many years a clear potential dependence of  $\alpha$  with potential has been difficult to prove experimentally with soluble redox species reacting at electrodes because the diffusion limit is reached at high ET transfer rates where one would expect the quadratic term to become important.

For heterogeneous electron transfer, the use of ordered organic monolayers (self-assembled monolayers or SAMs) at electrode surfaces as blocking films either with electroactive species in the electrolyte [26] or with electroactive groups tethered at the opposite end of the blocking molecule from the covalent attachment end [27] has provided a method to study the effect of electrode-redox center distance and the effect of the electrode potential on the electron-transfer rate.

The effect of tunneling distance in heterogeneous electron transfer at electrode surfaces has been shown by using blocking organized thin films (thickness less than 1.5 nm) where the electrons can tunnel through the films in the absence of defects or pinholes that would otherwise allow the access of electroactive species in direct contact with the electrode surface. For  $\omega$ -hydroxy-alkylthiol monolayers of different number of methylene units Miller and coworkers [26] showed that the ET heterogeneous rate constant,  $k_{ET}$ , decays exponentially with the number of methylene groups in the alkylthiol,  $n$ , which is equivalent to the distance from the redox

species to the electrode,  $x$ :

$$k_{\text{ET}}(x) = k_0(x = 0)e^{-\beta x} \quad (40)$$

where  $k_0$  is the preexponential rate coefficient and  $\beta$  the tunneling coefficient, assumed potential independent, and close to  $1 \text{ \AA}^{-1}$  [28, 29] for saturated alkylthiols in analogy to intramolecular through-bond electron transfer, and  $0.4\text{--}0.6 \text{ \AA}^{-1}$  for  $\pi$ -conjugated molecular spacers. Electron tunnel factors in ET through molecules and molecular interfaces is considered in Chapter 1.3 and a similar exponential decay has been observed in tunneling spectroscopy for tip-to-molecule distance as described in Chapter 3.3. Ratner and Whitesides [30] have recently introduced a simple experimental procedure to measure

rates of electron transport across organic thin films with a range of structures by using a Metal-SAM(1)SAM(2)-Metal junction using a mercury drop covered with C-16 alkylthiol. The current measured across these junctions obeys an exponential relation with a decay constant dependent on the molecular structure. Similar studies have been reported by Schiffrin [31], Lindsay [32], and Bard [33] with scanning tunneling microscopy (STM) examination of SAMs at electrode surfaces.

For ferrocene sites at the end of long alkanethiols self-organized at gold electrodes and diluted with unsubstituted thiols with the redox moiety in contact with the electrolyte (Fig. 4a), Chidsey has reported [34] curved Tafel plots (Fig. 4b), which could be fitted by equations derived from Marcus theory with values of  $\lambda = 0.85 \text{ eV}$  and  $Z = 6.73 \times 10^4 \text{ s}^{-1} \text{ eV}^{-1}$  for a reaction rate of  $k = 2.5 \text{ s}^{-1}$  at  $E^\circ$  in Fig. 4(b). Similar curvature in Tafel plots has been reported by Faulkner and coworkers [35] for adsorbed osmium complexes at ultramicro-electrodes (UME). The temperature dependence of the rate coefficient could also be fitted from Marcus equation and electron states in the metal and coupling factors given by quantum mechanics.

At high driving forces in Fig. 4(b), a plateau is reached instead of the inverted region predicted by Marcus theory due to the continuum of states in the

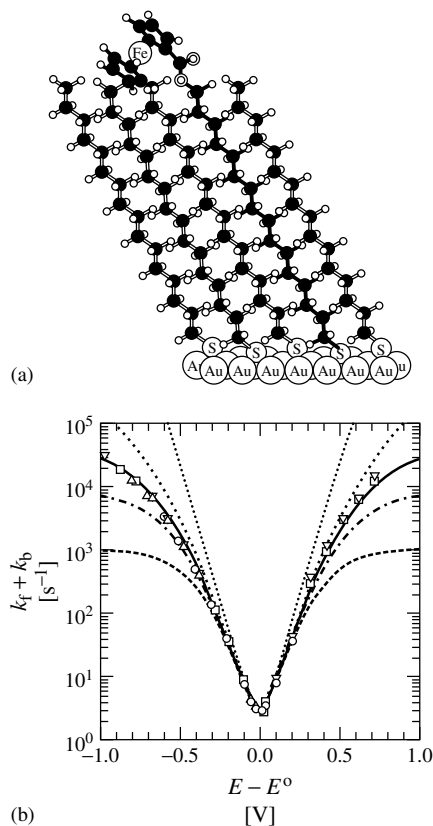


**Fig. 4** (a) Schematic representation of thiolated gold with ferrocene covalently attached to the alkylthiol end opposite to the S-Au bond. (b) Log  $(k_f + k_b)$  versus  $(E - E^\circ)$  for the oxidation–reduction of terminal ferrocene sites at SAM modified gold electrode (taken from Ref. [34]). The dotted line corresponds to calculation with the Butler–Volmer equation (29), the dashed line calculated curves from Marcus–Levich–Dogonazde theory.

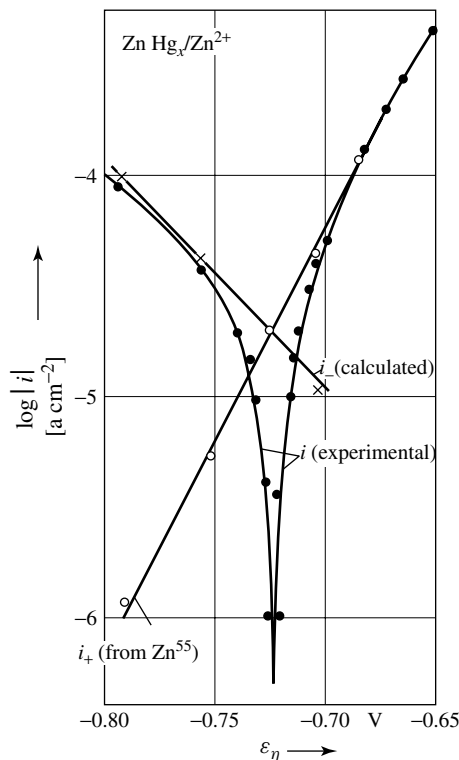
**Fig. 5** Log of current density versus potential curve of 0.1 M  $\text{ZnSO}_4$  at 0.6 atom % Zn amalgam electrode with  $50 \mu\text{M } [(\text{C}_4\text{H}_9)_4\text{N}]_2\text{SO}_4$ . Current densities were obtained from radiolabeled  $^{65}\text{Zn}$  amalgam. (Taken from Ref. [8].)

metal electrode unlike the inversion found for electron-transfer rates between two molecular states. The electronic states at the metal surface are considered in the Levich–Dogonadze theory [58], which takes into account the electronic states overlapping between the electrode and redox electrolyte and also describes the temperature dependence (see Chapter 1.2). Gerischer developed a quantum mechanics treatment for redox systems at metal and semiconductor electrodes, where the difference between metal and semiconductor electrodes is the integration over the electronic states in the electrode as in the Levich–Dogonadze theory [59]. In Gerischer model the electronic levels in the redox electrolyte are oxidized species (unoccupied states) and reduced species (occupied states) with a Gaussian distribution. The electronic overlap of these redox states with the states in the semiconductor or metal electrode describe the different contributions to the exchange current density and the current–potential dependence [3]. The current–potential relationship for electrode reactions at semiconductor electrodes present asymmetric curves due to the overlapping of the electronic structure of the semiconductor (electron or hole density of states) and the electronic states in the redox electrolyte.

#### 1.1.6

#### Ion-Transfer Reactions

Electrode reactions also characterized by exponential current–potential



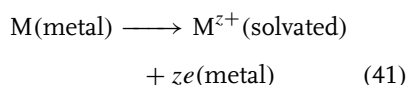
relationship are interfacial ion processes that can take place at

1. solid–liquid interface like in metal dissolution in liquid electrolyte
2. liquid–liquid interfaces like the interfaces between two immiscible electrolyte solutions (ITIES).

During the dissolution of a metal for instance, metal cations belonging to the metal crystallographic lattice can reach the surface and become *ad-atoms*, a term coined by Lorenz [38] to describe metal atoms adsorbed on surfaces. These adsorbed cations can loose electrons into the metal surface electronic plasmon and cross the electrical double layer to become solvated cations in the electrolyte. A very important role is the solvation process

that stabilizes the cation in solution. Note, however, that there is no electron transfer across the electrical double layer in the dissolution of a metal. Likewise, at ITIES not only electrons can be transferred across the liquid–liquid electrolyte boundary from donor redox states in one liquid phase to an acceptor redox states in the other, and vice versa; but also ion transfer at ITIES is possible with resolution of the ion being transferred as described in Chapter 4.2. The current–potential curve is also exponential in that case and can be described in a similar way to ion transfer at solid–liquid interfaces with surmounting an activation barrier by a Boltzman population of species with enough energy.

Gerischer [39] considered the process described by



where a metal ion at the surface metal lattice loses an electron (which remains in the metal) and crosses the double layer to become a solvated cation in the electrolyte. For this process an exponential current–potential curve is observed, which can be derived by considering the anodic ( $i_+$ ) and cathodic ( $i_-$ ) partial current densities proportional to the concentration of the reacting species and to the Boltzman factor  $e^{-Ei/kT}$ :

$$\begin{aligned} i_+ &= k'_+ c_{\text{MCT}} \exp\left(\frac{-\vec{E}_i}{RT}\right) \\ &= k_+ c_{\text{MCT}} \exp\left(\frac{\alpha z F}{RT} E\right) \end{aligned} \quad (42)$$

and

$$i_- = k_- c_o \exp\left(\frac{-\overleftarrow{E}_i}{RT}\right)$$

$$= k_- c_o \exp\left(\frac{(1-\alpha)zF}{RT} E\right) \quad (43)$$

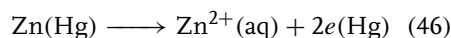
therefore the total current that flows at the interface is given by

$$\begin{aligned} i &= k_+ c_{\text{MCT}} \exp\left(\frac{\alpha z F}{RT} E\right) \\ &\quad - k_- c_o \exp\left(\frac{(1-\alpha)zF}{RT} E\right) \end{aligned} \quad (44)$$

or defining an exchange current density,  $i_o$  and overpotential,  $\eta$ :

$$\begin{aligned} i &= i_o \left[ \exp\left(\frac{\alpha z F}{RT} \eta\right) \right. \\ &\quad \left. - \exp\left(-\frac{(1-\alpha)zF}{RT} \eta\right) \right] \end{aligned} \quad (45)$$

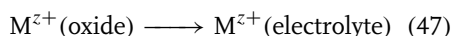
a typical ion-transfer electrode reaction is the dissolution of zinc amalgam into solvated  $\text{Zn}^{2+}$  cations in the aqueous electrolyte:



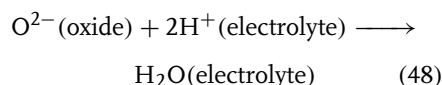
For this reaction a Tafel plot is shown in Fig. 5 as predicted by Eq. (45). A kinetic analysis of this data yields for the transfer coefficient:  $\alpha = RT/zF (\partial \ln i_o / \partial \epsilon_o) = 0.72$  for the charge-transfer valence  $z = 2$ .

The free-energy barrier for the flow of ionic charge across the oxide–electrolyte interface has an electrical contribution and consequently the current–potential curve can be described by a Butler–Volmer type equation [8].

The ion-transfer reactions at the oxide–electrolyte interface:



and,



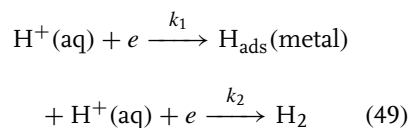
are also examples of interfacial ion-transfer reactions. Under steady state conditions, the net current at the interface is given by the sum of cation and anion partial ionic currents. Deposition and dissolution of the oxide requires that both cations and anions flow in the same direction while the corresponding electrical currents are opposite [39]. The steady state potential of the oxide electrode at a particular composition  $\text{MO}_n$  lies between the formal equilibrium potential with respect to oxygen and metal electrodes as required by the electroneutrality condition [40].

The transfer of ions across immiscible electrolyte interfaces (ITIES) can be described by a similar Butler–Volmer formalism and involves resolution of the transferred ions. The flux of ions can be measured by the electronic current in the external circuit generated at symmetrical reference electrodes reversible to one of the ions.

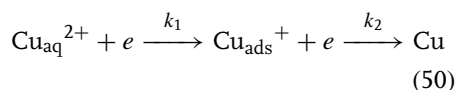
### 1.1.7

#### Multiple Electron Transfer

In general, reactions at electrodes involving more than one electron-transfer events occur in successive steps with participation of intermediaries, which in most cases are adsorbed at the electrode surface. For instance, consider



or,



Since the time scale for the electron-transfer event, ca.  $10^{-16}$  s is much smaller than the time scale of the fastest chemical

reorganization in the metal-ligand vibration scale,  $10^{-13}$  s or slower, the probability of simultaneous electron transfer in a single step is extremely low. Therefore, two one-electron steps with the stabilization of an intermediate state are more likely to occur than a single two-electron step. Figure 6 depicts the free-energy profile for a two-step electron-transfer electrode reaction, where the relative heights of the activation barriers for the elementary steps is differently influenced by the electrode potential. At  $E_1$ , the rate-determining step corresponds to the first electron transfer while at  $E_2$ , the rds is the second electron transfer and at  $E^*$  both transition states have the same activation barrier ( $k_2 = k_{-1}$ ) and therefore there is a shift in the position of the transition state from the first to the second electron-transfer process.

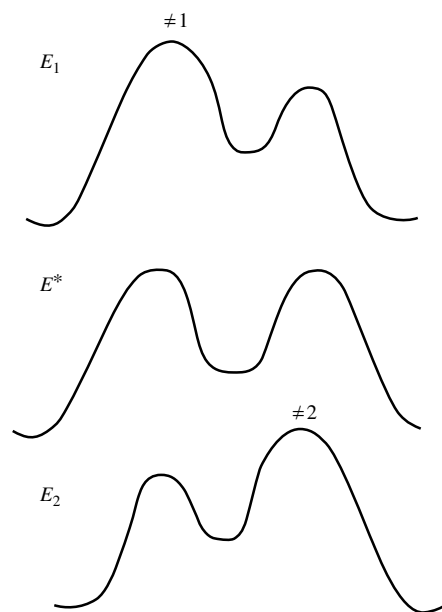
Note that both rate constants  $k_1$  and  $k_2$  may have different kinetics with  $i_{o,1}$  and  $\alpha_1$  and  $i_{o,2}$  and  $\alpha_2$  respectively and a general expression for a sequential two-electron reaction has been derived by Vetter [8]:

$$\begin{aligned} i = 2i_{o,1} \exp\left(\frac{\alpha_1 F \eta}{RT}\right) & \\ \times \frac{1 - \exp\left(-\frac{2F \eta}{RT}\right)}{1 + \left(\frac{i_{o,1}}{i_{o,2}}\right) \exp\left[-\frac{(1 + \alpha_2 - \alpha_1)F \eta}{RT}\right]} & \end{aligned} \quad (51)$$

where  $\eta = E - E^{\circ'}$  and  $E^{\circ'}$  is the standard electrode potential for the overall two-electron process. In Fig. 7 we represent the Tafel plot for the current potential relationship described by Eq. (51).

We can consider two limiting cases:

1. The first electron-transfer step is rds, then  $k_2 \gg k_{-1}$  in Eq. (51), and the forward rate coefficient  $k_f \approx k_1$  and



the backward rate coefficient  $k_b \approx (k_2/k_{-2})/k_{-1}$ .

2. Second electron-transfer step in Eq. (51) being rds.  $k_2 \ll k_{-1}$  then  $k_f \approx (k_1/k_{-1})k_2$  and,  $k_b \approx k_{-2}$ .

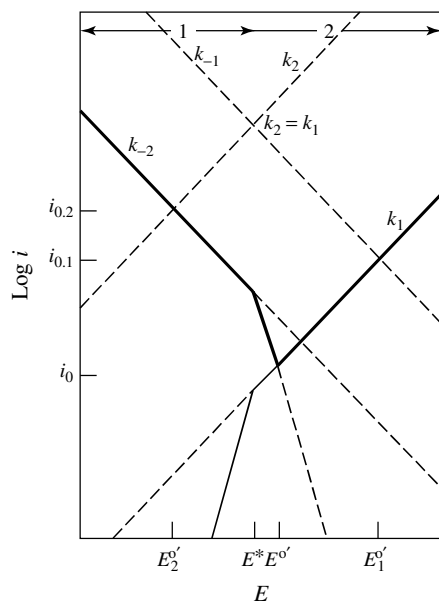


**Fig. 6** Standard free-energy diagram for a two-step electron-transfer electrode reaction with two potential dependent transition states.

The relative height of each individual activation barrier changes with electrode potential, as illustrated in Fig. 6.

As depicted in Fig. 7, at potentials more positive than  $E^*$ ,  $k_2 > k_{-1}$  and the first electron transfer is rds while for  $E < E^*$ ,  $k_{-1} > k_2$  and the second electron transfer becomes rate-determining. The Tafel slope in the first case is  $2RT/F$  and  $3RT/2F$  for the preequilibrium in the second case.

In multiple-electron electrode reactions extrapolation of Tafel lines from high overpotential regions to reversible potential for the overall reaction  $E'_0$ , does not yield the same apparent standard rate coefficient (exchange current density) and may be misleading:  $i_{0,2}$  is larger than  $i_{0,1}$ , the exchange current density for the kinetics that change more rapidly with potential. This feature distinguishes an  $n$ -electron sequential multistep reaction from a single  $n$ -electron charge-transfer step [8].

The rate-determining step, rds, for a given mechanism may change with potential, but this does not violate the principle of microscopic reversibility since inspection of Fig. 7 shows that, at any potential, the transition state is always the same for the forward and backward reactions in Eq. (51). Transition states at different electrode potentials, on the other hand, need not be the same (see Fig. 6). Furthermore, there is no reason, why the potential  $E^*$ , determined by kinetic factors,

**Fig. 7** Schematic representation of the variation of the individual rate coefficients  $k_i$  (broken lines) and the overall rate coefficient (solid line) for a two-electron electrode reaction as a function of the electrode potential.

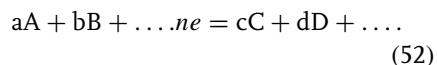
at which the transition of rds occurs, should be the same as the thermodynamic equilibrium potential  $E_e$ .

In Fig. 7, each transition state can be identified and is characterized by  $i_{o,i}$ ,  $E_{o,j}$  and  $\alpha_j$ ;  $i_{o,i}$  measures the barrier height of each transition state in the respective standard conditions, whereas at the formal standard potential,  $E^{\circ'}$ , for the overall reaction,  $k_f = k_b$  and this potential value is half way between  $E_1^{\circ'}$  and  $E_2^{\circ'}$ . The change in transition states with electrode potential is observed, for instance, in the complex oxygen electroreduction (4-electron and 4-proton) reaction, the mechanism of which may also change with pH.

#### 1.1.7.1 Stoichiometric Number

The concept of stoichiometric number was introduced in electrochemistry by Horiuti and Ikusima [42, 43] for the hydrogen electroreduction reaction. We need to introduce the stoichiometric number  $\nu$  in complex multielectron electrode kinetics in order to distinguish different possible mechanisms. The International Union of Pure and Applied Chemistry (IUPAC) defines the stoichiometric number in electrochemistry as a positive integer that indicates the number of identical activated complexes formed and destroyed in the completion of the overall reaction as formulated with the charge number,  $n$  [44, 45]

A general expression can be derived for the electrode reaction:

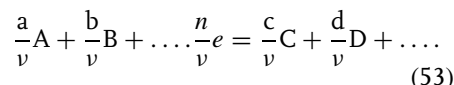


which takes place in several consecutive intermediate steps, the rate of one of them controlling the overall kinetics.

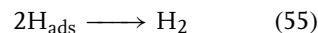
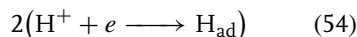
The reactants and products in the rate-determining step (rds) will be identified by  $R$  and  $P$ , respectively.

We shall assume that the completion of the overall process represented by Eq. (52) requires the formation and decomposition of  $\nu$  identical activated complexes.

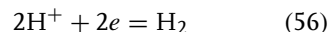
According to Parsons the rate-determining step can be represented [46] by



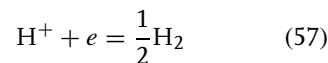
The stoichiometric number indicates the number of times the rate-determining step occurs in the overall stoichiometric reaction. For example, the Tafel mechanism for the reduction of  $H^+$  on metals occurs in two steps with Reaction (54) occurring twice for each time Reaction (56) takes place.



where  $H_{ad}$  indicates an adsorbed hydrogen atom (ad-atom) on the metal electrode. If the overall reaction is written in the form:



$\nu = 2$  and  $n = 2$ ; but if the reaction is represented as



then,  $\nu = 1$  and  $n = 1$ .

It is worthwhile noticing that, while  $\nu$  and  $n$  are arbitrary quantities that depend on the way we write the stoichiometric equation, the “electron number”  $n/\nu$  is characteristic of the electrode reaction kinetics. In the Tafel hydrogen reduction mechanism,  $n/\nu = 1$  and indicates the

number of electrons transferred for the completion of the rate-determining step.

The forward and backward reaction rate coefficients can be expressed by Eq. (17) with  $\Delta G^\ddagger$ , the standard free energy of formation of one mole of activated complex from reactants in Eq. (52), and should be replaced by the electrochemical free energy of activation,  $\overline{\Delta G_i^\ddagger}$ , for charged particles.

$$\overline{\Delta G_f^\ddagger} = \overline{\mu_\pm^\circ} - \overline{\mu_R^\circ} \quad (58)$$

$$\overline{\Delta G_b^\ddagger} = \overline{\mu_\pm^\circ} - \overline{\mu_P^\circ} \quad (59)$$

The standard electrochemical potentials of reactants and products may be written in terms of the chemical and electrical contributions:

$$\begin{aligned} \overline{\mu_R^\circ} &= \frac{a}{v} \mu_A^\circ + \frac{b}{v} \mu_B^\circ \\ &+ \frac{n}{v} \mu_e^\circ + \frac{n}{v} F \phi_M \end{aligned} \quad (60)$$

$$\overline{\mu_P^\circ} = \frac{c}{v} \mu_C^\circ + \frac{d}{v} \mu_D^\circ + \frac{n}{v} F \phi_S \quad (61)$$

In order to evaluate the potential dependence of the free energy of activation, without knowledge of the structure of the activated complex, it is assumed that the electrical contribution to the standard free energy of the transition state lies between that of the standard free energy of *P* and that to the standard free energy of *R* in the rds. The symmetry factor or transfer coefficient,  $\alpha$ , for the rds in analogy to the case for one-electron reactions is given by

$$\overline{\mu_\pm^\circ} = \mu_\pm^\circ + \frac{\alpha}{v} n F E \quad (62)$$

which after substitution in Eq. (17) with the free energy of activation given by Eqs. (58 and 59) is

$$k_b = \frac{k_B T}{h} \exp - \left[ \frac{\Delta G_f^\ddagger}{RT} + \frac{\alpha}{v} \frac{n F E}{RT} \right] \quad (63)$$

$$k_f = \frac{k_B T}{h} \exp - \left[ \frac{\Delta G_b^\ddagger}{RT} + \frac{(1 - \alpha)}{v} \frac{n F E}{RT} \right] \quad (64)$$

where  $\Delta G_i^\ddagger$  represents the nonelectrical contribution to the standard free energy of activation and  $E = (\phi_M - \phi_S) + \text{const.}$  It should be noted that the right-hand side of Eqs. (63 and 64) should be divided by the activity coefficient of the activated complex, which could be potential dependent [46].

Introducing the overpotential,  $\eta = E - E_e$ , and replacing

$$\begin{aligned} i &= i_o \left[ \exp \left( -\frac{\alpha}{v} \frac{n F \eta}{RT} \right) \right. \\ &\quad \left. - \exp \left( \frac{(1 - \alpha) n \eta}{v} \right) \right] \end{aligned} \quad (65)$$

and the exchange current density,  $i_o$

$$i_o = \frac{n}{v} F k_o [A]^{\frac{1-\alpha}{v}} [B]^{\frac{1-\alpha}{v}} [C]^{\frac{\alpha}{v}} [D]^{\frac{\alpha}{v}} \quad (66)$$

for a first-order reaction.

For  $|\eta| \gg vRT/\alpha nF$ , the Tafel approximation is valid and

$$\left( \frac{\partial \eta}{\partial \ln i} \right)_{T,P,c_i} = -\frac{vRT}{\alpha nF}$$

and

$$\left( \frac{\partial \eta}{\partial \ln i} \right)_{T,P,c_i} = \frac{vRT}{(1 - \alpha)nF} \quad (67)$$

and therefore the stoichiometric number,  $v$ , can be obtained from anodic and cathodic Tafel plots,

$$v = \frac{nF}{RT} \left\{ \left( \frac{\partial \ln i}{\partial E} \right)_a - \left( \frac{\partial \ln i}{\partial E} \right)_c \right\}^{-1} \quad (68)$$

if the rate-determining step is the same over the whole range of potentials from which Tafel slopes are obtained. Note that from a Tafel plot we can only determine the product  $\alpha n/v$ , not the quantities separately.



For small overpotentials,  $|\eta| \ll \nu RT / \alpha n F$  in the linear polarization region, an explicit expression for the stoichiometric number can be found:

$$\nu = -\frac{nFi_o}{RT} \left[ \frac{\partial \eta}{\partial i_c} \right]_{\eta=0} = \frac{nFi_o}{RT} \left( \frac{\partial \eta}{\partial i_a} \right)_{\eta=0} \quad (69)$$

which is valid if the reversible potential is far from the pzc, otherwise double-layer effects are important (see Sect. 1.1.10).

### 1.1.8

#### Mass Transport at Electrodes

In electrode reactions, the reactant has to find the electrode surface where electrons are taken or released, and therefore the mass transport of reactants and products becomes very important in the description of electrode reactions where we will be interested in current–time and current–potential relations. The master equation for mass transport to an electrode surface is the Nernst–Planck equation:

$$\vec{J}_i = -D_i \left( \vec{\nabla} c_i + c_i \frac{z_i F}{RT} \vec{\nabla} \phi + c_i \vec{v} \right) \quad (70)$$

which accounts for the flux of species  $i$  ( $\text{mol cm}^{-2} \text{s}^{-1}$ ) at a given distance from the electrode surface,  $D_i$  is the diffusion coefficient of the diffusing electroactive species ( $\text{cm}^2 \text{s}^{-1}$ ). The first term on the right hand side of Eq. (70) represents the transport mechanism by diffusion in a concentration gradient,  $\vec{\nabla} c_i$ , by random thermal motion of the particles, which tends towards uniform concentration of mobile species. The second and third term on the right hand side describe, respectively, migration under the influence of the electric field,  $\vec{E} = \vec{\nabla} \phi$ , and convection under the influence of a flow field, with the fluid velocity  $\vec{v}$  ( $\text{cm s}^{-1}$ ) and the particles

acquire a component of their velocity along the direction of the field. These effects will be treated in detail in Chapter 2.1: Diffusion and migration. However, in electrokinetic experiments, the migration contribution can be reduced by using an inert supporting electrolyte at a much higher concentration than that of the electroactive species so that the transport number of the electroactive species is negligible. Forced convection combined with diffusion can be controlled with hydrodynamic electrodes with a good mathematical description of the flow pattern and thus of the steady state current–potential relation. [9].

$$\frac{\partial c}{\partial t} = D \nabla^2 c - V_x \nabla c \quad (71)$$

The solution of this partial differential second-order equation depends on the initial and boundary conditions of the particular experiment, giving rise to a multitude of techniques. In Chapter 2.2, the digital simulation of voltammetry under stagnant and hydrodynamic conditions is described. By changing the electrode potential one can modify the boundary conditions and transient effects arise until a new steady state is reached.

The steady state diffusion is reached when

$$\frac{\partial c}{\partial t} = 0 \quad (72)$$

This condition can be accomplished when the concentration gradient close to the electrode surface is constant (linear) or its curvature is compensated by a term  $X$ :

$$\frac{\partial c}{\partial t} = D \nabla^2 c \pm X \quad (73)$$

where  $X$  can arise from the diffusion field geometry, that is, nonlinear terms like in cylindrical or spherical electrodes:

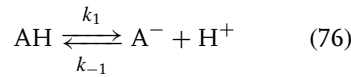
$$X_{\text{spherical}} = \frac{2}{r} D \frac{\partial c}{\partial r} \quad (74)$$

or,

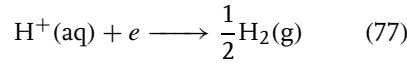
$$X_{\text{cylindrical}} = \frac{1}{r} D \frac{\partial c}{\partial r} \quad (75)$$

or approximations to these terms in ultra microelectrodes where the electrode size is smaller or comparable to the characteristic diffusion length at a given time, namely,  $r \leq \sqrt{(2Dt)}$ .

Two other sources of a term  $X$  that can compensate for the curvature of the concentration gradient at the electrode surface are a convective term  $X = c_i \vec{v}$ , where  $\vec{v}$  is the fluid velocity or a chemical reaction (not involving a charge-transfer step) term  $X = k_1 c_i$  coupled to the charge-transfer reaction, that is,



followed by the electron-transfer reaction:



The diffusion equation is

$$\frac{\partial c_{\text{AH}}}{\partial t} = D_{\text{H}} \frac{\partial^2 c_{\text{H}}}{\partial x^2} - k_1 c_{\text{HA}} + k_{-1} c_{\text{A}^-} c_{\text{H}^+} \quad (78)$$

which has a steady state at the electrode characterized by a reaction layer,  $x_{\text{R}} = \sqrt{(D_{\text{H}}/k_{-1}c_{\text{A}})}$ , a distance over which a proton once formed from dissociation of HA has a chance to diffuse before reacting with  $\text{A}^-$  [4].

In most practical applications, where the maximum yield of a product or electricity in electrochemical energy conversion systems is desired, the rate of mass transport should be fast enough in order not to limit the overall rate of the process. Conversely, in electroanalytical techniques, such as polarography or gas sensing, the reaction is limited by the transport of the reactant since the analyte bulk concentration

is to be determined from the limiting convective-diffusion current.

According to the classical treatment by Randles [47] for a simple electroreduction of O to R in solution and assuming, for simplicity, that the mass transport rate coefficients,  $k_{d,i}$  for the oxidized and reduced species are the same, the net current density under steady state conditions is

$$i = nFk_d[c_{\text{O}}^* - c_{\text{O}}^{\text{s}}] = nFk_d[c_{\text{R}}^{\text{s}} - c_{\text{R}}^*] \quad (79)$$

with the diffusion-limiting current densities for the anodic and cathodic processes given by.

$$i_{\text{L}} = nFk_d c_i^* \quad (80)$$

A diffusion layer of thickness  $\delta$ , which has a purely formal significance, can be defined as

$$\delta = \frac{D}{K_{d,i}} = \frac{(nFDAc_i)}{i} \quad (81)$$

In Eq. (25) we have considered the surface concentration of the reacting species equal to the analytical concentration in the bulk electrolyte. If we replace in Eq. (25) the surface concentrations from Eqs. (79–81):

$$\frac{c_i(0, t)}{c_i^*} = \left(1 - \frac{i}{i_{\text{L}}}\right) \quad (82)$$

we obtain

$$\frac{i}{i_{\text{o}}} = \left[ \left(1 - \frac{i}{i_{\text{L}, c}}\right) \exp\left(-\frac{\alpha n F \eta}{RT}\right) - \left(1 - \frac{i}{i_{\text{L}, a}}\right) \exp\left(\frac{(1 - \alpha) n F \eta}{RT}\right) \right] \quad (83)$$

Figure 8 depicts a plot of the current–potential curve calculated with Eq. (83),  $i/i_{\text{L}}$  versus  $\eta$  and the corresponding normalized concentration profiles at the limiting current and at equilibrium. The mass transport free Butler–Volmer

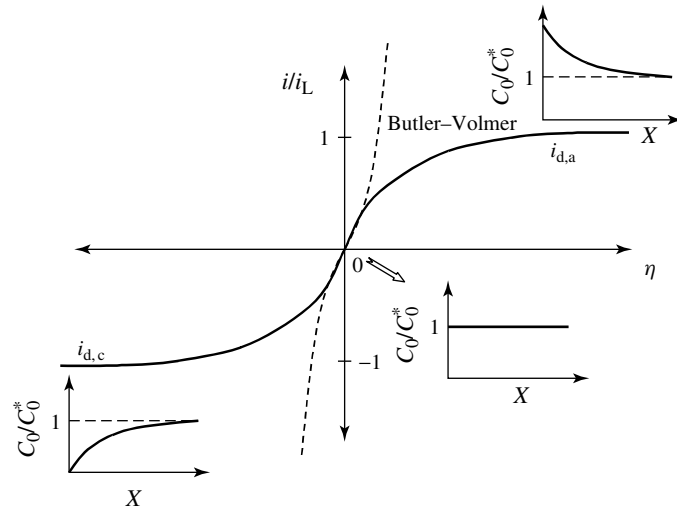


**Fig. 8** Plot of  $i/i_L$  versus  $\eta$  calculated with Eq. (83) (solid line) and Butler–Volmer current–potential curve calculated with Eq. (29) for  $\alpha = 0.5$  and  $n = 1$ . Inset: concentration profiles of the oxidized species normalized to the analytical concentration at limiting current and at equilibrium.

predicted current–potential curve calculated with Eq. (29) (dashed line) is shown for comparison.

We can reexamine Eq. (83), both in the Tafel region, for  $|\eta| \gg RT/\alpha nF$ :

$$\log i = \log i_o + \left(1 - \frac{i}{i_{L,c}}\right) \exp\left(-\frac{\alpha nF\eta}{RT}\right) \quad (84)$$

and for the linear polarization region, for  $|\eta| \ll RT/\alpha nF$ :

$$i = \frac{nF\eta}{RT} \left( \frac{1}{\left(\frac{1}{i_o}\right) + \left(\frac{1}{i_{L,c}}\right) + \left(\frac{1}{i_{L,a}}\right)} \right) \quad (85)$$

which in the absence of concentration polarization is coincident with Eq. (32).

Expressing Eq. (84) in terms of rate coefficient rather than current densities and rearranging terms, the rate coefficient obtained experimentally at constant

potential,  $k_{\text{obs}}$ :

$$k_{\text{obs}} = \frac{i}{nFc_i^*} \quad (86)$$

can be separated into the electrode reaction apparent rate coefficient for extrapolated infinitely fast mass transport conditions,  $k$ , and the mass transport rate coefficient,  $k_d$ :

$$\frac{1}{k_{\text{obs}}} = \frac{1}{k} + \frac{1}{k_d} \quad (87)$$

Heterogeneous electrode reactions can be compared with homogeneous kinetics in solution, with regard to mass transport. The second-order rate coefficient for a fast homogeneous reactions in solution,  $k(\text{hom})$ , which would be observed if diffusion were infinitely fast, can be related to the measured rate coefficient,  $k_{\text{obs}}(\text{hom})$  by application of Fick's first law in a spherical continuum diffusion field around the reacting molecule. At a collision distance  $r_{AB}$ , this corresponds to the average

concentration of molecules undergoing encounters equal to the average analytical concentration in the bulk solution [48].

$$k_{\text{obs}}(\text{hom}) = \frac{4\pi r_{\text{AB}} D_{\text{AB}}}{1 + \frac{4r_{\text{AB}} D_{\text{AB}}}{k(\text{hom})}} \quad (88)$$

where  $r_{\text{AB}}$  is the encounter distance of molecules A and B in solution and  $D_{\text{AB}}$  is the relative diffusion coefficient.

Rewriting Eq. (88) with  $k_d(\text{hom}) = 4\pi r_{\text{AB}} D_{\text{AB}} N_{\text{A}}$  where  $N_{\text{A}}$  is Avogadro's number:

$$\frac{1}{k_{\text{obs}}(\text{hom})} = \frac{1}{k(\text{hom})} + \frac{1}{k_d(\text{hom})} \quad (89)$$

The analogy in the mass transport effects in electrode reaction and homogeneous second-order fast reactions in solution becomes clear. In electrode kinetics, however, the charge-transfer rate coefficient can be externally varied over many orders of magnitude through the electrode potential and  $k_d$  can be controlled by means of hydrodynamic electrodes. For instance the mass transport rate coefficient,  $k_d$ , for a rotating disc electrode at the maximum practical rotation speed of 10 000 per min<sup>-1</sup> is approximately  $2 \times 10^{-2}$  cm s<sup>-1</sup>.

### 1.1.9

#### Electrochemical Reaction Order

The order of an electrochemical reaction is an empirical factor widely used in chemical kinetics, which may give an insight into the events at the molecular level for kinetics of complex reactions. It relates the reaction rate to the concentration of a particular species in the kinetic equation.

In electrode reactions, the reaction order with respect to the species  $k$  can be

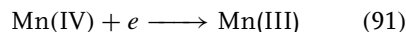
defined by

$$p_k = \left( \frac{\partial \log i_j}{\partial \log c_k} \right)_{c_{i \neq k}, E} \quad (90)$$

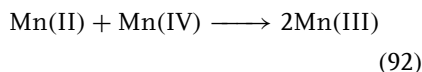
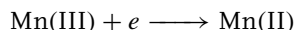
where  $i_j$  is a partial anodic or cathodic current density and  $c_k$  the concentration of species  $k$ .

Because of the strong dependence of the kinetics on potential, the determination of the electrochemical reaction order requires that the partial anodic or cathodic current densities be measured at constant potential in addition to the concentration of the other species being kept constant.

Vetter used extensively the concept of reaction order, for instance, as diagnostic of the mechanism of the electrode reaction:



on platinum electrode [8], which looks simple at first sight. However the reaction orders found experimentally are  $P_{\text{Mn(IV)}} = 0$  and  $P_{\text{Mn(III)}} = 1$ , which suggests the following mechanism:

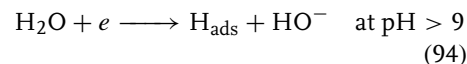


with the first electron transfer to Mn(III) rate-determining step.

For the HER on mercury the reaction order  $P_{\text{H}^+} = 1$  at pH less than 8 and  $P_{\text{H}^+} = 0$  at pH larger than 9, allows the following elementary steps to be distinguished:



and



## 1.1.10

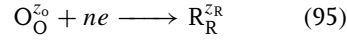
**Double-Layer Effects on the Current–potential Relationship**

Since the electrode reactions occur at charged interfaces the structure of this electrified interface influences the electrode kinetics of charged species. Frumkin [49] pointed out the importance of the double-layer structure on electrode kinetics for the hydrogen reduction reaction on mercury. The electrical potential at the plane where the reactant undergoes electron transfer to become a product influence the concentration of charged species different from the analytical concentration the bulk electrolyte due to the electrostatic work required for the charged reactant (product) to reach the electrode surface. Furthermore, the inner (Galvani) potential difference with respect to the solution ( $\phi_p - \phi_s$ ) is less than the applied electrode-electrolyte potential difference ( $\phi_M - \phi_s$ ).

The electrostatic work necessary to bring the electroactive ion to a charged interface, where the electrode reaction occurs, is equivalent to the electrostatic contribution to the free energy of activation in homogeneous reactions between ions in solution. When two ions of the same charge react, their kinetics are slower as compared to the uncharged species and conversely when two ions of different charge react, the apparent kinetics are faster than for the uncharged molecules.

When no specific adsorption occurs, the closest the reactant can get to the electrode surface is assumed to be the outer Helmholtz plane (OHP) and the reaction plane is identified with this OHP,  $\phi_p \approx \phi_2$ . The simplest case is when the reactant is the only ionic component of the solution, then the effects on electrode kinetics due to the properties of the interface

are maximum. For the electroreduction reaction:



two effects due to the double-layer structure can be described:

1. the concentration of the reacting ion,  $C_O^p$  in the outer Helmholtz plane, is different from the analytical concentration in the solution,  $C_O^s$ ,

$$C_O^p = C_O^s \exp \left[ -\frac{z_i F \Delta \phi_2}{RT} \right] \quad (96)$$

The electrical work to place a mole of O from the bulk solution in the OHP is  $z_i F \Delta \phi_2$  where  $\Delta \phi_2$  is the potential of the OHP with respect to the potential of the solution.

2. The driving force for the electrochemical reaction is the potential jump between the metal and the reaction site (in the absence of specific adsorption, identified with the OHP). The apparent rate coefficient for the reduction reaction involving n electrons is

$$k_{app} = k_{\phi_M = \phi_2} C_O^{\phi_2} \times \exp \left[ -\frac{\alpha n F (\phi_M - \phi_2)}{RT} \right] \quad (97)$$

By combining Eqs. (96 and 97) and replacing the concentration of O at the plane of reaction, the apparent rate constant can be expressed in terms of the applied electrode potential.

$$k_{app} = k_{\phi_M = \phi_2} C_O^s \exp \left[ -\frac{\alpha n F (\phi_M - \phi_s)}{RT} \right] \times \left\{ \exp \left[ \frac{(\alpha n - z) F (\phi_2 - \phi_s)}{RT} \right] \right\} \quad (98)$$

The first exponential term shows the potential dependence of the apparent

rate constant on the applied potential difference (metal–electrolyte solution),  $(\phi_M - \phi_S)$ . The second exponential term is the double-layer correction to the apparent rate constant due to concentration at the reaction plane and potential  $\phi_2$ . It is also shown that the same correction applies for the reverse reaction for  $z_r = z_o \pm n$  since the transition state and hence the reaction plane must be the same for the forward and backward processes.

It should be noticed that the Galvani potential difference,  $\Delta\phi_2$ , cannot be measured directly but its value can be derived from the Gouy–Chapman theory of the diffuse double layer. If the excess charge in the metal,  $q^m$ , is determined experimentally, that is, from the integration of differential capacity curves, then for a 1 : 1 electrolyte of concentration  $c^s$ , then  $\Delta\phi_2$  can be calculated:

$$\Delta\phi_2 = \frac{2RT}{z_i F} \sinh^{-1} \left[ \frac{q^m (2\pi)^{1/2}}{(2RT c^s \epsilon)^{1/2}} \right] \quad (99)$$

The double-layer correction of the observed electrode kinetics in Eq. (98) is more important at low ionic concentration, high ionic charge and close to the potential of zero charge (pzc). This correction can be minimized by using a supporting or inert electrolyte of high concentration so that most of the potential drops operates in the inner Helmholtz plane and  $\Delta\phi_2 \approx 0$ .

The consequence of double-layer correction on the exchange current density is

$$i_o = i_o(\text{app}) \exp \left[ -\frac{(\alpha n - z) F \Delta\phi_2}{RT} \right] \quad (100)$$

and on the apparent charge-transfer coefficient,

$$\alpha_{\text{app}} = \frac{\partial \ln i_{\text{app}}}{\partial E} = \frac{F}{RT} (\alpha n - z_o) \frac{\partial \Delta\phi_2}{\partial E} \quad (101)$$

Nonlinear Tafel plots are predicted by Eq. (101) when  $\Delta\phi_2$  changes appreciably with electrode potential: at low ionic concentrations and close to the pzc.

The apparent electrochemical reaction order is influenced by double-layer effects:

$$P_O^{\text{app}} = \left[ \frac{\partial \ln i_{\text{app}}}{\partial \ln c_O} \right]_E = P_O + (\alpha n - z_o) \frac{F}{RT} \left[ \frac{\partial \Delta\phi_2}{\partial \ln C_O} \right]_E \quad (102)$$

the double-layer correction in the second term of Eq. (102) due to interfacial potential distribution is zero at the pzc.

### 1.1.11

#### Adsorption and Electrocatalysis

Adsorption of reactants, intermediates and products at electrode surfaces significantly influence the current–potential relationship for electrode reactions. In particular species confined to electrode surfaces can be oxidized and reduced without the need for the reactants to diffuse towards the electrode surface. The adsorption free energy plays a key role in electrode kinetics and for charged species on the potential dependence.

An electrocatalytic reaction is an electrode reaction sensitive to the properties of the electrode surface. An electrocatalyst participates in promoting or suppressing an electrode reaction or reaction path without itself being transformed. For example, oxygen reduction electrode kinetics are enhanced by some five orders of magnitude from iron to platinum in alkaline solutions or from bare carbon to carbon electrodes modified with adsorbed iron or cobalt phthalocyanines or porphyrins and when certain metals are under potential deposited (upd).

As early as 1905, Tafel [11] showed that the kinetics of the proton reduction strongly depends on the nature of the electrode material. Thirty years later, Horiuti and Ikusima used the word “catalyst” instead of electrode [42], and Butler pointed out the very important role of adsorbed intermediates in the evolution of hydrogen [12, 13].

The main catalytic influence of the nature of the electrode material is through the adsorption of intermediates of complex electrode reactions. Horiuti and Polanyi [50] suggested that the activation energy of an electrode reaction should be related to the heat of adsorption of adsorbed intermediates by a relationship of the form of the Brønsted rule in homogeneous solutions. This corresponds to a vertical shift of the potential energy curves by an amount  $\beta\Delta H_{\text{ads}}^\circ$  with  $\beta$  a symmetry factor. Correlation of the activation energy or overpotential at a given current for a particular rds on different substrates with relative measures of the heat of chemisorption of intermediates have been successfully made for hydrogen evolution [51], oxygen evolution [52], and oxygen reduction [53], and so on. For the hydrogen electrode reaction (HER) on different metals, it is predicted that the curve  $\log i_o$  vs.  $\Delta G_{\text{ads}}^\circ$  goes through a maximum with decreasing  $\log i_o$  both at positive and negative values of  $\Delta G_{\text{ads}}^\circ$  due to the opposite effects of the free energy of adsorption on the geometric and exponential factors in the electrokinetic equation (volcano plots).

Several chapters in this volume describe new experimental evidence of adsorbate bonding with different “in situ” spectroscopic techniques, the effect of the interfacial structure on kinetics and mechanisms of selected electrode reactions with bond breaking and surface bonding like oxygen

reduction and CO and methanol oxidation. In particular, Chapter 5.1 analyzes electrocatalysis in depth.

### 1.1.12

#### Mixed Potential

At the equilibrium potential, both anodic and cathodic processes of a single electron-transfer reaction take place at the same exchange rate (a measure of which is  $i_o$ ) and the current through the external circuit is zero. The open-circuit potential is the thermodynamic equilibrium potential. When more than one reaction can take place at the electrode surface, on the other hand, the open-circuit potential is not a thermodynamic quantity but a “mixed potential” set up by the kinetics of both simultaneous electrode reactions that exchange electrons with the metal. At open circuit all the charge transferred from the electrode to the solution must be counterbalanced by the flow of charge in the opposite direction ( $I_a = I_c$ ) with no net flow of charge through the interface. Thus, anodic and cathodic processes are coupled through the charge exchanged and a net chemical reaction proceeds.

In order to explain the corrosion process of metals, Wagner and Traud [54] developed the “mixed potential” theory, which assumes that the current–potential relationship is given by

$$I(E) = \sum |I_{a,i}(E)| - \sum |I_{c,i}(E)| = 0 \quad (103)$$

The additive individual component currents are based on the simplifying assumption that the anodic and cathodic processes are statistically independent and that the electrode surface sites are indistinguishable for both reactions. Since the total anodic and cathodic currents equal at the

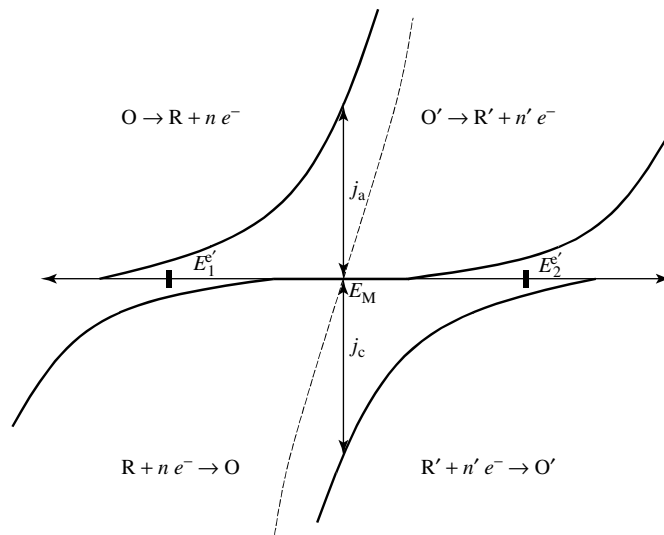


**Fig. 9** Schematic representation of the establishment of mixed potential,  $E_M$ , at an electrode. Partial current densities (solid lines) and total current density curve (broken line).

open-circuit or mixed potential,  $E_M$

$$\sum |i_{a,i}| A_{a,i} = \sum |i_{c,i}| A_{c,i} \quad (104)$$

where  $i_{k,i}$  represents the partial anodic and cathodic current densities and  $A_{k,i}$  the respective reaction areas.

In Fig. 9 we consider two simultaneous electrode reactions (O/R and O'/R') with transfer of  $n$  and  $n'$  electrons, respectively and formal equilibrium potentials  $E_1^e$  and  $E_2^e$ . At open circuit, the mixed potential,  $E_M$ , adopts intermediate values  $E_1^e < E_M < E_2^e$ , closer to the equilibrium potential of the faster partial reaction. The overall current–potential curve is indicated by the broken line. Notice that  $E_M$  is not determined by the thermodynamic values of  $E_1^e$  and  $E_2^e$  but by the kinetics of the respective reactions, that is, by the respective anodic and cathodic component curves in Fig. 9 with the condition of Eq. (104). These curves may be altered by mass transport, surface area and specific

properties; and consequently the mixed potential  $E_M$  may be susceptible to those kinetic factors, unlike the equilibrium potential of each partial electrode reaction, which is fixed by thermodynamics and the activities in the bulk solution. Unlike consecutive electron-transfer reactions the kinetics of which are determined by the slowest process, mixed potentials are determined by the fastest of several possible electrode reactions.

If one of the partial electrode reactions is the dissolution of the electrode (i.e. metal or semiconductor) the open-circuit potential is a corrosion potential and the system undergoes corrosion at a level given by the corrosion current ( $i_{\text{corr}}$ ), which measures the dissolution rate. The magnitude of  $i_{\text{corr}}$  for a corroding system may vary significantly over several orders of magnitude, like the exchange current densities of different individual electrode reactions span a range of orders of magnitude.



In Fig. 9, the occurrence of two simultaneous redox reactions at an electrode surface has been considered; however, in most corrosion problems, more than two reactions may take place and both forward and backward individual electrode reactions may not take place at significant rates in the potential range where the mixed potential is observed, owing to the slow kinetics of the participating reactions under those conditions.

Figure 10 illustrates the corrosion of two metals, M and M', in aqueous aerated (oxygenated) solutions. Three anodic partial reactions are considered: the active dissolution of two metals M and M' with different kinetics in the absence of their ions in the bulk electrolyte and decomposition of water with the evolution of oxygen. The kinetics of the latter process is so slow on most corroding metals that only at very negative potentials can dissolved oxygen be electroreduced and this eventually becomes limited by mass transport

due to the limited solubility of oxygen in water. At even more negative potentials, hydrogen evolution takes place on the electrode surface. The cathodic reduction of some dissolved metal ions in the solution adjacent to the electrode as a consequence of corrosion is also considered in Fig. 10 but the rate of oxygen reduction is the controlling factor in the overall rate. The measurable current–potential curve results from the balance of the anodic and cathodic processes as indicated by the broken line and the corrosion potential,  $E_M$ , is also shown. Metal M' is more noble than M and is not corroded because the oxygen reduction reaction is far too slow to bring M' to a potential where it can be corroded. Hydrogen evolution is a faster reaction but cannot corrode M' because its equilibrium potential is more negative than  $E_M^e$  and therefore the reaction cannot proceed on M' under those conditions.

It is well known that the reduction of organic molecules such as nitrobenzene

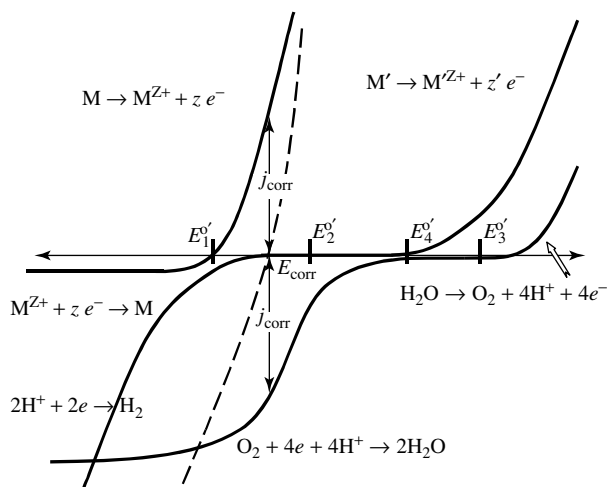


**Fig. 10** Representation of the formation of the corrosion potential,  $E_{\text{corr}}$ , by simultaneous occurrence of metal dissolution, hydrogen evolution, and oxygen reduction. Partial current densities (solid lines) and total current density curve (broken line).

with metals in acid leads to different final products depending on the nature of the metal employed and the composition of the electrolyte. The kinetics of hydrogen evolution, either from proton or from water, as well as the kinetics of dissolution of some metals, particularly those like Zn that can be complexed by  $\text{HO}^-$ , strongly depend on the pH and metal surface; the mixed potential is then fixed by the kinetics of hydrogen reduction and dissolution of the metal, which are relatively fast reactions. Organic electroreductions are slower processes and not likely to be potential-determining reactions, but they proceed through different reaction paths at different potentials depending on the mixed potential of the metal surface.

The theory of mixed potentials is based on the independence of partial anodic and cathodic reactions. However, in real corroding systems, coupling of these reactions, not only through exchanged charge at the interface, may sometimes occur as a result of (1) geometric surface limitations due to the blocking effect of the intermediates of one reaction on the kinetics of others taking place simultaneously at the same electrode surface and (2) changes in local pH due to the fact that some corrosion reactions such as hydrogen evolution may promote changes in the kinetics of other participating reactions.

Electroless deposition of metals like nickel-phosphorus, introduced in 1946 by Brenner and Riddell [55], is of great industrial importance and allows to deposit metals on nonconducting substrates such as printed circuit boards (copper), contacts (silver), and so on. Its mechanism is based on a particular case of mixed-potential where the partial electrode reactions are metal deposition at metal

nuclei and oxidation of organic and inorganic reductants. A quantitative treatment has been derived by Spiro [56] and practical aspects have been recently reviewed by O'Sullivan [57].

### 1.1.13

#### **Electrocrystallization**

The formation or dissolution of a new phase during an electrode reaction such as metal deposition, anodic oxide formation, precipitation of an insoluble salt, and so on involves surface processes other than charge transfer. For example, the incorporation of a deposited metal atom into a stable surface lattice site introduces an extra hindrance to the flow of electric charge at the electrode–solution interface and therefore the kinetics of these electrocrystallization processes are reflected in the overall electrode reaction.

During the initial stages of phase formation at electrodes (nucleation) incorporation of an adsorbed species into the surface lattice occurs only at “active sites” (crystal plane edges or kinks) where interactions with other species already in the lattice are possible. The process of formation of such nuclei may become kinetically limiting and supersaturation or overpotential is required for nuclei to be formed and survive. Depending on the relative time scale of nuclei formation and further growth or thickening of the deposit local potential distribution and mass transport conditions determine the morphology.

If the electrocrystallization is controlled by the formation of two or three-dimensional isolated nuclei, the current–potential relationship has a stronger overpotential dependence than predicted by the Butler–Volmer equation [58],

that is,

$$i = A \exp\left(\frac{B}{\eta^n}\right) \quad (105)$$

with  $n = 2$  for three-dimensional and  $n = 1$  for two-dimensional nucleation. Growth of isolated nuclei at an electrode surface is eventually limited when they start to coalesce due to their number and size and the size of the electrode area.

In metal deposition, depending on the binding energy of the metal to be deposited with respect to the foreign metal substrate, two limiting cases have been observed: (1) formation of structured underpotential deposited layers (upd) and further growth of the bulk metal phase on top of the two-dimension upd layer or (2) deposition in the overpotential region involving relatively few nuclei by three-dimensional nucleation and further growth. The influence of upd ad-atoms on electrode kinetics is treated in Chapter 4.3 and electrochemical nucleation and growth is described in Chapter 5.3.

### Acknowledgments

The author wishes to acknowledge financial support during the preparation of this chapter from Conicet, ANPCyT (Argentina), Fudetec, Motorola SPS, and the Guggenheim Foundation for a fellowship 2000/2001.

### References

1. E. Gileadi, M. Urbakh, (Eds.), *Thermodynamics and Electrified Interfaces*, Vol. 1. EoE, Wiley-VCH, Weinheim, Germany, 2002.
2. A. J. Bard, L. R. Faulkner, *Electrochemical Methods. Fundamentals and Applications*, 2nd ed., Wiley, New York, 2001.
3. H. Gerischer, D. M. Kolb, J. K. Saas, *Adv. Phys.* **1978**, 27, 437.
4. W. J. Albery, *Electrode Kinetics*, Oxford University Press, Clarendon Press, Oxford, 1975.
5. J. O'M. Bockris, K. N. Reddy, *Modern Electrochemistry*, Plenum Press, New York, 1970.
6. B. E. Conway, *Theory and Principles of Electrode Processes*, Ronald Press, New York, 1964.
7. P. Delahay, *Double Layer and Electrode Kinetics*, 2nd edn., Interscience Publishers, New York, 1966.
8. K. J. Vetter, *Electrochemical Kinetics (English Translation)*, Academic Press, New York, 1967.
9. C. M. A. Brett, A. M. Oliveira Brett, *Electrochemistry: Principles, Methods and Applications*, Oxford University Press, Oxford, 1993.
10. E. J. Calvo in *Comprehensive Chemical Kinetics* (Eds.: C. H. Bamford, R. G. Compton), Elsevier, Amsterdam, 1986, Vol. 26.
11. J. Tafel, *Z. Phys. Chem.* **1905**, 50A, 641.
12. J. A. V. Butler, *Trans. Faraday Soc.* **1932**, 28, 379.
13. J. A. V. Butler, *Proc. R. Soc. London, Ser. A* **1936**, 157, 423.
14. T. Erdey-Gruz, M. Volmer, *Z. Phys. Chem. Abt. A* **1931**, 157, 165.
15. R. A. Marcus (Nobel Lecture), *Angew. Chem., Int. Ed. Engl.* **1993**, 32, 1111.
16. R. A. Marcus, *J. Chem. Phys.* **1956**, 24, 966.
17. R. A. Marcus, *Discuss. Faraday Soc.* **1960**, 29, 21.
18. R. A. Marcus, *J. Phys. Chem.* **1963**, 67, 853.
19. R. Marcus, *J. Chem. Phys.*, **1965**, 43679.
20. R. Marcus, *J. Phys. Chem.* **1968**, 72, 891.
21. J. R. Miller, L. T. Calcaterra, G. L. Closs, *J. Am. Chem. Soc.* **1994**, 106, 3047.
22. A. L. Barker, J. V. Macpherson, C. J. Slevin et al., *J. Phys. Chem. B* **1998**, 102, 1586.
23. A. L. Barker, P. R. Unwin, S. Amemiya et al., *J. Phys. Chem. B* **1999**, 103, 7260.
24. M. Tsionsky, A. J. Bard, M. V. Mirkin, *J. Phys. Chem.* **1996**, 100, 17 881.
25. M. Tsionsky, A. J. Bard, M. V. Mirkin, *J. Am. Chem. Soc.* **1997**, 119, 10 785.
26. C. J. Miller in *Physical Electrochemistry, Principles, Methods and Applications* (Ed.: I. Rubinstein), Marcel Dekker, New York, 1995, Chap. 2.
27. H. O. Finklea, *Electroanal. Chem.* **1996**, 19, 109.
28. C. E. D. Chidsey, *J. Am. Chem. Soc.* **1997**, 119, 10 563.
29. S. Creager, S. J. Yu, D. Bamdad et al., *J. Am. Chem. Soc.* **1999**, 121, 1059.
30. R. Holmlin, R. F. Ismagilov, R. Haag et al., *Angew. Chem., Int. Ed.* **2001**, 40, 2316.

31. D. I. Gittins, D. Bethell, D. J. Schiffrin et al., *Nature* **2000**, 408, 67.
32. X. D. Cui, A. Primak, X. Zarate, J. Tomfohr, O. F. Sankey, A. L. Moore, T. A. Moore, D. Gust, G. Harris, S. M. Lindsay, *Science* **2001**, 294, 571.
33. F. F. Fan, J. Y. S. M. Dirk, D. W. Price et al., *J. Am. Chem. Soc.* **2001**, 123, 2454.
34. C. E. D. Chidsey, *Science* **1991**, 251, 919.
35. R. J. Forster, L. R. Faulkner, *J. Am. Chem. Soc.* **1994**, 116, 5444.
36. V. G. Levich in *Physical Chemistry. An Advanced Treatise* (Eds.: H. Eyring, D. Henderson, W. Jost), Academic Press, New York, 1970, pp. 985–1074, Vol. IXB.
37. H. Gerischer, *Adv. Electrochem. Electrochem. Eng.* **1961**, 1, 139.
38. W. Lorenz, *Z. Elektrochem.* **1953**, 57, 382.
39. H. Gerischer, *Z. Elektrochem.* **1953**, 57, 604.
40. K. Heusler, *Electrochim. Acta* **1983**, 28, 439.
41. E. J. M. O'Sullivan, E. J. Calvo in *Reactions at Metal Oxide Electrodes Comprehensive Chemical Kinetics* (Ed.: R. G. Compton), Elsevier, New York, 1987.
42. J. Horiuti, M. Ikusima, *Proc. Imp. Acad. (Tokyo)* **1939**, 15, 39.
43. J. Horiuti, *J. Res. Inst. Catal. Hokkaido Univ.* **1948**, 1, 8.
44. R. Parsons, *Pure Appl. Chem.* **1974**, 37, 501.
45. R. Parsons, *Pure Appl. Chem.* **1979**, 52, 233; reprinted in *Electrochim. Acta* **1981**, 26, 1869.
46. R. Parsons, *Trans. Faraday Soc.* **1951**, 47, 1332.
47. J. E. B. Randles, *Can. J. Chem.* **1959**, 37, 238.
48. J. D. Clark, R. P. Wayne in *Comprehensive Chemical Kinetics* (Eds.: C. H. Bamford, C. F. H. Tipper), Elsevier, Amsterdam, 1969, Vol. 2, Chap. 4, 377–462.
49. A. N. Frumkin, *Z. Phys. Chem.* **1933**, 164, 121.
50. J. Horiuti, M. Polanyi, *Acta Physicochim. URSS* **1935**, 2, 505.
51. J. O'M. Bockris, B. E. Conway, *J. Chem. Phys.* **1956**, 26, 532.
52. P. Ruetschi, P. Delahay, *J. Chem. Phys.* **1955**, 23, 1167.
53. A. J. Appleby, *Mod. Aspects Electrochem.* **1974**, 9, 369.
54. C. Wagner, M. Traud, *Z. Elektrochem.* **1938**, 44, 391.
55. A. Brenner, G. Riddell, *J. Res. Natl. Bur. Stand.* **1946**, 37, 31.
56. M. Spiro, *J. Chem. Soc., Faraday Trans. I* **1979**, 1507.
57. E. J. O'Sullivan in *Advances in Electrochemical Science and Engineering* (Eds.: R. C. Alkire, D. M. Kolb), Wiley-VCH, Weinheim, Germany, 2002.
58. T. Erdey-Gruz, M. Volmer, *Z. Phys. Chem. Abt. A* **1931**, 157, 177.

## 1.2

**Quantum Theory of Electrochemical Electron-Transfer Reactions**

Wolfgang Schmickler and Stefan Frank  
Abteilung Elektrochemie, University of Ulm,  
Ulm, Germany

## 1.2.1

**Introduction**

Electron-transfer reactions are amongst the most important processes in electrochemistry. Indeed, all electrochemical reactions involve an exchange of electrons between a particle and the electrode at some stage. Therefore, electron transfer has been the subject of intensive research ever since the rise of electrochemical kinetics toward the middle of the last century.

Much of our present understanding of electron-transfer reactions rests on concepts that were established in the pioneering papers by Marcus [1] and by Hush [2] in the 1950s. In particular, these works pointed out the important role that the reorganization of the solvent plays. Since that time the theory of these reactions has developed in various directions. A good review of the present state of the theory and its applications to physics, chemistry and biology can be found in the book by Kuznetsov [3]. Here we shall focus on a few topics relevant to electrochemical electron transfer at metal electrodes – semiconductors are treated in a recent monograph by Memming [4].

The formal development of the topic will rest on a model Hamiltonian proposed by one of us in the 1980s. From this we will first derive the Levich and Dogonadze theory [5], which was the first quantum theory for electron transfer in condensed media, and then obtain the classical potential-energy surfaces that are generalizations of those familiar with Marcus and Hush.

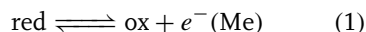
These surfaces will also serve as the basis for a discussion of solvent dynamics. The model Hamiltonian will then be extended to describe bond-breaking reactions, which will conclude the main part of this review. The last section is devoted to computer simulations, which can fill in some of the gaps that are missing in proper theory, and give quantitative results.

In this chapter, we attempt to address a broad audience that comprises both experimentalists and theoreticians. We therefore have to strike a compromise between readability and rigor and will not be able to cover some of the more formal aspects and second-order effects, for which the book by Kuznetsov [3] is a good reference. As an introduction, we start with a simple presentation of the Marcus theory, which should provide the necessary background for the more formal sections.

## 1.2.2

**A Simple Introduction to Marcus Theory**

We consider electron transfer from a metal electrode to a solvated species nearby according to the scheme



At first, we limit ourselves to the so-called *outer sphere* reactions in which chemical bonds are neither formed nor broken. During such a reaction, the charge on the reactant, and hence the configuration of its solvation sheath, changes. The order in which electron transfer and solvent reorganization occur is governed by the Frank–Condon principle: electron transfer is fast and occurs practically at a fixed position of the solvent. Obviously, it would be energetically unfavorable if electron transfer were to take place before

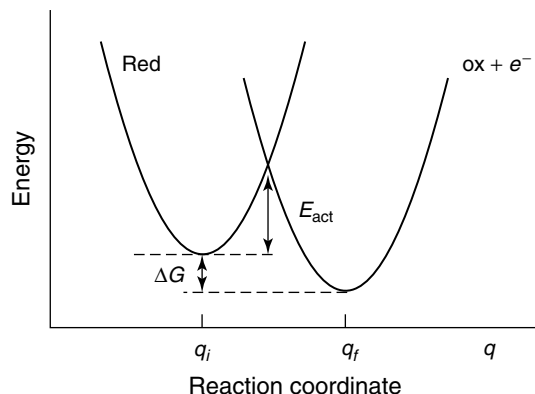


**Fig. 1** Potential energy vs. generalized solvent coordinate  $q$  in Marcus theory.

the solvent had started to reorganize, since the reactant would be surrounded by a solvation sheath pertaining to a different charge. Likewise, a solvent reorganization prior to electron transfer would require high energy, and is equally unlikely. Therefore, the solvation sheath must first take up a configuration between those for the initial and the final charge state, then the electron is transferred, and the system relaxes to its new equilibrium configuration.

These ideas can be put into quantitative terms within a simple, one-dimensional model in which the (free) energy of the system is plotted as a function of a generalized solvent coordinate  $q$  characterizing the solvation of the reactant. There are two such curves (see Fig. 1), one for each side of Eq. (1). Each curve attains its minimum at the equilibrium configuration for the corresponding state. If we develop each curve into a Taylor series about its minimum and keep terms up to second order, we obtain the *harmonic approximation* familiar through many branches of physics and chemistry in which each curve is represented by a parabola. We make the further assumption that the curvatures of both parabolas are equal – this can be

justified within an explicit model for the solvation [6].

The minima for the two parabolas correspond to the equilibrium configurations for the initial and the final states, and the difference between the values at the minima gives the free energy  $\Delta G$ , of the reaction. Changing the electrode potential affects the energy of the transferred electron, and hence  $\Delta G$ . The free energy of activation is the difference between the energies of the crossing point and the minimum of the initial state; it can easily be calculated within the harmonic approximation: Let the two parabolas for the initial ( $i$ ) and the final ( $f$ ) states be

$$\begin{aligned} U_i(q) &= \frac{1}{2}k(q - q_i)^2, \\ U_f(q) &= \frac{1}{2}k(q - q_f)^2 \end{aligned} \quad (2)$$

where  $q_i$  and  $q_f$  denote the two minima. A simple calculation gives, for the energy of activation

$$E_{\text{act}} = \frac{(\lambda + \Delta G)^2}{4\lambda} \quad (3)$$

where

$$\lambda = \frac{1}{2}k(q_i - q_f)^2 \quad (4)$$

is the so-called *energy of reorganization* for the solvent.

The preexponential factor  $Z$  for the rate constant can be calculated from the activated complex or from Kramer's theory (vide infra); it is independent of  $\Delta G$  or, in the electrochemical context, of the overpotential  $\eta$ . Thus, the rate constant can be written as

$$k = Z \exp -\frac{(\lambda + \Delta G)^2}{4\lambda k_B T} \quad (5)$$

where  $k_B$  is the Boltzmann's constant.

This expression gives the rate for a homogeneous electron-transfer reaction; it is usually associated with the name of Marcus, but the independent work of Hush is also equivalent. The sign convention in Eq. (3) is the usual one: a negative sign denotes a lowering of the free energy during the reaction; thus,  $-\Delta G$  measures the driving force for the reaction. An unusual feature is the quadratic dependence of the activation energy on  $\Delta G$ . As long as  $\lambda + \Delta G > 0$ , the reaction gets faster as the driving force increases, but for very large driving forces, where  $\lambda + \Delta G < 0$ , the reaction becomes slower. This is the so-called *inverted region*, whose existence has been established for homogeneous reactions. For reasons that will become apparent below, it cannot be accessed in heterogeneous reactions at metal electrodes.

In order to apply Eq. 5 to electrochemical reactions, we must make two modifications:

1. Equation 5 gives the rate for a reactant sitting at a given distance from the electrode. In order to get the total rate, we must integrate over all distances. Typically, the rate decreases exponentially with the distance, with a decay constant of  $\gamma \approx 1 \text{ \AA}^{-1}$ . Integration, therefore, adds an additional

factor  $C = 1/\kappa \approx 10^{-8} \text{ cm}$  to the pre-exponential factor.

2. For electrochemical reactions at metal electrodes, the reaction-free energy  $\Delta G$ , refers to the exchange with the Fermi level, and can then be related to the overpotential  $\eta$  by  $\Delta G = \pm e_0 \eta$ , where the sign depends on the direction of the current, anodic or cathodic. However, in a reduction reaction the electron can come from any occupied state, and in an oxidation it can be transferred to any empty level. Let us denote by  $\varepsilon$  the energy of a metal electron with respect to the Fermi level, and by  $\rho(\varepsilon)$ , the density of electronic states at the surface. To be specific, we consider electron transfer from the metal to a redox partner in the solution. The free energy for the transfer of an electron with energy  $\varepsilon$  is by an amount  $-\varepsilon$  lower than that for electron transfer from the Fermi level. The probability of finding an electron with that energy is given by  $\rho(\varepsilon)f(\varepsilon)$ , where  $f(\varepsilon)$  is the Fermi-Dirac distribution. Hence, the rate of electron transfer from the metal to the reactant is given by

$$k_{\text{red}} = ZC \int \rho(\varepsilon)f(\varepsilon) \times \exp -\frac{(\lambda - \varepsilon + e_0 \eta)^2}{4\lambda k_B T} d\varepsilon \quad (6)$$

where we have used the fact that a negative overpotential favors a reduction.

Equation (6) has also been derived by Gerischer [7, 8], but with a different interpretation. He defines

$$W_{\text{ox}}(\varepsilon, \eta) = (4\pi\lambda k_B T)^{(-1/2)} \times \exp -\frac{(\lambda - \varepsilon + e_0 \eta)^2}{4\lambda k_B T} \quad (7)$$

as the normalized density of oxidized or empty states in the solution. Since  $\rho(\varepsilon)f(\varepsilon)$  is the density of occupied states on the metal, Eq. (6) can be interpreted in the following way: The rate of exchange of electrons of energy  $\varepsilon$  is proportional to the density of occupied states on the metal times the density of empty states in the solution. Changing the overpotential simply shifts the density of oxidized states with respect to the Fermi level.

The form of Eq. (6), where the total rate is written as an integral over the energy  $\varepsilon$  of the transferring electron is found in several versions of the electron-transfer theory. For future reference, we write it as

$$k_{\text{red}} = ZC \int \rho(\varepsilon)f(\varepsilon)k_{\text{r}}(\varepsilon) d\varepsilon \quad (8)$$

where  $k_{\text{r}}(\varepsilon)$  is the *energy-resolved rate*.

The integration in Eq. (6) is to be performed over the conduction band of the electrode; in practice, it may be extended to  $\pm\infty$ , since the major contribution

to the integral comes from the vicinity of the Fermi level. If the density of states  $\rho(\varepsilon)$  is taken to be a constant, and the Fermi–Dirac distribution replaced by a step function, the integral can be performed explicitly:

$$k_{\text{red}} = ZC\rho\sqrt{\pi\lambda k_{\text{B}}T} \operatorname{erfc}\left(\frac{e_0\eta + \lambda}{(4\lambda k_{\text{B}}T)^{1/2}}\right) \quad (9)$$

Here  $\operatorname{erfc}$  denotes the complement of the error function. Equations (6) and (9) predict rate constants with a transfer coefficient of 1/2 for small overpotentials, and a constant rate  $k_{\text{lim}}$  for high overpotentials (see Fig. 2).

From the form of the current-potential curve, it is clear that the Marcus-inverted region cannot be accessed in a simple redox reaction on a metal electrode. For large overpotentials, the electrons are simply transferred to energy levels above the Fermi level so that the inverted part of the energy-resolved rate plays no role.

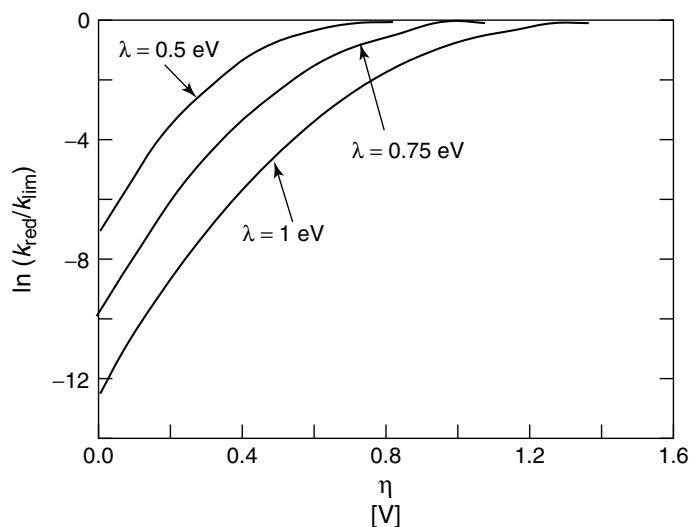


**Fig. 2** Logarithm of the normalized rate constant  $k_{\text{red}}/k_{\text{lim}}$  vs. overpotential for the reduction of a redox couple at a metal electrode according to Marcus theory (Eq. 9).



## 1.2.3

**Energy of Reorganization**

As outlined above, the energy of reorganization plays a major role in the electron-transfer theory. Generally it contains two contributions: one from the surrounding solvent and the other arising from changes in the bond lengths and vibration frequencies of the reacting complex itself. They are also referred to as *outer-sphere* and *inner-sphere* reorganization, respectively.

The reorganization of the solvent can be expressed through its polarization, which also contains two contributions: one from the electronic polarizability of the solvent molecules, and the other from the librational and vibrational motion. Only the latter are slower than the electron exchange as such, and contribute to the solvent reorganization energy  $\lambda_{\text{out}}$ . This takes a form that is reminiscent of the Born formula for the energy of solvation:

$$\lambda_{\text{out}} = \frac{1}{2\epsilon_0} \left( \frac{1}{\epsilon_{\infty}} - \frac{1}{\epsilon_s} \right) \times \int (\mathbf{D}_{\text{ox}} - \mathbf{D}_{\text{red}})^2 dV \quad (10)$$

Here,  $\epsilon_{\infty}$  and  $\epsilon_s$  are the optical and the static dielectric constants of the solution; the former appears because the contribution from the electronic polarizability has been subtracted.  $\mathbf{D}_{\text{ox}}$  and  $\mathbf{D}_{\text{red}}$  are the dielectric displacements when the reactant is in the reduced and in the oxidized form, respectively. The integral is to be performed over the space filled by the solution. When the reactant is close to the electrode surface, image terms arise, which contribute to the displacement.

The energy of reorganization is a molecular concept, and an equation such as (10), which is based on macroscopic electrostatics, can only be a rough approximation. Several other expressions, on the basis

of nonlocal electrostatics or involving the whole frequency spectrum of the dielectric constant, have been suggested, but the best estimates nowadays come from computer simulations.

The contribution from inner-sphere modes are easily obtained within the harmonic approximation. Let  $\Delta q$  be the change in the bond length of a mode with frequency  $\omega$  and effective mass  $m$ ; then its contribution to the energy of reorganization is

$$\lambda_i = \frac{1}{2} m \omega^2 \Delta q^2 \quad (11)$$

When electron transfer is accompanied by a significant change in frequency from  $\omega_1$  to  $\omega_2$ , an effective frequency  $2\omega_1\omega_2/(\omega_1 + \omega_2)$  can be used to a good approximation.

## 1.2.4

**Quantum-mechanical Theory****1.2.4.1 A Model for Electron Exchange Between a Metal and a Solvated Reactant**

Before we set up the model Hamiltonian for electrochemical electron transfer, we have to specify the models for the various parts of the system. For the electrons in the metal, we use the quasi-free electron model in which the electronic states are labeled by their quasi-momentum  $k$ . For outer-sphere electron transfer on metals, it is usually permissible to ignore the spin index – keeping it would introduce an additional factor of two, which can be incorporated into the interaction constants. On the reactant, we consider a single orbital, labeled  $a$ , with which the electrons are exchanged.

An important aspect of electron transfer is the accompanying reorganization of the solvent. The latter can be modeled as a phonon bath, or a collection of harmonic oscillators. Other models in terms of the

solvent polarization [9] or the orientation of the solvent dipoles [10] are equivalent. The formulation in terms of harmonic oscillators has the additional advantage that it is easy to include quantum modes: Most reactions are coupled to a few quantum modes, such as inner-sphere modes of the reactant, or even solvent modes in the first solvation shell [11]. These modes can be included in the collection of harmonic oscillators; of course, in contrast to the classical solvent modes they have to be treated by quantum mechanics.

The solvent modes can be separated into the slow librational and vibrational modes, and the fast electronic modes. Only the slow modes are represented in the phonon bath. The fast modes are supposed to be in electronic equilibrium with the transferring electron so that they simply renormalize the energy of the reactant's electronic states.

#### 1.2.4.2 The Model Hamiltonian

The quantitative formulation of the model outlined above is conveniently written in terms of second quantization. For this purpose, we introduce number operators  $n$  and creation and annihilation operators  $c^+$  and  $c$  for the various electronic states. Then the Hamiltonian takes the form

$$\begin{aligned}
 H = & \varepsilon_a n_a + \sum_k \varepsilon_k n_k + \sum_k [V_k c_k^+ c_a \\
 & + V_k^* c_a^+ c_k] + \frac{1}{2} \sum_v \hbar \omega_v (p_v^2 + q_v^2) \\
 & - n_a \left[ \sum_v \hbar \omega_v g_v q_v \right] \quad (12)
 \end{aligned}$$

The first term describes the electronic state of the reactant with energy  $\varepsilon_a$ , the next term represents the electrons in the metal. Electron exchange between the metal

and the reactant is incorporated in the third term; the amplitudes  $V_k$  characterize the strength of the electronic coupling between the two partners. The fourth term describes the bath of harmonic oscillators;  $q_v$  and  $p_v$  are dimensionless coordinates and momenta, and  $\omega_v$  the frequencies. The summation runs over both the classical solvent modes and over the quantum (inner-sphere) modes. The coupling of the oscillators to the redox couple is assumed to be linear and proportional to the charge, as given in the last term.

This Hamiltonian, which was introduced by Schmickler [12], is equivalent to earlier formulations by Levich and Dogonadze in terms of wave mechanics [5]; it is also related to the spin-boson model for homogeneous electron exchange [13] and to the Anderson-Newns model for specific adsorption [14].

Further treatment of this model depends on the magnitude of the electron-transfer term: if the amplitudes  $V_k$  are small, the first-order perturbation theory can be applied; if they are large, it is better to start from the adiabatic potential-energy surfaces.

#### 1.2.5

##### First-order Perturbation Theory

##### 1.2.5.1 Semiclassical Systems

We next consider the case in which the electron-transfer terms are small so that the first-order perturbation theory can be applied and assuming that all the phonon modes are classical – quantum modes will be considered below. In this case, the coordinates  $q_v$  of the oscillators can be treated as external parameters. It is then convenient to include the electron-phonon coupling – the last term in Eq. (12) – into the electronic energy of the reactant, and rewrite the first and last term as

$\tilde{\varepsilon}_a n_a$ , where

$$\tilde{\varepsilon}_a = \varepsilon_a - \sum_v \hbar \omega_v g_v q_v \quad (13)$$

To first order in the coupling constants  $V_k$ , the rate of electron transfer from a state  $k$  on the metal to the reactant at a given configuration  $q_v$  is given by Fermi's golden rule:

$$W_{ka}(q_v) = \frac{|V_k|^2}{\hbar} \delta(\tilde{\varepsilon}_a - \varepsilon_k) \quad (14)$$

The full derivation of the rate constant for this case can be found in Refs. [6, 15]. Here we list only the main steps involved:

- The delta function in Eq. (14) is replaced by its Fourier transform; this greatly simplifies the mathematics.
- Next the thermal average over all configurations  $q_v$  is performed. This results in an energy-resolved rate for the reduction:

$$k_r(\varepsilon_k) = \frac{|V_k|^2}{\hbar} \left( \frac{\lambda}{4k_B T} \right)^{1/2} \times \exp - \frac{(\varepsilon_a - \varepsilon_k)^2}{4\lambda k_B T} \quad (15)$$

for the rate at a given energy  $\varepsilon_k$ , which is to be compared with Eq. (5) of the simple Marcus theory. Here

$$\lambda = \frac{1}{2} \sum_v \hbar \omega_v g_v^2 \quad (16)$$

is the energy of reorganization of the phonon bath. Thus, in the semiclassical case the coupling to the bath is characterized by a single constant.

- To get the total rate, we have to sum over all occupied levels on the metal. This sum is converted into an integral:

$$\sum_{k, \text{occ.}} \mapsto \int d\varepsilon f(\varepsilon) \rho(\varepsilon) \quad (17)$$

- Finally, we relate  $\varepsilon_a$  to the overpotential  $\eta$  by noting that for  $\eta = 0$  the forward and backward rate must be equal; this gives:  $\varepsilon_a = \lambda + e_0 \eta$ . Further, we introduce the factor  $C$  converting bulk to surface concentrations (see Sect. 1.2.2), and take the coupling elements  $V_k$  as constant.

This procedure results in the following expression for the electrochemical rate constant for the reduction:

$$k_{\text{red}} = C \frac{|V_k|^2}{h} \left( \frac{\pi}{\lambda k_B T} \right)^{1/2} \times \int \rho(\varepsilon) f(\varepsilon) \exp - \frac{(\lambda - \varepsilon + e_0 \eta)^2}{4\lambda k_B T} \quad (18)$$

which differs from the Marcus–Hush expression in the preexponential factor, which is here determined by the square of the transition amplitude  $V_k$ . This is characteristic for the nonadiabatic, weak coupling case. Solvent dynamics, which is so important for the adiabatic, strong coupling case plays no role.

#### 1.2.5.2 Quantum Modes

When quantum modes are reorganized during the electron exchange, they have to be treated separately from the classical modes. We consider explicitly the case in which one such mode is present; the generalization to many modes is straightforward, though it results in rather cumbersome formulae.

The situation is simplest if the frequency  $\omega_i$  of the quantum mode is so high that its quantum of energy is much higher than the thermal energy,  $\hbar \omega_i \gg kT$ , so that it is not excited in the initial state. In this case, we only have to consider transitions from the ground state 0 to the  $n$ th excited state. Let

$$M_{0n} = |\langle \psi_0^i | \psi_n^f \rangle|^2 = \frac{1}{n!} \left( \frac{\lambda_i}{\hbar \omega_i} \right)^n \times \exp - \frac{\lambda_i}{\hbar \omega_i} \quad (19)$$

be the Frank–Condon factors for these transitions. Here,  $\psi_n^i, \psi_n^f$  are the vibronic wave functions for the initial and final states;  $\lambda_i$  is the energy of reorganization pertaining to the quantum mode. The rate of electron transfer involving the transition  $0 \rightarrow n$  is then obtained by multiplying the classical rate of Eq. (17) by the corresponding Frank–Condon factor, and by noting that the energy  $n\hbar\omega_i$ , which goes into the excitation of the quantum mode, is no longer available for the classical reorganization. The energy-reduced rate for the reduction is then

$$k_r(0 \rightarrow n) = M_{0n} \frac{|V_k|^2}{\hbar} \left( \frac{\pi}{\lambda k_B T} \right)^{1/2} \times \exp - \frac{(\lambda + n\hbar\omega_i - e_0\eta)^2}{4\lambda k_B T} \quad (20)$$

The total rate is obtained by summing over all final states  $n$ :

$$k_r = \sum_n k_r(0 \rightarrow n) \quad (21)$$

As long as  $e_0\eta < \hbar\omega$ , transitions from ground state to ground state dominate.

When the quantum of energy is of the same order of magnitude as the thermal energy,  $\hbar\omega \approx kT$ , we have to consider transitions from excited initial states  $m$  to final states  $n$ , and perform a thermal average over the initial states of the quantum modes:

$$k_r = \left\langle M_{mn} \frac{|V_k|^2}{\hbar} (\pi/\lambda k_B T)^{1/2} \times \exp - \frac{(\lambda + (n - m)\hbar\omega_i - e_0\eta)^2}{4\lambda k_B T} \right\rangle \quad (22)$$

where  $\langle \dots \rangle$  denotes a thermal average. A good general treatment of reactions involving quantum modes has been given by Tanaka and Hsu [16].

### 1.2.6 Adiabatic Reactions

When the electronic interaction is large, perturbation theory does not suffice. We consider the adiabatic limit in which the system is always in electronic equilibrium – the general case of an interaction with an intermediate strength has not yet been solved – and construct the potential-energy surface for the reaction.

The electronic interaction with the metal induces a broadening  $\Delta$  of the electronic level of the redox partner, which is determined by the matrix elements  $V_k$ :

$$\Delta = \pi \sum_k |V_k|^2 \delta(\omega - \varepsilon_k) \quad (23)$$

In principle,  $\Delta$  is a function of the electronic energy  $\varepsilon$ . When the reactant interacts with a broad electronic band, the width  $\Delta$  usually does not vary much in the relevant region near the Fermi level and can be taken as constant; this is the so-called *wide-band approximation*, which will be used here.

So far the adiabatic case has only been fully worked out for the semiclassical case in which quantum modes play no role. In this case, it is again convenient to use the  $q$ -dependent electronic energy  $\tilde{\varepsilon}_a$  introduced in Eq. (13). In the wide-band approximation, the broadening of this energy level takes the form of a Lorentzian so that its density of states becomes

$$\rho(\omega) = \frac{2\Delta}{[\omega - \tilde{\varepsilon}(q_v)]^2 + \Delta^2} \quad (24)$$

The reactant orbital is filled only partially up to the Fermi level of the metal, and its occupancy is given by

$$n(q_v) \equiv \langle n_a(q_v) \rangle = \frac{1}{\pi} \operatorname{arccot} \frac{\tilde{\varepsilon}_a}{\Delta} \quad (25)$$

where the Fermi level has been taken as the energy zero. The potential energy of the system, as a function of the coordinates  $q_v$ , is then

$$E[q_v] = \tilde{\varepsilon}_a n(q_v) + \frac{1}{2} \sum_v \hbar \omega_v q_v^2 + \frac{\Delta}{2\pi} \ln(\tilde{\varepsilon}_a^2 + \Delta^2) \quad (26)$$

where a constant term has been neglected.

With the aid of Eqs. (25 and 26) the potential energy of the system can be calculated as a function of the coordinates  $q_v$ . Of particular interest are the stationary points of this curve, at which the occupancy of the reactant obeys the self-consistency equation:

$$n^0 = \frac{1}{\pi} \operatorname{arccot} \frac{\varepsilon_a n_a - 2\lambda n^0}{\Delta} \quad (27)$$

which must be solved numerically. Depending on the values of the system parameters, this equation has either one or three solutions [17]. In the case in which the system is not too far from equilibrium, they can be stated in the following form:

- When the electronic interaction  $\Delta$  is large and the energy of reorganization  $\lambda$  is small, there is only one stationary state. This corresponds to an adsorbed state, which sits in a single potential well on the electrode surface.
- When the electronic interaction is weak and the energy of reorganization is large, there are three stationary solutions: two minima separated by a barrier. The two minima correspond to two different

charge states of the reactant. In an electron-transfer reaction, the system moves from one minimum via the barrier to the other minimum.

In mathematical terms, three stationary points exist if both the conditions

$$\frac{2\lambda}{\pi \Delta} > 1 \quad (28)$$

$$|\varepsilon - \lambda| \leq \frac{2\lambda}{\pi} |\arccos(\gamma) - \gamma(1 - \gamma^2)^{1/2}| \quad (29)$$

are fulfilled, where  $\gamma^2 = \pi \Delta / 2\lambda$ .

Within this formalism, it is in principle possible to calculate the potential-energy surfaces for electron-transfer reactions [17]. The important system parameters are  $\lambda$ ,  $\Delta$  and  $\varepsilon_a$ ; they can be estimated from quantum chemical calculations and computer simulations. At present, such surfaces involve fairly rough approximations; however, they are useful visualizations for understanding the dynamics of electron-transfer reactions. It is convenient to restrict the system to a minimum set of coordinates using a generalized solvent coordinate that follows a reaction path from one minimum of the surface via a saddle point to the other minimum. This coordinate can be normalized in such a way that its value at the two minima corresponds to the charge on the reactant in these configurations [18]. It, then, is identical to the reaction coordinate in the theory of Hush [2]. If quantum modes are reorganized during the electron transfer – typically, these would be inner-sphere modes – they have to be singled out and treated separately.

Figure 3 shows an adiabatic potential-energy surface for one single solvent coordinate  $q$ . Two minima are separated by a barrier. This barrier is the lower and the flatter the larger the electronic coupling between the reactant and the metal. For

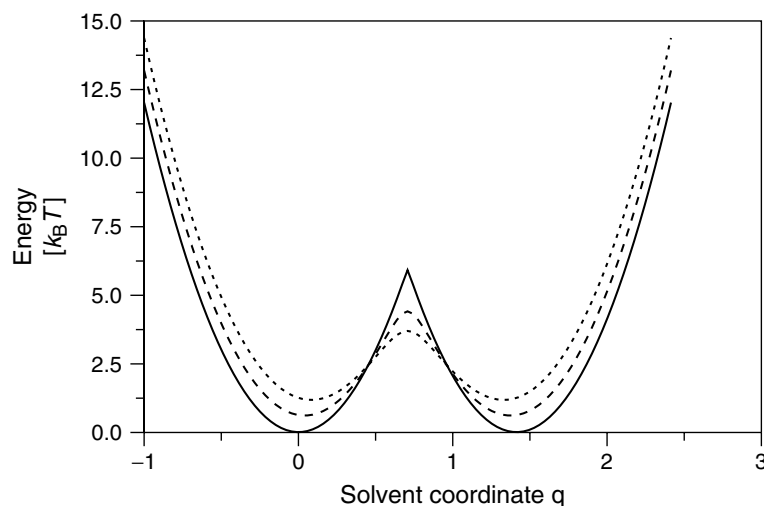


**Fig. 3** Adiabatic potential-energy curves for various values of the energy broadening  $\Delta$ ; full line:  $\Delta = 0.01$  eV; long dashes:  $\Delta = 0.05$  eV; short dashes:  $\Delta = 0.1$  eV. The energy of reorganization was taken as  $6 k_B T$ .

the lowest coupling shown, the surface resembles two intersecting parabola. This is the weakly adiabatic regime in which the electronic coupling is strong enough to establish electronic equilibrium, but too weak to lower the barrier.

#### 1.2.7

##### Solvent Dynamics

In the nonadiabatic case, electron transfer is a rare event. Therefore, the equilibrium distribution in the initial well is undisturbed, and the preexponential factor is determined by the electronic coupling between the reactants. In adiabatic reactions, the electronic system is in equilibrium at all points of the trajectory; therefore, the rate is not limited by electron transfer but by solvent dynamics.

The main points can be explained within the one-dimensional model outlined in the preceding section in which the free energy is taken to be a function of a generalized solvent coordinate – the two-dimensional

case involving an inner-sphere mode has been treated, amongst others, by Sumi and Marcus [19]. The simplest estimate for the rate of an adiabatic reaction is based on the transition-state theory. If the potential-energy well of the initial state is approximated by a harmonic oscillator of frequency  $\omega_i$ , the rate in that theory is given by

$$k = \frac{\omega_i}{2\pi} \exp -\frac{E_{\text{act}}}{k_B T} \quad (30)$$

where  $E_{\text{act}}$  is the energy of activation. However, as was pointed out by Kramers [20], the transition-state theory overestimates the rate since the population at the barrier may be depleted, and also because a system that has passed the saddle point can return, a phenomenon denoted as *barrier recrossing*. These effects can be described in terms of the *solvent friction*, which encompasses the influence of all the solvent modes that are not explicitly considered in the one-dimensional model. As a result, the preexponential factor is modified by an

additional transition factor:

$$\kappa = \frac{(\gamma^2/4 + \omega_b^2)^{1/2} - \gamma/2}{\omega_b} \quad (31)$$

where  $\gamma$  is the friction coefficient, and  $\omega_b$  is the barrier frequency obtained by approximating the barrier region by an inverted parabola. In effect, Eq. (31) describes a competition between the force exerted by the barrier, which is determined by  $\omega_b$  and the stochastic interaction with the surrounding bath characterized by  $\gamma$ . When the friction is weak,  $\gamma \ll \omega_b$ , the transition factor reduces to unity, and the transition-state theory holds. In the opposite limit, the case of strong friction, the transition factor simplifies to

$$\kappa = \frac{\gamma}{2\omega_b} \quad (32)$$

For electron transfer in solutions, it is often assumed that the strong friction limit holds. The friction coefficient has been identified with the inverse of the longitudinal relaxation time:

$$\gamma = \frac{1}{\tau_l}, \quad \text{where} \quad \tau_l = \frac{\varepsilon_\infty}{\varepsilon_s} \tau_D \quad (33)$$

and  $\tau_D$  is the usual relaxation time.

### 1.2.8

#### Computer Simulations

We have already emphasized the important role of the solvent dynamics and structure in the kinetics of electron-transfer reactions. During the last few years, a number of classical molecular dynamic (MD) simulations have been performed to obtain free energy surfaces of the reaction [21–27]. These simulations require explicit interaction potentials between the constituents of the system: the reactants, the solvent, and the electrode. Again, a generalized solvent coordinate is used to

represent the results; however, instead of the coordinate  $q$  defined in Sect. 1.2.6 most researchers use an electronic shift  $\delta E = -2\lambda q$ . As electron transfer requires relatively large fluctuations of the ion solvation, umbrella sampling techniques must be applied and in most cases it is not possible to obtain the electron-transfer rates directly from the MD trajectories. Instead, one applies transition-state theory or performs simulations near the saddle point in order to explore solvent dynamics near the barrier.

Rose and Benjamin [22] have computed the diabatic free energy surface of the redox pair  $\text{Fe}^{2+}/\text{Fe}^{3+}$  at a fixed distance from a Pt(100) surface (Fig. 4). Differences to a parabolic representation of the free energy are only significant far from equilibrium, which affects the reorganization energy  $\lambda$ , but hardly affects the free activation energy. In contradiction to a common assumption, the curvature at the potential minimum for the oxidized and the reduced states are slightly different. Both the electron-transfer rate  $k$  and the transfer coefficient  $\alpha$  depend on the applied overpotential  $\eta$ . In the regime of strong electronic coupling, they elucidate a classical transmission coefficient  $\kappa$  in agreement with Grote–Hynes theory [28], which is a generalization of Kramer’s theory; in particular,  $\kappa$  increases as the barrier becomes sharper.

Smith and Halley [23] performed simulations on a similar system for various fixed distances between the ion and the metal surface. They found a weak dependence of the reorganization energy on the separation, but strong variations of the thermodynamic driving force; even the direction of the reaction changed when the ion was moved away from the surface. Since their model includes an external electric field, but no realistic screening,

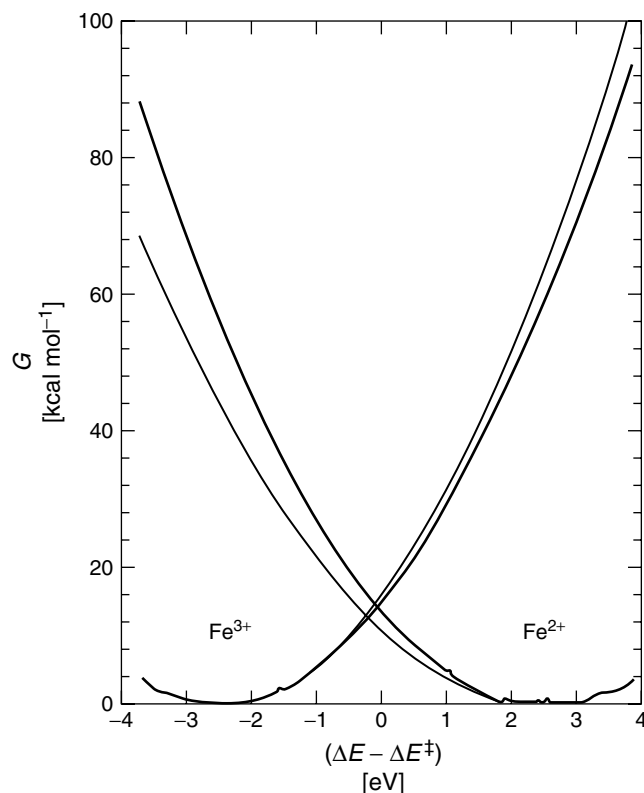


**Fig. 4** Diabatic solvent reorganization free energy curves for  $\text{Fe}^{2+}$  and  $\text{Fe}^{3+}$  [22]. The bold solid lines represent the molecular dynamics result, the thin solid lines the best parabolic fit of the region, near the bottom of each well.

it is difficult to assess the significance of their results. We note that their results contradict an earlier work of Straus and Voth [21].

In a series of publications, Voth and coworkers [21, 24, 25, 26, 27] explored various aspects of electron-transfer reactions. Their calculations are based on a version of the Anderson–Newns Hamiltonian presented in Sect. 1.2.4.2, which allows the direct computation of adiabatic free energy surfaces. For a  $\text{Fe}^{2+}/\text{Fe}^{3+}$  couple at a fixed distance to a Pt(111) surface, they compared a classical and a quantized water model [24]. The quantization

of the high-frequency degrees of freedom of water leads to a major shift in the thermodynamic driving force, and hence, in the solvation of the redox couple. Remarkably, the reorganization energy  $\lambda$  is almost unaffected; this means that the activation energy at equilibrium does not change, but only the equilibrium potential (Fig. 5). When the constraint of a fixed ion position is released and the ion is allowed to move [25], the adiabatic free energy surface is still very similar to the earlier case, but the barrier close to equilibrium is slightly higher. The ion is on average further away from the surface, weakening



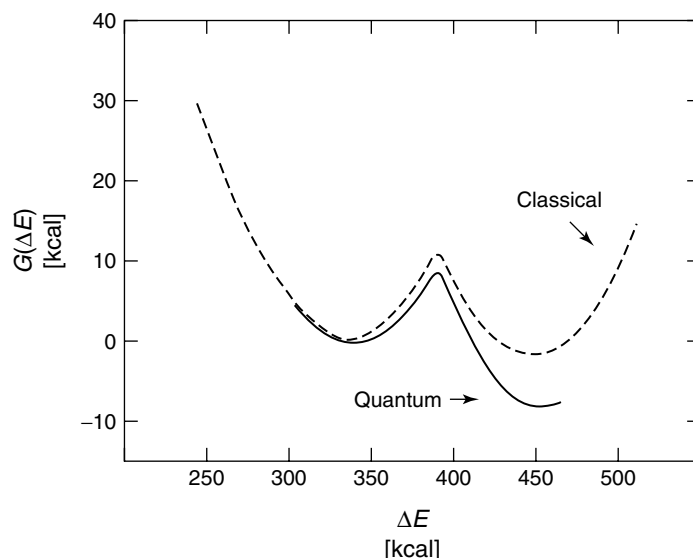


**Fig. 5** Adiabatic free energy curves for the  $\text{Fe}^{2+}/\text{Fe}^{3+}$  couple from molecular dynamics [25]. The solid line represents results for the quantized high-frequency degrees of water, the dashed line for the classical degrees of freedom only.

the electronic coupling. When the ion is moved away from the surface, the thermodynamic driving force can change for the same reason. The presence of a counterion causes nonmonotonical shifts in the barrier height and driving force depending on the separation of the two ions. For short distances, the reorganization energy is markedly increased. The influence of the electronic polarizability has been investigated for a  $\text{Na}^0/\text{Na}^{+1}$  couple by introducing a fluctuating charge on the water molecules [26]. The electronic polarizability causes a stronger solvation of the ion and a lower reorganization energy  $\lambda$ . The polarizable water can accommodate the change of the ion charge to some extent and less solvent reorganization is needed. Also, changes in the thermodynamic driving force are observed. For two different neutral redox species [27], the free energy surface shows four distinct wells, one

for the uncharged reactants, two for the transfer of an electron to one of the reactants, the other remaining neutral, and one for the transfer of one electron to each of the reactants (Fig. 6). Agreement with an analytic model for such a process [29] is satisfying, showing similar trends in the driving force of the elementary steps.

The solvent dynamics of a one-dimensional system was explored by Kuznetsov and Schmickler [30]. They singled out one important solvent coordinate and represented all the others by a heat bath. This is a similar concept to analytical theories such as Kramer's [20]. Adiabatic potential-energy surfaces were calculated from the Anderson–Newns Hamiltonian (see Fig. 3). The result is a symmetric double well, the barrier being the lower and the less sharp, the higher the electronic coupling  $\Delta$ . MD-simulations of a motion on this surface coupled to the heat bath

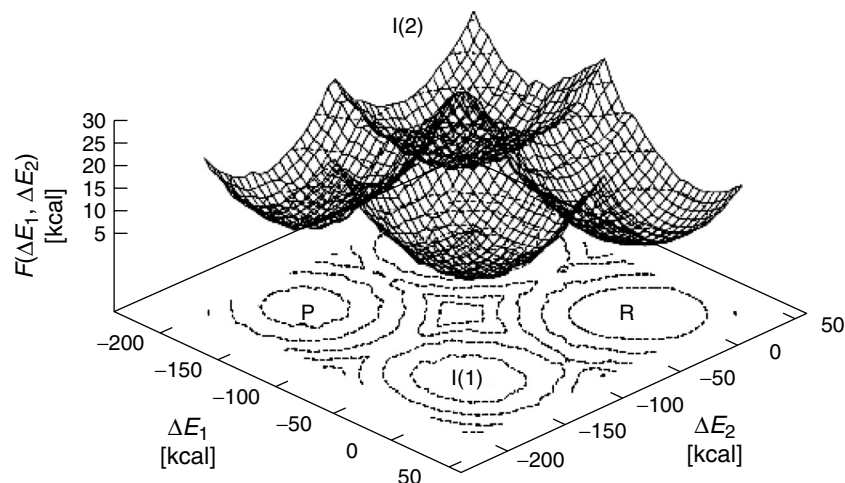


**Fig. 6** Adiabatic free energy surface for the electron transfer between two different redox couples and a metal electrode from molecular dynamic simulations [27].

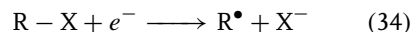
were performed. The time that was needed to cross the transition state starting from the reactant well with thermal velocity yields the reaction rate. The higher the friction exerted by the heat bath, the more the motion resembles a random walk, and the more likely is barrier recrossing (Fig. 7). The authors compare the reaction rates to the predictions of transition-state theory, and obtain a transmission coefficient  $\kappa$ . The results are in qualitative, but not in quantitative agreement with Kramer's theory [20].

#### 1.2.9

##### Bond Breaking Reactions

The models presented in the preceding section consider only elementary electron-transfer steps. In the same sense, many theories such as those of Marcus and Hush are restricted to outer-sphere reactions. For homogeneous electron transfer, bond breaking was considered in early papers by German and Dogonadze [31], and later by German and Kuznetsov [32]. For

electrochemical reactions, bond breaking was introduced into the Marcus–Hush framework by Savéant [33, 34]. Koper and Voth [35, 36] reformulated these ideas in terms of an extension of the model Hamiltonian of Eq. (12). The model applies to a reaction of the type:



Typically, R is an organic fragment, and  $\text{X}^-$  a halide anion. The electron-transfer step and bond breaking are assumed to be concerted; an example for such a reaction is the reductive cleavage of alkyl halides. The authors present both an analytical theory, [35] and molecular dynamic computer simulations [36], and calculate adiabatic energy surfaces. In both cases, the bond breaking is introduced in a similar way following Savéant's ideas. The  $\text{R} - \text{X}$  bond is described by a Morse potential, the interaction between the fragments R and  $\text{X}^-$  is described by the repulsive part of the same Morse potential. The following term is added to the Anderson–Newns Hamiltonian:

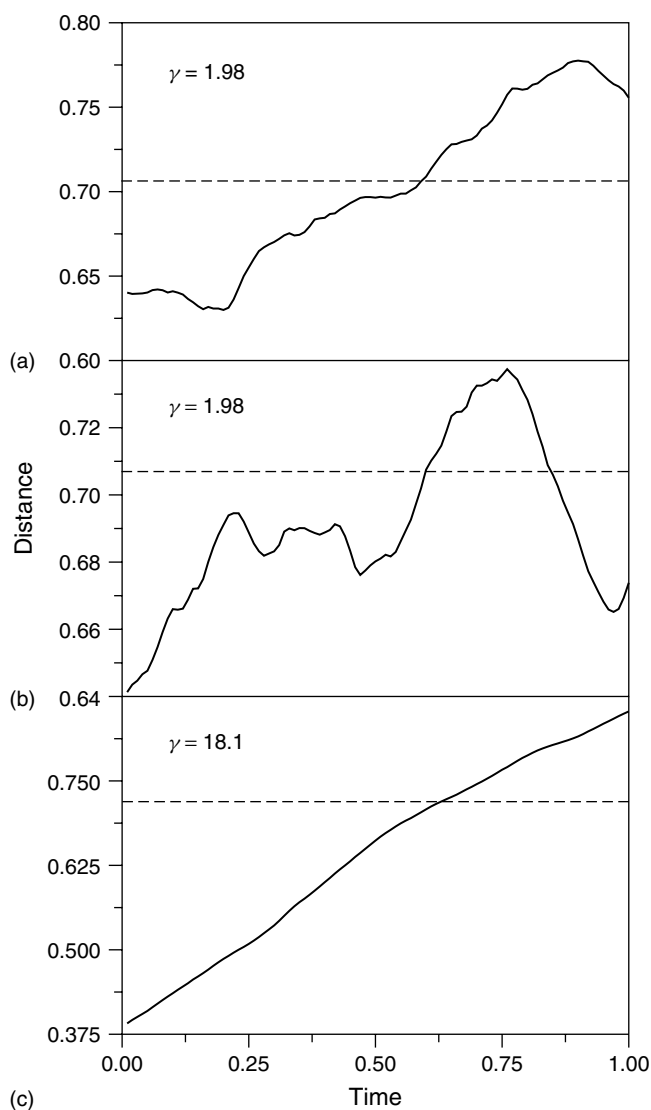


**Fig. 7** Molecular dynamic trajectories of a particle coupled to a heat bath on the potential-energy surface of Fig. 1. The saddle point is indicated by the dashed line. (a) and (b) are for relatively high friction and (c) low friction.  $\Delta = 0.05$  eV. The unit of time has been chosen such that the period of the harmonic oscillator is  $2\pi$ , and the friction coefficient  $\gamma$  is given in terms of this unit.

$$H_{\text{RX}} = (1 - n_a)D\{1 - \exp[-\kappa(r - r_0)]\}^2 + n_aD \exp[-2\kappa(r - r_0)] \quad (35)$$

where  $D$  is the dissociation energy of the bond, and  $r_0$  its equilibrium distance. The parameter  $\kappa$  determines the vibration frequencies and the anharmonicity. Since the bond is broken when the orbital  $a$  is occupied, that orbital is antibonding. All vibrations are assumed to be classical. The potential-energy surface calculated from analytical theory [35] for small electronic coupling  $\Delta$  shows a distinct well for the reactants and an exit channel for the products; both are separated by a saddle. These qualitative features are found again on the free energy surface calculated from MD simulations [36]; however, there are qualitative differences (Fig. 8). The product exit channel shows a shallow well for short distances between the fragments. This is a consequence of the microscopic solvation effects, which are not included in the analytical theory. However, the barrier that has to be overcome to separate the products is much lower than the barrier for the electron-transfer reaction itself, so fragment dissociation is never the rate-limiting step. Comparison to a linear response model on the basis of the results of the analytical theory, show quantitative deviations for the minima and curvature of the surface, as well as for the overpotential. These differences arise from nonlinear response of the solvent to the change in the charge on the redox center and the volume exclusion of the R fragment. Thus, the analytical theory gives rather a rough qualitative picture, but serves as a helpful visualization of the basic characteristics of the reaction.

The case of weak coupling, in which the first-order perturbation theory applies, was explored by Schmickler [37]. For the parameters chosen, the major contribution to the reaction rate comes from the

ground state of the bonding mode, but the energy of the final state is much larger than the thermal energy  $k_B T$ . This is energetically unfavorable, but the overlap with higher energetic states is better. As a consequence, the transfer coefficient  $\alpha$  at equilibrium is larger than 1/2. At higher overpotentials,  $\alpha$  approaches 0 as familiar from outer-sphere electron-transfer reactions. In comparison to Savéant's theory, the activation energy is smaller owing to the inclusion of tunneling effects.

#### 1.2.10

#### Conclusion

After fifty years of research, the theory of electrochemical electron-transfer reactions is well developed, and has provided us with a basic understanding of the essentials. However, a number of important questions are still open, and remain the subject of ongoing research. We list what we believe to be the most important points:

- At present, we have a theory for weak coupling on the basis of first-order perturbation, and for strong coupling, on the basis of the adiabatic limit. However, the intermediate case is unexplored; in particular, we do not fully know how the rate constant will behave as a function of the electronic coupling. A recent paper by Mohr and Schmickler [38] investigates this behavior, but the effects of solvent dynamics are not included in this work so that it will apply to very short timescales only.
- Although computer simulations have provided us with some insights into deviations from the harmonic approximation, much more work needs to be done in order to provide us with accurate potential-energy surfaces, and

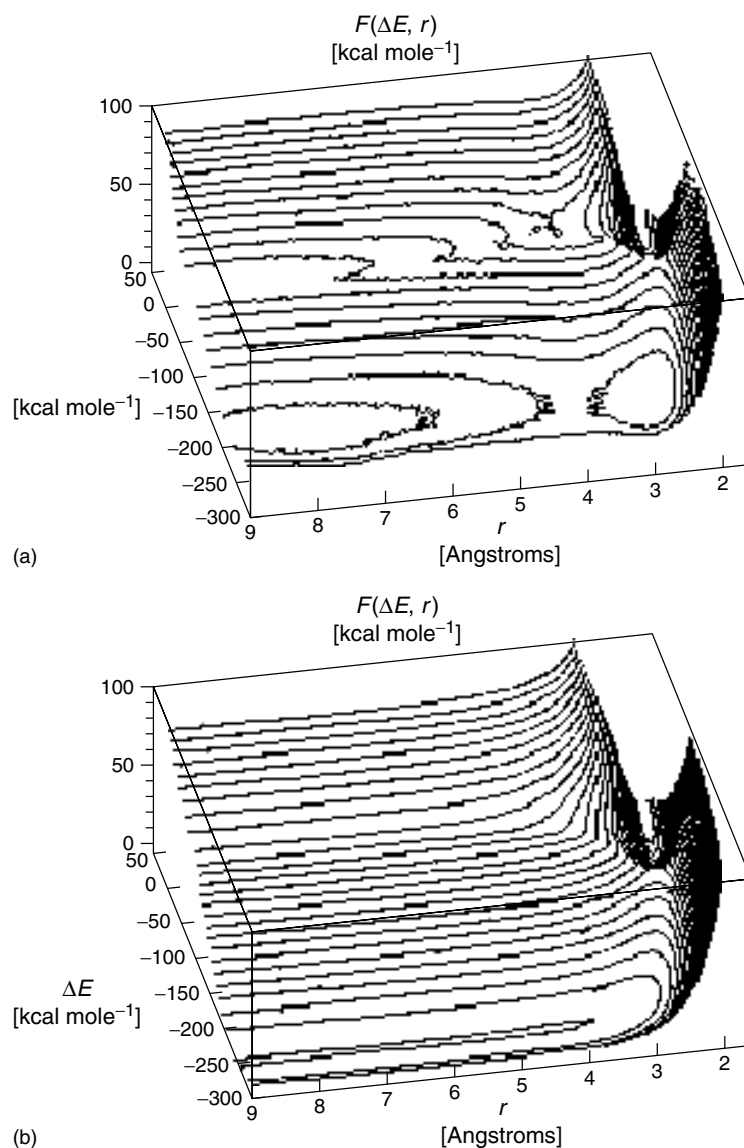


**Fig. 8** Adiabatic free energy surface for simultaneous electron transfer and bond breaking from MD simulations (upper) and a linear response solvent model (lower panel) [36].

also to explore subtle effects such as the variation of the electronic overlap with electrode potential.

- Solvent dynamics have been explored mainly within a wholly classical context;

its effect on quantum modes remains unexplored.

- During the last decade, long-range electron transfer along molecular chains has become very interesting, not least

because of its application to biological systems. While the superexchange theory [39, 40] is a good first approximation, it leaves many questions, in particular, the coupling to solvent and vibrational modes, open.

With these and other problems still open, the electron-transfer theory remains a vibrant field in physics, chemistry and biology alike.

### Acknowledgment

Financial support by the Volkswagenstiftung is gratefully acknowledged.

### References

1. R. A. Marcus, *J. Chem. Phys.* **1956**, 24, 966.
2. N. S. Hush, *J. Chem. Phys.* **1958**, 28, 962.
3. A. N. Kuznetsov, *Charge Transfer in Physics, Chemistry and Biology*, Gordon & Breach, Longhorne, Pa., 1995.
4. R. Memming, *Semiconductor Electrochemistry*, Wiley-VCH, Weinheim, Germany, 2000.
5. V. G. Levich, Kinetics of reactions with charge transport in *Physical Chemistry, An Advanced Treatise* (Eds.: H. Eyring, D. Henderson, W. Jost), Academic Press, New York, 1970, Vol. IXb, pp. 986–1014.
6. W. Schmickler, *Interfacial Electrochemistry*, Oxford University Press, New York, 1996.
7. H. Gerischer, *Z. Phys. Chem. N.F.* **1960**, 26, 223.
8. H. Gerischer, *Z. Phys. Chem. N.F.* **1961**, 27, 40, 48.
9. R. R. Dogonadze, Theory of molecular electrode kinetics in *Reactions of Molecules at Electrodes* (Ed.: N. S. Hush), Wiley-Interscience, London, 1971, pp. 135–227.
10. W. Schmickler, *Ber. Bunsen-Ges. Phys. Chem.* **1976**, 80, 834.
11. J. S. Bader, R. A. Kuharski, D. Chandler, *J. Chem. Phys.* **1990**, 93, 230.
12. W. Schmickler, *J. Electroanal. Chem.* **1986**, 204, 31.
13. A. J. Leggett, S. Chakravarty, A. T. Dorsey et al., *Rev. Mod. Phys.* **1987**, 59, 1.
14. D. M. Newns, *Phys. Rev.* **1969**, 178, 1123.
15. P. P. Schmidt, *Specialist Periodical Reports, Electrochemistry*, The Chemical Society, London, 1975, Vol. 5, pp. 21–131.
16. S. Tanaka, C.-P. Hsu, *J. Chem. Phys.* **1999**, 111, 11 117.
17. W. Schmickler, *Chem. Phys. Lett.* **1995**, 237, 152.
18. W. Schmickler, *Electrochim. Acta* **1996**, 41, 2329.
19. H. Sumi, R. Marcus, *J. Chem. Phys.* **1986**, 84, 4894.
20. H. A. Kramers, *Physica* **1940**, 7, 284.
21. J. B. Straus, G. A. Voth, *J. Phys. Chem.* **1993**, 97, 7388.
22. D. A. Rose, I. Benjamin, *J. Chem. Phys.* **1994**, 100, 3545.
23. B. B. Smith, J. W. Halley, *J. Chem. Phys.* **1994**, 101, 10 915.
24. J. B. Straus, A. Calhoun, G. A. Voth, *J. Chem. Phys.* **1995**, 102, 529.
25. A. Calhoun, G. A. Voth, *J. Phys. Chem.* **1996**, 100, 10 746.
26. A. Calhoun, G. A. Voth, *J. Electroanal. Chem.* **1998**, 450, 253.
27. A. Calhoun, G. A. Voth, *J. Chem. Phys.* **1998**, 109, 4569.
28. R. F. Grote, J. T. Hynes, *J. Chem. Phys.* **1980**, 95, 2715.
29. Y. G. Boroda, A. Calhoun, G. A. Voth, *J. Chem. Phys.* **1997**, 107, 8940.
30. A. M. Kuznetsov, W. Schmickler, *Chem. Phys. Lett.* **2000**, 327, 314.
31. E. D. German, R. R. Dogonadze, *Int. J. Chem. Kinet.* **1974**, 6, 467.
32. E. D. German, A. M. Kuznetsov, *J. Phys. Chem.* **1994**, 98, 6120.
33. J. M. Savéant, *J. Am. Chem. Soc.* **1987**, 109, 6788.
34. J. M. Savéant, *Acc. Chem. Res.* **1993**, 26, 455.
35. M. T. M. Koper, G. A. Voth, *Chem. Phys. Lett.* **1998**, 282, 100.
36. A. Calhoun, M. T. M. Koper, G. A. Voth, *J. Phys. Chem. B* **1999**, 103, 3442.
37. W. Schmickler, *Chem. Phys. Lett.* **2000**, 317, 458.
38. J. H. Mohr, W. Schmickler, *Phys. Rev. Lett.* **2000**, 84, 1051.
39. H. Taube, *Electron Transfer Reactions of Complex Ions in Solutions*, Academic Press, New York, 1970.
40. D. N. Beratan, J. J. Hopfield, *J. Am. Chem. Soc.* **1984**, 106, 1584.

### 1.3 Electronic Tunnel Factors in Molecular Electron Transfer and Molecular Conduction

*Abraham Nitzan  
Tel Aviv University, Tel-Aviv, Israel*

#### Abstract

Electron transmission through molecules and molecular interfaces has been a subject of intensive research owing to recent interest in electron transfer phenomena underlying the operation of the scanning tunneling microscope (STM) on one hand, and in the transmission properties of molecular bridges between conducting leads, on the other. In these processes, the traditional molecular view of electron transfer between donor and acceptor species give rise to a novel view of the molecule as a current carrying conductor, and observables such as electron transfer rates and yields are replaced by the conductivities, or more generally by current–voltage relationships, in molecular junctions. Such investigations of electrical junctions in which single molecules or small molecular assemblies operate as conductors, constitute a major part of what has become the active field of molecular electronics.

In this chapter, the author reviews the current knowledge and understanding of this field with particular emphasis on theoretical issues, and on the relationship between this new look at electron transfer phenomena and the traditional study of molecular electron transfer in solution. Different approaches to computing the conduction properties of molecules and molecular assemblies are reviewed, and the relationships between them is discussed.

#### 1.3.1 Introduction

Electron transfer, a fundamental chemical process underlying all redox reactions, has been under experimental and theoretical study for many years [1–6]. Theoretical studies of such processes seek to understand the ways in which their rate depends on donor and acceptor properties, on the solvent, and on the electronic coupling between the states involved. The different roles played by these factors and the way they affect qualitative and quantitative aspects of the electron transfer process have been thoroughly discussed in the past half-century. This kind of processes, which dominate electron transitions in molecular systems, is to be contrasted with electron transport in the solid state, that is, in metals and semiconductors. Electrochemical reactions that involve both molecular and solid-state donor/acceptor systems, bridge the gap between these phenomena [6]. Here, electron transfer takes place between quasi-free electronic states on one side, and bound molecular electronic states on the other.

The focus of the present discussion is another class of electron transfer phenomena: electron transmission between two regions of free or quasi-free electrons through molecules and molecular layers. Examples for such processes are photoemission (PE) through molecular overlayers, the inverse process of low energy electron transmission (LEET) into metals through adsorbed molecular layers and electron transfer between metal, and/or semiconductor contacts, through molecular spacers. Figure 1 depicts a schematic view of such systems. The “standard” electron transfer model in Fig. 1(a) shows donor and acceptor sites connected by a molecular bridge. In Fig. 1(b), the donor

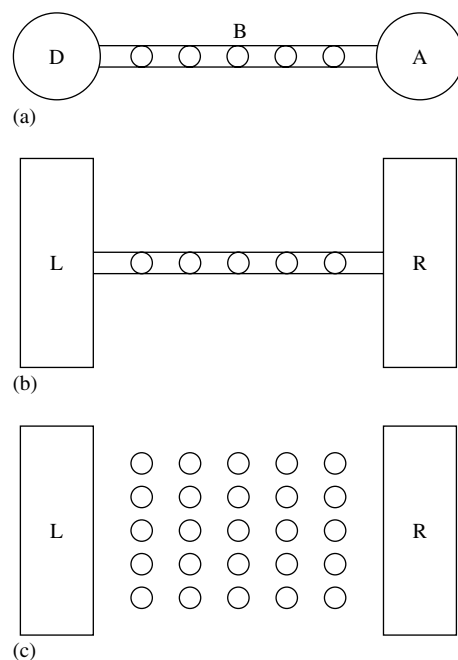


**Fig. 1** Schematic views of typical electron transmission systems. (a) A “standard” electron transfer system containing a donor, an acceptor, and a molecular bridge connecting them (not shown are nuclear motion baths that must be coupled to the donor and acceptor species). (b) A molecular bridge connecting two electronic continua, L and R, representing, e.g., two metal electrodes (c) same as (b) with the bridge replaced by a molecular layer.

and the acceptor are replaced by a continua of electronic states representing free space or metal electrodes. (This replacement can occur on one side only, representing electron transfer between a molecular site and an electrode). In Fig. 1(c), the molecular bridge is replaced by a molecular layer. A schematic view of the electronic states involved is shown in Fig. 2. The middle box represents the bridging molecule or molecular layer and a set of levels  $\{n\}$  represents the relevant molecular orbitals. In a “standard” electron transfer system, (Fig. 2a) this bridge connects the donor and acceptor species, now represented by potential surfaces associated with the vibronic structure of the corresponding intramolecular and solvent nuclear motions. When the bridge connects two metal electrodes (or separates a metal substrate from vacuum), these nuclear baths are replaced by manifolds of electronic states  $\{l\}$  and  $\{r\}$  that represent the continua of

free or quasi-free electron states in the substrates (or, depending on the process, in vacuum). In addition, coupling to the thermal environment (represented by the box  $\Theta$ ) may affect transmission through the bridge. The double arrows in the Figure represent the couplings between these different subsystems.

The first two of the examples given above, PE and LEET, involve electrons of positive energy (relative to zero kinetic energy in vacuum), and as such are related to normal scattering processes. The third example, transmission between two conductors through a molecular layer, involves negative energy electrons, and as such is closely related to regular electron transfer phenomena. The latter type of processes has drawn particular attention in recent years owing to the growing interest in conduction properties of individual molecules and of molecular assemblies. Such processes have become the subjects



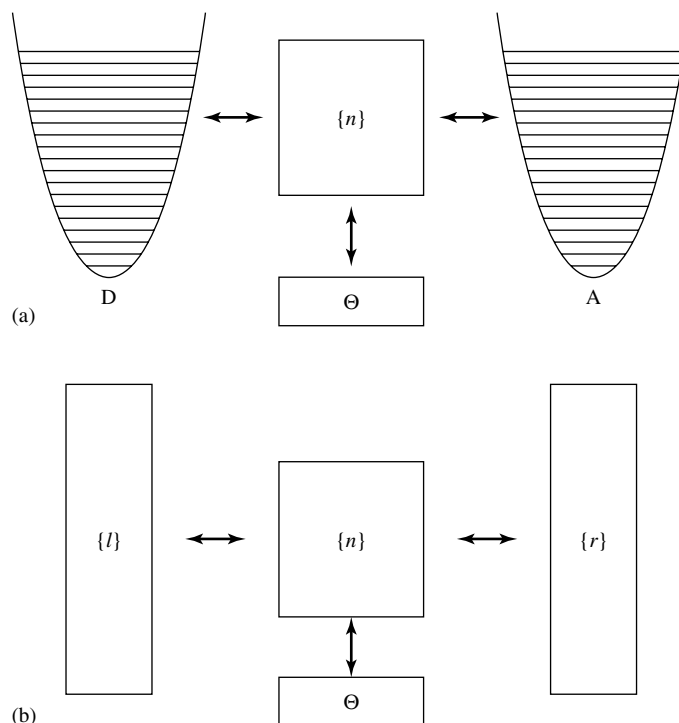


**Fig. 2** A schematic view of the electronic and nuclear states involved in typical electron transmission systems. See text for details.

of intensive research owing to recent interest in electron transfer phenomena underlying the operation of the STM on one hand, and in the transmission properties of molecular bridges between conducting leads on the other. In the latter case, the traditional molecular view of electron transfer between donor and acceptor species, gives rise to a novel view of the molecule as a current carrying conductor, and observables such as electron transfer rates and yields are replaced by the conductivities, or more generally, by current–voltage relationships, in molecular junctions. Of primary importance is the need to understand the interrelationship between the molecular structure of such junctions and their function, that is, their transmission and conduction

properties. Such investigations of electrical junctions in which single molecules or small molecular assemblies operate as conductors connecting “traditional” electrical components, such as metal or semiconductor contacts, constitute a major part of what has become the active field of molecular electronics [7–17]. Their diversity, versatility and amenability to control and manipulation, make molecules and molecular assemblies potentially important components in nano-electronic devices. Indeed, basic properties pertaining to single electron transistor behavior and to current rectification have already been demonstrated. At the same time, major difficulties lie on the way to real technological applications [18]. These difficulties stem from problems associated

with the need to construct, characterize, control and manipulate small molecular structures at confined interfaces with a high degree of reliability and reproducibility, and from issues of stability of such small junctions.

It should be obvious that while the different processes outlined above correspond to different experimental setups, fundamentally they are controlled by similar physical factors. Broadly speaking, we may distinguish between processes for which *lifetimes* or *rates* (more generally, the time evolution) are the main observables, and those that monitor *fluxes* or *currents*. In this review, we focus on the second class, which may be further divided into processes that measure current–voltage relationships, mostly near equilibrium, and those that monitor the nonequilibrium electron flux, for example, in photoemission experiments.

The focus of the following discussion is electron transfer between two conducting electrodes through a molecular medium. Such processes bear strong similarity to the more conventional systems that involve at least one molecular species in the donor/acceptor pair. However, important conceptual issues arise from the fact that such systems can be studied as part of complete electrical circuits, providing current–voltage characteristics that can be analyzed in terms of molecular resistance, conductance, and capacitance.

### 1.3.2

#### Standard Electron Transfer Theory

To set the stage for our later discussion, we first briefly review the rate expressions for “standard” electron transfer processes (Figs. 1a, 2a, 3a). We focus on the particular limit of nonadiabatic electron transfer, where the electron transfer rate is

given (under the Condon approximation) by the golden rule based expression

$$k_{\text{et}} = \frac{2\pi}{\hbar} |V_{\text{DA}}|^2 F \quad (1)$$

where  $V_{\text{DA}}$  is the coupling between the donor (D) and acceptor (A) electronic states and where

$$F = F(E_{\text{AD}}) = \sum_{\nu_{\text{D}}} \sum_{\nu_{\text{A}}} P_{\text{th}}(\varepsilon_{\text{D}}(\nu_{\text{D}})) \times |\langle \nu_{\text{D}} | \nu_{\text{A}} \rangle|^2 \delta(\varepsilon_{\text{A}}(\nu_{\text{A}}) - \varepsilon_{\text{D}}(\nu_{\text{D}}) + E_{\text{AD}}) \quad (2)$$

is the thermally averaged and Franck Condon (FC) weighted density of nuclear states. In Eq. (2),  $\nu_{\text{D}}$  and  $\nu_{\text{A}}$  denote donor and acceptor nuclear states,  $P_{\text{th}}$  is the Boltzmann distribution over donor states,  $\varepsilon_{\text{D}}(\nu_{\text{D}})$  and  $\varepsilon_{\text{A}}(\nu_{\text{A}})$  are nuclear energies above the corresponding electronic origin and  $E_{\text{AD}} = E_{\text{A}} - E_{\text{D}}$  is the electronic energy gap between the donor and acceptor states. In the classical limit,  $\Phi$  is given by

$$F(E_{\text{AD}}) = \frac{e^{-(\lambda + E_{\text{AD}})^2 / 4\lambda k_{\text{B}} \Theta}}{\sqrt{4\pi \lambda k_{\text{B}} \Theta}} \quad (3)$$

where  $k_{\text{B}}$  is the Boltzmann constant and  $\Theta$  is the temperature, and where  $\lambda$  is the reorganization energy, a measure of the electronic energy that would be dissipated after a sudden jump from the electronic state describing an electron on the donor to that associated with electron on the acceptor. If the donor (say) is replaced by an electrode [6, 19, 20], we have to sum over all occupied electrode states

$$\begin{aligned} |V_{\text{DA}}|^2 F &\Rightarrow \sum_{\mathbf{k}} f(\varepsilon_{\mathbf{k}}) F(\varepsilon_{\mathbf{k}} - e\Phi) |V_{\mathbf{kA}}|^2 \\ &= \int d\varepsilon f(\varepsilon) F(\varepsilon - e\Phi) \sum_{\mathbf{k}} \delta(\varepsilon - \varepsilon_{\mathbf{k}}) |V_{\mathbf{kA}}|^2 \end{aligned} \quad (4)$$

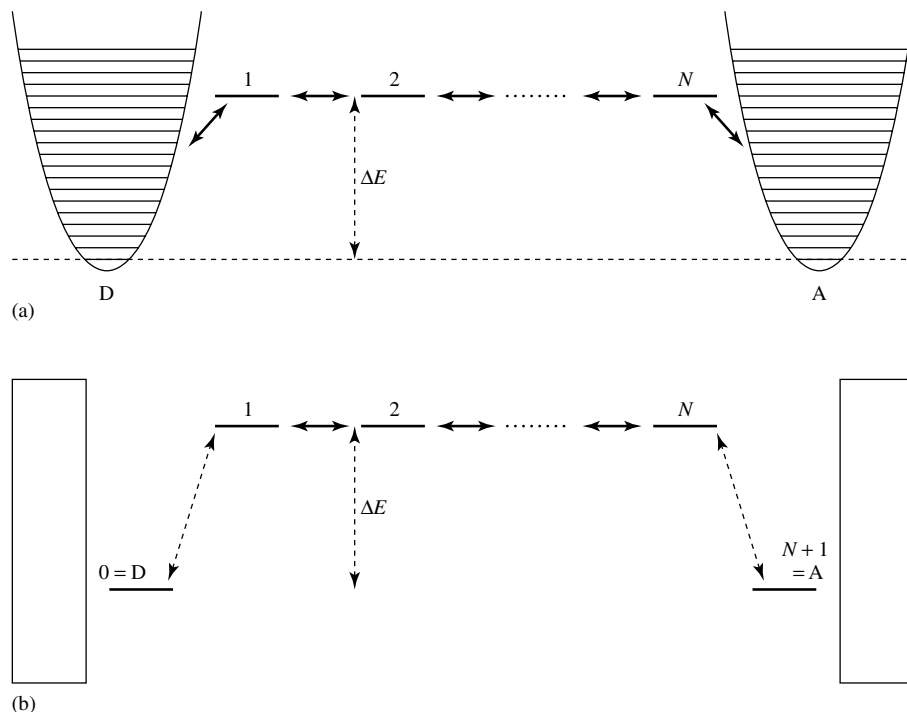


**Fig. 3** Simple level structure models (a) for molecular electron transfer and (b) for electron transmission. The molecular bridge is represented by a simple set of levels that represent local orbitals of appropriately chosen bridge sites. This set of levels is coupled to the donor and acceptor species (with their corresponding nuclear environments) in (a), and to electronic continua representing metal leads (say) in (b). In the latter case, the physical meaning of states 0 and  $N + 1$  depends on the particular physical problem: They can denote donor and acceptor states coupled to the continua of environmental states (hence the notation  $0 = D$ ,  $N + 1 = A$ ), surface localized states in an metal-molecule-metal junction, or they can belong to the right and left scattering continua.

where

$$f(\varepsilon) = \frac{1}{1 + e^{\varepsilon/k_B\Theta}} \quad (5)$$

is the Fermi–Dirac distribution function with  $\varepsilon$  measured relative to the electron chemical potential  $\mu$  in the electrode, and  $\Phi$ , which determines the position of the acceptor level relative to  $\mu$  is the *overpotential*. Defining

$$\sum_k \delta(\varepsilon - \varepsilon_k) |V_{kA}|^2 \equiv |V(\varepsilon)|^2 \quad (6)$$

the electron transfer rate takes the form

$$k_{et} = \frac{2\pi}{h} \int d\varepsilon \frac{e^{-(\lambda - e\Phi + \varepsilon)^2 / 4\lambda k_B\Theta}}{\sqrt{4\pi\lambda k_B\Theta}} \times |V(\varepsilon)|^2 f(\varepsilon) \quad (7)$$

Note that the reorganization energy that appears in Eq. (7) is associated with the change in the redox state of the molecular species only. The nominal change in the “oxidation state” of the macroscopic electrode does not affect the polarization state of the surrounding solvent because the transferred electron or hole does not stay localized.

Much of the early work on electron transfer have used expressions such as (1 and 7) with the electronic coupling term  $V_{\text{DA}}$  being used as a fitting parameter. More recent work has focused on ways to characterize the dependence of this term on the electronic structure of the donor/acceptor pair and on the environment. In particular, studies of bridge-mediated electron transfer, where the donor and acceptor species are rigidly separated by molecular bridges of well-defined structure and geometry, have been very valuable for characterizing the interrelationship between structure and functionality of the separating environment in electron transfer processes. As expected for a tunneling process, the rate is found to decrease exponentially with the donor-acceptor distance

$$k_{\text{et}} = k_0 e^{-\beta' R_{\text{DA}}} \quad (8)$$

where  $\beta'$  is the range parameter that characterizes the distance dependence of the electron transfer rate. The smallest values for  $\beta'$  are found in highly conjugated organic bridges for which  $\beta'$  is in the range of 0.2 to 0.6  $\text{\AA}^{-1}$  [21–32]. In contrast, for free space, taking a characteristic ionization barrier  $U_{\text{B}} = 5 \text{ eV}$ , we find  $\beta' = \sqrt{8mU_{\text{B}}/\hbar^2} \approx 2.4 \text{ \AA}^{-1}$  ( $m$  is the electron mass). Lying between these two regimes are many motifs, both synthetic and natural, including cytochromes and docked proteins [33–41], DNA [42–50], and saturated organic molecules [51–57]. Each displays its own characteristic range of  $\beta'$  values, and hence its own timescales and distance dependencies of electron transfer. A direct measurement of  $\beta'$  along a single molecular chain was recently demonstrated [58].

In addition, to bridge assisted transfer between donor and acceptor species, electron transfer has been studied in systems

in which the spacer is a well-characterized Langmuir–Blodgett film [59–61]. The STM provides a natural apparatus for such studies [58, 62–76]. Other approaches include break junctions [77–79] and mercury drop contacts [80–84].

Simple theoretical modeling of  $V_{\text{DA}}$  usually relies on a single electron (or hole) picture in which the donor-bridge-acceptor (DBA) system is represented by a set of levels:  $|D\rangle$ ,  $|A\rangle$ ,  $\{|1\rangle, \dots, |N\rangle\}$  as depicted in Fig. 3. In the absence of coupling of these bridge states to the thermal environment, and when the energies  $E_n$  ( $n = 1, \dots, N$ ) are high relative to the energy of the transmitted electron (the donor/acceptor orbital energies in Figs. 1a, 2a and 3a, or the incident electron energy in Figs. 1b to c, 2b and 3b), this is the superexchange model for electron transfer [85]. Of particular interest are situations where  $\{n\}$  are localized in space, so that the state index  $n$  corresponds to the position in space between the donor and acceptor sites (Fig. 3a) or between the two electron reservoirs (Fig. 3b). These figures depict generic tight binding models of this type, where the states  $n = 1, \dots, N$  are the bridge states, here taken as degenerate in zero order. Their localized nature makes it possible to assume only nearest-neighbor coupling between them, that is,  $V_{n,n'} = V_{n,n\pm 1}\delta_{n',n\pm 1}$ . We recall that the appearance of  $V_{\text{DA}}$  in Eq. (1) is a low-order perturbation theory result. A more general expression is obtained by replacing  $V_{\text{DA}}$  by  $T_{\text{DA}}$  where the  $T$  operator is defined by  $T(E) = V + VG(E)V$ , with  $G(E) = (E - H + (1/2)i\Gamma)^{-1}$  and where  $\Gamma$  stands for the inverse lifetime matrix of bridge levels. Assuming for simplicity that the donor level  $|D\rangle$  is coupled only to bridge state  $|1\rangle$  and that the acceptor level  $|A\rangle$  is coupled only to bridge level  $N$ , the effective coupling between donor and

acceptor is given by

$$T_{DA}(E) = V_{DA} + V_{D1}G_{1N}(E)V_{NA} \quad (9)$$

This naturally represents the transition amplitude as the sum of a direct contribution,  $V_{DA}$ , which is usually disregarded for long bridges and a bridge mediated contribution. In using  $T_{DA}$  instead of  $V_{DA}$  in Eq. (1), the energy parameter  $E$  in Eq. (9) should be taken to be equal to  $E_D = E_A$  at the point where the corresponding potential surfaces cross (or go through an avoided crossing). In the level structure of Fig. 3(a) that corresponds to the DBA system in Fig. 1(a), making the tight binding approximation and in the weak coupling limit,  $\max|V| \ll \min(E_B - E)$ , the Green's function element in (9) is given by

$$G_{1N}(E) = \frac{1}{E - E_N} \prod_{n=1}^{N-1} \frac{V_{n,n+1}}{E - E_n} \quad (10)$$

For a generalization of Eq. (10) that does not assume weak coupling see Refs. [86–88]. For a model with identical bridge segments,  $E_n$  and  $V_{n,n+1}$  are independent of  $n$  and will be denoted  $E_n = E_B$  and  $V_{n,n+1} = V_B$ . Using this in Eq. (1) leads to

$$k_{et} = \frac{2\pi}{\hbar} \left| \frac{V_{1D}V_{NA}}{V_B} \right|^2 \left( \frac{V_B}{\Delta E_B} \right)^{2N} F \quad (11)$$

where  $\Delta E_B = E_B - E$ . Similarly, for a bridge-assisted transfer between a molecule and an electrode, Eq. (7) applies with  $|V(\varepsilon)|^2$  given by

$$|V(\varepsilon)|^2 = \left( \frac{V_B}{\Delta E_B} \right)^{2N} \sum_k \delta(\varepsilon - \varepsilon_k) \times \left| \frac{V_{1k}V_{NA}}{V_B} \right|^2 \quad (12)$$

These results imply a simple form for the distance parameter  $\beta'$  of Eq. (8)

$$\beta' = \frac{2}{a} \ln \left( \frac{\Delta E_B}{V_B} \right) \quad (13)$$

where  $a$  measures the segment size, so that the bridge length is  $Na$ . The exponential dependence on the bridge length is a manifestation of the tunneling character of this process. For typical values, for example,  $\Delta E_B/V_B = 10$  and  $a = 5 \text{ \AA}$ , Eq. (13) gives  $\beta' = 0.92 \text{ \AA}^{-1}$ . More rigorous estimates of the electronic coupling term in electron transfer processes involve electronic structure calculation for the full DBA system. Such calculations, in the context of molecular conduction, will be discussed later.

### 1.3.3

#### Transmission Between Conducting Leads

Equations (1, 7 and 11) are expressions for the *rate* of electron transfer between donor and acceptor molecules or between a molecule and a metal electrode. As already mentioned, for electron transfer in metal-molecule-metal (MMM) junctions, the primary observable is the *current-voltage characteristics* of the system. Putting it in another way, while the primary observable in “standard” charge transfer processes involving molecular donors and/or acceptors is a *transient* quantity, in MMM junctions we focus on the *steady state* current through the junction for a given voltage difference between the two metal ends. Note that for electron transfer processes, in addition to *rates*, other observables are the *yields* of different products of the electron transfer reaction. Furthermore, for light induced electron transfer processes, the steady state current under a constant illumination can be monitored.

Consider first a simple model for a metal-insulator-metal (MIM) system in

which the insulator is represented by a continuum characterized by a dielectric constant  $\epsilon$  [89]. For specificity, assume that the electrode surfaces are infinite parallel planes perpendicular to the  $x$  direction. In this case, the transmission problem is essentially one-dimensional and depends only on the incident particle velocity in the  $x$  direction,  $v_x = \sqrt{2E_x/m}$ . In the WKB approximation, the transmission probability is given by

$$T(E_x) = \exp \left[ -\frac{4\pi}{\hbar} \int_{s_1}^{s_2} [2m(U_B(x) - E_x)]^{1/2} dx \right] \quad (14)$$

where  $U_B(x)$  is the barrier potential that determine the turning points  $s_1$  and  $s_2$  and  $m$  is the mass of the tunneling particle. The tunneling flux is given by  $T(E_x)n(E_x)\sqrt{2E_x/m}$ , where  $n(E_x)$  is the density per unit volume of electrons of energy  $E_x$  in the  $x$  direction.  $n(E_x)$  is obtained by integrating the Fermi–Dirac function with respect to  $E_y$  and  $E_z$ . When a potential  $\Phi$  is applied so that the right electrode (say) is positively biased, the net current density is obtained in the form [89]

$$J = \int_0^\infty dE_x T(E_x) \xi(E_x) \quad (15)$$

where

$$\begin{aligned} \xi(E_x) = & \frac{2m^2 e}{(2\pi\hbar)^3} \int_{-\infty}^\infty dv_y \int_{-\infty}^\infty dv_z [f(E) \\ & - f(E + e\Phi)] = \frac{4\pi m e}{(2\pi\hbar)^3} \int_0^\infty dE_r \\ & \times [f(E) - f(E + e\Phi)] \end{aligned} \quad (16)$$

and where  $E_r = E - E_x = (1/2)m(v_y^2 + v_z^2)$  is the energy in the direction perpendicular to  $x$ . In obtaining this result, it is assumed that the electrodes are chemically identical. At zero temperature,

and when  $\Phi \rightarrow 0$ ,  $f(E) - f(E + e\Phi) = e\Phi\delta(E - E_F)$ . Equations (15 and 16) then lead to an expression for the conduction per unit area, that is, the conductivity per unit length

$$\sigma_x = \frac{4\pi m e^2}{(2\pi\hbar)^3} \int_0^{E_F} dE_x T(E_x) \quad (17)$$

For finite  $\Phi$ , these expressions provide a framework for predicting the current–voltage characteristics of the junction; explicit approximate expressions were given by Simmons [89]. Here we only emphasize [89], that the dependence on  $\Phi$  arises partly from the structure of Eqs. (15) and (16), for example, at zero temperature

$$\begin{aligned} J = & \frac{4\pi m^2 e^2}{(2\pi\hbar^3)} \left[ e\Phi \int_0^{E_F - e\Phi} dE_x T(E_x) \right. \\ & \left. + \int_{E_F - e\Phi}^{E_F} dE_x (E_F - E_x) T(E_x) \right] \end{aligned} \quad (18)$$

but mainly from the voltage dependence of  $T$ . The simplest model for a metal–vacuum–metal barrier between identical electrodes without an external field is a rectangular barrier of height above the Fermi energy given by the metal work function. When a uniform electric field is imposed between the two metals, a linear potential drop from  $E_F$  on one electrode to  $E_F - e\Phi$  on the other is often assumed (see Fig. 4). In addition, the image potential experienced by the electron between the two metals will considerably modify the potential barrier. For a point charge  $e$ , located at position  $x$  between two conducting parallel plates that are a distance  $d$  apart, the image potential is

$$\begin{aligned} V_1 = & \left( -\frac{e^2}{4\pi\epsilon} \right) \\ & \times \left[ \frac{1}{2x} + \sum_{n=1}^\infty \left\{ \frac{nd}{[(nd)^2 - x^2]} - \frac{1}{nd} \right\} \right] \end{aligned} \quad (19)$$

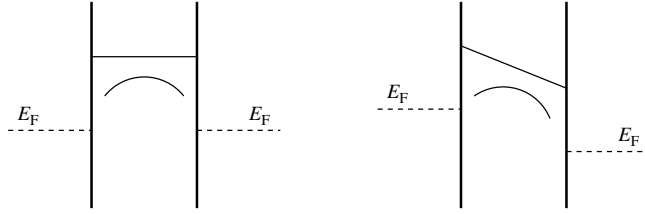


**Fig. 4** Tunneling gap between two metal electrodes in an unbiased (left) and a biased (right) situation. The bare gap, given by the work function  $W$ , is modified by the image interaction – the resulting barriers are represented by the curved lines.

where  $\varepsilon$  is the dielectric constant of the spacer. For  $x = d/2$ , this becomes

$$V_1 = -\frac{e^2 \ln 2}{2\pi \varepsilon d} \quad (20)$$

This negative contribution to the electron's energy reduces the potential barrier (Fig. 4), and has been invoked to explain the lower than expected barrier observed in STM experiments [90, 91]. Some points should however, be kept in mind. First, the classical result (19) fails close to the metal surface where quantum mechanical and atomic size effects change both the position of the reference image plane and the functional form of the image potential [92–96]. Second, consideration of the dynamic nature of the image response should be part of a complete theory [97–100]. The timescale of electronic response of metals can be roughly estimated from the plasma frequency to be  $\sim 10^{-16}$  s. This should be compared to the time during which a tunneling particle can respond to interactions localized in the barrier. For transmitted particles, this is the traversal time for tunneling [101, 102] that, for an electron traversing a 10 Å wide 1 eV barrier is of the order of  $\sim 1$  fs. This comparison would justify the use of the static image approximation in this context, but this approximation becomes questionable for deeper tunneling or narrower barriers.

The planar geometry implied by the assumption that transmission depends only on the energy of the motion parallel to the tunneling direction, as well as the explicit form of Eq. (14) are not valid for a typical STM configuration that involves a tip on one side and a structured surface on the other. To account for these structures, Tersoff and Hamman [103] have applied Bardeen's formalism [104], which is a perturbative approach to tunneling in arbitrary geometries. Bardeen's formula for the tunneling current is

$$I = \frac{4\pi e}{\hbar} \sum_{l,r} [f(E_l)(1 - f(E_r + e\Phi)) - (1 - f(E_l))f(E_r + e\Phi)] |M_{lr}|^2 \times \delta(E_l - E_r) = \frac{2\pi e}{\hbar} \sum_{l,r} [f(E_l) - f(E_r + e\Phi)] |M_{lr}|^2 \delta(E_l - E_r) \quad (21)$$

where

$$M_{lr} = \frac{\hbar^2}{2m} \int d\vec{S} (\psi_l^* \nabla \psi_r - \psi_l \nabla \psi_r^*) \quad (22)$$

is the transition matrix element for the tunneling process. This is just the Golden rule rate expression multiplied by the electron charge  $e$ , with  $M$  playing the role of coupling. In Ref. [103], only the first term in the square brackets of the first line appears. This gives the partial current from the negative to the positive

electrode. The net current is obtained by subtracting the reverse current as shown in Eq. (21). Also, compared with Ref. [103], Eq. (21) contains an additional factor of 2 that accounts for the spin multiplicity of the electronic states.

In Eqs. (21) and (22),  $\psi_\ell$  and  $\psi_r$  are electronic eigenstates of the negatively biased (left) and positively biased (right) electrodes, respectively,  $\Phi$  is the bias potential, and the integral is over any surface separating the two electrodes and lying entirely in the barrier region. The wave functions appearing in Eq. (22) are eigenfunctions of Hamiltonians that describe each electrode in the absence of the other, that is, interfaced with an infinite spacer medium. These functions therefore decay exponentially in the space between the two electrodes in a way that reflects the geometry and chemical nature of the electrodes and the spacer. For  $\Phi \rightarrow 0$ , Eq. (21) yields the conduction

$$g \equiv \frac{I}{\Phi} = \frac{4\pi e^2}{\hbar} \sum_{l,r} |M_{lr}|^2 \delta(E_l - E_F) \times \delta(E_r - E_F) \quad (23)$$

Tersoff and Hamman [103] have used substrate wave functions that correspond to a corrugated surface of a generic metal while the tip is represented by a spherical  $s$  orbital centered about the center  $\mathbf{r}_0$  of the tip curvature. In this case, they find

$$I \propto \sum_v |\psi_v(\mathbf{r}_0)|^2 \delta(E_v - E_F) \quad (24)$$

The rhs of Eq. (24) is the local density of states of the metal. While this result is useful for analysis of spatial variation of the tunneling current on a given metal surface, the contributions from the coupling matrix elements in Eq. (23) cannot be disregarded when comparing different metals and or different adsorbates [20].

### 1.3.4

#### The Landauer Formula

The results (14)–(17) and (21)–(23) are special cases of a more systematic representation of the conduction and the current–voltage characteristic of a given junction due to Landauer [105, 106]. Landauer’s original result was obtained for a system of two one-dimensional leads connecting two macroscopic electrodes (“electron reservoirs”) via a scattering object or a barrier characterized by a transmission function  $T(E)$ . The zero-temperature conductance, measured as the limit  $\Phi \rightarrow 0$  of the ratio  $I/\Phi$  between the current and the voltage drop between the reservoirs, was found to be

$$g = \frac{e^2}{\pi \hbar} T(E_F) \quad (25)$$

(The corresponding resistance,  $g^{-1}$ , can be represented as a sum of the intrinsic resistance of the scatterer itself,  $[(e^2/\pi \hbar)(T/(1-T))]^{-1}$  and a contribution  $(e^2/\pi \hbar)^{-1}$  from two contact resistances between the leads and the reservoirs. See Chapter 5 of Ref. [107] for a discussion of this point.) This result is obtained by computing the total unidirectional current carried in an ideal lead by electrons in the energy range  $(0, E) = (0, \hbar^2 k_E^2/(2m))$ . In a one-dimensional system of length  $L$ , the density of electrons, including spin, with wave vectors in the range between  $k$  and  $k + dk$  is  $n(k) dk = 2(1/L)(L/2\pi) f(E_k) dk = f(E_k) dk/\pi$ . The corresponding velocity is  $v = \hbar k/m$ . Thus

$$I(E) = e \int_0^{k_E} dk v(k) n(k) = e \int_0^{k_E} dk \left( \frac{\hbar k}{m} \right) \times \frac{f(E_k)}{\pi} = \frac{e}{\pi \hbar} \int_0^E dE' f(E') \quad (26)$$



At zero temperature, the net current carried under bias  $\Phi$  is

$$I = \frac{e}{\pi \hbar} \int_0^\infty dE (f(E) - f(E + e\Phi))$$

$$\xrightarrow{\Theta \rightarrow 0} \frac{e^2}{\pi \hbar} \Phi \quad (27)$$

Thus, the conductance of an ideal one-dimensional lead is  $I/\Phi = e^2/\pi \hbar = (12.9 K \Omega)^{-1}$ . In the presence of the scatterer, this is replaced by

$$I = \frac{e}{\pi \hbar} \int_0^\infty dE T(E) (f(E) - f(E + e\Phi))$$

$$\xrightarrow{\Theta \rightarrow 0, \Phi \rightarrow 0} \frac{e^2}{\pi \hbar} T(E_F) \Phi \quad (28)$$

which leads to (25). This result is valid for one-dimensional leads. When the leads have finite size in the direction normal to the propagation so that they support traversal modes, a generalization of (25) to this case yields [108]

$$g = \frac{e^2}{\pi \hbar} \sum_{i,j} T_{ij}(E_F) = \frac{e^2}{\pi \hbar} \text{Tr}(SS^\dagger)_{E_F} \quad (29)$$

where  $T_{ij} = |S_{ij}|^2$  is the probability that a carrier coming from the left (say) of the scatterer in transversal mode  $i$  will be transmitted to the right into transversal mode  $j$  ( $S_{ij}$ , an element of the  $S$  matrix, is the corresponding amplitude). The sum in (29) is over all transversal modes whose energy is smaller than  $E_F$ . The analog of Eq. (29) for the microcanonical chemical reaction rate was first written by Miller [109]. More generally, the current for a voltage difference  $\Phi$  between the electrodes is given by

$$I = \int_0^\infty dE [f(E) - f(E + e\Phi)] \frac{g(E)}{e} \quad (30)$$

$$g(E) = \frac{e^2}{\pi \hbar} \sum_{i,j} T_{ij}(E) \quad (31)$$

As an example, consider the case of a simple planar tunnel junction (see Eqs. (14)–(17)), where the scattering process does not couple different transversal modes. In this case, the transmission function depends only on the energy in the tunneling direction

$$\sum_{i,j} T_{ij}(E) = \sum_i T_{ii}(E) = \frac{L_y L_z}{(2\pi)^2} \int dk_y$$

$$\times \int dk_z T \left[ E - \left( \frac{\hbar^2}{2m} \right) (k_y^2 + k_z^2) \right]$$

$$= \frac{L_y L_z}{(2\pi)^2} \frac{2\pi m}{\hbar^2} \int_0^E dE_r T(E - E_r) \quad (32)$$

$E_r$  is defined below Eq. (16). Using this in Eq. (29) yields the conductivity per unit length

$$\frac{g}{L_y L_z} \equiv \sigma = \frac{4\pi m e^2}{h^3} \int_0^{E_F} dE_x T(E_x) \quad (33)$$

in agreement with Eq. (17).

Similarly, Eqs. (21 and 23) are easily seen to be equivalent to Eqs. (25 or 31) if we identify  $M_{lr}$  with  $T_{lr}$  in Eq. (37) below. An important difference between the results of (29 and 31) and results based on Bardeen's formalism, that is Eqs. (21 to 23), is that the former are valid for any set of transmission probabilities, even close to 1, while the latter yields a weak coupling result. Another important conceptual difference is the fact that the sums over  $l$  and  $r$  in Eqs. (21 to 23) is over zero order states defined in the initial and final subspaces, while the sums in Eqs. (29 to 31) is over scattering states, that is, eigenstates of the exact system's Hamiltonian. It is the essence of Bardeen's contribution [104] that in the weak coupling limit (i.e.

high/wide barrier), it is possible to write the transmission coefficient  $T_{ij}$  in terms of a golden rule expression for the transition probability between the zero order standing wave states  $|l\rangle$  and  $|r\rangle$  localized on the left and right electrodes, thus establishing the link between the two representations. (For an alternative formulation of this link, see Ref. [110])

To explore this connection on a more formal basis, we can replace the expression based on transmission coefficients  $T$  by an equivalent expression based on scattering amplitudes, or  $T$  matrix elements, between zero order states localized on the electrodes. This can be derived directly from Eqs. (29 or 31) by using the identity

$$\sum_{i,j} T_{ij}(E) = 4\pi^2 \sum_{l,r} |T_{lr}|^2 \times \delta(E - E_l) \delta(E - E_r) \quad (34)$$

On the left side of Eq. (34), a pair of indices  $(i, j)$  denote an exact scattering state of energy  $E$ , characterized by an incoming state  $i$  on the left (say) electrode and an outgoing state  $j$  on the right electrode. On the right,  $l$  and  $r$  denote zero order states confined to the left and right electrodes, respectively.  $T$  is the corresponding transition operator whose particular form depends on the details of this confinement. Alternatively, we can start from the golden-rule-like expression

$$\begin{aligned} I = e \frac{4\pi}{\hbar} \sum_{l,r} [f(E_l)(1 - f(E_r + e\Phi)) \\ - f(E_r + e\Phi)(1 - f(E_l))] |T_{lr}|^2 \\ \times \delta(E_l - E_r) = \frac{4\pi e}{\hbar} \sum_{l,r} [f(E_l) \\ - f(E_r + e\Phi)] |T_{lr}|^2 \delta(E_l - E_r) \end{aligned} \quad (35)$$

(An additional factor of 2 on the rhs accounts for the spin degeneracy). It is convenient to recast this result in the form

$$\begin{aligned} I = \frac{4\pi e}{\hbar} \int_0^\infty dE [f(E) - f(E + e\Phi)] \\ \times \sum_{l,r} |T_{lr}|^2 \delta(E - E_l) \delta(E - E_r) \\ = \int_0^\infty dE [f(E) - f(E + e\Phi)] \frac{g(E)}{e} \end{aligned} \quad (36)$$

where

$$\begin{aligned} g(E) \equiv \frac{4\pi e^2}{\hbar} \sum_{l,r} |T_{lr}|^2 \\ \times \delta(E - E_l) \delta(E - E_r) \end{aligned} \quad (37)$$

Note that Eqs. (34 and 37) imply again Eq. (31). For  $\Phi \rightarrow 0$ , Eqs. (36 and 37) lead to  $I = g\Phi$  with

$$g = g(E_F) \quad (38)$$

The analogy of this derivation of the result (23) is evident.

### 1.3.5

#### Molecular Conduction

Equations (36 to 38) provide a convenient starting point for most treatments of currents through molecular junctions where the coupling between the two metal electrodes is weak. In this case, it is convenient to write the system's Hamiltonian as the sum,  $H = H_0 + V$ , of a part  $H_0$  that represents the uncoupled electrodes and spacer and the coupling  $V$  between them. In the weak coupling, limit the  $T$  operator

$$\begin{aligned} T(E) &= V + VG(E)V; \\ G(E) &= (E - H + i\varepsilon)^{-1} \end{aligned} \quad (39)$$

is usually replaced by its second term only. The first “direct” term  $V$  can be

disregarded if we assume that  $V$  couples the states  $l$  and  $r$  only via states of the molecular spacer. Consider now a simple model where this spacer is an  $N$ -site bridge connecting the two electrodes so that Site 1 of the bridge is attached to the left electrodes and Site  $N$  – to the right electrode, a variant of Fig. 3(b). In this case, we have  $T_{lr} = V_{l1}G_{1N}V_{Nr}$ , so that at zero temperature [111]

$$\sum_{i,j} T_{ij}(E) = |G_{1N}(E_F)|^2 \times \Gamma_1^{(L)}(E_F)\Gamma_N^{(R)}(E_F) \quad (40)$$

and (using Eqs. 36 and 37)

$$I(\Phi) = \frac{e}{\pi\hbar} \int_{E_F - e\Phi}^{E_F} dE |G_{1N}(E, \Phi)|^2 \Gamma_1^{(L)}(E) \times \Gamma_N^{(R)}(E + e\Phi) \quad (41)$$

with

$$\Gamma_1^{(L)}(E) = 2\pi \sum_l |V_{l1}|^2 \delta(E_l - E);$$

$$\Gamma_N^{(R)}(E) = 2\pi \sum_r |V_{Nr}|^2 \delta(E_N - E) \quad (42)$$

The Green's function in Eq. (40) is itself reduced to the bridge's subspace by projecting out the metals' degrees of freedom. This results in a renormalization of the bridge Hamiltonian: in the bridge subspace

$$(E - H + i\eta)^{-1} \longrightarrow (E - H_B - \Sigma_B(E))^{-1} \quad (43)$$

where  $H_B = H_B^0 + V_B$  is the Hamiltonian of the isolated bridge entity with

$$H_B^0 = \sum_{n=1}^N E_n |n\rangle\langle n|;$$

$$V_B = \sum_{n=1}^N \sum_{n'=1}^N V_{n,n'} |n\rangle\langle n'| \quad (44)$$

and where, in the basis of eigenstates of  $H_B^0$

$$\Sigma_{nn'}(E) = \delta_{n,n'}(\delta_{n,1} + \delta_{n,N})[\Lambda_n(E) - (\frac{1}{2})i\Gamma_n(E)] \quad (45)$$

$$\Gamma_n(E) = 2\pi \sum_j |V_{nj}|^2 \delta(E - E_j) \quad (46)$$

$$\Lambda_n(E) = \frac{PP}{2\pi} \int_{-\infty}^{\infty} dE' \frac{\Gamma_n(E')}{(E - E')} \quad (47)$$

In Eq. (46), the sum is over both the right and the left manifolds (that is,  $j$  goes over all states  $\{l\}$  and  $\{r\}$  in these manifolds), so that  $\Gamma_n = \Gamma_n^{(L)} + \Gamma_n^{(R)}$ ;  $n = 1, N$ . The transmission problem is thus reduced to evaluating a Green's function matrix element and two width parameters. The first calculation is a simple inversion of a finite (order  $N$ ) matrix. The width  $\Gamma$  and the associated shift  $\Lambda$  represent the finite lifetime of an electron on a molecule adsorbed on the metal surface, and can be estimated, for example Ref. [111], using the Newns–Anderson model of chemisorption [112]. In the simple tight-binding model of the bridge and in the weak coupling limit,  $G_{1N}$  is given by Eq. (10) modified by the inclusions of the self-energy terms

$$G_{1N}(E) = \frac{V_{1,2}}{(E - E_1 - \Sigma_1(E))(E - E_N - \Sigma_N(E))} \times \prod_{j=2}^{N-1} \frac{V_{j,j+1}}{E - E_j} \quad (48)$$

Equations (40 to 48) thus provide a complete simple model for molecular conduction, equivalent to similar approximations used in theories of molecular

electron transfer (e.g. [113, 114] and references therein). For applications of variants of this formalism to electron transport in specific systems, see Refs. [86, 87, 115, 116]. In the following text, we discuss more general forms of this formulation.

### 1.3.6

#### Relation to Electron Transfer Rates

It is interesting to examine the relationship between the conduction of a molecular species and the electron transfer properties of the same species [117]. We should keep in mind that because of tunneling there is always an Ohmic regime near zero bias, with conduction given by the Landauer formula. Obviously, this conduction may be extremely low, indicating in practice an insulating behavior. Of particular interest, is to estimate the electron transfer rate in a given DBA system that will translate into a measurable conduction of the same system when used as a molecular conductor between two metal leads. To this end, consider a DBA system with a bridge that consists of  $N$  identical segments (denoted  $1, 2, \dots, N$ ) with nearest neighbor coupling  $V_B$ . The electron transfer rate is given by Eq. (11) that we rewrite in the form

$$k_{D \rightarrow A} = \frac{2\pi}{\hbar} |V_{D1} V_{NA}|^2 |G_{1N}(E_D)|^2 F \quad (49)$$

where, in the weak coupling limit,  $|V_B| \ll |E_B - E|$  (cf. Eq. 10)

$$G_{1N}(E) = \frac{|V_B|^{N-1}}{(E_B - E)^N} \quad (50)$$

and where  $F$  is the Franck–Condon-weighted density of nuclear states, given in the classical limit by Eq. (3). The appearance of  $F$  in Eq. (49) indicates that

the process is dominated by the change in the nuclear configuration between the two localization states of the electron. Suppose now that the same DBA complex is used to connect between two metal contacts such that the donor and acceptor species are chemisorbed on the two metals (denoted “left” and “right”, respectively). We wish to calculate the conduction of this junction and its relation to  $k_{D \rightarrow A}$ . First note that the conduction process does not involve localized states of the electron on the donor or the acceptor, so the factor  $F$  will be absent. (We will disregard energy loss arising from transient distortions of the nuclear configuration associated with transient populations of electronic states of the DBA complex). Assuming as before that states of the molecular complex are coupled to the metal only via the  $D$  and  $A$  orbitals, and that the latter are coupled only to their adjacent metal contacts, the conduction is given by an equation similar to Eq. (40), except that the bridge  $(1, \dots, N)$  is replaced by the complex  $DBA = (D, 1, \dots, N, A)$

$$g(E) = \frac{e^2}{\pi \hbar} |G_{DA}(E)|^2 \Gamma_D^{(L)}(E) \Gamma_A^{(R)}(E) \quad (51)$$

where, in analogy to Eq. (48)

$$\begin{aligned} G_{DA}(E) &= \frac{V_{D1} V_{NA}}{(E - E_D - \Sigma_D(E))(E - E_A - \Sigma_A(E))} \\ &\quad \times G_{1N}(E) \end{aligned} \quad (52)$$

Since the donor and acceptor species are chemisorbed on their corresponding metal contacts, their energies shift closer to the Fermi energies. We assume that this shift occurs uniformly in the DBA complex without distorting its internal electronic structure (strictly speaking this can happen only in the symmetric case of identical

donor and acceptors and identical metal electrodes, but the result of Eq. (53) below is probably a good approximation for more general cases because  $G_{1N}(E)$  is often not strongly dependent on  $E$ ). Assuming therefore that the denominator in Eq. (52) is dominated by the imaginary parts of the self-energies  $\Sigma$ , we get

$$g = g(E_F) = \frac{16e^2}{\pi\hbar} \frac{|V_{D1}V_{NA}|^2}{\Gamma_D^{(L)}(E_F)\Gamma_A^{(R)}(E_F)} \times |G_{1N}(E_F)|^2; \quad E_F = E_D = E_A \quad (53)$$

Comparing to Eq. (49) we get

$$g = \frac{e^2}{\pi\hbar} \frac{k_{D \rightarrow A}}{F} \frac{8\hbar}{\pi\Gamma_D^{(L)}\Gamma_A^{(R)}} \quad (54)$$

It has been argued that, Eq. (52) and therefore Eq. (54) holds the energy spacing  $E_B - E_F$  between the bridge levels and the Fermi energy is large relative to  $k_B T$ , Eq. (54) holds also when the electron transfer process involves thermal activation into the bridge states (and not only for the bridge assisted tunneling implied by Eq. 53) [118]. Using the classical expression for  $F$ , Eq. (3), we have in the present case  $F = (\sqrt{4\pi\lambda k_B T})^{-1} \exp(-\lambda/4k_B T)$ . For a typical value of the reorganization energy  $\sim 0.5$  eV, and at room temperature, this is  $\sim 0.02$  (eV) $^{-1}$ . Taking also  $\Gamma_D^{(L)} = \Gamma_A^{(R)} \sim 0.5$  eV leads to  $g \sim (e^2/\pi\hbar)(10^{-13}k_{D \rightarrow A}(s^{-1})) \cong [10^{-17}k_{D \rightarrow A}(s^{-1})] \Omega^{-1}$ . This sets a criterion for observing Ohmic behavior for small voltage bias in molecular junctions: With a current detector sensitive to pico-amperes,  $k_{D \rightarrow A}$  has to exceed  $\sim 10^6 s^{-1}$  (for the estimates of  $F$  and  $\Gamma$  given above) before measurable current can be observed at 0.1 V voltage across such a junction.

### 1.3.7

#### Quantum Chemical Calculations

The simple models discussed above are useful for qualitative understanding of molecular conductivity; however, the Landauer formula or equivalent formulations can be used as a basis for more rigorous molecular calculations using extended Huckel (EH) based computations [70–72, 79, 119–133] or Hartree–Fock (HF) [134–137]. These approaches follow similar semiempirical and ab initio calculations of electron transfer rates in molecular systems [138]; however, instead of focusing on the computation of the electronic coupling  $V_{DA}$  needed in Eq. (1), the sum in Eq. (34) is calculated directly. Structural stability considerations suggest that useful MMM bridges should involve strong chemisorption bonding between the molecule and the metal substrate, implying large electronic coupling between them [139]. It is, therefore, preferable to use a “supermolecule” approach, in which the quantum chemical calculations are carried out for a species that comprises the molecule and two clusters of metal atoms, so that the reduction that introduces the self energy  $\Sigma$  Eq. (43) is done at some deeper metal–metal contact. Such atomic level calculations usually start from a (nonorthogonal) basis set of atomic orbitals, so the formalism described above has to be generalized for this situation. (Alternatively, it has been shown by Emberly and Kirczenow [140, 141] that one can map the problem into a new Hilbert space in which the basis states are orthogonal.) We also relax the assumption that the molecule–metal contact is represented by coupling to a single molecular orbital. Defining the operator

$$\mathbb{H}(E) = EZ - H \quad \text{with } Z_{ij} = \langle i | j \rangle \quad (55)$$

The Green's function is  $G(E) = \mathbb{H}(E)^{-1}$ . In Eq. (55),  $i$  and  $j$  denote atomic orbitals that may be assigned to the supermolecule (M), the left metal (L) and the right metal (R) subspaces. Denoting formally the coupling between the subspace M and the subspaces  $K = L, R$  by the corresponding submatrices  $\mathbb{H}_{MK}$ , the Green's function for the supermolecule subspace is

$$G^{(M)}(E) = (\mathbb{H} - \Sigma^{(L)} - \Sigma^{(R)})^{-1} \quad (56)$$

with  $\Sigma^{(K)}$  is a matrix in the molecular subspace and

$$\Sigma^{(K)} = \mathbb{H}_{MK}(\mathbb{H}^{-1})_{KK}\mathbb{H}_{KM} \quad (57)$$

Eq. (57) is a compact notation for  $(\Sigma^{(K)})_{n,n'} = \sum_{k,k'} \mathbb{H}_{nk}(\mathbb{H}^{-1})_{kk'}\mathbb{H}_{k'n'}$  where  $k$  and  $k'$  are states in the metal  $K$  subspace. Using also

$$T_{lr} = \sum_{n,n'} \mathbb{H}_{ln} G_{nn'} \mathbb{H}_{n'r} \quad (58)$$

( $l$  and  $r$  in the metal L and R subspaces, respectively;  $n, n'$  in the supermolecule subspace) in Eq. (57) leads to

$$g(E) = \frac{e^2}{\pi\hbar} Tr \left[ G^{(M)}(E) \Gamma^{(R)}(E) \right. \\ \left. \times G^{(M)\dagger}(E) \Gamma^{(L)}(E) \right] \quad (59)$$

where, for example, for the "left" metal

$$\Gamma_{n,n'}^{(L)} = 2\pi \sum_l \mathbb{H}_{nl} \mathbb{H}_{ln'} \delta(E - E_l) \\ (n \text{ and } n' \text{ in the molecular subspace}) \quad (60)$$

In practice,  $\Sigma$  and  $\Gamma = -2\text{Im}(\Sigma)$  can be computed by using closure relations based on the symmetry of the metal lattice [130]. The trace in Eq. (59) is over all basis states in the (super)molecular subspace. The evaluation of the Green's function matrix elements and of this trace is straightforward in semiempirical single

electron representations such as the EH approximation, and can be similarly done at the HF level using, after convergence, the Fock rather than the Hamiltonian matrix in Expressions (55 to 60). (Note that the Fock operator depends on the ground state electronic configuration. The latter is taken in Refs. [134, 135] to be that of the isolated supermolecule, assuming that the contact with the bulk electrodes does not affect it appreciably. In particular, the supermolecule is usually assumed neutral in these calculations.)

An important attribute of the approach described above is that, within the approximation used, it provides the total current carried by the system, both through the unoccupied molecular levels (electron conduction) and the occupied ones (hole conduction). This results from the fact that the trace in Eq. (59) is over all the atomic orbitals that comprise the (super)molecular basis set, that upon diagonalization in the (super)molecular Hamiltonian will yield both occupied and unoccupied molecular orbitals. In a one-electron theory such as the EH approximation, both types of orbitals contribute in the same way. For example, the terms in Eq. (59) that describe an electron moving from the highest occupied molecular orbital (HOMO) into empty states of the anode, followed by an electron moving from the cathode into the HOMO (hole transport), and an electron moving from the cathode to the lowest unoccupied molecular orbital (LUMO), then moving on into the cathode (electron transport), are similar (their values depend on the energies of the molecular orbitals involved with respect to the Fermi energies), irrespective of whether the corresponding orbitals are occupied or not. The same is true in the HF calculation if the Koopman's theorem [142], stating that the HF orbital energies represent

the actual energies involved in removing an electron from an occupied orbital or putting an electron into an unoccupied one, holds. The Koopman's theorem is accurate only for large systems, and the approximation involved in applying it to small systems is one reason why HF is not necessarily superior to EH for calculating the conduction properties of small molecular junctions. This is true particularly for LUMO dominated conduction, because the HF is notoriously inadequate for electron affinities [143–146]. See Ref. [137] for further discussion of this point. Another potential (but in principle avoidable) problem in these calculations is associated with the finite, relatively small basis of atomic orbitals used. Close to resonance, when the electrode electrochemical potential  $\mu = E_F + e\Phi$  approaches the HOMO or LUMO energies, the corresponding HOMO or LUMO orbitals dominate the electron transfer and a small basis that correctly describes these orbitals is sufficient. When  $E_F$  is a distance  $\Delta E$  away from  $E_{\text{HOMO}}$  or  $E_{\text{LUMO}}$ , all molecular orbitals in the range  $\Delta E$  below  $E_{\text{HOMO}}$  and in a similar range above  $E_{\text{LUMO}}$  can contribute to the transmission probability and cannot be ignored, implying the need for a larger molecular basis [110]. We note in passing that the recently discussed transmission antiresonances [140, 141] associated with the nonorthogonality of the atomic orbital basis sets, have been shown [110] to be sometimes artifacts of a small basis calculation.

In spite of these limitations, EH- and HF-based calculations have provided important insight into the conduction properties of molecular junctions. In view of other unknowns, associated both with the uncertainty about the junction structure and with the simplified computation, the main value of the results obtained from such

calculations should be placed not in the absolute numbers obtained, but rather in highlighting the importance of the model parameters in determining the junction conduction behavior. Examples for qualitative issues that were investigated with these types of calculations include the effect of the nature (length and conjugation) of the molecular bridge [126, 127], the effect of the molecule–electrode binding and of the molecular binding site [130], the relation of conductance spectra to molecular electronic structure [79] and the effect of bonding molecular wires in parallel [128]. (See also Ref. [147])

### 1.3.8

#### Spatial-grid Based Pseudopotential Approaches

Another way to evaluate the expressions appearing in Eqs. (34 and 37) as well as related partial sums is closely related to the discrete variable representation of reaction probabilities as formulated by Seideman and Miller [148–150]. We have already seen that the sum

$$s(E) \equiv \sum_{l,r} |T_{lr}|^2 \delta(E - E_l) \delta(E - E_r) \quad (61)$$

which is related to the conduction by  $g(E) = (4\pi e^2/\hbar)s(E)$  (c.f. Eq. 37) can be represented by (c.f. Eq. 59)

$$s(E) = \frac{1}{4\pi^2} \text{Tr} [G^{(M)}(E) \Gamma^{(R)}(E) \times G^{(M)*}(E) \Gamma^{(L)}(E)] \quad (62)$$

If, instead of considering transitions from “left” to “right” electrode, we think of Eq. (61) as expressing a sum over transition probabilities from all initial ( $i$ ) states of energy  $E$  in the reactant space to all final ( $f$ ) states of the same energy in the product space,  $s(E)$

is also associated with the so called *cumulative reaction probability* [148–150], which in terms of the reaction S matrix is defined by  $N(E) = \sum_{i,f} |S_{if}(E)|^2 = 4\pi^2 s(E)$ , that is,  $N(E) = \sum_{i,f} \mathbf{T}_{if}(E)$ . Equation (62) now expresses the important observation that the cumulative reaction probability for a reactive scattering process can be expressed as a trace over states, *defined in a finite subspace that contains the interaction region*, of an expression that depends on the reduced Green's function and the associated self energy defined in that subspace. Following Seideman and Miller we can use a spatial grid representation for the states in this subspace, so that the trace in Eq. (62) becomes a sum over grid points. Also, in this representation the overlap matrix  $\mathbf{Z}$  is zero. In general, any subspace of position space that separate reactants from products (i.e. that encompasses the entire interaction region; the molecular bridge in our application) can be used in Eq. (62), provided that the consequences of truncating the “rest of the universe”, expressed by the corresponding  $\Sigma$  and  $\Gamma$  can be computed. The absorbing boundary condition Green's function (ABCGF) method of Seideman and Miller is based on the recognition that if this subspace is taken to be large enough so that its boundaries are far from the interaction region, the detailed forms of  $\Sigma$  and  $\Gamma$  are not important; the only requirement is that scattered waves that approach these boundaries will be absorbed and not reflected back into the interaction zone. In the ABCGF method, this is accomplished by taking  $\Sigma = -(1/2)i\Gamma = -i\varepsilon(\mathbf{r})$ , a local function in position space, taken to be zero in the interaction region and gradually increasing from zero when approaching the subspace boundaries. Its particular form is chosen to effect complete absorption of waves approaching the boundary to

a good numerical accuracy. Equation (62) then becomes

$$s(E) = 4Tr[G^{ABC}(E)_{\varepsilon_R} G^{ABC*}(E)_{\varepsilon_L}] \quad (63)$$

where  $G^{ABC}(E) = (E - H + i\varepsilon)^{-1}$ ;  $\varepsilon = \varepsilon_R + \varepsilon_L$  and where  $\varepsilon_R$  and  $\varepsilon_L$  are different from zero only on grid points near the right side (more generally the product side), and the left (reactant) side of the inner subspace, respectively.

A similar development can be done for the partial sum

$$s_l(E) \equiv \sum_r |T_{lr}|^2 \delta(E - E_r) \quad (64)$$

which, provided that  $l$  is taken as an eigenstate of the Hamiltonian describing the left electrode (or the reactant subspace), is related the “one to all” rate,  $k_l(E)$  to go from an initial state of energy  $E$  on the left electrode (or in reactant space) to all possible states on the right one (product space) according to  $k_l = (2\pi/\hbar)s_l$ . (The “microcanonical rate” is defined by  $k(E) = \rho_L^{-1}(E) \sum_l k_l \delta(E - E_l) = (2\pi/\hbar \rho_L(E))^{-1} 4\pi^2 s(E) = (\pi \hbar \rho_L(E))^{-1} N(E)$ .) We use the same definition of the coupling  $V$  between our subspace (bridge) and the reactant and product (electrode) states. Putting  $T = VGV$  in Eq. (64) we get

$$s_l(E) = \frac{1}{2\pi} \langle l | V G^{(M)} \Gamma^{(R)} G^{(M)*} V | l \rangle \quad (65)$$

Using again a position grid representation of the intermediate states used to evaluate this expression, and applying the same methodology as above, Eq. (65) can be recast in the form

$$\begin{aligned} s_l(E) &= \frac{1}{\pi} \langle l | V G^{ABC}(E)_{\varepsilon_R} G^{ABC*}(E) V | l \rangle \\ &= \frac{1}{\pi} \langle l | \varepsilon_L G^{ABC}(E)_{\varepsilon_R} G^{ABC*}(E)_{\varepsilon_L} | l \rangle \end{aligned} \quad (66)$$



The second part of Eq. (66) is obtained by using the identity  $\varepsilon_R|l\rangle = 0$  to write  $\varepsilon_R G^* V|l\rangle = \varepsilon_R(1 + G^* V)|l\rangle = \varepsilon_R G^*(G^{*-1} + V)|l\rangle$ , which, together with  $G^{*-1} = E - H_0 - V + i\varepsilon$ ,  $(E - H_0)|l\rangle = 0$  and  $\varepsilon|l\rangle = \varepsilon_l|l\rangle$ , yields the desired result.

The results (63 and 66) are very useful for computations of transmission probabilities in models in which the interaction between the transmitted particle and the molecular spacer is given as a position dependent pseudopotential. Applications to electron transmission through water and other molecular layers are discussed in Refs. [151–158].

### 1.3.9

#### Density Functional Calculations

Density functional methods provide a convenient framework for treating metallic interfaces [100]. Applications of this methodology to the problem of electron transport through atomic and molecular bridges have been advanced by several workers. In particular, Lang's approach [90, 159–165] is based on the density functional formalism [166, 167] in which the single electron wave functions  $\psi_0(\mathbf{r})$  and the electron density  $n_0(\mathbf{r})$  for two bare metal (jellium) electrodes is computed, then used in the Lippman–Schwinger equation

$$\begin{aligned} \psi(\mathbf{r}) = \psi_0(\mathbf{r}) + \int d\mathbf{r}' d\mathbf{r}'' G^0(\mathbf{r}, \mathbf{r}') \delta V \\ \times (\mathbf{r}', \mathbf{r}'') \psi(\mathbf{r}'') \end{aligned} \quad (67)$$

to get the full single electron scattering wave functions  $\psi(\mathbf{r})$  in the presence of the additional bridge. (Lang's earlier calculations [90, 168] use a related density functional approach to calculate the tunneling current between an atomic tip and a jellium electrode without an atomic or molecular bridge). In Eq. (67),  $G^0$  is the

Green's function of the bare electrode system and  $\delta V$  is the difference between the potential of the full system containing an atomic or a molecular spacer and that of the bare electrodes. In atomic units ( $|e|$ ,  $\eta$ ,  $m = 1$ ), it is

$$\begin{aligned} \delta V(\mathbf{r}, \mathbf{r}') = V_{ps}(\mathbf{r}, \mathbf{r}') + \left[ V_{xc}(n(\mathbf{r})) - V_{xc} \right. \\ \left. \times \left( n_0(\mathbf{r}) + \int d\mathbf{r}'' \frac{\delta n(\mathbf{r}'')}{|\mathbf{r} - \mathbf{r}''|} \right) \right] \end{aligned} \quad (68)$$

where  $V_{ps}$  is the sum of nonlocal pseudopotentials representing the cores of the spacer atoms and  $V_{xc}$  is the local density approximation (LDA) of the exchange-correlation potential.  $n$  is the electron number density for the full system (electrodes and atoms) and  $\delta n = n - n_0$ . Equation (67) yields scattering states that can be labeled by their energy  $E$ , momentum  $\mathbf{k}_{\parallel}$  in the direction ( $yz$ ) parallel to the electrodes and spin. In addition, Lang distinguishes between wave functions that in the electrode regions carry positive (+) or negative (−) momentum in the tunneling direction. Denoting by  $\mu_L$  and  $\mu_R$  the electron electrochemical potential in the left and right electrode, respectively, the zero-temperature electrical current density from left to right (for  $\mu_L > \mu_R$ ) is then

$$J(\mathbf{r}) = -2 \int_{\mu_L}^{\mu_R} dE \int d^2 K_{\parallel} Im\{\psi_+^* \nabla \psi_+\} \quad (69)$$

The factor 2 accounts for the double occupancy of each orbital. This approach was used recently [169] to calculate current through a molecular species, Benzene 1,4-dithiolate molecule (as used in the experiment described in Ref. [67]), between two jellium surfaces. The result demonstrates the large sensitivity of the computed current to the microscopic structure of the molecule–metal contacts.

A similar density functional approach, using an atomic level description of the electrodes, was described by Di ventra and Pantelides [170]. These authors used density-functional based ground state molecular dynamics [171] in order to get the relaxed structure of the metal-atomic system-metal junction; then evaluated the current through the relaxed structure.

The density-functional based calculations described above were done for small applied potential bias between the electrodes. In contrast, the density functional approach of Hirose and Tsukada [172] calculates the electronic structure of a metal-insulator-metal system under strong applied bias. The main difference from the density functional approaches described above comes in the way the effective one-electron potential is calculated. The potential used in this work contains the usual contributions from the Coulomb and the exchange-correlation interactions as well as from the ionic cores. However, the Coulomb (Hartree) contribution is obtained from the solution of a Poisson equation

$$\nabla^2 V_H(\mathbf{r}) = -4\pi[\rho(\mathbf{r}) - \rho_+(\mathbf{r})] \quad (70)$$

in the presence of the applied potential boundary conditions.  $\rho_+(\mathbf{r})$  is the fixed positive charge density, and the electron density  $\rho(\mathbf{r})$  is constructed by summing the squares of the wave functions over the occupied states. At the same time, the exchange-correlation potential is calculated in the standard LDA, neglecting the effect of the finite current that exists in the steady state system. The resulting formalism thus accounts approximately for nonequilibrium effects within the density functional calculation. (A simplified version of the same methodology has recently been presented by Mujica et al. [173].)

To end this brief overview of density-functional-based computations of molecular conduction, we should note that this approach suffers in principle from problems similar to those encountered in using the HF approximation, that is, the inherent inaccuracy of the computed LUMO energy and wave functions. The errors are different, for example HF overestimates the HOMO–LUMO gap (since the HF LUMO energy is too high [143–146, 174–176]) while density functional theory (DFT) underestimates it [167, 177]. Common to both approaches is the observation that processes dominated by the HOMO level will be described considerably better by these approaches than by processes controlled by coupling to the LUMO [137, 178].

### 1.3.10

#### Potential Profiles

The theoretical and computational approaches described above are used to compute both the Ohm-law conduction,  $g(E_F)$  of a molecular bridge connecting two metals, (Eqs. 37 or 59), and the current–voltage characteristics of the junction, also beyond the Ohmic regime (Eq. 36). We should keep in mind that these calculations usually disregard a potentially important factor – the possible effect of the imposed electrostatic field on the nuclear structure as well as on the electronic structure of the bridge. A change in nuclear configuration under the imposed electrostatic field is, in fact, not very likely for stable chemisorbed molecular bridges. On the other hand, the electronic wave functions can be distorted by the imposed field, and this in turn may affect the electrostatic potential distribution along the bridge, the electronic coupling between bridge segments and the position of the molecular energy levels vis-a-vis

the metal's Fermi energies. (In a single electron description, the local electrostatic potential will be an input, associated with the underlying many-electron response of the molecular bridge, to the position dependent energies of the bridge electronic states in the site representation.) These effects were, in fact, taken approximately into account by Hirose and Tsukada [172] and by Mujica, Roitberg and Ratner [173] by solving simultaneously, the coupled Schrödinger and Poisson equations. The latter yields the electrostatic potential for the given electron density and under the imposed potential boundary conditions.

The importance of the electrostatic potential profile on the molecular bridge in determining the conduction properties of a metal-molecule-metal junction was recently discussed by Tian et al [72] in conjunction with the current-voltage characteristics of a junction comprised of an STM tip, a gold substrate and a molecule with two bonding sites (e.g.  $\alpha, \alpha'$ -xylyl dithiol) connecting the two.

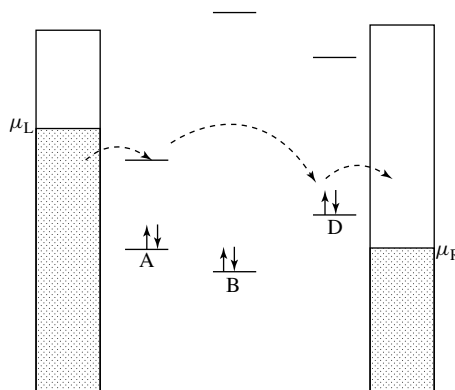
#### 1.3.11

##### Rectification

The possibility of constructing molecular junctions with rectifying behavior has been

under discussion ever since Aviram and Ratner [179] suggested that an asymmetric donor-bridge-acceptor system connecting two metal leads could rectify current. The proposed mechanism of operation of such a device is shown in Fig. 5. When the left electrode is negatively biased, that is, the corresponding electrochemical potentials satisfy  $\mu_L > \mu_R$  as shown, electrons can move from this electrode to the LUMO of molecular segment A, as well as from the HOMO of molecular segment D, to the right electrode. Completion of the transfer by moving an electron from A to D is assisted by the intermediate bridge segment B. When the polarity of the bias is reversed, the same channel is blocked. This simple analysis is valid only if the molecular energy levels do not move together with the metal electrochemical potentials, and if the coupling through the intermediate bridge is weak enough so that the orbitals on the D and A species maintain their local nature. Other models for rectification in molecular junctions have been proposed [180]. As discussed above, the expected rectifying behavior can be very sensitive to the actual potential profile in the ABD complex, which in turn depends on the molecular response to the applied bias [72, 181]. This explains why rectification is

**Fig. 5** A model for current rectification in a molecular junction: Shown are the chemical potentials  $\mu_L$  and  $\mu_R$  in the two electrodes, and the HOMO and LUMO levels of the donor, acceptor, and bridge. When the right electrode is positively biased, (as shown) electrons can hop from left to right as indicated by the dotted arrows. If the opposite bias can be set without affecting the electronic structure of the DBA system too much, the reverse current will be blocked.



often not observed even in asymmetric molecular junctions [181]. However, rectification has been observed in a number of metal-molecule-metal junctions, as well as in several STM experiments involving adsorbed molecules [61, 65, 182–185].

### 1.3.12

#### Carrier–carrier Interactions

The models and calculations discussed so far focus on processes for which the probability that a charge carrier populates the bridge is low so that carrier–carrier interactions can be disregarded. Electron–electron interactions were taken into account only in so far that they affected the single electron states, either in constructing the molecular spectrum (in the *ab initio* HF or DFT calculations) or in affecting the junction electrostatic potential through the electronic polarization response of the molecule or the metal contacts. When the density of carriers in the space between the metal contacts becomes large, Coulomb interactions between them have to be taken into account explicitly. Here we briefly discuss the effect of such interactions.

In classical (hopping) transport of carriers through insulating films separating

two metals, intercarrier interactions appear as suppression of current owing to film charging [186, 187]. In nano-junctions involving double barrier structures, increased electron population in the intermediate well under resonance transmission should affect the transport process for similar reasons. For example, consider a small metal sphere of radius  $R$  in the space between two metal electrodes (Fig. 6), and assume that both sphere and electrodes are made of the same metal of work function  $W$ . Neglecting possible proximity effect of these electrodes, the classical energy for removing an electron from the sphere to infinity is  $W + e^2/2R$  and the classical energy for the opposite process is  $W - e^2/2R$ . (From experimental and theoretical work on ionization potentials of small metal clusters [188] we know that the actual energies are approximately  $W + 0.4e^2/R$  and  $W - 0.6e^2/2R$ , respectively; with the differences arising from quantum size effects.) Here, the sphere plays the role of a molecular bridge in assisting electron tunneling between the two electrodes, and these energies now play the same role as the corresponding HOMO and LUMO energies of the bridge. This implies that a finite voltage difference is needed before current can flow in this sphere-assisted mode between the two

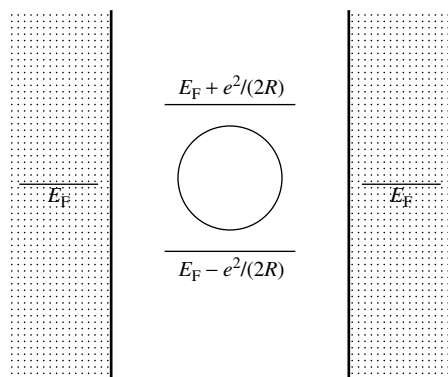


**Fig. 6** A nano-dot between two conducting leads: A model for Coulomb blockade phenomena.

metals, a phenomenon known as Coulomb blockade. For a larger potential bias, other conduction channels, corresponding to more highly charged states of the sphere give rise to the phenomenon of Coulomb steps [189]. For experimental manifestations of such and related phenomena, see, for example, Refs. [190–196]. The possibility to observe such phenomena in electrochemical systems was discussed by Kuznetsov and Ulstrup [197] and possibly demonstrated by Fan and Bard [198].

When the junction consists of a molecule or a few molecules connecting two metal leads, such Coulomb blockade phenomena are not expected to appear so clearly. The first Coulomb threshold is replaced, as just described, by the gap associated with the position of the metal's Fermi energies relative to the molecular HOMO and LUMO levels (modified by appropriate electron correlations). However, the discreteness (in the sense that  $\Delta E \gg k_B T$ ) of the molecular spectrum implies that for any given charging state of the molecule, for example, a molecule with one excess electron or one excess hole, there will be several distinct conduction channels that will appear as steps in the current versus voltage plot. It will be hard to distinguish between this structure and between a “genuine” Coulomb blockade structure. It should be emphasized that for potential applications, such as using the molecular junction in single electron transistor devices, the distinction between the origins of these conduction structures is in principle, not important.

However, understanding the role played by electron–electron interactions (in particular, correlation effects beyond the HF approximation) remains an important challenge in the study of molecular nanojunctions. Several recent theoretical works have addressed this problem within the

Hubbard model with [199–201] or without [202] the mean field approximation. In particular, Malysheva and Onipko have derived a tight binding analog of the model for negative differential resistance originally proposed by Davydov and Ermakov [203] (see also Refs. [204–206]). Numerical simulations [207] can assist in gauging the performance of the mean field approximations used in these calculations. Such models may be relevant to the understanding of recent experimental observation of negative differential resistance in a metal-self-assembled monolayer–metal junction with the SAM containing a nitroamine redox center [208].

We conclude this discussion by emphasizing again that understanding correlated carrier transport in molecular junctions continues to be an important experimental and theoretical challenge. Recent work by Gurvitz et al [209–211], using exactly solvable models of electron transport in two and three barrier structures, has indicated that new phenomenology may arise from the interplay of inelastic transitions and intercarrier interactions in the barrier. In fact, dephasing transitions in the barrier may prove instrumental in explaining the charge quantization that gives rise to the single electron transport behavior of such junctions (Sect. 6.3 in Ref. [212]).

### 1.3.13

#### Some Open Issues

This section discusses some subtle difficulties that are glossed over in most of the treatments of electron transmission using the formalisms described above. These should be regarded as open theoretical issues that should be addressed in future developments. The source of these problems is our simplified treatment of what is actually a complex many-body open system.

In particular, common ways of incorporating many-body-effect using single-body effective potentials become questionable in particular limits of timescales and interaction strengths.

One such issue, already mentioned, is the use of static image to account for the effect of metal polarizability (that is, the response of the metal electrons) on charge transfer processes at metal surfaces. Timescale estimates for electron tunneling in molecular systems are of the same order as metal plasma frequencies that measure the electronic response time of metals. However, static image theory has been used in the analysis of Sect. 1.3.3, and in other treatments of electron injection from metals into insulating phases [213]. To what extent dynamic image effects are important is not known, though theories that incorporate such effects have been developed [97–100].

Assuming that image interactions at metal surfaces should be accounted for in the static limit, namely that the metal responds instantaneously to the tunneling charge, opens other questions. Many calculations of electronic processes near metal surfaces [e.g. [89] (See Sect. 1.3.3 above)] *assume* that the metal electrons respond instantaneously to the *position* of the tunneling electron. Other calculations use *atomic or molecular orbitals*, or more general electronic charge distributions, and computing these under the given potential boundary conditions (see, e.g. Ref. [178]) implies that the corresponding orbitals or charge distributions are well defined on timescales shorter than the metal response times. (Computing molecular orbitals self-consistently with image interactions is the common practice in quantum chemistry calculations for solvated molecules using reaction field (cavity) models. Again we

have a choice: either imposing the reaction field on the electronic Hamiltonian in the position representation, thus modifying all Coulomb interaction terms, then calculate the electronic wave functions under the new potential, or compute the electronic wave functions with the original Hamiltonian under the imposed dielectric boundary conditions. The fact that the two representations are not equivalent is associated with the approximate nature of the approach, which replaces a detailed treatment of the electronic structure of the solvent by its electronic dielectric response and with the fact that the Schrödinger equations derived from them are nonlinear in the electronic wave functions).

Examination of the energies and timescales involved suggests that assuming instantaneous metal response to the electron position is more suitable in most situations than taking instantaneous response to the charge distribution defined by a molecular orbital, but the corresponding timescales are not different enough to make this a definite statement.

A similar issue appears in attempts to account for the electronic polarizability of a solvent in treating fast electronic processes involving solute molecules or excess electrons in this solvent. For example, in treating electron transmission in MIM junctions, the potential barrier that enters into expressions such as Eq. (14) depends on the electronic structure of the insulating spacer. For vacuum tunneling, a rectangular barrier, whose height above the metal Fermi energy is the metal work function, modified by image interactions as discussed above and in Sect. 1.3.3, seems appropriate. For a dielectric spacer, the barrier should be further modified by the fast (electronic) dielectric response of this spacer in the same way that it is modified by the electronic response of

the metal, raising issues similar to those discussed above.

An interesting point of concern is related to the way the Fermi distribution functions enter into the current equations. For example, Bardeen's transmission formula (21) is based on weak coupling between states localized on the two electrodes, the partial or unidirectional currents contain a product,  $f(1 - f)$ , that is, the probability that the initial state is occupied multiplied by the probability that the final state is not. In this viewpoint, the transitions occur between two weakly coupled systems, each of them in internal thermal equilibrium, which are out of equilibrium with each other because of the potential bias. Alternatively, we could work in the basis of exact eigenstates of the whole system comprising the two electrodes and the spacer between them. This system is in an internal nonequilibrium state in which transmission can be described as a scattering problem. The relevant eigenstates correspond to incident (incoming) waves in one electrode and transmitted waves in the other. The flux associated with those scattering states arising from an incident state in the negatively biased electrode is proportional to  $f(E)$ , while that associated with incoming waves in the positively biased electrode is proportional to  $f(E + e\Phi)$ . The net flux is therefore, found again to be proportional to the difference  $f(E) - f(E + e\Phi)$ . This argument cannot be made unless the process can be described in terms of coherent scattering states defined over the whole system. When inelastic scattering and dephasing processes take place, the description in terms of exact scattering states of the whole system becomes complicated [212, 214], although kinetic equations for electron transport can be derived for relatively simple situations [209–211]. On the other

hand, it appears that for weakly coupled contacts the perturbative approach that leads to Eq. (21) is valid. This approach describes the transmission in terms of electron states localized on the two electrodes where unidirectional rates appear with  $f(1 - f)$  factors, and can in principle be carried over to the inelastic regime. The exact correspondence between these different representations needs further study.

Finally, the theoretical and computational issues discussed in this chapter are based on the assumption that the electron tunnel factors do not depend on the interaction between the molecular system and its thermal environment. This assumption covers one important scenario of electron transmission. On the other extreme are systems in which electron transfer is thermally activated and long range electron transfer is dominated by hopping. An important example is provided by the recent results on long range electron transport in DNA [215–219]. The transition from tunneling to hopping and other issues involving thermal effects in long-range electron transfer have recently been discussed by several workers [220].

### Acknowledgments

This work was supported by the the Israel Science Foundation, the U.S. Israel Binational Science foundation and by the Israel Ministry of Science.

### References

1. J. Jortner, M. Bixon, (Eds.), *Advances in Chemical Physics: Electron Transfer – from Isolated Molecules to Biomolecules*, John Wiley & Sons, New York, 1999, Vol. 106.
2. A. M. Kuznetsov, *Charge Transfer in Physics, Chemistry and Biology*, Gordon & Breach, New York, 1995.

3. A. M. Kuznetsov, J. Ulstrup, A. M. Kuzne, T. Sov, *Electron Transfer in Chemistry and Biology: An Introduction to the Theory*, John Wiley & Sons, New York, 1998.
4. D. R. Lamb, *Electrical Conduction Mechanisms in Thin Insulating Films*, Methuen, London, 1967.
5. R. J. Miller, G. McLendon, A. Nozik et al., *Surface Electron Transfer Processes*, VCH Publishers, New York, 1995.
6. F. Schmickler, *Interfacial Electrochemistry*, Oxford University Press, Oxford, 1996.
7. R. M. Metzger in *Molecular Electronics – Science and Technology* (Ed.: A. Aviram), American Institute of Physics Conference Proceedings, New York, 1992, Vol. 262, p. 85.
8. C. A. Mirkin, M. A. Ratner, *Annu. Rev. Phys. Chem.* **1992**, 43, 719–754.
9. K. Sienicki, (Ed.), *Molecular Electronics and Molecular Electronic Devices*, CRC Press, New York, 1994.
10. M. C. Petty, M. R. Bryce, D. Bloor, (Eds.), *An Introduction to Molecular Electronics*, Oxford University Press, Oxford, 1995.
11. C. Joachim, S. Roth, (Eds.), *Atomic and Molecular Wires*, Kluwer, Dordrecht, The Netherlands, 1997, Vol. 341.
12. J. Jortner, M. Ratner, (Eds.), *Molecular Electronics*, Blackwell Science, Oxford, 1997.
13. L. Kouwenhoven, *Science* **1997**, 275, 1896, 1897.
14. A. Aviram, M. Ratner, (Eds.), *Molecular Electronics: Science and Technology*, New York Academy of Sciences, New York, 1998.
15. C. Dekker, *Phys. Today* **1999**, 52, 22–28.
16. M. A. Reed, *Proc. IEEE* **1999**, 87, 652–658.
17. A. G. Davies, *Philos. Trans. R. Soc. London Ser. A – Phys. Sci. Eng.* **2000**, 358, 151–172.
18. R. Landauer, *IEEE Trans. Electron Devices* **1996**, 43, 1637–1639.
19. R. A. Marcus, *J. Chem. Phys.* **1965**, 43, 679.
20. S. Gosavi, R. A. Marcus, *J. Phys. Chem.* **2000**, 104, 2067–2072.
21. M. R. Wasielewski, M. P. Niemczyk, D. G. Johnson et al., *Tetrahedron* **1989**, 45, 4785.
22. S. B. Sachs, S. P. Dudek, L. R. Sita et al., *J. Am. Chem. Soc.* **1997**, 119, 10 563.
23. V. Grosshenny, A. Harriman, R. Ziessel, *Angew. Chem., Int. Ed. Engl.* **1996**, 34, 2705.
24. J. M. Tour, *Chem. Rev.* **1996**, 96, 537.
25. A. Osuka, N. Tanade, S. Kawabata et al., *J. Org. Chem.* **1995**, 60, 7177.
26. A. C. Ribou, J. P. Launay, K. Takahashi et al., *Inorg. Chem* **1994**, 33, 1325.
27. S. Woitellier, J. P. Launay, C. W. Spangler, *Inorg. Chem.* **1989**, 28, 758.
28. A. Helms, D. Heiler, G. McLendon, *J. Am. Chem. Soc.* **1992**, 114, 6227.
29. L. M. Tolbert, *Acc. Chem. Res.* **1992**, 25, 561.
30. T. S. Arrhenius, M. Balnchard-Desce, M. Dvolaitzky et al., *Proc. Natl. Acad. Sci.* **1986**, 83, 5355.
31. P. Finkh, H. Heitele, M. Volk et al., *J. Phys. Chem.* **1988**, 92, 6584–6590.
32. R. F. Ziessel, *Chem. Educ.* **1997**, 74, 673–679.
33. M. J. Bjerrum, D. R. Casimiro, I. J. Chang et al., *J. Bioenerg. Biomembr.* **1995**, 27, 295.
34. R. Langen, I. J. Chang, J. P. Germanas et al., *Science* **1995**, 268, 1733–1735.
35. J. R. Winkler, H. B. Gray, *Chem. Rev.* **1992**, 92, 369.
36. M. Y. Ogawa, J. F. Wishart, Z. Young et al., *J. Phys. Chem.* **1993**, 97, 11 456.
37. S. S. Isied, M. Y. Ogawa, J. F. Wishart, *Chem. Rev.* **1992**, 92, 381.
38. K. S. Schanze, L. A. Cabana, *J. Phys. Chem.* **1990**, 94, 2740.
39. J. M. Vanderkooi, S. W. Englander, S. Papp et al., *Proc. Natl. Acad. Sci.* **1990**, 87, 5099.
40. C. E. Moser, C. C. Page, R. Farid et al., *J. Bioenerg. Biomembr.* **1995**, 27, 263–274.
41. M. W. Mutz, M. A. Case, J. F. Wishart et al., *J. Am. Chem. Soc.* **1999**, 121, 858, 859.
42. F. D. Lewis, T. F. Wu, Y. F. Zhang et al., *Science* **1997**, 277, 673–676.
43. R. E. Holmlin, P. J. Dandliker, J. K. Barton, *Angew. Chem., Int. Ed. Engl.* **1997**, 36, 2714.
44. P. Lincoln, E. Tuite, B. Norden, *J. Am. Chem. Soc.* **1997**, 119, 1454, 1455.
45. A. M. Brun, A. Harriman, *J. Am. Chem. Soc.* **1994**, 116, 10 383.
46. T. J. Meade, J. F. Kayyem, *Angew. Chem., Int. Ed. Engl.* **1995**, 34, 352–354.
47. P. F. Barbara, E. J. C. Olson, Experimental electron transfer kinetics in a DNA environment in *Advances in Chemical Physics: Electron Transfer – from Isolated Molecules to Biomolecules*, Pt 2 (Eds.: M. Bixon, J. Jortner), Horizon Pubs & Distributors Inc., 1999, pp. 647–676, Vol. 107.
48. K. Fukui, K. Tanaka, *Angew. Chem., Int. Ed. Engl.* **1998**, 37, 158–161.
49. E. Meggers, M. E. Michel-Beyerle, B. Giese, *J. Am. Chem. Soc.* **1998**, 120, 12 950–12 955.
50. E. Meggers, D. Kusch, M. Spichy et al., *Angew. Chem., Int. Ed. Engl.* **1998**, 37, 460–462.



51. K. P. Ghiggino, A. H. A. Clayton, J. M. Lawson et al., *New J. Chem.* **1996**, 20, 853.
52. H. Oevering, M. N. Paddon-Row, M. Heppener et al., *J. Am. Chem. Soc.* **1987**, 109, 3258.
53. M. T. Carter, G. K. Rowe, J. N. Richardson et al., *J. Am. Chem. Soc.* **1995**, 117, 2896.
54. H. L. Guo, J. S. Facci, G. McLendon, *J. Phys. Chem.* **1995**, 99, 8458.
55. B. Paulson, K. Pramod, P. Eaton et al., *Phys. Chem.* **1993**, 97, 13 042.
56. M. D. Johnson, J. R. Miller, N. S. Green et al., *J. Phys. Chem.* **1989**, 93, 1173.
57. C. A. Stein, N. A. Lewis, G. Seitz, *J. Am. Chem. Soc.* **1982**, 104, 2596.
58. V. J. Langlais, R. R. Schlittler, H. Tang et al., *Phys. Rev. Lett.* **1999**, 83, 2809–2812.
59. E. E. Polymeropoulos, D. Mobius, H. Kuhn, *Thin Solid Films* **1980**, 68, 173.
60. M. Fujihira, K. Nishiyama, H. Yamada, *Thin Solid Films* **1985**, 132, 77.
61. S. Roth, M. Burghard, C. M. Fischer, Resonant tunneling and molecular rectification in Langmuir-Blodgett films in *Molecular Electronics* (Eds.: J. Jortner, M. Ratner), Blackwell Science, Oxford, 1997, pp. 255–280.
62. E. Delamarche, B. Michel, H. A. Biebuyck et al., *Adv. Mater.* **1996**, 8, 718.
63. L. A. Bumm, J. J. Arnold, M. T. Cygan et al., *Science* **1996**, 271, 1705–1707.
64. U. Durig, O. Zuger, B. Michel et al., *Phys. Rev. B* **1993**, 48, 1711.
65. A. Dhirani, P. H. Lin, P. Guyot-Sionnest, *J. Chem. Phys.* **1997**, 106, 5249–5253.
66. L. Ottaviano, S. Santucci, S. D. Nardo et al., *J. Vac. Sci. Technol., A* **1997**, 15, 1014.
67. M. A. Reed, C. Zhou, C. J. Muller et al., *Science* **1997**, 278, 252–254.
68. D. Porath, O. Millo, *J. Appl. Phys.* **1997**, 81, 2241–2244.
69. D. Porath, Y. Levi, M. Tarabiah et al., *Phys. Rev. B* **1997**, 56, 9829–9833.
70. C. Joachim, J. K. Gimzewski, R. R. Schlittler et al., *Phys. Rev. Lett.* **1995**, 74, 2102.
71. S. Datta, W. D. Tian, S. H. Hong et al., *Phys. Rev. Lett.* **1997**, 79, 2530–2533.
72. W. D. Tian, S. Datta, S. H. Hong et al., *J. Chem. Phys.* **1998**, 109, 2874–2882.
73. J. R. Hahn, Y. A. Hong, H. Kang, *Appl. Phys. A -Mater. Sci. Process.* **1998**, 66, S467–S472.
74. W. Han, E. N. Durantini, T. A. Moore et al., *J. Phys. Chem.* **1997**, 101, 10 719–10 725.
75. Y. Manassen, D. Shachal, Scanning tunneling microscopy (STM) on physisorbed chemical groups of individual immobilized molecules, *Molecular Electronics: Science and Technology*, 1998, Vol. 852, pp. 277–289.
76. G. Nagy, *J. Electroanal. Chem.* **1996**, 409, 19–23.
77. J. M. Tour, L. Jones, D. L. Pearson et al., *J. Am. Chem. Soc.* **1995**, 117, 9529–9534.
78. C. Zhou, C. J. Muller, M. A. Reed et al., Mesoscopic phenomena studied with mechanically controllable break junctions at room temperature in *Molecular Electronics* (Eds.: J. Jortner, M. Ratner), Blackwell Science, Oxford, 1997, pp. 191–213.
79. C. Kergueris, J. P. Bourgoin, S. Palacin et al., *Phys. Rev. B: Condens. Matter* **1999**, 59, 12 505–12 513.
80. J. D. Porter, A. S. Zinn, *J. Phys. Chem.* **1993**, 97, 1190–1203.
81. K. Slowinski, R. V. Chamberlain, C. J. Miller et al., *J. Am. Chem. Soc.* **1997**, 119, 11 910–11 919.
82. K. Slowinski, K. U. Slowinska, M. Majda, *J. Phys. Chem.* **1999**, 103, 8544–8551.
83. K. Slowinsky, H. K. Y. Fong, M. Majda, *J. Am. Chem. Soc.* **1999**, 121, 7257–7261.
84. R. E. Holmin, R. F. Ismagilov, R. Haag, et al., *Angewandte Chemie* **2001**, 40, 2316.
85. H. M. McConnell, *J. Chem. Phys.* **1961**, 35, 508–515.
86. A. Onipko, Y. Klymenko, L. Malysheva et al., *Solid State Commun.* **1998**, 108, 555–559.
87. A. Onipko, Y. Klymenko, *J. Phys. Chem. A* **1998**, 102, 4246–4255.
88. B. L. Burrows, A. T. Amos, S. G. Davison, *Int. J. Quantum Chem.* **1999**, 72, 207–220.
89. J. G. Simmons, *J. Appl. Phys.* **1963**, 34, 1793–1803.
90. N. D. Lang, *Phys. Rev. B* **1987**, 36, 8173.
91. N. D. Lang, *Phys. Rev. B* **1988**, 37, 10 395.
92. N. Lang, W. Kohn, *Phys. Rev. B* **1973**, 7, 3541.
93. R. Monnier, J. P. Perdew, *Phys. Rev. B* **1978**, 17, 2595.
94. R. Monnier, J. P. Perdew, *Phys. Rev. B* **1980**, 22, 1124(E).
95. A. Kiejna, *Phys. Rev. B* **1991**, 43, 14 695–14 698.
96. K. L. Jensen, *J. Vac. Sci. Technol., B* **1998**, 17, 515–519.
97. P. A. Serena, J. M. Soler, N. Garcia, *Phys. Rev. B* **1986**, 34, 6767.
98. A. Liebsch, *Phys. Scr.* **1986**, 35, 354.

99. B. G. Rudberg, M. Johnson, *Phys. Rev. B* **1991**, 34, 9358.
100. A. Liebsch, *Electronic Excitations at Metal Surfaces*, Plenum Press, New York, 1997.
101. M. Buttiker, R. Landauer, *Phys. Rev. Lett.* **1982**, 49, 1739–1742.
102. M. Buttiker, *Phys. Rev. B* **1983**, 27, 6178–6188.
103. J. Tersoff, D. R. Hamman, *Phys. Rev. B* **1985**, 5031, 805.
104. J. Bardeen, *Phys. Rev. Lett.* **1961**, 6, 57.
105. R. Landauer, *IBM J. Res. Dev.* **1957**, 1, 223.
106. R. Landauer, *Philos. Mag.* **1970**, 21, 863–867.
107. Y. Imry, Physics of mesoscopic systems in *Directions in Condensed Matter Physics* (Eds.: G. Grinstein, G. Mazenko), World Scientific, Singapore, 1986, p. 101.
108. Y. Imry, *Introduction to Mesoscopic Physics*, Oxford University Press, Oxford, 1997.
109. W. H. Miller, S. D. Schwartz, J. W. Tromp, *J. Chem. Phys.* **1983**, 79, 4889–4898.
110. M. Galperin, D. Segal, A. Nitzan, *J. Chem. Phys.* **1999**, 111, 1569–1579.
111. V. Mujica, M. Kemp, M. A. Ratner, *J. Chem. Phys.* **1994**, 101, 6849–6864.
112. D. M. Newns, *Phys. Rev.* **1969**, 178, 1123.
113. J. N. Onuchic, D. N. Beratan, *J. Chem. Phys.* **1990**, 92, 722.
114. P. C. P. D. Andrade, J. N. Onuchic, *J. Chem. Phys.* **1998**, 108, 4292–4298.
115. A. Onipko, *Phys. Rev. B* **1999**, 59, 9995–10006.
116. A. Barraud, P. Millie, I. Yakimenko, *J. Chem. Phys.* **1996**, 105, 6972–6978.
117. A. Nitzan, *J. Phys. Chem. A* **2001**, 105, 2677.
118. D. Segal, A. Nitzan, M. A. Ratner et al., *J. Phys. Chem.* **2000**, 104, 2790.
119. P. Sautet, C. Joachim, *Chem. Phys.* **1989**, 135, 99.
120. P. Sautet, C. Joachim, *Chem. Phys. Lett.* **1991**, 185, 23.
121. P. Sautet, J. C. Dunphy, D. F. Ogletree et al., *Surf. Sci.* **1994**, 315, 127.
122. C. Chavy, C. Joachim, A. Altibeli, *Chem. Phys. Lett.* **1993**, 214, 569.
123. P. Doumergue, L. Pizzagalli, C. Joachim et al., *Phys. Rev. B* **1999**, 59, 15910–15916.
124. C. Joachim, J. K. Gimzewski, *Europhys. Lett.* **1995**, 30, 409.
125. C. Joachim, J. F. Vinuesa, *Europhys. Lett.* **1996**, 33, 635–640.
126. M. Magoga, C. Joachim, *Phys. Rev. B* **1997**, 56, 4722–4729.
127. M. Magoga, C. Joachim, *Phys. Rev. B* **1998**, 57, 1820–1823.
128. M. Magoga, C. Joachim, *Phys. Rev. B* **1999**, 59, 16011–16021.
129. M. P. Samanta, W. Tian, S. Datta et al., *Phys. Rev. B* **1996**, 53, R7626–R7629.
130. S. N. Yaliraki, M. Kemp, M. A. Ratner, *J. Am. Chem. Soc.* **1999**, 121, 3428–3434.
131. F. Biscarini, C. Bustamante, V. M. Kenkre, *Phys. Rev. B* **1995**, 51, 11089–11101.
132. E. G. Emberly, G. Kirczenow, *Phys. Rev. B* **1999**, 60, 6028–6033.
133. L. E. Hall, J. R. Reimers, N. S. Hush et al., *J. Chem. Phys.* **2000**, 112, 1510–1521.
134. F. Faglioni, C. L. Claypool, N. S. Lewis et al., *J. Phys. Chem.* **1997**, 101, 5996–6020.
135. C. L. Claypool, F. Faglioni, W. A. Goddard et al., *J. Phys. Chem.* **1997**, 101, 5978–5995.
136. S. Larsson, A. Klimkans, *Theochem. J. Mol. Struct.* **1999**, 464, 59–65.
137. S. N. Yaliraki, A. E. Roitberg, C. Gonzalez et al., *J. Chem. Phys.* **1999**, 111, 6997–7002.
138. M. D. Newton, *Chem. Rev.* **1991**, 91, 767.
139. T. Vondrak, C. J. Cramer, X. Y. Zhu, *J. Phys. Chem. B* **1999**, 103, 8915–8919.
140. E. Emberly, G. Kirczenow, *Phys. Rev. Lett.* **1998**, 81, 5205–5208.
141. E. G. Emberly, G. Kirczenow, *J. Phys. C: Condens. Matter* **1999**, 11, 6911–6926.
142. T. Koopmans, *Physica* **1933**, 1, 104.
143. M. F. Falcetta, K. D. Jordan, *J. Phys. Chem.* **1990**, 94, 5666.
144. M. F. Falcetta, K. D. Jordan, *J. Am. Chem. Soc.* **1991**, 113, 2903.
145. C.-S. Chen, T. H. Feng, J. S.-Y. Chao, *J. Phys. Chem.* **1995**, 99, 8629.
146. P. D. Burrow, A. E. Howard, A. R. Johnston et al., *J. Phys. Chem.* **1992**, 96, 7570.
147. Z. I. Miskovic, R. A. English, S. G. Davison et al., *J. of Phys. Condensed Matter* **1997**, 9, 10749–10760.
148. T. Seideman, W. H. Miller, *J. Chem. Phys.* **1992**, 97, 2499.
149. T. Seideman, W. H. Miller, *J. Chem. Phys.* **1992**, 96, 4412.
150. W. H. Miller, T. Seidman, Cumulative and state to state reaction probabilities via a discrete variable representation-absorbing boundary condition green's function in *Time-Dependent Quantum Molecular Dynamics: Experiment and Theory* (Ed.: J. Broeckhove), Plenum Press, New York, 1992.

151. D. Evans, I. Benjamin, T. Seidman et al., *Abstr. Papers Am. Chem. Soc.* **1996**, 212, 194.
152. A. Haran, A. Kadyshevitch, H. Cohen et al., *Chem. Phys. Lett.* **1997**, 268, 475–480.
153. A. Mosyak, A. Nitzan, R. Kosloff, *J. Chem. Phys.* **1996**, 104, 1549–1559.
154. A. Mosyak, P. Graf, I. Benjamin et al., *J. Phys. Chem. A* **1997**, 101, 429–433.
155. A. Nitzan, I. Benjamin, *Acc. Chem. Res.* **1999**, 32, 854–861.
156. I. Benjamin, D. Evans, A. Nitzan, *J. Chem. Phys.* **1997**, 106, 1291–1293, 6647–6654.
157. R. Naaman, A. Haran, A. Nitzan et al., *J. Phys. Chem. B* **1998**, 102, 3658–3668.
158. U. Peskin, A. Edlund, I. Bar-On et al., *J. Chem. Phys.* **1999**, 111, 7558–7566.
159. N. D. Lang, *Phys. Rev. B* **1988**, 38, 10 395.
160. N. D. Lang, A. Yacoby, Y. Imry, *Phys. Rev. Lett.* **1989**, 63, 1499.
161. N. D. Lang, *Phys. Rev. B* **1992**, 45, 13 599.
162. N. D. Lang, *Phys. Rev. B* **1995**, 51, 2029(E).
163. N. D. Lang, *Phys. Rev. B* **1995**, 52, 5335–5342.
164. N. D. Lang, P. Avouris, *Phys. Rev. Lett.* **1998**, 81, 3515–3518.
165. N. D. Lang, P. Avouris, *Phys. Rev. Lett.* **2000**, 84, 358–361.
166. R. G. Parr, W. Yang, *Density Functional Theory of Atoms and Molecules*, Oxford University Press, Oxford, 1989.
167. O. Gunnarsson, R. O. Jones, *Rev. Mod. Phys.* **1989**, 61, 689.
168. N. Lang, *Phys. Rev. Lett.* **1986**, 56, 1164.
169. M. Di Ventra, S. T. Pantelides, N. D. Lang, *Phys. Rev. Lett.* **2000**, 84, 979–982.
170. M. Di Ventra, S. T. Pantelides, *Phys. Rev. B* **1999**, 59, R5320–R5323.
171. G. Galli, M. Parrinello in *Computer Simulations in Material Science* (Eds.: V. Pontikis, M. Meyer), Kluwer, Dordrecht, The Netherlands, 1991.
172. K. Hirose, M. Tsukada, *Phys. Rev. B* **1995**, 51, 5278–5290.
173. V. Mujica, A. E. Roitberg, M. A. Ratner, *J. Chem. Phys.* **2000**, 112, 6834–6839.
174. A. Szabo, N. S. Ostlund, *Modern Quantum Chemistry: Introduction to Advanced Electronic Structure Theory*, McGraw-Hill, New York, 1989.
175. H. J. Silverstone, M. L. Yin, *J. Chem. Phys.* **1968**, 49, 2020.
176. S. Huzinaga, C. Arnau, *Phys. Rev. A* **1970**, 1, 1285.
177. H. Burke, E. K. U. Gross in *Density Functionals: Theory and Applications* (Ed.: D. Joubert), Springer, Berlin, 1998.
178. D. Lamoien, P. Ballone, M. Parrinello, *Phys. Rev. B: Condens. Matter* **1996**, 54, 5097–5105.
179. A. Aviram, M. A. Ratner, *Chem. Phys. Lett.* **1974**, 29, 277.
180. D. H. Waldeck, D. N. Beratan, *Science* **1993**, 261, 576, 577.
181. R. A. Marcus, *J. Chem. Soc., Faraday Trans.* **1996**, 92, 3905–3908.
182. M. Pomerantz, A. Aviram, R. A. McCorkle et al., *Science* **1992**, 255, 1115.
183. A. S. Martin, J. R. Sambles, *Adv. Mater.* **1993**, 5, 580–582.
184. A. S. Martin, J. R. Sambles, G. J. Ashwell, *Phys. Rev. Lett.* **1993**, 70, 218–221.
185. C. M. Fischer, M. Burghard, S. Roth et al., *Europhys. Lett.* **1994**, 28, 129–134, 375.
186. K. Nagesha, J. Gamache, A. D. Bass et al., *Rev. Sci. Instrum.* **1997**, 68, 3883–3889.
187. R. M. Morsolais, M. Deschenes, L. Sanche, *Rev. Sci. Instrum.* **1989**, 60, 2724–2732.
188. G. Makov, A. Nitzan, L. E. Brus, *J. Chem. Phys.* **1988**, 88, 5076–5085.
189. D. K. Ferry, S. M. Goodnick, *Transport in Nanostructures*, Cambridge University Press, Cambridge, 1997, Vol. 6.
190. R. Wilkins, E. Ben-Jacob, R. C. Jaklevic, *Phys. Rev. Lett.* **1989**, 63, 801–804.
191. M. A. Kastner, *Rev. Mod. Phys.* **1992**, 64, 849.
192. S. H. M. Persson, L. Olofsson, L. Gunnarsson, *Appl. Phys. Lett.* **1999**, 74, 2546–2548.
193. M. Dorogi, J. Gomez, R. Osifchin et al., *Phys. Rev. B: Condens. Matter* **1995**, 52, 9071–9077.
194. R. P. Andres, S. Datta, M. Dorogi et al., *J. Vac. Sci. Technol., A* **1996**, 14, 1178–1183.
195. R. P. Andres, T. Bein, M. Dorogi et al., *Science* **1996**, 272, 1323–1325.
196. A. N. Korotkov, Coulomb blockade and digital single electron devices in *Molecular Electronics* (Eds.: J. Jortner, M. Ratner), Blackwell Science, Oxford, 1997, pp. 157–189.
197. A. M. Kuznetsov, J. Ulstrup, *J. Electroanal. Chem.* **1993**, 362, 147–152.
198. F.-R. F. Fan, A. J. Bard, *Science* **1997**, 277, 1791–1793.
199. L. I. Malysheva, A. I. Onipko, *Phys. Rev. B* **1992**, 46, 3906–3915.
200. V. Mujica, M. Kemp, A. Roitberg et al., *J. Chem. Phys.* **1996**, 104, 7296–7305.

201. Y. Kawahito, H. Kasai, H. Nakanishi et al., *J. Appl. Phys.* **1999**, 85, 947–952.
202. Y.-Q. Li, C. Gruber, *Phys. Rev. Lett.* **1998**, 80, 1034–1037.
203. A. S. Davidov, V. M. Ermakov, *Physica* **1987**, 28D, 168–180.
204. H. L. Berkowitz, R. A. Lux, *J. Vac. Sci. Technol.* **1987**, B5, 967–970.
205. F. W. Sheard, G. A. Toombs, *Appl. Phys. Lett.* **1988**, 52, 1228–1230.
206. N. C. Kluksdahl, A. M. Krizan, D. K. Ferry et al., *Phys. Rev. B* **1989**, 39, 7720–7735.
207. A. Nakano, R. K. Kalia, P. Vashishta, *Phys. Rev. B: Condens. Matter* **1991**, 44, 8121–8128.
208. J. Chen, M. A. Reed, A. M. Rawlett et al., *Science* **1999**, 286, 1550–1552.
209. S. A. Gurvitz, H. J. Lipkin, Y. S. Prager, *Mod. Phys. Lett. B* **1994**, 8, 1377.
210. S. A. Gurvitz, H. J. Lipkin, Y. S. Prager, *Phys. Lett. A* **1996**, 212, 91–96.
211. S. A. Gurvitz, Y. S. Prager, *Phys. Rev. B* **1996**, 53, 15 932–15 943.
212. S. Datta, *Electric Transport in Mesoscopic Systems*, Cambridge University Press, Cambridge, 1995.
213. E. L. Wolf, *Principles of Electron Tunneling Spectroscopy*, Oxford University Press, New York, 1985.
214. E. Emberly, G. Kirczenow, *Phys. Rev. B* **2000**, 61, 5740–5750.
215. J. Jortner, M. Bixon, T. Langenbacher et al., *Proc. Natl. Acad. Sci. USA* **1998**, 95, 12 759–12 765.
216. M. Bixon, B. Giese, S. Wessely et al., *Proc. Natl. Acad. Sci. USA* **1999**, 96, 11 713–11 716.
217. B. Giese, S. Wesswly, M. Spormann et al., *Angew. Chem. Int., Ed. Engl.* **1999**, 38, 996–998.
218. Y. A. Berlin, A. L. Burin, M. A. Ratner, *J. Phys. Chem.* **2000**, 104, 443–445.
219. B. Giese, *Acc. Chem. Res.* **2000**, 33, 631–636.
220. A. Nitzan, *Annu. Rev. Phys. Chem.* **2001**, 52, 681–750.

## 2.1 Diffusion and Migration

*José A. Manzanares  
University of Valencia, Burjasot, Spain*

*Kyösti Kontturi  
Helsinki University of Technology, Espoo,  
Finland*

### Introduction

This chapter describes mass transport to electrodes by diffusion and migration. It is assumed throughout that there is no convective motion of the solution, and transport is described with respect to a reference frame fixed to the laboratory [1, 2]. Thus, many of the equations derived in this chapter cannot be directly applied to systems with bulk motion.

The chapter emphasizes migrational effects and provides analytical expressions for the electric potential drop in the solution under different experimental conditions. The fundamental concepts are discussed in detail, and a number of important restrictions are introduced for the sake of clarity. First, diluted solutions are considered throughout and the flux equations incorporate neither cross terms nor activity coefficients [2–5]. Second, one-dimensional systems are considered, except when presenting the transport equations in Sect. 2.1.1. Third, except in

a couple of sections, it is assumed that there are no homogeneous reactions. Insoluble species are also absent. Fourth, since the chapter is mainly of interest to cases in which mass transport is rate controlling, reversible electrode reactions are assumed and no kinetic effects are considered. Fifth, most sections involve steady state transport because the theoretical description of transient experiments in the presence of migration is difficult and quite often requires numerical solutions that bring much more mathematical complexity than new physical insights. Nevertheless, the effect of migration is analyzed in a simple transient case. Finally, the local electroneutrality (LEN) assumption is used. This is indeed a good approximation for most experimental situations, although deviations from LEN occur under some conditions. These deviations are discussed in the last section.

#### 2.1.1

##### Fundamental Concepts

This section presents the basic equations describing mass transport to electrodes: the flux equations, the continuity equation, and the LEN assumption. The flux equations are derived from the concept of electrochemical potential, which is used as a general term valid for both charged and

neutral species. The connection between electric conduction and the basic transport mechanisms, diffusion and migration, is discussed in detail, and the difference between ohmic and total electric potential gradient is emphasized. The spatial region in which mass transport takes place and the coupling between mass transport and the electrode reaction are discussed next. At this point, the one-dimensional geometry to be used henceforth is introduced. The electric potential drops in the system and the sign conventions are also defined. The boundary conditions for the transport equations are written in terms of the integral transport numbers. For the sake of simplicity, parallel reactions [6] and adsorption phenomena [7] are not considered.

#### 2.1.1.1 Diffusion–migration Flux Equations

The flux equations describing the behavior of electrochemical systems are intimately related to the Second Law of Thermodynamics. Consider two neighboring volume elements  $V'$  and  $V''$  of a solution having the same temperature and pressure, but different electrochemical potentials of their constituents. The difference between the electrochemical potential of species  $i$ ,  $\tilde{\mu}'_i$  and  $\tilde{\mu}''_i$ , in these volume elements implies that there is no distribution equilibrium and this species tends to move from one volume element to the other. This motion of species  $i$  from one volume element to its neighbor is generically called transport of species  $i$ . Since the transport of the different species in solution takes place under thermal and mechanical equilibrium, the change in internal energy  $U$  of these two volume elements is [1, 8, 9]

$$dU' = TdS' + \sum_i \tilde{\mu}'_i dn'_i \quad (1)$$

$$dU'' = TdS'' + \sum_i \tilde{\mu}''_i dn''_i \quad (2)$$

where  $T$  is the thermodynamic temperature,  $S$  the entropy, and  $n_i$  the number of moles of species  $i$ . Moreover, considering that the exchange of matter between  $V'$  and  $V''$  takes place without energy exchange with their surroundings, it is satisfied that  $dU' + dU'' = 0$  and  $dn'_i + dn''_i = 0$ . The Second Law of Thermodynamics requires that the entropy of the isolated system formed by the two volume elements must increase

$$T(dS' + dS'') = \sum_i (\tilde{\mu}''_i - \tilde{\mu}'_i) dn'_i \geq 0 \quad (3)$$

When the transport of species  $i$  is not coupled to that of other species, each individual term of this sum is positive. In this case,  $dn'_i$  is determined only by  $(\tilde{\mu}''_i - \tilde{\mu}'_i)$  and species  $i$  moves towards the region in which its electrochemical potential is lower, that is,  $dn'_i < 0$  when  $\tilde{\mu}''_i < \tilde{\mu}'_i$  and vice versa. This happens, for instance, in the case of ionic species in diluted solutions. When the transport of different species is coupled, one or more terms in the sum can be negative, but the sum is always positive.

The transport of species  $i$  can be described in terms of either its velocity  $\vec{v}_i$  or its flux density  $\vec{J}_i$ , which are related to each other by the molar concentration,  $\vec{J}_i = c_i \vec{v}_i$ . If the area of the surface separating the two volume elements is  $dA$  and its orientation is given by the unit vector  $\hat{n}$  (from  $V'$  to  $V''$ ), the number of moles of species  $i$  crossing the surface in a time  $dt$  is  $dn'_i = -\vec{J}_i \hat{n} dA dt$ .

When the difference between  $\tilde{\mu}''_i$  and  $\tilde{\mu}'_i$  is not too large, it can be assumed [10] that the rate of change of the amount of species  $i$ ,  $dn'_i/dt$ , is proportional to the difference  $\tilde{\mu}''_i - \tilde{\mu}'_i$  or, more exactly, to

the gradient of this potential normal to the surface,  $\partial \tilde{\mu}_i / \partial n \equiv \vec{\nabla} \tilde{\mu}_i \cdot \hat{n}$ . In this linear approximation, the velocity of species  $i$  is expressed as

$$\vec{v}_i = -u_i \vec{\nabla} \tilde{\mu}_i \quad (4)$$

where  $u_i$  is its mobility. Similarly, the flux density takes the form

$$\vec{J}_i = c_i \vec{v}_i = -u_i c_i \vec{\nabla} \tilde{\mu}_i = -\frac{D_i c_i}{RT} \vec{\nabla} \tilde{\mu}_i \quad (5)$$

where  $R$  is the universal gas constant and the Einstein relation between mobility and diffusion coefficient,  $D_i = u_i RT$ , has been used.

At constant temperature and pressure, the gradient  $\vec{\nabla} \tilde{\mu}_i$  originates from changes in composition and electric potential  $\phi$  so that

$$\vec{\nabla} \tilde{\mu}_i = RT \vec{\nabla} \ln c_i + z_i F \vec{\nabla} \phi \quad (6)$$

where  $F$  is the Faraday constant and  $z_i$  is the charge number of species  $i$ . Taking Eq. (6) to Eq. (5), the Nernst–Planck flux equation [11]

$$\vec{J}_i = -D_i (\vec{\nabla} c_i + z_i c_i f \vec{\nabla} \phi) \quad (7)$$

is obtained, where  $f$  denotes the ratio  $F/RT$ . The two terms in the right-hand side of this equation represent the transport mechanisms of diffusion and migration, respectively. Diffusion is a consequence of the random thermal motion of the particles, which tends to make the concentration of all species uniform. Migration accounts for the influence of the electric field,  $\vec{E} = -\vec{\nabla} \phi$ , on the random motion of the charged particles, and Eq. (7) shows that the particles acquire a component of their velocity along the direction of the electric field as a result of this influence.

### 2.1.1.2 Poisson Equation and the LEN Assumption

Equation (5) states that the flux density of species  $i$  in a diluted solution depends on  $\vec{\nabla} \tilde{\mu}_i$  but not on other gradients  $\vec{\nabla} \tilde{\mu}_{j \neq i}$ . In this sense, there is no correlation between the motions of two different species,  $i$  and  $j$ . The migrational term in Eq. (7), however, imposes a strong constraint on the motion of charged species by coupling their flux densities  $\vec{J}_i$ .

The electrical state of the system is so sensitive to small changes in composition [9] that the gradient  $\vec{\nabla} \phi$  in Eq. (7) cannot be assumed, in general, to be a simple constant [12], and an additional equation is required to determine it. Given the slowness of particle motion in solution, it is justified to use the Poisson equation from electrostatics to relate the changes in electric potential to the local electric charge density  $\rho_e$

$$\nabla^2 \phi = -\frac{\rho_e}{\varepsilon} = -\frac{F}{\varepsilon} \sum_i z_i c_i \quad (8)$$

where  $\varepsilon$  is the dielectric permittivity of the solution.

Consider, for example, a 10 mM 1:–1 electrolyte solution that contains a positive charge density of the order of  $10^6 \text{ C m}^{-3}$  counterbalanced by a negative charge of  $-10^6 \text{ C m}^{-3}$ . Since the dielectric permittivity of aqueous electrolyte solutions is of the order of  $10^{-9} \text{ C V}^{-1} \text{ m}^{-1}$ , the right-hand side of Eq. (8) is roughly the difference between two terms whose order of magnitude is  $10^{15} \text{ V m}^{-2}$ . The typical order of magnitude of the electric fields, however, can be estimated as  $10 \text{ V m}^{-1}$  and they are practically independent on position (except at the interfacial regions), so that  $\nabla^2 \phi$  is many orders of magnitude smaller than  $10^{15} \text{ V m}^{-2}$ . This means that the imbalance between cation and

anion concentrations in the system that is required to set up the typical electric potential distributions is many orders of magnitude smaller than the solution concentration. Therefore, the space charge density can be neglected and use can be made of the LEN assumption [13]

$$\sum_i z_i c_i = 0 \quad (9)$$

This equation replaces Eq. (8) in the description of transport processes. Though it is customary to use the equal symbol in Eq. (9), the electric charge density is not strictly zero, and the Poisson equation cannot be reduced to the Laplace equation  $\nabla^2 \phi = 0$ .

#### 2.1.1.3 Continuity Equation

The spatial variation of the flux density of species  $i$  is determined by the principle of conservation of the amount of substance for this species, which is represented by the continuity equation. Consider an arbitrary volume  $V$  in an electrolyte solution, in which the molar concentration of species  $i$  is  $c_i(\vec{r}, t)$ . The amount of substance of species  $i$  within  $V$  can change as a result of either a net flow of particles through the surface  $S$  enclosing the volume  $V$ , or due to homogeneous chemical reactions occurring within  $V$ . If the surface  $S$  is divided into surface elements of area  $dA$  perpendicular to the unit vector  $\hat{n}$  (oriented outwards from  $V$ ), the number of moles of species  $i$  entering  $V$  through this surface element in a time  $dt$  is  $dn_i = -\vec{J}_i \hat{n} dA dt$ . The homogeneous reactions generate or consume this species at a net rate  $r_i(\vec{r}, t)$ . Since the (net) accumulation rate of species  $i$  within  $V$  is given by the sum of the (net) generation rate due to the chemical reaction and the (net) incoming flux through  $S$ , it is concluded that

$$\begin{aligned} \frac{d}{dt} \iiint_V c_i(\vec{r}, t) dV &= \iiint_V \frac{\partial c_i}{\partial t} dV \\ &= \iiint_V r_i dV - \oint_S \vec{J}_i \hat{n} dA \\ &= \iiint_V (r_i - \vec{\nabla} \cdot \vec{J}_i) dV \end{aligned} \quad (10)$$

where Gauss' divergence theorem has been used. Moreover, since no restrictions apply to the volume  $V$ , Eq. (10) implies that

$$\frac{\partial c_i}{\partial t} + \vec{\nabla} \cdot \vec{J}_i = r_i \quad (11)$$

which is the continuity equation for species  $i$ .

#### 2.1.1.4 Ohm's Law and Migrational Transport Numbers

In a diluted electrolyte solution of uniform composition, the flux density  $\vec{J}_i = c_i \vec{v}_i$  is proportional to  $\vec{\nabla} \phi$ , and the conduction electric current density

$$\vec{I} \equiv F \sum_i z_i \vec{J}_i \quad (12)$$

satisfies Ohm's law

$$\vec{I} = -\kappa \vec{\nabla} \phi, \quad (\vec{\nabla} c_i = 0, \forall i) \quad (13)$$

where

$$\kappa \equiv \frac{F^2}{RT} \sum_i z_i^2 D_i c_i \quad (14)$$

is the electrical conductivity of the solution. The minus sign in Eq. (13) means that the electric current flows in the direction of decreasing electric potential. Equation (14) evidences that the conductivity of the solution is determined by all ionic species in solution, no matter whether they are active



or not. The migrational transport number

$$t_i \equiv \frac{z_i^2 D_i c_i}{\sum_j z_j^2 D_j c_j} \quad (15)$$

represents the relative contribution of species  $i$  to the conductivity of the solution.

Unfortunately, concentration gradients develop under most experimental conditions, and the motion of charge carriers takes place by both diffusion and migration as described by the Nernst–Planck equation, Eq. (7). In this case, Eqs. (14 and 15) provide the local (i.e. position-dependent) values of the conductivity and the transport number of species  $i$ , respectively. By writing the Nernst–Planck equation in terms of  $t_i$  as [1, 14]

$$\vec{J}_i = -\frac{t_i \kappa}{z_i^2 F^2} \vec{\nabla} \tilde{\mu}_i \quad (16)$$

Eq. (12) leads to the modified Ohm's law [5, 15]

$$\vec{I} = -\kappa (\vec{\nabla} \phi - \vec{\nabla} \phi_{\text{dif}}) \equiv -\kappa \vec{\nabla} \phi_{\text{ohm}} \quad (17)$$

in which

$$\vec{\nabla} \phi_{\text{ohm}} = \frac{1}{F} \sum_i \frac{t_i}{z_i} \vec{\nabla} \tilde{\mu}_i \quad (18)$$

is the ohmic potential gradient, and

$$\begin{aligned} \vec{\nabla} \phi_{\text{dif}} &= -\frac{F}{\kappa} \sum_i z_i D_i \vec{\nabla} c_i \\ &= -\frac{RT}{F} \sum_i \frac{t_i}{z_i} \vec{\nabla} \ln c_i \end{aligned} \quad (19)$$

is the diffusion potential gradient.

That is, the concentration gradients break the proportionality between the current density and the electric field; furthermore, in some cases,  $\vec{I}$  and  $\vec{\nabla} \phi$  are not even parallel vectors, a fact that is relevant to the tertiary current distribution [16].

This is due to the diffusion potential gradient that originates from the diffusion process, and therefore an expression similar to Ohm's law can only be recovered by subtracting the diffusion potential gradient from the total potential gradient, as shown by Eq. (17). A theoretical simplification sometimes used in the literature consists in neglecting the diffusion potential by assuming all ionic diffusivities to be equal [17, 18].

#### 2.1.1.5 Diffusion-conduction Flux Equation

The introduction of the modified Ohm's law, Eq. (17), in the Nernst–Planck equation, Eq. (7), leads to the following form of the flux equation

$$\vec{J}_i = -D_i (\vec{\nabla} c_i + z_i c_i f \vec{\nabla} \phi_{\text{dif}}) + \frac{t_i \vec{I}}{z_i F} \quad (20)$$

For the sake of simplicity, consider the case of a binary solution obtained by complete dissociation of a strong electrolyte  $A_{\nu_1} B_{\nu_2}$  into  $\nu_1$  ions  $A^{z_1}$  of charge number  $z_1$  and  $\nu_2$  ions  $B^{z_2}$  of charge number  $z_2$ ; obviously, the relation  $z_1 \nu_1 + z_2 \nu_2 = 0$  is satisfied. The ionic concentrations are then related to the stoichiometric electrolyte concentration  $c_{12}$  by the relations  $c_1 = \nu_1 c_{12}$  and  $c_2 = \nu_2 c_{12}$  which allows Eq. (20) to be rewritten as

$$\vec{J}_i = \nu_i \vec{J}_{12} + \frac{t_i \vec{I}}{z_i F} = -\nu_i D_{12} \vec{\nabla} c_{12} + \frac{t_i \vec{I}}{z_i F} \quad (21)$$

where  $\vec{J}_{12}$  is the electrolyte flux density, and

$$D_{12} = \frac{(\nu_1 + \nu_2) D_1 D_2}{\nu_2 D_1 + \nu_1 D_2} \quad (22)$$

is the Nernst–Hartley expression for the diffusion coefficient of the dissociated electrolyte [3].

Equations (20 and 21) describe ionic transport as a combination of electrolyte diffusion and ionic conduction, and hence the name diffusion–conduction flux equation is suggested. Its comparison with the diffusion–migration flux equation, Eq. (7), evidences the difference between migration and conduction. Migration is due to electric fields, either external or internal, and does not require a nonzero current density. Conduction is the ionic motion associated to the part of the electric field that is controlled externally. Note that the electric current density is a measurable magnitude but not the local electric field. Conduction requires a nonzero electric current density.

Note, finally, that the dissociated electrolyte satisfies Fick’s law,  $\vec{J}_{12} = -D_{12} \vec{\nabla} c_{12}$ , because both ions move at the same velocity in the absence of current ( $I = 0$ ), and the dissociated electrolyte is the only independently moving substance [1]. This is not in contradiction with the fact that the ionic diffusion coefficients are different to each other,  $D_1 \neq D_2$ , because the diffusion potential gradient affects the ionic motion even when  $I = 0$ . In conclusion, although the Nernst–Planck equation establishes that the flux of species  $i$  in a diluted solution is only proportional to the gradient  $\vec{\nabla} \tilde{\mu}_i$ , the contribution of the electric potential gradient to  $\vec{\nabla} \tilde{\mu}_i$  couples the transport of different species.

#### 2.1.1.6 Diffusion Boundary Layer

In general, the electrode reaction makes the concentration of species  $i$  to vary with the distance to the electrode surface. These concentration changes occur not only for the species participating in the electrode reaction, but also to other charged species because of their electrostatic coupling. The progress of the electrode reaction is accompanied by a propagation of

the concentration variations toward the interior of the solution, which affects a region that grows in thickness. It is possible, however, to confine the concentration variations to a “thin” region near the electrode by vigorous stirring, “thin” here means of the order of tenths of a millimeter. The solution can then be divided in two regions: the diffusion boundary layer (DBL) adjacent to the electrode surface, in which concentration varies with position and diffusion affects mass transport; and the bulk solution, in which concentration is made uniform by stirring and transport is due to migration and convection [5, 19, 20]. Although the transition between these two regions is actually smooth, it is practical to assume that the transition is abrupt and to assign a thickness  $\delta$  to the DBL, which can be empirically determined from the stirring rate or other hydrodynamic conditions [21, 22]. The thickness  $\delta$  is considered to be finite when describing steady state transport (indeed, this is a necessary condition for reaching the steady state); infinite DBL thickness, however, is assumed in Sect. 2.1.5.

In the following sections, the one-dimensional geometry described by Fig. 1 is considered. The electrode is located at  $x = 0$  and the DBL in the region  $0 < x < \delta$ . The electric current density  $I$  is positive for anodic oxidations and negative for cathodic reductions, in agreement with the IUPAC convention. The electric potential drop in the DBL is defined as the potential in the bulk solution ( $x = \delta$ ) relative to that at the electrode surface ( $x = 0$ ),  $\Delta\phi \equiv \phi^b - \phi^s$ .

#### 2.1.1.7 Faraday’s Law and Integral Transport Numbers

The charge transfer between an electrolyte solution and an electrode (quite frequently, a metal phase) can be represented by the

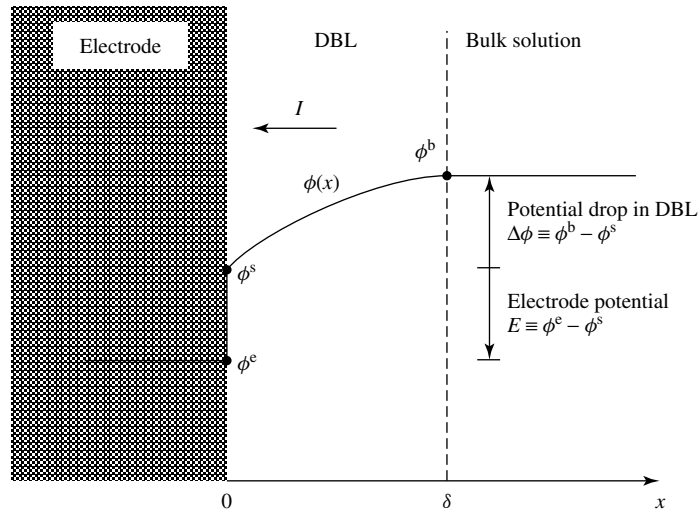


**Fig. 1** Schematic drawing of the system considered. The electric potential distribution has been shown for a cathodic process ( $I < 0$ ). Superscripts b, s, and e denote, respectively, bulk solution ( $x = \delta$ ), solution adjacent to the electrode surface ( $x = 0$ ), and electrode phase.

general electrode reaction equation

$$\sum_i \nu_i^r B_i^{z_i} + n e^- = 0 \quad (23)$$

where  $B_i$  and  $\nu_i^r$  are the molecular formula and the stoichiometric number of species  $i$ , respectively. The value of  $\nu_i^r$  is positive for products and negative for reactants. The stoichiometric number of the electron in the reaction,  $n = \sum_i z_i \nu_i^r$ , is positive for (anodic) oxidations and negative for (cathodic) reductions. The electrons in Eq. (23) are considered to be in the metal phase, and species  $B_i$  can be either in solution or in the electrode phase; it is obviously necessary that at least one active species  $B_i$  is in solution because Eq. (23) describes charge transfer between two phases.

The evolution of the electrode reaction needs the transport of reactants from the solution to its surface and products vice versa. Faraday's law establishes that the reaction rate  $d\xi/dt$  is proportional to the

conduction electric current density and, therefore, that the flux density of species  $i$  at the electrode surface is given by

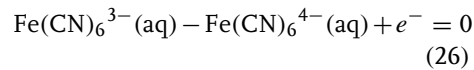
$$J_i^s = \frac{1}{A} \frac{dn_i}{dt} = \frac{\nu_i^r}{A} \frac{d\xi}{dt} = \nu_i^r \frac{I}{nF} \quad (24)$$

where  $A$  is the electrode surface area.

Equation (24) shows clearly that, at the electrode surface, the fraction of electric current density transported by species  $i$  is given by the magnitude

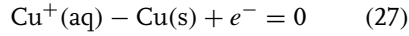
$$T_i^s \equiv \frac{z_i F J_i^s}{I} = \frac{z_i \nu_i^r}{n} \quad (25)$$

which is called the integral transport number of species  $i$  [23]; this magnitude is zero for the species that are not involved in the electrode reaction (i.e. the electroinactive species). It is important to observe that  $\sum_i T_i^s = 1$  but  $T_i^s$  is not bounded between 0 and 1. For example, in the electrode reaction

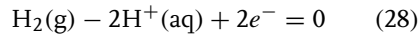


the transport numbers at the electrode surface are  $T_{\text{Fe(CN)}_6^{3-}}^s = -3$  and  $T_{\text{Fe(CN)}_6^{4-}}^s = 4$ .

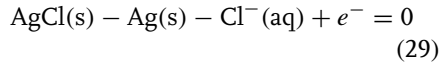
Some electrode reactions, such as the anodic dissolution of copper



the hydrogen evolution at a platinum electrode

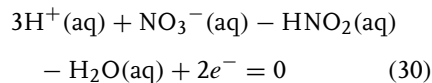


or the oxidation of silver at a Ag|AgCl electrode



involve only one electroactive species ( $\text{Cu}^+$ ,  $\text{H}^+$ , and  $\text{Cl}^-$ , respectively), which is denoted by subscript 1 henceforth. Since the current density in these processes is due to the single electroactive species,  $n = z_1 v_1^r$  and  $T_1^s = 1$ , while  $T_i^s = 0$  for  $i \neq 1$ . In these simple cases, the DBL becomes depleted of this species when  $J_1 < 0$  (i.e. the species is consumed at the electrode surface), and the potential drop satisfies  $z_1 \Delta\phi > 0$ . On the contrary, when  $J_1 > 0$ , the DBL becomes concentrated in species 1 and  $z_1 \Delta\phi < 0$ .

Note also that  $T_i^s$  is zero for neutral species but this does not imply that they are not transported towards or from the electrode. For example, in the case of nitrous acid in the electrode reaction



$T_{\text{HNO}_2}^s = 0$  but  $J_{\text{HNO}_2}^s = -I/2F$ , as can be easily deduced from Eq. (24). (For the neutral species, the transference number  $\tau_i \equiv T_i/z_i$  constitutes a good alternative to  $T_i$  [24].)

The integral transport number of species  $i$  can also be defined at locations different from the electrode surface as  $T_i \equiv z_i F J_i / I$  [23]. Under steady state conditions and in the absence of homogeneous reactions, both the current density  $I$  and the flux density  $J_i$  do not vary with position, and  $T_i$  takes the value specified by Eq. (25) throughout the whole system even when concentration gradients are present. Otherwise,  $T_i$  is position-dependent. It is important to observe that the integral transport numbers  $T_i$  are equal to the migrational transport numbers  $t_i$  in the absence of concentration gradients only; indeed, concentration gradients originate due to the fact that  $T_i \neq t_i$ .

#### 2.1.1.8 Nernst Equation and Concentration Overpotential

In order to drive an electric current density across the system depicted in Fig. 1, an electric potential difference must be applied between the electrode and the bulk solution. This potential difference can be expressed in terms of three contributions: the potential drop in the DBL, the equilibrium interfacial or Nernst potential drop, and the activation overpotential. For large enough kinetic currents, the latter contribution can be neglected [7, 25] and the potential difference required for the electrode process is  $E_{\text{eq}} - \Delta\phi$ , where  $E_{\text{eq}}$  is the equilibrium electrode potential (i.e. the electric potential of the electrode relative to that at the adjacent electrolyte solution). The value of  $E_{\text{eq}}$  is given by the Nernst equation. For the electrode Reaction (23), the Nernst equation takes the form

$$E_{\text{eq}} = E^\circ + \frac{RT}{nF} \sum_i v_i^r \ln \frac{c_i^s}{c_i^\circ} \quad (31)$$

where  $E^\circ$  is the standard (or, more exactly, the formal) electrode potential and  $c^\circ$  is

the standard concentration. The concentrations  $c_i^s$  of the active species in Eq. (31) are those at the electrode surface, which are evaluated by extrapolation to the electrode surface of the concentration profile within the DBL [19]. In other words, the electrode surface at position  $x = 0$  should be understood as the neutral solution just outside the electrical double layer (EDL). Similarly,  $\Delta\phi$  refers to the potential difference between the bulk solution and that point in the solution (that is, between the bulk solution|DBL and the EDL|DBL boundaries). Hence, no details of the EDL structure are considered when evaluating the equilibrium interfacial potential drop and the surface concentrations of the active species.

Since the interfacial concentrations of the active species vary with the electric current density,  $E_{\text{eq}}$  also does and its variation is often described in terms of the concentration overpotential [19, 26]

$$\eta_c \equiv E_{\text{eq}} - E_{\text{eq}}^b \equiv \frac{RT}{nF} \sum_i \nu_i^r \ln \frac{c_i^s}{c_i^b} \quad (32)$$

which represents the potential of the electrode in equilibrium with the interfacial concentrations that are established when a current density  $I$  is driven through the system,  $E_{\text{eq}}$ , relative to the (constant) potential of a similar electrode equilibrated with the bulk solution,  $E_{\text{eq}}^b$ . The potential difference between the electrode and the bulk solution is then  $E_{\text{eq}}^b + \eta_c - \Delta\phi$ .

Note, finally, that when the supporting electrolyte is used, the ionic strength of the DBL is not significantly affected by the concentration polarization of the active species, and therefore, their activity coefficients are practically independent of the current density [26]. This justifies the use of concentrations instead of activities in the above equations.

## 2.1.2

### Steady State Current–voltage Curves of Systems with One Active Species

The finite transport rate of the electroactive species toward the electrode surface implies the existence of a limiting current density, that is the most important consequence of mass transport. This limiting current density is defined by the condition of maximum concentration gradient of the electroactive species, which is achieved when the concentration of this species tends to zero at the electrode | depleted DBL interface (or, more accurately, at the EDL | DBL boundary).

In this section, the mass transport effects on the steady state current–voltage curves are described for the (relatively common) case of systems with only one electroactive species in solution. This species is denoted by subscript 1. The integration procedure of the transport equations in multi-ionic systems is presented first and the general current–voltage curve is derived. Except in Sect. 2.1.2.5, homogeneous reactions are assumed to be absent. The interesting case of excess supporting electrolyte, in which the active species is present in very small concentration and transport takes place mostly by diffusion, is discussed. Finally, the simple cases of binary and ternary solutions are considered to illustrate the conclusions drawn from the general solution.

#### 2.1.2.1 Integration of the Transport Equations

The fact that the flux density of the electroinactive species,  $i \neq 1$ , is zero simplifies significantly the solution of the transport equations. These species are in electrochemical equilibrium within the DBL, and hence their concentrations  $c_i$  are related to the electric potential  $\phi$  by the

Boltzmann equation

$$\frac{dc_i}{dx} = -z_i c_i f \frac{d\phi}{dx} \quad (i \neq 1, J_i = 0) \quad (33)$$

Thus, the ionic concentrations at the electrode surface,  $x = 0$ , are related to those in the bulk solution,  $x = \delta$ , by

$$c_i^s = c_i^b e^{z_i f \Delta\phi} \quad (i \neq 1, J_i = 0) \quad (34)$$

where  $\Delta\phi \equiv \phi^b - \phi^s$  is the electric potential drop across the DBL (see Fig. 1). Furthermore, the LEN assumption

$$\sum_i z_i c_i = z_1 c_1 + \sum_{i \neq 1} z_i c_i = 0 \quad (35)$$

implies that not only  $c_i$  ( $i \neq 1$ ) but also  $c_1$  is determined by  $\phi$ . Thus, for instance, the surface concentration of the electroactive species is

$$c_1^s = -\frac{1}{z_1} \sum_{i \neq 1} z_i c_i^s = -\frac{1}{z_1} \sum_{i \neq 1} z_i c_i^b e^{z_i f \Delta\phi} \quad (36)$$

The current–voltage relation can be obtained from the flux equation of the electroactive species

$$J_1 = \frac{I}{z_1 F} = -D_1 \left( \frac{dc_1}{dx} + z_1 c_1 f \frac{d\phi}{dx} \right) \quad (37)$$

by transforming the migration term with the help of Eq. (35) to

$$z_1 c_1 f \frac{d\phi}{dx} = -\sum_{i \neq 1} z_i c_i f \frac{d\phi}{dx} = \sum_{i \neq 1} \frac{dc_i}{dx} \quad (38)$$

Integration of Eq. (37) over the DBL then gives

$$\begin{aligned} -\frac{I\delta}{z_1 F D_1} &= \Delta c_1 + \sum_{i \neq 1} \Delta c_i \\ &= \sum_{i \neq 1} \left( 1 - \frac{z_i}{z_1} \right) \Delta c_i \end{aligned} \quad (39)$$

where  $\Delta c_i \equiv c_i^b - c_i^s$ . Introducing the limiting diffusion current density

$$I_{Ld,1} \equiv -\frac{z_1 F D_1 c_1^b}{\delta} \quad (40)$$

and using Eqs. (34 and 36), the current–voltage relation takes the form

$$I = I_{Ld,1} \sum_{i \neq 1} \frac{c_i^b}{c_1^b} \left( 1 - \frac{z_i}{z_1} \right) (1 - e^{z_i f \Delta\phi}) \quad (41)$$

Note that the definition of  $I_{Ld,1}$  has not been deduced from the condition  $c_1^s = 0$ , but it rather corresponds to a situation in which the transport of species 1 takes place mostly by diffusion, and hence its name. Moreover, Eq. (40) corresponds to the particular case in which there is only one active species; see Eq. (78) below for the general definition.

It is interesting to observe that species 1 is the only one that moves, while the inactive species are standing still over the system. In a sense, this is similar to the conduction of electrons in a metal, in which electrons move and the ions are standing on the crystal lattice and, therefore, Ohm's law is expected to be satisfied. Indeed, Eq. (37) shows that the electric current density is proportional to the electric field,  $I \equiv -\kappa_{\text{eff}}(d\phi/dx)$ , in which

$$\kappa_{\text{eff}}(x) = \frac{F^2}{RT} D_1 \sum_i z_i^2 c_i(x) \quad (42)$$

is the local effective conductivity and Eqs. (33 and 35) have been used. There is, however, a difference between these two systems. The “static” distribution of the inactive species is determined by the electric potential distribution and hence, although  $I$  is only due to species 1, all species are relevant to the conduction process.

The local ohmic behavior is not in contradiction with the fact that Eq. (41) shows a nonlinear variation of  $I$  with the potential drop  $\Delta\phi$ . At low potentials,  $f\Delta\phi \ll 1$ , the DBL is practically nonpolarized (i.e. the ionic concentrations take their bulk values throughout the DBL) and the slope of the current–voltage curve is  $\kappa_{\text{eff}}^b$ . When increasing  $\Delta\phi$ , the slope of the current–voltage curve decreases owing to the development of concentration polarization. The effective conductivity varies then with position and this makes the overall system behavior to be nonohmic.

#### 2.1.2.2 Solutions of Homovalent Ions, $|z_i| = z$

The theoretical analysis of ion transport requires the grouping of ions according to their valencies [27–31]. All ions of the same valency (a term used here as equivalent to charge number) are grouped together to constitute a “class” and the sum of their concentrations is termed the “class concentration” [32], denoted by  $C$ . The simplest transport problem involves only two classes corresponding to valencies  $z$  and  $-z$ . This is sometimes referred to as the homovalent case [33]. Some interesting conclusions are drawn from Eqs. (36 and 41) in this situation.

Denote the class of the electroactive species by subscript 1 and the other class by subscript 2. The LEN assumption requires the two class concentrations to be equal to each other

$$C_1 \equiv \sum_{z_i=z_1} c_i = \sum_{z_i=-z_1} c_i \equiv C_2 \equiv C \quad (43)$$

Equation (36) then simplifies to

$$c_1^s = C^b e^{-z_1 f \Delta\phi} + (c_1^b - C^b) e^{z_1 f \Delta\phi} \quad (44)$$

and the maximum potential drop in the DBL, which is attained under limiting

conditions  $c_1^s = 0$ , satisfies

$$e^{-z_1 f \Delta\phi_L} = \left(1 - \frac{c_1^b}{C^b}\right)^{1/2} \quad (45)$$

Thus, when the ionic strength of the solution is much larger than the concentration of the electroactive species ( $C^b \gg c_1^b$ ), that is, in the presence of excess supporting electrolyte case,  $z_1 \Delta\phi_L$  tends to zero and the electric potential drop is then negligible [5, 26, 34]. On the contrary, in the absence of a supporting electrolyte, the electroactive species is the only species of its class,  $C^b = c_1^b$ , and  $z_1 \Delta\phi_L$  diverges. The conclusion that migration is absent when the ionic strength of the solution is much larger than the concentration of the electroactive species is not restricted to the homovalent case; note that the equation  $I \equiv -\kappa_{\text{eff}}(d\phi/dx)$  implies that  $d\phi/dx$  decreases as  $\kappa_{\text{eff}}$  increases.

In homovalent systems, the current–voltage curve, Eq. (41), takes the form

$$I = I_L \frac{1 - e^{-z_1 f \Delta\phi}}{1 - e^{-z_1 f \Delta\phi_L}} \quad (46)$$

where

$$I_L = I_{Ld,1} \frac{2C^b}{c_1^b} \left[1 - \left(1 - \frac{c_1^b}{C^b}\right)^{1/2}\right] \quad (47)$$

is the limiting current density (i.e. that corresponding to  $c_1^s = 0$  and  $\Delta\phi = \Delta\phi_L$ ). The value of  $I_L$  varies between  $2I_{Ld,1}$  in the absence of supporting electrolyte ( $C^b = c_1^b$ ) and  $I_{Ld,1}$  in the presence of excess supporting electrolyte ( $C^b \gg c_1^b$ ). Migrational effects in homovalent solutions can therefore account for up to a factor 2 in  $I_L$ .

#### 2.1.2.3 Binary Electrolyte Solutions

When the solution contains only two ionic species, the concentration profiles

are linear and the diffusion and migration terms in the flux equations are independent on position within the DBL. The electroinactive species can be thought to be in equilibrium as a result of the balance of diffusional and migrational terms in its flux equation. The migrational contribution to the flux of the electroactive species is equal (due to the LEN assumption) to that of the inactive species, except for a sign reversal, and hence the flux of the electroactive species can be described as the sum of two diffusional contributions, Eq. (38). This means that the slopes of the concentration profiles are proportional to the electric current, Eq. (39), and the occurrence of a limiting current is clearly associated to the maximum concentration gradient that can be established over the DBL, that is, to vanishing concentrations at the electrode surface.

The current–voltage curve of this system is a particular case of Eq. (41), which takes the simple form [34]

$$I = I_L (1 - e^{z_2 f \Delta \phi}) \quad (48)$$

where

$$I_L = \left(1 - \frac{z_1}{z_2}\right) I_{Ld,1} = -\frac{(z_1 - z_2) F D_1 c_2^b}{\delta} \quad (49)$$

is the limiting current density. This curve has been plotted in Fig. 2. The figure

includes the case of both cathodic and anodic processes. Consider first that the electroactive species is an anion and, consequently, that  $I_L > 0$ ; note that the charge numbers have been defined with sign. In the depleted DBL adjacent to the anode, the current density is positive and tends to the limiting value when the (negative) potential drop increases in absolute value. In the concentrated DBL adjacent to the anode (for the same geometry described in Fig. 1, that is, electrode located at  $x = 0$  and DBL extending from  $x = 0$  to  $\delta$ ), the current is negative, and the potential drop is positive. Increasing the potential drop now leads to an increase of the electrical conductivity of the DBL, and hence of the slope of the current–voltage curve. When the electroactive species is a cation, these comments must be changed accordingly, but Fig. 2 remains valid.

Figure 3 shows the concentration,  $c_i(x)$ , and electric potential,  $\phi(x)$ , profiles given by

$$\frac{c_1}{c_1^b} = \frac{c_2}{c_2^b} = e^{z_2 f (\phi^b - \phi)} = 1 - \frac{I}{I_L} \left(1 - \frac{x}{\delta}\right) \quad (50)$$

which can be obtained by integration of Eq. (37) from  $x$  to  $\delta$ , after use of Eq. (38). In the depleted DBL, the interfacial

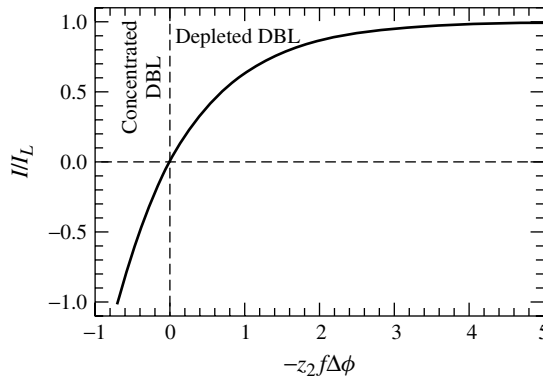


**Fig. 2** Current–voltage curves of a DBL containing a strong binary electrolyte. Magnitudes  $z_2$ ,  $\Delta\phi$ ,  $I$ , and  $I_L$  are defined with sign; subscript 2 denotes the electroinactive species. Negative values of  $I/I_L$  correspond to electrode dissolution (anodic or cathodic), and positive values to single ion discharge at the electrode.



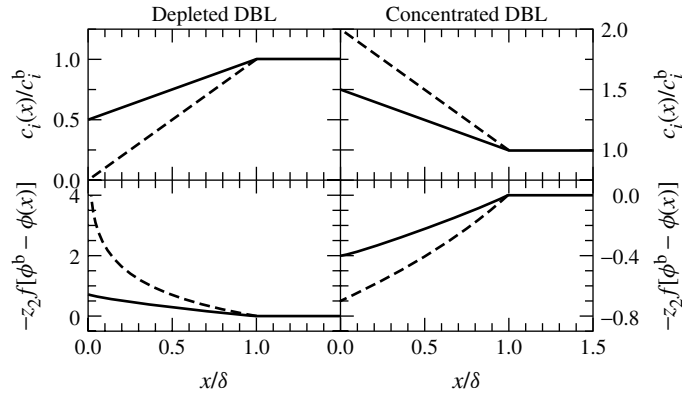


**Fig. 3** Concentration and electric potential profiles for depleted ( $I/I_L > 0$ ) and concentrated DBL ( $I/I_L < 0$ ). The continuous lines correspond to  $|I/I_L| = 0.5$  and the dashed lines to  $|I/I_L| = 1.0$ .

concentration  $c_i^s$  decreases with increasing  $\Delta\phi$ , and the limiting current  $I_L$  is reached when  $z_2\Delta\phi \rightarrow -\infty$  and  $c_i^s \rightarrow 0$ . In the concentrated DBL, the interfacial concentration  $c_i^s$  increases with increasing  $\Delta\phi$  (in absolute value).

It is important to stress that  $\Delta\phi$  is the potential drop in the DBL only. There is also a potential drop at the electrode|DBL interface that changes with concentration polarization. The variation of the latter is given by the concentration overpotential that, in this case, takes the form

$$\eta_c = \frac{1}{z_1 f} \ln \frac{c_1^s}{c_1^b} = \frac{1}{z_1 f} \ln \left( 1 - \frac{I}{I_L} \right) \quad (51)$$

Combining Eqs. (48 and 51), the current–voltage curve can be expressed as [34]

$$I = I_L \left\{ 1 - \exp \left[ \frac{z_2 - z_1}{z_1 z_2} f (\eta_c - \Delta\phi) \right] \right\} \quad (52)$$

where  $\eta_c - \Delta\phi$  is the change in the potential difference between the electrode and the bulk solution due to the passage of the electric current.

#### 2.1.2.4 Ternary Electrolyte Solutions. The Supporting Electrolyte

Consider a ternary system in which the common ion,  $i = 3$ , is an inactive species. (If the electroactive species were the common ion, the system behavior would be similar to that of a binary solution.) A key feature of systems with only one electroactive species is that there is a background concentration of indifferent electrolytes that maintain a fairly uniform conductivity of the DBL. This implies that the electric potential drop is small and is quite uniformly distributed over the DBL. The concentration profile of the electroactive species is (slightly) nonlinear, and the same is true in general for the inactive ions, but the system behavior is still quite simple. In the particular case  $z_1 = z_2$ , the concentration profile of the common ion is linear and is given by

$$c_3(x) = c_3^b - \frac{z_1 c_1^b}{z_1 - z_3} \frac{I}{I_{Ld,1}} \left( 1 - \frac{x}{\delta} \right) \quad (53)$$

which has been obtained by integration of Eq. (37) and making use of Eq. (38). The

distributions of the electric potential and concentration of the other inactive ion can be obtained from Eq. (33) as

$$f[\phi^b - \phi(x)] = \frac{1}{z_3} \ln \frac{c_3(x)}{c_3^b} = \frac{1}{z_2} \ln \frac{c_2(x)}{c_2^b} \quad (54)$$

Finally, the concentration profile of the electroactive species is determined from the LEN assumption, Eq. (35). Figure 4 shows these profiles for charge numbers  $z_1 = z_2 = 1, z_3 = -2$ , a concentration ratio  $c_1^b/c_2^b = 0.2$ , and current densities  $I/I_{Ld,1} = 0.5$  and  $1.0$ . The most significant characteristic shown by this figure is that the electric potential drop is very small, even for the case  $I/I_{Ld,1} = 1.0$ . As a consequence, ion transport takes place mostly by diffusion and the concentration profiles are practically linear. As could be expected from the ratio  $c_1^b/c_2^b = 0.2$ , the concentration changes associated to current transport are more important in relative terms for the electroactive species than for the inactive ones. A detail that can (hardly) be observed in Fig. 4 is that  $c_1^s \neq 0$

when  $I/I_{Ld,1} = 1.0$ , which is due to the fact that there is a small migrational contribution to the transport of this species. In other words, the limiting current is slightly larger than  $I_{Ld,1}$  under these conditions.

For the discussion of the current–voltage relation, the homovalent case of Eq. (46) is considered. In a ternary case, this equation becomes

$$I = -\frac{2z_1 F D_1 c_3^b}{\delta} (1 - e^{-z_1 f \Delta \phi}) \quad (55)$$

while Eqs. (45 and 47) simplify to

$$\Delta \phi_L = \frac{RT}{2z_1 F} \ln(1 + c_1^b/c_2^b) \quad (56)$$

and

$$I_L = -\frac{2z_1 F D_1 c_3^b}{\delta} \left[ 1 - \left( 1 - \frac{c_1^b}{c_3^b} \right)^{1/2} \right] \quad (57)$$

Equations (56 and 57) have been represented in Fig. 5 as a function of the electroactive/supporting electrolyte concentration ratio. When the electroactive species

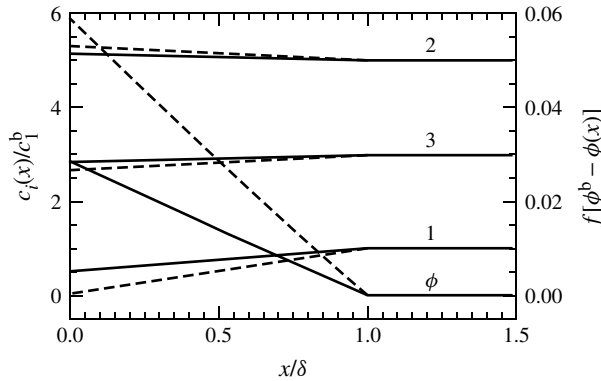


**Fig. 4** Electric potential and ionic concentration profiles (marked with the respective subscripts 1, 2, 3) in a ternary system with  $z_1 = z_2 = 1, z_3 = -2$ , for a concentration ratio electroactive to inactive cation  $c_1^b/c_2^b = 0.2$ , and two values of the electric current density:  $I/I_{Ld,1} = 0.5$  (continuous line) and  $1.0$  (dashed line).

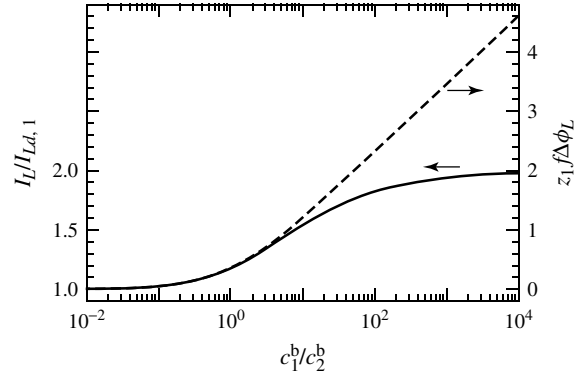


**Fig. 5** Dependence of the limiting current density (continuous line) and the electric potential drop (dashed line) in the DBL under limiting conditions on the electroactive/supporting electrolyte concentration ratio.

is a tracer ion,  $c_1^b/c_2^b \ll 1$ ,  $\Delta\phi_L \approx 0$  and

$$I_L \approx -\frac{z_1 F D_1 c_1^b}{\delta} \left( 1 + \frac{c_1^b}{4c_2^b} \right) \approx I_{Ld,1} \quad (58)$$

On the contrary, in the absence of supporting electrolyte,  $c_1^b/c_2^b \gg 1$ ,  $I_L \approx 2I_{Ld,1}$  and  $\Delta\phi_L$  diverges; the ratio  $I_L/I_{Ld,1}$  tends to  $(1 - z_1/z_3)$  when  $c_1^b/c_2^b \gg 1$  in systems with other charge numbers, as can be deduced from Eq. (49).

The current–voltage curves given by Eq. (55) have been represented in Fig. 6. The initial slope of these curves is  $\kappa_{\text{eff}}^b$ , which obviously increases with decreasing

ratio  $c_1^b/c_2^b$ , when the value of  $I_{Ld,1}$  is fixed (i.e.  $c_1^b$  is fixed). For very low values of this ratio,  $\Delta\phi$  is very small. It is then more relevant to consider also the variation of the electrode potential. Figure 7 shows the same curves as in Fig. 6 though presented in terms of  $\Delta\phi - \eta_c$ , where

$$\eta_c \equiv \frac{1}{z_1 f} \ln \frac{c_1^s}{c_1^b} \quad (59)$$

is the concentration overpotential. The potential drop  $\Delta\phi - \eta_c$  is the change in electrode potential (relative to bulk solution) due to the concentration polarization.

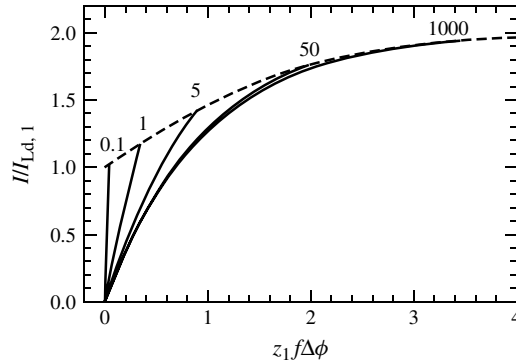


**Fig. 6** Current–voltage curves of a depleted DBL for different values of the electroactive/supporting electrolyte concentration ratio,  $c_1^b/c_2^b$ , shown on the curves.  $\Delta\phi$  is the electric potential drop in the DBL.

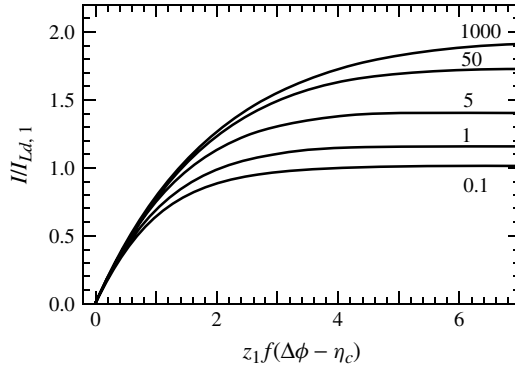


**Fig. 7** Current–overall voltage drop for different values of the electroactive/supporting electrolyte concentration ratio,  $c_1^b/c_2^b$ .

A validity test for the excess supporting electrolyte assumption (in the homovalent case) can be obtained by calculating the migrational flux from Eqs. (37 and 38) as

$$\begin{aligned} J_{1,\text{mig}} &\equiv -z_1 D_1 c_1 f \frac{d\phi}{dx} = \frac{z_1^2 c_1}{\sum_i z_i^2 c_i} J_1 \\ &= \frac{c_1}{2c_3} J_1 \quad (60) \end{aligned}$$

and comparing it to the diffusional flux

$$J_{1,\text{dif}} = J_1 - J_{1,\text{mig}} = J_1 \left( 1 - \frac{c_1}{2c_3} \right) \quad (61)$$

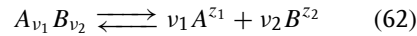
Equations (60 and 61) show clearly that the migrational contribution to  $J_1$  is negligible compared to the diffusional one in as much as  $c_1$  is negligible compared to  $c_3$ . Alternatively, the importance of migration can be estimated from Eq. (58), since the term  $c_1^b/4c_2^b$  accounts for the migrational contribution to  $I_L$ .

When the supporting electrolyte is electroinactive (and chemically inert), its presence can be totally ignored in the description of transport processes. The absence of migration and the zero flux condition for the inactive species implies that these species have an approximately uniform concentration throughout the DBL, which

is not affected by the passage of the electric current. It must be stressed, however, that this statement refers to the concentration gradients in relative terms to the bulk concentration of the respective species. In absolute terms, the concentration gradients of the inactive species are similar to that of the active species, and by no means the concentration gradient of the active species can be neglected. In fact, in the homovalent case, it can be easily shown that  $dc_1/dx \approx 2dc_3/dx \approx -2dc_2/dx$  when migration is negligible. A straightforward implication of these comments is that the LEN assumption cannot be used in conjunction with the excess supporting electrolyte assumption.

#### 2.1.2.5 Weak Binary Electrolyte

Consider an electrolyte  $A_{v_1} B_{v_2}$  dissociating into  $v_1$  ions  $A^{z_1}$  of charge number  $z_1$  and  $v_2$  ions  $B^{z_2}$  of charge number  $z_2$



where  $z_1 v_1 + z_2 v_2 = 0$ . Denote by  $c_{12} = \alpha c_{12,T}$  and  $c_{12,u} = (1 - \alpha) c_{12,T}$  the concentrations of dissociated and undissociated electrolyte fractions, respectively, being  $\alpha$  the degree of dissociation and  $c_{12,T} = c_{12} + c_{12,u}$  the total electrolyte

concentration. When the dissociation Reaction (62) is fast compared with the transport process, it can be assumed that the dissociated and undissociated electrolyte fractions are in equilibrium and the mass action law

$$K = \frac{c_1^{v_1} c_2^{v_2}}{c_{12,u}} = c_{12,T}^{v_{12}-1} \frac{v_1^{v_1} v_2^{v_2} \alpha^{v_{12}}}{1 - \alpha} \quad (63)$$

allows then to determine  $\alpha$  as a function of  $c_{12,T}$ . In deriving Eq. (63), the following relations have been used,  $c_1 = v_1 c_{12}$ ,  $c_2 = v_2 c_{12}$ , and  $v_{12} \equiv v_1 + v_2$ .

Because of the electrolyte dissociation, the flux densities  $J_i$  of the ions and that of the undissociated electrolyte

$$J_{12,u} = -D_{12,u} \frac{dc_{12,u}}{dx} \quad (64)$$

vary with position. The same applies to the flux density of the dissociated electrolyte,  $J_{12}$  [35]. The total electrolyte flux

$$J_{12,T} = J_{12,u} + J_{12} = -D_{12,u} \frac{dc_{12,u}}{dx} - D_{12} \frac{dc_{12}}{dx} = -D_{12,T} \frac{dc_{12,T}}{dx} \quad (65)$$

however, is constant throughout the system as required by the continuity equation, Eq. (11). In spite of this fact, the total electrolyte concentration  $c_{12,T}$  does not vary linearly with position because the effective diffusion coefficient of the electrolyte

$$D_{12,T} \equiv \frac{v_{12}(1 - \alpha)D_{12,u} + \alpha D_{12}}{v_{12}(1 - \alpha) + \alpha} \quad (66)$$

is a function of  $\alpha$ , and  $\alpha$  is a function of  $c_{12,T}$ . Exception is made for the special cases of very weak electrolyte ( $\alpha \rightarrow 0$ ,  $K \rightarrow 0$ ,  $D_{12,T} \rightarrow D_{12,u}$ ), very strong electrolyte ( $\alpha \rightarrow 1$ ,  $K \rightarrow \infty$ ,  $D_{12,T} \rightarrow D_{12}$ ), and  $D_{12,u} = D_{12}$ , when  $D_{12,T}$  is a constant and  $c_{12,T}$  varies linearly.

If only species 1 is electroactive, the boundary conditions at the electrode surface are  $J_{12,u}^s = 0$ ,  $J_2^s = 0$ , and  $J_1^s = I/z_1 F$ , and therefore the flux density  $J_{12,T}$  can be evaluated, from Eq. (21) and  $J_2^s = 0$ , as

$$J_{12,T} = -\frac{t_2}{z_2 v_2} \frac{I}{F} \quad (67)$$

The concentration profile of the electrolyte  $c_{12,T}$  could then be determined from Eqs. (63, 65, and 67), and the boundary value  $c_{12,T}^b$ . Note that the transport numbers are constant in a binary system.

For the determination of the current-voltage characteristics of this system, the integration of Eq. (65) over the DBL

$$\begin{aligned} -J_{12,T} \delta &= \frac{t_2}{z_2 v_2} \frac{I \delta}{F} \\ &= D_{12,u} \Delta c_{12,u} + D_{12} \Delta c_{12} \end{aligned} \quad (68)$$

can be conveniently rewritten in the form

$$I = I_{L,T} \left[ 1 - \frac{D_{12,u} c_{12,u}^s + D_{12} c_{12}^s}{D_{12,u} c_{12,u}^b + D_{12} c_{12}^b} \right] \quad (69)$$

where

$$I_{L,T} = \frac{z_2 v_2 F}{t_2 \delta} (D_{12,u} c_{12,u}^b + D_{12} c_{12}^b) \quad (70)$$

is the limiting current density defined from the condition that the electrolyte concentration (both dissociated and undissociated) becomes zero at the electrode surface when  $I \rightarrow I_{L,T}$ . This limiting current density reduces to

$$I_{L,u} \equiv \frac{z_2 v_2 F D_{12,u} c_{12,T}^b}{t_2 \delta} \quad (71)$$

and

$$I_L \equiv \frac{z_2 v_2 F D_{12} c_{12,T}^b}{t_2 \delta} = -\frac{z_1 v_{12} F D_{12} c_{12,T}^b}{\delta} \quad (72)$$

in the limits of very weak ( $\alpha \rightarrow 0$ ) and very strong electrolyte ( $\alpha \rightarrow 1$ ), respectively. Indeed, Eq. (70) can be easily transformed to

$$I_{L,T} = I_L \left[ \frac{D_{12,u}}{D_{12}} (1 - \alpha^b) + \alpha^b \right] \quad (73)$$

where  $\alpha^b$  is the degree of dissociation at  $x = \delta$ .

Figure 8 shows the dependence of the limiting current on the dissociation degree for the cases of 1:–1 and 2:–1 electrolytes and different values of the ratio  $D_{12,u}/D_{12}$ . At very low electrolyte concentration or very high dissociation constant, the electrolyte is completely dissociated and  $I_{L,T} = I_L$ . At very high electrolyte concentration or very low dissociation rate constant, the electrolyte is practically undissociated and  $I_{L,T} = I_{L,u}$ . The ratio  $I_{L,T}/I_L$  is then equal to  $D_{12,u}/D_{12}$ . Surprisingly, in this limit of negligible dissociation when there are no ions in solution, the system conducts electric current and, moreover, the limiting current can be greater than for a fully dissociated electrolyte if  $D_{12,u} > D_{12}$ . Note also from Fig. 8 that the limiting current density becomes independent of the dissociation

constant  $K$  when  $D_{12,u} = D_{12}$ , for in this case,  $I_{L,T} = I_{L,u} = I_L$ .

The paradoxical results mentioned above can be explained in terms of the electric potential drop across the DBL (see Appendix A for its derivation)

$$\Delta\phi = -\frac{RT}{z_2 F} \ln \frac{c_{12}^b}{c_{12}^s} - \frac{RT}{F} \frac{v_{12} D_{12,u}}{z_2 (v_{12} - 1) D_2} \times \left[ \frac{c_{12,u}^b}{c_{12}^b} - \frac{c_{12,u}^s}{c_{12}^s} \right] \quad (74)$$

This potential drop increases when  $K$  decreases and there are less ions to conduct the electric current. In particular,  $\Delta\phi_{\text{dif}}$  vanishes and  $\Delta\phi_{\text{ohm}}$  diverges when  $K \rightarrow 0$ , so that the sentence in the previous paragraph should have been written as follows: the system is able to conduct an electric current in the limiting case  $\alpha \rightarrow 0$ , provided that an infinite potential difference is applied across the depleted DBL.

The current–voltage curves of this system can be obtained by combining Eqs. (69 and 74). Figure 9 shows these curves for a 1:–1 electrolyte, with an electroactive cation, and different values of

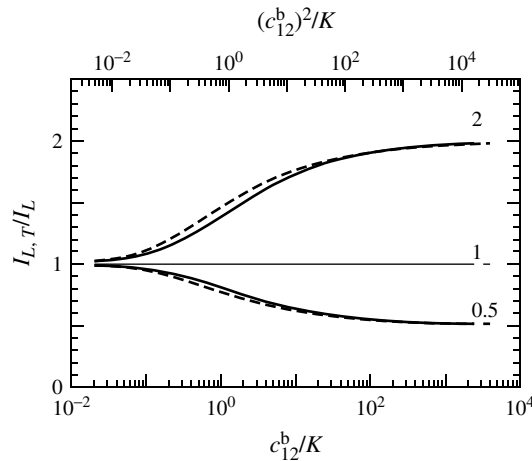
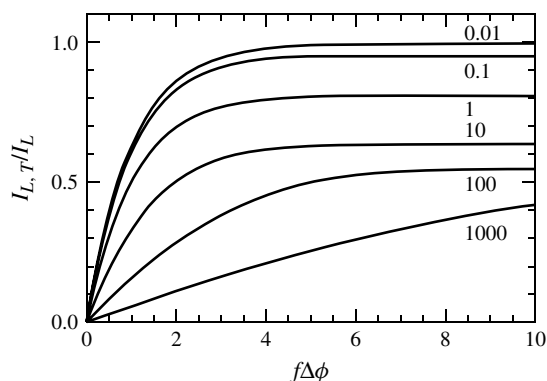


**Fig. 8** Limiting current density in a depleted DBL containing a weak electrolyte solution relative to the value corresponding to complete dissociation. The lower abcisa scale and the continuous lines correspond to a 1:–1 electrolyte. The upper abcisa and the dashed lines correspond to a 2:–1 electrolyte. The ratio  $D_{12,u}/D_{12}$  has been given the values 0.5, 1, and 2, as shown on the curves.

**Fig. 9** Current–voltage curves of a depleted DBL containing a weak 1 : –1 electrolyte for the values of the ratio  $c_{12,T}^b/K$ , which are shown on the curves. Both the ratio  $D_{12,u}/D_{12}$  and the transport number  $t_1$  have been set equal to 0.5.



the bulk electrolyte concentration relative to the dissociation constant,  $c_{12,T}^b/K$ . When the dissociation degree is close to one, that is at low values of the ratio  $c_{12,T}^b/K$ , the curves are practically identical to that in Fig. 2. However, when the ratio  $c_{12,T}^b/K$  is high and the electrolyte is mostly undissociated, the electric conduction becomes difficult. Thus, for instance, in the case  $c_{12,T}^b/K = 100$  where  $\alpha^b = 0.031$  and  $I_{L,T}/I_L = 0.516$ , the electric potential drop in the DBL,  $\Delta\phi$ , must be of the order of 15 times  $RT/F$  for the current density to be close to this limiting value. No need to mention that large values of the ratio  $c_{12,T}^b/K$  also imply lower concentration of the electroactive species close to the electrode and, therefore, larger electrode|solution potential drops (i.e. Nernstian potential drops in the case of reversible electrode reactions). However, the current–voltage curves do not change qualitatively when the electrode potential is taken into account in the voltage drop.

Note, finally, that the boundary condition  $J_{12,u}^s = 0$  requires (except in the trivial case  $I = 0$ , which lacks interest) that the dissociation degree  $\alpha$  is unity in the vicinity of the electrode, independent of the values of  $I$  and  $K$ . This is equivalent to stating

that the value of  $\alpha^s$  is independent of  $c_{12,T}^s$ , which is inconsistent with Eq. (63). It is then concluded that Eq. (63) is not valid in the vicinity of the electrode. The study of the limiting current without the assumption that the dissociation reaction is fast compared with the electrodiffusion process has been carried out by Kharkats and Sokirko [36, 37]. The validity of the dissociation equilibrium assumption and the drastic changes in concentrations that occur when  $I \rightarrow I_L$  have been considered by Vorotyntsev [38].

### 2.1.3

#### Steady State Current–overpotential Curves in the Presence of Supporting Electrolyte

The use of an excess amount of inactive electrolyte makes negligible the migrational contribution to mass transport and therefore simplifies the theoretical modeling of experimental observations. In particular, the absence of potential drop in the DBL eliminates the coupling of ionic fluxes. The current–voltage curves are then presented in terms of the concentration overpotential. Mass transport in the presence of homogeneous reactions can be described with relative simplicity in these systems, as shown in the last section.

### 2.1.3.1 Systems with One Electroactive Species

In the absence of migration, the flux density of the electroactive species is

$$J_1 = \frac{I}{z_1 F} \approx -D_1 \frac{dc_1}{dx} = -D_1 \frac{c_1^b - c_1^s}{\delta} \quad (75)$$

and the interfacial concentration can be expressed as

$$c_1^s = c_1^b \left( 1 - \frac{I}{I_{Ld,1}} \right) \quad (76)$$

where  $I_{Ld,1}$  is the limiting diffusion current density defined by Eq (40). Equation (76) can be rewritten in terms of the concentration overpotential, Eq. (32), as

$$I = I_{Ld,1} (1 - e^{z_1 f \eta_c}) \quad (77)$$

This equation is valid both for a depleted DBL, in which  $I/I_{Ld,1} > 0$  and  $z_1 \eta_c < 0$ , and for a concentrated DBL, in which  $I/I_{Ld,1} < 0$  and  $z_1 \eta_c > 0$ .

### 2.1.3.2 Systems with Several Electroactive Species

When several species are involved in the electrode reaction described by Eq. (23), the reaction rate is determined by the reactant ( $v_i^r < 0$ ) with slower diffusion rate. Thus, the limiting current exhibited by the system is the smallest of the limiting diffusion current densities [26]

$$I_{Ld,i} \equiv -\frac{n F D_i c_i^b}{v_i^r \delta} \quad (78)$$

of the reactants. Note that  $I$  can be either positive or negative, but it is always of the same sign as  $I_{Ld,i}$  for the reactants.

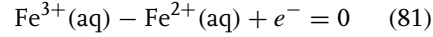
From Eqs. (25 and 78), the interfacial concentration of species  $i$  is given by

$$c_i^s = c_i^b + \frac{J_i \delta}{D_i} = c_i^b \left( 1 - \frac{I}{I_{Ld,i}} \right) \quad (79)$$

The concentration overpotential in Eq. (32) then takes the form

$$\eta_c = \frac{1}{nf} \sum_i v_i^r \ln \left( 1 - \frac{I}{I_{Ld,i}} \right) \quad (80)$$

Consider, for example, the anodic oxidation of iron(II)



in a situation in which the bulk (aqueous) solution is equimolar in ferrous and ferric ions. Since the ferrous ion is consumed at the electrode, the limiting current exhibited by the system is the diffusion limiting current of this ion and the current-overpotential curve is

$$\begin{aligned} \eta_c &= \frac{1}{f} \ln \frac{1 - I/I_{Ld,\text{Fe}^{3+}}}{1 - I/I_{Ld,\text{Fe}^{2+}}} \\ &= \frac{1}{f} \ln \frac{1 + (D_{\text{Fe}^{2+}}/D_{\text{Fe}^{3+}})I/I_{Ld,\text{Fe}^{2+}}}{1 - I/I_{Ld,\text{Fe}^{2+}}} \end{aligned} \quad (82)$$

which has been represented in Fig. 10.

### 2.1.3.3 Diffusion-reaction Processes

The general strategy for solving transport problems in which the electrode reaction, Eq. (23), is coupled to a homogeneous reaction in the DBL

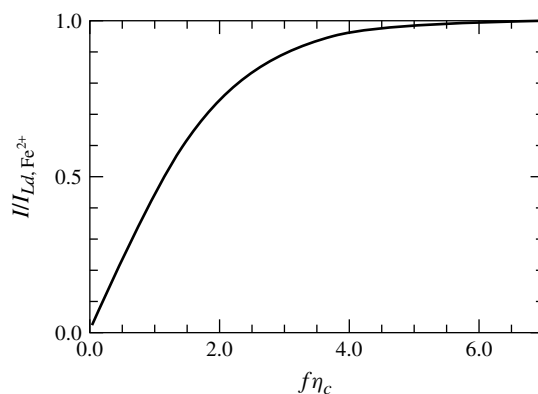
$$\sum_i v_i C_i^{z_i} = 0 \quad (83)$$

is outlined in this section. The stoichiometric numbers are defined to be positive for products and negative for reactants. Chemical equilibrium is assumed for both reactions, which is justified from the fact that chemical kinetics is usually much faster than diffusion processes.

The homogeneous reaction is considered to be reversible. The chemical equilibrium assumption,  $\sum_i v_i \tilde{\mu}_i \approx 0$  or  $K \approx \prod_i c_i^{v_i}$ , applied to transport problems



**Fig. 10** Current density versus concentration overpotential for the anodic oxidation of iron(II) from an equimolar solution of ferrous and ferric ions. The diffusion coefficients  $D_{\text{Fe}^{3+}} = 0.604 \times 10^{-5} \text{ cm}^2 \text{ s}^{-1}$  and  $D_{\text{Fe}^{2+}} = 0.719 \times 10^{-5} \text{ cm}^2 \text{ s}^{-1}$  [39] have been used.



means that the forward and backward reaction rates are much larger than the mass transport by diffusion, and hence their difference can be neglected in a first approximation. Actually, there is a small difference between the forward and backward reaction rates, the net reaction rate

$$r \equiv \frac{r_i}{v_i} = \frac{1}{v_i} \frac{dJ_i}{dx} \quad (84)$$

which is responsible for the spatial changes of the flux densities of the reactive species. In the description of transport processes, this equation can be used to set up relations among the flux density gradients of the reactive species and to evaluate the reaction rate. If the reaction rate constants are known, the validity of the fast chemical equilibrium assumption should also be checked a posteriori.

The continuity equation under steady state conditions, Eq. (84), states that the flux densities of the reactive species change with position because they are either consumed or generated in the homogeneous reaction. The reaction involves the transformation of chemical species by the exchange of atoms or groups of atoms among them, but the total amount of a

given chemical element is not modified. It is then correct to state that the sum of the flux densities, multiplied by a convenient stoichiometric coefficient, of all species that contain a given chemical element involved in Reaction (83) is independent of position. By consideration of all the chemical elements, a large number of equations are obtained. The elimination of those that are simply linear combinations of the others leads to a much smaller number of independent equations. Alternatively, those groups of atoms that are not modified by the reaction can be considered as a unique entity. This is the so-called formalism of constituents, which leads faster to the same number of independent equations. Consider, for instance, that the chemical reaction involves several species with a cyanide group. The reaction cannot make the cyanide group disappear but it can simply bind it to one or another chemical species. Thus, the flux of cyanide constituent (defined as the group of chemical species that contain cyanide) is not affected by the chemical reaction and is constant throughout the DBL (under steady state conditions).

These conservation equations (one for each constituent) are generically written in

the form

$$\frac{dJ_j}{dx} = \sum_i v_{j,i} \frac{dJ_i}{dx} = 0 \quad (85)$$

where the sum extends over all species  $i$  that contains the constituent (or chemical element)  $j$ , and  $v_{j,i}$  is the stoichiometric number of constituent  $j$  in species  $i$ . Taking into account that the flux densities of the different species at the electrode surface are given by Eq. (24), and neglecting migration owing to the presence of excess supporting electrolyte, Eq. (85) can be written as

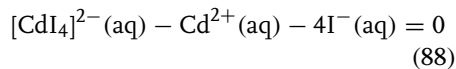
$$\begin{aligned} \sum_i v_{j,i} J_i &= - \sum_i v_{j,i} D_i \frac{dc_i}{dx} \\ &= \frac{I}{nF} \sum_i v_{j,i} v_i^r \end{aligned} \quad (86)$$

Note that the equation for the conduction current density, Eq. (12), is implicit in the system of Eqs. (86).

As an example, consider the dissolution of a cadmium metal electrode



in a solution containing iodide ion, which can complex to cadmium to form tetraiodocadmiate



Denoting the species  $\text{Cd}^{2+}$ ,  $\text{I}^-$ , and  $[\text{CdI}_4]^{2-}$  by subscripts 1 to 3, respectively, and considering cadmium Cd and iodine I as two constituents, Eq. (86) takes the form

$$D_1 \frac{dc_1}{dx} + D_3 \frac{dc_3}{dx} = - \frac{I}{2F} \quad (89)$$

$$D_2 \frac{dc_2}{dx} + 4D_3 \frac{dc_3}{dx} = 0 \quad (90)$$

where  $v_2^r = v_3^r = v_{1,1} = v_{\text{Cd},2} = 0$ ,  $v_1^r = v_{\text{Cd},1} = v_{\text{Cd},3} = v_{1,2} = 1$ ,  $n = 2$ , and  $v_{1,3} = 4$ . These two equations are to be solved together with the chemical equilibrium condition

$$K \approx \frac{c_3}{c_1 c_2^4} \quad (91)$$

using the bulk concentration values as boundary conditions. The diffusion coefficients and complexation equilibrium constants are  $D_1 = 0.7 \times 10^{-5} \text{ cm}^2 \text{ s}^{-1}$ ,  $D_2 = 2.0 \times 10^{-5} \text{ cm}^2 \text{ s}^{-1}$ ,  $D_3 = 0.5 \times 10^{-5} \text{ cm}^2 \text{ s}^{-1}$ , and  $K = 2 \times 10^6 \text{ M}^{-4}$  [39, 40].

A simple way to solve this equation system is to consider  $c_3$  as the independent variable and evaluate  $c_2$  and  $c_1$  from Eqs. (90 and 91), respectively. Finally, integration of Eq. (89) yields the position variable. Figure 11 shows the concentration profiles thus obtained for the cases of anodic dissolution ( $I > 0$ ) and cathodic discharge of cadmium ( $I < 0$ ). In the first case, the cadmium and complex ion concentration gradients are negative (i.e. surface concentration larger than bulk value) and the iodide concentration gradient is positive. The DBL is then concentrated in the cadmium constituent. In the second case, the cadmium ion is consumed by the electrode reaction and the DBL is depleted in the cadmium constituent. The reaction rate evaluated from Eq. (84) has also been represented. It is thus evidenced that the rate of the complexation reaction is large in the case of the anodic dissolution and that the reaction front shifts towards the bulk solution with increasing current. On the contrary, the reaction rate is negligible in the case of the cathodic discharge, in which the concentration profiles are practically linear. The electric current values have been presented relative to the limiting diffusion current density of cadmium ion,  $I_{L,1} = -2FD_1c_1^b/\delta$ . It can be

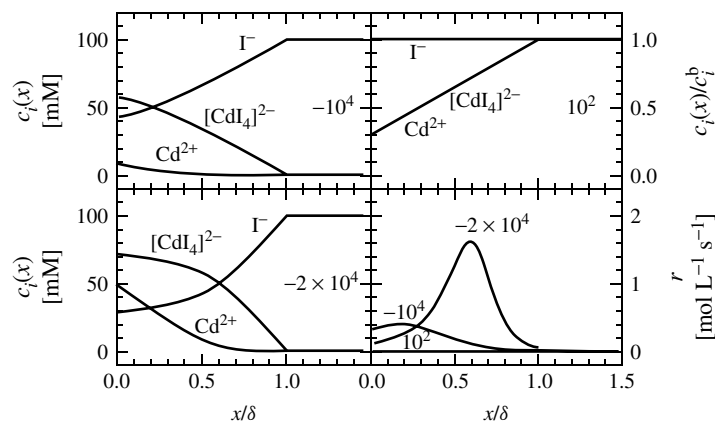


**Fig. 11** Concentration profiles in a cadmium iodide solution adjacent to a cadmium metal electrode and the rate of formation of tetraiodocadmiate ion. The bulk concentrations are  $c_1^b = 5 \mu\text{M}$ ,  $c_2^b = 100 \text{ mM}$ ,  $c_3^b = 1 \text{ mM}$ , and the three values of the electric current density have been considered:  $I/I_{Ld,1} = 10^2$  (cathodic cadmium discharge),  $-10^4$  and  $-2 \times 10^4$  (anodic cadmium dissolution).

deduced from Eq. (89) that the limiting current density (corresponding to  $c_1^s = c_3^s = 0$ ) is  $I_L = -2F[D_1c_1^b + D_3c_3^b]/\delta$ . For the bulk concentrations considered in Fig. 11,  $c_1^b = 5 \mu\text{M}$ ,  $c_2^b = 100 \text{ mM}$ ,  $c_3^b = 1 \text{ mM}$ , and a DBL thickness  $\delta = 10^{-3} \text{ cm}$ , these currents are  $I_{Ld,1} = -0.67$  and  $I_L = -97.2 \text{ mA cm}^{-2}$ .

#### 2.1.4

##### Steady State Current–voltage Curves of Systems with Several Active Species

There are electrochemical processes in which little or no supporting electrolyte is used. This is the case, for instance, of the study of overlimiting currents [34, 41, 42], and of microelectrode [43–45], and different voltammetric techniques [17, 18, 46–48], in which the absence of supporting electrolyte increases the sensitivity of the detection of the redox species. In this section, a general procedure for solving the electrodiffusion equations is presented. The procedure is based on determining

first the electric potential distribution and then the current–voltage curves or the ionic concentration distributions in the DBL. The generality of the method, and the inherent complexity of the nonlinear migration term in the flux equations could make it not very attractive for the nonexpert, and therefore simpler solutions based on the Goldman constant field (GCF) assumption are also presented. For the sake of simplicity, no homogeneous reactions are considered.

##### 2.1.4.1 Kramer's Integration Method

The mathematical difficulty of the electrodiffusion equations, Eq. (7), arises from the nonlinear migration term, which couples the Nernst–Planck equations of the different ionic species. By assuming that the electric field is constant (GCF assumption), this difficulty is removed and analytical solutions are easy to find. Unfortunately, the validity conditions for this approximation are not always satisfied in electrochemical systems [12, 49], and it

is then needed either to derive approximate expressions for the electric potential distribution in some other way [50] or to calculate the exact distribution as described below. In any case, if the electric field distribution  $E(x)$  or, equivalently, the electric potential distribution

$$\phi(x) = \phi^b + \int_x^\delta E dx \quad (92)$$

is considered to be known, the transport equations can be formally integrated by Kramer's transformation [51]. This consists of multiplying both terms of Eq. (7) by  $e^{z_i f \phi}$  and integrating from  $x$  to  $\delta$  to obtain [8, 52, 53]

$$c_i(x) = \left\{ c_i^b + \frac{J_i}{D_i} \int_x^\delta e^{z_i f [\phi(x') - \phi^b]} dx' \right\} \times e^{z_i f [\phi^b - \phi(x)]} \quad (93)$$

The surface concentration  $c_i^s$  is obtained by setting  $x = 0$  in this equation.

When the GCF approximation  $\phi(x) = \phi^b + (\delta - x)E$  is valid, the integral in Eq. (93) can be evaluated and this equation becomes

$$c_i(x) = \left( c_i^b - \frac{J_i}{z_i D_i f E} \right) e^{z_i f E(x - \delta)} + \frac{J_i}{z_i D_i f E} \quad (94)$$

#### 2.1.4.2 The Equation for the Electric Field under the LEN Assumption

Nikonenko and Urtenov [54, 55] have presented an algorithm for the solution of the steady state transport equations in multicomponent systems, which is based on calculating first the electric field  $E$  and then using Eqs. (92 and 93). Their method is outlined here for the particular case when the LEN assumption is used. Unlike Schlögl's

method, that uses the concept of valency classes [32], these authors proposed to rewrite the Nernst–Planck equation system for  $N$  species in terms of the magnitudes

$$S_k \equiv \sum_{i=1}^N z_i^k c_i, \quad k = 0, 2, 3, \dots, N \quad (95)$$

$$G_k \equiv \sum_{i=1}^N z_i^k J_i / D_i, \quad k = 0, 1, 2, \dots, N - 1 \quad (96)$$

instead of the  $N$  concentrations  $c_i$  and flux densities  $J_i$ . The LEN assumption in this notation takes the form  $S_1 \equiv \sum_i z_i c_i = 0$ , and this justifies the absence of index  $k = 1$  in Eq. (95). The aim of the method is obtaining an equation for the electric field in which the unknown concentrations are eliminated by using their relation to the flux densities, which are known from Eq. (24).

Multiplying the Nernst–Planck equation, Eq. (7), by  $-1/D_i$  and summing over species  $i$ , the electric field is eliminated and the concentration sum  $S_0 \equiv \sum_i c_i$  is shown to follow the linear profile

$$S_0(x) = S_0^b + (\delta - x)G_0 \quad (97)$$

Similarly, multiplying the Nernst–Planck equation by  $z_i/D_i$  and summing over species  $i$ , it is obtained that

$$G_1 = fES_2 \quad (98)$$

which could be used to evaluate the electric field if the relation between  $S_2$  and  $S_0$  were known. Note that  $S_2$  is equal to double the ionic strength of the solution, and the advantages of using it as a variable in the formulation of transport problems

have also been emphasized by other authors [17, 18]. Some simple cases are considered next and the general approach is presented later.

In the case of a binary solution,  $S_2 = -z_1 z_2 S_0$  the electric potential can be obtained from Eq. (98) as

$$\phi(x) = \phi^b + \frac{\Gamma}{f} \ln \frac{S_0(x)}{S_0^b} \quad (99)$$

where

$$\Gamma \equiv -\frac{1}{z_1 z_2} \frac{G_1}{G_0} \quad (100)$$

Moreover, introducing the limiting current density

$$I_L \equiv -\frac{S_0^b}{\delta} \frac{I}{G_0} \quad (101)$$

the steady state current–voltage curve can be deduced from Eq. (99) as

$$\begin{aligned} \Delta\phi &= -\frac{\Gamma}{f} \ln \frac{c_i^s}{c_i^b} \\ &= -\frac{\Gamma}{f} \ln \left( 1 - \frac{I}{I_L} \right) \end{aligned} \quad (102)$$

In a multi-ionic, homovalent solution,  $|z_i| = z$ ,  $S_2 = z^2 S_0$  and Eq. (99) is again obtained [56–58], though  $\Gamma$  is now defined as  $\Gamma \equiv G_1/z^2 G_0$ . Since the integral in Eq. (93) can be evaluated by using Eqs. (97 and 99) as

$$\begin{aligned} \int_0^\delta e^{z_i f(\phi - \phi^b)} dx &= -\frac{\int_0^\delta S_0^{z_i \Gamma} dS_0}{G_0(S_0^b)^{z_i \Gamma}} \\ &= \frac{S_0^b}{G_0(1 + z_i \Gamma)} \left[ \left( 1 + \frac{\delta G_0}{S_0^b} \right)^{1+z_i \Gamma} - 1 \right] \end{aligned} \quad (103)$$

the interfacial concentration is finally given by

$$\begin{aligned} c_i^s &= c_i^b \left\{ 1 + \frac{I_L}{(1 + z_i \Gamma) I_{Ld,i}} \right. \\ &\quad \times \left[ \left( 1 - \frac{I}{I_L} \right)^{1+z_i \Gamma} - 1 \right] \left. \right\} \left( 1 - \frac{I}{I_L} \right)^{-z_i \Gamma} \end{aligned} \quad (104)$$

which reduces to  $c_i^s = c_i^b(1 - I/I_L)$  in the binary case. In deriving Eq. (104), note that  $-J_i \delta / D_i c_i^b = I/I_{Ld,i}$ .

In the case of nonhomovalent multi-ionic systems, the solution procedure is necessarily more complicated because there is no simple relation such as  $S_2 = z^2 S_0$ , a problem that was first encountered and solved in different ways by Schlögl [59] and Brady and Turner [60]. If the system contains  $N$  different ionic species, the  $N$  Nernst–Planck equations for the  $N$  flux densities  $J_i$  are replaced by

$$\begin{aligned} G_k &= -\frac{dS_k}{dx} + fES_{k+1}, \\ k &= 0, 1, 2, \dots, N-1 \end{aligned} \quad (105)$$

In order to solve the system of Eqs. (105), a closure relation between  $S_N$  and other sums is needed. Such a relation is

$$\begin{aligned} S_N &= q_1 S_{N-1} - q_2 S_{N-2} + q_3 S_{N-3} \\ &\quad - \dots + (-1)^{N-1} q_N S_0 \end{aligned} \quad (106)$$

where

$$q_1 = z_1 + z_2 + \dots + z_N \quad (107)$$

$$\begin{aligned} q_2 &= z_1 z_2 + z_1 z_3 + \dots + z_1 z_N + z_2 z_3 + \dots \\ &\quad + z_2 z_N + z_3 z_4 + \dots + z_{N-1} z_N \end{aligned} \quad (108)$$

$$\begin{aligned} q_3 &= z_1 z_2 z_3 + \dots + z_1 z_2 z_N + z_1 z_3 z_4 + \dots \\ &\quad + z_1 z_3 z_N + \dots + z_{N-2} z_{N-1} z_N \end{aligned} \quad (109)$$

$$\begin{aligned} &\vdots \\ q_k &= \sum_{i_1=1}^{N+1-k} \sum_{i_2=i_1+1}^{N+2-k} \dots \sum_{i_k=i_{k-1}+1}^N z_{i_1} z_{i_2} \dots z_{i_k} \end{aligned} \quad (110)$$

Some particular cases are considered in the next sections.

#### 2.1.4.3 Ternary Electrolyte Solutions

In a ternary system ( $N = 3$ ), Eqs. (97 and 98) must be solved together with

$$G_2 = -\frac{dS_2}{dx} + fES_3 \quad (111)$$

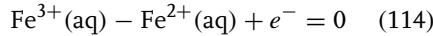
$$S_3 = q_1S_2 + q_3S_0 \quad (112)$$

After some algebra, Eq. (111) can be transformed into the following equation for the electric field

$$\frac{G_1}{E} \frac{dE}{dx} = (G_2 - q_1G_1)fE - q_3(fE)^2S_0(x) \quad (113)$$

which has to be integrated numerically from  $x = \delta$  to  $x$  using the boundary condition  $E^b = G_1/fS_2^b$ .

As an example, consider the case of a redox system such as  $\text{FeCl}_2 + \text{FeCl}_3$  in the absence of supporting electrolyte in a potential range in which the only possible electrode process is the anodic oxidation of ferrous ion



Denoting the ions  $\text{Fe}^{2+}$ ,  $\text{Fe}^{3+}$ , and  $\text{Cl}^-$  by subscripts 1, 2, and 3, respectively, the ion fluxes are  $J_1 = -J_2 = -I/F$ , and the parameters  $G_k$  take the values

$$G_0 = \left( \frac{1}{D_2} - \frac{1}{D_1} \right) \frac{I}{F} = 0.1904 \frac{I}{FD_1} \quad (115)$$

$$G_1 = \left( \frac{z_2}{D_2} - \frac{z_1}{D_1} \right) \frac{I}{F} = 1.5712 \frac{I}{FD_1} \quad (116)$$

$$G_2 = \left( \frac{z_2^2}{D_2} - \frac{z_1^2}{D_1} \right) \frac{I}{F} = 6.7136 \frac{I}{FD_1} \quad (117)$$

where  $D_1 = 0.719 \times 10^{-5} \text{ cm}^2 \text{ s}^{-1}$  and  $D_2 = 0.604 \times 10^{-5} \text{ cm}^2 \text{ s}^{-1}$  [39]. Equation (113) can be rewritten in terms of the

dimensionless electric field  $e \equiv fE\delta$  as

$$\frac{de}{d(x/\delta)} = e^2 \left\{ 0.2729 + e \left[ 0.7271 \left( 1 - \frac{x}{\delta} \right) + 11.456 \left( 1 + \frac{4c_2^b}{3c_1^b} \right) \frac{I_{Ld,1}}{I} \right] \right\} \quad (118)$$

where  $I_{Ld,1} = FD_1c_1^b/\delta$  is the limiting diffusion current density of ferrous ion.

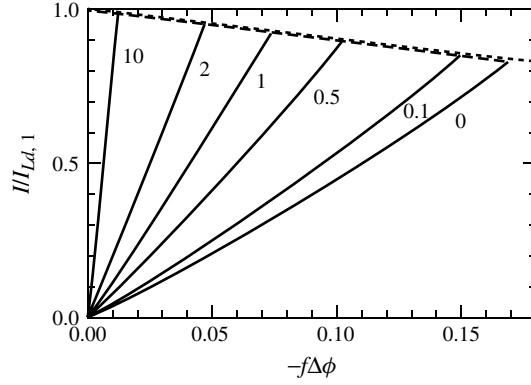
Equation (118) can be integrated by standard numerical methods, such as fourth-order Runge–Kutta method [61], starting from position  $x = \delta$ , in which the boundary condition  $e^b = G_1\delta/S_2^b$  is applied as

$$e \left( \frac{x}{\delta} = 1 \right) = \frac{I}{I_{Ld,1}} \frac{0.2619}{1 + 2c_2^b/c_1^b} \quad (119)$$

The potential drop  $\Delta\phi$  (and its distribution, if needed) can then be calculated by numerical integration of the electric field using, for example, a fourth-order Newton–Cotes method [61]. This procedure yields the current–voltage curves shown in Fig. 12 in the case of a DBL depleted of ferrous ions, that is, for  $I/I_{Ld,1} > 0$  and  $\Delta\phi < 0$ . These curves end when they meet the dashed line that corresponds to the limiting current density, that is, to vanishing surface concentration of ferrous ion. The limiting current density is a bit smaller than the limiting diffusion current density  $I_{Ld,1}$  because the ferrous cation is driven towards the anode by its concentration gradient against an electric field that pushes it away from the electrode. The strength of this electric field is reduced when the solution conductivity increases, that is, when the bulk concentration ratio  $c_2^b/c_1^b$  increases for a fixed value of  $c_1^b$ , and the limiting current density tends to  $I_{Ld,1}$  when this occurs.

The ionic concentration distributions in the DBL are represented in Fig. 13.

**Fig. 12** Current–voltage curves of a ternary system  $\text{FeCl}_2 + \text{FeCl}_3$  in the absence of supporting electrolyte for different values of the bulk concentration ratio  $c_2^b/c_1^b$  shown near the curves. The dashed line represents  $I_L/I_{Ld,1}$  obtained from the (exact) numerical solution, and the dotted line represents  $I_L/I_{Ld,1}$  obtained from the GCF assumption.



The ferrous ion concentration is obtained from Eq. (93) and using the relation  $-J_1\delta/D_1c_1^b = I/I_{Ld,1}$ . The chloride ion follows Boltzmann's equation  $c_3 = c_3^b e^{f(\phi - \phi^b)}$ , and the ferric ion concentration is obtained from the LEN assumption  $c_2 = (c_3 - 2c_1)/3$ .

Figures 12 and 13 evidence that the potential drop in the DBL is small and is distributed quite uniformly. It is then expected that the GCF assumption,  $E = -\Delta\phi/\delta$ , provides reasonable estimates. Indeed, by setting  $c_1^s = 0$  in Eq. (94), the limiting current density can be

estimated as

$$\frac{I_L}{I_{Ld,1}} = \frac{2f\Delta\phi}{1 - e^{-2f\Delta\phi}} \quad (120)$$

which has been represented in Fig. 12 and agrees very well with the exact numerical solution.

#### 2.1.4.4 Quaternary Electrolyte Solutions

Equations (97, 98 and 111), and

$$G_3 = -\frac{dS_3}{dx} + fES_4 \quad (121)$$

$$S_4 = q_1S_3 - q_2S_2 - q_4S_0 \quad (122)$$

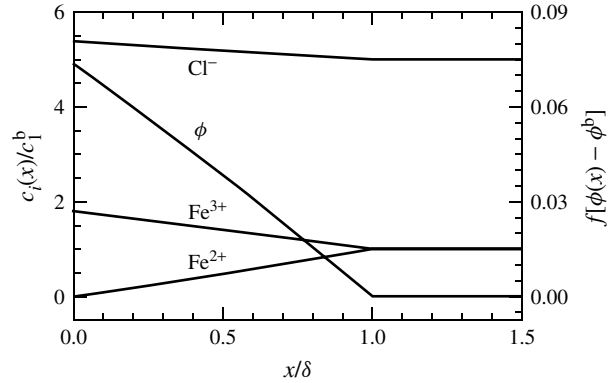


**Fig. 13** Electric potential and concentration profiles of  $\text{Fe}^{2+}$  ion ( $i = 1$ ),  $\text{Fe}^{3+}$  ion ( $i = 2$ ), and  $\text{Cl}^-$  ion ( $i = 3$ ) for a bulk concentration ratio  $c_2^b/c_1^b = 1.0$  and the limiting current density  $I = I_L = 0.9261I_{Ld,1}$ .

lead in this case to the following equation for the electric field

$$\begin{aligned} \frac{G_1}{E} \frac{d^2 E}{dx^2} - \frac{3G_1}{E^2} \left( \frac{dE}{dx} \right)^2 + (G_2 - q_1 G_1) \\ \times f \frac{dE}{dx} - (G_3 - q_1 G_2 + q_2 G_1 \\ + q_4 S_0 f E)(f E)^2 = 0 \end{aligned} \quad (123)$$

which has to be integrated numerically from  $x = \delta$  to  $x$  using the boundary conditions  $E^b = G_1/f S_2^b$  and

$$\left. \frac{dE}{dx} \right|_{x=\delta} = \frac{G_1}{f(S_2^b)^2} \left( G_2 - G_1 \frac{S_3^b}{S_2^b} \right) \quad (124)$$

Although the mathematical difficulty of this equation system is not very high, the GCF assumption, with the electric field estimated, for example, as  $E \approx E^b = G_1/f S_2^b$ , is a much simpler alternative to be considered when the ionic strength is roughly uniform over the DBL.

### 2.1.5

#### Ion Transport under Transient Conditions

Needless to say, transient transport conditions involve a higher level of mathematical complexity to the description of ion transport in electrochemical systems. The only case that can be worked out with ease is that of binary solutions. Ternary and multi-ionic solutions necessarily involve systems of partial differential equations coupled through the migration term that require advanced numerical methods. Given this situation, it is by no means surprising that most theoretical studies of transient problems neglect migration and use the diffusion equation (or Fick's second law) to describe the transport of ionic species. (The analysis of the role of supporting electrolytes in Sects. 2.1.2.2 and

2.1.2.4 was restricted to steady state conditions, but it is expected that a large excess of supporting electrolyte makes migration negligible under transient conditions too.)

This section describes diffusion and migration under transient conditions in some simple illustrative cases. For the sake of simplicity, an infinite DBL thickness  $\delta \rightarrow \infty$  is considered, which is justified in the absence of stirring. Current and voltage steps in semi-infinite planar geometry (and in the absence of homogeneous reactions) are described. Both Laplace transforms and Boltzmann's change of variables are used. The influence of migration is discussed analytically (whenever possible) by using the latter technique, which is introduced in Appendix B. Other solution techniques of the diffusion equation [62–64], and the electrodiffusion equations are available in the literature [13, 65–72]. Further information on electrochemical techniques can be found in Ref. [73].

#### 2.1.5.1 Fick's Second Law for a Strong Binary Electrolyte

The diffusion–conduction equation, Eq. (21), expresses the flux density of an ionic species from a strong binary electrolyte in terms of the electrolyte flux  $J_{12}$  and the current density  $I$ . Under transient conditions, both  $J_i$  and  $J_{12}$  are position-dependent, but  $I$  is not. Thus, taking into account Eq. (21) and the relation  $c_i = \nu_i c_{12}$ , the continuity equation, Eq. (11), leads to Fick's second law

$$\frac{\partial c_{12}}{\partial t} = D_{12} \frac{\partial^2 c_{12}}{\partial x^2} \quad (125)$$

The transient ionic electrodiffusion can then be described as electrolyte diffusion and solved by standard techniques [62–64].



### 2.1.5.2 Systems with One Active Species and Supporting Electrolyte

The transport of the active species in the presence of excess supporting electrolyte under transient conditions is described by the equation

$$\frac{\partial c_1}{\partial t} = D_1 \frac{\partial^2 c_1}{\partial x^2} \quad (126)$$

which is obtained from the continuity equation, Eq. (11), by neglecting the migrational contribution to the flux density  $J_1$ . Although Eq. (126) resembles Fick's second law, it should be observed that Fick's laws are valid for (neutral) electrolytes. Ion transport takes place by electrodiffusion and satisfies pseudo-Fick's laws only when migration is negligible.

For a simple electrode process, like cathodic deposition or anodic dissolution (without contribution of nucleation), the initial value is  $c_1(x, t = 0) = c_1^b$  and the boundary value at the bulk solution is  $c_1^b(t) = c_1^b$ . The boundary condition at the electrode surface can be either Eq. (24), in the form

$$\left. \frac{\partial c_1}{\partial x} \right|_{x=0} = -\frac{I(t)}{z_1 F D_1} \quad (127)$$

or the Nernst equation, Eq. (31), for the case of a single active species

$$E_{\text{eq}}(t) = E^\circ + \frac{RT}{z_1 F} \ln \frac{c_1^s(t)}{c^\circ} \quad (128)$$

When the system is perturbed by applying a known function,  $I(t)$ , Eq. (127) is used to evaluate the chronopotentiometric response of the system. Analogously, when the system is perturbed by applying a known function  $E_{\text{eq}}(t)$ , Eq. (128) describes the chronoamperometric response of the system.

### 2.1.5.3 Voltage Step in the Presence of Supporting Electrolyte

The boundary condition, Eq. (128), for a voltage step perturbation reads

$$c_1^s(t) = c_1^b \exp[z_1 f \Delta E H(t)] \quad (129)$$

where  $H(t)$  is the step function [ $H(t) = 0$  if  $t < 0$ ,  $H(t) = 1$  if  $t > 0$ ], and  $\Delta E$  is the width of the voltage step.

Using Laplace transformation with respect to time, the general solution of Eq. (126) in the Laplace domain is [62]

$$\begin{aligned} \tilde{c}_1(x, s) &= \frac{c_1^b}{s} + A e^{x(s/D_1)^{1/2}} \\ &+ B e^{-x(s/D_1)^{1/2}} \end{aligned} \quad (130)$$

where  $\tilde{c}_1(x, s)$  is the Laplace transformed concentration and  $s$  is the Laplace variable. Since the concentration must be bounded, the integration constant  $A$  vanishes. The boundary condition, Eq. (129), gives the value for  $B$ , resulting in

$$\begin{aligned} \tilde{c}_1(x, s) &= \frac{c_1^b}{s} \left[ 1 + (e^{z_1 f \Delta E} - 1) \right. \\ &\left. \times e^{-x(s/D_1)^{1/2}} \right] \end{aligned} \quad (131)$$

By inverse Laplace transformation, the concentration profile is obtained as

$$\begin{aligned} c_1(x, t) &= c_1^b [1 + (e^{z_1 f \Delta E} - 1) \text{erfc}(\zeta)] \\ &(t > 0) \end{aligned} \quad (132)$$

where  $\zeta \equiv x/(2D_1^{1/2}t^{1/2})$  is the Boltzmann variable (see Appendix B) and  $\text{erfc}$  stands for the complementary error function.

The electric current response is obtained from Eqs. (127 and 132) as

$$\begin{aligned} I(t) &= -z_1 F D_1 \left. \frac{\partial c_1}{\partial x} \right|_{x=0} \\ &= z_1 F c_1^b (e^{z_1 f \Delta E} - 1) \left( \frac{D_1}{\pi t} \right)^{1/2} \end{aligned} \quad (133)$$

If the potential step width is large enough,  $-z_1 f \Delta E \gg 1$ , the surface concentration of the electroactive species is negligible and Eq. (133) reduces to the Cottrell equation [73]

$$I(t) = -z_1 F c_1^b \left( \frac{D_1}{\pi t} \right)^{1/2} \quad (134)$$

#### 2.1.5.4 Current Step in the Presence of Supporting Electrolyte

Consider that the function  $I(t)$  in Eq. (127) is a current step  $I(t) = I_0 H(t)$ , where  $I_0$  is the constant current applied from  $t = 0$ . Equation (130) reduces now to

$$\tilde{c}_1(x, s) = \frac{c_1^b}{s} + \frac{I_0}{z_1 F D_1^{1/2}} s^{-3/2} e^{-x(s/D_1)^{1/2}} \quad (135)$$

whose inverse transform provides the concentration distribution

$$c_1(x, t) = c_1^b + \frac{2I_0 t^{1/2}}{z_1 F D_1^{1/2}} \times [\pi^{-1/2} e^{-\zeta^2} - \zeta \operatorname{erfc}(\zeta)] \quad (136)$$

The potential response is given by Eq. (128) with the surface concentration determined from Eq. (136) at  $\zeta = 0$ , that is,

$$E_{\text{eq}}(t > 0) = E^\circ + \frac{RT}{z_1 F} \times \ln \left[ \frac{c_1^b}{c^\circ} + \frac{2I_0}{z_1 F c^\circ} \left( \frac{t}{\pi D_1} \right)^{1/2} \right] \quad (137)$$

In cathodic processes ( $I_0 < 0$ ), the surface concentration becomes zero at the transition time

$$\tau = \pi D_1 \left( \frac{z_1 F c_1^b}{2I_0} \right)^2 \quad (138)$$

This relationship is called the Sand equation [73].

#### 2.1.5.5 Voltage Step in the Absence of Supporting Electrolyte

Although it is important for practical purposes to attempt the treatment of systems which are not stripped of so many features that they no longer bear resemblance to reality, the simultaneous treatment of a reasonable fraction of these features makes the mathematical problem so complex that there is a danger of obscuring the real problem [74]. It is then suggested to simplify the present analysis of a large voltage step in a ternary solution (where the common ion is inactive) by making equal all diffusion coefficients,  $D_i = D$ , for  $i = 1, 2, 3$ , and hence eliminating the diffusion potential. This allows for a better understanding of the effect of migration on the transient response of the system.

The treatment in Sect 2.1.4.3 is followed and magnitudes  $S_k$  and  $G_k$  are used instead of ionic concentrations and flux densities, respectively. However, the relations between  $c_1$ ,  $c_2$ ,  $c_3$ , and  $S_0$ ,  $S_2$ , are still needed because the Nernst equation, Eq. (31), involves ionic species.

The basic equations describing this problem are the continuity equations, Eq. (11), which owing to the simplifying assumption  $D_i = D$  reads as

$$\frac{\partial S_k}{\partial t} = -D \frac{\partial G_k}{\partial x} \quad (139)$$

and Eq. (105) for  $k = 0, 1$ , and  $2$ ,

$$G_0 = -\frac{\partial S_0(x, t)}{\partial x} \quad (140)$$

$$G_1 = -f \frac{\partial \phi(x, t)}{\partial x} S_2(x, t) \quad (141)$$

$$G_2 = -\frac{\partial S_2(x, t)}{\partial x} + q_1 G_1 + q_3 G_1 \frac{S_0(x, t)}{S_2(x, t)} \quad (142)$$

where the closure relation, Eq. (112), and Eq. (141) have been used to obtain Eq. (142). Equation (141) is Ohm's law, Eq. (13), for this system.

At the electrode surface, Eq. (24) requires that

$$G_0^s(t) = \frac{I(t)}{nFD} \sum_i v_i^r \quad (143)$$

$$G_2^s(t) = \frac{I(t)}{nFD} \sum_i z_i^2 v_i^r = \frac{I(t)}{FD} (z_1 + z_2) \quad (144)$$

which are used as boundary conditions in chronopotentiometric techniques or to evaluate the system response in chronoamperometric techniques. In the second equality of Eq. (144), the common ion is considered to be inactive,  $v_3^r = 0$ . The parameter  $G_1 = I(t)/FD$  is only a function of  $t$ .

Combining Eq. (139) for  $k = 0$  and Eq. (140), the partial differential equation for  $G_0$  is

$$\frac{\partial S_0}{\partial t} = -D \frac{\partial G_0}{\partial x} = D \frac{\partial^2 S_0}{\partial x^2} \quad (145)$$

which is subject to the initial and boundary conditions  $S_0(x, t = 0) = S_0^b$  and  $S_0(x \rightarrow \infty, t) = S_0^b$ , in addition to Eq. (143). The DBL thickness is considered to be infinite due to the absence of stirring. The solution of Eq. (145) can be obtained by following the method explained in Sect. 2.1.5.3 as

$$S_0(x, t) = S_0(\zeta) = S_0^b + (S_0^s - S_0^b) \text{erfc}(\zeta) \quad (146)$$

Combining Eq. (139) for  $k = 2$  and Eq. (142), the partial differential equation for  $S_2$  is

$$\frac{\partial S_2}{\partial t} = D \frac{\partial^2 S_2(x, t)}{\partial x^2} - q_3 D G_1 \frac{\partial}{\partial x} \left( \frac{S_0(x, t)}{S_2(x, t)} \right) \quad (147)$$

The difficulty introduced by the second term in the right-hand side of Eq. (147) makes it very convenient to introduce a further simplifying assumption.

When the number of electroactive species is conserved by the electrode reaction,  $\sum_i v_i^r = 0$ , it is satisfied that  $G_0^s = 0$ , and the only solution to Eq. (145) is the trivial result  $S_0 = S_0^b$ . This is the principle of unchanging total concentration established by Oldham and Feldberg [17]. Equation (147) then reduces to

$$\frac{\partial S_2}{\partial t} = D \frac{\partial^2 S_2}{\partial x^2} + \frac{q_3 I S_0^b}{F S_2^2} \frac{1}{S_2} \frac{\partial S_2}{\partial x} \quad (148)$$

The initial and boundary conditions for this equation are Eq. (31),  $S_2(x, t = 0) = S_2^b$  and  $S_2(x \rightarrow \infty) = S_2^b$ .

In the case of a large voltage step,  $f|\Delta E| \gg 1$ , Eq. (31) is approximated by the condition of zero surface concentration of the reactant,  $c_1^s(t) = 0$  (or  $S_2^s = -z_2 z_3 S_0^b$ ), and both boundary conditions for  $S_2$  turn out to be independent of time. This implies that  $S_2$  is a function of  $x$  and  $t$  through variable  $\zeta \equiv x/(2D_1^{1/2}t^{1/2})$ . Moreover, since the electric current density is obtained from Eqs. (142) and (144) as

$$\left. \frac{\partial S_2}{\partial x} \right|_{x=0} = \frac{I(t)}{FD} (z_3 - z_1) \quad (149)$$

it is concluded that  $I(t)$  is proportional to  $t^{-1/2}$ .

Equation (148) can then be transformed into the ordinary differential equation for  $S_2(\zeta)$  (see Appendix B)

$$0 = \frac{d^2 S_2}{d\zeta^2} + 2\zeta \frac{dS_2}{d\zeta} + \gamma \frac{(S_2^b)^2}{S_2^2} \frac{dS_2}{d\zeta} \quad (150)$$

Parameter  $\gamma$  in Eq. (150) is related to the current density by

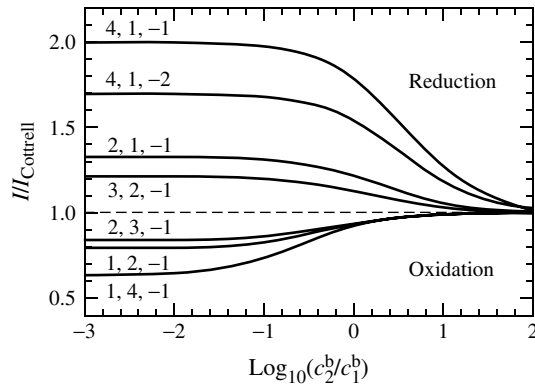


**Fig. 14** Current density in a voltage step of large width relative to that in absence of migration, given by Cottrell Eq. (152), as a function of the bulk concentration ratio product/reactant. The charge numbers  $z_1, z_2, z_3$  are shown close to the curves.

$$I = \gamma \frac{F(S_2^b)^2}{2q_3S_0^b} \left( \frac{D}{t} \right)^{1/2} \\ = \gamma \frac{(z_3 - z_1)(S_2^b)^2 \pi^{1/2}}{2q_3S_0^b(S_2^b + z_2z_3S_0^b)} I_{\text{Cottrell}} \quad (151)$$

where

$$I_{\text{Cottrell}} = (z_2 - z_1) F c_1^b \left( \frac{D}{\pi t} \right)^{1/2} \quad (152)$$

is the classical result obtained by Cottrell in the absence of migration. The value of  $\gamma$  must be obtained from the numerical solution of Eq. (150) by the shooting method starting from  $S_2(0) = S_2^s = -z_2z_3S_0^b$  and

$$\left. \frac{dS_2}{d\zeta} \right|_{\zeta=0} = \gamma \frac{(z_1 - z_3)(S_2^b)^2}{q_3S_0^b} \quad (153)$$

and modifying it by iteration until  $S_2(\infty) = S_2^b$  is satisfied.

Myland and Oldham [18] have compiled the results for the case in which the product of the electrode reaction is absent in bulk solution,  $c_2^b = 0$ . Figure 14 shows the current density as a function of the bulk product/reactant concentration ratio for several values of the charge numbers in the case of cationic redox couples. The current is then larger than in the absence of migration in the case of reductions and

smaller in the case of oxidations. It is observed that, for a given stoichiometric number of the electron  $n = z_2 - z_1$  in the electrode reaction, increasing the charge numbers of either the inactive anion or the active cations reduces the effect of migration. Moreover, the effect of migration is larger when  $|n|$  increases.

The results of these numerical simulations can be understood by the following intuitive arguments. Consider, for example, the oxidation of a cationic species [ $I > 0$ ,  $n > 0$ ,  $z_1 > 0$ ,  $z_2 = (n + z_1) > 0$ ,  $z_3 < 0$ ]. According to Ohm's law, the electric potential gradient in solution pushes the cations away from the anode, so that their gradients are smaller (in absolute value) than in absence of migration. Since the voltage step makes the surface concentration of the reduced species zero,  $c_1^s = 0$ , the flux density of this species at the electrode surface is only due to diffusion,

$$\left. \frac{dc_1}{dx} \right|_{x=0} = - \frac{I}{(z_1 - z_2)FD} \quad (154)$$

and a smaller concentration gradient implies then smaller current density. Contrarily, in the case of reduction of cations, migration pushes the cations towards the cathode, so that the concentration gradients are steeper. Since Eq. (154) still

applies, this implies larger current densities than in absence of migration.

Consider, finally, the oxidation of an anion [ $I > 0$ ,  $n > 0$ ,  $z_1 < 0$ ,  $z_2 = (n + z_1) < 0$ ,  $z_3 > 0$ ]. The electric potential gradient in solution pushes the anions towards the anode, so that the concentration gradients are steeper and the current density is larger than in the absence of migration. The opposite effect is observed in the reductions of anions.

### 2.1.6

#### Deviations from Local Electroneutrality

This last section is devoted to the space charge density and its variation with time and position. The dielectric permittivity of the solution is assumed to be constant, which is a good approximation for moderate concentrations and electric fields [75–77]. It is further assumed that the relaxation of the dielectric (i.e. the re-orientation of water molecules) is much faster than the redistribution of the space charge density [78].

#### 2.1.6.1 Space Charge Density

The Poisson equation, Eq. (8), identifies the space charge density in an electrolyte solution,  $\rho_e = F \sum_i z_i c_i$ , as the source of the electric field. Thus, whenever the electric field changes with position, there is a space charge distribution over the system.

In general,  $\rho_e$  is a function of both position and time. Its time derivative is

$$\begin{aligned} \frac{\partial \rho_e}{\partial t} &= -\varepsilon \frac{\partial^3 \phi}{\partial t \partial x^2} \\ &= \frac{\partial}{\partial x} \left[ \frac{\partial}{\partial t} \left( -\varepsilon \frac{\partial \phi}{\partial x} \right) \right] = \frac{\partial I_d}{\partial x} \end{aligned} \quad (155)$$

where  $I_d$  is the displacement current, that is, the time derivative of the electric displacement  $D = \varepsilon E$ . Alternatively,

$\partial \rho_e / \partial t$  can be evaluated from the continuity equation, Eq. (11) with  $r_i = 0$ , as

$$\begin{aligned} \frac{\partial \rho_e}{\partial t} &= F \sum_i z_i \frac{\partial c_i}{\partial t} \\ &= -F \sum_i z_i \frac{\partial J_i}{\partial x} = -\frac{\partial I}{\partial x} \end{aligned} \quad (156)$$

where  $I$  is the conduction electric current density. Equation (156) represents the conservation of electric charge and its combination with Eq. (155) leads to

$$\frac{\partial I_T}{\partial x} = \frac{\partial I}{\partial x} + \frac{\partial I_d}{\partial x} = 0 \quad (157)$$

which states that the total electric current density  $I_T$  that flows through an electrochemical cell is independent of position, and is made up of two contributions, the conduction and the displacement current densities [66–69, 79]

$$I_T = I + I_d = F \sum_i z_i J_i - \varepsilon \frac{\partial^2 \phi}{\partial t \partial x} \quad (158)$$

The current density  $I_T$  is equal to that due to the electrons flowing through the external circuit connected to the electrodes.

In the absence of concentration gradients, no space charge density can exist in the solution under steady state conditions. Moreover, if by any means some electrical charge density is generated at any position within the system, the time required for this charge to disappear (in fact, to migrate to the system boundaries) is of the order of nanoseconds. This time is the so-called electrical relaxation time of the system,  $\tau_e$ , and can be obtained from Eqs. (8, 13, and 156) as

$$\begin{aligned} \frac{\partial \rho_e}{\partial t} &= -\frac{\partial I}{\partial x} = \kappa \frac{\partial^2 \phi}{\partial x^2} \\ &= -\kappa \frac{\rho_e}{\varepsilon} \equiv -\frac{\rho_e}{\tau_e} \end{aligned} \quad (159)$$

so that  $\tau_e \equiv \varepsilon/\kappa \sim 10^{-9}$  s for a 100 mM aqueous solution.

Concentration gradients, however, are present in most situations of electrochemical interest, and the time evolution of  $\rho_e$  is then determined by the time variation of the conditions imposed on the system, which always involve times much larger than  $\tau_e$ .

Usually, space charge regions exist close to the system boundaries, such as the EDL at a planar electrode. In the presence of concentration gradients, Eq. (159) becomes

$$\begin{aligned} \frac{\partial \rho_e}{\partial t} &= \frac{\partial}{\partial x} \left( \kappa \frac{\partial \phi_{\text{ohm}}}{\partial x} \right) \\ &= \frac{\partial}{\partial x} \left( \kappa \frac{\partial \phi}{\partial x} \right) - \frac{\partial}{\partial x} \left( \kappa \frac{\partial \phi_{\text{dif}}}{\partial x} \right) \end{aligned} \quad (160)$$

which is much smaller, in magnitude, than  $\rho_e/\tau_e$ . Under equilibrium conditions,  $I = 0$ , the two terms on the right-hand side cancel out. In the presence of conduction current, these terms are very similar to each other and much larger in magnitude than  $\partial \rho_e / \partial t$ . An order of magnitude analysis of these two terms allows us to estimate the characteristic length for the space charge distribution,  $L_D$ . Because of the large electric fields existing in space charge regions, the ions have a strong tendency to migrate. If the ions were indeed migrating, the space charge distribution would disappear, so that the necessary condition for an equilibrium space charge distribution is that this tendency to migrate has to be compensated by a strong tendency to diffuse in the opposite direction [68]. The diffusional flux associated to concentration changes is of the order of  $Dc/L_D$ , where  $c$  is a typical ion concentration. The magnitude of the charge density can be estimated as  $\rho_e \approx Fc$ , and the Poisson

equation, Eq. (8) tells that the field associated to this charge density over a region of thickness  $L_D$  is of the order of  $\rho_e L_D / \varepsilon$ . The migrational flux density associated to this field is of the order of  $F D c \rho_e L_D / \varepsilon R T$ . The condition for the existence of an equilibrium space charge density is  $Dc/L_D \approx F D c \rho_e L_D / \varepsilon R T$ , which yields the expression of the Debye length

$$L_D \approx \left( \frac{\varepsilon R T}{F \rho_e} \right)^{1/2} \approx \left( \frac{\varepsilon R T}{F^2 c} \right)^{1/2} \quad (161)$$

Space charge distributions are then expected to exist over regions of thickness  $L_D$ , which is of the order of  $10^{-7}$  cm for a 100 mM aqueous solution. A practical consequence of this comment is that the behavior of electrochemical systems comprising microgeometries is affected by space charge layers [80–82].

Note, finally, that ionic motions associated to space charge redistribution involve distances of the order of  $L_D$ , which suggests that  $\tau_e$  can be interpreted as the time  $\tau_e \approx L_D^2 / D$  required for the ions to diffuse over  $L_D$  [79, 83–85].

### 2.1.6.2 Deviations from Local Electroneutrality

Planck suggested that the electric potential calculated from the LEN assumption,  $\phi^{(0)}$ , could be used to check the validity of this assumption [27, 31]. When this approximate electric potential is introduced in the Poisson equation, the space charge density obtained

$$\rho_r \equiv \varepsilon \frac{\partial E^{(0)}}{\partial x} = -\varepsilon \frac{\partial^2 \phi^{(0)}}{\partial x^2} \quad (162)$$

provides an idea of the deviations from LEN, which would be required to create the distribution  $\phi^{(0)}(x, t)$ . To make clear the difference between the true  $\rho_e$  in the Poisson equation, Eq. (8), and  $\rho_r$  defined

by Eq. (162), the latter is often named residual space charge density [13, 86].

Consider, for instance, the steady state electric field in a binary solution under current flow conditions with species 2 being inactive. From Sect. 2.1.4.2,  $\mathbf{E}^{(0)} = S_2/fG_1 = -z_2S_0/fG_0$  and the residual space charge density required to establish this approximate electric field is

$$\begin{aligned}\rho_r &= -\frac{\varepsilon RT}{z_2 F} \left( \frac{I}{I_L \delta} \right)^2 \left( \frac{c_2^b}{c_2(x)} \right)^2 \\ &= -\frac{\varepsilon RT}{z_2 F \delta^2} \left( \frac{I_L}{I} + \frac{x}{\delta} - 1 \right)^{-2} \quad (163)\end{aligned}$$

where Eqs. (97 and 101) have been used; note also that  $G_1 = z_1 G_0 = I/FD_1$ . This shows that significant deviations from the LEN only occur at the limiting current and close to the electrode surface  $x = 0$ , in which the ionic concentrations tend to zero and  $\rho_r$  diverges [34, 42, 87].

The actual space charge density in this binary solution can be obtained from the (exact) electric field  $\mathbf{E}$  by using the same formalism and the Poisson equation

$$\frac{d\mathbf{E}}{dx} = \frac{\rho_e}{\varepsilon} = \frac{FS_1}{\varepsilon} \quad (164)$$

First, integrating Eq. (105) for  $k = 0$

$$-G_0 = \frac{dS_0}{dx} - fES_1 \quad (165)$$

from  $x$  to  $\delta$ , and using Eq. (164), Eq. (97) is modified to

$$S_0(x) = S_0^b + (\delta - x)G_0 + \frac{\varepsilon E^2}{2RT} \quad (166)$$

where the electric field in bulk solution has been neglected. Then, substituting Eqs. (164 and 166) into Eq. (105) for  $k = 1$

$$-G_1 = \frac{dS_1}{dx} - fES_2 = \frac{dS_1}{dx} + z_1 z_2 fES_0 \quad (167)$$

and introducing the limiting current density  $I_L \equiv -S_0^b I / (\delta G_0)$  defined in Eq. (101), the equation for  $\mathbf{E}$  becomes

$$\begin{aligned}\frac{L_D^2}{E} \frac{d^2 \mathbf{E}}{dx^2} &= z_1 \frac{I}{I_L} \left\{ \frac{1}{fE\delta} - z_2 \left[ \frac{I_L}{I} + \frac{x}{\delta} - 1 \right. \right. \\ &\quad \left. \left. + (fEL_D)^2 \frac{I_L}{2I} \right] \right\} \quad (168)\end{aligned}$$

where  $L_D \equiv (\varepsilon RT / F^2 S_0^b)^{1/2}$  is the Debye length.

Analytical studies of Eq. (168) have used different changes of variables to write the electric field in terms of either Painlevé transcendents [68] or Jacobian elliptic functions [88]. Alternatively, asymptotic expansions have also been used [68, 87, 89, 90]. The approximate solution methods have neglected different terms of Eq. (168). Thus, while Urtenov and Nikonenko [55, 91, 92] have considered that the space charge density is quasi-uniform,  $dS_1/dx \approx 0$ , Bass [93] assumed that  $\varepsilon E^2 \ll RT S_0^b$  and  $I/I_L \ll \delta/L_D$  to express the electric field as the sum of the electroneutral electric field, which can be derived from Eq. (99), and a modified Gouy distribution corrected for the presence of current. In any case, both analytical and numerical [94, 95] solutions have shown that in the range of underlimiting currents, the deviations from LEN are confined to the EDL and that the latter is not significantly perturbed by the electric current.

In conclusion,  $\rho_r$  in Eq. (163) is a physically meaningful magnitude that is very similar to the actual  $\rho_e$  when LEN is a good approximation. Contrarily, when deviations from LEN occur, the actual electric potential surely differs from that obtained by using the LEN, and then the actual  $\rho_e$  is likely to show no resemblance to  $\rho_r$ .

Although the equations presented in this chapter cannot account for this fact,

overlimiting currents can be observed in practice [41]. The study of these currents requires not only to abandon the LEN assumption but also to take into account the electroconvective motions that originate due to the electrical force  $\rho_e \mathbf{E}$  acting on the electrolyte solution in space charge regions [68, 90, 91, 95–97].

### 2.1.6.3 Validity of the LEN Assumption

MacGillivray [98] was the first to provide a mathematical justification for the LEN assumption on the basis of the perturbation theory. The idea behind such a justification is that an order of magnitude analysis of the Poisson equation, Eq. (8), shows that

$$\begin{aligned} \frac{\rho_e}{Fc} &= -\frac{\varepsilon}{Fc} \left( \frac{d^2 \phi}{dx^2} \right) \approx \frac{\varepsilon}{Fc} \frac{RT/F}{L^2} \\ &= \left( \frac{L_D}{L} \right)^2 \equiv \lambda \ll 1 \end{aligned} \quad (169)$$

where  $L$  is a typical length for variation of the electric potential, which is considered to be of the order of the size of the electrochemical cell and hence much larger than the Debye length  $L_D$ . This suggests that the solution of the Nernst–Planck and Poisson equations can be found by writing the concentrations and the electric potential as an asymptotic expansion in terms of the “small parameter”  $\lambda \equiv (L_D/L)^2$ ,

$$c_i = c_i^{(0)} + \lambda c_i^{(1)} + \lambda^2 c_i^{(2)} + \dots \quad (170)$$

$$\phi = \phi^{(0)} + \lambda \phi^{(1)} + \lambda^2 \phi^{(2)} + \dots \quad (171)$$

Thus, the zeroth-order approximation (in  $\lambda$ ) of the Poisson equation is  $\rho_e^{(0)} = 0$ . In other words, the LEN assumption is a consequence of the Poisson equation when  $\lambda \ll 1$ . Moreover, the first-order term of the Poisson equation is

$$\lambda \rho_e^{(1)} = -\varepsilon \frac{d^2 \phi^{(0)}}{dx^2} \quad (172)$$

Since  $\phi^{(0)}$  is the electric potential calculated from the transport equations at zero order in  $\lambda$  (that is, making use of the LEN assumption), the residual space charge density defined in Eq. (162) is identified as  $\rho_e^{(1)}$ . The use of higher-order terms in the Expansions (170 and 171) is only needed when  $\rho_e^{(1)}$  is of the order of  $Fc$  [13, 27, 31, 67]. A different validity test for the LEN assumption, namely  $\lambda \rho_e^{(2)} \ll \rho_e^{(1)}$ , has been recently proposed by Feldberg (with a different notation) [99].

Note that it is possible to use either the full Poisson equation or the terms of its asymptotic expansion, such as the LEN assumption or Eq. (172), but  $\rho_e^{(0)}$  can never be interpreted as the full  $\rho_e$  in the Poisson equation. This would lead to the wrong conclusion that the LEN assumption implies a constant electric field.

## Appendix A

The total potential drop across the DBL in Eq. (74) can be obtained as the sum of the diffusion and ohmic potential drops. The former is given by Eq. (19) as

$$\Delta \phi_{\text{dif}} = -\frac{RT}{F} \left( \frac{t_1}{z_1} + \frac{t_2}{z_2} \right) \Delta \ln c_{12} \quad (173)$$

To integrate the ohmic potential gradient, it is convenient to introduce first the molar conductivity of the electrolyte as

$$\Lambda_{12} \equiv \frac{\kappa}{c_{12}} = -z_1 z_2 \frac{F^2}{RT} (v_2 D_1 + v_1 D_2) \quad (174)$$

where the last equality is known as the Nernst–Einstein relation [3]. Equation (17) then implies

$$d\phi_{\text{ohm}} = -\frac{I}{\kappa} dx = -\frac{I}{\Lambda_{12} c_{12}} dx \quad (175)$$

Eliminating the position variable from Eqs. (65) and (67) as



$$-dx = \frac{z_1 v_1 F}{t_2 I} (D_{12,u} dc_{12,u} + D_{12} dc_{12}) \quad (176)$$

and using Eq. (63) to deduce that  $d \ln c_{12,u} = v_{12} d \ln c_{12}$ , Eq. (175) is transformed to

$$\begin{aligned} d\phi_{\text{ohm}} &= \frac{z_1 v_1 F}{t_2 \Lambda_{12}} \frac{1}{c_{12}} (D_{12,u} dc_{12,u} \\ &+ D_{12} dc_{12}) = \frac{RT}{F} \left( \frac{v_{12} t_1}{z_1 v_1} \frac{dc_{12}}{c_{12}} \right. \\ &- \left. \frac{D_{12,u}}{z_2 D_2} \frac{dc_{12,u}}{c_{12}} \right) = \frac{RT}{F} \left[ \frac{v_{12} t_1}{z_1 v_1} d \ln c_{12} \right. \\ &- \left. \frac{v_{12} D_{12,u}}{z_2 (v_{12} - 1) D_2} d \left( \frac{c_{12,u}}{c_{12}} \right) \right] \quad (177) \end{aligned}$$

Straightforward integration over the DBL and addition of  $\Delta\phi_{\text{dif}}$  yields Eq. (74).

## Appendix B

The perturbation of the concentration field introduced by the electrode propagates at a finite rate determined by the diffusion coefficients and only affects a region close to the electrode whose thickness is of the order of the diffusion length  $2D_1^{1/2}t^{1/2}$ . Boltzmann showed that the diffusion equation, Eq. (126), can be reduced to an ordinary differential equation under certain conditions if expressed in terms of the variable  $\zeta \equiv x/(2D_1^{1/2}t^{1/2})$  [62, 100].

To obtain the diffusion equation in terms of the variables  $(\zeta, t)$ , the elementary concentration variation is first expressed as

$$dc_1 = \left( \frac{\partial c_1}{\partial \zeta} \right)_t d\zeta + \left( \frac{\partial c_1}{\partial t} \right)_\zeta dt \quad (178)$$

The partial derivatives of  $c_1$  with respect to  $x$  and  $t$  (at constant  $x$ ) are then given by

$$\begin{aligned} \left( \frac{\partial^2 c_1}{\partial x^2} \right)_t &= \left( \frac{\partial \zeta}{\partial x} \right)_t \left( \frac{\partial}{\partial \zeta} \left[ \left( \frac{\partial \zeta}{\partial x} \right)_t \left( \frac{\partial c_1}{\partial \zeta} \right)_t \right] \right)_t \\ &= \frac{1}{4D_1 t} \left( \frac{\partial^2 c_1}{\partial \zeta^2} \right)_t \quad (179) \end{aligned}$$

$$\begin{aligned} \left( \frac{\partial c_1}{\partial t} \right)_x &= \left( \frac{\partial c_1}{\partial \zeta} \right)_t \left( \frac{\partial \zeta}{\partial t} \right)_x + \left( \frac{\partial c_1}{\partial t} \right)_\zeta \\ &= -\frac{\zeta}{2t} \left( \frac{\partial c_1}{\partial \zeta} \right)_t + \left( \frac{\partial c_1}{\partial t} \right)_\zeta \quad (180) \end{aligned}$$

and the diffusion equation becomes

$$\frac{\partial^2 c_1}{\partial \zeta^2} + 2\zeta \frac{\partial c_1}{\partial \zeta} = 4t \frac{\partial c_1}{\partial t} \quad (181)$$

When the boundary conditions imposed by the experiment allow for the separation of variables  $\zeta$  and  $t$  (linear sweep voltammetry, for instance, does not), a solution of the form  $c_1(\zeta, t) = c_1^b + Z(\zeta)T(t)$  transforms Eq. (181) into

$$\frac{1}{Z} \left( \frac{d^2 Z}{d\zeta^2} + 2\zeta \frac{dZ}{d\zeta} \right) = \frac{4t}{T} \frac{dT}{dt} = \lambda \quad (182)$$

where  $\lambda$  is a constant.

In the chronoamperometric case, the boundary condition, Eq. (129), does not introduce any dependence on  $t$ , and  $\lambda = 0$  in Eq. (182). Then, the solution of this equation is

$$Z(\zeta) = c_1(\zeta, t) - c_1^b = A \text{erfc}(\zeta) + B \quad (183)$$

where  $\text{erfc}(\zeta)$  is the complementary error function. The boundary condition  $c_1(x \rightarrow \infty, t) = c_1^b$  imposes  $B = 0$ , and Eq. (132) is obtained.

In the chronopotentiometric case, the boundary condition, Eq. (127), becomes

$$\left. \frac{\partial c_1}{\partial \zeta} \right|_{\zeta=0} = T(t) \left. \frac{dZ}{d\zeta} \right|_{\zeta=0} = -\frac{2I_0}{z_1 F D_1^{1/2}} t^{1/2} \quad (184)$$

which makes  $\lambda = 2$  in Eq. (182). The solution of the ordinary differential equation for the function  $Z(\zeta)$  are the first integrals of the complementary error function [61]

$$Z(\zeta) = A[\pi^{-1/2} e^{-\zeta^2} - \zeta \text{erfc}(\zeta)] \quad (185)$$

where the boundary condition  $c_1(x \rightarrow \infty, t) = c_1^b$  has been taken into account.

Finally, the use of Eq. (184) to determine  $A$  yields Eq. (136).

$x$  position (m)  
 $z_i$  charge number, defined with sign

### List of important symbols

#### Latin symbols

$C$  class concentration ( $\text{mol m}^{-3}$ ), Eq. (43)  
 $c_i$  molar concentration ( $\text{mol m}^{-3}$ )  
 $D$  diffusion coefficient ( $\text{m}^2 \text{s}^{-1}$ )  
 $E_{\text{eq}}$  equilibrium  
 $\vec{E}, E$  electrode potential (V), Eq. (31)  
 $\vec{E}, E$  electric field ( $\text{V m}^{-1}$ )  
 $e \equiv f E \delta$  dimensionless  
 $e$  electric field, Eq. (118)  
 $F$  Faraday constant ( $\text{C mol}^{-1}$ )  
 $f \equiv F/RT$  ( $\text{V}^{-1}$ )  
 $G_k \equiv \sum_i z_i^k J_i / D_i$  ( $\text{mol m}^{-4}$ ), Eq. (96)  
 $I$  electric current  
 $I$  density ( $\text{A m}^{-2}$ ), Eqs. (12, 158)  
 $J_i$  ionic flux density ( $\text{mol m}^{-2} \text{s}^{-1}$ ), Eq. (5)  
 $K$  equilibrium constant  
 $[(\text{mol m}^{-3})^{\sum v_i}]$ , Eq. (63)  
 $L_D$  Debye length (m), Eq. (161)  
 $N$  number of ionic species, Eq. (95)  
 $n = \sum_i z_i v_i^r$  stoichiometric  
 $n$  number of the electron, Eq. (23)  
 $n_i$  number of moles of species  
 $i$  (mol)  
 $q_k$  auxiliary variable, Eq. (110)  
 $R$  gas constant ( $\text{J mol}^{-1} \text{K}^{-1}$ )  
 $r$  chemical reaction  
 $r$  rate ( $\text{mol m}^{-3} \text{s}^{-1}$ ), Eqs. (11, 84)  
 $S_k \equiv \sum_i z_i^k c_i$  ( $\text{mol m}^{-3}$ ), Eq. (95)  
 $s$  Laplace variable ( $\text{s}^{-1}$ ), Eq. (130)  
 $T$  temperature (K)  
 $T_i$  integral transport number, Eq. (25)  
 $t$  time (s)  
 $t_i$  migrational transport number,  
 $t_i$  Eq. (15)  
 $u_i$  ionic mobility ( $\text{m}^2 \text{V}^{-1} \text{s}^{-1}$ ),  
 $u_i$  Eq. (4)  
 $\vec{v}_i$  ionic velocity ( $\text{m s}^{-1}$ ), Eq. (4)

#### Greek symbols

$\alpha$  degree of dissociation, Eq. (63)  
 $\delta$  DBL thickness (m)  
 $\Delta$  difference defined as bulk minus  
 $\Delta$  surface value  
 $\varepsilon$  dielectric permittivity ( $\text{C V}^{-1} \text{m}^{-1}$ ),  
 $\varepsilon$  Eq. (8)  
 $\phi$  electric potential (V)  
 $\Gamma \equiv -G_1/z_1 z_2 G_0$   
 $\Gamma$  auxiliary variable, Eq. (100)  
 $\eta_c$  concentration  
 $\eta_c$  overpotential (V), Eq. (32)  
 $\kappa$  conductivity ( $\Omega^{-1} \text{m}^{-1}$ ), Eq. (14)  
 $\kappa_{\text{eff}} \equiv -I/(d\phi/dx)$  effective  
 $\kappa_{\text{eff}}$  conductivity ( $\Omega^{-1} \text{m}^{-1}$ ), Eq. (42)  
 $\Lambda_{12}$  molar conductivity  
 $(\text{m}^2 \Omega^{-1} \text{mol}^{-1})$ , Eq. (174)  
 $\tilde{\mu}_i$  electrochemical potential ( $\text{J mol}^{-1}$ )  
 $v_{12} \equiv v_1 + v_2$ , Eq. (63)  
 $v_i$  stoichiometric  
 $v_i$  number, Eqs. (62, 83)  
 $v_i^r$  stoichiometric number  
 $v_i^r$  in electrode reaction, Eq. (23)  
 $\rho$  charge density ( $\text{C m}^{-3}$ ), Eq. (8)  
 $\tau_e$  electrical relaxation  
 $\tau_e$  time (s), Eq. (159)  
 $\xi$  reaction coordinate (mol), Eq. (24)  
 $\zeta \equiv x/(2D^{1/2}t^{1/2})$   
 $\zeta$  Boltzmann variable, Eq. (132)

#### Subscripts and superscripts

$d$  displacement, Eq. (155)  
 $\text{dif}$  diffusion, Eqs. (19, 61)  
 $e$  electrical, Eq. (8)  
 $i$  ionic species  
 $ij$  dissociated electrolyte, Eq. (63)  
 $ij, T$  total electrolyte, Eq. (63)  
 $ij, u$  undissociated electrolyte, Eq. (63)  
 $j$  constituent, Eq. (85)  
 $k$  power of charge number, Eq. (95)  
 $L$  limiting, Eq. (47)

$Ld, i$	limiting diffusion (current density), Eq. (78)
mig	migration, Eq. (60)
ohm	ohmic, Eq. (18)
$T$	total, Eq. (158)
(i)	perturbation order, Eq. (170)
b	bulk solution ( $x = \delta$ )
o	standard state, Eq. (31)
r	electrode reaction, Eq. (23)
s	electrode surface ( $x = 0$ )

## References

1. R. Haase, *Thermodynamics of Irreversible Processes*, Addison-Wesley, New York, 1969.
2. K. Kontturi, *Acta Polytech. Scand.* **1983**, 152, 1–40.
3. R. A. Robinson, R. H. Stokes, *Electrolyte Solutions*, Butterworths, London, 1955.
4. N. Ibl in *Comprehensive Treatise of Electrochemistry* (Eds.: E. Yeager, J. O'M. Bockris, B. E. Conway et al.), Plenum Press, New York, 1983, Vol. 6, Chap. 1, pp. 1–63.
5. J. S. Newman, *Electrochemical Systems*, Prentice-Hall, Englewood Cliffs, N.J., 1991.
6. A. V. Sokirko, *J. Electroanal. Chem.* **1994**, 364, 51–62.
7. E. J. Calvo in *Comprehensive Chemical Kinetics* (Eds.: C. H. Bamford, R. G. Compton), Elsevier, Amsterdam, 1986, Vol. 26, Chap. 1, pp. 1–78.
8. R. Schlögl, *Stofftransport durch Membranen*, Steinkopff-Verlag, Darmstadt, 1964, Chap. 1, pp. 6–15, and Sect. 6.5, pp. 79–93.
9. E. A. Guggenheim, *Thermodynamics*, North Holland, Amsterdam, 1967, Chap. 8, pp. 298–302.
10. D. Kondepundi, I. Prigogine, *Modern Thermodynamics*, John Wiley & Sons, Chichester, 1998.
11. R. P. Buck, *J. Membr. Sci.* **1984**, 17, 1–62.
12. J. Pellicer, S. Mafé, V. M. Aguilera, *Ber. Bunsen-Ges. Phys. Chem.* **1986**, 90, 867–872.
13. S. Mafé, J. Pellicer, V. M. Aguilera, *J. Phys. Chem.* **1986**, 90, 6045–6059.
14. D. G. Miller, *Chem. Rev.* **1960**, 60, 15–37.
15. D. G. Miller, *J. Phys. Chem.* **1967**, 71, 3588–3592.
16. N. Ibl in *Comprehensive Treatise of Electrochemistry* (Eds.: E. Yeager, J. O'M. Bockris, B. E. Conway et al.), Plenum Press, New York, 1983, Vol. 6, Chap. 4, pp. 239–315.
17. K. B. Oldham, S. W. Feldberg, *J. Phys. Chem. B* **1999**, 103, 1699–1704.
18. J. C. Myland, K. B. Oldham, *Electrochem. Commun.* **1999**, 1, 467–471.
19. N. Ibl, *Pure Appl. Chem.* **1981**, 53, 1827–1840.
20. E. L. Cussler, *Diffusion, Mass Transfer in Fluid Systems*, 2nd ed., Cambridge University Press, Cambridge, 1997, Chap. 13, pp. 331–355.
21. J. N. Agar, *Discuss. Faraday Soc.* **1947**, 1, 26–37.
22. L. L. Bircumshaw, A. C. Riddiford, *Q. Rev. Chem. Soc. London* **1952**, 6, 157–185.
23. J. A. Manzanares, K. Kontturi in *Surface Chemistry and Electrochemistry of Membranes* (Ed.: T. S. Sørensen), Marcel Dekker, New York, 1999, Chap. 11, pp. 399–435.
24. K. Hattenbach, *Terminology for Electrodialysis*, European Society of Membrane Science and Technology, Geesthacht, Germany, 1988.
25. P. Delahay, *Double Layer and Electrode Kinetics*, Interscience Publishers, New York, 1965.
26. K. J. Vetter, *Electrochemical Kinetics*, Academic Press, New York, 1967, Chap. 2, pp. 157–184.
27. M. Planck, *Ann. Phys.* **1890**, 39, 161–186.
28. K. R. Johnson, *Ann. Phys. (Leipzig)* **1904**, 14, 995–1003.
29. H. Pleijel, *Z. Phys. Chem.* **1910**, 72, 1–37.
30. D. A. MacInnes, *The Principles of Electrochemistry*, Reinhold, New York, 1939, Chap. 13, pp. 220–245.
31. M. Planck, *Ann. Phys.* **1890**, 40, 561–576.
32. R. Schlögl, *Ber. Bunsen-Ges. Phys. Chem.* **1978**, 82, 225–232.
33. K. B. Oldham, Z. G. Zoski in *Comprehensive Chemical Kinetics* (Eds.: C. H. Bamford, R. G. Compton), Elsevier, Amsterdam, 1986, Vol. 26, Chap. 2, pp. 79–143.
34. V. G. Levich, *Physicochemical Hydrodynamics*, Prentice-Hall, Englewood Cliffs, N.J., 1962, Chap. 6, pp. 231–371.
35. Yu. I. Kharkats, *Sov. Electrochem.* **1988**, 25, 503–506.
36. A. V. Sokirko, Yu. I. Kharkats, *Sov. Electrochem.* **1989**, 25, 287–292.
37. Yu. I. Kharkats, A. V. Sokirko, *J. Electroanal. Chem.* **1991**, 303, 17–25.

38. M. A. Vorotyntsev, *Sov. Electrochem.* **1988**, 24, 1150–1154.
39. Y. Marcus, *Ion Properties*, Marcel Dekker, New York, 1997.
40. J. G. Stark, H. G. Wallace, *Chemistry Data Book*, John Murray, London, 1982.
41. V. K. Indusekhar, P. Meares in *Physicochemical Hydrodynamics* (Eds.: D. B. Spalding), Building & Sons, Guilford, 1977, pp. 1301–1313, Vol. II.
42. K. Aoki, *J. Electroanal. Chem.* **2000**, 488, 25–31.
43. K. B. Oldham, T. J. Cardwell, J. H. Santos et al., *J. Electroanal. Chem.* **1997**, 430, 25–37, 39–46.
44. M. F. Bento, L. Thouin, C. Amatore et al., *J. Electroanal. Chem.* **1998**, 443, 137–148.
45. M. F. Bento, L. Thouin, C. Amatore, *J. Electroanal. Chem.* **1998**, 446, 91–105.
46. A. M. Bond, S. W. Feldberg, *J. Phys. Chem. B* **1998**, 102, 9966–9974.
47. C. Amatore, L. Thouin, M. F. Bento, *J. Electroanal. Chem.* **1999**, 463, 45–52.
48. K. B. Oldham, *J. Phys. Chem. B* **2000**, 88, 4703–4706.
49. A. D. MacGillivray, D. Hare, *J. Theor. Biol.* **1969**, 25, 113–126.
50. A. V. Sokirko, J. A. Manzanares, J. Pellicer, *J. Colloid Interface Sci.* **1994**, 168, 32–39.
51. H. A. Kramers, *Physica* **1940**, 7, 284–330.
52. W. E. Morf, *Anal. Chem.* **1977**, 49, 810–813.
53. U. Behn, *Ann. Phys. Chem. N.F.* **1897**, 62, 54–67.
54. M. Kh. Urtenov, *Methods of Solution of the Nernst-Planck-Poisson Equation System [in russian]*, Kuban State University, Krasnodar, Russia, 1998.
55. V. V. Nikonenko, M. K. Urtenov, *Russ. J. Electrochem.* **1996**, 32, 187–194.
56. A. Guirao, S. Mafé, J. A. Manzanares et al., *J. Phys. Chem.* **1995**, 99, 3387–3393.
57. P. Ramírez, S. Mafé, A. Tanioka et al., *Polymer* **1997**, 38, 4931–4934.
58. J. A. Manzanares, G. Vergara, S. Mafé et al., *J. Phys. Chem. B* **1998**, 102, 1301–1307.
59. R. Schlögl, *Z. Phys. Chem. N. F.* **1954**, 1, 305–339.
60. J. F. Brady, J. C. R. Turner, *J. Chem. Soc., Faraday Trans. 1* **1978**, 74, 2839–2849.
61. M. Abramowitz, I. A. Stegun, *Handbook of Mathematical Functions*, Dover Publications, New York, 1965.
62. J. Crank, *The Mathematics of Diffusion*, 2nd ed., Oxford University Press, Oxford, 1977.
63. S. L. Marchiano, A. J. Arvia in *Comprehensive Treatise of Electrochemistry* (Eds.: E. Yeager, J. O'M. Bockris, B. E. Conway et al.), Plenum Press, New York, 1983, Vol. 6, Chap. 2, pp. 65–132.
64. D. Britz, *Digital Simulation in Electrochemistry*, Springer-Verlag, Berlin, Germany, 1988.
65. H. Cohen, J. W. Cooley, *Biophys. J.* **1965**, 5, 145–163.
66. J. R. Sandifer, R. P. Buck, *J. Electroanal. Chem.* **1975**, 79, 384–391.
67. J. R. Sandifer in *Ion-Transfer Kinetics* (Ed.: J. R. Sandifer), VCH Publishers, New York, 1995, Chap. 6, pp. 115–138.
68. I. Rubinstein, *Electro-diffusion of Ions*, SIAM, Philadelphia, Pa., 1990, Chap. 1, pp. 1–21.
69. W. D. Murphy, J. A. Manzanares, S. Mafé et al., *J. Phys. Chem.* **1992**, 96, 9983–9991.
70. G. R. Engelhardt, A. D. Davydov, *Russ. J. Electrochem.* **1994**, 30, 953, 954.
71. A. A. Moya, J. Castilla, J. Horno, *Ber. Bunsen-Ges. Phys. Chem.* **1995**, 99, 1037–1042.
72. A. A. Moya, J. Horno, *Electrochim. Acta* **1996**, 99, 1037–1042.
73. A. J. Bard, L. R. Faulkner, *Electrochemical Methods*, John Wiley & Sons, New York, 1980.
74. I. C. Bassignana, H. Reiss, *J. Phys. Chem.* **1983**, 87, 136–149.
75. D. C. Grahame, *J. Chem. Phys.* **1950**, 18, 903–909.
76. F. Booth, *J. Chem. Phys.* **1951**, 19, 391–394, 1327–1328, 1615.
77. I. C. Yeh, M. L. Berkowitz, *J. Chem. Phys.* **1999**, 110, 7935–7942.
78. J. M. G. Barthel, H. Krienke, W. Kunz, *Physical Chemistry of Electrolyte Solutions. Modern Aspects*, (Ed.: Deutsche Bunsen-Gesellschaft für Physikalische Chemie e.V.), Steinkopff, Darmstadt, 1998, Sect. 2.6.
79. S. Mafé, J. A. Manzanares, J. Pellicer, *J. Electroanal. Chem.* **1988**, 241, 57–77.
80. J. D. Norton, H. S. White, S. W. Feldberg, *J. Phys. Chem.* **1990**, 94, 6772–6780.
81. C. P. Smith, H. S. White, *Anal. Chem.* **1993**, 65, 3343–3353.
82. D. R. Baker, M. W. Verbrugge, *Proc. R. Soc. London, A* **1998**, 454, 1805–1829.
83. R. P. Buck, *J. Electroanal. Chem.* **1969**, 23, 219–240.
84. A. D. MacGillivray, *J. Chem. Phys.* **1970**, 52, 3126–3132.

85. J. L. Jackson, *J. Phys. Chem.* **1974**, 78, 2060–2064.
86. V. M. Aguilera, S. Mafé, J. Pellicer, *Electrochim. Acta* **1987**, 32, 483–488.
87. W. H. Smyrl, J. Newman, *Trans. Faraday Soc.* **1967**, 63, 207–216.
88. R. H. Tredgold, *Biochim. Biophys. Acta* **1972**, 274, 563–574.
89. J. Newman, *Trans. Faraday Soc.* **1965**, 61, 2229–2237.
90. A. V. Listovnichii, *Russ. J. Electrochem.* **1989**, 25, 1479–1482.
91. M. Kh. Urtenov, V. V. Nikonenko, *Russ. J. Electrochem.* **1993**, 29, 314–324.
92. V. V. Nikonenko, M. Kh. Urtenov, *Russ. J. Electrochem.* **1996**, 32, 195–198.
93. L. Bass, *Trans. Faraday Soc.* **1964**, 60, 1656–1663.
94. I. Rubinstein, L. Shtilman, *J. Chem. Soc., Faraday Trans. 2* **1979**, 75, 231–246.
95. J. A. Manzanares, W. D. Murphy, S. Mafé et al., *J. Phys. Chem.* **1993**, 97, 8524–8530.
96. I. Rubinstein, *React. Polym.* **1984**, 2, 117–131.
97. V. V. Nikonenko, V. I. Zabolotskii, N. P. Gnusin, *Sov. Electrochem.* **1989**, 25, 262–266.
98. A. D. MacGillivray, *J. Chem. Phys.* **1968**, 48, 2903–2907.
99. S. W. Feldberg, *Electrochem. Comm.* **2000**, 2, 453–456.
100. L. Boltzmann, *Ann. Phys.* **1894**, 53, 959–964.

## 2.2

### The Digital Simulation of Voltammetry under Stagnant and Hydrodynamic Conditions

Kerry A. Gooch, Fulian L. Qiu, and Adrian C. Fisher  
University of Bath, Bath, United Kingdom

#### 2.2.1

##### Introduction

##### 2.2.1.1 Digital Simulations

The advent of the personal computer has led to the rapid development of digital simulations in the field of electrochemistry. The motivation for these advances has been driven by many factors including: the desire to gain quantitative insights from electroanalytical measurements, extract kinetic and mechanistic information regarding the pathways of electrolysis reactions, and assist in the design of new quantitative electrochemical methods.

Quantification of the related phenomena proceeds by the definition of a model that describes the physical processes (e.g. mass transport, chemical reactivity, etc.) in terms of a set of mathematical expressions. Traditionally, workers have attempted to solve these relationships directly via standard mathematical methods; however, in many cases the complexity of the problem does not permit this analytical-solution approach. Digital simulation breaks down (discretizes) the problem into a series of steps that can be solved sequentially by the composition of a suitable computer program. This discretization process gives rise to a variety of different digital strategies with which electrochemical or related problems can be solved.

In this overview, three digital simulation approaches (the finite difference method (FDM), the finite element method (FEM),

and the boundary element method (BEM)) are discussed. Each has been used in varying degrees for the solution of the partial differential equations relating to the mass transport of material during electrolysis. At least one formulation strategy is outlined in detail for each method, to give workers, who are new to the field, a jump-off point to the extensive literature available. Although not included within this review, sample codes for the FDM can be found in a variety of publications, including, Feldberg [1], Bard and Faulkner [2], Britz [3], and Gosser [4]. Sample codes for the FEM and BEM are available on our website [5]. In each case, the general formulation stages are followed by a review of the digital simulation of mass transport using the specific technique. Special emphasis is placed on the literature associated with hydrodynamic techniques (e.g. the rotating disc, channel flow cell, or wall jet electrode), since there are already excellent overviews of diffusional applications using FDM (e.g. Ref. [3]).

##### 2.2.1.2 Simulation Methods. The Fundamentals

Irrespective of the simulation technique chosen, the key stages in the development of a numerical model and its validation are shared and these are indicated in Fig. 1.

The procedure begins with a proposed, realistic, or preliminary working physical model. A mathematical description is formulated, which in the case of transport-related problems proceeds via conservation of momentum, mass, charge, and energy.

For an electrolysis reaction, in which an electrode is sited in an electrolyte solution containing an electroactive species, the species distribution (in one spatial dimension) may be described by an expression of

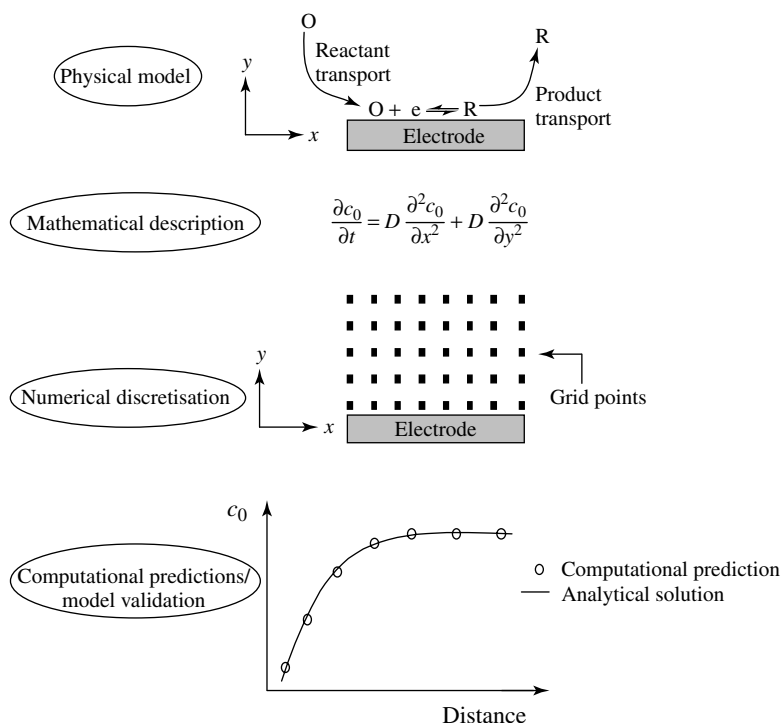


Fig. 1 Simulation procedure.

the form

$$\frac{\partial c}{\partial t} = D \nabla^2 c - V_x \nabla c \pm k \quad (1)$$

In Eq. (1),  $c$  is the reagent concentration,  $t$  the time,  $V_x$  the velocity, and  $k$  any kinetic terms (e.g. first-, second-order reactions, etc.). For more complex geometries, such as disc or band electrodes, the form of the transport equation becomes more complex but still retains terms of the same form as Eq. (1).

Next, digital solution of the model is required and this is achieved by discretization of Eq. (1). This process results in a set of algebraic equations that can then be employed to solve for the unknown variables.

To give a more general solution to the expressions, it is common to cast the equation variables in a dimensionless form. For example, the concentration,  $c$ , is cast dimensionless using

$$c^* = \frac{c}{c_{\text{BULK}}} \quad (2)$$

where  $c_{\text{BULK}}$  is the concentration of a specific starting material. Similarly, the distance parameter  $x$  can be cast into a dimensionless ( $X$ ) form

$$X = \frac{x}{\delta} \quad (3)$$

with  $\delta$  representing a fixed distance. The time variable,  $t$ , can be normalized by the

introduction of a fixed observation time,  $T$ ,

$$\tau = \frac{t}{T} \quad (4)$$

Additionally, dimensionless current, potential, reaction kinetic, and scan rate parameters may also be employed. The choice of  $\delta$ ,  $T$ , and so forth depends upon the specific problem tackled and a good overview may be found in the text by Britz [3].

Solution of Eq. (1) in the dimensionless form leads to the prediction of the temporal and spatial variation of  $c$ . These may be easily returned to dimensional variables by reverse transformation.

Once the predictions have been obtained, they need to be validated and this is often the most challenging aspect of the simulation procedure. Workers often configure codes so that they initially tackle documented problems with analytical solutions, providing a quantitative check on the simulations before extension to more complex problems.

#### 2.2.1.3 The Methods. An Overview

Before proceeding to the detailed development and numerical procedures for each method, it is of interest to note the relationship between the FDM, FEM, and BEM formulations. Although fundamentally different in their implementation, they are linked mathematically (Fig. 2).

By way of example, consider the numerical procedure for the solution of Fick's second law of diffusion in two dimensions

$$\frac{\partial c}{\partial t} = D \frac{\partial^2 c}{\partial x^2} + D \frac{\partial^2 c}{\partial y^2} \quad (5)$$

The FDM uses a truncated Taylor series (Sect. 2.2.2.2) to approximate the differential equation. This approach uses the original formulation of Fick's law and the variable of interest (concentration)

appears as the second derivative. The solution procedure requires discretization of the domain into a two-dimensional grid of points, at which the concentration is computed.

Implementation of the FEM requires integration of the differential equations once (by parts), to produce what is often referred to as the weak formulation (Sect. 2.2.3.2). In contrast to the FDM, the integral expression contains the variable and its first derivative, thus reducing the order of the differential by one with respect to the variable. Domain discretization uses a mesh of interconnecting elements and the variable approximated using a chosen interpolation function.

The BEM involves integration of the differential equation twice; this yields an expression that includes the variable and its derivative. Discretization employs a mesh of elements with the variable approximated using an interpolation function. In the BEM, the formulation permits (in some cases) the variable distribution within the domain to be related to the values only at the boundary. The integration procedure therefore effectively reduces the order of the digital simulation from a two- to a one-dimensional problem. This reduces the complexity of the grid and number of elements required in comparison to the FDM and the FEM.

The choice of the optimal method depends on the problem of interest. The FDM has found widespread application in the electrochemical field due to the relative ease of application, the routine modification for a variety of transport-related problems, and the simple modification for chemical reactivity issues. Apart from its popularity in the engineering fields, the FEM (Workers have used a variety of approaches based around the method of weighted residuals of which further detail



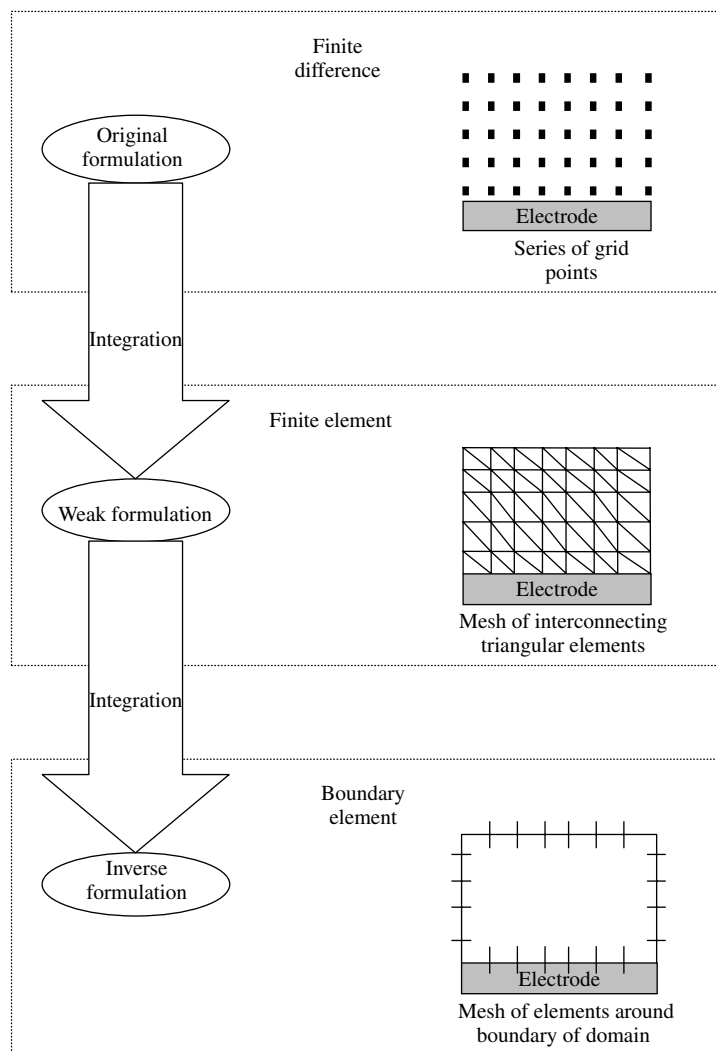


**Fig. 2** The relationship between the FDM, FEM, and BEM formulations.

can be found in Sect. 2.2.3.2.) has, more recently, also gained popularity in electrochemical applications. Merits of the FEM include a considerably reduced number of discretization steps within the domain and the ability to address complex or irregular geometries.

Perhaps the most neglected of the three techniques within electrochemistry is the

BEM. This in part has been due to the perceived difficulty [6] of implementation with some relatively involved mathematical steps required before numerical solution. In addition, the application of the method to problems of complex chemical reactivity is challenging. However, the method does possess some benefits over both the FEM and FDM. In particular,

the reduction in dimensionality brought about by the formulation procedure can give rise to significant time-savings and reduced grid-generation requirements when complex geometries and/or three-dimensional analysis of transport problems are required.

## 2.2.2 Finite Difference Methods

### 2.2.2.1 Introduction

The basis of the FDM was described as early as 1911 [7] and underwent significant development throughout the first half of the 1900s. Courant and coworkers [8] reported a detailed implementation and later Emmons [9] applied the method to a range of problems. In 1948, Randles simulated an electrochemical linear-sweep experiment [10] (with all of the calculations performed by hand). However, it was not until the 1960s with the work of Feldberg [1] that the digital simulation of electrode processes became a focused area of electrochemical research (Feldberg used a flux balance of material into and out of a box to derive the discretized form of the difference equations required for solution.). Many formulations using the FDM have since been reported and a number of the key methods have been highlighted below. The review begins with a detailed overview of the key steps required for the formulation of the explicit

FDM along with the application to a simple electrochemical simulation.

### 2.2.2.2 The Explicit Finite Difference (EFD) Method

Consider Fick's second law of diffusion (in one dimension):

$$\frac{\partial c}{\partial t} = D \frac{\partial^2 c}{\partial x^2} \quad (6)$$

This expression may be cast into a finite difference form via the following. The simulation domain ( $x = 0$  to  $x = \delta$ ) is divided into a series of equally spaced ( $\Delta x$ ) points as indicated in Fig. 3. The concentration close (e.g.  $c_{i-1}^t$  or  $c_{i+1}^t$ ) to an individual point ( $c_i^t$ ) is approximated using the Taylor expansion

$$\begin{aligned} f(x \pm \Delta x) &= f(x) \pm \Delta x f'(x) + \frac{(\Delta x)^2}{2!} \\ &\times f''(x) \pm \frac{(\Delta x)^3}{3!} f'''(x) \end{aligned} \quad (7)$$

where  $f'$ ,  $f''$ , and  $f'''$  are the first, second, and third derivatives of  $f$  respectively. If  $\Delta x$  is small, then the terms from  $(\Delta x)^3/3!$  may reasonably be neglected and expressions for the concentration at ( $c_{i-1}^t$  and  $c_{i+1}^t$ ) predicted

$$c_{i+1}^t = c_i^t + \Delta x \left( \frac{\partial c}{\partial x} \right) + \frac{(\Delta x)^2}{2!} \left( \frac{\partial^2 c}{\partial x^2} \right) \quad (8)$$

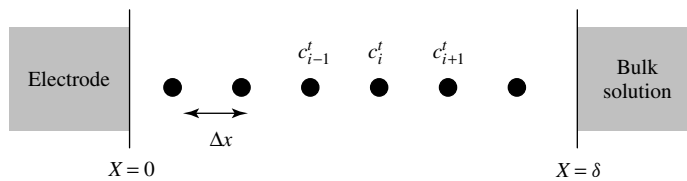


**Fig. 3** The discretization of a domain into a series of sample points, where the  $c_i^t$  represents the concentration at the point  $i$  at a specific time  $t$ .

$$c_{i-1}^t = c_i^t - \Delta x \left( \frac{\partial c}{\partial x} \right) + \frac{(\Delta x)^2}{2!} \left( \frac{\partial^2 c}{\partial x^2} \right) \quad (9)$$

summing Eqs. (8 and 9) yields

$$\frac{\partial^2 c}{\partial x^2} = \frac{1}{(\Delta x)^2} (c_{i+1}^t - 2c_i^t + c_{i-1}^t) \quad (10)$$

Similarly the variation of concentration at a point  $i$  during a small increment in time ( $\Delta t$ ) can be approximated as

$$\frac{\partial c}{\partial t} = \frac{c_i^{t+\Delta t} - c_i^t}{\Delta t} \quad (11)$$

$c_i^{t+\Delta t}$  and  $c_i^t$  are the concentrations at the point  $i$  at the new and old time intervals, respectively. Substituting Eqs. (10 and 11) into Eq. (6) followed by rearrangement gives the finite difference form of Fick's second law

$$c_i^{t+\Delta t} = (\lambda c_{i-1}^t + (1 - 2\lambda)c_i^t + \lambda c_{i+1}^t) \quad (12)$$

where

$$\lambda = \frac{D\Delta t}{(\Delta x)^2} \quad (13)$$

The above expression provides a direct method of obtaining the concentrations at

an individual point ( $i$ ) via the values at the previous time-step; hence this approach is termed an explicit formulation. Note that Eqs. (10 to 12) have been written in terms of the concentrations at the time interval  $t$ , this is referred to as a backwards difference approximation. Application of Eq. (12) permits the simulation of a variety of voltammetric measurements under diffusional transport control.

Consider a potential step experiment performed under conditions in which the analytical Cottrell equation is valid. Assuming that initially the solution contains a single electroactive reagent of concentration  $c_{\text{BULK}}$ . At  $t = 0$  the applied potential is insufficient to drive the electrolysis reaction, following the potential step at  $t > 0$ , the reagent is destroyed at the electrode surface at a transport limited rate. Digital simulation proceeds by dividing the domain  $\delta$  into  $NI$  finite difference points (Fig. 4a) and applying boundary conditions

$$t = 0 \quad c_i^t = c_{\text{BULK}} \quad i = 0, NI \quad (14)$$

$$t > 0 \quad c_i^t = 0 \quad i = 0 \quad (15)$$

$$c_i^t = c_{\text{BULK}} \quad i = NI \quad (16)$$

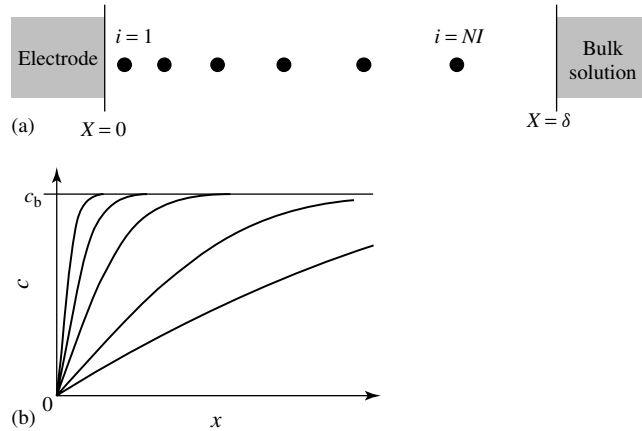


**Fig. 4** (a) Grid and (b) concentration distribution calculated using an EFD simulation.

The boundary condition (14) permits the calculation of new concentrations at all points ( $i$ ) for the time increment  $t + \Delta t$ , subject to the conditions specified in Eqs. (15 and 16). The current may be predicted by taking the concentration gradient at  $x = 0$

$$i = nFAD \left( \frac{\partial c}{\partial x} \right)_{x=0} \quad (17)$$

The choice of  $\delta$  should ensure that concentration changes from their bulk values occur within the simulation region. The simplest value for  $\Delta x$  would be given by  $\delta/NI$ , however, since the greatest change in concentration is usually found at or near the electrode surface, a grid that concentrates mesh points close to the surface would be desirable (Fig. 4a).

For one-dimensional simulations, Joslin and Pletcher [11] and Feldberg [12] have proposed alternative strategies based on a smooth spacing function and exponentially expanding grid, respectively. Recently Bieniasz [13] has reported a more sophisticated adaptation. The approach exploits a set of steps that recalculate the mesh point positions following a concentration distribution calculation. Irrespective of the choice of function, the overall goal is the accurate calculation of the concentration distribution – too few sample points yield an inaccurate (nonconverged) approximation.

Selection of  $\Delta t$  in electrochemical simulations has generally remained a fixed value, although, a few groups have reported a range of time-dependent variations [14–16]. However, with all of these approaches, one must be aware of an operating restriction of the EFD, which arises from the parameter  $\lambda$  Eq. (13). If its value exceeds 1/2, then the simulation will not give a stable solution. This condition arises from the formulation procedure

and is known as the von Neumann stability criterion [17], and it has been converted into a complete proof by John [18]. The stability criterion can prove problematic when a mesh contains small increments of  $\Delta x$ . For a fixed diffusion coefficient, this requires a small value of  $\Delta t$ , thus considerably increasing the real simulation time.

Extension of the EFD method to tackle convection and chemical reactions provides no conceptual problems. The convective term from Eq. (1) can be cast into the EFD form

$$\frac{\partial c}{\partial t} = V_x \left( \frac{c_i^t - c_{i-1}^t}{\Delta x} \right) \quad (18)$$

and summed with Eq. (10) to yield the EFD expression for the convective–diffusion equation. Similarly, kinetic complications arising from homogeneous chemical reactions can be introduced (e.g. for a first-order chemical reaction)

$$\frac{\partial c}{\partial t} = -kc_i^t \quad (19)$$

The ease of introduction of chemical reactivity into digital simulation methods provides a key advantage over analytical procedures that are difficult to solve for complex chemical problems. However, introduction of chemical reactivity needs to be tackled with care (especially when the rate constants are large). The rapid chemical depletion of one or more reagents within the simulation can result in finer mesh requirements or shorter time increments to retain stability and accuracy within the simulation. Readers are directed to a review by Speiser [19] in which these issues are highlighted in some detail.

The EFD method can be routinely applied to multidimensional spatial problems,

however the restriction imposed by  $\lambda$  has led workers to look for alternative formulation strategies to overcome these difficulties. In the next sections, some popular alternative formulations are examined.

### 2.2.2.3 The Crank & Nicolson (CN)

#### Method

The CN method [20, 21] was used by Randles [10] in his work carried out before the advent of modern computers. A central difference scheme is applied in which the diffusional term (10) is centered at the midpoint of the time-step

$$\frac{\partial^2 c^{(t+\Delta t/2)}}{\delta x^2} = \frac{1}{2(\Delta x)^2} (c_{i-1}^t - 2c_i^t + c_{i+1}^t + c_{i-1}^{t+\Delta t} - 2c_i^{t+\Delta t} + c_{i+1}^{t+\Delta t}) \quad (20)$$

The concentration at  $(t + \Delta t/2)$  is evaluated via linear interpolation using

$$c_i^{(t+\Delta t/2)} = \frac{(c_i^t + c_i^{t+\Delta t})}{2} \quad (21)$$

and leads to an equivalent expression to that of Eq. (12) for the explicit method

$$c_{i-1}^{t+\Delta t} - \frac{2(\lambda+1)}{\lambda} c_i^{t+\Delta t} + c_{i+1}^{t+\Delta t} = -c_{i-1}^t + \frac{2(\lambda-1)}{\lambda} c_i^t - c_{i+1}^t \quad (22)$$

where  $\lambda$  is given by Eq. (13). Unlike Eq. (11), the new concentrations cannot be directly obtained from Eq. (20) and hence the method is generally referred to as implicit (Some workers refer to the CN scheme as a semi-implicit method since the resulting expression contains both concentration terms centered at  $t$  and  $t + \Delta t$ ). Solution of Eq. (20) can be achieved, since for a general problem of  $NI$  points, a set of simultaneous equations

can be written in the tridiagonal form

$$c_0^{t+\Delta t} - \frac{2(\lambda+1)}{\lambda} c_1^{t+\Delta t} + c_2^{t+\Delta t} = -c_0^t + \frac{2(\lambda-1)}{\lambda} c_1^t - c_2^t \quad (23)$$

$$c_{i-1}^{t+\Delta t} - \frac{2(\lambda+1)}{\lambda} c_i^{t+\Delta t} + c_{i+1}^{t+\Delta t} = -c_{i-1}^t + \frac{2(\lambda-1)}{\lambda} c_i^t - c_{i+1}^t \quad (24)$$

$$c_{NI-1}^{t+\Delta t} - \frac{2(\lambda+1)}{\lambda} c_{NI}^{t+\Delta t} + c_{NI+1}^{t+\Delta t} = -c_{NI-1}^t + \frac{2(\lambda-1)}{\lambda} c_{NI}^t - c_{NI+1}^t \quad (25)$$

Application of appropriate boundary conditions yields a set of simultaneous equations that can be solved using a variety of methods including Gaussian elimination, of which the Thomas Algorithm [22] is a simplified version. Although formulation and implementation of the CN scheme is considerably more involved than the EFD, it does have advantages. In principle, the stability of the method is not restricted by the value of  $\lambda$ , therefore permitting the use of larger time increments within simulations. It has been noted that the CN method does possess some limitations that can be overcome by modification and the reader is directed to the text by Britz [3] for further details. The CN technique has been applied to simulate one-dimensional diffusion to planar and spherical electrodes and diffusion in redox polymers [23].

### 2.2.2.4 The Alternating Direction Implicit (ADI) Method

The ADI method was reported by Peaceman and Rachford [24] in 1955 and introduced into electrochemical applications by Heinze [25–27]. A fully implicit procedure is used to solve multidimensional diffusion or convective-diffusion problems.

One reported strategy [28] breaks each individual time increment into two half steps (in the case of a two-dimensional problem). In the first half-time increment, one of the dimensions is solved explicitly whilst the other is retained in implicit form, for example,

$$\begin{aligned} & (c_{i,j}^{t+\Delta t/2} - c_{i,j}^t) \\ &= \lambda_x (c_{i,j+1}^{t+\Delta t/2} - 2c_{i,j}^{t+\Delta t/2} + c_{i,j-1}^{t+\Delta t/2}) \\ &+ \lambda_y (c_{i+1,j}^t - 2c_{i,j}^t + c_{i-1,j}^t) \end{aligned} \quad (26)$$

where

$$\lambda_x = \frac{D\Delta t}{(\Delta x)^2} \quad \lambda_y = \frac{D\Delta t}{(\Delta y)^2} \quad (27)$$

and  $i, j, \Delta x$ , and  $\Delta y$  are defined in Fig. 5.

In the following half-time increment, the implicit/explicit directions are swapped

$$\begin{aligned} & (c_{i,j}^{t+\Delta t} - c_{i,j}^{t+\Delta t/2}) \\ &= \lambda_x (c_{i,j+1}^{t+\Delta t/2} - 2c_{i,j}^{t+\Delta t/2} + c_{i,j-1}^{t+\Delta t/2}) \\ &+ \lambda_y (c_{i+1,j}^{t+\Delta t} - 2c_{i,j}^{t+\Delta t} + c_{i-1,j}^{t+\Delta t}) \end{aligned} \quad (28)$$

Values at  $t + \Delta t/2$  are known from the previous time-step and the implicit terms are calculated at the interval  $t + \Delta t$ . The set of tridiagonal matrix equations obtained in each half-time increment may be solved

in an identical manner to those for the CN scheme.

The ADI method was used by Heinze [29] to assess the voltammetric properties at microdisc electrodes. Gavaghan [30] reported a thorough examination of optimum mesh generation and errors present in the FD analysis of the disc electrodes using the ADI method. More recently, the technique has been widely adopted in the field of scanning electrochemical microscopy [31–37] for the simulation of approach curve response and interfacial chemical reactivity.

The ADI method has also been applied to convective-diffusion problems to assess the influence of convective transport on the voltammetric response of microdisc electrodes [38] in channel cells. The convective component may be routinely introduced to Eq. (28) in an analogous manner to that noted for the EFD Eq. (18). The three-dimensional transport problem was addressed in an analogous manner to the two-dimensional problem by splitting each full time increment into three time-steps of one third, to allow the  $x$ ,  $y$ , and  $z$  directions to be solved implicitly.

#### 2.2.2.5 The Hopscotch (HS) Method

The HS method [39] was reported as an alternative strategy to ADI by Shoup and

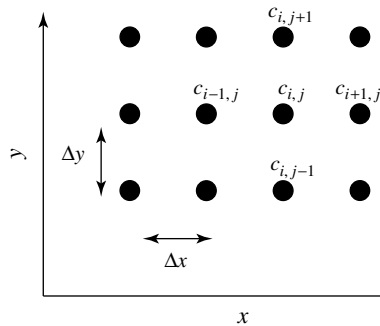


**Fig. 5** Two-dimensional mesh for diffusional calculations.

Szabo [40–42]. An implicit and explicit scheme is employed at alternating points within the two-dimensional mesh (Fig. 5), which allows the new concentrations to be calculated explicitly, but with the advantage of an implicit stability criteria [22]. A counter (a sum of the number of time increments plus the  $i$  and  $j$  pointers) is used to determine whether the calculation is performed explicitly (if the counter is odd)

$$\begin{aligned} & (c_{i,j}^{t+\Delta t} - c_{i,j}^t) \\ &= \lambda_x (c_{i,j+1}^t - 2c_{i,j}^t + c_{i,j-1}^t) \\ &+ \lambda_y (c_{i+1,j}^t - 2c_{i,j}^t + c_{i-1,j}^t) \quad (29) \end{aligned}$$

or implicitly (if the counter is even) at a specific grid point.

$$\begin{aligned} & (c_{i,j}^{t+\Delta t} - c_{i,j}^t) \\ &= \lambda_x (c_{i,j+1}^{t+\Delta t} - 2c_{i,j}^{t+\Delta t} + c_{i,j-1}^{t+\Delta t}) \\ &+ \lambda_y (c_{i+1,j}^{t+\Delta t} - 2c_{i,j}^{t+\Delta t} + c_{i-1,j}^{t+\Delta t}) \quad (30) \end{aligned}$$

The values of  $\lambda_x$  and  $\lambda_y$  are given by Eq. (27) and  $i$ ,  $j$ ,  $\Delta x$ ,  $\Delta y$  are defined in Fig. 5. When an implicit calculation is performed at the point  $i$ ,  $j$ , the surrounding mesh points will have been estimated explicitly at the new time increment using Eq. (29). The counter system ensures that at the next time-increment, the points that have previously been calculated explicitly will now be evaluated implicitly and vice versa. The approach allows unrestricted values of  $\lambda$  to be used and was demonstrated by Shoup and Szabo to give a good level of accuracy for the solution of transport limited current measurements at the microdisc electrode. Despite its relative ease of application and proven stability, the method has not been widely

adopted by workers in the electrochemical field. Modification of Eqs. (29 and 30) to include convective transport has been reported for hydrodynamic applications at a band ultramicroelectrode in a channel flow cell [43], and at a tubular band microelectrode in which the conditions for the current to be independent of flow rate are established [44].

#### 2.2.2.6 The Backwards Implicit (BI)

##### Method

The fully implicit BI method was used by Anderson [45, 46] to simulate the steady state current response to flow rate within a channel flow cell. Subsequently, this was implemented by Fisher and Compton [47] to evaluate the time-dependent convective-diffusion problem

$$\frac{\partial c}{\partial t} = D \frac{\partial^2 c}{\partial y^2} - V_x \frac{\partial c}{\partial x} \quad (31)$$

Cast into fully implicit form, the FD form of Eq. (31) is given by

$$\begin{aligned} & (c_{i,j}^{t+\Delta t} - c_{i,j}^t) \\ &= \lambda_y (c_{i+1,j}^{t+\Delta t} - 2c_{i,j}^{t+\Delta t} + c_{i-1,j}^{t+\Delta t}) \\ &- \lambda_c (c_{i,j+1}^{t+\Delta t} - c_{i,j}^{t+\Delta t}) \quad (32) \end{aligned}$$

where  $i$  and  $j$  are pointers as shown in Fig. 5,  $\lambda_y$  is given by Eq. (27) and

$$\lambda_c = \frac{V_x \Delta t}{(\Delta x)} \quad (33)$$

Following application of the boundary conditions, the set of tridiagonal simultaneous equations may be solved routinely as noted above. Compton and coworkers have used the technique extensively in mechanistic analysis including ECE reactions [48–53] and coupled kinetics reactions [54–59]. The technique has also been used to assess the influence of hydrodynamics on the

current density at microband, microstrip, and microdisc electrodes operating in channel-based cells [60–63]. In addition, the technique has been used to simulate voltammetric responses at wall jet and wall jet ring disc electrodes [64–67].

#### 2.2.2.7 The Fast Implicit Finite Difference (FIFD) Method

The *Fast Implicit Finite Difference* method, implemented by Rudolph [68, 69] has marginally higher computational requirements but has higher potential accuracy when tackling demanding problems. The FIFD formulation expresses the diffusional transport equation on an exponentially expanding spatial grid via

$$\begin{aligned} (c_i^{t+\Delta t} - c_i^t) &= D_{2i}^* (c_{i+1}^{t+\Delta t} - c_i^{t+\Delta t}) \\ &\quad - D_{1i}^* (c_i^{t+\Delta t} - c_{i-1}^{t+\Delta t}) \end{aligned} \quad (34)$$

where

$$D_{2i}^* = D^* \exp \left[ 2\beta \left( \frac{4}{3} - i \right) \right] \quad i > 1 \quad (35)$$

$$D_{1i}^* = D^* \exp \left[ 2\beta \left( \frac{5}{4} - i \right) \right] \quad i \geq 2 \quad (36)$$

with  $\beta$ , the grid expansion factor and

$$D^* = \frac{D\Delta t}{(\Delta x)^2} \quad (37)$$

The approach has undergone extensive development and interested readers are directed to the recent review by Speiser [19]. Feldberg and Rudolph [70] have adopted one of the developments to create a commercial electrochemical software package DigiSim [71, 72].

#### 2.2.2.8 The Strongly Implicit Procedure (SIP)

Compton and coworkers recently proposed the SIP [73] for a variety of

transport-related problems. The SIP was originally reported by Stone [74] in 1968 as an efficient approach to the solution of two- and three-dimensional transport problems. The SIP has been developed to tackle a range of steady state and time-dependent problems related to voltammetric measurements. In this approach, the fully implicit form of the two-dimensional transport equation is solved directly:

$$\begin{aligned} &-\lambda_y c_{i+1,j}^{t+\Delta t} - \lambda_x c_{i,j+1}^{t+\Delta t} + (2\lambda_x + 2\lambda_y + 1) \\ &\times c_{i,j}^{t+\Delta t} - \lambda_x c_{i,j-1}^{t+\Delta t} - \lambda_y c_{i-1,j}^{t+\Delta t} = c_{i,j}^t \end{aligned} \quad (38)$$

where  $\lambda_y$  and  $\lambda_x$  are given by Eq. (27). Using this approach, the system equations were cast into matrix form to yield

$$[A]\{p\} = \{q\} \quad (39)$$

where  $p$  is the vector of unknown concentrations,  $q$  the vector of known values, and  $[A]$  contains the coefficients from the right-hand side of Eq. (38). To overcome the traditional difficulties associated with solution of the pentadiagonal matrices, the matrix  $[A]$  can be modified by the addition of a further matrix  $[B]$  so that the summed matrices  $[A] + [B]$  can be factorized into upper and lower triangular matrices  $([L] + [U])$ .

$$[A][B] = [L][U] \quad (40)$$

This approach permits the efficient iterative solution of the matrix equations using a standard NAG routine (NAG FORTRAN Library (D03EBF)). The approach has been compared to the ADI and HS methods with the authors concluding that the SIP provides a highly efficient competitor to these strategies in both diffusion and convective-diffusion problems [75].



## 2.2.3

**Finite Element Methods**2.2.3.1 **Introduction**

The FEM is part of a larger group of techniques that exploit the method of weighted residuals (MWR) [76]. These use a set of weighting functions to allow the approximation of a variable over a domain. The choice of weighting function leads to a number of different alternative formulations, including the collocation method, subdomain method, method of moments, and the Galerkin method.

The FEM traces its lineage back to classical structural analysis [77] and Argyris [78], who introduced the concept underlying the FEM in 1954. In 1956, Turner and coworkers [79] made a key contribution to the area when they reported the use of pin-jointed bars and triangular plates for the analysis of aircraft structures. The term, *finite element*, however, was not widely adopted until Clough [80] used it in the title of a paper in 1960. The method has subsequently been applied to a vast range of problems, including, soil mechanics [81], aerodynamics [82], heat transfer [83], electric circuit analysis [84], and has also been described in a large number of texts [85–88]. Outlined below is one formulation strategy for the FEM analysis of one-dimensional diffusional transport.

2.2.3.2 **Formulation**

The key steps involved in the formulation of a one-dimensional diffusional problem under steady state conditions now follow:

$$D \frac{\partial^2 c}{\partial x^2} = 0 \quad (41)$$

The FEM uses a mesh of elements to cover the domain, as shown in Fig. 6

The variation of concentration  $c(x)$  along the element length  $l$  is defined by an interpolation function with the concentrations related to the values at the nodal points (Fig. 6)  $c_a$  and  $c_b$

$$c(x) = N_a c_a + N_b c_b \quad (42)$$

where the linear interpolation functions are given by

$$N_a = \frac{1}{l}(x_b - x) \quad (43)$$

$$N_b = \frac{1}{l}(x - x_a) \quad (44)$$

and  $x_a$  and  $x_b$  are the bounds of each element on Fig. 6. For an individual element, these relationships may be written in matrix form

$$c = \vec{N}^e \vec{c}^e \quad (45)$$

where

$$\vec{c}^e = \begin{bmatrix} c_a \\ c_b \end{bmatrix} \quad \vec{N}^e = [N_a \quad N_b] \quad (46)$$

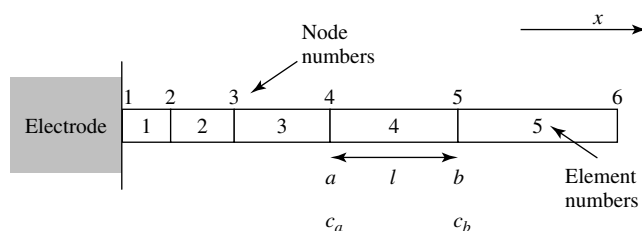


**Fig. 6** One-dimensional element mesh.

Summing the contribution from  $ne$  elements

$$c = \sum_{e=1}^{ne} \vec{N}^e \vec{c}^e \quad (47)$$

A weighted residual formulation [89, 90] is used in order to solve Eq. (41). This approach seeks to approximate the variation of concentration over a region in space using a residual  $R(x)$  such that

$$R(x) - \frac{\partial^2 c}{\partial x^2} = 0 \quad (48)$$

The aim of the numerical procedure is to ensure that the residual is minimized within the domain (ideally it will be zero). Mathematically, this is achieved by forcing  $R(x)$  to be zero (on average) over a given finite region in space by multiplying by a weighting function  $w(x)$

$$\int_a^b w(x) R(x) dx = 0 \quad (49)$$

The weighting function effectively distributes any residual error over the space interval defined by the bounds  $a$  and  $b$ . As noted, a number of possible routes to apply Eq. (49) exist, including: orthogonal collocation, the subdomain, and Galerkin methods [89 pg. 78, 91]. In the FEM, the Galerkin method exploits weighting functions that take the same form as the interpolation functions Eqs. (43, 44). The residual takes the same form as the original differential

$$R(x) - \frac{\partial^2 C}{\partial x^2} = 0 \quad (50)$$

where  $C$  is now an approximate solution for the concentration. Recasting Eq. (41) in weighted residual form gives

$$D \int_a^b N^e \frac{\partial^2 C}{\partial x^2} dx = 0 \quad (51)$$

and this is now integrated (by parts) to yield

$$D \int_a^b \frac{\partial \vec{N}^e}{\partial x} \frac{\partial C}{\partial x} dx - D \left( \vec{N}^e \frac{\partial C}{\partial x} \right) \Big|_a^b = 0 \quad (52)$$

From Eq. (47)

$$\frac{\partial C}{\partial x} = \frac{\partial \vec{N}^e}{\partial x} \vec{C} \quad (53)$$

and Eq. (52) can be rewritten

$$D \int_a^b \frac{\partial \vec{N}^e}{\partial x} \frac{\partial \vec{N}^e}{\partial x} dx \vec{C} - D \frac{\partial C}{\partial x} (\vec{N}^e) \Big|_a^b = 0 \quad (54)$$

Noting the second term of Eq. (54) relates to the boundary of the element and may be applied later; evaluation of Eq. (54) now requires the remaining integral. From Eq. (45), we can calculate

$$\frac{\partial \vec{N}}{\partial x} = \begin{bmatrix} -\frac{1}{l} & \frac{1}{l} \end{bmatrix} \quad (55)$$

it follows from Eq. (54)

$$\frac{D}{l} \begin{bmatrix} 1 & -1 \\ -1 & 1 \end{bmatrix} \vec{C} = 0 \quad (56)$$

written in matrix form for an individual element

$$[K]^e \vec{C} = \vec{P} \quad (57)$$

where

$$[K]^e = \begin{bmatrix} 1 & -1 \\ -1 & 1 \end{bmatrix} \quad (58)$$

( $[K]^e$  is usually referred to as the characteristic matrix of the element).

For a mesh of  $ne$  elements (Fig. 6), a global matrix (Fig. 7) is now constructed with contributions from each node summed into the relevant matrix position.

At this stage, any boundary conditions for the problem are introduced (e.g. flux

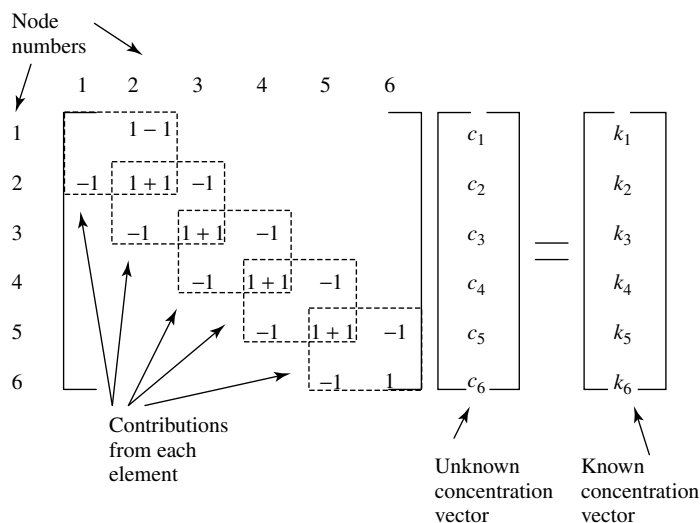


Fig. 7 Global matrix for a problem in which  $ne = 5$ .

or fixed values of concentration). For the internal nodes, it is assumed that the flux across the boundaries between each element are in balance leaving only the two values of flux at the external points of the mesh to be defined (if required). Left undefined, the values correspond to the Neumann boundary condition of no-flux. However, a fixed concentration, Dirichlet boundary condition, may be routinely introduced and further details can be found in [86 pg. 184]. It is apparent that the matrix formed is symmetric and banded around the center diagonal and this permits standard Gaussian elimination routines to be employed for solution of the matrices [92–94].

Formulation to introduce convective transport into electrochemical calculations provides no conceptual difficulties and readers are referred to the article by Stevens [95]. Similar procedures may be used to formulate two-dimensional analogies and these have been described previously [96, 97].

### 2.2.3.3 Applications

Early applications of the MWR/FEM in electrochemistry were reported by Whiting and coworkers [98] and Speiser and coworkers [99–105], who exploited the method for electroanalytical purposes. In 1984, Penczek and coworkers [91, 106] demonstrated the application of the FEM to finite and infinite one-dimensional diffusion problems relating to the voltammetry at mercury amalgam films.

Early two-dimensional simulations focused on the evaluation of the current distribution at microdisc electrodes [107, 108] and simulations of a variety of electrode geometries [109–111] including the influence of recessed microelectrode configurations [112]. Work has been also extended to cases involving coupled homogeneous kinetics, adsorption [113], and time-dependent redox polymer electrochemistry [114].

More recently, workers have reported the use of automatic mesh generation routines [115] and strategies that permit

the solutions to be obtained to a specified accuracy [116]. The FEM has been utilized to simulate hydrodynamic voltammetry at the rotating disc, channel, wall jet, and related electrode geometries [95, 117–119] and as a computer-aided design tool by Fisher and coworkers [120–124] for the development of new electroanalytical devices and to quantify voltammetry under microfluidic control.

Workers have also used a number of commercially available FEM packages to allow the simulation of immiscible liquid–liquid interfacial measurements [125–127] and approach curves for scanning electrochemical microscope applications [128]. Compton and coworkers have also used a commercial FEM package to model coupled heat and mass transport at a wire [129], and dissolution kinetics in flow-through devices [130].

## 2.2.4

### Boundary Element Method

#### 2.2.4.1 Introduction

The BEM forms part of a group of integral methods [131–142] that have been used sporadically for the simulation of electrochemically related problems. The BEM was described by Banerjee and coworkers and Brebbia and coworkers and has been outlined by them and others in detail in a number of engineering texts [6, 143–146]. A wide range of engineering-related problems have been tackled using the BEM including: heat transfer, fluid mechanics, and structural analysis.

The BEM uses an integral approach to solve the differential equations related to the transport of material within a domain. The differential equations are transformed into an equivalent integral equation at the boundary of the domain and discretized using a series of elements

that approximate the (nonlinear) variation of the variable at the boundary. Below, one formulation strategy for a one-dimensional diffusion-controlled problem is outlined Eq. (41).

#### 2.2.4.2 Formulation

The formulation procedure begins in an analogous manner to that of the FEM. For the case of the diffusional operator Eq. (41), the weighted residual form is given by Eq. (51) as before, integration (by parts) yields

$$D \int_a^b \frac{\partial w}{\partial x} \frac{\partial C}{\partial x} dx - D \left[ w(x) \frac{\partial C}{\partial x} \right]_a^b = 0 \quad (59)$$

A second integration gives the inverse formulation

$$D \int_a^b \frac{\partial^2 w}{\partial x^2} C dx + D \left[ w(x) \frac{\partial C}{\partial x} \right]_a^b - D \left[ C \frac{\partial w}{\partial x} \right]_a^b = 0 \quad (60)$$

The procedure yields an integral in which the differential operator acts on the weighting function and not  $C$ , plus two terms that are evaluated at the boundary. Careful selection of  $w$  such that

$$\frac{\partial^2 w}{\partial x^2} = 0 \quad (61)$$

reduces Eq. (60) to an integral expression relating to the boundary values of concentration, the weighting function, and the gradient of concentration. This procedure is referred to as the homogeneous solution method and has been applied to a range of one-dimensional problems. An alternative strategy usually adopted for solving two- and three-dimensional transport problems is the use of the Dirac delta function

$-\delta(x - \xi)$  such that

$$\frac{\partial^2 w}{\partial x^2} = -\delta(x - \xi) \quad (62)$$

when applied at the point  $x = \xi$ , further details may be found in [6 pg. 30]. The choice of  $w$  is discussed elsewhere [144] but is dependent upon the specific differential to be solved. A general solution that satisfies Eq. (61) is

$$w = Ax + B \quad (63)$$

where  $A$  and  $B$  are arbitrary constants. Selecting two solutions of Eq. (63) for example,

$$w_1 = x \quad (64)$$

$$w_2 = B \quad (65)$$

and then substituting these into Eq. (60) yields two simultaneous equations

$$-a \left( \frac{\partial C_a}{\partial x} \right) + C_a + b \left( \frac{\partial C_b}{\partial x} \right) - C_b = 0 \quad (66)$$

$$-\left( \frac{\partial C_a}{\partial x} \right) + \left( \frac{\partial C_b}{\partial x} \right) = 0 \quad (67)$$

where  $C_a$ ,  $C_b$ ,  $(\partial C_a / \partial x)$  and  $(\partial C_b / \partial x)$  correspond to the concentrations and fluxes at the boundary points  $a$  and  $b$  respectively. Application of boundary conditions (defining the flux or concentration at each boundary) permits the solution for the unknown values. Of particular interest to the electrochemist is the ability to gain a direct measure of the flux from the simulation unlike the FEM and the FDM that rely on a fine mesh normal to the surface.

Extension of the approach to convective and indeed migratory transport has been achieved in electrochemical applications and readers are referred to the article by Qiu, Wrobel, and Power [147] for further details.

### 2.2.4.3 Applications

Despite the potential of the BEM to reduce the dimensionality of the numerical solution and provide a direct measure of the interfacial flux, it has been poorly exploited by workers in the electrochemical field in comparison with the FDM and the FEM. By comparison, heat and mass transfer have been widely treated using the BEM in the engineering literature [148–151]. In 1984, the BEM was employed to calculate the primary current distribution during an electropolymerization reaction [152], the potential of the BEM for applications to irregular geometries was also noted. Hume and coworkers [153] used the approach to analyze mass transport effects of electrodeposition through polymeric masks.

Of related interest, Ramachandran and coworkers have reported a range of papers on the influence of mass transport [154–156], including diffusion-reaction problems [157]. Further work was reported on a variety of current distribution problems [158–161] in the early 1990s, with a comparison of the FEM and the BEM efficiency reported by Matlosz and coworkers [162]. A two-dimensional study of coplanar auxiliary electrodes was reported by Mehdizadeh and coworkers [163] and was used to assess the influence of the electrode configuration on uniform growth over the cathode electrode. Electroplating and corrosion protection in industrial cell configurations have also been addressed by Druesne and coworkers [164, 165].

In 1994, Barbero and coworkers [166] extended BEM applications in the electrochemical field to investigate convective electrodiffusion problems in charged membranes. Qiu, Wrobel, and Power have also outlined the application of the BEM to transport-related problems including detailed procedures for assessing current distribution effects controlled by combined

diffusion, convection, migration [147], examining binary and three electrolyte ion systems [167], and in the prediction of electrode topography [168].

The BEM has been applied in scanning electrochemical microscopy applications by Fisher and Denuault [169] to examine the influence of probe and substrate surface topography. In addition, time-dependent phenomena have been assessed in oil droplets [170, 171] and a range of microelectrode geometries using the dual reciprocity method (DRM) [172] closely related to the BEM [173].

### 2.2.5

#### Alternative Simulation Strategies

In addition to the topics reviewed above, which form the vast majority of the articles published to date in the field of electrochemical simulation, there are a number of other alternative methods that have been exploited by workers. These include, statistical techniques such as the Monte Carlo method [174–179], which has been exploited to examine the fractal nature of electrode surfaces and electrodeposited polymer film growth. The finite volume method, which has found significant application in the engineering literature [180, 181], remains poorly exploited in the electrochemical field [182, 183] as does the multidimensional unwinding method, which has been applied by Van Den Bossche and coworkers [184, 185] to multi-ion systems at the rotating disc electrode. For recent advances, readers are referred to the review of Speiser [19].

#### Acknowledgments

FLQ (GR/N00548) and KAG (studentship No. 9930027X) would like to thank the EPSRC for their support.

#### References

1. S. W. Feldberg in *Electroanalytical Chemistry* (Ed.: A. J. Bard), Marcel Dekker, New York, 1969, pp. 199–296.
2. A. J. Bard, L. R. Faulkner, *Electrochemical Methods*, John Wiley & Sons, New York, 1980.
3. D. Britz, *Digital Simulation in Electrochemistry*, 2nd ed., Springer-Verlag, Berlin, 1988.
4. D. K. Gosser, *Cyclic Voltammetry. Simulation and Analysis of Reaction Mechanisms*, Wiley-VCH, Weinheim, Germany, 1993.
5. <http://www.bath.ac.uk/~chsacf>.
6. P. A. Ramachandran, *Boundary Element Methods in Transport Phenomena*, 1st ed., Elsevier, Southampton, UK, 1994.
7. L. F. Richardson, *Philos. Trans.* **1911**, 210, 307–357.
8. R. Courant, K. Friedrichs, H. Lewy, *Math. Ann.* **1928**, 100, 32.
9. H. W. Emmons, *Q. Appl. Math.* **1944**, 2, 173–195.
10. J. E. B. Randles, *Trans. Faraday Soc.* **1948**, 44, 327–338.
11. T. Joslin, D. Pletcher, *J. Electroanal. Chem.* **1974**, 49, 171.
12. S. W. Feldberg, *J. Electroanal. Chem.* **1981**, 127, 1.
13. L. K. Bieniasz, *J. Electroanal. Chem.* **1993**, 360, 119–138.
14. J. B. Flanagan, K. Takahashi, F. Anson, *J. Electroanal. Chem.* **1977**, 81, 261.
15. J. W. Dillard, J. A. Turner, R. A. Osteryoung, *Anal. Chem.* **1977**, 49, 1246.
16. R. Seeber, S. Stefani, *Anal. Chem.* **1981**, 53, 1011–1016.
17. J. von Neumann, R. D. Richtmyer, *J. Appl. Phys.* **1950**, 53, 1021–1099.
18. F. John, *Common Pure Appl. Math.* **1952**, 5, 155–211.
19. B. Speiser in *Electroanalytical Chemistry* (Eds.: A. J. Bard, I. Rubinstein), Marcel Dekker, New York, 1996, pp. 1–108.
20. J. Crank, P. Nicolson, *Proc. Cambridge Philos. Soc.* **1947**, 43, 50–67.
21. J. Crank, *The Mathematics of Diffusion*, Clarendon Press, Oxford, 1956.
22. L. Lapidus, G. F. Pinder, *Numerical Solution of Partial Differential Equations in Science and Engineering*, John Wiley & Sons, New York, 1982.
23. M. Störzbach, J. Heinze, *J. Electroanal. Chem.* **1993**, 346, 1–27.

24. D. W. Peaceman, H. H. Rachford, *J. Soc. Ind. Appl. Math.* **1955**, 3, 28.
25. J. Heinze, M. Störzbach, *Ber. Bunsen-Ges. Phys. Chem.* **1986**, 90, 1043–1048.
26. J. Heinze, M. Störzbach, J. Mortensen, *J. Electroanal. Chem.* **1984**, 165, 61–70.
27. J. Heinze, M. Störzbach, J. Mortensen, *J. Electroanal. Chem.* **1988**, 240, 27–43.
28. M. K. Jain, *Numerical Solution of Differential Equations*, Wiley Eastern Limited, New Delhi, 1979.
29. J. Heinze, *J. Electroanal. Chem.* **1981**, 124, 73.
30. D. J. Gavaghan, *J. Electroanal. Chem.* **1998**, 456, 1–35.
31. A. J. Bard, F. R. F. Fan, F. F. Fu-Ren et al., *Anal. Chem.* **1989**, 61, 132.
32. C. Demaille, P. R. Unwin, A. J. Bard, *J. Phys. Chem.* **1996**, 100, 14 137–14 143.
33. J. L. Amphlett, G. Denuault, *J. Phys. Chem. B* **1998**, 102, 9946–9951.
34. A. J. Bard, M. V. Mirkin, P. R. Unwin et al., *J. Phys. Chem.* **1992**, 96, 1861–1868.
35. P. R. Unwin, A. J. Bard, *J. Phys. Chem.* **1991**, 95, 7814–7824.
36. J. V. Macpherson, P. R. Unwin, *J. Phys. Chem.* **1996**, 100, 19 475–19 483.
37. J. V. Macpherson, P. R. Unwin, *J. Phys. Chem.* **1994**, 98, 1704–1713.
38. J. Booth, R. G. Compton, J. A. Cooper et al., *J. Phys. Chem.* **1995**, 99, 10 942–10 947.
39. A. R. Gourlay, *J. Inst. Math. Appl.* **1970**, 6, 375.
40. D. Shoup, A. Szabo, *J. Electroanal. Chem.* **1982**, 140, 237–245.
41. D. Shoup, A. Szabo, *J. Electroanal. Chem.* **1984**, 160, 1–17.
42. D. Shoup, A. Szabo, *J. Electroanal. Chem.* **1986**, 199, 437–441.
43. P. Pastore, F. Magno, J. Lavagnini et al., *J. Electroanal. Chem.* **1991**, 301, 1–13.
44. H. R. Corti, D. L. Goldfarb, A. S. Ortiz et al., *Electroanalysis* **1995**, 7, 569–573.
45. S. Moldoveanu, J. L. Anderson, *J. Electroanal. Chem.* **1984**, 175, 67.
46. J. L. Anderson, S. Moldoveanu, *J. Electroanal. Chem.* **1984**, 179, 107–119.
47. A. C. Fisher, R. G. Compton, *J. Phys. Chem.* **1991**, 95, 7538–7542.
48. A. C. Fisher, R. G. Compton, *J. Appl. Electrochem.* **1992**, 22, 38–42.
49. R. G. Compton, B. A. Coles, A. C. Fisher, *J. Phys. Chem.* **1994**, 98, 2441–2445.
50. J. A. Alden, R. G. Compton, *J. Phys. Chem. B* **1997**, 101, 9606–9616.
51. J. A. Alden, M. A. Feldman, E. Hill et al., *Anal. Chem.* **1998**, 70, 1707–1720.
52. A. B. Miles, R. G. Compton, *J. Phys. Chem. B* **2000**, 104, 5331–5342.
53. A. B. Miles, R. G. Compton, *J. Electroanal. Chem.* **2001**, 499, 1–16.
54. R. G. Compton, M. B. G. Pilkington, G. M. Stearn, *J. Chem. Soc.* **1988**, 84, 2155–2171.
55. J. A. Alden, R. G. Compton, R. A. W. Dryfe, *J. Electroanal. Chem.* **1995**, 397, 11–17.
56. B. A. Coles, R. A. W. Dryfe, N. V. Rees et al., *J. Electroanal. Chem.* **1996**, 411, 121–127.
57. J. A. Alden, R. G. Compton, *J. Phys. Chem. B* **1997**, 101, 8941–8954.
58. F. Prieto, W. J. Aixill, J. A. Alden et al., *J. Phys. Chem. B* **1997**, 101, 5540–5544.
59. W. J. Aixill, J. A. Alden, F. Prieto et al., *J. Phys. Chem. B* **1998**, 102, 1515–1521.
60. R. G. Compton, A. C. Fisher, R. G. Wellington et al., *J. Phys. Chem.* **1993**, 97, 10 410–10 415.
61. C. W. Davies, M. K. Walters, A. C. Fisher et al., *J. Phys. Chem.* **1995**, 99, 10 942.
62. W. J. Aixill, A. C. Fisher, Q. Fulian, *J. Phys. Chem.* **1996**, 100, 14 067–14 073.
63. C. W. Davies, Q. Fulian, M. K. Walters et al., *Electroanalysis* **1996**, 11, 849.
64. R. G. Compton, A. C. Fisher, G. P. Tyley, *J. Appl. Electrochem.* **1991**, 21, 2–5.
65. A. C. Fisher, R. G. Compton, *J. Appl. Electrochem.* **1991**, 21, 208–212.
66. R. G. Compton, A. C. Fisher, M. H. Latham et al., *J. Phys. Chem.* **1992**, 96, 8363–8367.
67. J. C. Ball, R. G. Compton, C. M. A. Brett, *J. Phys. Chem. B* **1998**, 102, 162–166.
68. M. Rudolph, *J. Electroanal. Chem.* **1991**, 314, 13–22.
69. M. Rudolph, *J. Electroanal. Chem.* **1992**, 338, 85–98.
70. S. W. Feldberg, C. I. Goldstein, M. Rudolph, *J. Electroanal. Chem.* **1996**, 413, 25–36.
71. J. Mocak, S. W. Feldberg, *J. Electroanal. Chem.* **1994**, 378, 17–29.
72. M. Rudolph in *Physical Electrochemistry* (Ed.: I. Rubinstein), Marcel Dekker, New York, 1995, pp. 81–129.
73. R. G. Compton, R. A. W. Dryfe, R. G. Wellington et al., *J. Electroanal. Chem.* **1995**, 383, 13–19.
74. H. L. Stone, *Siam J. Numer. Anal.* **1968**, 5, 530.

75. J. A. Alden, R. G. Compton, *J. Electroanal. Chem.* **1996**, 402, 1–10.
76. B. A. Finlayson, *Br. Chem. Eng.* **1969**, 14, 53–57.
77. R. Courant, *Bull. Am. Math. Soc.* **1943**, 49, 1–23.
78. J. H. Argyris, *Aircraft Eng.* **1954**, 26, 347.
79. M. J. Turner, R. W. Clough, H. C. Martin et al., *J. Aerosol Sci.* **1956**, 23, 805.
80. R. W. Clough, Proceedings of 2nd ASCE Conference on Electronic Computation, Pittsburgh, Pa., 1960.
81. C. V. Girijavallabhan, L. C. Reese, *J. Soil Mech. Proc. ASCE* **1968**, 94, 473–496.
82. S. S. Rao, *Proc. Int. Symp. Disc. Methods Eng.* Milan, 1974, pp. 512–525.
83. S. G. Ravikumar, K. N. Seetharamu, P. A. Aswathanarayana, *Proc. Int. Conf. On Finite Elements in Computational Mechanics* 1985, 861, Vol. 2.
84. P. P. Silvester, R. L. Ferrari, *Finite Elements for Electrical Engineers*, 3rd ed., Cambridge University Press, Cambridge, 1996.
85. O. C. Zienkiewicz, R. L. Taylor, *The Finite Element Method*, 5th ed., Butterworth-Heinemann, Oxford, 2000.
86. S. S. Rao, *The Finite Element Method in Engineering*, Pergamon Press, Oxford, 1982.
87. G. Dhatt, G. Touzot, *The Finite Element Method Displayed*, John Wiley & Sons, New York, 1984.
88. C. Cuvelier, A. Segal, A. A. van Steenhoven, *Finite Element Methods and Navier-Stokes Equations*, D. Reidel, Dordrecht, The Netherlands, 1986.
89. J. Villadsen, M. L. Michelsen, *Solution of Differential Equations by Polynomial Approximation*, Prentice Hall, Englewood Cliffs, NJ, 1978.
90. G. Fairweather, *Finite Element Galerkin Methods for Differential Equations*, John Wiley & Sons, New York, 1978.
91. M. Penczek, Z. Stojek, J. Osteryoung, *J. Electroanal. Chem.* **1984**, 170, 99–108.
92. E. Isaacson, H. B. Keller, *Analysis of Numerical Methods*, John Wiley & Sons, New York, 1966.
93. L. W. Johnson, R. D. Riess, *Numerical Analysis*, 2nd ed., Addison-Wesley, Reading, Mass., 1982.
94. W. H. Press, S. A. Teukolsky, W. T. Vetterling et al., *Numerical Recipes in Fortran 77: The Art of Scientific Computing*, 2nd ed., Cambridge University Press, Cambridge, 1996.
95. N. P. C. Stevens, A. C. Fisher, *J. Phys. Chem. B* **1997**, 101, 8259–8263.
96. A. J. Chapman, *Heat Transfer*, 4th ed., Macmillan Publishing, New York, 1984.
97. J. P. Holman, *Heat Transfer*, 8th ed., McGraw-Hill, New York, 1997.
98. L. F. Whiting, P. W. Carr, *J. Electroanal. Chem.* **1977**, 81, 1–20.
99. B. Speiser, A. Rieker, *J. Electroanal. Chem.* **1979**, 102, 1–20.
100. B. Speiser, *J. Electroanal. Chem.* **1980**, 110, 69–77.
101. S. Pons, B. Speiser, J. F. McAleer, *Electrochim. Acta* **1982**, 27, 1177–1179.
102. B. Speiser, S. Pons, A. Rieker, *Electrochim. Acta* **1982**, 27, 1171–1176.
103. B. Speiser, *J. Electroanal. Chem.* **1984**, 171, 95–109.
104. P. Hertl, B. Speiser, *J. Electroanal. Chem.* **1987**, 217, 225–238.
105. P. Hertl, B. Speiser, *J. Electroanal. Chem.* **1988**, 250, 237–256.
106. M. Penczek, Z. Stojek, *J. Electroanal. Chem.* **1984**, 181, 83–91.
107. J. Galceran, D. J. Gavaghan, J. S. Rollet, *J. Electroanal. Chem.* **1995**, 394, 17.
108. M. Penczek, Z. Stojek, *J. Electroanal. Chem.* **1987**, 227, 271–274.
109. M. M. Stephens, E. D. Moorhead, *J. Electroanal. Chem.* **1987**, 220, 1–30.
110. N. P. C. Stevens, S. J. Hickey, A. C. Fisher, *An. Quim.* **1997**, 93, 225–232.
111. N. P. C. Stevens, F. L. Qiu, K. A. Gooch et al., *J. Phys. Chem. B* **2000**, 104, 7110–7114.
112. P. N. Bartlett, S. L. Taylor, *J. Electroanal. Chem.* **1998**, 453, 49–60.
113. E. D. Moorhead, M. M. Stephens, *J. Electroanal. Chem.* **1990**, 282, 1–26.
114. E. Deiss, O. Haas, C. Daul, *J. Electroanal. Chem.* **1992**, 337, 299–324.
115. T. Nann, J. Heinze, *Electrochem. Commun.* **1999**, 1, 289–294.
116. K. Harriman, D. Gavaghan, P. Houston et al., *Electrochem. Commun.* **2000**, 2, 150–170, 567–585.
117. R. Ferrigno, P. F. Brevet, H. H. Girault, *J. Electroanal. Chem.* **1997**, 430, 235–242.
118. N. P. C. Stevens, A. C. Fisher, *Electroanalysis* **1998**, 10, 16–20.



119. B. A. Coles, R. G. Compton, C. M. A. Brett et al., *J. Electroanal. Chem.* **1995**, 381, 99–104.
120. Q. Fulian, N. P. C. Stevens, A. C. Fisher, *J. Phys. Chem. B* **1998**, 102, 3779–3783.
121. K. A. Gooch, N. A. Williams, A. C. Fisher, *Electrochem. Commun.* **2000**, 2, 51–55.
122. Q. Fulian, A. C. Fisher, D. J. Riley, *Electroanalysis* **2000**, 12, 503–508.
123. F. L. Qiu, K. A. Gooch, A. C. Fisher et al., *Anal. Chem.* **2000**, 72, 3480–3485.
124. N. P. C. Stevens, K. A. Gooch, A. C. Fisher, *J. Phys. Chem. B* **2000**, 104, 1241–1248.
125. J. Josseland, J. Morandini, H. J. Lee et al., *J. Electroanal. Chem.* **1999**, 468, 42–52.
126. R. Ferrigno, H. H. Girault, *J. Electroanal. Chem.* **2000**, 492, 1–6.
127. H. J. Lee, C. Beriet, R. Ferrigno et al., *J. Electroanal. Chem.* **2001**, 502, 138–145.
128. Y. Lee, S. Amemiya, A. J. Bard, *Anal. Chem.* **2001**, 73, 2261–2267.
129. A. Beckmann, B. A. Coles, R. G. Compton et al., *J. Phys. Chem. B* **2000**, 104, 764–769.
130. B. A. Coles, R. G. Compton, M. Suarez et al., *Langmuir* **1998**, 14, 218–225.
131. S. Coen, D. K. Cope, D. E. Tallman, *J. Electroanal. Chem.* **1986**, 215, 29–48.
132. M. Fleischmann, J. Daschbach, S. Pons, *J. Electroanal. Chem.* **1989**, 263, 189–203.
133. J. Daschbach, S. Pons, M. Fleischmann, *J. Electroanal. Chem.* **1989**, 263, 205–224.
134. M. Rudolph, *J. Electroanal. Chem.* **1990**, 292, 1–7.
135. U. Kalapathy, D. E. Tallman, D. K. Cope, *J. Electroanal. Chem.* **1990**, 285, 71–77.
136. D. K. Cope, C. H. Scott, D. E. Tallman, *J. Electroanal. Chem.* **1990**, 285, 49–69.
137. D. K. Cope, D. E. Tallman, *J. Electroanal. Chem.* **1990**, 285, 79–92.
138. D. R. Baker, M. W. Verbrugge, J. Newman, *J. Electroanal. Chem.* **1991**, 314, 23–44.
139. M. V. Mirkin, A. J. Bard, *J. Electroanal. Chem.* **1992**, 323, 1–27, 29–51.
140. L. K. Bieniasz, *Comput. Chem.* **1992**, 16, 311–317.
141. L. K. Bieniasz, *J. Electroanal. Chem.* **1993**, 347, 15–30.
142. B. Pillay, J. Newman, *J. Electrochem. Soc.* **1993**, 140, 414–420.
143. P. K. Banerjee, R. Butterfield, *Boundary Element in Engineering Science*, McGraw-Hill, New York, 1981.
144. C. A. Brebbia, J. C. F. Telles, L. C. Wrobel, *Boundary Element Techniques. Theory and Application in Engineering*, Springer-Verlag, Berlin, Germany, 1984.
145. C. A. Brebbia, *Boundary Element Method for Engineers*, Pentech, London, 1984.
146. B. E. Beskos, *Boundary Element Methods in Mechanics, Computational Methods in Mechanics*, North Holland, Amsterdam, 1987, 1–25, Vol. 3.
147. Z. H. Qiu, L. C. Wrobel, H. Power, *Eng. Anal. Boundary Elements* **1995**, 15, 299.
148. P. H. L. Groenenboom, *Appl. Math. Modell.* **1982**, 6, 35.
149. C. A. Brebbia, P. Skerget, *J. Appl. Phys.* **1982**, 53, 8366.
150. W. L. Wendland, J. Zhu, *Math. Comput. Modell.* **1991**, 15, 19.
151. S. Y. Long, X. C. Kuai, J. Chen et al., *Eng. Anal. Boundary Elements* **1993**, 12, 293.
152. R. Bialecki, R. Nahlik, M. Lapkowski, *Electrochim. Acta* **1984**, 29, 905.
153. E. C. Hume, W. M. Deen, R. A. Brown, *J. Electrochem. Soc.* **1984**, 131, 1251.
154. P. L. Mills, S. Lai, M. P. Dudukovic et al., *Siam J. Sci. Stat. Comput.* **1988**, 9, 271.
155. P. A. Ramachandran, *Int. J. Numer. Methods Eng.* **1990**, 29, 1021.
156. P. A. Ramachandran, *Chem. Eng. J.* **1990**, 45, 49.
157. P. A. Ramachandran, *J. Comput. Phys.* **1992**, 102, 63.
158. J. F. Yan, S. N. R. Pakalapati, T. V. Nguyen et al., *J. Electrochem. Soc.* **1992**, 139, 1932.
159. P. Cicognani, F. Gasparoni, B. Mazza et al., *J. Electrochem. Soc.* **1990**, 137, 1689.
160. J. Horkins, L. T. Romankiw, *J. Electrochem. Soc.* **1989**, 136, 756.
161. E. K. Yung, L. T. Romankiw, *J. Electrochem. Soc.* **1989**, 136, 764.
162. M. Matlosz, C. Creton, C. Clerc et al., *J. Electrochem. Soc.* **1987**, 134, 3015.
163. S. Mehdizadeh, J. Dukovic, P. C. Andricacos et al., *J. Electrochem. Soc.* **1990**, 137, 110.
164. F. Druesne, P. Paumelle, *Corros. Prevention Control* **1998**, 45, 118.
165. F. Druesne, P. Paumelle, P. Villon, *Eng. Anal. Boundary Elements* **2000**, 24, 615.
166. A. J. Barbero, S. Mafe, P. Ramirez, *Electrochim. Acta* **1994**, 39, 2031.
167. Z. H. Qiu, L. C. Wrobel, H. Power, *J. Appl. Electrochem.* **1997**, 27, 1333.
168. Z. H. Qiu, H. Power, *J. Appl. Electrochem.* **2000**, 30, 575.

169. F. Qiu, A. C. Fisher, G. Denuault, *J. Phys. Chem. B* **1999**, 103, 4387, 4393.
170. F. L. Qiu, J. C. Ball, F. Marken et al., *Electroanalysis* **2000**, 12, 1012–1016.
171. J. C. Ball, F. Marken, F. L. Qiu et al., *Electroanalysis* **2000**, 12, 1017–1025.
172. F. L. Qiu, A. C. Fisher, *Electrochem. Commun.* **2000**, 2, 738–742.
173. D. Nardini, C. A. Brebbia in *Boundary Element Methods in Engineering* (Ed.: C. A. Brebbia), Springer-Verlag, Berlin, 1982, pp. 312–326.
174. B. Marner, W. Schmickler, *J. Electroanal. Chem.* **1986**, 214, 589–596.
175. B. Aurian-Blajeni, M. Kramer, M. Tomkiewicz, *J. Phys. Chem.* **1987**, 91, 600–605.
176. T. Pajkossy, L. Nyikos, *Electrochim. Acta* **1989**, 34, 171–179.
177. F. Sagués, J. M. Costa, *J. Chem. Educ.* **1989**, 66, 502–506.
178. S. Záliš, N. Fanelli, L. Pospíšil, *J. Electroanal. Chem.* **1991**, 314, 1–11.
179. G. Nagy, Y. Sugimoto, G. Denuault, *J. Electroanal. Chem.* **1997**, 433, 167–173.
180. H. K. Versteeg, W. Malalasekera, *An Introduction to Computational Fluid Dynamics: The Finite Volume Method*, Longman Group, Harlow, UK, 1995.
181. L. Ronghua, W. Wei, C. Zhongying, *Generalised Difference Methods for Differential Equations: Numerical Analysis of Finite Volume Methods*, Marcel Dekker, New York, 2001.
182. S. Bacha, A. Bergel, M. Comtat, *J. Electroanal. Chem.* **1993**, 359, 21–38.
183. Yu. V. Benderskii, V. G. Mairanosvkii, *Elektrokhimiya* **1992**, 28, 835–841.
184. B. Van Den Bossche, L. Bortels, J. Deconinck et al., *J. Electroanal. Chem.* **1995**, 397, 35–44.
185. B. Van Den Bossche, L. Bortels, J. Deconinck et al., *J. Electroanal. Chem.* **1996**, 411, 129–143.

### 3.1 NMR Spectroscopy in Electrochemistry

*YuYe Tong*  
*Georgetown University, Washington, Washing-*  
*ton DC*

*Eric Oldfield and Andrzej Wieckowski*  
*University of Illinois at Urbana-Champaign,*  
*Urbana, Illinois*

#### 3.1.1 Introduction

The fundamental physical origins of the different chemical reactivities of catalytic or functional metal surfaces – be they used as heterogeneous catalysts, electrocatalysts, substrates for materials engineering, or simply as templates for corrosion studies – are electronic [1]. Most surface processes can be considered to involve the optimization of the electronic interaction energy of the system through suitable geometric rearrangements. These surface processes necessarily involve the activation of one or more chemical ingredients together with the concomitant excitation of the many-electron metal surface. They are, therefore, in general rather complex processes.

In the gas (dry) phase, ultrahigh vacuum (UHV)-based surface science characterization techniques have been developed

for many years for scrutinizing complex surface processes [2]. Unfortunately, few of these techniques are readily applicable to investigating problems at the electrochemical interface, because of the ubiquitous presence of the condensed-phase electrolyte. In electrocatalysis/fuel cell applications, for instance, specific chemical and physical properties of the electrode become of paramount importance in terms of understanding the fundamental aspects of such interfacial electrochemical phenomena [3]. It is in this field of interfacial electrochemistry that the newly developed electrochemical nuclear magnetic resonance (EC-NMR) spectroscopy technique [4] is mainly applicable. This development is now beginning to bring results that illuminate both electronic and dynamic aspects of processes in real-world catalytic systems [4–10].

Technically, however, NMR probably possesses the lowest mass-detection sensitivity of any spectroscopic technique [11] and is still quite a challenging prospect. To appreciate the difficulties, note that a typical high-field NMR instrument needs  $\sim 10^{18}$ – $10^{19}$  NMR-active atoms, for example  $^{13}\text{C}$  spins, to make a signal detectable within a reasonable time period. However,  $1\text{ cm}^2$  of a single-crystal metal surface contains only about  $10^{15}$  atoms. Therefore, at least  $1\text{ m}^2$  surface area of NMR-active

atoms is needed to meet the sensitivity requirement, which is the primary reason that most surface NMR investigations reported so far have used high-surface-area materials. Nevertheless, there are several advantages to using NMR to investigate (electrochemical) surface processes. For example, NMR is extremely sensitive to local static (geometric), electronic, and dynamic structure [12]. Also, NMR can characterize samples in most types of catalysts – metal powders, oxide-supported metal catalysts, carbon-supported catalysts, and both metal and adsorbate structures can be probed. In addition, it is a nondestructive technique and can be applied under technically demanding environmental conditions close to real-world operating conditions. For example, it is possible to investigate graphite-supported metal catalysts in an electrochemical environment under potential control. Given adequate mass sensitivity then, NMR has a unique ability to provide a wealth of electronic and structural information on the atomic level, and in addition permits one to access motional information on adsorbates over a time-span unattainable by any other spectroscopic technique. As such, NMR of oxide-supported metal catalysts has therefore played an important historical role in the development of many fundamental aspects of gas-phase heterogeneous catalysis at transition metal surfaces [13–16], and the techniques developed, primarily by Slichter and coworkers [17], can be readily adapted to electrochemical systems.

EC-NMR was pioneered by Wieckowski's group [18] at the University of Illinois at the beginning of 1990s and, as noted above, has its roots in metal NMR of oxide-supported metal catalysts. However, interfacing solid-state NMR with interfacial electrochemistry is somewhat

more challenging than the more standard “gas-phase” techniques because of the basic incompatibility between NMR detection and the conducting requirements for proper electrode function. That is, the presence of conducting material in the NMR-detection coil greatly degrades the so-called quality factor of the NMR probe, which substantially decreases sensitivity. Nevertheless, the potential advantages of interfacing *in situ* solid-state NMR with electrochemistry for investigating the electrochemical interface are many. For example: NMR gives a direct probe of the Fermi level local densities of states – for both adsorbate and substrate; structure and bonding in an electrochemical environment can be investigated using a variety of NMR interactions; surface dynamics can be readily probed; and, of course, the effects of potential control can be investigated in working electrochemical systems – even where the adsorbates (such as CN on Pt) would not be accessible in conventional “gas-phase” or dry systems. Furthermore, by using high magnetic fields and high-surface-area electrode materials, the current state-of-the-art signal-detection sensitivity is in fact quite reasonable, and permits the routine acquisition of NMR spectra of surface species. As an example, we show in Fig. 1  $^{13}\text{C}$  NMR spectra of  $^{13}\text{CO}$  chemisorbed onto a 10-nm Pt sample having a CO coverage of about 0.8, recorded at room temperature and in, respectively, Fig. 1(a), 14.1 and Fig. 1(b), 8.5 T magnetic fields. The numbers of scans were 1600 and 2000, and the signal-to-noise (S/N) ratios (after using a 1-kHz line broadening) were 50 and 10, respectively, showing a significant S/N enhancement in the higher magnetic field. Sensitivity is also greatly enhanced at lower temperatures at which  $^{13}\text{C}$  NMR spectra can now be recorded in as little as 10 min.

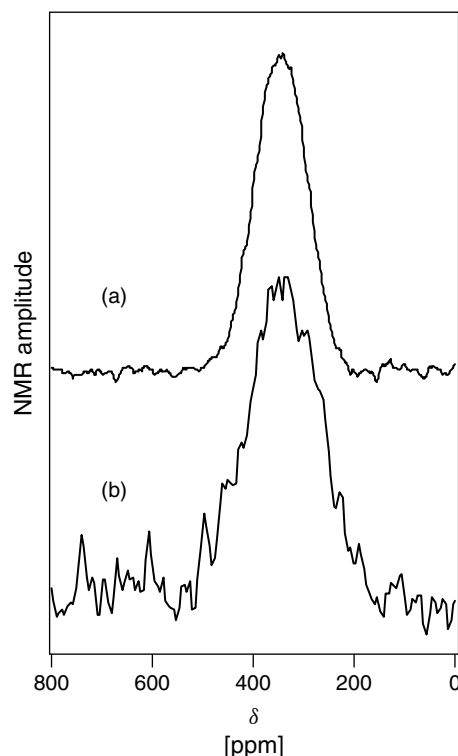
**Fig. 1**  $^{13}\text{C}$  NMR spectra of CO adsorbed on a 10-nm Pt electrocatalyst, recorded at room temperature and at (a) 14.1 T with 1600 scans and (b) 8.5 T with 2000 scans. The S/N ratios are ca. 50 and 10, respectively.

### 3.1.2

#### Principles of Solid-state Surface EC-NMR Spectroscopy

##### 3.1.2.1 Metal NMR Basics

In electrochemistry, electrodes are indispensable parts of an electrical circuit, so the EC-NMR of electrode surfaces in general has to deal with metallic systems. In NMR, in general, a specific resonance position (a frequency shift) with respect to a well-defined reference corresponds to a specific chemical environment (a structure) [12]. This shift is the chemical shift ( $\delta_{\text{CS}}$ ) in a molecule or the Knight shift ( $K$ ) [19] in a metal, and can be considered a fingerprint of the corresponding site or structure [20]. While the familiar chemical or orbital shift is ubiquitous, arising from the shielding of the external magnetic field at the nucleus by the otherwise quenched orbital angular momentum of the surrounding electrons, the Knight shift is metal-specific, being produced by nonzero magnetic interactions between nuclear and electronic spins since only electron spins at the Fermi energy can be polarized and thus create a nonzero spin density in an external magnetic field (the so-called Pauli paramagnetism). In addition, the Korringa relationship [21] (vide infra), which governs the nuclear spin–lattice relaxation in metals, is also metal-specific. Together, the Knight shift and the Korringa relation represent the two primary NMR probes of electronic structure in metals, and of surface molecular bonding in general.



Theoretically, the Hamiltonian of the nuclear–electron hyperfine interaction can be written for a nuclear spin  $I = 1/2$  as

$$H = \gamma_n \hbar I \mu_B \left\{ \frac{8\pi}{3} S(r) \delta(r) - \left[ \frac{S}{r^3} - \frac{3r(Sr)}{r^5} \right] - \frac{\ell}{r^3} \right\} \quad (1)$$

where  $\mu_B$  is the Bohr magneton and  $\gamma_n$  is the nuclear gyromagnetic ratio.  $I$ ,  $S$ , and  $\ell$  are the nuclear spin, electron spin, and electron orbital moments, respectively. The symbol  $r$  is the radius vector of an electron with respect to the nucleus at the origin. The first term in the brace in Eq. (1) is the Fermi contact term, the second (square bracket) is the dipole term, and the third ( $\ell/r^3$ ) is due to the orbital movement of electrons. In a diamagnetic molecule,

since all electron spins are paired up, the expectation values of the first and second terms become zero, leaving only the third term, which produces the usual so-called chemical or orbital shift,  $\delta_{CS}$ . In the case of a metal, the total line shift is the *sum* of the first term ( $K$ ) and the third term ( $\delta_{CS}$ ) in Eq. (1). In many cases,  $K$ , which arises from the hyperfine interaction of the observed nucleus with electron spins, dominates the purely chemical shift term,  $\delta_{CS}$ . The dipolar term normally contributes to relaxation, but not to the shift, since the trace of the operator is zero.

The Korringa relationship [21] indicates that  $1/T_1 \propto T$ , where  $T_1$  is the spin–lattice relaxation time and  $T$  is the absolute temperature of the sample. This unique temperature dependence of  $1/T_1$  is the NMR fingerprint of a metallic state. It results from the fact that only conduction electrons around the Fermi level can satisfy energy conservation for the electron–nuclear spin “flip-flop” relaxation process, and the fraction of these electrons is proportional to  $k_B T$ . When all relaxation mechanisms other than the first term in Eq. (1) can be neglected, and there are only  $s$ -like electrons at the Fermi level (such as in the alkali metals), the Korringa relationship takes its simplest form:

$$K^2 T_1 T = \left( \frac{\gamma_e}{\gamma_n} \right)^2 \left( \frac{h}{4\pi k_B} \right) = S \quad (2)$$

Here,  $\gamma_e$  and  $\gamma_n$  are the electronic and nuclear gyromagnetic ratios, respectively, and  $k_B$  is the Boltzmann constant. The Knight shift,  $K$ , also has a simple relationship with the electronic density of states at the Fermi level through the Pauli susceptibility,  $\chi_{\text{Pauli}}$ :

$$K = \chi_{\text{Pauli}} \frac{H_{\text{hf}}}{\mu_B} = \mu_B H_{\text{hf}} D(E_F) \quad (3)$$

where  $H_{\text{hf}}$  is the hyperfine field produced by an electron at the site of the nucleus, and  $D(E_F)$  is the (local) density of states at the Fermi level. Despite their simplicity, Eqs. (2 and 3) already give the simple physical picture that the NMR of metallic species can measure, in principle,  $D(E_F)$ . For systems having more than one band, which cuts the Fermi level, the deduction of multiple  $D(E_F)$ s becomes more involved, though the principles are the same. More specifically, for  $^{195}\text{Pt}$  [22] or chemisorbed  $^{13}\text{CO}$  [10], one can express the two primary metal NMR observables, the Knight shift  $K$  and the Korringa constant  $S(T_1 T)^{-1}$ , in terms of  $D(E_F)$ s. This is the so-called two-band model, the bands corresponding to metal  $s$  and  $d$  bands or to ligand ( $^{13}\text{CO}$ )  $5\sigma$  and  $2\pi^*$  bands. By experimentally measuring  $K$  and  $S(T_1 T)^{-1}$  (for the metal or ligand) and by solving two equations for two unknowns,  $s$  ( $5\sigma$ )- and  $d$  ( $2\pi^*$ )- $D(E_F)$  can be deduced. For more details, the reader is referred to Refs. [10, 20, 22].

It is important to note that many metallic properties, such as the Knight shift and the Korringa relationship, are determined by the finite and quasi-continuous nature of the Fermi level local density of states ( $E_F$ -LDOS). In the approximation most familiar to chemists, what this means is that the highest occupied molecular orbital–lowest unoccupied molecular orbital (HOMO–LUMO) gap in metals is much smaller than the thermal energy  $k_B T$ , and the value of the  $E_F$ -LDOS reflects the frontier orbital contributions in a metallic system [23]. The  $E_F$ -LDOS also represents a crucial metal surface attribute that can serve as an important conceptual bridge between the delocalized band structure (physics) picture and the localized chemical bonding (chemical) picture of metal–adsorbate interactions.

In addition to the determination of the chemical and/or Knight shift and the spin–lattice relaxation time in the laboratory frame ( $T_1$ ), there is another important NMR observable – the spin–spin relaxation time ( $T_2$ ). While the chemical and/or Knight shift contains essentially static structural information, the temperature and/or magnetic field dependence of the relaxation times, both  $T_1$  and  $T_2$ , are related to the dynamics of the observed nucleus.  $T_1$  measures the rate at which the spin system returns to thermal equilibrium with its environment (the lattice) after a perturbation, while  $T_2$  measures the rate of achieving a common spin temperature within the spin system. Both  $T_1$  and  $T_2$  provide exceptionally important information on motions, and can cover the timescale from  $\sim 10^{-9}$  to  $10^2$  s. Moreover, the temperature dependence of these motions provides important thermodynamic information in the form of activation energies for ligand motion on the catalyst surface.

### 3.1.2.2 EC-NMR Instrumentation

Two types of EC-NMR experiments have been carried out: electrode potential–dependent studies of an adsorbate ( $^{13}\text{CO}$ ,  $^{13}\text{CN}$ ) at room temperature [6, 8, 24], and temperature-dependent studies of an adsorbate [5, 10] and of platinum electrocatalysts [7, 25], down 10 K. For all of the EC-NMR measurements, the electrode materials, either polycrystalline platinum black or carbon-supported commercial fuel cell grade platinum electrodes, were immersed in a supporting electrolyte, typically 0.5 M  $\text{H}_2\text{SO}_4$ . For temperature-dependence studies, EC-NMR samples are prepared in a conventional three-electrode flow cell with oxygen-free  $\text{N}_2$  or Ar as a protecting gas, then together with supporting electrolyte and under the protection of

oxygen-free  $\text{N}_2$  or Ar, are transferred into a precleaned glass ampoule and flame-sealed. The potential drift of a sample in a conventional three-electrode cell, in an oxygen-free environment, is only a few millivolts over 12 h. The same observation holds after transferring the electrode material from the NMR ampoule back into the cell. These observations suggest that the surface potential does not change significantly once a sample is sealed (and does not change at all when the sample is frozen).

For room temperature electrode potential–dependence studies, we have incorporated an electrochemical cell inside the NMR probe [6]. This permits running NMR measurements while an (variable) external electrode potential is applied. Figure 2 shows a picture of a real EC-NMR probe as well as a schematic diagram of the setup. The working electrode material was loosely packed in the cell that was placed inside an NMR coil and electrical connection to an external circuit (potentiostat) made by inserting a Pt wire into the sample. (A very similar setup has also been developed by the Lausanne group [8, 24].) Our cell design permits both electrochemical sample preparation and characterization (voltammetry) and NMR data acquisition under active potential control, avoiding sample transfer from the preparative electrochemical cell. A very important technical issue here is that while the potentiostat is on, there is considerable “noise” injected into the NMR probe, since the potentiostat leads act as excellent “antennas” right inside the NMR coil! This noise has to be removed by using extensive electronic filtering of the electrochemical leads entering the probe, in order to eliminate extensive radio frequency (rf) pickup. The low-pass filter circuit elements  $L_{\text{counter}}C_{\text{counter}}$ ,  $L_{\text{ref}}C_{\text{ref}}$ , and  $L_{\text{wk}}C_{\text{wk}}$ .

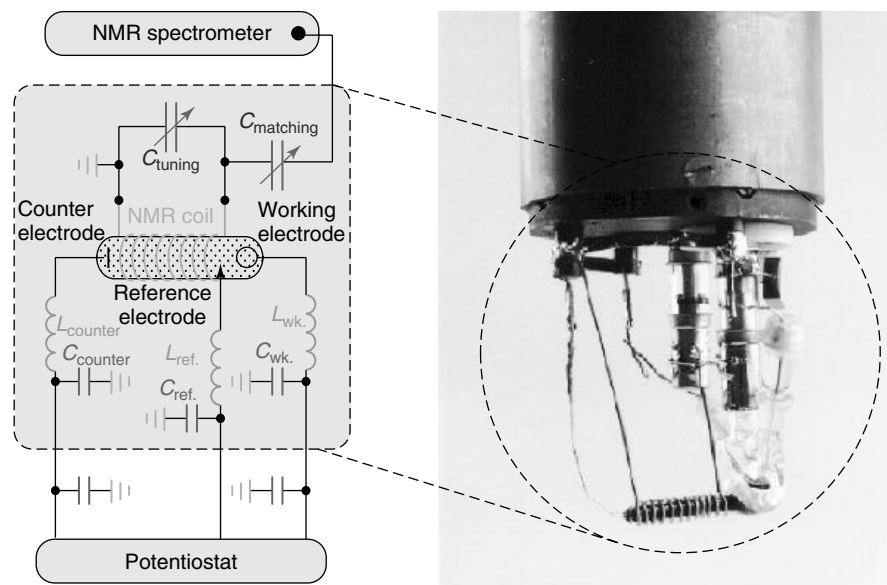


**Fig. 2** Schematic diagram (left) and picture (right) of an EC-NMR probe and its circuitry, showing the interface between NMR and electrochemistry.

in Fig. 2 were designed for this purpose, plus they serve a second purpose of acting as a high impedance to the rf pulses from the NMR spectrometer. These are typically  $\sim 1$  kW and may be incompatible with long potentiostat life.

Figure 3 shows another type of setup for an EC-NMR cell, developed by the Berkeley group to investigate  $^{13}\text{CO}$  adsorption from the gas phase onto a carbon-supported platinum electrocatalyst [26, 27]. In this system, a platinum electrocatalyst was pressed into a graphitized carbon cloth that was then cut into pieces and stacked into a cylindrical form that fits snugly into the cell's compartment. In order to reduce degradation in the quality factor of the NMR coil due to the presence of bulk electronic or ionic conductivity, the electrode layers were also alternately sandwiched with nonconductive fiberglass cloth. All the electrode layers were individually stitched with gold wire and

were then connected to each other and to the external potentiostat. Cyclic voltammograms of high quality are obtained by both types of EC-NMR cell.

### 3.1.3

#### Applications of Solid-state Surface EC-NMR Spectroscopy

##### 3.1.3.1 $^{195}\text{Pt}$ NMR of Carbon-supported Electrocatalysts and a Potential-scan-generated Sintering Effect

At the beginning of the 1980s, Slichter and coworkers discovered several unique features of the  $^{195}\text{Pt}$  NMR of oxide-supported small platinum particles [28]. They found that the overall  $^{195}\text{Pt}$  NMR lineshape was extremely broad, extending downfield some 4 kG from the position of bulk platinum ( $1.138 \text{ G kHz}^{-1}$ ), and contained a feature on the low-field side ( $1.089 \text{ G kHz}^{-1}$ ), which arose from the oxidized Pt surface atoms. Later on, van



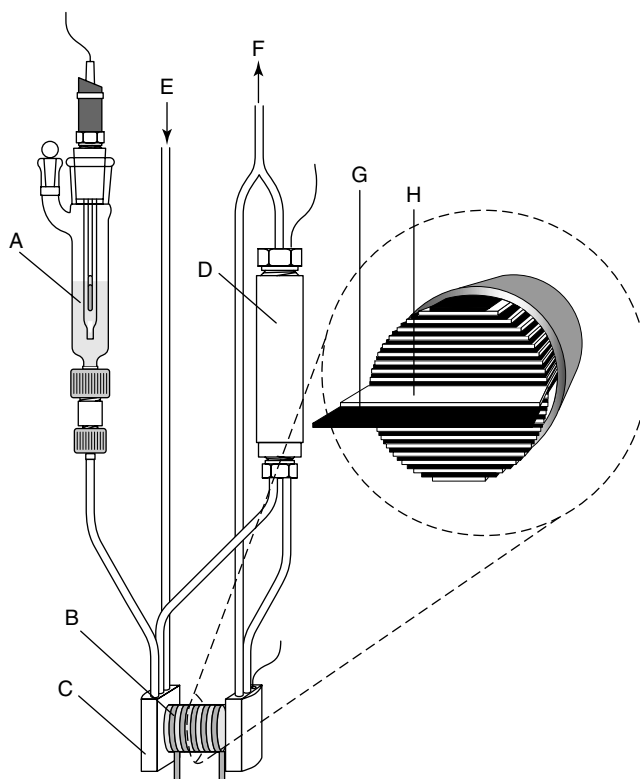


**Fig. 3** Schematic representation of the EC-NMR probe cell developed by the Berkeley group [27]: (A) reference electrode compartment; (B) NMR coil; (C) working electrode compartment; (D) counterelectrode compartment; (E) electrolyte inlet; (F) electrolyte outlet; (G) carbon-supported Pt electrocatalysts; and (H) fiberglass separator. (Reproduced with permission from Ref. [27], Copyright by © 2001 Electrochemical Society.)

der Klink and coworkers confirmed these observations, finding that the signal from clean-surface Pt atoms was centered at  $1.100 \text{ G kHz}^{-1}$  [29], a position clearly very different to the  $1.138 \text{ G kHz}^{-1}$  bulk position (the frequency difference is magnetic field dependent and is about 2.5 MHz in a field of 8.5 T). Ab initio theoretical calculations on a five-layer Pt (001) cluster [40] then demonstrated that the surface shift must be due to a gradual drop in the d-like Fermi level LDOS on moving from the inside of the particle to the surface. It

is this distinguishable surface signal that makes  $^{195}\text{Pt}$  NMR unique in investigating the surface physics and chemistry of nanoscale platinum particles.

We have observed that carbon-supported nanoscale platinum electrodes retain quite closely the  $^{195}\text{Pt}$  NMR spectral characteristics of isolated small platinum particles supported on oxides [4, 7, 25, 30], with the clean-surface platinum atoms also resonating at  $1.100 \text{ G kHz}^{-1}$  with respect to the value for bulk atoms,  $1.138 \text{ G kHz}^{-1}$ . We show in Fig. 4(a–c),  $^{195}\text{Pt}$  NMR spectra

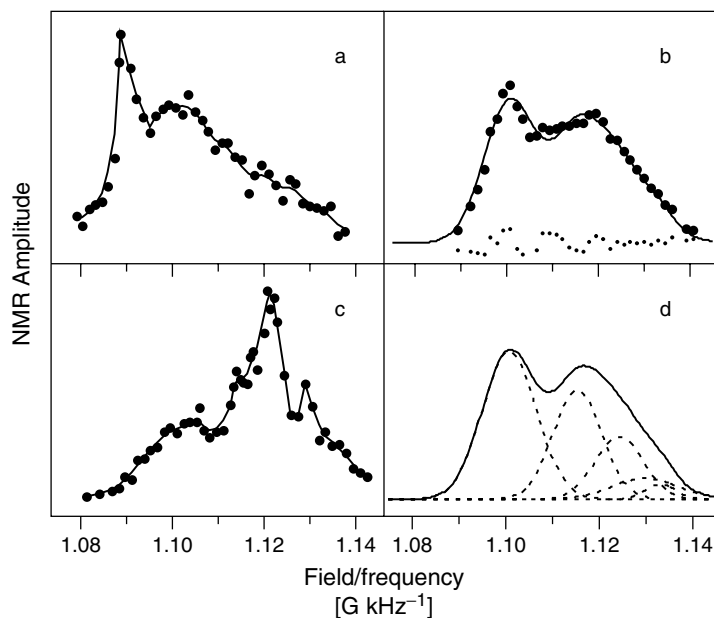


**Fig. 4** Typical point-by-point  $^{195}\text{Pt}$  NMR spectra showing electrochemical cleaning, sintering by potential cycling, and a layer-model analysis of the 2.5-nm sample: (a) as-received catalyst; (b) electrochemically cleaned in 0.5 M  $\text{H}_2\text{SO}_4$  by holding electrode potential at 0.45 V versus reversible hydrogen electrode (RHE); (c) cleaned by extensive potential cycling; and (d) layer-model deconvolution of spectrum (b). The solid line in (b) is the result of the simulation.

of a 2.5 nm carbon-supported commercial Pt electrocatalyst after different surface treatments. Figure 4(a) shows the spectrum of an as-received sample, while Fig. 4(b) shows a sample that has been electrochemically cleaned by holding the electrode potential within the electrochemical double-layer region with no potential cycling until the reduction current could no longer be measured. Figure 4(c) shows the spectrum obtained after extensive potential cycling (which is still widely used to clean electrode surfaces), and in which there are clearly discernable spectral differences, as discussed below.

In order to further analyze these results, we use a layer-model [31] (vide infra) deconvolution of the lineshape, and results

for the clean-surface spectrum (Fig. 4b) are shown in Fig. 4(d). The NMR layer model assumes that the nanoscale platinum particles can be represented by ideal cubo-octahedral particles built up layer-by-layer from a central atom, that NMR signals from atoms within a given layer can be approximated by a Gaussian, and that the average Knight shift of the  $n$ th layer,  $K_n$ , which is the center of the corresponding Gaussian, “heals” back exponentially towards the bulk platinum position when moving inwards. That is,

$$K_n = K_\infty + (K_0 - K_\infty) \exp\left(\frac{-n}{m}\right) \quad (4)$$

where  $n$  is the layer number, counting inwards from the surface layer (where

$n = 0$ ),  $m$  is the characteristic number (of layers) defining the “healing length” for the Knight shift, and  $K_0$  and  $K_\infty$  ( $= 3.34\%$ ) are the Knight shifts of the surface layer and the bulk, respectively. The relative contribution of each Gaussian is dictated by the fraction of the atoms within the corresponding layer, which can be determined from the size distribution of the sample. The healing length, defined as  $m$  times the distance between two consecutive layers (0.229 nm for Pt), is 0.46 nm ( $\cong 2$  Pt layers) from the deconvolution shown in Fig. 4(d). In addition, the shape of a  $^{195}\text{Pt}$  NMR spectrum conveys information on the size of the electrocatalyst. That is, the stronger is the surface peak, the higher is the dispersion, or the smaller is the particle size.

The surfaces of the as-received materials are covered by O and/or OH species, as indicated by the peak at  $1.098 \text{ G kHz}^{-1}$ . Remarkably, these surfaces were effectively cleaned simply by holding the electrode potential within the electrochemical double-layer region. This mild surface-reduction procedure should be contrasted to the rigorous and often technically demanding methods employed at the solid–gas interface, which usually involve several cycles of high-temperature calcination and reduction, limiting the choice of catalyst support to, typically, non-conductive oxides such as alumina, titania, and silica.

However, extensive potential cycling, which is a widely used in electrode-surface cleaning procedure, sinters the nanoscale electrocatalyst. Although the sample in Fig. 4(c) started with the same as-received electrocatalyst as that shown in Fig. 4(b), the dispersion estimated from the corresponding  $^{195}\text{Pt}$  NMR spectrum is only about 27% [30], far lower than the 50% obtained from Fig. 4(b). This dispersion

lowering provides clear evidence for sintering produced by potential cycling, an effect that clearly needs to be borne in mind when analyzing the results of both ligand and metal EC-NMR experiments.

### 3.1.3.2 Correlation between the Knight Shift of a Platinum Surface and the Electronegativity of the Adsorbate

Understanding how adsorbates modify the chemical and physical properties of metal surfaces has long been one of the central themes of surface science, and is of importance in relation to the ability to scientifically engineer metal surface properties for targeted applications, such as enhancing the CO tolerance of electrocatalysts used in fuel cells, or more generally in promoting metal surface catalysis. As demonstrated in Sect. 3.1.3.1, interfacial electrochemistry offers an elegant way to modify electrode surfaces while  $^{195}\text{Pt}$  NMR provides a powerful probe to follow the variations in the physical properties of metal surfaces caused by such modifications. By using this strategy, the influence of a series of different ligands (H, O, S,  $\text{CN}^-$ , CO, and Ru), electrochemically adsorbed onto carbon-supported nanoscale Pt particles from the same starting batch, has been investigated by  $^{195}\text{Pt}$  NMR, in an electrochemical environment [10].

The starting electrode material used for this series of experiments was the same as that used in the previous section. As shown there, the frequency difference between the resonance positions of surface and bulk platinum atoms at 8.5 T is about 2.5 MHz, large enough to provide a very convenient spectral visualization of how deep the influence of an adsorbate can go, as illustrated by the point-by-point  $^{195}\text{Pt}$  NMR spectra (recorded at 80 K) presented in Fig. 5. These spectra are normalized by equalizing their amplitudes

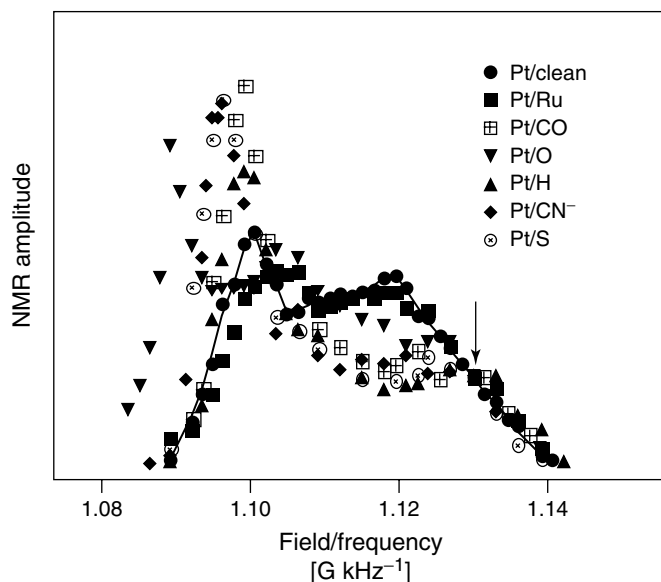


**Fig. 5** Superimposition of point-by-point, 8.47 T  $^{195}\text{Pt}$  NMR spectra of a 2.5 nm, carbon-supported Pt electrocatalyst without and with different chemisorbed ligand: Ru, CO, O, H,  $\text{CN}^-$ , and S. The spectra were normalized by equalizing the amplitude at  $1.131 \text{ G kHz}^{-1}$  (indicated by the arrow). The invariance of signals beyond  $1.131 \text{ G kHz}^{-1}$  provides experimental confirmation of the Friedel–Heine invariance theorem. The surface peaks range over  $\sim 11\,000 \text{ ppm}$ . (Reproduced with permission from Ref. [10], Copyright by © 2000 American Chemical Society.)

at  $1.131 \text{ G kHz}^{-1}$ , which is indicated by the arrow. The interesting observation here is that the position of the high-field signal intensity (above  $1.131 \text{ G kHz}^{-1}$ ), which is due to Pt atoms within the three innermost layers, is independent of adsorbate type. This independence provides direct experimental evidence for the validity of the Friedel–Heine invariance theorem [32, 33], which states that the integral electronic properties at an atom, such as its LDOS, are determined primarily by the surrounding medium, within a few electronic wavelengths. This is exactly what is observed – although the chemical identity of the adsorbates is quite varied, their influences, to a very

good approximation, do not go beyond their next-nearest neighbors. That is, the high-field signals are invariant towards “boundary” changes.

In complete contrast to the Friedel–Heine invariance of the electronic properties observed for the innermost platinum particle layers, the surface and subsurface NMR signals undergo major frequency shifts as different chemical species are adsorbed, as can be seen in Fig. 5. The NMR layer-model spectral deconvolution [31] technique was applied to these spectra in order to obtain the variations in the surface and subsurface Knight shifts. Because of the Friedel–Heine invariance, the NMR parameters (peak

position, width, relative intensity) for the three central layers were fixed to the clean-surface values, while the surface and subsurface peak positions were allowed to vary. For Pt/O, the position of the third layer was also varied, as a result of the long healing length in this system, plus the surface peak areas were also varied in some simulations, as a result of saturation effects caused by longer  $T_1$  values. The results of these simulations are shown in Fig. 6 and the surface and subsurface peak shift values obtained are plotted in Fig. 7 as a function of the Allred–Rochow electronegativity (defined as the electrostatic force exerted by the nucleus of the atom on its valence electrons) of the bonded adsorbate atom. Remarkably, both the surface and subsurface peak positions map almost linearly the electronegativity of the adsorbate. The reasons for this are as follows:

According to the layer model, Eq. (4), one has  $K_1 = K_\infty + (K_0 - K_\infty) \exp(-1/m)$  for the subsurface layer,  $n = 1$ . A simple mathematical conversion gives  $m =$

$1/\ln[(K_0 - K_\infty)/(K_1 - K_\infty)]$ . By replacing  $K_1$  and  $K_0$  by the correlation lines shown in Fig. 7,

$$K_0(\text{ppm}) = (-10.2 + 5.3\chi) \times 10^3 \quad (5)$$

$$K_1(\text{ppm}) = (-21.5 + 5.8\chi) \times 10^3 \quad (6)$$

$m$  (the healing length) can then be directly expressed as a function of the electronegativity  $\chi$ :

$$m = \frac{1}{\ln \left[ \frac{(23.2 + 5.3\chi)}{(11.9 + 5.8\chi)} \right]} \quad (7)$$

In Fig. 8, the healing length ( $= 0.229 m$ , where 0.229 nm is the layer thickness for Pt particles) is plotted as a function of the electronegativity, Eq. (7). This result shows that the larger the electronegativity of the adsorbate, the longer the healing length, that is, the deeper the influence of the adsorbate goes. It is also interesting to note that the value of the healing length  $m$  for hydrogen ( $\chi = 2.2$ ) adsorption obtained via Eq. (7) is about 2.9, which is very close to the  $m = 2.6$  value found

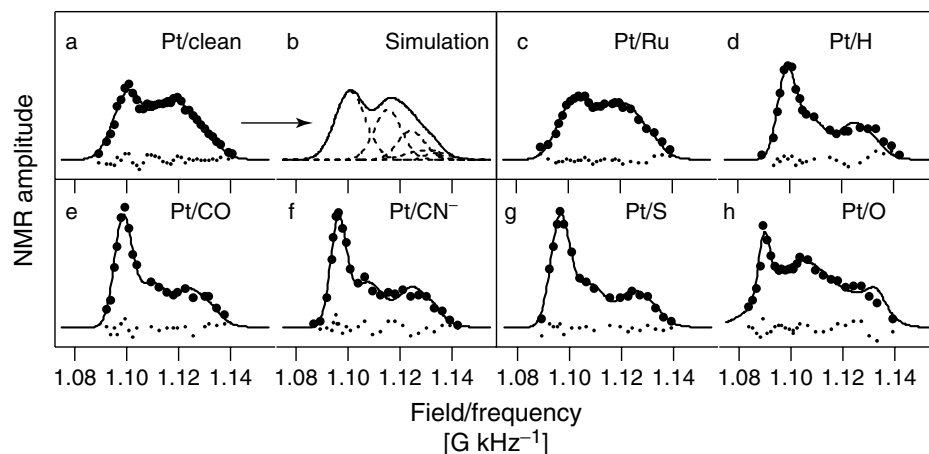


**Fig. 6** The NMR layer-model simulations of the  $^{195}\text{Pt}$  spectra shown in Fig. 5 and the small dots are the variances between the experimental and fitted values. (a) clean-surface Pt; (b) Simulation of (a); (c) Pt with adsorbed Ru; (d) Pt with

adsorbed H; (e) Pt with adsorbed CO; (f) Pt with adsorbed cyanide; (g) Pt with adsorbed S (from  $\text{Na}_2\text{S}$  solution); (h) Pt with adsorbed O. (Reproduced with permission from Ref. [10], Copyright by American Chemical Society 2000.)

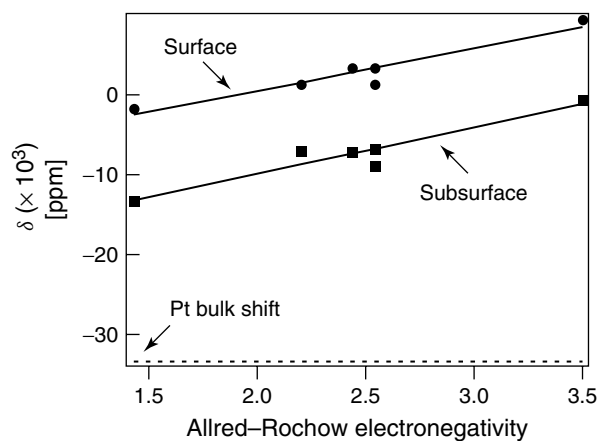


**Fig. 7** Correlation between surface/subsurface frequency shifts (with respect to the Pt NMR reference  $\text{H}_2\text{PtCl}_6$ ) and the Allred-Rochow electronegativity. The dashed horizontal line indicates the Knight shift of bulk platinum atoms. The solid straight lines are linear fits to the surface and subsurface shifts as a function of the electronegativity. Both have  $R^2$  values of ca. 0.92. (Reproduced with permission from Ref. [10], Copyright by American Chemical Society 2000.)

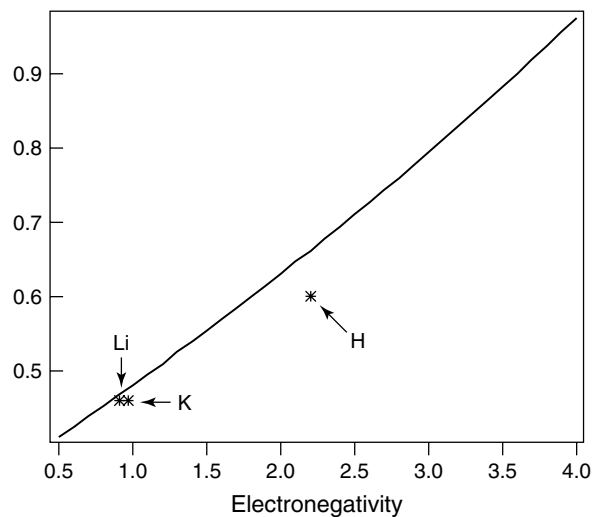


**Fig. 8** Solid curve showing the relationship between the healing length and electronegativity as determined from Eq. (7). For comparison, we also show the three experimental points based on previous observations. See the text for details. (Reproduced with permission from Ref. [10], © Copyright by American Chemical Society 2000.)

by a detailed layer-model analysis [31]. In addition, for the adsorption of the alkali metal elements ( $\chi \sim 1$ ), Eq. (7) predicts  $m \sim 2$ , virtually the same  $m$  as obtained for clean-surface Pt particles in an electrochemical environment. One would, therefore, expect that alkali adsorption would not significantly change the  $^{195}\text{Pt}$  NMR spectrum of small Pt particles after adsorption. This is exactly what has been observed experimentally (in a gas-phase system) [34]. For comparison, these three experimentally estimated points are also plotted in Fig. 8.

The invariance of the frequency shifts of the more buried (deeper than the third layer) Pt atoms to surface adsorbate electronegativity provides strong evidence demonstrating the applicability of Friedel–Heine invariance of the  $E_F$ -LDOS in these nanoscale electrocatalyst systems. This is a rather interesting extension of the original Friedel–Heine invariance theorem to nanoscale systems and may have utility in describing the electronic surface structure of metal catalysts in different chemical environments. These results may also be expected to lead to useful general correlations between electronic properties and more conventional chemical descriptors (such as ligand electronegativity), which could be helpful in understanding the electronic structure of metal–adsorbate interfaces by providing guidelines for engineering new electrode surfaces.

### 3.1.3.3 Correlation between the Clean-surface $E_F$ -LDOS of Metals and the Knight Shift of Adsorbates

Because NMR has elemental specificity and is also nondestructive, it offers unique opportunities for investigating electrochemical problems from both sides of the electrochemical interface. This strategy

has been applied to investigate the metal–CO interactions in a number of recent studies [25].

The discussions in the two previous sections demonstrate that there is an unambiguous NMR discrimination between the surface peak (at  $1.100 \text{ G kHz}^{-1}$  for nanoscale platinum particles) and the rest of the platinum sites. By carrying out detailed temperature-dependent  $T_1$  relaxation measurements on a given Pt sample, a value for  $S(T_1 T)^{-1}$  can be obtained, and by using the two-band model (see Sect. 3.1.2.1), a pair of surface Pt  $s$ - and  $d$ - $D(E_F)$ s can therefore be deduced. Similarly,  $S(T_1 T)^{-1}$  and  $K$  measurements on  $^{13}\text{C}$  adsorbed onto the metal surfaces can give the corresponding  $^{13}\text{C}$   $5\sigma$  and  $2\pi^*$  ( $E_F$ )s (see Sect. 3.1.3.4).

It is of fundamental interest to see if there exists any type of correlation between the clean-surface  $E_F$ -LDOS of the metal and the  $^{13}\text{C}$  Knight shift of the chemisorbed CO. The former is an important surface attribute defining the ability of the metal surface to donate (to act as a HOMO) as well as to accept (to act as a LUMO) electrons, while the latter measures, at least to a certain extent, the degree of metallization of chemisorbed CO (see Sect. 3.1.3.4). We show in Table 1, a set of data for atop CO on Pt and Pd, shown graphically in Fig. 9. The purely orbital contributions (chemical shifts) for atop CO on Pt and on Pd were calculated by using density functional theory (DFT) calculations on model  $\text{COPt}_7$  and  $\text{COPd}_7$  clusters in which CO sits atop the central metal atom, which is coordinated by the remaining six metal atoms. For  $\text{COPt}_7$ , a value of  $160 \pm 20 \text{ ppm}$  from tetramethylsilane (TMS) was obtained, while for  $\text{COPd}_7$ , the value was  $203 \pm 20 \text{ ppm}$ . These calculated values are in good agreement with available experimental data

**Tab. 1** Correlation between clean-surface  $E_F$ -LDOS and  $^{13}\text{C}$  shift of chemisorbed CO [25]. The Knight shift = total shift – chemical shift

Sample	Clean-surface $E_F$ -LDOS ( $\text{Ry}^{-1} \text{atom}^{-1}$ )	Total $^{13}\text{C}$ shift of $\text{CO}_{\text{chemisorbed}}$ (ppm w.r.t TMS)
$\text{PtCO}_7$	0	160
CO–Pt/oxides (dry)	14.8	330
CO–Pt/carbon (wet)	17.7 <sup>a</sup>	351 <sup>a</sup>
CO–Pt/carbon (wet)	18.6	383
$\text{PdCO}_7$	0	203
CO–Pd/oxides (dry)	24	500

<sup>a</sup>For an 8.8-nm sample.

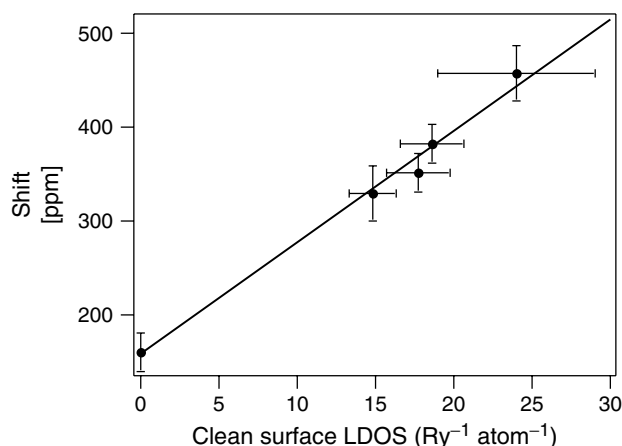


**Fig. 9** Correlation between the Fermi level total electronic densities of states at transition metal (Pt and Pd) surfaces (in  $\text{Ry}^{-1} \text{atom}^{-1}$ ) and the corresponding  $^{13}\text{C}$  Knight shift of chemisorbed CO. (Partially reproduced with permission from Ref. [25], © Copyright by American Chemical Society.)

while the standard deviations account for uncertainties caused by the use of different functionals and basis sets. The clean-surface  $E_F$ -LDOS for Pd was estimated on the basis of the changes in magnetic susceptibility of small Pd particles with respect to their bulk value, by application of the exponential healing model.

As shown in Fig. 9, the  $^{13}\text{C}$  NMR shift of CO responds linearly to the

clean-surface  $E_F$ -LDOS before adsorption. The straight line is a linear fit to the data, giving a slope of  $12 \text{ ppm/Ry}^{-1} \text{atom}^{-1}$ . This linear relationship can be readily related to the frontier orbital interpretation of the Blyholder model [35] – a higher clean-surface  $E_F$ -LDOS means more metal electrons and holes are available to engage in  $5\sigma$ -forward and  $2\pi^*$ -back donation. As the  $E_F$ -LDOS increases, CO becomes more metallic, which results in a larger



Knight shift. A correlation very similar in nature to this has also been found to exist in the “gas phase”, in which the C–O vibrational stretch frequency (after chemisorption) was shown to correlate linearly with the Pt clean-surface  $E_F$ -LDOS before chemisorption [36]. The higher the surface  $E_F$ -LDOS, the lower the C–O stretching frequency.

The linear relationship shown in Fig. 9 is important because it demonstrates the validity of the frontier orbital interaction picture of metal surface chemistry, in which the importance of the clean-surface  $E_F$ -LDOS is highlighted. In addition, it puts  $^{13}\text{C}$  NMR spectroscopy of chemisorbed CO on a firmer footing, by probing the electronic properties of transition metal surfaces *before* CO chemisorption.

### 3.1.3.4 Coupling EC-NMR with In Situ Infrared Spectroelectrochemistry

It is now clear that CO acquires metallic properties upon adsorption onto transition metal surfaces, as indicated by the presence of a Knight shift and a Korringa relationship, measured via  $^{13}\text{C}$  NMR. Furthermore, by using the experimentally measured  $^{13}\text{C}$  Knight shift and the Korringa constant, a phenomenological two-band model [10] permits a quantitative partitioning between the  $5\sigma$ - and  $2\pi^*$ - $D(E_F)$  at  $^{13}\text{C}$  to be obtained, providing insight into metal–CO bonding at the electronic level. These types of  $^{13}\text{C}$  NMR study have been carried out on  $^{13}\text{CO}$  chemisorbed (ex MeOH) onto a series of carbon-supported, fuel cell grade, commercial platinum electrocatalysts having different average particle size: 2.0, 2.5, 3.2, 3.9, and 8.8 nm, in which both metal and adsorption  $E_F$ -LDOS might be expected to vary with particle size. Shown

in Fig. 10 is a typical  $^{13}\text{C}$  NMR spectrum and temperature-dependent  $T_1$  data for the 8.8-nm sample [10]. The straight line through the origin is characteristic of the Korringa relationship, indicating the metallic state of adsorbed CO in this electrocatalyst system.

Table 2 collects all of the  $^{13}\text{C}$  NMR results together with values of the  $5\sigma$ - and  $2\pi^*$ - $D(E_F)$  deduced from these results, in addition to the corresponding infrared data [37] (*vide infra*). The results shown in Table 2 indicate that the major part of the total  $E_F$ -LDOS at  $^{13}\text{C}$  is from the  $2\pi^*$ -like electrons, with  $2\pi^*$ - $D(E_F)$  being about 10 times larger than the  $5\sigma - D(E_F)$ . These values are in good agreement with theoretical band structure calculations. The contribution to the spin–lattice relaxation rate ( $1/T_1$ ) is dominated by orbital and dipolar interactions, consistent with the dominance of  $\pi$ -like electrons at the Fermi level. Notice that while  $5\sigma - D(E_F)$  is almost a constant, the  $2\pi^*$ - $D(E_F)$  varies noticeably from sample to sample. However, since NMR only measures the electron density at a given energy level, that is, the Fermi level, it does not provide complete information about the total electron densities for forward-

**Tab. 2** The  $5\sigma$ - and  $2\pi^*$ - $D(E_F)$ s deduced by the two-band model from  $^{13}\text{C}$  NMR data of CO chemisorbed on Pt electrocatalysts [10] and the corresponding SNIFTIRS C–O vibrational stretching frequencies [37]

Size (nm)	$5\sigma$ - $D(E_F)$ (Ry molecule) $^{-1}$	$2\pi^*$ - $D(E_F)$ (Ry molecule) $^{-1}$	IR frequency (cm) $^{-1}$
8.8	0.6	6.4	2044
3.9	0.6	6.6	2043
3.2	0.6	6.5	2044
2.5	0.7	6.8	2038
2.0	0.6	7.3	2028

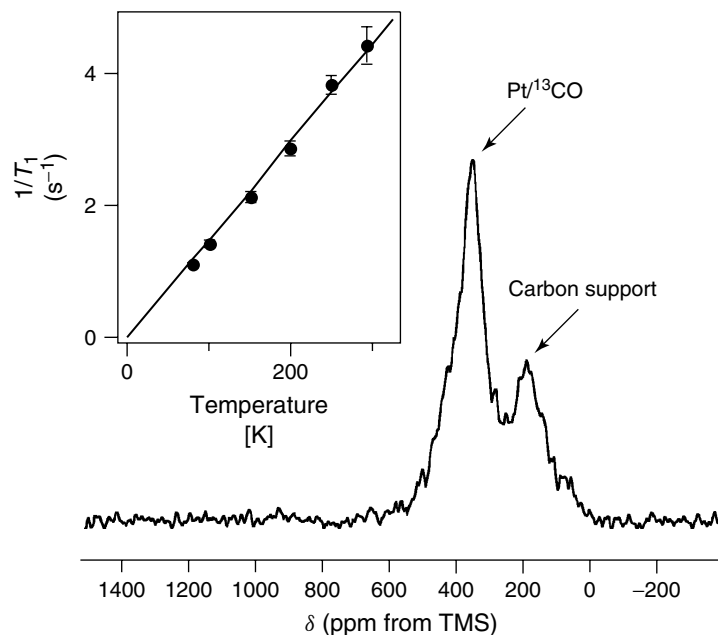


**Fig. 10** A typical  $^{13}\text{C}$  NMR spectrum and temperature-dependent  $T_1$  data for an 8.8-nm Pt/C sample. The straight line through the origin is characteristic of the Korringa relationship, indicating the metallic state of adsorbed CO in this electrocatalyst system. (Adapted from Ref. [10].)

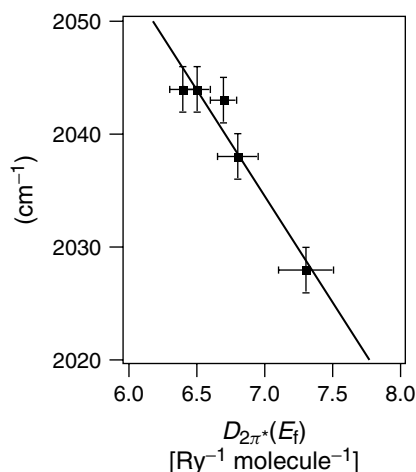
and backdonation, which are the integrals of the LDOS from the bottom of the conduction band to the Fermi level. Nevertheless, as can be seen in Table 2, the variation in the total  $E_F$ -LDOS between different samples are mainly due to changes in the  $2\pi^*-D(E_F)$ . This suggests that the changes in chemical properties of adsorbed CO are mainly determined by variations in backbonding. In particular, if the Fermi level cuts the tail of the  $2\pi^*$  band as it rises, then the increase in the  $2\pi^*-D(E_F)$  would indicate an enhancement in backdonation, and a decrease in the corresponding vibrational C–O stretch frequency.

In situ subtractively normalized interfacial Fourier transform infrared reflectance spectroelectrochemistry (SNIFTIRS) studies confirm this prediction [37]. They also

yield a linear correlation between  $\nu_{\text{CO}}$  and the  $2\pi^*-D(E_F)$ , Table 2, with a slope of  $-19 \pm 2 \text{ cm}^{-1}/(\text{Ry molecule})^{-1}$  and an intercept of  $2167 \pm 20 \text{ cm}^{-1}$ , as shown in Fig. 11. The latter value is quite close to the value expected for free CO,  $\nu = 2143 \text{ cm}^{-1}$ . On the basis of these results, the following overall physical picture of carbon monoxide adsorbed onto a platinum electrode can be proposed: Since the  $5\sigma$  orbital of CO is essentially nonbonding, with the lone pair concentrated on carbon and the  $2\pi^*$  orbital is a much less polarized antibonding orbital, the change in CO stretch frequency is mainly governed by changes in  $2\pi^*$  backdonation: the higher the backdonation, the lower the CO stretch frequency.

The above example demonstrates the complementary nature of in situ infrared

**Fig. 11** Correlations between  $\nu_{\text{CO}}$  and  $2\pi^*D(E_F)$ . The straight line is the linear fit that gives a slope of  $-19 \text{ cm}^{-1}/\text{Ry}^{-1} \text{ molecule}^{-1}$  and an intercept of  $2167 \text{ cm}^{-1}$ , with a  $R^2 = 0.98$ . (Part of the results shown in this figure has been published in Refs. [10, 37].)



spectroscopy and solid-state NMR, in providing insights into the details of surface chemistry of electro-chemisorbed CO on platinum. While SNIFTIRS – a major research technique of the interfacial electrochemical community – provides important qualitative information regarding the bond strengths of adsorbed CO, it offers somewhat less insight into the electronic relocations that occur within the bond, the electron distribution as a function of sample composition and morphological detail. For instance, how the bond changes as a function of particle size is difficult to learn using infrared alone. However, a  $^{13}\text{C}$  NMR analysis of the  $5\sigma$ - and  $2\pi^*$ - $E_F$ -LDOS at the carbon atom offers a quantitative description of metal–CO bonding in terms of changes in the  $E_F$ -LDOS. The joint SNIFTIRS/NMR approach provides new information on the electronic structure of the metal–solution interface, which is relevant to the characterization of industrial fuel cell catalysts, as well as other interfacial electrochemical systems of practical importance, by combining bond strength (IR) and quantitative  $E_F$ -LDOS results (NMR).

### 3.1.3.5 Surface Diffusion

The rationale behind using NMR to study surface diffusion is that the correlation time for diffusion,  $\tau$ , can be related to the temperature dependence of the NMR relaxation rates observed for diffusing atoms or molecules [12]. Under certain circumstances, such a relation can be expressed analytically, permitting a quantitative analysis of the data in dynamic and thermodynamic terms.

When using the temperature dependence of the nuclear spin–spin or nuclear spin–lattice relaxation rate to study molecular motion, as is the case with the surface diffusion we are dealing with here, there exist so-called “strong” and “weak” collision limits. Different mathematical relationships are needed to describe these limits. Consider the nuclear spin–spin relaxation rate ( $1/T_2$ ) as measured by a conventional Hahn-echo pulse sequence, and suppose that  $\Delta\omega$  is the amplitude of the local field fluctuation responsible for relaxation. Also assume that  $\tau$  is the correlation time for the motion, say a jump, which causes the local field to fluctuate. The strong collision limit is defined such that

$\tau \gg 1/\Delta\omega$ . At  $t = 0$ , that is, just after the first  $\pi/2$  pulse, which flips all nuclear spins into the  $xy$  plane, all spins are in phase, and they retain their phase memory until  $t = \tau$ , when the collision changes the direction of the local field. Since  $\tau$  is sufficiently long to dephase the spins, they lose all phase memory before the next collision. Therefore,  $1/T_2 = 1/\tau$ . In contrast, in the weak collision limit,  $\tau \ll 1/\Delta\omega$ . Since  $\tau$  is relatively short, insufficient dephasing builds up between two consecutive jumps. When the spin jumps randomly, many jumps are needed in order to accumulate sufficient dephasing, and one has  $1/T_2 = (\Delta\omega)^2\tau$ . In summary then, we have for these two limiting cases:

$$\frac{1}{T_2} = \frac{1}{\tau} \text{ for } \tau \gg \frac{1}{\Delta\omega} \quad (8)$$

and

$$\frac{1}{T_2} = (\Delta\omega)^2\tau \text{ for } \tau \ll \frac{1}{\Delta\omega} \quad (9)$$

Fortunately, the function

$$\frac{1}{T_2} = \frac{(\Delta\omega)^2\tau}{(1 + (\Delta\omega)^2\tau^2)} \quad (10)$$

satisfies both limiting cases. In fact, Eq. (10) is similar to the typical spectral density function used for a randomly fluctuating local field at a frequency  $\Delta\omega$ , and as we show below, the use of these simple relations leads to information on both the rates of surface diffusion and the associated energetics.

The temperature dependence of  $1/T_2$  for  $^{13}\text{CN}$  (a) [6] and for  $^{13}\text{CO}$  (b) [5] on polycrystalline platinum black at saturation coverage are shown in Fig. 12. For CO or CN adsorbed onto small

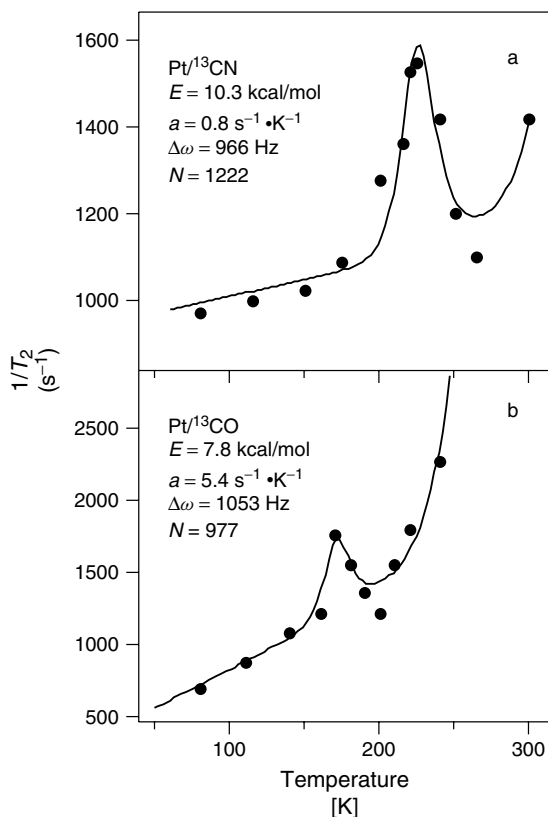
platinum particles,  $1/T_2$  can be expressed as

$$\begin{aligned} \frac{1}{T_2} &= \frac{1}{T_2^{\text{RL}}} + \frac{1}{T_2^{\text{Pt}}} + \frac{1}{T_2^{\text{dip}}} + \frac{1}{T_2^{\text{diff}}} \\ &= \frac{1}{T_2^{\text{RL}}} + aT + \frac{(\Delta\omega)^2\tau}{(1 + (\Delta\omega)^2\tau^2)} + \frac{1}{(N\tau)} \end{aligned} \quad (11)$$

where  $1/T_2^{\text{RL}}$  is the temperature-independent “rigid lattice” contribution, and  $1/T_2^{\text{Pt}} (= aT$ , where  $a$  is a constant and  $T$  the absolute temperature) accounts for the effects of platinum spins.  $1/T_2^{\text{dip}} = (\Delta\omega)^2\tau/(1 + (\Delta\omega)^2\tau^2)$ , where  $\Delta\omega$  is the dipolar field in Hertz and  $\tau = \tau_0 \exp(E/k_B T)$ , with  $\tau_0$  a preexponential factor, chosen to be  $10^{-13}$  s, and  $E$  is the activation energy for surface diffusion), arises from dipolar interactions between neighboring carbon-13 spins.  $1/T_2^{\text{diff}} (= 1/N\tau$ , where  $N$  is the number of jumps needed to dephase the carbon spins) comes from the field difference (positive or negative) between adjacent adsorption sites, due to the presence of a significant magnetic field inhomogeneity on the particle surface.

The solid lines in Fig. 12 are the fit to Eq. (11) with  $1/T_2^{\text{RL}}$ ,  $a$ ,  $\Delta\omega$ ,  $E$ , and  $N$  as fitting parameters. The results of the fits (in which  $1/T_2^{\text{RL}}$  are 293 and 930  $\text{s}^{-1}$  for CO and CN, respectively) are also shown in Fig. 12. Clearly, this simple model describes the experimental data very well, for both  $^{13}\text{CO}$  and  $^{13}\text{CN}$ . It is interesting to note that the activation energy found for CO (7.8  $\text{kcal mol}^{-1}$ ) is close to that found for CO on “dry” alumina-supported Pt clusters, as well as that found in single-crystal studies. The results of the fits also indicate that the activation energy for surface diffusion is higher for CN than for CO, while the difference in the constant  $a$  suggests, paradoxically, that platinum has more of an electronic influence on  $^{13}\text{C}$

**Fig. 12** Temperature dependence of spin–spin relaxation rates of chemisorbed and (panel a)  $^{13}\text{CN}$  and (panel b)  $^{13}\text{CO}$  on 10-nm Pt electrocatalyst surfaces. The solid lines are the fits to Eq. (11) and the numbers are the corresponding results of the fits. (Adapted from Refs. [5, 6].)



spin–spin relaxation of CO than on that of CN. The latter may, however, be related to the fact that the  $J$ -coupling is mediated by orbital electrons between  $^{13}\text{C}$  and  $^{195}\text{Pt}$  and is expected to be primarily influenced via  $\sigma$ -bonding rather than through  $\pi$ -bonding, for  $|\psi|^2 = 0$  at C for the  $2\pi^*$  orbital. If the  $^{195}\text{Pt}$ – $^{13}\text{C}$  dipolar interaction were the only mechanism for  $1/T_2^{\text{Pt}}$ , the ratio in  $a$  values would yield  $r_{\text{Pt–CN}}/r_{\text{Pt–CO}}$  equal to 1.9, which is unrealistic. Thus, while the activation values may indicate an overall stronger metal surface bonding for Pt–CN than for Pt–CO, the  $a$  values suggest that  $\sigma$ -bonding is stronger in the latter case. Finally,  $\Delta\omega$  for the  $^{13}\text{C}$ – $^{13}\text{C}$  dipolar interaction is essentially identical in each of the systems investigated, consistent

with a similar adsorbate coverage for both samples.

### 3.1.3.6 Isotopic Labeling for Site Selectivity

Isotopic labeling is a very useful and geometrically specific NMR technique when the natural abundance of the nucleus of interest is too low to be detected under normal conditions, such as with  $^{13}\text{C}$ ,  $^{15}\text{N}$ , and  $^{17}\text{O}$ . As an example, we consider here the bonding of a larger species, acetonitrile, bonded to Pt in an electrochemical environment [40].  $^{13}\text{C}$   $1/T_1$  versus  $T$  data for  $\text{CH}_3^{13}\text{CN}$  and  $^{13}\text{CH}_3\text{CN}$  adsorbed on platinum are shown in Fig. 13. A linear  $1/T_1$  versus  $T$  plot, reflecting Korringa behavior with

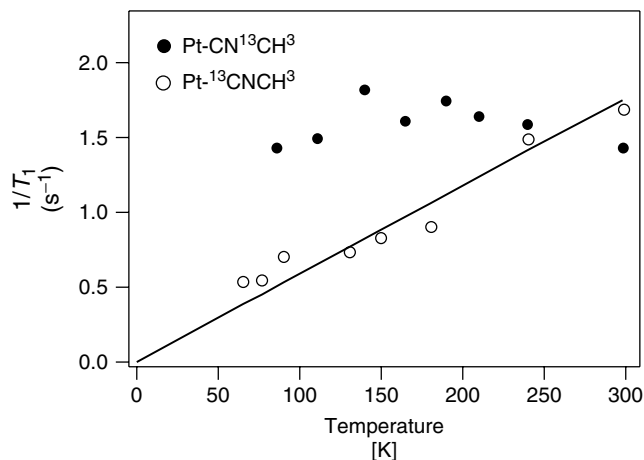


**Fig. 13** Temperature dependence of spin–lattice relaxation rates for chemisorbed  $\text{CH}_3^{13}\text{CN}$  and  $^{13}\text{CH}_3\text{CN}$ . The clear absence of a Korringa relationship for  $^{13}\text{CH}_3\text{CN}$  (solid circles) indicates that the carbon atom in the methyl group does not acquire any metallic character. (Adapted from Ref. [38].)

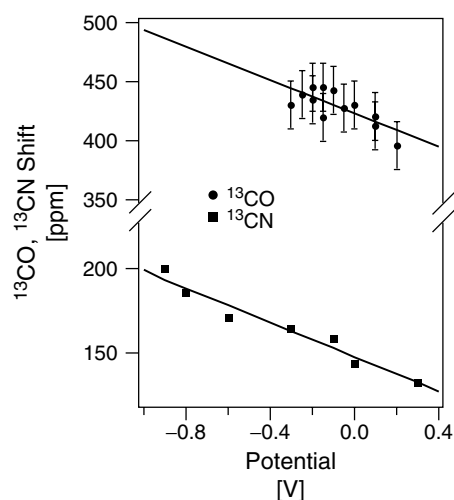
$T_1T = 170$  s K, is only obtained with the  $\text{CH}_3^{13}\text{CN}$  adsorbate. This proves that at least the carbon of the CN group is directly attached to platinum, and that the  $^{13}\text{C}$  has acquired metallic character. Note that the value of  $T_1T = 170$  s K for  $\text{CH}_3^{13}\text{CN}$  is quite close to that of  $^{13}\text{CN}$  (135 s K). The  $T_1T$  product for  $^{15}\text{N}$  in  $\text{CH}_3\text{C}^{15}\text{N}$  at room temperature is 224 s K, showing that the spin–lattice relaxation of  $^{15}\text{N}$  in chemisorbed  $\text{CH}_3\text{C}^{15}\text{N}$  is much more efficient than in chemisorbed  $\text{C}^{15}\text{N}$ , where  $T_1T$  varied in the range  $\sim 3000\text{--}4000$  s K. Indeed, after taking into account the  $\gamma_{^{13}\text{C}}/\gamma_{^{15}\text{N}} \sim 2.5$  factor in Eq. (3), the relaxation of  $^{15}\text{N}$  appears even more efficient than that of the “metallic”  $^{13}\text{C}$  in  $\text{CH}_3^{13}\text{CN}$ . This suggests that both C and N in the CN group are directly attached to the platinum surface, forming a side-on parallel orientation with respect to the Pt–Pt surface bonds. The clear absence of a Korringa relationship for  $^{13}\text{CH}_3\text{CN}$  (solid circles) indicates that the carbon atom in the methyl group does not acquire

any metallic character. This implies that neither C–C bonding nor antibonding orbitals are involved with bonding to the platinum surface, while both  $^{13}\text{C}$  and  $^{15}\text{N}$  atoms in the CN group are strongly involved, in contrast to the situation with the CN itself, in which cyanide has a C-down on-top bonding.

### 3.1.3.7 Potential-dependent EC-NMR

Understanding the nature of the electric field (electrode potential) effects on the electronic structure at the solid–liquid interface is an outstanding issue in electrocatalysis and in the theory of the electrical double layer. To illustrate such effects via NMR, we show in Fig. 14, the electrode potential–induced  $^{13}\text{C}$  line shifts for CO (circles) [8] and CN (squares) [6] on polycrystalline Pt. These results were obtained under active external potentiostatic control, and at room temperature, and the inset shows typical  $^{13}\text{C}$  NMR spectra of  $^{13}\text{CN}$ , recorded at

**Fig. 14** Electrostatic potential dependence of  $^{13}\text{C}$  shifts for  $^{13}\text{CO}$  (circles) and  $^{13}\text{CN}$  (squares) chemisorbed on a 10-nm Pt electrocatalyst. (Adapted from Ref. [4].)



different applied potentials. Apparently, for both adsorbates, there is a linear relation between the electrode potential and the line shift—the more negative the potential, the larger the frequency shift.  $^{13}\text{C}$  becomes more deshielded as the potential goes to more negative values, and the slope is about  $-71 \text{ ppm V}^{-1}$  for  $^{13}\text{CO}$  and  $-50 \text{ ppm V}^{-1}$  for  $^{13}\text{CN}$ . For CO on Pd, the slope was found to be even larger, that is, about  $-136 \text{ ppm V}^{-1}$  [8].

A similar response in C–O vibrational frequency,  $\nu_{\text{CO}}$ , to variations in the electrode potential has been reported [39]. There,  $\nu_{\text{CO}}$  decreased when the electrode potential became more cathodic. However, the origin of this so-called vibrational Stark effect has been controversial for some time, since a clear picture of how the short-range (electronic) bonding and the longer-range (electrostatic) field effects at surfaces are controlled by varying either the electrode or the surface potential, has not been available.

EC-NMR provides an additional technique with which to probe these questions, for several reasons. First, the response of  $^{13}\text{C}$  NMR to the electrode

potential has been found to be due essentially to the Knight shift [8]. The  $^{13}\text{C}$  chemical shift response of CO to electric fields (in biomolecules) has been estimated to be at most about  $-15 \text{ ppm V}^{-1}$ , much smaller than the values found at the electrochemical interface (see above). In addition, for CO on Pd, a corresponding change in the nuclear spin–lattice relaxation rate as a function of applied field has also been observed [8], indicating the electronic nature of the change in NMR shift. Second, the magnitude of the clean-surface  $E_{\text{F}}$ -LDOS of the adsorbent is responsible for the extent of the Knight shift as well as the vibrational stretch frequency of chemisorbed CO [25, 36]. That is to say, the higher the clean-surface  $E_{\text{F}}$ -LDOS, the larger (lower) will be the  $^{13}\text{C}$  Knight shift [25] (C–O stretch frequency [36]) of CO, after chemisorption. Both relationships are linear, with slopes of about  $12 \text{ ppm/Ry}^{-1}\cdot\text{atom}^{-1}$  and  $-4 \text{ cm}^{-1}/\text{Ry}^{-1}\cdot\text{atom}^{-1}$ , respectively, giving a ratio of  $-3 \text{ ppm/cm}^{-1}$ . This is to be compared with the ratio of  $-2.8 \text{ ppm/cm}^{-1}$ , obtained independently

from the slopes ( $-71 \text{ ppm V}^{-1}$  and  $25 \text{ cm}^{-1} \text{ V}^{-1}$ , respectively) of  $\delta(^{13}\text{C})$  and  $\nu_{\text{CO}}$  versus electrode potential relationships for CO on Pt black. Third, as shown in Sect. 3.1.3.4, variations in  $\nu_{\text{CO}}$  can be directly correlated with changes in  $2\pi^*$  backdonation – that is, the higher the backdonation, the lower the CO stretch frequency. When taken together, all these observations indicate that the potential dependence of both the  $^{13}\text{C}$  NMR shift and the vibrational stretch frequency of adsorbed CO are primarily electronic in nature, and originate from changes in the  $E_{\text{F}}$ -LDOS at the metal surface and at the adsorbate, induced by electrode polarization.

#### 3.1.4

##### Future Perspectives

EC-NMR has made considerable progress during the past few years. It is now possible to investigate in detail metal–liquid interfaces under potential control, to deduce electronic properties of electrodes (platinum) and of adsorbates (CO), and to study the surface diffusion of adsorbates. The method can also provide information on the dispersion of commercial carbon-supported platinum fuel cell electrocatalysts and on electrochemically generated sintering effects. Such progress has opened up many new research opportunities since we are now in the position to harness the wealth of electronic,  $E_{\text{F}}$ -LDOS as well as dynamic and thermodynamic information that can be obtained from NMR experiments. As such, it is to be expected that EC-NMR will continue to thrive and may eventually become a major characterization technique in the field of interfacial electrochemistry.

##### Acknowledgments

This work was supported by the United States National Science Foundation (grant CTS 97-26419), by an equipment grant from the United States Defense Advanced Research Projects Agency (grant DAAH 04-95-1-0581), and by the US Department of Energy under grant DEFG02-96ER45439.

##### References

1. A. Zangwill, *Physics at Surfaces*, Cambridge University Press, Cambridge, 1988.
2. G. A. Somorjai, *Introduction to Surface Chemistry and Catalysis*, John Wiley & Sons, New York, 1994.
3. A. Wieckowski, (Ed.), *Interfacial Electrochemistry – Theory, Experiment, and Applications*, Marcel Dekker, New York, 1999.
4. Y. Y. Tong, E. Oldfield, A. Wieckowski, *Anal. Chem.* **1998**, 70, 518A–527A.
5. J. B. Day, P.-A. Vuissoz, E. Oldfield et al., *J. Am. Chem. Soc.* **1996**, 118, 13 046–13 050.
6. J. J. Wu, J. B. Day, K. Franaszczuk et al., *J. Chem. Soc., Faraday Trans.* **1997**, 93, 1017–1026.
7. Y. Y. Tong, C. Belrose, A. Wieckowski et al., *J. Am. Chem. Soc.* **1997**, 119, 11 709, 11 710.
8. P.-A. Vuissoz, J.-P. Ansermet, A. Wieckowski, *Phys. Rev. Lett.* **1999**, 83, 2457–2460.
9. Y. Y. Tong, C. Rice, E. Oldfield et al. in *Theoretical Modeling of the Solid/Liquid Interface: Electronic Perspective and Comparison with Experiment* (Ed.: W. Halley), American Chemical Society, Washington, DC, 2001.
10. Y. Y. Tong, C. Rice, A. Wieckowski et al., *J. Am. Chem. Soc.* **2000**, 122, 1123–1129, 11 921–11 924.
11. M. E. Lacey, R. Subramanian, D. L. Olson et al., *Chem. Rev.* **1999**, 99, 3133–3152.
12. C. P. Slichter, *Principles of Magnetic Resonance*, 3rd Enlarged and Updated Edition, Springer-Verlag, Berlin, Germany, 1990.
13. J.-P. Ansermet, C. P. Slichter, J. H. Sinfelt, *Prog. NMR Spectrosc.* **1990**, 22, 401–421.
14. T. M. Duncan, *Colloids Surf.* **1990**, 49, 11–31.
15. M. Pruski in *Encyclopedia of Magnetic Resonance* (Eds.: D. M. Grant, R. K. Harris),



- John Wiley & Sons, New York, 1996, pp. 4638–4638, Vol. 7.
16. J. J. van der Klink, *Adv. Catal.* **2000**, *44*, 1–117.
  17. P.-K. Wang, J.-P. Ansermet, S. L. Rudaz et al., *Science* **1986**, *234*, 35–41.
  18. P. J. Slezak, A. Wieckowski, *J. Magn. Reson., Ser. A* **1993**, *102*, 166–172.
  19. W. D. Knight in *Solid State Physics* (Eds.: F. Seitz, D. Turnbull), Academic Press, New York, 1956, pp. 93–136, Vol. 2.
  20. J. J. van der Klink, H. B. Brom, *Prog. NMR Spectrosc.* **2000**, *36*, 89–201.
  21. J. Korrying, *Physica* **1950**, *16*, 601–610.
  22. J.-P. Bucher, J. J. van der Klink, *Phys. Rev. B* **1988**, *38*, 11 038–11 047.
  23. R. Hoffmann, *Rev. Mod. Phys.* **1988**, *60*, 601–628.
  24. P.-A. Vuissoz, J.-P. Ansermet, A. Wieckowski, *Electrochim. Acta* **1998**, *44*, 2457–2460.
  25. Y. Y. Tong, C. Rice, N. Godbout et al., *J. Am. Chem. Soc.* **1999**, *121*, 2996–3003.
  26. M. S. Yahnke, B. M. Rush, J. A. Reimer et al., *J. Am. Chem. Soc.* **1996**, *118*, 12 250, 12 251.
  27. B. M. Rush, J. A. Reimer, E. J. Cairns, *J. Electrochem. Soc.* **2001**, *148*, A137–A148.
  28. H. E. Rhodes, P.-K. Wang, H. T. Stokes et al., *Phys. Rev. B* **1982**, *26*, 3559–3568.
  29. J. J. van der Klink, J. Buttet, M. Graetzel, *Phys. Rev. B* **1984**, *29*, 6352–6355.
  30. C. Rice, Y. Y. Tong, E. Oldfield et al., *Electrochim. Acta* **1998**, *43*, 2825–2830.
  31. J. P. Bucher, J. Buttet, J. J. van der Klink et al., *Surf. Sci.* **1989**, *214*, 347–357.
  32. J. Friedel, *Adv. Phys.* **1954**, *3*, 446–507.
  33. V. Heine in *Solid State Physics* (Eds.: H. Ehrenreich, F. Seitz, D. Turnbull), Academic Press, New York, 1980, pp. 1–127, Vol. 35.
  34. Y. Y. Tong, G. A. Martin, J. J. van der Klink, *J. Phys. Condens. Matter* **1994**, *6*, L533–L538.
  35. G. Blyholder, *J. Phys. Chem.* **1964**, *68*, 2772–2778.
  36. Y. Y. Tong, P. Mériaudeau, A. J. Renouprez et al., *J. Phys. Chem. B* **1997**, *101*, 10 155–10 158.
  37. C. Rice, Y. Y. Tong, E. Oldfield et al., *J. Phys. Chem. B* **2000**, *104*, 5803–5807.
  38. J. Wu, C. Coretsopoulos, A. Wieckowski in *Electrochemical Society Proceedings*, The Electrochemical Society, Pennington, NJ, 1997, pp. 426–442, Vol. 97-17.
  39. D. K. Lambert, *Electrochim. Acta* **1996**, *41*, 623–630.
  40. M. Weinert, A. J. Freeman, *Phys. Rev. B* **1983**, *28*, 6262–6269.

## 3.2

**EPR Spectroscopy in Electrochemistry**

Jay D. Wadhawan, Richard G. Compton,\*  
Oxford University, Oxford, United Kingdom

## 3.2.1

**Introduction**

Electron paramagnetic resonance (EPR), or its equivalent term electron spin resonance (ESR), is an ideal spectroscopic tool to study the formation of paramagnetic species (such as radicals) during the course of electrolysis, as species with concentrations as low as  $10^{-8}$  M may be detected [1]. Further, electrolysis has consistently proved to be one of the most convenient and attractive techniques for the production of interesting radicals [2–5]. Additional advantages of using a spectroscopic approach in the interrogation of complex electrode reaction mechanisms are that it does not require the destruction (nor activation) of the sample, and that it permits an inference of the identity of paramagnetic species that are formed as intermediates in a plethora of electron-transfer processes. An example that illustrates this is the electrochemical reduction of 2,4-dichloronitrobenzene, studied by Lawless and Hawley [6]. In this reaction, the 2,4-dichloronitrobenzene radical anion undergoes a thermally-induced C–Cl bond cleavage to form the neutral chloronitrobenzene radical, which, after H atom abstraction from the solvent/electrolytic system, is subsequently further reduced. The question that arises is: which of the two C–Cl bonds is cleaved? Analysis of the EPR spectrum of the intermediates revealed that the *ortho*-chlorine is removed, leaving the *para*-chloronitrobenzene radical anion that is detected.

EPR spectroscopy was first applied to electrochemistry, albeit at low temperature, in 1958 by Ingram and coworkers [3], who demonstrated the formation of radical ion species from the potentiostatic electrolysis of various aromatic compounds in *N,N*-dimethylformamide (DMF). In these experiments, aliquots of sample were withdrawn during the course of electrolysis, frozen in liquid nitrogen, and subsequently examined by EPR. It was Maki and Geske [4, 5, 7, 8] who developed a complementary concept of electrochemical EPR by studying the solution-phase spectra of radicals that had been electrogenerated within the EPR cavity, thereby paving the way for two forms of electrochemical EPR methodology, via *in situ* techniques and *ex situ* techniques. In the former, paramagnetic species are generated within the EPR cavity, whilst in the latter, radicals that are externally generated are subsequently moved into the EPR cavity. It will be appreciated that the former technique is more advantageous than the latter, in that it may be used in the study of radicals with a shorter lifetime range. Whilst the *ex situ* technique has many merits, notably in Albery's use of a tube electrode with a mathematically well-defined flow of electrolytes in the study of the kinetics and mechanisms of a variety of electrode processes [9–14], this overview will be exclusively concerned with the more sensitive *in situ* approach to electrochemical EPR; the interested reader is referred to two earlier reviews by Waller and Compton [15, 16] that describe the historical development of electrochemical EPR.

The ability of the *in situ* electrochemical EPR technique to provide information on kinetics and mechanisms of electrode processes is the major reason for its adoption by electrochemists although its major limitation is that it requires

the presence of a paramagnetic reaction intermediate. Following Maki and Geske, Adams [17], Cauquis [18–22], Kashtening [23, 24], and Dohrmann [25–28] all developed cells based upon a variety of cell geometries, but these did not provide advances in the study of reaction kinetics; Sect. 3.2.3 covers the in situ electrochemical EPR cell designs that aim to remedy this, and Sect. 3.2.4 gives examples of the use of such cells in the analysis of kinetics and mechanisms. First, however, the underlying theoretical principles of electron paramagnetic resonance are covered, and from which, the similarity between this and its sister technique, nuclear magnetic resonance (NMR, see Chapter 3.1 of this volume), may be noted.

### 3.2.2

#### Principles of EPR Spectroscopy

This section outlines the theoretical concepts of EPR. The theory is similar to the related technique of NMR described in Volume 2 Chapter 3.1. In the following, a basic knowledge of quantum mechanics will be assumed. Throughout the following, the symbol **B** refers to the magnetic flux density (or magnetic induction field); the symbol **H** being reserved for the magnetic field strength. In SI units,  $\mathbf{H} = 4\pi \times 10^{-7} \mathbf{B}$ .

##### 3.2.2.1 EPR Theory

The origin of EPR spectroscopy lies in the fact that electrons have both electrostatic charge and spin angular momentum. The former is observed by electron-deflection from negatively charged surfaces, in for example, a cathode ray oscilloscope; the latter is easily verifiable in the classic Stern–Gerlach experiment [29, 30] in which a beam of S-state silver atoms is observed to split into two separate beams

upon passage through an inhomogeneous magnetic field.

The electronic charge (*e*) together with the angular momentum (**s**) confer a magnetic moment (**μ**) upon the electron, according to Eq. (1),

$$\boldsymbol{\mu} = g_e \gamma_e \mathbf{s} \quad (1)$$

in which  $\gamma_e$  is the magnetogyric ratio of the electron, given by the ratio  $-e/2m_e$ ,  $m_e$  representing the mass of the electron. The constant  $g_e$  is referred to as the electron *g*-factor and takes the value 2.002319314 for a free electron. The origin of this factor may be inferred from Dirac theory; the deviation from exactly 2 reflects the existence of a zero-point energy in the harmonic oscillating electromagnetic field. The interested reader is referred to Ref. [31] for further details regarding these phenomena.

The magnitude of the spin angular momentum vector (**s**) is given by

$$|\mathbf{s}| = \hbar \sqrt{s(s+1)} \quad (2)$$

in which *s* refers to the spin angular momentum quantum number. Experiment shows that  $s = 1/2$ , and the spin angular momentum vector is perceived to “precess” around the direction of the applied magnetic field (conventionally labeled the *z*-direction); the component of the spin angular momentum in this direction being  $\pm \hbar/2$  (Fig. 1). It is useful to introduce the quantum number  $M_s$  to label the allowed eigenvalues of  $s_z$ ,

$$s_z = M_s \hbar \quad (3)$$

Evidently,  $M_s = \pm 1/2$ . This space quantization of **s** and **μ** will necessarily cause the two possible electron energy states to split under the application of a magnetic field (the Zeeman Effect); the energy, *E*

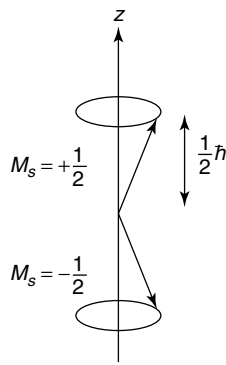


**Fig. 1** The precession of the spin angular momentum vector about a magnetic field applied in the z-direction.

of a magnetic dipole of moment  $\mu$  in the presence of a magnetic induction,  $\mathbf{B}$ , is given by

$$E = -\mu \cdot \mathbf{B} \quad (4)$$

The negative sign indicates that if the magnetic dipole is aligned parallel to the applied field, the interaction energy will be at a minimum; an antiparallel alignment corresponds to a maximum energy interaction. If the field is applied in the z-direction, Eq. (4) becomes

$$E = \frac{g_e \gamma_e M_s B_z}{\hbar} \quad (5)$$

Since  $M_s = \pm 1/2$ , only two energy states are possible as given above. In the absence of a magnetic field, the two energy states are necessarily degenerate; application of a magnetic field causes the spin states to adopt different energies, illustrated in Fig. 2. Note that the lower state ( $E_1$ ) has  $M_s = -1/2$ , whilst that antiparallel, upper state ( $E_2$ ), has  $M_s = +1/2$ . If the energy

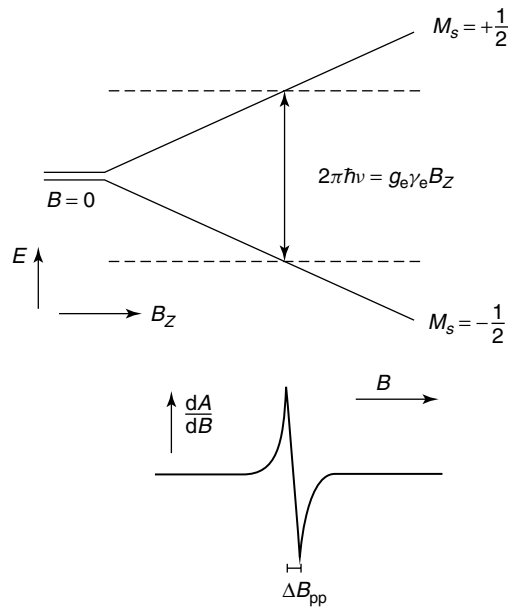


**Fig. 2** Splitting of the spin levels of a free electron in a magnetic field, of induction  $B_z$ . Also shown is the first derivative of the absorption intensity,  $A$ , with respect to  $B$ , as a function of  $B$ .

of the interaction is large when compared to  $kT$ , the alignment of the great majority of dipoles would correspond to the lower energy state. However, the energy of interaction in the EPR experiment is considerably smaller than  $kT$ .

Transitions between the two spin states may be induced by the application of electromagnetic radiation of the appropriate frequency,  $\nu$ , such that the applied energy,  $2\pi\nu\hbar$  exactly matches that of the Zeeman-level separation,  $g_e\gamma_e B_z$ , that is

$$\nu = \frac{g_e\gamma_e B_z}{2\pi\hbar} \quad (6)$$

This phenomenon is known as magnetic resonance; the frequency at which these transitions occur is called the resonant frequency. Resonance can be observed in two different ways; the frequency may be varied at a fixed magnetic field strength, or *mutatis mutandis* the converse. In practice, it is more beneficial to utilize the latter of these two methods. Equation (6) suggests that the resonant frequency of a free electron is 9.4 GHz for an applied magnetic field of 3400 G ( $1\text{ G} = 10^{-4}\text{ T}$ ). These approximate conditions are employed to experimentally observe EPR transitions; the frequency of 9.4 GHz is in the microwave region, corresponding to a wavelength  $\sim 3\text{ cm}$  (so-called “X-band”). Occasionally, measurements are undertaken under other conditions, such as Q-band (corresponding to  $\nu = 35\text{ GHz}$ ,  $B_z = 12\,500\text{ G}$ ,  $\lambda = 0.86\text{ cm}$ ) or S-band ( $\nu = 3.2\text{ GHz}$ ,  $B_z = 1140\text{ G}$ ,  $\lambda = 9.4\text{ cm}$ ).

In contrast to NMR spectra, EPR spectra are recorded as the first derivative of the intensity,  $A$ , of the absorption with respect to the field induction,  $B$ , and as a function of  $B$ , that is  $dA/dB$  versus  $B$ , as indicated in Fig. 2. The reasons for doing this lie in the phase-sensitive methods of detection employed in EPR, and consequently this way

of recording the spectrum depends upon the modulation used to amplify the absorption signal (*vide infra*). The peak-to-peak linewidth,  $\Delta B_{pp}$ , is generally taken as the abscissa distance between the maximum and the minimum of the  $dA/dB$  curve.

### 3.2.2.2 The $g$ -value

Until now only free electrons have been discussed. In reality, the electron responsible for the resonant absorption is normally an unpaired one within a molecule, thereby experiencing a local magnetic field different from the applied field, since the applied field will induce currents in the electrons of the molecule. The resonance condition is consequently modified to

$$\nu = \frac{g_e\gamma_e(1 - \sigma)B_z}{2\pi\hbar} \quad (7)$$

where  $\sigma$  represents a shielding constant similar to that in NMR spectroscopy. The  $g$ -factor of the molecule is then given by the quantity  $g = g_e(1 - \sigma)$ .

In addition to the magnetism arising from the electron spin, there may also be a contribution from the electronic orbital motion since atomic orbitals have associated angular momenta of magnitude  $\hbar\sqrt{\ell(\ell + 1)}$ , in which  $\ell = 0, 1$ , and  $2$  for s-, p-, and d-orbitals, respectively. Hence, occupied orbitals that are nondegenerate lead to nonzero angular momenta. An orbital angular momentum,  $\mathbf{l}$ , has an associated magnetic moment

$$\boldsymbol{\mu}_L = \gamma_e \mathbf{l} \quad (8)$$

For light atoms and certain linear radicals,  $\mathbf{s}$  and  $\mathbf{l}$  combine via the Russell–Saunders Coupling scheme to give a total angular momentum,  $\mathbf{j}$ . EPR spectroscopy then interrogates transitions between the different  $j$  levels. Hence, since the Hamiltonian operator for an electron spin in a molecule contains a term representing the effect of

the magnetic field on the electron spin magnetic moment, another for spin-orbit coupling, and another for the interaction of the applied field with the orbital angular momentum, the  $g$ -factor can absorb the effects of the orbital angular momentum operators, giving rise to an effective Spin Hamiltonian.

In most molecular radicals, the orbital contribution is lost (“quenched”), as the existence of covalent bonds lifts the degeneracy of the orbitals, and providing the electron is in an orbital sufficiently removed in energy from other levels, the effective  $g$ -value will be close to the “spin-only” value, and the resonance condition is given by

$$\nu = \frac{g\gamma_e B_z}{2\pi\hbar} \quad (9)$$

in which  $g$  is now a unique property of the whole molecule. The value of the  $g$ -factor will be independent of the magnetic field direction only in isotropic systems such as organic radicals in low-viscosity solutions in which there is rapid and random tumbling of the molecules so as to permit an average  $g$ -value to be observed. For the purposes of understanding liquid phase EPR spectra generated in electrochemical EPR experiments, this average value is sufficient. However, in a large number of other systems, the  $g$ -factor is anisotropic, varying markedly with the orientation of the sample (this is a consequence of its dependence upon the spin-orbit coupling). In these cases, especially for solid-state spectra, the  $g$ -factor must be regarded as a tensor [32]. Furthermore, the anisotropy of the  $g$ -tensor may contribute in some cases to the linewidth of the spectra from high-viscosity solution-phase radicals.

### 3.2.2.3 Linewidths

The linewidth of an EPR spectrum depends upon two instrumental factors, the

homogeneity of the magnetic field and the frequency of the magnetic induction modulation. Several other processes affect the linewidth and these are considered in turn. It should be noted that the two most frequently encountered lineshapes observed are Gaussian and Lorentzian. For a line centered at frequency  $\nu^*$ , a Lorentzian lineshape is given by the equation

$$f(\nu) = \frac{2T_2}{1 + 4\pi^2 T_2^2 (\nu - \nu^*)^2} \quad (10)$$

and a Gaussian lineshape by the equation

$$f(\nu) = T_2 \sqrt{2\pi} \exp[-2\pi^2 T_2^2 (\nu - \nu^*)^2] \quad (11)$$

where the symbol  $T_2$  is defined later. The Gaussian lineshape is observed when the line is the superposition of a large number of unresolved individual components, such a line being referred to as inhomogeneously broadened, and is commonly encountered in solid-state EPR spectra. More important is the Lorentzian lineshape, which is often observed for radicals in solution, when complications due to unresolved hyperfine splittings do not occur.

**3.2.2.3.1 Spin-lattice Relaxation** The transitions between eigenstates induced by the electromagnetic radiation necessarily involves a perturbation of the Boltzmann Distribution Law,

$$\frac{n_2}{n_1} = \exp\left[\frac{-(E_2 - E_1)}{kT}\right] \quad (12)$$

In this equation,  $k$  and  $T$  refer to the Boltzmann constant ( $1.380662 \times 10^{-23} \text{ J K}^{-1}$ ) and the absolute temperature, respectively, and  $n_i$  refers to the electron population of the  $i$ th non-degenerate energy level of energy  $E_i$ , as given in Fig. 2. At equilibrium, the lower state is more filled, and resonance initially induces more transitions from  $E_1$  to state  $E_2$  than the reverse. It is

expected that the populations will rapidly equalize, after which, there would be no resultant energy absorption, even though resonant transitions would still be occurring. This phenomenon is termed *saturation* and is observed when high microwave powers are applied. When low-power microwaves are employed, magnetic resonance transitions are observed and non-radiative “relaxation” processes occur. These processes oppose saturation and help restore the natural order of the thermal Boltzmann Distribution, and they are termed *spin-lattice relaxation phenomena*.

The mechanism for spin-lattice relaxation is as follows. All paramagnetic species in the sample have an associated magnetic field surrounding them with which each of the other paramagnetic species may interact. In liquids, the random molecular collisions that constitute Brownian motion permit these local magnetic fields to fluctuate; a fluctuation that occurs at the resonant frequency will induce a “radiationless” transition. The spin-lattice relaxation is characterized by a spin-lattice relaxation time,  $T_1$ , which thus effectively controls the degree of saturation.

Since the relaxation determines the lifetime,  $\Delta t$ , of a spin state, the Heisenberg Uncertainty Principle relates it to the uncertainty of the Zeeman eigenvalues,  $E_1$  and  $E_2$ , thereby allowing this phenomenon to affect the linewidth of EPR signals, as these depend inversely on  $T_1$ .

$$\Delta E \bullet \Delta t \approx \hbar \quad (13)$$

Clearly, if the spin-lattice interaction is strong,  $T_1$  is small,  $\Delta t$  is small, and  $\Delta E$  must be large, leading to a spread in the energy states between which transitions occur. Hence, absorption effectively occurs over a small range of magnetic field strengths. *Mutatis mutandis*, if the spin-lattice interaction is weak, narrow

absorption lines occur. The former situation is often encountered in the EPR spectra of transition metal ions, whilst the latter is usually found for organic radicals in solution.

Another form of spin-lattice relaxation occurs when there is a quadrupolar nucleus (*vide infra*) present in the paramagnetic species. Associated with this nucleus is an electric quadrupolar field, which will interact with gradients in the electric component of the microwave radiation. However, as this electric quadrupolar interaction is generally weak, it does not contribute much towards the relaxation.

**3.2.2.3.2 Spin-spin Relaxation** The second major nonradiative phenomenon is termed *spin-spin relaxation* and is characterized by a relaxation time  $T_2$ . The processes that contribute to  $T_1$  also influence  $T_2$ , which controls the linewidth (*vide supra*). However, the random forces that modulate the electron spin energy levels at low frequencies (below  $10^{10}$  Hz) contribute to  $T_2$ , whereas they have no influence upon  $T_1$ . Again, the source of the fluctuating magnetic field lies in the anisotropic magnetic interaction within the molecule, mainly due to the anisotropy in the  $g$ -tensor and to the dipolar hyperfine coupling with magnetic nuclei. This has assumed that the radical (or parent species) concentration is not too high; otherwise, spin exchange occurs as a result of radical-radical collisions, thereby causing a broadening of the EPR lines. The spin-spin process involves the interchange of the spins of the colliding radicals. At very high radical concentrations, the spin “sees” an average environment as it moves from radical to radical, and so the hyperfine splitting is lost and a single line results. This is the reason solid state EPR spectra are generally of a single line, as

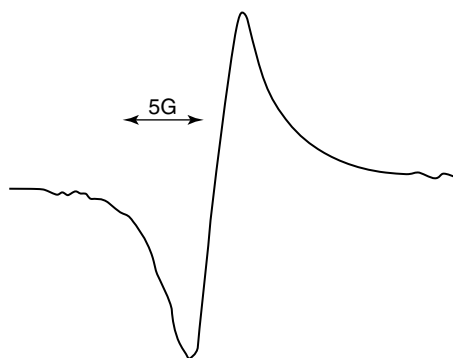


**Fig. 3** Typical EPR signal obtained upon reduction of poly(nitrostyrene) immobilized on an electrode.

shown in Fig. 3 for the poly(nitrostyrene) radical anion.

At high parent concentration, electron exchange may occur between radical and parent species, thereby inducing a line broadening; for example, the extent of such broadening has been used to calculate a rate constant for the chemical exchange between benzonitrile and the benzonitrile radical anion generated electrochemically in situ [33] yielding a rate constant of  $2 \times 10^8 \text{ dm}^3 \text{ mol}^{-1} \text{ s}^{-1}$ .

### 3.2.2.4 Hyperfine Structure

The most useful characteristic of EPR spectra in the identification of radical species is the splitting due to hyperfine coupling. This arises from the electron spin interacting with any magnetic nuclei in the molecule. Magnetic nuclei, with nuclear spin  $I$ , behave analogously to electrons when placed into a magnetic field. Hence the nuclear magnetic moment may be written in the form of Eq. 14,

$$\mu_N = g_N \gamma_N I \quad (14)$$

The  $g_N$  values are dimensionless and characteristic of the type of nucleus.  $\gamma_N$  is the nuclear gyromagnetic ratio. Some values are listed in Table 1, together with the corresponding quantum numbers  $I$  and  $M_I$ , in which the quantum number  $M_I$  allows for the space-quantization of

**Tab. 1** Characteristics of some nuclei

	Natural abundance %	Spin angular momentum	<i>g</i> -value
Electron	—	1/2	2.0023
<sup>1</sup> H	99.98	1/2	5.585
<sup>2</sup> D	0.02	1	0.857
<sup>6</sup> Li	7.43	1	0.8219
<sup>7</sup> Li	92.5	3/2	2.1707
<sup>12</sup> C	98.9	0	0
<sup>13</sup> C	1.1	1/2	1.405
<sup>14</sup> N	99.63	1	0.404
<sup>15</sup> N	0.37	1/2	−0.567
<sup>19</sup> F	100	1/2	5.257
<sup>23</sup> Na	100	3/2	1.477
<sup>31</sup> P	100	1/2	2.263

the magnetic field and is integral or half-odd integral in value. This range of  $(2I + 1)$  values can be expressed as the Clebsch–Gordon series,  $M_I = I, (I - 1), (I - 2), \dots, -(I - 1), -I$ .

It is instructive to consider the mechanism by which the hyperfine coupling arises. In a strong magnetic field, the interaction between an unpaired electron and a magnetic nucleus acts as a small perturbation  $\delta E$  to the Zeeman levels  $E_1$  and  $E_2$  of the electron spin. This perturbation is composed of two components,

$$\delta E = (\delta E)_{\text{isotropic}} + (\delta E)_{\text{anisotropic}} \quad (15)$$



The anisotropic term,  $(\delta E)_{\text{anisotropic}}$ , represents the dipolar interaction that depends upon the relative positions of the magnetic moments of the unpaired electron and the nucleus ( $\mu_e$  and  $\mu_N$ ). In single crystals, this gives helpful information on the crystal geometry; in polycrystalline substances, it causes line broadening. In liquid samples, however, since the molecules are constantly tumbling, the magnetic dipole–dipole interactions average to zero, except for a small amount that is dependent upon the liquid viscosity and hence gives rise to line broadening. The hyperfine structure due to radicals in solution, therefore, results from an isotropic term,  $(\delta E)_{\text{isotropic}}$ , which is a consequence of a nonclassical interaction, known as the Fermi-Contact interaction.

This interaction arises because of the presence of a small, but nevertheless finite spin density at the position of the nucleus. In a strong magnetic field applied in the  $z$ -direction, this term, referred to as the coupling constant,  $a$ , is proportional to the square of the electronic wave function at the nucleus,

$$a = \frac{8\pi}{3} g_e g_N \gamma_e \gamma_N |\psi(0)|^2 \quad (16)$$

Since only s-orbitals have a finite probability density at the nucleus (other orbitals all have nodes in their wave functions there), the contact interaction can only occur when the electron occupies a molecular orbital in which there is some s-orbital character.

Thus, for each nuclear spin state, a separate transition in the EPR spectrum will

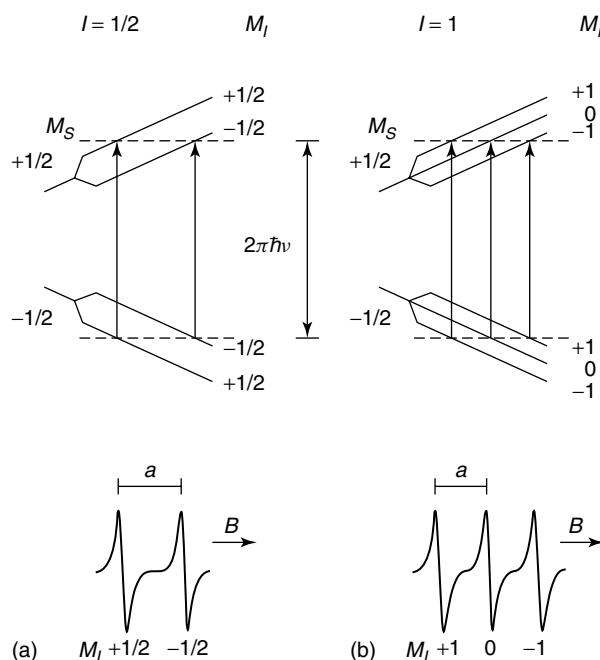


**Fig. 4** Splitting of an EPR signal by hyperfine interaction between the unpaired electron and a nucleus with spin quantum number (a)  $I = 1/2$  or (b)  $I = 1$ . Also shown are the EPR spectra anticipated for both cases.

be observed. This is illustrated in Fig. 4 in which the unpaired electron interacts with only one nucleus having a spin quantum number,  $I$ , of  $1/2$  or  $1$ , corresponding to a  $^1\text{H}$  or a  $^{14}\text{N}$  nucleus, respectively. The hyperfine coupling constant is the separation between the two lines, and is field-independent, and a characteristic of the nucleus–electron interaction. During the electronic transitions, the nuclear spin quantum number,  $M_I$ , does not change, and we may formulate the “first-order” selection rules,

$$\Delta M_S = \pm 1; \quad \Delta M_I = 0$$

The above rules are valid provided the magnitude of the hyperfine coupling is not too large; otherwise, the spins are partially coupled and the behavior is more complicated [32]. Hence, two hyperfine lines (a doublet) are detected in the spectrum resulting from the interaction of the unpaired electron with a proton, and three hyperfine lines (a triplet) when the electron interacts with a  $^{14}\text{N}$  nucleus. Quantitatively, under first-order conditions, the electronic energy levels of a one-electron, one-nucleus system are given by

$$E = M_S(-g_e\gamma_e\hbar B_z + aM_I) \quad (17)$$

The above can be extended for radicals containing more than one nucleus, by splitting the levels  $E_1$  and  $E_2$  in succession depending upon interaction with the nucleus in question. For a radical coupling to two spin- $1/2$  nuclei, the energy states are given by

$$E = M_S(-g_e\gamma_e\hbar B_z + a_1M_1 + a_2M_2) \quad (18)$$

in which  $a_1$  and  $a_2$  are the two coupling constants, and  $M_1$  and  $M_2$  are the nuclear spin quantum numbers. The EPR spectrum has four lines of equal intensity, and is described as being a “doublet

of doublets”. When, however,  $a_1 = a_2$ , the nuclei 1 and 2 are referred to as being *equivalent*. Typical EPR spectra are illustrated in Fig. 5 for the case of two equivalent spin- $1/2$  nuclei and equivalent spin-1 nuclei. In these cases, since there are certain spin configurations that are degenerate, some lines coincide.

In general,  $n$  equivalent nuclei with spin quantum number  $I$  give rise to  $(2nI + 1)$  equidistant hyperfine lines in the EPR spectrum. In particular, for an electron interacting with  $n$  equivalent protons ( $I = 1/2$ ),  $(n + 1)$  lines are produced whose relative intensities may be predicted from the coefficients of the binomial expansion of  $(1 + x)^n$ . These can be recalled most readily with the help of Pascal’s triangle, as shown in Fig. 6. Also shown in Fig. 6 are the relative line intensities for the coupling of  $n$  equivalent spin-1 nuclei with an electron (giving rise to  $(2n + 1)$  hyperfine lines). To illustrate this, Fig. 7 shows the EPR spectrum of the benzene anion. This species has six equivalent protons, and the EPR spectrum is clearly a  $1 : 6 : 15 : 20 : 15 : 6 : 1$  septet, as would be anticipated from the above ideas.

It is not immediately obvious how hyperfine splitting arises in the case of the benzene anion in which the electron occupies a  $\pi$ -orbital that has a nodal plane coincident with the plane of the aromatic ring. Similarly, it is not obvious as to why in the ethyl radical ( $\text{CH}_3\text{CH}_2\cdot$ ) the methyl (or  $\beta$ ) protons show a larger coupling constant than the  $\alpha$ -protons. This is rationalized below.

Consider an isolated  $>\text{C}\cdot\text{—H}$  unit with one electron in the  $\pi$ -orbital on the C-atom. This orbital is perpendicular to the plane of the three trigonal  $\sigma$ -bonds. Electrons in the C—H bond will keep apart, as they will mutually repel each other. This is represented in Fig. 8 in which two

“structures” are possible, depending upon whether the electron spin nearest the C-atom is parallel or antiparallel to the electron spin in the  $\pi$ -orbital. Exchange forces [32] cause the structure with the parallel spins at the C-atom to have slightly lower energy. Hence, the spins in the C–H bond are slightly polarized so that

the spin of the electron in the sigma orbital on the C-atom takes on slightly more of the character of the  $\pi$ -orbital. This means that the electron at the H atom must have a small excess of the opposite spin and this resides in the  $1s$  orbital used to form the C–H bond. The result is a finite spin density at the H-nucleus

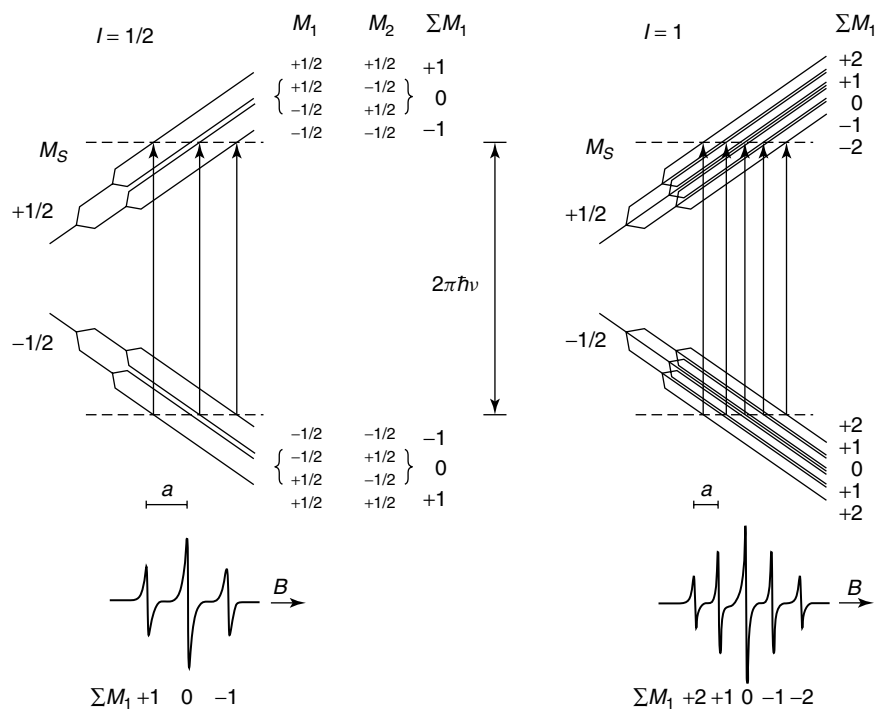


**Fig. 5** Splitting of an EPR signal by the hyperfine interaction between the unpaired electron and two equivalent nuclei.

$I = 1/2$	1	$n = 0$	$I = 1$	1
	1 1	1		1 1 1
	1 2 1	2		1 2 3 2 1
	1 3 3 1	3		1 3 6 7 6 3 1
	1 4 6 4 1	4	1	4 10 16 19 16 10 4
	1 5 10 10 5 1	5		
	1 6 15 20 15 6 1	6		

**Fig. 6** EPR line intensities for the coupling between two equivalent nuclei when  $I = 1/2$  (Pascal's Triangle) and  $I = 1$ .

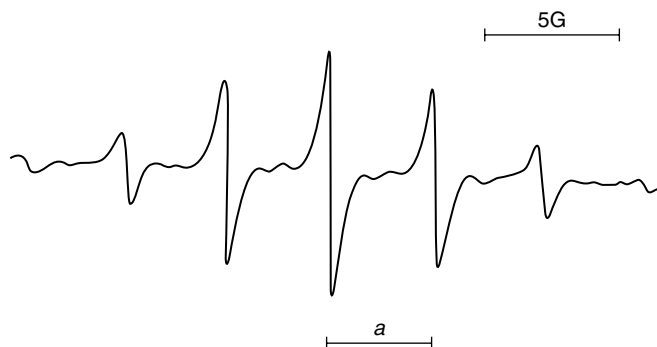


**Fig. 7** The EPR spectrum for the benzene anion in 1,2-dimethoxyethane at  $-80^{\circ}\text{C}$ .

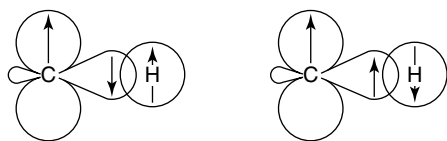


**Fig. 8** Canonical structures of the C-H fragment.

and, hence, a hyperfine splitting is seen. Quantitatively [32], the hyperfine coupling constant should be proportional to the  $\pi$ -electron density,  $\rho$ , on the carbon atom. This is expressed mathematically in McConnell's equation [34],

$$a(\text{H}) = Q\rho \quad (19)$$

where  $Q$  is a proportionality constant and takes a value of about  $-23\text{ G}$ . The negative coupling constant that is thus anticipated is because the unpaired spin density at the H atom is of opposite sign to that in the  $\pi$ -orbital on the C-atom.

The above can be easily extended to account for EPR signals at  $\beta$ -protons,

since exchange forces are capable of transmitting spin density through more than one bond. A more dominant effect, however, is due to hyperconjugation. This mechanism involves the direct overlap of the orbital containing the unpaired electron with the C-H  $\sigma$ -bonds formed by the  $\beta$ -hydrogens, as illustrated in Fig. 9. The magnitude of this interaction depends upon the relative orientation of the C-H bond to the orbital containing the unpaired electron. If the angle between the two is  $\theta$ , then

$$a(\text{H}) = A + B \cos^2 \theta \quad (20)$$

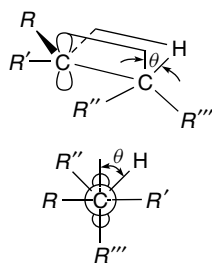


**Fig. 9** The magnitude of the hyperfine coupling between an electron and a  $\beta$ -proton depends on the dihedral angle,  $\theta$ , between the C-H bond and the p-orbital containing the unpaired electron.

where  $A$  is close to zero and  $B$  is about 46 G. In the ethyl radical, the methyl group can freely rotate and so an average value is seen. Since the averaged value of  $\cos^2 \theta$  is  $1/2$ , a value of ca. 23 G would be predicted for the coupling to these protons, in excellent agreement with the experimentally determined value (22.38 G).

### 3.2.2.5 EPR Instrumentation

Figure 10 shows a schematic illustration of an EPR spectrometer. An electromagnet supplies the adjustable applied magnetic field. Between the poles, the field is homogeneous to one part in  $10^5$ – $10^6$ . The stability of this uniform field is achieved by using a regulated power supply, any variation in the field being detected by a Hall effect device. Klystron oscillators generate microwaves, the frequency of which is determined by the voltage applied to the klystron. The stability of the microwave frequency is achieved using an automatic frequency control system. The microwaves travel through waveguides – hollow metal pipes of rectangular cross section with inside surfaces that are gold plated and whose dimensions are critically dependent

upon the wavelength of the radiation that is reflected off them – to the sample in the EPR cavity. The resonant cavity is located in the homogeneous part of the magnetic field. Within this, standing waves are set up by reflections off the end walls when the radiation is fed in through a small coupling hole from the waveguide; Fig. 11 shows the type of cavity most frequently encountered, a rectangular  $TE_{102}$  cavity. The standing wave permits the spatial separation of the electric and magnetic components of the microwave radiation. It can be seen that the magnetic component, which is responsible for inducing EPR transitions, has maximum intensity at the cavity center and is therefore concentrated upon the sample, when placed there. The distribution of the microwave field within the cavity is such that the sensitivity profile along the vertical axis of the cavity obeys a  $\sin^2$  relationship, with zero sensitivity at the cavity edges and maximum sensitivity in the cavity center [35]. The electric component has a node at the cavity center. This is advantageous, since aqueous samples in particular exhibit appreciable dielectric loss at microwave frequencies, which

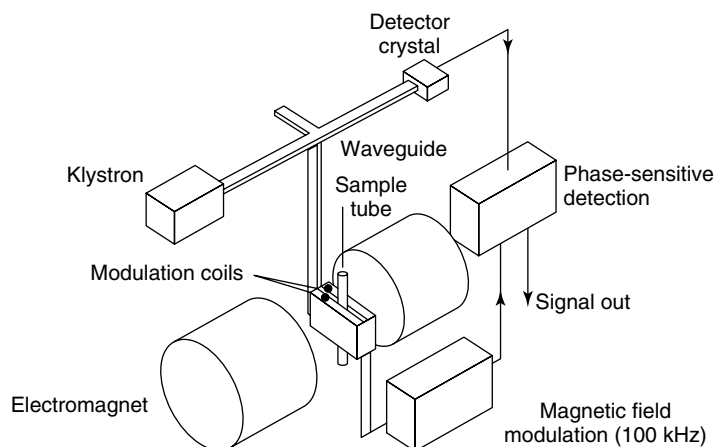
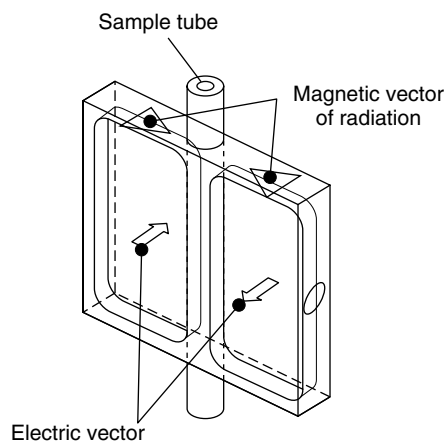


Fig. 10 The basic features of an EPR spectrometer.

Fig. 11 A TE<sub>102</sub> EPR cavity.

prevents the establishment of a standing wave; by containing these samples within a thin flat cell in which the solution is held on the nodal plane, thereby escaping interaction with the electric component of the microwave field, this problem is overcome. The cells used are fabricated from silica in preference to glass, since the latter contains paramagnetic impurities observable in the EPR spectrum. As well as the rectangular cavity described above, cylindrical cavities and microwave helices [36] have found application in electrochemical EPR.

The quality of the resonant EPR cavity is measured by its efficiency for integrating microwave energy. A measure of this efficiency is described by the quality factor ( $Q$ -factor),

$$Q = 2\pi \times \frac{\text{Energy Stored}}{\text{Energy Dissipated Per Cycle}} \quad (21)$$

A higher  $Q$  implies a greater capacity for energy storage, and only a narrower bandwidth of frequencies will be admitted into the cavity.

An attenuator and a ferrite insulator are placed between the klystron and the waveguide. The former allows regulation of

the power input, whilst the latter protects the klystron from reflected radiation. This radiation reaches the detector, a crystal diode via a “magic tee” bridge, as illustrated in Fig. 10. The bridge can be adjusted (“balanced”) so that no radiation reaches the detector if no absorption of microwaves occurs. At resonance, energy absorption by the bridge unbalances the bridge and microwave radiation is detected by the crystal diode detector.

One final point to note about the experimental EPR arrangement is that a second magnetic field is set up around the cavity using Helmholtz coils through which an alternating current is applied, thereby producing a sinusoidally varying magnetic field with time. This is known as field modulation, and, with a feedback mechanism acts to prevent saturation from arising. Further advantages include improvements in the signal-to-noise ratio made by increasing the modulation amplitude, although caution must be duly exercised, since if the modulation amplitude is approximately equal to the linewidth, the resolution deteriorates. Hence, modulation amplitude should generally not exceed about half the linewidth.

The ideas outlined in this section are treated in depth in the numerous textbooks on EPR [1, 32, 37–41]. In particular, the book by Symons [37] provides an excellent and stimulating introduction for chemists. All aspects of EPR instrumentation are thoroughly covered in the work by Poole [35].

### 3.2.3

#### In Situ Electrochemical EPR: Cell Design

In this section, contemporary methods for in situ electrochemical EPR are described, with particular emphasis given to the use of such techniques for the investigation of electrogeneration kinetics of short-lived intermediates and the mechanisms of their decay. The EPR-observable is the EPR signal intensity. Since there are many lines in each EPR spectrum, the EPR signal intensity is strictly the double integral of the EPR signal with respect to the magnetic field [42]. However, this can often be approximated by the peak-to-peak amplitude of the largest line in the spectrum, provided the peak-to-peak linewidth ( $\Delta B_{pp}$ ) is sufficiently small.

A full discussion of approximations to the double integral may be found in the review by Goldberg [42].

#### 3.2.3.1 The Bard–Goldberg Cell

**3.2.3.1.1 Cell Design** This in situ stationary solution cell developed by Bard and coworkers [43–45], is illustrated in Fig. 12. It is similar to the in situ flat cell pioneered by Adams and coworkers [17]. It consists of a platinum mesh working electrode (1 mm grid size) placed in a flat cell, with a U-shaped tungsten rod counter electrode along the cell edges, and a silver wire quasi-reference electrode located in the flat cell above the working electrode. Unlike the Adams cell design, ohmic drop problems were removed by the location of all three electrodes within the EPR cavity for electrolyte solutions in DMF. However, a careful choice of supporting electrolyte was necessary;  $\text{ClO}_2^\bullet$  radicals may be produced at the counter electrode when reductions occurred at the working electrode in the presence of perchlorate background electrolytes. The use

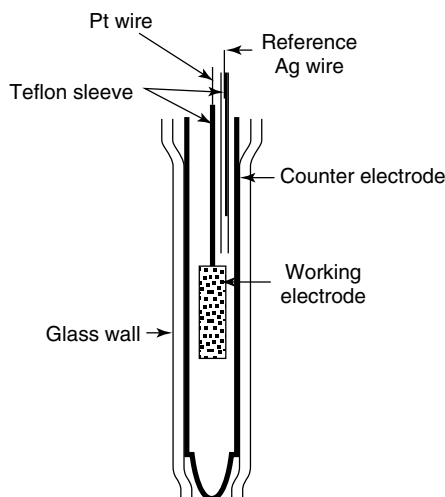


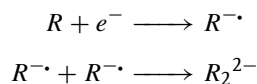
**Fig. 12** Schematic diagram of the Bard–Goldberg cell.

of tetrabutylammonium iodide as supporting electrolyte mitigated this problem, since nonparamagnetic iodine is formed at the counter electrode during reductions [43]. It was concluded that where radical formation is possible in this way, it might be necessary to add a nonradical producing electroactive substance so that the production of secondary radicals is prevented. Later work [45] confirmed these problems did indeed arise from radicals produced at the counter electrode.

**3.2.3.1.2 Typical Applications** Experiments performed with stable radical ions in DMF, such as those produced from the reduction of nitrobenzene, azobenzene, and 9,10-anthraquinone, indicated that the observed signal was stable for 20–30 s after generation by a current step, and after which natural convection set in, suggesting that kinetic measurements are possible from the magnitude of this constant steady state EPR signal, within the 20 s time limit [43].

It was further shown that the homogeneous kinetics of the radical ions produced electrochemically could be inferred from a current pulse experiment in which the EPR signal is measured during and following the current pulse. The signal transients were then analyzed in terms of working curves for first-order radical decomposition, second-order radical ion dimerization, and second-order radical ion-parent dimerization [44]. In this manner, the mechanism of the reduction of olefins was deduced, illustrated best by the dimerization of dimethyl fumarate radical anions. Analysis of the EPR signal transients generated by a current pulse yielded rate constants of  $160 \pm 26 \text{ dm}^3 \text{ mol}^{-1} \text{ s}^{-1}$  for radical-anion dimerization and  $50 \pm 30 \text{ dm}^3 \text{ mol}^{-1} \text{ s}^{-1}$  for radical anion-parent

dimerization [45]. Comparison of these data with the rate constants deduced from conventional cyclic voltammograms,  $160 \pm 40 \text{ dm}^3 \text{ mol}^{-1} \text{ s}^{-1}$  [45], suggesting that the mechanism is, in fact, a radical-anion dimerization,



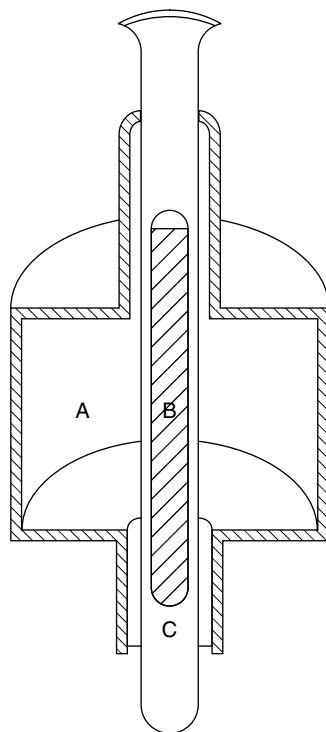
### 3.2.3.2 The Allendoerfer Cells

**3.2.3.2.1 Cell Design** Allendoerfer and coworkers [46–49] pioneered the electrochemical EPR cell design to exhibit maximum sensitivity to unstable radicals. These state-of-the-art in situ cells are probably the most sensitive for the detection of short-lived ( $\sim 10^{-5} \text{ s}$ ) paramagnetic intermediates. Two designs have emerged, one using a TE<sub>011</sub> cylindrical EPR cavity [46–48], the basis of which is illustrated in Fig. 13, and a cell based on a loop-gap resonator, Fig. 14 [49]. These designs and their applications to the study of radicals with small lifetimes are discussed in turn.

**3.2.3.2.2 The Coaxial Cell** The cylindrical TE<sub>011</sub> cavity is modified by centering a metallic rod along the axis of the cavity. A quartz cell contains this cylindrical metallic conductor, and the liquid sample is contained within the unfilled volume of the cell. For conventional EPR spectroscopy, the sensitivity of such a coaxial cavity was shown to be at least as good as that of a rectangular TE<sub>102</sub> cavity for lossy samples; but as an in situ cell for electrochemistry, a cell based upon the coaxial design exhibits greater sensitivity compared with in situ cells based upon the conventional EPR flat cell due to the significantly larger electrode area that can be accommodated when the



**Fig. 13** A schematic diagram of the Allendoerfer coaxial cell cavity design. A cross section of the  $TE_{011}$  cylindrical cavity (A) is shown. A metal cylinder (B) is located along the axis of the cavity within a silica sample tube (C).



central conductor of the coaxial cavity acts as the working electrode.

Initial experiments [47] involved a central conductor of 6 mm diameter and 50 mm length. One problem that arose was that the resonant frequency of the coaxial cavity was greater than the 9.0–9.8 GHz range of the employed klystron. To overcome this, the resonant frequency was lowered by surrounding the central metal rod with a material of suitable relative permittivity, such as Teflon<sup>(R)</sup>. It was shown that for a solid central conductor of good conductivity, the cavity  $Q$ -factor (a direct measurement of the EPR sensitivity) was not significantly different from that of the  $TE_{011}$  cavity employed.

To overcome some problems associated with using a solid central conductor, the inner part of the coaxial cavity was constructed from a finely wound shallow pitched helix, which stands freely against the inner wall of a quartz test tube (internal

diameter 6 mm). In this form, the standing microwave field “sees” only the portion of solution between the helix and the inner wall of the quartz tube and does not penetrate the inside of the helix, as shown

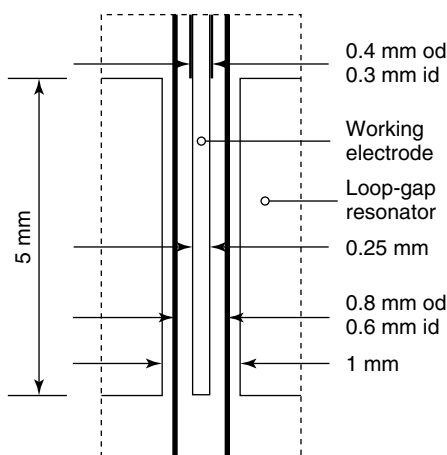


**Fig. 14** A schematic illustration of the active region of Allendoerfer's electrochemical loop-gap resonator geometry.

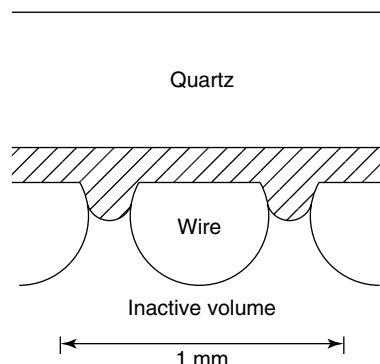


**Fig. 15** The EPR-visible part of the Allendoerfer coaxial cell is that between the wire helix and the quartz sample tube (shaded region). The inner part of the helix is free to house the reference and counter electrodes without interference with the EPR.

in Fig. 15. Since there is no penetration of microwaves within the helix, any material located here does not affect the EPR signal (or sensitivity), allowing the counter and reference electrodes to be placed here. The counter electrode is a platinum cylinder placed centrally along the cavity axis such that the current flow is radial, and so ensuring that there is a uniform current density over the whole cylindrical working-electrode surface. The uniform current density meant that potential control of the whole electrode can be achieved by monitoring a single point with a Luggin capillary.

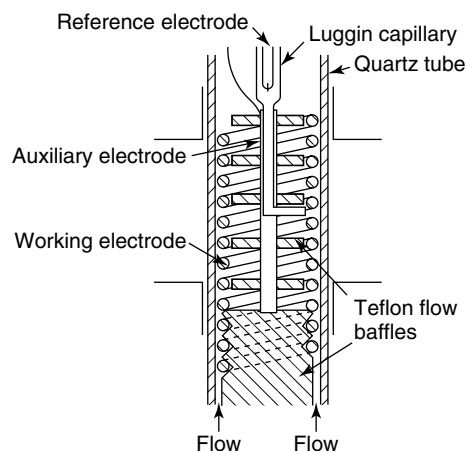
**3.2.3.2.3 Application** The surface area of the working electrode was estimated to be about  $22 \text{ cm}^2$ , significantly larger than in previous electrochemical EPR cell designs. The cell resistance was found to be  $13 \Omega$  when filled with  $0.1 \text{ M}$  tetrabutylammonium perchlorate in DMF [47], a value that compares favorably with the  $5\text{--}10 \text{ k}\Omega$  estimated by Bard and Goldberg [43] for an in situ cell based upon a conventional EPR flat cell. Electrochemical measurements made with this cell design were shown to be free from ohmic distortions, even when used with poorly conducting electrolytes, and that the cyclic voltammograms observed from

the in situ cell were indistinguishable from those obtained from normal polarographic cells, except for the large increase in current due to the large surface area. It was estimated that the uncompensated solution resistance was less than  $1 \Omega$ , even when highly resistive nonaqueous solvents were employed [47]. Radicals as short-lived as  $10^{-5} \text{ s}$  were anticipated to be amenable to study, providing a high concentration (approximately  $0.1 \text{ M}$ ) of electroactive material was used; in agreement with previous estimates [26] of the shortest-lived radical, it would be possible to study using in situ techniques.

A modification of the Allendoerfer cell has been described by Ohya-Nishiguchi and coworkers [50–52], whereby low-temperature studies were undertaken on the electrochemistry of twenty aromatic compounds. The low temperature was achieved by placing the electrolysis cell within a temperature control Dewar. However, it should be noted that this low-temperature in situ cell did not use a reference electrode.

In the study of short-lived radicals, the presence of efficient hydrodynamic flow is essential to sustain a constant supply of electroactive material to the working-electrode surface, and hence ensures a

**Fig. 16** The Allendoerfer–Carroll cell as modified to provide the capability for solution flow.



steady flux of radicals. Carroll adapted the Allendoerfer cell to this end [46, 48]. The changes to the helical arrangement are illustrated in Fig. 16. Solution is prevented from flowing into the central EPR inactive volume of the cell by a complex series of baffles. The value of flow coupled to the Allendoerfer cell was shown by the electroreduction of nitromethane in aqueous solutions; the radical anion of nitromethane was observed and this was shown to have a lifetime in the order of 10 ms. To date, this is the shortest radical lifetime observed by electrochemical EPR, although it has been calculated [50] that such a cell should be capable of observing radicals with lifetimes of  $10^{-5}$  s.

#### 3.2.3.2.4 The Loop-gap Resonator Cell

The loop-gap resonator was introduced into EPR spectroscopy by Froncisz and Hyde [53], who used an arrangement shown in Fig. 17. Its design and applications have been reviewed [54]. The loop behaves as an inductive element, whilst the gaps act as capacitive elements. It has been found [53] that increasing the number of gaps permits EPR spectroscopy to be undertaken on larger samples and at

higher frequencies. Loop-gap resonators have a number of advantages over conventional resonant cavities [53], notably their smaller size and greater observed signal intensity. For electrochemical purposes, these are beneficial; the former lead to smaller electrolysis currents and concomitantly less potential control problems, whilst the latter allows enhanced sensitivity on the basis of the total number of spins (that is spin concentration multiplied by sample volume), and is illustrated in Fig. 17 for the case of a small sample of  $\alpha, \alpha'$ -diphenyl- $\beta$ -picryl hydrazyl (DPPH).

Allendoerfer's loop-gap resonator cell design [49] is illustrated in Fig. 13. The working electrode comprises a gold wire (although a variety of other materials were also found to work equally as well) placed inside the active volume of the resonator; insertion into the resonator in this manner was found to have no deleterious effect, and little change in the resonator  $Q$ -factor. However, since the EPR active volume decreases, the energy density increases; hence, to avoid saturation, the microwave power must decrease. A platinum needle acted as the counter-electrode. For the purpose of generating

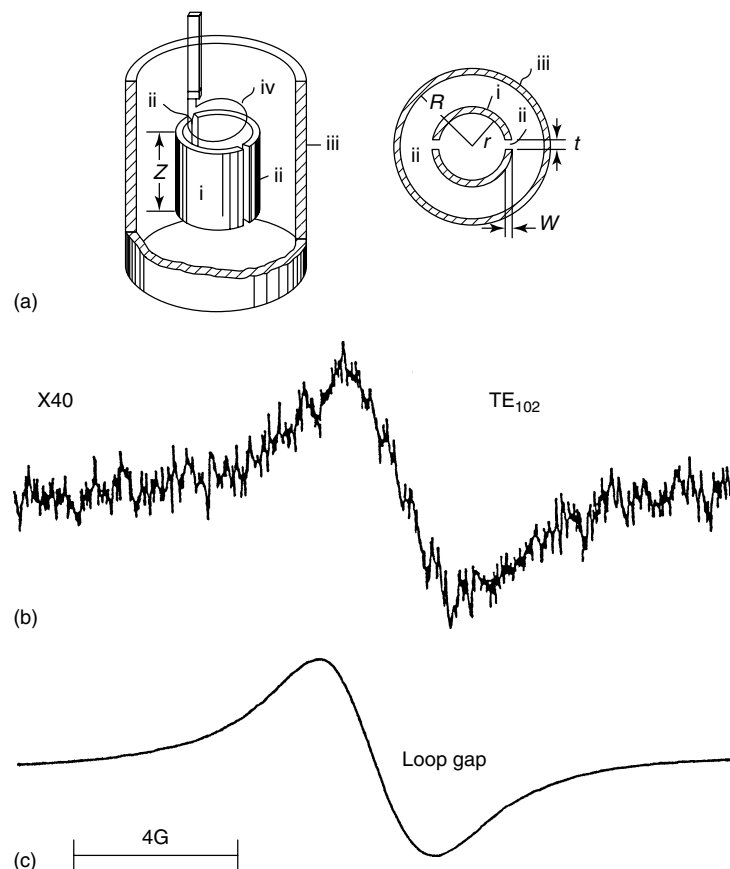


**Fig. 17** (a) The loop-gap resonator as used by Froncisz and Hyde. The principle components, (i) loop, (ii) gaps, (iii) shield, and (iv) inductive coupler are shown. The critical dimensions,  $Z$ , resonator length,  $r$ , resonator radius,  $R$ , shield radius,  $t$ , gap separation, and  $W$ , gap width are also indicated. The sample is inserted into the loop (i) through the coupler (iv). The microwave magnetic field in the loop is parallel to the axis of the loop and (b, c) Comparison of EPR spectra obtained of a point sample of DPPH measured at X-band in a rectangular  $TE_{102}$  cavity and in a loop-gap resonator of dimensions  $r = 0.6$  mm,  $Z = 5$  mm. The incident power was held constant at a low, nonsaturating level. The loop-gap resonator yields 37 times greater signal than the  $TE_{102}$  cavity.

radicals for EPR spectroscopy, this two-electrode arrangement was adequate, with the platinum electrode acting as a quasi-reference electrode in aqueous chloride. However, for the purposes of in situ electrochemical EPR, this arrangement was refined to accommodate a three-electrode

configuration employing a Ag|AgCl reference electrode.

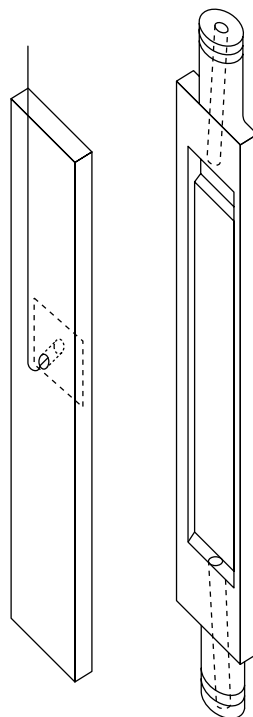
**3.2.3.2.5 Application** Allendoerfer and coworkers [49] observed the time-dependent formation and post electrolysis decay

**Fig. 18** Schematic illustration of the in situ channel flow cell.

of the dianion radical of *para*-nitrobenzoic acid in water at pH 11. It was found that the radical decay kinetics were not a simple function of pH or time.

### 3.2.3.3 The Channel Electrode Cell

**3.2.3.3.1 Cell Design** Compton and Coles designed a channel flow cell that could be used for in situ electrochemical EPR [55]. The design of this demountable flow cell, constructed in synthetic silica, is given in Fig. 18. A rectangular metal foil (such as platinum), cemented onto a silica plate, comprises the working electrode, with a fine lead out wire at the rear making the connection to the electrode. The whole cell is sealed together with a low-melting wax, which was found to be non-lossy. The cell is connected to Polytetrafluoroethane (PTFE) tubing for connection into a flow system, and is held within a TE<sub>102</sub> resonant cavity, accomplished by placing it inside a silica tube that runs right through the cavity and fixing its position with PTFE spacers. Movement of this supporting tube, which also serves to protect the cavity from any leakage, may finely adjust the cell position within the EPR cavity. Optimally, the cell is positioned at the point of maximum EPR sensitivity, which corresponds to the center of the EPR cavity, with the plane of the electrode parallel to the electric component of the microwaves standing wave. For an empty cell without electrode, the cavity *Q*-factor is 6400, which is lowered to 2500 when filled with an aqueous 0.1 M electrolytic solution. An empty cell with an electrode present has a *Q*-value of 4600, confirming that microwave losses due to the lead out wire are



acceptably low, whilst the *Q*-value when this cell is filled as before is 1200 – a value that is typically observed for conventional aqueous sample EPR methods.

The flow system used in conjunction with the channel unit is capable of a variable laminar flow, established by having a Reynolds Number,  $Re < 10^2$  (see Volume 2, chapter 2.2 (by Fisher), or equally Volume 3, chapter 3.5 (by Mount).), employing flow rates in the range  $10^{-4}$  to  $10^{-1} \text{ cm}^3 \text{ s}^{-1}$ , achieved using a gravity-fed system (so as to avoid variation in pumping pressure [56]) together with capillaries of different diameters and changes in reservoir height. A platinum gauze counter electrode is placed downstream of the working electrode and a saturated calomel or Ag|AgCl reference electrode upstream, both outside the cavity. The flow within the channel cell is parabolic, provided that there is a sufficiently long lead-in,

that is if the lead-in length is given by  $0.1 \times h \times Re$ , where  $h$  is the half-height of the channel [57]. This was verified experimentally by the observation of plug flow using a colored solution [55]. Edge effects were found to be negligible if the electrode size is less than 4 mm wide in a 6-mm channel. Further, because of the electrolyte resistance in the narrow gap through which solution flows [58], the potential may be slightly non-uniform [23, 59]. This effect may be anticipated to perturb the current density unless the distance over which radicals are formed is small compared with the total distance over which radicals are detected, thereby encouraging the use of small electrodes.

**3.2.3.3.2 Application** Channel electrodes have well-defined hydrodynamic properties [57], and the laminar flow convective-diffusion equation describing the mass transport regime (see Chapter 2.2 of this volume) within this cell at steady state for large electrodes is given by [60, 61]

$$D \frac{\partial^2 c(x, y)}{\partial y^2} - v_x \frac{\partial c(x, y)}{\partial x} = 0 \quad (22)$$

where  $D$  is the diffusion coefficient of the electroactive species,  $c(x, y)$  its concentration,  $x$ , the distance along the channel starting from the upstream edge of the electrode,  $y$  the distance normal to the electrode starting from the electrode surface, and  $v_x$ , the velocity of the solution in the  $x$ -direction. Equation (22) reflects the effects of convection in the direction of flow and diffusion in a direction ( $y$ ) perpendicular to this. Diffusion in the direction of flow can be shown [62] to be negligible for the case of macroelectrodes, although this is not the case for microelectrodes [63]. Since the velocity profile is parabolic,

$$v_x = v_0 \left( 1 - \frac{(h - y)^2}{h^2} \right) \quad (23)$$

where  $v_0$  is the mean solution velocity at the center of the channel. The velocity profile may be simplified for the case of macroelectrodes by employing the L  v  que Approximation [64],  $(y/2h) \ll 1$ , yielding,

$$v_x \approx 2v_0 \frac{y}{h} \quad (24)$$

Using this linearized form of the velocity parabola, the Levich equation [57] can be deduced for the case of a chemically and kinetically uncomplicated electron-transfer process,

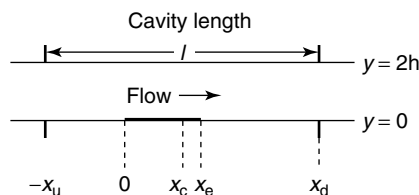
$$i_{\text{lim}} = 0.925nFc_{\text{bulk}}D^{2/3}V_f^{1/3} \times (h^2d)^{-1/3}wx_e^{2/3} \quad (25)$$

where  $d$  is the channel width,  $w$  is the electrode width,  $x_e$  is the electrode length, and  $V_f (= 4v_0dh/3)$  is the volume flow rate.

Two electrochemical EPR methodologies may be envisaged using a channel flow cell for the determination of kinetic and mechanism of radical decay. First is the measurement of the steady state EPR signal as a function of the electrode current and flow rate, and using variable flow rates to probe the radical lifetimes. Alternatively, if the electrogenerated radical is unstable, transient EPR signals may be recorded (at constant magnetic field induction) when the working electrode is open-circuited, after a steady state has been achieved. These are considered in turn for the case of a radical reacting via first-order kinetics. Physical application of these methods is reserved until later, Sect. 3.2.4.

For the steady state case, the EPR signal intensity,  $S$ , can be calculated by convoluting the  $\sin^2$  sensitivity of the cavity with the number of spins. Figure 19

**Fig. 19** The coordinate system defining the location of the channel electrode in the EPR cavity.



shows the coordinate system defining the position of the electrode relative to the EPR cavity.  $x_c$  denotes the center of the cavity and  $x = 0$  is the position of the upstream edge of the electrode. The cavity length,  $l = x_u + x_d$ , where  $-x_u$  and  $x_d$  denote the  $x$ -coordinates of the upstream and downstream edges of the cavity, respectively. Thus,  $x_c = x_d - l$ , where  $l$  is typically 24 mm and  $x_c$  is 15 mm. The  $\sin^2$  sensitivity profile allows maximum sensitivity at the center of the cavity ( $x = x_c$ ), whilst the sensitivity at the cavity edges ( $-x_u$  and  $x_d$ ) is effectively zero. Thus, integrating the spins throughout the cavity,

$$S = S_0 \int_{-x_u}^{x_d} \sin^2 \left[ \frac{(x - x_c)\pi}{\ell} \right] \times \left( \int_0^{2h} c(x, y) dy \right) dx \quad (26)$$

where  $S_0$  is the signal due to one mole of the EPR active species located at the center of the cavity, and the concentration of the paramagnetic species can be deduced from Eq. (22). Since the radical species is generated at the electrode, the integral can be shortened to

$$S = S_0 \int_0^{x_d} \sin^2 \left[ \frac{(x - x_c)\pi}{\ell} \right] \times \left( \int_0^{2h} c(x, y) dy \right) dx \quad (27)$$

This equation can be solved either analytically [55, 58] or numerically [65–68] using the Backward Implicit approach [69–71] for the case of macroelectrodes at steady

state to yield a current|EPR signal|flow rate relationship for two cases. First, where there is uniform concentration of radical at the electrode surface, and second, where there is a uniform current density at the electrode. The first case holds at all points on a reversible voltammetric wave and for an irreversible wave if the current is diffusion-limited; the second case holds near the foot of an irreversible wave. In both cases, it was found that the steady state EPR signal for a stable radical followed the following dependence upon the mass transport-limiting current and flow rate,

$$S \propto \frac{i}{V_f^{2/3}} \quad (28)$$

This dependence was experimentally verified for the case of the reduction of fluorescein to the semifluorescein radical anion [55]. For electrogenerated radicals that subsequently decay by first-order kinetics, the dependence of  $S$  upon the rate constant of the decay,  $k$ , is most conveniently expressed in terms of an EPR detection efficiency,  $M_K$ , given by

$$M_K = \frac{SV_f^{2/3}}{i} \quad (29)$$

where  $K$  is the normalized rate constant for the radical decay,

$$K = k \left( \frac{4h^4 \ell^2 d^2}{9V_f^2 D} \right)^{1/3} \quad (30)$$

For a stable radical,  $M_0$  is constant. Figure 20 shows how the ratio  $M_K/M_0$

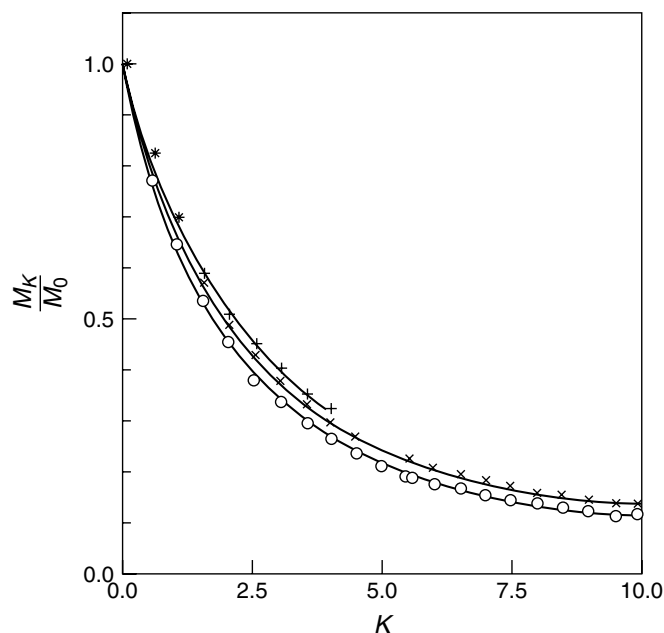


**Fig. 20** The variation of the EPR detection efficiency,  $M_K$ , with the normalized rate constant,  $K$ , for different sized electrodes (+, 2 mm; ×, 3 mm; O, 4 mm) located centrally in the cavity.

varies with  $K$  for an electrode positioned at the center of the EPR cavity for electrodes of practical dimensions. In these cases, the EPR signal and the Faradaic current are measured experimentally, for a range of flow rates, permitting the inference of  $K$  from the appropriate value of  $M_K$  in the working curve (Fig. 20). It follows from the definition of the normalized rate constant that a plot of  $K$  against  $V_f^{-2/3}$  allows the deduction of the rate constant for the decay process,  $k$ .

In Fig. 21, the quantity  $M_K$  is normalized with respect to the value  $M_K^{\text{ref}}$  obtained when the electrode is located at the cavity center. This figure describes the EPR signal dependence upon location of a 5 mm electrode within the EPR cavity. For high rate constants ( $K \geq 5.0$ ), the signal follows the  $\sin^2$  sensitivity profile of the

EPR cavity, since all the radicals are found adjacent to the electrode surface and decay before they can be transported away from the electrode; in contrast, at lower rates of decay, the curve deviates from  $\sin^2$  behavior, and a maximum is observed upstream of the cavity center. Hence, although the highest radical concentration is at the electrode surface, by generating radicals above the maximum sensitivity, a greater number of radicals occupy the EPR active area.

Attention is now turned to the use of EPR signal transients in the deduction of radical decay kinetics. The transient signals may be experimentally observed (at constant magnetic field induction) by either open-circuiting an electrode that had been previously held at a potential at which Faradaic processes occur, or



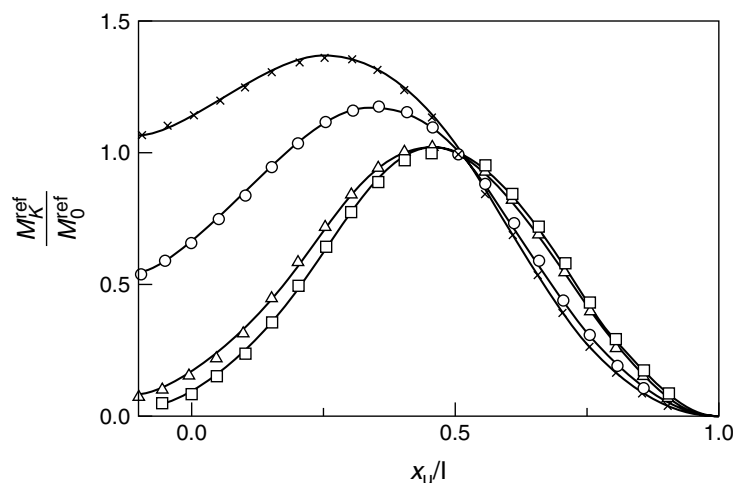


**Fig. 21** The variation of  $M_K^{\text{ref}}/M_0^{\text{ref}}$  for a 5 mm electrode with position of the electrode in the cavity for different rate constants ( $K = 0.0$ ,  $\times$ ;  $K = 1.0$ ,  $O$ ;  $K = 5.0$ ,  $\Delta$ ;  $K = 7.5$ ,  $\square$ ).

by stepping the potential between two defined values. The former method is normally adopted, since in the latter method, contributions to the radical decay may occur from, for example, the reoxidation of a radical-anion if it is generated by an electrochemically reversible reduction. Theory describing the transient EPR signals associated with the growth (when the current is stepped up from zero) or decay (when the current is stepped down to zero) of the electrogenerated radical upon a galvanostatic step at the working electrode, for first-order kinetics is given elsewhere [72]. For macroscopic electrodes, the relevant convective-diffusion equation is

$$\frac{\partial C(x, y)}{\partial t} = D \frac{\partial^2 C(x, y)}{\partial y^2} - v_x \frac{\partial C(x, y)}{\partial x} - kC(x, y) \quad (31)$$

where  $k$  is the first-order rate constant. The temporal EPR signal for a growth transient can be shown to be,

$$S(\tau) = S(\tau \rightarrow \infty)$$

$$\frac{1}{p} \sum_{n=0}^{\infty} \frac{b_n (K + p)^n J_n}{\Gamma\left(\frac{2n}{3} + \frac{5}{3}\right)} \times \mathbf{L}^{-1} \frac{\sum_{n=0}^{\infty} \frac{b_n K^n J_n}{\Gamma\left(\frac{2n}{3} + \frac{5}{3}\right)}}{\quad} \quad (32)$$

in which  $\tau$  is the normalized time variable,

$$\tau = t \left( \frac{9V_f^{2/3} D}{4h^4 d^2 \ell^2} \right)^{1/3} \quad (33)$$

$\mathbf{L}^{-1}$  represents the inverse Laplace Transformation (variable  $p$ ), and  $\Gamma(x)$  is the Gamma function [73]. The coefficients  $b_n$  are given by

$$b_n = \frac{3^{(n-2)/3}}{\pi} \sum_{n=0}^{\infty} \frac{\Gamma\left(\frac{1}{3}n + \frac{1}{3}\right)}{n!} \times \sin \left\{ \frac{2}{3}(n+1)\pi \right\} \quad (34)$$

and  $J_n$  are given by the expression

$$J_n = \int_0^{x_d} \sin^2 \left[ \pi \left( \frac{x - x_u}{\ell} \right) \right] \times \left[ \left( \frac{x}{\ell} \right)^{2(n+1)/3} - \left( \frac{x - x_e}{\ell} \right)^{2(n+1)/3} \right] \times U \left( \frac{x - x_e}{\ell} \right) d \left( \frac{x}{\ell} \right) \quad (35)$$

where  $U(x)$  is the unit step function.

Theoretical growth transients for various values of normalized rate constant are shown in Fig. 22 for an electrode located at the cavity center. For fast mass transport (or sluggish kinetics), the transient is governed by both the mass transport of material throughout the cavity and by the kinetic decay or the growth of the radical. As the normalized rate constant,  $K$ , increases (or as the mass transport decreases), the time taken for the transient to reach a steady state value decreases, and the transient changes shape until they attain a simple exponential form, which

for a decay transient is

$$S(t) = S(t = 0) \exp(-kt) \quad (36)$$

This can be rationalized on the basis of the decay within a convection-free “reaction layer” immediately adjacent to the electrode surface: the paramagnetic species are assumed to decay before they can diffuse sufficiently far from the electrode for them to experience a significant amount of transport by convection. Experimental transients obtained from the reduction of fluorescein to the semifluorescein radical anion, and from the reduction of 2-nitropropane verified these results [58, 72, 74].

This cell has been applied successfully for in situ electrochemical EPR, deducing both kinetics and reaction mechanisms, for radicals with lifetimes typically in the range 10 to 100 ms: Sect. 3.2.4 will examine its application to ECE [58], DISP1 [74], EC' [68], and comproportionation reaction mechanisms [75–77]. Other applications include the study of an ECEEE mechanism

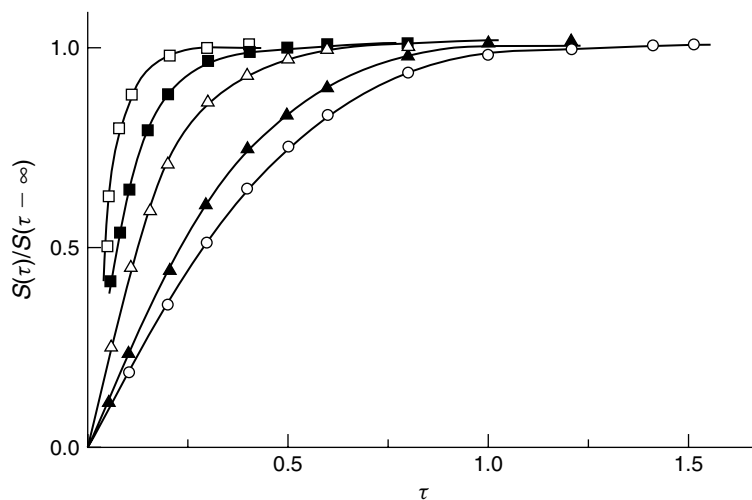


**Fig. 22** Calculated transients for a 4 mm electrode located at the cavity center for different values of  $K$  ( $K = 0.0$ ,  $\circ$ ;  $K = 0.1$ ,  $\blacktriangle$ ;  $K = 1.0$ ,  $\triangle$ ;  $K = 10.0$ ,  $\blacksquare$ ;  $K = 20.0$ ,  $\square$ ).

for the reduction of nitromethane in aqueous alkaline solution [78]. One last point to note is that since the cell is constructed of a transparent substance, silica, illumination of the electrode is possible, permitting photoelectrochemical EPR [55, 65–67, 79–81].

### 3.2.3.4 The Albery In Situ Tube Electrode Cell

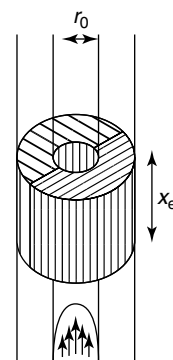
**3.2.3.4.1 Cell Design** Albery and coworkers [9–14] used tubular electrodes for ex situ electrochemical EPR experiments. The tubular electrode is equivalent to the channel electrode in all respects, except that the cross section is circular rather than rectangular [82, 137]. Like the later-developed channel flow cell, this setup (shown in Fig. 23) permits the interrogation of electrode reaction mechanisms of relatively long-lived radical species, [9–14] since the convective-diffusion equations are mathematically well defined, which at steady state are given by Eq. (37)

$$v_0 \left[ 1 - \left( \frac{r}{r_0} \right)^2 \right] \frac{\partial c}{\partial x} = D \left( \frac{\partial^2 c}{\partial r^2} + \frac{1}{r} \frac{\partial c}{\partial r} \right) \quad (37)$$

where  $v_0$  is the velocity of flow at the center of the tube,  $r_0$  is the radius of the tube,  $r$  is the radial distance from the center of the

tube,  $x$  is the distance down the tube,  $D$  is the diffusion coefficient of the species generated on the electrode, and  $c$  is its concentration. However, recognizing that an “ideal” electrochemical cell for both kinetic and mechanistic studies is of an in situ design with the electrode located within the EPR cavity for maximum sensitivity, with well-defined and calculable flow, experiments were undertaken using an in situ tubular electrode [83]. Figure 24 shows how the sensitivity of a standard rectangular TE<sub>102</sub> cavity to radicals varies with distance through the EPR cavity ( $\ell$ ). With the tube electrode outside the cavity (Curve a), the expected  $\sin^2$  dependence is observed [35]; moving the tube electrode into the cavity (Curve b) effects not only a lower sensitivity, but also a grossly distorted  $\sin^2$  curve. Furthermore, the sensitivity is negligible in the vicinity of the electrode, irrespective of the placement of the latter within the cavity. It was found that the sensitivity of the EPR cavity is not distorted if the tube electrode is replaced by a semiannular tube, as shown in Fig. 24 (Curve c). With the semiannular tube electrode positioned centrally within the EPR cavity, the expected  $\sin^2$  sensitivity profile is observed with the electrode centered at the maximum in the sensitivity curve,

**Fig. 23** The semiannular tube electrode as used by Albery and coworkers. The fine-hatched segment is made of platinum and the course-hatched segment of Teflon™. The parabolic velocity profile is shown. Typical dimensions are radius,  $r_0 = 0.5$  mm and the electrode length,  $x_e = 2.0$  mm.



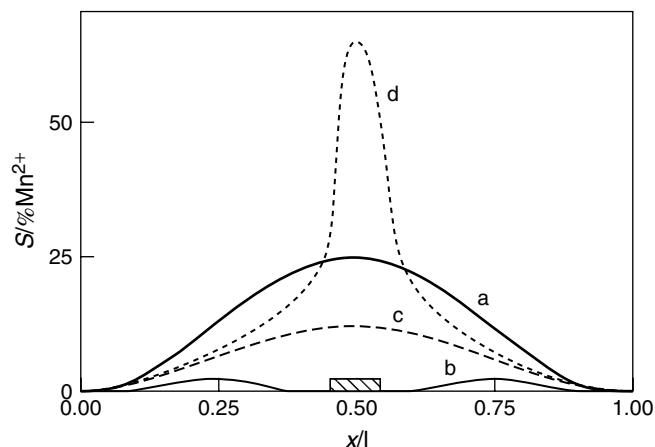


**Fig. 24** Variation of the sensitivity of the cavity with distance through the cavity. Curve a is obtained with no electrode inside the cavity; Curve b is obtained with a tube electrode consisting of a complete annulus at the cavity center. Curves c and d are obtained with an electrode at the center of the cavity consisting of a half annulus and an annulus with a missing sector, respectively.

albeit reduced by a factor of two, but nevertheless adequate for EPR measurements. Curve d in Fig. 24 shows the sensitivity when an annular electrode with a sector subtending  $10^\circ$  has been removed. The  $\sin^2$  function is now distorted, but the sensitivity at the electrode is enhanced by a factor of three when compared to Curve a. The difference between a complete annular electrode and a part-annular one is that in the former, the magnetic component of the standing microwave field induces eddy currents in the complete circle and therefore is unable to penetrate to the electrolyte solution. These eddy currents are minimized using an incomplete annulus. In the case of the semiannular electrode, there is a greater loss of sensitivity, but the standing microwave field is preserved.

**3.2.3.4.2 Application** For a semiannular tubular electrode, the limiting current is given by the appropriate form of the Levich

equation [10],

$$i_{\text{lim}} = 2.75nFD^{2/3}x_e^{2/3}V_f^{1/3}c_{\text{bulk}} \quad (38)$$

in which  $x_e$  is the electrode length and  $V_f$  the volume flow rate. Equation (38) was verified by experimental observations on the oxidation of *N,N,N',N'*-tetramethyl-*para*-phenylene diamine (TMPD) in aqueous sulfate solution. The diffusion coefficient calculated from these data was in agreement with literature values, showing the semiannular tube electrode to be a satisfactory hydrodynamic electrode.

As with the channel electrode cell, and following from the previous work undertaken using the *ex situ* tube electrode arrangement, the EPR signal ( $S$ ) is a function of the diffusion-limited current ( $i$ ) and the volume flow rate,

$$S = S_0 I_{x/\ell} (\ell - x_e)^{2/3} r_0^2 \frac{i}{nFD^{1/3}V_f^{2/3}} \quad (39)$$

where  $S_0$  is the EPR signal from one mole of spins at the center of the cavity, and  $I_{x/\ell}$  is a numerical factor that arises from convoluting the concentration profile with the sensitivity of the cavity; for the electrode just outside the cavity,  $I_0 = 0.53$ , while when the electrode is at the cavity center,  $I_{1/2} = 0.47$ . Experimental results, for the study of radicals in the coats of modified electrodes [83, 84], verified the predicted  $S \propto i/V_f^{2/3}$  dependence, suggesting that like the channel electrode EPR flow cell, this in situ cell is easily amenable to the study of electrode reaction mechanisms. However, it suffers from several disadvantages when compared to the channel cell. First, the Albery cell is not readily demounted, making examination and polishing of the electrode difficult. Second, it is uncertain whether eddy currents are induced in the electrode by the 100 kHz modulation, rendering areas of the electrode EPR-insensitive. Third, the channel electrode does not suffer as large an ohmic drop. Fourth, irradiation of the electrode is not possible, rendering this in situ cell inadequate in the study of photoelectrochemical phenomena.

### 3.2.3.5 The In Situ Coaxial Flow Cell

**3.2.3.5.1 Cell Design** Waller and Compton [85] effectively mimicked the Allendoerfer coaxial design (*vide supra*), whilst simultaneously maintaining the mathematically well-defined laminar flow of the channel flow cell. This improved cell for electrochemical EPR [85] allowed an improvement in the channel cell regarding lifetimes of radicals amenable to study, whilst retaining the hydrodynamic flow that is essential for the investigation of electrode reaction mechanisms.

The cell itself (see Fig. 25) comprises a TE<sub>011</sub> cylindrical cavity that is converted into a coaxial cavity by the addition of a smooth, polished copper rod that is positioned centrally within the cavity. The rod itself (diameter 9 mm) is located within a precision-bore silica tube, so that there is an annulus (of size  $2h$ ) around the rod, constrained to be of uniform thickness by a fine nylon thread running the length of the cavity. Typically  $2h \sim 100 \mu\text{m}$ , but this is adjustable by polishing the rod. The central 4 mm of the copper rod is insulated from the rest of the rod, as this part is the working electrode. To ensure a large negative potential window, this central part of the rod was plated with mercury. As in the case of the channel cell, this cell was connected to a reservoir-fed gravity flow system, with a platinum gauze counter electrode located outside the cavity and sufficiently away downstream so as to preclude counter electrode products from diffusing into the cavity, and an upstream reference electrode. Electrolyte solutions flow through the annular gap between the copper rod and the silica tube. Flow rates within the ranges  $10^{-4}$  to  $10^{-1} \text{ cm}^3 \text{ s}^{-1}$  were obtained in this manner. Since the flow pathway is narrow and resistive, the potentiostat was modified so as to provide high voltages to drive the current through the channel. Electrolyte resistance in the narrow gap through which the solution flows may lead to a non-uniform potential difference (*vide supra*), affecting the voltammetry only in poorly conducting nonaqueous solutions using low currents.

Like the Allendoerfer coaxial cells (*vide supra*), it was found that the resonant frequency of the cavity shifted above that of the empty cavity and outside the klystron tuning range as a result of the reduced effective cavity size produced by the addition of the copper rod. As

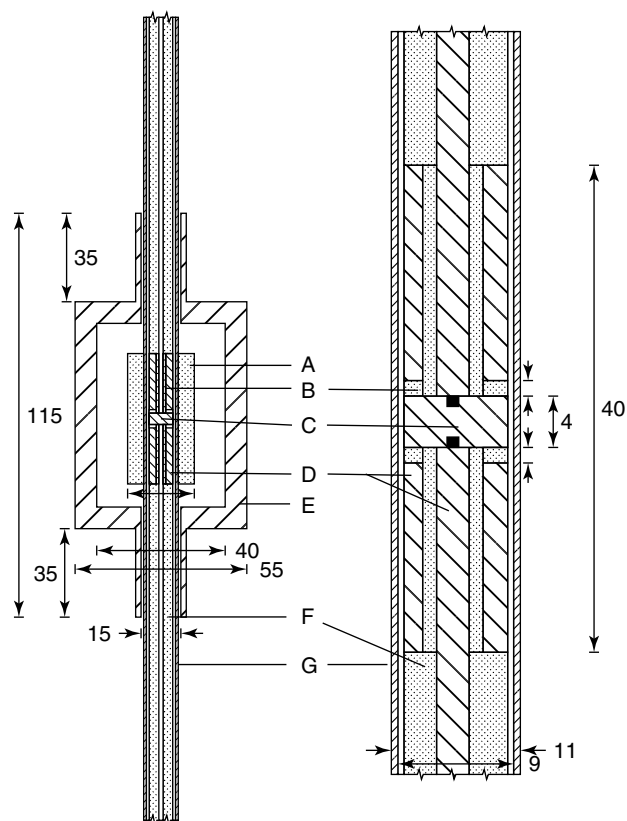


**Fig. 25** The in situ coaxial electrochemical EPR cell. A, Teflon™ annulus, B, Teflon™ insulator, C, mercury-plated copper electrode, D, copper, E, TE<sub>011</sub> cylindrical cavity, F, Teflon™ sheath, G, precision-bore silica tubing. The numbers shown represent the dimensions in mm.

above, this problem was eliminated by partially filling the cavity with a material of appropriate relative permittivity (such as a PTFE shielding around the silica tubing), shifting the resonant frequency back to typically 9.4 GHz.

The sensitivity of this modified cavity, as observed with a small crystal of DPPH, was found to follow a  $\sin^2$  function along the length of the cavity and at a fixed distance from the copper rod, as anticipated theoretically [35]. However, the EPR sensitivity was observed to vary in a  $\cos^2$  manner

around the copper rod at a fixed distance from the cavity. Since the cylindrical cavity sets up cylindrically symmetric standing microwave field patterns, this behavior can only be rationalized by a perturbation of the component of the magnetic field that is modulated at 100 kHz, caused by eddy currents induced in the copper rod by the 100 kHz component. Lenz's Law requires the induced magnetic field to oppose the applied field, and this effect is maximally observed when the applied field is perpendicular to the copper surface, and zero

when it is parallel to the copper surface. This  $\cos^2$  variation in sensitivity has also been observed in the Allendoerfer coaxial cell [46, 48]. This effect inevitably means that paramagnetic species will experience different amplitudes of the modulated field depending upon their location within the cell. However, it was shown that this will reduce the EPR signal by only a factor of one half from that which would be otherwise seen.

**3.2.3.5.2 Application** Laminar flow was established using flow rates such that the Reynolds Number,  $Re < 10$ . Thus, after sufficient lead-in (specifically  $0.1 \times Re \times h$ ), which in this case is negligible, a parabolic velocity profile develops across the flow-path. In this manner, the hydrodynamics of this electrochemical setup are equivalent to that of the channel electrode flow system; the mass transport-limiting current is therefore given by the Levich equation [86],

$$i_{\text{lim}} = 0.7767nF c_{\text{bulk}} D^{2/3} v_0^{1/3} h^{-1/3} \sigma x_e^{2/3} \quad (40)$$

in which  $\sigma$  is the circumference of the electrode,  $v_0$  is the mean solution velocity,

$x_e$  is the electrode length,  $D$  is the diffusion coefficient of the electrochemically active species, and  $n$  is the number of electrons transferred per mole reactant during the electrode reaction. The applicability of this equation was tested using the known one-electron reduction of fluorescein in aqueous alkali, to yield the semifluorescein radical anion, and it was found that the well-defined current|potential curves observed gave rise to linear Tafel plots, with the expected room temperature value of 59 mV decade<sup>-1</sup> slope. A linear Levich plot allowed inference of a diffusion coefficient of  $3.0 \times 10^{-6} \text{ cm}^2 \text{ s}^{-1}$ , in agreement with literature values [87]. Thus, the hydrodynamics of this particular flow cell are such that there is the expected parabolic, laminar flow.

Since the hydrodynamics are analogous to those experienced in the channel flow cell, it follows that steady state EPR signals should behave analogously, that is,

$$S \propto \frac{i}{V_f^{2/3}} \quad (41)$$

This equation should hold, providing the diffusion-layer thickness at the electrode is small when compared to the thickness of the flow-path. Figure 26 shows data

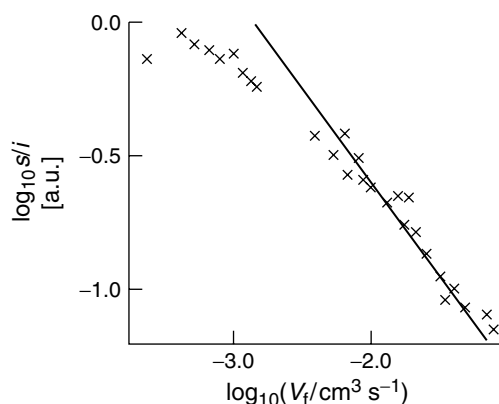


**Fig. 26** Steady state EPR signal|current|flow rate data.

obtained from the fluorescein system plotted according to Eq. (41). A straight line is observed for a wide range of flow rates; the line drawn has a gradient of  $-2/3$ , as predicted by the assumed theory. The deviation at low flow rates is entirely due to the diffusion layer becoming comparable in size to  $h$ ; less radical is produced than is predicted by assuming a wide channel [70, 89]. Hence at sufficiently slow flow rates, there is near-exhaustive electrolysis, and the cell behaves as a thin-layer cell [88], in which the current is given by

$$i = \frac{4}{3} n F v_0 h \sigma c_{\text{bulk}} \quad (42)$$

The full transition between the two limits has been calculated [70, 89] and corresponds to a flow rate of  $10^{-3} \text{ cm}^3 \text{ s}^{-1}$  for  $x_e = 4 \text{ mm}$  and  $2h = 100 \mu\text{m}$ . The EPR signal will be more sensitive to these effects than the observed current, since the EPR signal reflects the concentration of radicals throughout the channel, not merely the concentration gradient at the electrode surface.

### 3.2.3.6 The Bond In Situ Microelectrode Cell

**3.2.3.6.1 Cell Design** Bond and coworkers have designed various cells suitable for in situ electrochemical EPR [90–94]. These cells generally have a small volume and permit the recording of variable temperature EPR. In this section, only the most recently designed cell [94] will be discussed.

Figure 27 illustrates the all-glass cell used for electrochemical EPR over a wide temperature range. The reference electrode (either an Ag|AgCl or platinum) is fixed in the center of a Pt working-electrode coil, the latter extending to the bottom of the quartz tube. These electrodes have diameters of less than  $70 \mu\text{m}$ , so as to minimize the amount of metal present in the EPR cavity; the counter electrode is situated 15 mm above the working electrode outside the cavity, also permitting interference-free measurements from species diffusing from the counter electrode during electrolysis. With this design,

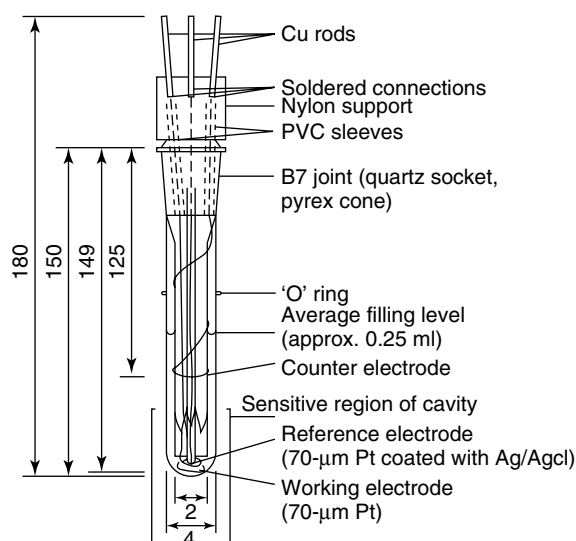


**Fig. 27** Schematic diagram of the in situ Bond cell for microelectrodes. All lengths are given in mm.



only a small volume of solution may be placed into the bottom of the cell, typically  $0.2\text{ cm}^3$ , allowing even lossy solvents to be used in electrochemical EPR work. Furthermore, by allowing complete sample handling under an inert atmosphere, the cell facilitates the study of electrochemically generated radicals that are highly oxygen and/or moisture sensitive. Furthermore, it was observed that this cell has a low  $RC$  time constant, making fast scan cyclic voltammetry viable [94].

**3.2.3.6.2 Application** This cell has been used for a variety of studies such as the oxidation of  $\text{Cr}(\text{CO})_2(\text{Ph}_2\text{PCH}_2\text{CH}_2\text{PPh}_2)_2$  [94], the reduction of  $[\text{Cp}_2\text{Ti}(\text{acac})]\text{ClO}_4$  ( $\text{Cp} = \eta^5\text{-C}_5\text{H}_5$ ,  $\text{acac} = \text{acetylacetone}$ ) [94], dipropylpyridine-3,4-dicarboxylate [95], and *S,S*-dipropylbenzene-1,3-dicarbothioate [95]. Generally, good voltammetric curves were obtained at room temperature, but these were often distorted at low temperatures (typically 180 K), possibly due to  $iR$  drop or due to the onset of thin-layer electrochemistry [94].

This cell has been recently compared with the channel flow cell [96]. Although the Bond cell has many advantages, its major limitation is that it does not permit the direct interrogation of electrode reaction mechanisms through the EPR signal in an analogous way to that by Compton and Coles (*vide supra*). Furthermore, the channel electrode cell is much more sensitive in detecting paramagnetic species than this cell by some orders of magnitude [96].

### 3.2.3.7 The In Situ Wall-jet Electrode Cell

**3.2.3.7.1 Cell Design** As described in Chapter 2.2 of this volume, a wall-jet electrode is a well-defined hydrodynamic electrode in which the convective mass

transport is the flow due to a jet of electrolyte striking a planar electrode surface at right angles, and rapidly spreads out over the electrode surface, the flow outside the jet being at rest [97]. Like the channel electrode, the wall-jet electrode is a non-uniformly accessible electrode, that is, the diffusion layer is not constant over the working electrode surface, making this electrode geometry successful in mechanistic discrimination [56].

The wall-jet electrode for in situ electrochemical EPR [98] is shown in Fig. 28. This arrangement is in fact a refinement to an in situ cell designed by Scholz and coworkers Fig. 29 [93], in which a jet of electrolyte impinges on a wire or mercury drop electrode. The modifications by Compton and coworkers [98] allow for controlled convection and enhancement of its sensitivity towards unstable radicals. The cell itself consists of a silica tube with a mercury working electrode placed at one end. Solution flows into the cell via the steel jet so that it impinges normally and centrally on the electrode surface. The system was connected to a gravity-fed flow system, with a silver or platinum pseudo-reference electrode positioned upstream of the mercury electrode and a platinum gauze counterelectrode located downstream of the cell.

The sensitivity profile of the cavity to radicals with the wall-jet cell placed along the vertical axis of the cavity, corresponding to a node in the electric component of the standing microwave field, with the working electrode surface at the cavity center, exhibited little distortion from the theoretically predicted  $\sin^2$  behavior, even though large amounts of metal (mercury and copper) are present. Measurement of the cavity  $Q$ -factor when the wall-jet cell containing acetonitrile and 0.5 M tetrabutylammonium perchlorate supporting electrolyte

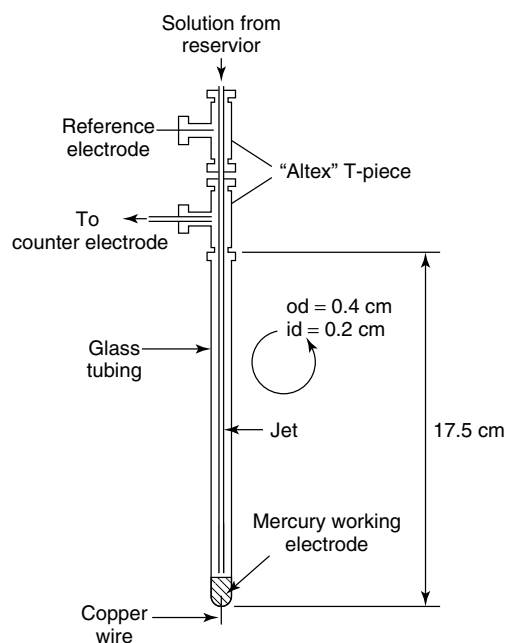
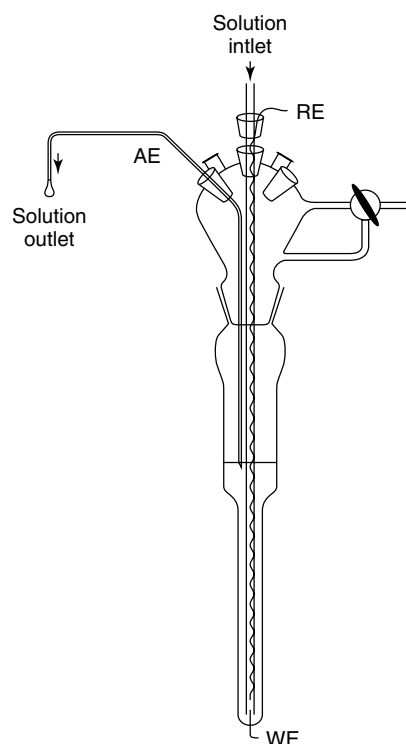


**Fig. 28** Schematic illustration of the in situ wall-jet EPR cell.



were present in the EPR cavity, revealed  $Q = 1000$ , which is a comparable value to that for the channel cell (*vide supra*).

**3.2.3.7.2 Application** Albery [99] and Matsuda [100] have derived an approximate equation for the mass transport-limited current for an  $n$ -electron transfer reaction at a wall-jet electrode,

$$i_{\text{lim}} = 1.59k_c n F D^{2/3} \nu^{-5/12} V_f^{3/4} \times a^{-1/2} R^{3/4} c_{\text{bulk}} \quad (43)$$

in which  $k_c$  is a constant determined by experiment to be close to 0.90 [99–101],  $\nu$  is the kinematic viscosity,  $a$  is the diameter of the jet, and  $R$  is the radius of the electrode. Analysis of the well-defined voltammograms for the reduction

**Fig. 29** Schematic of the Scholz design electrochemical EPR cell for use with flowing solutions.

of 1,4-benzoquinone in acetonitrile in terms of Eq. (43), by plotting  $i_{\text{lim}}$  against  $V_f^{3/4}$  revealed a straight line, and gave a diffusion coefficient in good agreement with literature values, indicating that the hydrodynamics of this cell are well defined and understood.

It has been seen that the other in situ hydrodynamic cells discussed above, the channel electrode cell and the tube electrode cell, both exhibit EPR signal ( $S$ ) characteristics dependent upon the ratio  $i/V_f^{2/3}$ . However, in the case of the wall-jet electrode under steady state conditions, in which the entire cell downstream of the working electrode is filled with radicals, the rate of loss of radicals from the cell is proportional to  $V_f$ , while the rate of their formation is proportional to  $i$ , thereby anticipating

$$S \propto \frac{i}{V_f} \quad (44)$$

This relationship was verified experimentally for the benzoquinone/acetonitrile system. The EPR signals were observed with excellent signal-to-noise ratio.

Analogous experiments in aqueous solutions gave similar responses. These present a more stringent test in terms of EPR compatibility since they are notoriously “lossy”; in order to reduce dielectric loss to acceptable levels, the internal diameter of the glass tube was reduced

to 0.15 cm. Although satisfactory hydrodynamic behavior was observed, when the cell dimensions were reduced for EPR compatibility and using a cell of the exact type to that described by Scholz [93], this was no longer the case – significant deviations from wall-jet behavior were found whatever the separation between the working electrode and the jet. Reproducibility problems were additionally encountered, in part due to the trapping of air bubbles within the cell, and due to a greater sensitivity of the cell to the exact location of the jet, pointing to loss of the wall-jet behavior and to the existence of “edge effects” caused by the walls of the cell.

In the Scholz design, the separation between the mercury working electrode and the jet is minimized so as to give rise to a “thin-layer cell” as shown in Fig. 30. Near-exhaustive electrolysis of the electroactive material is thus likely to occur, leading to large currents and a high sensitivity towards the detection of radicals that are stable on the experimental timescale; the shape of the mercury electrode is such that it may screen the working-electrode|electrolyte interface from the 100 kHz magnetic field modulation used in conventional EPR spectrometers, so that only radicals downstream of the shielded area will be EPR active; the wall-jet approach may be more suited in not only observing mechanistic pathways, but also

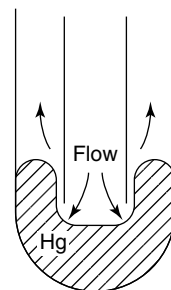


**Fig. 30** The flow pattern between the jet and the mercury working electrode under “thin-layer” conditions.

in the determination of EPR spectra from short-lived radicals. Furthermore, since the hydrodynamics of the Scholz flow-electrode design are not mathematically well described, it limits the use of its design for the study of electrode reaction mechanisms and kinetics.

### 3.2.3.8 The Dunsch–Petr–Neudeck Cell for In Situ UV-VIS EPR Spectroelectrochemistry

In situ electrochemical EPR is a versatile spectroelectrochemical technique as it allows quantitative inference of both the structure and concentration of paramagnetic species formed during electrochemical processes. However, this it is often difficult to distinguish between paramagnetic species that have been formed by the heterogeneous transfer of an electron and those formed subsequently

in homogeneous follow-on reactions. Furthermore, EPR alone cannot give structural information concerning diamagnetic reaction participants. Neudeck and coworkers [102–108] combined UV-VIS and EPR spectroscopies to give insights into whether primary or non-primary radicals are formed during electrolysis.

**3.2.3.8.1 Cell Design** The in situ electrochemical UV-VIS-EPR cell is shown schematically in Fig. 31. A  $TE_{102}$  cavity was modified to permit optical transmission. Fiber-optic light guides were used for the illumination of the EPR cavity as well as to connect the cavity to a photodiode array detector, the latter so as to improve UV-VIS measurements. The light guides were arranged near the walls of the cavity so that there was no loss in EPR sensitivity. Further, since the

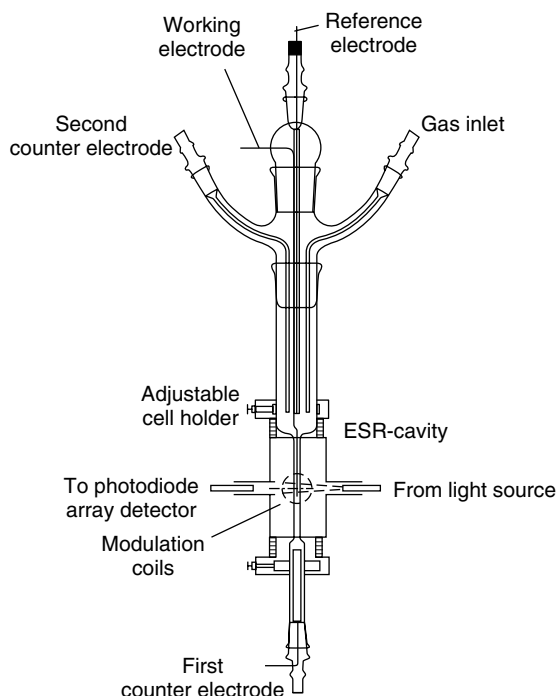


**Fig. 31** Schematic of the cell used for simultaneous in situ electrochemical EPR and UV-VIS measurements.

distance between the two light guides is just the cavity width, the sensitivity of the UV-VIS measurement is maximal. In order to minimize photochemical reactions from taking place, the light intensity used was kept to a minimum.

The electrochemical cell itself consisted of essentially a flat cell, fixed inside in the optimal position within the EPR cavity so as to ensure maximum sensitivity. The working electrode employed was either a platinum mesh [102] or later, a partly laminated gold mesh [103, 104]. An Ag|AgCl electrode was used as the reference, whilst two counter electrodes were employed to minimize oscillation of the cell voltage. The first counter electrode, a palladium sheet, is situated below the flat part of the cell, whilst the second, connected by a resistor to the potentiostat, is located above it.

**3.2.3.8.2 Application** The cell was tested with two electroactive compounds, *N,N,N',N'*-tetramethyl-*para*-phenylenediamine (TMPD) and *para*-aminodiphenylamine (PAD) in acetonitrile solutions. The former compound undergoes a one-electron oxidation to yield a dark blue cation radical,  $\text{TMPD}^{+\bullet}$  whilst the latter is thought to give rise to non-primary radicals upon oxidation, by disproportionation of the oxidation product, *N*-phenylquinonediimine with *para*-aminodiphenylamine. In this manner, absorbance|potential data (at a fixed wavelength) can be obtained together with the EPR signal|potential and cyclic voltammetric (current|potential) data.

For long-lived primary radicals, the EPR signal|potential curves should directly overlay a suitable normalized integrated charge|potential curve, since the former reflects the number of spins in the cavity and the latter, the number of radicals

formed. This was found to be so in the case of TMPD. The absorbance is also related to the concentration of the absorbing species. Measurements were conducted using 560-nm light, corresponding to the absorption of light by  $\text{TMPD}^{+\bullet}$ . Since the concentration of this species is not uniform, the Beer–Lambert law is replaced by a differential equation relating the intensity of light transmitted ( $I$ ) to the concentration of radicals ( $c$ ),

$$\frac{\partial I}{\partial x} = -\varepsilon c(x)I \quad (45)$$

where  $\varepsilon$  is the extinction coefficient at a fixed wavelength, and  $x$  is the thickness of the solution layer. Since the radical species is formed in the diffusion layer at the electrode, changing the scan rate of the cyclic voltammetric experiment perturbs the concentration gradient. It was found that in the range 20 to 200  $\text{mV s}^{-1}$ , the EPR signal|potential and the UV-VIS absorption|potential curves match up exactly, thereby allowing a semi-quantitative measurement of radicals, or UV-VIS absorbing compounds. At high scan rates ( $500 \text{ mV s}^{-1}$ ), the EPR signal|potential curve matches the integrated charge|potential curve, but deviates from the absorption curve, reflecting a greater concentration gradient at the electrode surface. At low scan rates ( $10 \text{ mV s}^{-1}$ ), further deviation due to diffusive processes occurs, permitting distinction between primary and non-primary radicals; at these scan rates, if non-primary radicals are formed, neither the EPR signal|potential curve nor the absorption|potential curve coincides with the charge|potential curve.

This cell design has been used to study conducting polymer films at electrode surfaces [104–108].

### 3.2.3.9 The Dryfe–Webster Cell for Charge Transfer Across a Liquid|Liquid Phase Boundary

**3.2.3.9.1 Cell Design** In situ EPR spectroscopy is an ideal method to detect and identify paramagnetic participants in liquid|liquid processes, but to our knowledge, has only been undertaken by Dryfe and coworkers [109, 110]. The cell used to perform the interfacial polarization-EPR experiments is shown in Fig. 32,

and is essentially a conventional silica flat cell [17] modified so that counter and reference electrodes can be inserted into both ends. It is assembled by first filling the higher density solvent through the capillary at the base of the cell using silicone tubing and a syringe, so that the solvent reaches the midpoint of the flat portion of the cell, and then sealing the silicone tubing using a Hoffmann clamp. The upper, less dense phase is then introduced into the cell from the top using a Pasteur pipette. Using this filling method, a liquid|liquid interface can be generated and maintained in the midportion of the flat part of the cell.

The EPR cell has two coiled platinum wire counter electrodes located outside the thin-layer section, and two silver wire reference electrodes flattened at one end to a thickness that enables their insertion into the flat part of the cell, positioned within 5 mm of the liquid|liquid interface. To obtain optimal control of the potential difference between the liquid phases, the portions of the reference electrodes outside the flat cell were jacketed in PTFE tubing and sealed so that they are only in contact with the solutions inside the flat part of the cell. The

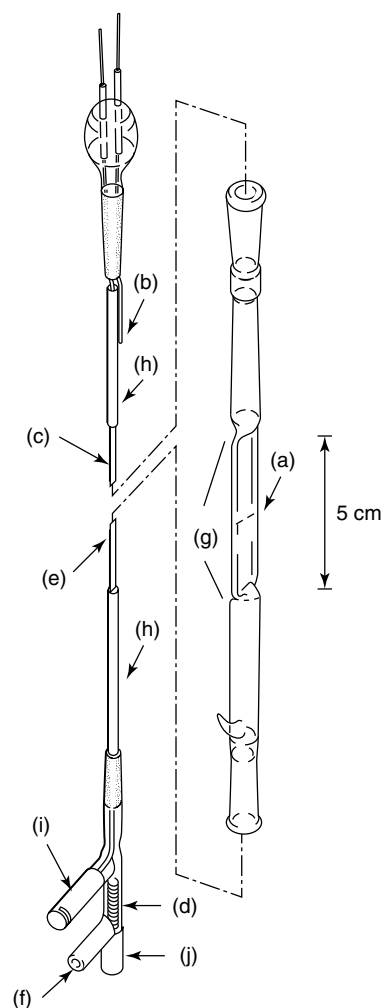
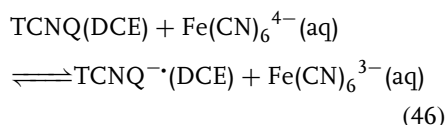


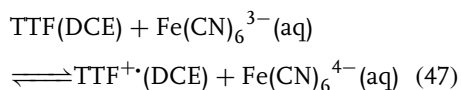
**Fig. 32** Silica cell for performing liquid|liquid electrochemical EPR experiments: (a) interface between two immiscible liquids, (b), platinum wire counter electrode 1, (c) silver wire reference electrode 1, (d) platinum wire counter electrode 2, (e) silver wire reference electrode 2, (f) capillary to fill lower portion of cell, (g) thin-layer portion of cell, (h) Teflon™/silicone rubber sleeves surrounding lower portions of reference electrodes, (i) electrical contact to reference electrode 2, and (j) electrical contact to counterelectrode 2.

inherent high resistivity of a flat cell combined with low dielectric solvents (such as 1,2-dichloroethane, DCE) can be partially overcome using this arrangement, and reasonable linear sweep voltammetry was observed using a four-electrode potentiostat. All experiments were undertaken in a TE<sub>102</sub> cavity.

**3.2.3.9.2 Typical Applications** EPR spectra were obtained for both the interfacial reduction of 7,7,8,8-tetracyanoquinodimethane (TCNQ) and oxidation of tetrathiafulvalene (TTF), when dissolved in DCE by the aqueous phase ferri/ferrocyanide redox couple, following the application of a potential difference directly to the liquid|liquid interface. Previous work [111, 112] suggested that a charge-transfer process occurs at the liquid|liquid interface, due to the heterogeneous reduction of TCNQ by the aqueous couple,



A similar mechanism can be written for the oxidation of TTF,



The presence of the organic ion radicals, and hence the occurrence of an electron-transfer process, was verified using EPR spectroscopy. The EPR spectra for TCNQ<sup>·-</sup> and TTF<sup>·+</sup> in DCE at room temperature consisted of single broad lines with  $\Delta B_{\text{pp}}$  of 5.2 and 3.0 G, respectively. The broad lines were thought not to arise by interaction of the radical ions with the aqueous phase iron complexes, since broad EPR spectra were also observed from TCNQ<sup>·-</sup> and TTF<sup>·+</sup> electrochemically

generated in the appropriate single-phase three-electrode cell [17] using DCE and the same supporting electrolyte, bis(triphenylphosphoranylidene)ammonium tetrakis(4-chlorophenyl)borate (BTPPA<sup>+</sup> TCPB<sup>-</sup>). The broad EPR spectra were thus explained by the strong ion-pairs formed between the product radical ions and the organic phase cation or anion, respectively undergoing fast electron exchange with neutral TCNQ or TTF [113].

EPR time-sweep experiments (see Fig. 33) for the oxidation of TTF, in which the magnetic field is held constant, corresponding to the maximum adsorption, by applying a potential difference ( $\Delta\phi_1$ ) between the silver quasi-reference electrodes located in each phase sufficient to cause an electron to be transferred across the water|DCE interface from TTF to Fe(CN)<sub>6</sub><sup>3-</sup>, showed increases in the EPR signal intensity, corresponding to the formation of TTF<sup>·+</sup>, exhibiting a square-root temporal dependence as expected for a potential-step occurring under planar diffusion (Volume 3 Chapter 2.3). Reversing, to a potential sufficiently negative to drive the back reaction ( $\Delta\phi_2$ ), immediately causes a decrease in the EPR signal intensity, since the radical cation is reduced to neutral TTF. Similar observations were made with TCNQ. Figure 33 also shows that when the potentiostatic circuit is broken after the formation of TTF<sup>·+</sup>, the EPR signal decreases, as TTF<sup>·+</sup>, a stable cation radical in DCE, diffuses away from the central, most sensitive part of the EPR cavity. Further application of this work to benzoquinones [110] permitted the deduction that at the aqueous|DCE interface, reduction of the parent compounds to yield semiquinones occurs without their immediate protonation.

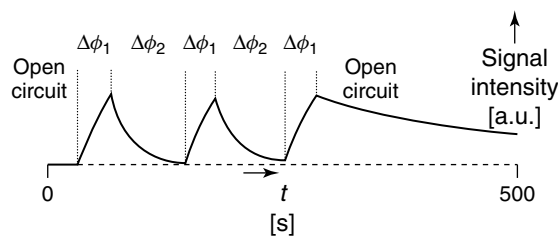


**Fig. 33** Time-sweep first derivative EPR spectrum of  $\text{TTF}^{+\bullet}$  recorded at constant magnetic induction using liquid|liquid electrochemical EPR cell. The organic phase (DCE) contained 5 mM TTF, 36 mM BTTPA<sup>+</sup> TCPB<sup>−</sup>. The aqueous phase contained 25 mM  $\text{K}_4[\text{Fe}(\text{CN})_6]$ , 25 mM  $\text{K}_3[\text{Fe}(\text{CN})_6]$ , and 0.1 M  $\text{Li}_2\text{SO}_4$ . EPR sweep time = 500 s, EPR sweep width = 10 G, modulation amplitude = 2.0 G, and time constant =  $10 \times 10^{-2}$  ms.  $\Delta\phi_1$  = oxidizing potential,  $\Delta\phi_2$  = reducing potential. The potential difference imposed to induce oxidation of the TTF was +0.7 V, whilst this process was reversed using a potential difference of −0.1 V (versus the silver pseudo-reference electrodes used).

### 3.2.4

#### Illustrative Examples of EPR in Electrochemistry

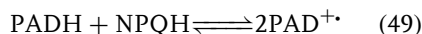
Applications of in situ electrochemical EPR are presented in this section.

##### 3.2.4.1 Radical and Radical Ion Identification

**3.2.4.1.1 The Anodic Oxidation of *para*-Aminodiphenylamine (PAD)** Allendoerfer and coworker [114] studied the oxidation of PAD at platinum electrodes in aqueous solution, in the pH range 1.2–4.8. Cyclic voltammetry in buffered solution produces a single peak, with  $E_{\text{mid}}$  ( $= 0.5(E_p^a + E_p^c)$ ) at 0.40 V versus SCE. This potential parameter was found to linearly shift with pH in the range pH 1–3, with a gradient corresponding to a proton:electron ratio of 1:1. Further, from the variation in peak potential separation with pH, this process was estimated to correspond to two electrons.

In unbuffered solutions at pH ~5.0, the cyclic voltammograms appeared to look

like two one-electron processes, suggesting the presence of a radical intermediate. An EPR study followed, confirming the presence of a radical, identified as being essentially  $\text{PAD}^{+\bullet}$ . A typical EPR spectrum of this radical is illustrated in Fig. 34. Since the  $\text{pK}_a$ 's of PAD are 4.4 and −0.072, a mechanism consistent with these observations suggested by Allendoerfer and Male is

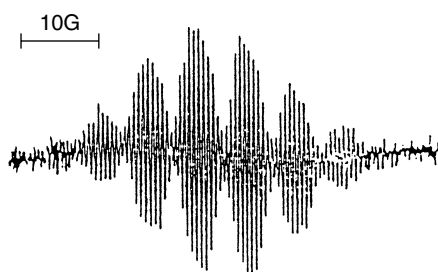


where NPQ is to *N*-phenylquinonediimine, and the extra H refers to the fact that the single protonated states are involved. The comproportionation reaction is postulated as the EPR spectrum corresponds to the unprotonated form of the radical. Further, since only a single reversible two-electron process is observed electrochemically, the comproportionation constant must be less than one.

Compton and coworkers [13] observed a similar comproportionation reaction for the case of *para*-phenylenediamine.



Fig. 34 Experimental EPR spectrum of  $\text{PAD}^{+\bullet}$ .



**3.2.4.1.2 The Reduction of Dicyanobenzene** Gennaro and coworkers [115] studied the reduction of 1,2-dicyanobenzene in acetonitrile at mercury electrodes. Two reduction signals were observed; the first (at  $-1.32\text{ V vs. SCE}$ ) was assigned to the 1,2-dicyanobenzene radical anion, the second (at  $-2.35\text{ V vs. SCE}$ ) attributed to further reduction of the radical anion, producing the 1,2-dicyanobenzene dianion, which was thought to immediately react with the solvent, producing benzonitrile, the reduction of which is thus observed. This reaction pathway was later confirmed by Compton and Waller [16] using in situ electrochemical EPR: Fig. 35 shows the EPR spectra observed by potentiostating at the appropriate voltages.

**3.2.4.1.3 The Reduction of  $\text{C}_{60}$**  This compound undergoes a series of reductions [116, 117]. Electrochemical EPR has been undertaken in toluene/acetonitrile mixtures [118], but it is notoriously difficult to unambiguously interpret these spectra [119, 120].

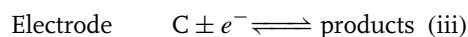
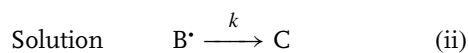
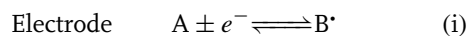
**3.2.4.1.4 Spin Trapping** If the radical to be investigated is extremely short-lived, it may not be possible to observe it directly. In these cases, the radical is “spin trapped” by chemically reacting it with a diamagnetic compound to produce a relatively

stable paramagnetic species. This technique was first introduced by Janzen and Blackburn [121, 122], using *N-tert*-butyl- $\alpha$ -phenylnitron (PBN) to spin-trap alkyl and alkoxy radicals. In a similar manner, Wadhawan and coworkers [123] were able to propose the existence of alkyl peroxides during sono-emulsion Kolbe electrosyntheses. It must be stressed that care should be taken to avoid electroactive spin traps; Bard and coworkers [124] showed that spin trapping is possible during electrochemical experiments, and that PBN is electroinactive in the potential range 1.5 to  $-2.5\text{ V}$  versus SCE in acetonitrile. The interested reader is referred to Kemp’s review on spin trapping [125] for further information.

### 3.2.4.2 Electrode Reaction Kinetics and Mechanism

This section shows the versatility of the channel flow EPR cell for mechanistic discrimination.

**3.2.4.2.1 EC Versus ECE** These reactions can be characterized by the general reaction scheme [126]



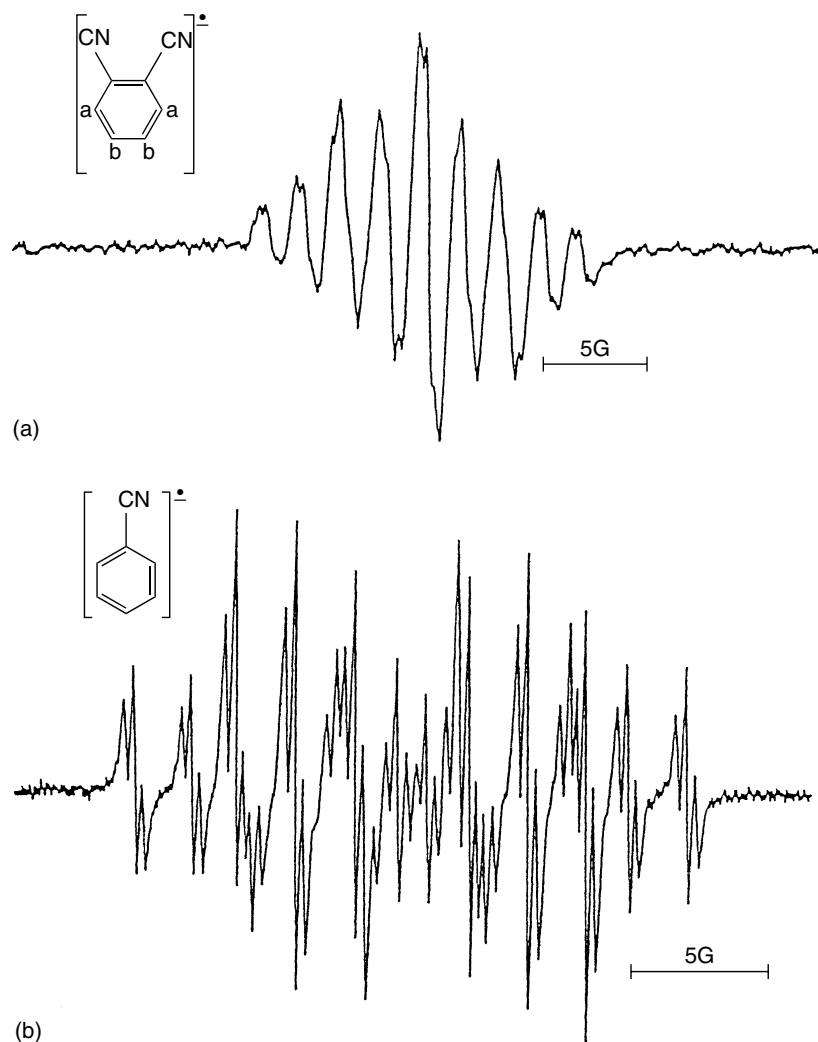


**Fig. 35** EPR spectrum obtained by in situ electrolysis of 1,2-dicyanobenzene at (a)  $-1.32$  V versus SCE, where the spectrum was shown to be that of 1,2-dicyanobenzene radical anion and (b)  $-2.35$  V versus SCE, where the spectrum corresponds to the benzonitrile anion radical.

Steps (i) and (ii) define a pure EC mechanism, while Steps (i), (ii), and (iii) correspond to an ECE mechanism. In effect, the mechanisms differ in terms of the electroactivity of the product, C, of reaction (ii) so that if C is more readily oxidized or reduced than A, the process is of the

ECE type, whereas if C is electrochemically inert, the process is designated EC. Analytical theory describing these processes in channel electrodes is established [127].

Compton and coworkers [58] deduced that the EPR signal for an ECE reaction follows that for a simple E reaction (Eq. 27),

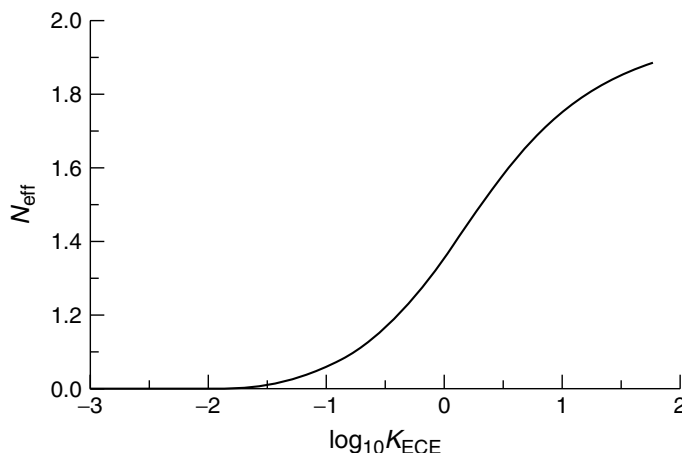


**Fig. 36** Working curve showing the relationship of  $N_{\text{eff}}$  and  $K$  for an ECE process.

provided the current,  $i$ , is replaced by that giving rise to unreduced  $B^*$ , namely,  $(i_A - i_C)$ . Further, a working curve, shown in Fig. 36 was described showing how a dimensionless rate constant,  $K$ , defined by

$$K = k \left( \frac{4h^4 x_e^2 d^2}{9V_f^2 D} \right)^{1/3} \quad (50)$$

varies with “the effective number of electrons”,  $N_{\text{eff}}$ , passed,

$$N_{\text{eff}} = \frac{\text{Total Limiting Current Observed}}{\text{Limiting Current For A Single Electron Transfer Process}} \quad (51)$$

The electrochemical reduction of 2-nitropropane at mercury-plated copper electrodes was investigated in aqueous solution, using Triton-X as a stabilizer. Two waves were observed, the first corresponding to the  $[(\text{CH}_3)_2\text{CHNO}_2]^-$  radical anion, as evidenced by electrochemical EPR. Upon removing the applied potential from the electrode, EPR signal transients were obtained, analysis of which in terms

of simple first-order kinetics (Eq. 36) permitted the inference of a rate constant,  $k$ . Plotting this parameter against  $V_f^{2/3}$ , gave a straight line graph that allowed extrapolation to zero flow rate to give a value of  $0.36 \pm 0.02 \text{ s}^{-1}$  for the first-order decay of the radical anion. The steady state EPR signal was found to be directly proportional to the generating current, until after the onset of the second voltammetric wave, when a dramatic decrease of EPR signal occurred. These features are both consistent with EC and ECE mechanisms. Conclusive evidence of the mechanistic discrimination between EC and ECE reactions came from analysis of the reduction current|flow rate data, shown in Fig. 37. It can be seen that at fast flow rates, the data tend towards one-electron behavior, whilst at slow flow rates, they tend towards two-electron behavior, indicative of an ECE reaction. Further analysis of the EPR signal|flow rates data permitted the determination of EPR detection efficiencies, from which a rate constant of  $0.28 \text{ s}^{-1}$  was obtained for radical decay.

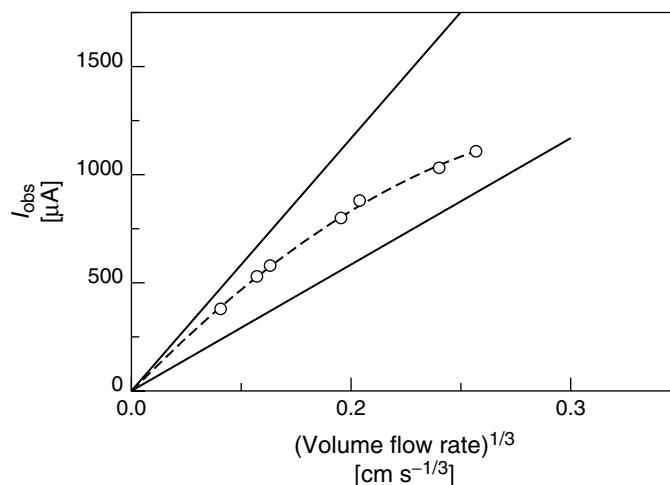
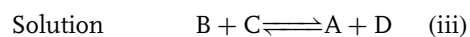
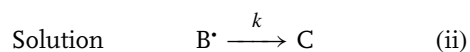
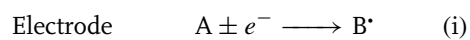


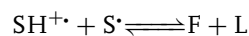
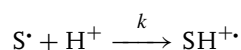
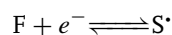
**Fig. 37** The limiting current|flow rate behavior for the reduction of 2-nitropropane in aqueous solution. The solid lines are calculated behavior for one- and two-electron processes.

**3.2.4.2.2 ECE Versus DISP1** DISP1 reactions are described by the following general kinetic scheme.



In this scheme, Step (ii) is rate limiting. Compton and coworkers [74] deduced the analytical theory for the solution of the relevant convective-diffusion equation at steady state for the above homogeneous kinetic scheme, in terms of a working curve, see Fig. 38.

The reduction of fluorescein (F) to give the semifluorescein ( $S^\bullet$ ) radical anion in aqueous solution at a silver channel electrode was studied [74]. Cyclic voltammetric experiments gave rise to linear Levich plots, but the size of the reduction wave increased with decreasing pH, suggesting that  $S^\bullet$  becomes unstable with respect to disproportionation to yield F and *leuco*-fluorescein (L),



where it was assumed that the protonation of  $S^\bullet$  is rate determining and irreversible, as it is accompanied by a change in hybridization from  $sp^2$  to  $sp^3$  at the central carbon atom. In a similar manner to that above, the current|flow rate data showed one-electron behavior at fast flow rates, but two-electron behavior at slow flow rates, indicative of either an ECE or a DISP process.

Analysis of EPR signal transients, obtained by open-circuiting the electrode, using simple first-order kinetics, was found to give an apparent rate constant of  $1.05 \text{ s}^{-1}$ , ruling out a DISP2 mechanism. Using experimentally determined values for the effective number of electrons transferred together with the working curves, values of  $K$ , were obtained for different flow rates. This is plotted in Fig. 39, where

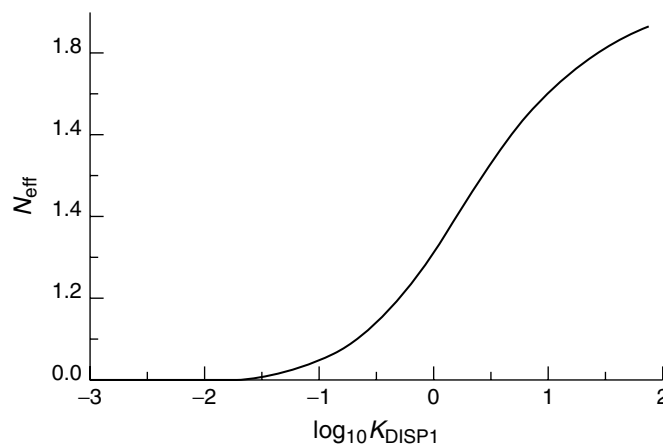
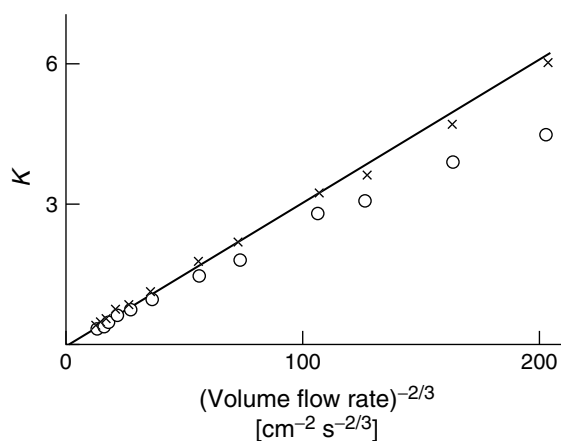


**Fig. 38** Working curve showing the relationship of  $N_{\text{eff}}$  and  $K$  for a DISP1 process.

**Fig. 39** Analysis of the limiting current/flow rate data at pH 9.68 assuming an ECE mechanism (O) or a DISP1 mechanism (x).



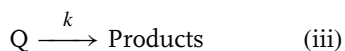
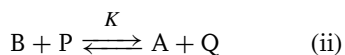
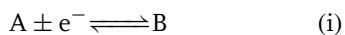
it is apparent that a rather better straight line is obtained assuming a DISP1 rather than ECE mechanism. Furthermore, the variation in the decadic rate constant observed from the extrapolated EPR transient data ( $k_{\text{app}}$ ) with pH using the relationship

$$k = \frac{1}{2} \lim_{V_f \rightarrow 0} k_{\text{app}} \quad (52)$$

which arises since two  $S^\bullet$  radicals are lost for each time that  $S^\bullet$  is protonated, is linear with a slope of  $-1$ ,

which would be that anticipated for the pseudo-first-order rate constant for the protonation of  $S^\bullet$ . Clearly, the analysis in terms of a DISP1 mechanism is in better agreement with experimental observations.

**3.2.4.2.3 EC'** Waller and coworkers employed the channel flow cell for the study of a catalytic mechanism [68]. The (pre-equilibrium) EC' mechanism can be defined by the following kinetic scheme.



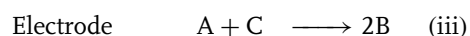
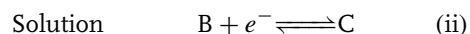
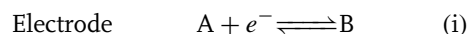
Solution of the appropriate convective-diffusion equations at steady state permits the behavior of this mechanism to be described in terms of a normalized rate constant:

$$K^* = kK \frac{[P]_{\text{bulk}}}{[A]_{\text{bulk}}} \left( \frac{h^2 x_e^2}{4\nu_0^2} \right)^{1/3} \quad (53)$$

where  $[P]_{\text{bulk}}$  and  $[A]_{\text{bulk}}$  are the bulk concentrations of  $P$  and  $A$ . Under conditions in which the Lévêque approximation is valid [63, 71], the current is a unique function of  $K^*$ . The observed behavior is best expressed in terms of the effective number of electrons transferred,  $N_{\text{eff}}$ . The EPR signal behavior may be deduced from numerical simulation of the concentration of the ion-radical species,  $B$ , as indicated in Sect. 3.2.3.

#### 3.2.4.2.4 Comproportionation Reactions

Comproportionation reactions are of the form  $Y + Y^{2-} \rightarrow 2Y^-$ . Spackman and coworkers [75] studied the effect of a homogeneous comproportionation reaction on an electrode reaction that proceeds stepwise via two single-electron transfers,



where  $E_{A|B}^0$  is more positive than  $E_{B|C}^0$ . For the Compton–Coles channel cell, the EPR signal from the regions adjacent to and downstream from the electrode is given

by the integral concentration of  $B$  (an anion radical) over the whole volume of the EPR cavity weighted by a  $\sin^2$  sensitivity profile,

$$S \propto \int_0^{2h} \left( \int_{x_{\text{offset}} - x_e/2}^{x_{\text{offset}} + x_e/2} b \sin^2 \left( \frac{\pi x}{2x_L} \right) + \int_{x_{\text{offset}} + x_e/2}^{x_L} b \sin^2 \left( \frac{\pi x}{2x_L} \right) \right) dx dz \quad (54)$$

where  $b$  is the concentration of  $B$ , found by numerical analysis of the pertinent convective-diffusion equation,  $2x_L$  is the length of the EPR cavity, and  $x_{\text{offset}}$  is the distance (offset) from the center of the electrode to the center of the cavity.

The behavior of the steady state EPR signal ( $S_1$ ) of  $B$  at a potential corresponding to steady state limiting current for the reduction of  $A$  to  $B$  is related to the generating current (provided  $B$  is stable), as indicated in Sect. 3.2.3,

$$S_1 \propto \frac{i}{V_f^{2/3}} \quad (55)$$

Stepping the potential so that the steady state limiting current for the reduction of  $B$  to  $C$  is established, gives rise to a new EPR signal ( $S_2$ ). Figures 40 and 41 show the dependence of the dimensionless parameter  $S_2/S_1$  upon the rate constant for step (iii) for the respective cases of equal and mixed diffusion coefficients. As  $k_{\text{III}}$  is initially increased from zero, the EPR signal ratio rises rapidly, but this tails off when the kinetics become mass transport-controlled.  $S_2/S_1$  never reaches the limiting value of two, as this is what would be expected if all  $C$  produced by the electroreduction of  $A$  is converted into  $B$  by comproportionation. Rather, for infinitely fast comproportionation kinetics, two separate spatial zones are established, one close to the electrode containing  $C$  (but

**Fig. 40** Working curve showing the relationship between  $S_2/S_1$  and  $\log(k_{III})$  for the channel electrode flow cell geometry of  $d = 0.591$  cm,  $2h = 0.036$  cm,  $w = 0.402$  cm and  $x_e = 0.425$  cm, and  $D_A = D_B = D_C = 1.75 \times 10^{-5}$  cm<sup>2</sup> s<sup>-1</sup> and a volume flow rate of  $10^{-2}$  cm<sup>3</sup> s<sup>-1</sup>.

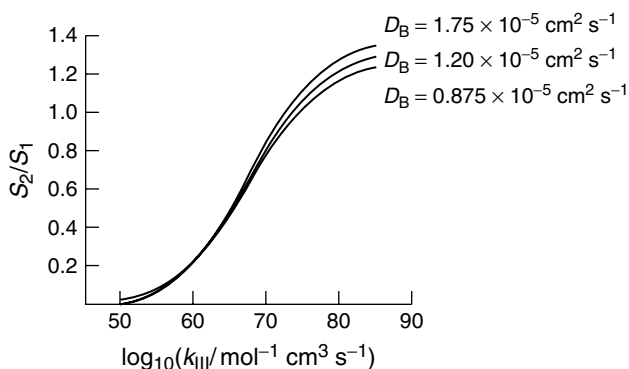
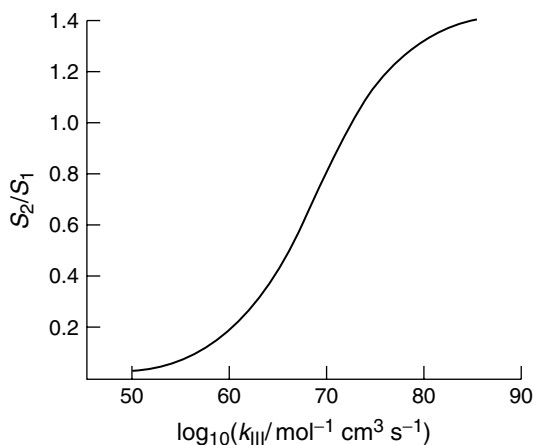


**Fig. 41** Working curve showing the relationship between  $S_2/S_1$  and  $\log(k_{III})$  for the channel electrode flow cell geometry of  $d = 0.591$  cm,  $2h = 0.036$  cm,  $w = 0.402$  cm and  $x_e = 0.425$  cm, and  $D_A = 1.75 \times 10^{-5}$  cm<sup>2</sup> s<sup>-1</sup>,  $D_C = 0.875 \times 10^{-5}$  cm<sup>2</sup> s<sup>-1</sup>, flow rate =  $10^{-2}$  cm<sup>3</sup> s<sup>-1</sup> with  $D_B = 0.875 \times 10^{-5}$ ,  $D_B = 1.20 \times 10^{-5}$ , and  $D_B = 1.75 \times 10^{-5}$  cm<sup>2</sup> s<sup>-1</sup>.

not A), and the other extending into the center of the channel containing A (but not C), with a sharp interface between the two zones.

The ratio of the diffusion coefficients of A and B has an effect upon the EPR signal ratio  $S_2/S_1$ . If  $D_B$  is decreased relative to  $D_A$ , assuming an initial condition  $D_A = D_B$ , both  $S_1$  and  $S_2$  increase but at different rates, so that  $S_2/S_1$  decreases. The

increased values  $S_1$  and  $S_2$  can be explained by noting that decreasing  $D_B$  narrows the diffusion layer of B, consequently reducing the flow rate of B out of the channel, leading to an accumulation of radicals in the channel flow cell.

Spackman and coworkers [75] looked at the case in which A is *p*-chloranil. First, with the electrode positioned at the center of the cavity, it was found that

at a potential ( $E_1$ ) corresponding to the formation of the anion radical (B), a plot of  $\log_{10} S_1/i_{\text{lim}}$  versus  $\log_{10} V_f$  gave a straight line with slope  $-2/3$ , as would be expected for a stable radical. EPR signal ( $S_2$ )|flow rate data were then obtained by potentiostatting the platinum foil working electrode at a potential ( $E_2$ ) corresponding to the reduction of the anion radical. Repositioning the electrode so that it was a few millimeters downstream of the cavity center, allowed a second set of  $S|V_f$  data at both potentials. In both cases, good agreement was obtained between experiment and theory.

The dependence of  $S_2/S_1$  on the location of the electrode within the cavity may be rationalized as follows. When the electrode is at  $E_1$ , B is generated by the electroreduction of A and then flows unperturbed out of the channel, so that a concentration profile of B within the channel is established, and so that the concentration of B decreases in both  $x$  and  $z$  directions. However, when the electrode potential is stepped to  $E_2$ , the concentration of B no longer varies monotonically with the  $x$  and  $z$  coordinates, but the precise distribution depends is determined by the electroreduction of B to C and the comproportionation reaction of A with C. In particular, at the downstream edge of the electrode, [B] rises rapidly with  $x$  and  $z$ , since B is no longer consumed electrochemically, but then passes through a maximum when C fully reacts. It is the position of this maximum within the EPR cavity that determines the ratio  $S_2/S_1$ .

In situ electrochemical EPR has been employed in the study of the comproportionation of methyl viologen [76, 77] and cyanophenyl paraquat [128].

**3.2.4.2.5 Photoelectrochemical EPR** The channel flow cell is ideally suited for the interrogation of photoelectrochemical

phenomena as it is constructed using silica – a transparent material. Further, the electrode material can be made to be a semiconducting material. Irradiation is simply achieved by illuminating the working electrode through the irradiation port machined on one face of the cavity, allowing the transmission of a high proportion of the interrogating light beam to the working electrode and uniform irradiation of the latter so that photochemical channel flow experiments can be routinely undertaken in an in situ mode [55, 65–67, 79–81]. In this manner, a variety of mechanisms have been studied, notably photo-ECE [67, 79], photo-CE [65], and photo-DISP2 [66].

#### 3.2.4.3 Modified Electrodes

In situ electrochemical EPR has been widely applied in the study of radical intermediates within polymer films on electrode surfaces. Examples include the electrochemical doping in polypyrrole [129, 130] and the anodic oxidation of poly(*N*-vinylcarbazole) films [131].

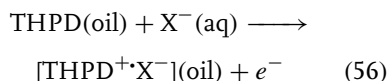
#### 3.2.4.4 Electrochemical EPR in Ionic Liquids

Ionic liquids are ideal solvents for conducting electrochemical experiments, notably due to their (1) high thermal stability and wide liquid range, (2) ability to act as solvents for many organic and inorganic materials, whilst still being highly polar, noncoordinating media, (3) high conductivity, and (4) negligible vapor pressure in contrast with conventional organic solvents, permitting their study under conditions of high vacuum. Surprisingly, little work on electrochemical EPR has been undertaken in these media. Allendoerfer and Osteryoung have pioneered this area [132], primarily focusing



upon measurements on polymers (such as polypyrrole [133] and polyaniline [134]) in 1-methyl-3-ethylimidazolium chloride and aluminum chloride.

Recently, Marken and coworkers [135] reported a novel method for the electro-generation of ionic liquids in which microdroplets of *N,N,N',N'*-tetrahexyl-*para*-phenylene diamine (THPD) are deposited upon the surface of a basal plane pyrolytic graphite (or gold) electrode and are immersed into an aqueous electrolyte solution. The ionic liquid is formed as a consequence of the requirement to maintain electroneutrality upon oxidizing THPD,



It has been shown that this process occurs at the three-phase boundary of THPD|aqueous electrolyte|solid electrode [135, 136]. In situ EPR transients for the oxidation and rereduction of THPD were seen to be consistent with the anion insertion process occurring at the triple phase junction [135].

### 3.2.5

#### Conclusion

In situ electrochemical EPR has been shown to be a useful technique for probing both the kinetics and mechanisms of electrode processes that produce or consume paramagnetic species. A variety of cell designs have been presented, illustrating the scope of this spectroelectrochemical technique.

#### Acknowledgments

We are gratefully indebted to all those who have worked with us in the pursuit of electrochemical EPR, notably Barry Coles,

Andy Waller, Rob Dryfe, Richard Webster, Nathan Lawrence, Frank Marken, and Andreas Neudeck. We thank John Freeman for the preparation of all of the figures in this manuscript.

#### References

1. A. Carrington, A. D. McLachlan, *Introduction to Magnetic Resonance*, Chapman & Hall, London, 1979.
2. G. K. Frenkel, P. H. Rieger, *J. Chem. Phys.* **1963**, 39, 309–318.
3. D. E. G. Austin, M. F. Peover, M. H. Ingram et al., *Nature* **1958**, 181, 1784–1785.
4. A. H. Maki, D. H. Geske, *J. Chem. Phys.* **1959**, 30, 1356–1357.
5. A. H. Maki, D. H. Geske, *J. Am. Chem. Soc.* **1960**, 82, 267–269.
6. J. G. Lawless, M. D. Hawley, *J. Electroanal. Chem.* **1969**, 23, App. 1–5.
7. A. H. Maki, D. H. Geske, *J. Chem. Phys.* **1960**, 33, 825–830.
8. A. H. Maki, D. H. Geske, *J. Am. Chem. Soc.* **1961**, 83, 1852–1856.
9. W. J. Albery, B. A. Coles, A. M. Couper et al., *J. Chem. Soc., Chem. Commun.* **1974**, 198–199.
10. W. J. Albery, B. A. Coles, A. M. Couper, *J. Electroanal. Chem.* **1975**, 65, 901–910.
11. W. J. Albery, A. T. Chadwick, B. A. Coles et al., *J. Electroanal. Chem.* **1977**, 75, 229–235.
12. W. J. Albery, R. G. Compton, A. T. Chadwick et al., *J. Chem. Soc., Faraday Trans. 1* **1980**, 76, 1391–1398.
13. W. J. Albery, R. G. Compton, I. S. Kerr, *J. Chem. Soc., Perkin Trans. 2* **1981**, 823–826.
14. W. J. Albery, R. G. Compton, *J. Chem. Soc., Faraday Trans. 1* **1982**, 78, 1561–1568.
15. R. G. Compton, A. M. Waller in *Spectroelectrochemistry* (Ed.: R. J. Gale), Plenum Press, New York, 1988, pp. 319–366.
16. A. M. Waller, R. G. Compton, *Comprehensive Chemical Kinetics*, Elsevier, Amsterdam, 1989, pp. 297–348, Vol. 29.
17. L. H. Piette, R. Ludwig, R. N. Adams, *Anal. Chem.* **1962**, 34, 916–919, 1587–1592.
18. G. Cauquis, J. P. Billon, J. Cambrisson, *Bull. Soc. Chim. Fr.* **1960**, 2062–2067.
19. G. Cauquis, J. P. Billon, J. Raison, *Bull. Soc. Chim. Fr.* **1967**, 199–205.

20. G. Cauquis, M. Genies, *Bull. Soc. Chim. Fr.* **1967**, 3220–3227.
21. G. Cauquis, M. Genies, H. Lemaire et al., *J. Chem. Phys.* **1967**, 42, 4642–4646.
22. G. Cauquis, C. Berry, M. Maivey, *Bull. Soc. Chim. Fr.* **1968**, 2510–2515.
23. B. Kastening, J. Divisek, B. Costissa-Mihelcic, *Faraday Discuss. Chem. Soc.* **1973**, 56, 341–348.
24. B. Kastening, J. Divisek, B. Costissa-Mihelcic et al., *Z. Phys. Chem.* **1973**, 87, 125–132.
25. J. K. Dohrmann, F. Galluser, H. Wittchen, *Faraday Discuss. Chem. Soc.* **1973**, 56, 350–358.
26. J. K. Dohrmann, K. J. Vetter, *J. Electroanal. Chem.* **1969**, 20, 23–29.
27. J. K. Dohrmann, F. Galluser, *Ber. Bunsen-Ges. Phys. Chem.* **1971**, 75, 432–437.
28. J. K. Dohrmann, *Ber. Bunsen-Ges. Phys. Chem.* **1970**, 74, 575–580.
29. O. Stern, *Z. Phys.* **1921**, 7, 249–252.
30. W. Gerlach, O. Stern, *Ann. Phys. (Leipzig)* **1924**, 74, 673–675.
31. A. I. Akhiezer, V. B. Berestetski, *Quantum Electrodynamics*, Monographs in Physics and Astronomy, Wiley Interscience, New York, 1965, Vol. XI, p. 1–50.
32. N. M. Atherton, *Electron Spin Resonance*, Ellis Horwood, Chichester, UK, 1973.
33. P. Ludwig, R. N. Adams, *J. Chem. Phys.* **1962**, 37, 828–831.
34. H. M. McConnell, D. B. Chestnut, *J. Chem. Phys.* **1958**, 28, 778–781.
35. C. P. Poole, *Electron Spin Resonance: A Comprehensive Treatise on Experimental Techniques*, 2nd ed., Wiley, New York, 1983.
36. P. Boyer, J. Dericbourg, *C. R. Acad. Sci. Paris* **1967**, 429–437.
37. M. C. R. Symons, *Electron Spin Resonance Spectroscopy*, Van Nostrand Reinhold, London, 1978.
38. F. Gerson, *High Resolution E.S.R. Spectroscopy*, John Wiley & Sons, New York, 1970.
39. K. A. McLauchlan, *Magnetic Resonance*, Oxford University Press, Oxford, 1972.
40. P. W. Atkins, *Molecular Quantum Mechanics*, 3rd ed., Oxford University Press, Oxford, 1997.
41. B. J. Tabner in *Spectroscopy* (Eds.: B. P. Straughan, S. Walker), Chapman & Hall, London, 1976, pp. 209–260, Vol. 1.
42. I. B. Goldberg, *Electron Spin Resonance: Royal Society of Chemistry Specialist Periodical Reports*, The Royal Society of Chemistry, London, 1981, pp. 1–20, Vol. 6.
43. I. B. Goldberg, A. J. Bard, *J. Phys. Chem.* **1971**, 75, 3281–3285.
44. I. B. Goldberg, A. J. Bard, *J. Phys. Chem.* **1974**, 78, 290–294.
45. I. B. Goldberg, D. Boyd, R. Hirasawa et al., *J. Phys. Chem.* **1974**, 78, 295–301.
46. J. B. Carroll, Ph. D. thesis, State University of New York at Buffalo, 1983.
47. R. D. Allendoerfer, G. A. Martinchek, S. Bruckenstein, *Anal. Chem.* **1975**, 47, 890–894.
48. R. D. Allendoerfer, J. B. Carroll, *J. Magn. Reson.* **1980**, 37, 497–501.
49. R. D. Allendoerfer, W. Froncisz, C. C. Felix et al., *J. Magn. Reson.* **1988**, 76, 100–106.
50. H. Ohya-Nishiguchi, *Bull. Chem. Soc. Jpn.* **1979**, 52, 2064–2068.
51. F. Gerson, H. Ohya-Nishiguchi, G. Wylder, *Angew. Chem., Int. Ed. Engl.* **1976**, 15, 552–556.
52. J. Bruken, F. Gerson, H. Ohya-Nishiguchi, *Helv. Chim. Acta* **1977**, 60, 1220–1227.
53. W. Froncisz, J. S. Hyde, *J. Magn. Reson.* **1982**, 47, 515–519.
54. J. S. Hyde, W. Froncisz, *Electron Spin Resonance: Specialist Periodical Reports*, The Royal Society of Chemistry, London, 1986, pp. 175–201, Vol. 10.
55. B. A. Coles, R. G. Compton, *J. Electroanal. Chem.* **1983**, 144, 87–94.
56. C. M. A. Brett, A. M. O. Brett, *Comprehensive Chemical Kinetics*, Elsevier, Amsterdam, 1988, pp. 355–376, Vol. 26.
57. V. Levich, *Physicochemical Hydrodynamics*, Prentice Hall, Englewood Cliffs, N.J., 1962.
58. R. G. Compton, D. J. Page, G. R. Sealy, *J. Electroanal. Chem.* **1984**, 161, 129–138.
59. I. B. Goldberg, A. J. Bard, S. W. Feldberg, *J. Phys. Chem.* **1972**, 76, 2550–2559.
60. P. R. Unwin, R. G. Compton, *Comprehensive Chemical Kinetics*, Elsevier, Amsterdam, 1989, pp. 190–296, Vol. 29.
61. J. A. Cooper, R. G. Compton, *Electroanalysis* **1998**, 10, 141–152.
62. J. B. Flanagan, L. Marcoux, *J. Phys. Chem.* **1974**, 78, 718–723.
63. J. A. Alden, R. G. Compton, *J. Electroanal. Chem.* **1996**, 404, 27–34.
64. M. A. Lévêque, *Ann. Mines Mem. Ser.* **1928**, 12, 201–208.

65. R. G. Compton, B. A. Coles, G. M. Stearn et al., *J. Chem. Soc., Faraday Trans. I* **1988**, 84, 2357–2363.
66. R. G. Compton, B. A. Coles, M. B. G. Pilkington, *J. Chem. Soc., Faraday Trans. I* **1988**, 84, 4347–4355.
67. R. G. Compton, B. A. Coles, M. B. G. Pilkington et al., *J. Chem. Soc., Faraday Trans.* **1990**, 86, 663–671.
68. A. M. Waller, R. J. Northing, R. G. Compton, *J. Chem. Soc., Faraday Trans.* **1990**, 86, 335–340.
69. S. Moldoveanu, J. L. Anderson, *J. Electroanal. Chem.* **1984**, 178, 45–49.
70. J. L. Anderson, S. Moldoveanu, *J. Electroanal. Chem.* **1984**, 179, 107–118, 119–128.
71. R. G. Compton, M. B. G. Pilkington, G. M. Stearn, *J. Chem. Soc., Faraday Trans. I* **1988**, 84, 2155–2164.
72. R. G. Compton, D. J. Page, G. R. Sealy, *J. Electroanal. Chem.* **1984**, 163, 65–69.
73. M. Abramowitz, I. A. Stegun, *Handbook of Mathematical Functions*, Dover Publications, New York, 1970, p. 283–285.
74. R. G. Compton, P. J. Daly, P. R. Unwin et al., *J. Electroanal. Chem.* **1985**, 191, 15–21.
75. R. G. Compton, B. A. Coles, R. A. Spackman, *J. Phys. Chem.* **1991**, 95, 4741–4748.
76. R. D. Webster, R. A. W. Dryfe, J. C. Eklund et al., *J. Electroanal. Chem.* **1996**, 402, 167–172.
77. C.-W. Lee, J. C. Eklund, R. A. W. Dryfe et al., *Bull. Korean Chem. Soc.* **1996**, 17, 162–167.
78. F. Prieto, R. D. Webster, J. A. Alden et al., *J. Electroanal. Chem.* **1997**, 437, 183–188.
79. R. G. Compton, R. G. Harland, M. B. G. Pilkington et al., *Port. Electrochim. Acta* **1987**, 5, 271–275.
80. R. G. Compton, R. A. W. Dryfe, J. C. Eklund, *Research in Chemical Kinetics* (Eds.: R. G. Compton, G. Hancock), Elsevier, Amsterdam, 1993, pp. 239–315, Vol. 1.
81. R. G. Compton, R. A. W. Dryfe, *Prog. React. Kinet.* **1995**, 20, 245–297.
82. R. G. Compton, P. R. Unwin, *J. Electroanal. Chem.* **1986**, 205, 1–20.
83. W. J. Albery, R. G. Compton, C. C. Jones, *J. Am. Chem. Soc.* **1984**, 106, 469–475.
84. W. J. Albery, C. C. Jones, *Faraday Discuss. Chem. Soc.* **1984**, 78, 193–199.
85. R. G. Compton, A. M. Waller, *J. Electroanal. Chem.* **1985**, 195, 289–296.
86. H. Matsuda, *J. Electroanal. Chem.* **1967**, 15, 325–328.
87. P. J. Daly, D. J. Page, R. G. Compton, *Anal. Chem.* **1983**, 55, 1191–1197.
88. B. H. Vassos, G. W. Ewing, *Electroanalytical Chemistry*, Wiley, New York, 1983, p. 130.
89. S. G. Weber, W. C. Purdy, *Anal. Chim. Acta* **1976**, 100, 531–535.
90. R. N. Bagchi, A. M. Bond, R. Colton, *J. Electroanal. Chem.* **1986**, 199, 297–303.
91. R. N. Bagchi, A. M. Bond, C. L. Heggie et al., *Inorg. Chem.* **1983**, 22, 3007–3013.
92. R. N. Bagchi, A. M. Bond, F. Scholz et al., *J. Electroanal. Chem.* **1988**, 245, 105–111.
93. R. N. Bagchi, A. M. Bond, F. Scholz, *J. Electroanal. Chem.* **1988**, 252, 259–264.
94. D. A. Fieldler, M. Koppenol, A. M. Bond, *J. Electrochem. Soc.* **1995**, 142, 862–868.
95. R. D. Webster, A. M. Bond, R. G. Compton, *J. Phys. Chem.* **1996**, 100, 10 288–10 296.
96. R. D. Webster, A. M. Bond, B. A. Coles et al., *J. Electroanal. Chem.* **1996**, 404, 303–311.
97. M. B. Glauert, *J. Fluid Mech.* **1956**, 1, 625–627.
98. R. G. Compton, C. R. Greaves, A. M. Waller, *J. Electroanal. Chem.* **1990**, 277, 83–88.
99. W. J. Albery, C. M. A. Brett, *J. Electroanal. Chem.* **1983**, 148, 201–207.
100. J. Yamada, H. Matsuda, *J. Electroanal. Chem.* **1973**, 44, 189–194.
101. R. G. Compton, C. R. Greaves, A. M. Waller, *J. Appl. Electrochem.* **1990**, 20, 575–585.
102. A. Petr, L. Dunsch, A. Neudeck, *J. Electroanal. Chem.* **1996**, 412, 153–159.
103. A. Neudeck, L. Kress, *J. Electroanal. Chem.* **1997**, 437, 141–148.
104. A. Neudeck, A. Petr, L. Dunsch, *J. Phys. Chem. B* **1999**, 103, 912–922.
105. P.-H. Aubert, A. Neudeck, L. Dunsch et al., *J. Electroanal. Chem.* **1999**, 470, 77–88.
106. A. Neudeck, A. Petr, L. Dunsch, *Synth. Met.* **1999**, 107, 143–158.
107. P. Rapt, R. Faber, L. Dunsch et al., *Spectrochim. Acta A* **2000**, 56, 357–362.
108. P. Rapt, A. Neudeck, A. Petr et al., *J. Chem. Soc., Faraday Trans.* **1998**, 94, 3625–3630.
109. R. A. W. Dryfe, R. D. Webster, B. A. Coles et al., *Chem. Commun.* **1997**, 779–780.
110. R. D. Webster, R. A. W. Dryfe, B. A. Coles et al., *Anal. Chem.* **1998**, 70, 792–800.

111. Y. Cheng, D. J. Schiffrin, *J. Chem. Soc., Faraday Trans.* **1994**, *90*, 2517–2521.
112. T. Solomon, A. J. Bard, *J. Phys. Chem.* **1995**, *99*, 17 487–17 492.
113. N. Haren, Z. Luz, M. Shporer, *J. Am. Chem. Soc.* **1974**, *96*, 4788–4793.
114. R. Male, R. D. Allendoerfer, *J. Phys. Chem.* **1988**, *92*, 6237–6243.
115. A. Gennaro, F. Marron, A. Maye et al., *J. Electroanal. Chem.* **1985**, *185*, 353–359.
116. R. G. Compton, R. A. Spackman, R. G. Wellington et al., *J. Electroanal. Chem.* **1992**, *327*, 337–341.
117. R. G. Compton, R. A. Spackman, R. G. Wellington et al., *J. Electroanal. Chem.* **1993**, *344*, 235–247.
118. S. A. Olsen, A. M. Bond, R. G. Compton et al., *J. Phys. Chem. A* **1998**, *102*, 2641–2652.
119. C. A. Reed, R. D. Bolskar, *Chem. Rev.* **2000**, *1000*, 1075–1189.
120. I. Noviandri, R. D. Bolskar, P. A. Lay et al., *J. Phys. Chem. B* **1997**, *101*, 6350–6359.
121. E. G. Janzen, B. J. Blackburn, *J. Am. Chem. Soc.* **1968**, *90*, 5909, 5910.
122. E. G. Janzen, B. J. Blackburn, *J. Am. Chem. Soc.* **1969**, *91*, 4481–4484.
123. J. D. Wadhawan, F. J. Del Campo, F. Marken et al., *J. Electroanal. Chem.* **2001**, *507*, 135–143.
124. A. J. Bard, J. C. Gilbert, R. D. Godwin, *J. Am. Chem. Soc.* **1974**, *96*, 620–621.
125. T. J. Kemp, *Prog. React. Kinet.* **1999**, *24*, 287–345.
126. A. C. Testa, W. H. Reinmuth, *Anal. Chem.* **1961**, *19*, 1320–1322.
127. P. D. Moorland, R. G. Compton, *J. Phys. Chem. B* **1999**, *103*, 8951–8959.
128. R. G. Compton, A. M. Waller, P. M. S. Monk et al., *J. Chem. Soc., Faraday Trans.* **1990**, *86*, 2583–2587.
129. A. M. Waller, A. N. S. Hampton, R. G. Compton, *J. Chem. Soc., Faraday Trans. I* **1989**, *85*, 773–778.
130. A. M. Waller, R. G. Compton, *J. Chem. Soc., Faraday Trans. I* **1989**, *85*, 977–982.
131. R. G. Compton, F. J. Davis, S. C. Grant, *J. Appl. Electrochem.* **1986**, *16*, 239–243.
132. M. A. M. Noel, R. D. Allendoerfer, R. A. Osteryoung, *J. Phys. Chem.* **1992**, *96*, 239–245.
133. J. F. Oudard, R. D. Allendoerfer, R. A. Osteryoung, *J. Electroanal. Chem.* **1988**, *241*, 231–238.
134. J. Tang, R. D. Allendoerfer, R. A. Osteryoung, *J. Phys. Chem.* **1992**, *96*, 3531–3537.
135. F. Marken, R. D. Webster, S. D. Bull et al., *J. Electroanal. Chem.* **1997**, *437*, 209–218.
136. J. C. Ball, F. Marken, Q. Fulian et al., *Electroanalysis* **2000**, *12*, 1017–1025.
137. B. A. Coles, R. G. Compton, *J. Electroanal. Chem.* **1981**, *127*, 37–43.

### 3.3 Spectroscopic Applications of STM and AFM in Electrochemistry

Nongjian Tao  
Arizona State University, Tempe, AZ

#### 3.3.1 Introduction

Scanning Tunneling Microscopy (STM) [1] and the related Atomic Force Microscopy (AFM) [2] are dream techniques that allow us to visualize atomic-scale phenomena on surfaces. Shortly after the inventions, the capability of the techniques for imaging electrode surfaces in solutions was recognized and applied to electrochemistry [3–6]. Since the pioneering works, various electrochemical phenomena have been imaged and studied with atomic or molecular resolution. Examples of such studies can be found in Volume 3 of this series and in many reviews [7–12]. In addition to high-resolution images, STM and AFM can provide local spectroscopy information of the surfaces and adsorbates. This chapter provides an introduction to the spectroscopy applications in electrochemistry. We start with a brief outline of STM and AFM fundamentals, and then illustrate the spectroscopy applications using selective examples.

#### 3.3.2 Electrochemical STM – Elementary Concepts

STM consists of a sharp metal tip that is placed over a conductive sample surface (Fig. 1). The conduction electrons are free to propagate within the tip and the sample, but classically forbidden in the gap between the tip and the sample in which the electron total energy is smaller than the potential energy. However, according

to quantum mechanics, the electrons can tunnel across the gap and give rise to a measurable tunneling current when a bias voltage is applied between the tip and the sample. The tunneling probability is proportional to the overlap of the electron clouds (wave functions,  $\psi_{\text{sub}}$  and  $\psi_{\text{tip}}$ ) that spill out of the tip and the sample surfaces. The overlap decreases exponentially as does the gap width, which leads to a simple relation between the tunneling current ( $I$ ) and the sample-tip distance ( $s$ ) by

$$I \propto \exp(-1.025\sqrt{\phi}s) \quad (1)$$

where  $\phi$  is the work function or the tunneling barrier height in eV and  $s$  is in Å. The work function is typically  $\sim 4$  eV, so the tunneling current decays about  $e^2 \sim 7.4$  times per Å, according to Eq. (1). The rapid decay means that only the atom in the closest proximity to the sample surface dominates the measured tunneling current, which is the basis of the atomic resolution imaging of STM. When scanning the STM tip across the sample surface with a piezoelectric transducer, the local tunneling current can be mapped. A more common approach is to keep a constant current by adjusting the vertical position of the tip with a feedback loop. The vertical position of the tip recorded as a function of the lateral position provides a three-dimensional image of the sample surface.

The simple exponential decay given by Eq. (1) was verified experimentally in vacuum over a wide range of tunneling current despite that the simple model ignores factors, such as imaging force experienced by the tunneling electrons [13]. Replacing the vacuum gap with an electrolyte, Eq. (1) holds approximately for a limited range of the gap with an effective barrier height ( $\phi$ ) somewhat smaller than

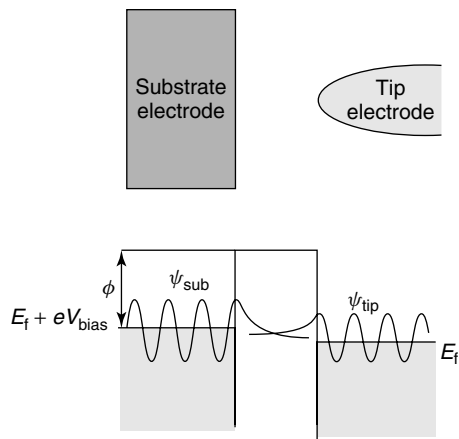


**Fig. 1** Electron tunneling between an STM tip and a conductive substrate.

the vacuum value [14–20]. However, when measuring the tunneling current over a wide range of the gap, Lindsay and coworkers [18, 19] observed a significant deviation from the simple exponential dependence. Hong and coworkers [20] reported that the tunneling barrier for the electron tunneling from tip to substrate was remarkably different from the reverse direction. Both the nonexponential decay and asymmetric tunneling demand a better understanding of electron tunneling across an electrolyte gap. Schmickler and Henderson [21] treated the water molecules in the tunneling gap as a dielectric medium and predicted a smaller tunneling barrier than in vacuum. Kuznetsov and Ulstrup considered the effects of solvent fluctuations on the tunneling barrier height and tunneling rate [22]. They found that the solvent fluctuations could enhance the tunneling rate, thus leading also to a lower effective barrier height. More elaborate models involving resonant tunneling through solvent states [18, 23] and ab initio simulations [24, 25] were also developed.

The STM image cannot always be literally interpreted as a geometrical topography of the sample surface because the tunneling current depends on the

electronic states of the tip and the sample surface. The tunneling current across a vacuum or insulation gap between the tip and the sample surface is given by [26]

$$I = \frac{4\pi e}{\hbar} \int_{-\infty}^{+\infty} [f(E_F - eV_{\text{bias}} + \varepsilon) - f(E_F - \varepsilon)] \rho_S(E_F - eV_{\text{bias}} + \varepsilon) \times \rho_T(E_F + \varepsilon) |M|^2 d\varepsilon \quad (2)$$

where  $f(E)$  is the Fermi–Dirac distribution function,  $E_F$  is the Fermi energy of the tip,  $V_{\text{bias}}$  is the bias voltage,  $\rho_T(\varepsilon)$  and  $\rho_S(\varepsilon)$  are the local density of states (DOS) of the tip and sample, respectively, and  $|M|^2$  is related to the overlap between the tip and the sample wave functions that decays according to Eq. (1). When the temperature is low, ( $k_B T \ll E_F$ ) and  $|M|^2$  is independent of energy, the tunneling current is a convolution of the tip and the sample DOS over an energy range  $eV_{\text{bias}}$ ,

$$I \approx \int_0^{eV_{\text{bias}}} \rho_S(E_F - eV_{\text{bias}} + \varepsilon) \times \rho_T(E_F + \varepsilon) d\varepsilon \quad (3)$$

In the presence of a molecular adsorbate, one may treat the combined adsorbate and the substrate as the sample. However,

many models have been proposed to treat the adsorbate more explicitly both in vacuum [27–35] and in aqueous solutions [21, 36–40]. For example, Kuznetsov and Ulstrup [36, 41] pointed out that a strong coupling between the electronic states of a molecule and the environmental fluctuations could affect the tunneling current by lowering the effective tunneling barrier and by momentarily bringing a molecular state to align with the substrate/tip Fermi levels. In addition to the adsorbate-solvent coupling, Schmickler and coworkers [38, 42] took into account the adsorbate-substrate coupling. They considered explicitly a resonant tunneling process when the molecular state was brought to align with the substrate/tip Fermi levels. We will return to these theories later.

### 3.3.3

#### Electrochemical AFM – Elementary Concepts

AFM is similar to STM in many aspects, but a fundamental difference between them is that STM measures the tunneling current, while AFM probes the force. So unlike STM, which requires a conductive surface or small adsorbates on a conductive surface, AFM can provide high-resolution images of both conductive and insulating surfaces. This is important for imaging large biological molecules or

poorly conductive materials on electrodes. The tip-sample force in AFM is typically detected by measuring the bending of a flexible cantilever on which the tip is attached (Fig. 2) [43]. As the tip approaches the sample surface, it first experiences long-range forces, such as the van der Waals and electrostatic interactions, then specific chemical bonds between the tip and the sample surface, followed by a rapid increase in the hard-core repulsive force [44]. In the electrochemical environment, additional forces such as ionic and hydration forces arise [45]. These forces will be discussed in greater details later.

AFM can be operated in either the attractive or repulsive-force modes. In the repulsive mode, or the so-called contact-mode AFM, the force is highly stable and images that show the periodic lattice structures of the samples are routinely obtainable. However, most of the reported images show either perfectly ordered atomic structures or defects that are much greater than an atom. Ohnesorge and Binnig [46] investigated this issue by imaging calcite in water. They observed atomic-scale defects when the net repulsive force applied on the sample surface by the AFM tip was 0.1 nN or smaller. Increasing the repulsive force, they found that sharp monoatomic steps were slowly wiped away because the large contact force resulted in a contact area between the tip and the sample much greater than

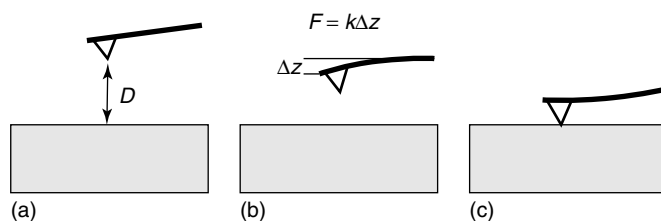


Fig. 2 Tip-sample interactions in AFM.

an atom. The subsequent AFM image, nevertheless, still showed well-ordered two-dimensional lattice structures owing to the periodic modulation of the force by the periodic lattice of the sample surface. The experiment shows that most AFM experiments operated with a contact force much greater than 0.1 nN are probably not truly atomic resolution.

The contact force can be avoided by operating in the attractive force mode or the noncontact mode. For high-sensitivity measurement of the attractive force, an AC technique was introduced. The technique measures the change in the resonance frequency of the AFM cantilever. When the tip is far away from the sample surface, the resonant frequency  $f_0$  is given by,

$$f_0 = 2\pi\sqrt{\frac{k}{m}} \quad (4)$$

where  $k$  is the spring constant of the cantilever and  $m$  is the effective mass. When the tip approaches the sample, the tip-sample interaction changes the spring constant by  $\Delta k = \partial F_{\text{tip-sample}}/\partial z$ . Consequently the resonance frequency changes by an amount of

$$\frac{\Delta f}{f_0} \approx \frac{\Delta k}{2k} \quad (5)$$

assuming that both the changes in the spring constant and oscillation amplitude of the cantilever are small [47]. One way to implement the idea for AFM imaging is to drive the AFM cantilever at or near the resonance frequency and measure the oscillation amplitude as the feedback signal. When the tip-sample interaction changes, the amplitude changes because of the change of the resonance frequency. This method has a low response time when the resonance is very sharp. The response time is usually acceptable for imaging in solutions because the cantilever experiences

much greater damping in solutions, which broadens the resonance. Faster response time can be achieved by directly following the resonance frequency [48]. This later technique has been used to obtain atomic resolution images of Si(111)  $-7 \times 7$  structure [49, 50]. We note that even if tip-sample contact is involved, the AC mode is still helpful for imaging soft materials, such as biological molecules adsorbed on electrodes, because the contact is intermittent. Commercial AFM, such as Tapping Mode AFM [51–53] from Digital Instruments and MAC Mode AFM [54–56] from Molecular Imaging Inc. are two examples.

### 3.3.4

#### Selective Examples of Applications

STM and AFM applications in electrochemistry as imaging tools are numerous. Novel nonimaging applications are also abundant in the literature [57, 58]. Because of space limitations, here we focus on tunneling spectroscopy and force spectroscopy applications using selective examples that are directly related to electrochemistry. Other important nonimaging applications that are relevant to electrochemistry include fabricating nanostructures [59–68] and probing fast kinetics [69–75].

#### 3.3.4.1 Tunneling Spectroscopy

The electronic states of a sample can be determined with STM by performing Scanning Tunneling Spectroscopy (STS). The concept of tunneling spectroscopy was developed as early as in the sixties using metal-oxide-metal junctions [26, 76]. The original idea of building the STM by Binnig and Rohrer was actually to perform tunneling spectroscopy locally on a small area. According to Eq. (3), the tunneling current is a convolution of the tip and



the sample DOS. In order to determine the sample DOS, one has to know the tip DOS, which is not always possible. However, for a given voltage range, the tip DOS is often weakly dependent on energy,  $\varepsilon$ , then Eq. (3) becomes,

$$\frac{dI}{dV} \approx \rho_S(E_F - eV_{\text{bias}} + \varepsilon) \quad (6)$$

Because the tunneling current is very sensitive to the tip-sample separation, the measured spectroscopic data are often normalized by  $I/V$  and given by  $[(V/I)(dI/dV)] = [(d \ln(I))/(d \ln(V))]$  [77].

In vacuum, STS is usually obtained by fixing the tip over the region of interest and then measuring tunneling current by sweeping the bias voltage. The method is, however, difficult to apply to STM in the electrochemical environment because the sweeping bias voltage induces a large polarization current that can overwhelm the tunneling current. Furthermore, faradic current at large bias voltage limits the spectroscopy to a relatively small range of bias voltage. Despite the difficulties, useful electronic information has been obtained by performing tunneling spectroscopy outside the electrochemical cell or by indirect methods.

**3.3.4.1.1 Redox States** An early attempt to extract DOS of redox molecules from tunneling current was made by Moriaki and coworkers [78]. They used thin  $\text{SiO}_2$  tunnel barriers on Pt silicide substrates for tunneling spectroscopy of complex ions, such as  $\text{Fe}(\text{CN})_6^{3-/4-}$  and  $\text{Fe}(\text{EDTA})^{1-/2-}$ . The energy dependent DOS extracted from the tunneling spectra was in good agreement with the Classical Marcus–Gerischer model [79]. The experiment was macroscopic because it measured a large number of molecules. In contrast, STS has the capability of

probing the electronic states of a single molecule or even a particular group within a molecule.

Schmickler and coworkers [38, 42] suggested that lowest unoccupied molecular orbital (LUMO) and highest occupied molecular orbital (HOMO) of molecules adsorbed on an electrode could be probed by STM. The LUMO (HOMO) is broadened and shifted as a result of the coupling of the molecule to the environment, which is described as density of oxidized (reduced) states. They have considered a coherent one-step electron transfer from the tip electrode to the substrate electrode or vice versa via a resonant transition through the oxidized states. An electron transfers from one electrode to the molecule and then to the second electrode before the molecule relaxes to the reduced state. This implies that the electron tunneling time is much faster than the vibration time of the molecule, which is on the order of  $10^{-14}$  s. If assuming the tunneling matrices, the tip, and the substrate DOS are independent of energy,  $\varepsilon$ , the model gives,

$$I \approx \int_0^{eV_{\text{bias}}} D_{\text{ox}}(\varepsilon - e\eta + eV_{\text{bias}}) d\varepsilon \quad (7)$$

where  $\eta$  is the overpotential and  $D_{\text{ox}}$  is the density of the oxidized states. When the molecule couples weakly to the substrate and the tip,  $D_{\text{ox}}$  takes the Gaussian form

$$D_{\text{ox}}(\varepsilon) = \sqrt{\frac{\pi}{k_B T \lambda}} \exp \left[ -\frac{(\varepsilon - \lambda)^2}{4k_B T \lambda} \right] \quad (8)$$

where  $\lambda$  is the reorganization energy. The tunneling spectrum,  $dI/dV_{\text{bias}}$  versus  $V_{\text{bias}}$  gives approximately the density of states ( $D_{\text{ox}}$ ). In electrochemical STM, the overpotential ( $\eta$ ) can be varied independent of the tip-substrate bias voltage ( $V_{\text{bias}}$ ). So by

measuring the tunneling current as a function of the overpotential with a fixed  $V_{\text{bias}}$ , one has a new way to perform tunneling spectroscopy. It follows from Eqs. (7 and 8) that  $I$  versus  $\eta$  gives also the density of states for a small  $V_{\text{bias}}$ .

Kuznetsov and Ulstrup [22, 36, 41] have considered another limit, a sequential two-step process, in which the electron transfers from the tip (substrate) to the molecule and reduces the molecule. The reduced states of the molecule are located below the Fermi level of the substrate, but a thermal fluctuation can shift the states up and then allow a second electron transfer from the molecule to the substrate (tip), returning the molecule to the oxidized state. Neglecting backward flowing current, the current caused by this two-step process is

$$I \approx \frac{R_{\text{sm}} R_{\text{mt}}}{R_{\text{sm}} + R_{\text{mt}}} \quad (9)$$

where  $R_{\text{sm}}$  and  $R_{\text{ms}}$  are proportional to the electron transfer rates from the substrate to the redox molecule, and from the redox molecule to the tip, respectively. Again, if we assume energy independent DOS for both the tip and the substrate, then  $R_{\text{sm}}$  and  $R_{\text{ms}}$  are given by,

$$R_{\text{sm}} \approx \int_{-\infty}^{+\infty} f(\varepsilon) \times \exp \left[ -\frac{(\varepsilon - E_0 - \lambda + \alpha e V_{\text{bias}})^2}{4k_{\text{B}} T \lambda} \right] d\varepsilon \quad (10)$$

and

$$R_{\text{mt}} \approx \int_{-\infty}^{+\infty} [1 - f(\varepsilon + e V_{\text{bias}})] \times \exp \left[ -\frac{(\varepsilon - E_0 + \lambda + \alpha e V_{\text{bias}})^2}{4k_{\text{B}} T \lambda} \right] d\varepsilon \quad (11)$$

where  $\alpha e V_{\text{bias}}$  is the energy shift in the redox levels caused by the tip-substrate bias voltage, and  $\alpha$  is between 0 and 1, reflecting the distribution of the bias voltage across the tunneling gap. This two-step electron transfer can also give rise to a maximum at a potential depending on the relative contributions from the two steps.

Friis and coworkers [80] considered an intermediate mechanism, in which an electron first transfers to the molecule and the molecule begins to relax towards the reduced state. However, before it is fully relaxed to the reduced state, an electron transfer from the molecule to the second electrode occurs when the temporarily occupied level passes the Fermi level of the second electrode. They called this process coherent two-step electron transfer. More recently, Kuznetsov and Ulstrup [81] have developed a systematic theory for the sequential two-step process. The electron transfers from one electrode to the molecule and reduces the molecule, and then transfers to the second electrode and reoxidizes the molecule, so the process is reviewed as a cycle of consecutive molecular reduction and reoxidation. A particular interesting feature in the theory is that each reduction-reoxidation cycle is composed of a large number of individual electron transfer events between the molecule and both the tip and the substrate. This significantly enhances the tunneling current compared to a single electron transfer.

Experimentally extracting redox state information from STS has been also pursued. Snyder and White measured STS of Fe-protoporphyrin IX multilayer films adsorbed on graphite electrode in air [82]. They observed an enhancement that was identical for both signs of the tip-substrate bias voltage. The data were interpreted in terms of tunneling via the adsorbate metal centers.

Tao studied electroactive molecule, Fe-protoporphyrins IX, coadsorbed with nonelectroactive protoporphyrins IX on graphite substrate in electrolyte [83]. Because of the difficulty in obtaining reliable STS in electrolyte, the apparent height of Fe-protoporphyrins IX relative to that of protoporphyrins IX was measured as a function of the electrochemical potential. A large increase in the tunneling current occurred when the potential was tuned to the redox potential. This observation was originally interpreted as a resonant tunneling via the oxidized state of Fe-protoporphyrins IX in terms of the coherent one-step model [83, 84], but the coherent one-step model predicts a maximum shifted away from the redox potential by  $\lambda$ , the reorganization energy. This, although, could be due to a small reorganization energy or experimental uncertainty in the potential, the sequential two-step electron transfer offers an alternative explanation [81].

Han and coworkers [85] studied STS of a series of metal-porphyrin compounds adsorbed onto a Au(111) electrode in an organic solvent (mesitylene). The molecules

were modified with thiol groups at one end so that they were tethered to the surface via the strong S-Au bonds. The derivative of these curves ( $dI/dV$ ) had a Gaussian-shaped peak at a voltage characteristic of the compound (Fig. 3). These bias-dependent features were not observed in the less electroactive molecules, so the STM was shown to be capable of distinguishing electroactive molecules from nonelectroactive molecules. They attempted to fit their data with both the coherent one-step and sequential two-step models outlined above. Both models yielded Gaussian-like peaks in the  $dI/dV_{\text{bias}}$  versus  $V_{\text{bias}}$  plot. The Gaussian predicted by the first model (Eqs. 7 and 8) was located at a lower potential than that by the second model, but they could not distinguish the two models within the experimental error.

Hipps and coworkers obtained STS metal-phthalocyanines adsorbed on Au(111) surfaces with STM in conjunction with the tunneling spectroscopy obtained with the metal-insulator junctions [86–88]. STM images showed that the molecules lay flat on

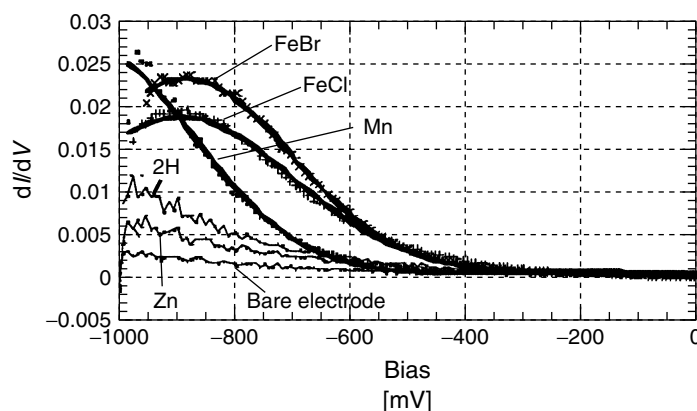


**Fig. 3** Derivatives ( $dI/dV_{\text{bias}}$ ) of the tunneling current versus bias voltage curves of Fe, Mn, Zn, and H embedded in tetraphenol porphyrin (TPP). (From Ref. [85] with permission.)

the surface, and the brightness of the central part of the molecule depended on the metal ion located there [86, 89]. The measured resonant tunneling via the molecular orbital shown in the STS was in good agreement with the macroscopic tunneling spectroscopy. Although the experiments were measured in vacuum, where reliable tunneling spectroscopy can be more easily obtained than in air or in water, they demonstrated a correlation between the orbital-mediated tunneling spectroscopy data and the redox potentials of the metal-phthalocyanines in solution [87, 90].

In addition to the relative simple redox molecules, electrochemical STM has been applied to study redox proteins, such as cytochrome *c* [91–93], blue copper protein *Pseudomonas aeruginosa* azurin [94–96], and PS I system [97]. An interesting observation by Ulstrup and coworkers is a “spike” localized near the center of each azurin molecule, which means a much higher electron tunneling through the region of the “spike” [94]. The “spike” was assigned to the electron transfer via the redox center, copper, in azurin, which enhanced the tunneling current. The tunneling current, however, depended only weakly on the bias voltage and the electrochemical overpotential, which could be because of the relative large bias voltage used in the experiment. This study provides the first evidence of local “spectroscopic” information of redox proteins with STM.

**3.3.4.1.2 Molecular Identifications** Because STM probes the electronic properties of the molecules, it can identify structurally similar molecules on the basis of the difference in the electronic states of the molecules. The works on redox molecules described above are good examples of such applications. Molecular

identification of other species has also been demonstrated. Schott and White [98] studied a mixed monolayer of halogen atoms (F, Cl, Br, and I) on Ag(111), in addition to the different radii and they observed differences in the tunneling spectra of the halogen species. Another interesting molecular identification with STM was carried in monolayer films of several primary substitute hydrocarbons  $\text{CH}_3(\text{CH}_2)_n\text{CH}_2\text{X}$  ( $\text{X}=\text{CH}_3$ , OH,  $\text{NH}_2$ , SH, Cl, Br, and I) on graphite–solution interfaces by Flynn and coworkers [99, 100]. The hydrocarbons formed well-ordered arrays on the surface. The  $\text{NH}_2$ , SH, Br, and I groups appeared as bright spots in the STM images while OH and Cl groups were not distinguishable from the alkyl chain, so it is possible to identify the molecules with different substitutes according to their “brightness” in the STM images. Claypool and coworkers imaged a series of substituted alkanes and alkanols on graphite [101]. They found that all the functional groups (halides, amines, alcohols, nitriles, alkenes, alkynes, ethers, thioethers, and disulfides) studied in their experiments could be distinguished from each other except for Cl and OH groups. Their results were consistent with quantum chemistry calculations [101]. Recently, Claypool and coworkers extended the study to  $\text{MoS}_2$  surface and the images of tetradecanol on  $\text{MoS}_2$  were nearly identical to those obtained on graphite [102].

**3.3.4.1.3 Molecular Electronics** As silicon-based microelectronics is heading towards the increasingly difficult road of nanometer scale, building electronic devices with individual molecules (molecular electronics) becomes a promising alternative [103, 104]. Indeed, many molecules possess wonderful electronic properties

that could be used as basic elements in a functional electronic device. A major challenge is to find a practical method to wire individual molecules to the outside world. STM can “wire” a single molecule with the sharp tip and probe electron transfer through individual molecules. A large number of works have already been performed [86, 88, 105–112]. Gimzewski and coworkers have published an excellent review recently [113], we describe here an interesting example that is based on the redox properties of molecules.

Gittins and coworkers [114] explored molecular electronics applications using STS and electrochemistry (Fig. 4). Their system consisted of gold nanoparticles attached to a gold electrode surface via the redox-active bipyridinium moiety. They controlled the electron transport between the nanoparticles and the electrode by controlling the redox state of the bipyridinium moiety. They measured the decay constant ( $k$  in Eq. 1) that dropped sharply on reduction of  $\text{bipy}^{2+}$  to  $\text{bipy}^{*+}$ , from  $\sim 16 \text{ nm}^{-1}$  to  $\sim 7 \text{ nm}^{-1}$ . They attributed the observed change to the injection of charge into the redox group, and thus showed that the electronic properties of the junction could be switched by the redox state. They also measured STS in mesitylene and observed a sharp peak in the  $dI/dV_{\text{bias}}$  versus  $V_{\text{bias}}$  plot (Fig. 4). Because of the stability of the  $\text{bipy}^{*+}$  state, the peak was interpreted as a two-step electron transfer through a temporary population of the molecular redox state.

#### 3.3.4.2 Force Spectroscopy

AFM has been applied to study various surface forces [44, 115–117]. The principle is similar to the surface force apparatus (SFA) that was developed some years ago [45]. SFA measures the force between two curved atomically smooth surfaces.

The separation between the two surfaces is controlled by a piezoelectric transducer and measured by an optical interferometric technique. Because SFA uses surfaces with known geometries, precise measurements of surface forces and energies are possible. However, SFA measures the force of a relative large surface area and is limited to atomically flat surfaces. That is why most of the SFA studies have been carried out on mica surfaces. AFM measure the force between a tip and a sample surface. A drawback is that the AFM tip geometry is not always precisely known, although attempts to control the tip geometry have been made by attaching an object with known geometry onto the regular AFM tip. Examples include colloidal particle [118, 119] and carbon nanotube [120]. However, being a local probe, AFM does not require atomically flat sample surfaces. Furthermore, AFM allows one to image the sample first and then place the tip over the region of interest.

As mentioned before, AFM can measure surface forces using two different operation modes, DC and AC. In the DC mode, one measures the deflection ( $\Delta Z$ ) of a cantilever as a function of the tip-sample distance ( $D$ ) that is varied usually by a piezoelectric transducer (Fig. 3). The tip-sample force is given by Hooke's law in terms of  $\Delta Z$ ,  $F = k\Delta Z$ , where  $k$  is the spring constant of the cantilever. This force clearly depends on the tip-sample distance,  $D$ , which is given by  $D = Z - \Delta Z$ , in the absence of sample deformation.  $Z$  in the expression is the displacement of the piezo and the one that can be controlled in the experiment. When the tip is far away from the sample (large  $D$ ), the force is zero. When the tip approaches the sample, it experiences various forces, electrostatic, van der Waals, double-layer, solvation forces, and so on. This is the regime of interest in

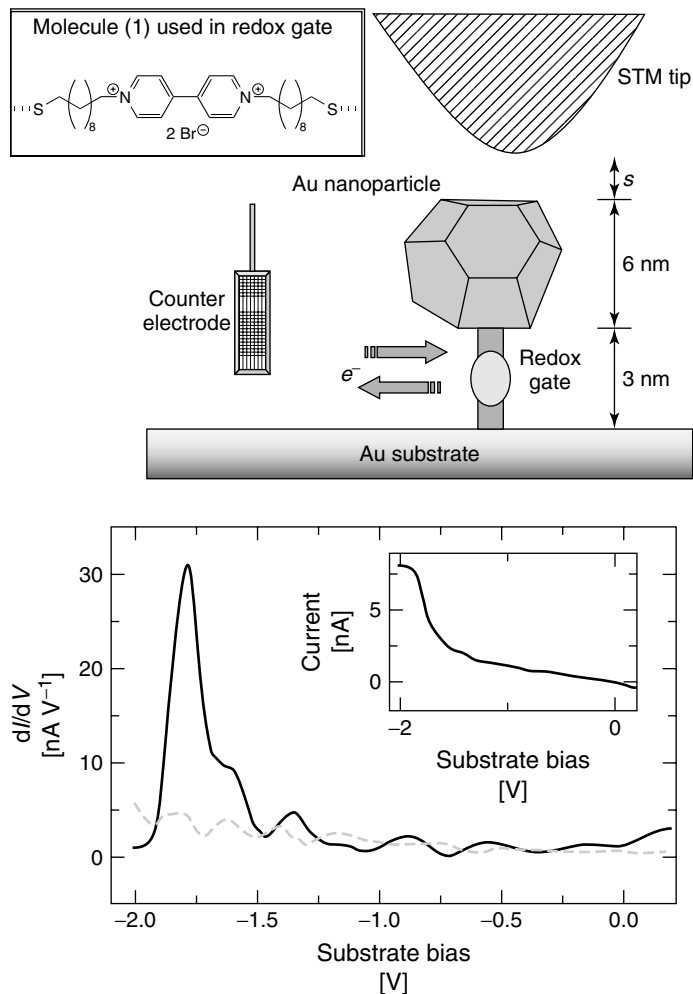


**Fig. 4** (a) Schematic representation of a nanoscopic device. Electrons can be injected into the redox gate by applying a suitable potential between the substrate and the counterelectrode. (b) A current–voltage curve (inset) and its derivative ( $dI/dV_{\text{bias}}$ ) in mesitylene. The dotted line corresponds to the control experiment, in which gold nanoparticles were deposited on a hexanedithiol monolayer. (From Ref. [114] with permission.)

terms of measuring surface forces. Finally, when  $D$  approaches zero, the tip is in contact with the sample surface. The plots of  $\Delta Z$  versus  $Z$  provide the tip-sample force,  $F(D)$ , and are often referred to as force-distance curves.

As we have already mentioned, the AC mode involves an oscillating AFM tip. When the tip is driven towards a sample surface, the oscillation is altered by the tip–sample interactions. If the cantilever is driven to oscillate at a fixed frequency,

the changes in the oscillation amplitude can be used to obtain the tip-sample force information. An alternative approach is to use a feedback to constantly monitor the resonance frequency that is changed by the tip-sample interactions. The AC force-distance curves are often referred to as dynamic force-distance curves. We note that for small oscillation amplitude, the change in the resonance frequency is proportional to the derivative of the force with respect to the tip-sample distance or differential stiffness (Eq. 5).

**3.3.4.2.1 Double-layer Forces** Double-layer forces arise when two charged surfaces separated with an electrolyte approach each other. The charge on each surface is balanced by an equal but oppositely charged region of counterions in the electrolyte. Some of the counterions are adsorbed on the surface, either transiently or permanently, within the so-called Helmholtz layer. Beyond the Helmholtz layer is a so-called diffuse electric double layer in which the ions are in rapid thermal motion. When bringing two such charged surfaces together, a double-layer force appears that can be traced to an electrostatic and entropic contribution. The electrostatic contribution favors an attraction between the surfaces because they are pulled together by the oppositely charged counterions. The entropic contribution is, however, repulsive because the configurational entropy favors more space between the surfaces. Because the van der Waals force always presents between two surfaces regardless the surface charge, it needs to be considered together with the double-layer force. Such a treatment was given by the well-known DLVO theory [45]. For a spherical tip geometry with a radius  $R$  and a flat substrate, the van der Waals

force is given by  $-H_a R/6D^2$  [45], where “-” sign reflects attractive force,  $H_a$  is Hamaker constant.

Assuming two semi-infinite surfaces with fixed surface charge density, Parsegian and Gingell [121] obtained an analytical expression for the double-layer force in the limit of small surface potentials ( $<25$  mV). Butt [122] calculated the double-layer force between a flat sample and a spherical tip with radius  $R$  using the Derjaguin approximation. If  $K_D R \gg 1$ , his results can be simplified to

$$F_{dl} = \frac{2\pi R}{\epsilon_0 \epsilon K_D} [(\sigma_T^2 + \sigma_S^2) e^{-2K_D D} + 2\sigma_T \sigma_S e^{-K_D D}] \quad (12)$$

where  $\sigma_T$ ,  $\sigma_S$  are the surface charge densities of the tip and sample, and  $K_D$  is the inverse of the Debye length ( $1/K_D$ ). The Debye length depends on the concentration and the valence of ions and is given by

$$\frac{1}{K_D} = \frac{c}{\sqrt{[X]}} \text{ nm} \quad (13)$$

where  $[X]$  is the electrolyte concentration in moles,  $c = 0.304$ ,  $0.176$ , and  $0.152$  for 1:1, 1:2 (or 2:1), and 2:2 electrolytes, respectively.

If  $\sigma_T < \sigma_S$ , that is, the tip is neutral, the first term in Eq. (6) dominates and the double-layer force decays exponentially with a decay length,  $1/2K_D$ . This term is always positive and thus gives a repulsive force, while the second term can be either repulsive or attractive. The second term decays with  $1/K_D$ , slower than the first term, so the second term dominates the solvation force at a large tip-sample separation.

The above models assume constant surface charge densities. Assuming constant surface potentials, Lin and coworkers [123] obtained

$$F_{\text{dl}} = 4\pi\epsilon\epsilon_0 R K_D \varphi_T \varphi_S e^{-K_D D} \quad (14)$$

where  $\varphi_T$  and  $\varphi_S$  are surface potentials of the tip and the sample, respectively. In most practical cases, it is likely that neither the surface charge nor the potential stays constant.

AFM has been used to measure double-layer forces between many insulator surfaces, including  $\text{Si}_3\text{N}_4$  tips on mica, diamond tips on mica, glass tips on glass, ZnS colloidal particle on mica, and polystyrene colloidal particle on polystyrene colloidal particle [119, 124, 125]. In these papers, the experimental data were fit with the second term of Eq. (6) or Eq. (8). The fitting allowed Weisenhorn and coworkers [124] to extract the Debye length, which was found to agree nicely with Eq. (7). In addition to ionic concentration, other experimental parameters, such as pH, were also varied, which allows the determination of the point of zero charge (isoelectric point) [126].

The double-layer forces between a metal and an insulator as well as between two metal surfaces have also been studied. For example, Biggs and coworkers [127, 128] have measured forces between a gold colloidal sphere and a flat gold substrate as a function of ionic concentration and pH. Several groups have carried out measurements of the double-layer forces with molecular adsorptions taking place on the metal surface [129–133].

Most of the studies were focused on relative low surface potentials because of the difficulty of making clean surfaces with high potentials. In the case of metal surfaces, one can easily obtain a high surface potential by applying an external potential

to the metal electrode relative to a reference electrode in the electrolyte [134–137]. Hillier and coworkers [137] studied the force between a silica probe and a gold electrode (Fig. 5). The force was attractive at open circuit, but it depended strongly on the potential applied to the gold and the type of the electrolyte. It was attractive at positive potentials and became repulsive at negative potentials. This was because the silica tip was negatively charged at a pH of 5.5. They carried out a systematic study of the force as function of the applied potential and found that the repulsive force decreased as the potential increased and passed through a minimum, which they referred to as the potential of zero force (pzf). They measured the pzf values in solutions of NaF, KCl, and KI, which showed a close correspondence between pzf and pzc (potential of zero charge). At large tip-surface separations, theoretical fits of the measured force to solutions of the Poisson–Boltzmann equation were excellent. At small separations, however, neither constant surface charge (Eq. 6) nor constant surface potential boundary conditions (Eq. 8) provided good fits. The poor fits at small separations were attributed to an overestimate of the Hamaker constant, an ill-defined position for the plane of surface charge, and the presence of short-range solvation forces.

Raiteri and coworkers [135] carried out a similar measurement of the force between a silicon nitride tip and a platinum or gold substrate and between two conductive surfaces, a gold sphere glued to an AFM cantilever and a gold electrode in 0.1 M KCl. They observed a large decrease in a repulsive force around the pzc of the gold electrode, which agreed qualitatively with the Poisson–Boltzmann theory. Arai and Fujihira [138] observed a similar repulsive



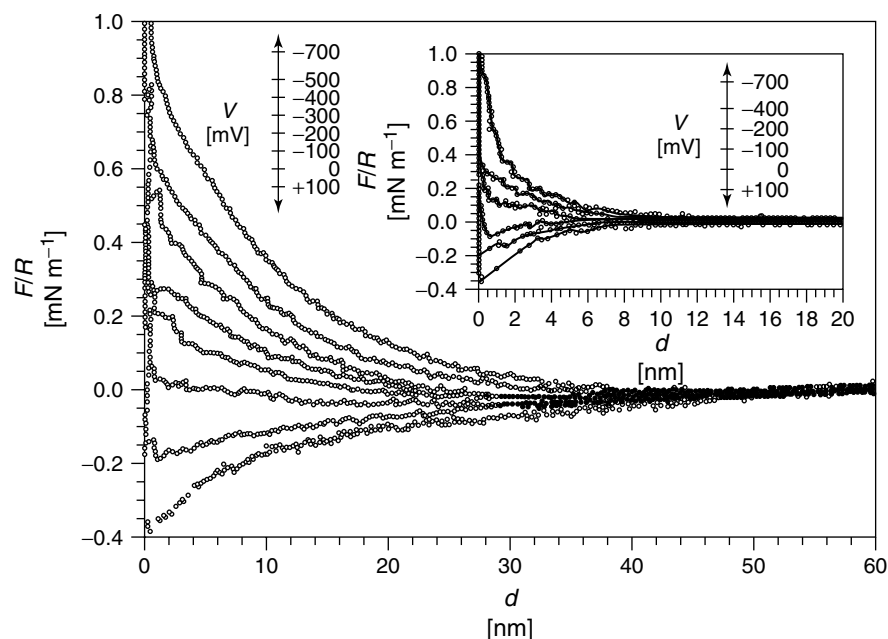


**Fig. 5** Force between silica sphere and gold electrode in an aqueous solution of 1 mM KCl at 25 °C and pH = 5.5 as a function of the applied potential at gold electrode. The curves correspond to, from top to bottom, electrode potentials of -700, -500, -400, -300, -200, -100, 0, and 100 mV (vs SCE). Electrostatic repulsion decreases as the electrode potential increases from -700 to 100 mV. Inset: force data for silica sphere and gold substrate in 10 mM KCl solution. (From Ref. [137] with permission.)

force between a gold-coated AFM tip and a gold substrate at pH = 10.9.

**3.3.4.2.2 Solvation Forces** When the tip-sample distance is smaller than a few nm, the DLVO theory, that is, an attractive van der Waals force and a repulsive double-layer force, is often not adequate. One possible reason is the break down of the approximation that both the tip and the substrate are treated as continuous media. Another reason is because other forces arise at the small distances. One of such forces is the so-called solvation force that arises when solvent molecules between the tip and substrate are ordered or form hydrogen-bonded network under the influence of the tip and the substrate.

When the tip approaches the substrate, it has to break the order or hydrogen-bonded network, so the measurement of solvation forces provides ordering information and discrete nature of solvent molecules near the solid surfaces. The most general type of solvation force is oscillatory, arising from the ordering of the solvent molecules into quasi-discrete layers near the surface. This solvation force can be approximately described by a cosine function with an exponentially decaying amplitude [45],

$$\sim \cos\left(\frac{2\pi D}{d}\right) e^{-D/d} \quad (15)$$

where  $d$  is the diameter of the solvent molecule. Both the oscillation period and

the characteristic decay length are close to  $d$ .

AFM has been used to study the solvation forces due to interfacial water and organic liquids [139–142]. Hoh and coworkers [140] observed a discrete (oscillating) adhesive interaction between an AFM tip and a solid surface. They attributed the oscillations to either individual hydrogen bonds between the tip and surface, or ordered water layers near the surface. O'Shea and coworkers used an AFM in the DC mode to measure the force on the AFM tip in octamethylcyclotetrasiloxane (OMCTS),  $n$ -dodecanol, and water during the tip approaching the graphite surface [141]. For both OMCTS and  $n$ -dodecanol, they observed an oscillatory force that was related to the layered structure of the solvents. But the oscillatory force did not appear in the case of water. Later they used a magnetically oscillated tip microscope to directly measure the local compliance of ordered liquid layers of OMCTS and  $n$ -dodecanol on graphite and on mica [141]. However, the spacing between layers of OMCTS was substantially smaller than the known smallest dimension of the molecule so that an orientation of the molecules in the layers could not be determined.

Using an AFM operated in the magnetic AC mode, Han and Lindsay [142] determined the layered structure of solvents at interfaces with high accuracy and reproducibility (Fig. 6). They found that the AFM cantilever amplitude oscillated in OMCTS and mesitylene as the tip approached the surface graphite. Similar oscillations were also found when the tip retracted away from the surface. The oscillations became smeared out gradually when increasing the tip-surface distance, showing a transition from highly ordered solidlike structure to liquid structure. The

oscillations reflect the layered structure of the solvents near the surface, and the oscillation periods give the spacing between two adjacent layers. For OMCTS, the period was found to be  $\sim 0.82$  nm, in good agreement with the oblate shape of OMCTS with a major diameter of 1.0 to 1.1 nm and a minor diameter of 0.7 to 0.8 nm. The data for mesitylene was similar to that of OMCTS, except that the average period of the layers was measured to be  $\sim 0.45$  nm. This spacing is consistent in that the mesitylene rings lie flat with respect to the graphite surface.

**3.3.4.2.3 Surface Stress** Surface stress is closely related to another quantity, surface tension ( $\gamma$ ), the energy cost per unit area to create a surface, according to

$$\sigma_{ij} = \gamma \delta_{ij} + \left. \frac{\partial \gamma}{\partial \varepsilon_{ij}} \right|_T \quad (16)$$

where  $\sigma_{ij}$ , and  $\varepsilon_{ij}$  are components of the surface stress and strain tensors, and  $\delta_{ij} = 1$  when  $i = j$  and  $\delta_{ij} = 0$  when  $i \neq j$ . So, in general, the surface tension and the surface stress are not identical. However, the two quantities are identical when the surface tension is independent of small strains (the second term in Eq. 9 vanishes). This is true only for liquid or liquidlike surfaces that are free to rearrange in response to small perturbations. Surface stress is an important thermodynamic quantity in electrochemistry and often known as “electrocapilarity”. The name originates from the measurements of the interfacial tension between a mercury electrode and an electrolyte in the earliest days of electrochemistry [143]. Since the surface tension of a liquid electrode is identical to the surface stress, the Lippmann equation can

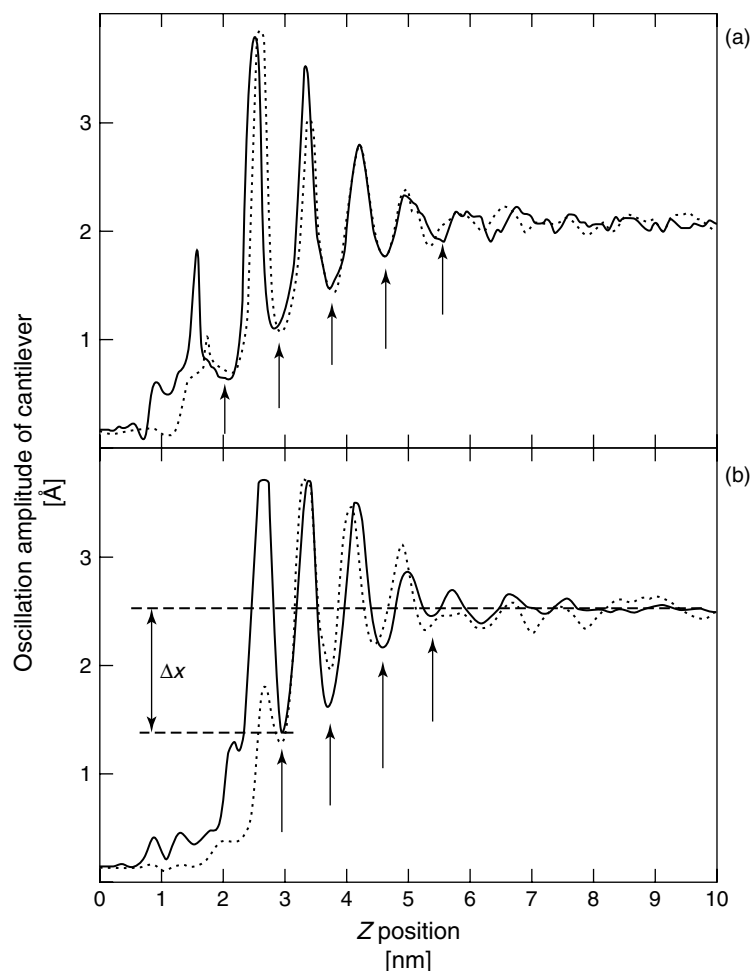


**Fig. 6** Two independent measurements of force spectra of the MAC mode AFM at OMCTS-graphite interface. The oscillation amplitude of the magnetic cantilever driven by an external magnetic field oscillates in both approaching (solid line) and retracting (dotted line) curves in the region of a few nanometers away from the surface due to ordered layers of OMCTS molecules at the interface. The arrows on this and subsequent plots correspond to repulsive-force maxima. (From Ref. [142] with permission.)

be derived for the mercury electrode that relates the electrode potential, the surface charge, and the interfacial stress. The Lippman equation predicts that the interfacial tension goes through a maximum at pzc, which has been used to determine pzc. Surface tension continues

to be a useful quantity to measure in today's research. For example, an electrochemical/thermodynamic procedure to determine surface tension, excess, and pressure has been developed and applied to study molecular adsorptions on well-defined crystals [144].

Surface stress can be measured by a number of experiments, including piezoelectric elements [145], ribbon electrodes [146], and more recently developed micromechanical sensors [147–149]. It can be also measured with AFM and STM, as demonstrated by several groups [150, 151]. The AFM and STM-based surface stress measurements usually detect the bending of a thin plate (cantilever) as a result of a surface stress change at one of the two surfaces. If the plate is isotropic and freely standing, the change in the surface stress can be calculated from the amount of bending by [152]

$$\Delta\sigma = \frac{Et^2}{4L^2(1-\nu)}\Delta z \quad (17)$$

where  $E$ ,  $t$ ,  $L$ , and  $\nu$  are the thickness, length, Young's modulus, and Poisson ratio of the cantilever, respectively. This equation has been widely used to determine changes in surface stress although one end of the cantilever is often clamped in experiments. Dahmen and coworkers [153] recently performed a finite element analysis of single crystal plates (anisotropic) with one end clamped. They concluded that Eq. (10) derived for the unconstrained bending could still be used in most cases with appropriate parameters.

It is clear from Eq. (10) that the bending of a cantilever because of a surface stress is  $\sim(L/t)^2\Delta\sigma$ , which requires long and thin cantilevers for high sensitivity. When trying to improve the sensitivity, one has to consider also the noise caused by environmental vibration in the measurement. In order to minimize the environmental vibration, one requires a high-resonance frequency,  $f = 0.163(t/L^2)\sqrt{E/\rho}$ , in which  $\rho$  is the density of the cantilever material. In AFM, microfabricated silicon or silicon nitride cantilevers coated with various

metals on one of the two faces are used to satisfy both requirements.

The microfabricated cantilever-based surface stress measurements have recently found many applications: changes in mass [154], heat dissipation [154, 155], magnetic field [156], infrared light [157], and polarized light [158], to name a few. There is a recent surge of interest in using the cantilevers for chemical and biological sensors in ambient air or aqueous environments [159–161]. For example, if one side of the cantilever with receptor molecules is coated and the other side is left “inert”, then a specific binding of chemical or biological species onto the receptor molecules results in a surface stress change in the cantilever. Fritz and coworkers [162] studied DNA hybridization and receptor-ligand binding using microfabricated cantilevers that were functionalized with a selection of biomolecules, and they were able to detect a single base mismatch between two 12-base pair DNA oligomers.

The microfabricated cantilevers have been used to study surface stress induced by electrochemical processes [163–166]. Brunt and coworkers [165, 166] monitored surface stress changes due to the electrochemical deposition and dissolution of a Pb and Ag on an Au(111)-coated AFM cantilevers. The changes corresponded nicely with the peaks in the cyclic voltammograms. Raiteri and coworkers [164] deposited the two sides of a gold-coated cantilever with different thiols, octadecanethiol, and 3-mercaptopropionic acid, respectively. The cantilever was exposed to a constant flow of aqueous electrolyte solution with varying pH and the surface stress-induced deflection in the cantilever was constantly measured. They found that the change in the surface stress had a minimum around pH 4 to 5. Increasing pH above 5 or decreasing it below 4

resulted in a bending of the cantilever toward the mercaptoprionic acid side. They attributed the observation to the proton dissociation of the carboxyl group, which lowered the free enthalpy of the carboxylate group. However, the simple mechanism was not adequate to explain the small increase in the surface stress when reducing the solution pH below 4. When replacing the mercaptoprionic acid monolayer with 2-aminoethanethiol and 2-mercaptoethanol, the surface stress increased monotonically with increasing pH. Another difference was that the surface stress change was much smaller than that of mercaptoprionic acid, in consistency with the smaller degrees of proton dissociation of 2-aminoethanethiol and 2-mercaptoethanol.

Measuring the surface stress of the AFM cantilever has a number of advantages over other approaches, but the approach is not

suitable if one wants to study the surface stress of a well-defined single crystal. This task can be performed with an STM setup [151, 167–169]. The sample in STM can be either a single crystal plate or thermally evaporated metal films on glass plate with one end clamped. One side of the single crystal plate must be covered with, for example, nail polish. An STM tip is placed over the other end to detect the surface stress-induced bending in the plate. The bending causes a change in the tunneling gap between the tip and sample and is reflected in a change of the tunneling current. The STM feedback maintains a constant current by adjusting the vertical position of the STM via a  $z$ -piezoelectric transducer. The amount of the adjustment gives the deflection,  $\Delta z$ , from which the surface stress is extracted using Eq. (10). A nice feature is that the same STM tip allows one also to image the surface.

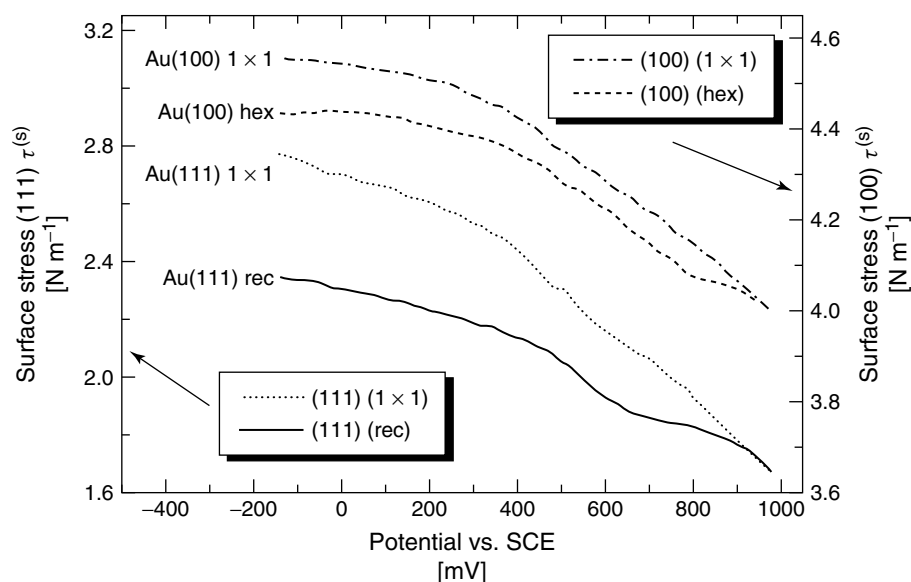


**Fig. 7** Surface stress versus the potential for the initially reconstructed and unreconstructed surfaces of Au(100) and Au(111). All measurements are from negative to positive potentials. (From Ref. [151] with permission.)

Using STM, Haiss and coworkers [168] studied the surface stress in the presence of anion adsorption on Au(111) as a function of the electrode potential. They found a linear dependence of the surface stress on the surface charge, with the slope depending on the type of electrolyte. However, the finding does not appear to be universal since the surface stress of Au(100) deviates significantly from the linear behavior at negative potentials [170]. Bach and coworkers [151] measured the change of the surface stress in the reconstruction of the Au(111) and the Au(100) surfaces in 0.1 M HClO<sub>4</sub> (Fig. 7). By controlling the electrochemical potential of the metal electrodes, the reconstruction was reversibly lifted. For both surfaces, the reconstruction relaxed the tensile stress by 22% and 5%, respectively, which can be understood since the average bond distances between the surface atoms are shorter in the reconstructed phases. In the case of the Au(111) surface, the energy gain due to the relaxation of the surface stress as estimated from the Frenkel–Kontorova model was close but not quite large enough to make the reconstruction energetically favored without the formation of the secondary herringbone structure of the solitons. For the Au(100) surface, the energy gain was found to be too small to cause the formation of the reconstruction.

### 3.3.5

#### Conclusion

Since the first applications of STM and AFM in electrochemistry more than a decade ago, both techniques have matured into powerful tools for imaging various electrochemical phenomena with high resolution. In addition to structural studies, many nonimaging applications based on STM and AFM have been demonstrated.

One important example is scanning tunneling spectroscopy that allows extraction of electronic states of the probed molecules. The electronic information can be used to identify structurally similar molecules, to obtain chemical reactivity of the molecules, and is directly relevant to the current effort of developing molecular electronics. However, in order to reliably extract the information, improvements in both the experimental method for measuring tunneling spectroscopy and theoretical description of the STM imaging mechanism in the electrochemical environment are needed. Another important example is the local force spectroscopy with AFM, which reveals not only various surface forces but also mechanical properties of individual molecules. The microfabricated cantilevers used as force sensors in AFM have found broad applications in chemical and biological sensors, in detecting infrared light, magnetic field, and other physical quantities and properties. Other nonimaging applications of STM and AFM in conjunction with the electrochemical techniques include nanofabrication and nanomanipulation, which will continue to play important roles in the emerging field of nanoscience and nanotechnology.

#### Acknowledgments

I am grateful to Shaopeng Wang, Salah Boussaad, Huixin He, and Yuwen Zhao for their comments and discussions. The lab has been supported by grants from NSF (CHE-9818073), PRF (33516-AC5, administered by the ACS), and AFOSR (F49620-99-1-0112).

#### References

1. G. Binnig, H. Rohrer, C. Gerber et al., *Phys. Rev. Lett.* **1982**, 49, 57–61.

2. G. Binnig, C. F. Quate, C. Gerber, *Phys. Rev. Lett.* **1986**, 56, 930–933.
3. R. Sonnenfeld, P. K. Hansma, *Science* **1986**, 232, 211–213.
4. H. Y. Liu, F. R. F. Fan, C. W. Lin et al., *J. Am. Chem. Soc.* **1986**, 108, 3838, 3839.
5. S. Manne, H. J. Butt, S. A. C. Gould et al., *Appl. Phys. Lett.* **1990**, 56, 1758, 1759.
6. S. Manne, P. K. Hansma, J. Massie et al., *Science* **1991**, 251, 183–186.
7. J. Lipkowsky, P. N. Ross, (Eds.), *Imaging of Surfaces and Interfaces*, Wiley-VCH, New York, 1999.
8. A. A. Gewirth, B. K. Niece, *Chem. Rev.* **1997**, 97, 1129–1162.
9. A. J. Bard, H. D. Abruna, C. E. Chidsey et al., *J. Phys. Chem.* **1993**, 97, 7147–7173.
10. T. P. Moffat, *Electroanal. Chem.* **1999**, 21, 211–316.
11. D. M. Kolb, *Electrochem. Acta* **2000**, 45, 2387–2402.
12. J. E. T. Andersen, J.-D. Zhang, Q. Chi et al., *Trend Anal. Chem.* **1999**, 18, 665–674.
13. C. J. Chen, *Introduction to Scanning Tunneling Microscopy*, Oxford University Press, New York, 1993.
14. J. H. Coombs, J. B. Pethica, *IBM J. Res. Dev.* **1986**, 20, 455–459.
15. R. Christoph, H. Siegenthaler, H. Rohrer et al., *Electrochim. Acta* **1989**, 34, 1011.
16. J. Wiechers, T. Twomey, D. M. Kolb et al., *J. Electroanal. Chem.* **1988**, 248, 451.
17. M. Bingelli, D. Carnal, R. Nyffenegger et al., *J. Vac. Sci. Technol., B* **1991**, 9, 1985–1992.
18. J. Pan, T. W. Jing, S. M. Lindsay, *J. Phys. Chem.* **1993**, 98, 4205–4208.
19. A. Vaught, T. W. Jing, S. M. Lindsay, *Chem. Phys. Lett.* **1995**, 236, 306–310.
20. Y. A. Hong, J. R. Hahn, H. Kang, *J. Chem. Phys.* **1998**, 108, 4367–4370.
21. W. Schmickler, D. Henderson, *J. Electroanal. Chem.* **1990**, 290, 283–291.
22. M. V. Vigdorovich, A. M. Kuznetsov, J. Ulstrup, *Chem. Phys.* **1993**, 176, 539–554.
23. G. Repphun, J. Halbritter, *J. Vac. Sci. Technol., A* **1995**, 13, 1693–1698.
24. W. Schmickler, *Surf. Sci.* **1995**, 335, 416–421.
25. I. Benjamin, D. Evans, A. Nitzan, *J. Chem. Phys.* **1997**, 106, 1291–1293.
26. J. Bardeen, *Phys. Rev. Lett.* **1960**, 6, 57–59.
27. J. Tersoff, D. R. Hamann, *Phys. Rev. B* **1985**, 31, 805–814.
28. S. M. Lindsay, O. F. Sankey, Y. Li et al., *J. Phys. Chem.* **1990**, 94, 4655–4660.
29. N. D. Lang, *Phys. Rev. Lett.* **1986**, 56, 1164–1167.
30. V. Mujica, M. Kemp, M. A. Ratner, *J. Chem. Phys.* **1994**, 101, 6849–6864.
31. H. Ou-Yang, B. Kallebring, R. A. Marcus, *J. Chem. Phys.* **1993**, 98, 7565–7824.
32. A. J. Fisher, P. E. Blöchl, *Phys. Rev. Lett.* **1993**, 70, 3263–3266.
33. D. N. Futaba, S. Chiang, *J. Vac. Sci. Technol., A* **1997**, 15, 1295–1298.
34. V. M. Hallmark, S. Chiang, *Surf. Sci.* **1995**, 329, 255–268.
35. X. W. Wang, N. J. Tao, F. Cunha, *J. Chem. Phys.* **1996**, 105, 3747–3752.
36. A. M. Kuznetsov, P. Sommer-Larsen, J. Ulstrup, *Surf. Sci.* **1992**, 275, 52–64.
37. J. E. T. Andersen, A. A. Kornyshev, A. M. Kuznetsov et al., *Electrochim. Acta* **1997**, 42, 819–831.
38. W. Schmickler, C. Widrig, *J. Electroanal. Chem.* **1992**, 336, 213–221.
39. H. Sumi, *J. Phys. Chem. B* **1998**, 102, 1833–1844.
40. A. K. Mishra, S. K. Rangarajan, *Theochem: J. Mol. Struct.* **1996**, 361, 101–109.
41. A. M. Kuznetsov, J. Ulstrup, *Mol. Phys.* **1992**, 87, 1189.
42. W. Schmickler, *J. Electroanal. Chem.* **1990**, 296, 283–289.
43. M. Tortonese, R. C. Barrett, C. F. Quate, *Appl. Phys. Lett.* **1993**, 62, 834–836.
44. S. M. Lindsay in *Scanning Tunneling Microscopy and Related Techniques* (Ed.: D. Bonnell), John Wiley & Sons, New York, 2000.
45. J. N. Israelachvili, *Intermolecular and Surface Forces*, Academic Press, London, 1992.
46. F. Ohnesorge, G. Binnig, *Science* **1993**, 260, 1451–1456.
47. F. J. Giessibl, *Phys. Rev. B* **1997**, 56, 16 010–16 015.
48. T. R. Albrecht, P. Grutter, D. Horne et al., *J. Appl. Phys.* **1991**, 69, 668–673.
49. F. J. Giessibl, *Science* **1995**, 267, 68–71.
50. F. J. Giessibl, *Appl. Phys. Lett.* **2000**, 76, 1470–1472.
51. Q. Zhong, D. Inniss, K. Kjoller et al., *Surf. Sci.* **2000**, 468, L688–L690.
52. P. K. Hansma, J. P. Cleveland, M. Radmacher et al., *Appl. Phys. Lett.* **1994**, 65, 1738–1741.

53. C. A. J. Putman, K. O. Vanderwerf, B. G. Degrooth et al., *Appl. Phys. Lett.* **1994**, *64*, 2454–2456.
54. S. M. Lindsay, Y. I. Lyubchenko, N. J. Tao et al., *J. Vac. Sci. Technol.* **1993**, *11*, 808–815.
55. E. I. Florin, M. Radmacher, B. Fleck et al., *Rev. Sci. Instrum.* **1994**, *65*, 639–643.
56. W. Han, S. M. Lindsay, T. Jing, *Appl. Phys. Lett.* **1996**, *69*, 4111–4113.
57. A. A. Kornyshev, M. Sumetskii in *Electrochemical Nanotechnology: In situ Local Probe Techniques of Electrochemical Interfaces* (Ed.: W. J. L. A. W. Plieth), Wiley-VCH, Weinheim, Germany, 1998, pp. 45–55.
58. N. J. Tao, C. Z. Li, H. X. He, *J. Electroanal. Chem.* **2000**, *492*, 81–93.
59. R. M. Nyffenegger, R. M. Penner, *Chem. Rev.* **1997**, *97*, 1195–1230.
60. L. A. Nagahara, T. Thundat, S. M. Lindsay, *Appl. Phys. Lett.* **1990**, *57*, 270–272.
61. D. M. Kolb, R. Ullmann, T. Will, *Science* **1997**, *275*, 1097–1099.
62. C. B. Ross, L. Sun, R. M. Crooks, *Langmuir* **1993**, *9*, 632–636.
63. W. J. Li, J. A. Nirtanen, R. M. Penner, *Appl. Phys. Lett.* **1992**, *60*, 1181–1183.
64. R. T. Potzshke, G. Staikov, W. J. Lorentz et al., *J. Electrochem. Soc.* **1999**, *146*, 141–149.
65. U. Stimming, R. Vogel, D. M. Kolb et al., *J. Power Sources* **1993**, *43*, 169–180.
66. D. Hofmann, W. Schindler, J. Kirchner, *Appl. Phys. Lett.* **1998**, *73*, 3279–3281.
67. R. Schuster, V. Kirchner, X. H. Xia et al., *Phys. Rev. Lett.* **1998**, *80*, 5599–5602.
68. C. Z. Li, N. J. Tao, *Appl. Phys. Lett.* **1998**, *72*, 894–897.
69. G. Binnig, H. Fuchs, E. Stoll, *Surf. Sci.* **1986**, *169*, L295–L298.
70. M. L. Lozano, M. C. Tringides, *Europhys. Lett.* **1995**, *30*, 537–542.
71. M. Sumetskii, A. A. Kornyshev, *Phys. Rev. B* **1993**, *48*, 17 493–17 506.
72. M. Sumetskij, A. A. Kornyshev, U. Stimming, *Surf. Sci.* **1994**, *307*, 23–27.
73. O. M. Magnussen, M. R. Vogt, *Phys. Rev. Lett.* **2000**, *85*, 357–360.
74. M. Giesen-Seibert, R. Jentjens, M. Poensgen et al., *Phys. Rev. Lett.* **1993**, *71*, 3521–3524.
75. M. Giesen, R. Randler, S. Baier et al., *Electrochim. Acta* **1999**, *45*, 527–536.
76. I. Giaever, *Phys. Rev. Lett.* **1960**, *5*, 147, 148.
77. R. M. Feenstra, J. A. Stroscio, A. P. Fein, *Surf. Sci.* **1987**, *181*, 295–306.
78. H. Morisaki, H. Nishikawa, H. Ono et al., *J. Electrochem. Soc.* **1990**, *137*, 2759–2763.
79. H. Gerischer, *Z. Phys. Chem. N. F.* **1961**, *27*, 48.
80. E. P. Friis, Y. I. Kharkats, A. M. Kuznetsov et al., *J. Phys. Chem. A* **1998**, *102*, 7851–7859.
81. A. M. Kuznetsov, J. Ulstrup, *J. Phys. Chem. A* **2000**, *104*, 11 531–11 540.
82. S. R. Snyder, H. S. White, *J. Electroanal. Chem.* **1995**, *394*, 177–185.
83. N. J. Tao, *Phys. Rev. Lett.* **1996**, *76*, 4066–4069.
84. W. Schmickler, N. J. Tao, *Electrochim. Acta* **1997**, *432*, 2809–2815.
85. W. Han, E. N. Durantini, T. A. Moore et al., *J. Phys. Chem.* **1997**, *10*, 10 719–10 725.
86. X. Lu, K. W. Hipps, X. D. Wang et al., *J. Am. Chem. Soc.* **1996**, *118*, 7197–7202.
87. U. Mazur, K. W. Hipps, *J. Phys. Chem. B* **1999**, *103*, 9721–9727.
88. L. Scudiero, D. E. Barlow, K. W. Hipps, *J. Phys. Chem. B* **2000**, *104*, 11 899–11 905.
89. X. Lu, K. W. Hipps, *J. Phys. Chem. B* **1997**, *101*, 5391–5396.
90. U. Mazur, K. W. Hipps, *J. Phys. Chem.* **1995**, *99*, 6684–6688.
91. J. E. T. Andersen, P. P. Moller, M. V. Pedersen et al., *Surf. Sci.* **1995**, *325*, 193–205.
92. B. Zhang, E. Wang, *Probe Microsc.* **1997**, *1*, 57–60.
93. J. D. Zhang, Q. Chi, S. J. Dong et al., *J. Electroanal. Chem.* **1996**, *379*, 535–539.
94. E. P. Friis, J. E. T. Andersen, Y. I. Kharkats et al., *Proc. Natl. Acad. Sci. USA* **1999**, *96*, 1379–1384.
95. E. P. Friis, J. E. T. Andersen, P. Moller et al., *J. Electroanal. Chem.* **1997**, *431*, 35–38.
96. J. J. Davis, C. M. Halliswell, H. O. A. Hill et al., *New J. Chem.* **1998**, *22*, 1119–1123.
97. I. Lee, J. W. Lee, R. J. Warmack et al., *Proc. Natl. Acad. Sci. USA* **1995**, *92*, 1965–1969.
98. J. H. Schott, H. S. White, *Langmuir* **1994**, *10*, 486–491.
99. D. M. Cyr, B. Venkataraman, G. W. Flynn et al., *J. Phys. Chem.* **1996**, *100*, 13 748–13 759.
100. H. B. Fang, L. C. Giancarlo, G. W. Flynn, *J. Phys. Chem. B* **1999**, *103*, 5712–5715.
101. C. L. Claypool, F. Faglioni, W. A. Goddard et al., *J. Phys. Chem. B* **1997**, *101*, 5978–5995.



102. C. L. Claypool, F. Faglioni, W. A. Goddard et al., *J. Phys. Chem. B* **1999**, *103*, 7077–7080.
103. C. Joachim, J. K. Gimzewski, A. Aviram, *Nature* **2000**, *408*, 541–548.
104. P. Ball, *Nature* **2000**, *406*, 118–120.
105. L. A. Bumm, J. J. Arnold, M. T. Cygan et al., *Science* **1996**, *271*, 1705–1707.
106. G. S. McCarty, P. S. Weiss, *Chem. Rev.* **1999**, *99*, 1983–1990.
107. G. Leatherman, E. N. Durantini, D. Gust et al., *J. Phys. Chem. B* **1999**, *103*, 4006–4010.
108. Y. Q. Xue, S. Datta, S. Hong et al., *Phys. Rev. B* **1999**, *59*, R7852–R7855.
109. D. J. Wold, C. D. Frisbie, *J. Am. Chem. Soc.* **2000**, *122*, 2970, 2971.
110. S. Datta, W. D. Tian, S. H. Hong et al., *Phys. Rev. Lett.* **1997**, *79*, 2530–2533.
111. C. Joachim, J. K. Gimzewski, *Chem. Phys. Lett.* **1997**, *265*, 353–357.
112. V. J. Langlais, R. R. Schlittler, H. Tang et al., *Phys. Rev. Lett.* **1999**, *83*, 2809–2812.
113. J. K. Gimzewski, C. Joachim, *Science* **1999**, *283*, 1683–1688.
114. D. I. Gittins, D. Bethell, D. J. Schiffrin et al., *Nature* **2000**, *408*, 67–69.
115. E. Meyer, H. Heinzelmann, P. Grutter et al., *J. Microsc.* **1988**, *152*, 269.
116. B. Cappelletti, G. Dietler, *Surf. Sci. Rep.* **1999**, *34*, 1–104.
117. S. Manne, H. E. Gaub, *Curr. Opin. Colloid Interface Sci.* **1997**, *2*, 145–152.
118. W. A. Ducker, T. J. Senden, R. M. Pashley, *Nature* **1991**, *353*, 239–241.
119. Y. Q. Li, N. J. Tao, J. Pan et al., *Langmuir* **1993**, *9*, 637–641.
120. H. J. Dai, J. H. Hafner, A. G. Rinzler et al., *Nature* **1996**, *384*, 147–151.
121. V. A. Parsegian, D. Gingell, *Biophys. J.* **1972**, *12*, 1192.
122. H.-J. Butt, *Biophys. J.* **1991**, *60*, 1438–1444.
123. X. Y. Li, F. Creuzet, H. Arribart, *J. Phys. Chem.* **1993**, *97*, 7272–7276.
124. A. L. Weisenhorn, P. Maivald, H.-J. Butt et al., *Phys. Rev. B* **1992**, *45*, 11 226–11 232.
125. D. T. Atkins, R. M. Pashley, *Langmuir* **1993**, *9*, 2232–2236.
126. R. Raiteri, S. Martinoia, M. Grattarola, *Biosens. Bioelectron.* **1996**, *11*, 1009–1017.
127. S. Biggs, P. Mulvaney, *J. Chem. Phys.* **1994**, *100*, 8501–8505.
128. S. Biggs, P. Mulvaney, C. Zukoski et al., *J. Am. Chem. Soc.* **1994**, *116*, 9150–9157.
129. V. Kane, P. Mulvaney, *Langmuir* **1998**, *14*, 3303–3311.
130. B. A. Hu K, *Langmuir* **1997**, *13*, 5418–5425.
131. C. Z. Hu K, J. K. Whitesell, A. J. Bard, *Langmuir* **1999**, *15*, 3343–3347.
132. S. Manne, J. P. Cleveland, H. E. Gaub et al., *Langmuir* **1994**, *10*, 4409–4413.
133. I. Larson, D. Y. C. Chan, C. J. Drummond et al., *Langmuir* **1997**, *13*, 2429–2431.
134. R. Raiteri, M. Preuss, M. Grattarola et al., *Colloids Surf., A* **1998**, *136*, 191–197.
135. R. Raiteri, M. Grattarola, H.-J. Butt, *J. Phys. Chem.* **1996**, *100*, 16 700–16 705.
136. T. Ishino, H. Hieda, K. Tanaka et al., *Jpn. J. Phys.* **1994**, *33*, L1552–L1554.
137. A. C. Hillier, S. Kim, A. J. Bard, *J. Phys. Chem.* **1996**, *100*, 18 808–18 817.
138. T. Arai, M. Fujihira, *J. Vac. Sci. Technol., B* **1996**, *14*, 1378–1382.
139. J. B. Pathica, W. C. Oliver, *Phys. Scr.* **1987**, *T19*, 61–66.
140. J. H. Hoh, J. P. Cleveland, C. B. Prater et al., *J. Am. Chem. Soc.* **1992**, *114*, 4917, 4918.
141. S. J. O'Shea, M. E. Welland, T. Rayment, *Appl. Phys. Lett.* **1992**, *60*, 2356–2358.
142. W. Han, S. M. Lindsay, *Appl. Phys. Lett.* **1998**, *72*, 1656–1658.
143. A. J. Bard, L. R. Faulkner, *Electrochemical Methods*, John Wiley & Sons, New York, 1980.
144. J. Lipkowski, L. Stolberg in *Adsorption of Molecules at Metal Electrodes* (Eds.: J. Lipkowski, P. N. Ross), VCH Publishers, New York, 1992, pp. 171–237.
145. R. E. Malpas, R. A. Fredlein, A. J. Bard, *J. Electroanal. Chem.* **1979**, *98*, 171.
146. K. F. Lin, T. R. Beck, *J. Electrochem. Soc.* **1976**, *123*, 1145.
147. R. E. Martinez, W. M. Augustyniak, J. A. Golovchenko, *Phys. Rev. Lett.* **1990**, *64*, 1035–1038.
148. A. J. Schell-Sorokin, R. M. Tromp, *Phys. Rev. Lett.* **1990**, *64*, 1039–1042.
149. D. Sader, H. Ibach, *Phys. Rev. B* **1991**, *43*, 4263–4267.
150. R. Berger, E. Delamarche, H. P. Lang et al., *Science* **1997**, *276*, 2021–2023.
151. C. E. Bach, M. Giesen, H. Ibach et al., *Phys. Rev. Lett.* **1997**, *78*, 4225–4228.
152. G. G. Stoney, *Proc. R. Soc. London, Ser. A* **1909**, *82*, 172–183.
153. K. Dahmen, S. Lehwald, H. Ibach, *Surf. Sci.* **2000**, *446*, 161–173.

154. R. Berger, H. P. Lang, C. Gerber et al., *Chem. Phys. Lett.* **1998**, 294, 363–369.
155. J. R. Barnes, R. J. Stephenson, M. E. Welland et al., *Nature* **1994**, 372, 79–81.
156. R. P. Cowburn, A. M. Moulin, M. E. Welland, *Appl. Phys. Lett.* **1997**, 71, 2202–2204.
157. P. I. Oden, P. G. Datskos, T. Thundat et al., *Appl. Phys. Lett.* **1996**, 69, 3277–3279.
158. P. Kremmer, A. M. Moulin, R. J. Stephenson et al., *Science* **1997**, 277, 1799–1802.
159. H. P. Lang, M. K. Baller, R. Berger et al., *Anal. Chem. Acta* **1999**, 393, 59–65.
160. T. Thundat, E. Finot, Z. Hu et al., *Appl. Phys. Lett.* **2000**, 77, 4061–4063.
161. H. F. Ji, E. Finot, R. Dabestani et al., *Chem. Commun.* **2000**, 6, 457, 458.
162. J. Fritz, M. K. Baller, H. P. Lang et al., *Science* **2000**, 288, 316–318.
163. H.-J. Butt, *J. Colloid Interface Sci.* **1996**, 180, 251–260.
164. R. Raiteri, H.-J. Butt, M. Grattarola, *Electrochem. Acta* **2000**, 46, 157–163.
165. T. A. Brunt, T. Rayment, S. J. O'Shea et al., *Langmuir* **1996**, 12, 5942–5946.
166. T. A. Brunt, E. D. Chabala, T. Rayment et al., *J. Chem. Soc., Faraday Trans.* **1996**, 92, 3807–3812.
167. W. Haiss, J. K. Sass, *J. Electroanal. Chem.* **1995**, 386, 267–270.
168. W. Haiss, R. J. Nichols, J. K. Sass et al., *J. Electroanal. Chem.* **1998**, 452, 199–202.
169. H. Ibach, C. E. Bach, M. Giesen et al., *Surf. Sci.* **1997**, 375, 107–119.
170. H. Ibach, *Electrochem. Acta* **1999**, 45, 575–581.

**3.4****In situ FTIR as a tool for mechanistic studies. Fundamentals and applications**

Francisco C. Nart and Teresa Iwasita  
Universidade de São Paulo, São Paulo, Brazil

**3.4.1****Historical Overview**

Electrochemistry experienced in the recent years the introduction of many in situ techniques for the purpose of improving the understanding of the electrode process at a molecular level. Among these techniques, the infrared spectroscopy plays a relevant role as a tool to study, in situ, the electrode surface. The molecular specificity permits the identification of adsorbates and reaction products and allows the study of physicochemical properties of adsorbed molecules.

The infrared spectroscopy has been used largely in Surface Science to study adsorbed molecules on surfaces in vacuum. The infrared beam is reflected at the crystal surface and the adsorbed molecules interact with the incident light [1, 2]. Greenler proposed the basic principles of the reflection-absorption spectroscopy in 1966 [3]. From his work, it becomes clear that the light interacting with the adsorbed molecules on a metal surface is only the parallel mode of the electric field of the incident radiation. This leads to the so-called *surface selection rule*, a central concept in reflection-absorption spectroscopy (see Sect. 3.4.2.1.2).

In situ infrared spectroscopy has been used in electrochemistry as early as 1970 [4]. Obviously, to apply the infrared spectroscopy to the study of the electrode surface, the strong absorption of light by the solvent must be minimized. One of the first attempts to use infrared spectroscopy as an in situ tool was

made using the so-called *attenuated total reflection (ATR)*, a technique largely used in infrared spectroscopy for liquid samples. In this technique, the infrared beam is introduced into a high refraction index infrared transparent crystal and the crystal put in contact with the sample. When the light hits the edge of the crystal in contact with a medium of lower refraction index, the light is totally reflected. If there is some absorbing species in the sample, then the refraction index will have an imaginary component that changes the refraction indexes at the wavelength where absorption exists. The light is then transmitted to the liquid sample and it is therefore attenuated at the detector.

The mostly used crystal as an ATR element and substrate for the electrode has been germanium [4, 5]. Germanium crystals have good transparency and good electrical conductivity, but are easily dissolved at positive potentials in aqueous solutions. The electrode can be deposited onto the crystal or, in some cases, the germanium can be used as an electrode for some processes in which the nature of the electrode does not affect the reaction, such as in outer sphere reactions.

The theory of internal reflection applied to electrochemical studies has been discussed in detail by Hansen [6] for both the infrared and the visible region of the electromagnetic spectrum. However, the ATR for electrochemical studies has been abandoned rapidly, because of the difficulties in obtaining an electrode with good optical transparency in the infrared region and good electrical conductivity. In general, the ATR crystal must be a semiconductor or insulating material. In cases in which the electrode is deposited on the surface of the element, the condition of optical transparency requires a very thin film in which the conductivity is very low. Moreover,

these very thin films are not enough to protect the crystal from corrosion in the usual electrochemical solutions.

Although ATR infrared spectroscopy for in situ studies of electrochemical systems presents many limitations, one interesting property of this technique is the amplification of the IR signal by excitation of surface plasmons. Osawa and coworkers used this technique to study the adsorption of water [7] and other molecules [8] on thin-film gold electrodes. However, the amplification of the IR signal through plasmon excitation is limited to metals such as gold, silver, and other sp metals.

Another important application of the ATR infrared spectroscopy is for the study of conducting polymers [9]. Most of these studies are conducted in nonaqueous media in which the corrosion of the ATR element is not important.

Though the internal reflection mode (ATR) encounters many applications, the external reflection mode is much more versatile to study metallic electrode surfaces. The external reflection mode has been introduced to study metallic electrode surfaces by Bewick and coworkers [10]. To minimize the strong attenuation of the radiation by the presence of a solvent in electrochemical systems, the electrode was placed very close to the infrared transparent window. Practically, the electrode is slightly pressed against the flat window surface leaving a very thin electrolyte layer between the electrode and the window.

At the beginning, a dispersive instrument was used. The signal-to-noise ratio was very poor, since the amount of species sampled was very low and the dispersive instrument has a low throughput. The low signal-to-noise ratio was then improved by applying to the electrode, a potential modulation of low frequency (typically between 7 and 10 Hz) and using a phase

detector (lock-in amplifier). This technique has been called *Electrochemically Modulated Infrared Spectroscopy (EMIRS)* [11]. The potential modulation, which is a square wave, and the spectra were collected at the two potentials of the step modulation. The spectra of each potential are added and then ratioed to obtain the  $\Delta R/R$ .

EMIRS has been successfully applied to many systems. Briefly it can be mentioned the study of adsorbates at the electrode surface [10], the detection of adsorbed reaction intermediates for the oxidation of small organic molecules [12], and the determination of the water structure in the double layer [13]. However, the potential modulation in EMIRS is its drawback, since it prevents the study of irreversible processes as the system must return to the same conditions each time the potential is changed. Other important limitations of EMIRS are related to both the electrical and chemical relaxation effects caused by the potential modulation at 12 Hz. The electrical relaxation is due to the high ohmic drop of the electrolyte confined in the thin solution layer required for the in situ measurements. The chemical relaxation is due to ion migration induced by the change in solution composition caused by the electrode potential change. These aspects have been discussed in detail in the following text [14–16] (see Sect. 3.4.2.3).

The introduction of Fourier Transformed Infrared Spectrometers to the electrochemical experiments eliminated the need of potential modulation to increase the signal-to-noise ratio. Fourier Transform Spectrometers present two advantages compared to the dispersive equipment [17], which have improved the possibilities of the in situ measurements. One advantage originates from the fact that the beam hits the sample without passing through a monochromator (Jacquinot

advantage), thus avoiding the losses caused by the monochromator components like slit and gratings. The net result is a better signal-to-noise ratio, eliminating the need of a phase detector. The other advantage is known as multiplex (or Fellgett) advantage, in which all the wave numbers can be sampled simultaneously, increasing the speed of spectral acquisition. However, the spectral acquisition at different potentials is necessary, since the Fourier transform equipments are single-beam devices and a reference spectrum is always needed. The use of Fourier Transform IR spectroscopy in in situ studies was introduced by Pons and coworkers [18, 19]. The technique was called Subtractively Normalized Interfacial Fourier Transform-Infrared Spectroscopy (SNIFTIRS) due to the way the spectra were acquired.

The use of Fourier Transform instruments eliminates much of the limitations of the EMIRS, since no more potential modulation is needed. The signal-to-noise ratio is far less than the dispersive instrument and can be improved statistically by adding more scans, since the spectral acquisition time is much lower. With the Fourier Transform equipment, also the irreversible processes can be studied, since it is no longer required to return to the same potentials as for modulation (see Sect. 3.4.4). This not only allows the acquisition of derivative or bipolar bands but also the acquisition of integral bands, as in the case of the adsorbed CO on platinum electrodes [20–25], which was impossible with EMIRS. The speed of spectral acquisition of Fourier Transform Infrared (FTIR) instruments allows also the follow-up of a reaction during a dynamic polarization curve [26, 27].

To avoid the spectral acquisition at two different potentials in order to have a reference spectrum, polarization modulation

has been used associated to the FTIRS. In theory this technique allows the acquisition of only integral bands, since this is based on the surface selection rule (see below Sect. 3.4.2.1.2), in which the s-polarized light is only active away from the electrode surface. This technique has been called *Fourier transform-infrared reflection-absorption spectroscopy FT-IRRAS* [28], although this acronym has been used also for the integral bands obtained without polarization modulation. The advantages and limitations of this technique have been analyzed in detail by Seki et al. [29]. The main limitation is that the reflectivity is different for the p- and s-polarized radiation, and it changes with the radiation energy, the incident angle, and thickness of the thin electrolyte layer. Thus the presence of water and ions in the solution can cause absorption bands even for species not adsorbed on the electrode. Therefore, compensating mechanisms are needed and even so, it is very difficult to prevent artifacts. In the case in which the bands of the adsorbed species are very close to the bands in solution, it is possible to mix the signals coming from each one [16, 30]. The polarization modulation has been used to study adsorbed CO [28] and  $\text{CN}^-$  [28, 29], since the bands of these species are far away from the bands of the water and ions used for the electrochemical experiments.

### 3.4.2

#### The External Reflectance Spectroscopy

##### 3.4.2.1 Fundamentals

Let us consider the reflection on a flat mirror-finished surface as depicted in Fig. 1. The complex electric field of the standing wave above the surface is the result of the vectorial sum of the incident and the reflected beam [1]. The magnitude

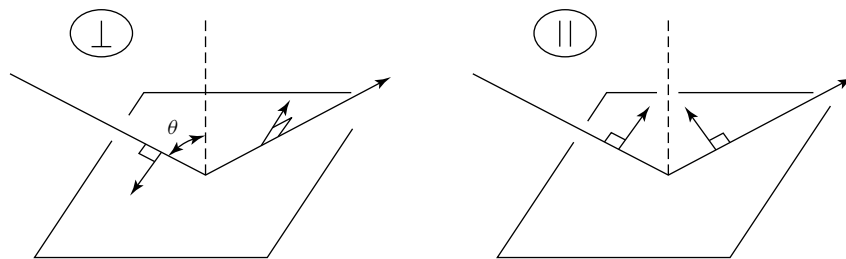


**Fig. 1** Reflection of the s-( $\perp$ ) and p-( $\parallel$ ) polarized light on a flat mirror surface. Note the direction of the electric field upon reflection.

of the field is a function of the incidence angle and of the light polarization. This is a consequence of the phase shift upon reflection. The phase shift for the electric field perpendicular to the incident plane (s-polarized radiation) is almost  $180^\circ$  for all the incident angles. For the electric field parallel to the incident plane (p-polarization), the phase shift is angle dependent and changes drastically between  $60^\circ$  and  $90^\circ$ , as can be seen in Fig. 2.

These results have two practical consequences for the reflection-absorption spectroscopy: (1) the dependence of the band intensity on the incident angle and

(2) the introduction of the surface selection rule.

**3.4.2.1.1 The Band Intensity** The absorption of infrared radiation by a submonolayer of an adsorbed species is the result of the interaction of the electric field of the radiation with the electric dipoles of the adsorbed species and with the electrons of the reflecting metallic surface. Therefore, the intensity of the absorption is determined by the electric properties of the metal. The absorption  $\Delta$  is the normalized difference between the reflectivity of the surface free from the absorbing

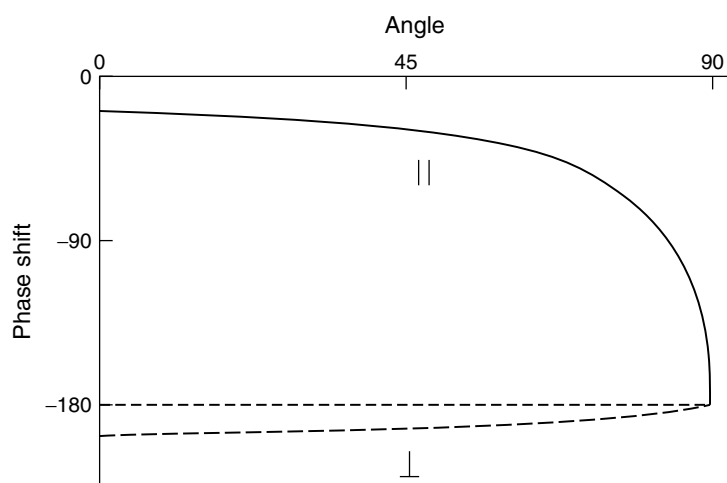


**Fig. 2** Phase shift for the reflected s-( $\delta_{\perp}$ ) and p-( $\delta_{\parallel}$ ) polarized light upon reflection on a metallic surface. (Data from Ref. [3] with permission.)

species ( $R_0$ ) and the surface covered with an absorbing layer ( $R$ ):

$$\Delta = \frac{R - R_0}{R_0} \quad (1)$$

The intensity of a band in the spectrum is the result of the dissipation of the electromagnetic radiation in the absorbing media at a given energy. Under these circumstances, the change in the energy flux is proportional to the mean quadratic field (see Appendix A). Therefore, it is important to understand the behavior of the electric field on a metallic surface to rationalize the factors affecting the intensity of light absorption.

The mean quadratic field, referred to the incident mean quadratic field in the same direction for the s-polarized radiation, is [6]

$$\frac{\langle E_{S1}^2 \rangle}{\langle E_{S1}^{02} \rangle} = \left[ (1 + R_S) + 2R_S^{1/2} \times \cos \left( \delta_S^r + 4\pi \left( \frac{z}{\lambda} \right) \xi_1 \right) \right] \quad (2)$$

where  $R_S$  is the s-polarized light reflectivity,  $\delta_S^r$  the phase angle of the reflected radiation,  $\lambda$  is the wavelength of the radiation,  $z$  is the position above the reflecting surface, and  $\xi = n \cos \theta$ , where  $n$  is the refraction index and  $\theta$  the incidence angle.

On the surface plane ( $z = 0$ ), the electric field is given by [6]

$$\frac{\langle E_{S1}^2 \rangle}{\langle E_{S1}^{02} \rangle} = \left[ (1 + R_S) + 2R_S^{1/2} \cos \delta_S^r \right] \quad (3)$$

since for a reflection on a metallic surface, the phase shift is almost  $\pi$ ,  $\cos \delta_S^r \approx -1$  and the mean quadratic field for this case is

$$\frac{\langle E_{S1}^2 \rangle}{\langle E_{S1}^{02} \rangle} = \left( 1 - R_S^{1/2} \right)^2 \quad (4)$$

Considering that for a metallic surface  $R_S \approx 1$ , the electric field at the surface is practically zero.

For the p-polarized light, the mean quadratic field is given by [6]

$$\begin{aligned} \frac{\langle E_{p1}^2 \rangle}{\langle E_{p1}^{02} \rangle} = & \cos^2 \theta_1 \left[ (1 + R_p) - 2R_p^{1/2} \right. \\ & \times \cos \left( \delta_p^r + 4\pi \left( \frac{z}{\lambda} \right) \xi_1 \right) \left. \right] \\ & + \sin^2 \theta_1 \left[ (1 + R_p) + 2R_p^{1/2} \right. \\ & \times \cos \left( \delta_p^r + 4\pi \left( \frac{z}{\lambda} \right) \xi_1 \right) \left. \right] \quad (5) \end{aligned}$$

The change in the intensity of the electric field for the p-polarized radiation is shown in Fig. 3. The intensity of the field increases for higher incidence angle up to ca.  $90^\circ$ . The best angle is around  $85^\circ$ , known as the *Brewster angle*.

From this discussion, two important consequences can be derived: (1) the s-polarized light does not interact with the species very close to the metallic surface (see Sect. 3.4.2.1.2). The immediate consequence is that adsorbed species cannot be sampled with s-polarized light but only with p-polarized light. (2) The intensity for the absorption of radiation is angle dependent and maximum for large angles in the case of metal/air or metal/vacuum surface.

For electrochemical applications, a very thin liquid electrolyte on the surface is needed, and for this a transparent window must be used to keep the electrolyte film in front of the surface. This makes the whole situation more complicated. The introduction of a very thin liquid film along with the transparent window (see below) changes the optimum incidence angle, as can be seen in Fig. 4, in which it is shown how the different media change the direction of the beam. It is worth noting the

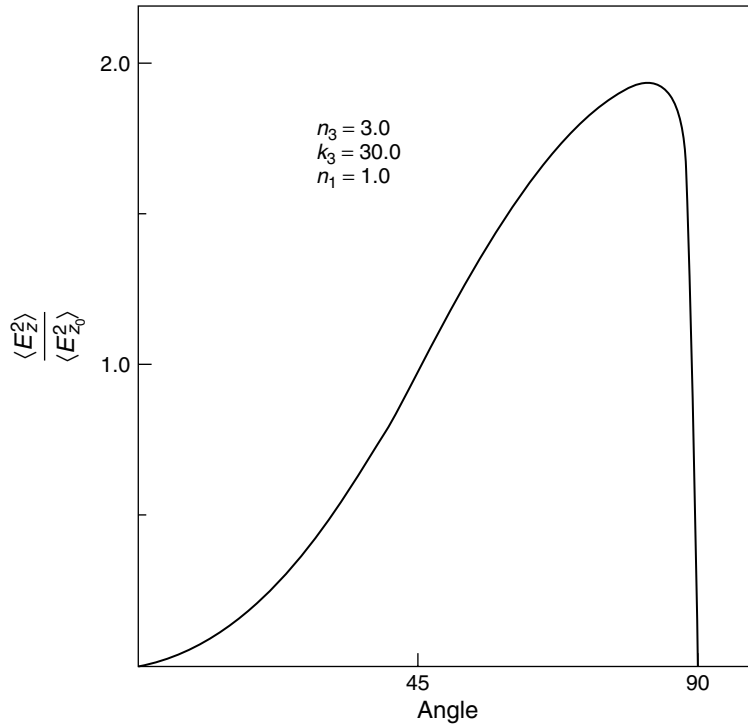


**Fig. 3** Change of the mean square electric field for the air/metallic surface with the incidence angle. The simulation parameters are shown in the figure.

qualitative differences if a flat or prismatic window is used.

The equations for a system consisting of metallic surface/thin-film electrolyte/prismatic window were developed by Seki et al. [29]. Briefly, the equations are

$$\frac{\langle E_{S2}^2 \rangle}{\langle E_{S2}^{02} \rangle} = [(1 + r_S)C + i(1 - r_S)S]^2 \quad (6)$$

and

$$\frac{\langle E_{P2}^2 \rangle}{\langle E_{P2}^{02} \rangle} = \left[ \cos \theta_1 (1 - r_P)C + i\xi_2 \left( \frac{n_1(1 + r_P)}{n_2^2} \right) S \right]^2$$

$$+ \left[ n_1 \sin \theta_1 \left( \frac{n_1(1 - r_P)}{n_2^2} \right) S + in_1 \sin \theta_1 \cos \theta_1 \left( \frac{(1 - r_P)}{\xi_2} \right) S \right]^2 \quad (7)$$

where

$$C = \cos \left[ 2\pi \xi_2 \left( \frac{z}{\lambda} \right) \right] \quad (8)$$

$$S = \sin \left[ 2\pi \xi_2 \left( \frac{z}{\lambda} \right) \right] \quad (9)$$

and

$$r_S = \frac{r_{S12} + r_{S23}e^{-2i\beta}}{1 + r_{S12}r_{S23}e^{-2i\beta}} \quad (10)$$

$$r_P = \frac{r_{P12} + r_{P23}e^{-2i\beta}}{1 + r_{P12}r_{P23}e^{-2i\beta}} \quad (11)$$



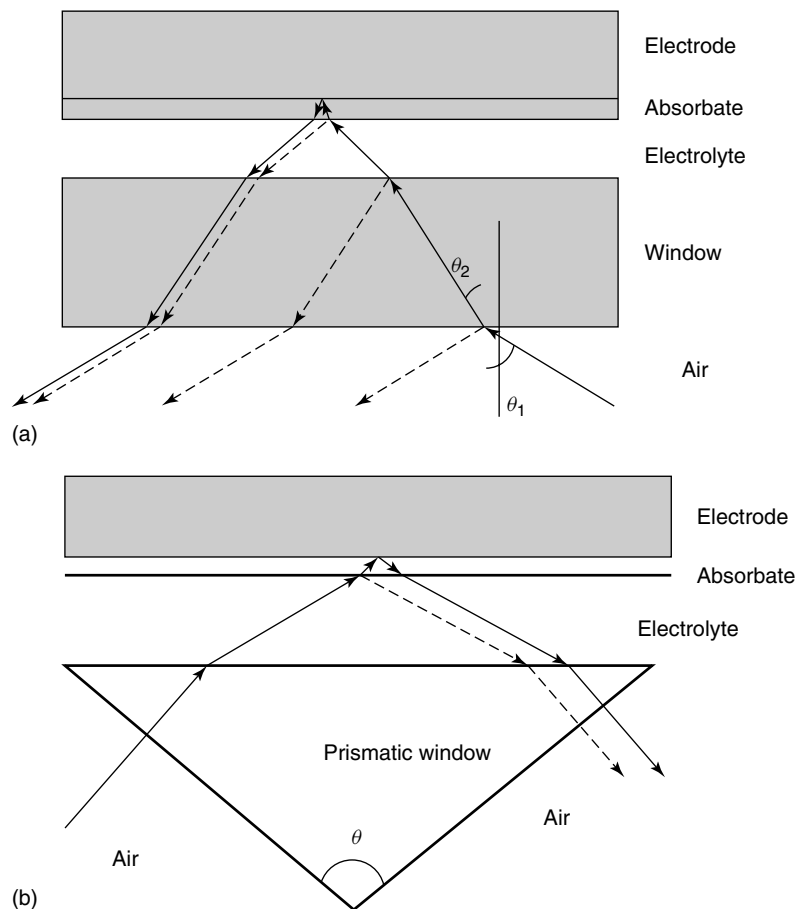


**Fig. 4** The reflection of the light beam for an electrochemical interface, including the window [(a) flat or (b) prismatic], showing the different internal reflections of the beam.

and  $r_{12}$  and  $r_{23}$  are the Fresnel coefficients for the window/electrolyte and electrolyte/metal interfaces, respectively.  $\beta$  is the energy attenuation in the solution phase and is given by

$$\beta = 2\pi \left( \frac{d}{\lambda} \right) \xi_2 \quad (12)$$

where  $d$  is the thickness of the thin electrolyte film.

So far the intensity of the electric field – which will be related to the

dispersion of the energy – was described in detail, but not the band intensity itself. The band intensity obviously depends on the magnitude of the electric field (see Appendix A), but the intensity of light absorption depends on the dynamic electric dipole moment of the species interacting with the electric field. For the band intensity in reflection-absorption spectra, one elegant and relatively simple equation has been presented by Persson [31]. According to this model, the adsorbed adlayer

is constituted by an ensemble of electric dipoles and the integrated band intensity is given by

$$\int d\nu \Delta(\nu) = \frac{16\pi^2}{\hbar c} \frac{N}{A} \mu^2 \Omega G(\alpha) \quad (13)$$

where  $N/A$  is the density of adsorbed particles,  $\mu$  is the dynamic dipole moment operator for the dipole perpendicular to the surface,  $\Omega$  is the vibrational frequency, and  $\nu$  is the frequency of the incident radiation.  $G(\alpha)$  is a function of the incident angle and of the dielectric constant  $\varepsilon$  of the metal and is defined [31] as

$$G(\alpha) = \frac{\sin^2 \alpha}{\cos \alpha} \left| \frac{\sqrt{\varepsilon} \cos \alpha}{\sqrt{\varepsilon} \cos \alpha - 1} \right| \quad (14)$$

Equation (13) is useful in understanding the different components affecting

the intensity in the reflection-absorption infrared spectroscopy. More specifically, both the dynamic dipole moment, which will depend on a specific vibration, combines with the surface properties through the  $G(\alpha)$  function. Therefore, quantitative studies from vibrational intensities must take into account the incidence angle at the electrode surface.

**3.4.2.1.2 Surface Selection Rule** The most important consequence of the behavior of the electric field upon reflection on a metal surface is the limitation of the dipole that can interact with the electric field at the surface. The phase shift of the electric field upon reflection for the s-polarized light on a metal surface leads to a vanishing electric field and therefore there is no interaction with the dipoles of the adsorbed molecules.

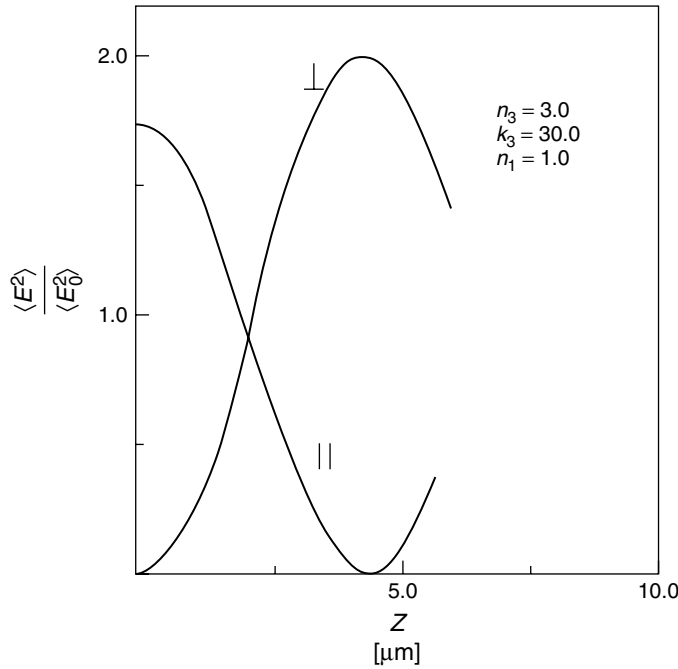


**Fig. 5** Change of the intensity of the reflected mean square electric field with the distance from the reflecting surface for the s- and p-polarized radiation.

The s-polarized radiation becomes active only for distances of ca. 5 nm above the surface. On the other hand, the electric field for the p-polarized light is a maximum at the surface and decreases when going away from the surface (see Fig. 5). The electric field for the p-polarized light is almost the same as the s-polarized light at ca.  $2.5\ \mu\text{m}$  for the metal/air interface for  $60^\circ$  of incidence angle at  $2000\ \text{cm}^{-1}$ . Therefore, the p-polarized light interacts with the dipoles at the surface and away from it. Since in order to interact with the electric field the dipole must present the same direction, it turns out that only the species with a nonzero dipole moment perpendicular to the surface will interact with the infrared beam. This is the *surface selection rule* and is an important tool in reflection-absorption spectroscopy applied to electrochemical systems in order to distinguish adsorbed species from species in solution and to assign specific adsorption geometry for the adsorbed species.

In Fig. 6, the s- and p-polarized spectra for adsorbed sulfate species on Au(111) [32] are presented to illustrate the use of the surface selection rule to differentiate adsorbed species from species in solution. In these spectra, the up band at  $1100\ \text{cm}^{-1}$  is visible in both spectra and this band is assigned to the dissolved sulfate. The down bands are seen only in the p-polarized spectrum, since the s-polarized light cannot sample the surface.

Another application of the surface selection rule is related to the fact that the p-polarized light has a specific direction on the surface, that is, the electric field of the p-polarized light will be perpendicular to the surface. Therefore, the assignment of the bonding of adsorbed species using the surface selection rule demands the information on the directions of the different dipole displacements of the adsorbed

molecule. This will tell which dipoles will be active for a given adsorption geometry thus affording for the ascertainment of the bonding of the adsorbed species to the surface. Obviously very simple linear molecules, like CO and  $\text{CN}^-$  will have practically only two bonding possibilities and the surface selection rule is not useful to determine the kind of bonding. However, for more complex species, the surface selection rule is of great help.

One interesting example is the application of the surface selection rule to assign the kind of bonding to the surface of the nitrate ion ( $\text{NO}_3^-$ ). This ion when isolated presents a  $D_{3h}$  symmetry (see Fig. 7).

In principle, the  $\text{NO}_3^-$  ions could adsorb with the plane of the molecule either parallel or perpendicular to the surface. For a parallel adsorption, the surface selection rule will allow only the out-of-plane bending modes, since the stretching modes present always the displacement parallel to the molecular plane. The perpendicular adsorption has two possibilities, that is, the nitrate ions can be adsorbed by coordination of either one or two oxygen to the surface. Experimentally, the stretching mode of the adsorbed nitrate ions [33, 34] is detected. Therefore it can be concluded that the ion is adsorbed with the molecular plane perpendicular to the surface, giving rise to a  $C_{2v}$  symmetry (see Fig. 8). The breakup of symmetry occurs because the oxygen in contact with the surface is no longer equivalent to the noncoordinating oxygen.

The stretching vibrational modes of the adsorbed  $\text{NO}_3^-$  are presented in Fig. 8, in which the symmetry and direction of displacement of each mode are indicated according to the character table for the  $C_{2v}$  point group (see Table 1). The symbols in the character table have the usual meaning [35]. Briefly, C is the

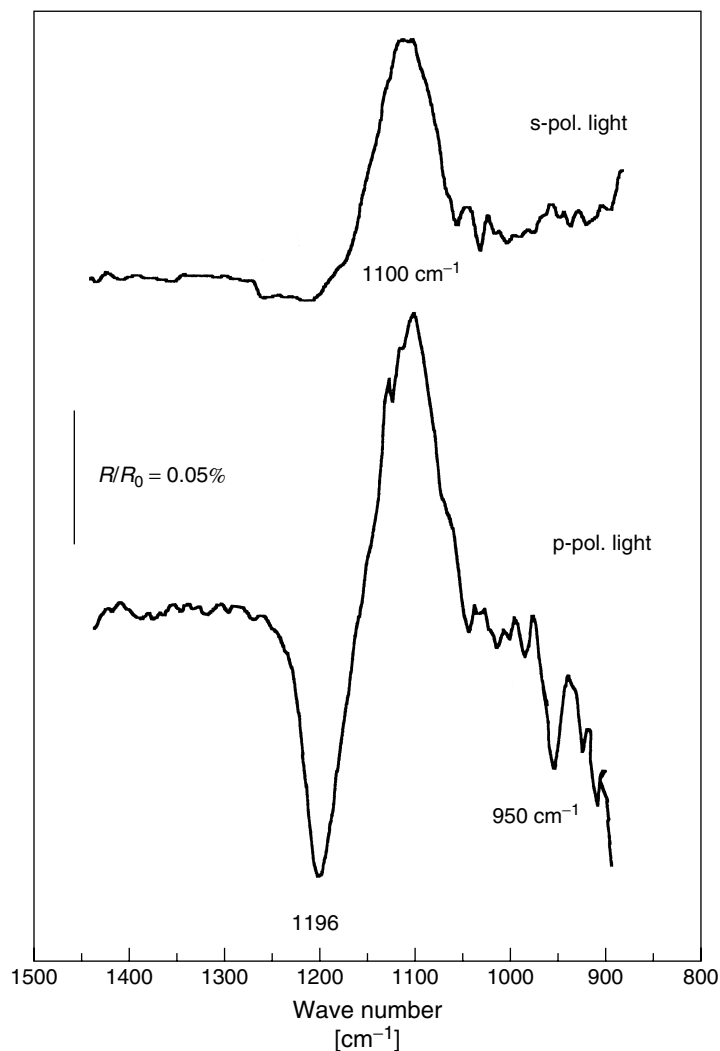


**Fig. 6** s- and p-polarized light spectra for the adsorbed sulfate species on Au(111) in  $0.69 \text{ mol L}^{-1}$  HF,  $0.5 \text{ mol L}^{-1}$  KF, and  $10^{-2} \text{ mol L}^{-1}$   $\text{K}_2\text{SO}_4$  solution. Ref. Pd/ $\text{H}_2$ . The s-polarized spectrum is extracted. (From Ref. [32] with permission.)

symmetry axis, the subscript 2 stands for an order two symmetry, and v is for vertical.  $\sigma$  is the reflection symmetry plane,  $I$  is the identity operation,  $T$  is the translator vector of the molecule in the indicated direction ( $x$ ,  $y$  or  $z$ ), and  $R$  is the rotation vector of the molecule

in the indicated direction and stands for the infrared activity.  $\alpha_{ij}$  are the components of the polarizability and accounts for the Raman activity. A and B are the nondegenerated species (one-dimensional representation). A represents a symmetric species with respect to the rotation

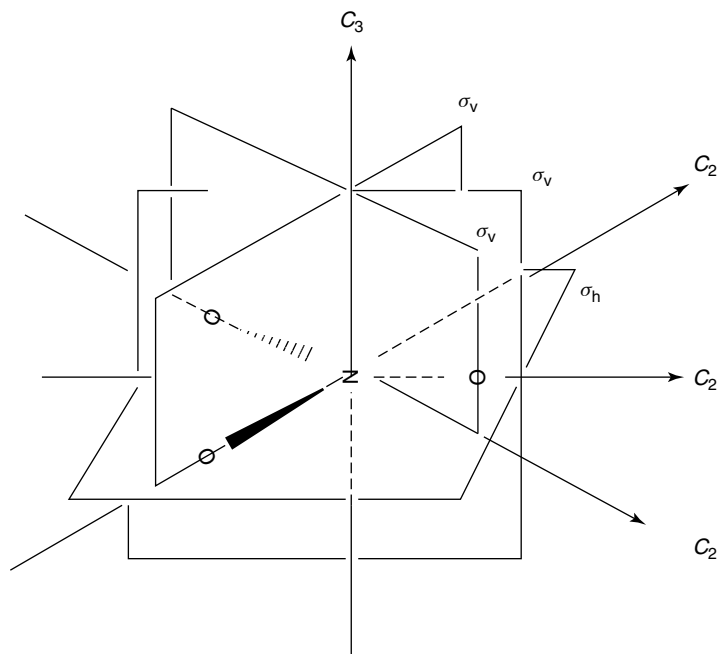
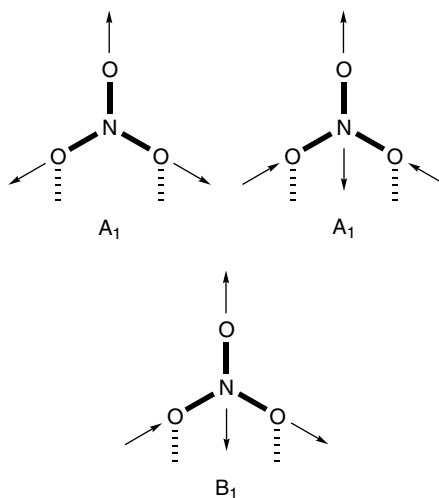


**Fig. 7** Sketch of the  $D_{3h}$  symmetry elements for the free nitrate ion.

**Fig. 8** Proposed N–O vibrations for the different modes of the adsorbed  $\text{NO}_3^-$  ions under a  $C_{2v}$  symmetry.



about the symmetry axis (represented by the character +1). The meaning of A is that upon the rotation operation the vibrational mode remains unchanged. B

represents the antisymmetric species with respect to the rotation about the symmetry axis (represented by the character -1), meaning that upon the symmetry

Tab. 1 Character table for the  $C_{2v}$  point group

$C_{2v}$	$I$	$C_2(z)$	$\sigma(xz)$	$\sigma(yz)$		
$A_1$	+1	+1	+1	+1	$T_z$	$\alpha_{xx}, \alpha_{yy}, \alpha_{zz}$
$A_2$	+1	+1	-1	-1	$R_z$	$\alpha_{xy}$
$B_1$	+1	-1	+1	-1	$T_x, R_y$	$\alpha_{xz}$
$B_2$	+1	-1	-1	+1	$T_y, R_x$	$\alpha_{yz}$

operation the vibrational mode has the direction inverted.

The character table allows identifying the active infrared modes. These modes are those with nonzero translation represented by  $T$  in the character table. For the  $C_{2v}$  point group, the A and B modes are active in the infrared spectroscopy. Adding to this analysis the surface selection rule, only those modes with translation in the direction perpendicular to the surface will be active. Considering that the surface is included in the  $xy$  plane, only the  $A_1$  modes can be active, since only the  $A_1$  have translation in the  $z$  direction. The  $A_1$  mode is the symmetric species with respect to the rotation about the symmetry axis, as described above. Therefore, for the adsorbed  $NO_3^-$  ion, only the symmetric modes will be active in the infrared spectroscopy.

A detailed assignment of vibration to a given molecule requires careful calculations, but for practical purposes, in the case of adsorbed species, it is possible to use the character table to assign the vibrations observed, once the vibrational modes of the free molecule (or ion) are known. In Fig. 8, the possible allowed vibrations are proposed for the adsorbed  $NO_3^-$  ion.

The in situ reflection-absorption spectrum of nitrate ions on a Au(100) electrode is shown in Fig. 9, in which two bands at 1436 and 1024  $cm^{-1}$  can be observed. The 1436  $cm^{-1}$  band has been assigned to the  $A_1$  symmetric mode for the nitrate ions

adsorbed forming a  $C_{2v}$  symmetry and the 1024  $cm^{-1}$  is the other  $A_1$  mode, corresponding to the activation of the totally symmetric  $NO_3$  stretching vibration [34]. This 1436  $cm^{-1}$  mode would be the  $\nu_3$  stretching vibration and the 1024  $cm^{-1}$  would be the  $\nu_1$  stretching vibration depicted in Fig. 8.

In the case of in situ infrared in electrochemical systems, strong limitations in the spectral range, due to the use of chemically inert windows, impede the observation of modes usually in the range of stretching vibrations for the inorganic molecules. Organic molecules usually display also bending modes in the same spectral range, but the kind of analysis is practically the same.

#### 3.4.2.2 Experimental Setup

The experimental setup for in situ infrared for electrochemical studies requires the construction of an electrochemical cell equipped with a window transparent to the infrared radiation and stable in aqueous electrolytes as used for the electrochemical studies. The window can be either flat or prismatic and is usually placed at the bottom of the cell. The prismatic window allows a more favorable angle of incidence.

The most commonly used window materials are  $CaF_2$  (900–77 000  $cm^{-1}$ ) and  $ZnSe$  (500–20 000  $cm^{-1}$ ). The  $BaF_2$  (770–66 000  $cm^{-1}$ ) can be used only in some solutions, since barium forms

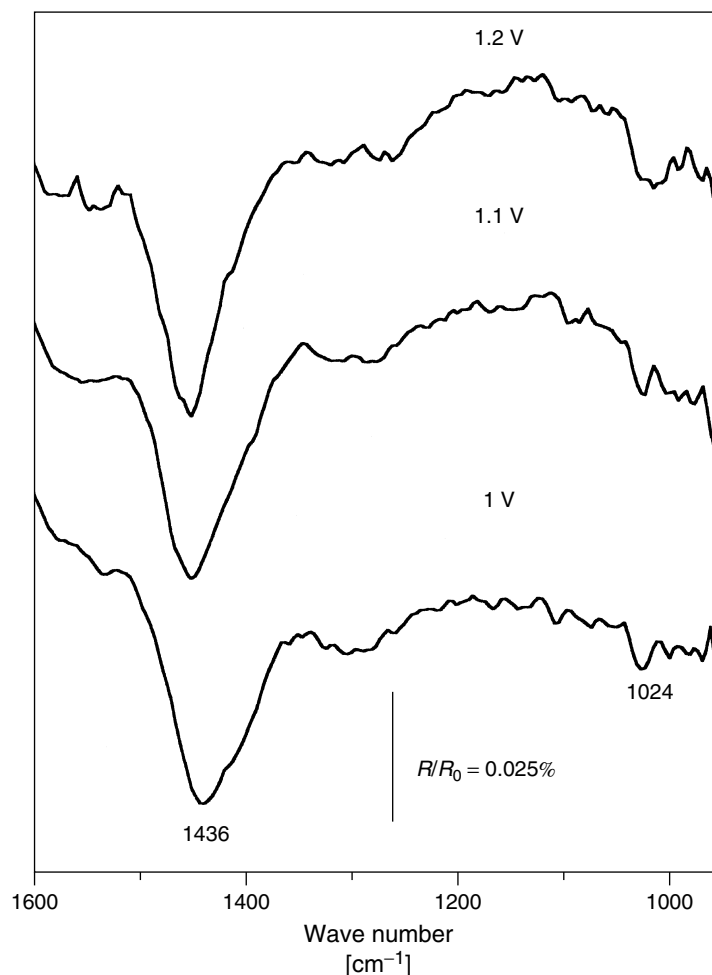


**Fig. 9** In situ FTIR p-polarized light spectra of adsorbed  $\text{NO}_3^-$  ions on  $\text{Au}(100)$  in  $1 \text{ mol L}^{-1}$  and  $0.05 \text{ mol L}^{-1}$   $\text{HNO}_3$ . Ref.  $\text{Pd}/\text{H}_2$ . (From Ref. [33] with permission.)

insoluble salts with sulfate, for example, and interferes with the spectral data. With prismatic windows with angles of ca.  $65^\circ$ , it is possible to obtain an incidence angle up to  $77^\circ$ . For a flat window, even for an incidence angle of  $60^\circ$  at the window/air interface, the maximum angle of incidence attainable is of ca.  $47^\circ$  [36].

A sketch of a typical electrochemical cell for in situ infrared spectroscopic

measurements is shown in Fig. 10. In the upper part is the entrance for the electrodes and gases. This kind of cell is to be placed vertically, which makes the optical setup slightly more complicated, but with clear advantages over the cell placed horizontally, since in the vertical cell solution leaks are rare, while in the horizontal cell the leaks are more common. Placing the cell vertically allows also

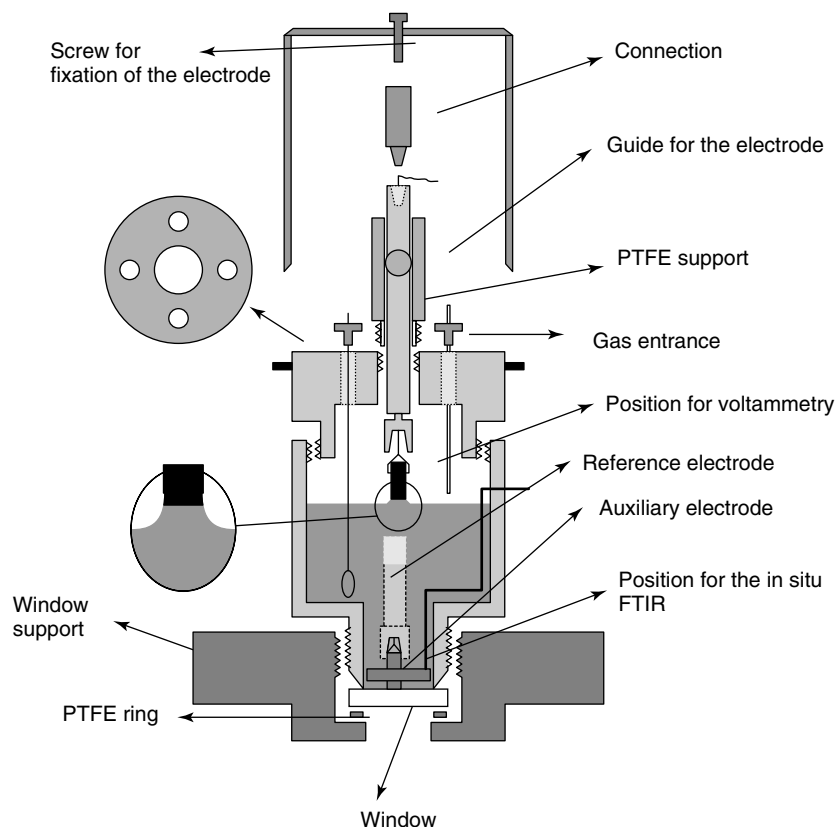


**Fig. 10** Sketch of an electrochemical cell used for in situ measurements specially designed to operate vertically.

the study of organic reactions, in which replacement of solution is needed in some cases. Other cells with distinct design can be seen in the literature [35–37].

The cell contains the three electrodes as any usual electrochemical cell for the control of potential. The working electrode is a reflecting surface and for this it must be polished to a mirror finish.

An important detail is the difference between the reflectivity using a flat window or a prismatic window for the in situ spectra. Simulating a change in absorbance in the thin-film layer, that is, a change in the solution composition, data of reflectivity are shown in Fig. 11(a, b)

for the setup using a prismatic and flat window, respectively [38]. The simulation shows a dramatic decrease in the reflectivity when a flat window is used. The differences in s- and p-reflectance are not as big as in the case of a prismatic window. Other important effects are the interference fringes for the flat window, which are more pronounced for the s-polarized light. The fringes are caused mainly by the flat window and not by the thin electrolyte layer, since the wavelength of the infrared radiation is larger than the thickness of the thin electrolyte film. Finally, it is important to stress that the reflectance is almost independent of the incidence angle up to  $40^\circ$ .



There is a maximum for 70° of incidence angle at the window. When a prismatic window is used, the radiation reflectivity is strongly dependent on the incidence

angle between 40° and 90° and there is a pronounced maximum around 70°.

The consequence of this behavior is that when a prismatic window is used, the

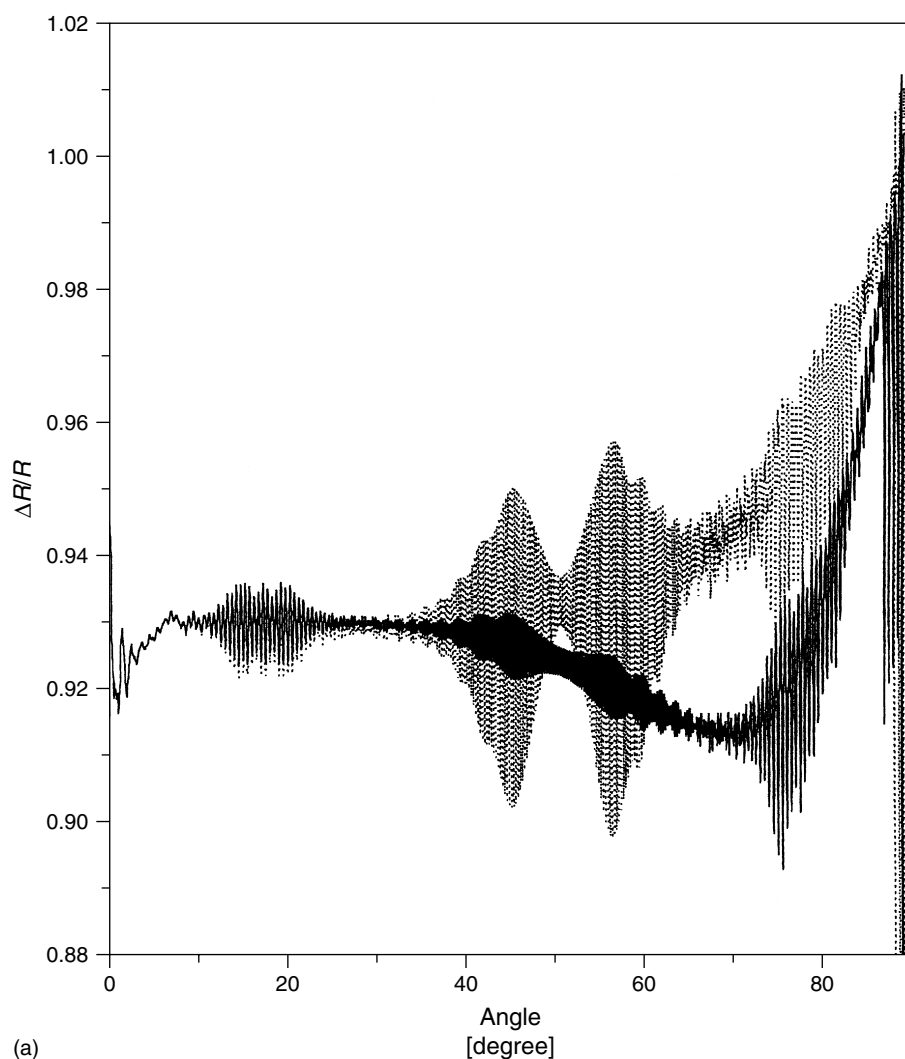
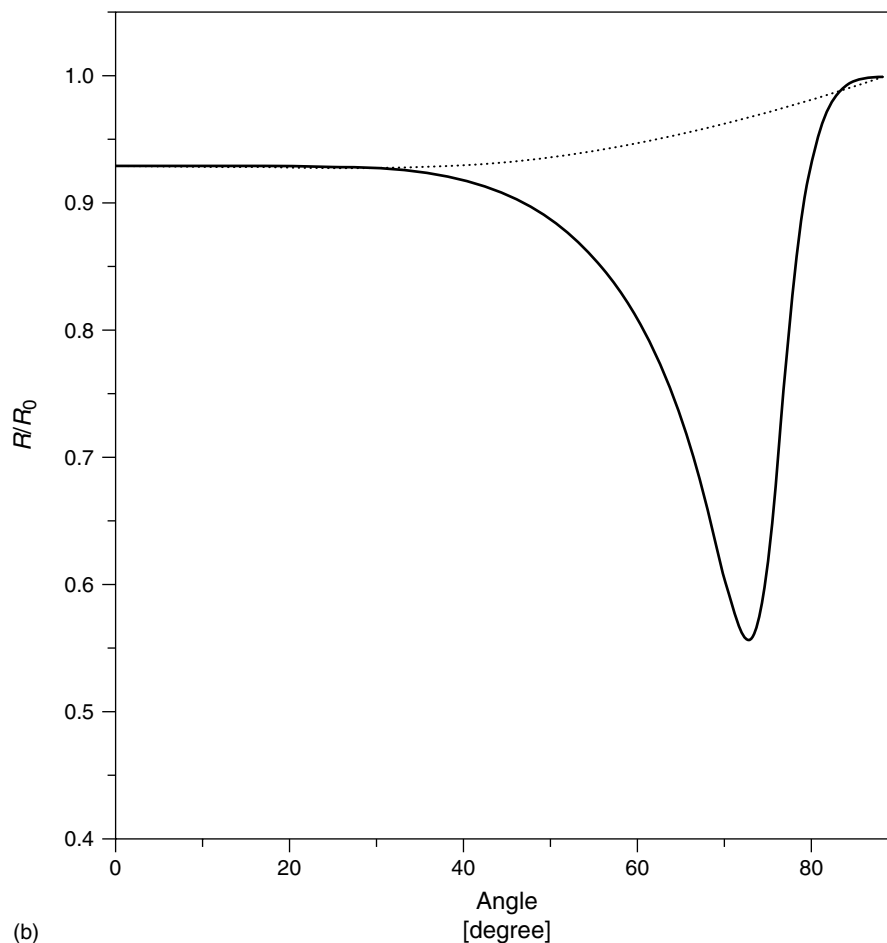


**Fig. 11** Simulated change in reflectivity for the system: (a) flat window/electrolyte/metal for a change in the absorption in the electrolyte layer (note the interference fringes caused by the internal reflections) and (b) prismatic window/electrolyte/metal. The parameters used in the simulation are:  $n_1 = 1.0$  (air);  $n_2 = 1.4$  ( $\text{CaF}_2$  window);  $n_3 = 1.32 + i0.015$  (electrolyte); and  $n_4 = 10.9 + 15.6$  (Pt). Electrolyte film thickness:  $2.0 \times 10^{-6}$  m; flat window thickness:  $2.0 \times 10^{-3}$  m. The change in absorbance in the electrolyte has been simulated by changing  $k$  by 0.01.



(b)

Fig. 11 (Continued)

large difference in reflectivity between s- and p-polarized light makes it difficult to distinguish between adsorbed species and species in solution, since the s-polarized signal will be much lower than the p-polarized signal. In summary, even if the s-polarized light spectral signal is too weak, this does not mean that the spectral feature is only due to adsorbed species. On the other hand, the use of a prismatic window will maximize the spectral signal from the surface and it will be of great

advantage for the in situ studies, since the overall signal-to-noise ratio will be very high compared with that obtained with a flat window.

#### 3.4.2.3 Transport Effects in the Thin Electrolyte Film

In one typical in situ FTIR experiment, it is necessary to measure a reference spectrum at a potential in which the electrochemical process does not take place and to measure a sample spectrum in which the desired

process takes place. The two spectra are ratioed to obtain the final spectrum as in Eq. (1). This kind of experiment was originally called *Subtractively Normalized Interfacial Fourier Transform-Infrared Spectroscopy* (SNIFTIRS).

In the process, of changing the potential to acquire the two spectra, the components of the solution contained in the thin electrolyte film between the electrode and the window can diffuse either to or from the thin layer. The diffusion inside the thin electrolyte layer is relatively slow [5]. Therefore the compensation of species that are consumed by reaction or adsorption is also slow. This is the reason that in SNIFTIRS spectra usually there are bands in both up and down direction with respect to the baseline. Taking  $R_0$  as the reference spectrum and  $R$  as the sample spectrum, down bands ( $R_0 > R$ ) correspond to the formation of species and up bands ( $R_0 < R$ ) to the consumption of new species (see Eq. 1).

These effects are particularly dramatic for platinum electrodes. Usually, a potential of 0.05 V in acidic solutions is used as reference both in studies of ion adsorption and organic molecules reaction. At this potential, the platinum electrode is covered with a monolayer of hydrogen. Changing the potential to higher values will cause hydrogen desorption leaving  $H^+$  ions in the thin layer causing pH changes.

Different groups [14–16] have addressed this problem in detail. It has been shown that two different kinds of problems can occur. Both double-layer charging and consumption of species can cause migration or diffusion of species into or from the thin solution layer, or pH changes can shift acid-base equilibria that can be sampled by the in situ FTIR spectra. In both cases, these effects can mask

the observation of the electrochemical process in study. The pH change effect was observed incidentally by Christensen et al. [39] during  $CO_2$  reduction in a phosphate buffer solution. The phosphate ions equilibria are very well-known and are easily observed in the in situ FTIR spectra. Corrigan and Weaver [15] demonstrated that the double-layer charging during the potential step used is already enough to produce ion migration inside the solution film as shown for the study of  $N_3^-$  ions adsorption on a polycrystalline gold electrode.

One example of ion equilibrium displacement in a phosphate buffer solution caused by pH changes [40] is shown in Fig. 12. The spectra were obtained using a potential step between  $-0.25$  V versus a reversible hydrogen electrode (RHE) and the potentials indicated in the figure. The spectra were taken with s- and p-polarized radiation to confirm that the changes in the spectra occur in the solution and not at the electrode surface.

The up bands are then those corresponding to the consumption of species after the potential step and the down bands are those corresponding to the species formed after the potential step. The bands are the  $1162$  and  $1075\text{ cm}^{-1}$ , corresponding to the antisymmetric and symmetric modes of the  $PO_2$  group, and the band at  $942\text{ cm}^{-1}$ , corresponding to the symmetric stretching of the  $P(OH)_2$  group of the  $H_2PO_4^-$ . On the other hand, the up bands at  $1091$  and  $991\text{ cm}^{-1}$  are assigned to the doubly degenerated stretching mode of the  $PO_3$  and the P–OH stretching vibration, respectively. Actually the  $HPO_4^{2-}$  species present the doubly degenerated mode at  $1072\text{ cm}^{-1}$ , but the down band at  $1075\text{ cm}^{-1}$  are overlapped and disturb the band at  $1072$

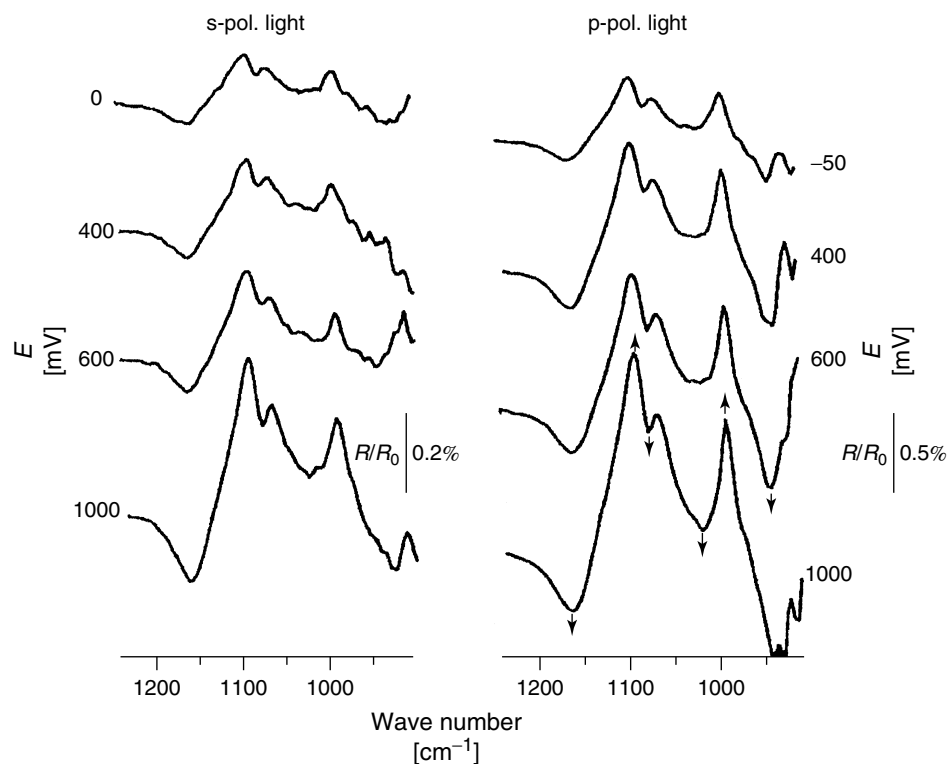
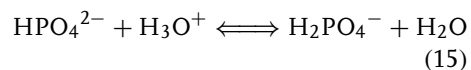


**Fig. 12** In situ FTIR spectra of the changes in phosphate protonation in solution for different applied potential step between  $-0.25$  V and the potentials indicated on a platinum electrode in a phosphate buffer  $\text{pH} = 7.4$ ; ionic strength 0.2.

Up bands at  $1162\text{ cm}^{-1}$ ,  $1018\text{ cm}^{-1}$ , and  $942\text{ cm}^{-1}$  are assigned to  $\text{H}_2\text{PO}_4^-$  and the down bands at  $1091\text{ cm}^{-1}$  and  $991\text{ cm}^{-1}$  to  $\text{HPO}_4^{2-}$ . (Data reproduced from Ref. [41] with permission.)

giving a peak at  $1091\text{ cm}^{-1}$ . In summary, from the spectral signals observed in the spectrum of Fig. 12, a phosphate buffer equilibrium has been sampled showing the reaction:



This is an example of how pH changes caused by  $\text{H}^+$  desorption during the potential step used for the measurement cause equilibrium changes in solution, and any possible band due to adsorbed phosphate is completely buried by the solution spectral signals. To minimize

these effects, an appropriate supporting electrolyte must be used to compensate the acid-base equilibrium changes. Other more complicated approaches, like a flow cell with an electrode with a small hole in the center to allow electrolyte flow, have been proposed [37]. The other version is a window with a hole that allows electrolyte flow [39]. However, the operation of such electrodes or windows is not easy and the fluctuations in the electrode-window distance preclude the compensation of the full spectrum of the optical path. So far, the use of a supporting electrolyte permitted the distinction of the solution

bands from the bands arising from the adsorbates [41].

### 3.4.3

#### **Infrared Spectroscopy under Equilibrium Conditions. Study of Adsorbed Sulfate Ions on Single-crystal Electrode Surfaces**

In this section, some selected applications of *in situ* infrared spectroscopy to study the reversible adsorption of anions on the electrode surface will be discussed. The relevant contribution of the *in situ* FTIR spectroscopy to this field was to permit the study of the structure of the adsorbed anions in the double-layer of the electrochemical interface for solid electrodes without a very well-defined double-layer region, as in the case of platinum electrodes. Moreover, the identification of the nature of adsorbed species using *in situ* infrared spectroscopy has been the object of intense debate and relevant contributions have been given.

##### **3.4.3.1 The Adsorption of Anions (The Electrical Double Layer)**

The use of *in situ* FTIR spectroscopy to study ions adsorption is related to the need of experimental tools to access the double-layer structure with molecular specificity. This is especially true for the solid metals, where the study of the double layer using the classical capacitance studies is not easy. Spectroscopy combined with *in situ* scanning tunneling microscopy (STM) [42, 43] constitutes a very powerful approach, allowing the determination of the molecular identity and organization of the double-layer components. However, it is not the purpose of this chapter to review in detail the double-layer structure, but rather, to show how *in situ* infrared spectroscopy can contribute to the understanding of the double layer at molecular specificity.

The simplest anion studied is the  $\text{CN}^-$ . The most recent studies on  $\text{CN}^-$  adsorption have been done by Tadjeddine and coworkers [44] using sum frequency generation, SFG a spectroscopic technique based on nonlinear optics. This technique is surface specific, since it is based on the property that when two laser beams meet at a nonsymmetric place, the frequency of the two beams is summed. Then, with a laser in the visible region and an infrared tunable laser, the vibrational bands can be sampled. According to the SFG measurements for the  $\text{CN}^-$  adsorption, two bands are observed and have been assigned to the C- and N-down cyanide ion adsorbed on the gold surface. Although many interesting studies on the  $\text{CN}^-$  and other anions adsorption can be found, in this chapter only the adsorption of sulfate ions will be addressed in detail to show the potentialities of *in situ* FTIR in the study of electrochemical systems.

The importance of sulfate ions is related to the fact that it is a largely used anion in supporting electrolytes both for fundamental studies and applications.

##### **3.4.3.1.1 The Adsorption of Sulfate on M(111) Single-crystal Electrodes**

One common feature of adsorbed sulfate ions on the M(111) faces of different fcc metals is that the vibrational features observed in the *in situ* FTIR spectra do not depend on the degree of dissociation of the species in solution. When sulfate ions are adsorbed from strongly acid solutions containing mainly bisulfate ions or from mildly acid solutions containing mainly sulfate ions, the vibrational feature observed is basically the same (see Fig. 13) [42, 45–47]. In the spectra of Fig. 13, it is possible to see the up band at  $1100\text{ cm}^{-1}$  for the solution with  $\text{pH} = 2.8$ . This band is the F mode of the free sulfate ions in solution. The absence of

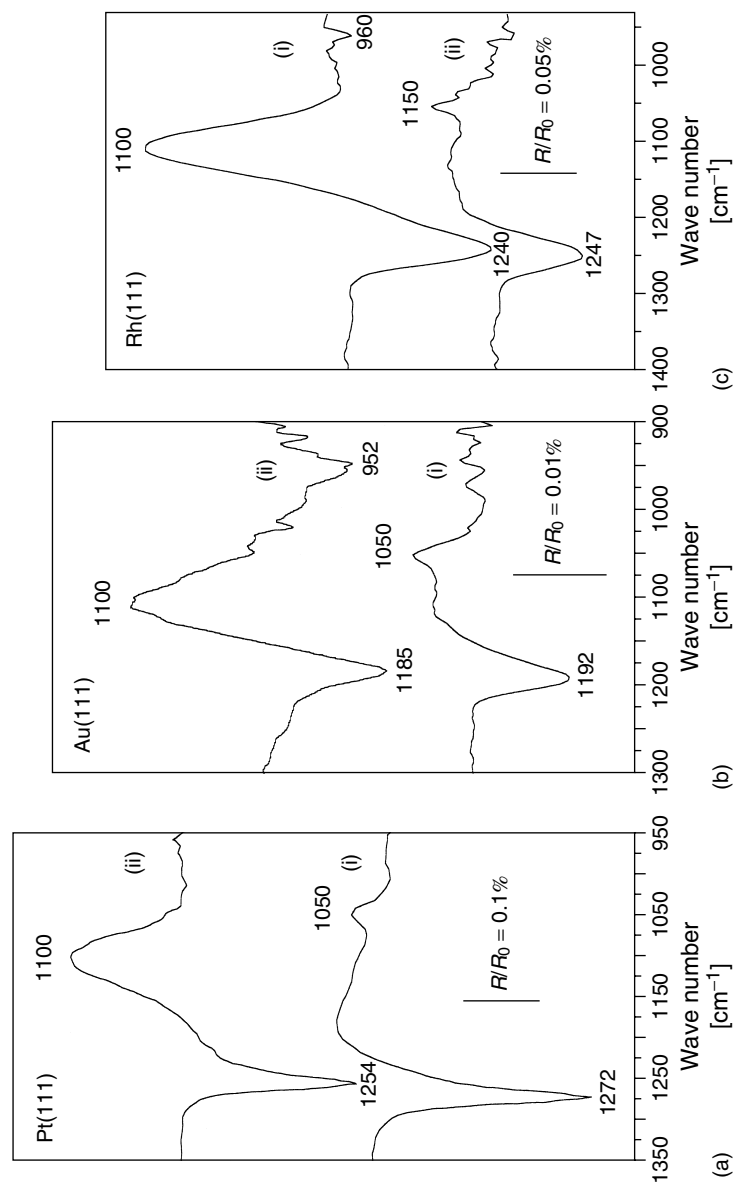


**Fig. 13** In situ FTIR spectra of adsorbed sulfate species on (a) Pt(111). (Data extracted from Ref. [45] with permission.) (b) Au(111). (Data extracted from Ref. [32] with permission.) (c) Rh(111) in (i) 0.69 mol L<sup>-1</sup> HF, 0.5 mol L<sup>-1</sup> K<sub>2</sub>SO<sub>4</sub> and (ii) 7.3 mol L<sup>-1</sup> HF and 10<sup>-2</sup> mol L<sup>-1</sup> K<sub>2</sub>SO<sub>4</sub>. (Data extracted from Ref. [46] with permission.)

up bands at  $950\text{ cm}^{-1}$  reveals that sulfate ions are unperturbed when dissolved, retaining the  $T_d$  symmetry. The up band, as discussed above (see Sect. 3.4.2.3), is due to the consumption of sulfate ions from the thin electrolyte film upon adsorption. For the same spectrum ( $\text{pH} = 2.8$ ), a down band can be observed between  $1200$  and  $1250\text{ cm}^{-1}$  for saturation coverage for the three metals, corresponding to the adsorbed ions. This band was not observed with s-polarized light, which confirms it is due to the adsorbed sulfate species (see Fig. 6 for the Au(111) case). Comparing the spectra obtained from the different solutions, it is clear that this feature is the same, independent of the species present in solution, indicating that either bisulfate is dissociated when adsorbed, or sulfate is protonated. Similar results are observed by other authors for Au(111) electrodes even for

neutral  $\text{SO}_4^{2-}$  solutions [42] (see Fig. 14). On the Au(111) electrode, a weak band at  $958\text{ cm}^{-1}$ , corresponding to the totally symmetric vibration has been observed (see Figs. 13(b) and 14). The activation of this band reveals the breakup of symmetry caused by the anion adsorption. This band has been assigned either to the activation of the totally symmetric mode of the  $\text{SO}_4^{2-}$  ion due to the breakup of symmetry or to the S–OH stretching vibration of adsorbed bisulfate [48]. Measuring the vibrational features of the adsorbed ion from a deuterated solution ( $\text{D}_2\text{SO}_4$  in  $\text{D}_2\text{O}$ ), Shingaya and Ito observed two bands, depending on the applied potential. For potentials between  $0.7$  and  $0.8\text{ V}$ , only one band at  $1153\text{ cm}^{-1}$  is found. At  $0.9\text{ V}$ , this band shifts to  $1170\text{ cm}^{-1}$  and a new band at ca.  $1200\text{ cm}^{-1}$  appears with a very weak intensity. The  $1170\text{ cm}^{-1}$  band loses intensity

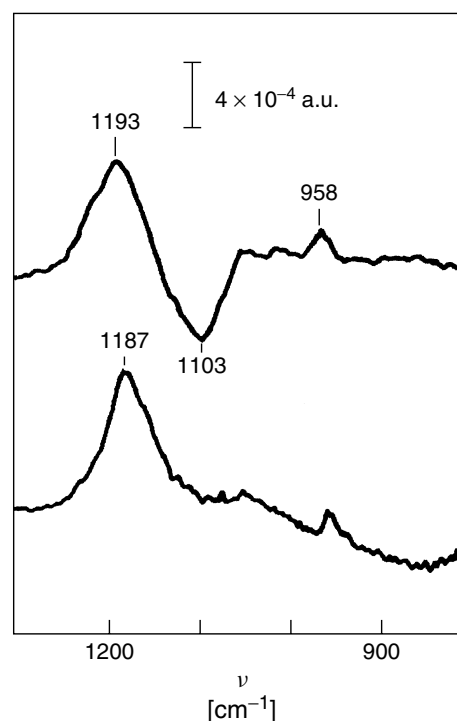


**Fig. 14** In situ FTIR spectra of adsorbed sulfate species on Au(111) in  $0.5\text{ mol L}^{-1}\text{ H}_2\text{SO}_4$  (lower) and  $0.1\text{ mol L}^{-1}\text{ Na}_2\text{SO}_4$  (upper). (Reproduced from Ref. [42] with permission.)

for more positive potentials and the band at  $1200\text{ cm}^{-1}$  starts to increase intensity and shifts strongly with the potential up to  $1230\text{ cm}^{-1}$  for 1.5 V.

An important observation is the intensity decrease of the low-energy band followed by the increase of the higher-energy band. There is also a concurrent change in the intensity of the  $950\text{ cm}^{-1}$  band. The authors [48] attributed this behavior to a mixture of sulfate and bisulfate on the surface in a given range of potential. The band at  $1153\text{ cm}^{-1}$  was assigned to the asymmetric stretching of the sulfate ions, while the  $1220\text{ cm}^{-1}$  band is due to the bisulfate. The  $950\text{ cm}^{-1}$  band was assigned to the S–OD stretching. Probably the  $1153\text{ cm}^{-1}$  band is not due to an

asymmetric mode, since this would have a dipole parallel to the surface, but when sulfate is adsorbed a  $C_{3v}$  symmetry could produce a second symmetric mode that can account for this band. The main argument used is that calculations (no detail has been given) show that the  $\text{SO}_3$  symmetric mode couples with the S–OH bending, but not with the S–OD and this would be the reason for the band splits at a certain potential. The main problem in this interpretation is the  $956\text{ cm}^{-1}$  band (compare Figs. 14 and 15) that has been observed also for nondeuterated solutions. It is therefore difficult to explain the absence of isotopic shift upon changing H for D in the S–OH stretching.

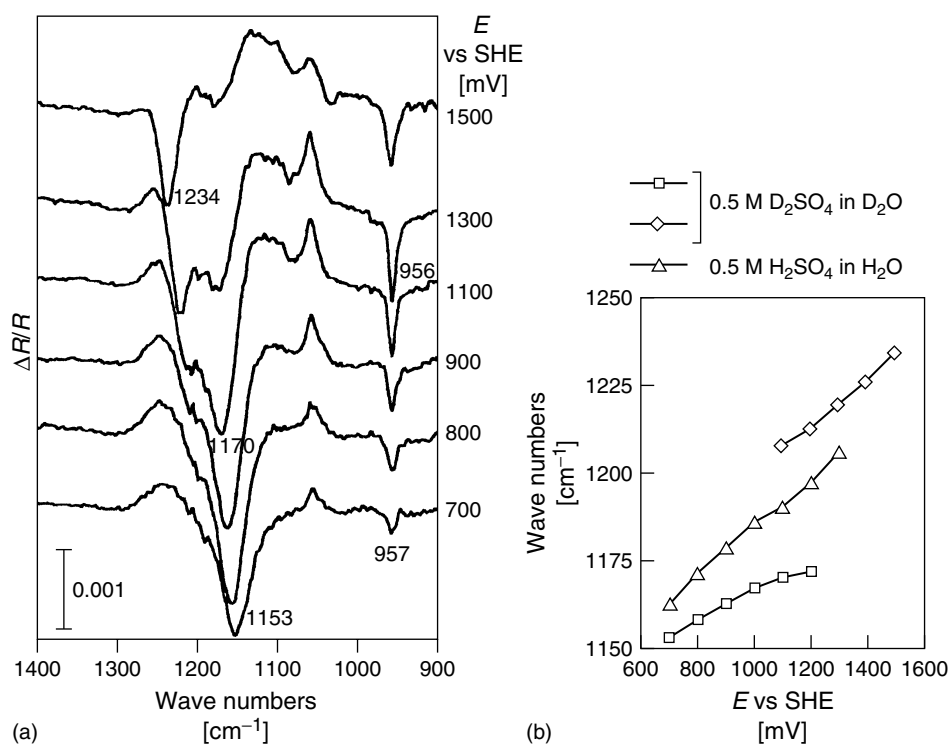


**Fig. 15** (a) In situ FTIR spectra of adsorbed sulfate species on Au(111) in  $0.5\text{ mol L}^{-1}\text{ D}_2\text{SO}_4$  in  $\text{D}_2\text{O}$  and (b) band center energy as a function of the applied potential. (From Ref. [48] with permission.)



More detailed results from the calculations are necessary to account for these differences. The controversy on the nature of the adsorbed sulfate species (sulfate or bisulfate) can be attributed to the limitations of the *in situ* FTIR spectroscopy in this case. Associated with the difficulty in identifying the nature of the adsorbed anion (sulfate or bisulfate) is the difficulty in determining the symmetry of the adsorbed species, which would give the clue in determining the coordination to the surface. The problem of the adsorbed sulfate is that only the symmetric modes will be active, according to the surface selection rule (see Sect. 3.4.2.1.2). It is assumed that the  $T_d$  symmetry is broken upon adsorption, since the oxygen atoms are no longer equivalent. The final symmetry will depend on the coordination to the surface. Coordinating one or three oxygen to the surface will lead to a  $C_{3v}$  symmetry, while coordinating two oxygen will lead to a  $C_{2v}$  symmetry. The  $C_{2v}$  symmetry has no degenerated modes, while the  $C_{3v}$  has two degenerated modes, one for the stretching modes. Therefore, for the free species in solution, the  $C_{2v}$  symmetry must present one more stretching mode than the  $C_{3v}$ . Because of the fact that the surface selection rule limits the active modes to those having the dynamic dipole moment perpendicular to the surface, two different coordinations will present the same number of bands. Considering only the number of bands, it is not possible to identify the symmetry of the adsorbed sulfate species; and consequently, it is not possible to assign unequivocally either the coordination or the nature of the adsorbed species. Other strategies have been used to clear these points.

Shingaya and coworkers have simulated the electrochemical environment in ultra high vacuum (UHV) by adding water and

$SO_3$  to a Pt(111) surface to compare it with *in situ* spectra [49]. They concluded that depending on the amount of water, the two species can be identified. Bands at 1230 and  $953\text{ cm}^{-1}$  were (arbitrarily) assigned to the bisulfate. This species would be converted into sulfuric acid (bands at 1276, 1043, and  $941\text{ cm}^{-1}$ ) when water evaporates. On the basis of these results, they concluded that there are two adsorbed species on Pt(111) electrodes, depending on the applied potential. Bisulfate species are adsorbed for potentials between 0.4 and 0.75 V (identified by the band at  $1230\text{ cm}^{-1}$ ) and sulfuric acid for potentials between 0.75 and 1.10 V (identified by the bands at  $1276\text{ cm}^{-1}$ ). Although this is an interesting approach to identify the fingerprints of adsorbed sulfate species, a definitive proof for bisulfate and sulfuric acid could be easily obtained in UHV by using deuterated water to confirm the presence of sulfuric acid. A mixture of different species at a given potential or surface condition cannot be ruled out and this is a further complication to the interpretation of *in situ* spectra.

Other explanations for the adsorbed species have also been given. Faguy and coworkers [50] suggested that the adsorbed species forms ion pairs with the hydronium ions close to the surface, and they even suggested that the ion is coordinated by three protonated oxygen [51]. This model tries to rationalize the discrepancy in the assignment of vibrational bands of the *in situ* FTIR spectra to sulfate or bisulfate. Actually, the close proximity of the coadsorbed hydronium ions can mimic the bisulfate situation and this could be also an explanation of the Shingaya and Ito results. A change in the hydronium ion concentration with potential may happen, producing a different number of hydrogen

bonding between the sulfate ions and the coadsorbed water.

Other strategy to identify the coordination and therefore to deduce the symmetry of adsorbed sulfate was presented by Lennartz and coworkers [43], using simultaneously in situ infrared spectroscopy and in situ STM. In this study, the authors used in situ STM to obtain the registry or the sulfate adlayer to the Cu(111) substrate by changing the bias current and obtaining an image containing the contrast due to both the adsorbed sulfate and the underlying Cu(111). Using Fourier Transform filtration, they were able to separate both signals and, since these were obtained from the same experiment, the overlap of the two images gave the registry between the adsorbate and the underlying surface. They observed for Cu(111) a bridging type adsorption of the sulfate using two oxygen resulting in a  $C_{2v}$  symmetry. Knowing the coordination, it is easier to obtain the symmetry and therefore the identity of the adsorbed species. For example, two-fold coordinated adsorbed bisulfate will have a  $C_s$  symmetry. Under this symmetry, the noncoordinated S–O and S–OH will produce two vibrations, other than the S–O<sub>2</sub> symmetric vibrations, with the component in the direction perpendicular to the surface. In the particular case of sulfate ions adsorbed on Cu(111), it is clear that the adsorbed ion is the dissociated sulfate and not the bisulfate ions, since only the strong symmetric band at 1205 to 1220  $\text{cm}^{-1}$  has been observed [43].

Another important result from in situ STM imaging of adsorbed sulfate on M(111), single-crystal metal electrodes is the observation of the adsorbate structure. It is found for Au(111) [42], Pt(111) [52], Rh(111) [53], Ir(111) [54], and Cu(111) [43] a  $\sqrt{3} \times \sqrt{7}$  structure. This kind of information can be used in determining lateral

interactions of the adsorbed ions, since the ion–ion distance can be measured. However, there are evidences that hydronium ions or water molecules are adsorbed between two neighboring ions in the  $\sqrt{7}$  direction. This obviously can break the chemical interaction, but probably not the dipole–dipole coupling since water and sulfate frequencies are well separated. The two ions adsorbed in the  $\sqrt{3}$  direction do not have water molecules in between and therefore chemical interactions can be operative as well.

Although the final symmetry cannot be deduced only from the spectroscopic data, it is important to stress that the spectroscopic data supply information on the strength of the chemical bonding [48] and on the effect of the applied electric field [55, 56]. Moreover, in situ STM data have been reported only for a full monolayer, but not for submonolayer coverage. The in situ FTIR is sensitive also in the submonolayer regime. By appropriate calibration (through the full monolayer as determined by in situ STM), it is possible to determine the adsorption isotherm, even for metals for which it is very difficult to obtain capacitance data.

#### 3.4.3.1.2 The Sulfate Ion Adsorbed on the M(100) and (110) Single-crystal Electrodes

The adsorbed sulfate species on other low-index planes of platinum and gold present a more complex spectroscopic structure [32, 46, 50, 57, 58]. Fig. 16 shows the spectra of adsorbed sulfate at saturation coverage for the three low-index planes of the platinum electrode in a solution of  $\text{pH} = 2.8$ . Clearly, a second band at 1008  $\text{cm}^{-1}$  can be easily identified for Pt(100) (weak) [57] and for Pt(110) (strong) [58]. These two planes do not match a  $C_{3v}$  symmetry for the adsorbed sulfate ions, and therefore we should

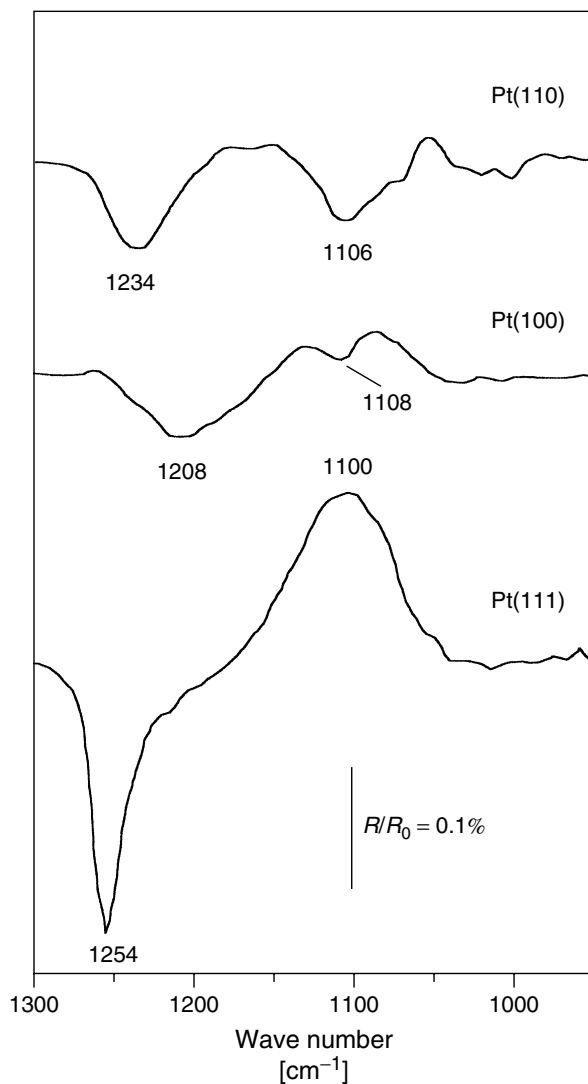


**Fig. 16** In situ FTIR spectra for the adsorbed sulfate species on platinum single-crystal electrodes in  $0.69 \text{ mol L}^{-1}$  HF,  $0.5 \text{ mol L}^{-1}$  KF, and  $10^{-2} \text{ mol L}^{-1}$   $\text{K}_2\text{SO}_4$ . Ref. Pd/ $\text{H}_2$ . (Data extracted from Ref. [45] (Pt(111)), Ref. [57] (Pt(100)), and Ref. [58] (Pt(110)) with permission.)

expect a  $C_{2v}$  symmetry if undissociated bisulfate ions are adsorbed. However, a  $C_{2v}$  symmetry has only two allowed bands, that is, the symmetric modes with respect to the symmetry axis (the  $A_1$  modes). A second

band indicates that either the adsorbed sulfate ion is tilted on the surface or that a second species is also adsorbed. A tilted adsorbed sulfate through a single oxygen will permit other vibrations to be active,

since the symmetry is no longer the  $C_{2v}$  and practically all modes will have some component of the dynamic dipole moment perpendicular to the surface.

The other possibility is that on Pt(100) and Pt(110), sulfate and bisulfate are coadsorbed on the surface. Comparing the bands for sulfate species adsorbed on polycrystalline platinum electrodes in strongly acid solutions, it is clear that

when bisulfate is the major species in solution, a band at ca.  $1100\text{ cm}^{-1}$  is observed [59]. A similar situation has been observed for adsorbed sulfate on Au(100) as shown in Fig. 17, in which two strong bands are observed at  $1165$  and  $1091\text{ cm}^{-1}$  for an applied potential of  $0.8\text{ V}$ . The  $1165\text{ cm}^{-1}$  band shifts to  $1185\text{ cm}^{-1}$ , but the  $1091\text{ cm}^{-1}$  band is practically insensitive to the applied potential. A weak

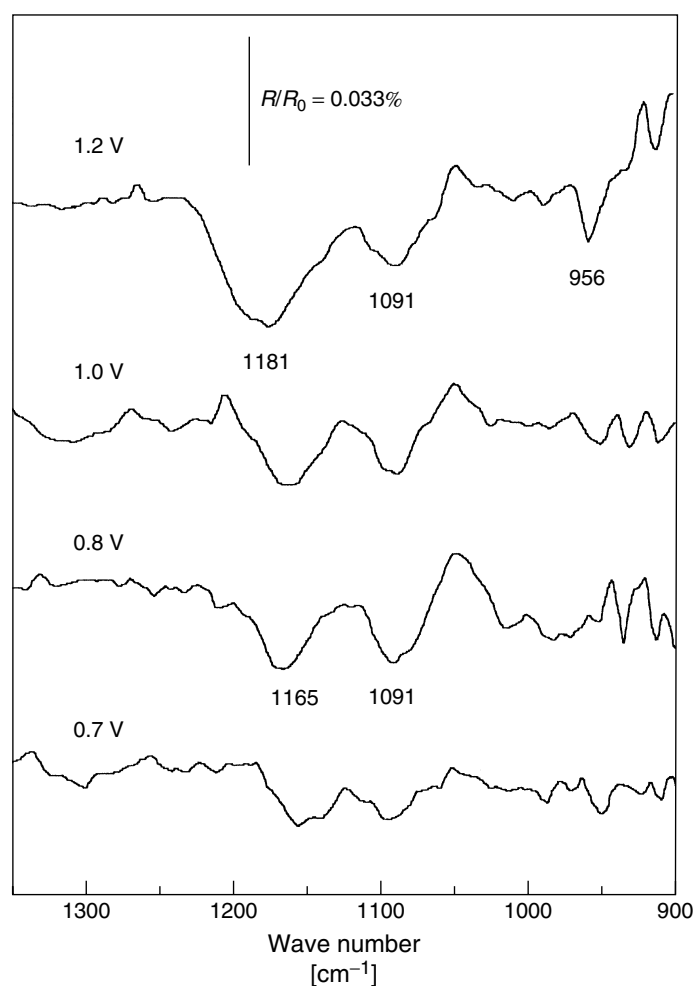


**Fig. 17** In situ FTIR spectra for the adsorbed sulfate species on Au(100) single-crystal electrode in  $7.3\text{ mol L}^{-1}\text{ HF}$  and  $10^{-2}\text{ mol L}^{-1}\text{ K}_2\text{SO}_4$ . Ref. Pd/H<sub>2</sub>. (Data reproduced from Ref. [34] with permission.)

band at  $956\text{ cm}^{-1}$  can be viewed in some spectra, which has been observed also for the sulfate adsorbed on Au(111). The presence of two strong bands suggests that probably at this solution pH, there is a mixture of sulfate and bisulfate on the surface. Indeed, the sulfate species adsorbed on Au(100) surfaces in solutions in which the undissociated sulfate is the major species, reveals only one strong band at  $1161$  to  $1190\text{ cm}^{-1}$ , indicating that when only sulfate is present in solution, the  $1091\text{ cm}^{-1}$  band is absent for the adsorbed species.

Interestingly the relative intensities of the  $1165$  to  $1185\text{ cm}^{-1}$  and  $1091\text{ cm}^{-1}$  features change with the applied potential. The  $1165$  to  $1185\text{ cm}^{-1}$  band is stronger than the  $1091\text{ cm}^{-1}$  at more positive applied potential, which could suggest that bisulfate can be further dissociated, since the applied potential induces a OH adsorption and therefore the acidity on the surface is changed favoring the bisulfate dissociation.

Summarizing, the adsorption of sulfate is of major interest in electrochemistry, since sulfuric acid solutions are largely used as a supporting electrolyte for many applications, including kinetic studies. So, the molecular structure of the double layer is an important piece of information in order to understand the effect of the double layer on the reaction kinetics. The infrared spectroscopy is an interesting tool to access this kind of data, providing information on the nature of the species, and with the help of *in situ* STM, the structure and coordination of the adsorbed ions. It is likely that this structure will not survive intact when faradaic reactions take place on the electrode surface, but certainly the structure formed will affect the threshold of the reaction, since different structures can account for different

barriers for surface reactions to start on the electrode surfaces.

#### 3.4.4

#### **Infrared Spectroscopy under Nonequilibrium Conditions. Study of Systems Relevant in Electrocatalysis**

One of the major successes of *in situ* FTIR spectroscopy concerns the study of complex electrode reactions. In this chapter, we present typical applications related to research in electrocatalysis of alcohol oxidation. With the aim to study electrocatalysis of reactions involving candidate substances for fuel cells applications, aliphatic alcohols of low molecular weight have been intensively investigated. In particular, remarkable progress in this direction was achieved in the last years in the case of methanol oxidation. In fact, the interest in establishing the nature of the adsorbed species of methanol was the motivation of one of the first papers using *in situ* infrared spectroscopy [60]. Because of the fact that adsorbed carbon monoxide is typically formed when small organic molecules interact with platinum, we start this section presenting data on the electrocatalysis of CO oxidation.

As explained in Sects. 3.4.2.1 and 3.4.2.2, application of the external reflectance technique requires the use of a thin layer of solution between the working electrode and the IR window. Because of this experimental approach, there has been some reticence to use the IR method under conditions of current flow. Criticism was centered on IR-drop effects and reactant-depletion problems in the solution thin layer. However, although IR drop and reactant depletion indeed occur, these problems can be experimentally minimized and should not be overestimated. On one side, usually employed solutions

have a good conductivity and, for instance, for a potential step of 100 mV within the H-region of platinum, charge compensation via ion migration can occur within tens of a second [30]. On the other side, since the Fourier transform method allows a fast rate of data acquisition, reactant depletion can be reduced to a negligible extent by using a reasonable experiment design, minimizing polarization time at each potential. Very valuable information can then be obtained under conditions of current flow.

#### 3.4.4.1 Carbon Monoxide

A significant number of studies using in situ FTIR spectroscopy have been devoted to adsorbed carbon monoxide. This is not surprising, in view of the supporting experimental and theoretical data on the CO system in UHV and the interest on carbon

monoxide as a model molecule in both electrochemical and UHV environments. UHV data have been used to compare the behavior of adsorbates at the electrochemical interface with that observed at metal/gas interfaces [23]. Also, spectroelectrochemical data on adsorbed CO are interesting in the study of the Stark effect, which can produce changes in band center frequency [55, 61] and integrated band intensity [56]. Spectroscopic studies of CO within this context have been reported and discussed elsewhere [30, 41]. In electrocatalysis, carbon monoxide can be considered as an intermediate (or poison) during the oxidation of small organic molecules (methanol, formic acid, ethanol, among others). In the present section, we have selected some studies concerning mainly this issue, using spectroscopic data to compare the CO behavior on different catalysts:

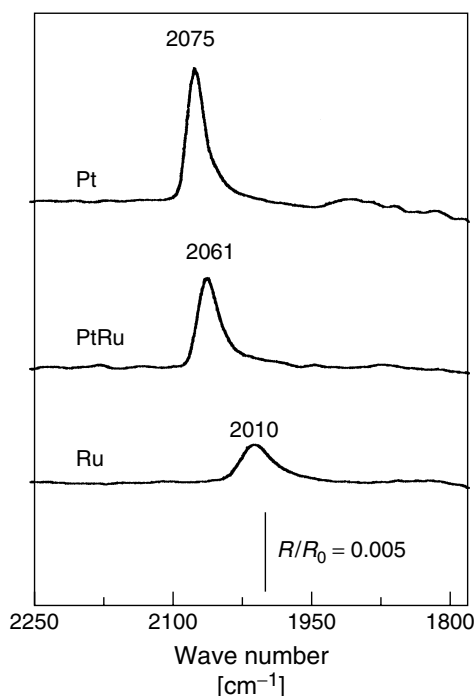


**Fig. 18** In situ FTIRS of a saturated CO monolayer adsorbed at 300 mV on Pt, Ru, and PtRu (50:50) electrodes in 0.1 M HClO<sub>4</sub>. Sample spectra measured at 300 mV, reference spectra obtained at 800 mV.

polycrystalline Pt, Ru, and (50:50) PtRu alloy [62], and single-crystal electrodes as Pt(111)Ru [63, 64] and (0001)Ru [65, 66].

**3.4.4.1.1 Adsorption and Oxidation of CO on Polycrystalline Substrates** In situ FTIR spectra in Fig. 18 show spectra for adsorbed CO at polycrystalline Pt, PtRu, and Ru, respectively. The surfaces were saturated with CO at 0.3 V in CO-saturated 0.1 M HClO<sub>4</sub> solutions. After elimination of bulk CO, sample spectra were collected at 0.3 V and corresponding reference spectra were measured at 0.8 V, a potential at which CO is completely oxidized.

Only linear-bonded CO is observed on the three surfaces. The ranges of observed frequencies are 2065 to 2075 cm<sup>-1</sup> for Pt, 2055 to 2065 cm<sup>-1</sup> for PtRu(50:50), and 2000 to 2020 cm<sup>-1</sup> for Ru.

Of major importance for the electrocatalysis, is the comparison of CO<sub>2</sub> production on the different materials as a function of potential. For this purpose, series of spectra were taken using the three catalysts in the potential range between 0.1 and 0.6 V versus RHE [62], as shown in Fig. 19 for the PtRu (50:50) alloy. The left side of Fig. 19, showing the bands for CO<sub>2</sub>, was calculated against a reference spectrum at 0.1 V. The increasing negative-going band represents the formation of CO<sub>2</sub> as the potential is stepped to higher values. The right side of the figure was calculated taking as a reference a spectrum at 0.8 V, a potential at which CO is completely oxidized. Here, the intensity of the negative-going bands is proportional to the CO coverage at the respective potentials. The integrated band intensities for CO<sub>2</sub>, at 2341 cm<sup>-1</sup> are plotted in Fig. 20. Accordingly, the catalytic activity for CO<sub>ad</sub> oxidation decreases in the order PtRu(50:50) > Ru > Pt.

#### Potential dependence of the band frequency

As the potential is stepped in the positive direction, the band center for adsorbed CO shifts to higher wave numbers for all electrode materials (Fig. 21). The following characteristics in the  $\nu - E$  relationship are noteworthy:

- For *pure platinum*, the band center exhibits first a linear dependence on potential with  $d\nu/dE = 28 \text{ cm}^{-1} \text{ V}^{-1}$ . As CO oxidation starts,  $\nu_{\text{CO}}$  remains approximately constant in the potential interval between 0.45 and 0.55 V and then decreases as the oxidation to CO<sub>2</sub> proceeds.
- For *pure ruthenium*, the band center frequency shifts linearly up to a potential of 0.3 V with  $d\nu/dE = 52 \text{ cm}^{-1} \text{ V}^{-1}$ . Then a more pronounced shift ( $d\nu/dE = 77 \text{ cm}^{-1} \text{ V}^{-1}$ ) is observed up to 0.45 V. The onset of oxidation can be extrapolated to 0.4 V, as judged from the CO<sub>2</sub> band intensity.
- For the *PtRu alloy*, the frequency shifts linearly with  $d\nu/dE = 32 \text{ cm}^{-1} \text{ V}^{-1}$  at low potentials and, as oxidation begins, the frequency drops immediately to lower values.

At constant (saturation) coverage, the marked effect of potential in pure Ru (highest  $d\nu/dE$  value) can be related to a stronger backbonding effect. This is also reflected in the lower frequency values of the CO<sub>L</sub> band at this metal as compared to the other two. Figure 21 gives also information on the properties of the adlayer as oxidation sets on. Thus, the faster red shift (to lower frequencies) of the band center frequency for PtRu beginning at the onset of CO oxidation indicates a rapid decrease of the lateral interactions, that is, oxidation of the CO adlayer probably occurs within a relatively loose structure. Contrasting, the

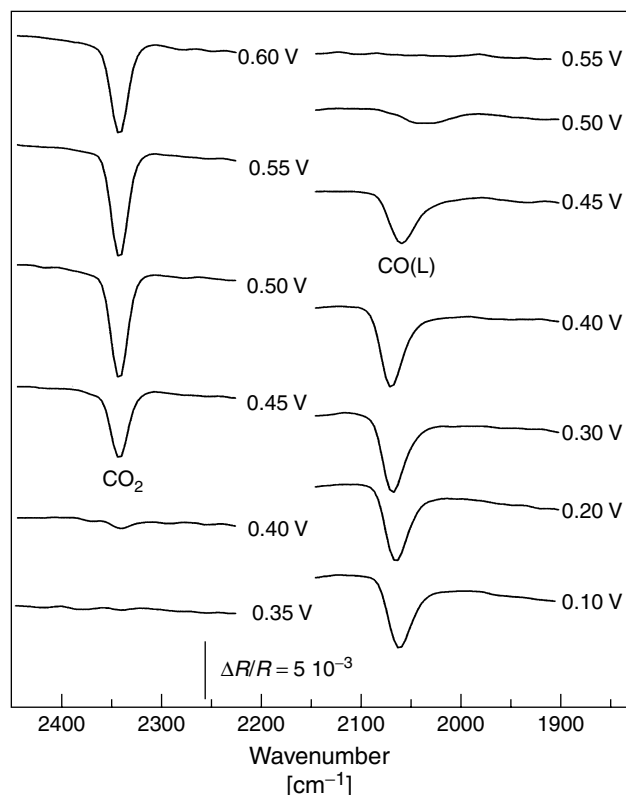


**Fig. 19** In situ FTIR spectra for saturated CO adsorbates on a PtRu(50:50) alloy electrode in 0.1 M HClO<sub>4</sub> from 100 mV to 600 mV at 50 mV interval. CO was adsorbed at 300 mV. For each spectrum, 100 interferograms were collected at 8 cm<sup>-1</sup> resolution, acquisition time ca. 44 s. Bands on the left side, corresponding to CO<sub>2</sub> produced during CO<sub>ads</sub> oxidation, were calculated against a reference spectrum taken at 100 mV (CO<sub>2</sub> was absent). Bands on the right side, corresponding to adsorbed CO, were calculated against a reference spectrum taken at 800 mV after complete oxidation of CO. (From Ref. [62] with permission.)

red shift observed on the pure metals is somewhat slower indicating that CO oxidation probably occurs only at the border of islands, the local CO coverage remaining relatively high.

Two different slopes observed for pure Ru at potentials prior to CO oxidation have been related to the possible interaction with adsorbed oxygen (Thermal desorption data from coadsorption of CO and O at

Ru(001) under UHV conditions [67] show a decrease of CO desorption energy from  $E_d = 140 \text{ kJ mol}^{-1}$  for the pure metal to  $E_d = 107 \text{ kJ mol}^{-1}$  in the presence of coadsorbed oxygen ( $\theta_O = 0.5$ )) [62, 67]. Such a behavior is expected in the presence of electronegative coadsorbates, which cause a withdrawal of metal electrons and diminish the metal- $\pi^*$  back donation. The consequences of this effect are



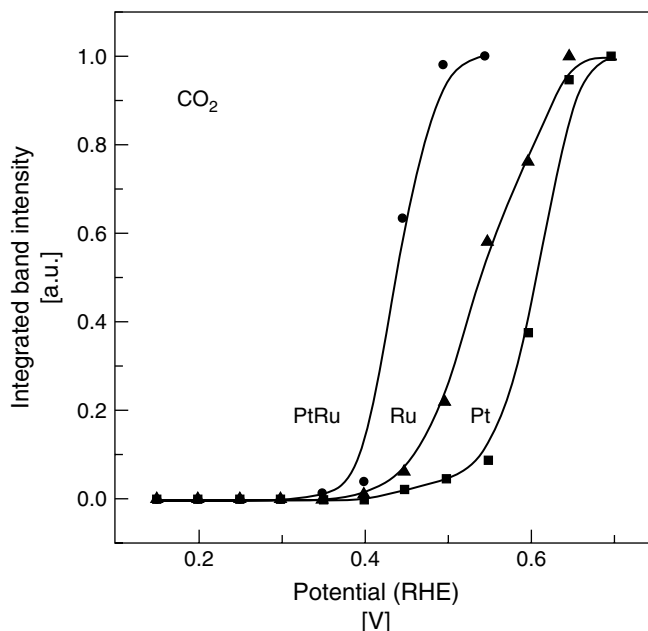


**Fig. 20** Integrated band intensity for  $\text{CO}_2$  as a function of potential. The intensities were calculated from series of spectra obtained at each catalyst as shown in Fig. 20 for the PtRu alloy. (From Ref. [62] with permission.)

a lowering of the metal-CO binding energy as observed in UHV [67] and a stronger C–O bond, which is reflected in the increase of  $\nu_{\text{CO}}$  shift between 0.35 and 0.45 V.

**The relative absorption coefficients of CO on Pt, Ru, and PtRu alloys** Spectra for CO submonolayers on the three materials are shown in Fig. 22. The degree of coverage  $\theta_{\text{CO}}$  indicated in the spectra was calculated using the ratio of the band intensity for  $\text{CO}_2$  to the maximum  $\text{CO}_2$  intensity, obtained after complete oxidation of a CO-saturated layer. Figure 22 shows that for comparable band intensities of  $\text{CO}_2$ , the corresponding intensity of the  $\text{CO}_{\text{ad}}$  feature largely differs for the three electrodes, the largest signal being observed at Pt and the smallest one at Ru.

A comparison of the absorption coefficients for CO on different materials requires a normalization, taking into account differences in electrode roughness. With the aim of normalization, one can use, again, the band intensity of  $\text{CO}_2$  produced upon total oxidation of the respective adlayer. The  $(\text{CO}_{\text{ads}})/(\text{CO}_2)$  intensity ratios are 0.87 (for Pt), 0.60 (for PtRu), and 0.25 (for Ru) with an estimated error of ca. 8% [62]. These normalized intensities of  $\text{CO}_{\text{ad}}$  reflect, in a first approximation, the relative values of the absorption coefficient of CO on the three substrates.

On the basis of the above discussion, the lower intensity of the CO band at Ru may really reflect a lower value for the dynamic dipole moment of the transition for CO on this metal as compared to the

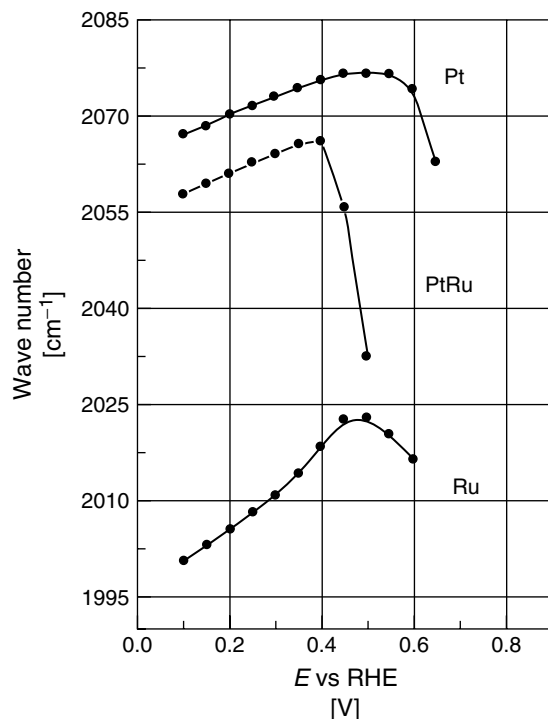


**Fig. 21** Dependence of the band center frequency on potential for saturated CO adlayers on Pt, Ru, and PtRu(50:50) alloy. The frequencies were taken from series of spectra measured at each catalyst as shown in Fig. 20 for the PtRu alloy. (From Ref. [62] with permission.)

other materials. In a study of the effects of coverage on the band intensity and band center of  $\text{CO}_{\text{ad}}$  at Ru(001), H. Pfnür and coworkers [68] have suggested that strong dipole–dipole coupling can reduce the dynamic dipole moment. Furthermore, these authors show that this effect markedly depends on the size of the CO islands. Indeed, the band intensity should be affected by lateral interactions to a larger extent, when adsorption takes place in the form of *large* islands, since in such a case most of CO molecules are surrounded by neighbors of an identical nature. Using a different theoretical approach, Persson and Rydberg [69] confirmed the predominance of dipole–dipole coupling in the coverage effects observed by Pfnür and coworkers [68], and explained the reduction of the band intensity as being due to

a screening effect caused by the electronic polarizability of the adsorbed molecules. In such a case, the reduced band intensity for CO could be caused by strong dipole–dipole coupling and/or large island domains; this would be an alternative (or additional) explanation for the lower rate of CO oxidation observed during oxidative stripping at pure ruthenium as compared to the alloy.

The dependence of  $\nu_{\text{CO}}$  on  $\theta_{\text{CO}}$  for Pt, PtRu, and Ru is shown in Fig. 23. A linear dependence of  $\nu_{\text{CO}}$  values is observed for all three materials, the respective  $d\nu_{\text{CO}}/d\theta_{\text{CO}}$  values being  $58 \text{ cm}^{-1}$  (for Pt),  $64 \text{ cm}^{-1}$  (for Ru), and  $50 \text{ cm}^{-1}$  (for PtRu). It can be stated that, from the spectroscopic point of view, the PtRu (50:50) alloy approaches more closely the behavior of pure Pt than that of pure Ru.

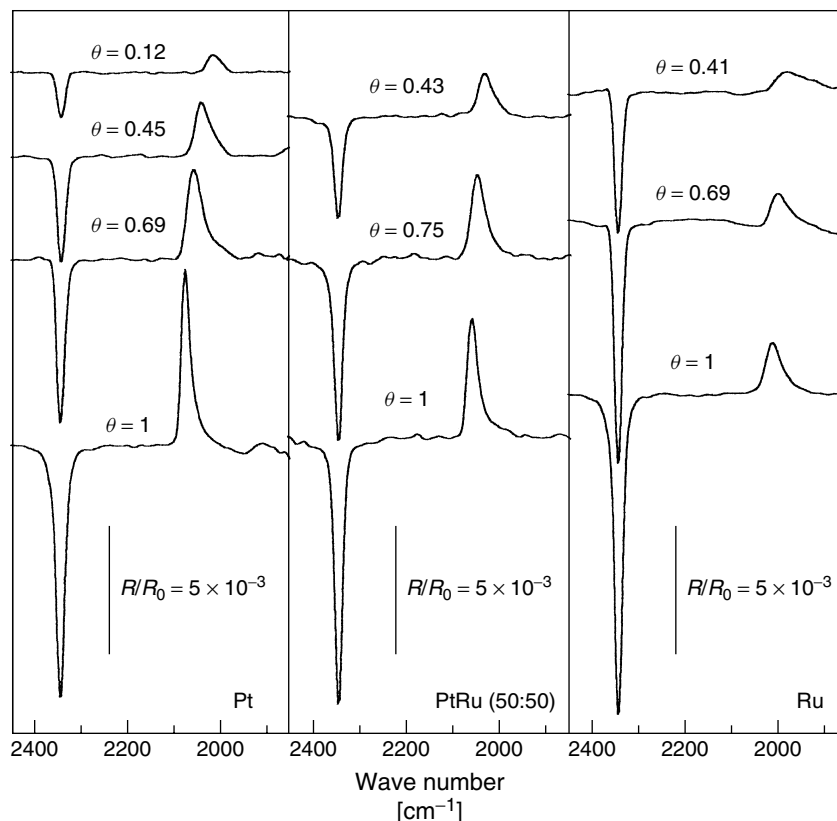


**Fig. 22** Comparison of in situ FTIR spectra for submonolayer CO adsorbates on Pt, PtRu(50:50), and Ru electrodes in 0.1 M HClO<sub>4</sub>. CO was adsorbed at 300 mV. Sample spectra were acquired at 300 mV and computed against a reference spectrum taken at 800 mV; 100 interferograms were collected at 8 cm<sup>-1</sup> resolution, acquisition time ca. 44 s. The CO coverages  $\theta_{\text{CO}}$  indicated on each spectrum were calculated from the ratio of the band intensity for CO<sub>2</sub> at each coverage to the CO<sub>2</sub> band obtained at saturation coverage. (From Ref. [62] with permission.)

#### 3.4.4.1.2 Adsorption and Oxidation of CO on Single-crystal Substrates

**CO adsorbed on Pt(111)/Ru** Attempts to study the influence of the surface structure on the rate of oxidation of CO, methanol, and ethanol motivated the preparation of catalysts using adsorbed Ru on well-defined Pt(111) surfaces [63]. However, the resulting structures, when investigated via STM, show that Ru segregates on the surface of Pt(111)

forming islands [70, 71]. The catalytic action is thus expected to occur at the border of Ru domains.

In situ FTIR spectra for adsorbed CO on this material are shown in Fig. 24(a, b) for two Ru coverages. At low Ru coverage ( $\theta_{\text{Ru}} = 0.2$ ), two bands related to CO bonded to Pt atoms in on-top and bridge positions are observed near 2058 cm<sup>-1</sup> and 1816 cm<sup>-1</sup>, respectively. A third band at 1982 cm<sup>-1</sup> corresponds to CO linearly bonded to Ru atoms. This feature is better

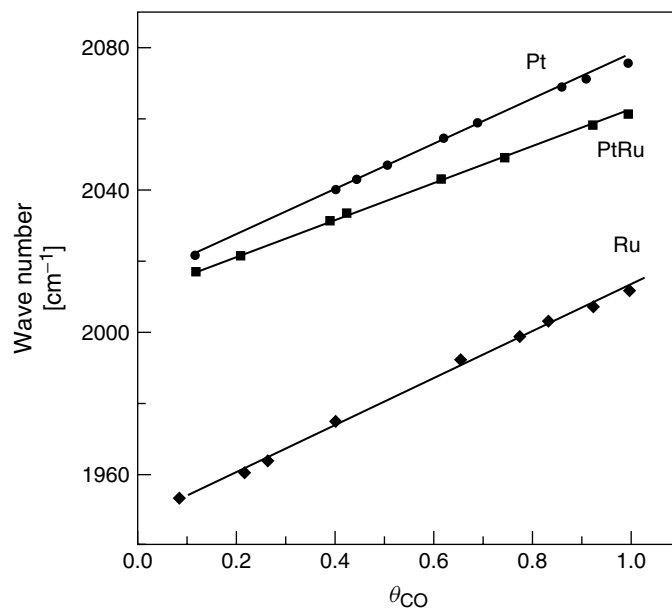


**Fig. 23** Dependence of  $\nu_{CO}$  on  $\theta_{CO}$  for submonolayer CO adsorbates on Pt, PtRu(50 : 50), and Ru electrodes in 0.1 M  $HClO_4$  at a constant potential of 300 mV: CO adsorption at 300 mV. Other details as in Fig. 23. (From Ref. [62] with permission.)

developed at the electrode with higher concentration of Ru, appearing at near  $2008\text{ cm}^{-1}$ . This and the band for  $CO_L$  at Pt sites ( $2047\text{ cm}^{-1}$ ) are the only prominent features observed.

It is noteworthy that for both surface coverages with Ru, Pt(111)/Ru exhibits features corresponding to CO frequencies near those of pure ruthenium and pure Pt as well. This is not the case for the PtRu (50 : 50) alloy, which exhibits only one band at frequencies close to those for pure Pt (Figs. 18 and 23). It can be thus stated that opposite to the Pt(111)/Ru electrode, the behavior of the alloy surface is that of a more homogeneous surface, with respect to the distribution of individual Pt and Ru atoms.

In Fig. 25, the band center frequencies for  $CO_L$  on different materials are plotted

as a function of the electrode potential; pure polycrystalline Ru is included for comparison. The Pt(111)/Ru samples exhibit values near to pure Pt(111) (at low Ru concentration) or pure Ru (at high Ru concentration).

Comparing the binary catalyst with the pure metals, it can be stated that the presence of Ru shifts the CO–Pt feature to lower wave numbers. Conversely, the presence of Pt shifts the CO–Ru feature to higher wave numbers. This observation can be related to the degree of backbonding. Since the work function of Pt(111) (5.93 eV) [72] is substantially higher than that of Ru (4.71 eV) [73], a significant electron transfer from Ru to neighboring Pt atoms is expected. Such an electronic effect should weaken the Ru–CO bond (because of decreased back donation) and

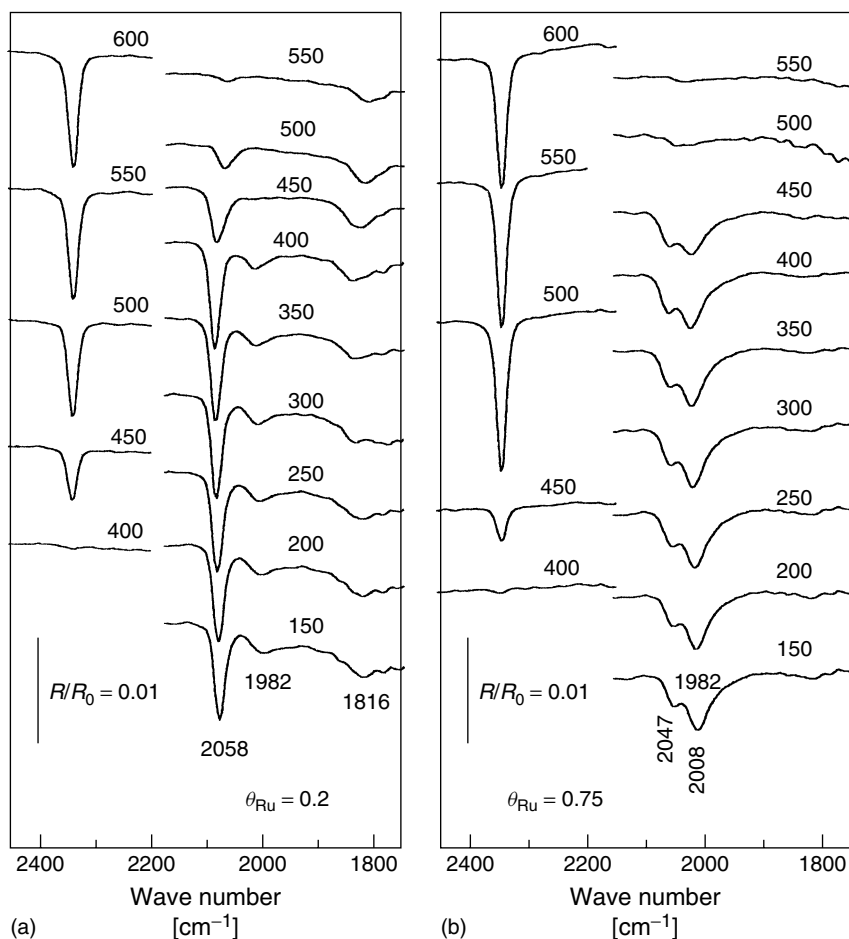


**Fig. 24** In situ FTIR spectra for adsorbed CO and for the CO<sub>2</sub> produced during the CO stripping in 0.1 M HClO<sub>4</sub> on Pt(111) modified with Ru. Ru coverage: (a) 0.2 mL and (b) 0.75 mL. After the formation of the CO adlayer at 0.1 V, CO was eliminated from the solution by N<sub>2</sub> bubbling. The potential was then changed from 0.1 V onwards in 50 mV steps. The sample potentials are indicated in the corresponding spectra. The CO<sub>2</sub> region (band at 2341 cm<sup>-1</sup>) was calculated with a reference spectrum taken at 0.1 V (a potential in which CO<sub>2</sub> is not formed). For the CO region, the reference spectrum was one taken at 0.8 V, that is, a potential in which CO<sub>ads</sub> was completely oxidized. (From Ref. [63] with permission.)

strengthen the Pt–CO bond (increased back donation). Thus, the relative values of the IR frequencies can be taken as a measure of the CO–Metal bond strength.

The rate of CO oxidation at 0.45 V on different PtRu materials was monitored

during several minutes via the changes in both CO and CO<sub>2</sub> signals. The result is plotted in Fig. 26. Surprisingly, the Pt(111)/Ru electrode containing 75% Ru presents the highest rate of CO oxidative stripping. The result can be rationalized in

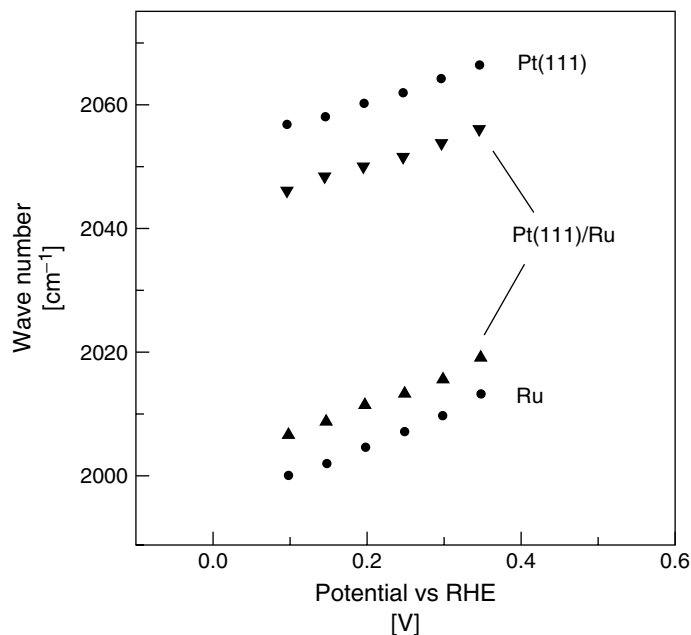


**Fig. 25** Comparison of the C–O stretch wave number for the  $\text{CO}_L$  on the Pt(111), Ru-modified Pt (111), and pure polycrystalline Ru as a function of potential. Data were derived from IR spectra as those in the figure. Experimental conditions as in Fig. 25. (From Ref. [63] with permission.)

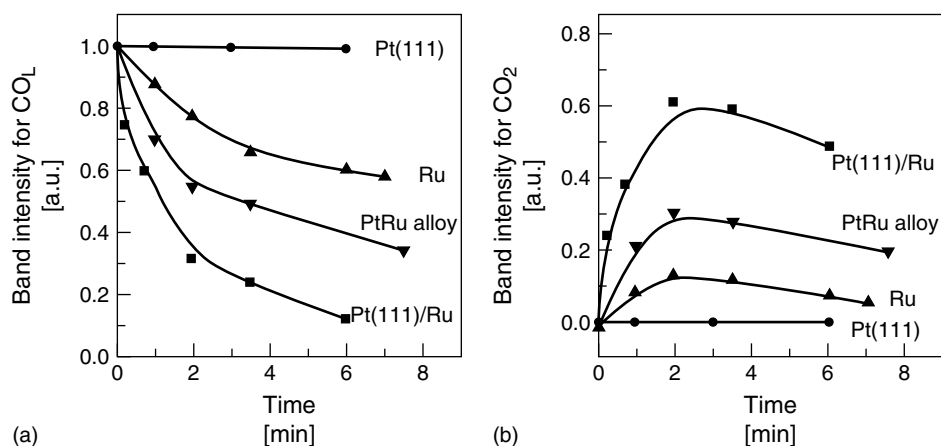
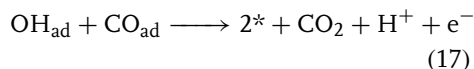
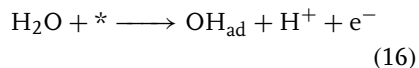


**Fig. 26** Change of the IR band intensity for adsorbed: (a) CO and (b) for  $\text{CO}_2$  during CO stripping at a constant potential of 0.45 V on Pt(111), Pt(111)/Ru with  $\theta_{\text{Ru}} = 0.75$ , PtRu(50:50) alloy, and pure polycrystalline Ru.

The respective surface was saturated with CO at 0.1 V after which, CO was eliminated from the electrolyte by nitrogen bubbling. (From Ref. [63] with permission.)

terms of a reaction mechanism as follows:



Where  $*$  represents a free site on the surface.

On pure Pt, the first step is rate determining, that is, the overall process starts as soon as OH adsorption sets in. The oxidation of the CO adsorbed layer is considered to initiate from sites that allow OH adsorption. On pure Ru, on the other hand, the second step seems to be rate determining. The adsorption of O-containing species has been reported already for potentials down to 0.2 V versus RHE [74], that is, well below the CO oxidation peak. This means that OH and CO can coexist on the surface within a certain potential region. The second step sets in only at a higher potential. In this model, the faster CO oxidation on the Pt(111)/Ru electrode can be explained by a decrease in the bond energy CO–Ru, reflected in the decrease of the backbonding effect.

**CO adsorbed on Ru(0001)** In situ FTIRS was used to study CO adlayers on Ru(0001) [65, 66]. Contrasting the behavior at polycrystalline Ru, where only the band for linear-bonded CO is observed (Fig. 27a), a saturated adlayer of CO adsorbed on Ru(0001) exhibits two different geometries. The spectra in Fig. 27(a) show two bands assigned to CO in linear and hollow position,  $\text{CO}_{\text{L}}$  and  $\text{CO}_{\text{H}}$ , respectively. This assignment is supported by STM data [66] showing this adsorption geometry in a  $c(2 \times 2)$ -2CO structure.

The potential dependence of the band intensity for both forms of adsorbed CO

and for the oxidation product,  $\text{CO}_2$ , is plotted in Fig. 27(b). The initial values of the band intensity for  $\text{CO}_{\text{L}}$  and  $\text{CO}_{\text{H}}$  are constant and start decreasing concomitant with the appearance of  $\text{CO}_2$  at ca. 200 mV versus Ag/AgCl. The intensity of the  $\text{CO}_2$  feature passes through a maximum at ca. 600 mV. From this potential onwards, the signal decreases, in spite of the fact that oxidation of  $\text{CO}_{\text{L}}$  continues up to a potential of 1100 mV. The latter process, however, is relatively slow and  $\text{CO}_2$  diffuses out of the thin layer, causing the observed decrease of the band intensity.

When analyzing the potential-dependent behavior of the band frequency, additional information on the surface structure and composition is useful. Thus, data from Auger and low-energy electron diffraction Spectroscopy (LEEDS) experiments were performed on emersed Ru(0001) electrodes [65]. In the range of potentials between  $-80$  mV and  $+200$  mV versus Ag/AgCl, a  $(2 \times 2)$  phase of oxygen exists on the surface [65]. Furthermore, oxygen was observed up to an emersion potential of 1100 mV, though forming another phase, which was suggested to be  $(1 \times 1)$ .

Four different potential regions are distinguished in Fig. 27(c) for the potential-dependent frequency of linear-bonded CO. The initial slope of the plot up to 175 mV,  $(d\nu_{\text{CO}}/dE) = 37 \text{ cm}^{-1} \text{ V}^{-1}$ , was interpreted as due to either a Stark effect or to electron back donation from the metal into the  $2\pi^*$  orbital of CO [30]. As the potential increases, between 200 and 425 mV versus Ag/AgCl, the slow oxidation of CO commences and the slope  $(d\nu_{\text{CO}}/dE)$  decreases slightly to  $29 \text{ cm}^{-1} \text{ V}^{-1}$ . The third region, with  $(d\nu_{\text{CO}}/dE) = 4 \text{ cm}^{-1} \text{ V}^{-1}$ , is accompanied with a significant increase of CO oxidation. At potentials between 625 mV and 1100 mV versus Ag/AgCl, the frequency changes again with a slope

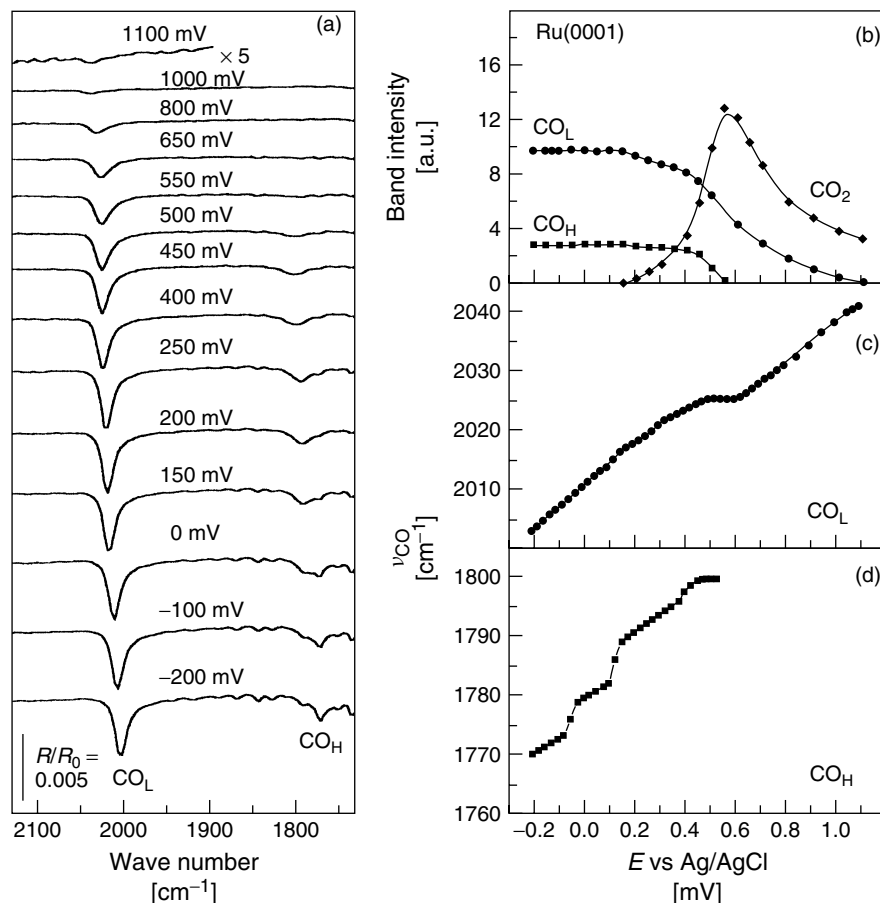


**Fig. 27** (a) In situ FTIR spectra for CO adsorbed at Ru(0001) at different potentials (vs Ag/AgCl/Cl<sup>-</sup>) as indicated. CO was adsorbed at -100 mV during 5 min, then the solution was replaced with pure base electrolyte (0.1 M HClO<sub>4</sub>). Spectra were normalized versus a spectrum taken at 1100 mV, after waiting for 2 min. in order to completely oxidize CO. (b) Integrated band intensities for  $\text{CO}_L$ ,  $\text{CO}_H$  from spectra is shown in (a).  $\text{CO}_2$  band intensity from the same experiments. (c), (d) Potential dependence of the band center frequency for  $\text{CO}_L$  and  $\text{CO}_H$ , respectively, from spectra shown in (a). (From Ref. [65] with permission.)

similar to the initial value for the saturated layer. Observing that CO oxidation slowly continues, it is obvious that the effect of potential on the band center frequency prevails over the lowering of the total CO coverage. That means that compact island domains of CO on the surface of Ru(0001) remain on the surface even at very high potentials [65].

At submonolayer coverage, a splitting of the  $\text{CO}_L$  feature was reported [65], which indicates different CO-adlayer structures that can be tuned by potential. It has been suggested that coadsorbed O, forming different structures depending on potential, plays an important role in the compression processes of the  $\text{CO}_L$  adlayer [65]. Confirming this interpretation, no splitting



of the  $\text{CO}_L$  adlayer was observed for electrodes pretreated by annealing at 1200 K in a hydrogen stream [66]. Under these conditions, the Ru oxide layer seems to be completely eliminated. The band for  $\text{CO}_H$ , Fig. 27(d), shows several transitions whose origin needs to be investigated. A series of spectra with different CO coverages exhibits this band only for the saturated adlayer [66].

#### 3.4.4.2 Methanol

The electrooxidation of methanol occupies, since many years, the center of interest in electrocatalysis of fuel cell reactions. Some of the most important findings on this issue are described in Chapter 5.2. We do not intend to review here all of the spectroscopic work done on methanol but to illustrate some highlights of the FTIRS method when applied to study the electrocatalysis of methanol oxidation.

It is well established that the rate of methanol electrooxidation at platinum can be enhanced in the presence of Ru as a cocatalyst. In Fig. 28 are represented in situ FTIR spectra obtained during oxidation of methanol on three different materials: Pt(111), Pt(111)/Ru(39%), and a PtRu alloy (85:15); the second electrode was prepared by adsorbing Ru from a  $\text{RuCl}_3$  solution onto a well prepared Pt(111) electrode [70]. For each material sample, spectra ( $R$ ) were obtained at the indicated potential and calculated as the ratio  $R/R_0$ , with  $R_0$  being a respective reference spectrum obtained at 0.05 V, a potential in which methanol adsorption is minimized.

For all electrodes, the band at  $2341\text{ cm}^{-1}$  is due to  $\text{CO}_2$  formed in the thin-layer cavity. Another feature due to a soluble species is the band at ca.  $1720\text{ cm}^{-1}$  due to a carbonyl group of the product formic acid c/o methyl formate (Methyl formate can

originate through a reaction of  $\text{HCOOH}$  with excess  $\text{CH}_3\text{OH}$ ). Other bands result from adsorbed species produced during methanol adsorption. Thus, the bands at ca.  $2050\text{ cm}^{-1}$  and  $1820\text{ cm}^{-1}$  are due, respectively, to linear and bridge adsorbed CO [60].

The spectra reveal that from all three materials, the alloy shows up (a) the largest production of  $\text{CO}_2$  and (b) the largest intensities for linear-bonded CO at low potentials. Thus, the gained information via IR spectroscopy is, not only the better performance of the alloy in relation to  $\text{CO}_2$  production but also its ability to adsorb methanol at lower potentials (observe the band intensity for CO at 0.15 mV). Besides this, for both PtRu materials, the CO band reaches at 0.30 to 0.35 V a stationary value and, in spite of a strong production of  $\text{CO}_2$  at 0.5 V, the band intensity for CO practically does not diminish. This indicates a high-rate methanol of readsorption at PtRu catalysts.

The catalytic mechanism of PtRu has been interpreted in terms of a so-called bifunctional effect of the surface in which Pt sites adsorb and dissociate methanol-forming CO and Ru atoms adsorb and dissociate water molecules, thus providing, at low potentials, oxygen atoms needed to complete the oxidation of adsorbed CO to  $\text{CO}_2$  [75]. The facts above, showing an increased rate of adsorption of methanol in the presence of Ru, indicate that the bifunctional mechanism alone does not fully describe the catalytic action of ruthenium.

#### 3.4.4.3 Ethanol

The electrocatalysis of ethanol oxidation using in situ FTIR spectroscopy was studied in several papers [76–80]. Some facts concerning the soluble reaction products at the low-index faces of Pt single-crystal

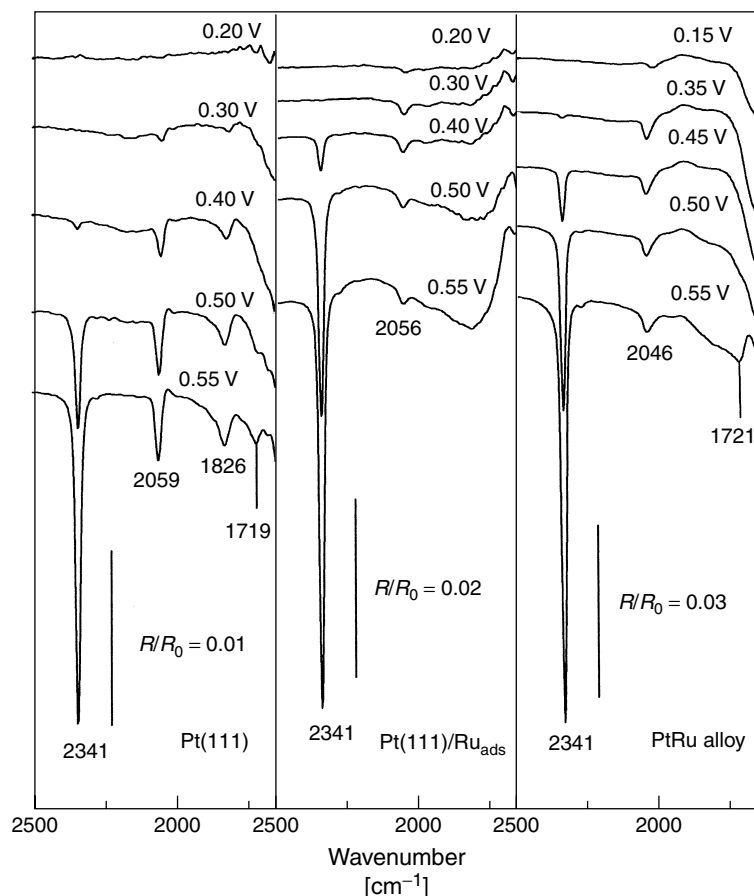


**Fig. 28** In situ FTIR spectra for Pt(111), Pt(111)/Ru 39%, and PtRu alloy (85 : 15) in 0.5 M  $\text{CH}_3\text{OH}$  + 0.1 M  $\text{HClO}_4$ . Potentials as indicated on each spectrum; reference spectrum taken at 0.05 V. (From Ref. [70] with permission.)

electrodes have been discussed by Chang et al. [77]. In a more or less quantitative manner, these authors used FTIR spectra to estimate the amount of adsorbed and soluble species formed during a potential scan. Some disagreement with later results in Ref. [80] concerning the intensity of CO bands may be explained in terms of a difference in the experimental approach.

As in the case of methanol, when Pt electrodes are contacted at 0.05 V versus RHE, with the solution containing

$\text{C}_2\text{H}_5\text{OH}$  + 0.1M  $\text{HClO}_4$ , ethanol adsorption is minimized. Therefore, this procedure allows the monitoring of the complete process of ethanol adsorption and oxidation as the potential is increased in the positive direction. Because of the well-known problem of surface poisoning by strongly adsorbed organic residues, data obtained under these conditions may not be observable in the second and following potential scans or when the electrode comes in contact with ethanol without potential control.

Spectral sequences during the electrochemical adsorption and oxidation of 0.1 M ethanol in 0.1 M HClO<sub>4</sub> on Pt(111) and Pt(100) are displayed in Fig. 29. In Table 2, the band assignments for the bands marked in the spectra are given. Acetaldehyde, acetic acid, and CO<sub>2</sub> have been earlier reported from in situ FTIR results, as products of ethanol oxidation [76]. In addition to these soluble products, a gain of bulk perchlorate ions (band at 1110 cm<sup>-1</sup>) can be observed in the spectra with increasing positive potentials.

These anions migrate into the thin layer of electrolyte to keep electric neutrality (note, that on positively increasing the potential, in addition to the double-layer charge changes, the hydrogen ions concentration in the thin layer of electrolyte increases. Both processes requiring the migration of negatively charged ions into the thin layer).

Adsorbed species observed are linear-bonded CO at ca. 2050 cm<sup>-1</sup> and acetate ions at 1404 to 1412 cm<sup>-1</sup> [82, 83]. Adsorbed acetate ions originate from

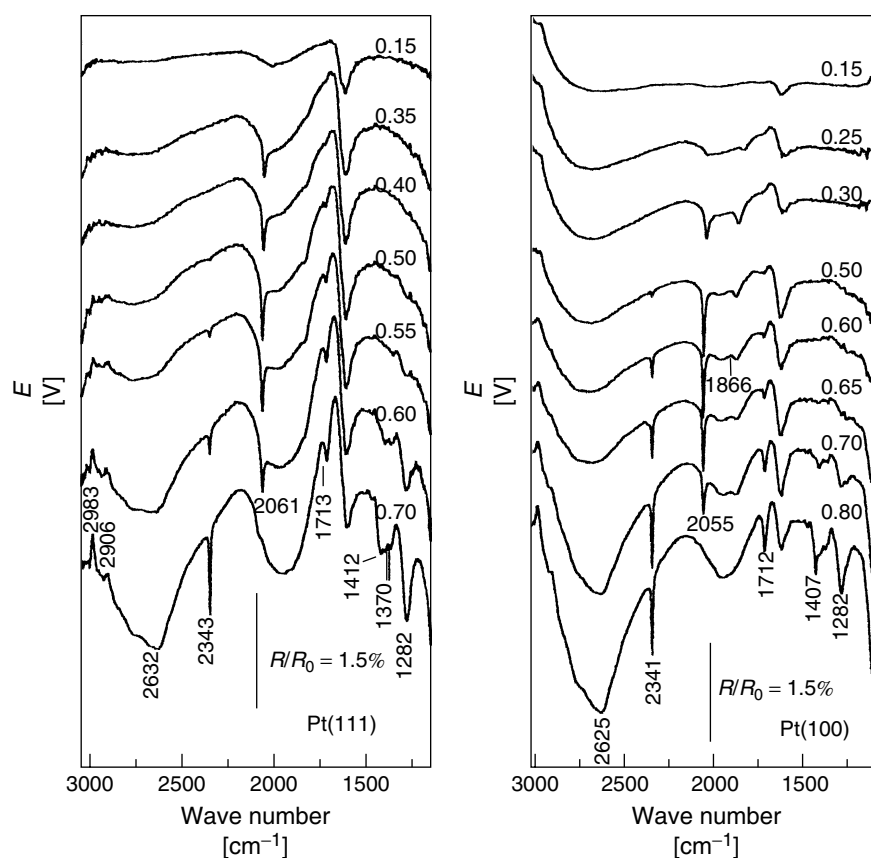


**Fig. 29** In situ FTIR spectra (256 scans, 8 cm<sup>-1</sup> resolution) at Pt(111) (left side) and Pt(100) (right side) in 0.1 M C<sub>2</sub>H<sub>5</sub>OH + 0.1M HClO<sub>4</sub>. Reference spectrum collected at 50 mV, and sample spectra collected at the indicated potential in 50 mV steps (some spectra were omitted for clarity). (From Ref. [80] with permission.)

**Tab. 2** Assignment of some of the fundamental bands in the spectra of Fig. 29

Wave number [cm <sup>-1</sup> ]	Functional group or chemical species	Mode, comments, references
2983, 2906	CH <sub>3</sub> , CH <sub>2</sub>	C–H str., 81
2632 (broad)	COOH	O–H str., 81
2341	CO <sub>2</sub>	C–O asym. str., 81
2055–2060	Adsorbed CO	Linearly bonded, 60
1713	COOH or CHO	C=O str., carbonyl, 81
1402	Adsorbed CH <sub>3</sub> COO <sup>-</sup>	C–O sym. str., 82
1370/1281	COOH	Coupl. C–O str. –OH def., 81
1100	ClO <sub>4</sub> <sup>-</sup>	Cl–O str. (F), 35

dissociation of acetic acid in the adsorbed state. Bridge-bonded CO, at about 1860 cm<sup>-1</sup> is observed at Pt(100) and to a minor extent at Pt(111). In the presence of bulk ethanol, as in the experiments in Fig. 29, positive-going features as those near 3000 cm<sup>-1</sup> (CH stretching region [83]) are due to consumption of bulk ethanol.

**3.4.4.3.1 Potential Dependence of the Band Intensities** The dependence of the band intensities for CO<sub>ad</sub> and CO<sub>2</sub> plotted

in Fig. 30(a, b) attest for the surface sensitivity of the reaction. At Pt(100) both linear and bridge-bonded CO start being formed short above 0.2 V. In the low-potential region, before oxidation begins, the site interconversion, CO-bridge → CO-linear, is observed. This phenomenon is well-known for CO formed at Pt(100) either from dissolved CO [23, 25] or from the adsorption of other fuels [84, 85]. At around 0.5 V, oxidation to CO<sub>2</sub> begins; maximum production of CO<sub>2</sub> is observed at 0.8 V. At this potential, all adsorbed

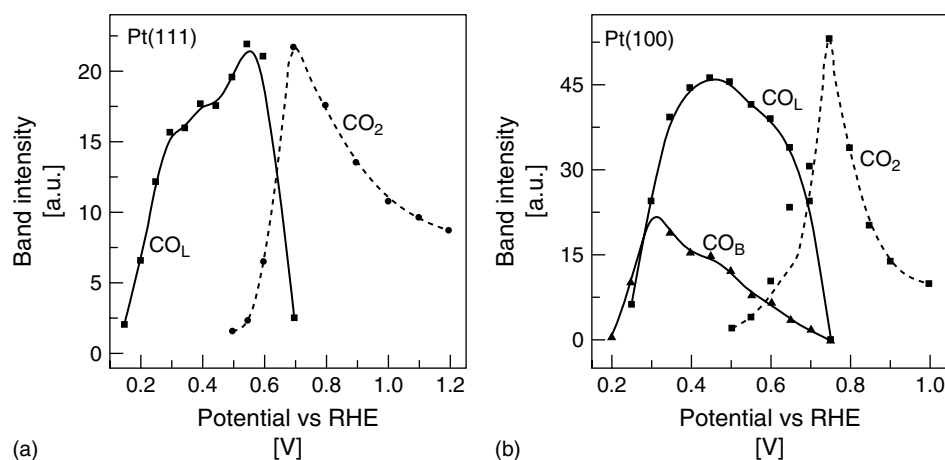


**Fig. 30** Band intensity for CO and CO<sub>2</sub> from spectra collected during the oxidation of 0.1 M ethanol in 0.1 M HClO<sub>4</sub> at (a) Pt(111) and (b) Pt(100). Experimental conditions as in Fig. 29. (From Ref. [80] with permission.)

CO is consumed and the  $\text{CO}_2$  signal decays as  $\text{CO}_2$  diffuses out of the thin-layer cavity.

At Pt (111), the formation of linear-bonded CO starts around 0.15 V. The integrated band intensity in Fig. 30(a), indicates a maximum for CO formation at 0.55 V. The arrest observed at intermediate potentials coincides with the beginning of the formation of acetaldehyde (band at 1713 in Fig. 29), thus indicating that this reaction competes with that producing CO (i.e. cleavage of the C–C bond).

A general phenomenon of small organic molecules is the presence of anodic currents during the negative-going sweep of the voltammogram as shown in Fig. 31. For the interpretation of this reactivation phenomenon, the formation of reaction products during a cyclic scan as shown in Fig. 32 should be considered. For these experiments, a  $60^\circ$   $\text{CaF}_2$  prism was used to monitor the bands for adsorbed

CO and  $\text{CO}_2$ . Formation of acetaldehyde can be followed without interference via a feature at  $933\text{ cm}^{-1}$  [77]. However, because of the cut off of  $\text{CaF}_2$  (around  $1000\text{ cm}^{-1}$ ), a flat ZnSe window had to be used to monitor the band intensity for acetaldehyde ( $933\text{ cm}^{-1}$ ). Data for acetic acid ( $1280\text{ cm}^{-1}$ ) in Fig. 32 were taken from the spectra obtained with the ZnSe window.

The changes for acetaldehyde and acetic acid resemble those reported by Chang et al. [77]. The onset of acetaldehyde formation, at about 0.4 V, is accompanied by a sluggish appearance of acetic acid. Both signals exhibit a pronounced increase in intensity at 0.6 V, coinciding with the onset of CO oxidation, that is, with a higher availability of Pt sites. It is interesting to note, during the positive-going polarization, that  $\text{CO}_2$  grows up to 1.0 V, that is, beyond the potential at which the surface becomes free from CO. This being an indication of the presence of other

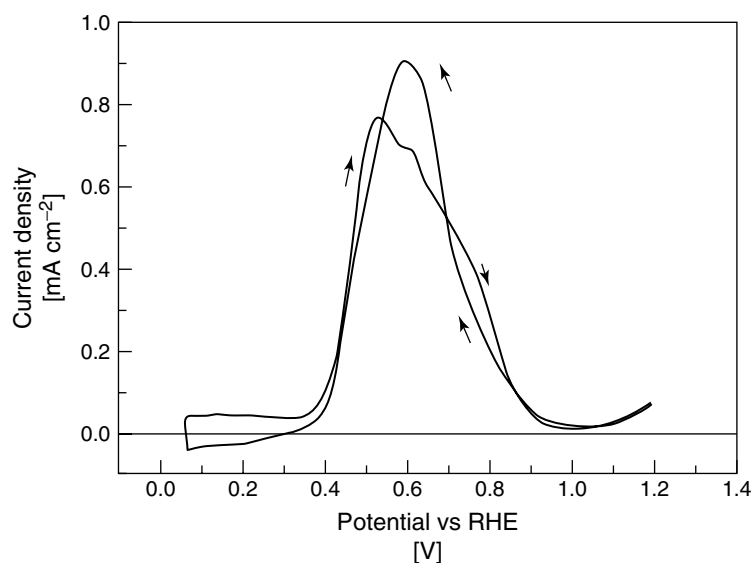


**Fig. 31** Cyclic voltammogram for a Pt(111) electrode in 1 M  $\text{C}_2\text{H}_5\text{OH}$  + 0.1 M  $\text{HClO}_4$  solution. Sweep rate 0.05 V/s.

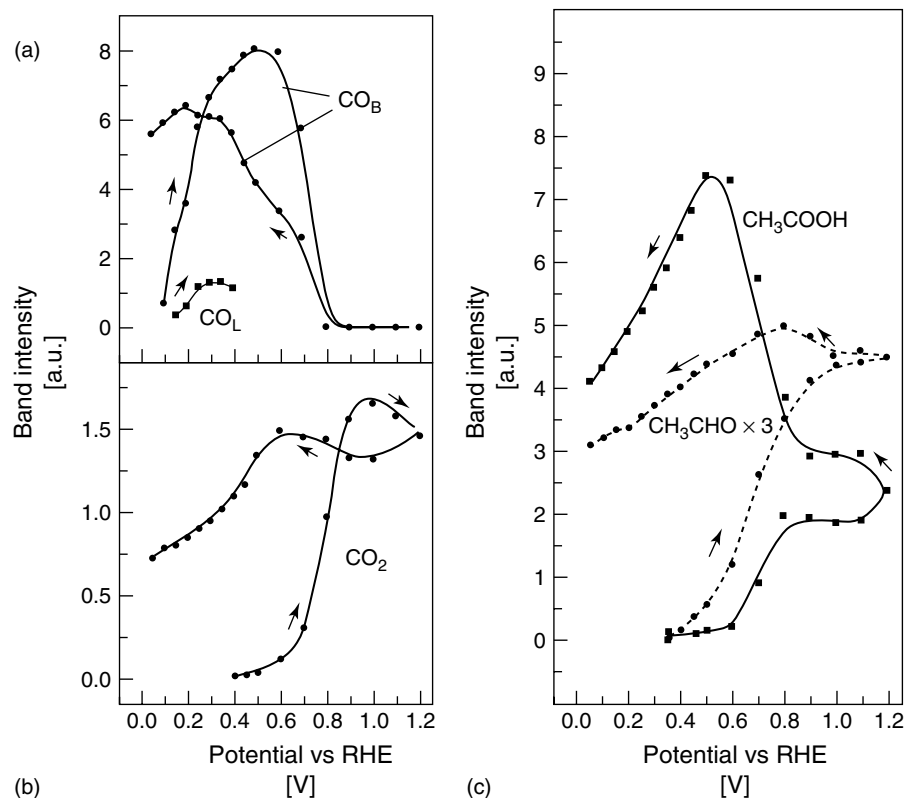


**Fig. 32** Potential dependence of the band intensities for CO, CO<sub>2</sub>, acetaldehyde, and acetic acid, from spectra obtained at Pt(111) during the oxidation of ethanol in 1 M C<sub>2</sub>H<sub>5</sub>OH + 0.1 M HClO<sub>4</sub>. After taking a reference spectrum at 0.05 V, potential steps were applied towards higher positive potentials and then back to the initial value. All spectra are referred to the first one taken at 0.05 V. A 60° prismatic CaF<sub>2</sub> window was used for CO and CO<sub>2</sub> and a flat ZnSe window for acetaldehyde and acetic acid. (From Ref. [80] with permission.)

strongly adsorbed species not observed in the spectra. As the applied polarization is reversed, both acetaldehyde and acetic acid increase slowly. However, at ca. 0.9 V, which is the potential at which the current in the voltammogram increases again, a pronounced increase of acetic acid is observed. Also, CO<sub>2</sub> and CO grow during the reverse scan from 0.8 V downwards. The recovering in activity has been related to a competition between water and the organic substance for Pt sites [86, 87]. Infrared spectroscopy data show that the

strength of water adsorption increases as the applied potential grows in the positive direction. During the negative-going scan, a decrease of water–platinum interaction favors the access of ethanol to the surface as indicated by the increase of the CO feature.

### 3.4.5

#### Final remarks

The examples presented in this chapter show the power of in situ FTIR

spectroscopy to study electrochemical systems. Under equilibrium conditions the infrared spectroscopy provides molecular level information on the double layer, contributing to the understanding of the physics and chemistry of the charged interface. Thus, the potential and structure dependence of ion adsorption and the geometry of the adsorbed ions as well, can be inferred from the inspection of the IR spectra.

On the other hand, under conditions of current flow, IR spectra can be used as a tool to obtain analytical information on electrochemical processes. This approach has provided valuable information on the electrocatalysis of the oxidation of organic substances, which is currently used for mechanistic interpretations and for the evaluation of catalytic materials.

### Acknowledgments

FAPESP and CNPq are gratefully acknowledged for their financial support.

### References

1. L. H. Little, *Infrared Spectra of Adsorbed Species*, Academic Press, London, 1966.
2. S. A. Francis, A. H. Ellison, *J. Opt. Soc. Am.* **1959**, *49*, 131–138.
3. R. G. Greenler, *J. Chem. Phys.* **1966**, *50*, 310–315.
4. A. H. Reed, E. Yeager, *Electrochim. Acta* **1970**, *15*, 1345–1354.
5. H. Neff, P. Lange, D. K. Roe et al., *J. Electroanal. Chem.* **1983**, *150*, 513–519.
6. W. N. Hansen, *J. Opt. Soc. Am.* **1968**, *58*, 380.
7. K. Ataka, M. Osawa, *Langmuir* **1998**, *14*, 951–959.
8. M. Osawa, K. Ataka, K. Yoshii et al., *J. Electrochem. Spectrosc.* **1993**, *64*, 371–379.
9. Z. Ping, G. E. Nauer, H. Neugebauer et al., *Electrochim. Acta* **1997**, *42*, 1693–1700.
10. A. Bewick, K. Kunitatsu, B. S. Pons, *Electrochim. Acta* **1980**, *25*, 465–480.
11. A. Bewick, K. Kunitatsu, B. S. Pons et al., *J. Electroanal. Chem.* **1984**, *160*, 47–61.
12. B. Beden, A. Bewick, C. Lamy, *J. Electroanal. Chem.* **1983**, *148*, 147–160.
13. A. Bewick, *J. Electroanal. Chem.* **1983**, *150*, 481–493.
14. T. Bae, D. A. Scherson, E. Yeager, *Anal. Chem.* **1990**, *62*, 45–49.
15. D. S. Corrigan, M. J. Weaver, *J. Electroanal. Chem.* **1988**, *239*, 55–66.
16. T. Iwasita, F. C. Nart, *J. Electroanal. Chem.* **1990**, *295*, 215–224.
17. P. R. Griffiths, J. A. de Haseth in *Chemical Analysis: A Series of Monographs on Analytical Chemistry and Its Applications* (Eds.: P. J. Elving, J. D. Winefordner), John Wiley & Sons, New York, 1986, Vol. 83, pp. 274–283.
18. S. Pons, *J. Electroanal. Chem.* **1983**, *150*, 495–504.
19. S. Pons, T. Davison, A. Bewick, *J. Electroanal. Chem.* **1984**, *160*, 63–71.
20. S. C. Chang, M. J. Weaver, *J. Chem. Phys.* **1990**, *92*, 4582–4594.
21. S. C. Chang, M. J. Weaver, *J. Phys. Chem.* **1990**, *94*, 5095–5102.
22. S. C. Chang, M. J. Weaver, *Surf. Sci.* **1990**, *230*, 222–236.
23. S. C. Chang, M. J. Weaver, *Surf. Sci.* **1990**, *238*, 142–162.
24. F. Kitamura, M. Takahashi, M. Ito, *Surf. Sci.* **1989**, *223*, 493–508.
25. F. Kitamura, M. Takahashi, M. Ito, *J. Phys. Chem.* **1988**, *92*, 3320–3323.
26. D. S. Corrigan, M. J. Weaver, *J. Electroanal. Chem.* **1988**, *241*, 143–162.
27. L. H. Leung, M. J. Weaver, *J. Phys. Chem.* **1988**, *92*, 4019–4022.
28. K. Kunitatsu, H. Seki, W. G. Golden et al., *Surf. Sci.* **1985**, *158*, 596–608.
29. H. Seki, K. Kunitatsu, W. G. Golden, *Appl. Spectrosc.* **1985**, *39*, 437–443.
30. T. Iwasita, F. C. Nart in *Advances in Electrochemical Science and Engineering* (Eds.: H. Gerischer, C. W. Tobias), Verlag Chemie, Weinheim, 1995, Vol. 4, pp. 123–216.
31. B. N. J. Persson, *Solid State Commun.* **1979**, *30*, 163–166.
32. I. R. Moraes, F. C. Nart, *J. Electroanal. Chem.* **1998**, *461*, 110–120.
33. M. C. P. M. da Cunha, M. Weber, F. C. Nart, *J. Electroanal. Chem.* **1996**, *414*, 163–170.
34. I. R. Moraes, M. C. P. M. da Cunha, F. C. Nart, *J. Bras. Chem. Soc.* **1996**, *7*, 453–460.

35. K. Nakamoto, *Infrared and Raman Spectra of Inorganic and Coordination Compounds*, 4th edition, John Wiley & Sons, New York, 1986.
36. P. Christensen, A. Hamnett in *Comprehensive Chemical Kinetics* (Eds.: R. G. Compton, A. Hamnett), Elsevier, Amsterdam, 1989, Vol. 29, pp. 1–104.
37. R. J. Nichols, A. Bewick, *Electrochim. Acta* **1988**, 33, 1691–1694.
38. E. L. de Sa, Ph. D. Thesis, Universidad de São Paulo, São Carlos, 1997.
39. P. Christensen, A. Hamnett, A. V. G. Muir, *J. Electroanal. Chem.* **1986**, 241, 361–371.
40. A. C. Chapman, L. E. Thirwell, *Spectrochim. Acta* **1964**, 20, 937.
41. T. Iwasita, F. C. Nart, *Prog. Surf. Sci.* **1997**, 55, 271–340.
42. G. J. Edens, X. Gao, M. J. Weaver, *J. Electroanal. Chem.* **1994**, 375, 357–366.
43. M. Lennartz, P. Broekmann, M. Arenz et al., *Surf. Sci.* **1999**, 442, 215–222.
44. A. Tadjeddine, A. Le Rille, *Electrochim. Acta* **1999**, 45, 601–609.
45. F. C. Nart, T. Iwasita, M. Weber, *Electrochim. Acta* **1994**, 39, 2093–2096.
46. I. R. Moraes, F. C. Nart, *J. Braz. Chem. Soc.* **2001**, 12, 138–143.
47. P. W. Faguy, N. Markovic, R. R. Adzic et al., *J. Electroanal. Chem.* **1990**, 289, 245–262.
48. Y. Shingaya, M. Ito, *J. Electroanal. Chem.* **1999**, 467, 299–306.
49. Y. Shingaya, M. Ito, *Surf. Sci.* **1997**, 386, 34–47.
50. P. W. Faguy, N. S. Marinkovic, R. R. Adzic, *Langmuir* **1996**, 12, 243–247.
51. P. W. Faguy, N. S. Marinkovic, R. R. Adzic, *J. Electroanal. Chem.* **1996**, 407, 209–218.
52. M. Funtikov, U. Stimming, R. Vogel, *J. Electroanal. Chem.* **1997**, 428, 147–153.
53. L. J. Wan, S. L. Yau, K. Itaya, *J. Phys. Chem.* **1995**, 99, 9507–9513.
54. L. J. Wan, M. Hara, J. Inukai et al., *J. Phys. Chem. B* **1999**, 103, 6978–6983.
55. F. C. Nart, T. Iwasita, *Electrochim. Acta* **1992**, 37, 2179–2184.
56. F. C. Nart, T. Iwasita, *Electrochim. Acta* **1996**, 41, 631–636.
57. F. C. Nart, T. Iwasita, M. Weber, *Electrochim. Acta* **1994**, 39, 2093–2096.
58. T. Iwasita, F. C. Nart, A. Rodes et al., *Electrochim. Acta* **1995**, 40, 53–59.
59. F. C. Nart, T. Iwasita, *J. Electroanal. Chem.* **1992**, 322, 289–300.
60. Beden, C. Lamy, A. Bewick et al., *J. Electroanal. Chem.* **1981**, 121, 343.
61. D. K. Lambert, *Electrochim. Acta* **1996**, 41, 623–630.
62. W. F. Lin, T. Iwasita, W. Vielstich, *J. Phys. Chem. B* **1999**, 103, 3250–3257.
63. W. F. Lin, M. S. Zei, M. Eiswirth et al., *J. Phys. Chem. B* **1999**, 103, 6968–6977.
64. S. Cram, K. A. Friedrich, K. P. Geyzers et al., *Fresenius' J. Anal. Chem.* **1997**, 358, 189–192.
65. W. F. Lin, P. A. Christensen, A. Hamnett et al., *J. Phys. Chem.* **2000**, 104, 6642–6652.
66. N. Ikemiyama, T. Senna, M. Ito, *Surf. Sci.* **2000**, 464, L681–L685.
67. T. E. Madey, C. Benndorf, *Surf. Sci.* **1985**, 164, 602–624.
68. H. Pfnür, D. Menzel, F. M. Hoffmann et al., *Surf. Sci.* **1980**, 93, 431–452.
69. B. N. J. Persson, R. Rydberg, *Phys. Rev. B* **1981**, 24, 6954–6970.
70. T. Iwasita, H. Hoster, A. John-Anacker et al., *Langmuir* **2000**, 16, 522–529.
71. H. Hoster, T. Iwasita, H. Baumgärtner et al., *PCCP* **2001**, 3, 337–346.
72. B. E. Nieuwenhuys, W. H. M. Sachtler, *Surf. Sci.* **1973**, 34, 225.
73. B. E. Nieuwenhuys, R. Bouwman, W. H. M. Sachtler, *Thin Solid Films* **1973**, 21, 5.
74. E. Ticianelli, J. G. Beery, M. T. Paffett et al., *J. Electroanal. Chem.* **1989**, 258, 61–77.
75. M. Watanabe, S. Motoo, *J. Electroanal. Chem.* **1975**, 60, 267–273.
76. T. Iwasita, B. Rasch, E. Cattaneo et al., *Electrochim. Acta* **1989**, 34, 1073–1079.
77. S.-C. Chang, L.-W. H. Leung, M. J. Weaver, *J. Phys. Chem.* **1990**, 94, 6013–6021.
78. F. Cases, M. López-Atalaya, J. L. Vázquez et al., *J. Electroanal. Chem.* **1999**, 278, 433–440.
79. T. Iwasita, E. Pastor, *Electrochim. Acta* **1994**, 39, 531–537.
80. X. H. Xia, H.-D. Liess, T. Iwasita, *J. Electroanal. Chem.* **1997**, 437, 233–240.
81. G. Socrates, *Infrared Characteristic Group Frequencies*, Wiley, New York, 1966.
82. A. Rodes, E. Pastor, T. Iwasita, *J. Electroanal. Chem.* **1994**, 376, 109–118.
83. J. Shin, W. J. Tornquist, C. Korzeniewski et al., *Surf. Sci.* **1996**, 364, 122–130.
84. X. H. Xia, T. Iwasita, F. Y. Ge et al., *Electrochim. Acta* **1996**, 41, 711–718.
85. T. Iwasita, X. H. Xia, E. Herrero et al., *Langmuir* **1996**, 12, 4260–4265.



86. T. Iwasita, X. H. Xia, *J. Electroanal. Chem.* **1996**, 411, 95–102.  
 87. T. Iwasita, X. H. Xia, H.-D. Liess et al., *J. Phys. Chem. B* **1997**, 101, 7542–7547.

## Appendix

If  $\mathbf{S}$  is the vector representing the electromagnetic energy flux intensity, the conservation equation will be

$$\frac{dw}{dt} + \text{div } \mathbf{S} = 0 \quad (\text{A1})$$

where  $dw/dt$  is the speed of energy dissipation.  $\mathbf{S}$  is the Poynting vector and is defined by Eq. (4)

$$\mathbf{S} = \mathbf{E} \times \mathbf{H} \quad (\text{A2})$$

Where  $\mathbf{E}$  is the electric field and  $\mathbf{H}$  is the magnetic field of the electromagnetic radiation. Giving that the electromagnetic radiation is a high-frequency radiation, the observed signal will be a time average of the radiation dissipation. The time average

of the Poynting vector is Eq. (4)

$$\langle S \rangle = \left( \frac{1}{2} \right) \text{Re}(\mathbf{E} \times \mathbf{H}^*) \quad (\text{A3})$$

Therefore, the rate of the radiation dissipation will be Eq. (2)

$$-\text{div} \langle S \rangle = \sigma \left( \frac{1}{2} \right) \mathbf{E} \times \mathbf{E}^* \quad (\text{A4})$$

where  $\sigma$  is the effective conductivity of the absorbing medium at the field frequency and the quantity  $\mathbf{E} \times \mathbf{E}^*$  is the time average of the  $\mathbf{E}^2$ , therefore

$$-\text{div} \langle S \rangle = \left( \frac{1}{2} \right) \sigma \langle \mathbf{E}^2 \rangle \quad (\text{A5})$$

Hence the rate of energy dissipation is proportional to the square of the mean electric field of the incident radiation and it is the result of the spectroscopic measurement. The intensity of the  $\langle \mathbf{E}^2 \rangle$  is directly related to the amount of dissipated energy by the absorbing medium.



## 4.1 Structure Relationships in Electrochemical Reactions

C. A. Lucas

*University of Liverpool, Liverpool, United Kingdom*

N. M. Marković

*University of California, Berkeley, California*

### 4.1.1 Introduction

In this report, we review recent studies of single-crystal transition metal electrode surfaces by combining in situ surface X-ray diffraction measurements with more traditional electrochemical techniques in order to probe the influence of the surface structure on the electrochemical reactivity. This functionality is generally termed *structure sensitivity*. In the last decade, the in situ surface X-ray diffraction technique has been a critical tool for determining the potential stability of specific surface structures in electrolyte *under* reaction conditions. On the other hand, the rotating ring disk electrode (RRDE) has been routinely used for determining the kinetics of electrochemical reactions on single-crystal surfaces and evaluating the potential-dependent surface coverage by an adsorbed species. In combination, the X-ray diffraction and RRDE

methods have provided remarkable insight into the surface electrochemistry and the “structure sensitivity” of many important electrochemical processes.

In this chapter, we review the progress in the surface science of electrochemical reactions. The methods of the surface X-ray diffraction and rotating ring disk experiments are described in Sect. 4.1.2, for surface X-ray diffraction – the focus being on the application of the technique to single-crystal electrodes in the electrochemical environment. Section 4.1.3 then describes the nature of the surface structures that are formed on “bare” single-crystal transition metal surfaces in electrolyte. The phenomena of surface reconstruction and surface relaxation are illustrated by detailed examples, namely Au(001) and Pt(110), in which the dependence of the surface structure on the applied electrode potential is described. Section 4.1.4 first describes the surface structures and energetics of anion adsorption onto different single-crystal electrode surfaces, that is, Pt and Au, and then the underpotential deposition (UPD) of metals onto the same substrates. Results from the different metal surfaces are presented in an attempt to understand the influence of the substrate on the structure of the overlayer and the effect of anions on the UPD process. The results highlight the strength of combining

RRDE measurements with X-ray diffraction results to investigate the detailed nature of the surface structures that are formed, particularly in coadsorption studies, for example, the influence of anion species on the UPD process. In Sect. 4.1.5, the oxygen reduction reaction (ORR) is used as a *model* electrochemical reaction to demonstrate the relation between the metal–O<sub>2</sub> energetics and reaction pathway/kinetics as well as the importance of the local symmetry of surface atoms in determining the electrocatalytic properties of metal surfaces.

#### 4.1.2

##### Methods

##### 4.1.2.1 X-ray Diffraction

**4.1.2.1.1 Theory** It is beyond the scope of this review article to provide a comprehensive description of basic X-ray diffraction from surfaces. Instead, readers are referred to the excellent reviews by Feidenhans'l [1], Fuoss and Brennan [2], and Robinson and Tweet [3] for explicit details. In this section, we will focus on some basic ideas that pertain to X-ray diffraction studies of surfaces in an electrochemical environment, in particular with regard to crystal-truncation rod (CTR) measurements.

Since the interaction of hard X-rays with matter is weak, provided that the exact Bragg conditions for a perfect crystal are not met, the kinematical scattering approximation, in which scattering is treated as a single event, can be used. For a crystal volume defined by  $N_1$ ,  $N_2$ , and  $N_3$  unit cells along the crystal axes defined by the vectors  $\mathbf{a}_1$ ,  $\mathbf{a}_2$ , and  $\mathbf{a}_3$ , the scattered intensity can be written as the product of two scattering amplitudes, one from the unit cell and one from the lattice of unit

cells. This gives

$$I(\mathbf{Q}) \propto F(\mathbf{Q})F^*(\mathbf{Q}) \frac{\sin^2(N_1\mathbf{Q}\cdot\mathbf{a}_1)}{\sin^2(\mathbf{Q}\cdot\mathbf{a}_1)} \times \frac{\sin^2(N_2\mathbf{Q}\cdot\mathbf{a}_2)}{\sin^2(\mathbf{Q}\cdot\mathbf{a}_2)} \frac{\sin^2(N_3\mathbf{Q}\cdot\mathbf{a}_3)}{\sin^2(\mathbf{Q}\cdot\mathbf{a}_3)} \quad (1)$$

where  $\mathbf{Q}$  is the momentum transfer, defined by the scattering angle  $2\theta$  and the unit cell structure factor,  $F$ , is given by

$$F(\mathbf{Q}) = \sum_{j=1}^n f_j \exp(i\mathbf{Q}\cdot\mathbf{r}_j) \quad (2)$$

where  $\mathbf{r}_j$  is the relative atomic position in the unit cell and the sum is over all of the atoms in the unit cell each having an atomic scattering factor  $f_j$  ( $f_j$  is  $\mathbf{Q}$ -dependent and proportional to the atomic number of the relevant atom). When the crystal is large, Eq. (1) produces a series of very sharp peaks in which  $\mathbf{Q}\cdot\mathbf{a}_i = \pi$ . If the scattering is from a single monolayer (ML), that is,  $N_3 = 1$  (the  $\mathbf{a}_3$  vector is along the surface normal), then the scattering normal to the crystal surface becomes completely diffuse.

Considering the case of a perfectly terminated crystal surface and assuming that the Bragg conditions are met in the plane of the crystal (i.e.  $\mathbf{Q}_x\cdot\mathbf{a}_1 = \mathbf{Q}_y\cdot\mathbf{a}_2 = n\pi$ ), then for a semi-infinite crystal, Eq. (1) reduces to

$$I(\mathbf{Q}) \propto \frac{N_1^2 N_2^2 F(\mathbf{Q})F^*(\mathbf{Q})}{2} \sin^2\left(\frac{\mathbf{Q}_z\cdot\mathbf{a}_3}{2}\right) \quad (3)$$

The Bragg points of the finite crystal are connected by streaks of intensity along the surface normal direction in the reciprocal lattice. At the minimum position, midway between Bragg reflections, the scattered intensity is similar to the scattering expected from a single monolayer. The streaks of intensity are known as crystal-truncation rods (CTRs) as they arise from

the truncation of the crystal lattice at the surface [3, 4].

Figure 1 illustrates some of the information that can be obtained from the analysis of CTR data. The intensity variation along a CTR as a function of the surface normal phase shift,  $\mathbf{Q} \cdot \mathbf{a}_3 = 2\pi l$ , is shown for the case of a perfect surface (solid line), a surface with a reduced density in the topmost atomic layer (dotted line), and a surface in which the topmost atomic layer is expanded away from the bulk crystal (dashed line). When  $l$  is an integer, the Bragg conditions are satisfied and the kinematical approximation breaks down. The minimum of the scattering is observed at the “anti-Bragg” positions when  $l$  has half-integer values. Surface roughness causes a decrease in the scattering at the anti-Bragg positions as shown by the dotted line in the figure, which is a calculation for a surface with only half of

the atoms in the surface layer present. Similar effects are observed when adsorbates are formed on crystal surfaces as a result of the difference in the scattering factors between the adsorbed atoms and the substrate atoms. Hence for a monolayer of adsorbed atoms, which have half of the scattering power of the substrate atoms, a similar result to the dotted line in Fig. 1 would be observed. Similarly, an adlayer with an increased surface density would cause an increase in the intensity at the anti-Bragg conditions. For CTRs measured with an in-plane contribution to the momentum transfer, the changes to the CTR profile are dependent on the relative phase of the scattering from the substrate and the adlayer, which can cause either an increase or decrease in the intensity at the anti-Bragg positions. Finally, a change in the lattice spacing at the surface causes asymmetry in the intensity

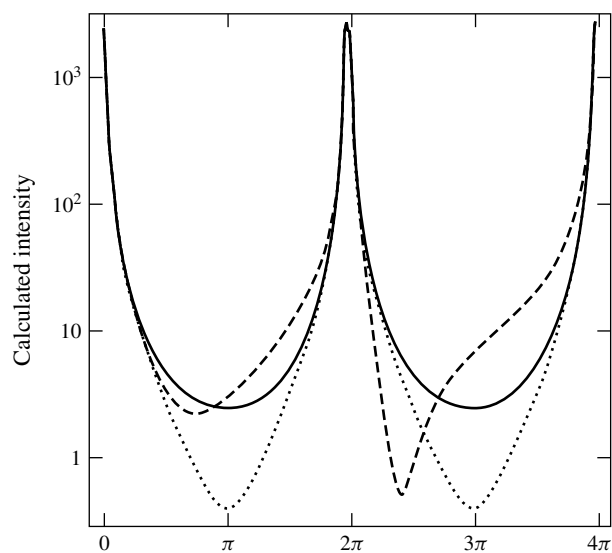


**Fig. 1** The intensity variation along a CTR as a function of the surface normal phase shift, calculated for a perfect surface (solid line), a surface with a lower density topmost atomic layer (dotted line) and a surface in which the topmost atomic layer is expanded by 10% of the layer spacing (dashed line).

around the Bragg reflections, as shown by the dashed line in Fig. 1, which is for a 10% expansion of the surface layer relative to the bulk. Again, similar effects are produced by adsorbates, as the adsorbate-substrate layer spacing is very often different from that of the bulk substrate layer spacing.

By careful modeling of CTR data, it is possible to extract structural information, such as surface coverage, surface roughness, and layer spacings (both adsorbate-substrate distances and the expansion/contraction of the substrate

surface atoms themselves). By combining specular CTR results (in which  $Q$  is entirely along the surface normal direction) with nonspecular CTR results (in which  $Q$  has an additional in-plane contribution), it is possible to build up a three-dimensional picture of the atomic structure at the electrode surface. If the surface or adlayer adopts a different symmetry from that of the underlying bulk crystal lattice, then the scattering from the surface becomes separate from that of the bulk in reciprocal space and it is possible to measure the surface scattering independently. This

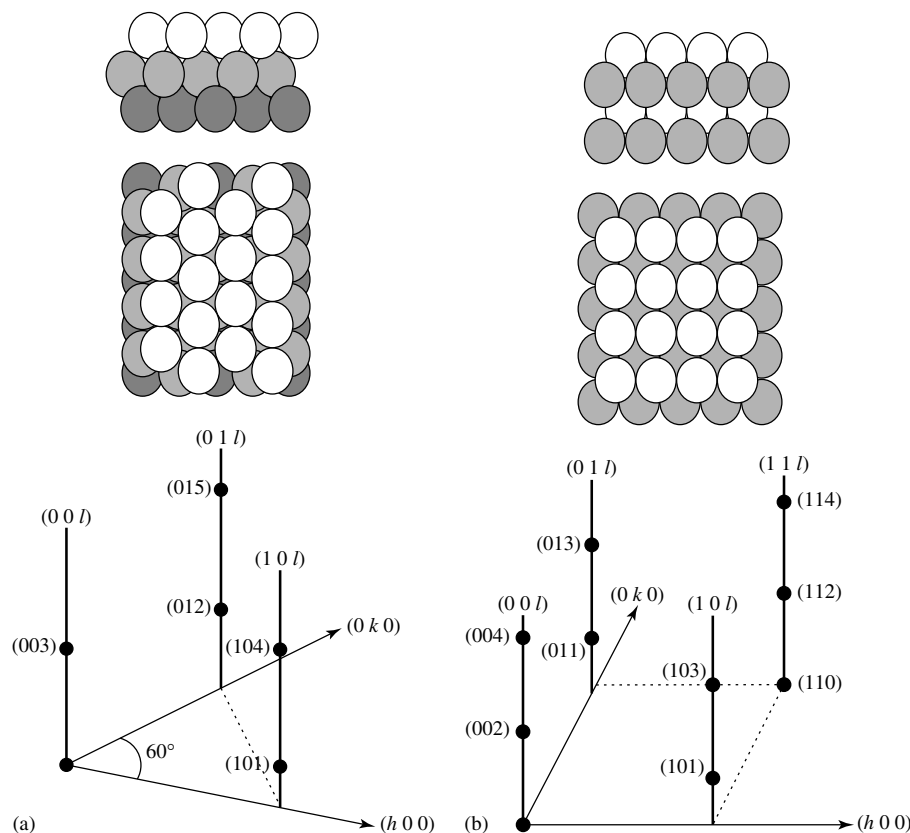
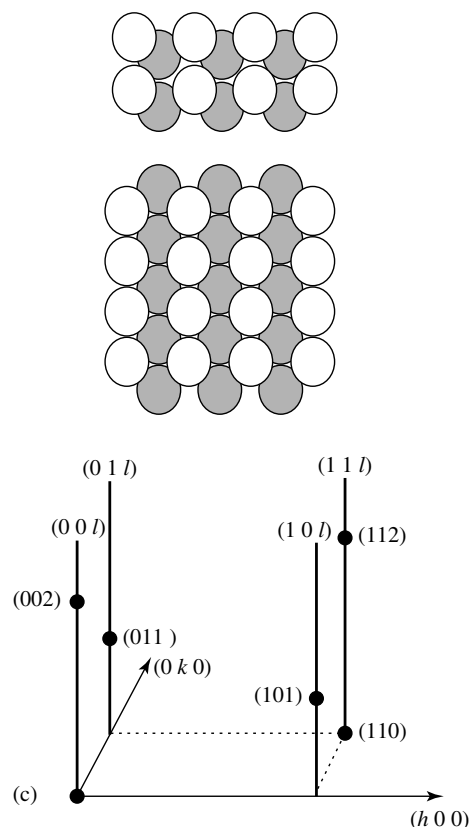


**Fig. 2** The real-space surface structures and corresponding reciprocal space lattices for: (a) (111); (b) (001); and (c) (110) surface terminations of an fcc crystal. The unit cells are shown in the real-space structures and the corresponding Bragg reflections indicated in the reciprocal space lattices.

Fig. 2 (Continued)



independent structural information can be combined with CTR analysis to give the registry of the surface layers with respect to the bulk lattice [1–3]. CTR and surface structure analysis are presented in Sects. 4.1.3 and 4.1.4 of this report for a variety of electrochemical surfaces.

**4.1.2.1.2 Reciprocal Lattices for Low-index fcc Metal Surfaces** This report describes results from the three low-index surfaces of metal crystals with the face centered cubic (fcc) crystal structure. As such, it is instructive to describe the reciprocal space lattice for each surface orientation so that the results from the X-ray diffraction experiments presented in Sects. 4.1.3 and

4.1.4 can be quoted without reference to the experimental details in each case. Figure 2 shows the reciprocal space lattices for the (111), (001), and (110) crystal faces with the corresponding real-space surface structures shown schematically in each case. In surface X-ray diffraction experiments, it is always desirable for the surface normal direction to be defined as the  $(0, 0, l)$  reciprocal space direction. This is also the convention adopted for low-energy electron diffraction (LEED) experiments.

The close-packed (111) surface is shown in Fig. 2(a). For this surface, a hexagonal unit cell is defined, such that the surface normal is along the  $(0, 0, l)_{\text{hex}}$  direction and

the  $(h, 0, 0)_{\text{hex}}$  and  $(0, k, 0)_{\text{hex}}$  vectors lie in the plane of the surface and subtend  $60^\circ$ . The units for  $h$ ,  $k$ , and  $l$  are  $a^* = b^* = 4\pi/\sqrt{3}a_{\text{NN}}$  and  $c^* = 2\pi/\sqrt{6}a_{\text{NN}}$  where  $a_{\text{NN}}$  is the nearest-neighbor distance in the crystal. Because of the ABC stacking along the surface normal direction, the unit cell contains three monolayers and the Bragg reflections are spaced apart by multiples of three in  $l$ . The basic scattering equation for an unrelaxed, unmodified (111) surface along the CTRs shown in Fig. 2(a) is then given by

$$I(h, k, l) \propto \left| \frac{f}{1 - \exp[2\pi i(h/3 - k/3 - l/3)]} \right|^2 \quad (4)$$

where  $f$  is the atomic form factor (including the Debye–Waller temperature factor [5]).

The (001) surface (Fig. 2b) is more open than the (111) surface and is indexed to a surface tetragonal unit cell. This is related to the conventional cubic unit cell by the transformations  $(1, 0, 0)_t = 1/2(2, 2, 0)_c$ ,  $(0, 1, 0)_t = 1/2(2, -2, 0)_c$ , and  $(0, 0, 1)_t = (0, 0, 1)_c$ . The units for  $h$ ,  $k$ , and  $l$  are  $a^* = b^* = 2\pi/a_{\text{NN}}$  and  $c^* = 4\pi/\sqrt{2}a_{\text{NN}}$ , where  $a_{\text{NN}}$  is the nearest-neighbor distance in the crystal. The CTR scattering, by analogy with Eq. (4), is given by

$$I(h, k, l) \propto \left| \frac{f}{1 - \exp[-\pi i(h + k + l)]} \right|^2 \quad (5)$$

Finally, the (110) reciprocal surface unit cell is rectangular as shown in Fig. 2(c) and the reciprocal lattice notation is such that  $h$  is along  $[1 \ -1 \ 0]$ ,  $k$  along  $[0 \ 1 \ 0]$ , and  $l$  is along the  $[1 \ 1 \ 0]$  surface normal. The units for  $h$ ,  $k$ , and  $l$  are  $a^* = c^* = 2\pi/a_{\text{NN}}$  and  $b^* = 4\pi/\sqrt{2}a_{\text{NN}}$ , where  $a_{\text{NN}}$  is the nearest-neighbor distance in the crystal. For this surface, the CTR scattering reduces to

the form

$$I(h, k, l) \propto \left| \frac{f}{1 - \exp[-2\pi i(h/2 + k/2 + l/2)]} \right|^2 \quad (6)$$

Equations (4–6) are by no means rigorous but they essentially form the basis for analyzing CTR data from the three low-index surfaces of fcc transition metals. The equations are easily modified to include surface relaxation effects, surface roughness, or adsorbed adlayer species and are used in the analysis of the results presented in Sects. 4.1.3 and 4.1.4 of this report.

**4.1.2.1.3 Experimental Details** The general experimental procedures used in X-ray diffraction measurements of electrochemical systems have been described in detail in previous articles [6–8]. After surface preparation of the electrode to be studied, the crystal is transferred (preferably whilst being protected from the atmosphere by a drop of electrolyte on the surface) into an X-ray electrochemical cell. The design of the electrochemical cell that we have used in our experiments is shown schematically in Fig. 3. In this design, the crystal is held in place by tightening down the central column of the cell, which is screw-threaded into the main body (all parts are made of Kel-F material, which can be chemically cleaned and is relatively easy to machine). The crystal surface then forms the highest part of the cell and so is easily accessible to the incident X-ray beam. Electrical contact to the working electrode and to a counter and reference electrode are made through feedthrough connections on the side of the cell. In our experiments, a palladium/hydrogen reference electrode was used, which was in direct contact with the electrolyte in the main body of the



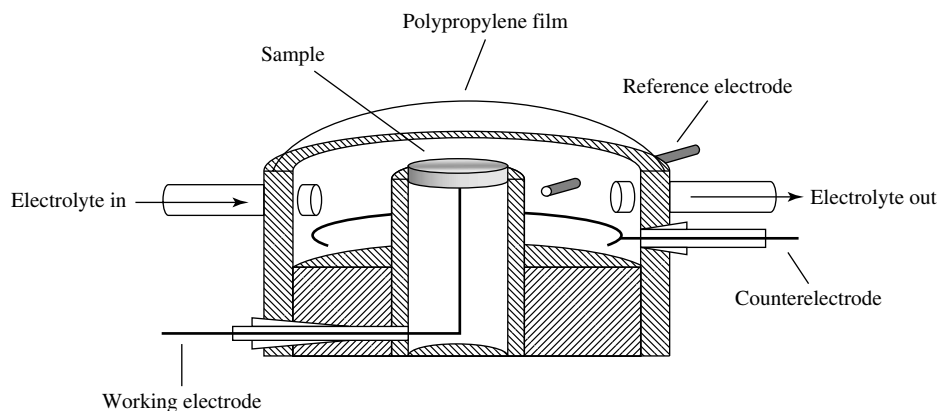


**Fig. 3** A schematic diagram of the electrochemical X-ray scattering cell.

cell. Care has to be taken in this situation as, depending on the nature of the electrochemical reactions that are being studied, there can be shifts in the reference potential. Two further connections form electrolyte feedthroughs to the cell and the liquid is contained within the cell by a thin ( $\sim 10\ \mu\text{m}$ ) polypropylene window sealed with an “o” ring. During the X-ray experiment, the electrochemical cell can be deflated to trap a thin layer of electrolyte ( $\sim 10\ \mu\text{m}$ ) between the electrode surface and the X-ray window to shorten the solution pathlength of the X-ray beam. Note that this cell design allows the sample to be oriented in any direction as the electrolyte is contained, that is, there is no need for any specialized diffractometer equipment in order to maintain a horizontal surface geometry. In order to minimize contamination from the atmosphere, the cell is surrounded by an outer shell containing a nitrogen atmosphere.

Most of the X-ray measurements described in this report were carried out at room temperature on beamline 7-2 at the Stanford Synchrotron Radiation Laboratory (SSRL) utilizing a focused monochromatic X-ray beam. Additionally,

some results by other authors are used, which were obtained on beamlines at the Brookhaven National Synchrotron Light Source (NSLS). For experimental details, readers are referred to the referenced work in each case. For a general description of the procedures used in synchrotron surface X-ray diffraction experiments, readers are referred to the excellent review by Feidenhans'l [1]. A typical procedure for any given electrochemical system used in our experiments is roughly as follows:

- (1) In the X-ray cell, immediately after mounting in the X-ray goniometer and being put under potential control, the cyclic voltammetry (CV) was measured for comparison with literature results. After the initial cycling, the electrode potential was transferred to computer control for the duration of the X-ray experiment. Although with time the features in the CV became distorted as the electrolyte made contact with the polycrystalline back and sides of the crystal, the general features were always observable for the duration of the experiment (typically up to a maximum of 24 h).

- (2) The X-ray spectrometer would be aligned with two or more Bragg reflections to relate the spectrometer angles to the reciprocal space lattice of the sample. Subsequently all data were measured in units of the sample reciprocal space (see previous section).
- (3) For a particular electrochemical system, the dependence of the X-ray scattering intensity at various key reciprocal space positions (usually at points on the CTRs) would be monitored as a function of the applied electrode potential over the potential range of interest. This potentiodynamic technique, which we have termed as *X-ray voltammetry* (XRV) [9], is described in more detail in Sect. 4.1.2.1.4.
- (4) The XRV measurement is used to identify structural changes that are occurring at different electrode potentials. These would then be probed with the electrode potential held at the relevant value. Typically, in searching for in-plane structures, scans along the  $(h, 0, 0)$ ,  $(0, k, 0)$ , and  $(h, k, 0)$  in-plane reciprocal space directions at small out-of-plane momentum transfer ( $l = 0.1\text{--}0.15$ ) were performed. From these scans, it would be hoped to locate scattering that had a different symmetry to that of the bulk CTR scattering. Data for CTR analysis would be obtained by performing rocking scans at sequential  $l$  values along a particular CTR. The rocking scans can then be integrated (either numerically or by fitting a functional form to the lineshape), which results in the CTR profile plotted as  $l$  versus integrated intensity. This data is suitable for analysis using the equations given in the previous section, modified by the appropriate instrumental resolution corrections [10].

**4.1.2.1.4 New Techniques** Surface X-ray diffraction is now a well-established technique for probing the atomic structure at the electrochemical interface and, since the first in situ synchrotron X-ray study in 1988 [6], several groups have used the technique to probe a variety of electrochemical systems. Most analysis has followed the methodology outlined in Sects. 4.1.2.1.1 to 4.1.2.1.3, whereby structural information at a fixed electrode potential is obtained by detailed measurement of the scattering from surface structures and modeling of the CTR profiles. In this section, a couple of recent applications of X-ray scattering are described that are particularly useful in studies of the electrochemical interface.

(1) *X-ray Voltammetry (XRV)*: XRV is a potentiodynamic measurement whereby the scattered X-ray intensity at a particular reciprocal lattice point is monitored as the potential is cycled. As can be seen from Fig. 1, positions on the CTRs are sensitive to surface expansion or to adsorption effects. By measuring the XRV at a number of different CTR positions, an insight into the nature of the structural changes at the surface can be obtained without recourse to the detailed measurement of the CTR profiles [11, 12]. If scattering as a result of an ordered surface layer with a different symmetry to that of the underlying bulk crystal is obtained, then the measurement of the potential dependence of this scattering directly indicates the potential range of stability of the structure. This information is particularly useful for comparison with CV results as features in the CV can be directly correlated with structural changes at the electrode surface. Several examples of this measurement are presented in Sects. 4.1.3 and 4.1.4 of this report.

(2) *Anomalous scattering techniques*: In Sect. 4.1.2.1.1, the atomic form factor,  $f$ , gives the scattering power of each atom within a particular unit cell structure. When the incident X-ray energy is away from atomic adsorption edges,  $f$  is  $\mathbf{Q}$ -dependent and related to the number of electrons that the atom has. However, if the X-ray energy is tuned near to an adsorption edge then  $f$  must be modified by the anomalous dispersion corrections according to

$$f(\mathbf{Q}, E) = f_0(\mathbf{Q}) - f'(E) - if''(E) \quad (7)$$

Close to an adsorption edge  $f'(E)$  can increase to  $\sim 10$  electrons and so can have a dramatic effect on the atomic form factor and hence the scattered X-ray signal. In the complex electrochemical environment, this effect can be extremely helpful in identifying structural models, especially in coadsorbate systems. For example, the contribution to the X-ray scattering from a particular atom in a structure may be effectively isolated by tuning the energy of the incident X-ray beam through an atomic adsorption edge. This can help the interpretation of X-ray diffraction data (examples are given in Sect. 4.1.4.2 for anion/metal coadsorption) and, additionally, may be used to probe oxidation states at surfaces and in adsorbates [13]. The combination of diffraction measurements with traditional extended X-ray absorption fine-structure (EXAFS) techniques (so-called diffraction anomalous fine-structure (DAFS) [14]) may lead to studies in which the local environment of atoms selected by the diffraction conditions is probed spectroscopically.

#### 4.1.2.2 Rotating Ring Disk Methods

A large array of experimental techniques has been developed to probe the behavior

of electrochemical reactions. Although several experimental methods are now routinely used in the surface electrochemistry, the rotating disk electrode (RDE) and rotating ring disk electrode (RRDE) techniques have become standard tools in determining kinetic parameters, reaction products, and potential-dependent surface coverage by adsorbates [15, 16]. The RDE is a solid disk embedded in an isolating material attached to the shaft that rotates about the electrode surface normal. The Navier–Stokes equation can be solved exactly for this system, providing exact correction for reactant mass transport limitations. As the concentration of dissolved gasses, viz.  $\text{H}_2$ ,  $\text{O}_2$ ,  $\text{CO}$ , and so on, in aqueous solutions is relatively low, for example,  $10^{-5}$ – $10^{-6}$  mol  $\text{cm}^{-2}$ , the mass-transfer limitation in the hydrogen oxidation reaction (HOR), oxygen-reduction reaction (ORR), and  $\text{CO}$  oxidation reaction are very significant, and the use of the RDE is absolutely essential for definitive kinetic studies. The most useful equation to study electrode kinetics that are under mixed control, that is, the case when the activation ( $i_{\text{ac}}$ ) and mass transport-controlled ( $i_{\text{L}} = B\omega^{1/2}$ ) current densities combine to yield the total current density as the sum of reciprocal, is

$$\frac{1}{i} = \frac{1}{i_{\text{ac}}} + \frac{1}{i_{\text{L}}} \quad (8)$$

where the diffusion limiting current is proportional to angular velocity  $\omega^{1/2}$  [15, 16].

The success of the RDE method has stimulated the development of several other rotating configurations. The RRDE is perhaps the most useful extension of the idea of the RDE. The RRDE was first developed by Frumkin and Nekrasov to detect unstable intermediates in electrode reactions. The RRDE, Fig. 4, consists of a central disk electrode surrounded by

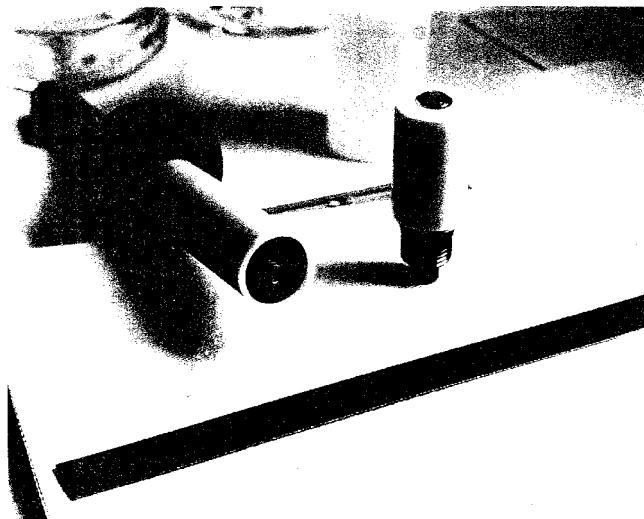


**Fig. 4** The RRDE consisting of a central disk electrode surrounded by a concentric insulating annulus and a concentric ring electrode.

a concentric insulating annulus (Teflon) and then a concentric ring electrode. To operate an RRDE, a bipotentiostat is needed, which can control the potential of the disk and the ring independently, in order to measure the current going through each of them separately. The reaction intermediates formed on the disk electrode can be monitored using the ring-collection properties. In the ring-collection mode, intermediates produced on the disk electrode can be “collected” by the ring electrode [16]. In the RRDE configuration, however, only a fraction of intermediates produced on the disk electrode will reach the ring electrode. This fraction is determined by the collection efficiency,  $N$ , which is defined as the ratio between the ring and disk currents,  $N = i_r/i_d$ . In Sect. 4.1.5, the collection mode of the RRDE is used to monitor the formation of intermediates during the ORR on the disk electrode.

The RRDE can also be useful to obtain accurate thermodynamic data without

interference from kinetic and double-layer effects. The best example is UPD of copper in solution containing  $\text{Br}^-$ , in which the amount of Cu UPD and/or bromide anion deposited/adsorbed on the disk electrode can be estimated using the two ring-electrode properties – ring shielding and ring collection [16]. For both modes, the UPD species is reduced to metal at the ring, and electroactive species in solution must undergo convective-diffusion controlled reduction at the ring electrode. The ring-shielding property of the RRDE is illustrated in Sect. 4.1.4.2.3 in which it is used to assess the *mass flux* of both the  $\text{Cu}^{2+}$  and the  $\text{Br}^-$  from and to the Pt(111) disk electrode. If either Br or Cu is adsorbed at the Pt(111) disk, the surface coverages  $\theta_{\text{Br,Cu}}$  can be assessed from the ring currents in either potentiodynamic or potentiostatic experiments:

$$\theta_{\text{Br,Cu}} = \frac{1}{Q} \frac{(1/\nu) \int (i_r - i_r^\infty) dE}{AnN} \quad (9)$$

$$\theta_{\text{Br,Cu}} = \frac{1}{Q} \frac{\int_0^\infty (i_{\text{r}(t)} - i_{\text{r}}^\infty) d\tau}{AnN} \quad (10)$$

where  $i_{\text{r}}^\infty$  and  $i_{\text{r}}$  are unshielded (no UPD process on the disk electrode) and shielded ring currents, respectively,  $N$  is the collection efficiency,  $v$  refers to the sweep rate,  $n$  is the number of electrons ( $n = 2$  for  $\text{Cu}^{2+}$  reduction to  $\text{Cu}^0$  and  $n = 1$  for  $\text{Br}^-$  oxidation to  $1/2 \text{Br}_2$  on the ring electrode), and  $Q$  is the charge corresponding to monolayer formation of ad-atoms on Pt(111) based on the surface atomic density of Pt(111)-( $1 \times 1$ ) ( $1.53 \times 10^{15}$  atoms  $\text{cm}^{-2}$ ), assuming one completely discharged ad-atom per platinum atom. (e.g.  $208 \mu\text{C cm}^{-2}$  for  $\text{Br}_{\text{ad}}$  and  $480 \mu\text{C cm}^{-2}$  for  $\text{Cu}_{\text{upd}}$ ). By combining the powerful in situ X-ray scattering technique with the elegant RRDE method, remarkable insight into the structural nature of the Pt(*hkl*)-UPD-anion electrochemical interface can be obtained as is demonstrated in Sect. 4.1.4.

#### 4.1.2.3 Surface Preparation

A key aspect in the study of single-crystal metal electrodes is the preparation of the surface prior to the experiment and the transfer of the crystal into the electrochemical environment. One approach is to prepare the surface in an ultrahigh vacuum (UHV) environment by cycles of ion sputtering and annealing. This methodology has the advantage that the surface quality can be checked during preparation by standard surface science techniques such as LEED and Auger electron spectroscopy. UHV preparation methods have been particularly useful in the study of Au(*hkl*) electrodes as the surfaces are relatively inert and the crystal can be transferred in air from the UHV system to the electrochemical cell. An alternative method for

the preparation of Au(*hkl*) is to use the flame-annealing technique [17]. After pretreatment to produce a flat, well-oriented surface, the crystal is heated in an hydrogen or butane flame and then allowed to cool in air before transfer to the cell. This method, or variations of it, can produce clean surfaces as evidenced by the subsequent observation of the Au surface reconstructions in electrolyte.

UHV preparation of crystal surfaces is time consuming and can be difficult for some metals. Furthermore, for more reactive metals than Au, it is transfer of the crystal after surface preparation that is vital, as it is important to minimize the interaction of the surface with the atmosphere. The development of the flame-annealing method by Clavilier and coworkers [18] has become of critical importance in surface electrochemistry. The hydrogen flame-annealing method has been developed to incorporate a cooling procedure whereby the crystal is cooled in a hydrogen or argon atmosphere before a drop of electrolyte is placed on the surface for transfer to the electrochemical cell. By using purified gases, the contact with oxygen is minimized during preparation and this procedure has been used successfully for the preparation of Pt(*hkl*) surfaces.

Unfortunately other metal surfaces, such as Cu, Ag, and Ni, cannot be prepared by flame-annealing methods. The most successful method for these surfaces has been to use a long preanneal of the surface in a forming gas, such as hydrogen, followed by a short electrochemical etch, rinsing with water and then direct transfer into the electrochemical cell [19–21]. The exact conditions for the etching procedure vary for different metals and even for different surface orientations of the same metal. For the results included in this report, readers are referred to the reference

material for precise descriptions of the surface preparation that was followed in each case.

#### 4.1.3

##### Surface Structures

Modern surface crystallographic studies have shown that on the atomic scale, most clean metals tend to minimize their surface energy by two kinds of surface atom rearrangements – relaxation and reconstruction [22–26]. In this review, the term surface reconstruction applies to the case in which there is lateral (i.e. in the surface plane) movement of surface atoms such that the surface layer has a symmetry that is different from that of the underlying bulk of the crystal. Hence, the surface layer has a two-dimensional unit cell that is different from the corresponding two-dimensional unit cell of a layer in the bulk. The periodicity of the surface can be defined by Woods' notation; for example, an unreconstructed surface would be termed as  $(1 \times 1)$ , whereas if the surface unit cell size was doubled in one of the primary vector directions, it would be termed as  $(2 \times 1)$ , and so on. On the other hand, surface relaxation applies to the case in which the surface layer is in a  $(1 \times 1)$  state but the layer is displaced along the surface normal direction from the position expected for bulk termination of the crystal lattice. In this section, both surface reconstruction and surface relaxation effects are described with specific examples chosen to illustrate the phenomena as they are observed in the electrochemical environment.

##### 4.1.3.1 Surface Reconstruction

###### 4.1.3.1.1 Gas–solid Interface Under UHV conditions, the clean low-index faces

of the fcc metals, Pt, Ir, and Au, have all been shown to reconstruct under certain conditions of sample temperature and surface preparation [24]. Given that the hexagonal (111) lattice planes form the most dense surfaces they have the least tendency to reconstruct and only the Au(111) surface exhibits a reconstruction at room temperature. The reconstruction is rather complex and involves a small increase in the surface density (23 surface atoms instead of 22), which leads to a large unit cell, the  $(23 \times \sqrt{3})$  structure, which is known as the “chevron” or “herringbone” reconstruction [27.] In contrast, the most open (110) surfaces have a strong tendency to reconstruct, exhibiting  $(1 \times n)$  periodicities [24]. The (110) surfaces of Pt, Ir, and Au usually reconstruct to form a  $(1 \times 2)$  or  $(1 \times 3)$  periodicity. After some initial controversy, it is now well established that the  $(1 \times 2)$  structure is characteristic of clean surfaces. These structures are called “missing-row” structures since every other row in the topmost atomic layer is missing. Hence, in the transition from the  $(1 \times 1)$  to the  $(1 \times 2)$  state, there is a 50% decrease in the density of the surface layer and significant mass transport must occur. Theoretical calculations have indicated that the  $(1 \times 2)$  reconstruction is stabilized on the 5d transition metal (110) surfaces due to the participation of the d electrons in bonding in the solid and the decrease of the kinetic energy of delocalized electrons at the surface [28]. For Au and Pt, contaminants seem to play the dominant role in the appearance of the  $(1 \times 3)$  structure, that is, it seems that the  $(1 \times 3)$  structures obtained in UHV are impurity-stabilized [29].

Perhaps the most intriguing reconstruction occurs on the (001) surfaces. For example, under UHV conditions, the

Au(001) surface exhibits a hexagonal reconstruction, that consists of a single, buckled, slightly distorted overlayer that is aligned close to the [110] bulk direction and is often referred to as a “ $5 \times 20$ ” reconstruction although, strictly speaking, the overlayer is incommensurate [30, 31]. Theoretical studies of the Au(001) surface suggest that the reconstruction forms because the energy gained from the formation of the more compact reconstructed top layer is greater than the energy lost as a result of the loss of registry with the substrate. The energy difference between the relaxed  $(1 \times 1)$  surface and the reconstructed surface is calculated to be  $\sim 0.2 \text{ eV atom}^{-1}$  [32]. X-ray measurements of the specular CTR at room temperature have shown that the reconstructed Au layer is 1.25 times denser than a bulk Au monolayer and that it is expanded away from the expected bulk position by  $\sim 20\%$  of the bulk lattice spacing [30]. Grazing incidence X-ray studies have shown that the overlayer is aligned approximately with the [110] direction although the detailed in-plane structure is dependent on the rate of cooling of the surface [31]. For slowly cooled samples, the overlayer is almost exclusively rotated by  $\pm 0.8^\circ$  from the [110] direction with a very small fraction of the domains unrotated. The in-plane surface diffraction pattern for this structure corresponds to a hexagon of spots centered around the origin of reciprocal space as shown in Fig. 5. In the [110] direction, the peaks are centered at  $(1.206, 1.206, 0)$ . The corresponding real-space structure is shown schematically in the lower part of the figure.

**4.1.3.1.2 Solid–solution Interface** Establishing the relationship between a surface structure in electrolyte and that observed in UHV has always been problematic, largely

due to the difficulty in preparing clean surfaces and transferring them to the electrochemical environment (see Sect. 4.1.2.3). Ex situ techniques, whereby the electrode is emersed from solution and transferred back into UHV for surface analysis, cannot give definitive results due to the loss of potential control and/or solution species. The advances in the application of in situ methods, for example, scanning tunneling microscopy (STM) [17, 21] and X-ray scattering, have alleviated this “emersion gap” problem, and provided definitive structure determination of metal surfaces in electrolyte and under potential control.

Studies of the reconstruction of (111) metal surfaces date back to the early 1970s, when it was reported that UHV-prepared Pt(111)- $(1 \times 1)$  surface remained intact after contact with solution [33, 34]. More recently systematic, in situ X-ray scattering [35] and STM [21, 28] studies have demonstrated that well-ordered P(111)- $(1 \times 1)$  structures, prepared either in UHV or by the flame-annealing procedure, are stable in aqueous solutions. As for Pt(111), the (111) surfaces of Ag and Cu exhibit a  $(1 \times 1)$  termination in the absence of any strongly adsorbing species, such as anion adsorption or UPD metals. In contrast, the Au(111) single-crystal surface exhibits a potential-dependent reconstruction that is unique among the fcc metal surfaces. As in UHV, the surface forms the  $(23 \times \sqrt{3})$  structure at negative electrode potentials whereas at positive potentials the unreconstructed  $(1 \times 1)$  surface is observed. The driving force for the  $(1 \times 1) \leftrightarrow (23 \times \sqrt{3})$  phase transition was proposed to be due to an induced surface charge density of  $0.07 \pm 0.02$  electrons per atom, that is, it was postulated that the formation of the surface reconstruction is driven by the induced surface charge [36.] Alternatively, it has been proposed that

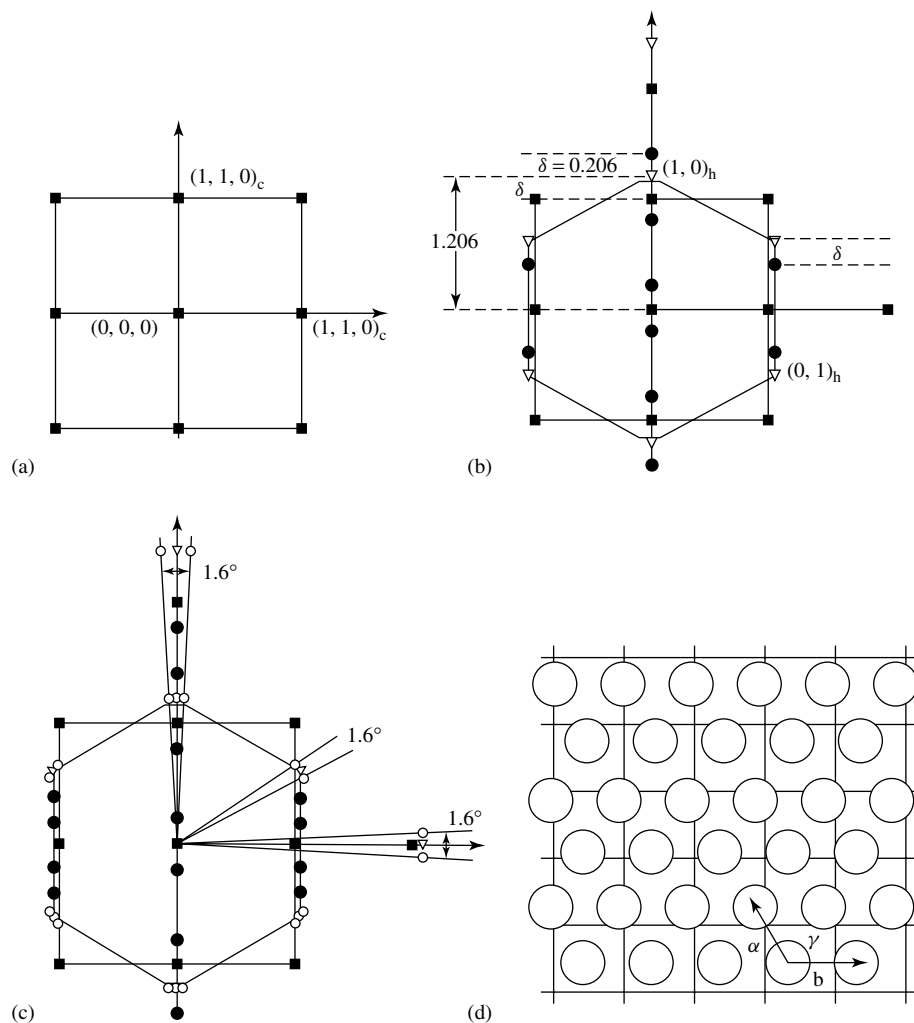


**Fig. 5** The in-plane diffraction pattern for the Au(001) surface. (a) The unreconstructed phase; (b) the distorted hexagonal phase; (c) the rotated, distorted hexagonal phase. In each case, the filled symbols represent the scattering from

the underlying Au(001) face with square symmetry and the open symbols the scattering due to the hexagonal surface reconstruction. (d) A real-space schematic picture of a rotated domain of the reconstruction.

adsorption/desorption of solution species is responsible for the changes in the surface structure [37]. Considering that the adsorption of ions from supporting electrolyte is closely related to the charge redistribution at the interface, it is very difficult to conclude unambiguously what

the real driving force for the potential-induced reconstruction of Au(111) is. At present, we consider the issue to be unresolved; for further details the readers are referred to Kolb's review on reconstruction phenomena at metal–electrolyte interfaces [17].



The structural behavior of the (001) surfaces in aqueous electrolytes has been more controversial. For example, the first *ex situ* experiments indicated that the Pt(001) – “ $5 \times 20$ ” structure transforms into the  $(1 \times 1)$  phase upon contact with aqueous solution or even when in contact with water vapor [38]. In contrast, Zei and coworkers found that the UHV-prepared reconstructed Pt(001) surface remained stable in contact with electrolyte, although no convincing evidence of potential-induced reconstruction was ever detected [39]. X-ray scattering measurements have unambiguously demonstrated that the Pt(001)- $(1 \times 1)$  surface is stable in the potential range between the adsorption of hydrogen and hydroxyl species and the reconstructed surface was never observed [40]. In contrast with Pt(001), the Au(001) surface in electrolyte exhibits a potential-induced reconstruction that is very similar to the temperature-induced reconstruction in UHV [7]. To illustrate the general phenomenon of surface reconstruction in electrolyte, representative results for this system are now presented to demonstrate the power of the X-ray diffraction technique in elucidating the potential-induced structural transformation of the Au(001) surface.

The potential stability of the gold surface reconstruction in the electrochemical environment has been studied by CV, *ex situ* emersion LEED experiments [17], STM, and X-ray diffraction [7]. In both acid and alkaline solutions, there is good agreement between the experimental techniques that the “ $5 \times 20$ ” reconstruction (see Fig. 5) is formed at cathodic potentials and that it can be reversibly lifted and formed upon cycling the applied potential anodically. Figure 6 shows representative in-plane X-ray diffraction results in the form of rocking scans through

the reciprocal lattice positions indicated in Fig. 5. Figure 6(c) shows a scan through the  $(1, 1, 0.4)$  position that corresponds to a point on the nonspecular  $(1, 1, l)$  CTR. This scan is representative of the in-plane mosaic spread of the crystal surface, which is  $\sim 0.5^\circ$  full-width at half-maximum (FWHM). Figures 6(a, b) show scans at the  $(1.206, 1.206, 0.4)$  position in 0.1 M KOH ( $-0.35$  V) and 0.1 M HClO<sub>4</sub> ( $-0.05$  V) solutions, respectively; the electrode potential chosen so that the surface is in the reconstructed state. In 0.1 M KOH, the scan shows a single broad peak aligned with the Au(110) direction. In 0.1 M HClO<sub>4</sub>, however, there is no longer a central peak but the scan displays two peaks rotated by  $\sim 0.75^\circ$  from the  $[110]$  direction. These results indicate good general agreement with UHV studies of the Au(001) surface [30, 31], although the rotated peaks observed in 0.1 M HClO<sub>4</sub> are unaccompanied by the strong central peak observed in the UHV studies, whereas in 0.1 M KOH no rotated domains are observed at all. We should note that the results shown in Fig. 6 were obtained after numerous cycles of the electrode potential in both electrolytes during which the reconstruction was lifted and reformed and so the results shown are representative of true equilibrium conditions.

Figure 7 shows some XRV measurements, which demonstrate the potential range of stability of the “ $5 \times 20$ ” reconstruction in the different electrolytes. Figure 7(a) shows the intensity dependence at the position of one of the rotated peaks in 0.1 M HClO<sub>4</sub>, Fig. 7(b) shows the intensity dependence at the unrotated peak position in 0.1 M KOH, and Fig. 7(c) shows data for the same solution obtained at  $(0, 0, 1.3)$ , a position close to the anti-Bragg position along the specular CTR

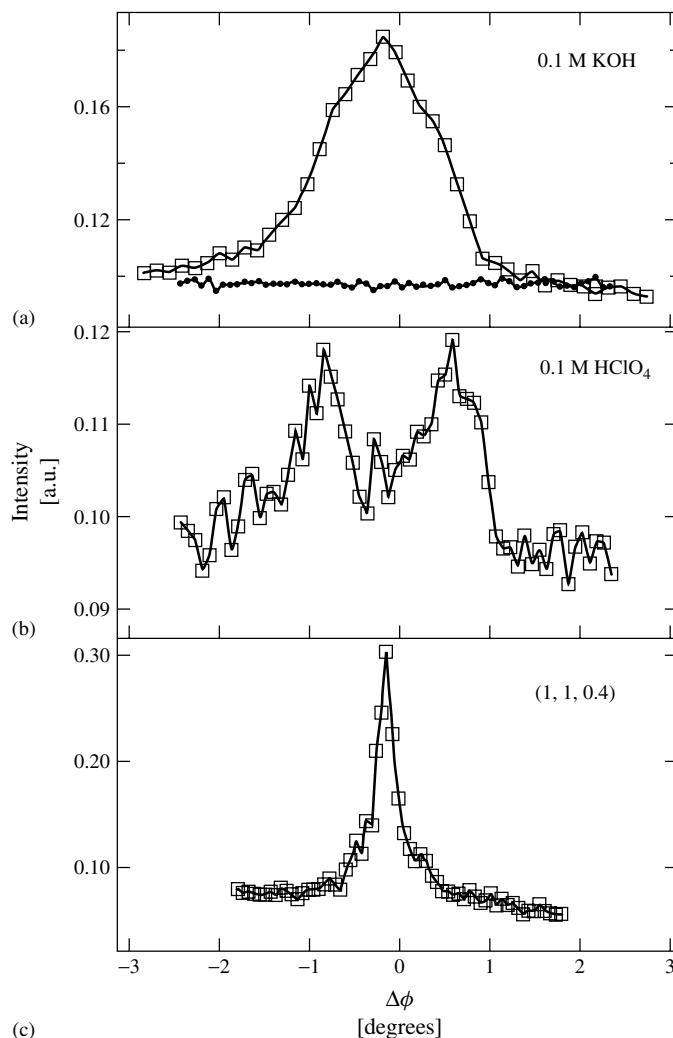


**Fig. 6** Rocking scans through: (a) (1.206, 1.206, 0.4) in 0.1 M KOH (at  $E = -0.35$  V); (b) (1.206, 1.206, 0.4) in 0.1 M HClO<sub>4</sub> ( $E = -0.05$  V); and (c) (1, 1, 0.4), a CTR position for a Au(001) electrode. These positions are illustrated in Fig. 5. The closed symbols in (a) show the measured profile in both solutions after the lifting of the reconstruction at positive potentials.

in which the reconstruction of the surface causes an increase in the scattered intensity due to the increased density of the surface layer. The results show the reversible lifting and formation of the reconstruction in both electrolyte solutions.

Because of the slow kinetics in the formation of the reconstructed surface, at the sweep rate used in these measurements,  $2.5 \text{ mV s}^{-1}$ , there is considerable hysteresis as the potential is cycled. Previous kinetic studies [8] have shown that

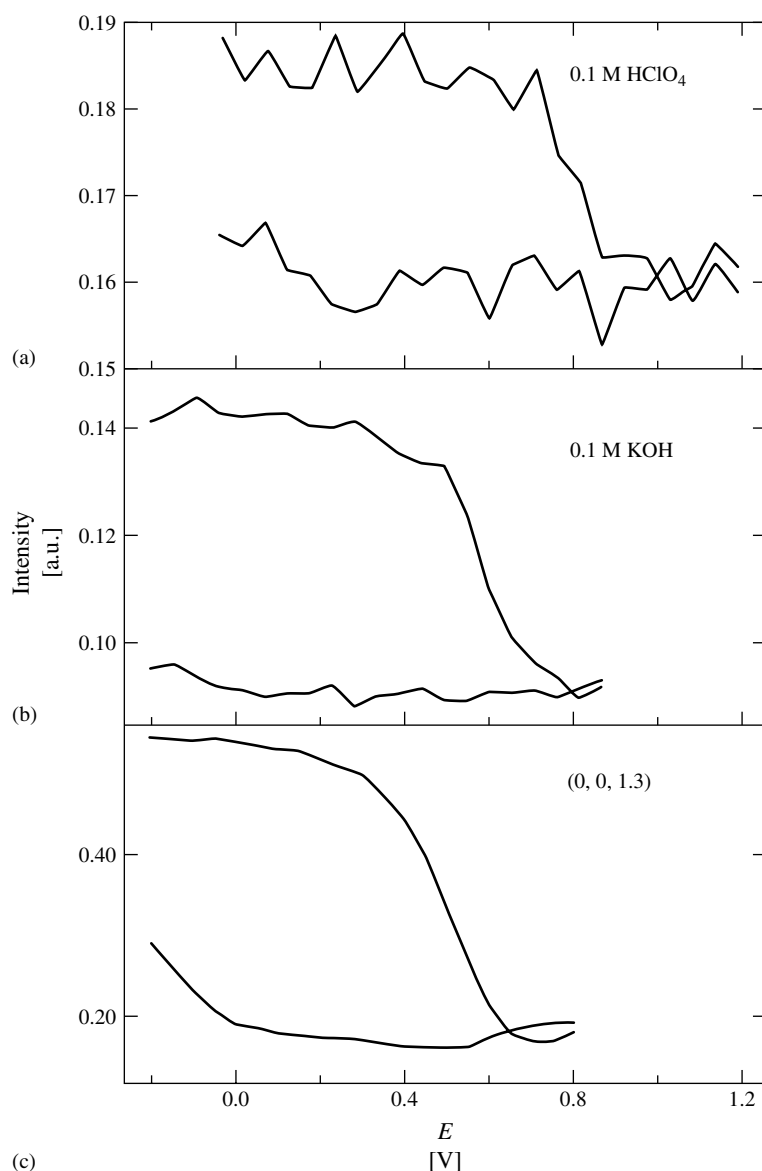


**Fig. 7** XRV measurements at: (a) the rotated peak position in 0.1 M HClO<sub>4</sub> (see Fig. 6b); (b) (1.206, 1.206, 0.4) in 0.1 M KOH; and (c) at (0, 0, 1.3), a position on the specular CTR, in the same solution as (b).

the reconstruction forms over a timescale of 15–100 s, which is consistent with the data shown in Fig. 7. The fact that the data at the CTR position, Fig. 7(c), shows the

same hysteresis implies that the kinetics are controlled by the large-scale movement of the Au surface atoms rather than any local ordering effects. As with the Au(111)

surface, it is difficult to propose an unique driving force for the surface reconstruction although it is interesting that the details of the reconstructed state (i.e. rotated vs. unrotated domains) appear to depend on the electrolyte.

The first insight into the structure of the (110) surfaces in electrolyte was also obtained from ex situ studies [17]. For example, the UHV-prepared Pt(110)-( $1 \times 2$ ) surface was found to be stable upon contact with several solutions, if the potential cycling was restricted to certain potential regions. More recently, the stability and structure of the Pt(110) surface in several electrolytes has been examined by in situ X-ray diffraction [41, 42]. The following results were obtained in 0.1 M NaOH solution, chosen so as to avoid any strongly adsorbing anions. The potential was cycled over the range 0.1–0.7, V, which corresponds to the hydrogen adsorption region ( $<0.3$  V) and the region in which reversible adsorption of OH species occurs. Over this entire potential range, diffraction peaks consistent with the presence

of a ( $1 \times 2$ ) reconstruction were observed. Figures 8(a, b) show longitudinal (along  $[0\ k\ 0]$ ) and rocking scans (approximately along  $[h\ 0\ 0]$ ) through the (0, 1.5, 0.1) superlattice Bragg reflection. The solid lines are fits of a Lorentzian lineshape to the data, which allow the correlation length of the ( $1 \times 2$ ) unit cell to be derived. From these measurements, and from similar scans through other superlattice reflections, a correlation length of  $\sim 350$  Å along the  $[1\ 0\ 0]$  direction and  $\sim 250$  Å along the  $[0\ 1\ 0]$  direction is calculated, in which these correspond to the parallel and perpendicular directions to the rows in the missing-row model of the ( $1 \times 2$ ) reconstruction. The larger correlation length corresponds to the limit of the instrumental resolution and so this only puts a lower limit on the domain size. Interestingly, there is no evidence of any shifts in the (0, 1.5) or (0, 2.5) in-plane reflections along the  $[0\ 1\ 0]$  direction, in contrast with the previously reported measurements of the UHV-prepared surface [43]. This shift was linked to the presence of randomly

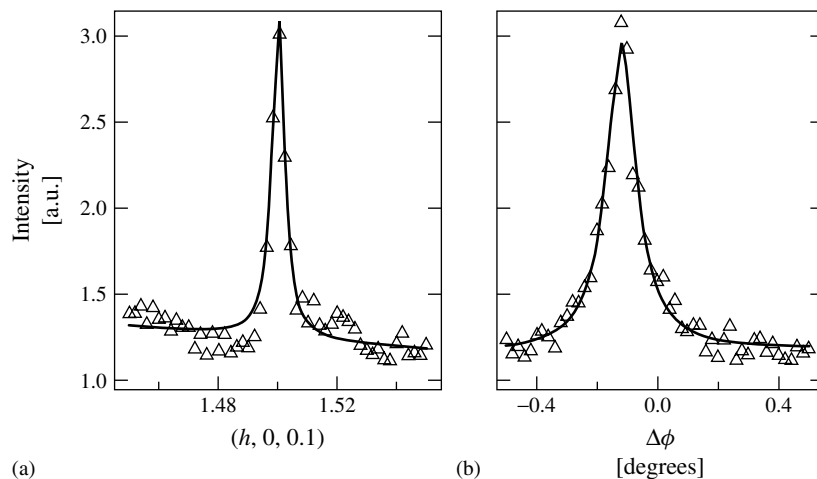


**Fig. 8** The measured X-ray intensity at (0, 1.5, 0.1): (a) along the  $[0\ 1\ 0]$  direction; and (b) along the  $[1\ 0\ 0]$  direction for a Pt(110) electrode in 0.1 M NaOH ( $E = 0.1$  V). The solid lines are fits of a Lorentzian lineshape to the data.

distributed single-height steps on the surface. The Lorentzian lineshape does not perfectly produce the data in the tails of the Bragg reflection (Fig. 8a) and this could be due to a residual step distribution. It is important to emphasize that the  $(1 \times 2)$  surface reconstruction was stable over a wide potential range, for example, even at 1.2 V there is still a strong  $(110)$ - $(1 \times 2)$  diffraction pattern. Upon sweeping the potential negatively, however, the  $(1 \times 2)$  reconstruction is finally lifted as the surface atoms move to accommodate the oxide reduction. It should also be noted that the  $\text{Pt}(110)$ - $(1 \times 2)$  structure was so stable in aqueous electrolytes that adsorption of CO on this surface did not induce the  $(1 \times 2) \leftrightarrow (1 \times 1)$  transition that is observed in UHV upon adsorption of CO [44]. The high stability of the  $\text{Pt}(110)$ - $(1 \times 2)$  structure implies that the potential-induced mobility of Pt surface atoms at the solid–liquid interface is significantly reduced compared to the temperature-induced mobility in UHV.

In contrast with  $\text{Pt}(110)$ , the reconstruction at the  $\text{Au}(110)$ –liquid interface can be reversibly lifted and reformed, implying that the mobility of gold surface atoms is appreciable even in contact with electrolyte. Depending on the nature of the supporting electrolyte, however, either the  $(1 \times 2)$  or  $(1 \times 3)$  reconstruction was found to be stable at negative potentials. In particular, Magnussen and coworkers [45] demonstrated that in perchloric acid the  $(1 \times 2)$  phase was stable at the potential of zero charge (denoted hereafter as the *pzc*). Positive of the *pzc*, the reconstruction is lifted and the  $\text{Au}(110)$ - $(1 \times 1)$  structure is clearly observed in STM experiments. The observed structural transformation is highly reversible, the  $(1 \times 2)$  structure being fully restored when the applied potential is negative of the *pzc*. Because of

the fact that the phase transition was observed at the *pzc*, it was proposed that the structural transformation of the  $\text{Au}(110)$  surface was governed by the specific (contact) adsorption of anions. In contrast, in an X-ray diffraction experiment, a  $(1 \times 3)$  reconstruction was observed in salt solutions (0.1 M NaCl) [46]. As for  $\text{Au}(111)$ , Ocko and coworkers postulated that the formation of the surface reconstruction was driven by the induced negative surface charge. It was also suggested that the  $(1 \times 3)$  reconstruction was stabilized over the  $(1 \times 2)$  structure due to the negative surface charge, by analogy to UHV results showing that  $\text{Ag}(110)$  underwent a  $(1 \times 1) \rightarrow (1 \times 2)$  transition after the adsorption of K on the surface [47]. As for the other Au surfaces, it is very difficult to resolve unambiguously the driving force for the potential-induced structural transformation, especially given that surface charge and anion adsorption are so strongly correlated.

#### 4.1.3.2 Surface Relaxation

The relaxation of metal surfaces under UHV conditions has been well studied by utilizing LEED  $I$ - $V$  analysis and a significant database now exists [23]. For unreconstructed low-index single-crystal surfaces, it is often found that the outermost layer of atoms is *contracted* toward the second layer, compared to the bulk layer spacing. Adsorption on the clean surface in UHV, however, usually reverses this trend and results in the outermost layer of metal atoms being *expanded* away from the second layer. The experimental data has led to interesting theoretical work aimed at establishing a fundamental understanding of surface relaxation [48]. The same concepts can be applied to the  $M(hkl)$ –electrolyte interface, and indeed relaxation has also been observed at the

Ag(*hkl*), Au(*hkl*), and Pt(*hkl*) surfaces in electrochemical environments [40, 46, 49]. As opposed to UHV systems, in the electrochemical environment, it is not possible to perform LEED experiments and surface relaxation effects can only be probed using X-ray diffraction techniques. As shown in Sect. 4.1.2.1, the analysis of CTR data is relatively simple to perform and can provide accurate values of surface relaxation in both the UHV environment and when the surface is in contact with the electrolyte. Additionally, the potential dependence of the surface relaxation can be probed by performing XRV measurements at suitable reciprocal lattice positions (see Sect. 4.1.2.1). The results can give good insight into the nature of the interaction between species that can be adsorbed from the electrolyte solution and the metal surface.

Toney and coworkers used X-ray scattering to probe the distribution of water molecules at the Ag(111)–electrolyte interface [49, 50]. In addition to observing a large increase in the density of the water layer adjacent to the Ag surface, they also observed an electrorestrictive effect in which the topmost Ag atomic layer was contracted into the surface (by 0.03 Å) relative to the bulk Ag(111) spacing by stepping from  $-0.23$  to  $0.52$  V (vs. an Ag/AgCl reference electrode) in  $0.002$  M NaF solution. This effect was obtained by modeling of nonspecular CTR data as the scattering contained no contribution from the incommensurate water adlayers. In a recent X-ray scattering study [51], Lucas and coworkers have used similar techniques to probe the relaxation of the Au(111) surface in its unreconstructed state. The results have been correlated with surface stress measurements and density functional theory (DFT) calculations that show corresponding changes in the density of

states of the Au surface atoms at the Fermi level.

Of the three low-index Pt surfaces that we have studied, the Pt(110)-(1 × 2) has the most dramatic dependence of the surface relaxation on the applied electrode potential [41, 42]. In the following discussion, the surface relaxation effects are interpreted as being caused by the specific nature of the adsorption sites on the Pt(110)-(1 × 2) surface and the strength of the adsorbate–metal bonding, the two of course being interrelated. The results were obtained in alkaline solution (Fig. 9), in which the surface relaxation is attributed to the adsorption of  $H_{\text{upd}}$  and  $OH_{\text{ad}}$  [41]. To confirm the dominant role of these adsorption processes, the charge associated with hydrogen adsorption and hydroxyl adsorption is also shown in Fig. 9. As shown in the previous section, the (1 × 2) surface reconstruction was stable over the entire potential range. However, changes in the diffracted intensities were observed, particularly along the CTRs. Such changes, in this case at (0, 0, 1.55) on the specular CTR, are shown in the lower part of Fig. 9. The changes in intensity indicate a potential dependence of the relaxation at the Pt(110) surface. Measurements at (0, 0, 2.45) showed the opposite behavior to those at (0, 0, 1.55), that is, the curve was inverted. These results suggest that additional expansion of the surface is caused both by hydrogen adsorption and hydroxyl adsorption. As discussed in Sect. 4.1.2.1.1, relaxation in the surface normal direction induced by  $H_{\text{upd}}$  at 0.05 V can be probed by modeling CTR data. The specular CTR, (0, 0, *l*) and nonspecular CTR, (0, 1, *l*), data are shown in Fig. 10. In order to model the data, the structural parameters derived by Vlieg and coworkers [52] for the Pt(110)-(1 × 2) surface in UHV were used, allowing the vertical displacements in the

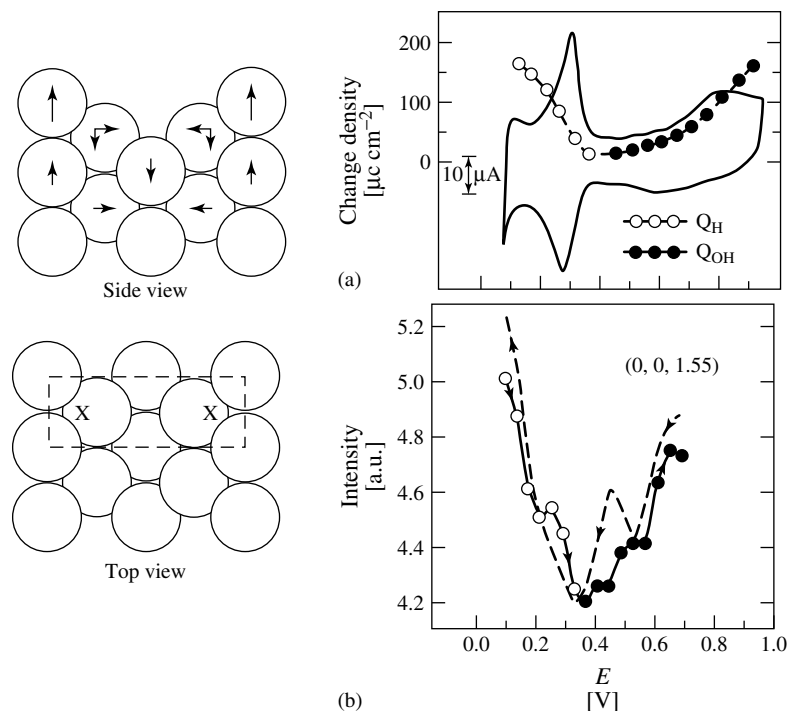


**Fig. 9** Left: A schematic illustration of the Pt(110)-(1 × 2) surface showing the directions of the atomic relaxations derived from fits to the X-ray scattering data. In the top view, the letter X indicates the most likely site for hydrogen adsorption. Right: (a) The CV of a Pt(110) disk electrode measured in an RRDE configuration ( $20 \text{ mV s}^{-1}$ ). The symbols correspond to the charge associated with hydrogen and hydroxyl adsorption. (b) The XRV measured at (0, 0, 1.55) for the positive (symbols) and negative (dashed line) sweep directions ( $2 \text{ mV s}^{-1}$ ).

top two Pt layers, the buckling in the third layer and an increased Debye–Waller factor (or roughness) of the first and second layers to vary. The best fit to the data (obtained by a least-squares method) is shown by the solid lines in Fig. 10. The dashed line represents a calculation of the CTRs according to the structural model proposed by Vlieg and coworkers [52]. The biggest discrepancy between the calculation for the model derived in previous work and the measured data occurs at the anti-Bragg position on the specular CTR. It was only possible to reproduce the data by including an expansion of the topmost layer spacing.

The magnitude of the relaxations derived from the best fit are as follows:  $0.35 \text{ \AA}$  expansion in the topmost layer (25% of the layer spacing), an inward displacement of  $0.08 \text{ \AA}$  in the second layer (6%), a buckling of  $0.08 \text{ \AA}$  in the third layer, and root-mean-square roughness of  $0.41$  and  $0.16 \text{ \AA}$  in the first and second layers, respectively (the bulk thermal roughness is  $0.05 \text{ \AA}$ ). The relaxation directions are indicated in the schematic model of the structure in Fig. 9.

The most striking difference between the structural model for the Pt(110)-(1 × 2) reconstruction in electrolyte and the model derived from UHV studies is

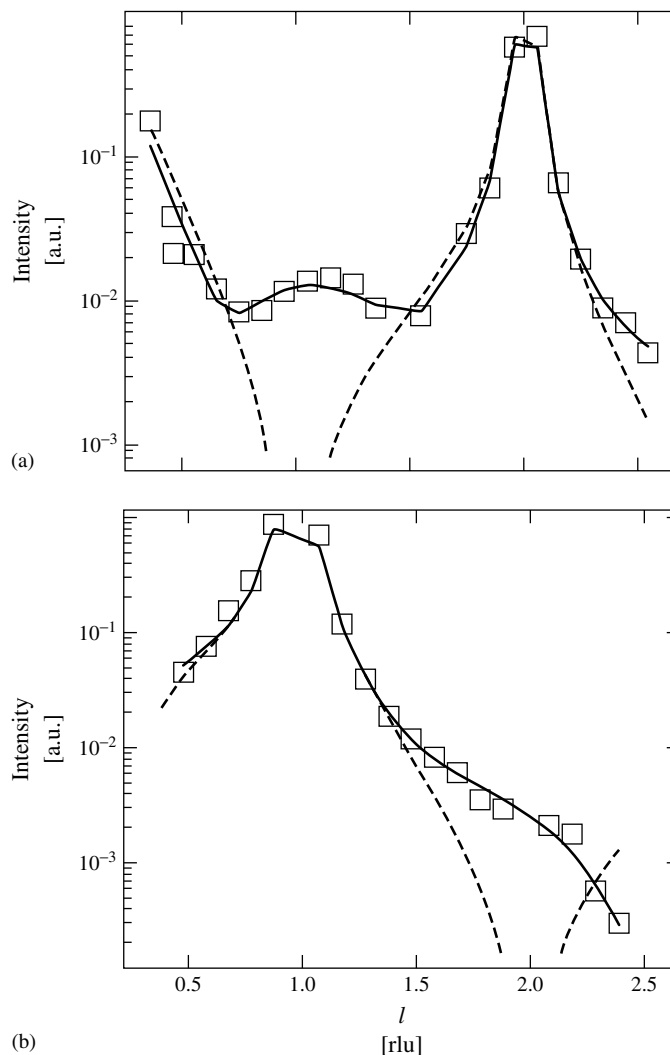


**Fig. 10** The measured CTR data: (a)  $(0, 0, l)$ ; and (b)  $(1, 0, l)$  for the Pt(110) electrode at an electrode potential of 0.1 V. The dashed lines are calculated for a contracted  $(1 \times 2)$  missing-row model that was found in UHV studies [52] and the solid lines are fits to the data indicating a 20% expansion of the surface [41].

in the relaxation of the topmost Pt atom in the unit cell. The contraction of the surface observed in vacuum studies has been explained on the basis of electrostatic considerations in which electrons are transferred from the top atom towards the

missing row with a resultant electrostatic force that pulls the ion cores into the surface [53]. In electrolyte, the situation is inherently more complex because of the presence of water, ions, and the electric field at the interface. In addition, the data



described above were taken in a potential region in which  $\sim 1$  monolayer of hydrogen is adsorbed onto the surface. Theoretical studies of hydrogen adsorption onto Pt surfaces have indicated that the most likely site for adsorption is the threefold coordinated site (indicated by the letter X in the top view of the surface in Fig. 9), with the d orbitals of the neighboring Pt atoms making a major contribution to the bonding. Full occupation of these sites agrees with the hydrogen coverage measured electrochemically. Interestingly, adsorption of hydrogen into these sites was proposed as the mechanism for an increased corrugation of the Pt(110) surface in UHV, in which a 20% expansion was observed by He diffraction [54].

#### 4.1.4

##### Adsorbate-modified Surfaces

It is well established that the adsorption of atoms and/or molecules on clean metal surfaces has a dramatic effect on the surface structure. The presence of the adsorbed layer usually alters the metal surface relaxation (see previous section) and can cause clean metal surfaces either to reconstruct or, more commonly, to deconstruct, that is, return from a reconstructed state to the  $(1 \times 1)$  phase. The thermodynamic driving force for adsorbate-induced restructuring is the formation of strong adsorbate–substrate bonds that are comparable to or stronger than the bonds between the substrate atoms. Within the framework of this article, we present a selected review of some recent studies of adsorption phenomena on single-crystal transition metals. The section is split into two parts: the first dealing with the adsorption of anions, in particular bromide, and the second describes metal UPD and gives

selected examples of coadsorption between metal UPD layers and anions.

##### 4.1.4.1 Anion Adsorption

The adsorption of anions on metal electrodes has been one of the major topics in surface electrochemistry. Anion adsorption has an important, and generally adverse, effect on the kinetics of electrochemical reactions and thus needs to be understood in some detail. Most of the recent progress has come from the combination of conventional electrochemical methods with ex situ and in situ surface-sensitive probes. Of particular interest are chemisorbed (also called contact adsorbed or specifically adsorbed) anions, whose adsorption is controlled by both electronic and chemical forces. In this report, we aim to highlight some of the general themes of this work by focusing on the adsorption of bromide anions onto Au and Pt electrodes. For the Au(001) and Au(111) electrodes, the focus is on the structural transitions that are observed as a result of atomic size effects. For Pt(111) and Pt(001), RRDE data are combined with X-ray scattering measurements to correlate structural changes with the potential-dependent surface coverage of the anion species.

**4.1.4.1.1 Au(111)/Br** X-ray diffraction and STM studies of the adsorption of bromide (and other halides) onto Au single-crystal electrodes have been reported in a series of papers from the Brookhaven group [55–57]. Figure 11(a) shows a CV for a Au(111) electrode in deaerated 0.1 M HClO<sub>4</sub> + 0.1 M NaBr solution. As discussed by Kolb [9], the peaks at  $-0.12$  V (anodic sweep) and  $-0.18$  V (cathodic sweep) are related to the lifting/forming of the Au surface reconstruction, which is

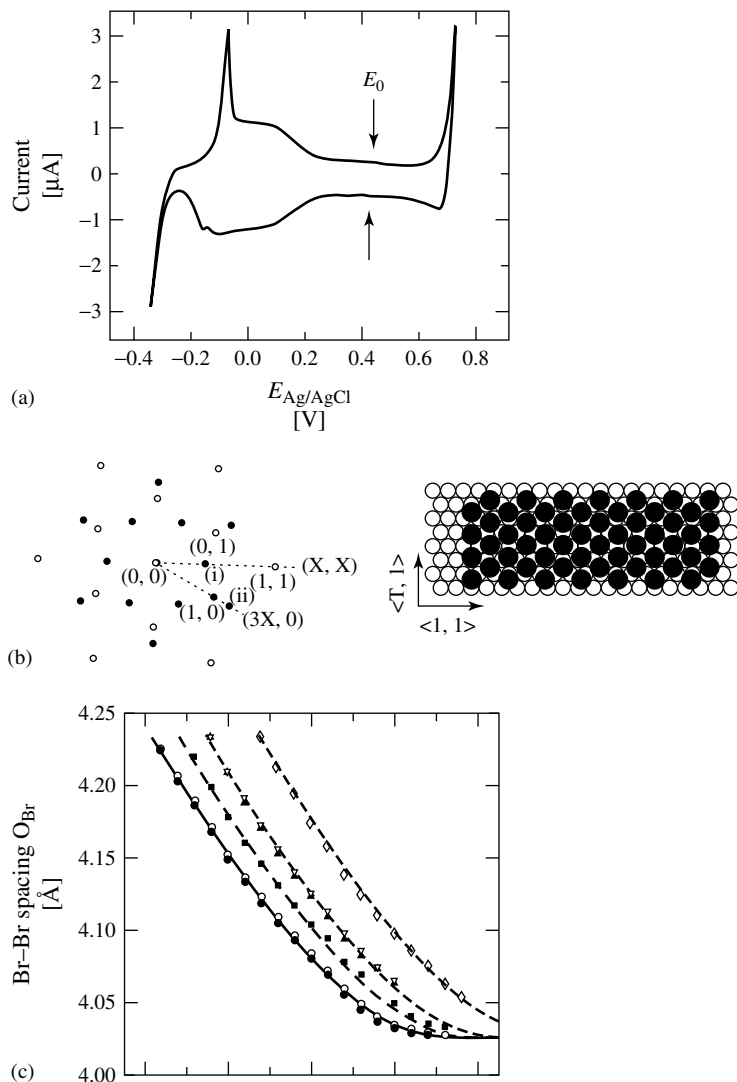


**Fig. 11** (a) The CV for a Au electrode in 0.1 M  $\text{HClO}_4$  + 0.1 M NaBr. (b) The in-plane X-ray diffraction pattern observed at potentials positive of  $E_0$ . Positions A, B, and C correspond to the first-, second-, and third-order diffraction peaks from the bromide adlattice, respectively (filled circles). Also shown is a schematic illustration of the corresponding bromide structure. (c) The bromide–bromide nearest-neighbor spacing (obtained from the X-ray measurements) as a function of the applied potential and solution concentration; 0.1 M (circles), 0.033 M (squares), 0.01 M (triangles), and 0.001 M (diamonds). The lines are polynomial fits to the data. (This figure is taken from Ref. [55].)

induced by a small amount of bromide adsorption/desorption. The major change in the bromide surface coverage occurs in the potential range  $-0.2$  to  $+0.2$  V, that is, from the reconstruction peak across the broad shoulder feature. At higher potentials, there is a small current associated with additional specific adsorption of bromide. At the position marked by  $E_0$  ( $0.42$  V), there is a small reversible peak, which is correlated with an order–disorder transition in the bromide adlayer. The ordering in the bromide adlayer was probed by X-ray diffraction measurements [55]. At potentials above  $0.2$  V, the Au surface is unreconstructed, however, no scattering from an ordered bromide structure was detected when the potential was below  $E_0$ . When the potential was raised above  $E_0$ , the in-plane diffraction pattern shown schematically in Fig. 11(b) was obtained. This pattern exhibits six hexagonally arranged pairs of diffraction peaks at the first-, second-, and third-order positions (marked by A, B, and C, respectively, in the figure). Rocking scans at these positions showed the presence of two rotated peaks (i.e. equidistant from the principal Au reciprocal lattice vector, as for the surface reconstruction of Au(001) in alkaline electrolyte – Sect. 4.1.3.1.2). This diffraction pattern indicates the presence of a rotated-hexagonal adlayer structure, shown schematically in Fig. 11(b).

The rotation angle and the radial peak positions for the bromide structure depend on the applied electrode potential over the range of which the structure was stable. In fact, the rotation angle ranged from  $\pm 3.2^\circ$  to  $\pm 4.7^\circ$ , whereas the position of the first-order peak varied from  $0.683$  to  $0.716$  [in units of Au(1,0,0)] as the potential was changed from  $0.42$  to  $0.76$  V. The change in the radial peak position can be correlated

with the change in the bromide–bromide nearest-neighbor spacing that is shown in Fig. 11(c) for four different solution concentrations of NaBr. At the potential at which the adlayer is formed ( $0.42$  V), the Br–Br spacing is  $4.24$  Å and it decreases down to a saturation value of  $4.03$  Å as the potential is increased. This saturation value is close to the van der Waals diameter of bromide ( $3.70$ – $4.00$  Å). The fact that the electrocompression is continuous and no discontinuities are observed in Fig. 11(c) implies that the adlayer does not lock-in to any high-order commensurate structures as this would give rise to a fixed Br–Br spacing in a certain potential range. Fits to the  $0.1$  M NaBr data to a third-order polynomial function are shown by the solid line in Fig. 11(c). The dashed lines were obtained by successive potential shifts of  $\sim 65$  mV per logarithm of NaBr concentration. Such a shift is consistent with the  $59$  mV shift expected for a nominal charge transfer of one electron from the bromide to the Au electrode, that is, the electrosorption valency,  $\gamma = -1$ .

**4.1.4.1.2 Au(001)/Br** Unlike the continuous electrocompression of the bromide adlayer observed on Au(111), the bromide adlayer on Au(001), a substrate with square symmetry, has been observed to undergo a commensurate-incommensurate transition in which a commensurate  $c(\sqrt{2} \times \sqrt{2})R45^\circ$  structure transforms continuously to an incommensurate  $c(\sqrt{2} \times p)R45^\circ$  structure [57]. The CV for Au(001) in  $0.05$  M NaBr is shown in Fig. 12. Three sharp peaks (labeled as P1, P2, and P3) are observed as the potential is swept between  $-0.25$  and  $0.6$  V; P1 corresponds to the lifting of the Au reconstruction to leave the surface in the  $(1 \times 1)$  state, P2 corresponds to the formation of the  $c(\sqrt{2} \times \sqrt{2})R45^\circ$  structure (as

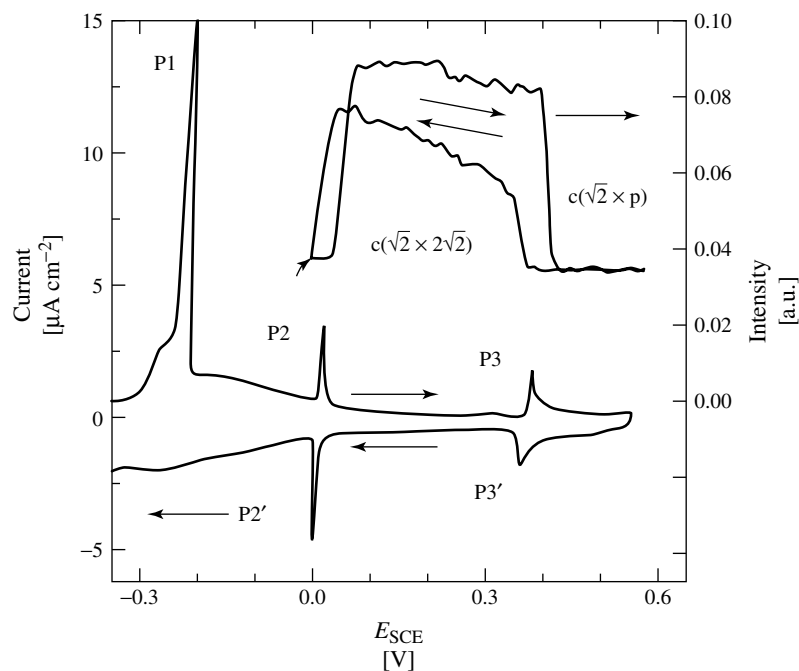


**Fig. 12** The CV for a Au(001) electrode in 0.05 M NaBr solution and the corresponding X-ray intensity at the position (0, 1, 0.1) in which scattering from a bromide adlayer was observed. (Taken from Ref. [57].)

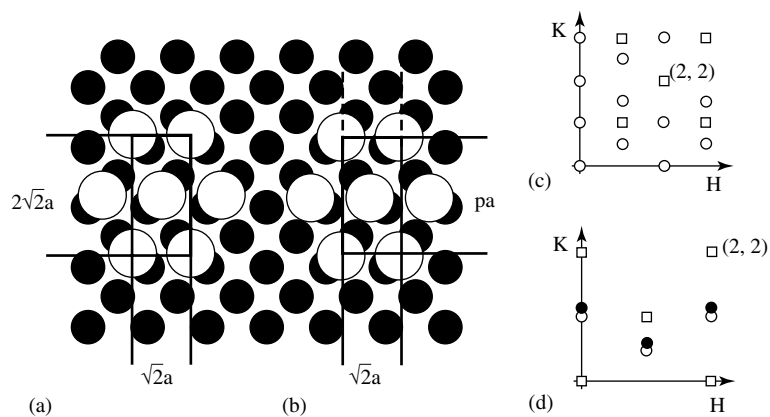


**Fig. 13** Real-space model (a, b) of the commensurate  $c(\sqrt{2} \times \sqrt{2})R45^\circ$  and incommensurate  $c(\sqrt{2} \times p)R45^\circ$  bromide structures observed on Au(001). The open circles correspond to bromide atoms. (c, d) show the corresponding in-plane reciprocal space patterns in which the squares are scattering from the Au substrate and the circles are Br reflections. In (d), the peaks move outward along K with increasing potential. (Taken from Ref. [57].)

shown in Fig. 12 by the intensity changes at the (1, 0, 0.1) reciprocal space position which is where scattering from such a structure would arise), and P3 corresponds to the commensurate-incommensurate phase transition. The  $c(\sqrt{2} \times \sqrt{2})R45^\circ$  structure is shown schematically in Fig. 13(a), which indicates that the surface coverage by bromide is  $\theta = 1/2$  and that the structure is close to an hexagonal arrangement, despite the square symmetry of the underlying substrate. This implies that the elastic interactions between the relatively large Br ad-atoms (which would favor hexagonal packing) dominate over the adsorbate–substrate interaction. The observed in-plane diffraction pattern is shown in Fig. 13(c) in which the squares correspond to substrate reflections and the circles to Br reflections. A similar Br structure was also observed for vapor-deposited Br on Au(001) [58].

At potentials positive of P3 (0.38 V), the bromide adlayer undergoes a commensurate-incommensurate transition that was signified by the movement of the low-order diffraction features continuously and uniaxially outward with increasing potential. As shown in the diffraction pattern (Fig. 13d), reflections were only observed at  $(1, 0.5 + \varepsilon/2)$ ,  $(0, 1 + \varepsilon)$ , and  $(2, 1 + \varepsilon)$ , along with symmetry equivalents ( $\varepsilon$  denotes the incommensurability). The real-space model of the structure is shown in Fig. 13(b). For the domain shown, the bromide lattice is commensurate along H (the  $\sqrt{2}$  direction) and incommensurate along K. As the potential increases above 0.38 V, the value of  $\varepsilon$  increases continuously and this corresponds to movement of the bromide atoms along the directions shown by the dashed lines in Fig. 13(b). In the incommensurate phase, the Br nearest-neighbor spacing is fixed at 4.078 Å, whereas the next-nearest-neighbor spacing

decreases from 4.56 Å ( $\varepsilon = 0$ , commensurate) to 4.14 Å ( $\varepsilon = 0.13$ ). This latter spacing is close to the minimum value observed on the Au(111) surface (4.02 Å).

**4.1.4.1.3 Pt(111)/Br** In contrast to anion adsorption onto gold electrodes, where a stable double-layer region occurs over a wide potential range, on platinum surfaces there is always strong competition between anions and either H or OH adsorption. This competition tends to inhibit the formation of ordered anion structures and can make the adlayers difficult to observe by X-ray scattering measurements. The interaction of bromide ions with Pt(*hkl*) surfaces has been studied extensively at the solid–electrolyte interface, perhaps even more so than at the vacuum interface. The modern in situ structural probes of STM and X-ray diffraction have played a significant role in understanding bromide ion adsorption on Pt(*hkl*) surfaces. What we will emphasize in this review is the importance of the surface geometry in the Pt-bromide energetics, and thus in the ordering of the adlayers.

Quantitative measurements of the coverage by  $\text{Br}_{\text{ad}}$  on Pt(111) surface were obtained by purely electrochemical methods, as described in detail in Ref. [59]. Briefly, by utilizing the ring-shielding properties of the RRDE, Sect. 4.1.2.2, it was possible to determine the potential-dependent surface coverage by bromide and its electrosorption valence ( $\gamma$ ) on Pt(111). The electrosorption valence

$$\gamma = \frac{i_{\text{d}}^{\infty}}{(i_{\text{r}}^{\infty} - i_{\text{r}}^{\text{fs}})/N} = 0.99 \quad (11)$$

is a measure of the degree of discharge of the ion upon adsorption, that is  $\gamma = 1$  for a univalent ion corresponds to complete discharge. Figure 14 shows that as the

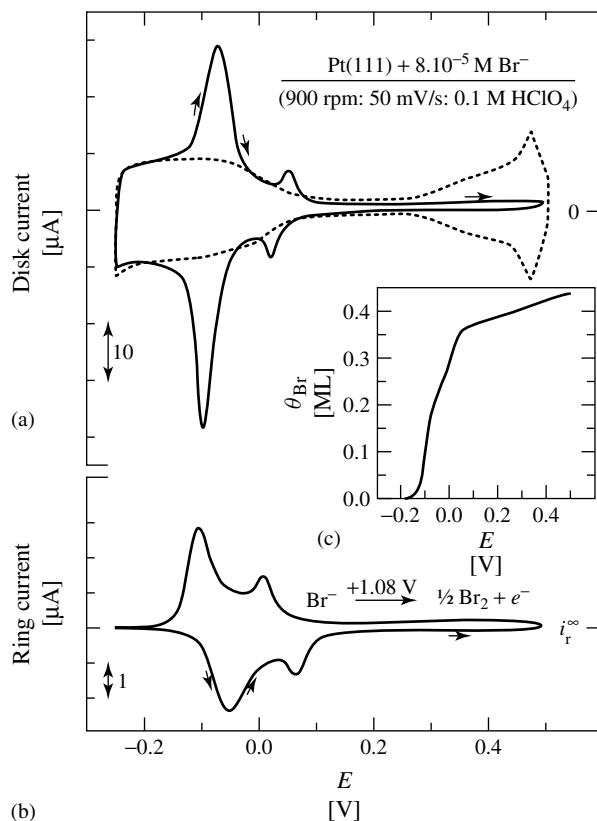


**Fig. 14** RRDE results for a Pt(111) electrode in 0.1 M  $\text{HClO}_4 + 10^{-4} \text{ M Br}^-$ : (a) Disk current; (b) corresponding ring current; and (c) the potential-dependent bromide coverage obtained from the results using Eq. (9).

Pt(111) disk potential is swept across the first voltammetric peak, the associated adsorption of bromide is demonstrated by the concomitant decrease of the ring current below its unshielded value. The same observation is made for the subsequent, more positive peak, which clearly relates this process to further bromide adsorption on the Pt(111) disk. Following these two characteristic voltammetric peaks, the Pt(111) disk current diminishes to a double-layer-like structure above  $\approx 0.2 \text{ V}$ . At the same time, the ring current remains below  $i_r^\infty$  until the positive potential limit is reached,

manifesting the continuous adsorption of bromide on the Pt(111) disk. The qualitative correspondence between ring and disk currents may be evaluated quantitatively in terms of  $\theta_{\text{Br}}$  according to Eq. (9); to avoid the mass transport resistances addressed in Sect. 4.1.2.2, the bromide adsorption isotherm is extracted from the negative-going sweep. The resulting  $\theta_{\text{Br}}$  versus  $E$  is shown in Fig. 14(c). As evident from the shape of curve, the adsorption of Br ( $\gamma_{\text{Br}} \approx 1$ ) is a two-step process, the first being displacement of the  $\text{H}_{\text{upd}}$  state in a narrow interval of potential, the second

a continuous compression until a close-packed adlayer with a maximum surface coverage of 0.44 Br per Pt surface atom is reached at  $\approx 0.6$  V. As demonstrated below, combining the purely electrochemical measurements of coverage with the structures observed by X-ray diffraction enables a reasonable physical picture of the adsorption process to emerge.

In a preliminary report of the results for bromide adsorption onto Pt(111), it was shown that an incommensurate “ $(3 \times 3)$ ” hexagonal bromide adlayer is present on the Pt(111) surface in the potential range 0.05–0.7 V [60]. From fits to the scattering profile at the lowest-order diffraction peak, the peak position

as a function of the electrode potential indicated that the hexagonal adlayer underwent a continuous electrocompression. By repeating the  $\text{Br}^-/\text{Pt}(111)$  experiments a number of times, however, it became apparent that the behavior of this structure was more complex than originally proposed [61]. Figure 15 is typical of the results obtained, showing scans along  $(h, 0, 0.1)$  through the first-order diffraction peak from the hexagonal bromide overlayer at different electrode potentials. At 0.2 V, there is a very strong peak due to the  $(3 \times 3)$  bromide adlayer located exactly at the commensurate  $(3 \times 3)$  position (domain size,  $D \sim 100$  Å) and an additional weak peak at slightly higher wave vector

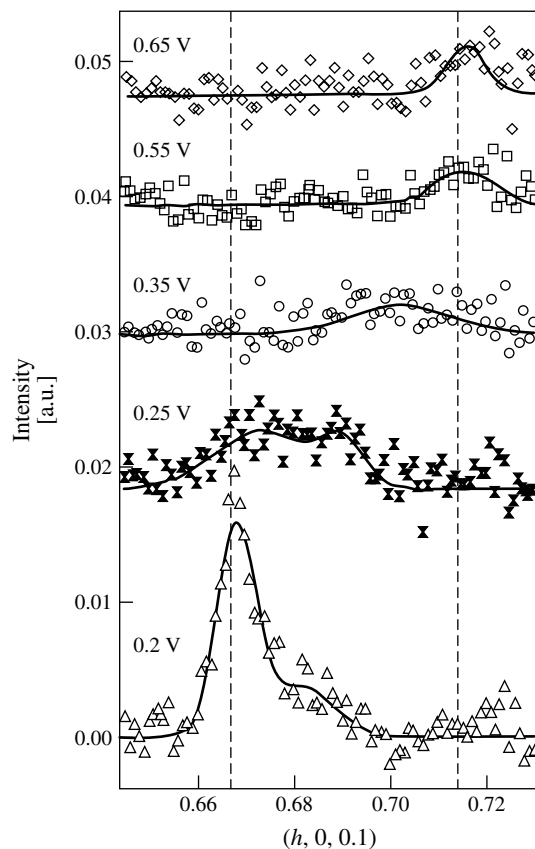


**Fig. 15** X-ray diffraction scans along  $(h, 0, 0.1)$  for  $\text{Br}^-/\text{Pt}(111)$  at different electrode potentials. The data were obtained by subtraction of a background scan performed at  $-0.2$  V. The solid lines are fits to the data and the dashed lines mark the positions  $h = 0.67$  and  $h = 0.71$ .

( $h = 0.68$ ). Upon stepping the electrode potential to 0.25 V, the intensity distribution shows only a very weak double peak lineshape. At 0.35 V, the scattered intensity is further reduced and it is almost impossible to distinguish any measurable feature from the background scattering. Upon stepping to higher potential, a weak peak gradually emerged at  $h = 0.715$ , becoming stronger as the potential was raised to a positive potential limit of 0.65 V. In Fig. 15, rocking scans through the peak, at any potential, showed the intensity to be centered along the Pt(1, 0, 0) lattice vector and there was no evidence of any rotation of the adlayer. Stepping the potential to  $-0.2$  V always caused the peak to disappear, consistent with the voltammetry results, which indicate complete desorption of bromide at this potential (see the isotherm in Fig. 14).

The isotherm for bromide adsorption (Fig. 14c) shows that increasing the potential in the “double-layer” region causes a continuous increase in the bromide coverage. The data shown in Fig. 15 and in other experiments, however, are not consistent with the notion that the additionally adsorbed bromide leads to a continuous compression of the incommensurate bromide adlayer, as this would cause the sharp peak at  $h = 0.67$  to shift gradually to higher wave vector. An alternative explanation of our results is that bromide forms a series of high-order commensurate (HOC) structures on the Pt(111) surface, that is, at all potentials the structure corresponds to a close-packed monolayer but that the periodicity depends critically on the ratio of the bromide and Pt lattice parameters. At 0.2 V, the unit cell corresponds to a  $(3 \times 3)$  structure with a basis of four Br atoms. At 0.6 V, the unit cell is a  $(7 \times 7)$  structure containing 25 Br atoms, that is, with a 7:5 ratio of the Br and Pt lattice parameters.

Both of these unit cells are relatively small (8.33 and 19.39 Å for the  $(3 \times 3)$  and  $(7 \times 7)$  structures, respectively) and so the adlayer is well ordered. In between these two phases, we note that HOC structures with intermediate Br–Br atomic spacings must have much larger unit cells ( $>30$  Å) [62]. Given that the maximum domain size that is observed is  $\sim 60$  Å, this could explain the decreased peak intensity (or disorder) in the intermediate potential region as the Br ad-atoms do not have enough mobility to form well-ordered structures with large unit cells.

**4.1.4.1.4 Pt(001)/Br System** As for the Pt(111)-Br system, the surface structure and potential-dependent surface coverages by Br on Pt(001) were obtained from the combination of X-ray scattering and RRDE measurements [63]. The effect of adsorbed bromide on the voltammetric features of Pt(001) recorded in 0.1 M HClO<sub>4</sub> is easily observed by comparing the voltammetry with and without Br<sup>−</sup>, as shown in Fig. 16. Close inspection of the voltammetry in Fig. 16(a) reveals that formation of a monolayer of hydrogen in the solution containing bromide occurs through two distinctive voltammetric features: a main sharp peak at  $-0.1$  V and a small peak at  $-0.175$  V. These two peaks correspond to simultaneous hydrogen adsorption/desorption with bromide desorption/adsorption on (001) terrace sites and most probably on  $(001) \times (111)$  terrace-step sites, respectively [63]. Further inspection of the RRDE results reveals that, the major adsorption peak on Pt(001) is not followed with a second sharp peak, as was found for the adsorption of Br<sup>−</sup> on Pt(111). The qualitative correspondence between ring and disk currents may be evaluated quantitatively in terms of  $\theta_{\text{Br}}$  as shown in the previous discussion for Br/Pt(111). The resulting



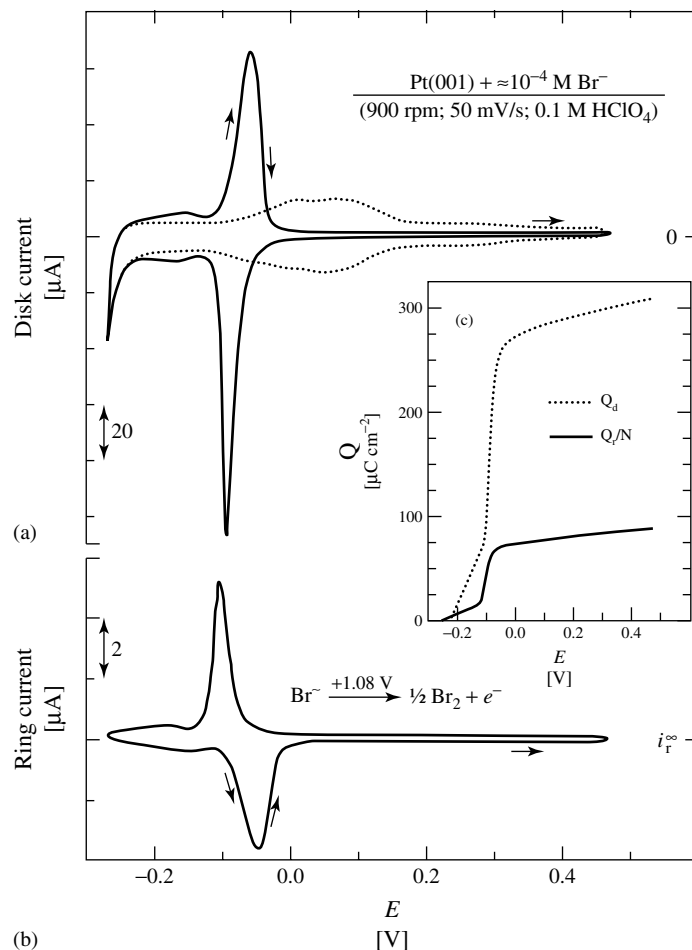


**Fig. 16** RRDE results for a Pt(001) electrode in 0.1M HClO<sub>4</sub> + 10<sup>-4</sup> M Br<sup>-</sup>: (a) Disk current; (b) corresponding ring current; and (c) the potential-dependent charge due to bromide adsorption obtained from (a) and (b).

bromide adsorption isotherm (charge) versus disk potential is shown in Fig. 16(c) yielding a maximum coverage of  $\approx 0.42$  ML at the positive potential limit of 0.5 V.

In the X-ray scattering experiments, no superlattice peaks were found at any potential for Br/Pt(001) in agreement with the STM results of Bittner and coworkers [64]. Despite the lack of adsorbate structures with long-range order in the

surface plane, information about the surface normal structure (the Pt–Br spacing) and local bonding sites for specifically adsorbed anions can be obtained from analysis of the specular and nonspecular CTRs [63]. Figures 17(a, b) show the specular (0, 0, *l*) CTR and nonspecular (1, 0, *l*) CTR measured at an electrode potential of  $-0.2$  V, where no bromide (or based on the adsorption isotherm for Br<sup>-</sup>, a negligible

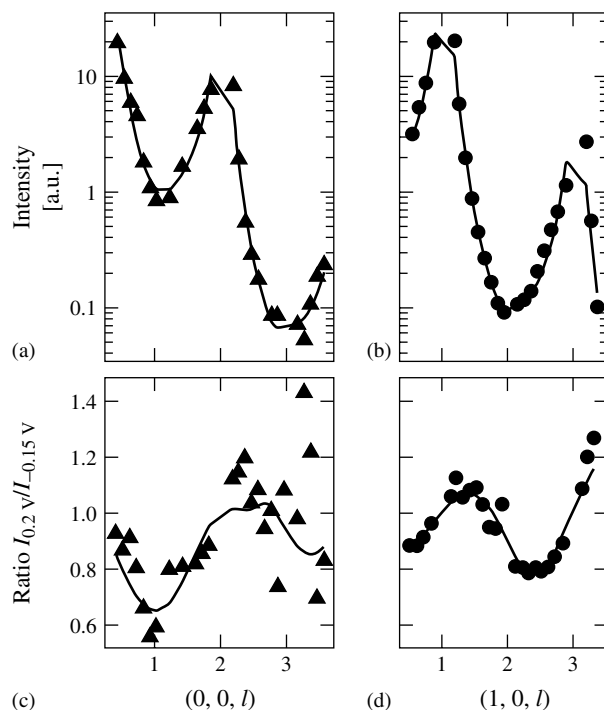


**Fig. 17** CTR data for the  $\text{Br}^-/\text{Pt}(001)$  system: (a)  $(0, 0, l)$ ; and (b)  $(1, 0, l)$  measured at  $-0.2$  V where no Br is adsorbed on the surface. The solid lines are a fit to the data including relaxation of the Pt surface. (c, d) show the changes in intensity measured at  $0.2$  V as referenced to the data at  $-0.2$  V. The fits to the data are described in the text.

amount) is expected to be present on the surface, but the coverage by hydrogen is essentially unity. The solid lines represent a simultaneous fit to the data in which the layer spacing between the first and second Pt layers and the occupancy and roughness (in the form of a static Debye–Waller factor) of the topmost Pt layer were varied. The best fit gave an occupancy of 0.81 in the surface Pt layer, a root-mean-square (r.m.s) roughness,  $\sigma = 0.09 \text{ \AA}$  and a surface expansion of the Pt lattice by 1.4% of the bulk lattice spacing ( $\sim 0.03 \text{ \AA}$ ). Figures 17(c, d) show the changes in the CTR data that occur upon the initial stage of bromide adsorption at *ca.*  $-0.2$  V, displayed as a

ratio of intensities along the CTR at  $0.2$  V (Figs. 17(a, b)) and  $-0.2$  V. Systematic changes in the data are apparent, which must be accounted for by changes in the Pt surface expansion and/or the presence of the adsorbed  $\text{Br}_{\text{ads}}$ . In calculating a fit to the ratio data, the total Br coverage was fixed to 0.35 (to be consistent with the RRDE results) and the partial  $\text{Br}_{\text{ads}}$  occupation of the three low-energy adsorption sites (hollow, bridge, and on-top) was varied. The only other parameters were the Br–Pt vertical separation and the Pt surface expansion. The best fit is shown by the solid lines in Figs. 17(c, d). The expansion of the topmost Pt layer is reduced to 1% and

the occupations (and heights) of bromide in the hollow, bridge, and on-top sites are 0.17 (1.8 Å), 0.08 (2.0 Å), and 0.09 (2.2 Å), respectively, with an r.m.s roughness of 0.19 Å. With such a limited data set there is obviously some ambiguity involved in assigning occupancies to the adsorption sites. However, a fit to the specular CTR data with Br<sub>ads</sub> located at a single height above the surface yielded an unreasonably large r.m.s roughness ( $\sigma = 0.7$  Å) and this suggests a distribution of heights consistent with the different adsorption sites. The covalent radii of Pt and Br<sub>ads</sub> are 1.14 and 1.30 Å, respectively, which gives calculated vertical separations of 1.60, 2.08, and 2.44 Å for the hollow, bridge, and on-top sites, respectively. These values are in good agreement with the CTR results and certainly indicate that the Pt–Br bond is covalent in nature.

**4.1.4.1.5 Summary of Anion Adsorption on Au(*hkl*) and Pt(*hkl*) Surfaces** As evident from the above discussion, the differences between the different anion structures are a consequence of two fundamental properties: the strength of the metal–anion interaction, and the symmetry of the anions with respect to the atomic geometry of the surface. The adsorption of bromide onto Au(111) leads to the formation of a rotated, hexagonal incommensurate adlayer, which undergoes compression and rotation as the potential is increased [55]. Bromide adsorption onto Pt(111) also leads to the formation of a hexagonal, incommensurate adlayer, however, the adlayer is aligned with the Pt lattice at all potentials and appears to form a series of HOC phases rather than exhibit continuous electrocompression [61]. In relation to the presence of HOC phases on the Pt(111) surface, in Sect. 4.1.4.2, we show

that copper UPD onto Pt(111) in the presence of halide anions also causes the formation of an aligned, incommensurate hexagonal CuBr (or CuCl) bilayer structure prior to formation of a full copper monolayer.

The absence of any ordered structures for the Br<sub>ad</sub> adlayer on Pt(001) contrasts with the ordered structures observed on Au(001), Au(111), and Pt(111). The ordered Br<sub>ads</sub> adlayer structures observed on Pt(111) and Au(111) are incommensurate, which means that there is no preference for any particular site. However, the energy minimum for adsorption at the hollow sites on (001) surfaces is considerably deeper than for the hollow sites on the (111) surfaces. This explains the appearance of the commensurate  $c(\sqrt{2} \times \sqrt{2})R45^\circ$  phase on the Au(001) surface, which is observed until increased bromide coverage drives the commensurate–incommensurate transition [57]. Initial adsorption of bromide into random hollow sites on Pt(001), therefore, seems likely, up to a maximum coverage determined by the lateral repulsion between bromide anions. Given that the second–near-neighbor distance for hollow sites is approximately 3.9 Å, this maximum coverage is quite low and further adsorption probably leads to occupation of other sites, as suggested by the CTR results. As the potential is increased, the Pt–Br bond becomes stronger, thus further reducing the mobility of the adsorbed atoms. This may be the mechanism that prevents the formation of any Br<sub>ads</sub> structure with long-range order on the Pt(001) surface.

#### 4.1.4.2 Underpotential Deposition

There are many different methods for producing bimetallic catalytic surfaces. Until recently, UHV-prepared surfaces had an

enormous advantage over the surfaces prepared by electrochemical methods because an UHV system equipped with modern surface-sensitive techniques provided microscopic structural information in a relatively direct fashion. Recently, however, the emergence of surface characterization techniques such as X-ray scattering and STM/atomic force microscopy (AFM), operating under electrochemical conditions, has allowed the electrodeposition method to become equally important in the synthesis of model bimetallic structures. In this section, we will focus on bimetallic Au and Pt single-crystal surfaces produced by the UPD solution phase method. UPD corresponds to the electrochemical adsorption, often of one monolayer, that occurs at electrode potentials positive of the Nernst potential below which bulk metal adsorption occurs [16]. Numerous experiments have shown that the UPD layer can dramatically alter the chemical and electronic properties of the interface. The UPD layer is also the first stage of bulk metal deposition and its structure, therefore, can strongly influence the structure of the bulk deposit. Early studies of UPD using polycrystalline substrates have, more recently, been extended to single-crystal substrates, which not only allows the role of surface atomic structure to be explored, but also permits the study of the interface structures by diffraction-based techniques, such as surface X-ray scattering. Quite a few systems have now been studied using this technique and this has led to a greater understanding of the physics determining the structure of the UPD layer, in particular with regards to the role of the electrode potential and of various other adsorbing species that can be present in solution. Many relevant papers in UPD studies are referenced in the review articles by Kolb [65] and Adzic [66]. For our purposes

here and to follow on from Sect. 4.1.4.1, we focus on the influence of anions on Cu UPD onto Au(111), Pt(111), and Pt(001).

#### 4.1.4.2.1 Cu UPD on Au(111) in Sulfuric Acid Solution

Cu UPD onto Au(111) in sulfuric acid has been an archetypal system for the study of anion coadsorption during metal UPD. The UPD of Cu occurs in two stages and there has been good agreement that in the second stage a full monolayer of Cu is formed. The first stage, however, has been somewhat controversial and a unique structural model was not confirmed until a detailed X-ray diffraction study by Toney and coworkers [67]. This is partly because the  $\text{Cu}^{2+}$  ion is not fully discharged to neutral  $\text{Cu}^0$  but carries an unknown charge that makes the surface coverage by Cu difficult to determine by cyclic voltammetry. The X-ray scattering experiment followed on from an ex situ LEED and Auger spectroscopy study in which it was proposed that the Cu atoms formed a honeycomb structure with  $(\sqrt{3} \times \sqrt{3})\text{R}30^\circ$  symmetry and a surface coverage of  $2/3$  ML per Au surface atom [68]. Toney and coworkers confirmed these results by performing a detailed surface X-ray diffraction study of the structure involving the measurement of the in-plane structure factors, the  $l$  dependence of some of the fractional-order reflections and the bulk CTRs passing through the Au Bragg reflections [67]. Figure 18(a) shows the in-plane diffraction pattern for the  $(\sqrt{3} \times \sqrt{3})\text{R}30^\circ$  structure together with some of the fractional-order rod data. The data in Fig. 18 immediately ruled out the  $(\sqrt{3} \times \sqrt{3})\text{R}30^\circ$  structure proposed from STM and AFM experiments (a triangular Cu adlayer) [69] as such a flat adlayer would give rise to fractional-order profiles that were far more intense and fall off slowly with  $L$ . The data in Fig. 18 is

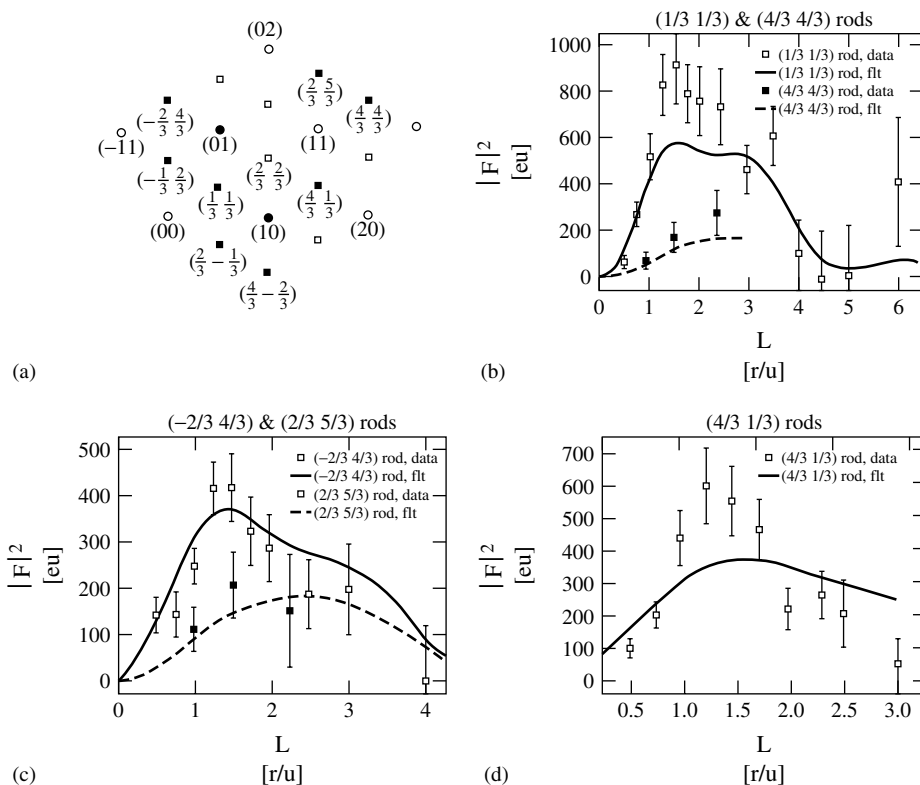


**Fig. 18** X-ray diffraction data for Cu/Au(111) in sulfuric acid solution at the first stage of Cu deposition: (a) In-plane diffraction pattern; (b)  $(1/3, 1/3, l)$  and  $(4/3, 4/3, l)$ ; (c)  $(-2/3, 4/3,$

$l)$  and  $(2/3, 5/3, l)$ ; (d)  $(4/3, 1/3, l)$ . The solid lines are fits to the data according to the structural model shown in Fig. 19. (Taken from Ref. [67].)

only consistent with a model consisting of atoms at different heights above the Au(111) surface.

Toney and coworkers considered a range of structural models containing both ordered Cu and sulfates and proposed the model shown in Fig. 19. In this model, Cu atoms form a honeycomb lattice ( $2/3$  ML coverage) and sulfate molecules are adsorbed in the honeycomb centers above the Cu atoms. Both Cu atoms and sulfate molecules occupy fcc threefold hollow sites on the Au(111) lattice. Three oxygen atoms of each sulfate molecule are bonded to Cu atoms and the remaining

oxygen atom points away from the surface. From the detailed analysis of the data, it was possible to determine several bond lengths in the structure. The Cu–O bond length was  $2.15 \text{ \AA}$ , a distance comparable to the Cu–O bond lengths in organic compounds, which implied that the sulfate molecules were chemically bonded to the Cu ad-atoms hence stabilizing the partial charge of the Cu. It should be noted that this open Cu structure is not found in UPD studies of Cu on Au(111) in perchloric acid solution thus confirming the crucial role of the sulfate anions in the UPD process.

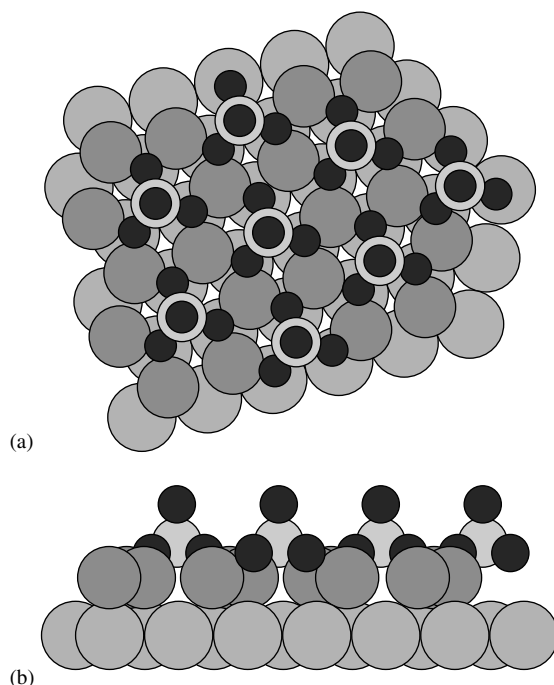


**Fig. 19** Interfacial structure of Cu/Au(111) derived from the data in Fig. 18. (a) Top view and (b) side view. The large light gray, medium gray, small light gray, and filled spheres represent Au, Cu, S, and O atoms, respectively. (Taken from Ref. [67].)

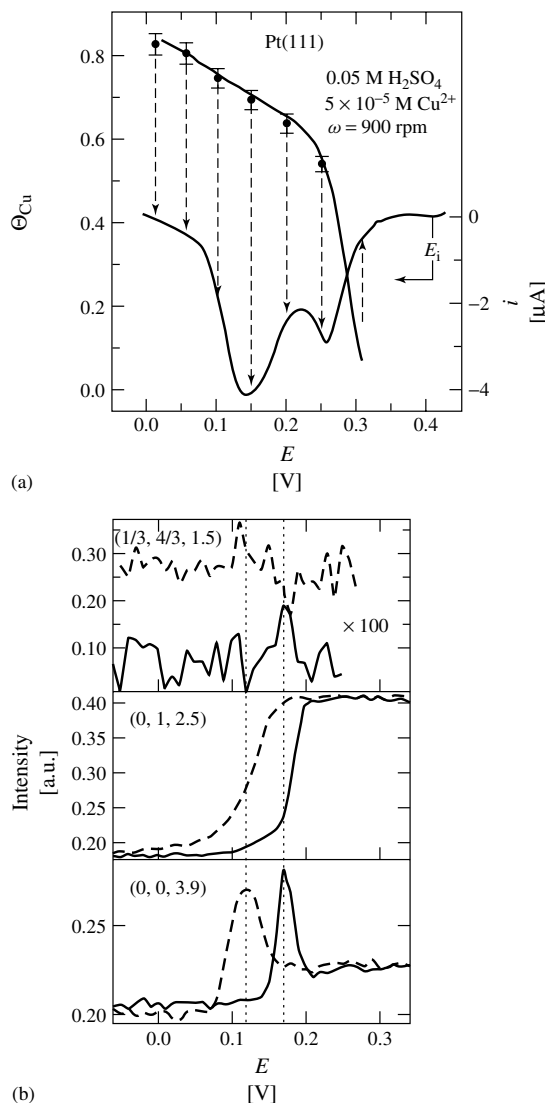
#### 4.1.4.2.2 Cu UPD on Pt(111) in Sulfuric Acid Solution

The interpretation of processes associated with the formation of the Cu monolayer on Pt(111), and the nature of the Pt(111)–Cu structure, have been the subject of considerable controversy. Overviews with some different perspectives can be found in Refs. [70–80]. The RRDE method was successfully applied to investigate the kinetics of  $\text{Cu}^{2+}$  deposition and to determine the potential-dependent surface coverage by  $\text{Cu}_{\text{upd}}$  ( $\Theta_{\text{Cu}(\text{upd})}$ ). The lower curve in Fig. 20(a) shows a cathodic sweep of the cyclic voltammogram (CV) measured on the disk electrode in an RRDE for UPD of Cu onto Pt(111) in sulfuric acid solution. The presence of sulfate anions in solution causes a splitting of the voltammetric Cu deposition peak. This result is in agreement with previous studies that, depending on the solution concentrations and sweep rates,

can show single peaks or double peaks in both sweep directions. The filled circles in Fig. 20(a) correspond to the Cu coverage obtained by potentiostatic measurements, in which the amount of Cu deposited on the disk electrode in a potential step from  $E_i$  (indicated in the figure) is assessed from the corresponding change in the constant  $\text{Cu}^{2+}$  flux to the ring electrode. The guide to the eye (solid line) shows that in the potential region in between the two peaks, the Cu coverage is constant in the range 0.6–0.7 ML (i.e. Cu atoms per Pt surface atom).

The structural details pertaining to Cu UPD have been derived from in situ X-ray scattering measurements [81]. The specular CTR results in Fig. 20(b) clearly indicate that UPD occurs in a two-stage process and the sharpness of the peak implies that the structure formed in the middle potential region is present over

**Fig. 20** (a) The lower curve shows the cathodic sweep of the cyclic voltammogram (CV) for a Pt (111) disk electrode in an RRDE configuration in 0.05 M  $\text{H}_2\text{SO}_4 + 10^{-5}$  M Cu. The closed circles represent the Cu coverage ( $\theta_{\text{Cu}}$ , atoms per surface Pt atom) assessed from changes in the ring current during Cu deposition onto the disk electrode as the potential is stepped (for each point) from  $E_i$ . (b) Changes in the X-ray scattering at (0, 0, 3.9), lower panel, (0, 1, 2.5), middle panel, and (1/3, 4/3, 1.5), top panel, as the electrode potential is swept at  $2 \text{ mV s}^{-1}$ . The solid lines and dashed lines are for the positive-going (anodic) and negative-going (cathodic) sweep directions, respectively.



a very narrow potential range. Indeed, at 0.15 V weak peaks, which could be indexed to a  $(\sqrt{3} \times \sqrt{3})\text{R}30^\circ$  superlattice, diffraction patterns were observed. For example, rocking scans through the  $(2/3, 2/3, 2)$ ,  $(1/3, 1/3, 1.5)$ , and  $(1/3, 4/3, 1.5)$  positions showed broad peaks, FWHM of  $0.84^\circ$ ,  $0.49^\circ$ , and  $1.72^\circ$ , respectively, which gives an ordered domain size in the

range 30–60 Å. This correlation length is at the limit of detection by X-ray scattering and the weak intensities coupled with the narrow stable potential range precludes a detailed structural analysis as performed for the Au/Cu/ $\text{H}_2\text{SO}_4$  system [67]. It should be noted, however, that there are a number of similarities, most noticeably that the superlattice structure factors

are not measurable at small out-of-plane momentum transfer. This implies that a similar structure may be responsible for the observed diffraction pattern, an assumption that can be tested by analysis of CTR data. In the top part of Fig. 20(b) is shown the X-ray scattering intensity at  $(1/3, 4/3, 1.5)$  as the potential is swept at the same rate as the data in the lower figures. Although the signal to noise is poor, it can clearly be seen that the scattering from the  $(\sqrt{3} \times \sqrt{3})R30^\circ$  structure is only present in the same narrow region highlighted by the changes at  $(0, 0, 3.9)$ .

To gain more insight into the nature of the Cu UPD structures, the  $(0, 0, l)$ ,  $(1, 0, l)$  and  $(0, 1, l)$  CTRs were measured at 0.0 and 0.15 V in order to derive structural models. Such results are relatively insensitive to the orientation of any adsorbed sulfate molecules and so the sulfate anion was approximated to a single molecule (i.e. single ion core) consisting of

one sulfur and two oxygen atoms ( $Z = 64$ ). Additional sensitivity to the coverage and location of the Cu atoms was obtained by performing the CTR measurements with incident X-ray energies of 8.78 keV (200 eV below the Cu K adsorption edge) and 8.94 keV (5 eV below the Cu K adsorption edge). In simulating the CTR data, the Cu atomic form factor in the scattering equations was replaced by the form of Eq. (7). At each electrode potential, a simultaneous fit to the CTR data ( $E = 8.78$  keV) and the ratio data set ( $R = I_{8.78 \text{ keV}}/I_{8.94 \text{ keV}}$ ) was performed. The structural parameters allowed to vary were the Cu coverage, Pt–Cu surface normal spacing, sulfate coverage, and Cu-sulfate surface normal spacing, along with their respective enhanced Debye–Waller-type roughness. Results of fits to the specular CTR data and ratio data at electrode potentials of 0.0 and 0.15 V are shown in Fig. 21 by the solid lines.

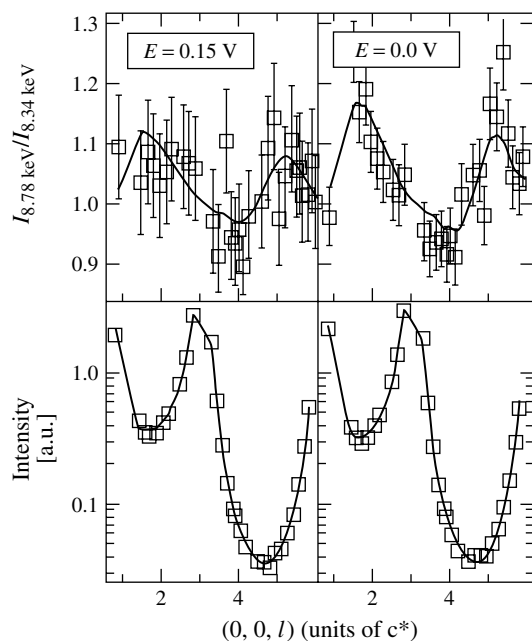


**Fig. 21** The measured specular CTR scattering for an incident X-ray energy of 8.78 keV (lower panels) and the ratio between a similar data set measured at 8.94 keV (upper panels) at electrode potentials of 0.15 V (left) and 0.0 V (right). The solid lines are fits to the data to a single structural model and the ratio data set is calculated by fixed changes in the Cu atomic form factor.



Use of the anomalous scattering technique enhances the accuracy of the Cu coverage determination. At 0.15 V, the Cu coverage is 0.60 with an adsorbed sulfate layer of coverage 0.22 on top of the Cu layer. By comparison with the structural model derived for the  $(\sqrt{3} \times \sqrt{3})R30^\circ$  Cu-sulfate structure on Au(111) (Fig. 19), it can be seen that the CTR results are in good agreement with that study. The bond lengths obtained for the Cu-sulfate bilayer are in good agreement with the Au study in which it was proposed that the sulfate is chemically bonded to the hexagonal Cu layer. At 0.0 V, the results give a Cu coverage of 0.81 ML per Pt surface atom with 0.21 ML of sulfate anions still adsorbed on top of the Cu layer. Because of the increase in Cu coverage, the sulfate anions are located at an increased height above the Cu adlayer presumably as the hollow sites in the hexagonal Cu adlayer have been filled by Cu ad-atoms. It is interesting that the Cu coverage derived by the CTR measurement are in good agreement with those obtained from the RRDE experiments and it appears, therefore, that it is not possible to complete a full Cu monolayer on the Pt(111) surface. The lower limit of potential (0.0 V) was chosen to avoid the formation of  $\text{Cu}^+$  via one-electron reduction of  $\text{Cu}^{2+}$  without further reduction to metallic copper. Fits to the nonspecular CTR data at both potentials (0.0 and 0.15 V), again to both raw data and ratio data sets, gave occupation of both types of threefold hollow sites, fcc and hexagonal close packed (hcp), although the fcc sites are favored (fcc/hcp = 0.51/0.09 at 0.15 V and 0.67/0.16 at 0.0 V). In contrast with the Au(111) system in which the Cu ad-atoms occupied only the fcc sites, it appears that on Pt(111) the energy difference between these sites may be smaller. Occupation of both types of threefold hollow site may

be responsible for the weak ordering of the intermediate Cu-sulfate bilayer phase and for the inability to complete the Cu monolayer at 0.0 V.

#### 4.1.4.2.3 Cu UPD onto Pt(111) in the Presence of Bromide Anions

The RRDE results for Cu UPD on Pt(111) in solution containing  $\text{Cu}^{2+}$  and  $\text{Br}^-$  ions are illustrated in Fig. 22. As the disk potential is swept across the Cu UPD region, both Cu UPD peaks recorded on the disk electrode, first at 0.25 V and the second at 0.15 V, are mirrored by the decrease in the ring current from its  $i_r^\infty$  value. Following these two characteristic Cu UPD peaks, the Pt(111)-disk current diminishes to a capacitive current below 0.1 V, manifesting the completion of the Cu monolayer on the Pt(111) disk electrode; consistent with the return of  $i_r$  to  $i_r^\infty$  in the same potential region. The fact that the ring-shielding current,  $i_r$ , mirrors the current on the disk electrode clearly indicates that both cathodic processes are primarily related with Cu UPD. The same observation is made for the subsequent positive sweep, at which there are two distinctive processes seen from the ring electrode; the first as a shoulder at *ca.* 0.375 V and second as a sharp peak at 0.425 V, both clearly related to stripping of Cu from the Pt(111) disk electrode. The total amount of Cu deposited by UPD was evaluated quantitatively by integration of the ring current, yielding a maximum Cu coverage of 0.95 ML (almost identical with the value inferred from disk measurements, the insert in Fig. 22). This rather small difference in the charge assessed from the disk and the ring measurements (*ca.*  $5 \mu\text{C cm}^{-2}$ ) suggests that the anion co-adsorption contributes insignificantly to the Coulombic charge passing the interface during Cu deposition.



(b)

as indicated by the bromide adsorption isotherm inferred from solution free of copper, insert of Fig. 23. In the potential region between 0.45 and 0.3 V, a small desorption of  $\text{Br}^-$  ( $\approx 2 \mu\text{C cm}^{-2}$ ) just preceding Cu deposition is demonstrated by the concomitant increase of the ring current above its unshielded value. As the disk potential is swept across the first UPD peak, the ring current remains

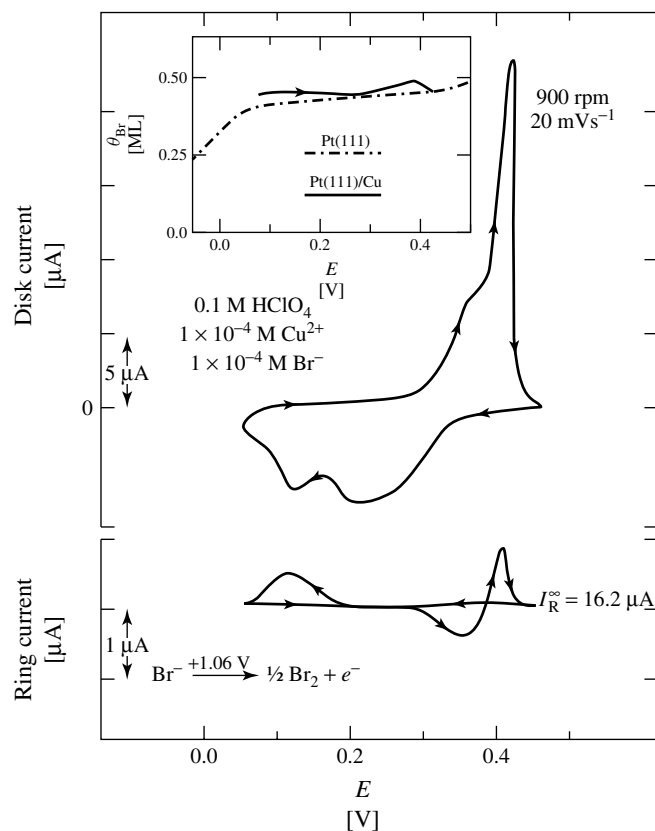


**Fig. 23** Top: Potentiodynamic curve for Cu UPD on a Pt(111) disk electrode. Bottom: Ring current corresponding to the change in the  $\text{Br}^-$  flux during copper deposition. Insert: Surface coverage of bromide at the disk electrode with and without copper present in solution (assessed from ring transients).

almost constant, manifesting an absence of either  $\text{Br}^-$  adsorption or desorption; the second Cu UPD peak is accompanied by the increase in the ring current from  $i_r^\infty$ , with completion of the Cu monolayer causing the ring current to return back to its unshielded value. The resulting  $\theta_{\text{Br}}$  from integration of the ring currents *versus* the potential of the Pt(111) surface in a solution containing  $\text{Cu}^{2+}$ , and the corresponding values for the Pt(111) surface in the solution free of  $\text{Cu}^{2+}$ , are shown in the insert of Fig. 23. Note that  $\theta_{\text{Br}}$

in between the two Cu UPD peaks is equal to the coverage following the complete stripping of Cu from the Pt(111) surface. Note also that after complete stripping of Cu, the Br coverage is exactly the same as in the case when the adsorption of  $\text{Br}^-$  on Pt(111) was monitored in a solution free of Cu. Remarkably, the total change in adsorption/desorption of  $\text{Br}^-$  during Cu UPD is rather low, *ca.*  $4 \mu\text{C cm}^{-2}$ .

X-ray scattering measurements of the Cu UPD layer on Pt(111) in solution containing bromide anions are summarized

in Fig. 24 [77, 80]. With the potential at 0.225 V, four symmetry-independent in-plane peaks were observed at (0, 0.735), (0.735, 0.735), (0, 1.47), (0.735, 1.47), as shown by the filled circles in the in-plane diffraction pattern illustrated in Fig. 24. The changes in the scattering intensity

of the fundamental peak (Fig. 24c) show that the structure responsible for this peak is potential dependent and present only in the potential region between the two Cu UPD peaks. The location of the fundamental peak at 0.735 (and higher-order peaks) shifted to 0.742 upon increasing the

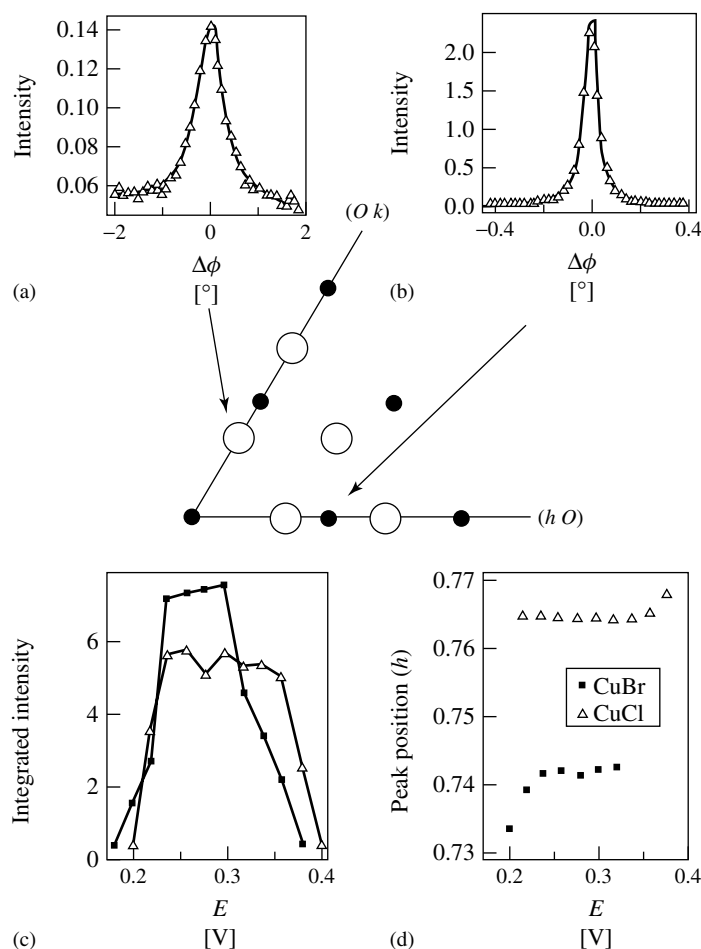


**Fig. 24** The in-plane X-ray diffraction pattern observed at 0.225 V for Cu UPD onto Pt(111) in solution containing  $\text{Br}^-$ . The Pt CTRs are represented by filled circles and the open circles correspond to scattering from the "4 × 4" structure. Rocking scans through (a) (0, 0.741 0.1) and (b) (1, 0, 0.1). (c) Integrated intensities obtained from scans such as the one shown in (a) for the CuBr bilayer (filled symbols) and CuCl bilayer (open circles) phases. (d) Corresponding position of the first-order diffraction peak from the CuBr and CuCl bilayer phases as a function of the electrode potential.

potential stepwise, as shown in Fig. 24(d). The comparable data for chloride solution is also shown. The location and symmetry of the in-plane peaks indicates that the adsorbed species form a hexagonal superstructure that is incommensurate with the underlying platinum lattice; the nearest commensurate unit cell is  $(4 \times 4)$ , which would have a fundamental peak at 0.750. Note that the chloride structure has a unit cell that is smaller than  $(4 \times 4)$ , and the bromide structure has one that is larger than  $(4 \times 4)$ , illustrating in a rather dramatic way the dominant role played by the anion and Cu-anion bonding in determining the structure of this intermediate phase. The inserts (a) and (b) in Fig. 24 show two rocking scans ( $\phi$  scans) through the  $(0, 0.735, 0.1)$  and  $(1, 0, 0.1)$  peaks, respectively. Both peaks have Lorentzian lineshapes with the width of the  $(0, 0.735)$  peak corresponding to a domain size of  $\approx 200$  Å, somewhat smaller than the estimated terrace size of the Pt(111) surface,  $\approx 1000$  Å. Additional information about the composition of the unit cell of this phase was obtained by utilizing “anomalous scattering” methods, that is, by measuring the relative intensities of the four in-plane peak intensities close to the Cu K adsorption edge (8979 eV). In general, the intensities of the relatively strong  $(0.735, 0.735)$  and  $(0, 1.47)$  peaks were weaker close to the Cu edge, indicating that the adsorbed superstructure does not consist of only Cu atoms (which would result in the reduction of the intensity of all in-plane peaks near the Cu edge) but must also include Br (for more details, see Ref. [80]). The simplest real-space structure consistent with the data has an hexagonal unit cell with the lattice spacing  $(0.735)^{-1}$  times the Pt lattice spacing, or 3.36 Å, and a two atom basis containing one copper and one bromide

atom arranged in two hexagonal layers, one of Cu and one of Br, each with the coverage of  $\approx 0.53$  ML.

#### 4.1.4.2.4 Cu UPD onto Pt(001) in the Presence of Bromide Anions

In pure perchloric acid, Cu is deposited as  $p(1 \times 1)$  islands on Pt(001) in a one-step adsorption process as evidenced by a single reversible change in the scattered X-ray intensity at  $(1, 0, 0.1)$ , an “anti-Bragg” point on the nonspecular CTR [82]. The effect of bromide adsorbed onto the surface (i.e. from solution) is to broaden the potential range of Cu deposition, although there is no evidence of a stagewise deposition process. This contrasts with results obtained on the Pt(111) surface in which two distinct steps in Cu UPD were observed (see previous section). With the electrode potential held at 0.43, 0.12, and  $-0.13$  V, in each case allowing enough time for the system to reach an equilibrium state, a search was performed for in-plane X-ray scattering peaks. In agreement with the results in Sect. 4.1.4.1.4, no peaks were found at 0.43 V, where only Br is adsorbed onto the surface. In addition, no peaks were found at 0.12 V, an intermediate potential in which on the Pt(111) surface under identical conditions the  $(4 \times 4)$  structure was observed. At  $-0.13$  V, however, peaks at reciprocal lattice positions, which could be indexed to a  $c(2 \times 2)$  structure, were found. The in-plane scattering in reciprocal space is represented in Fig. 25 together with some rocking scans at the various reciprocal lattice points that are indicated, (a)  $(1/2, 1/2, 0.1)$ , (b)  $(0, 1, 0.1)$ , and (c)  $(1/2, 3/2, 0.1)$ . As can be seen from Fig. 25, all of the measured  $c(2 \times 2)$  reflections were relatively broad compared to the peak at  $(1, 0, 0.1)$  on the Pt CTR and, from Lorentzian fits to the data (solid lines

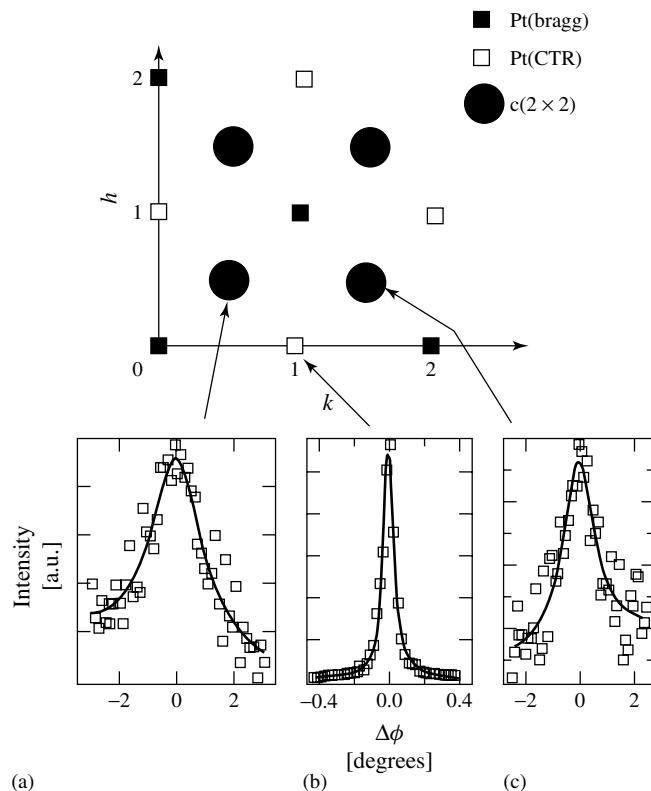


**Fig. 25** A representation of the in-plane X-ray scattering measured at  $-0.13$  V in solution containing  $0.1$  M  $\text{HClO}_4 + 10^{-3}$  M  $\text{Cu}^{2+} + 10^{-2}$  M  $\text{KBr}$ . The solid circles correspond to the measured  $c(2 \times 2)$  reflections and the squares to the location of bulk Pt CTRs and Pt Bragg reflections. The lower figures show scans through the indicated reciprocal lattice points at: (a)  $(1/2, 1/2, 0.1)$ ; (b)  $(0, 1, 0.1)$ ; and (c)  $(1/2, 3/2, 0.1)$ . In each case, the solid lines are fits of a Lorentzian lineshape to the data.

in Fig. 25), a domain size in the range  $30\text{--}60$  Å for the  $c(2 \times 2)$  structure was calculated. The  $c(2 \times 2)$  diffraction pattern was only formed if the electrode potential was held in the region below  $-0.12$  V and even then, only if the potential was approached from more negative potential. Once formed, the  $c(2 \times 2)$  structure was stable at negative potential until the onset of bulk Cu deposition.

In the previous section, anomalous scattering techniques were used to show

that the  $(4 \times 4)$  structure observed in the first stage of Cu deposition on Pt(111) contained both Cu and Br in the unit cell. Given that the  $c(2 \times 2)$  diffraction pattern in this study was obtained at  $-0.13$  V, a potential in which a significant amount of Cu is adsorbed onto the surface, similar measurements were made at several  $l$  values along the  $(1/2, 1/2, l)$  and  $(1/2, 3/2, l)$  rods. Measurements of the integrated intensities at  $8779$  eV,  $200$  eV below the Cu K adsorption edge, and  $8974$  eV,  $5$  eV

below the Cu edge, were performed but showed absolutely *no dependence* on the incident X-ray energy. Given that the dispersion corrections to the Cu atomic form factor change significantly over this energy range, this result implies that no Cu is contained in the  $c(2 \times 2)$  unit cell. It seems likely, therefore, that the  $c(2 \times 2)$  structure consists of an ordered Br lattice that is formed on top of a pseudomorphous Cu layer.

To obtain detailed structural information CTR measurements were modeled by a  $c(2 \times 2)$  Br adlayer on top of a  $p(1 \times 1)$  pseudomorphous Cu monolayer, where the respective coverages, surface normal spacings, and roughnesses were allowed to vary in order to fit the data. The CTRs passing through the bulk Pt Bragg reflections include contributions to the scattering both from the Cu and Br adlayers and the Pt lattice. To further test the model, the CTRs were measured with incident X-ray energies of 8779 and 8974 eV and the structural parameters were simultaneously refined to fit both the raw CTR data set (measured at 10 keV) and the intensity ratio  $I_{8779 \text{ eV}}/I_{8974 \text{ eV}}$ . This method increases the sensitivity of the fitting procedure to the Cu layer as shown in Sect. 4.1.4.2.2. CTR data taken with the potential held at  $-0.13$  V, where the  $c(2 \times 2)$  structure was present, is shown in the lower panels of Fig. 26. The top panels in Fig. 26 show the ratio data sets,  $I_{8779 \text{ eV}}/I_{8974 \text{ eV}}$ , which clearly indicates the sensitivity of the CTR measurements to the Cu adlayer. The solid lines in Fig. 26 correspond to the results of a simultaneous fit to these data sets in which the Cu coverage,  $\theta_{\text{Cu}}$ , Pt–Cu spacing,  $d_{\text{Pt–Cu}}$ , coverage of Br in a  $c(2 \times 2)$  adlayer, that is, two Br atoms per  $c(2 \times 2)$  unit cell,  $\theta_{\text{Br}}$ , Cu–Br spacing,  $d_{\text{Cu–Br}}$ , and the Cu and Br roughnesses were varied. The results are listed in Table 1. A

**Tab. 1** Structural parameters to the fit to the data in Fig. 26. The coverages,  $\theta_{\text{Cu}}$  and  $\theta_{\text{Br}}$ , are with respect to a full copper monolayer (one Cu atom per surface Pt atom) and a full  $c(2 \times 2)$  Br adlayer (0.5 Br atoms per surface Pt atom)

$\theta_{\text{Cu}}$	$1.0 \pm 0.06$
$d_{\text{Pt–Cu}}$	$1.75 \pm 0.05 \text{ \AA}$
$\sigma_{\text{Cu}}$	$0.13 \pm 0.05 \text{ \AA}$
$\theta_{\text{Br}} [c(2 \times 2)]$	$0.9 \pm 0.1$
$d_{\text{Cu–Br}}$	$1.79 \pm 0.08 \text{ \AA}$
$\sigma_{\text{Br}}$	$0.3 \pm 0.2 \text{ \AA}$

schematic of the structure is shown in Fig. 26.

Although the presence of Br anions considerably slows the kinetics of ordering, at negative potential ( $-0.13$  V) a complete pseudomorphous  $p(1 \times 1)$  Cu monolayer is formed on the Pt(001) surface. When this monolayer is completed, Br forms a  $c(2 \times 2)$  overlayer on top of the Cu monolayer. The Cu–Br spacing implies that, as was the case for the Pt–Br bond for Br adsorption onto Pt(001) (Sect. 4.1.4.1.4), the metal–halide bond is covalent in nature. The near-neighbor spacing in the Br adlayer is  $3.92 \text{ \AA}$ , which is similar to the near-neighbor spacing of Br adsorbed onto Pt(111) at positive electrode potential (Sect. 4.1.4.1.3). The Br coverage on the pseudomorphous Cu monolayer is nearly identical to the coverage measured on the Pt surface at positive potential and implies that close to a full Br monolayer remains on the electrode surface during Cu UPD. It is interesting that the bromide layer forms a structure with long-range order on the Cu monolayer and not on the Pt(001) surface in solution free of Cu.

#### 4.1.4.2.5 A Physical Model for Cu UPD

The results in this section have demonstrated that Cu UPD is a multistage

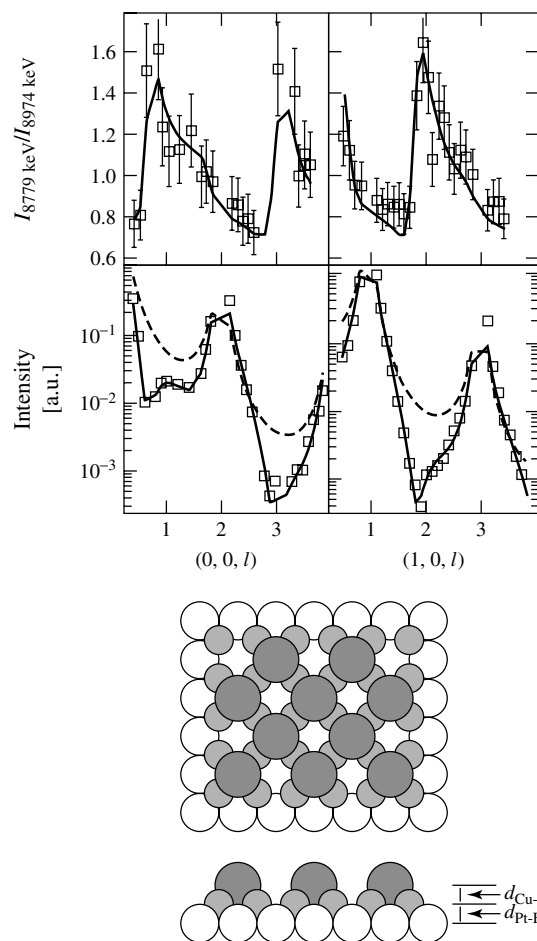


**Fig. 26** The measured CTRs at an electrode potential of  $-0.13$  V in  $0.1$  M  $\text{HClO}_4 + 10^{-3}$  M  $\text{Cu}^{2+} + 10^{-2}$  M  $\text{KBr}$  where the  $c(2 \times 2)$  structure is present. Upper panels: The ratio between CTR data sets taken with incident X-ray photon energies of  $8779$  and  $8974$  eV, that is,  $I_{8779 \text{ eV}}/I_{8974 \text{ eV}}$ . The solid lines are results of a simultaneous fit to all of the data according to the structural model that is schematically illustrated. The open circles are Pt substrate atoms, the shaded circles are Cu atoms, and the black circles are Br atoms that form the  $c(2 \times 2)$  structure. The side view indicates the surface normal spacings listed in Table 1.

process that, irrespective of the orientation of surface and/or the nature of specifically adsorbing anions, is governed by a complex interplay of  $\text{Cu}_{\text{upd}}$ -substrate,  $\text{Cu}_{\text{upd}}$ -anion, and the substrate-anion energetics. The structure of the adlayer depends strongly on the anion in the supporting electrolyte. In perchloric acid, the UPD layer on Pt(111) grows as progressively larger patches of Cu having the Pt lattice constant, that is, a pseudomorphic adlayer. From the electrocatalysis standpoint, the  $\text{Cu}_{\text{upd}}-\text{ClO}_4^-$  system is potentially the most interesting, because

a true bimetallic surface exists at which both Pt and Cu atoms can do catalysis. In either sulfate or halide-containing solutions, a multistep deposition occurs with the formation of ordered anion adlattices. Possible Pt(111)- $\text{Cu}_{\text{upd}}$ -anion and Pt(001)- $\text{Cu}_{\text{upd}}$ -anion structural models as a function of  $\text{Cu}_{\text{upd}}$  coverage are shown in Fig. 27. This model is very similar to previously proposed models for Cu UPD on Pt(111) [75] and Au(111) [83], and is based on the *enhanced* adsorption of halide and other anions on  $\text{Cu}_{\text{upd}}$ -modified Pt sites. Clearly,  $\text{Cu}_{\text{upd}}$  is either sandwiched



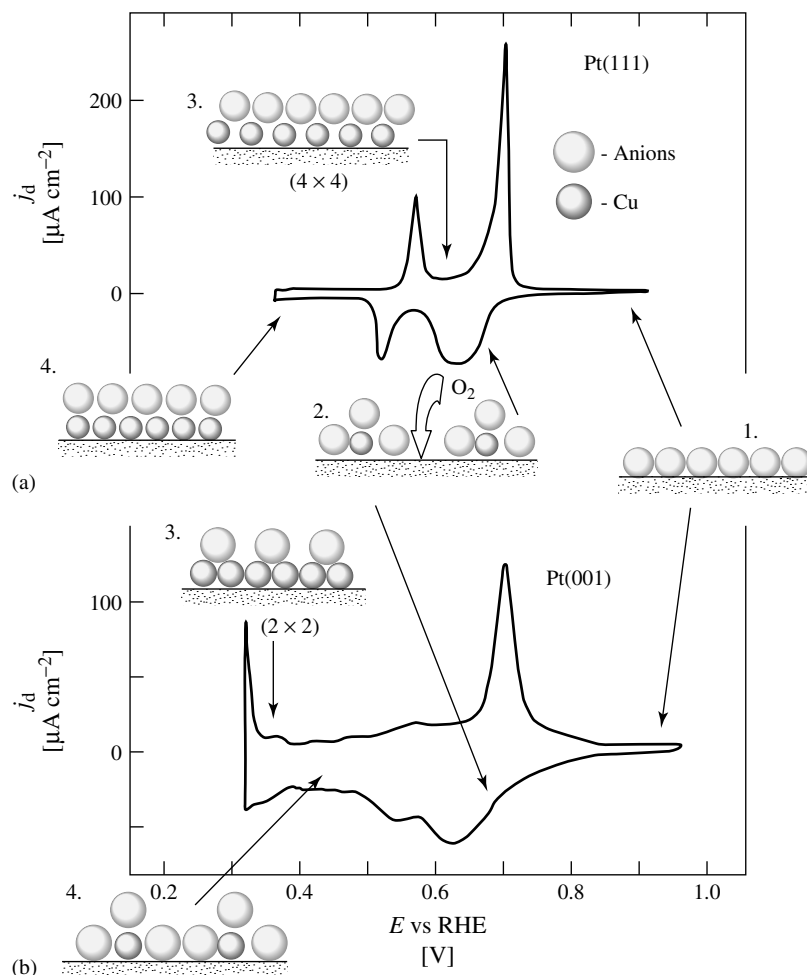


**Fig. 27** A cartoon schematic of the Cu UPD process on Pt in the presence of anion species. States 1–4 represent increasing Cu coverage, that is, consistent with a negative sweep of the electrode potential.

between the Pt surface and anions or is in contact with anions adsorbed on the adjacent Pt sites [77]. States 1a and 1b show a close-packed bisulfate/halide layer that is present on the Pt(111) and Pt(001) surfaces at potentials positive of Cu UPD. States 2a and 2b refer to the initial deposition of  $\text{Cu}_{\text{upd}}$  on Pt(111) and Pt(001) surfaces on which the  $\text{Cu}^{2+}$  ion is only partially discharged. At higher surface coverages

by  $\text{Cu}_{\text{upd}}$  ( $0.5 < \Theta_{\text{Cu}} < 1$ ), anions are either entirely displaced from the surface by  $\text{Cu}_{\text{upd}}$  (state 3a) or  $\text{Cu}_{\text{upd}}$  and anions form two-layer structures in which anions are adsorbed on both Pt as well as  $\text{Cu}_{\text{upd}}$  sites (state 3b in Fig. 27). Note that state 3a is representative of the ordered  $(4 \times 4)$   $\text{Cl}_{\text{upd}}\text{--Cl}_{\text{ad}}$  ( $\text{Br}_{\text{ad}}$ ) bilayer structure. In contrast with the Pt(111)– $\text{Cu}_{\text{upd}}$ –anion system, on Pt(001), in the same potential

range (0.1–0.4 V), a mixture of Cu and Br atoms is present on the Pt(001) surface in a disordered structure. Presumably the strong affinity of adsorbates for the Pt fourfold hollow site prevents the formation of a long-range ordered bilayer phase (for example, a (001) plane of Cu(I)Br) as adsorbate mobility is reduced on the (001) substrate. The final step in Cu UPD is the “filling-in” of the Cu<sub>upd</sub> monolayer to form a bilayer phase: that is, a pseudomorphic (1 × 1) Cu<sub>upd</sub> monolayer with either a disordered anion adlayer on the top of Pt(111)–Cu<sub>upd</sub> [80, 81], state 4a, or an ordered c(2 × 2) bilayer Cu<sub>upd</sub>–Br<sub>ad</sub> structure on the Pt(001) surface [82], state 4b. In both Cl<sup>−</sup> and Br<sup>−</sup> solutions, Cu UPD onto Pt(111) proceeds *via* the same intermediate phase. In sulfuric acid solution, however, the equivalent intermediate state on Pt(111) corresponds to the formation of the honeycomb ( $\sqrt{3} \times \sqrt{3}$ )R30° Cu<sub>upd</sub>–HSO<sub>4</sub> structure [81] that consists of both 0.22 ML bisulfate anions and 0.66 ML of Cu<sub>upd</sub> in the unit cell. The same structure was proposed for the Au(111)-sulfate system [67, 68]. The formation of the intermediate state (state 2) occurs over a very narrow region of potential. As will be shown in Sect. 4.1.5, the existence of bare platinum sites in state 2 (Fig. 27) is essential for the adsorption of O<sub>2</sub>, and this first-stage formation plays the key role in the activity of the Pt–Cu<sub>upd</sub> interface for the ORR.

#### 4.1.5

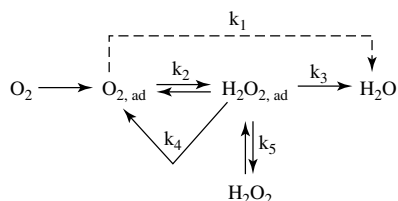
##### The Oxygen-reduction Reaction (ORR)

The main problem in the development of an efficient electrochemical energy conversion device (fuel cell) is in the sluggish ORR kinetics even on the most catalytically active electrode materials, for example, on

platinum group metals measurable currents are obtained only below 1 V. It is customary, therefore, in kinetic studies of the ORR to use the current density at a fixed potential, for example, at 0.9 V, as a measure of the reaction rate instead of the exchange current density, for example, at the reversible potential. Given that the reversible potential of the ORR is 1.23 V, virtually all reversible electrode potentials for solid elements are less positive, and consequently not many substrates may even be considered as oxygen electrodes. Besides the stability of electrode materials, the ORR is accompanied with many other complications, such as the necessity of cleaving the strong O–O bond (*ca.* 497 kJ mol<sup>−1</sup>) to produce the maximum efficiency in the 4e<sup>−</sup> process. Complete evaluation of electrocatalysis for the ORR must, therefore, accommodate many contributing factors, including variations of the free energy of activation, the heats of adsorption of reactive intermediates, and the preexponential surface coverage term, (1 −  $\Theta_{ad}$ ). In this section, closely following the microscopic description of clean and modified metal surfaces (presented in Sects. 4.1.3 and 4.1.4), we discuss recent efforts towards a fundamental understanding of electrocatalysis of the ORR on these surfaces.

##### 4.1.5.1 Reaction Pathway

The ORR is a multielectron reaction that may include a number of elementary steps involving different reaction intermediates. Of the various reaction schemes proposed for the ORR [84], the simplified version of the scheme given by Wroblowa and coworkers [85] appears to be the most effective one to describe the complicated reaction pathway by which O<sub>2</sub> is reduced at metal surfaces:



On the basis of this reaction scheme,  $O_2$  can be electrochemically reduced either directly to water with the rate constant  $k_1$  without intermediate formation of  $H_2O_{2,ad}$  (so-called “direct”  $4e^-$  reduction) or to  $H_2O_{2,ad}$  with the rate constant  $k_2$  (“series”  $2e^-$  reduction). The adsorbed peroxide can be electrochemically reduced to water with the rate constant  $k_3$  (“series”  $4e^-$  pathway), catalytically (chemically) decomposed on the electrode surface ( $k_4$ ), or desorbed into the bulk of the solution ( $k_5$ ). Although a number of important problems pertaining to the interpretation of the reaction pathway for the ORR on metal surfaces have yet to be resolved, it appears that a series pathway *via* an  $(H_2O_2)_{ad}$  intermediate may be operative on pure Pt, Au, and Cu and their bimetallic surfaces. This can be considered as a special case of the general mechanism in which  $k_1$  is essentially zero, that is, there is no splitting of the O–O bond before a peroxide species is formed. Peroxide, on the other hand, may ( $k_5 = 0$ ) or may not ( $k_5 \neq 0$ ) be further reduced to water. In either case, the rate-determining step appears to be the addition of the first electron to  $O_{2,ad}$ . The rate expression is then [86, 87],

$$i = nFKc_{O_2}(1 - \Theta_{ad})^x \exp\left(\frac{-\beta FE}{RT}\right) \times \exp\left(\frac{-\Delta G_{\theta}^*}{RT}\right) \quad (12)$$

where  $n$  is the number of electrons,  $K$  is the rate constant,  $c_{O_2}$  is the concentration of  $O_2$  in the solution,  $\Theta_{ad}$  is the total surface coverage by anions ( $\Theta_{ad}$ ) and  $OH_{ad}$  ( $\Theta_{OHad}$ ),  $x$  is either 1 or 2 depending on the site requirements of the adsorbates,  $i$  is the observed current,  $E$  is the applied potential,  $\Delta G_{\theta}^*$  is the standard free energy (“chemical”) of activation ( $\Delta G_{\theta}^* = \Delta G_0^* + \gamma \Delta G_{\Theta}^0 \Theta_{ad}$ ),  $\Delta G_0^*$  is the standard free energy of activation at zero coverage,  $\Delta G_{\Theta}^0$  is the difference in the heats of adsorption of reactance and products in the rate-controlling step ( $\Delta G_{\Theta}^0 = \Delta G_0^0 + r\Theta_{ad}$ ),  $\beta$  and  $\gamma$  are the symmetry factors (assumed to be 1/2), and  $r$  is a parameter characterizing the rate of change of the apparent standard free energy of adsorption of reaction intermediates with the surface coverage by adsorbing species. In deriving Eq. (12), it is assumed that the reactive intermediates,  $(O_2^-)_{ad}$  and  $(HO_2^-)_{ad}$ , are adsorbed only to low coverage, that is, they are not a significant part of  $\Theta_{ad}$ . In the following sections, this reaction pathway and rate expression are used to analyze the effects of various factors on the kinetics of the ORR on Pt(*hkl*), Au(*hkl*), and Cu(*hkl*) surfaces.

#### 4.1.5.2 ORR on Pt(*hkl*) Surfaces

During the past two decades, a great deal of work in surface electrochemistry has been aimed at elucidating the role of the local symmetry of surface atoms in electrocatalysis, particularly for the kinetics of the ORR on platinum single-crystal surfaces. It is now well established that the kinetics of the ORR on Pt(*hkl*) surfaces are sensitive to the surface structure [88, 89] and arise because of structure-sensitive adsorption of spectator species, such as  $H_{upd}$  [89, 90],  $OH_{ad}$  [91],  $HSO_{4(ad)}$  [90],  $Cl_{ad}$  [92], and  $Br_{ad}$  [87]. Within the limited scope of this report, it will not be possible to review all

of these results. Rather, we will show, using representative examples, the kind of information that can improve our understanding of the role of the local symmetry of platinum surface atoms in  $O_2$  reduction electrocatalysis. There are two general observations concerning the structure sensitivity of the ORR: (i) the *same* activation energy in both acid (at the reversible potential *ca.*  $42 \text{ kJ mol}^{-1}$  [93]) and alkaline solution (at  $0.8 \text{ V}$  *ca.*  $40 \text{ kJ mol}^{-1}$  [94]) has been found for all three  $Pt(hkl)$  surfaces; (ii) the structural sensitivity is most pronounced in electrolytes in which there is strong adsorption of anions. As a consequence, the structure sensitivity of the ORR on  $Pt(hkl)$  surfaces is mainly determined by the preexponential  $(1 - \Theta_{ad})$  coverage term.

**4.1.5.2.1 ORR at the  $Pt(hkl)$ -halide Interface** For the purpose of demonstrating the importance of the  $(1 - \Theta_{ad})$  term in the kinetics of the ORR on  $Pt(hkl)$ , two representative sets of polarization curves are shown in Figs. 28 and 29. Figure 28 shows that in the presence of  $Cl^-$ , the variation in activity increases in the order  $(001) < (110) < (111)$ . Figure 28(a) shows that the ORR on the  $Pt(111)$  surface in  $0.1 \text{ M HClO}_4 + 10^{-3} \text{ M } Cl^-$  is strongly inhibited, with an activity in a solution containing  $Cl^-$  being several orders of magnitude lower than in  $0.1 \text{ M HClO}_4$  [88, 92]. Figure 28(a) also shows that between  $0.3 < E < 0.9 \text{ V}$ , the ring currents were a small fraction of the disk currents, implying that on the surface highly covered with  $Cl_{ad}$ , oxygen reduction proceeds almost entirely through the  $4e^-$  reduction pathway. The appearance of peroxide oxidation currents on the ring electrode begins at potentials negative of  $0.25 \text{ V}$ , and parallels with the adsorption of hydrogen on  $Pt(111)$ . In contrast with

$Pt(111)$ , the ORR on  $Pt(110)$  (Fig. 28b) and  $Pt(001)$  (Fig. 28c) in  $Cl^-$ -containing solution is accompanied quantitatively with peroxide formation, implying that within the same potential limits  $H_2O_2$  is formed as an intermediate on the  $Pt(110)$  and  $Pt(001)$  electrodes covered with  $Cl_{ad}$ . On  $Pt(001)$  the percentage of  $H_2O_2$  produced between  $0.25 < E < 0.6 \text{ V}$  during the ORR is almost constant and is close to 25%. Note that, at potentials more negative than  $E = 0.3 \text{ V}$ , the surface coverage with  $Cl_{ad}$  is reduced substantially, but the  $O_2$ -reduction currents sharply decrease to diffusion-limiting currents for *ca.*  $2e^-$  per  $O_2$  molecule at the negative potential limit. In the same potential region, the  $O_2$ -reduction currents on the disk electrode are accompanied quantitatively by the  $H_2O_2$ -oxidation currents on the ring electrode, reaching maximum peroxide production of *ca.* 90% at  $0.075 \text{ V}$ . In  $Cl^-$ -free solution, however, a  $3e^-$  reduction is observed at the same potential limit [90]. This may suggest that  $Cl_{ad}$  is *always* present on  $Pt(001)$  covered by  $H_{upd}$  (as also observed for  $Br_{ad}$  on  $Pt(001)$  – see Sect. 4.1.4.1.4) thus, the availability of Pt atoms required for the breaking of the O–O bond are significantly reduced and the ORR proceeds entirely through the  $2e^-$  peroxide pathway on the  $Pt(001)$ - $H_{upd}$ - $Cl_{ad}$  surface. The amount of peroxide formed on the  $Pt(110)$  surface is substantially smaller, Fig. 28(b), *ca.* 2.5%, and no increase in peroxide formation was observed in the  $H_{upd}$  region.

As demonstrated recently [92], the key to resolving the structural sensitivity of the ORR and the HOR on  $Pt(hkl)$  surfaces in  $Cl^-$ -containing solution is to be found in understanding the interplay between the electronic properties (the work function) of the substrate and the match between the Pt surface atomic geometry and the

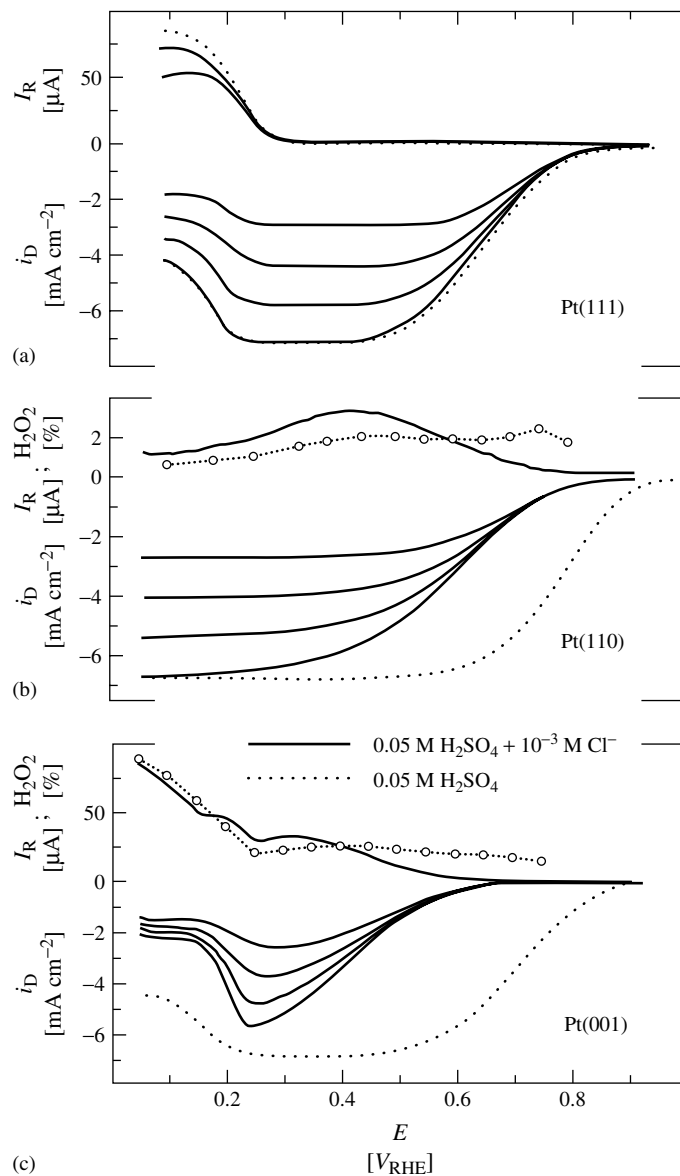


**Fig. 28** Polarization curves for Pt single-crystal electrodes in  $0.05\ M\ H_2SO_4$  with and without  $10^{-3}\ M\ Cl^-$ : (a) Pt(111); (b) Pt(110); and (c) Pt(001).

adsorbing anions. The high activity of the Pt(111)- $Cl_{ad}$  surface for the ORR can be attributed to the highest work function (the  $pzc$ ) of the Pt(111) surface. An obvious

consequence of this positive value of the  $pzc$  is that the onset of the desorption of  $Cl_{ad}$  occurs at more positive potentials on this surface. The fact that  $Cl_{ad}$  inhibits

the initial adsorption of  $O_2$  molecules, but does *not* affect the pathway of the reaction implies that the interaction of  $Cl_{ad}$  with the close-packed (111) surface is not very strong. On the other hand, the lower *pzc* of Pt(001) would require a larger shift in the thermodynamic driving force to displace  $Cl_{ad}$  from the surface, accounting for a strong deactivation of the ORR on the Pt(001)- $Cl_{ad}$  surface. The substantial production of peroxide on the Pt(001)- $Cl_{ad}$  surface is related to strong adsorption of  $Cl_{ad}$  on the fourfold hollow (001) sites, (similar to the mechanism that frustrates the ordering of Br on the Pt(001) surface – see Sect. 4.1.4.1.4) with a corresponding reduction in the available pairs of platinum sites required for the breaking of the O–O bond. This model may seem to conflict with the case of Pt(110), in which the kinetics of the ORR is higher than on the Pt(001) surface even though the *pzc* of the (110) surface has a lower value and interaction of  $Cl_{ad}$  with low coordinated (110) sites is as strong as on Pt(001). The key to resolving this seeming contradiction is, however, in the structure of the Pt(110) surface itself (as described in Sect. 4.1.3).  $Cl_{ad}$  is most probably adsorbed in the “troughs” or “missing rows” of the reconstructed (110) surface and, hence,  $O_2$  adsorption and the breaking of the O–O bond may take place on the top rows of platinum sites (the first atomic layer in the structural model shown in Fig. 9).

$Cl_{ad}$  is not observed to form any ordered structures on Pt(*hkl*) surfaces, in contrast with  $Br_{ad}$  on Pt(111) – see Sect. 4.1.4.1.3). Furthermore, the potential dependence surface coverage by  $Cl_{ad}$  cannot be discerned from RRDE measurements. As a consequence, it is difficult to find the relationship between the activity of the ORR and the potential dependence of  $Cl_{ad}$  surface coverage/structures. To get

insight into this relationship, the ORR has recently been studied on the Pt(111) surface in solution containing  $Br^-$  anions. As demonstrated in Sect. 4.1.4.1.3, the potential dependence of bromide adsorption/surface structure was obtained from a combination of RRDE and X-ray scattering measurements.

Figure 29(b) summarizes a family of polarization curves for the ORR on Pt(111) in 0.1 M  $HClO_4 + 10^{-4}$  M  $Br^-$  along with a representative polarization curve recorded in solution free of  $Br^-$  anions. In all experiments, the ring was potentiostated at 0.95 V, where oxidation of peroxide arriving at the ring is under diffusion control, Sect. 4.1.2.2. In pure perchloric acid, at low overpotentials, the ring currents were a very small fraction of the disk currents, implying that on the surface covered with reversible adsorbed  $OH_{ad}$  (the so-called “butterfly region”) oxygen reduction proceeds almost entirely through the direct  $4e^-$  pathway. The appearance of peroxide oxidation currents on the ring electrode begins at potentials negative of 0.0 V, and parallels the adsorption of hydrogen on Pt(111). At the negative potential limit, the limiting current corresponds to exactly two-electron reduction of  $O_2$ . Figure 29(b) shows that the ORR on the Pt(111) surface is strongly inhibited by  $Br^-$ , with an activity in the solution containing  $Br^-$  being several orders of magnitude lower than in pure perchloric acid. Figure 29(b) shows that  $O_2$  reduction on the Pt(111)-Br surface starts at *ca.* 0.3 V ( $\Theta_{Br} \approx 0.4$  ML and  $\Theta_{OH} \approx 0.0$  ML in Fig. 29a) and is under combined kinetic-diffusion control between  $0.1 < E < 0.3$  V. Figure 29(b) also shows that peroxide was detected on the ring electrode in the same potential region, indicating that  $H_2O_2$  is formed as an intermediate on the electrode covered with  $\theta_{Br} \approx 0.4$ –0.35 ML. At potentials

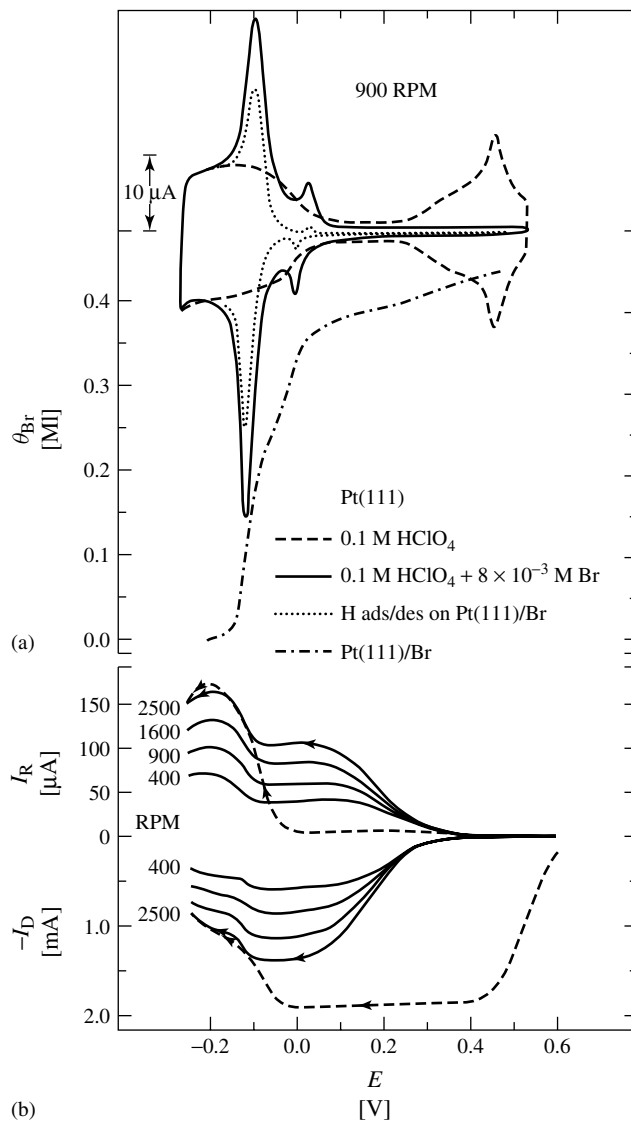


**Fig. 29** (a) CV for Pt(111) in 0.1 M HClO<sub>4</sub> (dashed line) showing the effect of Br<sup>-</sup> in solution (solid line) and the effect on the adsorption/desorption of hydrogen (dotted line). The Br coverage is shown by the dot-dashed line. (b) Polarization curves for the ORR on Pt(111) in 0.1 M HClO<sub>4</sub> + 10<sup>-4</sup> M Br<sup>-</sup>.

more negative than  $E = 0.1$  V, the surface coverage with Br decreases substantially, for example, from  $\theta_{\text{Br}} \approx 0.35$  ML to  $\theta_{\text{Br}} \approx 0.25$  ML, and the O<sub>2</sub>-reduction

currents increase to a diffusion-limiting current for 3e<sup>-</sup> per O<sub>2</sub> molecule. In the same potential region, the O<sub>2</sub>-reduction currents are accompanied quantitatively by

the  $\text{H}_2\text{O}_2$ -oxidation currents on the ring electrode, implying that in the presence of  $\text{Br}^-$  anions  $\text{O}_2$  reduction does *not* proceed entirely through the  $4\text{e}^-$  reduction, as found for the  $\text{Pt}(111)\text{-Cl}_{\text{ad}}$  system [92]. It was proposed that strongly adsorbed Br can simultaneously suppress the initial adsorption of the  $\text{O}_2$  molecule and the formation of pairs of platinum sites needed for the breaking of the O–O bond [87]. On the basis of this proposition, the physical model that appears to rationalize the ORR on the  $\text{Pt}(111)\text{-Br}_{\text{ad}}$  electrode is one in which the active sites for the adsorption of molecular  $\text{O}_2$  are the small number of “bare” platinum sites that are created when desorption of  $\text{Br}_{\text{ad}}$  takes place from the  $\text{Pt}(111)$  surface. Finally, by comparing the ORR in Fig. 29 with the potential stability of the  $\text{Br}_{\text{ad}}$  structure in Fig. 15, one can find *no* correlation between the ordered surface structure and the kinetics of the ORR.

The analysis for the ORR on  $\text{Pt}(111)$  has shown that the Tafel plot of mass transport corrected currents for the ORR at the  $\text{Pt}(111)$  surface in solution containing  $\text{Br}^-$  is *ca.*  $118 \text{ mV dec}^{-1}$ . The fact that the  $\text{Pt}(111)\text{-Br}_{\text{ad}}$  surface has a single slope of  $118 \text{ mV dec}^{-1}$  strongly suggests that the apparent standard free energy of adsorption of the reaction intermediates is *not* affected by the neighboring  $\text{Br}_{\text{ad}}$ , that is, the adsorption of reaction intermediates that are formed during the ORR on the  $\text{OH}_{\text{ad}}$ -free  $\text{Pt}(111)$  surface obeys the Langmuirian conditions. In contrast, the Tafel plot in  $0.1 \text{ M HClO}_4$  solution free of  $\text{Br}^-$  deviates significantly from  $120 \text{ mV dec}^{-1}$ , similarly to what is found in the literature for the  $\text{O}_2$  reduction on a polycrystalline Pt electrode [95]. A number of theories have been proposed to explain the transition in the Tafel slope on polycrystalline Pt electrodes,

which is usually from *ca.*  $60 \text{ mV dec}^{-1}$  at low current densities to  $120 \text{ mV dec}^{-1}$  at high current densities [86]. The change in the slope has been attributed to the change from Temkin to Langmuirian conditions for the adsorption of reaction intermediates [95], or as being due to a change in the surface coverage by  $\text{PtOH}_{\text{ad}}$ , which effects the adsorption of molecular  $\text{O}_2$  [96]. In both theories, the first charge-transfer step has been proposed as the rate-determining step. It has, however, been very difficult to obtain definitive evidence that will support either theory, since both the nature of intermediates in the ORR have never been probed experimentally and the surface coverage by  $\text{OH}_{\text{ad}}$  species was poorly defined. By eliminating the surface heterogeneity with single-crystal electrodes, it was proposed that there are two modes of action of the  $\text{OH}_{\text{ad}}$  state on the kinetics of the ORR on the  $\text{Pt}(111)$  surface [97]: (i)  $\text{OH}_{\text{ad}}$  can block the adsorption of  $\text{O}_2$  on active platinum sites, that is, they compete for the same sites; and (ii)  $\text{OH}_{\text{ad}}$  can alter the adsorption energy of intermediates (the  $r_{\text{ad}}$  follows the Temkin conditions) that are formed during the ORR on the bare Pt sites neighbored by the  $\text{OH}_{\text{ad}}$ .

**4.1.5.2.2 ORR at the  $\text{Pt}(hkl)\text{-Cu}_{\text{upd}}$  Interfaces** Studies of the kinetics of the ORR on platinum single-crystal electrodes modified by UPD metal ad-atoms are of interest primarily from a fundamental science perspective. Since it is possible to begin the experiment with a clean  $\text{Pt}(hkl)$  surface in which the ORR is well known, the change in both rate and reaction pathway with the addition of another metal to the surface, usually in a highly structured manner, can provide some insight into the ORR on metals that are otherwise difficult to study, for example, Cu, Pb, and Bi. Only the results



on Cu<sub>upd</sub>-modified surfaces are reviewed here because trace levels of copper may be present in real systems, mostly as a corrosion product, thus the effects of Cu UPD on Pt will serve as a model system to understand why a small amount of Cu UPD has a devastatingly inhibiting effect on the ORR. The first result for the ORR on the Pt(111)-Cu<sub>upd</sub> electrode was published by Abe and coworkers [76]. By using STM and hanging meniscus rotating disk electrode (HMRDE) methods, the authors demonstrated a close correlation between the inhibition of the ORR with the microstructure of Cu<sub>upd</sub> adlayer. In sulfuric acid solution, threefold hollow platinum sites are still accessible for O<sub>2</sub> adsorption inside the honeycomb ( $\sqrt{3} \times \sqrt{3}$ )R30° structure that forms at *ca.* 0.5 V, but the reduced geometry favors 2e<sup>−</sup> reduction to peroxide versus 4e<sup>−</sup> reduction to water. The correlation between the surface structure of Cu<sub>upd</sub> and the kinetics of the ORR can be examined by using a combination of RRDE and X-ray scattering measurements (the X-ray diffraction measurements are described in Sect. 4.1.4.2). These results reveal that there is *no* correlation between the ORR kinetics and the *ordered* Cu<sub>upd</sub> surface structures irrespective of the nature of the specifically adsorbing anions [98]. The effect of Cu<sub>upd</sub> on the ORR at the Pt(111) interface in 0.05 M H<sub>2</sub>SO<sub>4</sub> and 0.05 M H<sub>2</sub>SO<sub>4</sub> + 10<sup>−3</sup> M Cl<sup>−</sup> are shown in Figs. 30(a, b). For comparison, the polarization curves for the ORR in Cu<sup>2+</sup>-free solutions under the same experimental conditions are shown as dotted curves. Clearly, in a solution containing Cu<sup>2+</sup> ions, the ORR is strongly inhibited in both Cl<sup>−</sup>-free and Cl<sup>−</sup>-containing solutions. Very similar behavior was also observed on a polycrystalline electrode [99, 100] and Pt(111) [76, 98] in different acid solutions. Given that Cu UPD is a rather slow

process, the ORR currents at the Cu<sub>upd</sub>-modified surfaces can also be measured under steady state conditions, see the closed circles in Fig. 30. In these experiments, the ORR is more inhibited than in the potentiodynamic experiments. As shown in Fig. 30, the deactivation is more pronounced in the presence of Cl<sup>−</sup> ions, presumably due to stronger interaction of specifically adsorbed chloride (Cl<sub>ad</sub>) than bisulfate (H<sub>2</sub>SO<sub>4(ad)</sub>) anions with the Pt-Cu<sub>upd</sub> surface. Analysis of the RRDE data (Fig. 30) also revealed that the mechanism for the ORR on Cu<sub>upd</sub>-modified electrodes is the same as on unmodified Pt(111), that is, proceeds mostly as a 4e<sup>−</sup> reaction pathway with negligible solution phase peroxide formation, (*ca.* 3%). It is surprising, however, that a relatively small amount of Cu<sub>upd</sub> has such a devastating effect on the rate of ORR. This anomalously large inhibition by a very small amount of Cu<sub>upd</sub> is attributed to enhanced anion adsorption on platinum atoms adjacent to Cu<sub>upd</sub> atoms [98], see Sect. 4.1.4.2 and Fig. 27. The predominant role of anions in determining the rate of the ORR on Cu<sub>upd</sub>-modified platinum single-crystal surfaces is supported by the fact that the activity of the ORR decreases in the same sequence as the Cu-anion bond strength increases: Pt-Cu<sub>upd</sub>-HSO<sub>4,ad</sub> ≫ Pt-Cu<sub>upd</sub>-Br<sup>−</sup>. The model that rationalizes these results is one in which the active sites for the adsorption of molecular O<sub>2</sub> are the small number of platinum “islands” created in state 2 in Fig. 27. It is important to note that in the Cu UPD potential region, Cu<sub>upd</sub> is always covered with anions, even at the most negative potentials at which Pt(001) and Pt(111) are covered by nominally 1 ML of Cu<sub>upd</sub>. It is obvious, therefore, that is impossible to determine the true catalytic activity of an anion-free pseudomorphic (1 × 1)

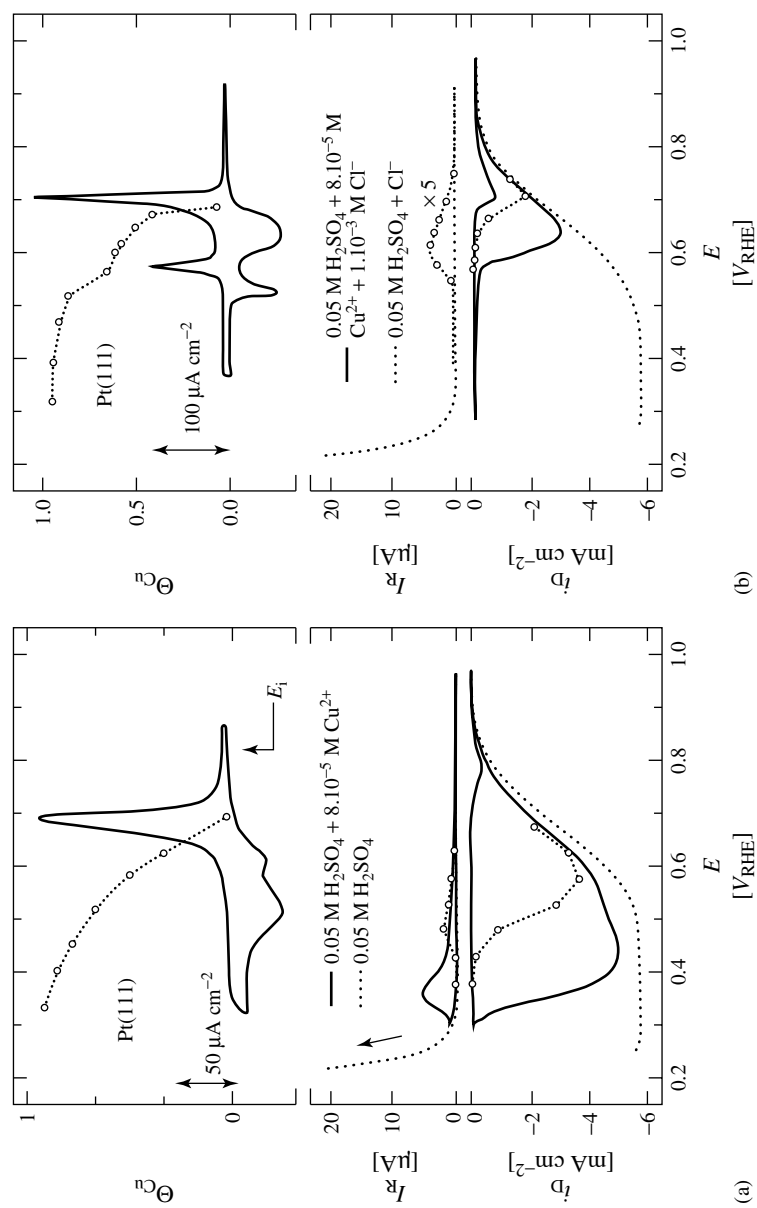


**Fig. 30** The effect of  $\text{Cu}_{\text{upd}}$  on the ORR at the Pt(111) interface in (a)  $0.05 \text{ M H}_2\text{SO}_4 + 10^{-4} \text{ M Cu}^{2+}$ , represented at the bottom of (a) and (b). In both cases, the solution contains  $10^{-4} \text{ M Cu}^{2+}$ . The corresponding Cu coverages (open circles) obtained from RRDE experiments (disk currents are shown by solid lines) are represented at the top.

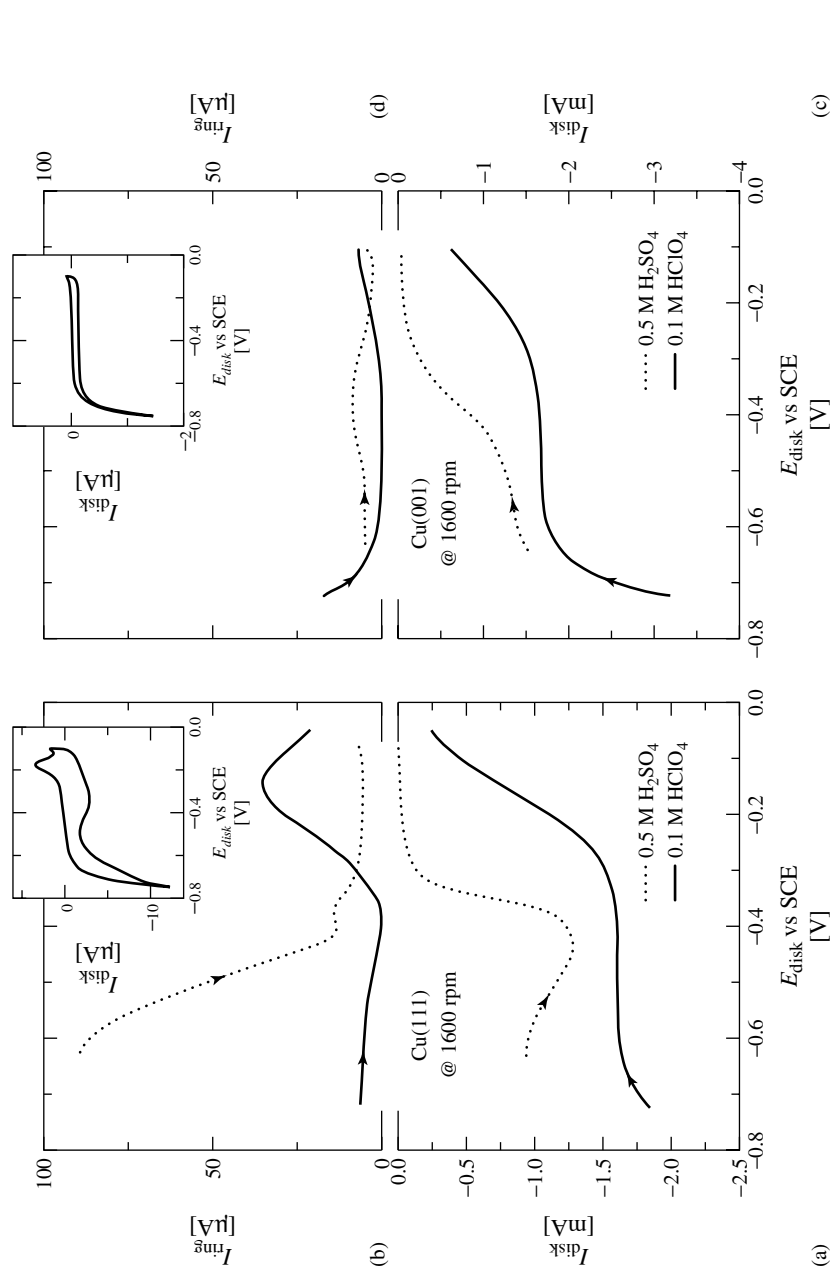


**Fig. 31** Polarization curves (positive sweeps) of the ORR on (a, b) Cu(111) and (c, d) Cu(001) electrodes in 0.5 M  $\text{H}_2\text{SO}_4$  (dashed lines) and 0.1 M  $\text{HClO}_4$  (solid lines). Insets: The corresponding CVs obtained on the disk electrodes in 0.1 M  $\text{HClO}_4$  in the absence of  $\text{O}_2$ .

Cu<sub>upd</sub> monolayer. One way to overcome this problem is to study the ORR on Cu single-crystal surfaces.

#### 4.1.5.3 ORR on Cu(*hkl*) Surfaces

In contrast with the extensive studies of the ORR on Pt(*hkl*) surfaces, there has been no substantial fundamental study of the effects of anion adsorption on the kinetics of the ORR on Cu(*hkl*) surfaces. Very recently, by utilizing the RRDE technique, Brisard and coworkers [101] have shown that the ORR on Cu(111) and Cu(001) surfaces in sulfuric acid solution is a structure-sensitive process, see Fig. 31. As for Pt(*hkl*), an interpretation of the variation in the activity of this process with the different low-index crystal surfaces of Cu can be presented on the basis of the premise of the structure-sensitive adsorption of sulfuric acid anions on Cu(*hkl*) surfaces, for example, as for Pt(*hkl*) with the  $(1 - \Theta_{\text{ad}})$  term.

A comparison of the polarization curves (positive sweeps) of the ORR on Cu(111) and Cu(001) at the same rotation rate (1600 rpm), Fig. 31, shows relatively small, for example, less than a factor of 2, differences in activity, but very different reaction pathways below  $-0.4$  V. Since very little is known about the nature of adsorbed anions on Cu(*hkl*) in sulfuric acid solution, or how the adsorption sites might differ between the different surfaces, it is difficult to rationalize the structural sensitivity of the ORR on Cu(*hkl*). For the Cu(111)-SO<sub>4,ad</sub> interface, both Wilms and coworkers [102] and Li and Nichols [103] found by STM that a complex incommensurate ordered structure of sulfate anions formed at the Cu(111) surface throughout the  $-0.1$  to  $-0.4$  V potential region in H<sub>2</sub>SO<sub>4</sub>. This ordered structure does not appear to lie along any high symmetry directions of the Cu(111) substrate but it

forms a particularly stable adlayer between  $-0.3 < E < -0.1$  V. In addition, by utilizing a potentiostatic STM image, it was shown that disordering of this structure coincides with the onset of formation of the cathodic peak, for example, with the desorption of (bi)sulfate anions at  $-0.35$  V in Fig. 31(a). Given that the onset of the ORR on the Cu(111) surface in Fig. 31(a) is observed at the same potential, it was suggested that the kinetics and reaction pathway of the ORR is controlled by the number of Cu “bare” sites on which the adsorption of O<sub>2</sub> molecules may take place. Although structural information regarding the surface coverage of (bi)sulfate anions on Cu(001) is lacking, it is reasonable to suggest that the ORR pathway on Cu(001) is the same as on Cu(111).

The overall inhibiting effect of anion adsorption on the kinetics of the ORR was determined by comparing the ORR on Cu(111) and Cu(001) in 0.5 M H<sub>2</sub>SO<sub>4</sub> and 0.1 M HClO<sub>4</sub> [101]. Figure 31(a) shows that in 0.1 M HClO<sub>4</sub> the initial reduction of O<sub>2</sub> molecules is associated with production of peroxide on the ring electrode (Fig. 31b). A comparison of the voltammetric curve of Cu(111) in 0.1 M HClO<sub>4</sub> solution free of O<sub>2</sub> (inset of Fig. 31b) with the polarization curves for the ORR in Fig. 31(a), suggests that the amount of peroxide formed on the disk electrode is determined by the potential-induced change in the surface coverage of OH<sub>ad</sub> on the Cu(111) surface [101]. Thus, the decrease in the surface coverage by OH<sub>ad</sub> on Cu(111) results in an increase in the rate of the ORR on the Cu(111) surface, as observed for the ORR on Pt(*hkl*) in the potential region of the structure-sensitive adsorption of OH<sub>ad</sub> [97]. Further inspection of Fig. 31 shows that the combined kinetic-diffusion control of the ORR on Cu(111) and Cu(001) is followed with the smooth transition to a

well-defined diffusion-limiting current for the  $4e^-$  reduction ( $-0.65 < E < -0.3$  V), consistent with an absence of peroxide on the ring in this potential region. The fact that the ORR on Cu(111) and Cu(001) is orders of magnitude lower in sulfuric acid solution than in pure perchloric acid, indicates that the compact layer of strongly adsorbed bisulfate anions suppresses the initial adsorption of the  $O_2$  molecule on these surfaces, for example, the kinetics of the ORR on Cu(*hkl*) is determined by the  $(1 - \Theta_{ad})$  term in Eq. (12).

#### 4.1.5.4 ORR on Au(*hkl*) Surfaces

The ORR on gold single-crystal surfaces, was also found to be structure sensitive in both alkaline and acid solutions. In fact, the first observation that the rate of the ORR is structure sensitive was made from measurements of the ORR on gold single-crystal surfaces in alkaline solution [104, 105]. In acid solutions [105, 106], the order of activity increases in the sequence: Au(111) < Au(110) < Au(001). In contrast with Pt(*hkl*) and Cu(*hkl*) surfaces, the ORR on Au(*hkl*) surfaces in acid solution is a very slow process. Because of the very weak interaction of  $O_2$  molecules with gold, two-electron reduction with 100% production of peroxide was commonly observed on all Au(*hkl*) surfaces. The ORR on Au(*hkl*) in alkaline solution represents one particularly interesting example of a structure-sensitive reaction. In independent studies by two research groups [104, 105], the Au(001) surface in alkaline solution was found to be the most active of the low-index surfaces (by nearly four orders of magnitude) and was reported as even more active than polycrystalline platinum under the same experimental conditions. In spite of efforts by many research groups to determine the origin of this catalytic activity,

the reason for this remarkable effect remains unclear. It was reported [104] that the unique catalytic activity of the Au(001) surface only appears in the potential region in which  $OH_{ad}$  is adsorbed on the surface, see Fig. 32. Figure 32 also shows that at potentials negative of the potential for Au(001)- $OH_{ad}$  formation, the surface provides only  $2e^-$  reduction. On the basis of this evidence, it was proposed that the change in the catalytic activity of the Au(001) surface from  $4e^-$  to  $2e^-$  reduction was due to the existence of a AuOH layer. On the other hand, it was also proposed that the higher activity of Au(001) for the ORR is related to the dissociative adsorption of  $HO_2^-$  anions on the four-fold symmetry sites that occur only on the (001)-(1 × 1) surface [105]. Consequently, the change in the oxygen-reduction pathway from  $4e^-$  to  $2e^-$  reduction is due to potential-induced reconstruction of the (1 × 1) surface to a structure similar to the “hex” reconstruction found in UHV. The results in Sect. 4.1.3.2.1 (Fig. 7) indicate that the  $(1 \times 1) \leftrightarrow$  “hex” reconstruction is not the dominant mechanism for this change in reaction pathway since the transition in reduction kinetics occurs in a much narrower potential range than the  $(1 \times 1) \leftrightarrow$  “hex” transition. Furthermore, the time constant for the two transitions differs by approximately two orders of magnitude, with the structural transition being the slower.

#### 4.1.5.5 Summary of the ORR

Just as in heterogeneous catalysis, the ultimate challenge in electrocatalysis is to relate the microscopic details of adsorbed states of reaction intermediates to the macroscopic measurement of kinetic rates. There are many strategies that may be employed in this endeavor. Here we develop the relation between

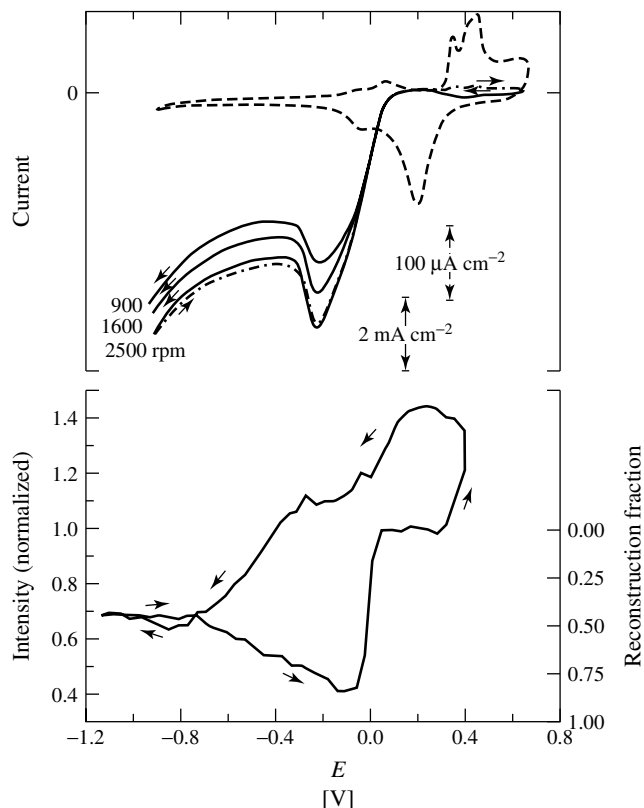


**Fig. 32** Top: Polarization curves for the ORR on Au(001) in 0.1 M KOH at different rotation rates. The dashed line shows the CV. Bottom: Corresponding changes in the X-ray scattering signal at (0, 0, 2.3) where the scattered intensity depends on the presence of the surface reconstruction, that is, deconstruction leads to an increase in the intensity. The fraction of the surface that is reconstructed is shown on the right-hand axis.

the kinetics of the ORR and two factors: a chemical-dependent part,  $\Delta G_{\theta}^* = \Delta G_0^* + \gamma \Delta G_{\Theta}^0 \Theta_{\text{ad}}$ , and the preexponential  $(1 - \Theta_{\text{ad}})$  term. The first term is mainly determined by the nature of interaction of  $\text{O}_2$  molecules and reaction intermediates with the electrode surface, that is, by the  $\text{M}-\text{O}_2$  energetics and the ability of the substrate (M) to break the  $\text{O}-\text{O}$  bond. The preexponential  $(1 - \Theta_{\text{ad}})$  term is, however, mainly determined by the interplay between the electronic properties

(the work function, for example, the  $pzc$ ) of the substrate and the match between the surface atomic geometry of the single crystals and the geometry of adsorbing spectator species ( $\text{H}_{\text{upd}}$ ,  $\text{OH}_{\text{ad}}$ , and anions), that is, by the ability of the surface to adsorb molecular  $\text{O}_2$ . In the following discussion, these two terms are used to analyze the difference in the kinetics of the ORR on  $\text{Pt}(hkl)$ ,  $\text{Au}(hkl)$ , and  $\text{Cu}(hkl)$  and the structure sensitivity of the ORR on  $\text{M}(hkl)$  surfaces. One should keep in mind,

however, that a compensation effect exists between the preexponential factor and the heat of activation.

Given that the energetics of  $O_2$  molecules and intermediates on  $Pt(hkl)$ ,  $Au(hkl)$ , and  $Cu(hkl)$  in solution is not known, the  $\Delta G_\theta^* = \Delta G_0^* + \gamma \Delta G_0^0 \Theta_{ad}$  term cannot be determined on these electrodes. However, one can use the values of thermodynamic functions that are obtained from UHV measurements and test them in the electrochemical system for consistency. Two general features in the energetics of the  $O_2$  interaction clearly emerge from the UHV studies: (i) although the heat of adsorption of oxygen increases in the order  $Pt(hkl) < Cu(hkl) \ll Au(hkl)$ , the heats of  $O_2$  adsorption are relatively insensitive to the surface structure of the substrate [107, 108]; and (ii) the energetics of interaction are strongly coverage dependent [23]. The coverage dependence on single-crystal surfaces arises primarily from adsorbate–adsorbate repulsive interactions rather than surface heterogeneity [109]. As we demonstrate below, on the basis of “UHV-like” arguments for the M- $O_2$  energetics and the potential-dependent surface coverage of spectator species (from Sects. 4.1.3 and 4.1.4), one can develop a very reasonable relation between the kinetics of the ORR and the parameters  $\Delta G_0^*$ , and  $(1 - \Theta_{ad})$ .

We first discuss the structure sensitivity on the same metal substrates. The fact that the kinetics of the ORR on  $Pt(hkl)$  (Figs. 28 and 29),  $Cu(hkl)$  (Fig. 31), and  $Au(hkl)$  (Fig. 32) are orders of magnitude lower in acid solutions containing strongly adsorbing anions indicates that the structure sensitivity is due primarily to the structure-sensitive adsorption of spectator species, for example, by the  $(1 - \Theta_{ad})$  term. The  $(1 - \Theta_{ad})$  term is determined by both the  $pzc$  of the substrate as well as the match

between surface atomic geometry of the single crystals and the geometry of adsorbing spectator species. The importance of the  $pzc$  in controlling the  $(1 - \Theta_{ad})$  term is obvious from the  $Pt(hkl)$ – $Cl_{ad}$  system in which, due to the high anodic  $pzc$  of  $Pt(111)$  and the ability of this surface to desorb  $Cl_{ad}$  at the most positive potentials, this surface is the most active for the ORR. In sulfuric acid solution, however, an exceptionally large deactivation is observed at the  $Pt(111)$  surface. For this system, the  $(1 - \Theta_{ad})$  term is affected more with the symmetry factors than with the  $pzc$  of the surface; for example, due the strong adsorption of the (bi)sulfate anion, which is induced by the geometrical match between the hexagonal (111) surface and the  $C_{3v}$  geometry of the oxygen atoms of the sulfate anions, the ORR is strongly deactivated on the  $Pt(111)$  surface. The exceptionally low activity of  $Cu(111)$  and  $Au(111)$  in sulfuric acid solution is also related to the strong interaction of bisulfate anions with the (111) surface atoms.

The most direct probe of the  $pzc$  effects in the kinetics of the ORR can be obtained by comparing the catalytic activities of  $Pt(hkl)$  versus  $Cu(hkl)$ . On both surfaces, in solution free of strongly adsorbing anions, the reaction mechanism is the same (the  $4e^-$  reduction), the formation of peroxide appears to precede the breaking of the O–O bond [91]. Owing to the relatively high energy of adsorption of oxygen on  $Cu$  (*ca.*  $200 \text{ kJ mol}^{-1}$  on  $Cu$  vs.  $350 \text{ kJ mol}^{-1}$  on  $Pt$  [23]), the exceptionally large difference in catalytic activity between  $Cu$  and  $Pt$  cannot be explained by a difference in the isosteric heat of adsorption of  $O_2$  on these two surfaces. We propose, therefore, that the main contribution to the deactivation of the ORR on  $Cu(hkl)$  is due to the  $(1 - \Theta_{ad})$  term, which is controlled by the low

$pzc$  of Cu, leading to high coverages of oxide/anions at low overpotentials and the inability of Cu to adsorb  $O_2$  molecules. It is interesting that although the  $pzc$  of Au is much higher than on Cu, Au(*hkl*) is catalytically inactive in acid solution and the ORR proceeds as a  $2e^-$  process [105]. This can be attributed to the very low heat of adsorption of  $O_2$  on Au, which is well established in UHV [23]. Therefore, in acid solutions, the main difference in the ORR pathway on Pt(*hkl*) and Cu(*hkl*) (*ca.*  $4e^-$  reduction) versus Au(*hkl*) ( $2e^-$  reduction) lies rather in the chemical  $\Delta G_\theta^*$  term than the  $(1 - \Theta_{ad})$  term. While the  $\Delta G_\theta^*$  term is determining the reaction pathway, the  $(1 - \Theta_{ad})$  term is determining the availability of Au sites for  $O_2$  adsorption. Because of the high  $pzc$  of Au, desorption of anions/oxides occurs at more positive potentials than on Cu and, in turn, the *onset* potential for the ORR is more positive on Au(*hkl*) than on Cu(*hkl*) surfaces. What is influencing the electrocatalytic activity of Au(001) in alkaline solution is, however, still a mystery. Further work is needed in order to understand the ability of the Au(001) surface to break the O–O bond at such low overpotentials.

#### 4.6

#### Conclusion

In this chapter, we have attempted to show that in situ structural analysis techniques and traditional electrochemical measurements can be combined to obtain detailed insight into electrochemical reactions on single-crystal electrode surfaces. Thus, it is possible to establish a link between macroscopic electrochemical phenomena and atomic-scale surface structures. X-ray diffraction is a relatively new technique that takes advantage of the high brightness of synchrotron radiation sources to

attain surface sensitivity. We have highlighted the applicability of this technique to studies of the electrochemical interface, in particular, with the ability to probe changes in the surface atomic structure as the electrode potential is changed and different reaction conditions prevail. The X-ray technique is particularly powerful when combined with RRDE measurements because RRDE can supply element-specific adsorption isotherms, which are key to the interpretation of the X-ray data. In turn, structural results obtained from X-ray diffraction measurements can give vital insight into the kinetics of electrochemical reactions, such as the oxidation–reduction reaction, which are crucially dependent on the exact nature of the available adsorption sites on an electrode surface.

Several future developments of the experimental techniques and materials are anticipated. For example, the study of bimetallic crystals relevant to applications in electrocatalysis, nanoparticle systems, and further applications of spectroscopic techniques in combination with X-ray scattering studies. The work highlighted in this chapter lays the foundation for these developments.

#### Acknowledgment

This work was supported by the Director, Office of Energy Research, Materials Sciences Division (MSD) of the U.S. Department of Energy (DOE) under contract no. DE-AC03-76SF00098. Research was carried out in part at SSRL, which is funded by the Division of Chemical Sciences (DCS), U.S. DOE and at the XMaS UK-CRG beamline at the ESRF, Grenoble. CAL is grateful for the support of an EPSRC Advanced Research Fellowship.



## References

1. R. Feidenhans'l, *Surf. Sci. Rep.* **1989**, 10, 105.
2. P. H. Fuoss, S. Brennan, *Annu. Rev. Mater. Sci.* **1990**, 20, 365.
3. I. K. Robinson, D. J. Tweet, *Rep. Prog. Phys.* **1992**, 55, 599.
4. I. K. Robinson, *Phys. Rev. B* **1986**, 33, 3830.
5. B. E. Warren, *X-ray Diffraction*, Dover Publications, New York, 1990.
6. M. G. Samant, M. F. Toney, G. L. Borges et al., *J. Phys. Chem.* **1988**, 92, 220.
7. B. M. Ocko, J. Wang, A. Davenport et al., *Phys. Rev. Lett.* **1990**, 65, 1466.
8. I. M. Tidswell, N. M. Markovic, C. A. Lucas et al., *Phys. Rev. B* **1993**, 47, 16 542.
9. C. A. Lucas, *J. Phys. D: Appl. Phys.* **1999**, 32, A198.
10. M. F. Toney, D. G. Wiesler, *Acta Crystallogr., Sect. A* **1993**, 49, 624.
11. C. A. Lucas, N. M. Markovic, P. N. Ross, *Surf. Sci.* **2000**, 448, 65.
12. C. A. Lucas, N. M. Markovic, B. N. Grgur et al., *Surf. Sci.* **2000**, 448, 77.
13. E. D. Specht, F. J. Walker, *Phys. Rev. B* **1993**, 47, 13 743.
14. H. Stragier, J. O. Cross, J. J. Rehr et al., *Phys. Rev. Lett.* **1992**, 69, 3064.
15. W. J. Albery, M. L. Hitchman, *Ring-Disc Electrodes*, Clarendon Press, Oxford, 1971.
16. A. J. Bard, L. R. Faulkner, *Electrochemical Methods*, John Wiley & Sons, New York, 1980.
17. D. Kolb, *Prog. Surf. Sci.* **1996**, 51, 109.
18. J. Clavilier, *J. Electroanal. Chem.* **1980**, 107, 211.
19. M. Samant, M. Toney, G. Borges et al., *Surf. Sci.* **1988**, 193, L29.
20. Y. S. Chu, I. K. Robinson, A. A. Gewirth, *Phys. Rev. B* **1997**, 55, 7945.
21. O. M. Magnussen, J. Scherer, B. M. Ocko et al., *J. Phys. Chem.* **2000**, 104, 1222.
22. G. A. Somorjai, M. A. Van Hove, *Prog. Surf. Sci.* **1989**, 30, 201.
23. G. A. Somorjai, *Introduction to Surface Chemistry and Catalysis*, John Wiley & Sons, New York, 1993.
24. P. A. Thiel, P. J. Estrup in *CRC Handbook of Surface Imaging and Visualization* (Ed.: A. T. Hubbard), CRC Press, Boca Raton, Fla., 1995.
25. R. I. Masel, *Principles of Adsorption and Reaction on Solid Surfaces*, John Wiley & Sons, New York, 1996.
26. M. A. Van Hove, K. Hermann, P. R. Watson et al., *Surf. Rev. Lett.* **1999**, 6, 805.
27. A. R. Sandy, S. G. J. Mochrie, D. M. Zehner et al., *Phys. Rev. B* **1991**, 43, 4667.
28. K.-M. Ho, K. P. Bohnen, *Phys. Rev. Lett.* **1987**, 59, 1833.
29. I. K. Robinson, P. J. Eng, C. Romainczyk et al., *Phys. Rev. B* **1993**, 47, 10 700.
30. B. M. Ocko, D. Gibbs, K. G. Huang et al., *Phys. Rev. B* **1991**, 44, 6429.
31. D. Gibbs, B. M. Ocko, D. M. Zehner et al., *Phys. Rev. B* **1990**, 42, 7330.
32. N. Takeuchi, C. T. Chan, K. M. Ho, *Phys. Rev. Lett.* **1989**, 63, 1273.
33. R. M. Ishikawa, A. T. Hubbard, *J. Electroanal. Chem.* **1976**, 69, 317.
34. E. Yeager, W. E. O'Grady, M. Woo, *J. Electrochem. Soc.* **1978**, 125, 348.
35. I. M. Tidswell, N. M. Markovic, P. N. Ross, *J. Electroanal. Chem.* **1994**, 376, 119.
36. J. Wang, B. M. Ocko, A. J. Davenport et al., *Science* **1992**, 255, 1416.
37. K. P. Bohnen, D. M. Kolb, *Surf. Sci.* **1998**, 407, L629.
38. F. T. Wagner, P. N. Ross, *J. Electroanal. Chem.* **1983**, 150, 141.
39. M. S. Zei, N. Batina, D. M. Kolb, *Surf. Sci.* **1994**, 306, L519.
40. I. M. Tidswell, N. M. Markovic, P. N. Ross, *Phys. Rev. Lett.* **1993**, 71, 1601.
41. C. A. Lucas, N. M. Markovic, P. N. Ross, *Phys. Rev. Lett.* **1996**, 77, 4922.
42. N. M. Markovic, B. N. Grgur, C. A. Lucas et al., *Surf. Sci.* **1997**, 384, L805.
43. I. K. Robinson, Y. Ku, L. C. Feldman, *Phys. Rev. B* **1984**, 29, 4762.
44. T. Gritsch, D. Coulman, R. J. Behm, G. Ertl, *Phys. Rev. Lett.* **1989**, 63, 1086.
45. O. M. Magnussen, J. Wiechers, R. J. Behm, *Surf. Sci.* **1993**, 289, 139.
46. B. M. Ocko, G. Helgeson, B. Schardt et al., *Phys. Rev. Lett.* **1992**, 69, 3350.
47. C. L. Fu, K. M. Ho, *Phys. Rev. Lett.* **1989**, 63, 1617.
48. P. J. Feibelman, *Surf. Sci.* **1996**, 360, 297.
49. M. F. Toney, J. N. Howard, J. Richer et al., *Nature* **1994**, 368, 444.
50. M. F. Toney, J. N. Howard, J. Richer et al., *Surf. Sci.* **1995**, 335, 326.

51. R. J. Nichols, T. Nouar, C. A. Lucas, W. Haiss, W. A. Hofer, *Surf. Sci.* **2002**, 513, 263–271.
52. E. Vlieg, I. K. Robinson and K. Kern, *Surf. Sci.* **1990**, 233, 248.
53. M. W. Finnis, V. Heine, *J. Phys. F* **1974**, 4, L37.
54. E. Kirsten et al., *Surf. Sci.* **1990**, 231, L183.
55. O. M. Magnussen, B. M. Ocko, J. X. Wang et al., *J. Phys. Chem.* **1996**, 100, 5500.
56. B. M. Ocko, O. M. Magnussen, J. X. Wang et al., *Physica B* **1996**, 221, 238.
57. B. M. Ocko, O. M. Magnussen, J. X. Wang et al., *Phys. Rev. B* **1996**, 53, R7654.
58. E. Bertel, E. P. Netzer, *Surf. Sci.* **1980**, 97, 409.
59. H. A. Gasteiger, N. M. Markovic, P. N. Ross, *Langmuir* **1996**, 12, 1414.
60. C. A. Lucas, N. M. Markovic, P. N. Ross, *Surf. Sci.* **1996**, 340, L949.
61. C. A. Lucas, N. M. Markovic, P. N. Ross, *Phys. Rev. B* **1997**, 55, 7964.
62. P. Zeppenfeld, U. Becher, K. Kern et al., *Phys. Rev. B* **1992**, 45, 5179.
63. N. M. Markovic, C. A. Lucas, H. A. Gasteiger et al., *Surf. Sci.* **1996**, 365, 229.
64. A. M. Bittner, B. Wintterline, B. Beran et al., *Surf. Sci.* **2001**, 335, 291.
65. D. M. Kolb in *Advances in Electrochemistry and Electrochemical Engineering* (Eds.: H. Gerischer, C. W. Tobias), John Wiley & Sons, New York, 1978.
66. R. R. Adzic in *Advances in Electrochemistry and Electrochemical Engineering* (Eds.: H. Gerischer, C. W. Tobias), John Wiley & Sons, New York, 1984.
67. M. F. Toney, J. N. Howard, J. Richer et al., *Phys. Rev. Lett.* **1995**, 75, 4472.
68. Z. Shi, J. Lipkowski, *J. Electroanal. Chem.* **1994**, 364, 289.
69. O. M. Magnussen, J. Hotlos, R. J. Nichols et al., *Phys. Rev. Lett.* **1990**, 64, 2929.
70. J. H. White, H. D. Abruna, *J. Phys. Chem.* **1990**, 94, 894.
71. R. Michaelis, M. S. Zei, R. S. Zhai et al., *J. Electroanal. Chem.* **1992**, 339, 299.
72. R. Durand, R. Faure, D. Aberdam et al., *Electrochim. Acta* **1992**, 37, 1977.
73. N. Markovic, P. N. Ross, *Langmuir* **1993**, 9, 580.
74. N. M. Markovic, H. A. Gasteiger, P. N. Ross, *Langmuir* **1995**, 11, 4098.
75. R. Gomez, H. S. Yee, G. M. Bommarito et al., *Surf. Sci.* **1995**, 335, 101.
76. T. Abe, G. M. Swain, K. Sashikata et al., *J. Electroanal. Chem.* **1995**, 382, 73.
77. N. M. Markovic, C. Lucas, H. A. Gasteiger et al., *Surf. Sci.* **1997**, 372, 239.
78. A. C. Finnefrock, L. J. Buller, K. L. Ringland et al., *J. Am. Chem. Soc.* **1997**, 119, 11703.
79. N. M. Markovic, H. Gasteiger, C. Lucas et al., *Surf. Sci.* **1995**, 335, 91.
80. I. M. Tidswell, C. A. Lucas, N. M. Markovic et al., *Phys. Rev. B* **1995**, 51, 10205.
81. C. A. Lucas, N. M. Markovic, P. N. Ross, *Phys. Rev. B* **1997**, 56, 3651.
82. C. A. Lucas, N. M. Markovic, P. N. Ross, *Phys. Rev. B* **1998**, 57, 13184.
83. S. Wu, Z. Shi, J. Lipkowski et al., *J. Phys. Chem.* **1997**, 101, 10310.
84. K. Kinoshita, *Electrochemical Oxygen Technology*, John Wiley & Sons, New York, 1992.
85. H. Wroblowa, Y. C. Pan, J. Razumney, *J. Electroanal. Chem.* **1976**, 69, 195.
86. M. R. Tarasevich, A. Sadkowski, E. Yeager in *Comprehensive Treatise in Electrochemistry* (Eds.: J. O. M. Bockris, B. E. Conway, E. Yeager et al.), Plenum Press, New York, 1983.
87. N. M. Markovic, H. A. Gasteiger, B. N. Grgur et al., *J. Electroanal. Chem.* **1999**, 467, 157.
88. F. El Kadiri, R. Faure, R. Durand, *J. Electroanal. Chem.* **1991**, 301, 177.
89. N. M. Markovic, R. R. Adzic, B. D. Cahan et al., *J. Electroanal. Chem.* **1994**, 377, 249.
90. N. M. Markovic, H. A. Gasteiger, P. N. Ross, *J. Phys. Chem.* **1995**, 99, 3411.
91. N. M. Markovic, H. A. Gasteiger, P. N. Ross, *J. Phys. Chem.* **1996**, 100, 6715.
92. V. Stamenkovic, N. M. Markovic, P. N. Ross Jr, *J. Electroanal. Chem.* **2000**, 500, 44.
93. B. N. Grgur, N. M. Markovic, P. N. Ross Jr, *Can. J. Chem.* **1997**, 75, 1465.
94. T. J. Schmidt, B. N. Grgur, N. M. Markovic et al., *J. Electroanal. Chem.* **2001**, 500, 36.
95. A. Damjanovic in *Comprehensive Treatise in Electrochemistry* (Eds.: J. O. M. Bockris, B. E. Conway), Plenum Press, New York, 1969.
96. M. R. Tarasevich, *Electrochimica* **1973**, 9, 578.

97. N. M. Markovic, P. N. Ross Jr in *Interfacial Electrochemistry-Theory, Experiments and Applications* (Ed.: A. Wieckowski), Marcel Dekker, New York, 1999.
98. N. M. Markovic, B. N. Grgur, C. A. Lucas, P. N. Ross, *Electrochim. Acta.* **1998**, *44*, 1009–1017.
99. G. Kokkinidis, D. Jannakoudakis, *J. Electroanal. Chem.* **1984**, *162*, 163.
100. S. A. S. Machado, A. A. Tanaka, E. R. Gonzales, *Electrochim. Acta* **1991**, *36*, 1325.
101. G. M. Brisard, N. Bertrand, P. N. Ross et al., *J. Electroanal. Chem.* **2000**, *480*, 219.
102. M. Wilms, P. Broekmann, C. Stuhlmann et al., *Surf. Sci.* **1998**, *416*, 121.
103. W. H. Li, R. J. Nichols, *J. Electroanal. Chem.* **1998**, *456*, 153.
104. R. R. Adzic, N. M. Markovic, V. B. Vesovic, *J. Electroanal. Chem.* **1984**, *165*, 105, 121.
105. J. D. E. McIntyre, Peck in *The Physics and Chemistry of Electrocatalysis* (Eds.: J. D. E. McIntyre, M. J. Weaver, E. Yeager), The Electrochemical Society, Pennington, N.J., 1984.
106. R. R. Adzic in *Electrocatalysis* (Eds.: J. Lipkowski, P. N. Ross), Wiley-VCH, New York, 1998.
107. G. Ertl, N. Neumann, K. M. Streit, *Surf. Sci.* **1977**, *64*, 393.
108. P. A. Thiel, R. J. Behm, P. R. Norton et al., *J. Chem. Phys.* **1983**, *78*, 7448.
109. W. T. Lee, L. Ford, P. Blowers et al., *Surf. Sci.* **1998**, *416*, 141.

## 4.2

**Theoretical Aspects Associated with Charge-transfer Kinetics across Interfaces between Two Immiscible Electrolyte Solutions**

*David J. Fermín, Henrik Jensen, and Hubert H. Girault*  
*Ecole Polytechnique Fédérale de Lausanne,*  
*Lausanne, Switzerland*

## 4.2.1

**Introduction and Scope**

Charge-transfer reactions at interfaces between two immiscible electrolyte solutions (ITIES) have been the subject of a tremendous amount of research from an experimental and theoretical point of view in the last thirty years. The relevance of this kind of molecular interfaces has been addressed in various review articles and books, expanding from fundamental charge transfer at interfaces to drug delivery in biological systems, ion-selective electrodes, sensors, artificial photosynthesis, and so forth [1–5]. The scope of this chapter is to review the theoretical models developed in recent years for rationalizing the kinetic behavior of electron and ion transfer across ITIES. This chapter does not intend to provide an exhaustive account of experimental developments and specific models but an overview of the more general theoretical descriptions in a critical fashion. In doing so, we have made an attempt to present the basic description of each model employing a homogenized terminology.

The discussions will be mostly centered on ideal systems in which the reactants are considered as particles with given redox properties and solvation energies present at the interfacial region between two dielectric media. In the case of electron transfer (ET), we shall concentrate

on models within the framework of the transition state theory. On the other hand, ion transfer will be examined not only from the viewpoint of charge transfer in polar media but also in terms of ion transport in heterogeneous systems.

## 4.2.2

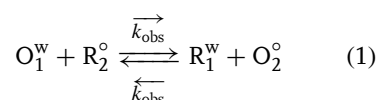
**Heterogeneous Electron Transfer across ITIES**

ET reactions across a liquid|liquid junction are undergoing a renaissance as a result of the increasing interest in molecular electrochemistry. The pioneering work by Samec [6, 7], Kharkats [8], Girault and Schiffrin [9], and later by Marcus [10–12] established fundamental aspects that experimental evaluation is yet to ascertain. For instance, the dependence of the bimolecular ET rate constant on the Galvani potential difference and the distance separating the redox species are among the most controversial issues in this area. Throughout the 1980s and early 1990s, few experimental works were reported on the dynamics of ET as probed by cyclic voltammetry and electrochemical impedance spectroscopy employing four-electrode potentiostats [13–21]. However, the analysis of these data was rather limited because of the primitive knowledge of the structure and potential distribution across ITIES. More recently, the introduction of spectroelectrochemical techniques, Scanning Electrochemical Microscopy (SECM), and dynamic photoelectrochemistry has provided new insights into the correlation between structure and reactivity at these interfaces. As a result, not only has our understanding of the fundamental properties of ITIES significantly increased but we are also able to envisage novel potential applications as well as rationalize important aspects concerning life-sustaining redox

biological processes [1]. In this section, we shall highlight fundamental aspects in relation to the energetic and dynamics of heterogeneous ET bringing about some relevant examples.

#### 4.2.2.1 Thermodynamic Aspects in Connection to Heterogeneous ET

The thermodynamic driving force for an ET process across liquid|liquid junctions is determined by the difference in the redox potential of both species as well as the Galvani potential difference. Considering the general reaction



the equality in the electrochemical potential determines that the ratio of the activities of the redox species is linked to the Galvani potential difference by

$$\Delta_o^{\text{w}}\phi = \Delta_o^{\text{w}}\phi_{\text{et}}' - \frac{RT}{nF} \ln \left( \frac{c_{\text{O}_1}^{\text{w}} c_{\text{R}_2}^{\circ}}{c_{\text{R}_1}^{\text{w}} c_{\text{O}_2}^{\circ}} \right) \quad (2)$$

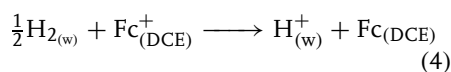
where the formal potential,  $\Delta_o^{\text{w}}\phi_{\text{et}}'$ , is determined by

$$\Delta_o^{\text{w}}\phi_{\text{et}}' = \left[ E_{\text{O}_2/\text{R}_2}^{\circ, \circ} \right]_{\text{SHE}} - \left[ E_{\text{O}_1/\text{R}_1}^{\circ, \text{w}} \right]_{\text{SHE}} \quad (3)$$

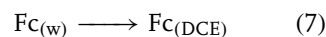
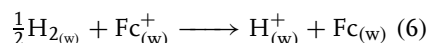
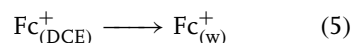
By definition, both redox potentials in Eq. (3) have to be referred to a common reference potential, in this case that of the standard hydrogen electrode (SHE). Obviously, some thermodynamic assumptions have to be introduced in order to evaluate  $[E_{\text{O}_2/\text{R}_2}^{\circ, \circ}]_{\text{SHE}}$ , which denotes the formal redox potential of a redox couple in the organic phase versus the SHE in water.

A simple approach to this problem involves the estimation of  $[E_{\text{O}_2/\text{R}_2}^{\circ, \circ}]_{\text{SHE}}$  for a given redox couple that can be further used as a reference potential in the organic phase. For instance, the redox couple

ferricenium/ferrocene ( $\text{Fc}^+/\text{Fc}$ ) has been employed in numerous studies in organic solvents as a reference potential [22]. In the case of the water|DCE junction, the following reaction can be envisaged:



where the subscript “w” and “DCE” correspond to the water and 1,2-dichloroethane electrolyte phases, respectively. In order to estimate the formal Gibbs energy for Reaction (4), the following thermodynamic cycle can be introduced:



From Eqs. (4 to 7), it follows that

$$\left[ E_{\text{Fc}^+/\text{Fc}}^{\circ, \circ} \right]_{\text{SHE}} = \Delta_o^{\text{w}}\phi_{\text{Fc}^+}' + \left[ E_{\text{Fc}^+/\text{Fc}}^{\circ, \text{w}} \right]_{\text{SHE}} - \frac{\Delta G_{\text{Fc}}^{\text{w} \rightarrow \circ}}{F} \quad (8)$$

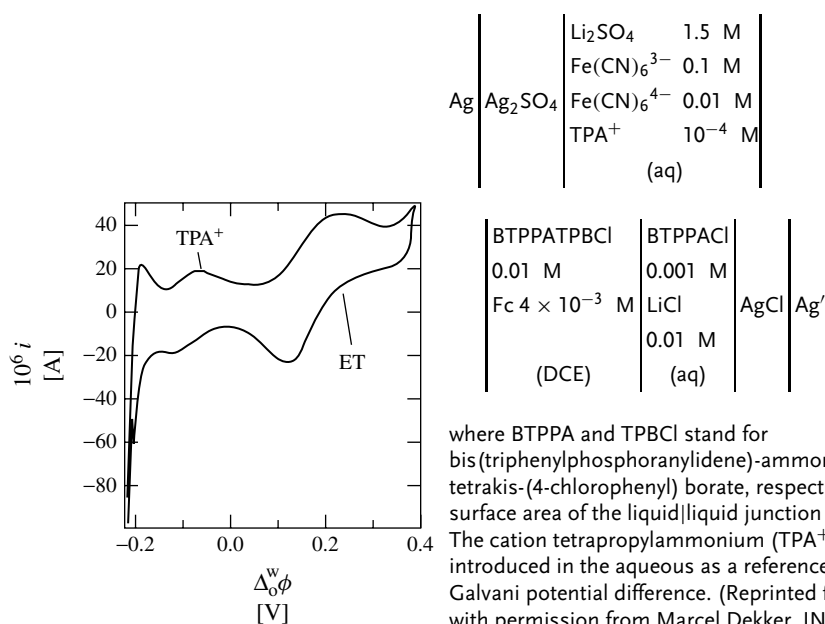
where the three terms correspond to the formal transfer potential of ferricenium, the formal redox potential of  $\text{Fc}^+/\text{Fc}$  in water versus the SHE, and the Gibbs energy associated with the partition of ferrocene between the two phases, respectively. Independent evaluation of the three constants provided  $E_{\text{Fc}^+/\text{Fc}}^{\circ, \circ} = 0.638 \pm 0.020$  V versus SHE [5]. Taking this value as a reference, the redox potential of several couples in DCE often found in the literature can be summarized as exemplified in Table 1. These data allow predicting whether the formal ET potential as defined by Eq. (3) is effectively located within the ideally polarizable window. This condition, also referred to as redox potential matching, is essential for studying ET processes at ITIES under potentiostatic control.

**Tab. 1** Formal redox potential versus SHE in water for species often employed in electrochemical studies at the water|1,2-dichloroethane interface

Redox couple	$[E^{o',DCE}]_{SHE}/V$
Decamethylferrocene <sup>+/0</sup>	0.07
Dimethylferrocene <sup>+/0</sup>	0.55
Diferrocenylethane <sup>+/0</sup>	0.55
Butylferrocene <sup>+/0</sup>	0.56
Ferrocene <sup>+/0</sup>	0.64
Trianisilamine <sup>+/0</sup>	0.76
Tri(bromophenyl)amine <sup>+/0</sup>	1.10
Tetraphenylborate <sup>0/-</sup>	0.93
Tetrakis(4-chlorophenyl)-borate <sup>0/-</sup>	1.15
Tetracyanoquinodimethane <sup>0/-</sup>	-0.29
Chloranil <sup>0/-</sup>	-0.17
Benzoquinone <sup>0/-</sup>	-0.43

The condition of redox potential matching is illustrated in Fig. 1. Considering the concentration ratio of ferri/ferrocyanide indicated in the cell representation and  $E_{Fe(CN)_6^{3-}/Fe(CN)_6^{4-}}^{o',o}$  as  $0.36 \pm 0.01$  V, the value of  $\Delta_o^w \phi_{et}^{o'}$  in the presence of Fc should be located close to 0.16 V. The cyclic voltammogram features a response with a half-wave transfer potential that coincides with  $\Delta_o^w \phi_{et}^{o'}$ . The signal observed at more negative potentials corresponds to the transfer of tetrapropylammonium employed as internal reference for the estimation of the Galvani potential difference ( $\Delta_o^w \phi_{TPA^+}^{o'} = -0.093$  V [23]). It should be noted that the half-wave potential associated with the ET across the ITIES is not necessarily correlated to the formal

**Fig. 1** Cyclic voltammogram at the water|1,2-dichloroethane interface in the presence of ferricyanide/ferrocyanide couple and ferrocene (Fc) at  $10 \text{ mV s}^{-1}$ . This experiment was performed with a four-electrode potentiostat, while the electrochemical cell can be represented as

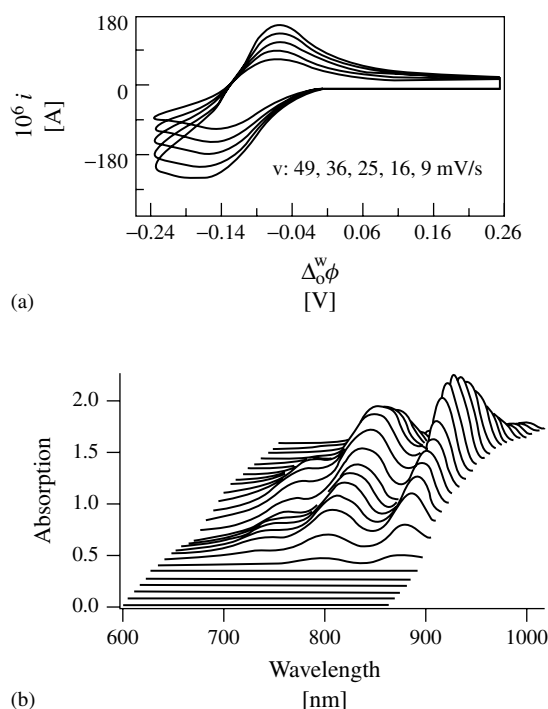


ET potential. This process involves the diffusion of four species, consequently, if the concentration of the reactants in both phases is similar, then rather large peak-to-peak separations could be observed [24]. In the particular case of Fig. 1, the redox couple in the aqueous phase is largely in excess with respect to the organic phase, therefore its concentration can be taken as constant and the ET rate is only controlled by the diffusion of tetracyanoquinodimethane (TCNQ). Under these conditions, commonly referred to as the constant composition approximation, the aqueous phase behaves as a "solid electrode" with the Fermi level defined by the electrochemical potential of the ferri/ferrocyanide couple.

Another well-studied redox system at liquid|liquid interfaces involves the electron acceptor TCNQ [14, 15, 25, 26]. Cyclic

voltammograms obtained in the presence of an excess of ferri/ferrocyanide are exemplified in Fig. 2(a). As expected for a quasi-reversible ET process, the peak current increases linearly with the square root of the scan rate. The spectral changes obtained in situ by Total Internal Reflection from the DCE phase are also contrasted in Fig. 2(b) as a function of the Galvani potential difference. The spectra evolution shows the bands associated with the radical  $\text{TCNQ}^{\cdot-}$  generated from the heterogeneous ET reaction. Indeed, the differential spectroscopic signal at 670 nm exhibits the same potential dependence of the current [26]. This close correlation between electrochemical and spectroscopic behavior indicates that the dynamic of ET can be evaluated by both approaches. Furthermore, consistent data for this system has also been gathered employing

**Fig. 2** Cyclic voltammograms of the heterogeneous reduction of tetracyanoquinodimethane (TCNQ) by the ferricyanide/ferrocyanide couple across the water|DCE interface at various scan rates (a). The composition of the electrochemical cell is as in Fig. 1 but with a ratio 0.01/0.4 M  $\text{Fe}(\text{CN})_6^{3-}/\text{Fe}(\text{CN})_6^{4-}$  and  $6 \times 10^{-4}$  M TCNQ in DCE. Absorption spectra obtained in total internal reflection from the DCE phase as the potential is swept from 0.190 to 0.260 V, with a difference 40 mV between each spectrum (b). The spectra show the main features of the radical  $\text{TCNQ}^{\cdot-}$  as the potential is swept toward the reduction potential. (Fig. 2a was reprinted from Ref. [25] with permission from Royal Society of Chemistry. Fig. 2b was reprinted from Ref. [26] with permission from Elsevier Science.)



techniques based on SECM at nonpolarizable interfaces [27, 28]. Consequently, we shall adopt this system as an example for some of the discussions in connection to fundamental aspects on ET.

#### 4.2.2.2 Electron-transfer Kinetics

As in any interfacial redox process, the rate of heterogenous ET across ITIES is determined by the interfacial concentration of the reactants and the phenomenological bimolecular ET rate constant ( $k_{\text{obs}}$ ). Expressions concerning the mass transport of species involved in the redox processes have been addressed for a variety of geometries, for example, planar diffusion [24], spherical diffusion at microinterfaces [29], as well as for “approach curves” familiar from techniques based on SECM [30–35]. In this section, we shall concentrate instead on the physical aspects underlying the rate constant of heterogeneous ET. In particular, the dependence of  $k_{\text{obs}}$  on the thermodynamic driving force as well as the nature of the activation energy will be highlighted.

**4.2.2.2.1 The Phenomenological Butler–Volmer Expression** Considering symmetric energy surfaces for the initial and final states of the reaction described in Eq. (1), the activation energy will be affected by a fraction  $\alpha_{\text{obs}}$  of the Galvani potential difference

$$\Delta G_{\text{act}} = \Delta G_{\text{act,eq}} - \alpha_{\text{obs}}(\Delta_o^w \phi - \Delta_o^w \phi_{\text{eq}}) \quad (9)$$

where  $\Delta G_{\text{act,eq}}$  and  $\Delta_o^w \phi_{\text{eq}}$  correspond to the Gibbs activation energy and the Galvani potential difference at the equilibrium state. The effect on the ET rate constants can be phenomenologically described as

$$\overrightarrow{k}_{\text{obs}} = \overrightarrow{k}_{\text{obs}}^{\circ} \exp\left(\frac{\alpha_{\text{obs}} n F \Delta_o^w \phi}{RT}\right) \quad (10)$$

and

$$\overleftarrow{k}_{\text{obs}} = \overleftarrow{k}_{\text{obs}}^{\circ} \exp\left[-\frac{(1 - \alpha_{\text{obs}}) n F \Delta_o^w \phi}{RT}\right] \quad (11)$$

where the preexponential parameters can be evaluated at the standard potential

$$\begin{aligned} k^{\circ} &= \overrightarrow{k}_{\text{obs}}^{\circ} \exp\left(\frac{\alpha_{\text{obs}} n F \Delta_o^w \phi^{\circ}}{RT}\right) \\ &= \overleftarrow{k}_{\text{obs}}^{\circ} \exp\left[-\frac{(1 - \alpha_{\text{obs}}) n F \Delta_o^w \phi^{\circ}}{RT}\right] \end{aligned} \quad (12)$$

From Eqs. (10 to 12), the faradaic current as a function of the applied potential can be expressed in terms of the concentration of each of the reactants at the respective interfacial reaction planes (position along the  $z$ -axis),

$$\begin{aligned} I &= n F A k_{\text{obs}}^{\circ} \left\{ c_{\text{O1}}^w(z_{\text{O1}}) c_{\text{R2}}^{\circ}(z_{\text{R2}}) \right. \\ &\quad \times \exp\left[\frac{\alpha_{\text{obs}} n F (\Delta_o^w \phi - \Delta_o^w \phi^{\circ})}{RT}\right] \Big\} \\ &\quad - n F A k_{\text{obs}}^{\circ} \left\{ c_{\text{R1}}^w(z_{\text{R1}}) c_{\text{O2}}^{\circ}(z_{\text{O2}}) \right. \\ &\quad \times \exp\left[\frac{-(1 - \alpha_{\text{obs}}) n F (\Delta_o^w \phi - \Delta_o^w \phi^{\circ})}{RT}\right] \Big\} \end{aligned} \quad (13)$$

Equation (13) can be rewritten in terms of the overpotential  $\eta = \Delta_o^w \phi - \Delta_o^w \phi_{\text{eq}}$ , as

$$\begin{aligned} I &= I_0 \left\{ \frac{c_{\text{O1}}^w(z_{\text{O1}}) c_{\text{R2}}^{\circ}(z_{\text{R2}})}{c_{\text{O1}}^w c_{\text{R2}}^{\circ}} \right. \\ &\quad \times \exp\left(\frac{\alpha_{\text{obs}} n F \eta}{RT}\right) \\ &\quad - \frac{c_{\text{R1}}^w(z_{\text{R1}}) c_{\text{O2}}^{\circ}(z_{\text{O2}})}{c_{\text{R1}}^w c_{\text{O2}}^{\circ}} \\ &\quad \times \exp\left[\frac{-(1 - \alpha_{\text{obs}}) n F \eta}{RT}\right] \Big\} \end{aligned} \quad (14)$$



where

$$I_0 = nFAk_{\text{obs}}^{\circ} [c_{\text{O1}}^{\text{w}} c_{\text{R2}}^{\circ}]^{1-\alpha_{\text{obs}}} [c_{\text{O1}}^{\text{w}} c_{\text{R2}}^{\circ}]^{\alpha_{\text{obs}}} \quad (15)$$

If we assume that the concentrations at the reaction planes are equal to that in the bulk, Eq. (14) is simplified to the corresponding Butler–Volmer expression for ET at ITIES,

$$I = I_0 \left\{ \exp \left( \frac{\alpha_{\text{obs}} n F \eta}{RT} \right) - \exp \left[ \frac{-(1 - \alpha_{\text{obs}}) n F \eta}{RT} \right] \right\} \quad (16)$$

This simplistic derivation opens up some important questions that we shall address in the next sections. Firstly, the observed ET rate constant needs to be considered in terms of microscopic parameters such as the distance separating the redox species, the adiabatic properties of the systems, and the thermodynamic driving force. If the reactants feature ionic species, the concentration profiles at the interfaces arising from polarization effects can introduce

substantial deviations from Eq. (16). Another parameter to be dealt with from first basis is  $\alpha_{\text{obs}}$ . Does this parameter only reflect the fraction of the Galvani potential difference acting on the  $\Delta G_{\text{act}}$  as indicated in Eq. (9)?

#### 4.2.2.2.2 The Rate Constant of Electron Transfer

We shall commence by assuming that the liquid|liquid interface can be described in terms of a sharp boundary between water and a lower dielectric medium. The single ET process of Eq. (1) involves the approaching of the reactants to the interface as schematically represented in Fig. 3. The observed rate of ET is given by

$$j_{\text{obs}} = k_{\text{obs}} c_{\text{O1}}^{\text{w}} c_{\text{R2}}^{\circ} \quad (17)$$

where  $k_{\text{obs}}$  is the phenomenological bimolecular ET rate constant (units of  $\text{cm}^4 \text{mol}^{-1} \text{s}^{-1}$ ). This rate constant effectively corresponds to an integral over all distance  $l$  and the characteristic angles defining the position of the reactants at the interface (Fig. 3). Following a Marcus

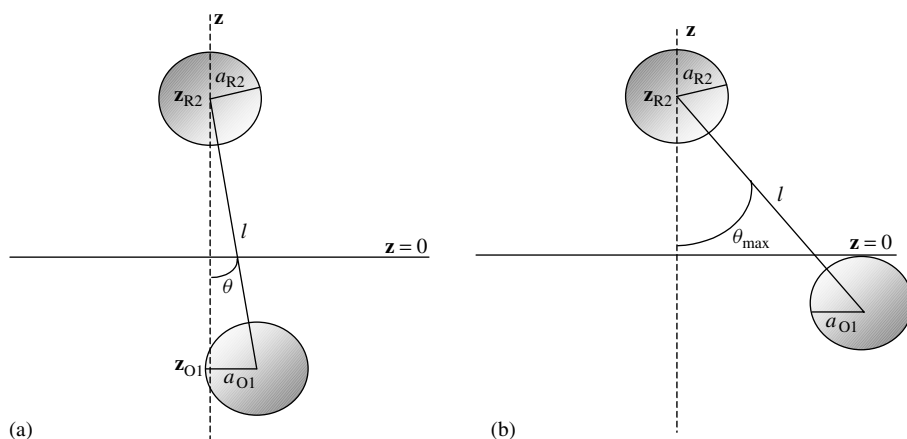


**Fig. 3** (a) Schematic representation of the coordinates for the calculations of the hypervolume as described by Marcus in Ref. [10]. (b) The maximum value of the angle  $\theta$  for a given  $z_{R2}$  and  $l$  arrangement.

type of analysis [7, 9–12],

$$k_{\text{obs}} = \kappa \nu \nu \exp\left(\frac{-\Delta G_{\text{act}}}{k_B T}\right) \quad (18)$$

where  $\kappa$  is the transmission coefficient,  $\nu$  is the frequency of molecular motion, and  $\nu$  is the “volume” per unit of area in which the reactants are separated by a distance  $(l + \Delta l)$ .  $\Delta l$  is defined as the region where the contribution to the total ET is maximized. As discussed later, the activation free energy  $\Delta G_{\text{act}}$  is dependent on the reorganization energy term as well as the work terms associated with approaching reactants and separating the products. If we consider the arrangement depicted in Fig. 3, it follows that [10]

$$\begin{aligned} \nu &= \int_{l=a_{R2}+a_{O1}}^{\infty} \int_{z_0=a_{R2}}^{l-a_{O1}} \int_{\theta=0}^{\theta_{\text{max}}(z_0, l)} \int_{\Phi=0}^{2\pi} l^2 \\ &\quad \times \sin \theta \, d\Phi \, d\theta \, dz_0 \, dl \frac{k(l)}{k(l_{\text{max}})} \\ &= \pi \int_{l=a_{R2}+a_{O1}}^{\infty} (l - a_{R2} - a_{O1})^2 l \\ &\quad \times \frac{k(l) dl}{k(l_{\text{max}})} \end{aligned} \quad (19)$$

where  $\Phi$  corresponds to the angle along the plane of the interface. Assuming that the ions cannot penetrate the phase boundary,  $\theta_{\text{max}}$  can be defined as the maximum angle  $\theta$  obtained for a given value of  $z_1$  and  $l$  as depicted in Fig. 3(b). In Eq. (19), the parameter  $k(l)$  is given by

$$k(l) = \kappa(l) \exp\left[\frac{-\Delta G_{\text{act}}(l)}{k_B T}\right] \quad (20)$$

and  $l_{\text{max}}$  corresponds to the characteristic distance at which the weighting factor  $k(l)$  is maximized. Drawing analogies with the behavior observed for ET in bulk liquids, Marcus suggested that  $k(l)$  can go through a maximum at

a distance close to  $a_{O1} + a_{R2}$ , and exponentially decrease as  $l$  increases for larger distances. Consequently, taking  $k(l)/k(l_{\text{max}}) = \exp[-\beta(l - a_{O1} - a_{R2})]$ , it follows that the integration in Eq. (19) results in

$$\nu = 2\pi(a_{O1} + a_{R2})\beta^{-3} \quad (21)$$

Equation (21) is associated with the limiting case for a sharp phase boundary between both liquids. Marcus also estimated the hypervolume for the case in which both reactants are allowed to penetrate the interfacial region in such a way that their centers can effectively reach the liquid boundary. For such configuration, the limits of the integrations in Eq. (19) are different and  $\nu'$  approaches to

$$\nu' \approx \pi(a_{O1} + a_{R2})^3 \beta^{-1} \quad (22)$$

If we consider that the sum of the ionic radii is of the order of  $10 \text{ \AA}$  and  $\beta = 1 \text{ \AA}^{-1}$ , it can be estimated that the hypervolume, and consequently the rate constant, is approximately two orders of magnitude larger for the case in which the ions are allowed to penetrate the interfacial region.

Marcus proposed that the analysis involving Eqs. (18 to 22) was also valid in the adiabatic limit. Smith and coworkers criticized this point on the basis of the fact that the transmission coefficient exhibits a complex dependent on the distance separating the redox species, and therefore should be considered in the integration step [36]. Let us consider the Landau–Zener transmission coefficient

$$\kappa = \frac{2\zeta}{(1 + \zeta)} \quad (23)$$

where

$$\zeta = 1 - \exp(-2\pi\Gamma) \quad (24)$$

and

$$\Gamma = \frac{|H|^2 \pi^{3/2}}{2\pi \hbar \nu (k_B T \lambda)^{1/2}} \quad (25)$$

where the parameter  $H$  corresponds to electronic coupling matrix element

$$H = H_0 \exp \left[ \frac{-\beta(l - a_{O1} - a_{R2})}{2} \right] \quad (26)$$

and  $\lambda$  is the local reorganization energy. From classical transition state theory, the Landau–Zener approximation accounts for the probability of ET upon multiple passages through the transition state region of the energy surface. Equation (23) is equal to 1 for adiabatic ET processes and decreases toward the nonadiabatic limit. On the basis of this spatial dependence of the transmission coefficient as well as the Gibbs activation energy (as discussed in the next section), it is clear that a more complete model will include the integration not only of the hypervolume as implicitly done for Eqs. (21 and 22) but also of the local ET rate constant and even the concentration profile of the reactants at the interface [36].

The meticulous analysis by Smith and coworkers allows illustrating the effect of each of the spatially dependent parameters on the integrand of Eq. (19) [36]. Including all terms in the integrand, it follows

$$\begin{aligned} k_{\text{obs}} = & \int_{l=a_{R2}+a_{O1}}^{\infty} \int_{z_0=a_{R2}}^{l-a_{O1}} \int_{\theta=0}^{\theta_{\text{max}}(z_0, l)} \int_{\Phi=0}^{2\pi} \nu_K \\ & \times \exp \left[ \frac{-\Delta G_{\text{act}}(l)}{k_B T} \right] l^2 g_{R1}(\mathbf{z}) g_{O2}(\mathbf{z}) \\ & \times \sin \theta \, d\Phi \, d\theta \, dz \, dl \end{aligned} \quad (27)$$

where  $g$  is the corresponding concentration profile along the  $\mathbf{z}$ -axis. Neglecting distance dependence on the Gibbs energy of activation and the concentration profiles, the solution of Eq. (27) in the

nonadiabatic limit (i.e.  $\kappa = 4\pi\Gamma$ ) can be approximated to

$$\begin{aligned} k_{\text{obs}} \approx & 2\pi \kappa \nu (a_{O1} + a_{R2}) \beta^{-3} \\ & \times \exp \left( \frac{-\Delta G_{\text{act}}}{k_B T} \right) \end{aligned} \quad (28)$$

which is identical in form to the previous Marcus derivation (Eq. 18) taking the hypervolume as in Eq. (21). A numerical comparison between the limiting case given by Eq. (28) and the full integration of Eq. (27) is displayed in Fig. 4 as a function of the parameter  $\Gamma$ . It is observed that away from the nonadiabatic limit, Eq. (28) provides bimolecular rate constants one or two orders of magnitude smaller than for the “complete” model.

A further refinement introduced by Smith and coworkers involves the resolution of the general integrand (27) taking into account the distance dependence of the reorganization energy. As discussed in the next section, the solvent reorganization term is not only dependent on the distance separating the redox couples but also on their relative positions with respect to the  $\mathbf{z}$ -axis. Fig. 5 shows the value of the integrand calculated from the nonadiabatic limit of the Marcus expression, as well as from the general model excluding concentration profiles. In general, these simulations show that the integrand is more sharply dependent on the distance  $l$  in the generalized model. In order to illustrate the contribution of the various physical elements involved in the ET dynamics, we shall look closer at the reorganization energy as well as the interfacial distribution of reactants (which is connected to the characteristic work terms for approaching reactants to the interface).

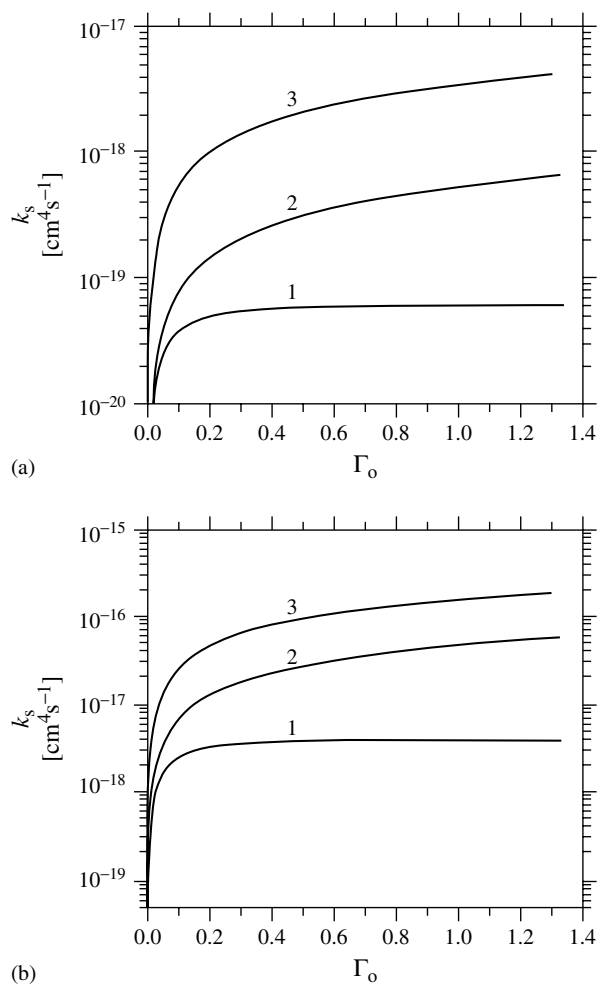


**Fig. 4** Calculated electron-transfer rate constants as a function of the adiabatic parameter  $\Gamma$  for  $a_{O1} = a_{R2} = 3 \text{ \AA}$  and  $\lambda = 1 \text{ eV}$ . The parameter  $\beta$  was evaluated as 0.25 and  $1 \text{ \AA}^{-1}$  for (a) and (b), respectively. Curve 1 was estimated from Eq. (28), employing the approximation  $\kappa = \kappa_{LZ}(I = a_{O1} + a_{R2})$ . Curve 2 is obtained from the full numerical integration of Eq. (27). Curve 3 was calculated as in curve 2, but assuming a concentration profile of the two reactants that increases toward the interface. (Reprinted from Ref. [36] with permission from Elsevier Science.)

**4.2.2.2.3 The Solvent Reorganization Energy** The Gibbs energy of activation already included in Eq. (18) can be described in terms of the total reorganization energy

( $\lambda$ ), the concentration independent term of the Gibbs energy of ET ( $\Delta G_{et}^{\circ'}$ ), as well as work terms for approaching reactants ( $w_p$ ) and separating products ( $w_s$ ) to and from

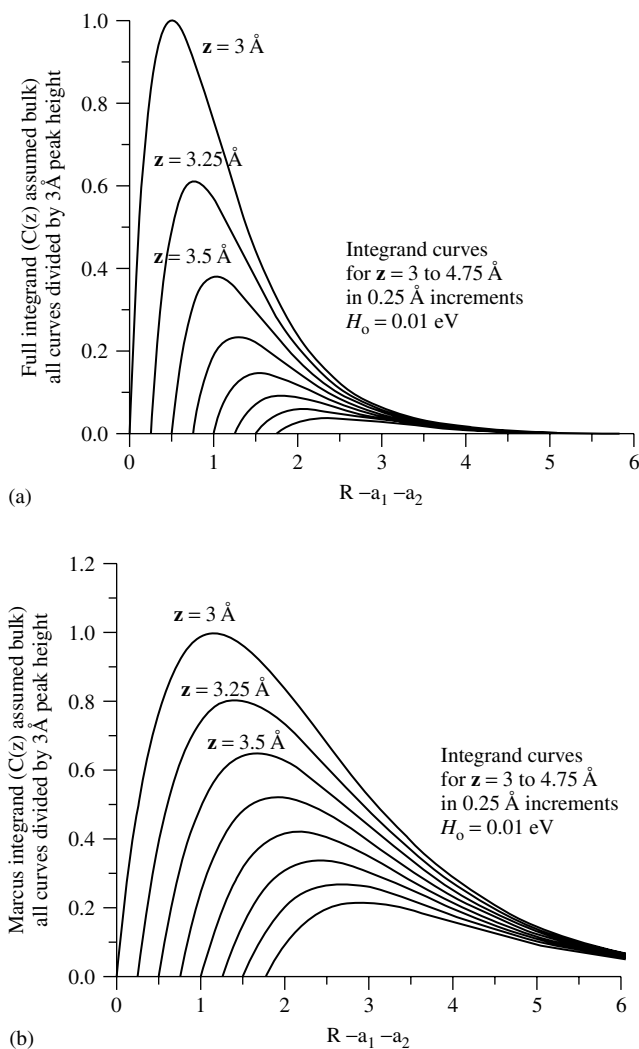


**Fig. 5** Evaluation of the full integrand of Eq. (27) as a function of the distance  $l$  employing Eq. (29) for  $\Delta G_{\text{act}}$ , Eq. (32) for  $\lambda_s$ , and Eq. (26) for  $H$  (a). Other parameters were evaluated as  $\varepsilon_w^s = \varepsilon_o^s = 30$ ,  $\varepsilon_w^{\text{op}} = \varepsilon_o^{\text{op}} = 2$ ,  $H_0 = 0.01$  eV,  $\beta = 1$  Å<sup>-1</sup>, and  $\Delta G_{\text{et}}^{\text{op}} = 0$ . The integrand corresponding to Eq. (19) under identical condition is shown in (b). The dependence of the integrand on the distance is sharper in (a) than in (b) owing to the inclusion of the distance dependent of  $\Delta G_{\text{act}}$  and  $\lambda_s$ . (Reprinted from Ref. [36] with permission from Elsevier Science.)

the interface

$$\Delta G_{\text{act}} = \frac{\lambda}{4} \left( 1 + \frac{\Delta G_{\text{et}}' + w_s - w_p}{\lambda} \right)^2 \quad (29)$$

where  $\Delta G_{\text{et}}'$  is given by

$$\Delta G_{\text{et}}' = -nF(\Delta_o^w \phi - \Delta_o^w \phi_{\text{et}}') \quad (30)$$

The term in Eq. (30) corresponds to the so-called driving force for the ET process. Considering that reactants and products involve ionic species, the work terms ( $w_p$ ) and ( $w_s$ ) feature a chemical part associated with their solvation energies and an electrostatic term that is determined by the local potential distribution. This electrostatic term is rather important as it may account for part of the potential dependence of the phenomenological ET rate constant. We shall give a closer look to this point in the next section.

The contribution of the solvent reorganization energy to the total  $\lambda$  as considered by Kharkats [8] and later by Marcus [11]. The expressions obtained appeared not entirely consistent, but successive revision established that the key aspect lies in separating the static and optical terms of the integral of the electric displacement vectors over the volume of the two liquids system [37]

$$\lambda_s = \frac{1}{2\epsilon_0} \left[ \iiint_{\infty-V_w-V_o} \frac{1}{\epsilon_{\text{st}}} (\vec{D}_f - \vec{D}_i)^2 dv \right]_{\text{static}} - \frac{1}{2\epsilon_0} \left[ \iiint_{\infty-V_w-V_o} \frac{1}{\epsilon_{\text{op}}} (\vec{D}_f - \vec{D}_i)^2 dv \right]_{\text{optical}} \quad (31)$$

where  $\vec{D}_i$  and  $\vec{D}_f$  are the displacement vectors for the initial and final states, respectively. Integration of Eq. (31), considering a sharp boundary between two

dielectric media and for the general geometrical arrangement depicted in Fig. 3(a), provides an expression for  $\lambda_s$  of the form

$$\begin{aligned} \lambda_s = & \frac{(ne)^2}{4\pi\epsilon_0} \left( \frac{1}{\epsilon_o^{\text{op}}} - \frac{1}{\epsilon_o^s} \right) \left( \frac{1}{2a_{\text{R2}}} \right) \\ & + \frac{(ne)^2}{4\pi\epsilon_0} \left( \frac{1}{\epsilon_w^{\text{op}}} - \frac{1}{\epsilon_w^s} \right) \left( \frac{1}{2a_{\text{O1}}} \right) \\ & + \frac{(ne)^2}{4\pi\epsilon_0} \left( \frac{1}{4z_{\text{R2}}} \right) \\ & \times \left( \frac{\epsilon_o^{\text{op}} - \epsilon_w^{\text{op}}}{\epsilon_o^{\text{op}}(\epsilon_o^{\text{op}} + \epsilon_w^{\text{op}})} - \frac{\epsilon_o^s - \epsilon_w^s}{\epsilon_o^s(\epsilon_o^s + \epsilon_w^s)} \right) \\ & + \frac{(ne)^2}{4\pi\epsilon_0} \left( \frac{1}{4z_{\text{O1}}} \right) \\ & \times \left( \frac{\epsilon_w^{\text{op}} - \epsilon_o^{\text{op}}}{\epsilon_w^{\text{op}}(\epsilon_w^{\text{op}} + \epsilon_o^{\text{op}})} - \frac{\epsilon_w^s - \epsilon_o^s}{\epsilon_w^s(\epsilon_w^s + \epsilon_o^s)} \right) \\ & - \frac{(ne)^2}{4\pi\epsilon_0} \left( \frac{2}{l} \right) \left( \frac{1}{\epsilon_o^{\text{op}} + \epsilon_w^{\text{op}}} - \frac{1}{\epsilon_o^s + \epsilon_w^s} \right) \end{aligned} \quad (32)$$

where  $\epsilon^{\text{op}}$  and  $\epsilon^s$  are the optical and static dielectric constants,  $n$  is effective number of electrons transferred, and  $e$  is the elementary charge. Taking  $\epsilon_w^{\text{op}} = \epsilon_o^{\text{op}} = \epsilon^{\text{op}}$  and  $\epsilon_w^s = \epsilon_o^s = \epsilon^s$ , Eq. (32) reduces to the well-known expression obtained for homogeneous ET,

$$\lambda_s^{\text{hm}} = \frac{n^2}{4\pi\epsilon_0} \left( \frac{1}{2a_{\text{O1}}} + \frac{1}{2a_{\text{R2}}} - \frac{1}{l} \right) \times \left( \frac{1}{\epsilon^{\text{op}}} - \frac{1}{\epsilon^s} \right) \quad (33)$$

If we take 1,2-dichloroethane as the organic solvent, Eq. (32) can be simplified to

$$\begin{aligned} \lambda_s^{\text{w|DCE}} = & \frac{n^2}{4\pi\epsilon_0} \left( \frac{0.189}{a_{\text{R2}}} + \frac{0.275}{a_{\text{O1}}} \right. \\ & \left. + \frac{0.029}{z_{\text{R2}}} - \frac{0.014}{z_{\text{O1}}} - \frac{0.494}{l} \right) \end{aligned} \quad (34)$$

It can be noticed that the dominant factors in Eq. (34) are related to the ionic size and the distance separating the redox species. Assuming 0.5 nm for the ionic radii of both reactants in a face-to-face configuration and a total distance  $l$  of 1 nm,  $\lambda_s^{\text{w|DCE}}$  can be estimated to be of the order of 0.7 eV. This magnitude is considerably larger than the common internal reorganization terms for species in which no substantial changes are seen in the structures during the redox process. Therefore, it is expected that the solvent reorganization energy will provide the most important contribution to the total  $\lambda$ .

Marcus also calculated the chemical part of the work term for the formation of the precursor complex [11]

$$w_p^\circ = \left( \frac{1}{4\pi\epsilon_0} \right) \left[ - \left( \frac{(z_{R2})^2}{4d_o\epsilon_o^s} - \frac{(z_{O1})^2}{4d_w\epsilon_w^s} \right) \times \left( \frac{\epsilon_w^s - \epsilon_o^s}{\epsilon_w^s + \epsilon_o^s} \right) + \frac{2}{l} \frac{z_{O1}z_{R2}}{\epsilon_w^s + \epsilon_o^s} \right] \quad (35)$$

It should be noticed that this expression is obtained for a sharp boundary between the dielectric; therefore it may not be directly applicable in the mixed-solvent region model. The equivalent expression for the successor complex ( $w_s^\circ$ ) can be easily obtained by replacing the charges of the reactants by the corresponding products. For the sake of comparison, if we introduce the parameters employed earlier for estimating  $\lambda_s^{\text{w|DCE}}$ , it can be obtained that they are of the order of 10 and 80 meV, respectively. For this calculation we have also assumed that  $z_{O1} = z_{O2} = +1$  and  $z_{R1} = z_{R2} = 0$ . It can be clearly seen that  $w_p^\circ$  and  $w_s^\circ$  are expected to be rather small in comparison to  $\lambda_s^{\text{w|DCE}}$ , therefore the activation energy (see Eq. 29) is mostly controlled by the latter. It should also be mentioned that Benjamin and Kharkats have developed expressions for  $\lambda_s$  for all

possible locations of the reactants at the interface, including the case in which one of them is allowed to cross from one phase to the other [38]. This analysis provides a quantitative comparison between the homogeneous limit (Eq. 33) and the corresponding heterogeneous case (Eq. 32).

#### 4.2.2.2.4 Potential Dependence of the Heterogeneous Electron-transfer Rate Constant

Some of the earlier works devoted to rationalize the dependence of the observed ET rate constant on the applied potential were based on basic models for charge transfer in polar media. Two of the main issues arising from these considerations are the structure of the liquid|liquid boundary and the distribution of the electrostatic potential. In the pioneering work by Samec in 1979, the potential dependence of  $k_{\text{obs}}$  was considered assuming a model involving two diffuse layers separated by an ion-free compact layer [7]. The region delimited by the inner layer establishes the distance for maximum probability of ET ( $R^*$ ). In this case, the element  $\delta R^*$  is estimated by the space volume of the ion of radius  $a_{O1}$  located in one of the reaction plane and certain molecular volume adjacent to the phase boundary,

$$\delta R^* = 2a_{O1}AV_m \quad (36)$$

The density probability of the precursor complex,  $\Phi(R^*)$ , can be obtained by a distribution of the type

$$\Phi(R^*) = a_{O1}a_{R2} \times \exp \left[ \frac{-z_{O1}\Delta_w^{z_{O1}}\phi + z_{R2}\Delta_o^{z_{R2}}\phi}{kT} \right] \quad (37)$$

where “ $z_{O1}$ ” and “ $z_{R2}$ ” correspond to the position of the edges of the inner layer. From Eqs. (36 and 37), and considering

that the ET probability at the precursor complex is determined by  $\Delta G_{\text{act}}$  (Eq. 29), the rate constant of ET can be evaluated as

$$k_{\text{obs}} = k_{\text{obs}}^{\text{pzc}} \exp \left[ \frac{-z_{\text{O}1} \Delta_{\text{w}}^{\text{zO}1} \phi - z_{\text{R}2} \Delta_{\text{o}}^{\text{zR}2} \phi}{RT} \right] \times \exp \left( \frac{-\alpha n \Delta_{\text{zR}2}^{\text{zO}1} \phi}{RT} \right) \quad (38)$$

where

$$k_{\text{obs}}^{\text{pzc}} = 2a_{\text{O}1} V_{\text{m}} B^* \exp \left( \frac{-\lambda}{4RT} \right) \times \exp \left( \frac{-\alpha n F \Delta_{\text{o}}^{\text{w}} \phi_{\text{et}}'}{RT} \right) \quad (39)$$

$$\alpha = \frac{1}{2} + \frac{nF}{4\lambda} (\Delta_{\text{zR}2}^{\text{zO}1} \phi - \Delta_{\text{o}}^{\text{w}} \phi_{\text{et}}') \quad (40)$$

and  $B^*$  involved the overlap integral of the wave function associated with the initial and final states. Although the preexponential term is not fully developed as discussed in Sect. 4.2.2.2.2, the whole quantity can be experimentally accessed by measurements of the phenomenological rate constant at the potential of zero charge (*pzc*). On the other hand, a very important implication from Eq. (38) is that the dependence of the  $k_{\text{obs}}$  on the Galvani potential difference may only arise from changes in the interfacial concentration of the reactants and not by the Gibbs energy of activation.

Girault and Schiffrin proposed a model in which the interface features a mixed-solvent region [9]. To approach this region, the reactants and products undergo changes in their solvation energies and ionic atmosphere. Consequently, the work terms associated with the formation of the precursor complex and dissociation of the successor complex also feature some

potential independent parameters,

$$w_{\text{p}} = w_{\text{p}}^{\circ} + z_{\text{O}1} F \Delta_{\text{w}}^{\text{zO}1} \phi + z_{\text{R}2} F \Delta_{\text{o}}^{\text{zR}2} \phi \quad (41)$$

$$w_{\text{s}} = w_{\text{s}}^{\circ} + z_{\text{O}2} F \Delta_{\text{o}}^{\text{zO}2} \phi + z_{\text{R}1} F \Delta_{\text{w}}^{\text{zR}1} \phi \quad (42)$$

The terms  $w_{\text{p}}^{\circ}$  and  $w_{\text{s}}^{\circ}$  are associated with the changes in solvation energy and ionic atmosphere experienced by the reactants and products in the mixed-solvent region. The second and third terms in Eqs (41 and 42) reflect the work involved to displace the ions in and out of the electrified interfaces. Effectively,  $\Delta_{\text{w}}^{\text{zO}1} \phi$  and  $\Delta_{\text{o}}^{\text{zR}2} \phi$  are the potential drop developed between the reaction plane and the bulk of the corresponding electrolyte phase. In the original analysis by Samec [7], these electrostatic components provide the most important contributions to the work terms. This is simply because of the assumption that chemical changes in the ionic environment can be neglected outside the “inner compact layer.”

The approach followed by Girault and Schiffrin [9] was based on the “encounter preequilibrium” model, previously employed for ET in condensed phase [39] and metal|electrolyte interfaces [40]. It follows from this model,

$$k_{\text{obs}} = K_{\text{p}}^{\text{e}} k_{\text{et}} \quad (43)$$

where  $K_{\text{p}}^{\text{e}}$  is the equilibrium constant for forming the precursor complex, which is given by

$$K_{\text{p}}^{\text{e}} = \delta R^* \exp \left( \frac{-w_{\text{p}}}{RT} \right) \quad (44)$$

Similar to the previous consideration,  $\delta R^*$  corresponds to the “reaction zone” where the molecules feature the appropriate configuration for the ET step. Considering Eqs. (20, 29, 30, and 41 to 44), an expression for  $k_{\text{obs}}$  identical in form



to Eq. (38) can be obtained but with a preexponential factor of the form

$$k_{\text{obs}}^{\text{pzc}} = \delta R^* \nu_{\text{eff}} \exp\left(\frac{-\lambda}{4RT}\right) \exp\left(\frac{-w_{\text{p}}^{\circ}}{RT}\right) \times \exp\left[\frac{\alpha(w_{\text{p}}^{\circ} - w_{\text{s}}^{\circ} + nF\Delta_{\text{o}}^{\text{w}}\phi_{\text{et}}^{\circ'})}{RT}\right] \quad (45)$$

here  $\nu_{\text{eff}}$  is the effective electron hopping frequency. It should also be noticed that if the potential independent components of the work terms are negligible with respect to the reorganization energy and the thermodynamic driving force, Eq. (45) reduces to an expression similar to Eq. (39). Apparently, this might be physically plausible if we compare the values of  $\lambda_{\text{s}}^{\text{w|DCE}}$ ,  $w_{\text{p}}^{\circ}$ , and  $w_{\text{s}}^{\circ}$  as derived from Eqs. (34 and 35).

As we mentioned previously, the potential dependence of  $k_{\text{obs}}$  can arise from changes in the Gibbs energy of ET or from concentration polarization effects. Schmickler approached this problem by simulating the potential dependence of the distribution of ionic species using a lattice-gas model [41]. These simulations showed that as far as the distance separating the redox species is smaller than the Debye length of each space charge region, the potential dependence would be mostly controlled by the concentration polarization phenomena. This conclusion appears more consistent with the “mixed-solvent region” model, which allows a close approach between the two reactants. Some experimental reports have shown deviations from the Butler–Volmer behavior, which could reflect concentration polarization phenomena. However, as reviewed in the next section, a clear dependence of the ET rate constant and the Galvani potential difference have been observed, suggesting that the potential and ionic distribution are

far more complex than what is described by current modeling.

#### 4.2.2.3 Selected Experimental Results

The first quantitative evaluations of heterogeneous electron transfer rate constants were performed employing cyclic voltammetry and electrochemical impedance spectroscopy at polarizable interfaces [13, 14, 17, 21]. Careful choice of redox couples and electrolyte composition was essential in order to avoid interference from coupled ion-transfer processes. From these early studies, rate constants typically of the order of  $10^{-22} \text{ cm}^4 \text{ s}^{-1}$  were measured for the ET between hexacyanoferrate and various redox couples in the organic phase. A common aspect to all these measurements is the redox potential matching, which allows to onset the ET reaction within the polarizable window commonly obtained for liquid|liquid junctions. Obviously, this boundary condition does not permit studying redox processes featuring large values of  $\Delta G_{\text{et}}^{\circ'}$ . As discussed later, dynamic studies far from equilibrium provide very useful information on fundamental parameters such as the preexponential factor in Eq. (28) and the reorganization energy (Eq. 32).

The particular case of hexacyanoferrate and TCNQ (see Fig. 2) have been studied not only by electrochemical impedance spectroscopy [14] but also by Potential Modulated Reflectance Spectroscopy (PMR) [26], SECM [42], and Microelectrochemical Measurements at Expanding Droplets (MEMED) [27, 28]. Considering that the composition of the electrolyte varied for all these approaches, rate constants between  $10^{-23}$  and  $10^{-22} \text{ cm}^4 \text{ s}^{-1}$  were consistently obtained for this system. Cheng and Schiffrin demonstrated that these figures are consistent with the basic expressions derived by Marcus for a

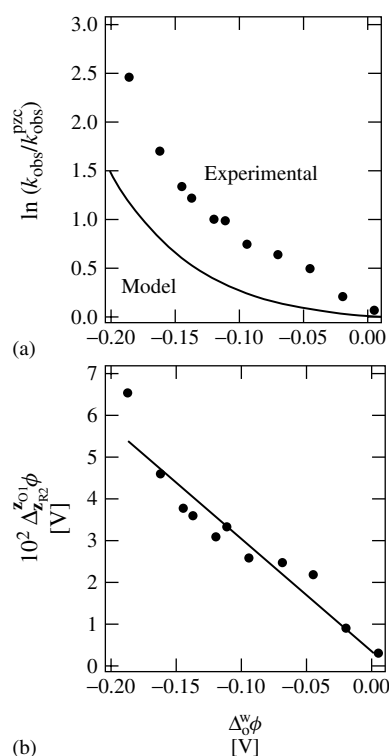


**Fig. 6** Potential dependence of the electron-transfer rate constant ( $k_{\text{obs}}$ ) normalized to the value at the  $pzc$  ( $k_{\text{obs}}^{\text{pzc}}$ ) for the TCNQ reduction by hexacyanoferrate at the water|DCE interface. Full line was estimated from Eq. (38), assuming that the potential drop across the inner layer is negligible ( $\Delta_{\text{z}_{\text{R2}}}^{\text{O1}}\phi \approx 0$  V). Dependence of the potential drop across the ET reaction plane with the Galvani potential difference, as obtained from recalculation of the two trends in (a), assuming a transfer coefficient of 0.5 (b). These results suggest that approximately 30% of the Galvani potential difference is developed between the reacting species under the experimental conditions defined in Fig. 2. (Reprinted from Ref. [26] with permission from Elsevier Science.)

sharp liquid|liquid boundary Eqs. (28 and 32) [14].

The potential dependence of the observed ET rate constant from hexacyanoferrate (II) to TCNQ is shown in Fig. 6 [26]. The rate constants were estimated from chronoabsorptometric and PMR measurements under the conditions described in Fig. 2. Deviations from the Butler–Volmer behavior are evident at potentials away from the  $pzc$ , which were also pointed out by Cheng and Schiffrin in a previous paper [14]. The theoretical curve shown in Fig. 6 illustrates a simulation of the potential dependence of the observed rate constant normalized to the value at the  $pzc$  employing Eq. (38). The potential drop between the plane at  $\text{z}_{\text{O1}}$  and  $\text{z}_{\text{R2}}$  was initially neglected and only the contribution associated with concentration polarization

was considered. The interfacial potential was estimated using a Poisson–Boltzman distribution of the ionic species. The substantial underestimation of the experimental points can be taken as evidence that a finite fraction of the applied potential is developed between the reaction planes  $\text{z}_{\text{O1}}$  and  $\text{z}_{\text{R2}}$ . Assuming a transfer coefficient  $\alpha = 0.5$ , Fig. 6(b) shows that the local potential could be up to 30% of the total Galvani potential difference.

The dependence of the observed ET rate constant on the thermodynamic driving force indeed remains rather controversial. Unlike electrochemical and spectroelectrochemical approaches at polarizable interfaces, techniques based on SECM and dynamic photoelectrochemical measurements have allowed probing rate constants far away from equilibrium conditions. In

SECM, redox-active species are generated in the proximity of the interface by an approaching microelectrode. The feedback current at the microelectrode tip contain information on the rate of ET at the liquid|liquid boundary. On the other hand, the photoinduced ET involving dyes and redox species at either side of the interface manifest itself as photocurrent responses [5, 43–47]. These photoresponses are proportional to the ratio between the rate constants of excited state decay and heterogeneous ET. The common point between these two approaches is that highly reactive species are generated at the interface, either by light or by an approaching microelectrode; therefore large driving forces for the ET can be attained.

Tsionsky and coworkers studied the dynamics of ET from various redox couples located in the aqueous phase to the oxidized zinc tetraphenylporphyrin in benzene by SECM. The driving force was varied by changing the concentration ratio of a common ion ( $\text{ClO}_4^-$ ) and by using different redox couples in the aqueous phase. It was observed that for driving forces smaller than 0.5 eV, the potential dependence of the observed rate constant exhibits a Butler–Volmer behavior. Ignoring concentration polarization effects, this dependence is consistent with Eq. (38). For larger driving forces, the observed rate constant becomes potential independent suggesting a diffusion control regime. It should be mentioned that the redox couples in the aqueous phase are in large excess with respect to the zinc porphyrin in the organic phase in order to avoid coupling of diffusion profiles in both phases (the constant composition approximation). Interestingly, a different behavior is observed in the presence of a C-10 surfactant as depicted in Fig. 7(a). The adsorbed lipid layer effectively increases the distance

separating the redox couple, therefore increasing the solvent reorganization energy (see Eq. 32). In this case, a decrease in  $k_{\text{obs}}$  with increasing potentials at high values of driving force has been observed. This phenomenon was taken as first evidence of the Inverted Marcus Region at a polarized interface. However, the limited number of experimental points does not allow quantifying parameters such as the reorganization energy term.

Barker and coworkers employed essentially the same approach but reducing the concentration of the redox couple in the aqueous phase. Although the analysis of the approaching curves is further complicated by the coupling of diffusion regimes in either side of the interface, the most important aspect is that the overall rate of ET decreases. Consequently, rate constants of fast reactions, which previously appeared diffusion-controlled, were accurately measured. This analysis provided a dependence of the rate constant on the driving force as illustrated in Fig. 7(b). The authors rationalized the limited number of experimental points employing Eqs. (18, 29, and 30), providing values for the reorganization energy and the preexponential factor of 0.55 eV and  $8.3 \times 10^{-20} \text{ cm}^4 \text{ s}^{-1}$ , respectively. In principle, the value for  $\lambda_s$  is consistent with Eq. (32), assuming a face-to-face approach and for  $l \sim a_{\text{O1}} + a_{\text{R2}}$ .

The previous works based on SECM have not addressed the specific contributions of the Galvani potential difference and the formal ET potential to the thermodynamic driving force. Our recent work based on photoinduced ET at externally polarizable interfaces quantitatively tackles this problem employing the thermodynamic relations discussed in Sect. 4.2.2.1 [48]. The advantage of this approach is that the driving force can be changed potentiostatically as well as by changing the redox

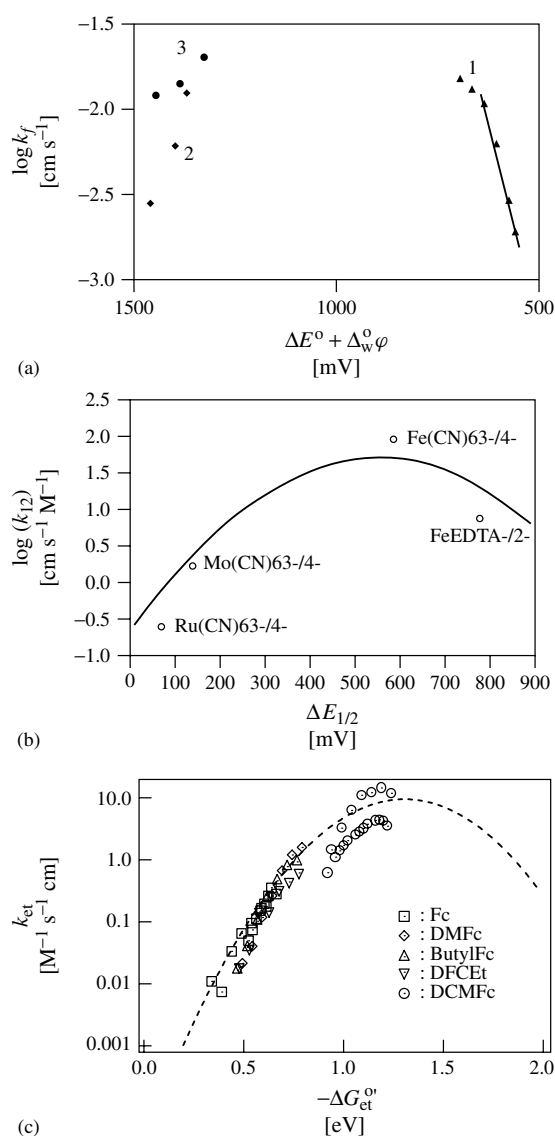


**Fig. 7** “Driving force” dependence of  $k_{obs}$  obtained for the reduction of ZnPor<sup>+</sup> in benzene by various redox couples in the aqueous phase as probed by SECM in the presence of a full monolayer of C10-lipid (a). As the driving force increases,  $k_{obs}$  increases in the presence of Fe(CN)<sub>6</sub><sup>4-</sup> (curve 1), but decreases for Co (II) sepalchrate (curve 2) and V<sup>2+</sup> (curve 3). A similar analysis is presented in (b) but in the absence of the C-10 lipids and for substantially smaller concentration of the aqueous redox couple. The curve in (c) was obtained from photocurrent measurements at the polarizable water|DCE interface in the presence of water-soluble porphyrin dimer (ZnTPPS : ZnTMPyP) and ferrocene (Fc), dimethylferrocene (DMFc), butylferrocene (ButylFc), diferrocenylethane (DfcEt), and decamethylferrocene (DCMFc). (Figs. a, b and c were reprinted from Refs. [32, 34], respectively, with permission from the American Chemical Society.)

couple acting as quencher in the organic phase. From the photocurrent analysis, the phenomenological rate constant of ET as a function of the driving force is illustrated in Fig. 7(c). It can be observed that the ET from the redox couple in the organic phase to the excited state of the porphyrin dimer exhibits a rather high reorganization

energy, which shift the inverted region beyond 1 eV. The number of experimental points obtained from a family of ferrocene derivatives allows a confident analysis in terms of Eq. (29). This rather high reorganization energy can also be explained in terms of Eq. (34), assuming  $a_{Fc} \sim 0.2$  nm,  $a_{por} \sim 0.7$  nm, and  $l \sim 1$  nm.

Finally, it is rather interesting to notice that Figs. 7(b and c) provide pre-exponential factors of the order of  $5 \times 10^{-20} \text{ cm}^4 \text{ s}^{-1}$ . Comparing with the simulations in Fig. 4, it can be concluded that the experimental data is consistent with a highly nonadiabatic limit ( $\Gamma \rightarrow 0$ ), in which the expressions derived by Marcus and Smith and coworkers do converge. This low electronic coupling between the redox species may arise from the difference in the solvation properties, which induces interfacial separation distances of the order of 1 nm.

#### 4.2.3

##### **Ion-transfer Reactions**

Ion-transfer reaction at interfaces between immiscible electrolyte solutions (ITIES) has been an area of active research for more than two decades [49–52]. Several research groups have developed theories dealing with the fundamental features of ion-transfer processes at (ITIES) [7, 53–68]. The theoretical work has often been initiated by advances in experimental techniques used to obtain kinetic information on the ion-transfer kinetics [53, 69–74]. More recently, computer simulations have given important information on the microscopic surface structure [51, 57, 75–78]. The microscopic nature of the ion-transfer event has been discussed in the theoretical works on ion transfer, and different factors that are potentially important for the ion-transfer event at ITIES have been suggested: elasticity of the inner layer, surface structure in general, the electric potential energy (dependent on the Galvani potential), hydrodynamic friction, and changes in solvation.

There are two main approaches to describe ion-transfer reactions, that is, as an

activated process and as a pure transport process. Usually, the ion transport across a liquid|liquid interface has been described using the Nernst–Planck equation [60, 61] or the Langevin equation [57–59, 65]. The basic ideas of these independent theories will be reviewed starting from first principles and a more generalized approach will be outlined. In a recent theoretical work the transport description has been combined with a microscopic theory on the mechanism of ion transfer [68]. Other models for ion transfer will be dealt with briefly in a separate paragraph [55, 64–66, 79].

##### **4.2.3.1 Kinetics of Ion-transfer Reactions Based on the Assumption of an Activated Ion-transfer Event**

The simplest kinetic approach is to consider an ion-transfer reaction as an activated process as schematically shown in Fig. 8, but we shall consider the transfer of the ion across the complete interface at which the Galvani potential difference between the two phases varies. This derivation may be termed *the global approach*.

For this simple kinetic model, the Gibbs energy in the adjacent phases is defined by the standard electrochemical potential, which can be defined as the concentration independent part of the electrochemical potential.

The current is defined by

$$I = zFA \left( \overrightarrow{k} c^w - \overleftarrow{k} c^o \right) \quad (46)$$

where  $\overrightarrow{k}$  and  $\overleftarrow{k}$  are the forward and backward global rate constants with units of  $\text{cm s}^{-1}$ . The bulk concentrations are given by  $c^w$  and  $c^o$ . The charge of the ion is  $z$ ,  $A$  is the surface area, and  $F$  is the Faraday constant. At equilibrium, the Galvani potential difference is equal to the standard transfer potential defined by

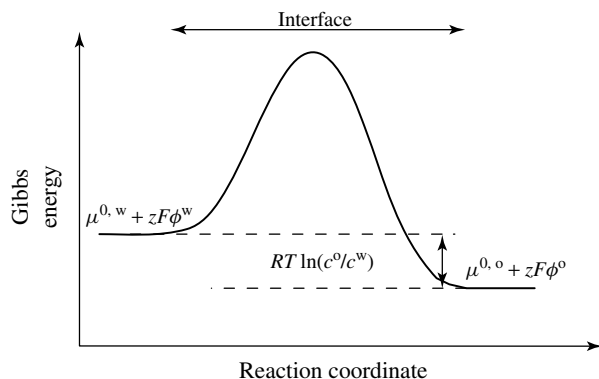


**Fig. 8** Standard Gibbs energy profile for global ion-transfer reactions.

$$\Delta_{\text{o}}^{\text{w}}\phi_i^{\text{o}} = \frac{\Delta G_{\text{tr},i}^{\text{o},\text{w} \rightarrow \text{o}}}{z_i F} \quad (47)$$

where  $\Delta G_{\text{tr},i}^{\text{o},\text{w} \rightarrow \text{o}}$  is the standard Gibbs energy of transfer from water to the organic phase. At the standard transfer potential the activation energy barrier is regarded as symmetrical. In the standard case at equilibrium we have  $c^{\text{w}} = c^{\text{o}} = c$  and  $\Delta_{\text{o}}^{\text{w}}\phi_{\text{eq}} = \Delta_{\text{o}}^{\text{w}}\phi^{\text{o}'}$ . When we apply a Galvani potential difference different from the standard transfer value, only a fraction,  $\alpha$ , of the driving force is active on lowering the energy barrier:

$$I = zFAk^{\text{o}}c \left[ e^{zF\alpha(\Delta_{\text{o}}^{\text{w}}\phi - \Delta_{\text{o}}^{\text{w}}\phi^{\text{o}'})} - e^{-zF(1-\alpha)(\Delta_{\text{o}}^{\text{w}}\phi - \Delta_{\text{o}}^{\text{w}}\phi^{\text{o}'})} \right] \quad (48)$$

In the general case, this equation becomes

$$I = zFAk^{\text{o}} \left[ c^{\text{w}} e^{zF\alpha(\Delta_{\text{o}}^{\text{w}}\phi - \Delta_{\text{o}}^{\text{w}}\phi^{\text{o}'})} - c^{\text{o}} e^{-zF(1-\alpha)(\Delta_{\text{o}}^{\text{w}}\phi - \Delta_{\text{o}}^{\text{w}}\phi^{\text{o}'})} \right] \quad (49)$$

If this simple kinetic approach can be used as a primary model, it is difficult to ascribe a physical meaning to the rate constants. Indeed, these rate constants correspond to the transfer of an ion across

the entire interfacial region composed of two back-to-back diffuse layers. The only merit of this global approach is to yield an expression that in essence can be considered as a Butler–Volmer equation for an ion-transfer reaction. Many groups have observed this Butler–Volmer behavior, as originally suggested by Gavach [53]. Figure 9 illustrates the results obtained by means of chronocoulometry for the transfer of acetylcholine.

#### 4.2.3.2 Interfacial Reaction Independent of the Local Electric Field

Another way to treat an ion-transfer reaction is to consider the reaction as an elementary “jump” across a thin interfacial layer, which we will call the reaction plane, but it may also be called “inner layer” or “mixed-solvent layer” depending on the interfacial model used. The interface (about 1 nm thick) comprises back-to-back diffuse layers.

With the notation of Fig. 10, the current now reads

$$I = zFA \left( \overrightarrow{k} c^{\text{a}} - \overleftarrow{k} c^{\text{b}} \right) \quad (50)$$

where  $\overrightarrow{k}$  and  $\overleftarrow{k}$  represent the rate constants of the ion-transfer reaction

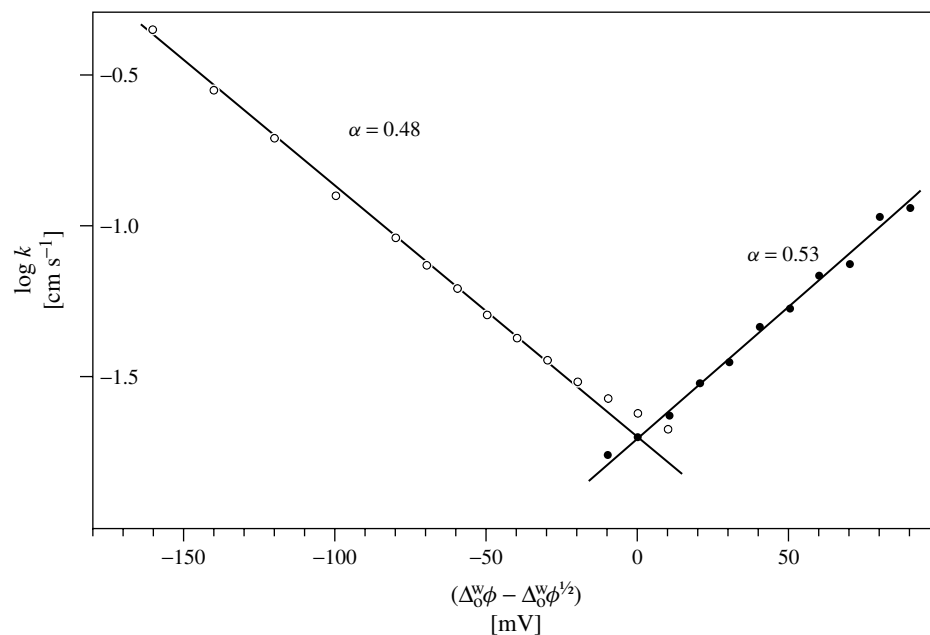


**Fig. 9** Tafel plots for ion transfer of acetylcholine. From water to DCE (o) and from DCE to water (●).

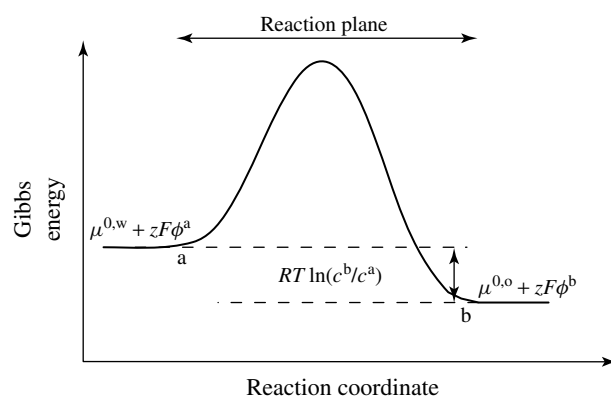
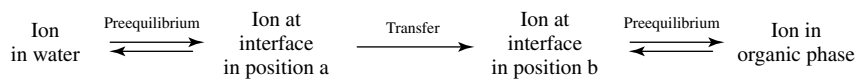


**Fig. 10** Standard Gibbs energy profile for an elementary ion-transfer reaction.



**Scheme 1** Elementary steps for kinetically controlled ion transfer.

across the reaction plane and where the concentrations  $c^a$  and  $c^b$  are the concentrations on both sides of the reaction plane. In a first approximation, we can assume that the rate constants are potential-independent and that the only consequence of the interfacial polarization is to vary the interfacial ion concentration as described by Boltzmann statistics:

$$c^a = c^w e^{-zF\Delta_w^a\phi/RT} \quad (51)$$

$$c^b = c^o e^{-zF\Delta_o^b\phi/RT} \quad (52)$$

In the application of these two equations it is assumed that there is a preequilibrium between the reaction plane and the bulk regions.

It is important to realize that the application of the above scheme and Eqs. (51 and 52) are based on the assumption that the ion transfer is slow compared to diffusion of ions to a and b from bulk solutions. By substitution in Eq. (50), we obtain

$$I = zFA \left( \overrightarrow{k} c^w e^{-zF\Delta_w^a\phi/RT} - \overleftarrow{k} c^o e^{-zF\Delta_o^b\phi/RT} \right) \quad (53)$$

Furthermore, if the positions a and b are close, we can assume that the electrical potential difference between these two points is negligible. In this case, Eq. (53) reduces to

$$I = zFA \left[ \overrightarrow{k} c^w e^{\alpha zF\Delta_o^w\phi/RT} - \overleftarrow{k} c^o e^{-(1-\alpha)zF\Delta_o^w\phi/RT} \right] \quad (54)$$

The proportion of the Galvani potential difference occurring in the aqueous phase is termed  $\alpha$ . At equilibrium, at the standard transfer potential, we have

$$\begin{aligned} \overrightarrow{k} e^{\alpha zF\Delta_o^w\phi^\circ/RT} &= \overleftarrow{k} e^{-(1-\alpha)zF\Delta_o^w\phi^\circ/RT} \\ &= k^\circ \end{aligned} \quad (55)$$

If we further assume that  $\alpha$  does not vary with  $\Delta_o^w\phi$  (which is a very rough approximation), the following expression for the current ensues:

$$I = zFAk^\circ \left[ c^w e^{\alpha zF(\Delta_o^w\phi - \Delta_o^w\phi^\circ)/RT} - c^o e^{-(1-\alpha)zF(\Delta_o^w\phi - \Delta_o^w\phi^\circ)/RT} \right] \quad (56)$$

This result is similar to what was obtained in the simple approach (Eq. 49). The fundamental difference is that now it is possible to relate  $k^0$  to the microscopic features of the ion transfer.

#### 4.2.3.3 Interfacial Reaction Dependent on the Electric Field

Still considering an ion-transfer reaction as an interfacial process, Eq. (50) remains. However, we will now assume that the rate constants depend on the applied Galvani potential difference according to

$$\overrightarrow{k} = \overrightarrow{k}_0 e^{\beta zF\Delta_b^a\phi/RT} \quad (57)$$

$$\overleftarrow{k} = \overleftarrow{k}_0 e^{-(1-\beta)zF\Delta_b^a\phi/RT} \quad (58)$$

In these equations it is assumed that transition state theory can be applied in the description of the ion transfer. By substitution in Eq. (50), the following equation is obtained:

$$I = zFA \left[ \overrightarrow{k}_0 c^a e^{\beta zF\Delta_b^a\phi/RT} - \overleftarrow{k}_0 c^b e^{-(1-\beta)zF\Delta_b^a\phi/RT} \right] \quad (59)$$

If we still assume that there are equilibria between the interfacial position and the bulk, we have

$$I = zFA \left[ \overrightarrow{k}_0 c^w e^{-\beta zF\Delta_a^b\phi/RT} e^{-zF\Delta_w^a\phi/RT} - \overleftarrow{k}_0 c^o e^{(1-\beta)zF\Delta_a^b\phi/RT} e^{-zF\Delta_o^b\phi/RT} \right] \quad (60)$$



We can define the potential  $\phi^\#$  such that

$$\Delta_a^\# \phi = \beta \Delta_a^b \phi \quad (61)$$

$$\Delta_\#^b \phi = (1 - \beta) \Delta_a^b \phi \quad (62)$$

Equation (60) then reads

$$I = zFA \left[ \overrightarrow{k_0} c^w e^{-zF\Delta_w^\# \phi / RT} - \overleftarrow{k_0} c^\circ e^{-zF\Delta_\#^\circ \phi / RT} \right] \quad (63)$$

The coefficient  $\alpha$  can be defined as

$$\Delta_w^\# \phi = \alpha \Delta_w^\circ \phi \quad (64)$$

$$\Delta_\#^\circ \phi = (1 - \alpha) \Delta_w^\circ \phi \quad (65)$$

Equation (63) can now be written as

$$I = zFA \left[ \overrightarrow{k_0} c^w e^{\alpha zF\Delta_w^\circ \phi / RT} - \overleftarrow{k_0} c^\circ e^{-(1-\alpha)zF\Delta_w^\circ \phi / RT} \right] \quad (66)$$

At the formal standard transfer potential, we have

$$\overrightarrow{k_0} e^{\alpha zF\Delta_w^\circ \phi^\circ / RT} = \overleftarrow{k_0} e^{-(1-\alpha)zF\Delta_w^\circ \phi^\circ / RT} = k^\circ \quad (67)$$

By defining  $k^\circ$  in this way, we recover an expression of the current similar to Eq. (49). This approach may be compared with the of work Koryta [54] and Samec [7]. In the latter, an activation energy and a solvent reorganization energy are explicitly associated with the rate constant of ion transfer. (The microscopic transport of ions across the ITIES may also be described using the Langevin equation, see Refs. [58, 59], which relates the microscopic rate of particle motion,  $v$ , of a particle of mass  $m$  with coordinate  $x$  and time  $t$ , to the regular potential of the field  $U(x, t)$ , a phenomenological friction coefficient,  $\beta$ , and a function  $A(x, t)$  describing

the random force caused by fluctuations in the condensed medium:

$$\frac{dv}{dt} = -\beta v - \frac{1}{m} \left[ \frac{dU(x, t)}{dx} + A(x, t) \right]$$

The derivative of  $U$  with respect to position is the regular force acting on the particle. However, this so-called stochastic approach results in similar Nernst–Planck type equations albeit with microscopic diffusion coefficient differing from the traditional macroscopic diffusion coefficient. The microscopic diffusion coefficient,  $\bar{D}$ , is related to  $\beta$ , through  $\bar{D} = (k_B T) / (\beta m)$ .

#### 4.2.3.4 Kinetics of Ion-transfer Reactions Based on a Transport Description

Another way to treat ion-transfer reactions is to consider them as a special case of ionic conductivity across an interface. From a phenomenological viewpoint, anionic flux can be written [80]:

$$\mathbf{J}_i = -c_i \tilde{u}_i \mathbf{grad} \tilde{\mu}_i \quad (68)$$

By taking into account that the electrochemical potential can be considered as the sum of a standard term, which is solvent dependent, a concentration/activity term, and an electrical term, we have

$$\begin{aligned} \mathbf{J}_i(x) = & -c_i \tilde{u}_i(x) [\mathbf{grad} \mu_i^\circ(x) \\ & + RT \mathbf{grad} \ln c_i(x) \\ & + z_i F \mathbf{grad} \phi(x)] \end{aligned} \quad (69)$$

which is identified as the Nernst–Planck equation:

$$\begin{aligned} \mathbf{J}_i(x) = & -RT \tilde{u}_i(x) \mathbf{grad} c_i(x) - z_i F c_i(x) \\ & \times \tilde{u}_i(x) \mathbf{grad} [\phi(x) - \phi_i^\circ(x)] \end{aligned} \quad (70)$$

with  $\phi_i^\circ(x) = -\mu_i^\circ / z_i F$ .

To integrate this equation, we can rewrite it in the following way:

$$\begin{aligned} J_i(x) = & -RT\tilde{u}_i(x) \\ & \times \text{grad} \left\{ c_i e^{z_i F[\phi(x) - \phi_i^\circ(x)]/RT} \right\} \\ & \times e^{-z_i F[\phi(x) - \phi_i^\circ(x)]/RT} \end{aligned} \quad (71)$$

If we consider the ion-transfer reaction as the crossing of the inner layer, we have to integrate this equation between a in the water phase and b in the oil phase.

$$\begin{aligned} J_i \int_b^a \frac{e^{z_i F[\phi(x) - \phi_i^\circ(x)]/RT}}{\tilde{u}_i(x)} dx = & -RT \\ & \times \int_b^a d \left\{ c_i e^{z_i F[\phi(x) - \phi_i^\circ(x)]/RT} \right\} \end{aligned} \quad (72)$$

If  $\phi(x) - \phi_i^\circ(x)$  varies linearly through the interface, by defining

$$y_b = \frac{z_i F}{RT} [\phi(b) - \phi_i^\circ(b)] \quad (73)$$

$$y_a = \frac{z_i F}{RT} [\phi(a) - \phi_i^\circ(a)] \quad (74)$$

we can write

$$\frac{z_i F[\phi(x) - \phi_i^\circ(x)]}{RT} = y_b + (y_a - y_b) \frac{x}{L} \quad (75)$$

If it is assumed that the ionic mobility is constant through the interface, we have

$$\begin{aligned} \frac{J_i}{\tilde{u}_i} \int_0^L e^{y_b + (y_a - y_b)x/L} dx = & -RT \\ & \times \int_b^a d \left\{ c_i e^{z_i F[\phi(x) - \phi_i^\circ(x)]/RT} \right\} \end{aligned} \quad (76)$$

Solving this integral leads to

$$\begin{aligned} \frac{J_i}{\tilde{u}_i RT} e^{y_b} \int_0^L e^{(y_a - y_b)x/L} dx = & \frac{L J_i}{\tilde{u}_i RT} \\ & \times \left[ \frac{e^{y_a} - e^{y_b}}{(y_a - y_b)} \right] = -RT [c_i^a e^{y_a} - c_i^b e^{y_b}] \end{aligned} \quad (77)$$

We then obtain an equation for the ion flux:

$$J_i = \frac{\tilde{u}_i RT}{L} \left[ \frac{c_i^a e^{y_a} - c_i^b e^{y_b}}{e^{y_a} - e^{y_b}} \right] (y_a - y_b) \quad (78)$$

The parameter  $y$  is defined as

$$y = \frac{y_a - y_b}{2} = \frac{z_i F}{2RT} (\Delta_b^a \phi - \Delta_b^a \phi_i^\circ) \quad (79)$$

The ion flux can now be expressed as

$$\begin{aligned} J_i = & \frac{2\tilde{u}_i RT y}{L} \left( \frac{c_i^a e^{2y} - c_i^b}{e^{2y} - 1} \right) \\ = & \frac{\tilde{u}_i RT}{L} \frac{y}{\sinh y} (c_i^a e^y - c_i^b e^{-y}) \end{aligned} \quad (80)$$

The approach outlined above is essentially equivalent to that suggested by Kakiuchi [60], which again relies on the work of Goldman for ion transfer across membranes. Expressions for the ion-transfer rate constants may be obtained as below if we recall that the ionic flux across the interface can be described according to Eq. (50).

$$\vec{k} = \left( \frac{\tilde{u}_i RT}{L} \right) \left( \frac{y e^y}{\sinh y} \right) \quad (81)$$

$$\overleftarrow{k} = \left( \frac{\tilde{u}_i RT}{L} \right) \left( \frac{y e^{-y}}{\sinh y} \right) \quad (82)$$

Since it may be noted that

$$\lim_{y \rightarrow 0} \frac{y e^y}{\sinh y} = \lim_{y \rightarrow 0} \frac{y e^{-y}}{\sinh y} = 1 \quad (83)$$

It immediately follows that a useful definition for  $k_i^\circ$  is

$$k_i^\circ = \left( \frac{\tilde{u}_i RT}{L} \right) \quad (84)$$

The equations describing  $\vec{k}$  and  $\overleftarrow{k}$  can easily be incorporated into Eq. (50) to describe the entire current potential characteristic. Note that in this treatment the

ion transfer is treated as a transport process and  $\tilde{u}_i$  is a phenomenological mobility of the ion in the inner layer. This model has successfully accounted for experimental data [71] and the experimental values of  $\alpha$  and  $k^\circ$  can be given phenomenological meanings. Within the framework of the model suggested by Kakiuchi, the ion-transfer rate constant can be related to the microscopic structural features of the liquid|liquid reaction plane describing the ionic mobility and interface width.

By analogy to the derivation of Eqs. (56 and 66), we can obtain an expression for  $J_i$  on the basis of the bulk concentration of the ion in water and oil. The concentration of the ion at a and b may be expressed according to Eqs. (51 and 52) if we again assume the formation of a preequilibrium according to Sch. 1, or in other words that the ion transfer/transport across the liquid|liquid interface is slow compared to the diffusion/migration of the ion in the diffuse layers. Under such conditions the following expression for  $J_i$  ensues:

$$J_i = \frac{\tilde{u}_i RT}{L} \frac{y}{\sinh y} \left( c_i^w e^{-z_i F \Delta_w^a \phi / RT} \times e^{z_i F (\Delta_b^a \phi - \Delta_b^a \phi_i^\circ) / 2RT} - c_i^\circ e^{-z_i F \Delta_o^b \phi / RT} \times e^{-z_i F (\Delta_b^a \phi - \Delta_b^a \phi_i^\circ) / 2RT} \right) \quad (85)$$

We can define a potential  $\phi^\#$  such that

$$\Delta_\#^a \phi = \Delta_b^\# \phi = \frac{1}{2} \Delta_b^a \phi \quad (86)$$

leading to the following expression:

$$J_i = \frac{\tilde{u}_i RT}{L} \frac{y}{\sinh y} \times \left( c_i^w e^{-z_i F (\Delta_w^\# \phi + 1/2 \Delta_b^a \phi_i^\circ) / RT} - c_i^\circ e^{-z_i F (\Delta_o^\# \phi - 1/2 \Delta_b^a \phi_i^\circ) / RT} \right) \quad (87)$$

In general,  $1/2 \Delta_b^a \phi_i^\circ$  can be approximated by  $1/2 \Delta_o^w \phi_i^\circ$  and we can therefore write

$$J_i = \frac{\tilde{u}_i RT}{L} \frac{y}{\sinh y} \times \left( c_i^w e^{-z_i F (\Delta_w^\# \phi + 1/2 \Delta_o^w \phi_i^\circ) / RT} - c_i^\circ e^{-z_i F (\Delta_o^\# \phi - 1/2 \Delta_o^w \phi_i^\circ) / RT} \right) \quad (88)$$

Finally, by defining  $\alpha$  as the fraction of the total potential drop between the two bulk phases occurring from bulk water to the middle point of the potential drop between a and b, we arrive at the following result:

$$J_i = \frac{\tilde{u}_i RT}{L} \frac{y}{\sinh y} \times \left( c_i^w e^{z_i F (\alpha \Delta_o^w \phi - 1/2 \Delta_o^w \phi_i^\circ) / RT} - c_i^\circ e^{-z_i F [(1-\alpha) \Delta_o^w \phi - 1/2 \Delta_o^w \phi_i^\circ] / RT} \right) \quad (89)$$

It should be noted that in order to apply this refined model in general it is necessary to know the potential drop across the inner layer. We can recover Eq. (56) if we make the assumption that  $\alpha$  is independent of  $\Delta_o^w \phi$  and define  $k^\circ$  according to the following equation valid at equilibrium at the formal standard transfer potential:

$$\frac{\tilde{u}_i RT}{L} \frac{y}{\sinh y} e^{z_i F (\alpha \Delta_o^w \phi_i^\circ - 1/2 \Delta_o^w \phi_i^\circ) / RT} = \frac{\tilde{u}_i RT}{L} \frac{y}{\sinh y} \times e^{-z_i F ((1-\alpha) \Delta_o^w \phi_i^\circ - 1/2 \Delta_o^w \phi_i^\circ) / RT} = k^\circ \quad (90)$$

Note, however, that this approach leads to a different dependence of  $k^\circ$  on  $\Delta_o^w \phi_i^\circ$ . An interesting point concerns the fact that when  $\alpha$  is close to 0.5, the dependence of  $k^\circ$  on  $\Delta_o^w \phi_i^\circ$  vanishes.

#### 4.2.3.5 General Treatment of Ion-transfer Reactions at ITIES

In recent theoretical work on ion transfer at ITIES, the ion transfer through the diffuse layer has been analyzed [62, 63, 67]. In the following we will assume that the ion transport from bulk solution to the interface can be described according to the Nernst–Planck equation. No specific assumptions regarding the ion distribution or the potential profile will be made. The ion flux across the diffuse layers can then be obtained by solving the following equations:

$$J_i \int_{-\infty}^a e^{z_i F \phi(x)/RT} dx = -RT \times \tilde{u}_i^w \int_{-\infty}^a d(e^{z_i F \phi(x)/RT}) \quad (91)$$

$$J_i \int_b^{\infty} e^{z_i F \phi(x)/RT} dx = -RT \times \tilde{u}_i^o \int_b^{\infty} d(e^{z_i F \phi(x)/RT}) \quad (92)$$

Note that in these equations the integration limits  $\infty$  and  $-\infty$  represent the bulk phases of the oil and water phase, respectively, which is identified as the position from the interface in which the Galvani potentials equal the bulk phase values. Upon integration, the following expressions are obtained:

$$J_i = -RT \tilde{u}_i^w \frac{(c_i^a e^{z_i F \phi^a/RT} - c_i^w e^{z_i F \phi^w/RT})}{\int_{-\infty}^a e^{z_i F \phi(x)/RT} dx} = \frac{-RT \tilde{u}_i^w}{A^w} (c_i^a e^{z_i F \Delta_w^a \phi/RT} - c_i^w) \quad (93)$$

$$J_i = -RT \tilde{u}_i^o \frac{(c_i^o e^{z_i F \phi^o/RT} - c_i^b e^{z_i F \phi^b/RT})}{\int_b^{\infty} e^{z_i F \phi(x)/RT} dx} = \frac{RT \tilde{u}_i^o}{A^o} (c_i^o - c_i^b e^{z_i F \Delta_o^b \phi/RT}) \quad (94)$$

where  $A^w$  and  $A^o$  are given by

$$A^w = \int_{-\infty}^a e^{z_i F \Delta_w^x \phi/RT} dx \quad (95)$$

$$A^o = - \int_b^{\infty} e^{z_i F \Delta_o^x \phi/RT} dx = \int_{-\infty}^b e^{z_i F \Delta_o^x \phi/RT} dx \quad (96)$$

The concentrations of the ion at a and b are then obtained as

$$c_i^a = e^{-z_i F \Delta_w^a \phi} \left( -\frac{J_i A^w}{RT \tilde{u}_i^w} + c_i^w \right) \quad (97)$$

$$c_i^b = e^{-z_i F \Delta_o^b \phi} \left( -\frac{J_i A^o}{RT \tilde{u}_i^o} + c_i^o \right) \quad (98)$$

In the case of small  $A^w$  and  $A^o$ , the traditional Boltzmann distribution is recovered. This situation corresponds to the case in which the potential drops between a and “w” and between b and “o” are small. These expressions can be inserted into Eq. (50) to obtain the following result:

$$J_i = \frac{\overrightarrow{k} c_i^w e^{-z_i F \Delta_w^a \phi/RT} - \overleftarrow{k} c_i^o e^{-z_i F \Delta_o^b \phi/RT}}{1 + \overrightarrow{k} \frac{A^w}{RT \tilde{u}_i^w} e^{-z_i F \Delta_w^a \phi/RT} - \overleftarrow{k} \frac{A^o}{RT \tilde{u}_i^o} e^{-z_i F \Delta_o^b \phi/RT}} \quad (99)$$

Note that a potential dependence may easily be incorporated into an expression for  $\overrightarrow{k}$  and  $\overleftarrow{k}$  as in Eqs. (57 and 58). A Butler–Volmer type expression is obtained (Eq. 53) when  $A^w$  and  $A^o$  can be approximated to zero in Eqs. (97 and 98). Alternatively, Eqs. (97 and 98) can be incorporated into Eq. (80) if the ion transfer is described as a pure

transport process:

$$J_i = \frac{(c_i^w e^y e^{-z_i F \Delta_w^a \phi / RT} - c_i^o e^{-y} e^{-z_i F \Delta_o^b \phi / RT}) \frac{\tilde{u}_i}{L} \frac{y}{\sinh y}}{1 + \left( \frac{A^w}{RT \tilde{u}_i^w} e^y e^{-z_i F \Delta_w^a \phi / RT} - \frac{A^o}{RT \tilde{u}_i^o} e^{-y} e^{-z_i F \Delta_o^b \phi / RT} \right) \frac{\tilde{u}_i}{L} \frac{y}{\sinh y}} \quad (100)$$

As in Eq. (80), we have here specified a linear potential profile across the interface. If we define  $\vec{k}$  and  $\overleftarrow{k}$  as in Eq. (81 and 82), we recover Eq. (99). The potential dependence on the rate constant is, however, somewhat different from what is obtained from expressions based on transition state theory (Eqs. 57 and 58). In a practical situation it can be assumed that  $a$  and  $b$  are approximately equal. Then the potential drop in the aqueous phase is simply obtained as  $\Delta_a^w \phi \approx \alpha \Delta_o^w \phi$ .

Regardless of whether the transfer or transport approach is followed, the flux equation can, in principle, be solved for any given potential profile in the diffuse layers. Usually, the potential profile is quite well described using the Poisson–Boltzmann equation, which in the case of a  $z:z$  supporting electrolyte can be solved analytically. More advanced theories may also be applied [81, 82]. In a recent theoretical study based on the idea of determining the permeabilities of the diffuse double layers and the interface independently, different potential profiles were analyzed. The Poisson–Boltzmann potential profile, a stepwise linear potential profile, and a potential step profile were compared. Interestingly, even a very simple stepwise potential profile is hardly distinguishable from the linear potential profile and the relatively complicated Poisson–Boltzmann

potential distribution when realistic parameters of the ion and diffuse layers are used [62]. From these considerations it may thus be concluded that traditional steady state current voltage curves generally do not give much information about the inner layer processes.

In general, experimental studies on ion-transfer reactions lead to values of “apparent” rate constants. In this connection it is interesting to note that the nominator in Eq. (99) is essentially similar to the expression for  $J_i$  in Eq. (66) obtained from the simple Butler–Volmer approach. It thus immediately follows that the correction of an experimentally determined apparent rate constant based on Eq. (66) (equivalent to the Frumkin correction used for ET at solid electrodes) is not in direct agreement with the more general treatment leading to Eq. (99). This point was first recognized by Senda [63], who termed the denominator of Eq. (99) the Levich correction.

#### 4.2.3.6 The Marcus Model for Ion Transfer at Liquid|Liquid Interfaces

Recently, Marcus has attempted to treat the ion transfer as a combined activation-controlled and transport-controlled process [68]. In the Marcus theory for ion transfer between two immiscible solutions, the ion transport is described using a Nernst–Planck type equation [57]. This equation leads to an expression of  $k^\circ$  similar to that obtained by Kakiuchi [60],

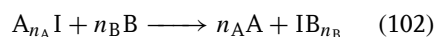
$$k^\circ = \frac{\tilde{u} RT}{L} = \frac{D}{L} \quad (101)$$

The experimentally determined  $k^\circ$  leads to a phenomenological diffusion coefficient that is in the order of  $10^{-8} \text{ cm}^2 \text{ s}^{-1}$ , assuming an interface thickness of 10 Å.

A central point in the Marcus theory is the experimentally and theoretically verified presence of protrusions at the

liquid|liquid interface. It is assumed that the ion transfer occurs via attachment of the ion to a protrusion in one phase. The probability of forming a protrusion of height  $h$  is given by  $P(h)$ . The probability of forming a protrusion is related to the Gibbs energy of formation of the protrusion.

The overall process of transfer of an ion I from a solvent A to a solvent B can be shown schematically as



Here  $n_A$  and  $n_B$  denotes a measure of the solvation of I in A and B.

The attachment and detachment of an ion to a protrusion in A is described by the rate constants  $k^A$  and  $k_-^A$ . Using these rate constants as well as the rate constant of detachment of the ion in solvent B, it is possible to describe the ion flux across the inner layer.

$$J = [k^A c_i(z_a) - k_-^A c_i(z_a)] P(h_a) \Delta h_a \quad (103)$$

$$J = k_-^B c_i(z_b) P(h_b) \Delta h_b \quad (104)$$

The overall rate constant of ion transfer is obtained as

$$\frac{1}{k_{\text{rate}}} = \frac{1}{k_{\text{assn}}^A} + \frac{1}{K_{\text{eq}}^A k_{\text{diff}}^A} + \frac{1}{K_{\text{eq}}^B k_{\text{diss}}^B} \quad (105)$$

In this equation the rate constants and equilibrium constants may be estimated using the transition state theory. In this treatment an activation energy can easily be incorporated in the expressions for  $k^A$  and  $k_{\text{diss}}^B$  using the transition state theory.

$$k_{\text{assn}}^A = k^A P(h_a) \Delta h_a \quad (106)$$

$$K_{\text{eq}}^A = \frac{1}{2g} \langle \pi r^2 \rangle \sigma P(h_a) \Delta h_a \quad (107)$$

$$K_{\text{eq}}^B = \frac{1}{2g} \langle \pi r^2 \rangle \sigma P(h_b) \Delta h_b e^{-[\mu(z_b) - \mu(z_a)] / k_B T} \quad (108)$$

The electrochemical potential of the ion at  $z_b$  and  $z_a$  is given by  $\mu(z_b)$  and  $\mu(z_a)$ , respectively. Within the framework of a transition state model, the  $(x, y)$  oscillation of the ion transverse to the protrusion is considered. The thermally averaged mean square displacement or the  $(x, y)$  oscillator is given by  $\langle r^2 \rangle$ . The surface density of protrusions is termed  $\sigma$  and  $g$  is a structural factor. It is instructive to consider one of the limiting situations in which  $K_{\text{eq}}^A k_{\text{diff}}^A$  is the rate-controlling step. In this case the expression for  $k_{\text{rate}}$  reduces to

$$k_{\text{rate}} = K_{\text{eq}}^A k_{\text{diff}}^A = \frac{1}{2} g \langle \pi r^2 \rangle \sigma P(h_a) \Delta h_a k_{\text{diff}}^A \quad (109)$$

The expression for  $k_{\text{diff}}^A$  is essentially the same as that derived by Kakiuchi for an ion-transfer reaction given in Eq. (82). It thus immediately follows that the apparent good agreement between experimentally determined ion-transfer rate constants and Kakiuchi's model is also consistent with the Marcus model. Furthermore, the small phenomenological diffusion coefficient needed to fit the data to Eqs. (80 to 84) may simply be explained by a small  $K_{\text{eq}}^A$ .

The Marcus theory is difficult to apply directly in a practical situation, owing to lack of knowledge of the probability of the formation of protrusions. One way to overcome this problem could be to employ capillary wave theory for the interface between two immiscible electrolyte solutions. Recently, theoretical efforts have been made to describe capillary waves at soft electrified interfaces [83]. It may be possible to use such theories to quantify the value of  $P(h) \Delta h$ . One of the major complications is related to the fact that the surface tension is dependent on the Galvani potential difference between the two

phases, which means that  $P(h_a)\Delta h_a$  is potential-dependent. Theoretical [77] and experimental [84, 85] studies have been undertaken to clarify the dependence of the surface structure on an electric field, but more studies are clearly needed before quantitative predictions can be made. In particular, a clear-cut experimental evidence of a link between protrusions at liquid|liquid interfaces and ion transfer is still lacking.

#### 4.2.3.7 Other Models

Another model that treats the ion transfer across ITIES as an activated transport process by applying classical transition state theory has been suggested by Girault and Schiffrin [55]. Also in this case the equation describing the ion flux across the interface is similar to that obtained by the Butler–Volmer approach. Naturally, the interpretation of the  $\alpha$  values and  $k^\circ$  is somewhat different in that case. Experimentally [85] and theoretically [79], the effect of solvent viscosity on the ion-transfer process has been confirmed indicating the importance of this parameter.

Aoki has modeled ion transfer as a combined transport and activated process [65]. In this approach the activation energy for ion transfer is a combination of an electric potential energy, an activation energy due to solvation changes, and an energy required to form a pore into the interface. The microscopic ion transport is described using the Langevin equation. In certain cases, such as when viscous effects are pronounced, the theory is in good agreement with the Butler–Volmer equation. A limiting factor in this theory is related to the fact that it cannot successfully account for the experimentally observed concave variation of the logarithm to the ion-transfer rate constant with the Galvani potential difference.

In a model put forward by Indenbom, the ITIES is considered as an elastic film in which forces of interfacial tension counteract the forces of an external electric field [64]. This causes a potential-dependent compressed grooved structure of the interface at which ion transfer takes place when the compression reaches a critical state. The validity of this picture will rely on detailed molecular dynamics studies of the microscopic features of ion transfer across ITIES. In this connection it is relevant to mention the work of Cunnane and coworkers in which the kinetics of ion transfer across a monolayer adsorbed at a liquid|liquid interface is discussed in terms of the energy required to form a pore of a size similar to that of the transferring ion [56].

Schmickler has treated the ion-transfer process within the framework of a lattice-gas model [66]. In this model the interface is treated as an extended region in which the two solvents mix. The reaction rate is generally obtained using the transition state theory in combination with Kramers theory depending on whether frictional forces are important.

The central idea in Schmickler's model is to treat the liquid|liquid system as an infinite three-dimensional lattice. The fraction of sites occupied by the two kinds of solvent molecules at a position  $z$  are termed  $f_1(z)$  and  $f_2(z)$ .

$$f_1(z) = \begin{cases} 1 - \frac{1}{2e^{z/\delta}} & \text{for } z \leq 0 \\ \frac{1}{2e^{-z/\delta}} & \text{for } z \geq 0 \end{cases} \quad (110)$$

$$f_2(z) = 1 - f_1(z) \quad (111)$$

In these equations,  $\delta$  represents the width of the interface.

The final result is shown to be in good agreement with a Butler–Volmer

behavior. Schmickler's treatment may be useful in a theoretical modeling of the transfer process, in particular to determine the potential of mean force acting on the ion. Qualitative experimental predictions may also be made. This model can, for instance, successfully account for the dependence of the solvation energy on the ion-transfer rate constant. It may be noted that no assumptions regarding the microscopic structure of the liquid|liquid interface are made in this description and, for instance, surface tension is not considered explicitly. An advantage of this relatively simple model is that additional complications such as ion pairing of supporting electrolyte ions can be described [86].

#### 4.2.4

#### Conclusion and Outlook

The analysis presented in this review appears to show that while classical transition state theory provides a good account for experimental observation concerning ET kinetics, the picture is less clear for ion-transfer processes. Our understanding remains hindered by the primitive knowledge of the ITIES structure at a microscopic level, despite current efforts based on computer modeling [41, 51, 66, 87]. The potential distribution across the interface is also an essential piece of information that is yet to be clarified in the liquid|liquid context. Furthermore, these analyses have excluded any specific interaction of ions at the interface, which can also exert a profound effect on the reactivity of the system. In order to address all these aspects, it is crucial to develop novel spectroscopic techniques coupled to electrochemical systems.

Dynamic studies of heterogeneous ET across ITIES consistently suggest that

these processes are strongly nonadiabatic. The maximum values of rate constants measured either by SECM or photoelectrochemical techniques are of the order of  $10^{-19} \text{ cm}^4 \text{ s}^{-1}$ , which coincide with the nonadiabatic limit obtained from the models outlined in Sect. 4.2.2. The low electronic coupling between reactants is a result of the typical separation distances at the interface. These distances are also responsible for reorganization energies close to 1 eV as estimated from experimental data.

Undoubtedly, a key development that will clarify basic aspects in connection to ET dynamic is the effective control on the distance separating the redox species. It can be envisaged that redox couples linked by functionalized spacers, which allow highly ordered self-assembling structures, could provide very valuable information on the rate of interfacial ET and the effect of the interfacial potential. In this case, electronic coupling between reactants could be quite substantial and sophisticated modeling will be required to fully rationalize these findings. Ultrafast photoinduced processes can be effectively approached by spectroscopic Pump-Probe methods down to the femtosecond timescale.

The ion-transfer theories outlined in this chapter are all based on idealized models. In practice, complications in the measurements related to adsorption of the transferring ion or chemical reactions associated with the ion transfer arise. Detailed theoretical descriptions of the microscopic nature of such complications are still lacking. One of the most interesting feature of simple ion transfers concerns the fact that they always appear fast, and indeed as the experimental techniques have been improved, the measured values have increased even for similar ion transfers. One way to clarify the microscopic features of



ion-transfer reactions could be to perform photoinduced ion-transfer reactions in a controlled way. Such an experiment could, for instance, be carried out using a surfactant that upon illumination generates an ion that can transfer across the interface.

## References

1. F. Reymond, D. J. Fermín, H. J. Lee et al., *Electrochim. Acta* **2000**, 45, 2647–2662.
2. A. G. Volkov, D. W. Deamer, *Liquid-Liquid Interfaces: Theory and Methods*, CRC Press, Boca Raton, Fla., 1996.
3. A. G. Volkov, D. W. Deamer, D. I. Tanelian et al., *Liquid Interfaces in Chemistry and Biology*, John Wiley & Sons, New York, 1998.
4. R. Lahtinen, D. J. Fermín, K. Kontturi et al., *J. Electroanal. Chem.* **2000**, 483, 81–87.
5. D. J. Fermín, R. Lahtinen in *Dynamic Aspects of Heterogeneous Electron Transfer Reactions at Liquid/Liquid Interfaces* (Ed.: A. Volkov), Marcel Dekker, Boca Raton, Fla., 2001, pp. 179–228.
6. Z. Samec, V. Marecek, J. Weber, *J. Electroanal. Chem.* **1978**, 96, 245–247.
7. Z. Samec, *J. Electroanal. Chem.* **1979**, 99, 197–205.
8. Y. I. Kharkats, *Sov. Electrochem.* **1976**, 12, 1257.
9. H. H. J. Girault, D. J. Schiffrin, *J. Electroanal. Chem.* **1988**, 244, 15–26.
10. R. A. Marcus, *J. Phys. Chem.* **1990**, 94, 4152–4155, 7742.
11. R. A. Marcus, *J. Phys. Chem.* **1990**, 94, 1050–1055.
12. R. A. Marcus, *J. Phys. Chem.* **1991**, 95, 2010–2013.
13. Y. Cheng, D. J. Schiffrin, *J. Electroanal. Chem.* **1991**, 314, 153–163.
14. Y. Cheng, D. J. Schiffrin, *J. Chem. Soc., Faraday Trans.* **1993**, 89, 199–205.
15. Y. F. Cheng, D. J. Schiffrin, *J. Chem. Soc., Faraday Trans.* **1994**, 90, 2517–2523.
16. V. J. Cunnane, G. Geblewicz, D. J. Schiffrin, *Electrochim. Acta* **1995**, 40, 3005–3014.
17. G. Geblewicz, D. J. Schiffrin, *J. Electroanal. Chem.* **1988**, 244, 27–37.
18. S. Kihara, M. Suzuki, K. Maeda et al., *J. Electroanal. Chem.* **1989**, 271, 107–125.
19. E. Makrlík, *Z. Phys. Chem.* **1987**, 268, 212–214.
20. M. Lher, R. Rousseau, E. Lhostis et al., *C. R. Acad. Sci. Paris*, t. 322, Série IIb **1996**, 322, 55–62.
21. Q. Z. Chen, K. Iwamoto, M. Seno, *Electrochim. Acta* **1991**, 36, 291–296.
22. S. Daniele, M. A. Baldo, C. Bragato, *Electrochem. Commun.* **1999**, 1, 37–41.
23. H. H. Girault, see the web site [dcwww.epfl.ch](http://dcwww.epfl.ch) for a comprehensive list of free energy of ion transfer at various liquid/liquid interfaces.
24. A. A. Stewart, J. A. Campbell, H. H. Girault et al., *Ber. Bunsen-Ges. Phys. Chem.* **1990**, 94, 83–87.
25. Z. Ding, P.-F. Brevet, H. H. Girault, *Chem. Commun.* **1997**, 2059–2060.
26. Z. F. Ding, D. J. Fermin, P. F. Brevet et al., *J. Electroanal. Chem.* **1998**, 458, 139–148.
27. J. Zhang, C. J. Slevin, L. Murtomaki et al., *Langmuir* **2001**, 17, 821–827.
28. J. Zhang, P. R. Unwin, *J. Phys. Chem. B* **2000**, 104, 2341–2347.
29. B. Quinn, R. Lahtinen, L. Murtomaki et al., *Electrochim. Acta* **1998**, 44, 47–57.
30. A. J. Bard, D. E. Cliffel, C. Demaille et al., *Ann. Chim.* **1997**, 87, 15–31.
31. A. L. Barker, J. V. Macpherson, C. J. Slevin et al., *J. Phys. Chem. B* **1998**, 102, 1586–1598.
32. A. L. Barker, P. R. Unwin, S. Amemiya et al., *J. Phys. Chem. B* **1999**, 103, 7260–7269.
33. M. Tsionsky, A. J. Bard, M. V. Mirkin, *J. Phys. Chem.* **1996**, 100, 17 881–17 888.
34. M. Tsionsky, A. J. Bard, M. V. Mirkin, *J. Am. Chem. Soc.* **1997**, 119, 10 785–10 792.
35. C. Wei, A. J. Bard, M. V. Mirkin, *J. Phys. Chem.* **1995**, 99, 16 033–16 042.
36. B. B. Smith, J. W. Halley, A. J. Nozik, *Chem. Phys.* **1996**, 205, 245–267.
37. H. H. Girault, *J. Electroanal. Chem.* **1995**, 388, 93–100.
38. I. Benjamin, Y. I. Kharkats, *Electrochim. Acta* **1998**, 44, 133–138.
39. N. Sutin, *Acc. Chem. Res.* **1982**, 15, 275.
40. J. T. Hupp, M. J. Weaver, *J. Electroanal. Chem.* **1983**, 152, 1–14.
41. W. Schmickler, *J. Electroanal. Chem.* **1997**, 428, 123–127.
42. B. Liu, M. V. Mirkin, *J. Am. Chem. Soc.* **1999**, 121, 8352–8355.
43. D. J. Fermín, Z. Ding, H. Duong et al., *J. Phys. Chem. B* **1998**, 102, 10 334–10 341.
44. D. J. Fermín, H. Duong, Z. Ding et al., *Electrochem. Comm.* **1999**, 1, 29–32.
45. D. J. Fermín, H. Duong, Z. Ding et al., *Phys. Chem. Chem. Phys.* **1999**, 1, 1461–1467.

46. D. J. Fermín, H. Duong, Z. Ding et al., *J. Am. Chem. Soc.* **1999**, 121, 10 203–10 210.
47. H. Jensen, J. J. Kakkassery, H. Nagatani et al., *J. Am. Chem. Soc.* **2000**, 122, 10 943–10 948.
48. N. Eugster, D. J. Fermín, H. H. Girault, *J. Phys. Chem. B* **2002**, 106, 3428–3433.
49. P. Vanysek, *Electrochim. Acta* **1995**, 40, 2841–2847.
50. H. H. Girault, *Mod. Aspects Electrochem.* **1993**, 25, 1–62.
51. I. Benjamin, *Annu. Rev. Phys. Chem.* **1997**, 48, 407.
52. Z. Samec, T. Kakiuchi, *Adv. Electrochem. Sci. Eng.* **1995**, 4, 297–361.
53. C. Gavach, B. D'Epenoux, F. Henry, *J. Electroanal. Chem.* **1975**, 64, 107–115.
54. J. Koryta, P. Vanysek, M. Brezina, *J. Electroanal. Chem.* **1977**, 75, 211–228.
55. H. H. J. Girault, D. J. Schiffrin, *J. Electroanal. Chem.* **1985**, 195, 213–227.
56. V. J. Cunnane, D. J. Schiffrin, M. Fleischmann et al., *J. Electroanal. Chem.* **1988**, 243, 455–464.
57. I. Benjamin, *J. Chem. Phys.* **1992**, 96, 577–585.
58. Y. Y. Gurevich, Y. I. Kharkats, *J. Electroanal. Chem.* **1986**, 200, 3–16.
59. Z. Samec, Y. I. Kharkats, Y. Y. Gurevich, *J. Electroanal. Chem.* **1986**, 204, 257–266.
60. T. Kakiuchi, *J. Electroanal. Chem.* **1992**, 322, 55–61.
61. T. Kakiuchi, J. Noguchi, M. Senda, *J. Electroanal. Chem.* **1992**, 327, 63–71.
62. K. Kontturi, J. A. Manzanares, L. Murtomäki, *Electrochim. Acta* **1995**, 40, 2979–2984.
63. M. Senda, *Electrochim. Acta* **1995**, 40, 2993–2997.
64. A. V. Indenbom, *Electrochim. Acta* **1995**, 40, 2985–2991.
65. K. Aoki, *Electrochim. Acta* **1996**, 41, 2321–2327.
66. W. Schmickler, *J. Electroanal. Chem.* **1997**, 426, 5–9.
67. L. Murtomäki, A. K. Kontturi, D. J. Schiffrin, *J. Electroanal. Chem.* **1999**, 474, 89–93.
68. R. A. Marcus, *J. Chem. Phys.* **2000**, 113, 1618–1629.
69. Z. Samec, V. Marecek, J. Weber et al., *J. Electroanal. Chem.* **1981**, 126, 105–119.
70. P. D. Beattie, A. Delay, H. H. Girault, *Electrochim. Acta* **1995**, 40, 2961–2969.
71. T. Kakiuchi, Y. Takasu, *J. Phys. Chem. B* **1997**, 101, 5963.
72. Z. F. Ding, F. Reymond, P. Baumgartner et al., *Electrochim. Acta* **1998**, 44, 3–13.
73. Z. F. Ding, R. G. Wellington, P. F. Brevet et al., *J. Electroanal. Chem.* **1997**, 420, 35–41.
74. D. J. Fermín, Z. Ding, P. F. Brevet et al., *J. Electroanal. Chem.* **1998**, 447, 125–133.
75. I. Benjamin, *Chem. Rev.* **1996**, 96, 1449–1475.
76. I. Benjamin, *Science* **1993**, 261(5128), 1558–1560.
77. K. J. Schweighofer, I. Benjamin, *J. Electroanal. Chem.* **1995**, 391, 1–10.
78. P. A. Fernandes, M. N. D. S. Cordeiro, J. A. N. F. Gomes, *J. Phys. Chem. B* **1999**, 103, 6290–6299.
79. R. Ferrigno, H. H. Girault, *J. Electroanal. Chem.* **2001**, 496, 131–136.
80. Z. Samec, V. Marecek, D. Homolka, *J. Electroanal. Chem.* **1985**, 187, 31–51.
81. Q. Cui, G. Zhu, E. Wang, *J. Electroanal. Chem.* **1995**, 383, 7–12.
82. L. I. Daikhin, A. A. Kornyshev, M. Urbakh, *J. Electroanal. Chem.* **2000**, 483, 68–80.
83. Z. H. Zhang, I. Tsuyumoto, S. Takahashi et al., *J. Phys. Chem. A* **1997**, 101, 4163–4166.
84. Z. H. H. Zhang, I. Tsuyumoto, T. Kitamori et al., *J. Phys. Chem. B* **1998**, 102, 10 284–10 287.
85. Y. Shao, H. H. Girault, *J. Electroanal. Chem.* **1990**, 282, 59–72.
86. C. M. Pereira, W. Schmickler, F. Silva et al., *J. Electroanal. Chem.* **1997**, 436, 9–15.
87. I. Benjamin, *ACS Symp. Ser.* **1994**, 568, 409–422.

## 4.3

**The Influence of Ad-atom Adsorption on Reaction Rates and Mechanisms**

Georgios Kokkinidis

Aristotle University of Thessaloniki, Thessaloniki, Greece

## 4.3.1

**Introduction**

It is well known that many chemical reactions do not by themselves occur at a significant rate, although thermodynamics predict that they are very favorable. The rate of such reactions, however, may be increased by several orders of magnitude by a catalyst. The catalyst (homogeneous or heterogeneous) is a substance, which alters the rate of a chemical reaction without itself being consumed or generated in the process. Similarly, there are many electrochemical reactions that also do not proceed with a sufficient rate because of poor kinetics. For these reactions, it is again necessary to find an active *electrode/catalyst* or, better, an *electrocatalyst*, otherwise high overpotentials should be applied in order to promote the reaction. Thus, the term *electrocatalysis* was introduced for the heterogeneous charge-transfer reactions that take place at the electrode/electrolyte solution interface. The objective of electrocatalysis is to discover electrocatalysts that allow electrode reactions to occur with a sufficient rate at potentials very close to the equilibrium potential and, in some cases, to improve the selectivity with respect to the reaction products.

The catalytic role of an electrode is revealed by writing the rate of an electrochemical reaction as follows [1]:

$$v = \frac{j}{nF} = \left( c \frac{kT}{h} e^{-\Delta G^{\circ\#}/RT} \right) \times e^{-\alpha F \Delta \Phi / RT} \quad (\text{for a cathodic process}) \quad (1)$$

This equation makes it clear that electrocatalysis consists of two terms: an electrical one (the term depending on the potential difference across the interface) and a chemical one (the Arrhenius term), which depends on the nature of the electrode material.

Although by applying high overpotentials one can increase the rate of an electrochemical reaction on a given electrode/catalyst even by more than 10 orders of magnitude, the activity of the electrode, the Arrhenius term, still remains the most important fact in electrocatalysis. This is obvious, since the energy efficiency of any cell is determined mainly by the overpotentials necessary at the anode and cathode. The lower the overpotentials, the better is the energy efficiency. Furthermore, the application of high overpotentials usually introduces problems due to the interference of undesired reactions (e.g. the hydrogen or the oxygen evolution reaction, the electrodisolution of the electrode, etc.).

The catalytic activity of an electrode depends on its electronic – and perhaps crystallographic – properties. When the reactants or intermediates are adsorbed on the electrode surface, the reaction rate will depend additionally on the heat of adsorption, on the strength of bond-forming or bond-breaking, and on the properties of the adsorption isotherm. All these factors may be changed by the modification of the electrode surface from adsorbed species existing in the solution, not participating in the reaction. These species can sometimes improve the catalytic activity of the bare material. For example, heavy metal atoms (e.g. Pb, Tl, and Bi) deposited in the underpotential region have been shown to increase the catalytic activity of noble metal electrodes (e.g. Pt, Au, Ag, Pd, etc.) for several technologically interesting

electrochemical reactions. Such reactions are the reduction of oxygen, the oxidation of organic fuels, the reduction of aromatic nitro compounds, and so forth. Although noble metals are considered to be the best electrocatalysts in contemporary electrocatalysis, their modification by foreign metal ad-atoms deposited in the underpotential region may improve their catalytic activity for certain electrochemical reactions.

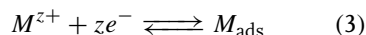
#### 4.3.2

##### **Metal Ad-atoms Deposited in the Underpotential Region**

Foreign metal ad-atoms can be deposited on an electrode electrochemically in the so-called underpotential region, that is, the potential region positive to the reversible Nernst potential for the bulk metal deposition.

$$\Delta E = E_{\text{ads}} - E_{\text{Nernst}} \geq 0 \quad (2)$$

The underpotential deposition (abbreviated to UPD) of a metal  $M$  on a foreign metal substrate  $M'$  is a process that takes place according to the reaction



This Faradaic adsorption of  $M^{z+}$  ions dissolved in the solution of the supporting electrolyte leads to the formation of sub- and monolayer coverages of discharged  $M$  ad-atoms and constitutes the first stage in electrocrystallization. The UPD process was studied rather extensively because of its importance in investigating a wide variety of electrochemical phenomena, such as adsorption on electrified interfaces, charge-transfer reactions, surface diffusion, nucleation and growth, double-layer changes, and, of course, because of its

fundamental and practical significance in electrocatalysis.

The UPD process was studied for a large number of systems using both polycrystalline and monocrystalline electrodes as substrates and the progress of understanding all related parameters was covered in depth in several review articles [2–5]. Here we will give only an outline of some thermodynamic and structural aspects, which will be useful for the better understanding of the role of the UPD ad-atoms as reaction modifiers in electrocatalysis.

The equilibrium potential for the UPD process (Reaction 3) may be formulated as [3]

$$E_{\text{ads}}(\theta) = E^0 + \left( \frac{RT}{zF} \right) \ln \left( \frac{f_{M^{z+}} c_{M^{z+}}}{f_{\text{ads}} \theta} \right) \quad (4)$$

where  $f_{M^{z+}}$  and  $f_{\text{ads}}$  are the activity coefficients of the metal ion in solution and the bulk deposit ( $f_{\text{ads}} = 1$  for  $\theta \approx 1$ ),  $c_{M^{z+}}$  is the metal ion concentration in solution, and  $\theta$  the UPD ad-atom coverage. Since  $\theta$  takes values between 0 and 1, Eq. (4) yields an equilibrium potential that is always more positive than the corresponding Nernst potential for the bulk metal deposition. Moreover, Eq. (4) implies that the submonolayer equilibrium potential shifts toward more positive potentials by  $60/z$  mV  $\text{dec}^{-1}$  for constant  $\theta$  with increasing the metal ion concentration in solution.

There are two excess parameters, the charge  $\sigma = (\partial \gamma / \partial E)_{\mu}$  and the surface concentration  $\Gamma = -(\partial \gamma / \partial \mu)_E$  from which the electrosorption valency may be defined and experimentally determined:

$$\ell = \frac{1}{F} \left( \frac{\partial \sigma}{\partial \Gamma} \right)_E \quad (5)$$

The symbols in all the above expressions have their usual meaning.

The electrosorption valency expresses the charge flow during the electrosorption process at a constant potential. It takes values ranging between zero and the ionic charge  $z$ . Values very close to  $z$  show that the adsorbed species are almost completely discharged, while values of  $\ell$  lower than  $z$  indicate adsorption with partial charge transfer. The adsorbed species are recognized as ad-atoms when  $\ell$  takes values very close or equal to  $z$ .

Saturate coverages with ad-atoms are obtained at potentials close to the potential for the bulk metal deposition. The maximum surface concentration is about  $\Gamma_{\max} \approx 2 \times 10^{-9} \text{ mol cm}^{-2}$ . This surface concentration corresponds to a maximum amount of charge  $\sigma_{\max} \approx z 200 \text{ } \mu\text{C cm}^{-2}$  [3, 4].

The extent of the UPD region depends on the binding energies between the adsorbed atoms and the atoms of the substrate metal. There exists a linear relationship between  $\Delta E_p$  and  $\Delta \Phi$ , where  $\Delta \Phi$  is the difference in the work functions between the substrate and the adsorbed metal. This linear correlation is expressed by a semiempirical Eq. (3):

$$\Delta E_p = 0.5 \Delta \Phi \quad (6)$$

$\Delta E_p$  is defined as the difference between the bulk and the most positive adsorption peak of the corresponding cyclic voltammogram for the UPD. The linear correlation holds for systems with polycrystalline substrate electrodes, while for systems with single-crystal electrodes some deviations were observed [3]. This behavior suggests that the binding energies of the UPD are not only determined by the difference in the electronegativities expressed as  $\Delta \Phi$  but they are also influenced by the lateral interactions that are governed by the crystallographic orientation of the substrate.

From theoretical considerations of bond formation in electrosorbates it was concluded that the underpotentially deposited metal ad-atoms can approximately be considered to be covalently bonded and nearly completely discharged if the difference in the Pauling's electronegativities of the substrate and adsorbed metal is  $|\Delta \chi| \leq 0.5$  [6]. That means these systems have electrosorption valency  $\ell/z \approx 1$ . Systems in which the electrosorption valency is equal to the ionic charge are those resulting from the UPD of heavy metal ions on noble and transition metal electrodes.

There are a number of parameters that can actually determine the structure of the UPD monolayers [4]. The most outstanding ones are certainly the structure of the substrate, the ratio between the diameter of the adsorbed species and the distance of two adjacent adsorption sites, and of course the degree of the UPD ad-atom coverage. At low surface coverages a UPD metal monolayer consists of isolated  $M$  ad-atoms or partially discharged and desolvated ions, which are randomly distributed on the substrate owing to the lateral repulsion. With the increase in the degree of coverage some ordering occurs and at high surface coverages the UPD layer may form a sequence of two-dimensional periodic superlattice structures with electronic properties closely approaching those of the bulk metal.

On single-crystal electrodes the UPD deposits often form well-defined, ordered monolayers. Hypothetical superlattice structures have been proposed, which rely on the charges determined for the various peaks observed in the cyclic voltammograms. The anions of the supporting electrolytes influence the shape and the position of the UPD peaks in the cyclic voltammograms, although the superlattice structures are not always affected by

interactions between the ad-atoms and the anions adsorbed on the UPD monolayer [7].

In the beginning, conventional electrochemical techniques had been used to study the UPD, both on polycrystalline and single-crystal electrodes. The work done on single-crystal electrodes included both low index planes and stepped surfaces. The technique developed by Clavilier et al. [8, 9] (the so-called flame annealing technique) has led to a revolution in electrochemical studies, since single crystals of platinum and gold can be relatively easily formed and precisely oriented using an optical technique. Single-crystal surfaces were previously prepared in an ultrahigh vacuum (UHV) chamber by sputtering and annealing, and their structure was defined by low energy electron diffraction (LEED) [10–12]. The results of the various techniques were compared mainly in connection with the hydrogen adsorption on platinum [13, 14].

The electrochemical methods provide only indirect information about the structure of the UPD ad-atom layers in an atomic scale. In order to obtain more direct information about the structure of the UPD ad-atom layers, many investigators have adopted the use of in situ techniques, in which the electrode surface is examined with surface science methods. The methods mainly used are in situ X-ray diffraction [7, 15–17], in situ scanning tunneling microscopy (STM) [18–23], and in situ atomic force microscopy (AFM) [24]. These methods have provided detailed information on the atomic structure, the thermodynamic stability, and the dependence of the structure on the potential for several UPD systems. However, little attempt has been made (and this mainly concerns the reduction of oxygen) to correlate directly the structure of the ad-atom

layers to their influence on the catalytic activity of the substrate. The reason is that the superlattice structures of the ad-atom layers are influenced by the strong adsorption of intermediates involved in the mechanism of many electrocatalytic reactions. For example, the rate of formic acid oxidation on Pt modified by Pb ad-atoms is different if lead is adsorbed before or after formic acid [25].

#### 4.3.3

##### Electrocatalysis by Ad-atoms

Modified electrodes with ad-atoms (usually deposited in the underpotential region) exhibit enhanced electrocatalytic activity for several categories of electrochemical reactions. The most extensively studied reactions are those related to the development of low-temperature fuel cell technology, namely, the reduction of oxygen and the oxidation of organic fuels. The ad-atoms may influence the rate and the mechanism of electrochemical reactions through [26–29]

1. the third-body effect,
2. the prevention of poison formation,
3. the bifunctional mechanism, and
4. the modification of the electronic properties of the electrode surface.

In the third-body mode of action, the ad-atoms are considered as inert species, actually not participating in the reaction. Their presence acts only to diminish the places where the poison formation reaction can take place. The poisoning reaction requires greater number of neighboring sites (say Pt surface atoms) not occupied by ad-atoms than the main reaction that proceeds in parallel through reactive (not strongly adsorbed) intermediates. The

enhanced reactivity in the presence of ad-atoms results from decreased poisoning and, thereby, an increase in the rate of the reaction branch, which requires smaller number of neighboring sites.

Blocking of poison formation through the third-body mechanism is physical. Ad-atom coverages at around 0.5, although permitting the adsorption/dehydrogenation step (which is necessary for initiating the oxidation of an organic molecule), prevent the strong adsorption of intermediates, which poison the electrocatalyst surface. In some cases, it is believed that adsorbed hydrogen is involved in the poison formation reaction. The ad-atoms block the adsorption of hydrogen, thus inhibiting the poison reaction. The required coverage by the ad-atoms should be greater than 0.5 in the hydrogen potential region to avoid poison formation.

The bifunctional mechanism refers not only to catalysts modified by ad-atoms but also to electrocatalysis on bimetallic surfaces. The oxidation of methanol on Pt–Ru alloy surfaces is a typical example of bifunctional mechanism. The role of the modifier is to supply oxygen for the oxidation of either reactive or poisoning intermediates. The potential in which increased reaction rates are observed is governed by the potential in which the adjacent modifier or ad-atom adsorbs oxygen, which should be less positive than that of platinum. The bifunctional mechanism reduces the oxidation overpotential, which is particularly important for fuel cells. The bifunctional mechanism refers also to catalysts on which chemisorption of reducible groups and reductive cleavage of bonds might increase the electrocatalyst selectivity. A bridge adsorption for the reactive intermediate is assumed to explain the selective bond cleavage, in which a

substrate atom and an adjacent ad-atom are involved.

Finally, the ad-atoms may cause local electronic changes on the substrate, thus affecting the reactant–substrate interactions. The role of ad-atoms on the modification of the catalytic properties of metal surfaces has been extensively studied [30–32]. The behavior of these systems has been rationalized in terms of changes in adsorption bond strength of the reactant species caused by changes in catalyst (metal) work function, which results from the electronic interactions of the ad-atoms with the active metal surface [30–32].

#### 4.3.4

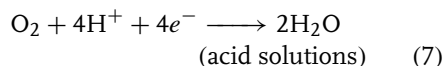
#### Reactions Catalyzed by Ad-atoms

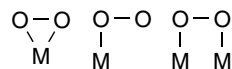
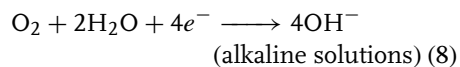
##### 4.3.4.1 Reduction of Oxygen

The reduction of oxygen is one of the most extensively studied electrochemical reactions. There are two reasons for the increased interest for this reaction, *firstly*, its fundamental significance with respect to electrode kinetics and, *secondly*, its role in the area of electrochemical energy conversion and corrosion. The kinetics and mechanism of oxygen electroreduction greatly depends on the electrode material. Oxygen reduction is also a very sensitive reaction to the surface structure, as shown by studies on single-crystal electrodes of different metals. There are several extended reviews and book chapters, which cover all these aspects of oxygen electroreduction [33–37].

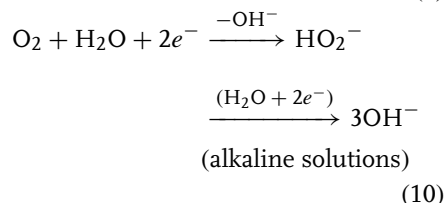
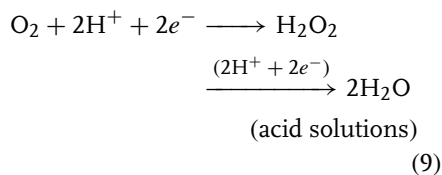
In aqueous solutions, oxygen reduction is considered to proceed by two overall reaction pathways [38].

The direct four-electron pathway:





The peroxide pathway:



Depending on the electrode material, the reduction of oxygen occurs by one or the other reaction pathway. The two reaction pathways may also take place in parallel. The most powerful technique for the quantitative determination of the extent of these reactions was proved to be the rotating ring-disc electrode voltammetry, which allows the detection of hydrogen peroxide on the ring electrode.

On some electrodes, hydrogen peroxide cannot undergo further reduction and is obtained as the final reaction product. Electrodes on which the two-electron reduction to hydrogen peroxide predominates are Au, Hg, and various carbon materials. Electrodes on which the four-electron reduction to water is predominant include Ag, Pt, and the Pt family metals. Platinum is considered to be the best electrocatalyst for oxygen reduction, since the reduction on this electrode occurs with the lowest overpotential. The reaction pathway that is more favorable depends on the way molecular oxygen is adsorbed on the metal surface. Three different models for adsorption have been proposed, the Griffith's model, the Pauling's model, and the bridge model [38, 39]:

The end-on adsorption (Pauling's model) favors the two-electron reduction of  $\text{O}_2$  to  $\text{H}_2\text{O}_2$ . The bridge model, with the two bonds with two metal sites, favors the direct four-electron reduction of  $\text{O}_2$  to  $\text{H}_2\text{O}$  through rupture of the O—O bond.

Metal ad-atoms deposited in the underpotential region strongly influence the rate and mechanism of oxygen reduction. Positive and/or negative catalytic effects were observed depending on the substrate electrode. The work done was reviewed by Adzic [26] and Kokkinidis [27]. It was reported that Pb, Tl, and Bi ad-atoms catalyze the reduction of oxygen on Au and carbon electrodes. The half-wave potential is shifted toward less negative potentials and the two-electron reduction to hydrogen peroxide is transformed to the four-electron reduction to water. The catalytic action is mainly observed in alkaline electrolytes and at potentials of low UPD ad-atom coverages. Similar behavior was also observed on ruthenium [40]. Ruthenium partially oxidized, which is inactive for  $\text{O}_2$  reduction in alkaline solutions, can be made very active by Pb and Tl ad-atoms. Traces of Pb and Tl are sufficient to activate the four-electron reduction on this electrode.

In contrast to positive catalysis on gold and carbon electrodes, Pb, Tl, and Bi ad-atoms cause a negative catalytic effect on Pt and Ag electrodes. The four-electron reduction on the bare metals changes to two-electron reduction on the electrodes covered by the modifiers. This partial inhibition occurs at negative potentials, in the mass-transport control region, where almost complete UPD ad-atom coverages are obtained. Finally, the reduction of



oxygen on Pt [41] and Au [42] is completely inhibited by Cu ad-atoms deposited at underpotentials.

Figure 1 shows, as an example, the rotating-disc voltammograms of oxygen reduction on Ag(100) in the absence and in the presence of  $\text{Pb}^{2+}$  ions in solution [43]. The cyclic voltammogram for the UPD of Pb on the Ag(100) single-crystal electrode is given for comparison. It should be noted that the observed potential shift of the inhibition effect

reflects the concentration-dependence of the UPD process according to Eq. (4).

Figure 2 shows ring-disc measurements for  $\text{O}_2$  reduction on Au and Au/ $\text{Tl}_{\text{ads}}$  in an alkaline solution, obtained from Ref. [44] (Fig. 2a), and on Pt and Pt/ $\text{Pb}_{\text{ads}}$  in an acid solution, obtained from Ref. [45] (Fig. 2b). The ring currents indicate the production of hydrogen peroxide as a function of the disc potential. The positive catalytic effect observed on Au and Au(hkl) electrodes was attributed by Jüttner [46] to

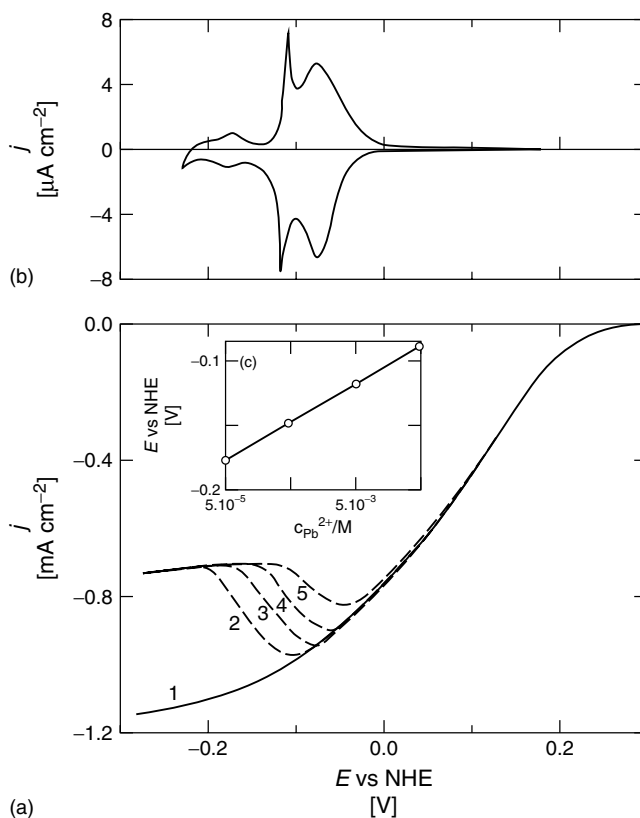


**Fig. 1** (a) Current–potential curves of  $\text{O}_2$  reduction on Ag(100) in aerated solution of 0.5 M  $\text{HClO}_4 + x\text{M Pb}(\text{ClO}_4)_2$ . ( $\nu = 1 \text{ mV s}^{-1}$ ;  $f = 25 \text{ Hz}$ ).  $x/\text{M}$ : (1) 0; (2)  $5 \times 10^{-5}$ ; (3)  $5 \times 10^{-4}$ ; (4)  $5 \times 10^{-3}$ ; and (5)  $5 \times 10^{-2}$ . (b) Cyclic voltammogram for the UPD of Pb on Ag(100) in 0.5 M  $\text{HClO}_4 + 5 \times 10^{-3} \text{ M Pb}(\text{ClO}_4)_2$ . ( $\nu = 10 \text{ mV s}^{-1}$ ). (c) Potential variation of the descending part of curves 2 to 5 versus  $C_{\text{Pb}^{2+}}$ . (Reproduced from Ref. [43] with permission.)

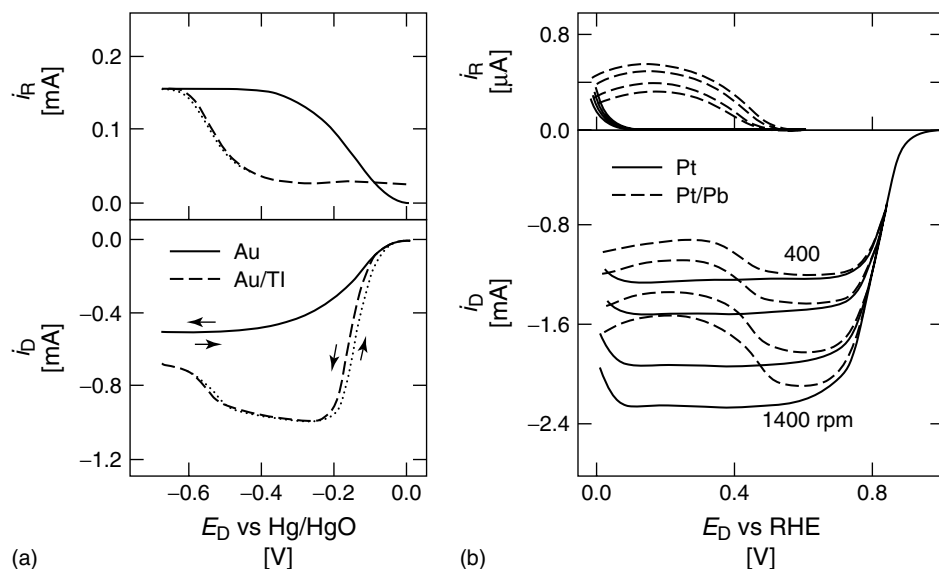


**Fig. 2** (a) Current-potential curves of  $O_2$  reduction on a Au-Au rrde in 0.1 M NaOH without (full line) and with (dashed line)  $6.6 \times 10^{-6}$  M Tl(I) ( $\nu = 10$  mV s $^{-1}$ ).  $E_R = 0.1$  V. (b) Current-potential curves of  $O_2$  reduction on a

Pt-Pt rrde in 0.2 M HClO $_4$  without (full lines) and with (dashed lines)  $2 \times 10^{-5}$  M  $Pb^{2+}$  ( $\nu = 40$  mV s $^{-1}$ ).  $E_R = 1.2$  V. (Reproduced from Refs. [44, 45] with permission.)

the change of the adsorption configuration from end-on on bare Au to bridge adsorption on Au partially covered by the modifiers Au-O-O-M (M = Pb, Tl, Bi). As mentioned earlier, this mode of adsorption favors the O-O bond cleavage. At high ad-atom coverages the bridge adsorption does not exist any more and oxygen is reduced to  $H_2O_2$  as on bulk Pb, Tl, and Bi electrodes.

The influence of the structure of the ad-atom layers on the reduction of oxygen was examined by using in situ optical and scanning probe microscopies. With these techniques reliable information on the structure of the ad-atom layers can be obtained during the course of oxygen or hydrogen peroxide reduction. In most systems studied, the UPD adlattice structures are not affected by the presence of molecular oxygen in solution. On the basis of

AFM observations, Chen and Gewirth [24] reported that the maximum catalytic activity for  $H_2O_2$  electroreduction on Au(111) modified by Bi UPD monolayers is observed in a narrow potential region, where the  $(2 \times 2)Bi$  structure is obtained. At potentials negative to this region, the rectangular Bi structure is formed and the reduction of  $H_2O_2$  is almost completely suppressed. The  $(2 \times 2)Bi$  structure enables the heterobimetallic bridge adsorption (Au-O-O-Bi), which, according to the views of Jüttner [46], may explain the enhanced reactivity.

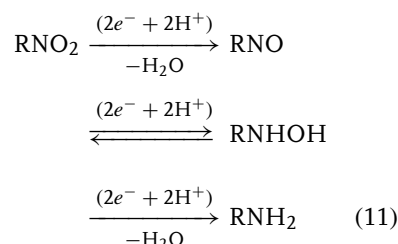
More recent studies combined the in situ techniques with the use of single-crystal electrodes in a rotating geometry, the so-called rotating hanging meniscus electrode (RHME) [47-49] or in the most desired geometry of a rotating ring-disc electrode. This combination provides

unique possibilities for studying structural effects in O<sub>2</sub> electrocatalysis. Adzic et al. [50] studied the effect of Tl adlayers on the reduction of oxygen on Au(111) in acid solutions by using X-ray diffraction and the RHME. They found that the reduction mechanism changes from a four-electron reduction at a low Tl coverage to a two-electron reduction at a higher Tl coverage. The (2 × 2)Tl structure is conducive to the four-electron reduction, while the close-packed rotated hexagonal Tl phase, which exists at more negative potentials, is responsible for the two-electron reduction. The reduction of oxygen does not change the Tl coverage, although it decreases the in-plane diffraction intensity. This indicates that O<sub>2</sub> molecules interact with the Tl ad-atoms and provide direct evidence that oxygen reduction is, indeed, an *inner-sphere* and not an *outer-sphere* reaction.

Finally, it is worth mentioning the pronounced inhibition effect of oxygen reduction on Au(100) and Pt(111) electrodes caused by bromide adsorption (Fig. 3). It is well known that the specific adsorption of halide anions inhibit the reduction of oxygen, but information of the inhibition mechanism in an atomic level was attempted for the first time by Adzic and Wang [51]. As shown in Fig. 3, the  $c(\sqrt{2} \times 2\sqrt{2})R45^\circ$  adlayer structure on Au(100) and the (3 × 3)Br structure on Pt(111) cause a complete inhibition of the two-electron reduction on Au(100) and the four-electron reduction on Pt(111) surfaces, respectively. The reduction can take place only at potentials more negative than the low potential limit of the existence of these structures. The stability of the structure of the Br adlayers during oxygen reduction was checked by measuring the X-ray intensity as a function of the potential in the absence and in the presence of oxygen in solution.

#### 4.3.4.2 Reduction of Nitro and Nitroso Compounds

The reduction of nitro compounds has played an important role in the development of organic electrochemistry. The nitro group is one of the most easily reducible groups. In aqueous solutions the general reduction mechanism, first proposed by Haber, is



According to this mechanism, nitro compounds are reduced to the corresponding hydroxylamines or amines by an irreversible four- or six-electron process that proceeds through nitroso intermediates. Nitroso intermediates are not stable on the electrode surface because their reduction potential is more positive than that of the initial nitro compounds. Azoxy, azo, and hydrazo derivatives can also be obtained by electrolysis, particularly in alkaline solutions, as a result of chemical follow-up reactions rather than electrochemical reactions. The electrochemistry of all these compounds has been discussed in reviews [52–54]. Among the different nitro compounds, nitrobenzene has played a central role and its reduction is one of the most thoroughly studied electrochemical reaction. The reduction involves adsorption of reactants and intermediates and follows direct electron-exchange mechanism on most cathodes except of platinum, in which the reduction proceeds by an electrocatalytic hydrogenation mechanism.

The influence of ad-atoms on the reduction of nitro and nitroso compounds on

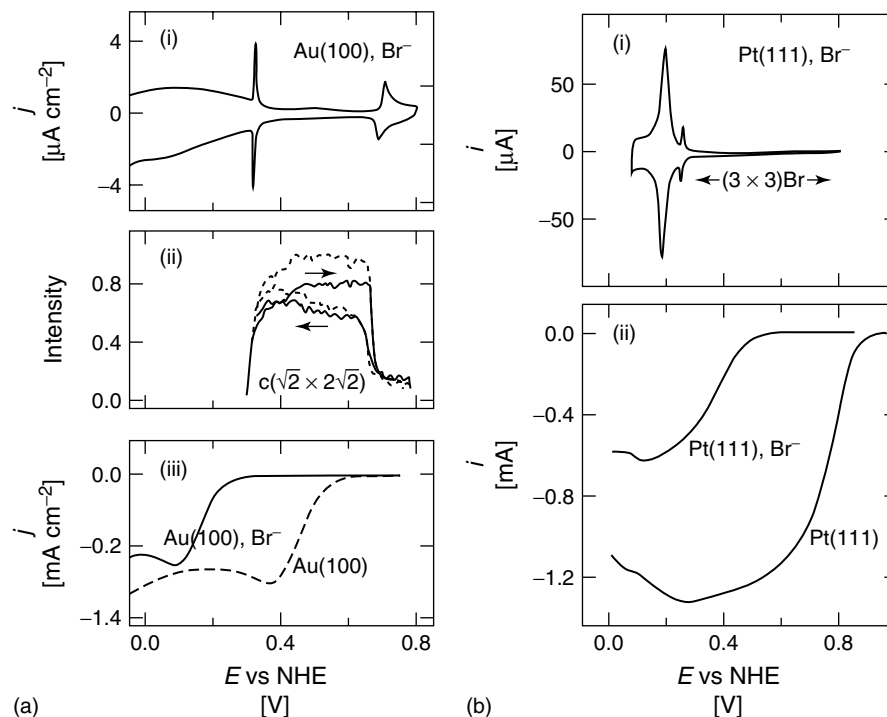


**Fig. 3** (a) (i) Voltammetry curve of the Au(100) electrode in 0.1 M  $\text{HClO}_4$  + 20 mM  $\text{Br}^-$  ( $\nu = 10 \text{ mV s}^{-1}$ ). (ii) X-ray intensity at (1/2, 1/2, 0.1) position in the absence (dashed line) and in the presence (full line) of oxygen. (iii)  $\text{O}_2$  reduction on Au(100) without and with 20 mM  $\text{Br}^-$  ( $\nu = 20 \text{ mV s}^{-1}$ ). (b) (i) Voltammetry curve of the Pt(111) electrode in 0.1 M  $\text{HClO}_4$  + 20 mM  $\text{Br}^-$  ( $\nu = 20 \text{ mV s}^{-1}$ ). (ii)  $\text{O}_2$  reduction on a hanging meniscus rotating Pt(111) disc electrode in 0.1 M  $\text{HClO}_4$  without and with 20 mM  $\text{Br}^-$  ( $\nu = 20 \text{ mV s}^{-1}$ ;  $f = 625 \text{ rpm}$ ). (Reproduced from Ref. [51] with permission.)

Ag, Au, and Pt electrodes has been studied during the last two decades [55–61]. It was found that ad-atom layers of Pb, Tl, and Bi deposited at underpotentials have a strong influence on the performance of the above substrates for the nitro and nitroso group electroreduction, both in terms of the improvement of the catalytic activity and the catalytic selectivity of these electrodes.

**Reduction of nitrobenzene on Ag/Pb(upd) and Au/Pb(upd)** The electrocatalytic influence of Pb(upd) adlayers on the reduction of nitrobenzene on Ag [55] and Au [56] electrodes was studied in acidic

solutions. On the bare metals, nitrobenzene is reduced to aniline. The UPD of Pb on Ag and Au causes a partial inhibition of nitrobenzene reduction. The step of the reduction of the intermediate hydroxylamine to aniline is completely inhibited when the silver and gold substrates are screened off by a lead monolayer. Figure 4 shows the polarization curves for the nitrobenzene and nitrosobenzene reduction on Ag(111) and Ag(111)/Pb(upd) electrodes. The limiting current of nitrobenzene falls from the six-electron level to the four-electron level at potentials more negative than the third UPD peak

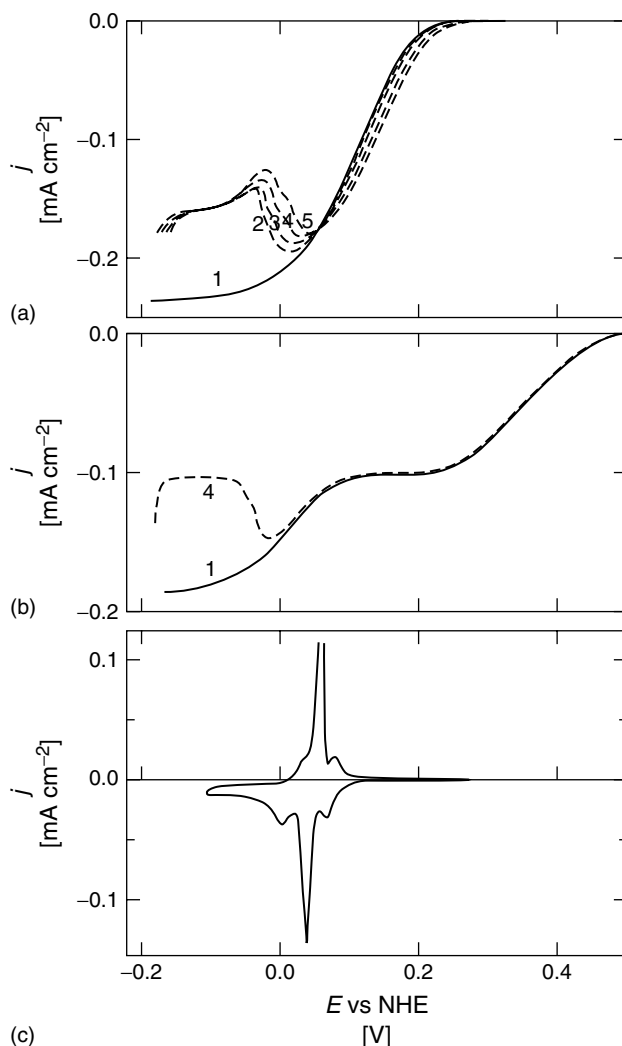


**Fig. 4** Steady state Current–potential curves for (a)  $\text{Ph-NO}_2$  ( $5 \times 10^{-4}$  M) and (b)  $\text{Ph-NO}$  ( $5 \times 10^{-4}$  M) reduction on Ag(111) in  $0.2 \text{ M LiClO}_4 + 7.5 \times 10^{-3} \text{ M HClO}_4$  in methanol without  $\text{Pb(ClO}_4)_2$  (1) and with  $\text{Pb(ClO}_4)_2$ ; (2)  $5 \times 10^{-4}$ ; (3)  $10^{-3}$ ; (4)  $2.5 \times 10^{-3}$ ; and (5)  $5 \times 10^{-3}$  M. (c) Cyclic voltammogram for the UPD of Pb on Ag(111) in the same electrolyte with  $2.5 \times 10^{-3} \text{ M Pb(ClO}_4)_2$  ( $\nu = 10 \text{ mV s}^{-1}$ ). (Reproduced from Ref. [55] with permission.)

at which complete ad-atom coverage is obtained. In this potential region, lead forms on Ag(111) a rotated hexagonal close-packed structure as revealed by

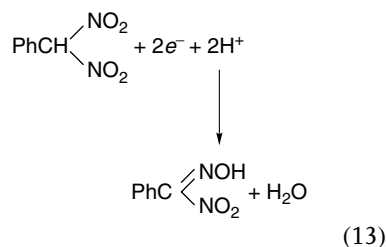
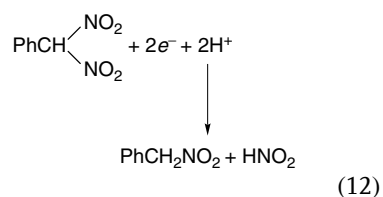
X-ray diffraction [15] and STM [20] studies. Also, the second reduction wave of nitrosobenzene, which corresponds to the reduction of phenylhydroxylamine to

aniline, is completely suppressed in the same potential region.

**Reduction of aromatic nitro and nitroso compounds on Pt/M(upd)**

In contrast to silver and gold electrodes, interesting catalytic effects were found for the reduction of aromatic nitro compounds on Pt surfaces modified by Pb, Tl, and Bi UPD adlayers in aqueous solutions [57–59]. On clean Pt the reduction of nitro compounds occurs in the potential region where hydrogen is evolved and no separate well-formed reduction waves are obtained. On Pt/M(upd) the reduction begins at more positive potentials and diffusion-controlled limiting currents are obtained. Generally, the catalysis of the reduction of nitro compounds was attributed [57] to the change of the nitro group reduction mechanism from catalytic hydrogenation on clean Pt to direct electron-transfer mechanism on Pt surfaces covered by the UPD adlayers, as on metals with high hydrogen overvoltage (Scheme 1).

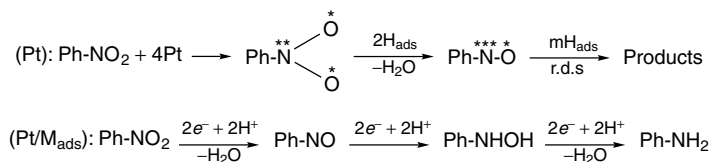
In the case of phenyldinitromethane [58] the UPD-modified surfaces exhibit also remarkable electrocatalytic selectivity as regards the final reduction products under electrolysis conditions. From the two competitive reaction routes



Reaction (12), producing phenylnitromethane, predominates on Pt/Tl(upd), while on Pt/Pb(upd) the major reaction is the reduction to *o*-nitrobenzaldehyde.

Also, in the case of the reduction of benzofuroxan [59] the UPD adlayers of Pb, Tl, and Bi strongly modify the catalytic activity and selectivity of the platinum electrode. Figure 5 shows the rotating-disc voltammograms for benzofuroxan reduction on Pt and Pt/M(upd), M = Pb, Tl, Bi.

On bare platinum the reduction proceeds via catalytic hydrogenation to *o*-nitroaniline (Scheme 2), which is reduced further to *o*-phenylenediamine. On the other hand, on UPD-modified platinum surfaces, the reduction occurs at much more positive potentials and follows the electronation mechanism, that is, the direct exchange of electrons between the dinitroso tautomeric form and the modified electrode surface. The first step is now the reduction to *o*-benzoquinone dioxime that appears as a stable intermediate over a wide potential range (0.60 to 0.45 V) before it is reduced further to the final products.



**Scheme 1** Reduction of nitrobenzene on Pt and Pt/M<sub>ads</sub> (M = Pb, Tl).

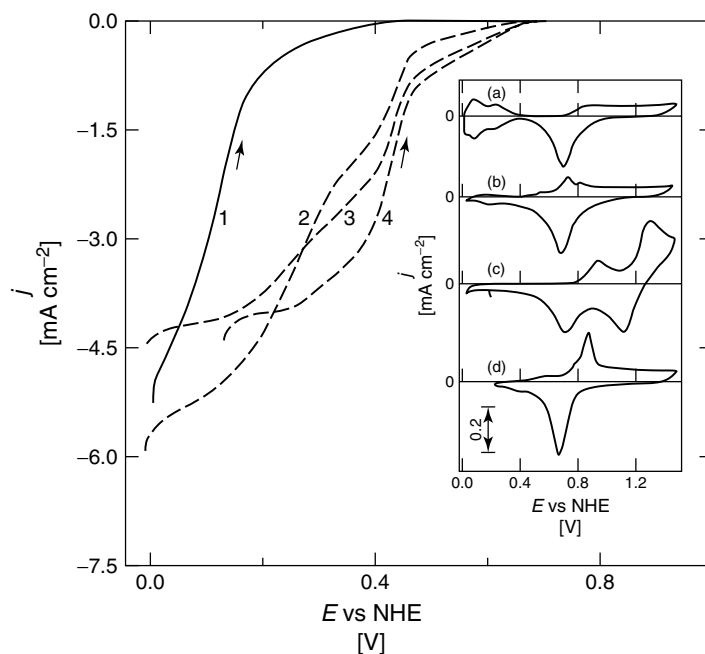
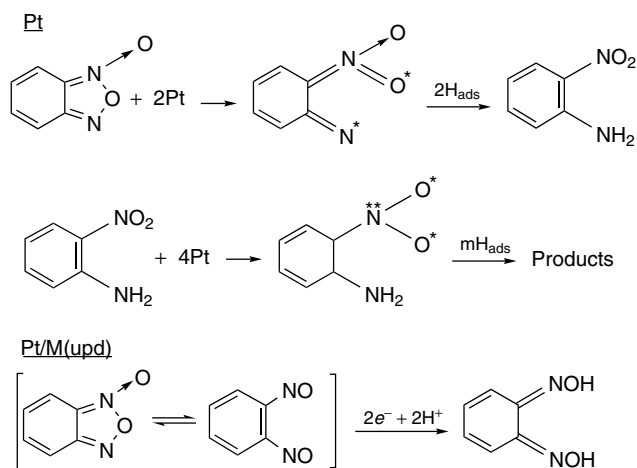
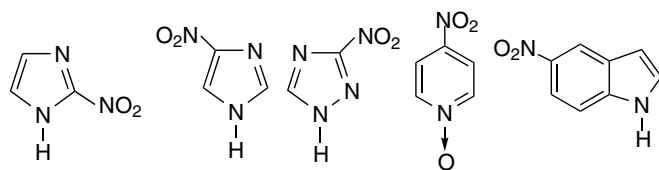


**Fig. 5** Current-potential curves for benzofuroxan ( $10^{-3}$  M) reduction on a Pt rotating-disc electrode in 0.5 M  $\text{HClO}_4$  without (1) and with (2)  $10^{-3}$  M  $\text{TlClO}_4$ ; (3)  $10^{-3}$  M  $\text{Pb}(\text{ClO}_4)_2$ ; (4)  $10^{-3}$  M  $\text{Bi}(\text{ClO}_4)_3$  ( $\nu = 10 \text{ mV s}^{-1}$ ;  $f = 25 \text{ Hz}$ ). Inset: Cyclic voltammograms for the UPD of Pb, Tl, and Bi on Pt in 0.5 M  $\text{HClO}_4$ . (a) Without ions; (b) with  $5 \times 10^{-4}$  M  $\text{Pb}^{2+}$ ; (c) with  $5 \times 10^{-4}$  M  $\text{Tl}^+$ ; and (d) with  $5 \times 10^{-4}$  M  $\text{Bi}^{3+}$ . Scan rate  $\nu = 50 \text{ mV s}^{-1}$ . (Reproduced from Ref. [59] with permission.)



**Scheme 2** Reduction of benzofuroxan on Pt and Pt/M(upd) (M = Pb, Tl, Bi).



**Reduction of heterocyclic nitro compounds on Au/M(upd)** Overlayers of Pb and Tl ad-atoms, deposited on Au in the underpotential region, exert pronounced catalytic effects on the reduction of some *N*-heterocyclic nitro compounds [56, 60, 61].

The behavior of these compounds differs from that of nitrobenzene. The strong electron-attracting heterocyclic nuclei, on the one hand, renders the nitro group more easily reducible and, on the other hand, helps to stabilize the hydrated form of the nitroso intermediates.

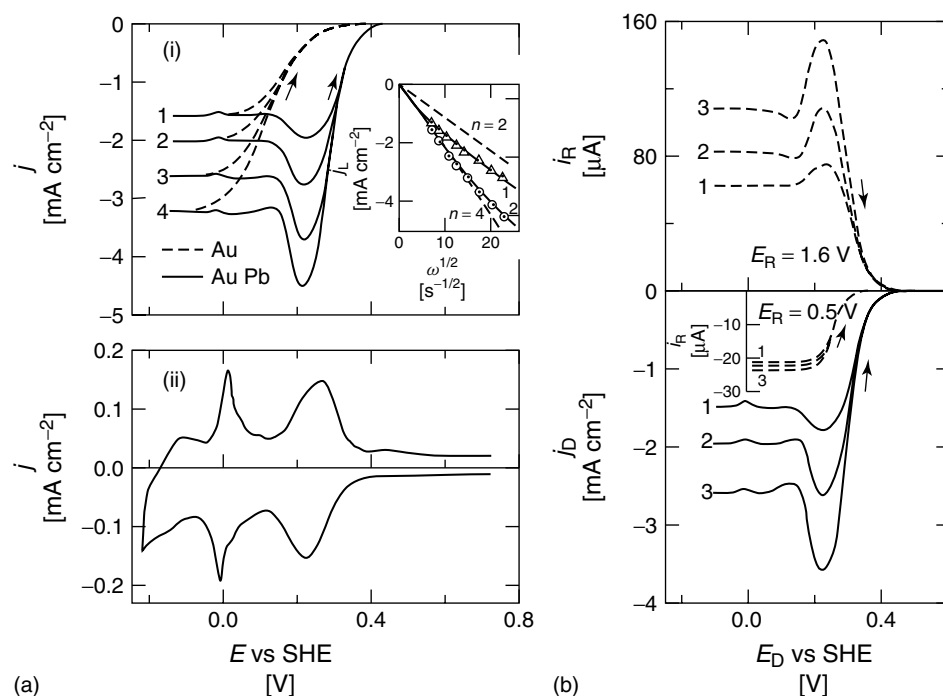


**Fig. 6** (a) (i) Current-potential curves for the reduction of 3-nitro-1,2,4-triazole ( $10^{-3}$  M) on a Au disc electrode in 0.2 M  $\text{HClO}_4$  without (dashed lines) and with (full lines)  $5 \times 10^{-4}$  M  $\text{Pb}(\text{ClO}_4)_2$  ( $\nu = 20 \text{ mV s}^{-1}$ ).  $f/\text{Hz}$ : (1) 12.5; (2) 25; (3) 50; and (4) 83.3. The inset shows the  $j_L$  versus  $\omega^{1/2}$  ( $\omega = 2\pi f$ ) plots at (1)  $-0.1$  V and (2)  $+0.21$  V. (ii) Cyclic voltammogram for the

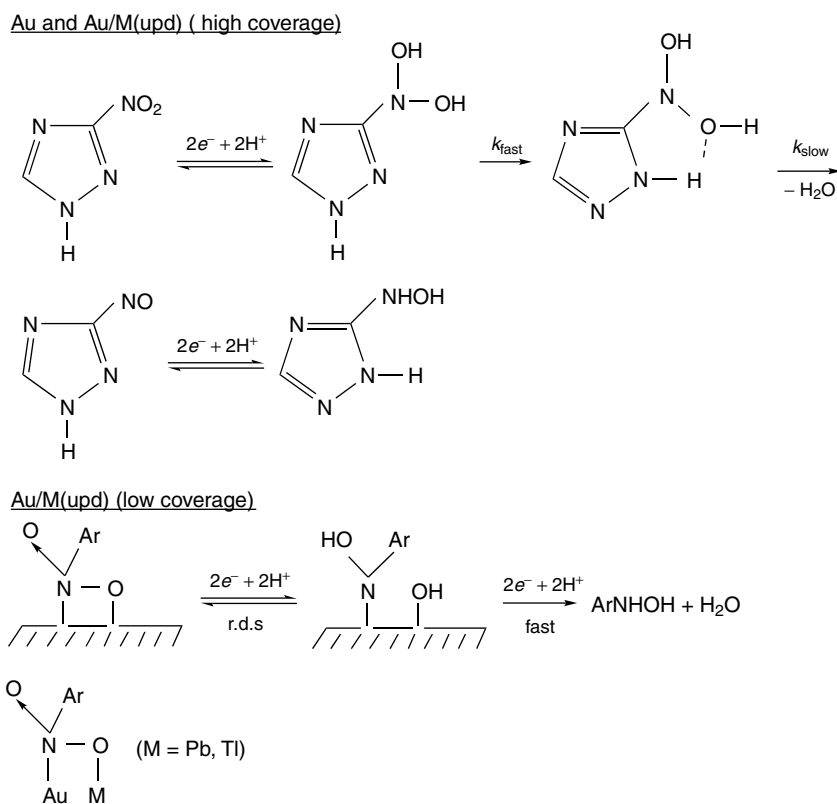
UPD of Pb on Au in 0.2 M  $\text{HClO}_4$ .  $\text{C}_{\text{Pb}^{2+}} = 5 \times 10^{-4}$  M;  $\nu = 50 \text{ mV s}^{-1}$ . (b) Au-Au rotating ring-disc ( $N = 0.18$ ) measurements for 3-nitro-1,2,4-triazole ( $10^{-3}$  M) in 0.2 M  $\text{HClO}_4$  +  $5 \times 10^{-4}$  M  $\text{Pb}(\text{ClO}_4)_2$  ( $\nu = 20 \text{ mV s}^{-1}$ ).  $f/\text{Hz}$ : (1) 12.5; (2) 25; and (3) 50. (Reproduced from Ref. [56] with permission.)



The effect of covering a gold disc with Pb ad-atom layers on the reduction of 3-nitro-1,2,4-triazole is shown in Fig. 6(a). Nitrotriazole undergoes a four-electron reduction both on Au and Au/Pb(upd) [56]. However, the reduction mechanism depends on the UPD ad-atom coverage. On bare Au and Au surfaces with almost complete ad-atom layer ( $E < 0.15$  V), the four-electron reduction follows the ECE mechanism (Scheme 3). The reaction proceeds through a  $N,N'$ -dihydroxyamine derivative (the hydrated form of the nitroso intermediate) that is reduced further after an irreversible loss of water. Because of the slow rate of the dehydration

reaction, the limiting current exhibits kinetic character.

On Au partially covered by Pb ad-atoms ( $E = 0.4$  to  $0.2$  V), an electrocatalytic mechanism appears to be operative. The reduction proceeds through chemisorption of the nitro group and reductive cleavage of one of the two N–O bonds, which leads directly to the hydroxylamino compound and gives diffusion-controlled four-electron limiting currents. As in the case of oxygen reduction, a bridge adsorption of the nitro group with a bridge complex involving a substrate (Au) and an adsorbed atom ( $M = \text{Pb, Tl}$ ) was assumed to explain the strong chemisorption on Au



**Scheme 3** Reduction mechanism of 3-nitro-1,2,4-triazole on Au and Au/M(upd) (M = Pb, Tl).

partially covered by ad-atoms. Analogous behavior was also observed with the other heterocyclic nitro compounds [60, 61].

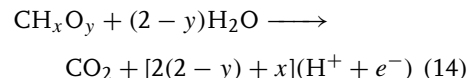
The ring-disc measurements presented in Fig. 6(b) confirm the above mechanisms. The final product of the reduction of nitrotriazole both at potentials of diffusion-controlled and kinetically controlled limiting currents is hydroxylaminotriazole, which is collected by the ring electrode at  $E_R = 1.6$  V. In the potential region, where the current is kinetically controlled, the intermediate nitrosotriazole was detected at  $E_R = 0.5$  V. In fact, the nitroso compound detected on the ring electrode is not that formed on the disc, because it is rapidly reduced further, but that produced from the dihydroxyamine intermediate upon its dehydration across the gap from disc to ring. Dihydroxyamine itself is not oxidized back to nitrotriazole on the ring, as one would expect, because it is rapidly stabilized by intramolecular hydrogen bonds.

The reduction of the above *N*-heterocyclic nitro compounds on Au modified by ad-atoms may be used as model reactions for studying the surface geometric and electronic structure in electrocatalysis. By using Au, Ag, or Pt single-crystal electrodes, it could be possible to correlate the catalytic activity with the superlattice structures of the ad-atoms.

#### 4.3.4.3 Oxidation of Small Organic Molecules

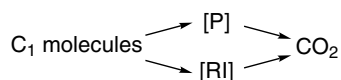
The electrooxidation of simple one-carbon molecules ( $C_1$  molecules), such as methanol, formaldehyde, and formic acid, became the subject of considerable and continuous interest. This is quite reasonable since these compounds, particularly methanol, are potential fuels for fuel cells. The complete oxidation of the

first two fuels to  $CO_2$  requires the donation of oxygen, which comes either from water or hydroxyl ions depending on the pH of the solution. In aqueous acid solutions the overall reaction may be written as



Since all hydrogen atoms must be abstracted from the fuel, the electrocatalyst must support the dehydrogenation. Electrodes that can be used as efficient anodes in  $C_1$  electrocatalysis are those with great affinity toward dehydrogenation reactions, namely, Pt and some other metals of the Pt-Group. Unfortunately, the current densities obtained with these electrodes are very low owing to poisoning effects. The main effect of poisoning is to block sites on the electrode surface.

Many efforts have been made to identify the nature of the poisoning species. The most successful techniques are the in situ IR reflectance spectroscopies. Intensive work has been done both on polycrystalline and single-crystal electrodes. The work done has been reviewed by Bewick and Pons [62], Beden and Lamy [63], and more recently by Sun [64]. It is now recognized that CO (either linearly or bridge-bonded to the surface) is the poison and not formyl species (COH), as believed previously [65, 66]. Carbon monoxide is formed by dehydration in the case of HCOOH and by dehydrogenation in the case of HCHO and  $CH_3OH$ . The CO formation reaction constitutes the one branch of the so-called “dual mechanism,” originally suggested by Capon and Parsons for the electrochemical oxidation of  $C_1$  molecules [65, 66]. The other branch is the reaction through reactive intermediates.



[P] is the poison and [RI] the reactive intermediates. All species involved in the mechanisms may be considered as reactive intermediates, if they are not strongly bonded to the surface and are oxidized to CO<sub>2</sub>.

The importance of the oxidation of C<sub>1</sub> molecules in electrochemical energy conversion has prompted intense research efforts to find new more active electrocatalysts or to improve the activity of existing catalysts, for instance, platinum. Efforts to enhance the catalytic properties of metal electrodes toward C<sub>1</sub> electrooxidation include both bulk alloys and pure metal surfaces modified by ad-atoms (modifiers), usually deposited in the underpotential region.

Generally, the ad-atoms cause positive catalytic effects with significant enhancement of the electrocatalytic activity of platinum in several cases. Several reviews have been published on this subject [26–28, 67]. Very recently Ross [68] and Jarvi and Stuve [29] have discussed the more recent advances in our understanding of the fundamentals of C<sub>1</sub> electrocatalysis by ad-atoms. The different types of enhancement (third-body effect, bifunctional mechanism, poison destabilization, and electronic modification) are well documented. The new information obtained from the in situ spectroscopic studies about the nature of poisons and the dependence of their coverages on potential, as well as the use of single-crystal electrodes with defined surface structure and specific reactivity, enables a deeper insight in the electrocatalysis by ad-atoms. As a general rule, one can say that, except for methanol, the more susceptible

the electrode to poisoning, the more important is the enhancement caused by ad-atoms.

#### Formic acid electrocatalysis by ad-atoms

The electrooxidation of formic acid on noble metals, such as Pt, Pd, Rh, Ir, is a classical example of a self-poisoning reaction. The currents obtained are very low and depend strongly on the potential sweep direction (anodic or cathodic) and the crystallographic orientation of the electrode surface. The Pt(111) face with the hexagonal lattice structure was found to be the surface that gives the higher currents and is less sensitive to poisoning effects [69, 70]. Foreign metal ad-atoms cause striking catalytic effects on the oxidation of formic acid on polycrystalline and single-crystal electrodes. Ad-atoms may be deposited either by UPD or irreversibly by immersing the electrode into the metal solution at open circuit. The early work was reviewed by Adzic [26], while the most recent work by Jarvi and Stuve [29].

Modifiers that can enhance the electrocatalytic activity of Pt, Pd, Rh, and Ir electrodes are Pb, Tl, Bi, Cd (see Ref. [26] and references therein). Among these modifiers, lead appears to be the stronger promoter in formic acid electrocatalysis [26, 71–74]. Figure 7 shows the effect of the UPD of Pb on formic acid electrooxidation on Pt. As seen, very high currents are obtained on Pt/Pb(upd) in the range between 0.3 and 0.7 V. Another important observation is the coincidence of the currents during the positive and the reverse negative potential scans, which is considered as an evidence of reduced poisoning effects.

The more recent studies on formic acid electrooxidation refer to Pt single-crystal electrodes modified by ad-atoms with

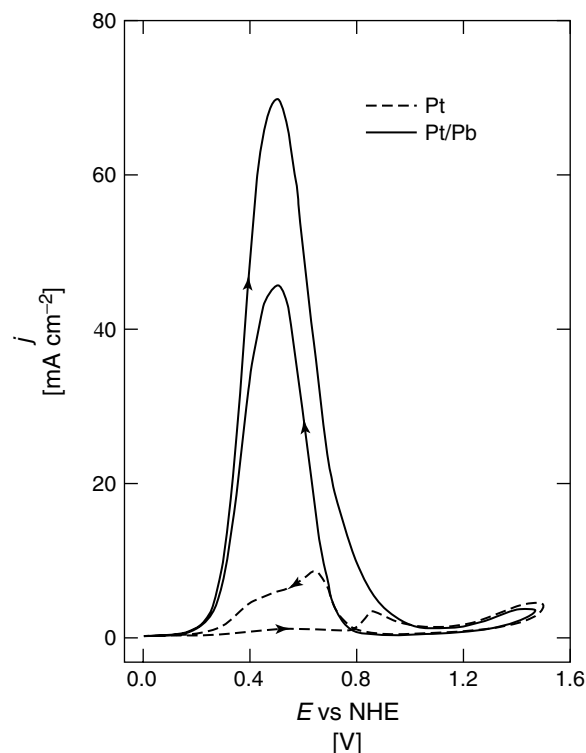


**Fig. 7** Voltammetric curves for formic acid (0.265 M) oxidation on a Pt electrode in 1 M  $\text{HClO}_4$  without (dashed line) and with (full line)  $10^{-3}$  M  $\text{Pb}^{2+}$  ions. Scan rate  $\nu = 50 \text{ mV s}^{-1}$ . (Reproduced from Ref. [71] with permission.)

controlled coverage, which are adsorbed irreversibly on the Pt surface. Ad-atoms deposited in this way include Pd [75, 76], Pb [77], Sb [78], As [79], and Bi [78, 80]. Palladium is the stronger promoter for formic acid oxidation. Indeed, adsorbed Pd drastically enhances the electrocatalytic activity of the Pt(100) electrode toward formic acid oxidation (Fig. 8). High current densities are obtained at low potentials (0.22 V vs. RHE), where bare Pt is not active. The catalytic activity reaches a maximum at  $\theta_{\text{Pd}} = 0.6$  [75]. Multilayers of Pd, epitaxially grown on Pt single-crystal electrodes, also exhibit enhanced catalytic activity toward formic acid oxidation [76]

compared to that of massive Pd single-crystal electrodes. Palladium overlayers show higher resistivity against CO poisoning than bare Pd, which was attributed to electronic effects.

#### Formaldehyde electrocatalysis by ad-atoms

Poisoning effects during the electrooxidation of formaldehyde were mainly observed in acid solutions. Ad-atoms deposited at underpotentials enhance the electrocatalytic activity of the Pt electrode toward  $\text{HCHO}$  oxidation [81–83]. According to Motoo and Shibata [82], ad-atoms that do not adsorb oxygen (e.g. Pb, Tl, Bi) have only a small influence resulting

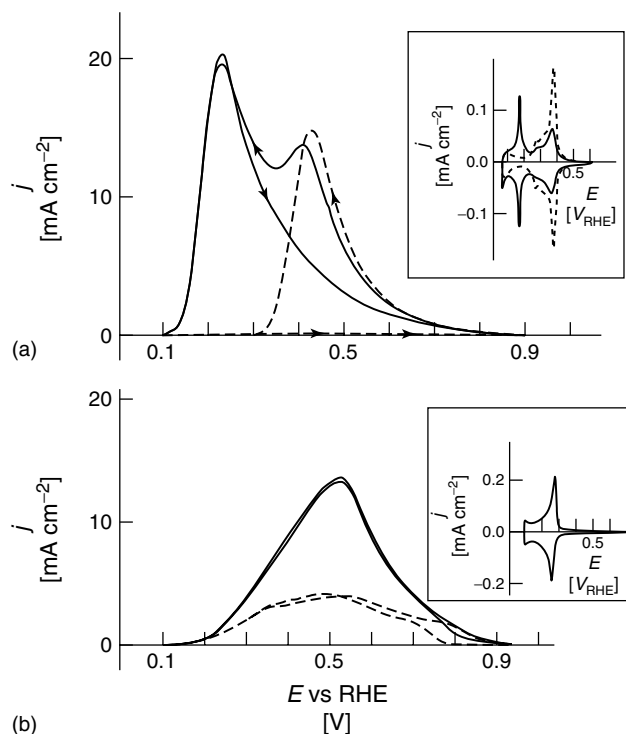


**Fig. 8** (a) Cyclic voltammograms of Pt(100) (dashed line) and Pt(100)/Pd<sub>ads</sub> ( $\theta = 0.32$ ) (full line) in 0.25 M HCOOH + 0.5 M H<sub>2</sub>SO<sub>4</sub>. (b) Cyclic voltammograms of Pd (dashed line) and Pt(100)/Pd<sub>ads</sub> ( $\theta = 1.06$ ) (full line) in the same electrolyte. The insets show blank voltammograms in 0.5 M H<sub>2</sub>SO<sub>4</sub>. (Reproduced from Ref. [75] with permission.)

from geometric factors (third-body mechanism), while oxygen adsorbing ad-atoms (e.g. Ru, Ge, Sn, Sb) give rise to a greater enhancement. The ad-atoms facilitate the donation of oxygen through the bifunctional mechanism, thus lowering the oxidation overpotential.

**Methanol electrocatalysis by ad-atoms** The oxidation of methanol takes place at potentials more positive than that needed for formic acid. Even on platinum, which is the most active electrocatalyst, the oxidation occurs at high overpotentials and significant currents are obtained only in

the potential region of Pt-oxide formation. Many efforts have been made to promote the activity of Pt by adding a second metal, either as ad-atoms or by alloying it with Pt. These studies are extensive and overviews of the literature may be found in Refs. [26, 28, 29, 68].

Here, we will restrict ourselves to pointing out that ad-atoms, such as Pb and Bi, which are strong promoters for formic acid electrocatalysis, only slightly increase the activity of Pt for methanol oxidation [83–86]. The most successful promoter for methanol electrocatalysis is Ru and perhaps Sn, albeit not as ad-atoms.

Pt-Ru alloys are now recognized as the best electrocatalysts for methanol oxidation exhibiting lower overpotentials and long-term stability, both important factors for direct methanol fuel cells. In a series of excellent papers, Gasteiger et al. [87–90] have provided valuable information regarding the reactivity of Pt–Ru alloys. The effect of Ru on the kinetics of CH<sub>3</sub>OH electrooxidation was rationalized in terms of the bifunctional action and a series reaction mechanism. The Pt sites act as centers for the adsorption/dehydrogenation of methanol-producing poison and carbonaceous intermediates, and Ru sites act as centers for adsorbing oxygen-containing species at less positive potential than Pt. The oxygen species on Ru sites oxidize both CO and the reactive carbonaceous intermediates by surface diffusion reactions. The surface composition of Ru alters the balance between the reaction rates of CO formation and oxidation with the 7 to 10% Ru surface being the optimum surface composition for enhanced reactivity.

#### 4.3.4.4 Oxidation of Bigger Organic Molecules

Other organic molecules, whose oxidation can be catalyzed by ad-atoms, include primary and secondary alcohols [85, 91–93], diols and polyols [94–100], and different monosaccharides [101–105]. Aldehydes are oxidized at more positive potentials compared to the oxidation potentials of primary alcohols and their oxidation is catalyzed only by oxygen-adsorbing ad-atoms [106, 107].

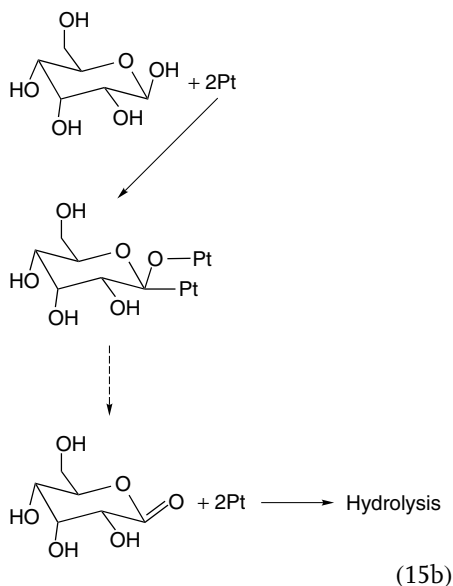
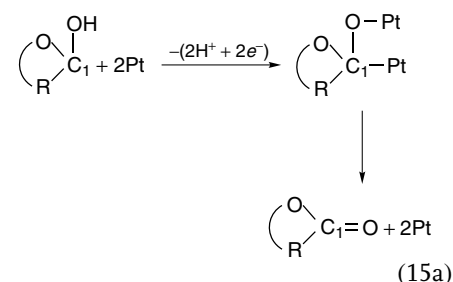
Generally, submonolayers of ad-atoms of heavy metals (such as Pb, Tl, Bi, Cd, etc.) deposited in the underpotential region increase the catalytic activity of Pt toward the electrooxidation of alcohols and sugars both in aqueous, acid, and alkaline solutions. The catalytic effect is more

pronounced in alkaline solutions, in which the currents on the modified surfaces are much higher compared to those obtained on platinum without ad-atoms. It should be noted that in alkaline media the catalytic effect is observed only at very low concentrations (around  $10^{-6}$  M) of heavy metal ions in the solution. At higher concentrations, negative catalytic effects are observed rather than positive catalysis. In general, the main products formed during the oxidation of primary and secondary alcohols are the corresponding aldehydes and ketones, while the main product of the oxidation of glucose is gluconic acid.

In acid solutions the catalytic effect caused by ad-atoms is characterized by the shift of the onset of oxidation toward less positive potentials and an increase of the peak current density by a factor of 2 to 5, depending on the kind of ad-atom and the organic substance being oxidized. In alkaline solutions the catalytic effect is mainly recognized by an immense increase of the oxidation current, especially with Pb and Bi ad-atoms. In alkaline solutions the poisoning effect is not so significant, since strongly adsorbed intermediates are not involved in the oxidation mechanism.

On the contrary, in acid solutions strongly adsorbed species are supposed to be formed during the oxidation of alcohols and sugars. The catalytic effect was generally interpreted in terms of a decrease of the electrode poisoning. The nature of the poisoning species produced during the dissociative chemisorption of aliphatic alcohols [108–111] and ethylene glycol [112] on Pt has been studied by *in situ* reflectance spectroscopies. It was demonstrated that CO is the main poisoning species and that the coverage of the surface by adsorbed CO decreases with

the increase of the carbon chain. The formation of CO results from the dissociative chemisorption and the C<sub>1</sub>–C<sub>2</sub> bond breaking. In the case of D-glucose oxidation on Pt, the poisoning species is believed to be a gluconolactone type intermediate [113, 114], which is also considered as the reactive intermediate producing gluconic acid upon hydrolysis.



However, more recent studies by in situ IR spectroscopy [115, 116] have demonstrated that the catalytic decomposition of glucose

on Pt produces CO, which should be the major adsorbate responsible for poisoning of the electrode surface.

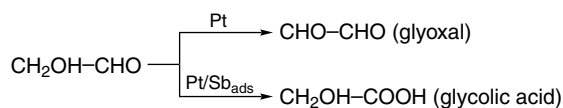
The structure of the organic molecules should also be considered in interpreting the catalytic effects caused by the modifiers. This can be deduced from the comparative studies (performed in acid solutions) of the UPD effect on the oxidation of two different series of organic compounds with the same functional group, such as aliphatic primary alcohols [85] and monosaccharides [103]. The lack of uniform catalytic behavior (based on current densities) leads to the conclusion that besides the third-body effect of the ad-atoms that is physical in nature the specific interacting forces of the reaction intermediates with the modified electrode surface must also play a significant role in the electrocatalytic process.

Finally, ad-atom-modified electrodes may also exhibit selectivity regarding the products obtained after electrolysis. Selective oxidation is particularly important in organic electrosynthesis. Two examples of selective oxidation of organic compounds will be discussed: the oxidation of glycolaldehyde in acid solutions on Pt and Pt/Sb<sub>ads</sub> [117] and the oxidation of gluconic acid in alkaline solutions on Pt and Pt/Pb<sub>ads</sub> [118].

On smooth Pt the main product of glycolaldehyde oxidation is glyoxal, while on Pt/Sb<sub>ads</sub> it is glycolic acid [117] (Scheme 4).

The Sb ad-atoms increase the reaction rate of both the oxidation of the CHO group to COOH group and the oxidation of the CH<sub>2</sub>OH group to CHO group, but the enhancement of the first reaction is much

**Scheme 4** Selective oxidation of glycolaldehyde on Pt and Pt/Sb<sub>ads</sub>.



more significant than that of the second one. Thus, the CHO group is selectively oxidized on the Pt electrode modified by the Sb ad-atoms.

In the case of D-gluconic acid [118], analysis of the oxidation products by ionic chromatography has shown that on smooth Pt the main products are oxalic, tartaric, 5-keto-D-gluconic, and D-glucuronic acids. On Pt modified by Pb ad-atoms, D-gluconic acid is selectively oxidized to 2-keto-D-gluconic acid, which is obtained with relatively high yield (33%). The reaction rate and the orientation of D-gluconic acid depend on the nature of the electrode. On bare Pt the reaction rate is very low and the oxidation occurs preferably at C<sub>6</sub> yielding D-glucuronic acid. On Pt/Pb<sub>ads</sub> the rate of reaction is significantly increased and the oxidation occurs at C<sub>2</sub> producing 2-keto-D-gluconic acid. On Pt/Pb<sub>ads</sub> no D-glucuronic acid was obtained. This means that oxidation at C<sub>6</sub> does not occur at all, indicating that the presence of ad-atoms changes the way that the reacting molecules link and interact with the electrode surface.

#### 4.3.4.5 Reversible Redox Reactions

It is known that some redox systems show poor reversibility on platinum. This is due to the fact that a monolayer of chemisorbed species from the redox components is formed that hinders the exchange of electrons between the rest of the diffusing molecules and the electrode.

Underpotentially deposited ad-atom layers of Pb, Tl, and Bi improve markedly the reversibility of the redox systems: hydroquinone/*p*-benzoquinone [119, 120], pyrocatechol/*o*-benzoquinone [120], adrenaline/adrenalinequinone [121], hexahydroxybenzene/tetrahydroxy-1,4-benzoquinone [122], *p*-benzoquinone dioxime/*p*-dinitrosobenzene [123], as well as the

oxidation of some dienolic compounds, such as ascorbic acid [124, 125] and rhodizonic acid [122]. Figure 9 presents an example of how the UPD of Tl affects the cyclic voltammetric behavior of the system pyrocatechol/*o*-benzoquinone on the Pt electrode.

The improvement of the reversibility of the redox systems was attributed by Kokkinidis et al. [120, 122] to the change of the reaction mechanism. The reaction mechanism changes from an *inner-sphere* mechanism involving adsorbed intermediates on bare Pt to an *outer-sphere* one without complications from adsorption of the reacting molecules on Pt/M<sub>ads</sub> (M = Pb, Tl, Bi).

#### 4.3.4.6 Inorganic Electrochemical Reactions

Inorganic electrochemical reactions influenced by ad-atoms include the oxidation of hydrazine and the reduction of some oxo-anions.

The influence of the UPD of heavy metals on the oxidation of hydrazine on Pt was studied in aqueous acid and alkaline solutions [126]. Adlayers of Pb, Tl, Bi, Cu, Cd, Ag cause a complete inhibition of the four-electron oxidation of hydrazine to nitrogen. On the Pt-modified surfaces the oxidation commences at sufficiently positive potentials where appreciable dissolution of ad-atoms occurs.

On the contrary, UPD monolayers of Pb, Tl, and Bi markedly catalyze the reduction of chromates (Cr<sub>2</sub>O<sub>7</sub><sup>2-</sup>) [127] and persulfates (S<sub>2</sub>O<sub>8</sub><sup>2-</sup>) [127, 128] on Pt. The *E*<sub>1/2</sub> of the reduction waves shifts toward more positive potentials and diffusion-controlled limiting currents are attained within the UPD region. The catalytic activity was interpreted in terms of preventing the covering of the Pt surface by species resulting from the dissociative



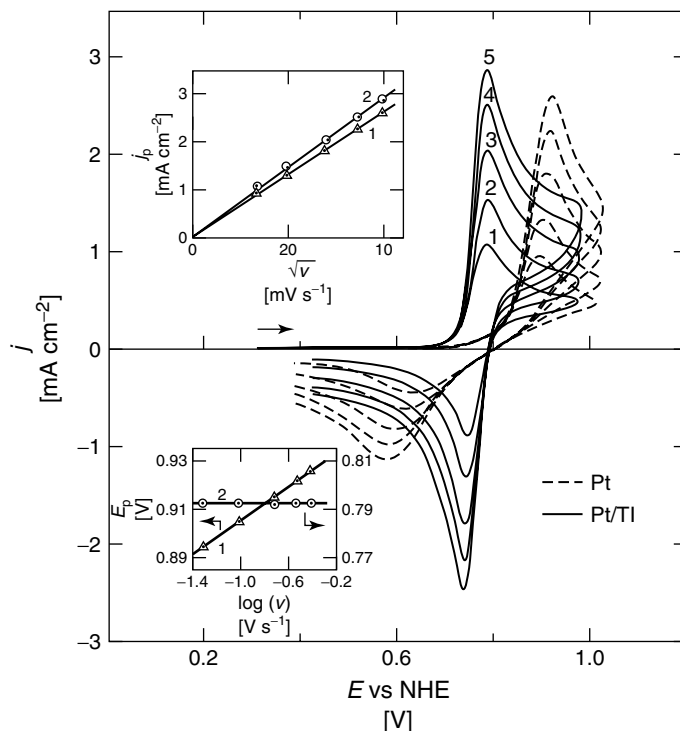


**Fig. 9** Cyclic voltammograms for pyrocatechol ( $2.5 \times 10^{-3}$  M) on Pt in 0.5 M  $\text{HClO}_4$  without (dashed lines) and with (full lines)  $10^{-3}$  M  $\text{TiClO}_4$ . Scan rate  $\nu/\text{mV s}^{-1}$ : (1) 50; (2) 100; (3) 200; (4) 300; and (5) 400. The insets show plots of  $j_p$  versus  $\nu^{1/2}$  and  $E_p$  versus  $\log \nu$  without (1) and with (2)  $\text{TiClO}_4$ . (Reproduced from Ref. [120] with permission.)

chemisorption of  $\text{Cr}_2\text{O}_7^{2-}$  and  $\text{S}_2\text{O}_8^{2-}$  anions, thus leading to faster electron exchange for the charge-transfer step involved in the reaction mechanisms. In the case of dichromate reduction in acid solutions, a remarkable discontinuity in the voltammetric behavior was observed when the potential was scanned in the positive direction. This behavior is related to the anodic desorption of the UPD monolayers, which in the presence of  $\text{Cr}_2\text{O}_7^{2-}$  ions occurs very abruptly owing to the competitive adsorption of dichromates.

Finally, the reduction of  $\text{NO}_3^-$  anions on  $\text{Ag}(\text{hkl})$  electrodes is strongly inhibited by Pb and Tl ad-atom layers [129]. The

inhibition effect was correlated to the superlattice structures of the UPD ad-atoms on the different Ag single-crystal surfaces.

#### 4.3.5

#### Conclusion

The influence of ad-atoms on reaction rates and mechanisms has attracted the interest of many researchers over the last 25 years. The most extensively studied reactions are the reduction of oxygen and the oxidation of organic fuels because of the importance of these reactions in electrochemical energy conversion. The challenge was to improve the catalytic activity of Pt and

to develop new, more efficient electrocatalysts for these reactions. On the other hand, studies on ad-atom-modified electrodes have allowed us to understand how surface geometric and electronic structure influences catalytic activity and reactivity. Significant progress has been made toward this direction by using single-crystal electrodes with well-defined structures of substrate and ad-atom layers in combination with in situ spectroscopies and scanning probes. These techniques have provided information on reaction intermediates (reactive or poisons) and surface properties under operating conditions that can help us to directly correlate the surface structure and composition with the catalytic activity. We already know enough about oxygen reduction, but there is still much to learn about the oxidation of organic fuels.

Except the enhancement of the electrocatalytic activity, ad-atoms may also improve the selectivity of the surface of the electrocatalysts regarding the final reaction products. Little work has been done in this direction. Probably in the future, electrodes modified by ad-atoms will be more attractive as potential catalysts in selective electrocatalysis. The improvement of the selectivity would require thorough mechanistic studies in order to get a better understanding of the various factors that may influence the selectivity of these electrodes.

## References

1. J. O'M. Bockris, A. K. N. Reddy, *Modern Electrochemistry*, Plenum Press, New York, 1977, Vol. 2.
2. W. J. Lorenz, H. D. Herrman, N. Wüthrich et al., *J. Electrochem. Soc.* **1974**, *121*, 1167–1177.
3. D. M. Kolb in *Advances in Electrochemistry and Electrochemical Engineering* (Eds.: H. Gerischer, C. W. Tobias), Wiley, New York, 1978, pp. 125–271, Vol. 11.
4. K. Jüttner, W. J. Lorenz, *Z. Phys. Chem. N.F.* **1980**, *122*, 163–185.
5. S. Szabó, *Int. Rev. Phys. Chem.* **1991**, *10*, 207–248.
6. J. W. Schultze, F. D. Koppitz, *Electrochim. Acta* **1976**, *21*, 327–343.
7. M. F. Toney, J. G. Gordon, M. G. Samant et al., *Langmuir* **1991**, *7*, 796–802.
8. J. Clavilier, R. Faure, G. Guinet et al., *J. Electroanal. Chem.* **1980**, *107*, 205–209.
9. J. Clavilier, D. Armand, S. C. Sun et al., *J. Electroanal. Chem.* **1986**, *205*, 267–277.
10. A. T. Hubbard, R. M. Ishikawa, J. Katekaru, *J. Electroanal. Chem.* **1978**, *86*, 271–288.
11. P. N. Ross, *J. Electrochem. Soc.* **1979**, *126*, 67–77.
12. P. N. Ross, F. T. Wagner in *Advances in Electrochemistry and Electrochemical Engineering* (Eds.: H. Gerischer, C. W. Tobias), Wiley, New York, 1984, pp. 69–112, Vol. 13.
13. R. R. Adzic in *Modern Aspects of Electrochemistry* (Eds.: R. E. White, J. O. 'M. Bockris, B. E. Conway), Plenum Press, New York, 1990, pp. 163–236, Vol. 21.
14. R. Parsons, G. Ritzoulis, *J. Electroanal. Chem.* **1991**, *318*, 1–24.
15. M. G. Samant, M. F. Toney, G. L. Borges et al., *J. Phys. Chem.* **1988**, *92*, 220–225.
16. M. F. Toney, J. G. Gordon, M. G. Samant et al., *Phys. Rev.* **1992**, *B45*, 9362–9374.
17. J. Wang, B. M. Ocko, A. J. Davenport et al., *Phys. Rev.* **1992**, *B46*, 10 321–10 338.
18. M. P. Green, K. J. Hanson, D. A. Scherson et al., *J. Phys. Chem.* **1989**, *93*, 2184–2187.
19. M. Binggeli, D. Carnal, R. Nyffenegger et al., *J. Vac. Sci. Technol.* **1991**, *B9*, 1985–1992.
20. U. Müller, D. Carnal, H. Siegenthaler et al., *Phys. Rev.* **1992**, *B46*, 12 899–12 901.
21. X. Gao, A. Hamelin, M. J. Weaver, *Phys. Rev.* **1992**, *B46*, 7096–7102.
22. K. Sashikata, N. Furuya, K. Itaya, *J. Electroanal. Chem.* **1991**, *316*, 361–368.
23. D. M. Kolb, *Electrochim. Acta* **2000**, *45*, 2387–2402.
24. C.-H. Chen, A. A. Gerwirth, *J. Am. Chem. Soc.* **1992**, *114*, 5439, 5440.
25. X. Xia, T. Iwasita, *J. Electrochem. Soc.* **1993**, *140*, 2559–2565.
26. R. R. Adzic in *Advances in Electrochemistry and Electrochemical Engineering* (Eds.:

- H. Gerischer, C. W. Tobias), Wiley, New York, 1984, pp. 159–260, Vol. 13.
27. G. Kokkinidis, *J. Electroanal. Chem.* **1986**, 201, 217–236.
  28. R. Parsons, T. VanderNoot, *J. Electroanal. Chem.* **1988**, 257, 9–45.
  29. T. D. Jarvi, E. M. Stuve in *Electrocatalysis* (Eds.: J. Lipkowski, P. N. Ross), Wiley, New York, 1998, pp. 75–153.
  30. N. D. Lang, S. Holloway, J. K. Norskov, *Surf. Sci.* **1985**, 150, 24–28.
  31. M. P. Kiskinova, *Stud. Surf. Sci. Catal.* **1992**, 70, 1–137.
  32. C. G. Vayenas, I. V. Yentekakis in *Handbook of Heterogeneous Catalysis* (Eds.: G. Ertl, H. Knözinger, J. Weitkamp), Wiley-VCH, Weinheim, New York, 1997, pp. 1310–1325, Vol. 3.
  33. A. Damjanovic in *Modern Aspects of Electrochemistry* (Eds.: J. O'M. Bockris, B. E. Conway), Plenum Press, New York, 1969, pp. 369–483, Vol. 5.
  34. M. R. Tarasevich, A. Sadkowski, E. Yeager in *Comprehensive Treatise of Electrochemistry* (Eds.: B. Conway, J. O'M. Bockris, E. Yeager et al.), Plenum Press, New York, 1983, pp. 301–332, Vol. 7.
  35. K. Kinoshita, *Electrochemical Oxygen Technology*, Wiley, New York, 1990.
  36. A. J. Appleby, *J. Electroanal. Chem.* **1993**, 357, 117–179.
  37. R. Adzic in *Electrocatalysis* (Eds.: J. Lipkowski, P. N. Ross), Wiley, New York, 1998, pp. 197–242.
  38. E. Yeager, *Electrochim. Acta* **1984**, 29, 1527–1537.
  39. P. Fischer, J. Heitbaum, *J. Electroanal. Chem.* **1980**, 112, 231–238.
  40. N. Anastasijevic, Z. M. Dimitrijevic, R. R. Adzic, *Electrochim. Acta* **1992**, 37, 457–464.
  41. G. Kokkinidis, D. Jannakoudakis, *J. Electroanal. Chem.* **1984**, 162, 163–173.
  42. T. Abe, G. M. Swain, K. Sachikata et al., *J. Electroanal. Chem.* **1995**, 382, 73–83.
  43. A. Swetanova, K. Jüttner, *J. Electroanal. Chem.* **1981**, 119, 149–164.
  44. R. Amadelli, N. Markovic, R. Adzic et al., *J. Electroanal. Chem.* **1983**, 159, 391–412.
  45. S. A. S. Machado, A. A. Tanaka, E. R. Gonzalez, *Electrochim. Acta* **1994**, 39, 2591–2597.
  46. K. Jüttner, *Electrochim. Acta* **1984**, 29, 1597–1604.
  47. F. El Kadiri, R. Faure, R. Durand, *J. Electroanal. Chem.* **1991**, 301, 177–188.
  48. N. M. Markovic, R. R. Adzic, B. Cahan et al., *J. Electroanal. Chem.* **1994**, 377, 249–259.
  49. N. M. Markovic, H. A. Gasteiger, P. N. Ross, *J. Phys. Chem.* **1995**, 99, 3411–3415.
  50. R. R. Adzic, J. Wang, B. M. Ocko, *Electrochim. Acta* **1995**, 40, 83–89.
  51. R. R. Adzic, J. X. Wang, *Electrochim. Acta* **2000**, 45, 4203–4210.
  52. W. Kemula, T. M. Krygowski in *Encyclopedia of Electrochemistry of the Elements* (Eds.: A. J. Bard, H. Lund), Marcel Dekker, New York, 1979, pp. 77–208, Vol. 13.
  53. H. Lund in *Organic Electrochemistry* (Eds.: M. M. Baizer, H. Lund), 3rd ed., Marcel Dekker, New York, 1991, pp. 401–432.
  54. A. Cyr, P. Huot, J.-F. Marcoux et al., *Electrochim. Acta* **1989**, 34, 439–445.
  55. G. Kokkinidis, K. Jüttner, *Electrochim. Acta* **1981**, 26, 971–977.
  56. G. Kokkinidis, A. Papoutsis, G. Papanastasiou, *J. Electroanal. Chem.* **1993**, 359, 253–271.
  57. G. Kokkinidis, P. Jannakoudakis, *Electrochim. Acta* **1984**, 29, 821–828.
  58. G. Kokkinidis, E. Coutouli-Argyropoulou, *Electrochim. Acta* **1985**, 30, 493–499.
  59. G. Kokkinidis, N. Argyropoulos, *Electrochim. Acta* **1985**, 30, 1611–1620.
  60. A. Papoutsis, G. Kokkinidis, *J. Electroanal. Chem.* **1994**, 371, 231–239.
  61. G. Kokkinidis, A. Kelaidopoulou, *J. Electroanal. Chem.* **1996**, 414, 197–208.
  62. A. Bewick, B. S. Pons in *Advances in Infrared and Raman Spectroscopy* (Eds.: R. J. H. Clark, R. E. Hester), Wiley Heyden, London, 1985, pp. 1–63, Vol. XII.
  63. B. Beden, C. Lamy in *Spectroelectrochemistry-Theory and Practice* (Ed.: R. G. Gale), Plenum Press, New York, 1988, pp. 189–261, Chap. 5.
  64. S.-G. Sun in *Electrocatalysis* (Eds.: J. Lipkowski, P. N. Ross), Wiley, New York, 1998, pp. 243–290.
  65. A. Capon, R. Parsons, *J. Electroanal. Chem.* **1973**, 44, 1–7.
  66. A. Capon, R. Parsons, *J. Electroanal. Chem.* **1973**, 45, 205–231.
  67. B. Beden, J.-M. Léger, C. Lamy in *Modern Aspects of Electrochemistry* (Eds.: J. O'M. Bockris, B. E. Conway, R. E. White), Plenum Press, New York, 1992, pp. 97–264, Vol. 22.

68. P. N. Ross in *Electrocatalysis* (Eds.: J. Lipkowski, P. N. Ross), Wiley, New York, 1998, pp. 43–74.
69. J. Clavilier, R. Parsons, R. Durand et al., *J. Electroanal. Chem.* **1981**, 124, 321–326.
70. R. R. Adzic, A. V. Tripkovich, W. O'Grady, *Nature* **1982**, 296, 137, 138.
71. R. R. Adzic, D. N. Simic, A. R. Despic et al., *J. Electroanal. Chem.* **1975**, 65, 587–601.
72. R. R. Adzic, D. N. Simic, A. R. Despic et al., *J. Electroanal. Chem.* **1977**, 80, 81–99.
73. D. Pletcher, V. Solis, *J. Electroanal. Chem.* **1982**, 131, 309–323.
74. M. Shibata, S. Motoo, *J. Electroanal. Chem.* **1985**, 188, 111–120.
75. M. J. Llorca, J. M. Feliu, A. Aldaz et al., *J. Electroanal. Chem.* **1994**, 376, 151–160.
76. M. Baldauf, D. M. Kolb, *J. Phys. Chem.* **1996**, 100, 11 375–11 381.
77. S. A. Campbell, R. Parsons, *J. Chem. Soc., Faraday Trans.* **1992**, 88, 833–841.
78. E. Herrero, J. M. Feliu, A. Aldaz, *J. Electroanal. Chem.* **1994**, 368, 101–108.
79. A. Fernandez-Vega, J. M. Feliu, A. Aldaz et al., *J. Electroanal. Chem.* **1991**, 305, 229–240.
80. E. Herrero, A. Fernandez-Vega, J. M. Feliu et al., *J. Electroanal. Chem.* **1993**, 350, 73–88.
81. D. M. Spasojevic, R. R. Adzic, A. R. Despic, *J. Electroanal. Chem.* **1980**, 109, 261–269.
82. S. Motoo, M. Shibata, *J. Electroanal. Chem.* **1982**, 139, 119–130.
83. M. Beltowska-Brzezinska, J. Heitbaum, W. Vielstich, *Electrochim. Acta* **1985**, 30, 1465–1471.
84. B. Beden, F. Kadirgan, C. Lamy et al., *J. Electroanal. Chem.* **1981**, 127, 75–85.
85. G. Kokkinidis, D. Jannakoudakis, *J. Electroanal. Chem.* **1983**, 153, 185–200.
86. M. Shibata, S. Motoo, *J. Electroanal. Chem.* **1987**, 229, 385–394.
87. H. A. Gasteiger, N. Markovic, P. N. Ross et al., *J. Phys. Chem.* **1993**, 97, 12 020–12 029.
88. H. A. Gasteiger, N. Markovic, P. N. Ross et al., *J. Electrochem. Soc.* **1994**, 141, 1795–1803.
89. H. A. Gasteiger, N. Markovic, P. N. Ross et al., *Electrochim. Acta* **1994**, 39, 1825–1832.
90. N. M. Markovic, H. A. Gasteiger, P. N. Ross et al., *Electrochim. Acta* **1995**, 40, 91–98.
91. G. Kokkinidis, A. Papoutsis, *J. Electroanal. Chem.* **1989**, 271, 233–247.
92. D. Sazou, N. Xonoglou, G. Kokkinidis, *Collect. Czech. Chem. Commun.* **1986**, 51, 2444–2454.
93. C. T. Hable, M. S. Wrighton, *Langmuir* **1993**, 9, 3284–3290.
94. G. Kokkinidis, D. Jannakoudakis, *J. Electroanal. Chem.* **1982**, 133, 307–315.
95. F. Kadirgan, B. Beden, C. Lamy, *J. Electroanal. Chem.* **1982**, 136, 119–138.
96. F. Kadirgan, B. Beden, C. Lamy, *J. Electroanal. Chem.* **1983**, 143, 135–152.
97. M. Shibata, N. Furuya, M. Watanabe, *J. Electroanal. Chem.* **1989**, 267, 163–170.
98. G. Pierre, A. Ziode, M. L. Kordi, *Electrochim. Acta* **1987**, 32, 601–606.
99. P. Ocon, B. Beden, H. Huser et al., *Electrochim. Acta* **1987**, 32, 387–394.
100. P. Ocon, B. Beden, C. Lamy, *Electrochim. Acta* **1987**, 32, 1095–1101.
101. M. Sakamoto, K. Takamura, *Bioelectrochem. Bioenerg.* **1982**, 9, 571–582.
102. N. Xonoglou, G. Kokkinidis, *Bioelectrochem. Bioenerg.* **1984**, 12, 485–498.
103. G. Kokkinidis, N. Xonoglou, *Bioelectrochem. Bioenerg.* **1985**, 14, 375–387.
104. N. Xonoglou, I. Moutzisz, G. Kokkinidis, *J. Electroanal. Chem.* **1987**, 237, 93–104.
105. G. Kokkinidis, J.-M. Léger, C. Lamy, *J. Electroanal. Chem.* **1988**, 242, 221–242.
106. M. Shibata, S. Motoo, *J. Electroanal. Chem.* **1985**, 187, 151–159.
107. M. Shibata, S. Motoo, *J. Electroanal. Chem.* **1986**, 201, 23–32.
108. B. Beden, M. C. Morin, F. Hahn, C. Lamy, *J. Electroanal. Chem.* **1987**, 229, 353–366.
109. H. Hitmi, E. M. Belgsir, J.-M. Léger et al., *Electrochim. Acta* **1994**, 39, 407–415.
110. S.-G. Sun, D.-F. Yang, Z.-W. Tian, *J. Electroanal. Chem.* **1990**, 289, 177–187.
111. E. Pastor, S. Wasmus, T. Iwasita et al., *J. Electroanal. Chem.* **1993**, 350, 97–116.
112. F. Hahn, B. Beden, F. Kadirgan et al., *J. Electroanal. Chem.* **1987**, 216, 169–180.
113. S. Ernst, J. Heitbaum, C. H. Hamann, *Ber. Bunsen-Ges. Phys. Chem.* **1980**, 84, 50–55.
114. Yu. B. Vassiliev, O. A. Khazova, N. N. Nikolaeva, *J. Electroanal. Chem.* **1985**, 196, 105–125, 127–144.
115. T. T. Bae, E. Yeager, *J. Electroanal. Chem.* **1991**, 309, 131–145.
116. F. Largeaud, K. B. Kokoh, B. Beden et al., *J. Electroanal. Chem.* **1995**, 397, 261–269.
117. M. Shibata, N. Furuya, M. Watanabe, *J. Electroanal. Chem.* **1993**, 344, 389–393.

118. K. B. Kokoh, P. Parrot, E. M. Belgsir et al., *Electrochim Acta* **1993**, 38, 1359–1365.
119. R. Wetzell, L. Müller, P. Göttlich, *Z. Phys. Chem.* **1977**, 258, 528–532.
120. G. Kokkinidis, *J. Electroanal. Chem.* **1984**, 172, 265–279.
121. M. Sakamoto, K. Takamura, *Bioelectrochem. Bioenerg.* **1983**, 10, 251–260.
122. G. Kokkinidis, D. Sazou, I. Moutziz, *J. Electroanal. Chem.* **1986**, 213, 135–147.
123. G. Kokkinidis, G. Papanastasiou, *J. Electroanal. Chem.* **1988**, 257, 239–255.
124. K. Takamura, M. Sakamoto, *J. Electroanal. Chem.* **1980**, 113, 273–283.
125. M. J. Walls, J. M. Feliu, A. Aldaz et al., *J. Electroanal. Chem.* **1989**, 260, 237–244.
126. G. Kokkinidis, P. Jannakoudakis, *J. Electroanal. Chem.* **1981**, 130, 153–162.
127. G. Kokkinidis, D. Sazou, *J. Electroanal. Chem.* **1987**, 237, 137–144.
128. G. Kokkinidis, D. G. Zatkas, D. Sazou, *J. Electroanal. Chem.* **1988**, 256, 137–148.
129. C. Mayer, K. Jüttner, W. J. Lorenz, *J. Appl. Electrochem.* **1979**, 9, 161–169.

## 4.4

**Electrochemistry in Micelles and Microemulsions***James F. Rusling**Departments of Chemistry and Pharmacology  
University of Connecticut, Storrs, CT, USA*

## 4.4.1

**Introduction**

Analytical and synthetic electrochemistry is usually done in homogeneous aqueous solutions or organic solvents. However, there are advantages in some cases in using microheterogeneous fluids such as micellar solutions and microemulsions [1–3]. These include solubilization of organics and biomolecules, manipulation of electrode surface properties, stabilization or destabilization of reactive intermediates [4, 5], control of reaction pathways, and enhancement of rates of mediated reactions [6, 7]. Advantages also accrue from the low cost [8] and low toxicity of micellar solutions and microemulsions compared to pure aprotic solvents often used for organic electrochemistry. Electrochemical methods can also be used to characterize micelles and microemulsions via the measurement of diffusion coefficients of electroactive probes [4, 5, 9].

Micelles and microemulsions depend on surfactants for their internal structure. Surfactants (surface-active agents or detergents) are amphiphilic molecules with charged or polar head groups attached to one or more hydrocarbon tails (Fig. 1). Micelles are aggregates that form in water when concentrations of surfactants exceed a critical micelle concentration (CMC). Microemulsions are microheterogeneous fluids made from oil, water, and surfactants, and sometimes cosurfactants. They appear homogeneous to the eye but contain dynamic heterogeneous nanostructures that

can be tuned for specific applications by adjusting the relative amounts of the components [1–3].

The aim of this chapter is to describe electrochemistry in micelles and microemulsions in fundamental and practical terms. A major focus is on the use of these media to purposely influence the desired outcome of electrochemical reactions. The chapter also describes how electrochemical methods can be used for structural characterization of these fluids. In the next section (Sect. 4.4.2), we discuss structures, properties, and dynamics of micelles and microemulsions. Subsequent sections present relevant aspects of direct electrochemistry and electrochemical catalysis in micelles and microemulsions.

## 4.4.2

**Surfactant-stabilized Microheterogeneous Fluids**4.4.2.1 **Structures of Micelles and Microemulsions**4.4.2.1.1 **Surfactants and Micellar Structure**

The formation of micellar aggregates from ionic surfactants in water causes sharp discontinuities in conductivity and surface tension. Water-soluble surfactants form spherical or globular micelles at concentrations near the CMC (Fig. 2). Micelle formation is thermodynamically favored in water for water-soluble surfactants such as cetyltrimethylammonium bromide (CTAB), sodium dodecyl sulfate (SDS), and Brij 35, and is driven by hydrophobic interactions between the tails [10]. The charged or polar head groups face the water phase and the hydrocarbon tails reside in the interior of the micelle. For ionic surfactants in water, the head group region is only partly neutralized by counterions, setting up an interfacial

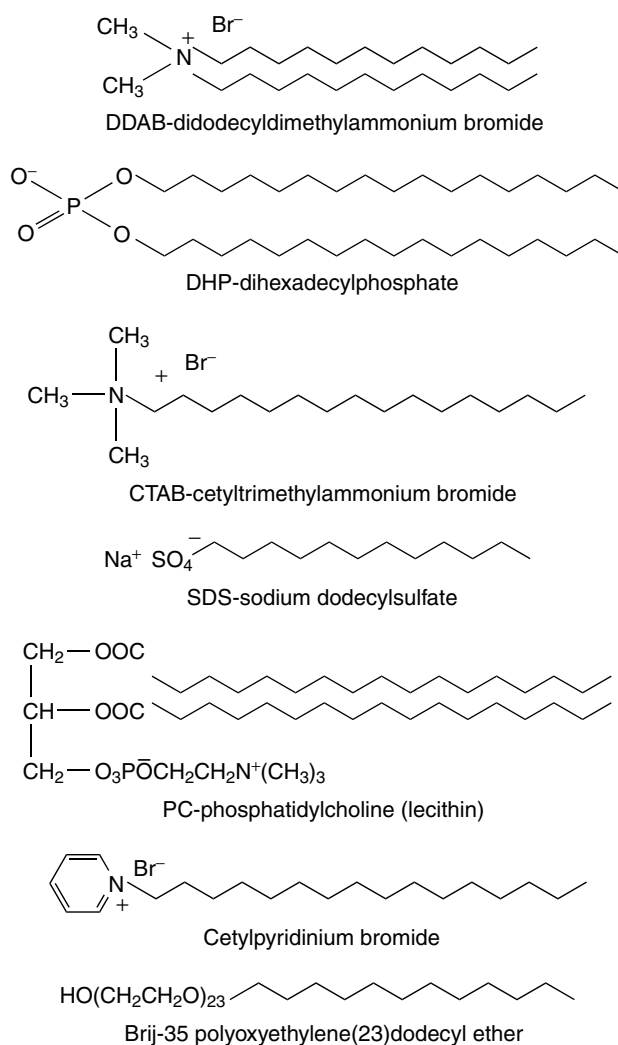


**Fig. 1** Amphiphilic molecules (surfactants) used to make micellar solutions and microemulsions.

potential on the order of 100 mV [3]. This interfacial region consists of an electrical double layer (i.e. head groups and counterions) called the *Stern layer* and provides binding sites for solutes of the opposite charge. If salt is added to a micellar solution, the surface potential is partly neutralized and the micelle grows

larger. Micelles having a single narrow size distribution are called *monodisperse*.

Hydrophobic cores of globular micelles typically have diameters of 1 to 3 nm. Micellar core volume ( $V_c$ ) can be estimated from the average number of surfactant molecules per micelle, that is, the aggregation number ( $N_{ag}$ , ca. 30–200),

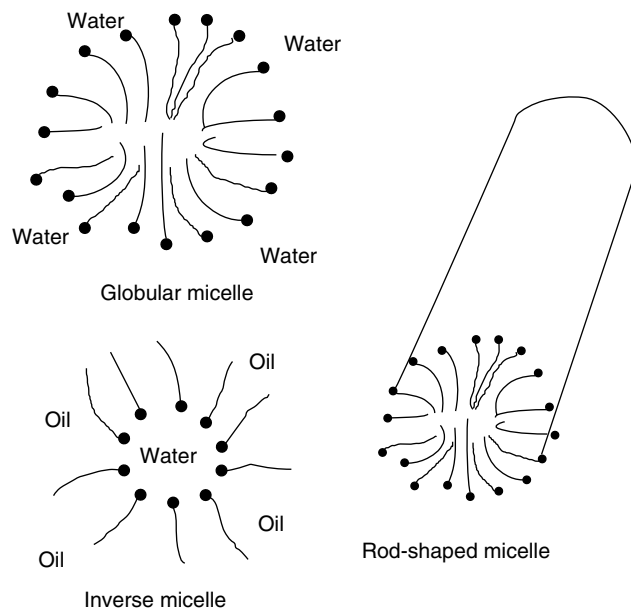


**Fig. 2** Oversimplified representations of micellar structures. Surfactants are represented with dark circles for head groups and curved lines for hydrocarbon tails.

via [10]

$$V_c = m'(27.4 + 26.9n')\text{\AA} \quad (1)$$

for a single chain surfactant  $m' = N_{\text{ag}}$  for a double chain surfactant  $m' = 2N_{\text{ag}}$  and  $n'$  is the number of carbon atoms in the tail less one. Solubilization of nonpolar molecules occurs in hydrophobic regions of the micelles but near the Stern layer [3].

At intermediate concentrations considerably above the CMC, rod-shaped micelles often form. At very high concentrations, lamellar aggregates and other condensed phases form. In organic solvents, some surfactants form spherical inverse micelles with the head groups facing small pools of trapped water, with hydrocarbon tails facing the bulk solvent phase (Fig. 2).

Structures of micelles depend on the structures and concentrations of the surfactant molecules. The *surfactant packing*

*parameter*,  $v/a_0l_c$ , can be used to predict the shape of the aggregate formed [11]. To a first approximation,  $a_0$  is the area of the head group, and the other terms are found from

$$l_c = 1.5 + 1.26n\text{\AA} \quad (2)$$

$$v = 27.4 + 26.9n'\text{\AA} \quad (3)$$

where  $n$  is the number of carbons in the tail of length  $l_c$ , and  $n' = n - 1$ . For a double chain molecule,  $n'$  is multiplied by 2. Values of  $v/a_0l_c < 1/3$  suggest spherical micelles,  $1/3 > v/a_0l_c > 1/2$  predicts rod-shaped micelles,  $1/2 > v/a_0l_c > 1$  suggests lamellar structures including bilayers, and  $v/a_0l_c > 1$  implies that reverse micelles will form in organic solvents. The packing parameter is influenced to some extent by added salt, which decreases average head group area, and by other experimental variables [12].



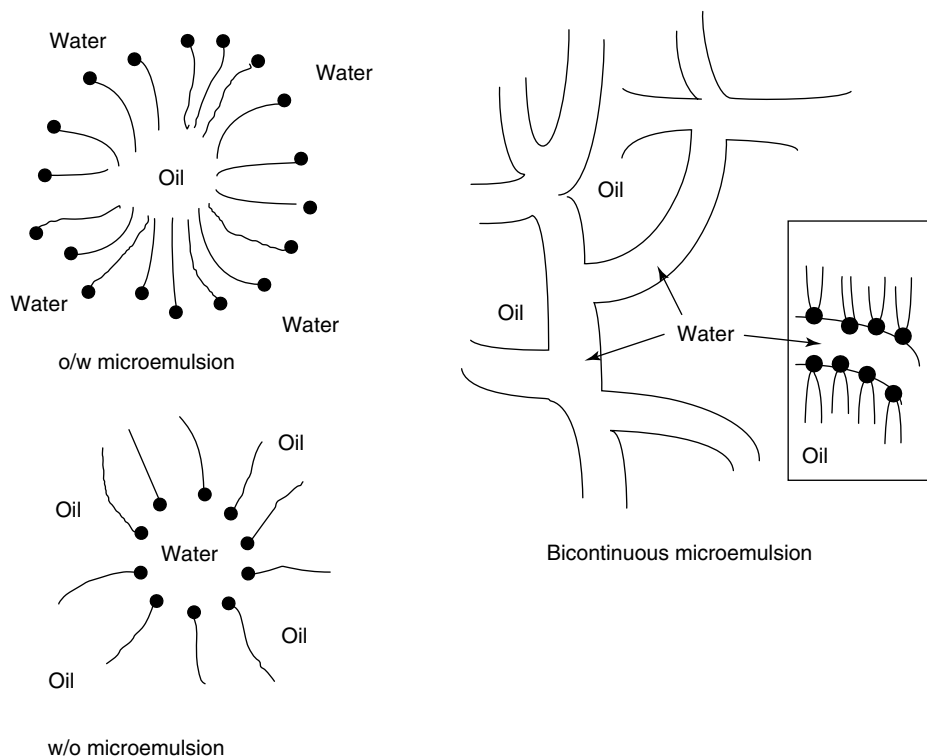


**Fig. 3** Oversimplified representations of microemulsion structures.

**4.4.2.1.2 Microemulsion Structure** Surfactant molecules residing at oil–water interfaces lower the interfacial free energy to nearly zero and drive the formation of optically clear, thermodynamically stable microemulsions [1–5]. Charged or polar head groups of the surfactants (Fig. 1) face the water phase and hydrocarbon tails extend into the oil phase. Microemulsions can contain droplets of oil in a continuous water phase (oil-in-water or o/w microemulsions) or droplets of water in a continuous oil phase (water-in-oil or w/o microemulsions). These droplets have diameters in the range 10 to 100 nm, larger than most micelles but much smaller than droplets in emulsions. As with micelles, the surface charge on the droplets

leads to interfacial potentials on the order of 100 mV.

A third type of microemulsion does not contain droplets but features continuous oil and water phases intertwined in dynamic extended networks (Fig. 3). Conductivity is imparted to microemulsions by ionic surfactants or salt in a continuous water phase. Thus, o/w and bicontinuous microemulsions can be made in conductive forms suitable for electrochemical experiments.

The surfactant packing parameter  $v/a_0l_c$  can be used to predict what types of nanostructures in microemulsions can form using specific surfactants. Amphiphilic molecules with  $0.5 < v/a_0l_c < 1$  tend to form three-component o/w and

bicontinuous microemulsions. Surfactants with  $v/a_0l_c < 0.5$  usually require cosurfactants such as long-chain alcohols to form microemulsions and those with  $v/a_0l_c > 1$  tend to form w/o microemulsions. These rules provide guidelines, but the type of microemulsion obtained also depends on ratios of oil, water, cosurfactant, and surfactant [2].

#### 4.4.2.2 Dynamics

A major influence on the mass transport of electroactive solutes ensues when

they are bound to micelles, microemulsion droplets, or interfacial surfactant layers in bicontinuous microemulsions. Binding can occur by coulombic or hydrophobic interactions. An understanding of the influence of solute binding on electrochemical experiments relies on the knowledge that micelles and microemulsion nanostructures exist in mobile equilibria with solutes and surfactant monomers (Fig. 4). Ejection of a monomer or solute from globular aggregates occurs on the microsecond timescale, and recapture is diffusion

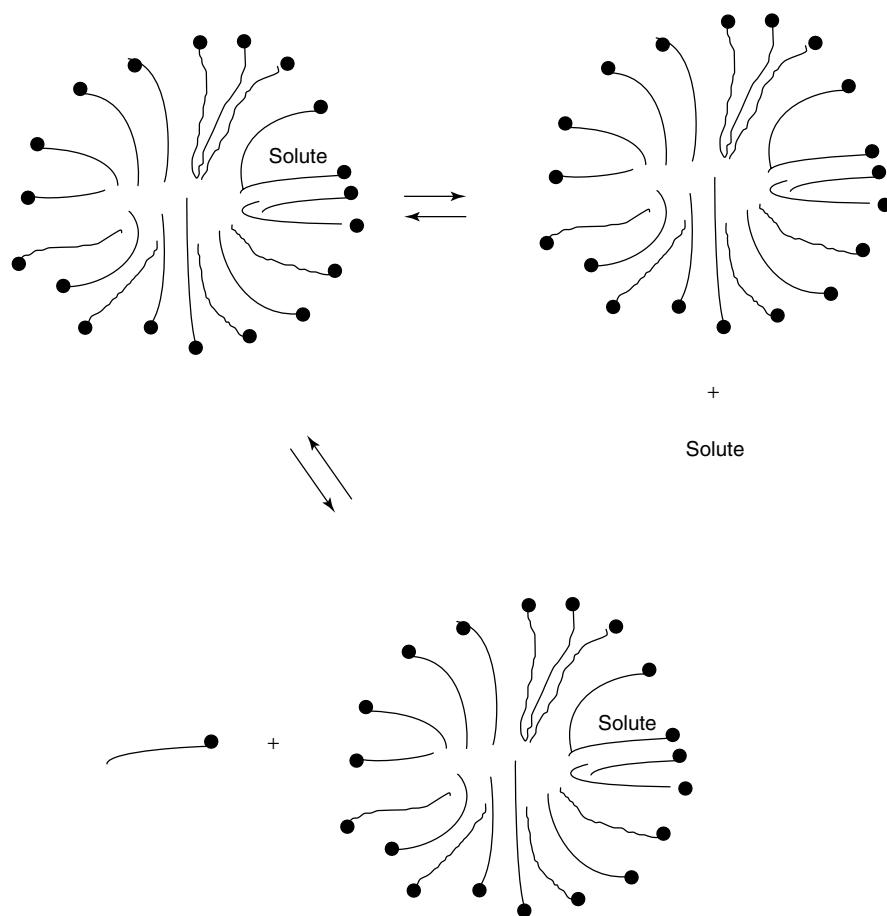


**Fig. 4** Dynamic equilibria involving micelles, solutes and surfactant monomers.

controlled, that is, on the nanosecond timescale. Recapture rates do not depend strongly on solute structure, but exit rate constants range from  $10^3$  to  $10^7 \text{ s}^{-1}$ , and decrease with the size and solubility of the solute [3, 4].

Multiply charged ions have a strong coulombic attraction to oppositely charged micelles; for example,  $\text{Ru}(\text{bpy})_3^{2+}$  [bpy = 2,2'-bipyridine] binds strongly to SDS micelles. Such solutes reside on the micelle surface, although the ligands can contribute hydrophobic interactions to the binding. Nonpolar solutes like aromatic hydrocarbons reside in hydrophobic regions close to the Stern layer of the micelles. Spectroscopic studies show that their microenvironments are more polar in ionic micelles than in hydrocarbon oils but less polar than in water [13].

#### 4.4.2.3 Surfactant Aggregates on Solid Surfaces

Adsorption of surfactants on charged metal oxides is understood better than on solid electrodes and instructive parallels can be drawn [14]. For ionic surfactants of opposite charge to the metal oxide surface, the first stage of adsorption from very dilute aqueous solutions is thought to result from neutralization of the surface charge [15–17]. Well below the CMC, surfactants adsorb individually with little intermolecular interaction. As the concentration increases, adsorption increases sharply and surface aggregates begin to form. It was suggested that at this point the surface is characterized by patches of bilayers [15, 18]. In the inner adsorbate layer, head groups face the solid surface. The outer layer of the surfactant has its charged head groups facing the water phase. Once the high charge density patches are covered with

bilayers, other regions of the surface begin filling in.

Atomic force microscopy (AFM) [19–21] provides a more detailed molecular picture of adsorbates at concentrations above the CMC. Adsorbed cationic surfactant  $\text{C}_{14}\text{TAB}$  (tetradecyltrimethylammonium bromide) was arranged in surface micelles on silica and in long cylinders on mica. Double-chained DDAB was organized in bilayers on mica. These structures result from the balance of adsorbate–surface interactions and aggregate curvature controlled by intermolecular interactions.

Ionic surfactants above the CMC form full coverage aggregates on metal and carbon electrodes [4, 22, 23]. Multilayers may form at extreme potentials of the opposite sign of the surfactant head group. Developing a definitive molecular picture of the aggregate structure based only on electrochemical results is difficult. Spectroscopy of the electrode–adsorbate solution interface has helped elucidate structural features [4, 14].

A few general features of the surfactant adsorbate structure can be extracted from the information available. At potentials negative of the point of zero charge (PZC) on hydrophilic metal and carbon electrodes, cationic surfactants adsorb head down. Positive of the PZC, anionic surfactants adsorb head down. Nonionic surfactants may adsorb head down on hydrophilic electrodes on either side of the PZC. Adsorption of cationic surfactants may be head down even at potentials positive of the PZC. This may involve adsorbed anions such as chloride on the electrode. Surface aggregate structures above the CMC may include bilayers, surface micelles, or cylinders depending on the nature of the surfactant, the electrode surface, and the applied potential.

## 4.4.3

**Electrochemistry in Micellar and Microemulsion Systems****4.4.3.1 Mass Transport – Diffusion**

Mass transport rates of electroactive solutes can be affected greatly by micelles and microemulsions. In cyclic voltammetry, for the reaction of a reversibly reduced or oxidized solute (O or R),



the peak current ( $I_p$ ) in a quiet solution depends on the apparent diffusion coefficient  $D'$  as given by the Randles–Sevcik equation [24]:

$$I_p = 0.4463nFAC^* \left( \frac{nF}{RT} \right)^{1/2} \nu^{1/2} D'^{1/2} \quad (5)$$

where  $n$  is the number of electrons transferred per molecule,  $F$  is Faraday's constant,  $A$  is the electrode area,  $C^*$  is the solute concentration,  $R$  is the gas constant,  $T$  is the temperature in Kelvin, and  $\nu$  is the scan rate. Equation (5) predicts a linear plot of  $I_p$  versus  $\nu$  for a reversible reduction or oxidation. The slope of this plot can be used to estimate  $D'$  in a micellar solution or microemulsion.

Linear sweep voltammetry at ultramicroelectrode disks of radius  $r < 10 \mu\text{m}$  under mass transport control, usually achieved at scan rates  $< 50 \text{ mV s}^{-1}$ , provides a limiting current  $I_L$  that depends directly on  $D'$  [25]:

$$I_L = 4nFD'C^*r \quad (6)$$

A number of other electrochemical methods can also be employed to obtain  $D'$  [4, 9].

$D'$  is influenced by binding to micelles, microemulsion droplets, or surfactant monolayers at o/w interfaces, as well

as obstruction effects.  $D'$  for water-soluble, unbound electroactive ions can be interpreted in terms of obstruction by oil droplets in o/w microemulsions [5, 9] as in Eq. (7):

$$D' = D_0(1 - \phi_c)^{p+1} \quad (7)$$

where  $\phi_c$  is the volume fraction of the oil in the microemulsion,  $D_0$  is the diffusion coefficient of the free ion in water, and  $p$  is a fitted coefficient.  $D'$  values of unbound water-soluble ions in microemulsions are typically 40 to 80% of those in water. Diffusion of electroactive species residing in a single microphase of bicontinuous microemulsions is somewhat obstructed by the o/w network.

Solutes bound to micelles, droplets, or interfacial regions can have  $D'$  values  $\geq$  tenfold smaller than their  $D$  values in the corresponding homogeneous solvent. For aggregates with a single size distribution, where the equilibrium between the bound and the free solute is fast with respect to the timescale of the electrochemical experiment,  $D'$  is given by a two-state model [4, 5]:

$$D' = f_a D_0 + f_b D_1 \quad (8)$$

where  $f_a$  is the mole fraction of the unbound solute,  $f_b$  is the fraction of the bound solute,  $D_0$  is the diffusion coefficient of the free solute, and  $D_1$  is that of the micelle or droplet in the fluid. Equation (8) represents the usual case in micelles and microemulsions when  $D'$  is estimated by cyclic, rotating disk, or ultramicroelectrode voltammetry at relatively low scan rates [4].

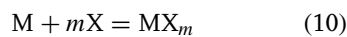
$D_1$  can be used to estimate the hydrodynamic radius ( $r_h$ ) of a micelle or microemulsion droplet via the

Stokes–Einstein equation:

$$D_1 = \frac{kT}{6\pi\eta r_h} \quad (9)$$

where  $k$  is Boltzmann's constant,  $\eta$  is the viscosity, and  $T$  is the temperature in Kelvin.  $D_1$  can be obtained by using equilibrium expansions of Eq. (7) describing  $D'$  versus total concentration of an electroactive probe,  $C_X$  [4, 5]. At typical surfactant and probe concentrations, more than one electroactive probe (X) can bind to a micelle or droplet (M) in the overall

reaction:



$$K^m = \frac{[MX_m]}{[M][X]^m} \quad (11)$$

Assuming  $[X] \ll C_X$ , that is, that the probe is almost entirely bound, Eq. (8) can be expressed as

$$D' = \frac{D_0}{1 + C_M K^m C_X^{m-1}} + \frac{C_M K^m C_X^{m-1} D_1}{1 + C_M K^m C_X^{m-1}} \quad (12)$$

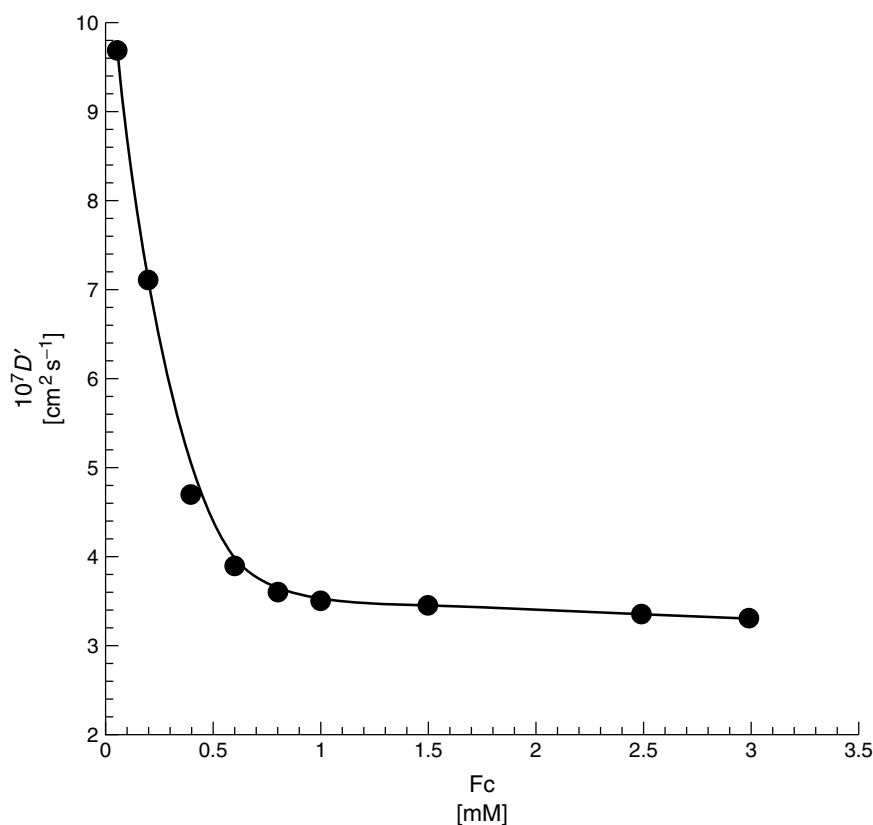


**Fig. 5** Influence of the concentration of ferrocene (Fc) on  $D'$  measured by cyclic voltammetry at a glassy carbon electrode in 0.15 M CTAB/0.1 M tetraethylammonium bromide. Points are experimental; line is best fit to Eq. (12) with  $n = 3$  by nonlinear regression, giving  $D_1 = 3.3 \times 10^{-7} \text{ cm}^2 \text{ s}^{-1}$  for the rod-shaped micelles. (Reproduced with permission from Ref. [4], Copyright 1994 by Marcel Dekker.)

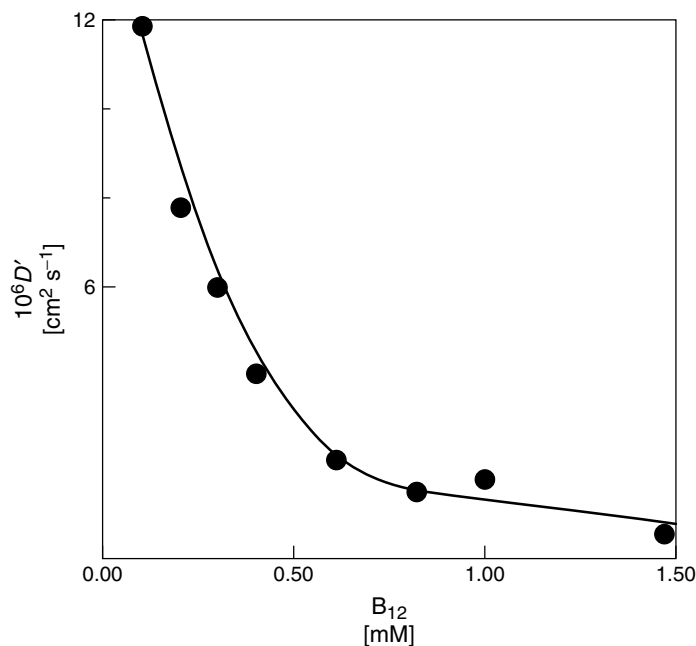


**Fig. 6** Influence of concentration of cobalt(II) corrin complex vitamin B<sub>12</sub> on  $D'$  measured by linear sweep voltammetry at a 10- $\mu$ m radius carbon ultramicroelectrode in w/o microemulsion made with 0.2 M aerosol AT, 4 M water, and isooctane. Points are experimental; line is best fit to Eq. (12) with  $n = 3$  by nonlinear regression giving  $D_1 = 0.63 \times 10^{-6} \text{ cm}^2 \text{ s}^{-1}$  for the water droplets. Using this value with Eq. (9) gave a hydrodynamic radius of 7.5 nm. (Adapted with permission from Ref. [27], Copyright by American Chemical Society.)

Equation (12) holds for micelles and w/o or o/w microemulsions with single size distributions. It describes the dependence of  $D'$  on  $C_M$  at constant  $C_X$  and on  $C_X$  at constant  $C_M$ .  $K$  is an apparent binding constant for a single probe molecule.

Plots of  $D'$  versus  $C_X$  at constant  $C_M$  are useful for determining  $D_1$  because the aggregate size is likely to remain constant for the full set of  $C_X$ . When  $C_M$  is increased, aggregate size and shape may change [3, 4]. If  $K$  is too large, no dependence of  $D'$  versus  $C_X$  will be observed.

Figure 5 illustrates agreement of  $D'$  versus  $C_X$  data with Eq. (12) for rod-shaped

micelles using micelle-soluble ferrocene (Fc) as the electroactive probe. Fitting Eq. (12) to the data is typically done with  $D_0$ ,  $D_1$ , and  $K$  as parameters. A series of nonlinear regressions are done, each with a different fixed integer value  $m = 2, 3, \dots, q$ , until the minimum standard deviation of the regression in the series is found [26].

Figure 6 illustrates the use of Eq. (12) for a w/o microemulsion. Ultramicroelectrodes were used to obtain  $D'$  for the water droplets using a water-soluble electroactive probe. Results of the regression analysis allow an estimate of the hydrodynamic radius of the spherical droplet.

Inspection of Figs 5 and 6 shows that at high probe concentration, limiting values of  $D'$  tend toward  $D_1$ . Thus, a reasonable estimate of  $D_1$  for monodisperse systems can be obtained by measuring  $D'$  at relatively large probe concentrations, for example, 2 to 5 mM. For polydisperse systems, additional equilibria must be considered. A three-state model was used to develop a version of Eq. (12) for two micellar size distributions, and applied to systems with coexisting globular and rod-shaped micelles [4].

#### 4.4.3.2 Formal Potentials

Binding electroactive solutes to micelles or microemulsion droplets influence formal potentials ( $E^{\circ'}$ ) estimated by voltammetry. The *pseudophase equilibrium* approach can predict  $E^{\circ'}$  in the microheterogeneous media. Equilibria of micelles or droplets with both forms of the redox couple must be considered via a square scheme (Scheme 1) for the reversible redox couple A/B.

The *pseudophase equilibrium model* considers solutes to be dissolved in continuous and discrete (micelles or droplets) “phases” in a way similar to the partition in conventional two-phase systems of oil and water [3, 4]. The equilibrium distribution constants are

$$K_0 = \frac{[A_W]}{[A_M]} \quad \text{and} \quad K_r = \frac{[B_W]}{[B_M]}$$

Subscript W refers to the water or continuous phase, and subscript M refers to the micellar or droplet phase. In general,

the reversible midpoint or formal potential in the microheterogeneous fluid ( $E_M^r$ ) is

$$E_M^r = E_W^{\circ'} + \frac{RT}{nF} \ln \frac{K_0(1 + K_r)}{K_r(1 + K_0)} - \frac{RT}{2nF} \ln \frac{D'_0}{D'_r} \quad (13)$$

where  $D'$ 's are measured diffusion coefficients in the microheterogeneous solutions,  $E_W^{\circ'}$  is the formal potential of A/B in the continuous phase, and the other constants have their usual electrochemical meanings. There are several limiting cases allowing simplifications:

**Case 1.** A and B exist mainly in the bound form, and  $K_r, K_0 \ll 1$ .

$$E_M^r = E_W^{\circ'} + \frac{RT}{nF} \ln \frac{K_0}{K_r} \quad (14)$$

Examples include multiply charged metal complexes  $ML^{3+}/ML^{2+}$  in SDS micelles [28].

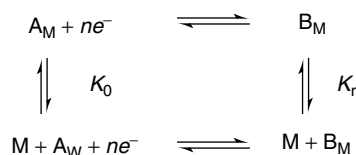
**Case 2.** B is entirely bound but A is not bound.

$$E_M^r = E_W^{\circ'} + \frac{RT}{nF} \ln \frac{1 + K_r}{K_r} - \frac{RT}{2nF} \ln \frac{D'_0}{D'_r} \quad (15)$$

An example is ferrocene bound to positively charged alkyltrimethylammonium micelles, where oxidation product ferricinium ion dissociates when formed [29].

#### 4.4.3.3 Electrode Kinetic Effects

Attempts were made several decades ago to describe the influence of adsorbed surfactants on the apparent heterogeneous



Scheme 1

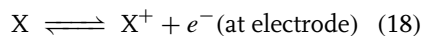
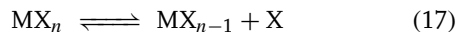
electron transfer rate constant  $k^{\circ'}$  using Eq. (16) [4, 9]:

$$k^{\circ'} = k_0(1 - \theta) + \theta k_1 \quad (16)$$

where  $k_0$  is the rate constant on a bare electrode,  $k_1$  is the rate constant on a fully coated electrode, and  $\theta$  is fractional surface coverage of surfactant. While many systems deviate from Eq. (16) at large  $\theta$ , a decreased  $k^{\circ'}$  in micellar solutions and microemulsions is often found.

For a reactant molecule or ion in a micellar solution or microemulsion, predictions of electron transfer kinetics at electrodes need to consider [14]: (1) the distance between the electrode and the reactant, (2) the environment surrounding the reactant at the time of electron transfer, (3) structure and dynamics of surfactant aggregates on the electrode, and (4) dynamics of interactions of the reactant with surfactant structures on the electrode and with micelles. A molecular picture of these events during electron transfer is by no means clear, and quantitative predictions are not possible at this time. A qualitative view of the above factors is given in the following paragraphs.

When small electroactive ions or molecules are bound to larger aggregates like micelles or microemulsion droplets, the reactant (probe) is transported to the electrode along with the larger, slower diffusing aggregate. Equation (12) describes the influence of concentration of surfactant or reactant on electrochemically measured diffusion coefficients. At  $[X] > 2$  mM, the measured apparent diffusion coefficient  $D'$  approaches the diffusion coefficient of the micelle  $D_1$ . This implies electrolysis of one reactant X per micelle. This electrolyzed X could reside within  $MX_n$ , or be released by dissociation, as illustrated in Eqs. (17 and 18) for an oxidation:



When  $MX_n$  reaches the electrode, either an electron is donated directly from one of the bound Xs or dissociation (Eq. 18) yields a free X that donates the electron.

Both coulombic and hydrophobic interactions of reactants with adsorbed surfactant on electrodes are important in determining electron transfer kinetics. Reactants in micellar solutions and microemulsions can be preconcentrated into adsorbed surfactant films on electrodes [30], yielding mixed layers of reactants and nonelectroactive surfactants. Coulombic effects in micellar solutions may result in small kinetic enhancements when ionic reactants interact with oppositely charged surfactant adsorbed on electrodes. Partial inhibition of electron transfer can occur by coulombic repulsion if the charge sign on the reactant and adsorbed surfactant are the same. Hydrophobic molecules and ions may show a small amount of preconcentration on the electrode.

Studies of oxidations in micellar CTAB and SDS media [31] suggested average microenvironments for ferrocene during electron transfer in micellar solutions that are more polar than in apolar solvents but less polar than in water. Similar microenvironmental polarity is found for hydrophobic solutes in micelles [13].

Studies of electroactive surfactants 1 to 4 (Fig. 7) in dilute or micellar solutions have provided insight into adsorbate structure, interactions, and dynamics at electrodes [14]. Ordered films were formed on glassy carbon electrodes from dilute solutions of 3. Single-molecule residence times on the electrode in micromolar solutions were 4.5 s for Fc-C8, 14 s for Fc-C12, and 66 s for Fc-C16. Bilayers of 3 were



adsorbed on electrodes from microemulsions made with 3, oil, water, and alcohol.

Comparisons of electrochemical  $k^{\circ'}$  values of surfactants 1 and 2 in microemulsions and micellar solutions helped establish qualitative pictures of dynamics at relevant electrode-fluid interfaces. Rate constants for oxidations of ferrocene (Fc) 2-Fc (1) and 5-Fc (2) were similar in homogeneous DMF and DMSO on Pt and glassy carbon electrodes [32, 33]. However, in aqueous CTAB micelles, electron transfer rates were in the order  $\text{Fc} > 2\text{-Fc} > 5\text{-Fc}$ , with tenfold differences in successive values. This was attributed to 2-Fc and 5-Fc achieving head down orientations on the electrode prior to electron transfer. Adsorbed  $\text{CTA}^+$  on the electrode seems to help order 1 and 2 on the electrode prior to electron transfer.

In a bicontinuous CTAC microemulsion, ferrocene had a  $k^{\circ'}$  twice as large as 1 and 2 [33], but values for 2-Fc and 5-Fc were similar. These relatively small differences in electron transfer rates in the microemulsion cannot be explained by head down–tail up orientation of 1 and 2 at the time of electron transfer as proposed for micellar solutions. The results suggest an increased disorder and mobility in the electrode–fluid interface in the CTAC microemulsion compared to micellar CTAB solutions.

Alcohols are often used as cosurfactants in microemulsions, and insight has been obtained from the electrochemistry of ferrocene alcohols (4). Oxidations of  $\text{FcOHC}_{10}$ ,  $\text{FcOHC}_{14}$ , and  $\text{FcOHC}_{18}$  [34] were nearly reversible and controlled by diffusion in microemulsions of DDAB, CTAC, or SDS. In micellar solutions, electrode reactions were more complex and reflected strong adsorption of the ferrocene alcohols onto the electrode.

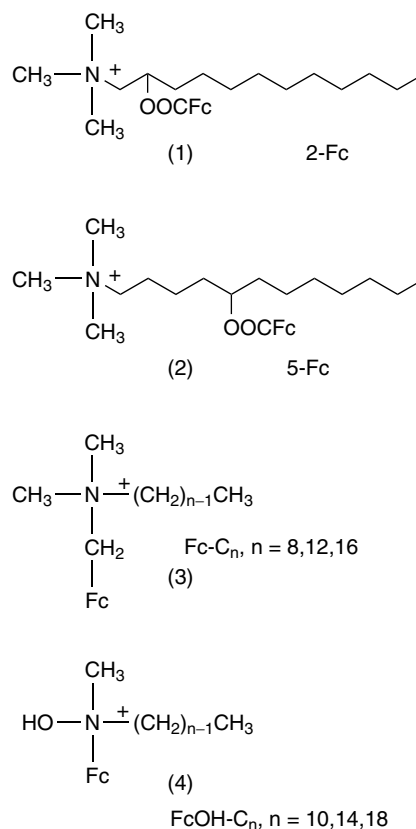


**Fig. 7** Electroactive ferrocene-containing surfactants.

In microemulsions, the alcohols are distributed between the oil–water interfaces and the oil phase of the microemulsions, with increases in chain length favoring binding at the oil–water interface. Results of these and other studies [35–37] suggest that the presence of sufficient cosurfactant can improve interfacial fluidity and facilitate electron transfer at electrodes.

In general, then, surfactant aggregates on electrode surfaces can control electron transfer kinetics. Aggregates such as bilayers, cylinders, or surface micelles adsorb onto electrodes in solutions with surfactant concentrations above the CMC.

On hydrophilic electrodes, head down adsorption of surfactants seems to be preferred.

The electroactive reactant may replace adsorbed surfactant at a site on the electrode and approach the electrode closely. In micellar CTAB, this may occur with reactants 1, 2, and 3. However, adsorbed reactant is unlikely to replace all of the adsorbed nonelectroactive surfactant in micellar solutions well above the CMC, and mixed adsorbate layers form on the electrode. Alternatively, if surfactants remain strongly adsorbed, hydrophobic reactants could enter the surface film and approach the electrode to within roughly one head group diameter prior to electron transfer. Both possibilities can be inferred for specific experimental systems. Comparisons of ferrocene, 1 and 2 suggested that underivatized ferrocene may approach the electrode within the distance of one head group. Small reactants typically have  $k^o'$  values in micellar solutions consistent with this view [4]. Thus, depending on the ability of the solute to compete with nonelectroactive surfactant for sites on the electrode, electron transfer can take place to adsorbed reactant or to reactant that approaches the electrode to within a distance of roughly one surfactant head group.

There are several molecular scenarios for the delivery of micelle-bound reactants into adsorbed surfactant films on electrodes. One possibility is dissociation (Eq. 17) followed by entry of the reactant into the aggregate film on the electrode, orientation near the surface, and electron transfer. Making the analogy between these latter processes and the adsorption rates of 3, entry into the films and orientation is expected to occur on a millisecond timescale.

Alternatively, a micelle in solution could join with aggregates on the electrode

surface, bringing the reactant close enough to the electrode for electron transfer, analogous to the joining of micelles and submicellar aggregates on the millisecond timescale. This process may be indistinguishable from Eqs. (17 and 18) by voltammetry [14].

A picture of the microemulsion–electrode interface emerges through comparison with the micellar case. Although the surfactant is adsorbed onto electrodes from both types of fluids, the adsorbate in microemulsions is likely to be more disordered and more fluid. Results for ferrocene alcohols 4 suggest that there is no long-chain alcohol cosurfactant strongly adsorbed onto electrodes. However, some alcohol may be distributed into a dynamic surfactant layer on the electrode. Oils in some microemulsions could also penetrate the surfactant layer on the electrode, perhaps inducing disorder and increased fluidity. However, much more information is needed before a comprehensive understanding of electron transfer processes at electrodes in microemulsion is reached.

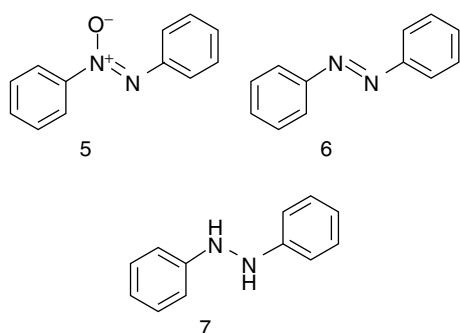
#### 4.4.4

##### Pathway Control of Organic Reactions

##### 4.4.4.1 Direct Electrolyses

Control of organic reaction pathways can be achieved by using micellar media and microemulsions. In the following sections, selected cases are presented rather than a comprehensive review.

Products of the reduction of *nitrobenzene* in water depend on pH [38]. In neutral and weakly acid media, phenylhydroxylamine is always the product. In stronger acid ( $\text{pH} < 4$ ), phenylhydroxylamine is reduced to aniline. In alkaline media, dimeric products azoxybenzene (5), azobenzene (6), or hydrazobenzene (7) are formed.



Under conditions where phenylhydroxylamine is the product, a single four-electron voltammetric peak is found for nitrobenzene. However, at pH > 10 containing surface-active camphor or gelatin, a single one-electron wave for reduction of nitrobenzene to its anion radical is found, with a subsequent three-electron wave at more negative potentials [4]. Similar behavior occurs in SDS micelles and was attributed to hydrophobic-based stabilization of the nitrobenzene anion radical by the micelles [39]. Surfactant solutions allow electrochemical generation of relatively stable radical anions of nitrobenzene and its derivatives, and have been used for electron spin resonance (ESR) studies.

Electrolysis of nitrobenzene at  $-1.5$  V versus Ag/AgNO<sub>3</sub> in DDAB/hexane/water microemulsions, even when acidified, gave dimers 5 or 6 as products [40]. No hydroxylamine or aniline was detected, suggesting that the reaction takes place at sites of low proton availability.

Direct reductions of organohalide pollutants have been done in solutions containing ionic and nonionic surfactants [41], but often with low current efficiencies. One interesting approach involved the use of an acid-labile nonionic surfactant, 1% oil, and water for the dechlorination of hexachlorobenzene. This allowed facile

recovery of lesser-chlorinated products by breaking the microemulsion with acid [42].

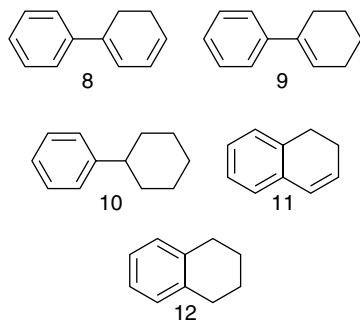
Micelles can also facilitate one-electron dimerizations over two-electron reductions. An example is electrohydrodimerization of activated olefins, including the commercially important conversion of acrylonitrile to adiponitrile in the Monsanto process, which employs an emulsion of acrylonitrile, water, and short-chain tetraalkylammonium salts [43]. High selectivity for the dimer adiponitrile can also be achieved by using millimolar concentrations of nonionic surfactants such as Triton X-100 [44]. Surfactant adsorbed on the electrode is thought to create reaction sites of low proton availability, shutting down the competing two-electron reduction that requires protons. Other organic dimerizations also benefit from using micellar solutions [4].

A variety of electrochemical oxidations and reductions have been examined in micellar solutions. For further information, the reader is directed to comprehensive reviews [4, 22, 30, 41, 45].

Only a few other direct electrochemical reductions have been studied in microemulsions. Reductions of naphthalene and biphenyl resulted in selective reduction of a single benzene ring in the polyaromatic hydrocarbon [40], as in 8 to 12. Products 8 and 9, in addition to biphenyl, were also found from catalytic reduction of polychlorinated biphenyls in microemulsions [46].

#### 4.4.4.2 Electrochemical Polymerization in Microemulsions

Microemulsions may have advantages over conventional solvents for synthesizing conducting polymers. W/o microemulsion droplets can serve as microreactors to control polymer growth kinetics and particle size [47].



W/o microemulsions of water, aniline, light petroleum, and nonionic surfactant Empilan NP-5 have been utilized for electrochemical polymerization of aniline to polyaniline [48]. Improved homogeneity and conductivity was achieved compared with polyaniline grown in water. The heterogeneous nature of the microemulsion directed the mode of polymer growth and improved conductivity and structural features.

Poly(*p*-phenylene) was made by electrochemical polymerization in o/w microemulsions [49] of benzene, sulfuric acid, and anionic, cationic, or neutral surfactant. Benzene radical cation was stabilized by the anionic surfactant, resulting in polymer with less cross-linking, smaller particle size, and a relatively narrow size distribution. With cationic surfactants, the radical cation destabilized the water droplets and led to a broader size distribution of polymer particles.

Stepwise polymer film formation in a microemulsion has been explored [50]. The first step was the partial polymerization of a microemulsion containing acrylamide, styrene, pentanol, water, and SDS. Addition of potassium persulfate and azo-bis-isobutyronitrile gave a viscous mixture that was used to coat the electrode surface. Evaporation of pentanol left a highly porous surface onto

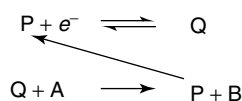
which pyrrole was electrochemically polymerized. This porous composite had a large surface area for electrochemical reactions and allowed greater permeation by reactants.

Nonconductive w/o microemulsions were used for electrochemically induced polymerization at a specially designed solid polymer working electrode. Using a microemulsion of water, toluene, and sodium bis(2-ethylhexyl) sulfosuccinate (AOT), acrylamide was polymerized *via* persulfate reduction [51]. An applied potential initiated polymerization, which continued for several hours after the power was off. This resulted in a latex suspension with comparable molecular weight and particle size to those obtained by thermal or UV initiation. The degree of stirring controlled the particle size (7–130 nm).

The influence of structure and concentration of cosurfactant amides in the above w/o microemulsions was investigated by ultramicroelectrode voltammetry [36]. Oxidation of amides was detected only above a threshold concentration. The threshold decreased as the chain length of amide increased because longer chain amides were more extensively adsorbed at the oil–water interface. Increasing the amount of acrylamide makes the interfacial region more fluid and increases the permeability to electroactive species so that electron transfer can occur more easily [37, 52].

#### 4.4.4.3 Mediated Reactions in Micellar Solutions

Micellar rate enhancement of thermal and light-initiated biomolecular reactions often occurs via preconcentration of the two reactants in the micelles [3]. In electrochemical catalysis (Scheme 2), the analogous situation can occur for participants in biomolecular reactions coadsorbed into surfactant films on electrodes. Interfacial

**Scheme 2** Simple pathway for electrochemical catalysis.

preconcentration in micellar solutions can be exploited in electrochemical catalysis in which a catalyst (mediator, P/Q) is added to the system to shuttle electrons between the electrode and a reactant that is otherwise difficult to oxidize or reduce [30]. Rate-determining steps (r.d.s.) in electrochemical catalysis are often bimolecular, for example, the reaction between Q and A in Scheme 2.

The observed rate of a chemical reaction in micellar solutions is the sum of rates in the continuous and micellar phases [3]. Consider a bimolecular chemical reaction between Q and A in which the reactants are totally bound to micellar aggregates. The rate constant  $k_{\text{obs}}$ , obtained on the basis of amounts of Q and A in the total system volume ( $V_t$ ), is given by

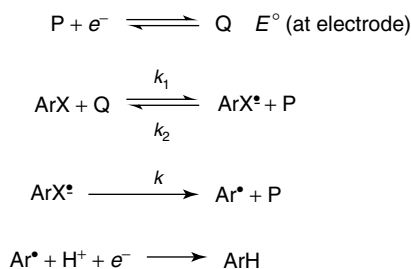
$$k_{\text{obs}} = \frac{k_M [\text{Q}]_M [\text{A}]_M}{[\text{Q}][\text{A}]} \quad (19)$$

where  $k_M$  is the rate constant in the micellar phase, denoted by subscript M. The concentration of the reactant in the micellar phase is the total concentration divided by the volume fraction of the micelles,  $\phi_M$ , so that

$$k_{\text{obs}} = \frac{k_M}{\phi_M^2} \quad (20)$$

Equation (20) shows that  $k_{\text{obs}}$  is enhanced by compartmentalization of all the reactants into micellar volume  $V_t \phi_M$ . In electrochemical catalysis in micellar solutions, large rate enhancements are observed when the reaction occurs in surfactant aggregates on the electrode surface [4, 30]. In this case, the compartmentalization volume where the bimolecular r.d.s. occurs is that of the surfactant film on the electrode.

Catalytic reductions of organohalides are examples of electrochemical catalysis that can give large rate enhancements in micellar solutions [4, 30]. Anthracene derivatives and metal complexes catalyze these two-electron carbon-halogen cleavage reactions. The pathway is shown in Scheme 3. Catalyst P is dissolved in the micellar solution or immobilized on the electrode. At applied potentials near  $E^\circ$ , P is reduced to Q, which reacts with aryl halide ArX, regenerating P. This latter reaction is often the r.d.s. Subsequent steps yield hydrocarbon ArH. Since catalyst P is regenerated in the pathway, the voltammetric peak current of P is larger in the

**Scheme 3** Electrochemical catalytic reduction of aryl halides.

presence of ArX. This “catalytic current” can be used to estimate rate constants.

Mediator 9-phenylanthracene (9-PA) was used to reduce 4-bromobiphenyl in CTAB solutions on Hg electrodes [4, 30]. Voltammetry showed a large preconcentration of 9-PA in a thick film of CTAB on the Hg surface. Reduction of 9-PA at  $-2.2$  V versus SCE gave the anion radical that was stabilized by the positively charged CTAB film. The observed  $k_1$  for reaction of 9-PA anion radical with 4-bromobiphenyl was  $10^7 \text{ M}^{-1} \text{ s}^{-1}$  in  $0.1 \text{ M}$  CTAB compared to  $300 \text{ M}^{-1} \text{ s}^{-1}$  in DMF, demonstrating a large rate enhancement in the micellar solution. Electrolysis using this system showed a clean, high-yield conversion of 4-bromobiphenyl to biphenyl.

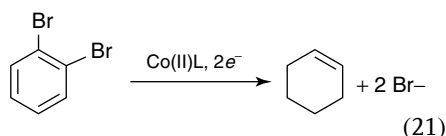
Other catalysts with  $E^\circ$  values more positive than  $-2$  V showed smaller rate enhancements because a thick CTAB film apparently does not form on Hg electrodes at these potentials. Negatively charged clays on electrode surfaces have been used to form films of cationic micelles on electrodes for organohalide reductions positive of  $-2$  V. Details of these and other mediated reactions in micellar solutions are found in reviews [4, 30].

#### 4.4.4.4 Mediated Reactions in Microemulsions

**4.4.4.4.1 Reductive Dehalogenations** Microemulsions are usually more useful than micelles for electrochemical synthetic applications because larger amounts of polar and nonpolar reactants can be solubilized. Electrochemical catalysis has been used in microemulsions for the electrolytic conversion of organohalide pollutants to hydrocarbons [53] using mediators such as metal phthalocyanines and cobalt complexes. Microemulsions were used for the complete electrochemical catalytic

dechlorination of polychlorinated biphenyl (PCB) mixtures [46, 54–56] and the pesticide DDT [56, 57] and were also employed for mediated electrolytic dechlorination of PCBs adsorbed onto soils and clays [55]. The reactions were most successful with a lead cathode in a simple, undivided, two-electrode electrochemical reactor operated under constant-current using zinc phthalocyanine as a mediator.

The catalytic conversion of *trans*-1,2-dibromocyclohexane (DBCH) to cyclohexene with macrocyclic cobalt complexes [6, 58] was used as a probe to investigate the kinetics of mediated electrochemical reactions in microemulsions. The P/Q catalyst couples were macrocyclic cobalt complexes  $\text{Co}^{\text{II}}\text{L}/\text{Co}^{\text{I}}\text{L}$  such as cobalt corrins, salen, porphyrins, and phthalocyanines.



In bicontinuous DDAB microemulsions,  $\text{Co}^{\text{II}}\text{L}$  mediators reside in the water phase and DBCH in the oil phase, and the reaction (Eq. 21) probably occurs at the o/w interface. Cyclic voltammetry (Fig. 8) shows the reversible  $\text{Co}^{\text{II}}/\text{Co}^{\text{I}}$  reduction–oxidation peaks of the mediator and an increase in reduction current when DBCH is added. Direct reduction of DBCH occurs at a much more negative potential.

The catalytic current was used to estimate the apparent rate constant  $k_1$  for the DBCH reaction with  $\text{Co}^{\text{I}}\text{L}$  [58]. A linear plot of  $\log k_1$  versus  $E^{\circ'}$  of the mediator (Fig. 9) in DDAB microemulsions and organic solvents was obtained. A similar linear plot was found for the catalytic reduction of benzyl bromide in microemulsions [59]. These plots suggest that the bimolecular reactions in these microemulsions are controlled mainly by

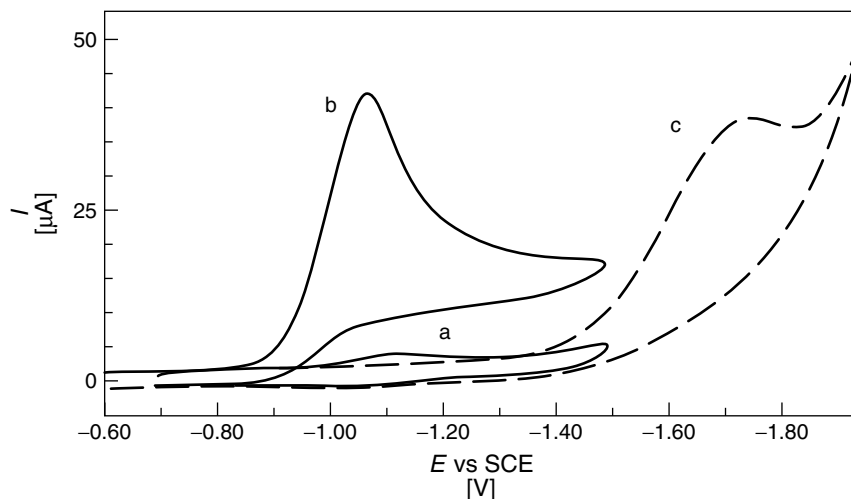


**Fig. 8** Cyclic voltammograms at  $0.1 \text{ V s}^{-1}$  on glassy carbon electrodes in a DDAB microemulsion: a)  $0.4 \text{ mM Co(salen)}$  alone; b)  $0.4 \text{ mM Co(salen)} + 1.5 \text{ mM DBCH}$ ; and c)  $1.5 \text{ mM DBCH}$  alone without catalyst. (Adapted with permission from Ref. [58], Copyright by American Chemical Society.)

the intrinsic activation free energy of the reaction via  $E^{\circ'}$ , and not by partition between oil and water phases. This situation requires sufficiently large o/w interfacial area of the fluid.

As with micelles, incorporation of reactants into an adsorbed surfactant layer on an electrode [6, 7] can lead to high reactant concentrations in a restricted reaction volume and enhanced rates of bimolecular reactions. Conversely, when reactants in a bimolecular r.d.s. reside separately in oil and water phases in microemulsions with insufficient interfacial area or slow partition dynamics, the reaction rate may be slower than in a homogeneous solution [27].

The reduction of DBCH was also effected by using carbon electrodes coated with catalytic films made by covalently linking poly-L-lysine (PLL) onto oxidized carbon electrodes, then attaching a reversible cobalt corrin catalyst [60]. Covalent linkage was necessary for stability of the catalytic films in microemulsions. Conversion of

DBCH to cyclohexene in microemulsions was achieved with turnover numbers much higher than with dissolved catalysts. The catalytic properties of these PLL-Co films could be controlled by microemulsion composition [61], and anionic micelles formed within the cationic films in SDS microemulsions.

Turnover rates for the reduction of DBCH to cyclohexene mediated by the PLL-Co film in bicontinuous SDS microemulsions were controlled by the difference between the reduction potential of the reactant and  $E^{\circ'}$  of the catalyst in the film, similar to dissolved cobalt complex catalysts. High conductivity and low viscosity of the bulk microemulsion also facilitated fast catalyst turnover.

**4.4.4.4.2 Bond Forming Reactions** Mediated electrochemical synthesis in microemulsions can be used to construct bonds. Carbon-carbon linkages between an alkyl halide RX and an activated olefin

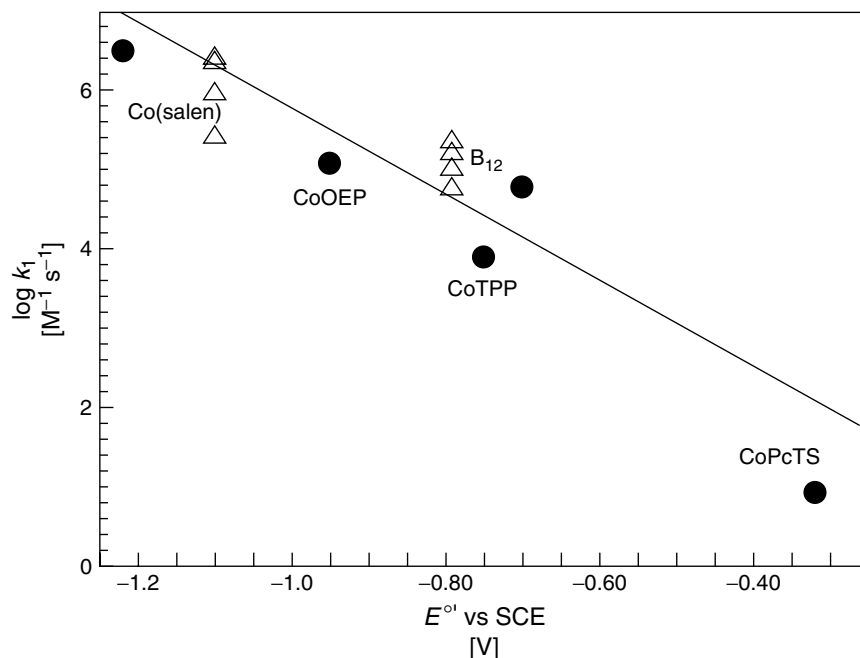
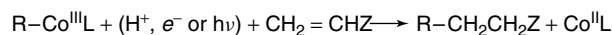
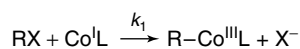
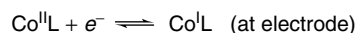


**Fig. 9** Influence of catalyst formal potential ( $E^\circ$ ) on  $\log k_1$  for reaction of  $Co^I L$  with DBCH in a bicontinuous microemulsion ( $\Delta$ ) of DDAB/water/dodecane (21/39/40) and in dimethylformamide ( $\bullet$ ) for dissolved catalysts vitamin B<sub>12</sub>, Co(salen), cobalt phthalocyaninetetrasulfonate (CoPCTS), cobalt tetraphenylporphyrin (CoTPP), and cobalt octaethylporphyrin (CoOEP). Points from reactions in the microemulsion ( $\Delta$ ) represent apparent  $k_1$  values for 0.4, 0.5, 1.0, and 2.0 mM catalyst in order of decreasing  $\log k_1$ . (Adapted with permission from Ref. [58], Copyright by American Chemical Society.)



**Scheme 4** Mediated electrochemical bond formation.

are made by using  $Co^{II}L$  complexes as mediators as in Scheme 4.

Here, X represents a halogen atom and Z is an electron-withdrawing group. Electrochemically reduced mediator  $Co^I L$  reacts with alkyl halide RX to yield intermediate  $R-Co^{III}L$ , which is cleaved at a more negative potential or by visible

light. The resulting alkyl anion or radical is trapped by an activated olefin to form a carbon-carbon bond.

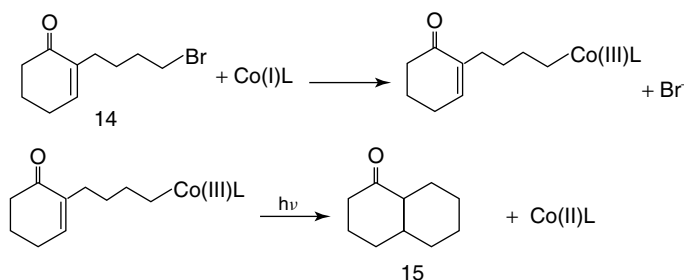
Several examples of mediated bond formation are given below. Conjugated additions of alkyl iodides to 2-cyclohexen-1-one gave 3-alkyl cyclohexanones 13 (Scheme 5) [62] in 70 to 80% yields in



$$\begin{array}{l} \text{Co(II)L} + \text{RI} \longrightarrow \text{R-Co(III)L} + \text{I}^- \\ \text{R-Co(III)L} + \text{cyclohex-2-en-1-one} \xrightarrow{h\nu} \text{cyclohex-2-en-1-one-3-R} + \text{Co(II)L} \end{array}$$

Catalysis using vitamin B<sub>12</sub> at  $-1.5$  V versus SCE at carbon electrodes in CTAB and SDS bicontinuous microemulsions converted 2-(3-bromopropyl)-2-cyclohexen-1-one (16) to the 5-endo-trig cyclization product 4-hydrindanone (17) in 62 to 70% yields (Scheme 7) [64]. Similar conditions gave only 7 to 19% of 17 in DMF, MeOH, or MeOH/water. The microemulsions seem to provide reaction sites of low proton availability to inhibit protonation of a key carbanion intermediate whose protonation would prevent cyclization.

Finally, phase transfer catalysis was achieved in DDAB microemulsions. Dichlorocarbene was generated at a carbon cathode from dichlorodibromomethane used as the



### Scheme 7

oil constituent of a microemulsion [65]. Tetrabutylammonium bromide helped to catalyze this reaction in the oil phase. The carbene reacted with cyclohexene to generate 7,7-dichloro-bicycloheptane. The best current efficiency was 80%.

#### 4.4.5

##### Summary

This chapter describes the electrochemistry of small reactants dissolved in micellar solutions and microemulsions. A major influence of these microheterogeneous fluids on reversible reactants is slowing down mass transport. These phenomena enable electrochemical probes to be used to characterize aggregate mass transport and size in the fluids. Tuning the compositions of micelles and microemulsions can control pathways and kinetics of direct organic reactions, polymerizations, and mediated electrochemical reactions.

##### Acknowledgments

The author's work on micelles and microemulsions described in this chapter was initially supported by US PHS Grant No. ES03154 from the National Institute of Environmental Health Sciences, NIH. More recent synthetic aspects were supported by Grants nos. CTS-9306961, CTS-9632391, and CTS-9982854 from NSF. The contents of this chapter are solely the responsibility of the author and do not necessarily represent official views of NIH or NSF.

##### References

1. P. L. Luisi, L. Magid, *CRC Crit. Rev. Biochem.* **1987**, 20, 409–474.
2. M. Bourrel, R. S. Schechter, *Microemulsions and Related Systems*, Marcel Dekker, New York, 1988.
3. J. H. Fendler, *Membrane Mimetic Chemistry*, John Wiley & Sons, New York, 1982.
4. J. F. Rusling in *Electroanalytical Chemistry* (Eds.: A. J. Bard), Marcel Dekker, New York, 1994, pp. 1–88, Vol. 19.
5. J. F. Rusling in *Modern Aspects of Electrochemistry* (Eds.: B. E. Conway, J. O'M. Bockris), Plenum Press, New York, 1994, pp. 49–104, No. 26.
6. J. F. Rusling, D.-L. Zhou, *J. Electroanal. Chem.* **1997**, 439, 89–96.
7. J. F. Rusling in *Reactions and Synthesis in Surfactant Systems* (Eds.: J. Texter), Marcel Dekker, New York, 2001; in press.
8. S. Friberg, *Adv. Colloid Interface Sci.* **1990**, 32, 167–182.
9. R. A. Mackay, *Colloids Surf.* **1994**, 82, 1–23.
10. C. Tanford, *The Hydrophobic Effect*, 2nd ed., John Wiley & Sons, New York, 1980.
11. J. Israelachvili, *Intermolecular and Surface Forces*, 2nd ed., Academic Press, San Diego, Calif., 1992.
12. D. F. Evans, D. J. Mitchell, B. W. Ninham, *J. Phys. Chem.* **1986**, 90, 2817–2825.
13. K. Kalyanasundaram, *Photochemistry in Microheterogeneous Systems*, Academic Press, New York, 1987.
14. J. F. Rusling, *Colloids Surf.* **1997**, 123–124, 81–88.
15. J. H. Harwell, J. C. Hoskins, R. S. Schecter et al., *Langmuir* **1985**, 1, 251.
16. M. A. Yeskie, J. H. Harwell, *J. Phys. Chem.* **1988**, 92, 2346.
17. P. Chandar, P. Somasundaran, N. Turro, *J. Coll. Interface Sci.* **1987**, 117, 31.
18. J. F. Scamehorn, R. S. Schecter, W. H. Wade, *J. Colloid Interface Sci.* **1982**, 85, 463.
19. S. Manne, H. E. Gaub, *Science* **1995**, 270, 1480, 1481.
20. S. Manne, J. P. Cleveland, H. E. Gaub et al., *Langmuir* **1994**, 10, 4409.
21. E. J. Wanless, W. A. Ducker, *J. Phys. Chem.* **1996**, 100, 3207.
22. T. C. Franklin, S. Mathew in *Surfactants in Solution* (Eds.: K. L. Mittall), Plenum Publishing, New York, 1989, pp. 267–286, Vol. 10.
23. N. Shinozuka, S. Hayano in *Solution Chemistry of Surfactants* (Eds.: K. L. Mittall), Plenum Publishing, New York, 1979, pp. 599–623, Vol. 2.
24. A. J. Bard, L. R. Faulkner, *Electrochemical Methods*, John Wiley & Sons, New York, 1980.

25. M. Fleishmann, S. Pons, D. R. Rolison, P. P. Schmidt, *Ultramicroelectrodes*, Datatech, North Carolina, 1987.
26. J. F. Rusling, T. F. Kumosinski, *Nonlinear Computer Modeling of Chemical and Biochemical Data*, Academic Press, San Diego, 1996.
27. A. Owlia, Z. Wang, J. F. Rusling, *J. Am. Chem. Soc.* **1989**, *111*, 5091–5098.
28. Y. Ohsawa, Y. Shimazaki, S. Aoyagui, *J. Electroanal. Chem.* **1980**, *114*, 235.
29. Y. Ohsawa, S. Aoyagui, *J. Electroanal. Chem.* **1982**, *136*, 353.
30. J. F. Rusling, *Acc. Chem. Res.* **1991**, *24*, 75–81.
31. A. P. Abbott, C. L. Miaw, J. F. Rusling, *J. Electroanal. Chem.* **1992**, *327*, 31–46.
32. A. P. Abbott, G. Gounili, J. M. Bobbitt et al., *J. Phys. Chem.* **96**, 11 091–11 095.
33. G. Gounili, J. M. Bobbitt, J. F. Rusling, *Langmuir* **1995**, *11*, 2800–2805.
34. X. Zu, J. F. Rusling, *Langmuir* **1997**, *13*, 3693–3699.
35. E. Garcia, S. Song, L. E. Oppenheimer et al., *Langmuir* **1993**, *9*, 2782.
36. E. Garcia, J. Texter, *J. Colloid Interface Sci.* **1994**, *162*, 262.
37. B. Antalek, A. J. Williams, E. Garcia et al., *Langmuir* **1994**, *10*, 4459.
38. A. J. Fry, *Synthetic Organic Electrochemistry*, 2nd ed., Wiley, New York, 1989.
39. G. L. McIntire, D. M. Chiappardi, R. L. Casselberry et al., *J. Phys. Chem.* **1982**, *86*, 2632.
40. H. Carrero, J. Gao, J. F. Rusling et al., *Electrochem. Acta* **1999**, *45*, 503–512.
41. N. J. Bunce, S. G. Merica, J. Lipkowski, *Chemosphere* **1997**, *35*, 2719–2726.
42. S. G. Merica, C. E. Banceu, W. Jedral et al., *Environ. Sci. Technol.* **1998**, *32*, 1509–1514.
43. D. Pletcher, F. C. Walsh, *Industrial Electrochemistry*, 2nd ed., Blackie Academic, London, 1993.
44. M. R. Moncelli, F. Pergola, G. Aloisi et al., *J. Electroanal. Chem.* **1983**, *172*, 233.
45. R. A. Mackay, J. Texter, (Eds.), *Electrochemistry in Colloids and Dispersions*, VCH Publishers, New York, 1992.
46. S. Zhang, J. F. Rusling, *Environ. Sci. Technol.* **1993**, *27*, 1375–1380.
47. J. F. Rusling, C. J. Campbell in *Encyclopedia of Surface and Colloid Science* (Ed.: A. Hubbard), Marcel Dekker, New York, 2002, 4143–4161.
48. H. S. O. Chan, L. M. Gan, C. H. Chow et al., *J. Mater. Chem.* **1993**, *3*, 1109–1115.
49. A. Manna, K. Bandyopadhyay, K. Vijayamohan et al., *Langmuir* **1998**, *14*, 84–90.
50. D. A. Kaplin, S. Qutubuddin, *Synth. Met.* **1994**, *63*, 187–194.
51. E. Garcia, L. E. Oppenheimer, J. Texter in *Electrochemistry of Colloids and Dispersions* (Eds.: R. A. Mackay, J. Texter), VCH Publishers, New York, 1992.
52. E. Garcia, S. Song, L. E. Oppenheimer et al., *Colloids Surf., A* **1995**, *94*, 131–136.
53. J. P. Zelina, J. F. Rusling in *Environmental Analysis and Remediation* (Eds.: R. A. Meyers), John Wiley & Sons, New York, 1998, pp. 1567–1583.
54. E. Couture, J. F. Rusling, S. Zhang, *Trans. Inst. Chem. Eng. (U.K.)* **1992**, *70*:B, 153–157.
55. S. Zhang, J. F. Rusling, *Environ. Sci. Technol.* **1995**, *29*, 1195–1199.
56. J. F. Rusling, S. Schweizer, S. Zhang et al., *Colloids Surf.* **1994**, *88*, 41–49.
57. S. Schweizer, Q. Huang, J. F. Rusling, *Chemosphere* **1994**, *28*, 961–970.
58. D.-L. Zhou, J. Gao, J. F. Rusling, *J. Am. Chem. Soc.* **1995**, *117*, 1127–1134.
59. D.-L. Zhou, H. Carrero, J. F. Rusling, *Langmuir* **1996**, *12*, 3067–3074.
60. D.-L. Zhou, C. K. Njue, J. F. Rusling, *J. Am. Chem. Soc.* **1999**, *121*, 2909–2914.
61. C. K. Njue, J. F. Rusling, *J. Am. Chem. Soc.* **2000**, *122*, 6459–6463.
62. J. Gao, J. F. Rusling, D.-L. Zhou, *J. Org. Chem.* **1996**, *61*, 5972–5977.
63. J. Gao, C. K. Njue, J. K. N. Mbindyo et al., *J. Electroanal. Chem.* **1999**, *464/1*, 31–38.
64. J. Gao, J. F. Rusling, *J. Org. Chem.* **1998**, *63*, 218, 219.
65. C. J. Campbell, J. F. Rusling, *Langmuir* **1999**, *15*, 7416, 7417.



## 5.1 Electrocatalysis

*Enrique Herrero, Juan M. Feliu, Antonio Aldaz  
Universidad de Alicante, Alicante, Spain*

### 5.1.1

#### Introduction: Concept of Electrocatalysis and Electrocatalyst

The concept of a catalyst is quite clear in chemistry. It was first defined by Ostwald in the nineteenth century as a substance that only modifies the velocity of a chemical reaction without suffering any chemical change in the process. This definition is based on a comparison between the rates of the reaction in the presence and in the absence of the catalyst. Two different types of catalysis can be defined: homogeneous catalysis, in which the catalyst and all the species involved in the reaction are in the same phase and heterogeneous catalysis, when the catalyst constitutes a different phase than that containing the reaction species and the reaction takes place on the surface of the catalyst. An inaccurate extrapolation of the definition of the catalyst to electrocatalyst would indicate that all the electrode materials are electrocatalyst since the electrode reactions are heterogeneous reactions in which an inert material (the electrode) is always present and normally does not suffer any chemical change in the

process. However, the right definition of an electrocatalyst requires the comparison of rates in the presence and the absence of the electrode material. The problem arises just in the possibility of performing this comparison since, in most cases, there is no homogeneous electrochemical reaction with which to compare.

Although the definition of catalyst cannot be directly extrapolated for that corresponding to electrocatalyst, the concepts underlying the definition can be effectively used. In a catalyzed reaction, there is a specific interaction between the catalyst and some species involved in the chemical reaction. The specific interaction is then the key point in the catalysis definition and, thus, the electrocatalyst can be defined as an electrode material that interacts specifically with some species involved in the reaction and remains unaltered after the reaction. This definition allows a good distinction between electrocatalyzed and non-electrocatalyzed reactions: the existence of specific surface interactions is characteristic of an electrocatalyzed reaction.

It is implicit in the definition of the electrocatalyst that this specific alters the energetics of the reaction path, that is, it changes the activation energy, and thus the velocity of reaction. The lack of experimental or calculated rates for the reaction in absence of an electrocatalyst is then

not necessary to define an electrocatalytic reaction. Moreover, if several electrode materials are used and the reaction rates for a given reaction depends on the electrode material (and/or surface structure), it can be said that these electrodes are acting as a true electrocatalyst with different efficiency. These different reaction rates can only be justified if there is a specific interaction between the electrode and the species. On the other hand, if the reaction is insensitive to the electrode material, these electrodes are not interacting with the reaction species and are not electrocatalysts. When comparing the catalytic activity of several electrodes, the comparisons have to be made either at constant overpotential and measuring the current density (value that is proportional to the reaction rate) or at constant current density and measuring the overpotential. Of course, the final goal is always higher rates at lower overpotentials.

As a first step, it is important to define which reactions are susceptible to be catalyzed. In principle, the reaction rates of any process can be increased. In a heterogeneous process, such as electrode reactions, the diffusion of the active species to the electrode may be the rate-determining step of the whole process. In that case, any improvement in the rate of the electron-transfer step would not produce any change in the overall rate of the process, since the mass-transfer process is still the limiting step. The electrode reaction will behave then as a reversible diffusion-controlled reaction. Whenever the reaction in the actual experimental conditions is not diffusion controlled, it may be interesting to find a better electrocatalyst for it. The criteria for defining a reaction as diffusion controlled depends on the technique employed for the study. According to the technique, several

parameters can be measured. For instance, when using a stationary technique in which the diffusion layer is constant, the limiting diffusion current for any species can be written as

$$j_{\text{lim},i} = k_i c_i^\infty \quad (1)$$

where  $c_i^\infty$  is the bulk concentration of  $i$  and  $k_i$  is the mass-transfer coefficient, which is a function of the diffusion coefficient and can be calculated for the different electrochemical techniques. For a general reaction  $\text{Ox} + ne^- = \text{R}$ , the relationship between the stationary current and the potential is

$$E = E^\circ + \frac{RT}{nF} \ln \frac{k_{\text{R}}}{k_{\text{Ox}}} + \frac{RT}{nF} \ln \frac{(j - j_{\text{lim,Ox}})}{(j_{\text{lim,R}} - j)} \quad (2)$$

Whenever a process studied with a stationary technique follows Eq. (2), the process is mass controlled and improvement in the reaction rates will not increase the overall reaction rate. If not, it may be interesting to find a better electrocatalyst.

Improvement of the reaction rates is not the only attribute sought in an electrocatalyst. Often, a higher selectivity versus any competitive reaction that may take place is also required. For that reason, catalysts given higher reaction rates but lower material yields are normally not used. Thus, a good electrocatalyst is the one that gives high current densities at low overpotential and with high selectivity for the desired product.

When studying the electrocatalytic behavior of a given material, several properties may influence its overall performance: the electronic properties, the surface structure, and the different types of sites present on it, the particle size, surface composition, and so on. The variety of these

properties makes it difficult to understand what the role of the electrocatalyst in a reaction is. This way any interpretation may be proposed. In this short chapter, we will focus on the most fundamentals aspects of the electrocatalysis, that is, how the different properties of a given material relate to its electrocatalytic behavior. In order to understand the fundamentals of electrocatalysis, it is important to limit and control the number of possible variables for a given experiment. Single-crystal metal electrodes are normally used in these studies, since they possess a very well-defined structure and allow to establish a correlation between surface structure and its catalytic activity. For that reason, we will emphasize the results obtained on well-defined metal electrode surfaces. Despite the use of single-crystal electrodes in the last decades, the number of studies is rather limited and only a few systems have been investigated systematically. However, it is worth noting that the results shown here will have to be later applied to the real surfaces employed in more applied processes. Several general articles about electrocatalysis can be found in the literature [1–8].

## 5.1.2

### Electronic Effects in Electrocatalysis

#### 5.1.2.1 Specific Interaction and Transfer Rates

The specific interaction between the electrode material and some of reacting species has to be defined formally by the overlap of the electronic states of the reactant and the electrode material at the transition state. A weak overlap electron-transfer reaction is defined as that in which the energy of the transition state is not affected by the proximity of the reacting species to the electrode. Conversely, in strong overlap

reactions the energy of the transition state is affected greatly by the proximity of the electrode and the reacting species. A strong overlap takes place when specific interaction between the surface and some of the reactant species exists.

These situations are depicted in Fig. 1 for a multistep reaction  $\text{Ox} + ne^- = \text{R}$ . In this figure, A denotes the transition state and P and S, respectively, denote the precursor and successor states that precede and follow the transition state. The full line represents the energetics of the process for a large distance between reactive species and electrode. If the reacting species come closer to the electrode surface and these species have attractive interactions with the electrode surface, the dashed and dotted lines are obtained, where the dotted line represents a stronger overlap than the dashed line. In this simplest model, the transition state corresponds to the same reaction coordinate.

These curves can be related to the inner- and outer-sphere reactions pathways. The full line represents the outer-sphere reaction, whereas the inner-sphere reactions are depicted by the dashed and dotted lines. As can be seen, outer-sphere reactions are always weak overlapping reactions, that is, reactions in which the electrode is not acting as an electrocatalyst. Inner-sphere reactions can be either strong or weak overlap reactions, depending on the properties of the reactant species and electrode material. From a chemical point of view, a chemical bond between the reactant species and the electrode is formed in the strong overlap cases, that is, the reactant species are chemisorbed on the electrode surface.

From a practical point of view, it is important to distinguish between electrocatalyzed and nonelectrocatalyzed reactions. In addition to the criteria given above, in

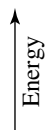


**Fig. 1** Schematic free energy profile scheme for an electron electroreduction. O, oxidized species; R, reduced species; A, transition state; and P and S, the precursor and successor states, respectively, that precede and follow the transition state. (—) for a large distance between the reactive species and the electrode. (----) Energetics of the process in which the reacting species come closer to the electrode surface and these species have attractive interactions with the electrode surface. (· · · · ·) Same as a dashed line but with a stronger overlap.

situ infrared and Raman spectroscopies allow the detection of adsorbed species on the electrochemical interface. These species present vibrational frequencies that depend on the electrode material and that are different than those found for the species in solution, a clear indication that the species are interacting with the electrode surface. In other cases, the detection of intermediate adsorbed species is not possible and indirect methods have to be used to determine if the electrode is acting as an electrocatalyst. Normally, if the reaction rates depend on the electrode

material and its surface structure, it can be said that the electrode is acting as an electrocatalyst. However, different reaction rates on different electrode materials may be the consequence of changes in the specific reactant solvation at the interface or electrostatic double-layer effects, and not a consequence of a strong overlap transfer [9].

In the simplest cases, it is possible to compare rates for homogeneous and heterogeneous electron-transfer reactions. According to the Marcus theory for homogeneous outer-sphere reactions [10],



the reaction rate is given by

$$k_1 = A_1 \exp\left(\frac{-\lambda}{4RT}\right) \quad (3)$$

where  $\lambda$  is the reorganization factor and  $A_1$ , the preexponential factor [10]. Analogously, the reaction rate for heterogeneous reactions is

$$k_2 = A_2 \exp\left(\frac{-\lambda}{2RT}\right) \quad (4)$$

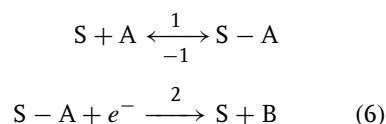
Dividing Eqs. (3 and 4) leads to

$$\frac{k_1}{A_1} = \left(\frac{k_2}{A_2}\right)^{1/2} \quad (5)$$

When the reaction rates for the homogeneous and heterogeneous reaction rates fulfill Eq. (3), it is clear that the reaction is taking place through an outer-sphere mechanism, and the electrode material is not acting as a true electrocatalyst.

### 5.1.2.2 Adsorption and Electrocatalysis

As stated previously, adsorption of some species involved in the electrochemical reaction is the key parameter to consider an electrode material as an electrocatalyst. Therefore, it is important to relate the activity of such a material with its adsorption properties. Let us consider first the simplest reaction  $A + e^- \rightarrow B$ , in which A is the only species adsorbed on the catalyst, and try to relate the reaction rate to the adsorption properties of the surface S. A simple reaction mechanism is



where S stands for an adsorption site. Assuming that the adsorption

step (Reaction (1)) takes place through Langmuir kinetics and  $k_1, k_{-1} > k_2$  and using the steady state approximation, the reaction rate  $\nu$  can be written as

$$\nu = \frac{k_2 K_1 C_A}{1 + K_1 C_A} \quad (7)$$

where  $K_1$  is the equilibrium constant for Reaction (1), and  $k_2$  the rate constant for step 2. Now, it is desirable to express both the constants as a function of the Gibbs energy of adsorption ( $\Delta G_1^\circ$ ).  $K_1$  can be readily written as

$$K_1 = \exp\left(-\frac{\Delta G_1^\circ}{RT}\right) \quad (8)$$

$k_2$  can be expressed as a function of the activation energy ( $E_{A2}$ ) and the electrode potential,  $E$ :

$$\begin{aligned} k_2 &= k_2^\circ \exp\left(-\frac{E_{A2}}{RT}\right) \\ &\times \exp\left(-\frac{\beta_2 F(E - E^\circ)}{RT}\right) \end{aligned} \quad (9)$$

where  $\beta$  is the symmetry factor for the electron-transfer step and  $E^\circ$  is the standard potential for the overall reaction. For a given series of homologous reactions (in this case, the reaction  $S - A + e^- \rightarrow B$  using different surfaces), the activation energy can be written as a function of the Gibbs energy change of the reaction using the Brønsted relationship [11]:

$$E_A = E_A^\circ - \gamma \Delta G^\circ \quad (10)$$

where  $\gamma$  is the transfer coefficient (generally close to 0.5) and  $E_A^\circ$  is the intrinsic activation energy for the surface in which the Gibbs energy of the reaction of the adsorbed species is zero. Substituting Eq. (10) into Eq. (9), the following equation can be obtained:

$$\begin{aligned}
k_2 &= k_2^\circ \exp\left(-\frac{E_{A2}}{RT}\right) \\
&\times \exp\left(-\frac{\beta_2 F(E - E^\circ)}{RT}\right) \\
&= k_2^\circ \exp\left(-\frac{E_{A2}^\circ + \gamma_2 \Delta G_2^\circ}{RT}\right) \\
&\times \exp\left(-\frac{\beta_2 F(E - E^\circ)}{RT}\right) \quad (11)
\end{aligned}$$

The Gibbs energy of the second step ( $\Delta G_2^\circ$ ) of the overall process is related to the overall Gibbs energy ( $\Delta G_T^\circ$ ) and the Gibbs energy of adsorption ( $\Delta G_1^\circ$ ) according to

$$\Delta G_2^\circ = \Delta G_T^\circ - \Delta G_1^\circ \quad (12)$$

where  $\Delta G_1^\circ$  depends on the electrode material. Substituting Eq. (12) into Eq. (11)

$$\begin{aligned}
k_2 &= k_2^\circ \exp\left(-\frac{E_{A2}^\circ + \gamma_2 \Delta G_T^\circ - \gamma_2 \Delta G_1^\circ}{RT}\right) \\
&\times \exp\left(-\frac{\beta_2 F(E - E^\circ)}{RT}\right) \quad (13)
\end{aligned}$$

and grouping all the constant terms for the series of homologous reactions ( $\Delta G_T^\circ$  and  $E_{A2}^\circ$ ) into  $k_2^a$ , the following expression can be obtained:

$$\begin{aligned}
k_2 &= k_2^a \exp\left(\frac{\gamma_2 \Delta G_1^\circ}{RT}\right) \\
&\times \exp\left(-\frac{\beta_2 F(E - E^\circ)}{RT}\right) \quad (14)
\end{aligned}$$

Substituting Eqs. (8 and 14) into Eq. (7) yields

$$\begin{aligned}
\nu &= \frac{k_2^a \exp\left(-\frac{(1 - \gamma_2) \Delta G_1^\circ}{RT}\right)}{1 + \exp\left(-\frac{\Delta G_1^\circ}{RT}\right) C_A} \\
&\times \exp\left(-\frac{\beta F(E - E^\circ)}{RT}\right) C_A \quad (15)
\end{aligned}$$

As can be seen, the reaction rate  $\nu$  is a function of the Gibbs energy of adsorption, the electrode potential, and the concentration of A. In fact, the reaction rate can be divided into two separate terms: one containing the dependence of  $\Delta G_1^\circ$  and  $C_A$  and the other one that depends on the electrode potential. If the catalytic activity of several surfaces is compared at constant potential, the reaction rate will depend only on  $\Delta G_1^\circ$  and  $C_A$ . In Fig. 2, the term

$$k_2^\neq = \frac{k_2^a \exp\left(-\frac{(1 - \gamma_2) \Delta G_1^\circ}{RT}\right) C_A}{1 + \exp\left(-\frac{\Delta G_1^\circ}{RT}\right) C_A} \quad (16)$$

has been plotted versus the Gibbs energy of adsorption. It follows that  $k_2^\neq$ , and obviously the reaction rate, increases with the Gibbs energy of adsorption, reaches a maximum, and then decreases, giving a curve known as the volcano curve. This kind of curve is very common in catalyzed processes, not only in the simple process that has been considered here, since most reaction kinetics can be described by mathematical expressions similar to Eq. (14), and therefore have the same qualitative behavior. This behavior demonstrates that adsorption increases reaction rates provided that its energy is not too high. In such case, the adsorbed intermediate is too stable to react on to the products. This idea is called, in heterogeneous catalysis, the Principle of Sabatier [12]. The comparisons in electrochemistry are performed using the exchange current density ( $j_0$ ) instead of the reaction rate. It can be easily demonstrated that  $j_0$  follows the same dependence on  $\Delta G_1^\circ$  that the reaction rate, and therefore, volcano curves are obtained. In fact, such curves have been obtained for several electrochemical processes, such as hydrogen evolution [13], ethylene oxidation [14],

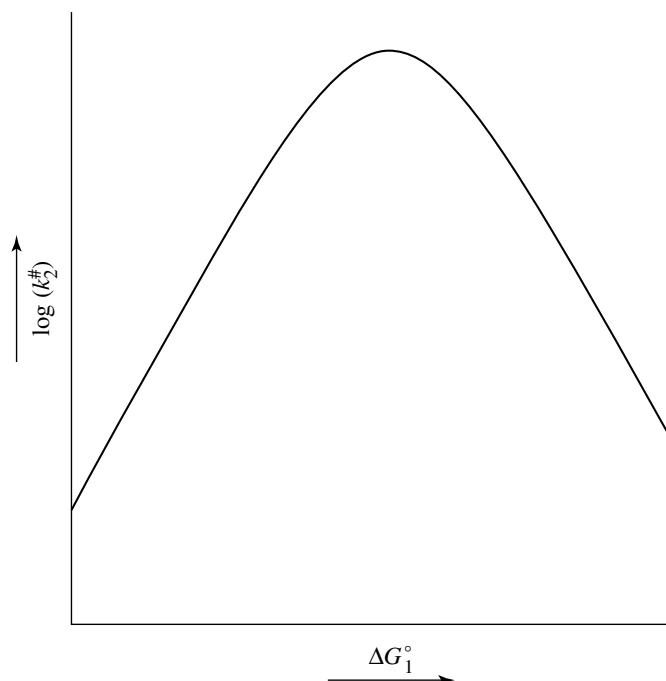
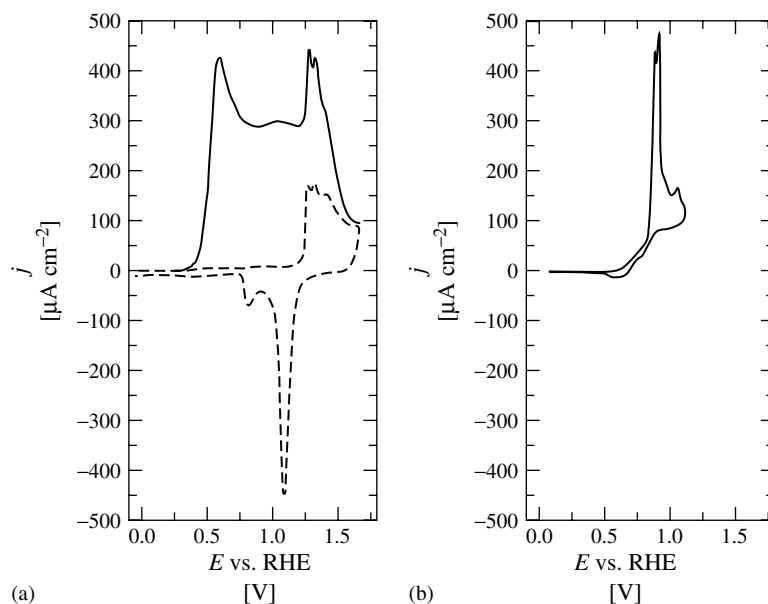


Fig. 2 Generalized representation of  $k_2^\ddagger$  versus  $\Delta G_1^\circ$ .

formic acid oxidation [15, 16], and oxygen reduction [17]. In all these cases, the reactions proceed through mechanisms much more complicated than those studied here and for instance, the nature of the relevant adsorbed species for hydrogen evolution is unclear [18]. An additional complication of the electrochemical processes is the possible dependence of  $\Delta G_1^\circ$  with the applied potential. Even in the simplest case, this dependence arises either from the specific interaction of the reacting species with the electrode material, or from the specific interaction of any competing species (water, anions) present in solution. In fact, the concept of the adsorption isotherm of a molecule in solution is more complicated than that in the gas phase and has to take into account the presence of other species. Additional comments on this problem will be made in the next paragraph.

In other processes that involve two adsorbed species that react (for instance, Langmuir–Hinselwood mechanisms), the dependence of the reaction rate with the adsorption energy is more complicated since two adsorption energies are involved. For this case, the ideal electrocatalyst is the one that has intermediate adsorption energy for both adsorbed species. If the chemistry of the two adsorbed species is different, which is normally the case, it is difficult to find a surface that has the right combination of adsorption energies for both species.

CO oxidation (among other oxidation reactions of interest in electrocatalysis) belongs to this type of reactions. It has been normally proposed that adsorbed CO reacts through a Langmuir–Hinselwood mechanism with adsorbed OH from water dissociation. Therefore, this reaction



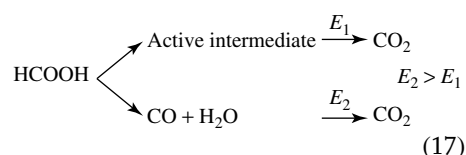
**Fig. 3** Voltammetric profiles of CO oxidation on CO-saturated 0.1 M HClO<sub>4</sub> solutions. (a) Au(110) electrode. The dashed line corresponds to the voltammetric profile obtained in the supporting electrolyte alone. Scan rate 100 mV cm<sup>-1</sup>. (Reproduced with permission from Ref. [24]). (b) Pt(111) electrode. Scan rate 20 mV cm<sup>-1</sup>. (Reproduced with permission from Ref. [25].)

requires a metal that adsorbs OH and CO with moderate energies. We can then compare, in this case, the performance of platinum and gold for the oxidation. To assess the interactions between the CO molecule and the electrode surface, in situ Fourier Transform Infrared (FTIR) spectroscopy has been used. For platinum electrodes, strong absorption bands from adsorbed CO have been detected [19–21], even after CO has been eliminated from solution, whereas, in the case of gold, very weak absorption bands are only observed when CO is present in solution [22, 23]. Therefore, it can be concluded that CO is strongly adsorbed on the platinum surface in comparison to gold surfaces. Although the adsorption energy for OH on both surfaces is different, being lower for the more noble metal (gold), the main factor

in the differences of both electrocatalytic activities is the CO-adsorption energies. In spite of the fact that the catalytic performance of these metals towards CO oxidation is far from optimum ( $\Delta G$  values for the reaction indicates that solution CO should be oxidized at 0.0 V), the oxidation of CO from solution on gold takes place at less positive potentials than on platinum (Fig. 3) [24, 25]. The low activity of the platinum surface is related to the strong adsorption of CO, which hinders its oxidation. In this case, the strong adsorption not only stabilizes the adsorbed CO but also prevents OH from adsorption since it completely covers the platinum surface.

Other reaction mechanisms present additional complications. That is the case of the parallel-path mechanisms,

especially when an intermediate is strongly adsorbed on the surface poisoning the active sites and thus preventing further reaction of the molecule. These parallel-path mechanisms are often found for the oxidation of organic molecules in which the poisoning intermediate is normally the adsorbed CO. The simplest parallel-path mechanism is that of the oxidation of formic acid. Schematically, it can be written that



The simplicity of this reaction scheme makes formic acid oxidation a model reaction in electrocatalysis. For these reactions, it is important to assess the catalytic activity of the surface for both paths (specially the determination of the reaction path through the active intermediate) in order to investigate the catalytic effects of a given surface. The problem is the reciprocal interference of the paths that makes difficult the evaluation of the reaction rates of both paths separately. The reaction rate for the active intermediate path can be obtained only in the absence of surface poison. In order to achieve that condition, several strategies have been used. The simplest strategy is to measure the current density. After cleaning the surface of the poison (that normally can be achieved at potentials above 0.75 V), the electrode potential is then stepped to a lower value at which the oxidation of the molecule takes place. As the electrode surface at time zero (just after the step) is free from the poison, the current extrapolated at  $t = 0$  is the reaction rate through the active intermediate path. This method has been used for formic acid and methanol [26, 27]. This strategy has

also been used in combination with a linear potential sweep in the technique known as pulsed voltammetry [28, 29] (Fig. 4).

Another important characteristic of these reactions is the different behavior of the molecules when adsorbed on electrochemical and ultrahigh vacuum (UHV) environments. In UHV, formic acid dissociates on a platinum surface to yield only  $\text{H}_2$  and  $\text{CO}_2$ , and CO is not a reaction intermediate [30, 31]. The differences can be attributed to the presence of water molecules on the electrochemical environments. The presence of water, a polar molecule, guides the adsorption process of the reacting molecule. Methanol adsorption on Pt(111) surfaces provides a clear example of such changes induced by the presence of water (or a solvent). In UHV, methanol adsorbs on the Pt(111) surface through the oxygen atom after losing the hydrogen bonded to it. In electrochemical environments, the first step in the methanol oxidation is the breaking of one out of the three C–H bonds, and the molecule adsorbs on the surface with the OH group pointing outwards [26]. The polar nature of the OH group and its interactions with the water molecule (also polar) prevent the adsorption through the oxygen group.

### 5.1.3

#### Surface Structure Effects

##### 5.1.3.1 Role of the Surface Symmetry in Electrocatalysis

It is clear that adsorption processes are structure sensitive, that is, the adsorption of species depends on the structure of the surface site. This change in structure may involve several changes: first, the surface will have a different energy, as revealed by the dependence of the work function with the surface

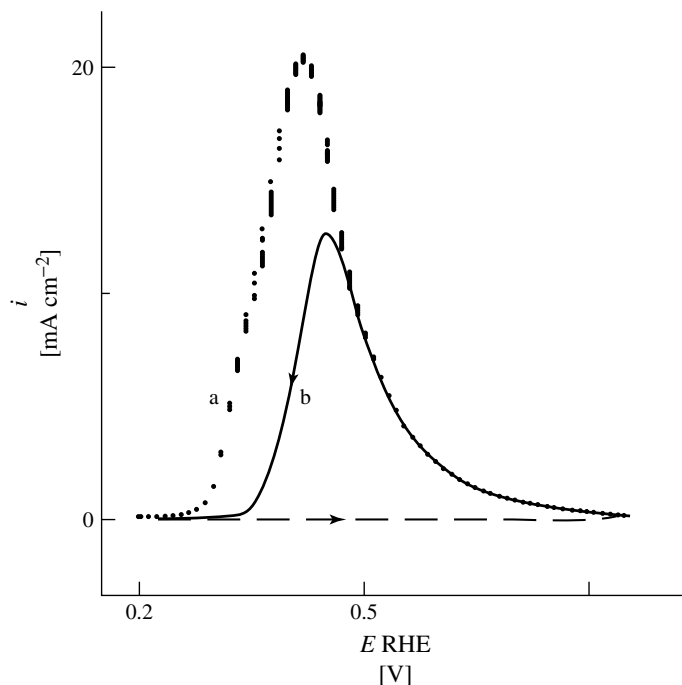


**Fig. 4** (a) Pulsed voltammogram; and (b) stationary voltammogram for a Pt(100) electrode in 0.5 M  $\text{H}_2\text{SO}_4$  + 0.1 M  $\text{HCOOH}$  solution (—), pulsed voltammogram (----). Pulse voltammetry conditions: sampling window time: 0.30 s; poison oxidation pulse length: 0.360 s; potential of pulse: 0.95 V; time between the end of the poison oxidation pulse and the opening of the sampling window: 0.015 s. Sweep rate:  $10 \text{ mV s}^{-1}$ . (Reproduced with permission from Ref. [28].)

structure. As generally accepted, there is a linear relationship between the work function and the potential of zero charge (PZC) of the electrode [32, 33], which in turn plays an important role in the adsorption process of the different species and in the properties of the double layer. In this way, the changes in the surface energy plays a double role in the electrocatalysis, one linked to the changes in the adsorption energy of the molecules and the second role related to the changes in the double-layer structure. The interfacial structure has been proved to affect the oxidation/reduction of the charges species at potentials close to the

PZC, altering the typical Butler–Volmer kinetics [34].

Second, the changes in surface geometry will lead to changes in the geometry of the adsorption sites and the distance between them. The effect of the changes in the site geometry can be studied easily using low-index single-crystal electrodes, since they have a defined surface structure and few different types of sites. For instance, (111) surfaces of face centered cubic (fcc) metals have on top, bridged-bonded and two different types of three hollow sites (tetrahedral and octahedral), whereas (100) surfaces have on top, bridged-bonded and four hollow sites. If the most favorable site

for the adsorption of a given species is the hollow sites, there will be significant differences in the energy of adsorption in the (111) and (100) surfaces, owing to the different geometry of the sites, and thus an effect in the electrocatalysis of the species will be observed. In other cases, the species may bond to the surface through more than one surface site. In this case, the right surface requires not only the right adsorption sites, but also these sites have to be at a distance compatible with the geometry of the adsorbing molecule.

In most cases, it is almost impossible to decouple the effects of the surface energy changes and the changes in the site geometry. Moreover, in electrochemistry, adsorption is always a competitive process since there are other species, like the solvent or the supporting electrolyte, which can be adsorbed on the electrode surface apart from the electroactive species. In some cases, these competing adsorption processes govern the adsorption of the electrocatalytically active species. Owing to the intrinsic difficulty in assigning the changes of the adsorption to any specific property of the surface, we will term the effect related to the surface properties as surface structure effects. It is clear that the interpretation becomes more difficult when polycrystalline materials are to be considered.

As aforementioned, surface structure effects on adsorption are well known in electrochemistry. A typical example is CO adsorption on low-index single-crystal platinum surfaces. For CO, three different adsorption geometries exist: on-top, bridge-bonded, and multibonded. The relative population of each adsorption species and the surface structure of adsorbate layer are dependent on the surface structure and metal (see for instance Refs. [19–21]

(Fig. 5)). Moreover, multibonded CO, in which CO is coordinated to three platinum atoms, is only observed on the Pt(111) surface. Additionally, the formation of multibonded CO not only requires a three-fold symmetry surface but also long-range order [35]. Experiments performed using stepped surfaces show that the multibonded CO does not appear on surfaces having short terraces with (111) symmetry. This effect suggests that long-range order domains will have a different reactivity. Additionally, the IR frequencies for on-top CO are also dependent on the surface symmetry [19–21]. Changes in the IR frequency are associated to changes in the bonding energy of the CO molecule to the surface. If the adsorption energy of the surface is different for the same adsorption site in surfaces with different geometry, the energy of the surface is playing a role in the adsorption process of CO. This example clearly illustrates the interrelation between the different properties (symmetry, energy, etc.) of a given surface regarding its adsorption properties and the difficulty to assign the changes in its adsorption properties to a given structural factor.

The changes in the adsorption properties are not only restricted to changes in the binding geometry for the adsorption or surface structure. When the species has several groups that are liable to bond to the surface, changes in the surface structure may lead to changes in the binding group. That is the case for urea adsorbed on platinum single-crystal electrodes. On Pt(100), urea is always bonded to the surface through the two nitrogen atoms of the molecule [36]. On the other hand, the adsorption is coverage sensitive on Pt(111). For low urea coverages, the adsorption takes place through only one nitrogen atom, whereas for high urea coverages, the

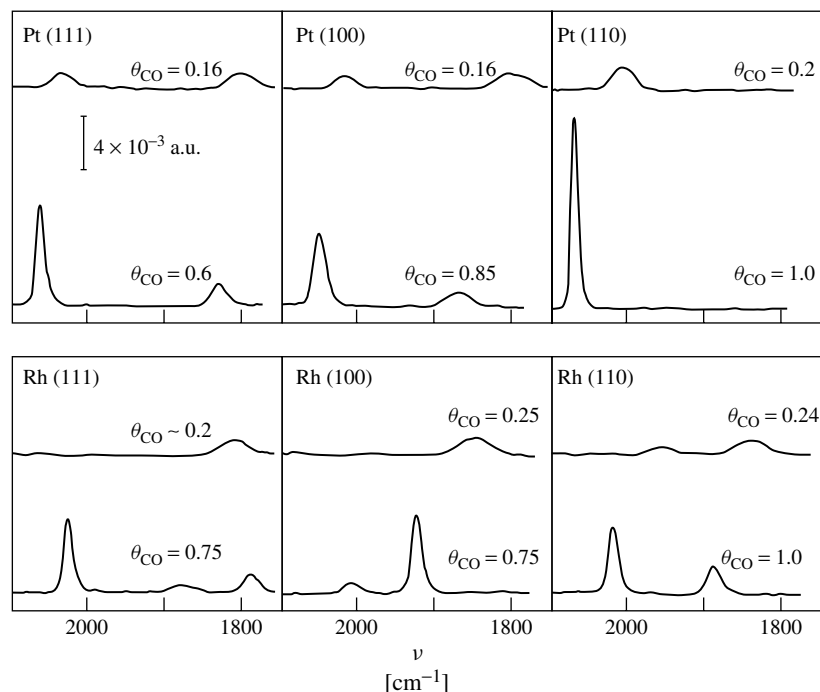
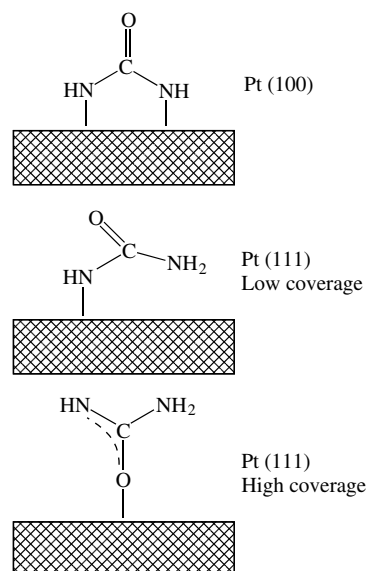


**Fig. 5** FTIR spectra for CO irreversibly adsorbed on platinum and rhodium low-index surfaces in 0.1 M HClO<sub>4</sub> at 0.25 V versus SCE at saturation and low CO coverages. The reference spectrum was acquired at 0.45–0.5 V after CO oxidation. (Reproduced with permission from Ref. [19].)



adsorption is through the oxygen of the carbonyl group [37] (Fig. 6).

The identification of the different adsorbed species and its relation with the catalytic activity of the surface is much more troublesome. The problem generally arises from the short life of the adsorbed intermediates, which makes difficult its detection with the usual techniques. In spite of this fact, the effects of the surface structure on electrocatalysis are beginning to be well documented. The typical example is again formic acid oxidation

**Fig. 6** Proposed adsorption modes of urea on Pt(111) at low and high urea coverages and on Pt(100). (Reproduced with permission from Ref. [37].)



on platinum single-crystal electrodes. The effect of the surface structure affects both the direct and the poisoning paths for the formic acid oxidation [38]. Among the three basal planes, the lowest poisoning rate corresponds to Pt(111), which also shows the lower catalytic activity [39, 40]. When comparing the intrinsic activity of Pt(111) and Pt(100) in sulfuric acid medium, it can be seen that the current densities for the Pt(100) surface at 0.5 V versus RHE are 10 times higher than those obtained on Pt(111) [28, 29]. Similar behavior is obtained for methanol on platinum electrodes (Table 1) [27]. These results clearly indicate that the reactivity of the molecule depends on the electrode surface structure.

Methanol oxidation also illustrates the effect of the competing adsorption on the electrocatalysis. The presence of a strong adsorbing anion on the supporting electrolyte hinders the oxidation of the molecule (Fig. 7). Thus, the current densities for methanol oxidation in phosphoric acid solution are lower than those obtained in sulfuric acid, being the highest values those obtained in perchloric acid solution [26, 27]. This is because the oxidation of methanol molecules takes place at potentials in which the anions are adsorbed on the electrode surface. Therefore,

the first step in the adsorption process of the species of interest is the replacement of the adsorbed anions. The stronger the anion adsorption, the more difficult the displacement of the anion by the incoming molecule is, resulting in a lower current. The voltammetric characteristics for formic acid or methanol oxidation remain essentially the same, but lower currents are obtained when anions are strongly adsorbed on the electrode surface.

Until this point, the use of low-index crystal surface electrodes has allowed to get insight into the electrocatalytic phenomena. However, real surfaces are far from being perfect and comprise several types of sites, including step and kink sites, and the size of the ordered domains is rather limited. For that reason, it is also important to rationalize the effect of such sites in the reaction, using stepped and kinked surfaces. Because of its complexity, there are few examples of these effects in the literature, but the research on the subject is expected to become more and more important.

The presence of defects in a given surface structure may also play an important role in the electrocatalytic process. Normally, long-range ordered domains are separated from each other by step or kink sites. The substrate atoms that belong to kink or step sites have special adsorption properties since they have a lower coordination number, that is, they have a lower number of nearest neighbor substrate atoms than the surface atoms in a well-ordered domain. These properties may result in an increased catalytic activity. In order to model the real surfaces, stepped and kinked surfaces are used since they have a well-defined distribution of these sites and they can be prepared reproducibly.

A clear example of the role of defect sites in electrocatalysis can be found in

**Tab. 1** Maximum voltammetric peak current densities ( $j_{CV}$ ), and instantaneous current densities at 0.2 V ( $j_{E=0.2}$ ) and 0.4 V ( $j_{E=0.4}$ ) (vs. Ag/AgCl) for methanol oxidation in 0.1 M  $H_2SO_4$  + 0.1 M  $HClO_4$  for Pt(111), Pt(110), and Pt(100) electrodes. Data taken from Ref. [27]

	Pt(111)	Pt(110)	Pt(100)
$j_{CV}$ (mA cm <sup>-2</sup> )	0.74	24.5	4.2
$j_{E=0.2}$ (mA cm <sup>-2</sup> )	0.57	6.5	5.2
$j_{E=0.4}$ (mA cm <sup>-2</sup> )	4.8	17.0	6.1

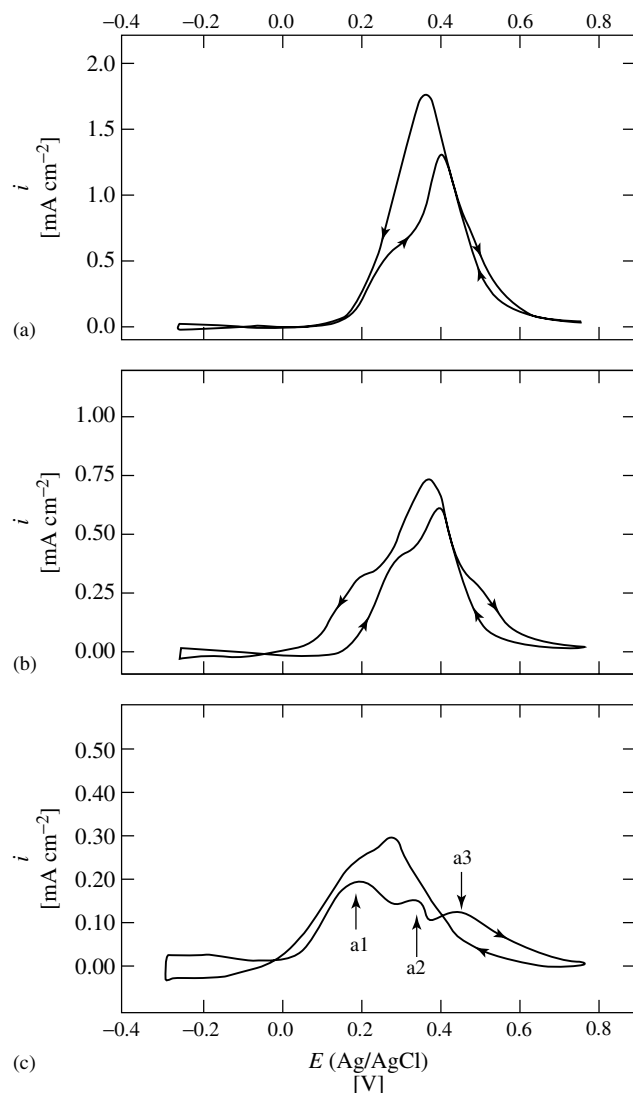


**Fig. 7** Voltammetric profiles for the Pt(111) electrode in: (a) 0.1 M  $\text{HClO}_4$  + 0.2 M  $\text{CH}_3\text{CH}_2\text{OH}$ ; (b) 0.1 M  $\text{H}_2\text{SO}_4$  + 0.2 M  $\text{CH}_3\text{CH}_2\text{OH}$ ; and (c) 0.1 M  $\text{H}_3\text{PO}_4$  + 0.2 M  $\text{CH}_3\text{CH}_2\text{OH}$ . Scan rate  $50 \text{ mV s}^{-1}$ . (Reproduced with permission from Ref. [27].)

the oxidation of adsorbed CO on Rh(111) electrodes [41]. For well-ordered surfaces, the stripping of the adsorbed CO and the recovery of the clean surface is quite difficult. However, this process is considerably easier in a stepped surface.

This fact clearly indicates the necessity of defect sites in the surface structure of the Rh(111) surface in order to oxidize the adsorbed layer.

Glucose oxidation is a clear example of the effects of the domain size of the

electrode in the electrocatalysis [42–45]. This molecule is relatively big and has several groups that can be attached to the electrode surface. Consequently, it prefers relatively flat areas to adsorb and oxidize. For this reason, the maximum catalytic activity is found for the Pt(111) [42–44] and Pt(100) electrodes [44]. If stepped surfaces are used, the oxidation current is proportional to the terrace size [44], a clear indication of the influence of the domain sizes in the reaction (Fig. 8). Moreover, an additional oxidation process at low potentials appears that corresponds to the oxidation on the step sites at which glucose adsorption would be more reactive.

### 5.1.3.2 Chiral Surfaces

As aforementioned, defect sites (kink sites) may have an important role in electrocatalysis. Kink sites have an

additional property – they are chiral. This means that it is possible to prepare two nonoverlapping specular surfaces having the same type of kink site. Analogously to the chiral molecules, the kink sites have been termed as *R* or *S* depending on its symmetry [46, 47]. If an enantiomer interacts with a chiral site, the reactivity can be dependent on the symmetry of the chiral site, leading to the formation of different reaction products and/or to different reaction rates. Therefore, chiral surfaces exhibit stereoselective activity.

In order to observe the stereoselective behavior of the surface, the kink site and a chiral center of the enantiomeric molecule have to be involved in the adsorption process that yields the reaction products. Moreover, owing to the symmetry rules, crossed activity has to be observed, that is, the behavior of an *R* surface with an *S*

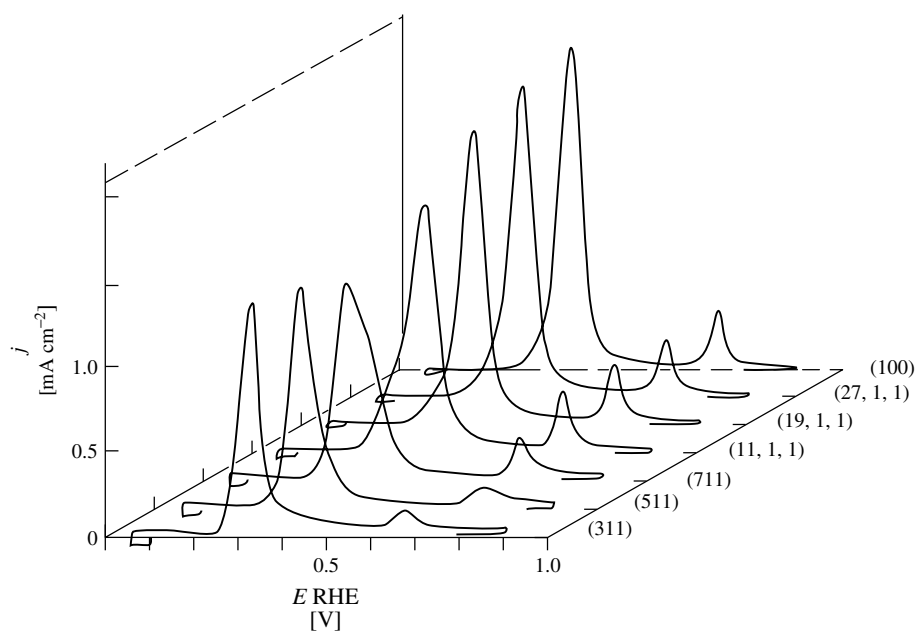


**Fig. 8** Voltammetric profiles for the oxidation of 0.01 M glucose in 0.1 M HClO<sub>4</sub> on different Pt(s):[*n*(100) × (111)] stepped surfaces. Scan rate 50 mV s<sup>−1</sup>. (Reproduced with permission from Ref. [44].)

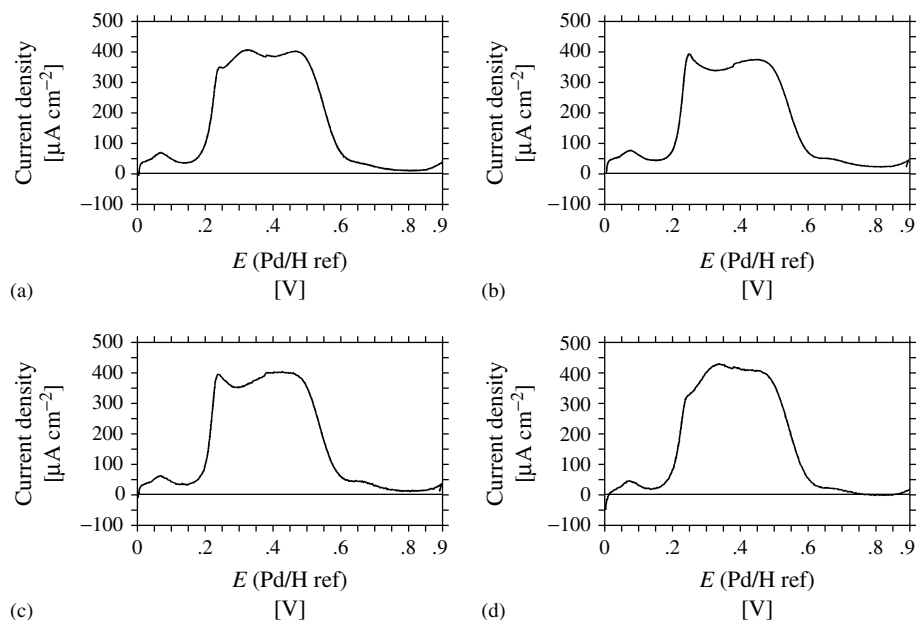


**Fig. 9** Voltammograms for glucose oxidation on the two chiral Pt(643) electrodes in 0.05 M  $\text{H}_2\text{SO}_4$  supporting electrolyte. (a)  $\text{Pt}(643)^S$  electrode in 5 mM D-glucose; (b)  $\text{Pt}(643)^S$  electrode in 5 mM L-glucose; (c)  $\text{Pt}(643)^R$  electrode in 5 mM D-glucose; and (d)  $\text{Pt}(643)^R$  electrode in 5 mM L-glucose. Scan rate:  $50 \text{ mV s}^{-1}$ . (Reproduced with permission from Ref. [47].)

molecule should be the same as that of an S surface with an R molecule. Such behavior has been observed with L- and D-glucose and the R and S Pt(643) surfaces [47, 48]. As can be seen in Fig. 9, the voltammetric profile for the oxidation of the molecule depends on the surface symmetry and the glucose isomer. The main difference is the apparition of a new peak at 0.31 V in the S–D and R–L combinations, which is absent in the other two cases. The current density at 0.31 V increases with the kink density, thus proving its relationship with the site symmetry.

#### 5.1.4

#### Surface Composition Effects

In many cases, the most active metals available have only a limited catalytic

activity for the reaction considered. In those cases, an alternative is to try to modify the surface properties of the metal in order to increase its activity. In most cases, this can be achieved by depositing a foreign ad-atom on the surface. This particular case can be compared to alloys but it should be remembered that bulk properties are different, that is, the bulk phase is a pure metal and only the surface has a different composition in the case of a modified electrode. It is assumed that the foreign ad-atom will maintain the surface structure of the substrate, leading to the growth of a well-defined surface layer. The new species on the surface can affect the desired reaction in three different ways. (1) It may change the electronic properties of the surface in such a way that the adsorption of the reactant

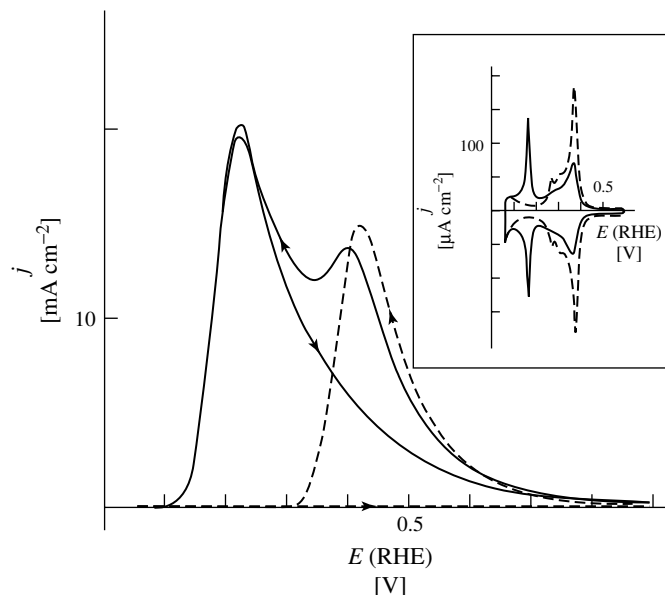


**Fig. 10** Quasi-stationary voltammetric profiles of Pt(100) (-----) and Pd–Pt(100) ( $\theta_{\text{Pd}} = 0.32$ ) (—) electrodes in 0.25 M HCOOH + 0.5 M H<sub>2</sub>SO<sub>4</sub> solution. Inset: blank voltammograms of the same electrodes in 0.5 M H<sub>2</sub>SO<sub>4</sub> solution. Scan rate 50 mV s<sup>−1</sup>. (Reproduced with permission from Ref. [49].)

is modified and the catalytic properties of the surface are enhanced. (2) It also may affect the availability of adsorption sites required for a given reaction, that is, blocking the possibility of a poisoning reaction. (3) It may provide new reaction sites for some of the reactive species, acting as a bifunctional catalyst. We will explain these effects with some examples.

#### 5.1.4.1 Changes in the Electronic Properties of the Metal

When a foreign ad-atom is deposited on a surface, the electronic properties of the ensemble ad-atom–surface atom are different from that of the original surface atoms. One of the clearest examples is that of formic acid oxidation on Pt(100) + Pd [49]. On the unmodified Pt(100) electrode, the voltammetric profile for formic acid

oxidation is shown in Fig. 10 (dashed line). As can be seen, no current is recorded in the positive-going scan, since the surface is completely covered by the poison (CO). In the negative-going scan, the maximum current is round 17 mA cm<sup>−2</sup> at 0.45 V (close to the intrinsic activity of Pt(100) electrodes). When palladium is deposited on the electrode surface, the oxidation peak shifts to 0.21 V, both in the positive- and negative-going scans (Fig. 10, full line). This peak reaches its maximum when the palladium coverage is ca. 0.5, with an intensity of ca. 55 mA cm<sup>−2</sup>. The current density at 0.21 V for the Pd-modified surface is much higher than the intrinsic activity at this potential obtained for the unmodified Pt(100) surface and for a palladium electrode (negligible currents are recorded in both scans for the unmodified

electrode at this potential, see Fig. 4), and the oxidation potential has diminished ca. 0.3 V.

It is worth noting that the catalytic effect of the ad-atom-modified electrodes can be different from that found for an alloy of these metals, since even in the case of solid solutions in the whole composition range, the surface structure is not the same. In the alloy, there is a microscopic mixture of the two species participating in the alloy, whereas in the ad-atom-modified electrodes, the ad-atoms are deposited on top of the surface. Moreover, the surface concentration of the different metallic atoms in the alloy can be completely different from that obtained in the bulk, making the interpretation of the results obtained with the alloy electrodes more difficult. In this respect, much more research is needed in order to fully understand the different behavior of the alloys.

#### 5.1.4.2 Ensemble Effects

In the previous section, we have discussed the cases in which the ad-atom plays a positive influence on the catalytic properties of the surface. In other cases, the ad-atom may not exert any effect. The only consequence of the presence of the ad-atom is that some of the active catalytic sites of the surface become blocked. It is said that the ad-atom is acting like a third body. In some cases, a third-body effect may result in a surface that has some interesting properties. That is the case when the reaction mechanism has parallel paths, or there is a competing reaction. If the site requirements for the different paths are different, the catalytic activity of the ad-atom-modified surface may be altered. These effects are known as ensemble effects, since they require a given structure of the adlayer to appear.

In the case of formic acid oxidation, this effect is well documented. It has been proposed that the dissociation of formic acid to yield water and CO (the poisoning intermediate) requires two adjacent sites, whereas the direct oxidation through the active intermediate demands only one site [50]. If the ad-atom deposits randomly on the electrode surface, there will be a coverage at which the distribution of the ad-atoms does not leave two adjacent sites. In that case, the dissociation reaction to yield the CO molecule is completely inhibited. Of course, the reaction through the active intermediate exhibits lower currents, since the number of available adsorption sites on the surface are lower, but the electrode presents the advantage of a very low poisoning rate and stable currents with time. A good example of this behavior is found for selenium-modified Pt(111) surfaces [50]. As the selenium coverage is increased, the currents at 0.5 V and the total poison accumulation decrease linearly, as expected for ad-atoms acting only as a third body. At a selenium coverage of 0.28 (coverage at which 84% of the surface platinum sites have been blocked by the ad-atom) the poison formation is completely inhibited whereas the surface still oxidizes formic acid [50].

#### 5.1.4.3 Bifunctional Catalysts

For some reactions, two or more species have to be adsorbed on the surface for the reaction to proceed. That is the case, for instance, of CO oxidation on metal electrodes. As aforementioned, CO and an oxygen-containing species have to be adsorbed on the electrode surface. For such cases, electrocatalysis is much more difficult, since the adsorption energy for the different species has to be the adequate for the reaction to proceed. In some cases, the adsorption energy is good for one of

the reactant species but not for the other, resulting in low current densities for the process. If it is possible to find an ad-atom that has more adequate adsorption energy for the second adsorbing species, the surface will exhibit better catalytic properties. In this case, the reaction will take place preferentially between one species adsorbed on the original surface and the second species adsorbed on the ad-atom. That kind of catalyst is called a bifunctional catalyst.

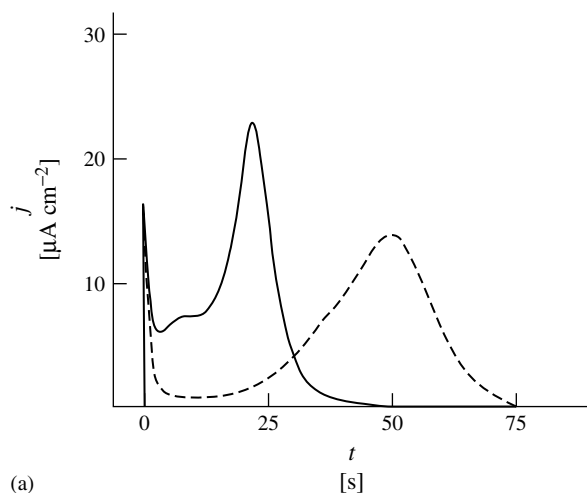
The typical example of a bifunctional catalyst is the ruthenium-modified platinum surfaces for the oxidation of methanol [51–58]. Of all the metals studied, platinum is the one that displays the best catalytic activity for methanol oxidation. However, its catalytic activity is still too low for practical purposes. The problem arises from the necessity of the adsorption of a second species able to transfer the oxygen group required for its complete oxidation to  $\text{CO}_2$ . Ruthenium is known to have a better affinity for OH than platinum but its interaction with methanol is very poor [59]. Thus, a platinum surface, which has good interaction energy with methanol, modified with ruthenium, whose interaction with OH is better than that of platinum, exhibits better catalytic properties than platinum.

The observed catalytic enhancement is potential dependent, since the adsorption energy for OH is also potential dependent. The energy of OH adsorption increases with the potential. Ruthenium adsorbs OH at less positive potentials than platinum, and therefore the onset for methanol oxidation takes place at lower potentials [56]. If the potential is increased, the adsorption energy for OH will increase. At a specific potential, the energy of OH adsorption will be too high for the reaction, and the modified surface will display lower catalytic

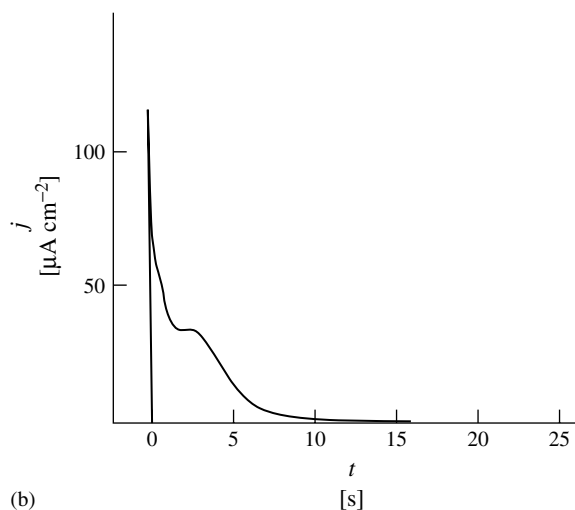
activity than the platinum surface [56]. This kind of bifunctional mechanism is also operative for CO oxidation on the same electrode surface.

It is important to establish if the mechanism of the observed catalytic effect played by an ad-atom is electronic or if the ad-atom is acting as a bifunctional catalyst. The problem arises from the fact that both effects can be considered as short-range effects, that is, the catalytic enhancement is only observed in the surface substrate atoms closest to the ad-atom. For the electronic effects, it is known that the effect induced by an ad-atom extends to the first and second row or neighboring atoms to the ad-atoms [60]. For the bifunctional catalyst, the pair responsible for the catalytic effect is the combination of an active site in the ad-atom and an active site in the surface close to it. This way, the determination of the electrocatalytic mechanism requires a detailed knowledge of the distribution of the ad-atom on the surface and the condition under which the catalytic enhancement is found. These questions are currently under investigation.

That is the case, for instance, of CO oxidation in surfaces modified with arsenic and bismuth (Fig. 11) [61, 62]. Both ad-atoms catalyze the oxidation of adsorbed CO layers. From the measured IR frequencies for CO, it is clear that arsenic and bismuth alter the surface energy of the electrode. However, the frequency shifts are in opposite directions, the effect of arsenic is a blue shift of the frequencies whereas the presence of bismuth causes a red shift [62]. If the effective mechanism of these ad-atoms were an electronic effect, the effects of bismuth and arsenic would be the opposite. Owing to the fact that the electrocatalytic effect is only observed at potentials at which the ad-atoms adsorb OH, the



(a)



(b)

**Fig. 11** CO-oxidation transients for Pt(111) at 0.70 V for (a)  $\Theta_{\text{As}} = 0.04$  and  $\Theta_{\text{CO}} = 0.68$ ; (b)  $\Theta_{\text{Bi}} = 0.10$  and  $\Theta_{\text{CO}} = 0.56$  (—),  $\Theta_{\text{As}} = 0.00$  and  $\Theta_{\text{CO}} = 0.56$  (----). (Reprinted with permission from Ref. [62].)

main electrocatalytic mechanism of these ad-atoms is a bifunctional mechanism.

#### 5.1.4.4 Modeling of the Catalytic Effects

The last point in electrocatalytic studies is trying to model the catalytic effect of the ad-atoms to achieve a full knowledge of its

effect and to be able to predict its catalytic properties regarding other molecules or other surface ad-atoms systems. Owing to the complexity of the simulations, it is important to have a well-defined system in which the experimental data are well understood. The most comprehensive simulations use clusters to model the



surface and tried to determine the most favorable adsorption sites and the activation energy for the process. However, as a result of the long computational times required to calculate the different parameters of the process, the size of the cluster are limited to a small number of metal atoms and to one or two different species adsorbed on the cluster surface in most of the cases. Therefore, the results obtained with these simulations represent a semiquantitative approach to the process. Moreover, the fact that the solvent is absent from most of the simulations and the lateral interactions between adsorbed species are not taken into account, the applications to electrochemical problems are more limited. However, some studies have tried to calculate the activation energy for the CO-oxidation process in a platinum surface with and without ruthenium, obtaining a potential dependence of the activation energy [63, 64].

In other cases, a simpler simulation based on statistical models is preformed. This kind of simulation was performed to determine the effect of the different ad-atoms in the oxidation of formic acid on

platinum electrodes [65]. In this model, the ad-atoms can play an effective catalysis on the process or act as a simple third body. In the first case, the activity of the surface is directly proportional to the number of pair ad-atom–surface sites, whereas in the latter case, the activity is proportional to the number of unoccupied surface sites. Since oxidation of formic acid takes place through a parallel-path mechanism, the effects of different levels of poisoning are also considered. For the cases in which the surface is completely covered by poison, both types of ad-atoms (the catalytically effective ad-atoms and the third-body ad-atoms) produce similar qualitative effects, that is, both types increases the current for the oxidation of formic acid [65]. Of course, the catalytic enhancement is higher in the case of the ad-atoms that modifies the electronic properties of the surface, since the global effect will be the combination of the electronic enhancement and the third-body effect (any ad-atom always acts as a third body). This is the case, for instance, for the Pt(100) surfaces modified with ad-atoms [65–67]. For the surfaces with low poisoning, that is, the Pt(111)

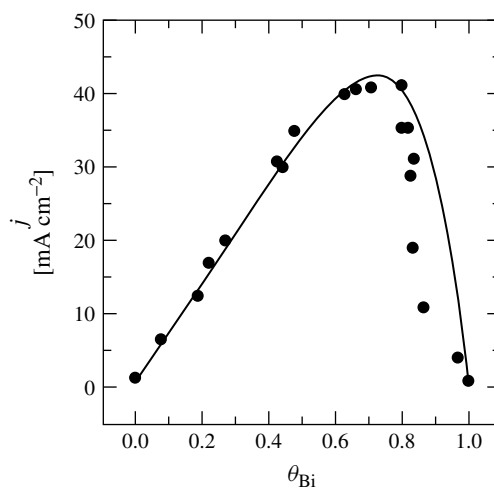


**Fig. 12** Comparison between experimental (●) and theoretical currents versus coverage curves for the electrooxidation of formic acid at Bi–Pt(111) electrode in 0.25 M HCOOH + 0.5 M H<sub>2</sub>SO<sub>4</sub>. (Reproduced with permission from Ref. [65].)

electrode, the distinction between the effects of both types of ad-atoms is clear. For the electronically effective ad-atoms, the catalytic activity of the surface increases with the ad-atom coverage until it reaches a maximum when 75% of the initial surface sites have been covered, that is, bismuth-modified Pt(111) surfaces (Fig. 12) [65, 68]. For the ad-atoms acting only as a third body, the current of the oxidation of formic acid diminishes with the ad-atom coverage, as observed with the selenium-modified Pt(111) surfaces [65].

## References

1. A. J. Appleby in *Comprehensive Treatise of Electrochemistry* (Eds.: B. Conway, J. O'M. Bockris, E. Yeager et al.), Plenum Press, New York, 1983, pp. 173–239, Vol. 7.
2. L. I. Kristalik in *Advances in Electrochemistry and Electrochemical Engineering* (Eds.: P. Delahay, C. Tobias), John Wiley & Sons, New York, 1970, pp. 283–339, Vol. 7.
3. R. Parsons, *Proc. Conf. 75th Anniv. Real Soc. Esp. de Fis. Y Quim*, Madrid, 1981, pp. 352–358.
4. J. O'M. Bockris, A. Reddy, *Modern Electrochemistry*, Plenum Press, New York, 1970.
5. J. O'M. Bockris, S. U. M. Khan, *Surface Electrochemistry*, Plenum Press, New York, 1973.
6. R. Adzic in *Modern Aspects of Electrochemistry* (Eds.: R. E. White, J. O'M. Bockris, B. E. Conway), Plenum Press, New York, 1990, pp. 163–236, Vol. 21.
7. J. Lipkowski, P. N. Ross, (Eds.), *Electrocatalysis*, Wiley-VCH, New York, 1998.
8. A. Wieckowski, (Ed.), *Interfacial Electrochemistry*, Marcel Dekker, New York, 1999.
9. M. J. Weaver in *Chemical Kinetics* (Ed.: R. G. Compton), Elsevier, Amsterdam, 1987, pp. 1–60, Vol. 27.
10. R. A. Marcus, *J. Electroanal. Chem.* **2000**, 483, 2.
11. J. N. Brønsted, K. J. Pedersen, *Z. Phys. Chem.* **1923**, 108, 185.
12. R. I. Masel, *Principles of Adsorption and Reaction on Surfaces*, John Wiley & Sons, New York, 1996.
13. S. Trasatti, *J. Electroanal. Chem.* **1972** 39, 163.
14. A. T. Kuhn, H. Wroblowa, *Trans. Faraday Soc.* **1967**, 63, 1458.
15. A. Capon, R. Parsons, *J. Electroanal. Chem.* **1973**, 44, 239.
16. R. R. Adzic, D. N. Simic, A. R. Despicm et al., *J. Electroanal. Chem.* **1977**, 80, 81.
17. A. J. Appleby, *Catal. Rev.* **1970**, 4, 221.
- 18a. S. Schuldiner, *J. Electrochem. Soc.* **1963**, 110, 332.
- 18b. S. Schuldiner, *J. Electrochem. Soc.* **1968**, 115, 362.
19. S.-C. Chang, M. J. Weaver, *Surf. Sci.* **1990**, 238, 142.
20. S.-C. Chang, J. D. Roth, Y. Ho et al., *J. Electron Spectrosc. Relat. Phenom.* **1990**, 54/55, 1185.
21. S.-C. Chang, J. D. Roth, M. J. Weaver, *Surf. Sci.* **1991**, 244, 113.
22. S.-C. Chang, A. Hamelin, M. J. Weaver, *J. Phys. Chem.* **1991**, 95, 5560.
23. S.-C. Chang, A. Hamelin, M. J. Weaver, *Surf. Sci.* **1990**, 239, L543.
24. G. J. Edens, A. Hamelin, M. J. Weaver, *J. Phys. Chem.* **1996**, 100, 2322.
25. A. Wieckowski, M. Rubel, C. Gutierrez, *J. Electroanal. Chem.* **1995**, 382, 97.
26. K. Franaszczuk, E. Herrero, P. Zelenay et al., *J. Phys. Chem.* **1992**, 96, 8509.
27. E. Herrero, K. Franaszczuk, A. Wieckowski, *J. Phys. Chem.* **1993**, 97, 9730.
28. J. Clavilier, *J. Electroanal. Chem.* **1987**, 236, 87.
29. A. Fernández-Vega, J. M. Feliu, A. Aldaz et al., *J. Electroanal. Chem.* **1991**, 305, 229.
30. M. R. Columbia, P. A. Thiel, *Surf. Sci.* **1990**, 235, 53.
31. M. R. Columbia, A. M. Crabtree, P. A. Thiel, *J. Am. Chem. Soc.* **1992**, 114, 1231.
32. S. Trasatti in *Advances in Electrochemistry and Electrochemical Engineering* (Eds.: H. Gerischer, C. W. Tobias), Wiley Interscience, New York, 1977, pp. 213–321, Vol. 10.
33. W. Schmickler, *Interfacial Electrochemistry*, Oxford University Press, New York, 1996.
34. A. N. Frumkin, *Z. Electrochem.* **1955**, 59, 809.
35. A. Rodes, R. Gómez, J. M. Feliu et al., *Langmuir* **2000**, 16, 811.
36. V. Climent, A. Rodes, J. M. Orts et al., *Langmuir* **1997**, 13, 2380.
37. V. Climent, A. Rodes, J. M. Orts et al., *J. Electroanal. Chem.* **1999**, 461, 65.
38. C. Lamy, J. M. Leger, C. Clavilier et al., *J. Electroanal. Chem.* **1983**, 150, 71.

39. S. Motoo, N. Furuya, *Ber. Bunsen-Ges. Phys. Chem.* **1987**, 91, 457.
40. S. Motoo, N. Furuya, *J. Electroanal. Chem.* **1985**, 184, 303.
41. R. Gómez, J. M. Orts, J. M. Feliu et al., *J. Electroanal. Chem.* **1997**, 432, 1.
42. K. Popovic, A. Tripkovic, N. Markovic et al., *J. Electroanal. Chem.* **1990**, 295, 79.
43. K. Popovic, A. Tripkovic, N. Markovic et al., *J. Electroanal. Chem.* **1991**, 313, 181.
44. M. J. Llorca, J. M. Feliu, A. Aldaz et al., *J. Electroanal. Chem.* **1991**, 316, 175.
45. A. Rodes, M. J. Llorca, J. M. Feliu et al., *Anal. Quim.* **1996**, 92, 118.
46. C. F. McFaden, P. S. Cremer, A. J. Gellman, *Langmuir* **1996**, 12, 2483.
47. G. A. Attard, A. Ahmadi, J. M. Feliu et al., *Langmuir* **1999**, 15, 1420.
48. G. A. Attard, A. Ahmadi, J. M. Feliu et al., *J. Phys. Chem. B* **1999**, 103, 1381.
49. M. J. Llorca, J. M. Feliu, A. Aldaz et al., *J. Electroanal. Chem.* **1994**, 376, 151.
50. M. J. Llorca, E. Herrero, J. M. Feliu et al., *J. Electroanal. Chem.* **1994**, 373, 217.
51. M. Watanabe, S. Motoo, *J. Electroanal. Chem.* **1975**, 60, 267.
52. K. Franaszczuk, J. Sobkowski, *J. Electroanal. Chem.* **1992**, 327, 235.
53. T. Iwasita, F. C. Nart, W. Vielstich, *Ber. Bunsen-Ges. Phys. Chem.* **1990**, 94, 1030.
54. H. A. Gasteiger, N. Markovic, P. N. Ross et al., *J. Phys. Chem.* **1993**, 97, 12 020.
55. H. A. Gasteiger, N. Markovic, P. N. Ross et al., *Electrochim. Acta* **1994**, 39, 1825.
56. E. Herrero, K. Franaszczuk, A. Wieckowski, *J. Electroanal. Chem.* **1993**, 361, 269.
57. W. Chrzanowski, A. Wieckowski, *Langmuir* **1997**, 13, 5974.
58. T. Frelink, V. Visscher, J. A. R. van Veen, *Surf. Sci.* **1995**, 335, 353.
59. B. J. Kennedy, A. W. Smith, *J. Electroanal. Chem.* **1990**, 293, 103.
60. P. J. Fiebelman, D. R. Ramman, *Phys. Rev. Lett.* **1984**, 52, 61.
61. E. Herrero, J. M. Feliu, A. Aldaz, *J. Catal.* **1995**, 152, 264.
62. E. Herreo, A. Rodes, J. M. Pérez et al., *J. Electroanal. Chem.* **1995**, 393, 87.
63. A. B. Anderson, E. Grantscharova, *J. Phys. Chem.* **1995**, 99, 9143.
64. A. B. Anderson, E. Grantscharova, S. Seong, *J. Electrochem. Soc.* **1996**, 143, 2075.
65. E. Leiva, T. Iwasita, E. Herrero et al., *Langmuir* **1997**, 13, 6287.
66. A. Fernández-Vega, J. M. Feliu, A. Aldaz et al., *J. Electroanal. Chem.* **1988**, 258, 101.
67. J. Clavilier, A. Fernández-Vega, J. M. Feliu et al., *J. Electroanal. Chem.* **1989**, 261, 113.
68. J. Clavilier, A. Fernández-Vega, J. M. Feliu et al., *J. Electroanal. Chem.* **1988**, 258, 89.

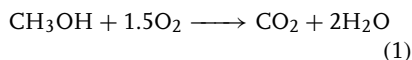
## 5.2 CO, Formic Acid, and Methanol Oxidation in Acid Electrolytes – Mechanisms and Electrocatalysis

Wolf Vielstich  
Instituto de Quimica de Sao Carlos-SP,  
USP, Brasil

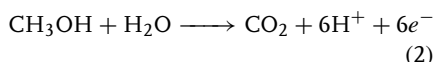
### 5.2.1

#### Scope of the Chapter

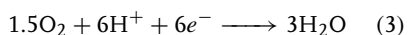
The anodic oxidation of methanol was considered as one of the most interesting subjects in electrochemistry during the last 15 years. Besides very characteristic reaction pathways and electrocatalytic effects, the methanol molecule with its four hydrogen atoms is the basis of a high-energy density liquid fuel. The reaction of methanol with oxygen follows the chemical route



with a reaction enthalpy of  $726.6 \text{ kJ mol}^{-1}$  and with a Gibbs Free Energy of  $702.5 \text{ kJ mol}^{-1}$  under standard conditions. The high-energy density of a combination of liquid methanol and liquid oxygen was already used since 1940 by Wernher von Braun, for the propulsion of the first rocket in space. But in the 1960s, the electric energy onboard the space ship was not taken from a methanol/oxygen fuel cell, but from a hydrogen/oxygen system. At this time, the electric data of a methanol/oxygen fuel cell had not been sufficient for this application. Especially in acid solution, the rate of methanol oxidation

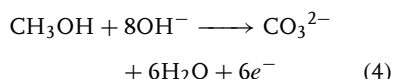


in combination with oxygen reduction at the cathode



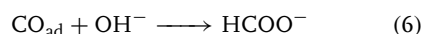
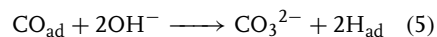
was very low, even with platinum as a catalyst [1].

By the above reasons, the possibility of using methanol in an *alkaline electrolyte* was studied, showing a much better rate of oxidation at more suitable potentials [2]. But the following equation:

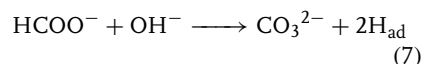


shows that part of the electrolyte is consumed and carbonate ions are formed. After consumption, the cell has to be filled again. Nevertheless, some applications of an alkaline system have been studied [3]. It is interesting to note that at platinum, formate is the main intermediate of the reaction [4].

The electrochemistry for CO and formic acid also are different in alkaline solution. As opposed to acid solutions, two chemical pathways introduce a catalytic conversion of CO and  $\text{OH}^-$  ions to hydrogen as active material. From the adsorbed state, carbonate ions and/or formate can be formed [5, 6].



Formate reacts with an additional  $\text{OH}^-$  ion also to carbonate ions and hydrogen



In both cases, the charge-transfer step is the oxidation of hydrogen.

The interest in the oxidation of CO, formic acid, and methanol in *acid media* did come relatively late. It was only in 1986 that the European Community started a project for an acid methanol fuel cell, a direct methanol fuel cell, DMFC [7, 8]. This development is still

going on. In the following text, we will therefore concentrate our survey mainly on *methanol*. But *CO* and *formic acid* are directly connected with this approach, due to the fact that formic acid is formed in one pathway of methanol oxidation, and CO is playing an important role as adsorbed product or main intermediate, depending on operating conditions such as electrode potential, catalyst, and temperature.

In acid media, platinum is an essential part of a catalyst, because at platinum the adsorbed methanol molecule is especially able to start different reaction pathways already at room temperature, while, for example, at ruthenium a temperature of about 60 °C is necessary. For this reason, the reactions of CO and formic acid have to be studied on ruthenium and PtRu catalysts also.

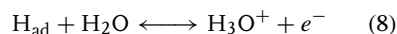
In the following paragraph, we will start with some thermodynamic considerations and then we will give a survey on CO oxidation and the reaction pathways of formic acid and methanol oxidation.

### 5.2.2

#### Basic Facts

##### 5.2.2.1 Thermodynamics, Open-circuit Potentials

From thermodynamics, one obtains the electrode potential on the basis of a reversible process at the surface of the catalyst. Our top example is the hydrogen electrode with its high exchange current at platinum in acid solution:



For our model species, carbon monoxide, formic acid, and methanol, such an equilibrium does not exist. Nevertheless, the open-circuit potential observed for formic acid and methanol is not too far from the thermodynamic values. Thermodynamic

data are obtained via the Gibbs free energy change  $\Delta G$ , accompanying a chemical reaction at the absolute temperature  $T$ , and is related to the corresponding changes in enthalpy and entropy

$$\Delta G = \Delta H - T \Delta S \quad (9)$$

The reaction of methanol and oxygen, for example, can be an electrochemical one (Eqs. 1–3), split into two separated charge-transfer processes at the anode and cathode. Then we have as maximum possible electromotive force

$$E = \frac{-\Delta G}{nF} \quad (10)$$

This is the potential difference between the oxygen and the methanol electrode. With the thermodynamic potential of oxygen, +1.23 V versus hydrogen, we now can place the thermodynamic data for methanol in relation to the hydrogen reference electrode. In addition, we can calculate the “ideal efficiency” of the methanol/oxygen reaction by relating  $\Delta G$  to the change in enthalpy:

$$\eta_{\text{id}} = \frac{\Delta G}{\Delta H} [\%] \quad (11)$$

Doing the same for CO and HCOOH, we can list our data in Table 1 below.

While the theoretical potential of CO and methanol are positive to the hydrogen reference, for formic acid the data is negative. But experiments show (Sect. 5.2.3) that open-circuit potentials are much more positive than the thermodynamic values, especially in the case of formic acid. This is a consequence of the missing reaction equilibrium. In addition, the increase in rate positive to the open-circuit potential is much less than in the case of hydrogen oxidation. The rate of charge transfer at a given potential depends strongly on the catalyst and its surface structure.

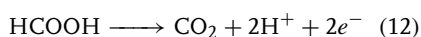
**Tab. 1** Thermodynamic data for the oxidation reactions of hydrogen, CO, formic acid, and methanol under standard conditions at 25 °C, standard potential  $\varphi^0$ , and ideal efficiency

Fuel	Reaction	$n$	$-\Delta H^0$ [kJ mol <sup>-1</sup> ]	$-\Delta G^0$ [kJ mol <sup>-1</sup> ]	$\varphi^0$ [V]	%
Hydrogen	$H_2 + \frac{1}{2}O_2 \rightarrow H_2O_l$	2	286.0	237.3	0.000	83.0
CO	$CO + \frac{1}{2}O_2 \rightarrow CO_2$	2	283.1	257.2	0.163	90.9
Formic Acid	$HCOOH + \frac{1}{2}O_2 \rightarrow CO_2 + H_2O_l$	2	270.3	285.5	0.251	105.6
Methanol	$CH_3OH + \frac{3}{2}O_2 \rightarrow CO_2 + 2H_2O_l$	6	726.6	702.5	0.015	96.7

### 5.2.2.2 Reaction Pathways

In the introduction (Sect. 5.2.1), we learned already that in alkaline solution CO shows two possible reaction pathways. In acid solution this is not the case. But we have now to discuss the different pathways for formic acid and methanol.

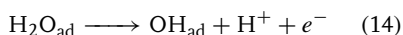
As already proposed by Capon and Parsons [9], the anodic reaction of formic acid at platinum proceeds indeed via a dual-path mechanism. One pathway is producing CO<sub>2</sub> in a direct way via *dehydrogenation*



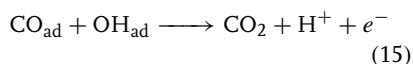
and in a parallel pathway a surface-blocking residue is formed via *dehydration*,



followed by the oxidation of the adsorbate as the rate-determining step:



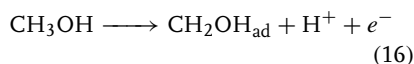
and



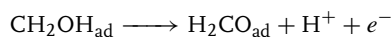
The “direct” pathway possibly involves a reactive intermediate like COOH [9]. This step is still unknown, but the formation of hydrogen atoms has been shown using a palladium membrane as sensor [10, 11].

On the other hand, CO is a very well-known intermediate (or product, depending on potential and catalyst used). The existence of the direct path above is proven by an experiment with upd-lead [12]. It was shown that at a coverage of 84% of the platinum surface (1) an additional formation of adsorbate is not possible and (2) on 16% free surface sites the oxidation of formic acid continues. A second proof of the dual-pathway model has been made via a Differential electrochemical mass spectrometry (DEMS) experiment and it will be discussed in Sect. 5.2.3.1.

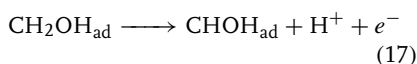
Methanol oxidation takes place via at least two different pathways. The main route is producing CO again as a poisoning adsorbate. In a second alternative, formic acid is formed, which reacts in solution with methanol to methylformate (Sect. 5.2.3). The first route leads to hydrogen-containing species as formulated by Bagotzki and coworkers [13]:



or



or





or

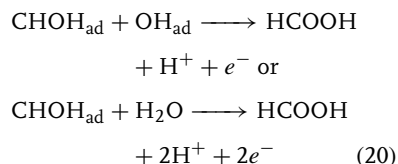


or



The presence of adsorbed CO was shown by in situ Fourier Transform Infrared Spectroscopy (FTIRS) [14] and the presence of adsorbed COH by FTIRS [15], the relative amounts depending on methanol concentration. COH is favored by low methanol concentrations as proved via Thermal Desorption Spectroscopy (TDS) [16a]. For the complete oxidation to  $\text{CO}_2$ , again  $\text{OH}_{\text{ad}}$  is required as in the above case of formic acid.

The existence of formic acid formation on a second path has been proved by the DEMS-technique (Sect. 5.2.3). A possible step of formation could be



The rate of HCOOH formation is still unknown. The DEMS technique shows only the part of HCOOH that has been transformed to mass 60 ( $\text{HCOOCH}_3$ ) via the reaction with methanol in solution (Sect. 5.2.3). As shown by several authors, we have last not least a pathway via formation of formaldehyde. The rate of formation is not easy to be measured [16b].

#### 5.2.2.3 Bifunctional Mechanism of Methanol Oxidation

The kinetic of methanol oxidation [17] is determined by the fact that the product

of Reaction (18), adsorbed CO, requires a catalyst other than platinum, while on the other side Pt atoms are necessary for the dehydrogenation steps. The blocking residue CO needs a surface with the easy formation of an OH-bond out of the surrounding water molecules, and this at low potentials. A model catalyst for this procedure is ruthenium (Sect. 5.2.3.3). At room temperature, this metal is ineffective as opposed to the first steps in methanol oxidation. Therefore, for this bifunctional function of the reaction to the final products of  $\text{CO}_2$  and water, one needs a surface arrangement of different metal sites, for example, clusters containing Pt and Ru atoms. The principle of the bifunctional action is illustrated in Fig. 1.

The metal sites for adsorption and dehydrogenation should be platinum or even better, a PtRu combination (see below); the sites for  $\text{OH}_{\text{ad}}$  formation should preferably be ruthenium.  $\text{OH}_{\text{ad}}$  formation on platinum needs a much higher anodic potential. A special question arises: what is the most suitable distribution of the two different surface sites, requiring three neighboring Pt sites close to at least one Ru site, supposed to be? In the following paragraphs, we will learn that for a smooth model surface we have to use an alloy, the optimum ratio of Pt: Ru sites depending on operating conditions such as temperature and methanol concentration.

### 5.2.3

#### Oxidation of CO, Formic Acid, and Methanol at Pt Metals

##### 5.2.3.1 Results via CV and MSCV

Online observation of mass signals from volatile reaction partners offers, in addition to a current–potential plot, useful information on the studied reaction (DEMS technique, in Ref. [18–20]). For

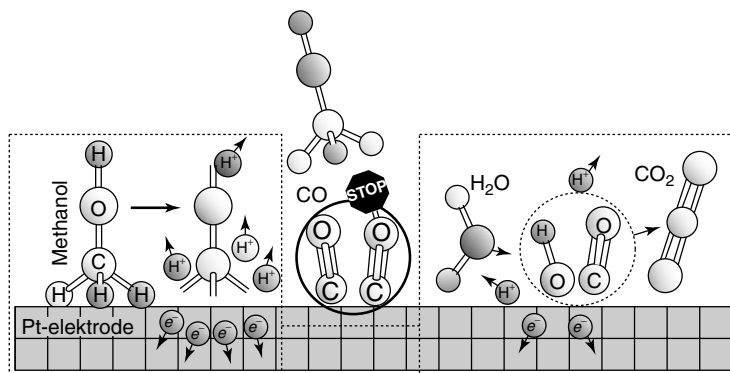


**Fig. 1** Illustration of the different reaction steps during methanol oxidation on a model catalyst surface, from left to right: three sites methanol adsorption, dehydrogenation, adsorption of blocking CO intermediate, formation of  $\text{OH}_{\text{ad}}$  from a water molecule, reaction with CO and desorption as  $\text{CO}_2$ .

mass signals also, cyclic voltammograms (CVs) can be resolved up to more than  $100 \text{ mV s}^{-1}$  [21]. Besides the amount of

information given in a first survey, a continuous control of electrode reactions as function of time is possible.

In the following text, we will characterize the oxidation of our small organic molecules by CVs and simultaneously by mass spectrometric cyclic voltammograms (MSCV) as well as by the respective potential scans.

#### 5.2.3.1.1 Carbon Monoxide Oxidation

The current/potential behavior of CO on a porous Pt surface is demonstrated after CO adsorption in a flow cell experiment [22] via a potential scan in a solution free of CO, starting at 50 mV versus RHE [23]. Figure 2 shows a first low current region (peak I) between 0.3 and 0.55 V, in the upper part, well below oxide formation on platinum. The following three peaks,

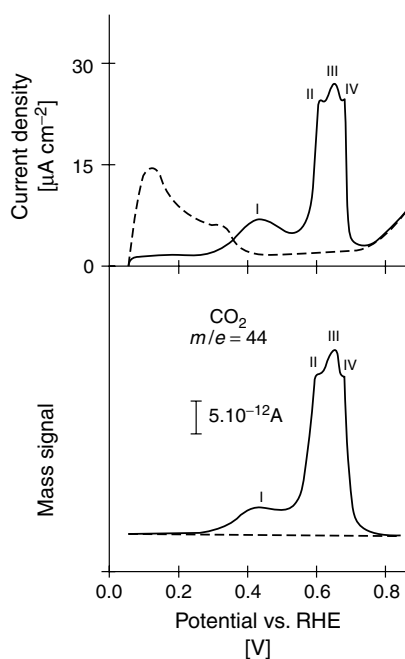


**Fig. 2** Simultaneous recording of current and mass signal  $e/m = 44$  for the oxidation of adsorbed CO during a potential scan at Pt in  $0.05 \text{ M HClO}_4$ ,  $E_{\text{ad}} = 50 \text{ mV}$ ,  $t_{\text{ad}} = 10 \text{ min}$ ,  $10 \text{ mV s}^{-1}$ . Dashed trace: supporting electrolyte only [23].



II to IV, are close together between 0.6 and 0.7 V. The relative contribution of these peaks to the total charge is strongly dependent on the structure of the polycrystalline surface. The lower curve with the mass signal of  $\text{CO}_2$  shows that in all cases, a close relation exists between the current and the mass signal. The peaks therefore are related to  $\text{CO}_{\text{ad}}$  and the oxidation product is  $\text{CO}_2$  only. We learn from the beginning of CO oxidation at 0.3 V that at room temperature, the overpotential for CO oxidation amounts to more than 100 mV (Table 1).

In a second experiment, we turn from a porous Pt surface to the well-defined surface of a Pt(111) single crystal [23, 24]. The potential scans of Fig. 3 show that the overpotential is the same as for the polycrystalline surface, and peak I appears in both cases again, but the multiplicity of the large current peak is missing. The main oxidation peak on Pt(100) is much sharper and more positive than for Pt(111). From this it follows that for a given oxidation time, the CO coverage is always smaller on Pt(111) than on Pt(100).

**5.2.3.1.2 Methanol Oxidation** The mechanism of methanol oxidation with its parallel pathway characteristic is much more complicated than CO oxidation. We therefore begin our study with simultaneous registration of CVs and MSCVs. Figure 4 shows results for porous Pt electrodes in a 1 M  $\text{CH}_3\text{OH}$  sulfuric acid solution. Comparing part (a) and part (b) of the figure, it is clear that the products  $\text{CO}_2$  and also  $\text{HCOOH}$  are following the current over the total experimental region up

to 1.4 V. Note the two orders of magnitude difference in the mass signal intensity for  $\text{CO}_2$  and methyl formate. Obviously, for the oxidation of methanol also, platinum shows a high overpotential of ca. 0.6 V (compare with the thermodynamic data in Sect. 5.2.2). We will discuss the formation of current peaks in the CVs later, under Sect. 5.2.3.2.3

Interesting new information can be obtained by taking a first anodic scan, after contacting the electrode with methanol at 0.05 V, where adsorbed hydrogen still inhibits methanol adsorption. Figure 5 shows the resolution of reaction steps as a function of the potential [26, 27]. The increase in  $\text{CO}_2$  formation not before 400 mV demonstrates that the current

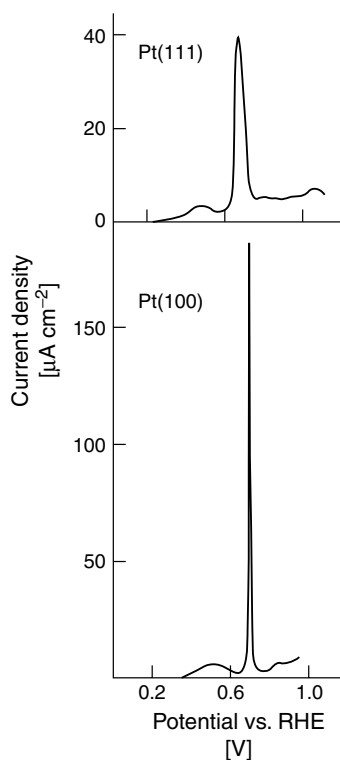


**Fig. 3** Potentiodynamic profiles for the oxidation of CO adsorbate on single-crystal Pt surfaces, obtained by the flow cell technique as in Fig. 2, but  $t_{\text{ad}} = 3$  min [23].

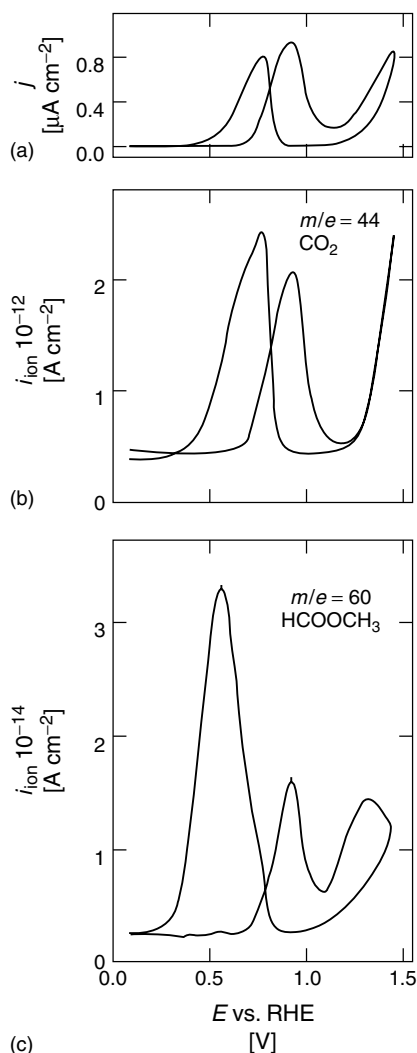


**Fig. 4** Methanol oxidation at porous Pt in 1 M  $\text{CH}_3\text{OH}$  and 0.5 M  $\text{H}_2\text{SO}_4$ .

(a) CV with  $20 \text{ mV s}^{-1}$ ; (b) simultaneously recorded mass signal  $m/e = 44$  ( $\text{CO}_2$ ); and (c) MSCV for  $m/e = 60$  ( $\text{HCOOCH}_3$ ) [25].

In closing our first view on methanol oxidation in acid media, we should give some results about the influence of surface structure on the electrocatalytic activity. For this purpose, we have plotted, in Fig. 6, the first potential scans (in anodic and cathodic direction) for methanol oxidation at the three main single surfaces of platinum [26–29]. Pt(111) and Pt(110) show the highest activity at low potentials. A strong early dehydrogenation obviously occurs on Pt(100). For recent details, see T. Iwasita in Ref. [26, 27]. The discussion of the current maximum on Pt(111) will be done with the help of information from FTIRS, mentioned below in Sect. 5.2.3.2.

**5.2.3.1.3 Formic Acid Oxidation** Cyclic voltammograms taken at platinum in a DEMS experiment [30, 31] show the  $\text{CO}_2$  signal following the current as in the case of Methanol oxidation (Fig. 7). In the potential range up to 1.5 V, we have again three anodic current peaks, but the bulk oxidation begins for formic acid at a much lower potential. Studying the activity of the single-crystal surfaces [29, 32, 33], one finds strong activity for Pt(111) (Fig. 13), and a very low one on Pt(110) and Pt(100). Adzic and coworkers [33] have demonstrated that the addition of the three CVs combines to the diagram for polycrystalline platinum.

The existence of a dual-pathway mechanism can easily be demonstrated by using labeled  $\text{H}^{13}\text{COOH}$  in the following DEMS experiment (Fig. 8) [30, 31]. After cycling in the basic electrolyte, changing to 0.04 M

during the anodic peak between 200 and 350 mV is due to the oxidation of hydrogen atoms out of the dehydrogenation step [10, 11]. The desorption of hydrogen atoms that are already present on the surface, is involved also. The oxidation of methanol up to  $\text{CO}_2$  during a first potential scan starts only above 450 mV.

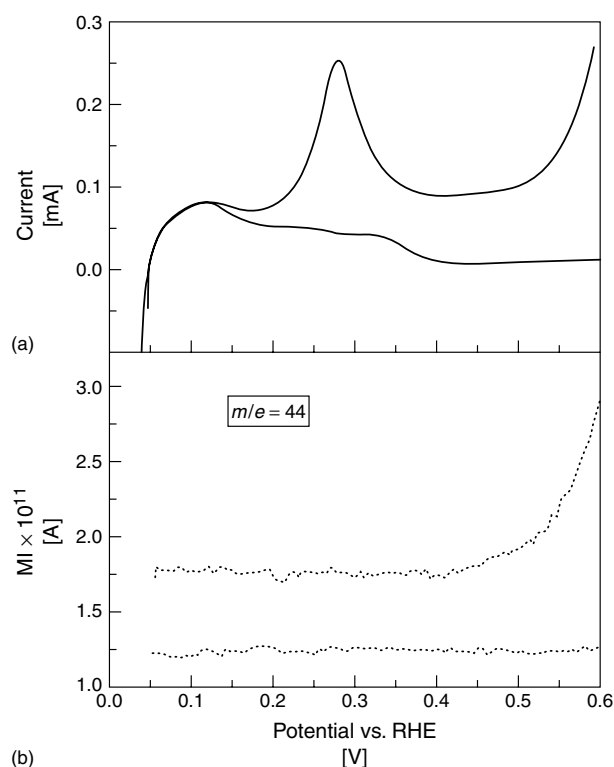


**Fig. 5** First potential scan at a porous platinum layer after contact with solution at +0.05 V, CV and MSCV as in Fig. 4, but 0.2 M  $\text{CH}_3\text{OH}/0.1 \text{ M HClO}_4$ ,  $10 \text{ mV s}^{-1}$ : (a) current; (b) mass signal for  $\text{CO}_2$ , traced line: base signal without methanol [26, 27].

$\text{H}^{13}\text{COOH}/0.5 \text{ M H}_2\text{SO}_4$  solution under potential control at 0.2 V for 3 min. It follows exchange of the solution first against 0.5 M  $\text{H}_2\text{SO}_4$  and finally against  $\text{H}^{12}\text{COOH}/0.5 \text{ M H}_2\text{SO}_4$ . Then the potential scan is started in the anodic direction. The mass signals for the oxidized adsorbate ( $m/e = 45$ ) start only above 0.5 V, before this happens  $\text{HCOOH}$  from the bulk is oxidized to  $^{12}\text{CO}_2$  ( $m/e = 44$ ). The direct pathway is active at the covered surface. About the adsorbates, we now will learn more from IR experiments in the next paragraph.

### 5.2.3.2 Study of Adsorbates via FTIRS

**5.2.3.2.1 Carbon Monoxide** Carbon monoxide adsorbed at the interface electrode/electrolyte shows a strong surface-sensitive behavior [34]. We will show this for Pt(111) as a model substrate. Depending on the potential, CO can be adsorbed in three different forms: linearly bonded (atop), bridge bonded, and threefold bonded. With the shift in the strength of the C–O bond, the frequency (or alternatively, the wave number) are varying in a clear manner.

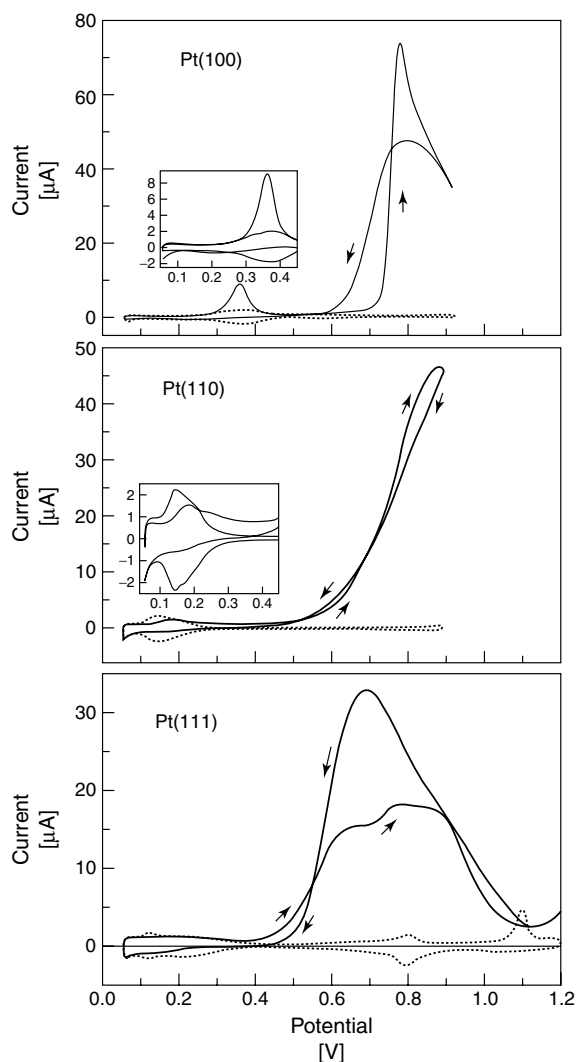


**Fig. 6** First potential scan after methanol adsorption at 0.05 V as in Fig. 5, but single-crystal surfaces Pt(100), Pt(110), and Pt(111), 50 mV s<sup>-1</sup> [26, 27].

In Fig. 9, this fact is shown for the case of a CO-saturated 0.1 M HClO<sub>4</sub> solution and two different potentials, (a) -0.01 V and (b) 0.34 V versus RHE. The reference spectrum used during the

in situ FTIR experiment was 0.75 V RHE [35].

The positive going bands are due to the loss of CO molecules, the negative going band at 2345 cm<sup>-1</sup> results from the CO<sub>2</sub>

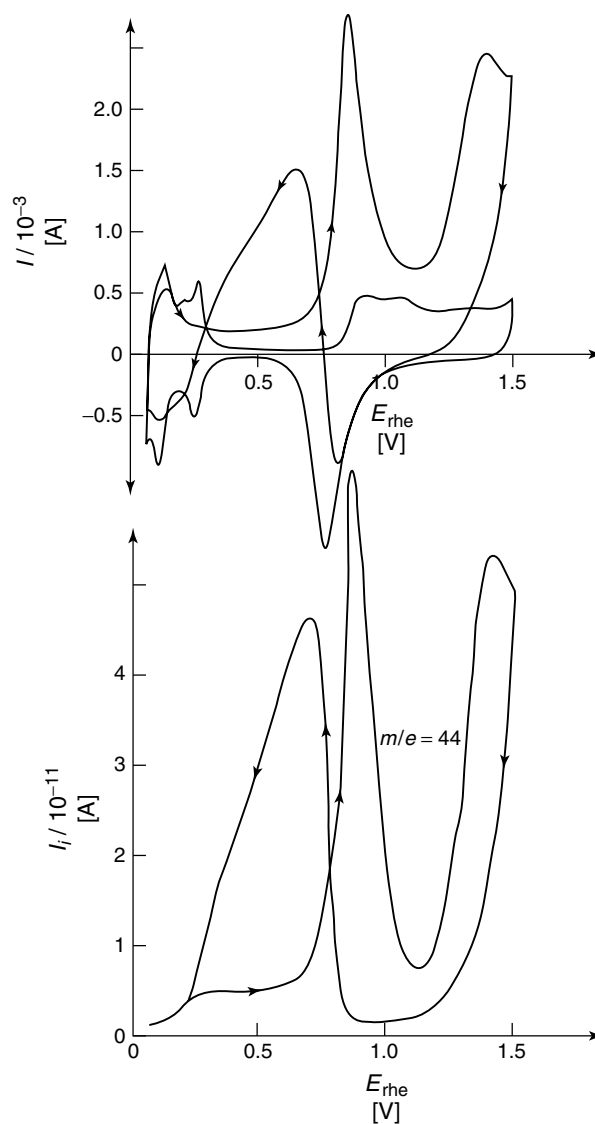


**Fig. 7** Formic acid oxidation at porous Pt, CV, and MSCV as in Fig. 4, but  $12.5 \text{ mV s}^{-1}$  and  $0.01 \text{ M HCOOH}$  solution [30, 31].

formed during the potential step to  $0.75 \text{ V}$  and trapped in the thin layer between electrode and IR-window (Chapter 3.1 of this volume). The thin-layer thickness was

minimized, such that at least 90% of the  $\text{CO}_2$  produced was from electrooxidation of the adsorbate and not from the solution-phase CO.

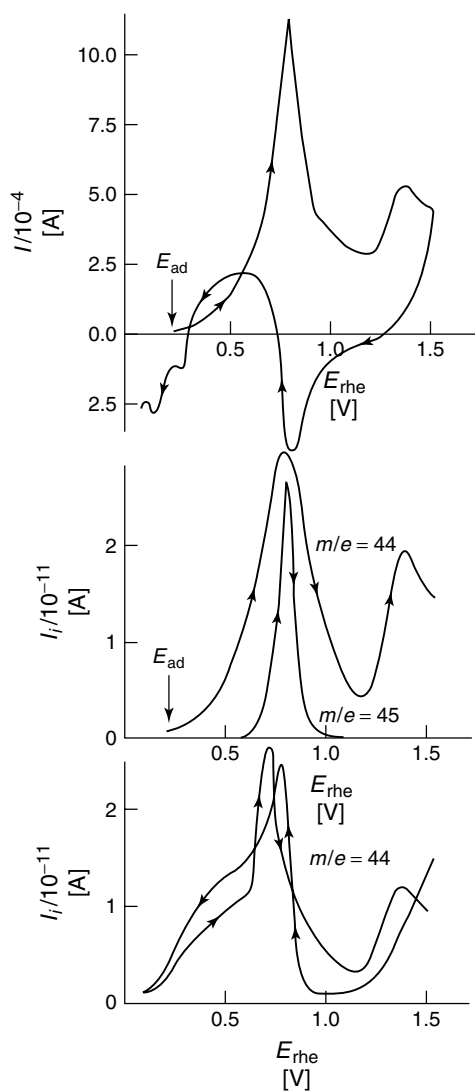


**Fig. 8** CV and MSCV of formic acid oxidation as in Fig. 7, but using preadsorbed  $\text{H}^{13}\text{COOH}$  in order to form a labeled adsorbate up to saturation coverage, followed by oxidation of  $\text{H}^{12}\text{COOH}$  at the covered surface. The second MSCV below shows, in addition, the first cathodic and the second anodic scan [30, 31].

Spectrum (A) shows a sharp CO band at  $2066\text{ cm}^{-1}$  attributed to atop CO and a much weaker band at  $1773\text{ cm}^{-1}$  for threefold adsorbed CO. At  $0.34\text{ V}$ , we have a drastic change from the presence of threefold-bonded to bridge-bonded CO at  $1850\text{ cm}^{-1}$ . By taking data

over a wider range of potentials, one gets the change in band intensity as a function of the potential for the species studied [35].

Comparing the IR data from Fig. 10 with adlayer structures obtained from scanning tunneling microscopy (STM),

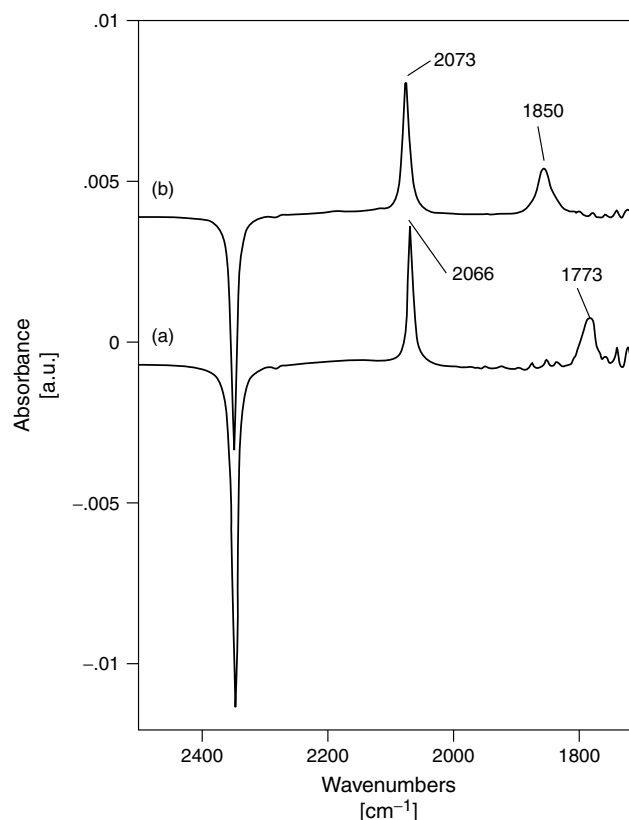


**Fig. 9** Potential-difference infrared spectra in a CO-saturated 0.1 M  $\text{HClO}_4$  solution at (a)  $-0.01$  V and (b)  $0.34$  V versus RHE, reference was made by stepping to  $0.75$  V RHE [35].

one understands that adlayer structure and bonding properties reflect each other. Obviously, bridge- and threefold-bonded CO requires the presence of a  $(2 \times 2)$  or  $(\sqrt{19} \times \sqrt{19})$  structure.

Not only does the integrated band intensity change with the potential, but the frequency (or wave number) also shifts. Figure 11 shows the potential dependence of these two band parameters for atop CO on polycrystalline ruthenium. In this case, we follow the stripping of a saturated adlayer formed at  $0.3$  V using a pure  $0.1$  M

$\text{HClO}_4$  as electrolyte. Relative to platinum, the wave numbers are shifted to lower values. Oxidation to  $\text{CO}_2$  starts at Ru more than  $100$  mV earlier than on Pt, a fact that will be discussed in Sect. 5.2.3.3.

**5.2.3.2.2 Formic Acid** In situ IR spectra taken during the first anodic polarization at the Pt(111) model electrode in  $\text{HCOOH}$  solution give important new information. After contacting the solution at  $0.05$  V, using a flow cell procedure [22], a series of spectra was collected at fixed potentials

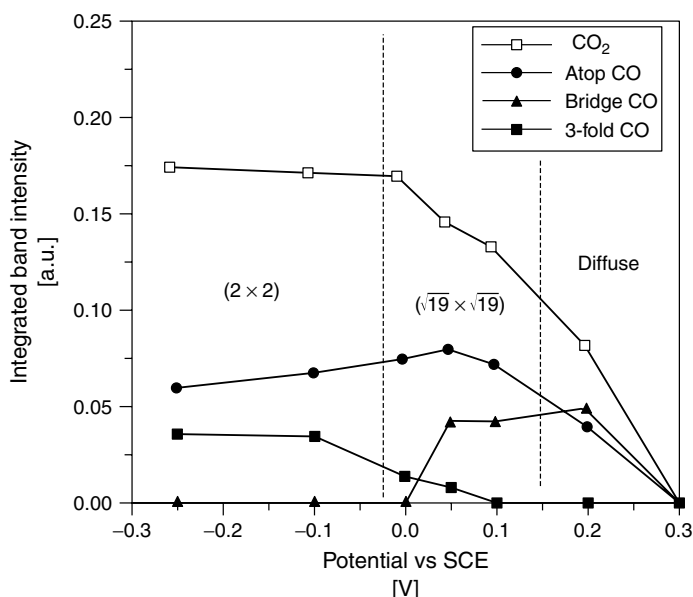


**Fig. 10** Plot of integrated infrared band intensities for linearly, bridge- and threefold-bonded CO adsorbed on Pt(111), together with spectra for CO<sub>2</sub>, obtained along with stepping to the 0.75 V versus RHE reference; all data were taken with CO-saturated 0.1 M HClO<sub>4</sub> [35].

(Fig. 12). Atop CO (near 2050 cm<sup>-1</sup>) and bridge-bonded (at 1870 cm<sup>-1</sup>) are formed. Obviously both types of adsorbate are formed with increasing intensities up to a maximum of 0.3 to 0.45 V. It has been established that on this surface no interconversion between bridged and atop CO occurs with increasing positive potential. [37]. As shown in further studies [38], the direct pathway of HCOOH oxidation via dehydrogenation is the main pathway on Pt(111).

**5.2.3.2.3 The Anodic Maximum of Formic Acid Oxidation below 0.5 V** Small organic molecules as formic acid, formaldehyde, and methanol do show anodic maxima when the applied polarization is reversed also. At potentials above 0.8 V

at polycrystalline Pt, the current decay during the positive going scan was explained in terms of the formation of platinum oxide [39] and the increase in current during the scan in negative direction as due to HCOOH oxidation on the clean surface after oxide reduction. This interpretation, however, cannot explain decays at potentials near 0.5 V as, for example, observed for formic acid (Fig. 13). For methanol in sulfuric acid, Markovic and Ross [40] state that sulfate adsorption, which is a reversible process, hinders the adsorption of organic species. Herrero and coworkers [41] stated that sulfate/water interactions [42, 43] are responsible for this effect. But the reversible behavior is observed in H<sub>3</sub>PO<sub>4</sub> also [41], and even in the presence of a much less adsorbable electrolyte as HClO<sub>4</sub> (Fig. 13).



**Fig. 11** Potential dependence of band parameters for spectra obtained during CO stripping of a saturated adlayer, formed at 0.3 V RHE on polycrystalline Ru in 0.1 M HClO<sub>4</sub>: (a) integrated band intensities, normalized with the maximum value obtained after complete oxidation of CO at 0.8 V, the CO<sub>2</sub> band at 2341 cm<sup>-1</sup> was calculated with the reference spectrum taken at 0.1 V where no CO<sub>2</sub> is formed; (b) C–O stretch wave numbers [36].

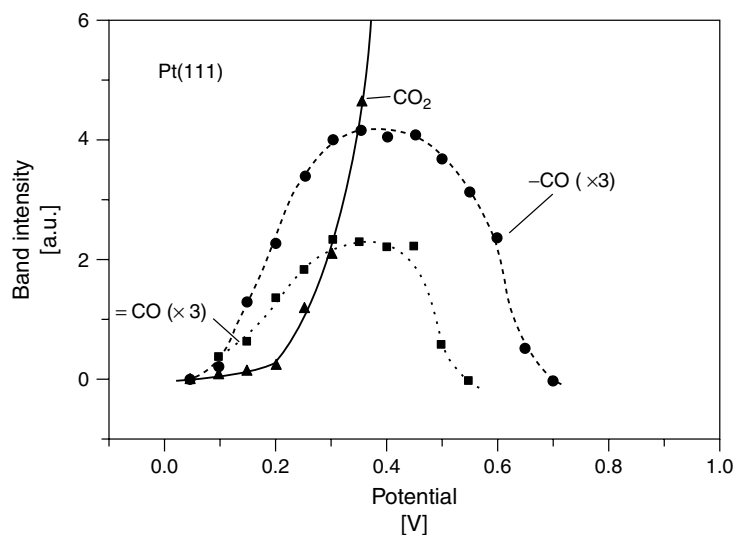
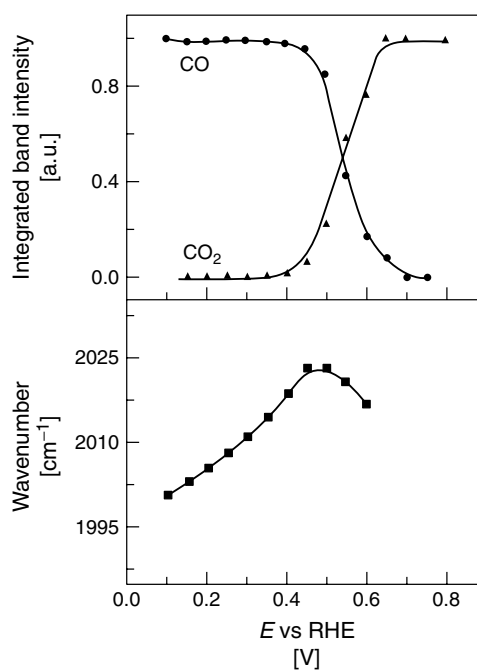


**Fig. 12** Integrated IR band intensities of CO<sub>L</sub> (atop), CO<sub>B</sub> (bridge-bonded), and CO<sub>2</sub> during the first anodic scan at Pt(111) in 0.1 M HCOOH/0.1 M HClO<sub>4</sub> as function of potential [38].

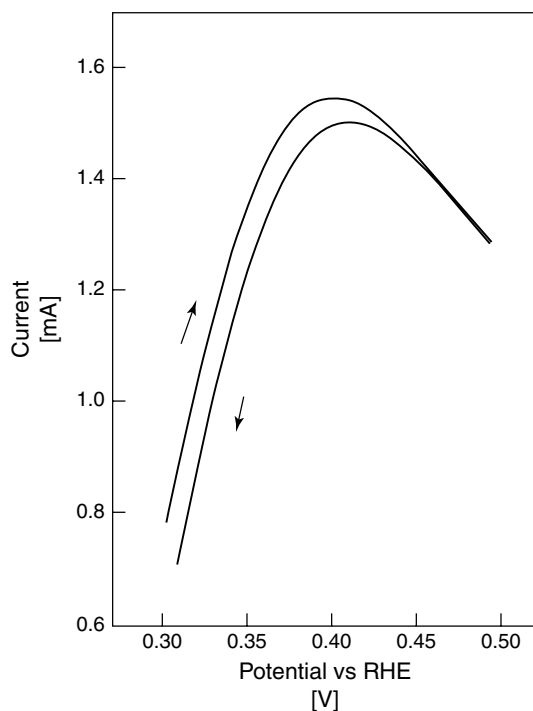


**Fig. 13** CV for a Pt(111) electrode in 0.1 M HCOOH/0.1 M HClO<sub>4</sub> [44, 45]. The potential is reversed at 0.5 V, sweep rate 50 mV s<sup>-1</sup>.

A first satisfactory explanation of the symmetric current/potential response can be given via a recent infrared spectroscopy study [44, 45].

Potential-dependent bands for the OH stretching and HOH bending mode of water have been analyzed and interpreted in terms of the interactions of water molecules with the electric field of the double layer and with the metal surface [46]. In short, the shift of the bending mode in the potential region of 0.4 to 0.9 V indicates O-adsorbed water molecules being oriented from a tilted to perpendicular position at the surface (Fig. 14). With increasing potential, water dipoles acquire a configuration of minimum interaction

energy with the electric field in the double layer. In this position, participation of the 3a orbital of the H<sub>2</sub>O molecule results in an increased HOH-bond angle and, consequently, in a red shift of the bending mode. Obviously, the interaction of water with the platinum surface seems to be stronger than assumed so far. The interaction leads to a partial dissociation of water, a phenomenon observed for several adsorbed weak acids. Since the dissociation of water produces OH, the interaction described can play an important role in the electrocatalytic properties of the system.

It is interesting to observe that using the Pt(111) surface, a *symmetric* current response is present, even when the

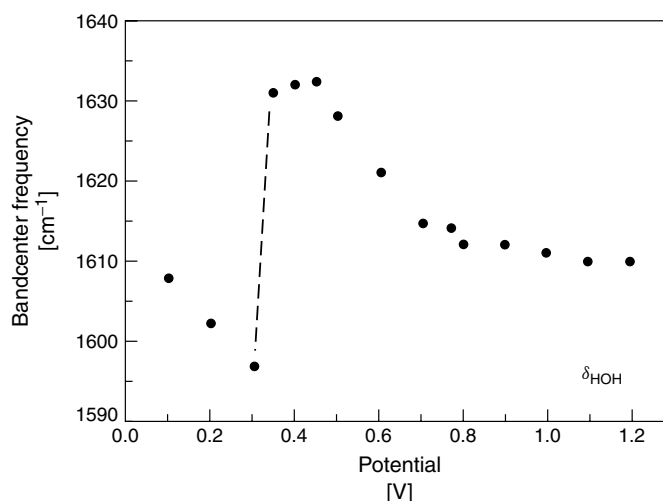


**Fig. 14** Potential dependence of the wave number for the in-plane deformation (scissor mode) of water adsorbed at Pt(111) [44, 45].

potential scan is reversed already near 0.5 V. A similar behavior was reported by Capon and Parsons [9] for polycrystalline platinum. Obviously, the process for the current decay depends reversibly on the potential. This can be explained assuming that a stronger H<sub>2</sub>O interaction is unfavorable for HCOOH adsorption. In addition, the onset of current near 0.2 V, well below the beginning of CO oxidation, proves that the direct reaction pathway of HCOOH oxidation is active. This reaction model is supported by the fact that the CV of CO oxidation shows also a maximum in the negative scan, if the energy of adsorption is low as in the case of silver [45], but *not* for the strongly adsorbing metal platinum [44, 45].

**5.2.3.2.4 Methanol** The adsorption model presented above for HCOOH emphasizes that organic species have to compete with water for an adsorption site, that is, we assume an energy barrier for

the desorption of water comparable with that of the studied organic molecules. TDS data of gas/solid interfaces indicate a chemisorbed state of water at 170 to 180 K [47, 48]. Assuming a first-order kinetic and a preexponential factor of  $10^{13} \text{ s}^{-1}$ , the bond strength of water should be in the order of 42 kJ mol<sup>-1</sup> [49]. The peak temperatures for desorption at Pt(111) are 190 K for CH<sub>3</sub>OH, 170 K for HCOOH, and 200 K for C<sub>2</sub>H<sub>5</sub>OH [47, 48]. Accordingly, the adsorption energy for the undissociated molecules should be in the same order as that of water. Calculated from TDS data, the bond strength of CO lies in the order of 108 kJ mol<sup>-1</sup> [50]. Assuming the same relationship in ultrahigh vacuum (UHV) as at the electrochemical interface, a competition with water for Pt sites can be expected from small organic molecules, but not from CO. And indeed, the absence of a “reactivation peak” had been observed on voltammograms at polycrystalline [51] and single-crystal platinum [52] in CO-saturated solution.

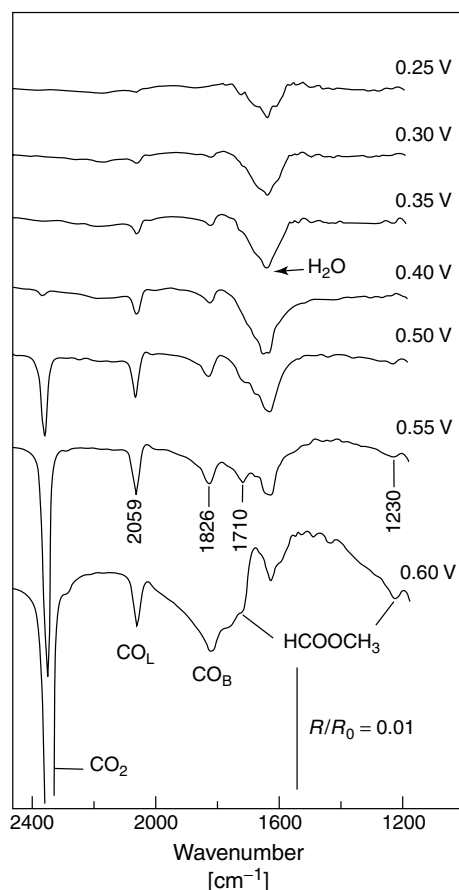


**Fig. 15** In situ FTIR spectra at Pt(111) in 0.5 M CH<sub>3</sub>OH/0.1 M HClO<sub>4</sub> at different potentials, reference spectra at 0.1 V versus RHE (256 scans, 8 cm<sup>-1</sup> resolution) [53].

Figure 15 shows in situ FTIR spectra during the oxidation of methanol on Pt(111) in 0.5 M CH<sub>3</sub>OH/0.1 M HClO<sub>4</sub> at potentials between 0.25 and 0.60 V [53]. Besides CO<sub>2</sub> production, formation of atop CO and bridged CO, one has bands due to HCOOCH<sub>3</sub> formation near the interface at 1710 and 1230 cm<sup>-1</sup>. The development of the (integrated) band intensities with electrode potential is given in Fig. 16. As in the case of HCOOH oxidation (Fig. 12), both types of CO adsorbates are formed with a maximum near 0.5 V together with an early CO<sub>2</sub> production, obviously due to

a direct pathway of methanol oxidation. Adding ruthenium clusters to the Pt(111) surface (for details see the next paragraph), the weak band of bridge-bonded CO is not more observed and CO<sub>2</sub> production starts ca. 100 mV earlier.

Infrared spectroscopy is able to prove the development of two more multibonded adsorbates, the earlier-discussed COH<sub>ad</sub>, and a CH<sub>x</sub>OH<sub>ad</sub> species. These bands have been discovered years later than the different CO adsorbates because of their relatively slow development with time [15]. The time-resolved formation is presented

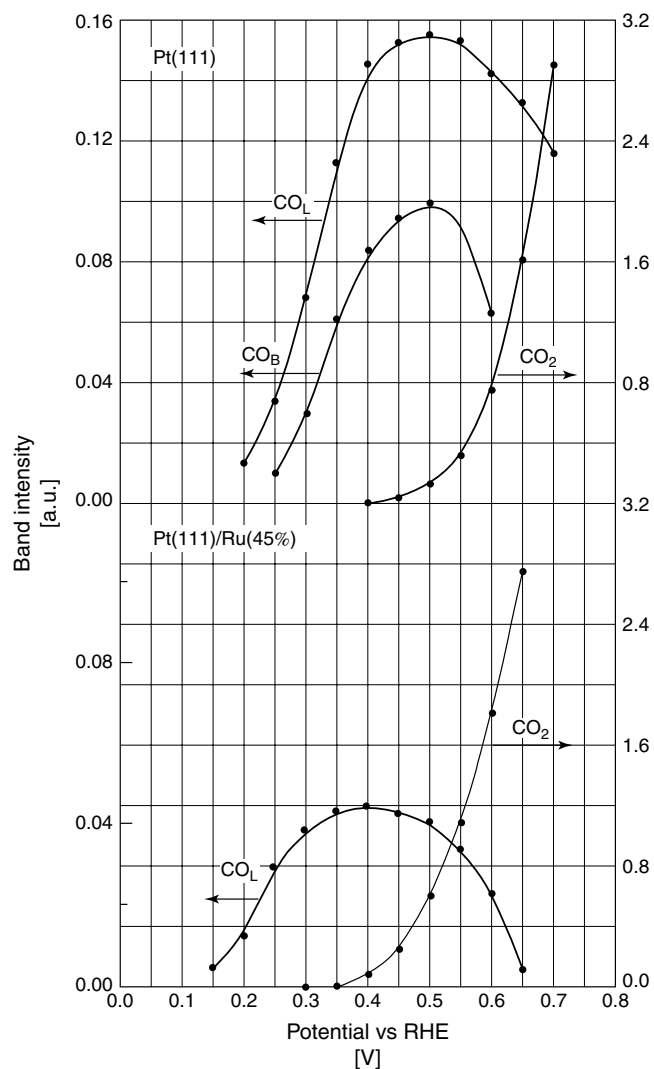


**Fig. 16** Integrated IR band intensities of  $\text{CO}_L$  (atop),  $\text{CO}_B$  (bridge-bonded), and  $\text{CO}_2$  during methanol oxidation at Pt(111) and at Ru(45%)/Pt(111) in 0.5 M  $\text{CH}_3\text{OH}$ /0.1 M  $\text{HClO}_4$  as function of potential [53].

in Fig. 17 for smooth polycrystalline Pt from 1 M  $\text{CH}_3\text{OH}$ /0.1 M  $\text{HClO}_4$  solution. Atop CO signals are given for comparison. It is important to note that an adsorption

band for a species like  $\text{HCO}$ , which was discussed also as an alternative [54], has to be expected according to calculations near  $1900\text{ cm}^{-1}$ . On the other hand, the

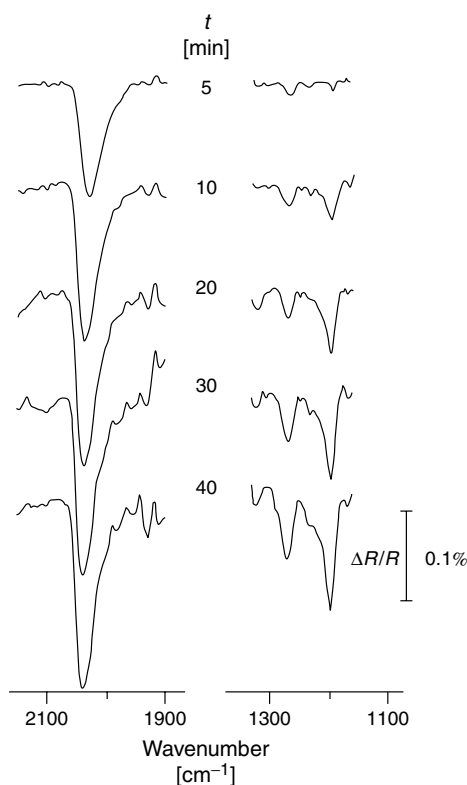


**Fig. 17** In situ FTIR spectra (1024 scans,  $8\text{ cm}^{-1}$  resolution) at smooth polycrystalline platinum, time-resolved formation of atop CO (ca.  $2050\text{ cm}^{-1}$ ), threefold-bonded COH ( $1256\text{ cm}^{-1}$ ), and  $\text{CH}_x\text{OH}$  ( $1200\text{ cm}^{-1}$ ), adsorbed from  $1\text{ M CH}_3\text{OH}$  and  $0.1\text{ M HClO}_4$ , adsorption potential  $350\text{ mV}$ , reference potential  $50\text{ mV}$  versus RHE [15].

experimental data for COH fits well with the theoretical value [55–58]. In addition, the preliminary note, favoring HCO [54] was found to be an experimental error. The nature of the adsorbate was later clearly shown to be COH, via a DEMS experiment (Ref. [18–20]) by using labeled isotopes [7].

Additional experiments with the same electrolyte, but using single-crystal surfaces, show that for Pt(111) and Pt(100) the  $1260\text{ cm}^{-1}$  COH band starts developing near  $150\text{ mV}$  versus RHE [26, 27].

#### 5.2.3.3 Metal Alloys and Binary Metal Catalysts

It is now well established that Pt metal combinations such as PtRe, PtSn, PtIr, and

especially PtRu show a drastic enhancement in catalytic activity for methanol oxidation. The first results have been published already more than 30 years ago, see for example Ref. [59] on PtRu, [60] on PdRu, [61, 62] on PtMo and PtSn, but especially [63] on PtRu, on Raney metals of Pd, Ru, Pt, Rh, Ir, Os and their mixtures. Different results have been obtained by the different authors, but the positive effects of ruthenium in combination with platinum were never in doubt.

The mechanism of the ruthenium effect was first described by Watanabe and Motoo [17], postulating a *bifunctional mechanism* in which platinum serves as catalyst for a dissociative methanol adsorption and

ruthenium (in the form of islands, clusters, or atoms) for the formation of a Ru-OH species, being used finally for a successive oxidation of methanol adsorbates (Fig. 1). It has to be noted that at room temperature ruthenium does not adsorb methanol [64], the first step of adsorption takes place in the presence of Pt sites only.

In the following, we discuss the PtRu system as a model catalyst. Binary PtRu electrocatalysts are presently studied in many different forms, PtRu alloys [65–68], Ru electrodeposits on Pt [69, 70], PtRu

codeposits [71–73], Ru adsorbed on Pt [74], and Ru evaporated on Pt [75]. All these materials present an enhanced activity for methanol oxidation.

The determination of the surface composition of PtRu samples has been the matter of several investigations. The simple use of CVs has the handicap that features, clearly associated with the Ru coverage as in the case of hydrogen for platinum, do not exist (Fig. 18). Watanabe and Motoo [17] suggested the formation of RuOH in the potential range between 0.34 and 0.9 V of the CV. They defined the ratio

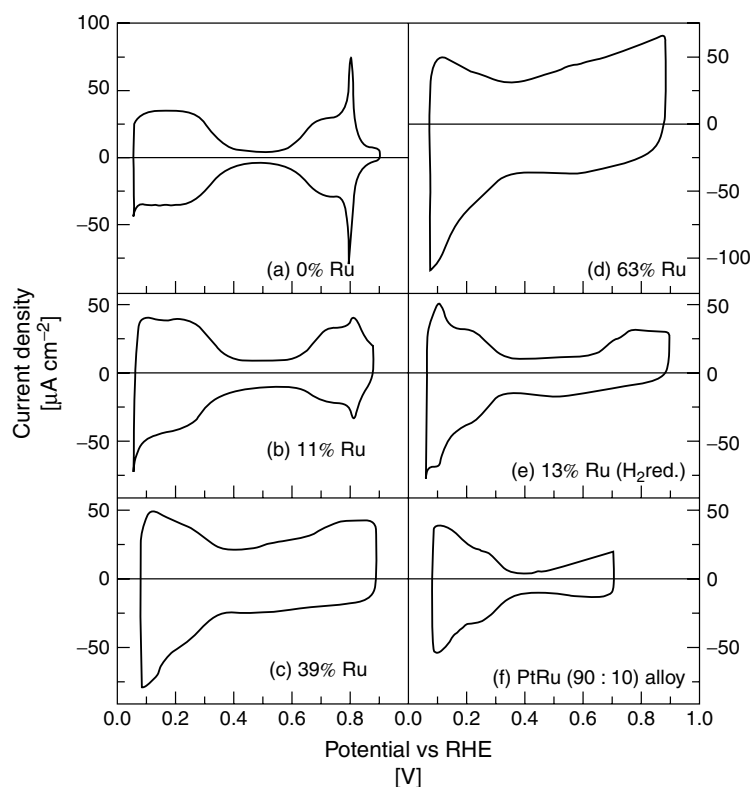


**Fig. 18** CVs at  $50 \text{ mV s}^{-1}$  for Pt(111), different Ru-modified Pt(111) surfaces and a PtRu alloy in  $0.1 \text{ M HClO}_4$ ,  $25^\circ \text{C}$ ; (a) Pt(111), (b–d) using spontaneous Ru adsorption, (e) Ru adsorption and simultaneous reduction by hydrogen [75].

between the charge for RuOH formation and the charge for H atom desorption as a measure for the degree of coverage with Ru atoms. Frelink and coworkers [76] assumed a two-electron process for RuO formation. Since methanol oxidation is a surface-sensitive process, IR spectroscopy using single-crystal surfaces covered with submonolayers of ruthenium is an obvious approach for a better understanding [26–29].

For a first evaluation of the PtRu surface composition, we compare in Fig. 18 the CVs of a clean Pt(111) surface with the CVs of Ru-modified Pt(111) and a PtRu alloy. For Pt(111), the characteristic features for

hydrogen adsorption/desorption and the so-called anomalous states are observed. As the surface becomes covered with increasing amounts of Ru, the sharp peak at 0.78 V decreases and the charge for the formation of Ru oxides in the double-layer region increases. The sample prepared via Ru reduction with hydrogen (Fig. 18e) exhibits a sharp peak at ca. 0.1 V. The forms of the CVs of Fig. 18(b–d) confirm the lack of clear features indicating well-defined surface processes that could be used for coverage determinations. For Ru-modified Pt(100), the existence of more than one surface process has been clearly observed [77].

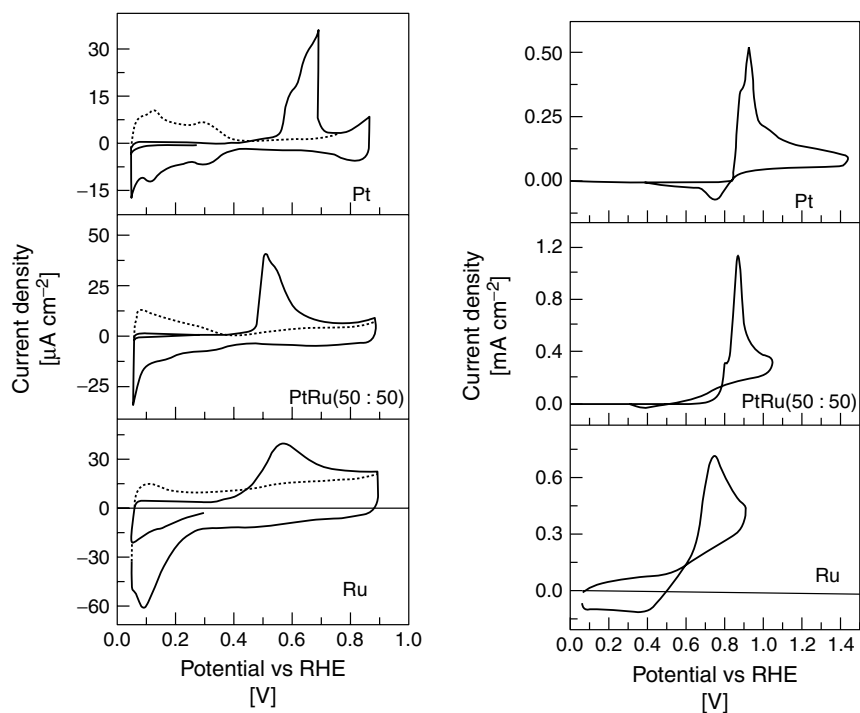


**Fig. 19** CVs for oxidative stripping of CO (left side) and oxidation from CO-saturated solution (right side), 0.1 M HClO<sub>4</sub>; for stripping saturation of surface with CO at 0.3 V; dashed: second scan coinciding the CV of a clean surface in the supporting electrolyte, 50 mV s<sup>-1</sup> [36].



**5.2.3.3.1 CO Oxidation** For the characterization of electrode activity, usually two different CVs are taken: a stripping voltammogram (left side of Fig. 19) or a voltammogram in CO-saturated solution (right side of Fig. 19). As can be seen in the figure, the optimum PtRu composition is very different in both cases. For a stationary rate of CO oxidation from solution, pure ruthenium is by far the best catalyst. When taking a stripping voltammogram, clearly a binary metal surface is the better option. At room temperature, one finds an optimum composition near Pt:Ru = 1:1 [78] up to Pt:Ru = 1:2 [79], depending on potential. This fact demonstrates that at a CO-free surface the overall reaction, adsorption and oxidation, is best catalyzed by a one-to-one addition of platinum atoms to ruthenium. For the oxidation of methanol, at least at room temperature, this is not the case, probably because of the fact that for adsorption of

the methanol molecule, three neighboring Pt sites are needed.

**5.2.3.3.2 Oxidation of Methanol** The oxidation of methanol via a binary catalyst will be discussed for PtRu combinations as a model system. As known from early investigations [59, 63] and already demonstrated here with the IR results of Fig. 16, PtRu surfaces are strongly enhancing the oxidation of methanol. In order to approach the behavior in the stationary case, we analyze the activity mainly in the form of  $i(t)$ -curves.

In Fig. 20, electrocatalytic activities at room temperature are compared as function of Ru percentage at the surface, for Ru-modified Pt(111) and UHV prepared alloy electrodes [75]. Disc-shaped PtRu alloys (Johnson–Matthey) of 5 mm diameter and 2 mm thickness were polished to a mirror finish and treated in UHV by Ar sputtering and heating according to Ref. [80]. After

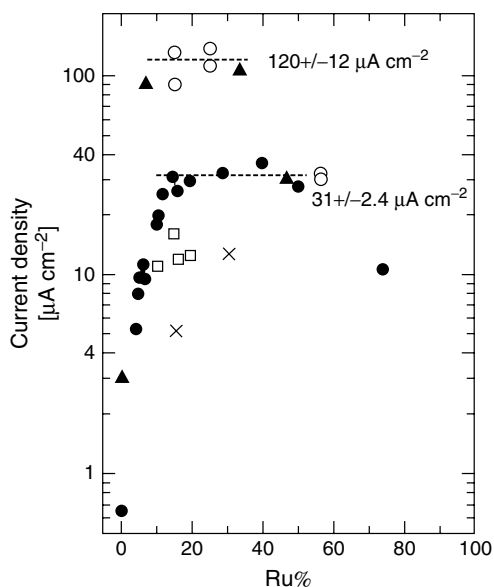


**Fig. 20** Plot of current densities for methanol oxidation from amperometric curves at 0.5 V after 300s and for different PtRu surfaces [75]. (●) Ru/Pt(111) formed by spontaneous adsorption, (□) Ru-modified Pt(111) via Ru adsorption and simultaneous reduction by hydrogen, (×) Ru coverage by UHV vapor deposition, data obtained after 20 min, (○) UHV-prepared PtRu alloys (see text), (▲) data of UHV-prepared PtRu alloys from Ref. [67] for comparison.

application of a potential step from 0.05 to 0.5 V, the current was measured after 20 min [75]. For spontaneous adsorbed Ru, a pronounced growth in activity is observed with increasing coverage, followed by a broad maximum near  $30 \mu\text{A cm}^{-2}$  between 15 and 50% Ru. Related to clean Pt(111) (see in figure), the activity is increased by a factor of ca. 50. Ru deposits obtained via reduction of Ru with hydrogen or via evaporation of Ru present a three times lower activity than spontaneous adsorbed Ru. Highest data are obtained by the alloy samples. Values measured by Gasteiger and coworkers [67] are also plotted in the figure. A maximum of activity of ca.  $120 \mu\text{A cm}^{-2}$  is observed between 10 and 40% Ru. Again three times more activity is shown than using spontaneous adsorbed ruthenium.

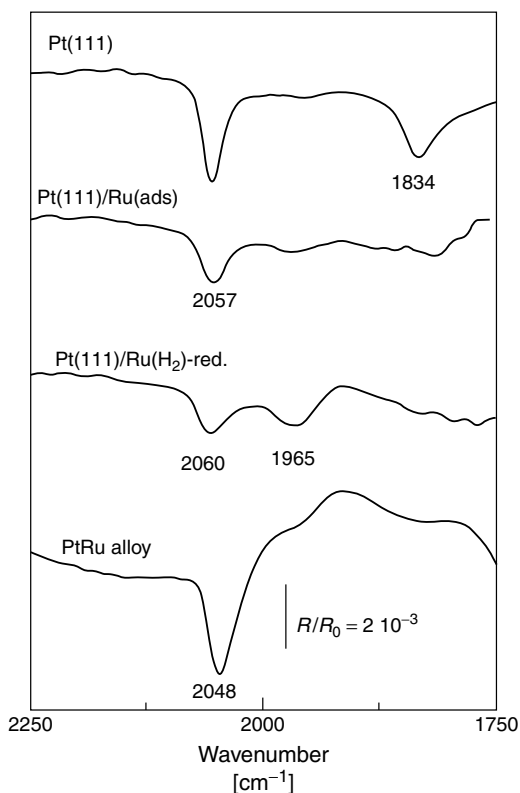
According to a model suggested for the bifunctional mechanism, a surface structure having one Ru atom neighboring three Pt sites represents the optimum geometry for methanol oxidation [81]. On account of this, it was predicted that activity/composition plots should have a maximum near 10%. The experimental results do not support such a prediction. This is not surprising since an ordered surface structure as ideally proposed [81] does not exist in real systems, even for ordered structures like Pt(111). In this respect, it is noteworthy that Pt deposited onto Ru(001) under UHV conditions segregates into clusters also [82]. In addition, the model calculation giving a sharp peak near 10% Ru [81] only holds if the dissociative adsorption of methanol is rate determining. But the benefit of a homogeneous distribution of Pt and Ru sites in contrast to an island structure must be emphasized. Thus, in Fig. 20, the alloys are present by a factor of three higher currents than spontaneous adsorbed Ru/Pt(111) electrodes.

But so far, a *direct proof* for a homogeneous distribution of Pt and Ru in the alloy does not exist.

The data of Fig. 20 show that for alloys, under the experimental conditions of room temperature and 0.5 M  $\text{CH}_3\text{OH}$  concentration, the rate of reaction is more or less independent of surface composition in the range between 10 and 40% Ru. Within this range, neither the number of Pt sites (necessary for methanol dissociation) nor of Ru sites (necessary for water dissociation) can be regarded as rate-limiting factors. Obviously, the kinetic limitation is caused by the reaction between adsorbed CO and RuOH. Therefore, a homogeneous distribution of Pt and Ru atoms must have a strong influence on the rate. Indeed, the optimum distribution is that of alloys. For samples forming Ru islands, the method of preparation must be chosen in such a way that the diameters of the islands are as small as possible. In order to have a first approximation of cluster size, in situ IR spectroscopy can be of help, as shown below.

Cramm and coworkers studied the CO-IR signal on Ru-modified Pt(111) surfaces [83]. With increasing Ru coverages from 25 to 60%, an increasing signal for CO adsorbed at Ru sites was observed. Near the  $2070 \text{ cm}^{-1}$  band for atop CO on Pt sites, a new band near  $2010 \text{ cm}^{-1}$  clearly develops. The influence of the preparation procedure on the CO-Ru adsorption band is shown in Fig. 21. From the two electrodes with adsorbed Ru-clusters, only for ruthenium adsorbed via hydrogen a band at  $1965 \text{ cm}^{-1}$  is clearly observed. The difference in signal should be attributed to the formation of different size Ru islands, depending on the preparation method. Larger islands seem to be formed by the  $\text{H}_2$ -reduction procedure. This justifies the relatively low activity of the latter

**Fig. 21** Comparison of CO bands in FTIR spectra for methanol on different samples of Fig. 20: Pt(111), Pt(111) with spontaneously adsorbed Ru(39%), with Ru reduced by hydrogen and PtRu alloy, 15% of Ru each [75].



sample. Obviously, surface structure and Pt/Ru distribution determine the electrocatalytic activity.

The behavior of the PtRu system for methanol oxidation changes strongly with increasing temperature. At 40 to 60 °C, ruthenium can adsorb and oxidize methanol also. Therefore, less Pt sites are necessary for the steps of adsorption and dehydration. Results on PtRu surfaces show indeed a shift of the optimum PtRu ratio to higher Ru contents near 50% [84]. For porous PtRu clusters on carbon black at 60 °C, Watanabe and Motoo [17] have shown an optimum PtRu ratio near 50%.

Beside the successful system PtRu, many other platinum metal combinations

have been checked as catalyst for methanol oxidation, for example, PtPd, PtAu, PtIr, and PtOs [85], or even multimetal systems like PtRuOs and PtRuOsIr [86]. The current/potential plots do not markedly differ and are therefore difficult to analyze. In addition, a current normalization via  $\text{mgPt cm}^{-2}$  or  $\text{mgMetal cm}^{-2}$  or via BET was performed. A more realistic determination of the active surface has been suggested using oxidative stripping of CO [73]. Investigations on smooth PtSn alloys [81, 87] have been negative in spite of the fact that a number of publications show increased activities for Sn, electrodeposited on platinum (for a survey, see [88]).

Binary catalysts other than PtRu show increased activity for the oxidation of CO and HCOOH also. For CO, the alloy Pt<sub>3</sub>Sn alloy was studied in detail and with interesting results [81, 87].

**5.2.3.3.3 Ad-atom Effects on Formic Acid Oxidation** Submonolayers of some metal atoms, irreversible adsorbed or underpotentially deposited (upd) [89] on a metal substrate, can present electrocatalytic properties different from those of the pure metals. They may be similar to those of alloys or codeposited metals [90]. Typical examples are submonolayers of As, Sn, Bi, Tl, and Pb on platinum [91–93]. Since a upd layer can exist within a given potential range only, this modified catalyst may not fulfill the conditions for technical application.

A noticeable increase in activity on formic acid oxidation was already observed 30 years ago [94], at polycrystalline platinum in the presence of  $10^{-5}$  M Pb

ions in solution. These ions form surface ad-atoms at potentials of interest between ca. 100 and 500 mV RHE. Figure 22 shows CVs obtained at smooth Pt, with and without the addition of Pb<sup>2+</sup> ions to the electrolyte. The current is increased by two orders of magnitude. As already discussed in Sect. 5.2.2.2, the Pb ad-atoms catalyze the *direct* pathway of formic acid oxidation. To our knowledge, the PtPb system is the only upd catalyst with successful stationary data. At  $10 \text{ mA cm}^{-2}$  and at room temperature, a cathodic shift of potential by 200 mV was observed for hours [95].

Ad-atom electrocatalysis in the case of formic acid oxidation can be divided into two terms: (1) inhibition of surface poisoning by CO formation (indirect pathway), and (2) true enhancement of the rate of oxidation (direct pathway). For most ad-atoms, these effects are mixed. An example for the mixed case is the Sb ad-atom adsorption on Pt(100) [96]. The reaction takes place on single Pt sites and randomly

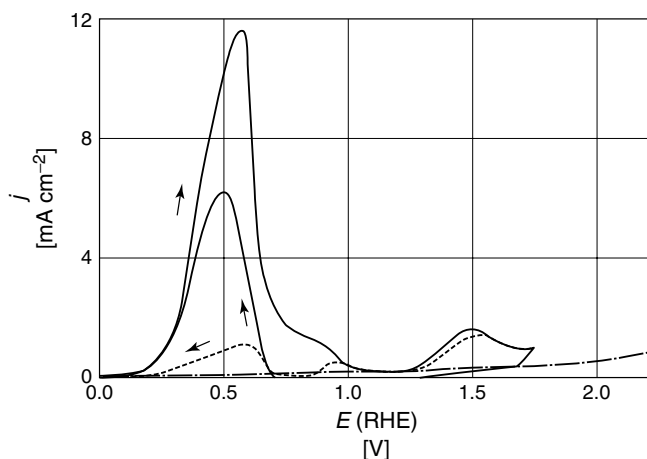


**Fig. 22** Cyclic Voltammograms for formic acid oxidation at smooth polycrystalline platinum, without addition (dotted lines) and with lead ions in the electrolyte (full lines); 1 M HCOOH/1 M H<sub>2</sub>SO<sub>4</sub>,  $10^{-5}$  M Pb<sup>2+</sup>,  $50 \text{ mV s}^{-1}$  [94].

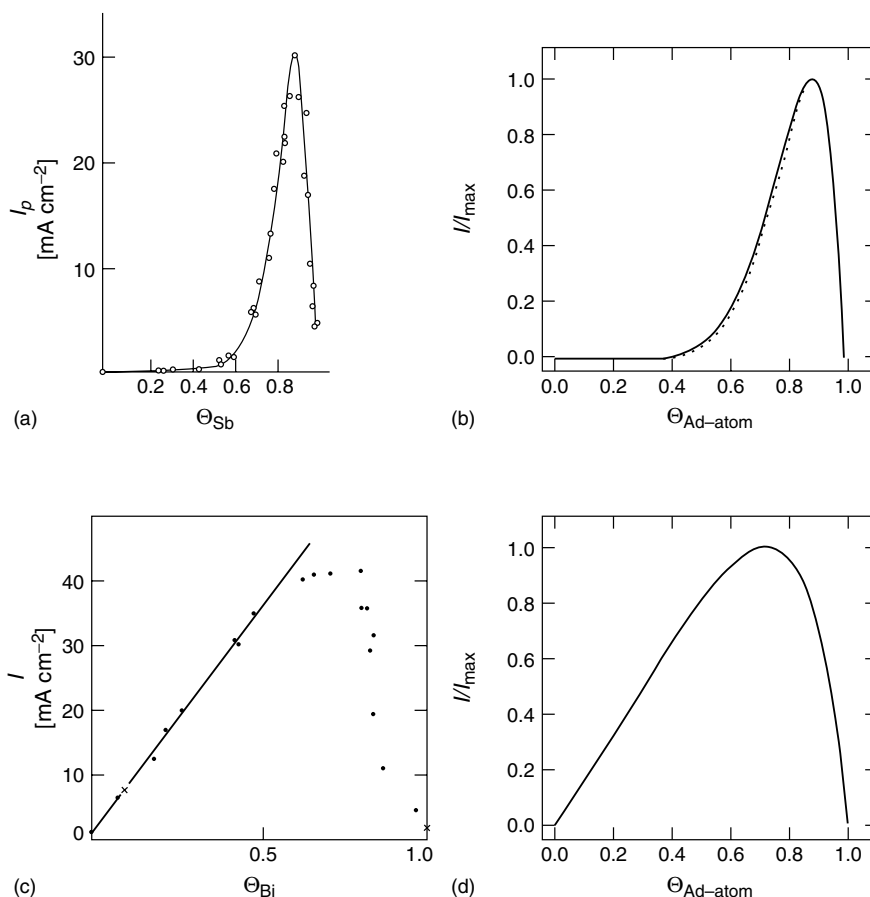


**Fig. 23** Comparison of experimental and simulated current/ $\Theta_{\text{ad-atom}}$  plots for the oxidation of formic acid. (a) Sb-modified Pt(100) surface [96]; (b) simulated curve for a pure third-body effect (current proportional to the

number of *isolated* Pt sites) [97]; (c) Bi-modified Pt(111) surface [101]; (d) simulated curve for a true catalytic effect (current proportional to number of *ad-atom-free* Pt sites [97]).

distributed ad-atoms may block neighboring places, making some isolated sites available for the direct oxidation. In addition, the rate of reaction per free Pt site is enhanced. In Fig. 23, we have in (a, b) a comparison between the experimental current/ $\Theta_{\text{Sb}}$  plot and a simulation under the conditions of randomly distributed ad-atoms and a reaction rate proportional

to the number of isolated Pt sites [97]. All other places are occupied by ad-atoms or by poison. This effect had been called *third-body effect* [98]. On well-defined surfaces, some ad-atoms form geometric arrangements. Thus, Se atoms can form a  $(2 \times 2)$  layer on Pt(111), exhibiting isolated Pt sites, surrounded by Se atoms occupying three-fold places [99]. In such an arrangement,

the third-body effect is particularly effective (*ensemble effect*). A true enhancement effect with a current density of  $3.2 \text{ mA cm}^{-2}$  (at the poison-free surface) and  $40 \text{ mA cm}^{-2}$  at a  $\Theta_{\text{Bi}} = 0.8$  was observed for Bi on Pt(111) [96]. This represents an increase in rate per free Pt site by a factor of ca. 70. In addition, Bi coverages of only 10% totally inhibit the formation of CO [100]. The rate of reaction depends, for this system, on the number of ad-atom/free site pairs. In this case, in Fig. 23(c, d), the experimental plot [101] is again compared with the simulated curve [97].

#### 5.2.4

##### Surface Structure and Methanol Electro catalysis

From the discussions in the above chapters, we learned already that surface structures are of special importance for methanol oxidation as a result of the required bifunctional catalyst properties. A first step to use STM images to gain a better insight into this matter was done by Cramm and coworkers [83]. Electrodeposits of Ru islands on Pt(111) in 0.1 M  $\text{HClO}_4$  were characterized by STM images. Islands of monoatomic height and between 2 to 5 nm of diameter are shown for two different Ru coverages. More recent results will be presented in the following paragraph.

##### 5.2.4.1 Ex Situ STM Images Taken during Methanol Oxidation via UHV Transfer

In order to follow the morphology of a Ru/Pt(111) surface during methanol oxidation, the following modification of an Omicron standard preparation and analysis chamber was made [102]. The manipulator was extended by a platinum shield to avoid foreign metal deposition. The external load-lock chamber was modified to

allow insertion of a mini electrochemical cell. With these additions, a UHV transfer from the electrochemical cell to the STM position and back was possible.

An example of the results obtained is given in Fig. 24 (a, c), which show the morphology shortly after preparation of the electrode. After UHV transfer to the electrochemical cell, methanol was oxidized at this surface at 500 mV for 50 min. It followed cleaning with water and UHV transfer back to the STM. From Fig. 24 (b, d), it can be concluded that almost no change in morphology took place.

In a second experiment, the activity of different PtRu model surfaces is characterized via current/time curves after a potential step from 300 to 500 mV (Fig. 25) [103]. Because of the pronounced differences in activity, the plots are given in a half logarithmic scale. Two layer islands (A) and smooth Ru surface alloys (B) show strong decay and lower currents than Ru monolayers on smooth Pt(111) (C). Ion bombardment before (D) or after (E) Ru island formation increases the activity. But highest current densities were obtained for the PtRu(85 : 15) electrode (F) with the by far finest distribution of Ru and Pt atoms in the surface.

All current–time plots in Fig. 25 show a marked decay with time. This phenomenon will be discussed in the next paragraph.

##### 5.2.4.2 Current Decay at Smooth Surfaces

When comparing the catalytic properties of different smooth surfaces, it is essential to have a suitable measure or definition for the catalytic activity itself. For this purpose, current–time curves at potentials between, 0.35 V and 0.5 V versus RHE, had been used [67, 104]. As a common feature for all model catalysts, the resulting  $i(t)$ -curves show a pronounced decay at

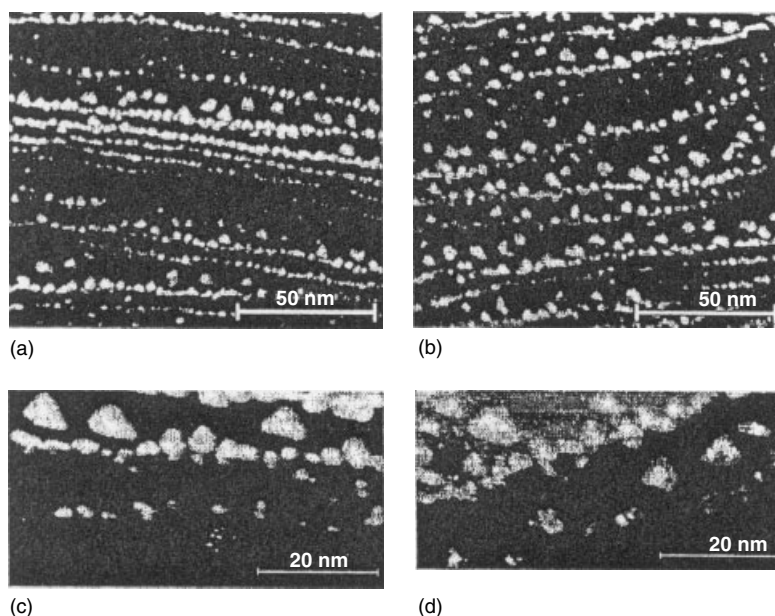


**Fig. 24** Morphology of a Ru/Pt(111) electrode taken via STM before and after 50 min methanol oxidation at 500 mV in 0.5 M CH<sub>3</sub>OH/0.1 M HClO<sub>4</sub>. Potential step from 50 to 500 mV RHE [103].

the beginning, which becomes less steep after ca. 10 min (Figs. 25 and 26). All smooth probes present a current decay that was also observed for spontaneously adsorbed Ru at Pt(111) [74, 75]. In most publications, the current density after 10 to 30 min has been regarded as a good measure for the catalytic activity of the respective surface. However, in all cases, it is clearly visible that at this time a steady state was yet not reached, this way of defining the catalytic activity appearing thus unsatisfactory. Same decay curves as in Fig. 26 have been reported for all three single-crystal Pt surfaces and potentials below 550 mV [74, 105]. Already at 600 mV, Stuve and coworkers report about a stationary current at Pt (111), 10s after potential step from 55 to 600 mV [106].

Three main points should be discussed in connection with the above observation. First, there is a pronounced decay of the current occurring at the beginning of the experiment. The current decreases by a factor of about two during the first 10 min of application of the potential step. A current limitation by mass transport is unlikely for CH<sub>3</sub>OH concentrations of 0.5 M; current densities in the 100 mA cm<sup>-2</sup> range could be achieved from that point of view.

A second important aspect of the current–time response is the fact that the current does not look like it is going to reach some steady state value even after 30 minutes. In fact, the decay is observed over hours [104].

The third and probably most interesting feature is that in many cases the current–time curves measured on freshly

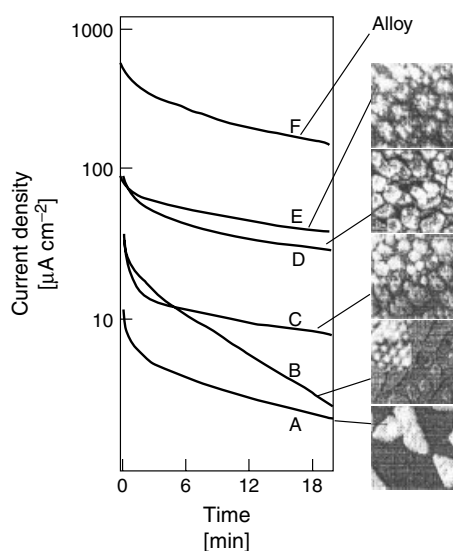


**Fig. 25** Structure of PtRu model electrodes and catalytic activity for methanol oxidation after a potential step from 300 to 500 mV RHE; current/time curves under conditions as in Fig. 24 [103]; (A) Two layer Ru island formation on Pt(111) by Ru evaporation at 400 K; (B) Smooth Ru/Pt(111) surface alloy; (C) Ru evaporated on smooth Pt(111); (D) Ru evaporated on a rough Pt(111) surface; (E) Ru evaporated on Pt(111) and roughened via ion bombardment; (F) Sputtered PtRu alloy (85 : 15), STM image not possible.

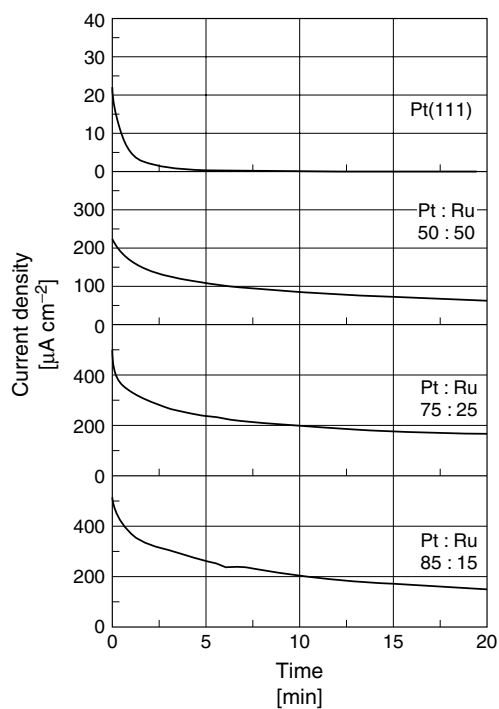


**Fig. 26** Current–time curves after potential step from 300 to 500 mV RHE for different *smooth* catalysts as indicated; 0.5 M CH<sub>3</sub>OH/0.1 M HClO<sub>4</sub>; room temperature [104].



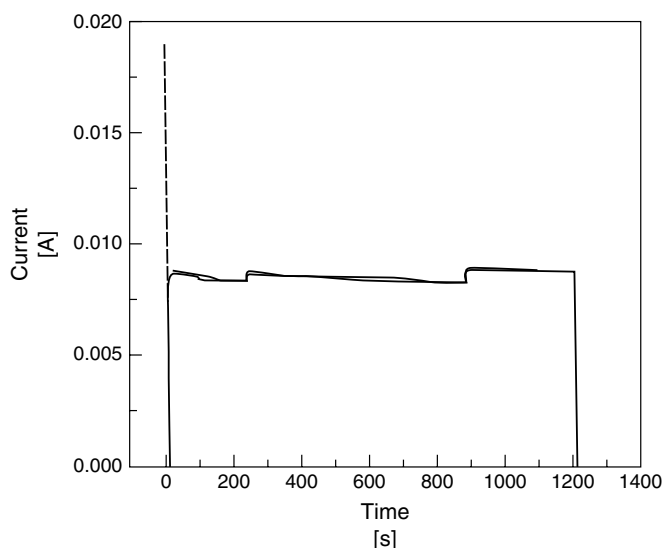


**Fig. 27** Current/time curve for a *porous* PtRu electrodeposited (81:19) on a gold substrate. The steps at ca. 4 min and 14 min are caused by the production of CO<sub>2</sub> bubbles [104].

prepared rough electrode (also on technical fuel cell electrodes) exhibit no decay (Fig. 27). The electrode for this experiment was prepared on a gold substrate (Electrodeposit from 20 mM H<sub>2</sub>PtCl<sub>6</sub> + 2 mM RuCl<sub>3</sub> + 0.1 M HCl;  $E = 100$  mV versus RHE;  $t = 15$  min.) and according to energy dispersive X-ray spectroscopy (EDXS) the catalyst composition was Pt:Ru = 81:19 [104]. The constant current response observed here is comparable to that reported by Chu and Gilman [107] for methanol oxidation at porous PtRu alloys as well as by Aramata and Masuda [108] for porous PtRuAu alloys and 50 °C. In agreement with this behavior, Motoo and coworkers [109] measured a constant cell voltage during polarization of a methanol-zinc cell at 125 mA cm<sup>-2</sup> and 40 °C. However, this behavior of rough electrodes cannot be generalized and, depending on experimental variables

during their preparation, technical PtRu electrodes may present a slow loss of activity. Thus, the main difference between both types of materials is that smooth electrodes *always* present such a current decay. The difference in behavior of both types of materials is probably related to the microstructure of the surface.

Rough surfaces, as those of technical electrodes, are characterized by the presence of a large amount of defects (steps, kinks, etc.) and it is well known that such defects exhibit enhanced catalytic activity for the oxidation of organic residues. Recently, Souza and coworkers [110] observed that electrodeposited PtRu electrodes do present a higher capacity of breaking the C–C bond and producing CO<sub>2</sub> than do smooth materials of the same composition. In this context, it could be possible that hydrogenated residues easily undergo oxidation to CO<sub>2</sub> on defect

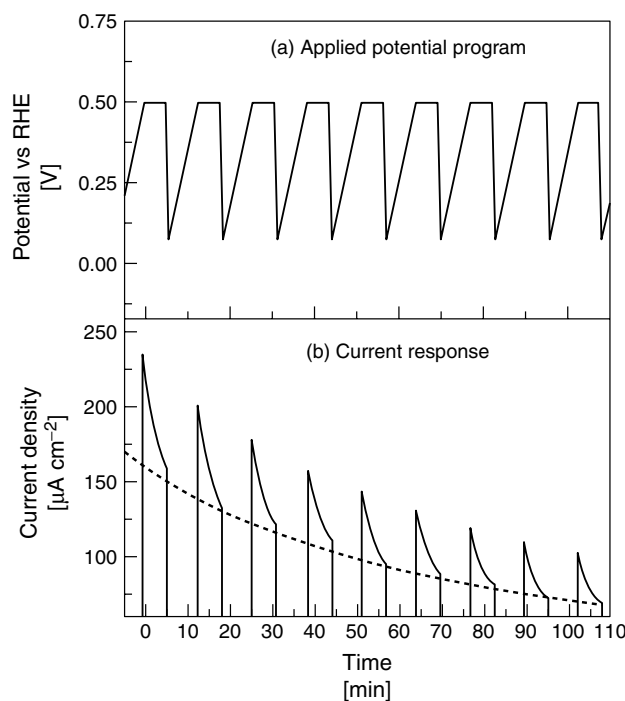


**Fig. 28** Current/time curves for a *smooth* PtRu(85 : 15) alloy as in Fig. 26, but with load interruptions by turning back the potential to its initial value [104].

sites at rough electrodes while smooth surfaces present a lower activity towards this process.

For a better understanding of the first strong decay on smooth electrodes, the potential was repeatedly changed between 75 and 500 mV [104]. After resetting the potential to 500 mV (Fig. 28), the current is higher than at the end of the preceding wave, but the initial value is not recovered. At the beginning of each cycle, we observe an initial fast decay. The deactivation of the smooth PtRu surface has at least two components – a partially reversible one and a second one causing a slow loss in activity that cannot be reversed at low potentials.

The *initial decay*, being a reversible process, could be related to the formation of Ru oxides such as RuO<sub>2</sub> or RuO<sub>3</sub>, their relative ratio depending on potential [111]. These oxides, having Ru in a high valence state, must have a covalent character and it is doubtful as to whether or to what extent they can act as oxygen donors. However, the presence of oxides at low potentials is an indication of the propensity of Ru to adsorb and dissociate water. Thus, adsorbed OH could be present at the Ru surface, being the oxygen donor for the oxidation of organic compounds. X-Ray Photoelectron Spectroscopy (XPS) data for electrodes immersed at 300 and 50 mV versus RHE support the assumption

that oxidation of the Ru component is a quasi-reversible process, undergoing composition changes in the timescale of minutes [112].

The slow deactivation of smooth surfaces could be due to a further accumulation of carbon monoxide blocking active sites. But IR data show that a Pt(111) surface becomes saturated with CO after 2 min, applying a potential step from 50 to 500 mV. On Ru-modified Pt(111), the formation of adsorbed CO is even faster [104]. On the other hand, at sufficient anodic potentials, for example above 1 V RHE, adsorbed poisoning particles obviously can be oxidized. This fact suggests that  $C_nH_m$  compounds, possibly formed during methanol adsorption [56, 110], could be responsible for the slow deactivation.

The slow decay follows the relation

$$\frac{1}{j(t)} = \frac{1}{j^*} + bt \quad (21)$$

with  $j^* = j(t = 0)$  and  $b$  as a characteristic constant. The current must be proportional to the number of active surface sites,  $N(t)$ :

$$j(t) = k'N(t) \quad (22)$$

Eq. (21) suggests a second-order kinetic on  $N(t)$ , which slowly causes the blockage of the surface

$$dN(t) = kN(t)^2 \quad (23)$$

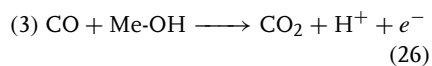
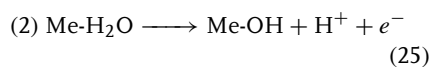
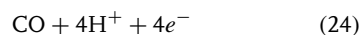
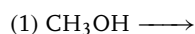
Plotting the reciprocal current versus the time, one observes that for  $t > \text{ca. } 10 \text{ min}$  all curves for smooth alloys follow a function in the described manner [104]. Interestingly, literature results measured at  $60^\circ\text{C}$  follow the same behavior [67].

Using the gradient of the reciprocal current,  $b$ , as a parameter characterizing the deactivation, one observes that the effective activity is, in all cases, reciprocal to the value of  $b$  [102, 104].

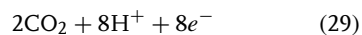
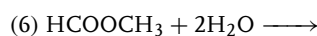
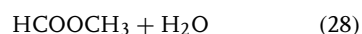
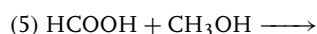
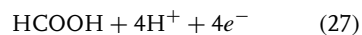
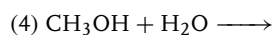
#### 5.2.4.3 Rate-determining Step of Methanol Oxidation

Coming back to the well-analyzed intermediates of methanol oxidation, one has to consider the following scheme for the mechanism:

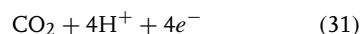
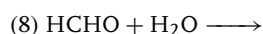
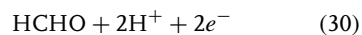
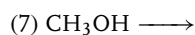
Path one



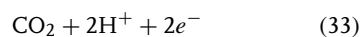
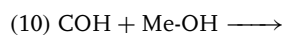
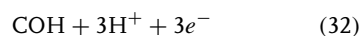
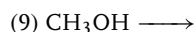
Path two



Path three



Path four



Path four is observed at low concentrations of methanol only ( $<0.1 \text{ M}$ ), and path two will cover not much more than 10% of the total process. Therefore, for the discussion of the rate-determining step, we

have to consider the different issues of path one. If Step (24) is rate determining, adsorption and/or dissociation of the methanol molecule should be slow, that is, the current should depend on methanol concentration. Otherwise the reactive desorption of the surface-blocking CO is the slowest part of the reaction. In this case, the current must be independent of methanol concentration; Step, (25 or 26) being the slowest process.

Literature data show that depending on the experimental conditions, both phenomena can be observed. Chu and Gilman [107] did find for a PtRu(48:52) alloy at 25 and 60 °C, and Schmidt and coworkers [113] for a porous PtRu(52:48) surface at 25 °C, an increase in current by a factor of about 1.3, changing methanol concentration from 0.5 M to 2.0 M. For a porous PtRuAu alloy (Pt:Ru = 50:50) at 50 °C, Aramata and Masuda [108] report a much stronger dependence on concentration between 0.05 and 0.5 M CH<sub>3</sub>OH. Recently, Valdecir-Paganin and coworkers [114] did study the dependence on

methanol concentration for five different porous catalysts and with five different methanol concentrations between 0.1 and 3.0 M. Interestingly, for an E-TEK PtRu(50:50) catalyst, again a strong influence of methanol concentration was found. For PtRu(84:16) and PtRu(75:25), a higher activity was observed, being almost constant between 0.5 and 3 M (Fig. 29). The last data are in good agreement with the plots in Fig. 20. Obviously, in the high activity PtRu region and for 25 °C, the rate-determining reaction is the oxidation of adsorbed CO (Steps 2 and 3 in our scheme for the mechanism) while outside this region (e.g. for the catalysts PtRu(50:50)) the available Pt sites are not enough for a sufficient rate of adsorption of methanol. For Pt(90:10) and of course for pure platinum, the number of Pt sites is high, but the bifunctional mechanism is hindered or even not possible at all.

For a methanol concentration smaller than ca. 0.3 M, we obviously have in all cases the effect of a too low rate of methanol adsorption. In the region of

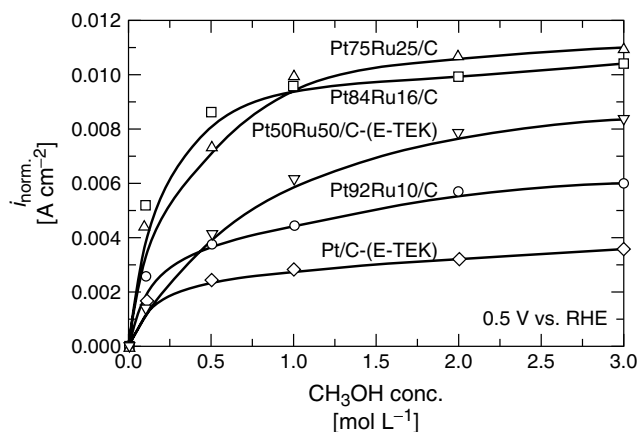


**Fig. 29** Current density, taken 30 min after applying the load, as a function of methanol concentration for different porous catalysts at 25 °C [114].

highest catalytic activity and between 0.5 and 3.0 M of methanol concentration, no change in current is observed, that is, step one is not rate-determining. The rate seems to be proportional to expressions such as Pt-CO/Ru-CO and Ru-OH/Pt-OH. Changing PtRu composition between ca. 15 and 40% Ru, both expressions may compensate each other.

### 5.2.5

#### Instabilities – Oscillations during the Oxidation of Formic Acid, Methanol, and Carbon Monoxide

##### 5.2.5.1 General Conditions for Electrochemical Instabilities

Common for the three molecules CO, HCOOH, and CH<sub>3</sub>OH is the occurrence of maxima in the CV even at concentrations above 1 M in solution, that is, without mass-transfer limitations (Figs. 6 and 7). According to the early study of Bonhoeffer [115] and Franck [116], a negative slope in the steady state current/potential plot (decrease of current with increase of overvoltage,  $di/d\varphi < 0$ , that is, a negative impedance  $Z$  of the interface, Fig. 30) is one physical condition for the phenomenon of oscillations in the case of an applied constant current. Using a potentiostatic circuit, the additional condition  $|z| < R_E$  has to be met, in order to observe bistability or oscillations (see below).

For a better understanding, we study the equivalent circuit of Fig. 31. The output of a potentiostat delivers the voltage  $U$ , applied between the working

electrode and the reference electrode. The working electrode is represented by double-layer capacity  $C_D^W$  and faradaic impedance  $Z_F^W(\omega)$ . Finally the ohmic resistance  $R_E$  is the electrolyte resistance between the working electrode and the Luggin capillary of the reference electrode. The resistance of the counterelectrode and the resistance between the Luggin capillary and the counterelectrode does not have to be considered in a potentiostatic circuit. The applied voltage  $U$  is composed of the voltage drop over  $R_E$ ,  $iR_E$ , and of the potential difference  $\varphi$  between the working and reference electrode, the electrode potential,  $U = iR_E + \varphi$ .

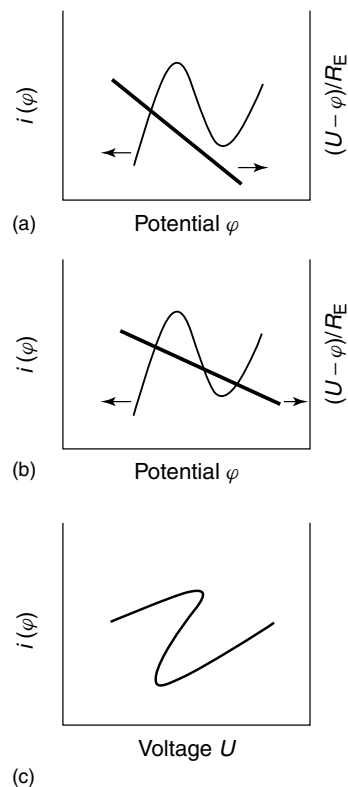


**Fig. 30** N-shaped current–potential curves  $i(\varphi)$  ( $\varphi$  potential of the working electrode) and load lines  $(U - \varphi)/R_E$ ;  $U$  applied voltage,  $R_E$  ohmic resistance: (a) single stationary case; (b) three stationary states (bistability); (c) plot of current  $i$  against the external voltage  $U$ .

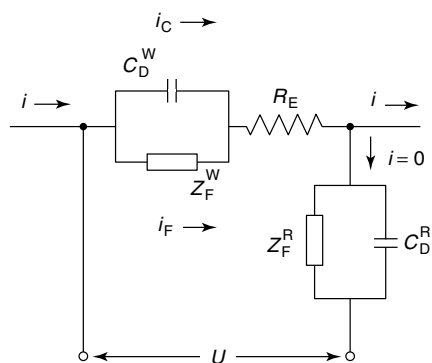


**Fig. 31** Equivalent circuit for the connection of a potentiostat to a working and reference electrode of an electrochemical cell, with double-layer capacities  $C_D^W$ ,  $C_D^R$ , and faradaic impedances  $Z_F^W$ ,  $Z_F^R$  of a working and reference electrode, ohmic resistance  $R_E$  (in most cases electrolyte resistance between the working electrode and end of the Luggin capillary of the reference electrode, and possible external resistance in connection with the working electrode),  $U$  applied voltage,  $i = i_C + i_F$ .

The current through the interface electrode/electrolyte has two pathways,  $i_F$  and  $i_C$ . For the respective differential equation follows:

$$\begin{aligned} i &= \frac{(U - \varphi)}{R_E} = i_C + i_F \\ &= AC_D \frac{d\varphi}{dt} + i_F(\varphi) \end{aligned} \quad (34)$$

with  $A$  as the electrode surface. For a stationary state, with  $i_C = 0$ , we may have the electrode potential  $\varphi_{SS}$ , and Eq. (34) reduces to

$$i = i_F(\varphi_{SS}) = \frac{(U - \varphi_{SS})}{R_E} \quad (35)$$

Two of the possible load lines  $(U - \varphi)/R_E$  against  $\varphi$  are plotted for different values of  $U$  and  $R_E$  in Fig. 30(a, b). The load line in Fig. 30(a) shows one intersection with the  $N$ -shaped  $i(\varphi)$  curve, that is, one steady state. In Fig. 30(b), the two outer intersections are necessarily stable, being on branches with positive slopes. A perturbation of the middle state leads to one of the branches with positive slopes, and the system is therefore called *bistable*. Finally, Fig. 30(c) shows the plot of the current against the applied voltage  $U$ , indicating the influence of the voltage drop  $iR_E$ .

The stability of the potentiostatic circuit is checked by applying a small potential perturbation  $\delta\varphi$ :

$$\begin{aligned} i_F(\varphi) &= i_F(\varphi_{SS} + \delta\varphi) \\ &= i_F(\varphi_{SS}) + \left( \frac{di_F}{d\varphi} \right)_{\varphi=\varphi_{SS}} \times \delta\varphi \end{aligned} \quad (36)$$

where  $(di_F/d\varphi)$  is by definition equal to  $Z_F^{-1}$ . Introducing Eqs. (36 and 34), it follows:

$$\begin{aligned} \Delta i &= \Delta i_C + \Delta i_F \\ &= AC_D \frac{d\delta\varphi}{dt} + \frac{di_F}{d\varphi} \times \delta\varphi \text{ and} \\ \Delta i &= \frac{\Delta(U - \varphi)}{R_E} = \frac{-\delta\varphi}{R_E}, \text{ or} \\ \frac{-\delta\varphi}{R_E} &= AC_D \frac{d\delta\varphi}{dt} + Z_F^{-1} \times \delta\varphi, \text{ or} \\ \frac{d(\delta\varphi)}{dt} &= -(AC_D)^{-1} (Z_F^{-1} + R_E^{-1}) \delta\varphi, \text{ or} \\ \delta\varphi &= \delta\varphi(t=0) \times \exp\{-(AC_D)^{-1} \\ &\quad \times (Z_F^{-1} + R_E^{-1})t\} \end{aligned} \quad (37)$$

Equation (37) shows the time dependence of the perturbation. It follows that  $\varphi_{SS}$  becomes *stable* as long as  $Z_F^{-1}$  has positive values, that is, as long as

$$Z_F > 0 \quad (38)$$

For  $Z_F > 0$ , one has always a function  $\exp(-at)$ .

On the other hand, the system becomes *unstable* as soon as the exponent is positive, that is, for

$$Z_F < 0 \text{ and } |Z_F| < R_E \quad (39)$$

In the case that the current is held constant (*galvanostatic circuit*, which can be approximated with a potentiostatic circuit by introducing a large ohmic resistance  $R_E$ ) and the voltage  $U$  is variable, the condition for instability reduces to Eq. (38), because the second part of the conditions in Eq. (39) is met by definition.

For the evaluation of possible perturbations, that is, of the presence of negative faradaic impedances  $Z_F$ , we now follow the approach of Koper [117] and introduce the Butler–Volmer expression for our current–potential curve

$$i_F(\varphi) = nFA(\varphi)c_s(\varphi)k(\varphi) \quad (40)$$

with  $n$  number of electrons,  $A$  available electrode area,  $c_s$  concentration at the interface, and  $k(\varphi)$  the electrochemical rate constant.

From Eq. (40), it follows for the faradaic impedance

$$Z_F^{-1} = \frac{di_F}{d\varphi} = nF \left\{ A c_s \left( \frac{dk(\varphi)}{d\varphi} \right) + A k(\varphi) \left( \frac{dc_s}{d\varphi} \right) + c_s k(\varphi) \left( \frac{dA}{d\varphi} \right) \right\} \quad (41)$$

We may have three causes for an  $N$ -shaped current–potential curve, which possesses a negative impedance in a limited potential region, that is,  $Z_F^{-1}$  becoming negative values:

1. The rate constant  $k(\varphi)$  decreases with  $\varphi$  if either a species that catalyses the reaction at low potentials is desorbing

at higher overpotentials or a substance that hinders the reaction adsorbs more strongly at higher potentials, as for example, in the case of water molecules.

2. A coulombic repulsion between electroactive species at the electrode, that is,  $dc_s/d\varphi < 0$ .
3. A decrease in the active surface  $A$ , for example, by adsorption of a species that completely inhibits the reaction, or by formation of a passivating layer.

Especially, the last point has to be considered in our investigation of small molecules producing strongly adsorbed CO.

Comparing Fig. 30 with Fig. 4, we can assume that in the potential region between 1.0 and 1.3 V, methanol oxidation could be an example for a negative differential resistance (NDR) system. In addition, from Fig. 30, it can be concluded that  $N$ -shaped systems with a *negative differential resistance* can oscillate at constant potential (*current oscillations*), but not at constant current. As we see below under Sect. 5.2.5.3 and Fig. 35, indeed, current oscillations are to be observed. The surface properties are modified by an electrochemical reaction alone, by the formation of platinum oxide. This Pt-O formation is followed by a chemical reaction between the oxide and methanol in solution.  $\text{CO}_2$  is produced, and the current at the free surface sites increases to form new surface oxide, until the surface coverage approaches its maximum and the chemical reaction becomes stronger again. And the cycle starts anew. A characteristic of the (simple) NDR oscillators is that only *one* potential-dependent process is involved, that is, the electrochemical oxide formation.

An electrochemical oscillator works under galvanostatic conditions (*potential oscillations*) if the mechanism involves two

different potential-dependent processes. In general, potential oscillations appear in the region of the positive part of the steady state curve. A simple example of the phenomenon are the *potential oscillations* to be observed during the oxidation of hydrogen at platinum in acid solution, using mixtures of a large amount of hydrogen with some percent of carbon monoxide [118]. After the application of a constant current, the potential of hydrogen oxidation increases from values below 100 mV RHE up to ca. 800 mV, because of the poisoning of Pt sites, more and more with adsorbed CO. The oxidation of CO, starting slowly above 600 mV, becomes really effective near the maximum of the oscillations. At the free platinum sites, hydrogen is adsorbed, and the potential drops down steeply versus the reversible hydrogen potential again, a new cycle starts. The potential-depending rates of adsorption and desorption of the blocking adsorbate CO are next to hydrogen oxidation – the second potential-dependent process. But, where is the point of negative resistance – the negative slope of one of these two processes? It is the well-known branch of the steady state curve of hydrogen oxidation above ca. 800 mV RHE. As already discussed in Sect. 5.2.3.2, in the case of formic acid (Fig. 13), a competition for free surface sites between hydrogen and adsorbed water takes place. Koper and Sluyters have shown that for such instabilities, an inductive loop and/or a negative faradaic impedance in a Niquist plot are characteristic (Fig. 36) and called *hidden negative differential resistance* (HNDR) [119, 120]. The mathematical description of an HNDR oscillator has been given, for instance, by Krischer [121–125] after studying, as a model system, hydrogen oxidation at a rotating Pt disc in 0.5 M H<sub>2</sub>SO<sub>4</sub>/10<sup>−2</sup> M Cl<sup>−</sup> with the addition of

small amounts of metal ions [121–123]. Here, we have the HNDR in form of decreased hydrogen oxidation via potential-dependent Cl<sup>−</sup> ion adsorption.

#### 5.2.5.2 Potential Oscillations during Formic Acid Oxidation

The explanation for the instability at the electrochemical interface during formic acid oxidation is very similar to that of the above-mentioned H<sub>2</sub>/CO model. Coming back to the dual-path process of formic acid oxidation (Eqs. 12–14), the direct oxidation to CO<sub>2</sub> is equivalent to hydrogen oxidation, and the pathway via CO formation replaces the CO adsorption from the gas phase. The origin of an NDR is the competition for adsorption at free sites between HCOOH and water – the bond strength water-metal becoming stronger with increasing potential (compare Fig. 13). The pathway via dehydration (Step 13) takes care that the NDR is hidden in a certain potential region.

Potential oscillations during formic acid oxidation had been observed already in the 1920s [126]. As Fig. 32 shows [127], the upper potential limit is between 800 and 900 mV, as in the case of H<sub>2</sub>/CO oscillations. Introducing a model simulation, only the four (or five) rate constants of Eqs. (12–14) have to be employed. This has been done quite successfully by Okamoto and coworkers [128], reproducing the fingerprints of their experimental results.

The surface coverages of CO and H<sub>2</sub>O being of importance, Okamoto applied the following equations [128]:

$$\frac{d\theta_{\text{CO}}}{dt} = k_2(1 - \theta_{\text{CO}} - \theta_{\text{H}_2\text{O}}) - k_4(\theta_{\text{CO}} \times \theta_{\text{H}_2\text{O}}) \quad (42)$$

$$\frac{d\theta_{\text{H}_2\text{O}}}{dt} = k_3\theta_{\text{CO}}(1 - \theta_{\text{CO}} - \theta_{\text{H}_2\text{O}}) - k_{-3}\theta_{\text{H}_2\text{O}} - k_4(\theta_{\text{CO}} \times \theta_{\text{H}_2\text{O}}) \quad (43)$$



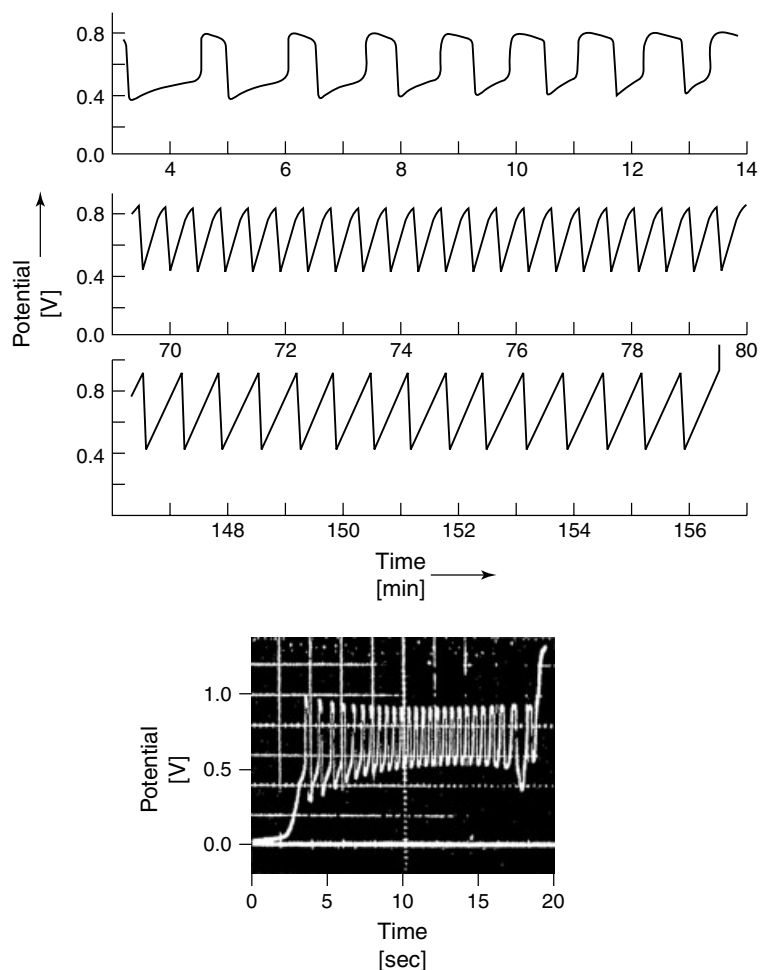


**Fig. 32** Potential oscillations during formic acid oxidation at a smooth polycrystalline platinum electrode: (a) 5 M HCOOH/0.5 M H<sub>2</sub>SO<sub>4</sub>, applied current density of 1.5 mA cm<sup>-2</sup>; (b) 1 M HCOOH and 0.5 M H<sub>2</sub>SO<sub>4</sub>, 0.25 mA cm<sup>-2</sup> [127].

$$\frac{dE}{dt} = \frac{1}{C_d} [I - 2Fh\{k_1(1 - \theta_{CO} - \theta_{H_2O}) + k_4(\theta_{CO} \times \theta_{H_2O})\}] \quad (44)$$

with  $k_1$  to  $k_4$  rate constants, including the concentrations of formic acid and water,  $k_{-3}$  the rate constant of the backward

reaction,  $I$  the applied current,  $C_d$  the double-layer capacity,  $E$  the electrode potential,  $F$  the Faraday constant, and  $h$  the number of sites on a unit surface area of platinum.

Different types of potential oscillations had been observed during formic acid oxidation at a *rotating electrode*, that is, with

additional control of mass transfer at the interface [129].

Potential-controlled *current oscillations* do occur at single-crystal platinum surfaces also [130–132]. And finally, a special case of mass-transfer influence was reported by Raspel and Eiswirth [133]. Starting with a low concentration of protons in a formic acid solution, the pH in the double layer of a hanging meniscus at platinum single-crystal surfaces can move to lower values. In this case, again current oscillations at constant potentials are found. It is important to note that the oscillations can be stopped by *stirring the solution*. This observation supports the above assumption that mass-transfer processes like diffusion can be responsible for the occurrence of oscillations also.

Interestingly, new impedance results (Fig. 33) show that a Nyquist plot can also be an indication for dynamic instability [131, 132]. For earlier observations, using  $\text{CH}_2\text{O}$  in 0.1 M NaOH on

a rhodium rotating disk electrode (RDE), see Ref. [134].

### 5.2.5.3 Current Oscillations during Methanol Oxidation

As already mentioned in the introduction, platinum oxides can be reduced via a chemical reaction with a fuel like methanol in solution. Figure 34 shows the effect, observed also by introducing  $\text{HCOOH}$  and  $\text{CH}_2\text{O}$  for comparison [127, 135]. At constant methanol concentration, the rate of this reaction depends on the amount of oxide coverage. On the other hand, at the applied potential, the current for oxide formation is decreasing with coverage. After reaching a maximum value, the rate of chemical oxide reduction decreases, and then the current of oxide formation again increases in this part of the cycle. Figure 35 shows current oscillations observed for *gas diffusion electrodes* in contact with a methanol solution at 1.2 and 1.5 V

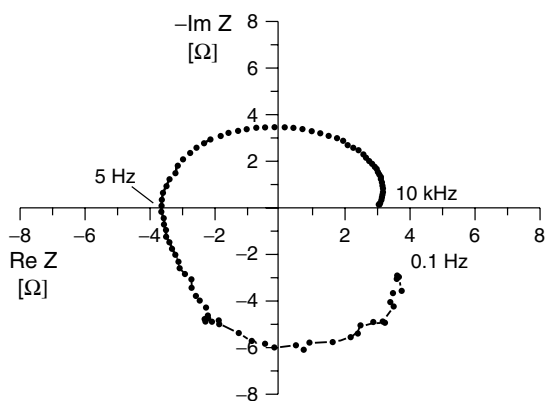


**Fig. 33** Nyquist plot for formic acid oxidation on platinum, obtained at +740 mV versus SHE, that is, in the region of the positive slope of  $i(\varphi)$  (compare Fig. 7), showing an inductive loop and negative faradic impedance; 0.1 M  $\text{HCOONa}/0.033 \text{ M } \text{H}_2\text{SO}_4$ , indicating a dynamic instability [131, 132], as already mentioned under Sect. 5.2.5.1.

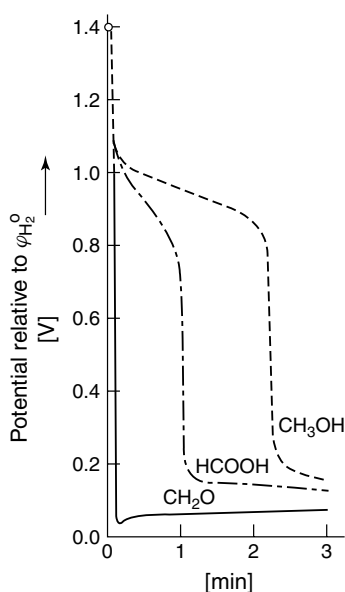
**Fig. 34** Reduction of Pt oxide, formed in 2.5 M  $\text{H}_2\text{SO}_4$ , by dipping the platinized Pt electrode in 0.1 M fuel/2.5 M  $\text{H}_2\text{SO}_4$  solution [127, 135].

RHE [136]. As the figure suggests, the cycle frequency follows the applied potential as parameter.

Two additional comments are of importance. (A) The oscillations of Fig. 35 *cannot* be observed at *smooth platinum surfaces*. Obviously, the diffusion in the electrolyte-filled part of the pores of the *gas diffusion electrode*, used in the experiment, is essential for the effect. (B) Indeed, if we disturb this mass-transfer process in the pores of the above-studied porous methanol electrode, the oscillations immediately vanish. Disturbance is possible by applying *oxygen* to the gas chamber of the porous electrode. This results in a strong chemical reaction with the methanol in the pores, forming  $\text{CO}_2$  [136]. On the other side, applying *nitrogen* to the gas chamber has no effect on the oscillations.

For a somewhat complicated case, Schell and coworkers [137] have studied voltammetric responses, using a rotating platinum disc in *alkaline* solution. Oscillation had been observed for potentials above 700 mV RHE. Note, that in alkaline solution, the formation of  $\text{PtOH}$  starts already on leaving the hydrogen region [138]. High-order periodic responses were obtained in experiments in which the system was allowed to relax under fixed conditions, following the transfer of the electrode to the methanol solution.

And again, *potential oscillations* of different types between 600 and 900 mV RHE are observed also, using smooth platinum in 0.5 M  $\text{CH}_3\text{OH}/0.5$  M  $\text{H}_2\text{SO}_4$  [139].



#### 5.2.5.4 Current Oscillations during CO Oxidation at a Rotating Disc

According to a recent experiment, using a rotating platinum electrode [140], current oscillations are observed also during potentiostatic oxidation of carbon monoxide. Figure 36 shows the current/time behavior after application of 0.95 V on a rotating polycrystalline platinum electrode. Oscillations can only be observed in a small potential window between 0.9 and 1.0 V *and* in the presence of the rotations of the electrode. The current density seems to be small enough to ensure that the potential drop at the interface is only negligibly disturbed by the ohmic drop in the solution. Therefore, the sources of instability should be of a chemical nature. The oscillations are probably connected to the initial stages of platinum oxide formation and the interference on this process by CO adsorption and/or oxide reduction. Because of the low solubility of CO in the electrolyte, the rate of mass transfer to

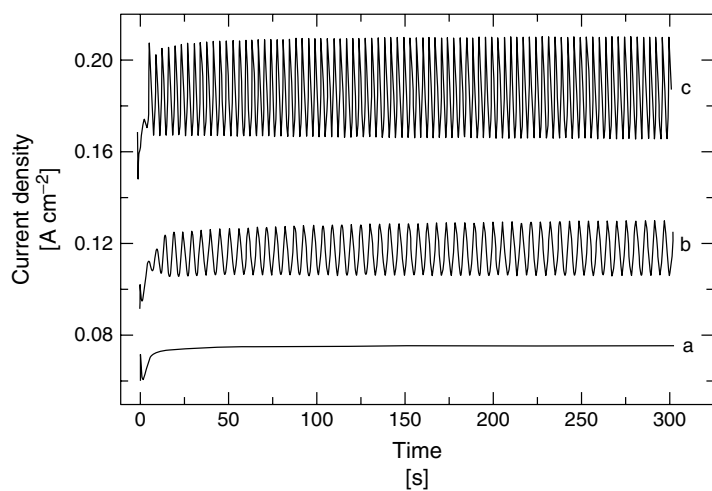


**Fig. 35** Current Oscillations during methanol oxidation at a Pt catalyzed gas diffusion electrode ( $0.4 \text{ mgPt cm}^{-2}$ ), supplied with nitrogen to the gas side;  $2.0 \text{ M CH}_3\text{OH}/0.5 \text{ M H}_2\text{SO}_4$ ; controlled potentials versus RHE (a) 1.0; (b) 1.2; and (c) 1.5 Volt [136].

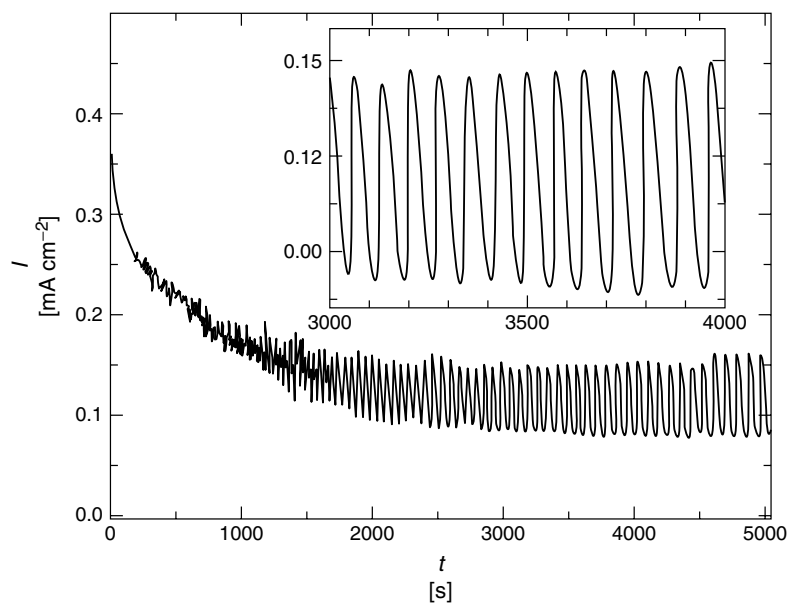


**Fig. 36** Current/time transient of a rotating platinum electrode (1.000 rpm) in CO-saturated  $0.1 \text{ M HClO}_4$  at  $0.95 \text{ V}$  versus RHE. Initial instants after potential application, the insert shows a time window [140].

the surface (e.g. via convection) is of importance. At a rotating electrode, one has above 1.0 V versus RHE limiting current, being constant also during the negative scan and passing the sharp maximum of the anodic scan (Fig. 4 in Ref. [140]).

#### 5.2.6

##### Nonelectrochemical Pathway of Methanol Oxidation

During investigations of DMFCs, it was observed that as a result of the diffusion of methanol molecules through the electrolyte to the three-phase boundary of the cathode, the potential of the oxygen electrode may shift to more negative values. In addition, a higher consumption of methanol was found [57, 88]. It was assumed that this effect results from simultaneous oxygen reduction and methanol oxidation at the platinum surface used,

the oxygen reduction being only slightly poisoned by the adsorbed methanol. This explanation was supported by investigations of Chu and Gilman using rotating Pt disc electrodes [141]. But, recently it has been shown that a *chemical pathway*, the purely heterogeneous reaction of methanol and oxygen to form carbon dioxide, has to be considered also [136]. This can be studied best in the presence of large amounts of both reactants. Therefore, a higher methanol concentration was used in the electrolyte near the oxygen cathode.

In the experiments of Fig. 37, we present first oxygen reduction (curve (a), oxygen supplied on the gas side of the Pt catalyzed diffusion electrode only) without methanol in the electrolyte. Of course, a standard oxygen-reduction behavior results. For comparison, in curve (b), a 2 M methanol solution is used and nitrogen is supplied to the gas chamber of the gas diffusion

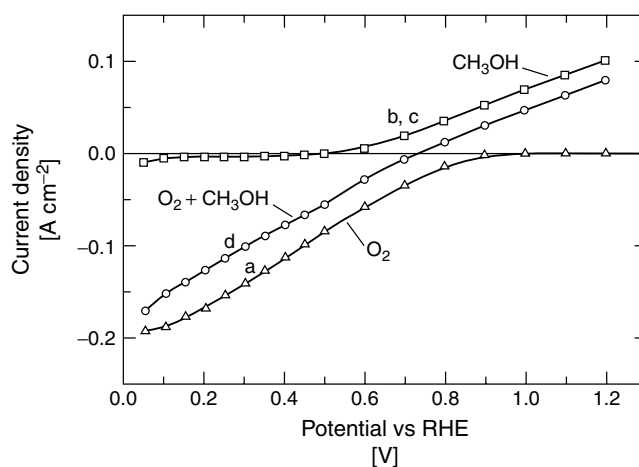


**Fig. 37** Stationary current/potential curves of a Pt catalyzed gas diffusion electrode as in Fig. 33. Points taken after 3 to 5 min, room temperature; (a) 0.5 M  $H_2SO_4$ , oxygen supplied to the gas chamber only; (b) 2.0 M  $CH_3OH/0.5$  M  $H_2SO_4$ , nitrogen supplied to gas chamber and solution; (c) methanol solution and nitrogen supplied to the gas chamber as in (b), but oxygen supplied to the solution; (d) methanol in solution and oxygen supplied to the gas chamber [136].

electrode. The current/potential plot of a methanol anode is obtained. With curve (c), the effect of adding oxygen to the methanol solution is studied. Because of the low oxygen solubility in the electrolyte, practically no change is observed because of the minimum oxygen reduction current. With curve (d) finally, we have the case of a strong heterogeneous chemical reaction of methanol with oxygen at the platinum surface, supplying methanol to the solution and oxygen to the gas chamber of the diffusion electrode. Below 0.7 V curve (d) is comparable with curve (a), but the currents are up to  $30 \text{ mA cm}^{-2}$  smaller than those without methanol in solution. The anodic part shows methanol oxidation, but again with a substantial loss in the rate. If the strong effect of methanol, presented in the difference between curve (d) and (a), is due to a chemical reaction, the product of this reaction,  $\text{CO}_2$ , must be found also below 0.5 V, where no anodic oxidation of methanol takes place at the platinum.

The carbon dioxide produced was collected by precipitation at three tubes in series with  $0.5 \text{ M Ba(OH)}_2 + 0.1 \text{ M BaCl}_2$  solution and the determination of concentration was made by potentiometric titration with standard acid ( $0.5 \text{ M HCl}$ ) [142]. The formation of  $\text{CO}_2$  was followed at different potentials between 0.1 and 0.5 V for the conditions of curves (a), (b), and (d) at intervals of 60 min. Only for the conditions of curve (d), methanol in the electrolyte and  $\text{O}_2$  supplied to the gas diffusion electrode,  $\text{CO}_2$  was found, ca.  $1.8 \times 10^{-3} \text{ mol h}^{-1}$  at a difference in current between (a) and (d) of ca.  $35 \text{ mA cm}^{-2}$ . Obviously, the difference in current is due to methanol consumption via a chemical pathway at the three-phase boundary of the Pt gas diffusion electrode.

Recently, another method was suggested to measure the current efficiency for  $\text{CO}_2$

production during methanol oxidation, using online mass spectrometry in combination with a dual thin-layer flow through cell [143].

As shown decades ago, *formaldehyde* also is obtained via a nonelectrochemical reaction at Pt surfaces ([25, 143] and references therein). In acid solution, formaldehyde reacts with water to form the *gem*-diol  $\text{H}_2\text{C(OH)}_2$  [134]. Using a sensitive fluorescence assay, Korzeniewski and Childers [144] followed the formation of *gem*-diol during the oxidation of methanol out of a  $15 \text{ mM CH}_3\text{OH}/0.1 \text{ M HClO}_4$  solution at smooth platinum for different methanol oxidation potentials. Above 500 mV RHE, a strong drop of the conversion of methanol to the *gem*-diol is observed.

## References

1. A. Kutschker, W. Vielstich, *Electrochim. Acta* **1963**, 8, 985–989.
2. W. Vielstich, *Chem.-Ing.-Tech.* **1963**, 35, 362.
3. E. Guth, E. J. Haase, H. G. Plust et al., *Proc. 21st Ann. Power Sources Conf.*, Atlantic City, 1967, p. 29ff.
4. O. Bloch, M. Prigent, J. C. Balaceanu, *The Electrochemical Society Meeting*, Indianapolis, 1961, Ext. Abstr. No 116.
5. G. Grüneberg, Dissertation Uni Braunschweig, 1958.
6. W. Vielstich, *Fuel Cells*, John Wiley & Sons, London, UK, 1970, pp. 103–107.
7. T. Iwasita, W. Vielstich, E. Santos, *J. Electroanal. Chem.* **1987**, 229, 367–376.
8. A. Hamnett, *Catal. Today* **1997**, 38, 445–457.
9. A. Capon, R. Parsons, *J. Electroanal. Chem.* **1973**, 45, 205.
10. V. S. Bagotzki, Yu. B. Vasiliev, *Electrochim. Acta* **1966**, 11, 1439.
11. W. Güther, W. Vielstich, *Electrochim. Acta* **1982**, 27, 811–816.
12. X. H. Xia, T. Iwasita, *J. Electrochem. Soc.* **1993**, 140, 2559–2565.
13. V. S. Bagotzki, Yu. B. Vasiliev, O. K. Khasova, *J. Electroanal. Chem.* **1977**, 81, 229.

14. A. Bewick, K. Kunitatsu, S. Pons, J. W. Russel, *J. Electroanal. Chem.* **1984**, 160, 47.
15. T. Iwasita in *Advances in Electrochemical Science and Engineering* (Eds.: H. Gerischer, C. W. Tobias), Wiley-VCH, Weinheim, Germany, 1995, pp. 123–216, Vol. 4.
- 16a. S. Wilhelm, T. Iwasita, W. Vielstich, *J. Electroanal. Chem.* **1987**, 238, 383–391.
- 16b. K. I. Ota, Y. Nakagawa, M. Takahashi, *J. Electroanal. Chem.* **1964**, 179, 179.
17. M. Watanabe, S. Motoo, *J. Electroanal. Chem.* **1975**, 60, 267–273.
18. B. Bittins, E. Cattaneo, P. Königshoven et al. in *Electroanalytical Chemistry* (Ed.: A. J. Bard), Marcel Dekker, New York, 1991, pp. 182–219, Vol. 17.
19. H. Baltruschat in *Interfacial Electrochemistry* (Ed.: A. Wieckowski), Marcel Dekker, New York, 1999, pp. 577–597.
20. P. A. Christensen, A. Hamnett, *Techniques and Mechanisms in Electrochemistry*, Blackie Academic, Chapman & Hall, London, 1994, pp. 217–224, 278–283.
21. O. Wolter, C. Giordano, J. Heitbaum et al., *Proc. Symp. Electrocatalysis*, The Electrochemical Society, Pennington, N.J., 1982, pp. 235–253.
22. P. Stonehart, *Electrochim. Acta* **1973**, 18, 63.
23. E. Santos, E. Leiva, W. Vielstich et al., *J. Electroanal. Chem.* **1987**, 227, 199–211.
24. L. H. Leung, A. Wieckowski, M. J. Weaver, *J. Phys. Chem.* **1988**, 92, 6985–6990.
25. T. Iwasita, W. Vielstich, *J. Electroanal. Chem.* **1986**, 201, 403–408.
26. X. H. Xia, T. Iwasita, F. Ge et al., *Electrochim. Acta* **1996**, 41, 711–718.
27. T. Iwasita in *Handbook of Fuel Cells* (Eds.: W. Vielstich, A. Lamm, H. Gasteiger), John Wiley & Sons, Chichester, UK; in press.
28. J. Clavilier, C. Lamy, J. M. Leger, *J. Electroanal. Chem.* **1981**, 125, 249.
29. S.-Ch. Chang, L. H. Leung, M. Weaver, *J. Phys. Chem.* **1990**, 94, 6013–6021.
30. J. Willsau, Dissertation Uni Bonn, 1985, pp. 80–84.
31. J. Willsau, J. Heitbaum, *Electrochim. Acta* **1986**, 31, 943–948.
32. J. Clavilier, R. Parsons, R. Durand et al., *J. Electroanal. Chem.* **1981**, 124, 321.
33. R. R. Adzic, A. V. Tripkovic, W. E. O'Grady, *Nature* **1982**, 296, 137.
34. R. R. Adzic in *Handbook of Fuel Cells* (Eds.: W. Vielstich, A. Lamm, H. Gasteiger), John Wiley & Sons, Chichester, UK; in press.
35. I. Villegas, M. J. Weaver, *J. Chem. Phys.* **1994**, 101(2), 1648–1660.
36. W. F. Lin, T. Iwasita, W. Vielstich, *J. Phys. Chem. B* **1999**, 103, 3250–3257.
37. F. Kitamura, M. Takahashi, M. Ito, *Surf. Sci.* **1989**, 223, 493.
38. T. Iwasita, X. H. Xia, E. Herrero et al., *Langmuir* **1996**, 12, 4260–4265.
39. J. Giner, *Ber. Bunsen-Ges. Phys. Chem.* **1959**, 63, 386.
40. N. Markovic, P. Ross, *J. Electroanal. Chem.* **1992**, 330, 499.
41. E. Herrero, K. Franaszczuk, A. Wieckowski, *J. Phys. Chem.* **1994**, 98, 5074.
42. O. M. Magnussen, J. Hageböck, J. Hotlos et al., *Faraday Discuss.* **1992**, 94, 329.
43. G. J. Edens, X. Gao, M. J. Weaver, *J. Electroanal. Chem.* **1994**, 375, 357.
44. T. Iwasita, X. H. Xia, H. D. Liess et al., *J. Phys. Chem. B* **1997**, 101, 7542–7547.
45. A. Rincon, M. C. Perez, G. Orozco et al., *Electrochem. Commun.* **2001**.
46. T. Iwasita, X. H. Xia, *J. Electroanal. Chem.* **1996**, 411, 95.
47. B. A. Sexton, K. Rendulic, A. E. Hughes, *Surf. Sci.* **1982**, 121, 181.
48. G. B. Fisher, J. L. Gland, *Surf. Sci.* **1980**, 94, 446–455.
49. P. A. Thiel, T. E. Madey, *Surf. Sci. Rep.* **1987**, 7, 211–385.
50. R. W. McCabe, L. D. Schmidt, *Surf. Sci.* **1977**, 66, 101–124.
51. J. A. Caram, C. Gutiérrez, *J. Electroanal. Chem.* **1991**, 305, 259.
52. A. Wieckowski, M. Rubel, C. Guitérrez, *J. Electroanal. Chem.* **1995**, 382, 972.
53. T. Iwasita, X. H. Xia, H.-D. Liess, W. Vielstich, *J. Phys. Chem. B* **1997**, 101, 7542–7547.
54. J. Willsau, J. Heitbaum, *J. Electroanal. Chem.* **1985**, 185, 181–183.
55. J. M. Bowmann, J. S. Bittmann, L. B. Harding, *J. Chem. Phys.* **1986**, 85, 911.
56. S. Wilhelm, T. Iwasita, W. Vielstich, *J. Electroanal. Chem.* **1987**, 238, 383–391.
57. A. Hamnett in *Interfacial Electrochemistry* (Ed.: A. Wieckowski), Marcel Dekker, New York, 1999, pp. 843–883.
58. W. Vielstich, P. A. Christensen, S. A. Weeks et al., *J. Electroanal. Chem.* **1988**, 242, 327–333.
59. J. O'M. Bockris, H. Wroblowa, *J. Electroanal. Chem.* **1964**, 7, 428.

60. O. A. Petrii, B. I. Podlovchenko, A. N. Frumkin et al., *J. Electroanal. Chem.* **1965**, 10, 253.
61. J. A. Shropshire, *J. Electrochem. Soc.* **1965**, 112, 465.
62. J. A. Shropshire, *J. Electrochem. Soc.* **1967**, 114, 773.
63. H. Binder, A. Köhling, G. Sandstede in *From Electrocatalysis to Fuel Cells* (Ed.: G. Sandstede), University of Washington Press, Seattle, 1972, pp. 43–79.
64. K. Franaszczuk, J. Sobkowski, *J. Electroanal. Chem.* **1992**, 327, 235.
65. T. Iwasita, F. C. Nart, W. Vielstich, *Ber. Bunsen-Ges. Phys. Chem.* **1990**, 94, 1030–1034.
66. H. A. Gasteiger, N. Markovic, P. N. Ross et al., *J. Phys. Chem.* **1993**, 97, 1220–1229.
67. H. A. Gasteiger, N. Markovic, P. N. Ross et al., *J. Electrochem. Soc.* **1994**, 141, 1795–1803.
68. N. Markovic, H. A. Gasteiger, P. N. Ross et al., *Electrochim. Acta* **1995**, 40, 91–98.
69. K. A. Friedrich, K. P. Geyzers, U. Linke et al., *J. Electroanal. Chem.* **1996**, 402, 123–128.
70. W. Chrzanowski, A. Wieckowski, *Langmuir* **1998**, 14, 1967–1970.
71. M. Krausa, W. Vielstich, *J. Electroanal. Chem.* **1994**, 379, 307–314.
72. M. P. Hogarth, J. Munk, A. K. Shukla et al., *J. Appl. Electrochem.* **1994**, 24, 85.
73. J. P. Iudice de Souza, T. Iwasita, F. C. Nart et al., *J. Appl. Electrochem.* **2000**, 30, 43–48.
74. W. Chrzanowski, H. Kim, A. Wieckowski, *Catal. Lett.* **1998**, 50, 69–75.
75. T. Iwasita, H. Hoster, A. John-Anacker et al., *Langmuir* **2000**, 16, 522–529.
76. T. Frelink, W. Visscher, J. A. R. van Veen, *Surf. Sci.* **1995**, 335, 353–360.
77. W. Chrzanowski, A. Wieckowski, *Langmuir* **1997**, 13, 5974–5978.
78. H. Gasteiger, N. Markovic, P. N. Ross et al., *J. Phys. Chem.* **1994**, 98, 617–625.
79. W. F. Lin, M. S. Zei, M. Eiswirth et al., *J. Phys. Chem.* **1999**, 103, 6968–6977.
80. H. A. Gasteiger, P. N. Ross, E. J. Cairns, *Surf. Sci.* **1993**, 293, 67–80.
81. P. N. Ross in *Electrocatalysis* (Eds.: J. Lipkowski, P. N. Ross), Wiley-VCH, New York, 1998, pp. 43–74.
82. F. Bautier de Mongeot, M. Scherer, B. Gleich et al., *Surf. Sci.* **1998**, 411, 249–362.
83. S. Cramm, K. A. Friedrich, K. P. Geyzers et al., *Fresenius' J. Anal. Chem.* **1997**, 358, 189–192.
84. H. A. Gasteiger, N. Markovic, P. N. Ross et al., *Electrochim. Acta* **1994**, 39, 1825.
85. A. Hamnett in *Interfacial Electrochemistry* (Ed.: A. Wieckowski), Marcel Dekker, New York, 1999, 843–883.
86. E. Reddington, A. Sapienza, B. Gurau et al., *Science* **1998**, 280, 1735–1739.
87. K. Wang, H. Gasteiger, N. Markovic et al., *Electrochim. Acta* **1996**, 41, 2587.
88. S. Wasmus, A. Küver, *J. Electroanal. Chem.* **1999**, 461, 14–31.
89. D. M. Kolb in *Adv. Electrochem. a. Electrochem. Engrn.* (Eds.: H. Gerischer, C. W. Tobias), John Wiley & Sons, New York, 1978, p. 125, Vol. 11.
90. R. A. Hess, Ch. C. Liang, US Patent 3 340 097, 1967 (applied 1964).
91. M. Watanabe, S. Motoo, *J. Electroanal. Chem.* **1977**, 78, 243.
92. R. R. Adzic, *Proc. Symp. Electrocatal.* **1982**, 82, 309.
93. E. Herrero, K. Franaszczuk, A. Wieckowski, *J. Electroanal. Chem.* **1993**, 361, 269.
94. E. Schwarzer, W. Vielstich, *Chem.-Ing.-Tech.* **1973**, 45, 201.
95. A. Castro-Luna, T. Iwasita, W. Vielstich, *J. Electroanal. Chem.* **1985**, 196, 301.
96. A. Fernandez-Vega, J. M. Feliu, A. Aldaz et al., *J. Electroanal. Chem.* **1989**, 258, 101.
97. E. Leiva, T. Iwasita, E. Herrero et al., *Langmuir* **1997**, 13, 6287.
98. M. Angerstein-Kozłowska, B. McDougall, B. E. Conway, *J. Electrochem. Soc.* **1973**, 122, 756.
99. M. Llorca, E. Herrero, J. M. Feliu et al., *J. Electroanal. Chem.* **1994**, 373, 217.
100. E. Herrero, A. Fernandez-Vega, J. M. Feliu et al., *J. Electroanal. Chem.* **1993**, 350, 73.
101. A. Fernandez-Vega, J. M. Feliu, A. Aldaz et al., *J. Electroanal. Chem.* **1989**, 305, 229.
102. H. Hoster, T. Iwasita, H. Baumgärtner et al., *PCCP* **2001**, 3, 337–346.
103. H. Hoster, doctor thesis, Uni-Bw München 2002.
104. H. Hoster, T. Iwasita, H. Baumgärtner et al., *J. Electrochem. Soc.* **2001**, 148, A496.
105. K. Franaszczuk, E. Herrero, P. Zelenay et al., *J. Phys. Chem.* **1992**, 96, 8509–8516.
106. S. Srimarulu, T. D. Jarvi, E. M. Stuve, *Electrochim. Acta* **1998**, 44, 1127–1134.



107. D. Chu, S. Gilman, *J. Electrochem. Soc.* **1996**, *143*, 1685.
108. A. Aramata, M. Masuda, *J. Electrochem. Soc.* **1991**, *138*, 1949–1957.
109. M. Watanabe, M. Uchida, S. Motoo, ECS Meeting, Boston, Mass., Ext. Abstr. 339, 1986.
110. I. A. Rodrigues, J. P. I. Souza, F. C. Nart, *Langmuir* **1997**, *13*, 6829.
111. R. Liu, H. Iddir, Q. Fan et al., *J. Phys. Chem. B* **2000**, *104*, 3518–3531.
112. H. Kim, I. Rabelo de Moraes, G. Tremiliosi-Filho et al., *Surf. Sci.* **2001**, *474*, L203–L212.
113. T. J. Schmidt, H. Gasteiger, R. J. Behm, *Electrochem. Commun.* **1999**, *1*, 1–4.
114. V. A. Paganin, W. Lizcano-Valbuena, E. R. Gonzales, *Electrochim. Acta* **2000**, *47*, 3715–3722.
115. K. F. Bonhoeffer, G. Vollheim, *Z. Naturforsch.* **1953**, *8b*, 406.
116. U. F. Franck, R. FitzHugh, *Z. Elektrochem.* **1961**, *65*, 156.
117. M. T. M. Koper, *Electrochim. Acta* **1992**, *37*, 1771–1778.
118. T. Yamazaki, T. Kadera, *Electrochim. Acta* **1991**, *36*, 639–646.
119. M. T. M. Koper, J. H. Sluyters, *J. Electroanal. Chem.* **1991**, *303*, 73.
120. M. T. M. Koper, J. H. Sluyters, *J. Electroanal. Chem.* **1994**, *371*, 149.
121. K. Krischer in *Modern Aspects of Electrochemistry* (Eds.: J. O'M. Bockris, B. E. Conway, R. White), Kluwer Academic Publishers, New York, 1999, pp. 1–142, Vol. 32.
122. K. Krischer, N. Mazouz, P. Grauel, *Angew. Chem.* **2001**, *113*, 842–863.
123. K. Krischer, N. Mazouz, P. Grauel, *Angew. Chem., Int. Ed. Engl.* **2001**, *40*, 850–861.
124. K. Krischer, M. Lübke, W. Wolf et al., *Electrochim. Acta* **1995**, *40*, 69.
125. M. Wolf, K. Krischer, M. Lübke et al., *J. Electroanal. Chem.* **1995**, *385*, 85.
126. E. Müller, S. Tanaka, *Z. Elektrochem.* **1928**, *34*, 256.
127. W. Vielstich, *Fuel Cells*, John Wiley & Sons, London, UK, 1970, pp. 88–91.
128. H. Okamoto, N. Tanaka, M. Naito, *Chem. Phys. Lett.* **1996**, *248*, 289–295.
129. F. N. Albahadily, M. Schell, *J. Electroanal. Chem.* **1991**, *308*, 151–173.
130. N. Markovic, P. Ross, *J. Phys. Chem.* **1993**, *97*, 9771–9778.
131. P. Strasser, M. Eiswirth, G. Ertl, *J. Chem. Phys.* **1997**, *107*, 991–1003.
132. P. Strasser, *Interface* **2000**, *9*, 46–52.
133. F. Raspel, M. Eiswirth, *J. Phys. Chem.* **1994**, *98*, 7613–7618.
134. J. F. Walker, *Formaldehyde*, 3rd ed., Reinhold Publishing, New York, 1964.
135. J. E. Oxley, G. K. Johnson, B. T. Buzalski, *Electrochim. Acta* **1964**, *9*, 897.
136. W. Vielstich, V. A. Paganin, F. Lima et al., *J. Electrochem. Soc.* **2001**, *148*, A502.
137. Y. Xu, A. Amini, M. Schell, *J. Phys. Chem.* **1994**, *98*, 12 759–12 767.
138. E. Santos, M. C. Giordano, *J. Electroanal. Chem.* **1984**, *172*, 201.
139. M. Krausa, W. Vielstich, *J. Electroanal. Chem.* **1995**, *399*, 7–12.
140. D. C. Azevedo, A. L. N. Pinheiro, E. R. Gonzales, *Electrochem. Solid-State Lett.* **2002**, *5*, A51–54.
141. D. Chu, S. Gilman, *J. Electrochem. Soc.* **1994**, *141*, 1770.
142. G. H. Jeffery, J. Bassett, J. Mendham et al., *Vogel's Textbook of Quantitative Chemical Analysis*, 5th ed., John Wiley & Sons, New York, 1989, p. 297.
143. H. Wang, Th. Löffler, H. Baltruschat, *J. Appl. Electrochem.* **2001**, *31*, 759–765.
144. C. Korzeniewski, Ch. L. Childers, *J. Phys. Chem. B* **1998**, *102*, 489–492.

## 5.3

**Electrochemical Nucleation and Growth**

*Benjamin R. Scharifker and Jorge Mostany  
Universidad Simón Bolívar, Caracas,  
Venezuela*

## 5.3.1

**Phase Formation on Electrodes**

The onset of stable structures, known as nuclei, is characteristic of the phase formation phenomena [1]. These structures are aggregates of atoms or molecules, and they become centers for the propagation of the two-dimensional or three-dimensional new phase. The phase formation process is supported by material originated from the bulk of the mother phase and invariably, during electrochemically driven phase formation processes, occurs also with chemical reactions taking place at the interface between the developing phase and the electrolyte solution. A sequence of events lead to the formation and growth of the new phase; these include adsorption of precursors on the electrode substrate, frequently accompanied also by charge transfer, formation of two- or three-dimensional nuclei, and the growth of the new phase. The supersaturation (or excess Gibbs energy) of the system decreases with the formation and growth of the new phase; hence the overall process is categorized as a first-order phase transformation.

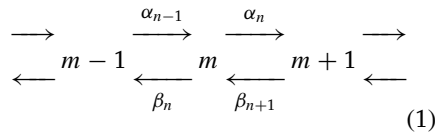
An appropriate description of the energetics and kinetics of the nucleation process requires consideration of the equilibrium properties of the bulk phases involved as well as contributions that arise from the formation and growth of the interface between them. Clusters that constitute the seeds of the phase transformation are usually composed of a small number of atoms or molecules. For such small entities, the surface or interfacial properties

will play dominant roles in preserving the excess energy and, in some cases, this might result in a long lasting metastable equilibrium, with indefinite preservation of the supersaturated state. Thus, in terms of classical thermodynamics, the total free energy of a spherical drop in equilibrium with its vapor is obtained from the properties of the condensed bulk phase as well as the interface. The Kelvin equation [2]  $\ln(p/p_\infty) = 2\sigma\Omega_L/rkT$  states that the excess vapor pressure of a drop varies with the surface tension or free energy of the surface,  $\sigma$ , and the molar volume of the condensed phase  $\Omega_L$ , and also with the inverse of the radius of curvature of the surface,  $1/r$ ;  $p_\infty$  is the equilibrium vapor pressure of the flat surface between phases with the same chemical composition. According to this expression, small clusters will not be stable unless the pressure of the vapor surpasses their equilibrium vapor pressure, and this will invariably occur at a value higher than the equilibrium pressure of the bulk phase. Under such conditions, the increasing volume of the new phase reduces the free energy, whereas the free energy change due to the expansion of the surface is always positive. Therefore, the combined contributions due to formation of a bulk phase and a surface produce a maximum of  $\Delta G$ , occurring under given conditions at a certain size of the aggregate of the new phase, thus defining the critical radius  $r^*$ . The critical radius must be exceeded for a nucleus to grow irreversibly, and this may happen through fluctuations in temperature, pressure or composition, or, in electrochemical systems, by changes of the electrical potential.

For a simple electrochemical process,  $M_{(sol)}^{z+} + ze^- = M_{(ads)}$ , the equilibrium potential  $E_{rev}$  is given by the Nernst equation  $E_{rev} = E^\circ + RT/zF \ln(a_{M_{eq}^{ads}}/a_{M^{n+,sol}})$ , where  $E^\circ$  is the

standard potential of the redox equilibrium between bulk metal and a solution of  $M^{n+}$ ,  $a_{M_{eq}^{ads}}$  is the equilibrium surface activity of ad-atoms, and  $a_{M^{n+,sol}}$  is the activity of  $M^{n+}$  in solution. This quantity may be modified at will varying the electrode potential to a new value  $E = E_{rev} + \eta$ , where  $\eta$  is the overpotential at which the surface activity of M satisfies the relation  $a_{M_{eq}^{ads}}/a_{M_{eq}^{ads}} = \exp(-zF\eta/RT)$ . It can be shown that both the energy of formation of the critical nucleus,  $\Delta G^* = 16\pi\sigma^3 M^2 \phi(\theta)/3\rho^2 (zF\eta)^2$  (the function  $\phi(\theta)$  of the contact angle  $\theta$  between the nucleus and the substrate will be defined later), as well as its radius,  $r^* = -2\sigma/zF\eta$ , depend on the overpotential [3]. This illustrates the possibility of controlling, rapidly, precisely, and reversibly, the conditions that determine the occurrence of electrochemical nucleation processes.

A critical cluster of atoms is at a maximum of free energy. Considering then that the appearance of critical nuclei is the limiting step of the nucleation process and that the probability of their formation would be proportional to  $\exp(-\Delta G^*/kT)$ , the nucleation rate will be proportional to  $\exp(-16\pi\sigma^3 M^2 \phi(\theta)/3\rho^2 z^2 \eta^2 kT)$ , where  $M$  is the molar mass of the deposit and  $\rho$  is its mass density. The preexponential factor derives from kinetic arguments, considering that the populations of clusters of different sizes are in a steady state, determined by a sequence of reactions such as



Thus, consecutive addition (and detachment) of atoms leads eventually to the formation of supercritical nuclei that grow irreversibly and are not further considered in the steady state equations. Becker and

Döring [4] provided an analytical solution considering a system of constant composition in which supercritical clusters are reintroduced into the system as the equivalent amount of discrete units. A steady state expression of the nucleation rate follows,  $J_s = Z\alpha_{m^*}c_{m^*}$ , where  $\alpha_{m^*}$  is the net probability of addition of an atom per unit time from a critical cluster of size  $m^*$ , and  $c_{m^*}$ , the equilibrium concentration of critical clusters, is related to the monomer concentration through the Boltzmann equation,  $c_{m^*} = c_1 \exp(-\Delta G_{m^*}/kT)$  and the nondimensional Zeldovich factor  $Z$ , which accounts for the fact that the steady state concentration at  $m^*$  is only 1/2 of the concentration at equilibrium, and that critical clusters may still decay [5].

Classical nucleation theory uses macroscopic properties characteristic of bulk phases, like free energies and surface tensions, for the description of small clusters. These macroscopic concepts may lack physical significance for typical nucleus sizes of often a few atoms as found from experimental studies of heterogeneous nucleation. This has prompted the development of microscopic models of the kinetics of nucleation in terms of atomic interactions, attachment and detachment frequencies to clusters composed of a few atoms and with different structural configurations, as part of a general nucleation theory based on the steady state nucleation model [6]. The size of the critical nucleus follows straightforwardly in the atomistic description from the logarithmic relation between the steady state nucleation rate and the overpotential. It has been shown that at small supersaturations, the atomistic description corresponds to that of the classical theory of nucleation [7].

Given that in electrochemical systems the supersaturation of a developing

phase is determined by the overpotential, experimental studies of the kinetics of phase formation processes are generally conducted under potentiostatic conditions. At constant potential then, it is generally considered that the steady state nucleation rate  $J_s$  maintains a constant value  $A$ , which depends on the applied overpotential. The nucleation frequency  $A$  may be determined from the analysis of the current that represents the overall rate of electrodeposition. Analyses of current transients, together with direct observation of the electrode surface, constitute the most common methods for the study of nucleation processes.

In many cases of electrochemical phase formation reactions, the charge-transfer step is fast and the rate of growth of mature supercritical nuclei is well described by mass transport of electrodepositing species to hemispherical growth centers [8]. The current attending the growth of an isolated nucleus is proportional to the square root of its age,  $I(t) = \pi z F (2Dc)^{3/2} (Mt/\rho)^{1/2}$ , where  $c$  is the molar concentration and  $D$  is the diffusion coefficient of electrodepositing species in solution. On the other hand, the rate of appearance of nuclei on a surface with a number density  $N_0$  of active sites for nucleation may be expressed as  $dN/dt = A(N_0 - N)$ , where  $A$  is the nucleation rate per site, from which the number density of nuclei on the surface as a function of time will be given by  $N = N_0[1 - \exp(-At)]$ . Depending on the frequency at which nuclei appear and the corresponding rate at which active sites are depleted, the nucleation process may be classified as “instantaneous” or “progressive”. When  $A$  is very large ( $A \gg 1/t$ ), depletion of nucleation sites

occurs at very early stages, the above expression soon reduces to  $N = N_0$ , and nucleation is “instantaneous”. Conversely, for very small  $A$ , the number density of nuclei increases initially linearly with time,  $N = N_0At$ , and nucleation is said to be “progressive”.

In multiple nucleation conditions, the current density may be expressed as a convolution of the growth current of individual nuclei and their birth rate on the surface. In the very initial stages, nuclei are small in both size and number, and they grow independently of each other. The current transient is then given by  $i(t) = \pi z F (2Dc)^{3/2} (Mt/\rho)^{1/2} N_0 \Phi(\sqrt{At})$  [9], where  $\Phi(\sqrt{At})$  is the Dawson integral,  $\Phi(\sqrt{At}) = 1 - (e^{-At}/\sqrt{At}) \int_0^{\sqrt{At}} e^{\lambda^2} d\lambda$ . For,  $At \geq 20$ ,  $\Phi(\sqrt{At}) \rightarrow 1$  and the equation above describes a current density proportional to  $N_0 t^{1/2}$ , corresponding to instantaneous nucleation; for  $At \leq 0.2$  nucleation is progressive,  $\Phi(\sqrt{At}) \rightarrow (2/3)At$  and the current density is proportional to  $(2/3)N_0 At^{3/2}$  [10, 11].

An overall description of the nucleation and growth process valid for all times is in general complicated by interactions among growing centers. When growth is diffusion controlled, then overlap of the spherical diffusional fields supporting the growth of individual nuclei must be considered, eventually collapsing into a single planar field to the plane of the electrode. The many-body problem that ensues has been approached following several strategies. General models not restricted to the instantaneous case, and allowing determination of  $A$  and  $N_0$  from current transients, consider two-dimensional projections of the hemispherical diffusional fields around individual nuclei onto the plane of the electrode [12] and estimate their overlap using the Avrami

theorem [13]. The current density is then given by [11]:

$$i(t) = \frac{zFDc}{(\pi Dt)^{1/2}} \times \frac{1 - \frac{e^{-At}}{(At)^{1/2}} \int_0^{(At)^{1/2}} e^{\lambda^2} d\lambda}{1 - \left(\frac{1 - e^{-At}}{At}\right)} \times \left\{ 1 - \exp \left[ -(2\pi)^{3/2} D \left( \frac{cM}{\rho} \right)^{1/2} \times N_0 t \left( 1 - \left( \frac{1 - e^{-At}}{At} \right) \right) \right] \right\} \quad (2)$$

The expression above describes appropriately experimental current transients obtained in studies of electrodeposition processes for numerous systems. The electrodeposition of Hg may be considered as a model system for the study of the fundamentals of electrochemical phase formation, and is briefly discussed here (see Sect. 5.3.4.4). Analysis of current transients allows determining the values of the nucleation rate and the number density of active sites. The experimentally observed dependence of the nucleation rates on overpotential and the charge transferred during the electrodeposition reaction are in agreement with fundamental theoretical postulates. The number density of nuclei observed microscopically on the surface, on the other hand, are in good agreement with those predicted from the nucleation rates obtained. Overall, experimental studies show the dominant role of deposit|substrate interactions during the electrochemical phase formation phenomena.

Detailed knowledge of the mechanisms and kinetics of phase formation are of practical interest for applications in surface finish, electrometallurgy, electrocatalysis,

and more recently in microelectronics and the manufacture of nanostructures. The experimental conditions of the electrochemical processes (including current density, potential, electrolyte composition, or the use of complexing agents) have substantial effects on the morphology and properties of the electrodeposits [14]. In particular, interest in developing efficient and environmentally friendly energy sources has motivated the study of the catalytic properties of micro- and nano-metallic clusters of noble and transition metals. These clusters may be deposited on metal surfaces or dispersed in three-dimensional structures, such as porous matrices, polymeric membranes, or thin conductive polymer films, to catalyze reactions such as oxygen reduction or the oxidation of hydrogen or organic molecules. Because of the strong effects of surface structure on reactivity, available theories of phase formation have become especially useful for controlling the size, morphology, density, and spatial distribution of metallic electrodeposits on electrodes.

### 5.3.2

#### Thermodynamics of Electrochemical Phase Formation

The thermodynamic treatment of phase transitions is usually based upon the equilibrium properties of the bulk phases involved. A description of the formation of a new phase requires consideration of at least two additional factors, the contribution of changes in the surface states to the total energy, and the influence of these changes on the rate of formation of the new phase.

Transformation of one phase into another will occur only when both phases are not at mutual equilibrium; the greater the deviation from equilibrium, the greater

the driving force for the transformation. If both phases are well developed, that is, if they are sufficiently large for the contributions of surface effects to be ignored, then the slightest deviation from equilibrium will cause a displacement of the boundary between phases, to counterbalance the deviation. However, if the phases are not well developed, that is, when one of them does not even exist, then the initial surface contributions to the total energy can be sufficiently important so as to impede the formation of a new phase. Such systems are in metastable equilibrium, and may remain in such condition for considerable periods of time. Common examples of metastable equilibria are supersaturated vapors (whether overcooled or overcompressed) and supercooled liquids, some of which, as in the case of glasses, remain indefinitely as stable amorphous solids.

The new phase generates from the metastable system necessarily in the form of nuclei. These are small clusters of atoms or molecules that in the prevailing conditions have developed into a size sufficiently large to grow spontaneously, ensuring their own viability and, eventually, the stability of the new phase. The intensive properties of nuclei differ from the bulk phase only because of their small size. This point of view is not necessarily correct since the properties, structure, and even the composition of small clusters may not be identical to those of the corresponding bulk phase, but the notion of a "nucleus" determined essentially by its size is useful to relate the macroscopic and microscopic descriptions of phase formation, as described below.

Leaving aside for the moment the problem of the origin of the nucleus and considering only the conditions for its further growth, the effect of its small size is manifested by an overwhelmingly

large ratio of surface to volume, which for macroscopic bodies tends to zero. Lord Kelvin [2] demonstrated that the larger the vapor pressure in equilibrium with a small drop of liquid at a given temperature, the smaller the radius  $r$  of the drop. If the drop is not sufficiently small, then its surface energy may be expressed as the product of the surface area  $4\pi r^2$ , and the macroscopic surface tension,  $\sigma$ , corresponding to  $r \rightarrow \infty$ . The thermodynamic potential of the total system, composed of vapor V and liquid L, is expressed by the equation,

$$\delta G = \mu_V dn_V + \mu_L dn_L + \sigma dS \quad (3)$$

where  $n_V$  and  $n_L$  represent the number of molecules on V and L,  $\mu_V$  and  $\mu_L$  are the chemical potentials referred to a molecule in the bulk phase at the given temperature and pressure, and  $S$  is the surface area of the drop. Thermodynamic equilibrium determined by the condition  $\delta G = 0$  and for a closed system,

$$\mu_V - \mu_L + 4\pi\sigma \frac{d(r^2)}{dn_L} = 0 \quad (4)$$

Designating the volume occupied by a molecule in the liquid phase as  $\Omega_L$ , then  $n_L = 4\pi r^3/3\Omega_L$ , and,

$$\mu_V - \mu_L + \frac{2\sigma\Omega_L}{r} = 0 \quad (5)$$

In the limiting case of  $r \rightarrow \infty$ , this expression reduces to the ordinary equilibrium condition between macroscopic phases,  $\mu_V = \mu_L$ . Differentiating Eq. (5) and considering that  $d\mu_V = \Omega_V dp$  and  $d\mu_L = \Omega_L dp$ , where  $\Omega_V$  is the volume per molecule in the gaseous phase, then

$$(\Omega_V - \Omega_L)dp = 2\sigma\Omega_L d\left(\frac{1}{r}\right) \quad (6)$$

Neglecting  $\Omega_L$  in comparison with  $\Omega_V$  and considering the vapor as an ideal

gas, for which  $\Omega_V = kT/p$ , where  $k$  is Boltzmann's constant and  $T$  the temperature, then

$$\ln\left(\frac{p}{p_\infty}\right) = \frac{2\sigma\Omega_L}{rkT} \quad (7)$$

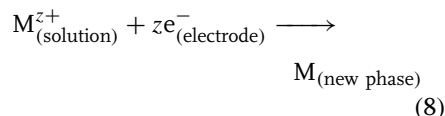
where  $p/p_\infty$  is the ratio between the pressures exerted over the surface of radius of curvature  $r$  and a flat surface, of infinite radius of curvature. This is the starting point of the classical theory of nucleation. According to Eq. (7), small clusters of the new phase are characterized by an excess vapor pressure. If the supersaturation pressure is larger than  $p$ , then the cluster will continue growing; if it were less than  $p$ , it would tend to evaporate. Since every cluster had to be initially of molecular size (and therefore  $p \gg p_\infty$ ), it still remains to be explained how a nucleus of a new phase ever appears. The reason is that all systems at finite temperature undergo fluctuations, which eventually produce a cluster with an equilibrium vapor pressure less than or equal to that of the supersaturated state. Hence a new phase will be formed, and according to classical theory, will continue growing. But before entering into a detailed discussion of the matter, we will describe briefly some fundamental concepts necessary to discuss equilibrium and phase transformations in electrochemical systems.

### 5.3.3

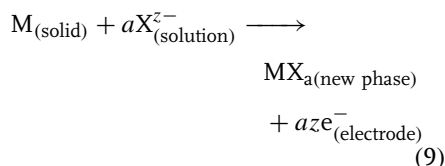
#### Electrochemical Nucleation Kinetics

Electrochemical nucleation can be considered as a series of partial reactions in which at least one step involves charge transfer by electrons or ions through the solution|electrode interface. The rate of the process is determined by the potential difference existing across the double layer in

reactions such as



for metal ion reduction to the corresponding metallic phase, or



for anodic deposit formation.

According to Erdey-Grüz and Volmer [15], the supersaturation  $c/c_\infty$ , where  $c$  is the concentration of ions in solution in equilibrium with a surface of radius of curvature  $r$ , and  $c_\infty$  is the corresponding concentration of ions in equilibrium with a planar surface, is directly determined by the overpotential,  $\eta = E - E_{\text{rev}}$ , where  $E$  is the electrode potential and  $E_{\text{rev}}$  is the equilibrium potential, in the absence of net current flow for a single electrode reaction.

For the metal electrode|solution interface,

$$\eta = \left(\frac{RT}{zF}\right) \ln\left(\frac{c}{c_\infty}\right) \quad (10)$$

where  $F$  is Faraday's constant. This relation expresses that through external control of the electrical potential, the conditions governing the electrochemical nucleation process can be precisely and reversibly controlled.

#### 5.3.3.1 The Classical Nucleation Model

From Eq. (3), the Gibbs energy of formation of a nucleus may be formally described as [3]

$$\Delta G = \delta G_{\text{volume}} + \delta G_{\text{surface}} \quad (11)$$

where

$$\delta G_{\text{volume}} = \left(\frac{4}{3}\right) \pi r^3 \Delta G_V \quad (12)$$

where  $\Delta G_V$  is the Gibbs energy of formation of the bulk phase per unit volume, and

$$\delta G_{\text{surface}} = 4\pi r^2 \sigma \quad (13)$$

$\delta G_{\text{volume}}$  is always a negative quantity, the thermodynamic way of expressing the spontaneity of the process, arising from the greater stability of the new phase with respect to the initial state. On the other hand, the interfacial contribution,  $\delta G_{\text{surface}}$ , is necessarily positive; otherwise the new phase would immediately become dispersed in the initial phase. For small values of  $r$ , the second term predominates, and the total change in Gibbs energy involved in the formation of a nucleus is also positive, that is,  $(\partial \Delta G / \partial r)_{\text{small } r} > 0$ . However, for larger values of  $r$ , the first term of Eq. (11) predominates and  $(\partial \Delta G / \partial r)_{\text{large } r} < 0$ . It is then evident that a particular value of the radius  $r = r^*$  exists, in which the Gibbs energy change is maximum,  $(\partial \Delta G / \partial r)_{r^*} = 0$ . Thus equating the first derivative of Eq. (11) to zero,

$$\left(\frac{\partial \Delta G}{\partial r}\right)_{r^*} = 4\pi (r^*)^2 \Delta G_V + 8\pi (r^*) \sigma = 0 \quad (14)$$

from which  $r^*$ , known as the critical radius, is obtained as

$$r^* = -\frac{2\sigma}{\Delta G_V} \quad (15)$$

Clusters with radius of curvature less than  $r^*$  will minimize their energy by disappearing in the initial phase, while larger ones will grow spontaneously. A

cluster with radius  $r^*$  is designated as a “critical nucleus” an entity in precise equilibrium with the initial phase as implied by  $(\partial \Delta G / \partial r)_{r^*} = 0$ , with equal probabilities of growing or decaying. If  $r \rightarrow r + \delta r$ , the cluster will grow irreversibly; alternatively, if  $r \rightarrow r - \delta r$ , it will disappear. Equation (15) is a direct consequence of Eq. (7), and is known as the Gibbs–Kelvin equation, relating the Gibbs energy of an interface with its radius of curvature. The reversible work required to form a critically sized cluster from the supersaturated phase can be obtained from Eq. (14), integrating between  $r = 0$  and  $r = r^*$  [3],

$$\begin{aligned} \Delta G_{\text{homo}}^* &= \left(\frac{16\pi}{3}\right) \frac{\sigma^3}{(\Delta G_V)^2} \\ &= \left(\frac{\sigma}{3}\right) 4\pi (r^*)^2 \end{aligned} \quad (16)$$

which has been designated here as  $\Delta G_{\text{homo}}^*$  (in homogeneous phase) to emphasize that Eq. (16) refers to the work of formation of a nucleus from the bulk phase.

A comparison of Eqs. (15 and 7) reveals that both the radius of the critical nucleus and the work needed to form it are functions of the ratio  $c/c_\infty$ . When  $c = c_\infty$ , that is, when the solution is saturated in relation to an interface of infinite radius of curvature, the work required to form a nucleus tends to infinite, and the phase transition does not occur. As the supersaturation ratio  $c/c_\infty$  increases, the radius of the critical nucleus, and hence its reversible work of formation, diminishes.

Supersaturation is one of the principal factors determining the work required to form a critical nucleus, but there are other factors worth considering too. In the majority of cases and especially under electrochemical conditions, formation of a new phase occurs on a surface. The



interaction between the substrate and the new phase has a strong influence on the reversible work of formation of the critical nucleus, thus nucleation occurs onto those sites on the surface with the minimal work of formation of critical clusters, the so-called *active sites*, to be treated further below.

Consider the deposition of a liquid phase in the solid|solution interface. The liquid surface makes contact with the solid at a characteristic angle  $\theta$ , the contact angle [16], defined as the angle between the tangent planes to the solid and liquid phases on the contact line, as shown in Fig. 1.

At any point along the equilibrium line between the contacting phases, there are three surface tension forces  $\sigma_{i,j} : \sigma_{1,2}$  between the liquid drop and the solution, at the contact angle  $\theta$  with respect to the surface;  $\sigma_{1,3}$  between the solid and the solution, directed along the plane of the surface, and  $\sigma_{2,3}$  due to the solid|liquid interface, also along the plane but opposing  $\sigma_{1,3}$ . To maintain equilibrium, the solid reacts with an additional force perpendicular to the surface and directed towards the bulk of the solid. The equilibrium condition is expressed by the Young equation

$$\sigma_{2,3} - \sigma_{1,2} \cos \theta - \sigma_{1,3} = 0 \quad (17)$$

A second relation between the three forces is obtained using Dupre's equation, defining the reversible work  $W_{2,3}$  needed to separate a unit area of the solid|liquid interface. Conservation of energy requires that [17]

$$\sigma_{2,3} + W_{2,3} = \sigma_{1,3} + \sigma_{1,2} \quad (18)$$

subtracting Eq. (17) from Eq (18),

$$W_{2,3} = \sigma_{1,2}(1 + \cos \theta) \quad (19)$$

This quantity is maximum when  $\theta = 0^\circ$ , that is, when the liquid completely wets the solid and  $W_{2,3}$  is zero when  $\theta = 180^\circ$  and the liquid evades the solid, a characteristic behavior that constitutes an effective method to determine the interaction energy between surfaces.

The work of formation of a liquid drop onto a surface may be written as

$$\Delta G = \Delta G_V V + \sigma_{1,2} S_{1,2} + \sigma_{2,3} S_{2,3} + \sigma_{1,3} S_{1,3} \quad (20)$$

where  $V$  is the volume of the drop and  $S_{1,2}$ ,  $S_{2,3}$  and  $S_{1,3}$  are the surface areas of the different interfaces involved. To calculate the work of formation of the critical nucleus, it is sufficient to know the relation  $\phi(\theta)$  between the volume of the spherical shell in contact with the solid,  $v$ , and the volume of a sphere with an equal

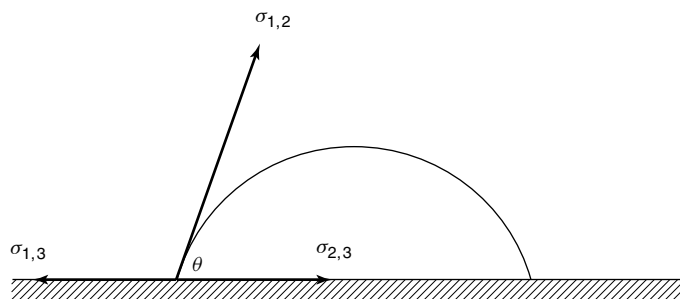


Fig. 1 Model of a liquid drop on a solid surface.

radius of curvature,  $V_e$ , in equilibrium with the supersaturated solution. The heterogeneous work of formation of the critical nucleus on the surface would be given by the corresponding work to form a sphere with the same radius of curvature, Eq. (16), multiplied by  $\phi(\theta)$

$$\begin{aligned}\Delta G_{\text{hetero}}^* &= \Delta G_{\text{homo}}^* \phi(\theta) \\ &= \left[ \frac{16\pi(\sigma_{1,3})^3}{3(\Delta G_V)^2} \right] \phi(\theta) \quad (21)\end{aligned}$$

The volume of the spherical shell is  $v = (2 - 3 \cos \theta + \cos^3 \theta) \pi r^3 / 3$  whereas that of the sphere is  $V_e = 4\pi r^3 / 3$ , thus,

$$\phi(\theta) = \frac{v}{V_e} = \frac{(2 - 3 \cos \theta + \cos^3 \theta)}{4} \quad (22)$$

$0 \leq \phi(\theta) \leq 1$ , nucleation at an interface requires always less energy than within the bulk phase.

To describe electrochemical phase formation processes, it is necessary to establish the role of the overpotential on the formation of nuclei. Under electrochemical conditions, the Gibbs energy of interfacial phase formation  $\Delta G_V$ , appears from the charge transfer of ionic species across the double layer, and can be defined in terms of the product of the net charge of formation of a cluster and the applied overpotential:

$$\Delta G_V = \frac{-zF\eta\rho}{M} \quad (23)$$

where  $\rho$  is the density of the deposit and  $M$  is the molar mass of the electrodepositing species. Then, the free energy of critical nucleus formation may be expressed as

$$\Delta G_{\text{hetero}}^* = \frac{16\pi\sigma^3 M^2 \phi(\theta)}{3(\rho z F \eta)^2} \quad (24)$$

where, to simplify the notation,  $\sigma_{1,3}$  has been written as  $\sigma$ . From this expression,

$$r^* = \frac{2\sigma M}{\rho z F |\eta|} \quad (25)$$

Figure 2 shows the free energy of hemispherical clusters ( $\theta = 90^\circ$ ,  $\phi(\theta) = 1/2$ ) of mercury as a function of the radius, for different values of the overpotential.

### 5.3.3.2 Nucleation on Electrode Surfaces

The probability of formation of a critical nucleus is proportional to  $\exp(-\Delta G^*/kT)$  [18], hence the rate of nucleation will be proportional to  $\exp(-4\pi\sigma(r^*)^2\phi(\theta)/3kT)$  and this exponential term is central to the theory of nucleation; a full description of the nucleation rate however requires also determining the preexponential factors. According to Farkas [19], each cluster is characterized by its number of molecules,  $n$ , and through kinetic arguments it is possible to evaluate the evolution of  $n$ . Since  $n$  is an integer, it can only vary in  $\pm 1$  due to random addition or loss of molecules.  $n$  may in principle change in 2 or even more units due to attachment of dimers, trimers, and so forth, but these events will be infrequent and may be neglected. This argument leads to an expression for the nucleation rate that contains an indeterminate integration constant, that Becker and Döring managed to eliminate reintroducing clusters attaining a given size, bigger than critical, as an equivalent number of monomers [4]. In this way, a steady state is maintained even though the system is closed, and under these conditions the number of clusters of a given size remain constant. Thus, a steady state distribution of cluster sizes may be defined, and the nucleation rate is then

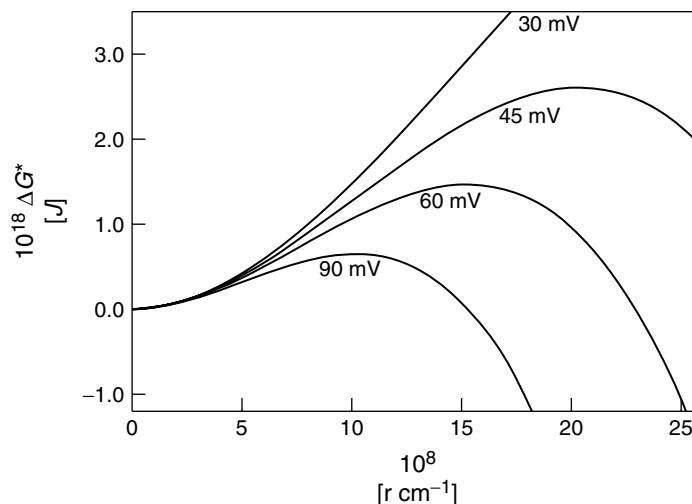
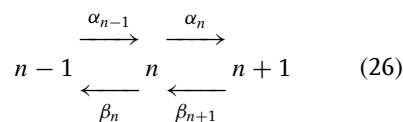


**Fig. 2** Free energy of formation of hemispherical mercury clusters from  $\text{Hg}_2^{2+}$  aqueous solution at different overpotentials, as a function of nucleus size.  $\sigma = 300 \text{ dyn cm}^{-1}$ , obtained from electrocapillary curves of Hg in  $\text{KNO}_3$  solution at  $E_{\text{Hg(II)/Hg}}^\circ = 0.8 \text{ V}$ .

expressed as the rate of aggregation of molecules to the critical nucleus, times the steady state concentration of clusters of critical size.

The treatment of Zeldovich [5] does not differ in essence from the already stated argument and allows for a more precise evaluation of critical parameters with a minimal of assumptions. It follows considerations from the Kramers theory of transition states, according to which the passage through the activated state is subject to random external influences, similar to those affecting the Brownian movement of particles in intense fields [20]. Thus, the system contains a constant number of molecules suffering statistical fluctuations at temperature  $T$ . If  $C_n(t)$  is the concentration of clusters of  $n$  molecules at time  $t$ , then, allowing only transitions between contiguous neighbors, that is, from  $n$  to  $n - 1$  or  $n + 1$ ,



The change in concentration of clusters of  $n$  molecules may be written as  $dC_n(t)/dt = \alpha_{n-1}C_{n-1}(t) - (\alpha_n + \beta_n)C_n(t) + \beta_{n+1}C_{n+1}(t)$ , which has the form of Kolmogorov differential equation for Markov processes in discrete number space and continuous time [21].  $\alpha_n$  and  $\beta_n$  are respectively the net probabilities of incorporation or loss of molecules by a cluster per unit time, and these may be defined formally as the aggregation or detachment frequencies times the surface area of the cluster of  $n$  molecules. Given the small size of the clusters,  $\alpha_n$  and  $\beta_n$  are not simple functions of  $n$  and in general they are unknown. However, if  $\alpha_n$  and  $\beta_n$  are not functions of time, then an equilibrium distribution  $C_n^\circ$  of cluster sizes exists, such that  $dC_n^\circ/dt = 0$  for  $C_n(t) = C_n^\circ$ , and the following differential

equation may be stated if we consider that in equilibrium, the number of clusters that progress from  $n$  to  $n + 1$  equals those decaying from  $n + 1$  to  $n$  per unit time:

$$\frac{\partial C_n(t)}{\partial t} = \frac{\partial}{\partial n} \left\{ \alpha_n C_n^\circ \frac{\partial}{\partial n} \left( \frac{C_n(t)}{C_n^\circ} \right) \right\} \quad (27)$$

This expression holds if the time during which the macroscopic phase transition occurs is large compared to the characteristic times of the accretion and decay processes,  $\alpha_n^{-1}$  and  $\beta_n^{-1}$ .

Equation (27) is the Fokker–Planck equation and describes diffusion in the presence of an external force,  $\alpha_n$  plays a role similar to that of the diffusion coefficient in the Fick equation; for the special case of  $C_n^\circ = C^\circ = \text{constant}$ , substituting  $\alpha_n$  for  $D$ , we obtain Fick's law,

$$\frac{\partial C_n(t)}{\partial t} = D \frac{\partial^2 C_n(t)}{\partial n^2} \quad (28)$$

However, the field of force or gradient in the Gibbs energy introduced by Eqs. (11–13) must be, in general, retained to describe the random diffusion of clusters through the distribution of their sizes. The equilibrium concentration of  $n$ -mers is given by

$$C_n^\circ = C_1 \exp \left( \frac{-\Delta G_n^\theta}{kT} \right) \quad (29)$$

where  $\Delta G_n^\theta$  is the standard Gibbs energy of formation of a  $n$ -mer from  $n$  monomers and  $C_1$  is the concentration of monomers in the initial phase. Referring to Eq. (16) describing the Gibbs energy of a critical cluster (cf. Fig. 2), it is clear that  $C_n^\circ$  is minimal at  $n = n^*$  ( $n^*$  is the number of molecules constituting the critical nucleus) or  $r = r^*$  and that  $\Delta G^* = \Delta G_{n^*}^\theta$  therefore constitutes the activation Gibbs energy for nucleation. Substituting

Eq. (29) in Eq. (27),

$$\frac{\partial C_n(t)}{\partial t} = \frac{\partial}{\partial n} \left\{ \alpha_n \frac{\partial C_n(t)}{\partial n} + \frac{\alpha_n C_n(t)}{kT} \frac{\partial (\Delta G_n^\theta)}{\partial n} \right\} \quad (30)$$

To solve this equation, it is convenient to define a “critical region” of values of  $n$  in which the Gibbs energies of clusters differ from the maximum  $\Delta G^*$  less than  $kT$ , the energy of thermal fluctuations (cf. Fig. 3), extending a cluster size range of  $(2\pi kT/\gamma)^{1/2}$ , where  $\gamma = -(\partial^2 \Delta G_n^\theta / \partial n^2)_{n^*}$ .

Since the Gibbs energy of activation is maximal at the critical nucleus,  $(\partial \Delta G_n^\theta / \partial n)_{n^*} = 0$  and to a first approximation the variation of  $\Delta G$  within the critical region may be neglected; the second term in the right-hand side of Eq. (30) will be small compared to the first and a steady state solution is readily found at fixed supersaturation and when clusters attaining a given supercritical size are instantaneously extracted from the system and replaced by an equivalent amount of monomers. Under these conditions,  $\partial C_n(t) / \partial t = 0$  and the steady state nucleation rate  $J_s$  may be expressed as

$$J_s = -\alpha_{n^*} \left( \frac{\partial C_n}{\partial n} \right)_{n^*} \quad (31)$$

which is clearly a diffusion equation that may be solved approximately with the limiting layer model. Thus replacing  $-(\partial C_n / \partial n)_{n^*}$  by  $C_{n^*} / \Delta n$ , where  $\Delta n$  is the width of the critical region,  $(2\pi kT/\gamma)^{1/2}$  and taking account that diffusion occurs at both sides of the critical region, then [22]

$$J_s = \frac{2\alpha_{n^*} C_{n^*}}{(2\pi kT/\gamma)^{1/2}} \quad (32)$$

Thus the steady state nucleation rate is expressed as the product of the equilibrium

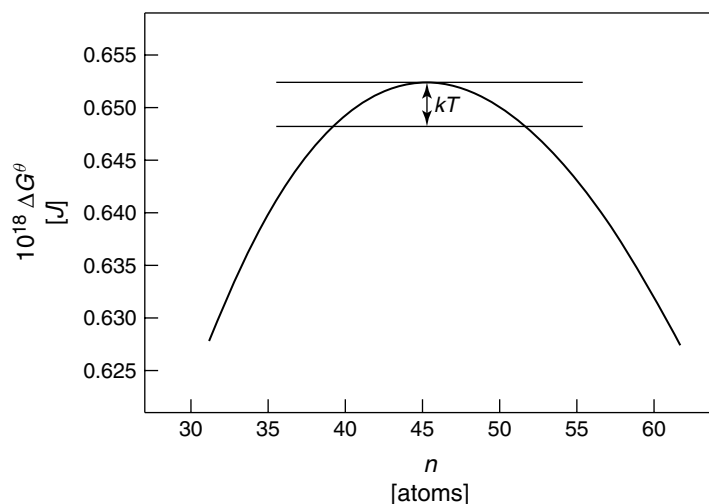


**Fig. 3** Critical region around  $n^*$  within which the energies of hemispherical mercury clusters at  $\eta = -90$  mV differ from  $\Delta G^*$  less than  $kT$ .

concentration of critical clusters,  $C_{n^*}^o$ , the rate of attachment of monomers to critical clusters,  $\alpha_{n^*}$ , and a “nonequilibrium factor”, known as the Zeldovich factor  $Z$ , which takes into account that the steady state concentration of  $n^*$  is only 1/2 of the equilibrium value and that supercritical clusters may still decay. The Zeldovich factor is thus defined as

$$Z = \sqrt{-\frac{1}{2\pi kT} \left( \frac{\partial^2 \Delta G_n^\theta}{\partial n^2} \right)_{n^*}} \quad (33)$$

The treatment as outlined above provides a good approximation of the steady state nucleation rate under conditions in which  $\Delta G^*$  may be calculated. The principal difficulty in finding the nucleation rate is in evaluating the equilibrium concentration of clusters in terms of their formation free energies. The classical way of realizing this is to consider all clusters as chemically equivalent,  $\Delta G_n^\theta$  is obtained from the Gibbs energy change for their formation from monomers, as a sum of “volume” and “surface” terms (cf. Eq. 11).

For small clusters, this procedure is prone to criticism on several grounds. The thermodynamic properties of small clusters, for instance, surface tension or composition, are supposed to be identical to those of the equilibrium bulk phase. In particular, it is considered that clusters are of homogeneous chemical composition, but this is hardly so in clusters that are only a few nm in diameter, given that for them the width of the interfacial boundary would be comparable to the radius of curvature. It is then inappropriate to extrapolate the normal notion of surface tension to such small clusters [23]; since the surface tension arises from the steep discontinuity between phases, it should be lower at high curvatures [24]. The surface width of the liquid–vapor transition region has been calculated, and for simple liquids is about seven or eight molecular diameters [25]. This means that the thermodynamic properties of a system composed of, for example, argon vapor and argon clusters smaller than  $\sim 300$  molecules will differ from those of a system composed of

bulk liquid and vapor phases at the same temperature. This is the basis of the diffuse drop model [26], according to which the nucleus presents uniform properties at low supersaturations, with interfacial energies independent of radius of curvature. At increasing supersaturation, the work of formation decays progressively, the interface becomes diffuse, and the composition of the nucleus becomes nonuniform throughout. At even higher supersaturation, the composition at the center of the nucleus approaches that of the external phase; the radius first decreases but then passes through a minimum and then diverges, as the work of formation tends to zero at very high supersaturation. Hence, unless the interfacial energy can be determined, the Gibbs energy of formation of small clusters, needed for the estimation of the nucleation rate, will remain unknown. In an experimental study of the electrochemical nucleation of metals from molten salts, Hills and coworkers [27] observed that the radius of critical nuclei passed through a minimum as the supersaturation increased. The diffuse liquid drop model predicts this behavior, but its adoption shifts the problem from determining the surface tension of small clusters to the no simpler task of calculating the Gibbs energy of formation of a nonhomogeneous phase. An alternative description is to introduce in the classical expression of the energy of formation of the surface, Eq. (11), the surface tensions between the liquid and the supersaturated phase at the different overpotentials [28], instead of the equilibrium surface tension between the liquid and the supersaturated phase. This is a remarkable result; extrapolation of macroscopic properties of materials to small clusters conducts to reasonable agreement between experimental

data and the kinetic equations derived from the classical theory of nucleation.

### 5.3.3.3 Microscopic Approach to Phase Formation: The Atomistic Model

As discussed in the previous section, the liquid drop model confronts serious difficulties in describing the nucleation rate when the critical size is of just a few atoms, as is commonly found in experimental studies of electrochemical nucleation. For such small clusters, not only is it inappropriate to use the macroscopic surface energy to calculate the nucleation rates, the concept of interfacial energy itself is open to question. For instance, all atoms are on the surface in clusters smaller than six atoms. On this basis, Walton [29] developed an expression for the concentration of clusters using statistical mechanics, avoiding the concept of surface energy and deriving the nucleation rate from purely kinetic considerations. Walton's treatment follows closely the classical work of Volmer [30] but using partition functions instead of classical thermodynamics to determine the equilibrium concentration of clusters. The expression obtained for  $C_n^\circ$  is [29]

$$\frac{C_n^\circ}{N_0} = \left( \frac{C_1}{N_0} \right)^n \exp \left( \frac{E_n}{kT} \right) \quad (34)$$

where  $N_0$  is the number density of adsorption sites on the surface, which is assumed to be much higher than  $C_1$ , the number density of adsorbed atoms, and  $E_n = \varepsilon_n - n\varepsilon_1$  is the energy of formation of the cluster, taking as zero the potential energy of the adsorbed atom.  $E_n$  is found minimizing the formation energies of all possible configurations of  $n$  atoms in all possible orientations, which may be accomplished, for example, by trial and error. The nucleation rate is calculated assuming that all clusters larger than

critical are immediately extracted from the system; the critical nucleus is defined as that cluster for which the probability of growing is less than or equal to 1/2 but, upon incorporating one atom, attains a probability of growing larger than 1/2. The probability of supercritical clusters decaying and turning subcritical is considered as very slim and is therefore neglected. The nucleation rate is then expressed as

$$J = R \frac{\sigma_{n^*}}{a} \left( \frac{R_a^2}{\nu} \right)^{n^*} \times \exp \left\{ \frac{[(n^* + 1)Q_{ad} + E_{n^*} - Q_D]}{kT} \right\} \quad (35)$$

where  $R$  is the incidence rate of atoms to the surface,  $\sigma_{n^*}$  is the capture cross section of critical nuclei,  $a$  is the distance between adsorption sites,  $\nu$  is an attempt frequency,  $Q_{ad}$  is the bond energy with the surface, and  $Q_D$  is the activation energy for surface diffusion. Since  $n^*$  can only adopt integer values, the same size of critical nucleus should operate over a range of temperatures, and discontinuities in the temperature-dependence of the nucleation rate are to be expected upon changes of the critical size along temperature intervals. Regarding the clustering process as an infinite chain of intermediates with relative concentrations determined by their respective rates of growth and decay [31] avoids altogether having to consider the notion of critical nucleus but, unfortunately, does not lead to analytical expressions for the nucleation rate without a number of additional assumptions, although it is possible to obtain explicit expressions for certain limiting cases [32].

Stoyanov [6] reexamined Walton's atomistic theory of heterogeneous nucleation and derived the nucleation rate avoiding

both the notion of critical nucleus as well as that of equilibrium concentration of clusters, starting from the expression for the nucleation rate obtained by Becker and Döring [4], that is,

$$J_s = \frac{\omega_{+1} C_1}{1 + \sum_{i=2}^m \frac{\omega_{-2}\omega_{-3}\cdots\omega_{-i}}{\omega_{+2}\omega_{+3}\cdots\omega_{+i}}} \quad (36)$$

where  $\omega_{+i}$  and  $\omega_{-i}$  are the frequencies of attachment and detachment of atoms, respectively, from a cluster of  $i$  atoms, given by

$$\omega_{+i} = \alpha_i \frac{C_i}{N_0} \nu \exp \left( -\frac{Q_D}{kT} \right)$$

and

$$\omega_{-i} = \beta_i \nu \exp \left[ -\frac{(E_i - E_{i-1} + Q_D)}{kT} \right] \quad (37)$$

where  $\alpha_i$  is the number of ways of forming a cluster of size  $i + 1$  incorporating one ad-atom to a cluster of size  $i$  and  $\beta_i$  is the number of ways an atom can detach from a cluster of size  $i$ . Given that for each birth,  $i \rightarrow i + 1$ , there is a corresponding death,  $i + 1 \rightarrow i$ ,  $\alpha_i$  and  $\beta_i$  are related by

$$\alpha_i = \beta_{i+1} \quad (38)$$

The sum in the denominator in Eq. (36) is taken to an arbitrary size  $m$  that may be defined as, for example, the minimal size experimentally observable. Thus  $J_s$  turns into the rate of conversion of the largest invisible clusters into detectable clusters and, since the rate in the steady state is equal for clusters of all sizes, the size of the critical nucleus does not need to be defined. Substituting Eqs. (37) and (38) in Eq. (36), the steady state nucleation rate is

obtained as

$$J_s = \omega_{+1} C_1 \left/ \left[ 1 + \sum_{i=2}^m \prod_{j=2}^i (\beta_j N_0 \times \exp(-E_j/kT)) \times \exp(-E_{j-1}/kT) / \beta_{j+1} C_1 \right] \right. \quad (39)$$

Since  $E_1 = 0$  and  $\alpha_1 = \beta_2$ , the product in the denominator may be expanded, and

$$J_s = \frac{\omega_{+1} C_1}{1 + \sum_{i=1}^m \frac{\beta_2}{\alpha_i} \left( \frac{N_0}{C_1} \right)^{i-1} \exp\left(\frac{-E_i}{kT}\right)} \quad (40)$$

Equation (40) reduces into Eq. (35) if any of the terms in the sum in the denominator is much larger than others, in which case the notion of critical nucleus is recovered.

The rate of electrochemical phase formation according to the atomistic model was derived by Milchev and coworkers [7] considering that the frequencies of attachment of atoms to form stable clusters of  $n^*$  atoms and detachment to form unstable clusters of  $n^* - 1$  atoms, is given by

$$\omega_{+n^*-1} = k_{+n^*-1} c \times \exp\left(-\frac{U_{n^*-1} - (1 - \alpha_e)ze_0(E_0 + \eta)}{kT}\right) \quad (41)$$

and

$$\omega_{-n^*} = k_{-n^*} \exp\left(-\frac{U_{-n^*} + \alpha_e ze_0(E_0 + \eta)}{kT}\right) \quad (42)$$

where  $U_{n^*-1}$  and  $U_{-n^*}$  are the energies of transfer of electrodepositing ions from solution to clusters and vice versa,  $c$  is the concentration of electrodepositing ions in solution,  $\alpha_e$  is the electronic transfer coefficient,  $e_0$  is the charge of the electron, and  $E_0$  is the equilibrium potential of the

electrodeposition reaction. According to Eq. (41),  $U_{-n^*} - U_{n^*-1} = \varphi_{n^*}$  represents the separation work of an atom from the cluster of  $n^*$  atoms. Furthermore, if the number density  $N_0$  of sites available for adsorption of atoms on the surface is in large excess with respect to the number density  $N_1$  of adsorbed atoms, then this latter is given by

$$N_1 = \left( \frac{N_0 - N_1}{N_0} \right) \exp\left(\frac{ze_0\eta}{kT}\right) \quad (43)$$

so that

$$\frac{\omega_{-n^*}}{\omega_{+n^*-1}} = \frac{k_{-n^*}}{k_{+n^*-1}} \frac{1}{c} \exp\left(-\frac{\varphi_{n^*}}{kT}\right) \times \exp\left(-\frac{ze_0(E_0 + \eta)}{kT}\right) \quad (44)$$

and the nucleation rate is expressed as

$$J_s = ZcN_0 \exp\left(-\frac{U_n - (1 - \alpha_e)ze_0E_0}{kT}\right) \times \exp\left(-\frac{\Phi(n^*)}{kT}\right) \times \exp\left(\frac{(n^* + 1 - \alpha_e)ze_0\eta}{kT}\right) \quad (45)$$

where  $Z$  contains the ratio of products of frequencies of attachment and detachment from clusters up to the critical and  $\Phi(n) = n\varphi_{1/2} - \Sigma\varphi_i$  represents the difference in energy of  $n$  atoms when they are part of an infinitely large crystal on the one hand, and when they form an independent cluster on the electrode surface on the other, that is,  $\Phi(n)$  represents the surface energy of the cluster of  $n$  atoms.

#### 5.3.4

#### Experimental Studies of Electrochemical Phase Formation

Metal electrodeposition occurs at the interface between an electronically conducting substrate and an ionically conducting



electrolyte. The sequence of events leading to the formation of a new phase may include the adsorption of metal ad-atoms, as well as two-dimensional or three-dimensional nucleation, followed by the growth of the bulk deposit. The particular mechanism for the growth of the new phase on the conductive substrate is determined by a balance of the interactions between ad-atoms and the substrate,  $\Psi(\text{Me}_{\text{ads}}-\text{S})$ , and the crystallographic compatibility of the substrate with the bulk metal deposit [1]. Under quasi-equilibrium conditions, in which low supersaturations and the absence of kinetic limitations might be assumed, phase formation occurs through two fundamental mechanisms: if the energy of metal|substrate interactions dominates,  $\Psi(\text{Me}_{\text{ads}}-\text{S}) < \Psi(\text{Me}_{\text{ads}}-\text{Me})$ , then the concentration of ad-atoms  $\text{Me}_{\text{ads}}$  is small and the formation of three-dimensional clusters is favored. On the other hand, if  $\Psi(\text{Me}_{\text{ads}}-\text{S}) > \Psi(\text{Me}_{\text{ads}}-\text{Me})$ , then the degree of commensurability between the crystalline habits of the substrate and the adsorbate determines if the new phase grows as epitaxial bidimensional layers or as three-dimensional nuclei.

#### 5.3.4.1 Three-dimensional Nucleation

Experimental studies of electrochemical phase formation may be carried out by direct observation of the number of nuclei on the electrode surface at different stages of the growth process [33, 34], or by relating the electrical current with the number density of nuclei on the electrode [8, 35], in which case it is necessary to establish also the rate of growth of the deposit. In many cases of electrochemical phase formation reactions, particularly during the electrodeposition of metals from molten salts [36], or aqueous solutions, [37], the charge-transfer step is fast and the rate

of growth of mature, supercritical nuclei, are well described by the mass transfer of the electrodepositing species to growth centers. Nuclei are small and they may be regarded as ultramicroelectrodes [38]; the diffusion-controlled current flux to an isolated hemisphere of radius  $r_0$  on the surface is [8, 39]

$$I = 2\pi zFDcr_0 \quad (46)$$

Where  $zF$  is the molar charge transferred during the electrodeposition process and  $D$  is the diffusion coefficient of the electrodepositing species in the bulk of the solution. The same current also causes the growth of the deposit, thus, following Faraday's law:

$$I = \frac{zF\rho}{M} \frac{dV}{dt} \quad (47)$$

and accordingly,

$$2\pi zFDcr_0 = \frac{zF\rho}{M} 2\pi r_0^2 \frac{dr}{dt} \quad (48)$$

from which the radius of an isolated nucleus of age  $t$  is given by

$$r_0 = \sqrt{\frac{2DcMt}{\rho}} \quad (49)$$

and the growth current of an isolated nucleus as a function of time is

$$I(t) = \frac{\pi zF(2Dc)^{3/2} M^{1/2} t^{1/2}}{\rho^{1/2}} \quad (50)$$

In general, experimental studies of the kinetics of formation of metallic phases on electrodes are performed potentiostatically, stepping the potential from a positive to a negative value with respect to the reversible potential of the electrodeposition reaction. Under potentiostatic conditions, it is generally assumed that both the steady state nucleation rate  $J_s$  and the growth rate

of nuclei will remain a constant, with rates depending on the applied overpotential. The value  $A$  of the steady state nucleation rate can be obtained from analysis of the current, which represents the overall rate of the electrodeposition process. For a real surface at constant overpotential, the rate of formation of nuclei over a given number of active sites  $N_0$  may be expressed as [12]

$$\frac{dN}{dt} = (N_0 - N) \quad (51)$$

Integration with initial condition  $N = 0$  at  $t = 0$  gives the number density of nuclei as a function of time:

$$N = N_0[1 - \exp(-At)] \quad (52)$$

Typical values of  $N_0$  are  $10^4 \text{ cm}^{-2} < N_0 < 10^{10} \text{ cm}^{-2}$ , frequently dependent of the potential but always smaller than the number density of atoms on the surface, of ca.  $10^{15} \text{ cm}^{-2}$  [40, 41]. For small values of  $A$  ( $\ll 1/t$ ), Eq. (52) reduces to  $N = N_0At$  and the nucleation process is said to be progressive, while for large values of  $A$ ,  $N = N_0$  and the saturation number density of nuclei is achieved immediately after applying the potential step, and nucleation is instantaneous. Under conditions of multiple nucleation, the current density can be expressed as the convolution of the growth rates of individual nuclei at time  $t$  after having born at time  $u$  (Eq. 50) and their appearance on the surface,  $dN/du = AN_0 \exp(-Au)$ , Eqs. (51 and 52) [9]:

$$i(t) = \frac{\pi z F (2Dc)^{3/2} M^{1/2}}{\rho^{1/2}} \times \int_0^t (t-u)^{1/2} \frac{dN}{du} du \quad (53)$$

The solution of Eq. (53) may be expressed as

$$i(t) = \frac{\pi z F (2Dc)^{3/2} M^{1/2} N_0 t^{1/2}}{\rho^{1/2}} \Phi \quad (54)$$

where

$$\Phi = 1 - \frac{e^{-At}}{(At)^{1/2}} \int_0^{(At)^{1/2}} e^{\lambda^2} d\lambda \quad (55)$$

$\Phi(At)^{1/2}$  is Dawson's integral, a tabulated function [42]. For,  $At \geq 20$ ,  $\Phi \rightarrow 1$  and Eq. (54) describes the current density corresponding to "instantaneous" nucleation, proportional to  $N_0 t^{1/2}$ ; for  $At \leq 0.2$ ,  $\Phi \rightarrow (2/3)At$  and the current density is proportional to  $(2/3)N_0 A t^{3/2}$ , corresponding to the limiting case of "progressive" nucleation.

Equation (54) and the limiting cases of "instantaneous" and "progressive" nucleation are valid only during the initial stages of the electrocrystallization process, when the number and size of the nuclei are sufficiently small so as for growth to occur independently from each other. The general description of the current transient requires consideration of interactions among nuclei [9–12, 43–48]. Initially, as discussed above, nuclei grow independently of each other and the process is controlled by hemispherical diffusion to isolated nuclei – the "short time" behavior. After some time, the diffusion fields around nuclei overlap and eventually the growth of the deposit is controlled by linear diffusion towards the planar electrode surface – the "long time" behavior. To overcome the difficulties encountered in describing this many-body problem, some approaches have taken into account the overlap of three-dimensional diffusional fields using Avrami's theorem [13], either considering slices [45] or two-dimensional projections on the electrode surface in the form of

circular “diffusion zones” [9, 11, 12, 43, 44]. Other treatments have avoided the Avrami approach altogether, considering mean field approximations [46] or using statistical mechanics to calculate nucleus growth [48], but restricting consideration to only the limiting case of instantaneous nucleation. Other developments [49, 50] have considered the changes in concentration occurring around nuclei during their diffusion-control growth and the effect of these changes on the nucleation rates and on the spatial distribution of nuclei, but do not discuss how to determine the nucleation rate  $A$  and the number density of active sites  $N_0$  from experimental data.

Models allowing to determine  $A$  and  $N_0$  obtain the current transient from the material flux to “free”, noninteracting, growth centers, considering circular diffusion zones around them, with time-dependent radii  $r_d$ . As shown in Fig. 4, these are two-dimensional projections of three-dimensional fields that define, for a hemispherical nuclei of radius  $r_0$ , an equivalent area toward which the same amount of matter that diffuses spherically to a three-dimensional nucleus diffuses by planar diffusion.

The mass balance results in

$$\frac{\pi z F (2Dc)^{3/2} M^{1/2} (t-u)^{1/2}}{\rho^{1/2}} = \times \frac{z F D c (\pi r_d^2)}{\pi D (t-u)^{1/2}} \quad (56)$$

where the term at the left is the current to a single hemispherical nucleus, Eq. (52), and the right-hand side term is the Cottrell current for a plane electrode of equivalent area  $\pi r_d^2$ , generated at the moment of birth of the nucleus. Accordingly, the radial flux (flux density  $\times$  area) equated to the planar flux to the equivalent diffusion zone, defines its area as [12]

$$\pi r_d^2 = (2\pi)^{3/2} D \left( \frac{cM}{\rho} \right)^{1/2} (t-u) \quad (57)$$

However, nuclei do not grow independently of each other and their interactions results in overlap of the diffusion fields around them. Overlap may be accounted for using Avrami’s theorem, [13]

$$\theta_d = 1 - \exp(-\theta_{ex}) \quad (58)$$

where  $\theta_d$  is the fraction of electrode surface covered by planar diffusion zones and  $\theta_{ex}$  is the “extended” coverage, that is, the fraction of surface that would be covered in absence of overlap,

$$\theta_{ex} = \frac{\pi^{3/2} (2Dc)^{3/2} M^{1/2}}{\rho^{1/2}} A N_0 \times \int_0^t (t-u) \exp(-Au) du \quad (59)$$

that after integration yields

$$\theta_{ex} = 2\pi \left( \frac{2MDc}{\rho} \right)^{1/2} N_0 (\pi Dt)^{1/2} t^{1/2} \Theta = \alpha At \Theta \quad (60)$$

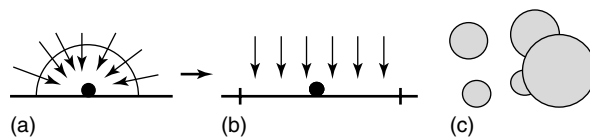


**Fig. 4** (a) Hemispherical diffusion fields; (b) projection to the electrode surface as planar diffusion zones; and (c) their overlap on the plane of the surface.

where  $\alpha = (2\pi)^{3/2} D(cM/\rho)^{1/2} N_0/A$  and

$$\Theta = 1 - \frac{(1 - e^{-At})}{At} \quad (61)$$

The coverage of the electrode surface with diffusion zones, considering overlap, is then given by the following expression:

$$\theta_d = 1 - \exp[-\alpha(At - 1 + e^{-At})] \quad (62)$$

The “instantaneous” limit corresponds to the  $\alpha \rightarrow 0$  limit, high nucleation rate  $A$  on small number density of active sites  $N_0$ , while the “progressive” situation results when the value of  $A$  is low and/or  $N_0$  is elevated, that is, when  $\alpha \rightarrow \infty$ . The current density is obtained as the planar diffusive flux to an electrode of fractional area  $\theta_d$ :

$$i(t) = \frac{zFDc}{\delta} \theta_d \quad (63)$$

The length of the diffusion layer is obtained from the balance between Eqs. (54 and 63) [11]

$$\frac{\pi z F (2Dc)^{3/2} M^{1/2} N_0 t^{1/2}}{\rho^{1/2}} \Phi = \frac{zFDc}{\delta} \theta_{ex} \quad (64)$$

as

$$\delta = (\pi Dt)^{1/2} \frac{\Theta}{\Phi} \quad (65)$$

According to this expression [11], the rate of expansion of the diffusion layer depends on the nucleation rate  $A$ , but not on the density of active sites. For instantaneous nucleation,  $\delta = (\pi Dt)^{1/2}$ , whereas for progressive nucleation,  $\delta = (3/4)(\pi Dt)^{1/2}$ . From Eqs. (54, 60 and 64), the current density is described as [11, 12]

$$i(t) = \frac{zFDc}{(\pi Dt)^{1/2}} \frac{1 - \frac{e^{-At}}{(At)^{1/2}} \int_0^{(At)^{1/2}} e^{\lambda^2} d\lambda}{1 - \left( \frac{1 - e^{-At}}{At} \right)}$$

$$\times \left\{ 1 - \exp \left[ - (2\pi)^{3/2} D \left( \frac{cM}{\rho} \right)^{1/2} \times N_0 t \left( 1 - \left( \frac{1 - e^{-At}}{At} \right) \right) \right] \right\} \quad (66)$$

#### 5.3.4.2 Two-dimensional Electrocrystallization

Two-dimensional phase formation occurs preferentially when a strong substrate-metal interaction exists, a process that typically involves the formation of growth centers a few atoms thick, that expand and coalesce to form a monolayer that serves as a precursor deposit to subsequent two-dimensional metal layers.

As discussed before, for a determinate supersaturation level  $\Delta\mu$ , ion transfer from solution to electrode across the electrochemical double layer occurs accompanied by the corresponding free energy change,  $\Delta G_V(n) = -nze|\eta|$ . A fraction  $\phi(n)$  of this energy is consumed in the formation of the new nucleus|solution and nucleus|surface interfaces, giving for the total change of Gibbs free energy associated with the formation of a cluster comprising  $n$  atoms,  $\Delta G_V(n) = -nze|\eta| + \phi(n)$ . This expression has a minimum  $\Delta G^*$  for the equilibrium form of the crystal with the lower surface energy  $\sigma_i$  among the  $i$  crystalline faces, as determined by the Gibbs–Curie expression [51],  $\phi = \sum_i \sigma_i A_i = \min$  (for constant volume  $V$ ).

In the case of epitaxial grow over an ideal substrate, the surface energies of the two-dimensional clusters reduce to border energies  $\varepsilon_i$  (J cm<sup>-1</sup>), as the emergence of the new phase is balanced by disappearance of substrate area. Under these conditions, the 2D crystal satisfies the Gibbs–Curie condition for the excess free energy, in analogy to the three-dimensional case;  $\phi = \sum_i \varepsilon_i L_i = \min$  (at

constant area), where  $L_i$  is the border length of the 2D crystal. By appropriate considerations for simple geometrical forms [52], the number of atoms of the critical 2D nucleus may be obtained from

$$n^* = \frac{b\Omega\varepsilon^2}{(ze|\eta|)^2} \quad (67)$$

where  $b$  is a geometrical factor,  $\Omega$  the area occupied by an atom in the cluster surface, and  $\varepsilon$  the mean value of the border energies for the  $i$  crystalline faces, from which the free energy of the critical 2D nuclei is  $\Delta G^* = ze|\eta|n^*$ . The Volmer–Weber expression applied to the two-dimensional case gives

$$J = A_{2D} \exp\left(-\frac{b\Omega\varepsilon^2}{ze|\eta|kT}\right) \quad (68)$$

where  $A_{2D}$  may be considered constant, although it encloses the potential-dependent contributions coming from the Zeldovich factor  $Z$  and the probability of attachment to critical nuclei  $\omega_{n^*}n^*$ .

Analysis of  $\ln(J)$  versus  $1/|\eta|$  relationships from experimental data allows to determine the nucleation parameters  $n^*$  and  $\Delta G^*$  for the critical nucleus, through the relation [52]

$$\frac{d \ln J}{d|\eta|} = -\frac{1}{KT} \frac{d\Delta G^*}{d|\eta|} = n^* \frac{zF}{RT} \quad (69)$$

The description of the current transient arising from nucleation and growth of two-dimensional monolayers, considers as limiting step the attachment of atoms or molecules to the edge of the growing two-dimensional centers. The required charge to form a disc-shaped nuclei of radius  $r$  and height  $h$  is  $Q(r) = zF\pi r(t)^2 h\rho/M$ , from which the instantaneous current  $i(r, t) = zF2\pi r(t)h\rho/M dr(t)/dt$  may be obtained differentiating with respect to time. If  $k$  (in moles  $\text{cm}^{-2} \text{s}^{-1}$ ) is the

rate of attachment of atoms to the growth center, the radial expansion rate would be  $dr(t)/dt = Mk/\rho$  and the temporal dependence of the radius  $r(t) = Mkt/\rho$ . These expressions lead to the following equation for the current associated with the growth of an isolated disc-shaped nucleus:

$$i_{2D}(t) = \frac{2\pi n F k^2 h M}{\rho} t \quad (70)$$

As previously considered with respect to the three-dimensional nucleation situation, the expression for the current transient corresponding to multiple two-dimensional nucleation requires consideration of the coalescence of growth centers, which diminishes the edge length available for attachment of new atoms or molecules, and produces a decay of the current. By means of the Avrami theorem (see Sect. 5.3.4.1), the following expressions are obtained for the limiting cases of instantaneous and progressive two-dimensional nucleation:

$$I_{2D, \text{inst}} = \frac{2\pi z F M h N_0 k^2 t}{\rho} \times \exp\left(-\frac{\pi N_0 M^2 k^2 t^2}{\rho^2}\right) \quad (71)$$

$$I_{2D, \text{prog}} = \frac{\pi z F M h N_0 k^2 t^2}{\rho} \times \exp\left(-\frac{\pi A N_0 M^2 k^2 t^3}{3\rho^2}\right) \quad (72)$$

#### 5.3.4.3 Spatial Distribution of Nuclei

The fundamental reason to study nucleation kinetics under potentiostatic conditions is to maintain constant supersaturation and hence a constant nucleation rate, except for nonstationary effects occurring at the onset of the potential step. However, the irreversible growth of the

nuclei diminishes the concentration of electrodepositing species and inhibits the nucleation rate in their vicinity. Thus the number of nuclei that ultimately attain stable growth over the surface depends on the local variations of the nucleation rate, as a result of changes in concentration occurring during the growth process. At sufficiently high overpotentials and in the presence of excess supporting electrolyte, the local nucleation rate at a given moment  $t$  and at a distance  $r$  from the center of a nucleus of age  $\tau = (t - u)$  and radius  $r_0 = (2DcM/\rho)^{1/2}\tau^{1/2}$  is given by [53]

$$A(r, t) = A_0 \left( 1 - \frac{(2DcM/\rho)^{1/2}\tau^{1/2}}{r} \right)^{n^*+1} \quad (73)$$

where  $A_0$  is the noninhibited nucleation rate at a sufficiently large distance from a growing nucleus. The local variation of the nucleation rate due to the growth of nuclei is shown in Fig. 5.

Thus, the probability of forming a nucleus somewhere in the electrode surface at a given moment  $t$  is affected by the presence of a nucleus  $i$  located at a distance  $r_i$ ; this may be expressed as  $p_i(r_i, t) = A(r_i, t)/A_0$ . If the effects of several nuclei in the vicinity of the site were independent, then the joint nucleation probability would be expressed as  $p(r_i, t) = \prod p_i(r_i, t)$ , but the radial symmetry of the diffusional hemispherical fields generated by the growth of nuclei is robust [54], thus the concentration of electrodepositing species is determined by the nucleus that exerts the more intense diffusional field on the particular site, acting then as the most influential neighbor, and superseding the effects induced by other smaller or more distant neighbors. Then the local nucleation rate is not determined by the combined effects of all the nuclei surrounding the particular site, but only by the “most influential neighbor” [50]. This most influential neighbor

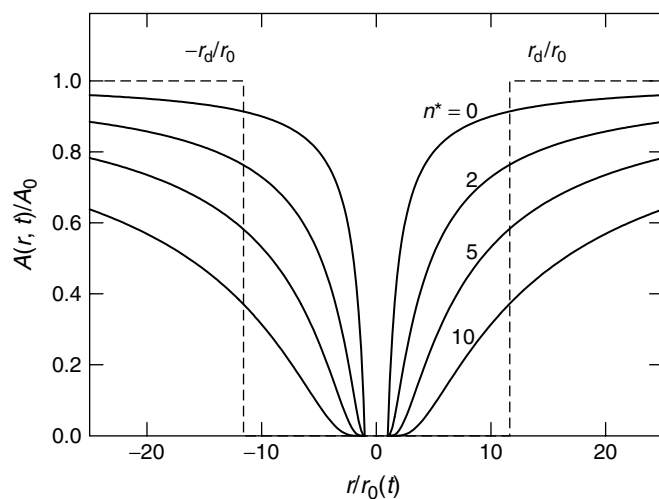


**Fig. 5** Local nucleation rate around a growing nucleus of radius  $r_0$ , for different critical nucleus sizes. Also shown is the exclusion zone of radius  $r_d$ , defining regions inside ( $A = 0$ ) and outside ( $A = A_0$ ) the exclusion zone.

and its effects on the nucleation process may be identified defining a circular zone around each nucleus, inside which formation of further nuclei is excluded. The overall rate of nucleation will diminish as a result of the decreased supersaturation caused by the growth of nuclei, and will eventually vanish as the exclusion zones expand and overlap, covering all the area available. In Fig. 5, the size of the exclusion zone has been identified with that of the diffusion zones considered on the current transient analysis. Under this assumption, the saturation number density of nuclei on the electrode surface is given by

$$N_S = AN_0 \int_0^\infty \exp \left[ - (2\pi)^{3/2} D \times \left( \frac{cM}{\rho} \right)^{1/2} N_0 \frac{(Au - 1 - e^{-Au})}{A} \right] \times e^{-Au} du \quad (74)$$

Evaluation of  $N_S$  from Eq. (74) requires numerical methods, but for the particular case of “progressive” nucleation, that is, when nucleation is slow and occurs on a large number density of active sites, then [55]  $N_S = \{AN_0/[2(8\pi cM/\rho)^{1/2}D]\}^{1/2}$ . Values of  $N_S$  obtained from this expression agree favorably with experimental number densities of Pb, Ag, and Hg nuclei obtained by direct microscopic observation of electrode surfaces [56–58].

Local variations of the nucleation rate affect not only the saturation number density of nuclei, but also their spatial distribution [59, 60], and this can be studied analyzing images of the electrode surface. The spatial distribution of nuclei is represented in Fig. 6 by the probability density of the distances between nearest neighbors, in nondimensional, normalized form. For

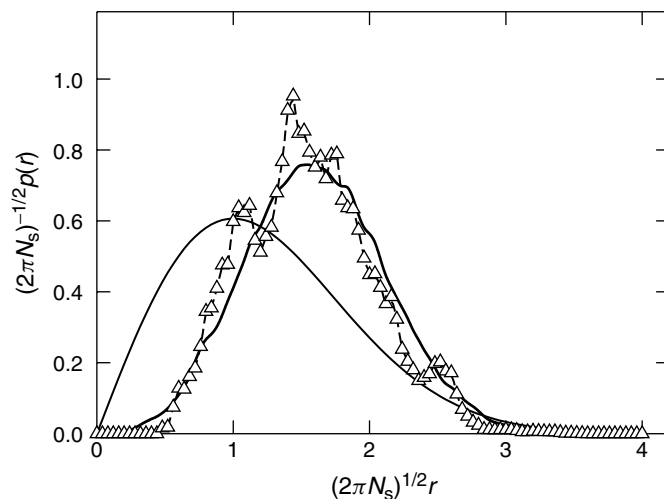


**Fig. 6** Normalized probability density of nearest neighbor distances for  $2.2 \times 10^6$  drops/cm<sup>2</sup> of mercury, electrodeposited onto vitreous carbon at 220 mV from 0.01 mol dm<sup>-3</sup> Hg<sup>2+</sup> aqueous solution ( $\Delta$ ) [58]. Also shown are the probability densities corresponding to uniformly distributed drops (thin line) and excluded nucleation for distances less than  $r_d = [(8\pi cM/\rho)^{1/2}D(t-u)]^{1/2}$  from each drop (heavy line), obtained from digital simulations [59].

uniformly distributed nuclei, the nearest neighbor distribution can be obtained as follows [56]. The probability of finding the nearest neighbor at a distance  $r$  from a given nucleus,  $P(r)$ , can be expressed as the product of the probability of not finding one at a distance less than  $r$ , and the probability of finding one between  $r + dr$ :

$$dP(r) = p(r)dr = \left[ 1 - \int_0^r p(u) du \right] \times 2\pi N_S r dr \quad (75)$$

This may be now expressed as  $dP(r)/[1 - P(r)] = 2\pi N_S r dr$ , and after integration becomes  $P(r) = 1 - \exp(-\pi N_S r^2)$ . Thus,

$$p(r)dr = 2\pi N_S r \exp(-\pi N_S r^2) \quad (76)$$

The probability density in Eq. (76) has maximum value for  $r_m = 1/(2\pi N_S)^{1/2}$ , and we may express it in nondimensional form in terms of this characteristic distance, as

$$(2\pi N_S)^{-1/2} p(r) = (2\pi N_S)^{1/2} r \times \exp\left(-\frac{1}{2}[(2\pi N_S)^{1/2} r]^2\right) \quad (77)$$

This normalized distribution does not depend on the number density of nuclei on the electrode surface, and only denotes the ordering pattern of nuclei on the electrode surface. If nuclei were, for example, ordered on a square array, then the distance between nearest neighbors would be  $1/N_S^{1/2}$  and the probability of finding the nearest neighbor would change from 0 to 1 at a nondimensional distance  $N_S^{-1/2}/(2\pi N_S)^{-1/2} = (2\pi)^{1/2} = 2.507$ . In a hexagonal array, all nearest neighbors are separated by a nondimensional distance  $(4\pi/\sqrt{3})^{1/2} = 2.694$ . For a random uniform distribution, the probability density is maximum at the characteristic distance, that is,  $(2\pi N_S)^{-1/2}/(2\pi N_S)^{-1/2} = 1$ . In nondimensional coordinates, the maximum of the distribution shifts to higher

distances as the ordering of the nuclei on the plane increases. As is shown in Fig. 6, inhibition of nucleation in the vicinity of growing nuclei induces a certain degree of ordering, which may be advantageous, for example, in the preparation of catalysts to reduce sintering and to assist accessibility of the catalytic sites by reacting species.

In general [50, 56–58], electrodeposited nuclei at low overpotentials are uniformly distributed, reflecting a random distribution of active sites on the electrode surface, while at higher overpotentials the spatial distribution of nuclei is affected by inhibition of the nucleation rate in their vicinity.

#### 5.3.4.4 Experimental Examples

Mercury electrodeposition is a model system for experimental studies of electrochemical phase formation. On the one hand, the product obtained is a liquid drop, corresponding very well with the liquid drop model of classical nucleation theory. Besides, electron transfer is fast [61] and therefore the growth of nuclei is controlled by mass transport to the electrode surface [44]. On the other hand, the properties of the mercury|aqueous solution interface have been the object of study for over a century and hence are fairly well understood. The high overpotential for proton reduction onto both mercury and vitreous carbon favor the study of the process over a wide range of overpotentials. In spite of the complications introduced by the equilibrium between the  $\text{Hg}^{2+}$ ,  $\text{Hg}_2^{2+}$ , and  $\text{Hg}$  species, this system offers an excellent opportunity to verify the fundamental postulates of the electrochemical nucleation theory. In fact, the dependence of the nucleation rate on the oxidation state of the electrodeposing species is fully consistent with theory: critical nuclei appear with similar sizes and onto similar number densities of active sites



either from  $\text{Hg}_2^{2+}$  or  $\text{Hg}^{2+}$  solutions, as expected from the identical interactions between deposit and substrate in both cases. This demonstrates the dominant role of the interaction between the surface and the deposit in the phase formation process, as discussed before. Fig. 7 shows a family of current transients obtained for mercury electrodeposition from  $\text{Hg}(\text{I})$  solution onto vitreous carbon at different potentials.

A similar family of theoretical current transients, obtained from evaluation of Eq. (66) with the known values of  $z$ ,  $F$ ,  $c$ ,  $M$ , and  $\rho$  corresponding to the reduction of  $\text{Hg}(\text{I})$  to  $\text{Hg}(0)$ , is shown in Fig. 8.

As shown in both the experimental and theoretical transients, the currents first increase as a result of the formation of mercury drops and their growth controlled by radial diffusion, decaying at longer times due to the onset of semi-infinite planar diffusion. The diffusion coefficients may be obtained either from  $i$  versus  $t^{-1/2}$  plots

for sufficiently long times, at which linear dependence is observed in accordance with Cottrell behavior, or by hydrodynamic methods using rotating electrodes. In the particular case of mercury, nucleation may be realized also from  $\text{Hg}(\text{II})$  solutions, and Fig. 9 shows the nucleation rates as a function of the overpotential from both  $\text{Hg}(\text{I})$  and  $\text{Hg}(\text{II})$  solutions, obtained from the analysis of current transients.

According to Eq. (45), the atomistic theory predicts a linear dependence of the nucleation rate with overpotential for constant size of the critical nucleus, as shown in Fig. 7. Also, in accordance with Eq. (45), the value of the slope doubles for mercury deposition from  $\text{Hg}(\text{II})$  as compared with deposition from  $\text{Hg}(\text{I})$ . The slopes of logarithmic plots of the nucleation rate as a function of the overpotential, such as that shown in Fig. 9, confirm the small sizes of critical nuclei in electrochemical phase formation processes. Frequently, as suggested by the

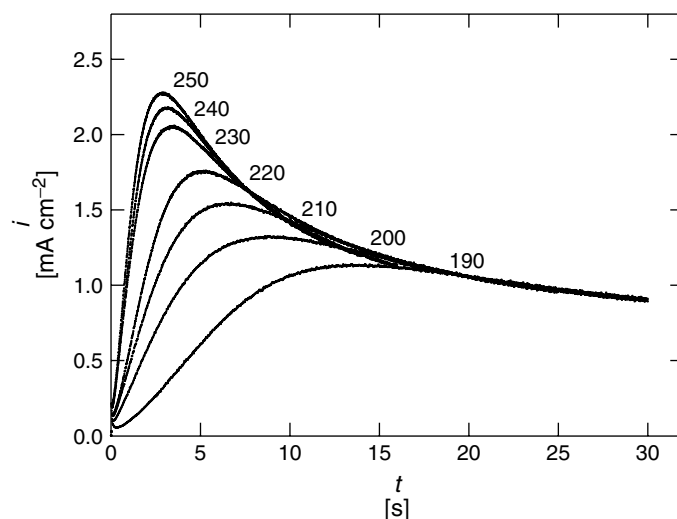


**Fig. 7** Current transients recorded during Hg electrodeposition onto vitreous carbon from  $0.01 \text{ mol dm}^{-3} \text{ Hg}_2^{2+}$  solutions in  $\text{KNO}_3$   $1 \text{ mol dm}^{-3}$  at the indicated overpotentials (in mV) [58].

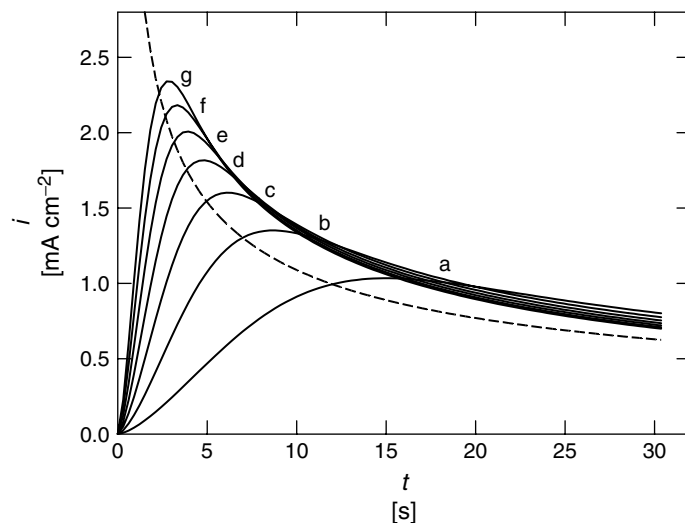


**Fig. 8** Current transients according to Eq. (66), for mercury electrodeposition from 10 mM  $\text{Hg}_2^{2+}$  solutions, with  $D = 10^{-5} \text{ cm}^2 \text{ s}^{-1}$ , at nucleation rates  $A$  and number densities of active sites  $N_0$ , respectively, of: (a)  $0.02 \text{ s}^{-1}$  and  $0.4 \times 10^6 \text{ cm}^{-2}$ ; (b)  $0.04 \text{ s}^{-1}$  and  $0.6 \times 10^6 \text{ cm}^{-2}$ ; (c)  $0.06 \text{ s}^{-1}$  and  $0.8 \times 10^6 \text{ cm}^{-2}$ ; (d)  $0.08 \text{ s}^{-1}$  and  $1.0 \times 10^6 \text{ cm}^{-2}$ ; (e)  $0.10 \text{ s}^{-1}$  and  $1.2 \times 10^6 \text{ cm}^{-2}$ ; (f)  $0.12 \text{ s}^{-1}$  and  $1.4 \times 10^6 \text{ cm}^{-2}$ ; and (g)  $0.14 \text{ s}^{-1}$  and  $1.6 \times 10^6 \text{ cm}^{-2}$ . The broken line indicates the Cottrell diffusive limiting current to the electrode surface.

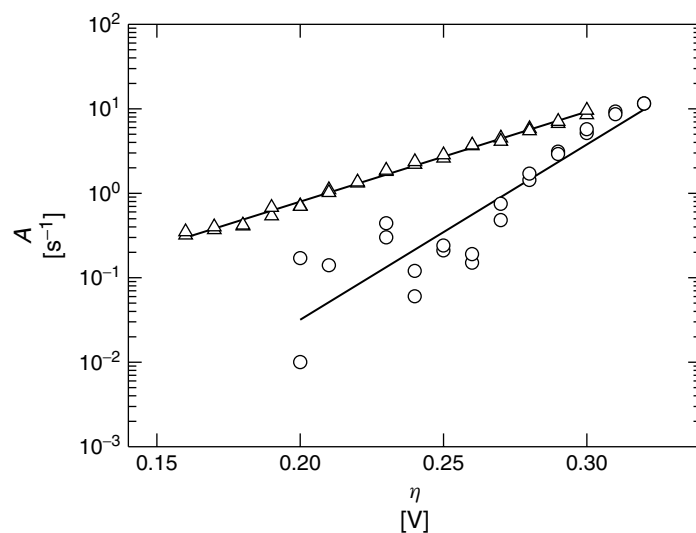


**Fig. 9** Nucleation rates of Hg onto vitreous carbon from  $0.01 \text{ mol dm}^{-3}$   $\text{Hg}_2^{2+}$  (○) and  $0.01 \text{ mol dm}^{-3}$   $\text{Hg}^{2+}$  (Δ) solutions, as a function of the overpotential [58].

slopes in Fig. 9, single atoms adsorbed on the surface grow irreversibly and play the role of critical nuclei.

Usually, only a small fraction of the surface is active for nucleation, the number density of active sites is potential dependent, and much less than the atomic density of the surface [40]. Analysis of transients by means of Eq. (66) allows also obtaining the number densities of sites on the electrode surface. As shown in Fig. 10, nucleation of mercury either from  $\text{Hg}_2^{2+}$  or  $\text{Hg}^{2+}$  solutions takes place at a given overpotential onto a similar number of sites, as would be expected from the identical interactions between the electrodeposited atoms and the substrate in both cases. This observation reaffirms the dominant role of the surface|deposit interactions in phase formation phenomena.

We have presented here some of the fundamental aspects of electrochemical

phase formation processes, and some illustration has been given by way of a specific example, the electrodeposition of mercury. Many other theoretical and experimental studies show that electrochemical methods may be advantageously used for the electrodeposition of a wide variety of materials. Electrochemical phase formation offers possibilities for controlling the chemical nature, size, morphology, and spatial distribution of dispersed and nanostructured deposits of a variety of materials, including metals [62, 63], semiconductors [64], or conducting polymers [65]. Controlled monodisperse deposition of materials at nanoscopic scales, which has been shown to be achievable with electrochemical methods, is necessary for optimal performance of a variety of devices and processes, such as, for example, quantum dots or clean electrochemical energy converters.

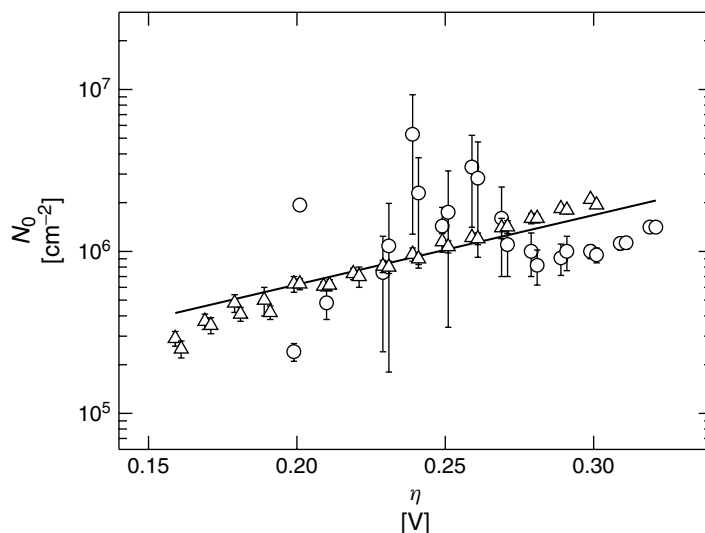


**Fig. 10** Number densities of nucleation sites on the surface of vitreous carbon as a function of the overpotential, obtained from analysis of current transients obtained during mercury deposition from  $0.01 \text{ mol dm}^{-3} \text{ Hg}_2^{2+}$  (o) and  $0.01 \text{ mol dm}^{-3} \text{ Hg}^{2+}$  ( $\Delta$ ) aqueous solutions [58].

## References

1. E. Budevski, G. Staikov, W. J. Lorenz, *Electrochemical Phase Formation and Growth*, John Wiley & Sons, New York, 1996.
2. W. Thomson, *Proc. R. Soc. Edinb.* **1870**, 7, 63.
3. J. W. Gibbs, *Collected Works (Thermodynamics)*, Yale University Press, New Haven, 1948, Vol. I.
4. R. Becker, W. Döring, *Ann. Phys.* **1935**, 24, 719.
5. J. B. Zeldovich, *Acta Phys. Chem. USSR* **1943**, 18, 1.
6. S. Stoyanov, *Thin Solid Films* **1973**, 18, 91.
7. A. Milchev, S. Stoyanov, R. Kaishev, *Thin Solid Films* **1974**, 22, 255.
8. G. J. Hills, D. J. Schiffrin, J. Thompson, *Electrochim. Acta* **1974**, 19, 657.
9. M. Sluyters-Rehbach, J. H. O. J. Wijenberg, E. Bosco et al., *J. Electroanal. Chem.* **1987**, 236, 1.
10. B. R. Scharifker, J. Mostany, M. Palomar-Pardavé et al., *J. Electrochem. Soc.* **1999**, 146, 1005.
11. L. Heerman, A. Tarallo, *J. Electroanal. Chem.* **1999**, 470, 70.
12. B. R. Scharifker, J. Mostany, *J. Electroanal. Chem.* **1984**, 177, 13.
13. M. Avrami, *J. Chem. Phys.* **1939**, 7, 1103.
14. W. J. Basirun, D. Pletcher, A. Saraby-Reintjes, *J. Appl. Electrochem.* **1996**, 26, 873.
15. T. Erdey-Grúz, M. Volmer, *Z. Phys. Chem.* **1931**, 157, 165.
16. T. Young, *Philos. Trans. R. Soc. (Londres)* **1805**, 1, 65.
17. R. Aveyard, D. A. Haydon, *An Introduction to the Principles of Surface Chemistry*, Cambridge University Press, Cambridge, 1973, p. 74.
18. M. Volmer, A. Weber, *Z. Phys. Chem.* **1926**, 119, 277.
19. L. Farkas, *Z. Phys. Chem.* **1927**, 125, 236.
20. H. A. Kramers, *Physica* **1940**, 7, 284.
21. E. Parzen, *Stochastic Processes*, Holden-Day, San Francisco, 1962.
22. J. Frenkel, *Kinetic Theory of Liquids*, Clarendon Press, Oxford, 1946.
23. E. A. Guggenheim, *Trans. Faraday Soc.* **1940**, 36, 408.
24. R. C. Tolman, *J. Chem. Phys.* **1949**, 17, 333.
25. K. S. C. Freeman, I. R. McDonald, *Mol. Phys.* **1973**, 26, 529.
26. J. W. Cahn, J. E. Hilliard, *J. Chem. Phys.* **1959**, 31, 688.
27. G. J. Hills, D. J. Schiffrin, J. Thompson, *Electrochim. Acta* **1974**, 19, 671.
28. R. McGraw, H. Reiss, *J. Stat. Phys.* **1979**, 20, 385.
29. D. Walton, *J. Chem. Phys.* **1962**, 37, 2182.
30. M. Volmer, *Z. Elektrochem.* **1929**, 35, 555.
31. G. Zinsmeister, *Vacuum* **1966**, 16, 529.
32. R. M. Logan, *Thin Solid Films* **1969**, 3, 59.
33. R. Kaishev, B. Mutaftchiew, *Electrochim. Acta* **1965**, 10, 643.
34. S. Toshev, A. Milchev, K. Popova et al., *C.R. Acad. Bulg. Sci.* **1969**, 22, 1413.
35. M. Fleischmann, H. R. Thirsk, *Electrochim. Acta* **1960**, 2, 22.
36. F. Lantelme, J. Chevalet, *J. Electroanal. Chem.* **1981**, 121, 311.
37. B. R. Scharifker, G. J. Hills, *J. Electroanal. Chem.* **1981**, 130, 81.
38. B. R. Scharifker in *Modern Aspects of Electrochemistry* (Eds.: J. O. 'M. Bockris, B. E. Conway, R. E. White), Plenum Press, New York, 1992, p. 467, Vol. 22.
39. S. Fletcher, *J. Chem. Soc., Faraday Trans. 1* **1983**, 79, 467.
40. J. Mostany, J. Mozota, B. R. Scharifker, *J. Electroanal. Chem.* **1984**, 177, 25.
41. E. Michailova, A. Milchev, *J. Appl. Electrochem.* **1990**, 21, 170.
42. M. Abramowitz, I. A. Stegun, *Handbook of Mathematical Functions*, Dover Publications, New York, 1965, p. 298.
43. G. Gunawardena, G. Hills, I. Montenegro et al., *J. Electroanal. Chem.* **1982**, 138, 225.
44. B. Scharifker, G. Hills, *Electrochim. Acta* **1983**, 28, 879.
45. E. Bosco, S. K. Rangarajan, *J. Electroanal. Chem.* **1982**, 134, 213.
46. P. A. Bobbert, M. M. Wind, J. Vlieger, *Physica A* **1987**, 146, 69.
47. M. V. Mirkin, A. P. Nilov, *J. Electroanal. Chem.* **1990**, 283, 35.
48. M. Tokuyama, *Physica A* **1990**, 169, 147.
49. A. Milchev, W. S. Kruijt, M. Sluyters-Rehbach et al., *J. Electroanal. Chem.* **1993**, 362, 21.
50. E. García-Pastoriza, J. Mostany, B. R. Scharifker, *J. Electroanal. Chem.* **1998**, 441, 13.
51. P. Curie, *Bull. Soc. Mineral.* **1885**, 8, 145.
52. R. Kaishev, *Bull. Acad. Bulg. Sci. Phys.* **1951**, 2, 191.
53. W. S. Kruijt, M. Sluyters-Rehbach, J. H. Sluyters et al., *J. Electroanal. Chem.* **1994**, 371, 13.

54. L. C. R. Alfred, K. B. Oldham, *J. Electroanal. Chem.* **1995**, 396, 257.
55. B. R. Scharifker, *Acta Cient. Venez.* **1984**, 35, 211.
56. A. Serruya, J. Mostany, B. R. Scharifker, *J. Chem. Soc. Faraday Trans.* **1993**, 89, 255.
57. A. Serruya, B. R. Scharifker, I. González et al., *J. Appl. Electrochem.* **1996**, 26, 451.
58. A. Serruya, J. Mostany, B. R. Scharifker, *J. Electroanal. Chem.* **1999**, 464, 39.
59. B. R. Scharifker, J. Mostany, A. Serruya, *Electrochim. Acta* **1992**, 37, 2503.
60. J. Mostany, A. Serruya, B. R. Scharifker, *J. Electroanal. Chem.* **1995**, 383, 37.
61. P. Bindra, A. P. Brown, M. Fleischmann et al., *J. Electroanal. Chem.* **1975**, 58, 39.
62. J. L. Fransaer, R. M. Penner, *J. Phys. Chem. B* **1999**, 103, 7643.
63. G. Oskam, P. C. Searson, *J. Electrochem. Soc.* **2000**, 147, 2199.
64. R. M. Penner, *Acc. Chem. Res.* **2000**, 33, 78.
65. M. F. Suárez, R. G. Compton, *J. Electroanal. Chem.* **1999**, 462, 211.

